NUREG/CP-0091
Vol. 4

Proceedings of the U.S. Nuclear Regulatory Commission

Fifteenth Water Reactor Safety Information Meeting

Volume 4
- Separate Effects/Experiments and Analyses
- Source Term Uncertainty Analysis
- Integral Systems Testing
- 2D/3D Research

Held at
National Bureau of Standards
Gaithersburg, Maryland
October 26-29, 1987

U.S. Nuclear Regulatory Commission

Office of Nuclear Regulatory Research

Proceedings prepared by
Brookhaven National Laboratory

NOTICE

These proceedings have been authored by a contractor of the United States Government. Neither the United States Government nor any agency thereof, or any of their employees, makes any warranty, expressed or implied, or assumes any legal liability or responsibility for any third party's use, or the results of such use, of any information, apparatus, product or process disclosed in these proceedings, or represents that its use by such third party would not infringe privately owned rights. The views expressed in these proceedings are not necessarily those of the U.S. Nuclear Regulatory Commission.

Available from

Superintendent of Documents
U.S. Government Printing Office
P.O. Box 37082
Washington D.C. 20013-7082

and

National Technical Information Service
Springfield , VA 22161

NUREG/CP-0091
Vol. 4
R2, R4

Proceedings of the U.S. Nuclear Regulatory Commission

Fifteenth Water Reactor Safety Information Meeting

Volume 4
- Separate Effects/Experiments and Analyses
- Source Term Uncertainty Analysis
- Integral Systems Testing
- 2D/3D Research

Held at
National Bureau of Standards
Gaithersburg, Maryland
October 26-29, 1987

Date Published: February 1988

Compiled by: Allen J. Weiss

Office of Nuclear Regulatory Research
U.S. Nuclear Regulatory Commission
Washington, DC 20555

Proceedings prepared by
Brookhaven National Laboratory

ABSTRACT

This six-volume report contains 140 papers out of the 164 that were presented at the Fifteenth Water Reactor Safety Information Meeting held at the National Bureau of Standards, Gaithersburg, Maryland, during the week of October 26-29, 1987. The papers are printed in the order of their presentation in each session and describe progress and results of programs in nuclear safety research conducted in this country and abroad. Foreign participation in the meeting included twenty-two different papers presented by researchers from Belgium, Czechoslovakia, Germany, Italy, Japan, Russia, Spain, Sweden, The Netherlands and the United Kingdom. The titles of the papers and the names of the authors have been updated and may differ from those that appeared in the final program of the meeting.

PROCEEDINGS OF THE
15th WATER REACTOR SAFETY INFORMATION MEETING

October 26-29, 1987

Published in Six Volumes

GENERAL INDEX

REGISTERED ATTENDEES (NON-NRC)
15th WATER REACTOR SAFETY INFORMATION MEETING

D. ACKER
CEA FRENCH ATOMIC ENERGY COMMISSION
DEMT/SMTS/RDMS
GIF S/YVETTE 91191
FRANCE

H. ADACHI
JAPAN ATOMIC ENERGY RES. INSTITUTE
TOKAI-MURA
IBARAKI 319-11
JAPAN

L. J. AGEE
ELECTRIC POWER RESEARCH INSTITUTE
3412 HILLVIEW AVENUE
PALO ALTO CA 94303
USA

H. AKIMOTO
JAPAN ATOMIC ENERGY RES. INSTITUTE
TOKAI-MURA
IBARAKI 319-11
JAPAN

P. ALBRECHT
UNIVERSITY OF MARYLAND
DEPT. OF CIVIL ENGINEERING
COLLEGE PARK MD 20742
USA

D. J. ALEXANDER
OAK RIDGE NATIONAL LAB.
P.O. BOX X, BLDG 4500-S
OAK RIDGE TN 37831
USA

R. P. ALLEN
BATTELLE PACIFIC NORTHWEST LAB.
P.O. BOX 999
RICHLAND WA 99352
USA

K. K. ALMENAS
UNIVERSITY OF MARYLAND
COLLEGE PARK MD 20742
USA

A. ALONSO
MADRID POLYTECHNICAL UNIVERSITY
JOSE GUTIERREZ ABASCAL, 2
MADRID 28006
SPAIN

M. AMIN
SARGENT & LUNDY
55 E. MONROE
CHICAGO IL 60603
USA

P. S. ANDERSEN
DYNATREK, INC.
2115 E. JEFFERSON STREET
ROCKVILLE MD 20852
USA

J. M. ANDERSON
BECHTEL
15740 SHADY GROVE RD.
GAITHERSBURG MD 20850
USA

F. ARAYA
JAPAN ATOMIC ENERGY RES. INSTITUTE
3000 TRINITY DR.
LOS ALAMOS NM 87544
USA

W. C. ARCIERI
ENSA, INCORPORATED
15825 SHADY GROVE ROAD
ROCKVILLE MD 20850
USA

K. H. ARDRON
CENTRAL ELECTRICITY GENERATING BOARD
BDCD
GLOUCESTER
UK

J. G. ARENDTS
EG&G IDAHO, INC.
P.O. BOX 1625
IDAHO FALLS ID 83415
USA

D. A. ARMSTRONG
WASHINGTON PUBLIC POWER SUPPLY SYS.
3000 G. WASH. WAY-P.O. BOX 968
RICHLAND WA 99352
USA

A. ARNAUD
CEA FRENCH ATOMIC ENERGY COMMISSION
CEN CADARACHE
ST. PAUL LEZ DURANCE 13115
FRANCE

W. W. ASCROFT-HUTTON
HM NUCLEAR INSTALLATIONS INSPECTORATE
BAYNARDS HOUSE, CHEPSTOW PLACE
LONDON W24TF
UK

V. G. ASMOLOV
I. V. KURCHATOV INST. OF ATOMIC ENERGY
KURCHATOV SQUARE
MOSCOW 123182
USSR

D. AXFORD
ATOMIC ENERGY OF CANADA, LTD.
15 ISABEL STREET
PETAWAWA ONTARIO K8H1Z1
CANADA

W. J. BABYAK
WESTINGHOUSE BETTIS ATOMIC PWR LAB
P.O. BOX 79
WEST MIFFLIN PA 15122
USA

A. J. BAKER
HM NUCLEAR ISTALLATIONS INSPECTORATE
ST. PETERS HOUSE, BALLIOL ROAD
BOOTLE MERSEYSIDE L203LZ
UK

J. L. BALLIF
SCIENTECH
P.O. BOX 1406
IDAHO FALLS ID 83403-1406
USA

W. H. BAMFORD
WESTINGHOUSE
P.O. BOX 2728
PITTSBURGH PA 15230
USA

M. C. BAMPTON
BATTELLE PACIFIC NORTHWEST LAB
P.O. BOX 999
RICHMOND WA 99352
USA

K. K. BANDYOPADHYAY
BROOKHAVEN NATIONAL LAB.
BLDG. 129
UPTON NY 11973
USA

R. A. BARI
BROOKHAVEN NATIONAL LAB.
BLDG 130
UPTON NY 11973
USA

B. R. BASS
OAK RIDGE NATIONAL LAB.
P.O. BOX Y
OAK RIDGE TN 37831
USA

J. A. BAST
GENERAL ELECTRIC COMPANY
P.O. BOX 1072
SCHENECTADY NY 12301
USA

R. C. BAUER
WESTINGHOUSE BETTIS ATOMIC PWR LAB
P.O. BOX 79
WEST MIFFLIN PA 15122
USA

K. R. BAUMGARTEL
GESELLSCHAFT FUR REAKTORSICHERHEIT
SCHWERTNERGASSE 1
KOELN 8046
FRG

S. L. BAXTER
UNIVERSITY OF MARYLAND
4100 CONNECTICUT AVENUE
BALTIMORE MD 21045
USA

P. D. BAYLESS
EG&G IDAHO, INC.
P.O. BOX 1625
IDAHO FALLS ID 83415
USA

A. BECERRA
INSURGENTES SUR 1776
MEXICO CITY
MEXICO 01030
MEXICO

R. J. BEELMAN
EG&G IDAHO, INC.
P.O. BOX 1625
IDAHO FALLS ID 83415
USA

J. G. BENNETT
LOS ALAMOS NATIONAL LAB.
P.O. BOX 1663, MS J570
LOS ALAMOS NM 87544
USA

E. D. BERGERON
SANDIA NATIONAL LABORATORIES
P.O. BOX 5800, DIV 6413
ALBUQUERQUE NM 87185
USA

K. D. BERGERON
SANDIA NATIONAL LABORATORIES
P.O. BOX 5800
ALBUQUERQUE NM 87185
USA

E. BESWICK
CENTRAL ELECTRICITY GENERATING BOARD
BOOTHS HALL, CHELFORD ROAD
KNUTSFORD CHESHIRE WA16800
UK

P. BEZLER
BROOKHAVEN NATIONAL LABORATORY
BLDG. 129
UPTON NY 11973
USA

M. J. BIRD
UKAEA/AEE WINFRITH
DORCHESRER
DORSET DT280H
UK

D. P. BIRMINGHAM
BABCOCK & WILCOX
1562 BEESON STREET
ALLIANCE OH 44601
USA

H. M. BLEAKLEY
UKAEA/SRD
WIGSHAW LANE, CULCHETH
WARRINGTON WA34NE
UK

J. L. BOCCIO
BROOKHAVEN NATIONAL LABORATORY
BUILDING 130
UPTON NY 11973
USA

B. R. BOHER
FRAMATOME
254 RAINPRINT SQUARE
MURRYSVILLE PA 15668
USA

J. M. BOONE
DUKE POWER
422 SOUTH CHURCH ST.
CHARLOTTE NC 28242
USA

R. B. BORSUM
BABCOCK & WILCOX CO.
7910 WOODMONT AVE., SUITE 220
BETHESDA MD 20814
USA

W. M. BOWEN
BATTELLE PACIFIC NORTHWEST LAB.
P.O. BOX 999
RICHLAND WA 99352
USA

D. R. BRADLEY
SANDIA NATIONAL LABORATORIES
P.O. BOX 5800
ALBUQUERQUE NM 87185
USA

M. BRANDANI
ANSALDO
VIA D'ANNUNZIO 113
GENOVA 16129
ITALY

R. J. BREEDING
SANDIA NATIONAL LABORATORIES
P.O. BOX 5800, DIV 6413
ALBUQUERQUE NM 87185
USA

D. BREWER
DUKE POWER
422 SOUTH CHURCH ST.
CHARLOTTE NC 28242
USA

I. BRITTAIN
UKAEA/AEE WINFRITH
DORCHESRER
DORSET DT280H
UK

J. M. BROUGHTON
EG&G IDAHO, INC.
P.O. BOX 1625
IDAHO FALLS ID 83415
USA

R. H. BRYAN
OAK RIDGE NATIONAL LAB.
P.O. BOX Y
OAK RIDGE TN 37831
USA

B. J. BUESCHER
EG&G IDAHO, INC.
P.O. BOX 1625
IDAHO FALLS ID 83415
USA

N. E. BUTTERY
CENTRAL ELECTRICITY GENERATING BOARD
BERKELEY NUCLEAR LABORATORIES
BERKELEY GLOUCESTERSHIRE GL139PB
UK

A. L. CAMP
SANDIA NATIONAL LABORATORIES
P.O. BOX 5800, DIV 6412
ALBUQUERQUE NM 87185
USA

N. G. CATHEY
EG&G IDAHO, INC.
P.O. BOX 1625
IDAHO FALLS ID 83415
USA

S. CHAKRABORTY
EIR-EIDG. INST. FUR REAKTORFORSCHUNG
WURENLINPEN CH5303
SWITZERLAND

Y. CHEN
INSTITUTE OF NUCLEAR ENERGY RESEARCH
P.O. BOX 3-3
LUNG-TAN TAIWAN 32500
ROC

J. C. CHEN
LEHIGH UNIVERSITY
WHITAKER LAB #5
BETHLEHEM PA
USA

T. CHEN
ADVANCED NUCLEAR FUELS CORP.
2101 HORN RAPIDS RD., P.O. BOX 130
RICHLAND WA 99352
USA

H. S. CHENG
BROOKHAVEN NATIONAL LAB.
BLDG 475B
UPTON NY 11973
USA

J. CHENG
UNIVERSITY OF MARYLAND
DEPT. OF CIVIL ENGINEERING
COLLEGE PARK MD 20742
USA

A. CHEUNG
WESTINGHOUSE
P.O. BOX 355
PITTSBURGH PA 15230
USA

G. K. CHOPRA
ARGONNE NATIONAL LAB.
9700 S. CASS AVE.-BLDG 208
ARGONNE IL 60439
USA

J. CHRISTENSEN
BATTELLE PACIFIC NORTHWEST LAB.
P.O. BOX 999
RICHLAND WA 99352
USA

R. CLASPER
UKAEA/SRD
WIGSHAW LANE, CULCHETH
WARRINGTON WA34NE
UK

J. W. CLEVELAND
SEA CONSULTANTS, INC.
2001 GATEWAY PLACE, SUITE 610-W
SAN JOSE CA 95110
USA

M. COLAGROSSI
ENEA/DISP
VIA VITALIANO BRANDATI 48
ROME 00144
ITALY

R. K. COLE
SANDIA NATIONAL LABORATORY
P.O. BOX 5800, DIVISION 6418
ALBUQUERQUE NM 87185
USA

M. W. CONEY
CENTRAL ELECTRICITY GENERATING BOARD
CERL-KELVIN AVE.
LEATHERHEAD KT227SE
UK

I. COOK
UKAEA
CULHAM LABORATORY
ABINGTON OXFORDSHIRE OX14 3DB
UK

K. Y. COOK
OAK RIDGE NATIONAL LAB.
P.O. BOX X, 45005
OAK RIDGE TN 37831
USA

B. A. COOK
EG&G IDAHO, INC.
P.O. BOX 1625
IDAHO FALLS ID 83415
USA

W. R. CORWIN
OAK RIDGE NATIONAL LAB.
P.O. BOX Y, BLDG. 9204-1
OAK RIDGE TN 37831
USA

R. COWARD
MPR ASSOCIATES, INC.
1050 CONNECTICUT AVE N.W.
WASHINGTON DC 20036
USA

S. R. COWNE
BALTIMORE GAS & ELECTRIC
CALVERT CLIFFS - P.O. BOX 1535
LUSBY MD 20657
USA

W. R. CRAMOND
SANDIA NATIONAL LABORATORY
P.O. BOX 5800
ALBUQUERQUE NM 87185
USA

M. W. CRUMP
COMBUSTION ENGINEERING
1000 PROSPECT HILL ROAD
WINDSOR CT 06095
USA

W. H. CULLEN
MATERIALS ENGINEERING ASSOCIATES, INC.
9700-B MARTIN LUTHER KING HWY
LANHAM MD 20706
USA

G. E. CUMMINGS
LAWRENCE LIVERMORE NATIONAL LAB.
P.O. BOX 808, L-198
LIVERMORE CA 94550
USA

R. A. CUSHMAN
NIAGARA MOHAWK POWER CO.
301 PLAINFIELD ROAD
SYRACUSE NY 13212
USA

D. A. DAHLGREN
SANDIA NATIONAL LABORATORY
P.O. BOX 5800
ALBUQUERQUE NM 87185
USA

P. M. DALING
BATTELLE PACIFIC NORTHWEST LAB.
P.O. BOX 999
RICHLAND WA 99352
USA

P. S. DAMERELL
MPR ASSOCIATES, INC.
1050 CONNECTICUT AVE N.W.
WASHINGTON DC 20036
USA

J. DARLASTON
BERKELEY NUCLEAR LABS
C.E.G.B.
BERKELEY GLOS GL139PB
UK

G. DAVIS
COMBUSTION ENGINEERING
1000 PROSPECT HILL ROAD
WINDSOR CT 06095
USA

G. DeSIASSI
BROOKHAVEN NATIONAL LAB.
BLDG. 129
UPTON NY 11973
USA

R. S. DENNING
BATTELLE COLUMBUS
505 KING AVENUE
COLUMBUS OH 43201
USA

V. DEVITA
ROCKETDYNE (ETEC)
DESOTO AND NORDHOFF
CANOGA PARK CA 91304
USA

R. deWIT
NATIONAL BUREAU OF STANDARDS
RM A113, MATERIALS BLDG
GAITHERSBURG MD 20854
USA

D. R. DIERCKS
ARGONNE NATIONAL LAB.
9700 S. CASS AVE.
ARGONNE IL 60439
USA

M. diMARZO
UNIVERSITY OF MD.
MECH. ENG. DEPT.
COLLEGE PARK MD 20742
USA

S. R. DOCTOR
BATTELLE PACIFIC NORTHWEST LAB.
P.O. BOX 999
RICHLAND WA 99352
USA

C. V. DODD
OAK RIDGE NATIONAL LAB.
P.O. BOX X, 45005, MS-151
OAK RIDGE TN 37831
USA

P. K. DOHERTY
COMBUSTION ENGINEERING
WINDSOR
CT 1000 PROSPECT HILL ROAD 06095
USA

B. J. DOLAN
DUKE POWER
422 SOUTH CHURCH ST.
CHARLOTTE NC 28242
USA

J. DRCEC
NUCLEAR POWER PLANT KRSKO
YRBINA 12, 68270 KRSKO
KRSKO 68270
YUGOSLAVIA

S. S. DUA
GENERAL ELECTRIC COMPANY
175 CURTNER AVE.
SAN JOSE CA 925125
USA

S. W. DUCE
EG&G IDAHO, INC.
P.O. BOX 1625
IDAHO FALLS ID 83415
USA

J. J. DUCO
CEA FRENCH ATOMIC ENERGY COMMISSION
DAS/SASC,CEN/FAR,BP NO 6
FONTENAY-AUX-ROSES CEDEX CEDEX 92265
FRANCE

R. DUFFEY
EG&G IDAHO, INC.
P.O. BOX 1625
IDAHO FALLS ID 83415
USA

S. R. DUGAN
UNIVERSITY OF MARYLAND
RT. 1
COLLEGE PARK MD 21093
USA

K. DWIYEDY
VIGINIA POWER
5000 DOMINION BLVD.
GLEN ALLEN VA 23060
USA

D. B. EBELING-KONING
WESTINGHOUSE
P.O. BOX 355, M/S E 4-12A
PITTSBURGH PA 15230
USA

J. L. EDSON
EG&G IDAHO, INC.
P.O. BOX 1625
IDAHO FALLS ID 83415
USA

G. R. EIDAM
BECHTEL
P.O. BOX 72
MIDDLETOWN PA 17057
USA

D. M. EISSENBERG
OAK RIDGE NATIONAL LAB.
P.O. BOX Y, BLDG.9104-1 MS-1
OAK RIDGE TN 37831
USA

J. EKMAN
ROLLS ROYCE & ASSOCIATES LTD.
P.O. BOX 31
DERBY DE2 8BJ
UK

Z. J. ELAWAR
ARIZONA NUCLEAR POWER PROJECT
11226 NORTH 23RD AVE.
PHOENIX AZ 85029
USA

T. W. ELLISON
GENERAL ELECTRIC COMPANY
P.O. BOX 1072
SCHENECTADY NY 12301
USA

G. T. EMBLEY
KNOLLS ATOMIC POWER LABORATORY
BOX 1072
SCHENECTADY NY 12301
USA

D. ERB
DEPARTMENT OF ENERGY
WASHINGTON DC 20545
USA

H. A. ERNST
GEORGIA INSTUTUTE OF TECHNOLOGY
ATLANTA GA 30332
USA

M. ERVE
SIEMENS/KWU
HAMMERBACHERSTRASSE 12 + 14
ERLANGEN D-8520
FRG

H. FABIAN
SIEMENS/KWU
HAMMERBACHERSTRASSE 12 + 14
ERLANGEN D-8520
FRG

A. M. FABRY
SCK-CEN
200 BOERETANG
2400 MOL
BELGIUM

C. R. FARRAR
LOS ALAMOS NATIONAL LAB.
MS 5576
LOS ALAMOS NM 87545
USA

J. FELL
UKAEA/AEE WINFRITH
DORCHESTER
DORSET DT280H
UK

D. FIELHUBER
UTC
1000 ABERNATHY RD.
ATLANTA GA 30328
USA

H. E. FLORA
UNITED ENGINEERS
305 17TH STREET
PHILADELPHIA PA 19101
USA

E. FOTOPOULOS
BECHTEL
15740 SHADY GROVE ROAD
GAITHERSBURG MD 20877
USA

E. C. FOX
OAK RIDGE NATIONAL LAB
P. O. BOX X
OAK RIDGE TN 37831
USA

M. D. FRESHLEY
BATTELLE PACIFIC NORTHWEST LAB.
P. O. BOX 999
RICHLAND WA 99352
USA

B. C. FRYER
ADVANCED NUCLEAR FUELS CORP.
2101 HORN RAPIDS RD., P.O. BOX 130
RICHLAND WA 99352
USA

E. L. FULLER
ELECTRIC POWER RESEARCH INSTITUTE
3412 HILLVIEW AVE., P.O. BOX 10412
PALO ALTO CA 94303
USA

S. F[illegible]
TQ[illegible]
8 S[illegible] TA-15080-KU
YO[illegible] KANAGAWA-KEN 235
JAPAN

J. L. GANDRILLE
FRAMATOME
TOUR FIAT CEDEX 16
PARIS FR 92084
FRANCE

F. J. GARDINER
BECHTEL POWER COMPANY
GAITHERSBURG
MD 15740 SHADY GROVE RD. 20878
USA

P. T. GEORGE
CENTRAL ELECTRICITY GENERATING BOARD
BOOTHS HALL
KNUTSFORD CHESHIRE
UK

J. A. GIESEKE
BATTELLE COLUMBUS
505 KING AVENUE
COLUMBUS OH 43201
USA

P. A. GILLES
FRAMATOME
505 KING AVENUE
COLUMBUS OH 43201
USA

T. GINSBERG
BROOKHAVEN NATIONAL LAB
BLDG 820M
UPTON NY 11973
USA

B. GITNICK
ENSA, INC.
P.O. BOX 5537
ROCKVILLE MD 20855
USA

M. W. GOLAY
MASS. INSTITUTE OF TECHNOLOGY
77 MASS. AVE
CAMBRIDGE MA 02139
USA

M. GOMOLINSKI
CEA FRENCH ATOMIC ENERGY COMMISSION
CEN-FAR, IPSN
FONTENAY-AUX-ROSES CEDEX 92265
FRANCE

R. L. GOODMAN
BATTELLE PACIFIC NORTHWEST LAB
P.O. BOX 999
RICHLAND WA 99352
USA

N. GOTOH
HITACHI, LTD
3-1-1, SAIWAI-CHO
HIYACHI IBARAKI 317
JAPAN

S. R. GREENE
OAK RIDGE NATIONAL LAB
P.O. BOX Y, BLDG 9104-1
OAK RIDGE TN 37831
USA

G. A. GREENE
BROOKHAVEN NATIONAL LAB
BLDG 820M
UPTON NY 11973
USA

W. L. GREENSTREET
OAK RIDGE NATIONAL LAB
P.O. BOX Y, BLDG 9201-3, MS 2
OAK RIDGE TN 37831
USA

M. V. GREGORY
SAVANNAH RIVER LABORATORY
773-41A
AIKEN SC 29808
USA

E. F. GRIER
LAUREL INDUSTRIES
SUITE 1001, 16 11 N. KENT ST.
ARLINGTON VA 22209
USA

P. GRIFFITH
MASSACHUSETTS INST. OF TECH.
ROOM 7-044
CAMBRIDGE MA 02139
USA

P. GRUBER
KRAFTWERK UNION AG
HAMMERBACHERSTRASSE 12 + 14
ERLANGEN D-8520
FRG

P. GRUNER
GESELLSCHAFT FUR REAKTORSICHERHEIT
SCHWERTNERGASSE 1
COLOGNE 5000
FRG

W. E. GUNTHER
BROOKHAVEN NATIONAL LAB
BLDG 130
UPTON NY 11973
USA

J. G. GUPPY
BROOKHAVEN NATIONAL LAB
BLDG 475B
UPTON NY 11973
USA

D. E. GUYON
WESTINGHOUSE BETTIS ATOMIC PWR LAB
P.O. 79
WEST MIFFLIN PA
USA

G. L. GYOREY
GENERAL ELECTRIC
19941 WINTER LN
SARATOGA CA 015070
USA

F. M. HAGGAG
OAK RIDGE NATIONAL LAB
P.O. BOX X, BLDG 4500-S
OAK RIDGE TN 37831
USA

R. E. HALL
BROOKHAVEN NATIONAL LABORATORY
BLDG 130
UPTON NY 11973
USA

R. G. HANSON
EG&G IDAHO, INC.
P.O. BOX 1625
IDAHO FALLS ID 83415
USA

D. J. HANSON
EG&G IDAHO, INC.
P.O. BOS 1625
IDAHO FALLS ID 83415
USA

Y. A. HASSAN
TEXAS A & M, DEPT. OF NUCLEAR ENGR.
COLLEGE STATION TX 77843
USA

J. R. HAWTHORNE
MATERIALS ENGINEERING ASSOCIATES, INC.
9700-B MARTIN LUTHER KING HWY
LANHAM MD 20706
USA

M. HAYASHI
JAPAN NUS
875 FUTOCHO KOUHOKUKU
YOKOHAMA
JAPAN

Y. HAYASHI
KANSAI ELECTRIC POWER CO., INC.
1100 17TH STREET N.W. SUITE 500
WASHINGTON DC 20036
USA

M. R. HAYNS
UKAEA/SRD
WIGSHAW LANE, CULCHETH
WARRINGTON WA37NB
UK

T. J. HEAMES
SAIC
2109 AIR PARK RD. SE
ALBUQUERQUE NM 87106
USA

R. A. HEDRICK
TECHNOLOGY FOR ENERGY CORP.
P.O. BOX 22996
KNOXVILLE TN 37933
USA

J. A. HEIL
NETHERLANDS ENERGY RES FOUNDATION
POSTBOX 1
PETTEN NH 175520
NETHERLANDS

J. C. HELTON
ARIZONA STATE UNIVERSITY
TEMPE AZ 85287
USA

F. P. HENNESSY
E.I. DUPONT
117 COUNTRY PLACE DR.
N. AUGUSTA SC 29841
USA

H. K. HERKENRATH
COMMISSION OF EUROPEAN COMMUNITIES
J.R.C. ISPRA
ISPRA VA 21020
ITALY

R. J. HERTLEIN
KRAFTWERK UNION AG
HAMMER&ACHERSTRASSE 12 + 14
ERLANGEN D-8520
FRG

R. T. HESSIAN
STONE & WEBSTER
3 EXECUTIVE CAMPUS
CHERRY HILL NJ 08053
USA

G. F. HEWITT
UKAEA/WRPD
B 392, HARWELL LABORATORY
OXFORDSHIRE OX10 0DY
UK

E. F. HICKEN
GESELLSCHAFT FUR REAKTORSICHERHEIT
FORSCHUNGSGELAENDE
GARCHING 8046
FRG

D. HICKS
UKAEA/WRPD
B 329, HARWELL LABORATORY
OXFORDSHIRE OX11 0RA
UK

L. J. HIGGINBOTHAM
UNIVERSITY OF MARYLAND
1200 FALLS ROAD
BALTIMORE MD 21011
USA

J. C. HIGGINS
BROOKHAVEN NATIONAL LABORATORY
P. O. 130, 321 LEWIS
UPTON NY 11973

P. R. HILL
PENNSYLVANIA PWR & LIGHT CO.
2 NORTH NINTH STREET
ALLENTOWN PA 18101
USA

J. H. HINTON
SAVANNAH RIVER LABORATORY
707-C RM. 329
AIKEN SC 29808
USA

T. J. HIRONS
LOS ALAMOS NATIONAL LAB
P.O. BOX 1663, MS E561
LOS ALAMOS NM 87545
USA

A. L. HISER
MATERIALS ENGINEERING ASSOCIATES, INC.
9700-B MARTIN LUTHER KING HWY
LANHAM MD 20706
USA

N. HOBSON
NATIONAL NUCLEAR CORP.
BOOTHS HALL, CHELFORD ROAD
KNUTSFORD CHESHIRE
UK

S. A. HODGE
OAK RIDGE NATIONAL LAB
P.O. BOX Y, BLDG 9104-1
OAK RIDGE TN 37831
USA

L. G. HOEGBERG
SWEDISH NUCLEAR POWER INSPECTORATE
SEHLSTEDTSGATAN 11, BOX 27106
STOCKHOLM 310252
SWEDEN

P. HOFMANN
KERNFORSCHUNGSZENTRUM (K.F.K.)
P.O. BOX 3640
D-7500 KARLSRUHE 1
FRG

C. HOFMAYER
BROOKHAVEN NATIONAL LAB
BLDG 129
UPTON NY 11973
USA

G. S. HOLMAN
LAWRENCE LIVERMORE NATIONAL LAB
P. O. BOX 808, L-197
LIVERMORE CA 94550
USA

H. L. O. HOLMSTROM
TECHNICAL RESEARCH CENTRE OF FINLAND
P. O. BOX 169
HELSINKI SF00181
FINLAND

K. W. HOLTZCLAW
GENERAL ELECTRIC COMPANY
175 CURTNER AVENUE, M/C 754
SAN JOSE CA 95125
USA

R. G. HOPPE
WESTINGHOUSE BETTIS ATOMIC PWR LAB
P.O. BOX 79
WEST MIFFLIN PA 15122
USA

J. HORTAL
BROOKHAVEN NATIONAL LAB
BLDG 475B
UPTON NY 11973
USA

P. Y. HOSEMANN
EIR-EIDG. INST. FUR REAKTORFORSCHUNG
WURENLINGEN CH5303
SWITZERLAND

T. W. HSU
VIRGINIA POWER
5000 DOMINION BLVD.
GLEN ALLEN VA 23060
USA

Y. Y. HSU
UNIVERSITY OF MARYLAND
RT. 1
COLLEGE PARK MD 20742
USA

J. M. HU
UNIVERSITY OF MARYLAND
DEPT. OF CIVIL ENGINEERING,
COLLEGE PARK MD 20742
USA

E. W. HUNT, JR.
SAVANNAH RIVER LABORATORY
773-41A, 182
AIKEN SC 29808
USA

P. H. HUTTON
BATTELLE PACIFIC NORTHWEST LAB
P.O. BOX 999
RICHLAND WA 99352
USA

J. G. HWANG
ENSA, INC.
P.O. BOX 20130
SAN JOSE CA 95160
USA

M. L. HYDER
SAVANNAH RIVER LABORATORY
773-41A
AIKEN SC 29808
USA

T. IGUCHI
JAPAN ATOMIC ENERGY RES. INSTITUTE
TOKAI-MURA
IBARAKI 319-11
JAPAN

H. INHABER
NUS CORPORATION
910 CLOPPER ROAD
GAITHERSBURG MD 20878
USA

G. R. IRWIN
UNIVERSITY OF MD., DEPT. OF MECH. ENG.
COLLEGE PARK MD 20742
USA

T. ISHIDA
JAPAN INSTITUTE OF NUCLEAR SAFETY
MITA KOKUSAI BLDG., 1-4-28, MITA
MINATO-KU, TOKYO 108
JAPAN

M. ISHII
ARGONNE NATIONAL LABORATORY
9700 S. CASS AVENUE
ARGONNE IL 60439
USA

S. K. ISKANDER
OAK RIDGE NATIONAL LAB
P.O. BOX X
OAK RIDGE TN 37831
USA

K. ITOH
JAPAN NUS COMPANY
2864-3 NARACHO MIDORIKU
YOKOHAMA JAPAN
JAPAN

R. IVANY
COMBUSTION ENGINEERING
1000 PROSPECT HILL ROAD
WINDSOR CT 06095-500
USA

T. IWAMURA
JAPAN ATOMIC ENERGY RES. INSTITUTE
TOKAI-MURA
IBARAKI 319-11
JAPAN

J. L. JACOBSON
EG&G IDAHO, INC.
P.O. BOX 1625
IDAHO FALLS ID 83415
USA

P. JAMET
CEA FRENCH ATOMIC ENERGY COMMISSION
DEMT/SMTS/EMSI
GIF S/YVETTE 91191
FRANCE

J. F. JANSKY
BTB-LEONBERG
TONWEG-3
LEONBERG
FRG

D. B. JARRELL
BATTELLE PACIFIC NORTHWEST LAB
S10 SIGMA 3 3160 G. W. WAY
RICHLAND WA 99352
USA

L. JARRIEL
INTERNATIONAL TECHNOLOGY INC.
575 OAK RIDGE TURNPIKE
OAK RIDGE TN 37830
USA

R. P. JENKS
LOS ALAMOS NATIONAL LAB
P.O. BOX 1663, MS K555
LOS ALAMOS NM 87545
USA

G. W. JOHNSEN
EG&G IDAHO, INC.
P.O. BOX 1625
IDAHO FALLS ID 83415
USA

E. R. JOHNSON
WESTINGHOUSE ELECTRIC CORP.
P. O. BOX 2728
PITTSBURGH PA 15230
USA

W. R. JOHNSON
U. OF VIRGINIA
NUCLEAR ENERGY DEPT.-REACTOR BLDG
CHARLOTTESVILLE VA 22903
USA

A. B. JOHNSON
BATTELLE PACIFIC NORTHWEST LAB
P.O. BOX 999
RICHLAND WA 99352
USA

E. R. JOHNSON
WESTINGHOUSE
P.O. 355
PITTSBURGH PA 15230
USA

R. JOO
CNSNS
INSURGENTES SUR 1776
MEXICO CITY D.F. 01030
MEXICO

J. A. JOYCE
U.S. NAVAL ACADEMY
MS 11C
ANNAPOLIS MD 21402
USA

S. P. KALRA
ELECTRIC POWER RESEARCH INSTITUTE
P.O. BOX 10412
PALO ALTO CA 94303
USA

F. B. K. KAM
OAK RIDGE NATIONAL LAB
P.O. BOX X, 3001
OAK RIDGE TN 37831
USA

L. D. KANNBERG
BATTELLE PACIFIC NORTHWEST LAB
P.O. BOX 999
RICHLAND WA 99352
USA

M. F. KANNINEN
SOUTHWEST RESEARCH INSTITUTE
6220 CULEBRA RD.
SAN ANTONIO TX 78284
USA

H. KANTEE
IMATRON YHTIÖ OY (IYO)
P.O. BOX 138
HELSINKI SF00101
FINLAND

H. KARWAT
TECHNICAL UNIVERSITAT MUNCHEN
8046 GARSHING FORSCHUNGSGELANDE
GARCHING D8046
FRG

W. Y. KATO
BROOKHAVEN NATIONAL LABORATORY
BLDG. 197C
UPTON NY 11973
USA

K. R. KATSMA
EG&G IDAHO, INC.
P.O. BOX 1625
IDAHO FALLS ID 83415
USA

R. KAWABE
ENERGY RESEARCH LAB., HITACHI, LTD.
1168 MORIYAMA-CHO
HITACHI-SHI IBARAKI-KEN 316
JAPAN

W. KAWAKAMI
JAPAN ATOMIC ENERGY RES. INSTITUTE
1233 WATANUKI-MACHI
TAKASAKI GUNMA KEN 370-12
JAPAN

J. M. KELLY
BATTELLE PACIFIC NORTHWEST LAB
P.O. BOX 999
RICHLAND WA 99352
USA

R. M. KEMPER
WESTINGHOUSE
4043 W. BENDEN DRIVE
MURRYSVILLE PA 15663
USA

M. F. KENNEDY
ENSA, INC.
4550 N. BAILEY
BUFFALO NY 14226
USA

R. C. KERN
UAI/CDC
6003 EXECUTIVE BLVD.
ROCKVILLE MD 20852
USA

J. G. KEUSENHOFF
GESELLSCHAFT FUR REAKTORSICHERHEIT
SCHWERTNERGASSE 1
COLOGNE 5000
FRG

S. KIM
KOREAN ATOMIC ENERGY RESEARCH INST.
DAEDUK-DANJI, P.O. BOX 7
CHOONG-NAM
KOREA

F. D. KING
SAVANNAH RIVER LABORATORY
773-41A, ROOM 252
AIKEN SC 29808
USA

W. L. KIRK
LOS ALAMOS NATIONAL LAB
P.O. BOX 1663
LOS ALAMOS NM 87545
USA

M. KODA
MITSUBISHI ATOMIC POWER INDUSTRIES
SHIBAKOUEN
MINATO-KU, TOKYO 105
JAPAN

S. J. KOSKI
TVO POWER COMPANY LTD.
SF-27160 OLKILUOTO
SUOMI
FINLAND

C. A. KOT
ARGONNE NATIONAL LAB
9700 S. CASS AVE-BLDG 335
ARGONNE IL 60439
USA

J. J. KOZIOL
COMBUSTION ENGINEERING, INC.
1000 PROSPECT HILL ROAD
WINDSOR CT 06095-0500
USA

B. KUCZERA
KERNFORSCHUNGSZENTRUM (KFK)
P.O. BOX 3640
D-7500 KARLSRUHE 1
FRG

Y. KUKITA
JAPAN ATOMIC ENERGY RES. INSTITUTE
TOKAI-MURA
IBARAKI 319-11
JAPAN

Z. R. KULJIS
COMBUSTION ENGINEERING
1000 PROSPECT HILL ROAD
WINDSOR CT 06095
USA

D. KUPPERMAN
ARGONNE NATIONAL LABORATORY
9700 S. CASS AVENUE
ARGONNE IL 60302
USA

R. J. KURTZ
BATTELLE PACIFIC NORTHWEST LAB
P.O. BOX 999
RICHLAND WA 99352
USA

K. P. KUSSMAUL
UNIVERSITY OF STUTTGART
PFAFFENWALDRING 32
SUTTGART 80 7000
FRG

T. E. LAATS
EG&G IDAHO, INC.
P.O. BOX 1625
IDAHO FALLS ID 83415
USA

F. LAM
ONTARIO HYDRO
700 UNIVERSITY AVE., H-11
TORONTO M5G1X6
CANADA

R. T. LANCET
ROCKWELL INTERNATIONAL
6716 DARYN DR.
WESTHILLS CA 91307
USA

P. M. LANG
U.S. DEPARTMENT OF ENERGY
NE-42
WASHINGTON DC 20545
USA

R. E. LANG
DEPARTMENT OF ENERGY
9800 S. CASS AVE.
ARGONNE IL 60439
USA

B. P. LAUZAU
AMERICAN ELECTRIC POWER SERVICE CORP
1 RIVERSIDE PLAZA
COLUMBUS OH 43215
USA

S. Y. LEE
ARGONNE NATIONAL LABORATORY
9700 S. CASS AVENUE
ARGONNE IL 60439
USA

M. LEE
BROOKHAVEN NATIONAL LABORATORY
BUILDING 130
UPTON NY 11973
USA

J. R. LEHNER
BROOKHAVEN NATIONAL LABORATORY
BUILDING 130
UPTON NR 11973
USA

I. S. LEVY
BATTELLE PACIFIC NORTHWEST LAB
P.O. BOX 999
RICHLAND WA 99352
USA

C. K. LEWE
NUS CORPORATION
910 CLOPPER ROAD
GAITHERSBURG MD 20878
USA

K. J. LIESCH
GESELLSCHAFT FUR REAKTORSICHERHEIT
FORSCHUNGSGELAENDE
GARCHING 8046
FRG

T.-K. LIN
INSTITUTE OF NUCLEAR ENERGY RESEARCH
P.O. BOX 3
LUNG-TAN TAIWAN
ROC

C. W. LIN
ROBERT L. CLOUD ASSOCIATES
125 UNIVERSITY AVENUE
BERKLEY CA 94710
USA

F. W. LINCOLN
WESTINGHOUSE
W. MIFFLIN PA
USA

W. B. LOEWENSTEIN
ELECTRIC POWER RESEARCH INSTITUTE
3412 HILLVIEW AVE., P.O. BOX 10412
PALO ALTO CA 94303
USA

R. J. LOFARO
BROOKHAVEN NATIONAL LAB
BLDG 130
UPTON NY 11973
USA

J. V. LOPEZ
ETSII CATEDRA DE TECHNOLOGIA NUCLEAR
JOSE GUTIERREZ ABASCAL, 2
MADRID 28006
SPAIN

F. J. LOSS
MATERIALS ENGINEERING ASSOCIATES, INC.
9700-B MARTIN LUTHER KING HWY
LANHAM MD 20706
USA

A. L. LOWE
BABCOCK & WILCOX
P.O. BOX 10935
LYNCHBURG VA 24506
USA

R. J. LUTZ, JR.
WESTINGHOUSE ELECTRIC
P.O. BOX 355
PITTSBURGH PA 15230
USA

P. E. MacDONALD
EG&G IDAHO, INC.
P.O. BOX 1625
IDAHO FALLS ID 83415
USA

I. K. MADNI
BROOKHAVEN NATIONAL LAB
BLDG 130
UPTON NY 11973
USA

J. MALHERBE
CEA FRENCH ATOMIC ENERGY COMMISSION
DEMT/SMTS/RDMS
GIF S/YVETTE 91191
FRANCE

A. P. MALINAUSKAS
OAK RIDGE NATIONAL LAB
P.O. BOX X, BLDG 4500S (S-135
OAK RIDGE TN 37831
USA

A. N. MALLEN
BROOKHAVEN NATIONAL LAB
BLDG 475B
UPTON NY 11973
USA

P. MARSILI
ENEA/DISP
VIA VITALIANO BRANCATI 48
ROME 00144
ITALY

J. MARTIN
MASS. INST. OF TECHNOLOGY
77 MASSACHUSETTS AVE., RM 24-210
CAMBRIDGE MA 02139
USA

A. MARYRAY
TEXAS UTILITIES ELECTRIC
400 NORTH OLIVE STREET, L. B. 81
DALLAS TX 75201
USA

F. MASUDA
TOSHIBA CORP.
9-3-104, 5-CHOME (5080
YOKOHAMA
JAPAN

M. J. MATSUBARA
CEN. RES. INST. OF ELEC. POWER INDUSTRY
11-1 IWATO-KITA, 2-CHOME
KOMAE TOKYO 157
JAPAN

B. MAVKO
J. STEFAN INSTITUTE
JAMOVA 39
LJUBLJANA 6111
YUGOSLAVIA

R. K. McCARDELL
EG&G IDAHO, INC.
P.O. BOX 1625
IDAHO FALLS ID 83415
USA

D. J. McCLOSKEY
SANDIA NATIONAL LABORATORY
P.O. BOX 5800
ALBUQUERQUE NM 87185
USA

G. E. McCREERY
EG&G IDAHO, INC.
P.O. BOX 1625
IDAHO FALLS ID 83415
USA

W. H. McELROY
BATTELLE PACIFIC NORTHWEST LAB.
P.O. BOX 999
RICHLAND WA 99352
USA

M. McGUIRK
BABCOCK & WILCOX
P.O. BOX 10935, 3315 OLD FOREST RD.
LYNCHBURG VA 24506-0935
USA

R. N. H. McMILLAN
UKAEA/SRD
WIGSHAW LANE, CULCHETH
WARRINGTON WA34NE
UK

D. M. MEARS
BABCOCK & WILCOX
P.O. BOX 10935, 3315 OLD FOREST RD.
LYNCHBURG VA 24506-0935
USA

C. MEDICH
VIA NINO BIXIO
PIACENZA
ITALY

J. A. MEINCKE
CONSUMER POWER CO.
1945 W. PARNALL RD.
JACKSON MI
USA

G. M. MELIN
CEA FRENCH ATOMIC ENERGY COMMISSION
SETH/LES - C.E.N.G. - 85X
GRENOBLE CEDEX 38041
FRANCE

B. MERCER
UNIVERSITY OF MARYLAND
COLLEGE PARK MD 20742
USA

O. M. MERCIER
EIR-EIDG INST. FUR REAKTORFURSCHUNG
WURENLINGEN CH5303
SWITZERLAND

Y. MEYZAUD
FRAMATOME
TOUR FIAT CEDEX 16
PARIS FR 92084
FRANCE

J. S. MILLER
GULF STATES UTILITIES CO.
P. O. BOX 220
ST. FRANCISVILLE LA 70775
USA

C. S. MILLER
EG&G IDAHO, INC.
P.O. BOX 1625
IDAHO FALLS ID 83415
USA

R. L. MILLER
WESTINGHOUSE HANFORD COMPANY
P.O. BOX 1970
RICHLAND WA 99352
USA

H. A. MITCHELL
INTERNATIONAL TECHNOLOGY CORP.
575 OAK RIDGE TURNPIKE
OAK RIDGE TN 37830
USA

S. M. MODRO
EG&G IDAHO, INC.
P.O. BOX 1625
IDAHO FALLS ID 83415
USA

C. L. MOHR
MOHR & ASSOCIATES
1440 AGNES
RICHLAND WA 99352
USA

R. O. MONTGOMERY
TEXAS A&M UNIVERSITY
NUCLEAR ENGINEERING DEPT.
COLLEGE STATE TX 77843
USA

B. S. MONTY
WESTINGHOUSE ELECTRIC
P.O. BOX 355
PITTSBURGH PA 15235
USA

J. MORIN
SAVANNAH RIVER LABORATORY
773-41A
AIKEN SC 29808
USA

G. A. MORTENSEN
EG&G IDAHO, INC.
P.O. BOX 1625
IDAHO FALLS ID 83415
USA

F. E. MOTLEY
LOS ALAMOS NATIONAL LAB
P.O. BOX 1663
LOS ALAMOS NM 87545
USA

L. D. MUHLSTEIN
WESTINGHOUSE HANFORD COMPANY
P.O. BOX 1970
RICHLAND WA 99352
USA

Y. MURAO
JAPAN ATOMIC ENERGY RESEARCH INC
TOKAI-MURA
IBARAKI 319-11
JAPAN

R. C. MURRAY
LAWRENCE LIVERMORE NATIONAL LAB
P.O. BOX 808,L-197
LIVERMORE CA 94550
USA

S. A. NAFF
KRAFTWERK UNION AG
HAMMERBACHERSTRASSE 12 + 14
ERLANGEN D-8520
FRG

R. K. NANSTAD
OAK RIDGE NATIONAL LAB
P.O. BOX X, BLDG 4500-S
OAK RIDGE TN 37831
USA

D. J. NAUS
OAK RIDGE NATIONAL LAB
P.O. BOX Y, BLDG 9204-1
OAK RIDGE TN 37831
USA

H. H. NEELY
ROCKWELL INTERNATIONAL
6633 CANOGA AVENUE
CANOGA PARK CA 91304
USA

L. A. NEIMARK
ARGONNE NATIONAL LABORATORY
9700 S. CASS AVENUE
ARGONNE IL 60302
USA

L. Y. NEYMOTIN
BROOKHAVEN NATIONAL LAB
BLDG 475B
UPTON NY 11973
USA

S. J. NIEMCZYK
GULL ASSOCIATES
1545 18TH ST. NW #112
WASHINGTON DC 20036
USA

M. V. NIKITIN
SCIAE, INTERNATIONAL RELATIONS DEPT
STAROMONETNYI, 26
MOSCOW 109180
USSR

S. NISHINO
ELECTRIC POWER RESEARCH INSTITUTE
3412 HILLVIEW AVE., P.O. BOX 10412
PALO ALTO CA 94303
USA

C. K. NITHIANANDAN
BABCOCK & WILCOX
LYNCHBURG VA 24503
USA

K. K. NIYOGI
UNITED ENGINEERS & CONST. INC.
30 S. 17TH STREET
PHILADELPHIA PA 19101
USA

Y. NOGUCHI
CHUBU ELECTRIC POWER CO. INC
900 17TH ST. N.W., SUITE 714
WASHINGTON DC 20006
USA

P. NORTH
EG&G IDAHO, INC.
P. O. BOX 1625
IDAHO FALLS ID 83415
USA

J. G. O'BRIEN
UNIVERSITY OF MARYLAND
RT. 1
COLLEGE PARK MD 21093
USA

C. F. OBENCHAIN
EG&G IDAHO, INC.
P. O. BOX 1625
IDAHO FALLS ID 83415
USA

K. OKABE
MITSUBISHI ATOMIC POWER INDUSTRIES
4-1, SHIBAKOUEN 2-CHOME
MINATO-KU TOKYO
JAPAN

R. C. OLSON
BALTIMORE GAS & ELECTRIC
CALVERT CLIFFS - P.O. BOX 1535
LUSBY MD 20657
USA

H. P. OLSON
SAVANNAH RIVER LABORATORY
AIKEN SC 29808
USA

A. M. OMAR
ATOMIC ENERGY CONTROL BOARD
270 ALBERT STREET
OTTAWA K1P5S9
CANADA

A. OMOTO
TOKYO ELECTRIC POWER
POTOMAC
MD. 8605 TIMBER HILL LANE 20854
USA

A. T. ONESTO
ETEC
P.O. BOX 1449
CANOGA PARK CA 91304
USA

D. J. OSETEK
EG&G IDAHO, INC.
P.O. BOX 1625
IDAHO FALLS ID 83415
USA

L. J. OTT
OAK RIDGE NATIONAL LAB
P.O. BOX Y, BLDG 9104-1
OAK RIDGE TN 37831
USA

J. PAN
UNIVERSITY OF MICHIGAN
2250 G. G. BROWN
ANN ARBOR MI 48109
USA

B. PANELLA
POLITECNICO DI TORINO
CORSO DUCA DEGLI ABRUZZI, 24
TORINO 10100
ITALY

M. V. PAREDE
BABCOCK & WILCOX
P.O. BOX 10935, 3315 OLD FOREST RD
LYNCHBURG VA 24506-0935
USA

A. C. PAYNE, JR
SANDIA NATIONAL LABORATORY
P.O. BOX 5800
ALBUQUERQUE MN 87185
USA

G. PETRANGELI
ENEA/DISP
VIA VITALIANO BRANCATI 48
ROME 00144
ITALY

L. PETRUSHA
BABCOCK & WILCOX
P.O. BOX 10935, 3315 OLD FOREST ROD.
LYNCHBURG VA 24506-0935
USA

D. A. PETTI
EG&G IDAHO, INC.
P.O. BOX 1625
IDAHO FALLS ID 83415
USA

L. K. PIPLIES
COMMISSION OF EUROPEAN COMMUNITIES
I-21020
ISPRA I-21020 ISPRA
ITALY

M. P. PLESSINGER
EG&G IDAHO, INC.
P.O. BOX 1625
IDAHO FALLS ID 83415
USA

M. G. PLYS
FAUSKE & ASSOCIATES, INC
16W070 W. 83RD STREET
BURR RIDGE IL 60521
USA

M. Z. PODOWSKI
RENSSELAER POLYTECHNIC INST.
TROY NY 12180
USA

G. J. POSAKONY
BATTELLE PACIFIC NORTHWEST LAB.
P.O. BOX 999
RICHLAND WA 99352
USA

T. PRATT
BROOKHAVEN NATIONAL LABORATORY
BUILDING 130
UPTON NY 11973
USA

D. A. PRELEWICZ
ENSA, INC.
P.C. BOX 5537
ROCKVILLE MD 20855
USA

J. G. PRUETT
OAK RIDGE NATIONAL LAB
P.O. BOX X, BLDG 4500S MS-135
OAK RIDGE TN 37831
USA

C. E. PUGH
OAK RIDGE NATIONAL LAB
P.O. BOX Y
OAK RIDGE TN 37831
USA

W. R. QUEALY
HM NUCLEAR ISTALLATIONS INSPECTORATE
ST. PETERS HOUSE, BALLIOL ROAD
BOOTLE MERSEYSIDE L203LZ
UK

K. RAES
BATTELLE FRANKFURT
AM ROMERHOF 35
FRANKFORT
FRG

F. RAHN
ELECTRIC POWER RESEARCH INSTITUTE
3412 HILLVIEW AVE
PALO ALTO CA 94303
USA

N. C. RASMUSSEN
MASS. INSTITUTE OF TECHNOLOGY
ROOM 24-205
CAMBRIDGE MA 02139
USA

M. REICH
BROOKHAVEN NATIONAL LAB
BLDG. 129
UPTON NY 11973
USA

H. RENNER
NUS CORPORATION
910 CLOPPER ROAD
GAITHERSBURG MD 20878
USA

L. N. RIB
LNR ASSOCIATES
2505 GRIMSBY COURT
POTOMAS MD 20854
USA

D. R. RILEY
ELECTRIC POWER RESEARCH INST
501 FOREST AVE # 601
PALO ALTO CA 94301
USA

C. L. RITCHEY
BABCOCK & WILCOX
P.O. BOX 10935, 3315 OLD FOREST RD
LYNCHBURG VA 24506-0935
USA

C. M. ROBERTS
UNIVERSITY OF MARYLAND
COLLEGE PARK MD 20742
USA

D. E. ROBERTSON
BATTELLE PACIFIC NORTHWEST LAB
P.O. BOX 999
RICHLAND WA 99352
USA

G. E. ROBINSON
PENN STATE UNIVERSITY
231 SACKETT BLDG
UNIVERSITY PARK PA 16902
USA

U. S. ROHATGI
BROOKHAVEN NATIONAL LAB
BLDG 475B
UPTON NY 11973
USA

J. V. ROTZ
BECHTEL
15740 SHADY GROVE RD.
AITHERSBURG MD 20877
USA

J. C. ROUSSEAU
CEA FRENCH ATOMIC ENERGY COMMISSION
CENTRE D'ETUDES NUCLEAIRES
GRENOBLE 38041
FRANCE

D. RUBIO
ELECTRIC POWER RESEARCH INSTITUTE
3412 HILLVIEW AVE.
PALO ALTO CA 94303
USA

K. D. RUSSEL
EG&G IDAHO, INC.
P.O. BOX 1625
IDAHO FALLS ID 83415
USA

B. SAFFELL
BATTELLE COLUMBUS DIVISION
505 KING AVENUE
COLUMBUS OH 43201
USA

H. SAKAMOTO
NUCLEAR POWER ENGINEERING TEST CENTER
3-13, 4-CHOME, TORANOMON
MINATO-KU, TOKYO 105
JAPAN

H. SAKURAGI
JAPAN INSTITUTE OF NUCLEAR SAFETY
MITA KOKUSAI BLDG., 1-4-28, MITA
MINATO-KU, TOKYO 108
JAPAN

J. SALUJA
VIKING SYSTEMS INTERNATIONAL
121 N. HIGHLAND AVE.
PITTSBURG PA 15206
USA

L. E. SALYARDS
BALTIMORE GAS & ELECTRIC
CALVERT CLIFFS - P.O. BOX 1535
LUSBY MD 20657
USA

M. SARRAM
UNITED ENGINEERS & CONST. INC.
30 S. 17TH ST., P.O. BOX 8223
PHILADELPHIA PA 19101
USA

I. SATO
JAPAN STEEL WORKS
4 CHATSU-MACHI
MURORAN HOKKAIDO
JAPAN

D. G. SATTERWHITE
EG&G IDAHO, INC.
P.O. BOX 1625
IDAHO FALLS ID 83415
USA

M. B. SATTISON
EG&G IDAHO, INC.
P.O. BOX 1625
IDAHO FALLS ID 83415
USA

J. C. SCARBOROUGH
JCS LIMITED
6936 RACE HORSE LANE
ROCKVILLE MD 20852
USA

P. J. SCHALLY
GESELLSCHAFT FUR REAKTORSICHERHEIT
SCHWERTNERGASSE 1
KOELN 5060
FRG

A. P. SCHMITT
CEA FRENCH ATOMIC ENERGY COMMISSION
CEN-FAR, IPSN
FONTENAY-AUX-ROSES CEDEX 92265
FRANCE

R. R. SCHULTZ
EG&G IDAHO, INC.
P.O. BOX 1625
IDAHO FALLS ID 83415
USA

C. W. SCHWARTZ
UNIVERSITY OF MD., DEPT. OF CIVIL ENG.
COLLEGE PARK MD 20742
USA

J. H. SCOBEL
WESTINGHOUSE
MEC E 3-21
PITTSBURGH PA 15230
USA

F. SEARS
NORTHEAST UTILITIES
P. O. BOX 270
HARTFORD CT 06141-0270
USA

S. S. SETH
THE MITRE CORPORATION
7525 COLSHIRE DRIVE, MAIL - W721
McLEAN VA 22102
USA

R. T. SEWELL
RISK ENGINEERING INC.
5255 PINE RIDGE ROAD
GOLDEN CO 80403
USA

W. J. SHACK
ARGONNE NATIONAL LABORATORY
BUILDING 212
ARGONNE IL 60302
USA

VIK SHAH
EG&G IDAHO, INC.
11428 ROCKY ..E PIKE, SUITE 410
ROCKVILLE MD 20852
USA

R. H. SHANNON
CONSULTANT
P.O.BOX 2264
ROCKVILLE MD 20852
USA

R. SHARMA
AMERICAN ELECTRIC POWER SERVICE CORP
1 RIV[illegible]SIDE PLAZA
COL[illegible] OH 43216
USA

R. [illegible]
EG&G IDAHO, INC.
P.O. BOX 1625
IDAHO FALLS ID 83415
USA

J. M. SHEA
NORTHEAST UTILITIES
107 SELDEN ST., W-15
BERLIN CT 06037
USA

L. SHEN
ATOMIC ENERGY COUNCIL,EXECUTIVE YUAN
57, LANE144, KEELUNG RD., SEC.4
TAIPEI TAIWAN 107
ROC

G. L. SHERWOOD, JR.
U.S. DEPARTMENT OF ENERGY
GERMANTOWN MD 20767
USA

P. SHEWMON
ADVISORY COMM. ON REACTOR SAFEGUARDS
2477 LYTHAM ROAD
COLUMBUS OH 43220
USA

D. J. SHIMECK
WESTINGHOUSE
RD2, BOX 194
EXPORT PA 15632
USA

M. SHIMIZU
JAPAN ATOMIC ENERGY RES. INSTITUTE
TOKAI-MURA IBARAKI-KEN 319-11
JAPAN

M. S. SHINKO
EMERGENCY RESPONSE TEAM
P.O. BOX 129
WASHINGTON GROVE MD 20880
USA

E. G. SILVER
OAK RIDGE NATIONAL LAB
P.O. BOX Y, BLDG.9201-3, MS 5
OAK RIDGE TN 37831
USA

F. A. SIMONEN
BATTELLE PACIFIC NORTHWEST LAB
P.O. BOX 999
RICHLAND WA 99352
USA

B. M. SLAUGHTER
OAK RIDGE NATIONAL LAB
P.O. BOX X, BLDG 4500-S
OAK RIDGE TN 37831
USA

M. K. SMITH
BABCOCK & WILCOX
P.O. BOX 10935, 3315 OLD FOREST RD.
LYNCHBURG VA 24506-0935
USA

A. W. SNYDER
SANDIA NATIONAL LABORATORY
P.O. BOX 5800, DIVISION 6[illegible]0
ALBUQUERQUE NM 87185
USA

K. SODA
JAPAN ATOMIC ENERGY RES. INSTITUTE
TOKAI-MURA IBARAKI-KEN 319-11
JAPAN

H. G. SONNENBURG
GESELLSCHAFT FUR REAKTORSICHERHEIT
FORSCHUNGSGELAENDE
GARCHING 8046
FRG

P. SOO
BROOKHAVEN NATIONAL LAB
BLDG 830
UPTON NY 11973
USA

J. L. SPRUNG
SANDIA NATIONAL LABORATORY
P.O. BOX 5800
ALBUQUERQUE NM 87185
USA

D. SQUARER
WESTINGHOUSE R&D
1310 BEULAH RD.
PITTSBURGH PA 15235
USA

M. G. SRINIVASAN
ARGONNE NATIONAL LAB
9700 S. CASS AVE.-BLDG 335
ARGONNE IL 60439
USA

K. E. ST. JOHN
YANKEE ATOMIC ELECTRIC COMPANY
1671 WORCESTER RD.
FRAMINGHAM MA 01701
USA

H. STADTKE
COMMISSION OF EUROPEAN COMMUNITIES
121020, ISPRA
ISPRA
ITALY

R. STEELE
EG&G IDAHO, INC.
P.O. BOX 1625
IDAHO FALLS ID 83415
USA

J. P. STEELMAN
BALTIMORE GAS & ELECTRIC
LUSBY POST OFFICE
LUSBY MD 20657
USA

N. PONOMAREV- STEPNOI
I. V. KURCHATOV INST. OF ATOMIC ENERGY
KURCHATOV SQUARE
MOSCOW 123182
USSR

P. M. STOOP
NETHERLANDS ENERGY RES.FOUNDATION ECN
3 WESTERDUINWEG, P.O. BOX 1
PETTEN (NH) 1755 ZG
NETHERLANDS

E. STUBBE
TRACTEBEL
31 RUE DE LA SCIENCE
BRUSSELS 1040
BELGIUM

M. SUBUDHI
BROOKHAVEN NATIONAL LAB
BLDG 130
UPTON NY 11973
USA

W. SUGNET
ELECTRIC POWER RESEARCH INSTITUTE
3412 HILLVIEW AVE.
PALO ALTO CA 94303
USA

R. M. SUMMERS
SANDIA NATIONAL LABORATORY
P.O. BOX 5800, DIVISION 6418
ALBUQUERQUE NM 87185
USA

B. SUN
ELECTRIC POWER RESEARCH INSTITUTE
3412 HILLVIEW AVE.
PALO ALTO CA 94303
USA

R. K. SUNDARAM
YANKEE ATOMIC ELECTRIC COMPANY
1671 WORCESTER ROAD
FRAMINGHAM MA 01519
USA

D. G. SWANSON
PDI TECHNOLOGY
246 VIKING AVE
BREA CA 92621
USA

H. TAKAHASHI
MITSUBISHI ATOMIC POWER INDUSTRIES
4-1, SHIBAKOUEN 2-CHOME
MINATO-KU TOKYO
JAPAN

Y. K. TANG
ELECTRIC POWER RESEARCH INSTITUTE
3412 HILLVIEW AVE.
PALO ALTO CA 94303
USA

H. T. TANG
ELECTRIC POWER RESEARCH INST.
3412 HILLVIEW AVE.
PALO ALTO CA 94303
USA

K. TASAKA
JAPAN ATOMIC ENERGY RES. INSTITUTE
TOKAI-MURA IBARAKI-KEN 319-11
JAPAN

J. H. TAYLOR
BROOKHAVEN NATIONAL LAB
BLDG 130
UPTON NY 11973
USA

T. A. THEOFANOUS
UNIV. OF CALIF., SANTA BARBARA
817 SEA RANCH DRIVE
SANTA BARBARA CA 93109
USA

E. W. THOMAS
BECHTEL EASTERN POWER
SHADY GROVE ROAD
GAITHERSBURG MD
USA

B. J. TOLLEY
COMMISSION OF THE EUROPEAN COMM
200, RUE DE LA LOI
BRUSSELS 1049
BELGIUM

B. TOLMAN
EG&G IDAHO, INC.
2355 TASMAN
IDAHO FALLS ID 83401
USA

K. TOMOMURA
CENTURY RESEARCH CENTER CORPORATION
3-6-2 NIHONBASHI- HONCHO 3-CHOME
CHUO-KU, TOKYO 103
JAPAN

L. S. TONG
TAI
9733 LOOKOUT PLACE
GAITHERSBURG MD 20879
USA

F. TOTSUKA
ENERGY RESEARCH LAB., HITACHI, LTD.
1-29-4 HANAYAMA-CHO
HITACHI-SHI IBARAKI-KEN 316
JAPAN

H. E. TRAMMELL
OAK RIDGE NATIONAL LAB
P.O. BOX Y, BLDG 9701-3
OAK RIDGE TN 37831
USA

T. M. TRAN
TENNESSEE VALLEY AUTHORITY
400 SUMMIT HILL
KNOXVILLE TN 37902
USA

J. R. TRAVIS
LOS ALAMOS NATIONAL LAB
GROUP T-3, M/S B216
LOS ALAMOS NM 87545
USA

D. E. TRUE
ERIN ENGINEERING
1850 MT. DIABLO BLVD., SUITE 600
WALNUT CREEK CA 94596
USA

A. A. TUDOR
SAVANNAH RIVER LABORATORY
773-41A
AIKEN SC 29808
USA

N. K. TUTU
BROOKHAVEN NATIONAL LABORATORY
BUILDING 82/JM
UPTON NY 11973
USA

T. UESHIMA
ELECTRIC POWER RESEARCH INSTITUTE
3412 HILLVIEW AVE., P.O. BOX 10412
PALO ALTO CA 94303
USA

T. UMEMOTO
ISHIKAWAJIMA-HARIMA HEAVY INDUSTRIES
1-SHIN-NAKARA,ISOGO-KU
YOKAHAMA 235
JAPAN

K. D. UNDERWOOD
UNIVERSITY OF MARYLAND
COLLEGE PARK MD 20742
USA

S. UNWIN
BROOKHAVEN NATIONAL LABORATORY
BLDG. 130
UPTON NY 1[illegible]73
USA

R. A. VALENTIN
ARGONNE NATIONAL LAB
9700 S. CASS AVE.-BLDG 208
ARGONNE IL 60439
USA

R. M. VAN KUIJK
N. V. KEMA
POSTBUS 9035, UTRECHTSEWEG 310
6800 ET ARNHEM
NETHERLANDS

N. VASUDEVAN
BABCOCK & WILCOX
P.O. BOX 10935, 3315 OLD FOREST ROAD
LYNCHBURG VA 24506-0935
USA

C. H. VERTES
WESTINGHOUSE
NORTHERN PIKE RD.
MONROEVILLE PA 15146
USA

O. YESCOVI
SIET
NINO BIXIO 27
PIACENZA
ITALY

W. E. VESELY
SAIC
SUITE 245, 2929 KENNY ROAD
COLUMBUS OH 43221
USA

J. L. VON HERRMANN
IT-DELIAN
2011 EYE STREET
WASHINGTON DC 20006
USA

W. A. VON RIESEMANN
SANDIA NATIONAL LABORATORY
P.O. BOX 5800, DIVISION 6442
ALBUQUERQUE NM 87185
USA

M. WALTER
UNIVERSITY OF MARYLAND
663 W. FAYETTE STREET
BALTIMORE MD 21201
USA

S. F. WANG
INSTITUTE OF NUCLEAR ENERGY RESEARCH
P.O. BOX 3-13
LUNG-TAN TAIWAN 32500
ROC

M. E. WATERMAN
EG&G IDAHO, INC.
11428 ROCKVILLE PIKE, #410
ROCKVILLE MD 20852
USA

W. L. WEAVER
EG&G IDAHO, INC.
P.O. BOX 1625
IDAHO FALLS ID 83415
USA

E. T. WEBER
WESTINGHOUSE HANFORD COMPANY
P.O. BOX 1970
RICHLAND WA 99352
USA

J. R. WEEKS
BROOKHAVEN NATIONAL LAB
BLDG 130
UPTON NY 11973
USA

P. A. WEISS
SIEMENS-KWU
HAMMERBACHERSTRASSE 12 + 14
ERLANGEN D-8520
FRG

A. J. WEISS
BROOKHAVEN NATIONAL LAB
BLDG 197C
UPTON NY 11973
USA

E. WENZINGER
MPR ASSOCIATES, INC.
1050 CONNECTICUT AVE N.W.
WASHINGTON DC 20036
USA

E. T. WESSEL
EDWARD T. WESSEL, CONSULTING ENG.
316 WOLVERINE STREET
HAINES CITY FL 33844
USA

R. A. WESTON
COMBUSTION ENGINEERING
1000 PROSPECT HILL RD
WINDSOR CT 06095
USA

H. WESTPHAL
GESELLSCHAFT FUR REAKTORSICHERHEIT
SCHWERTNERGASSE 1
COLOGNE 5000
FRG

D. L. WHITCOMB
WASHINGTON PUBLIC POWER SUPPLY SYS.
3000 G. WASH. WAY-P.O. BOX 968
RICHLAND WA 99352
USA

T. J. WHITEHEAD
SAIC
101 S. PARK AVE
IDAHO FALLS ID 83402
USA

P. G. WHITKOP
SAVANNAH RIVER LABORATORY
773-41A
AIKEN SC 29808
USA

G. M. WILKOWSKI
BATTELLE-COLUMBUS DIVISION
505 KING AVENUE
COLUMBUS OH 43201
USA

K. A. WILLIAMS
SAIC
2109 AIR PARK RD. SE
ALBUQUERQUE NM 87106
USA

F. WINEGARDNER
BATTELLE PACIFIC NORTHWEST LAB
P.O. BOX 999
RICHLAND WA 99352
USA

F. WINKLER
KRAFTWERK UNION AG
HAMMERBACHERSTRASSE 12 + 14
ERLANGEN D-8520
FRG

L. WOLF
PROJECT HDR/KERNFORSCHUNGSZENTRUM
POSTFACH 3640
7500 KARLSRUHE 1
FRG

K. WOLFERT
GESELLSCHAFT FUR REAKTORSICHERHEIT
FORSCHUNGSGELAENDE
GARCHING 8046
FRG

Y. C. WONG
CEGB, GENERATION DEV. & CONST. DIV.
BARNETT WAY
BARNWOOD GLOUCESTER GL4 7RS
UK

G. WONG
GENERAL PUBLIC UTILITIES
1 UPPER POND ROAD
PARSIPPANY NJ 07054
USA

L. R. WYGO
GENERAL ELECTRIC COMPANY
P.O. BOX 1072, BUILDING P-1, ROOM 111
SCHENECTADY NY 12301
USA

W. WULFF
BROOKHAVEN NATIONAL LAB
BLDG 475B
UPTON NY 11973
USA

G. YAGAWA
UNIVERSITY OF TOKYO
HONGO, BUNKYOKU
TOKYO 113
JAPAN

K. K. YOON
BABCOCK & WILCOX
P.O. BOX 10935, 3315 OLD FOREST ROAD
LYNCHBURG VA 24506-0935
USA

E. YOSHIKOWA
NUCLEAR POWER ENGINEERING TEST CENTER
NO. 2 AKIYAMA BLDG., 6-2, 3-CHOME, MINA
TOKYO 105
JAPAN

R. YOUNG
UKAEA/SRD
WIGSHAW LANE
CULCHETH WARRINGTON WA3 4NE
UK

J. ZDAREK
CZECHOSLOVAK EMBASSY
3900 LINNEAN AVE. N.W.
WASHINGTON DC 20008
CZECHOSLOVAKIA

K. ZIEGLOWSKI
KWU-OFFENBACH
6050 OFFENBACH BERLINER STR.
FRG

R. ZIPPER
GESELLSCHAFT FUR REAKTORSICHERHEIT
SCHWERTNERGASSE 1
COLOGNE
FRG

R. ZOBRAN
MPR ASSOCIATES, INC.
1050 CONNECTICUT AVE N.W.
WASHINGTON DC 20036
USA

PROCEEDINGS OF THE
FIFTEENTH WATER REACTOR SAFETY INFORMATION MEETING

October 26-29, 1987

TABLE OF CONTENTS - VOLUME 4

SOURCE TERM UNCERTAINTY ANALYSIS

Chairperson: L. Chan (NRC)

INTEGRAL SYSTEMS TESTING

Chairperson: R. Lee (NRC)

INTEGRAL SYSTEM TESTING
(Cont'd)

2D/3D RESEARCH
Chairperson: G. S. Rhee (NRC)

UNCERTAINTIES IN MODELLING AND SCALING OF CRITICAL FLOWS AND PUMP MODEL IN TRAC-PF1/MOD1

Upendra S. Rohatgi and Wen-Shi Yu
Brookhaven National Laboratory
Department of Nuclear Energy
Upton, New York 11973

The USNRC has established a Code Scalability, Applicability and Uncertainty (CSAU) evaluation methodology to quantify the uncertainty in the prediction of safety parameters by the best estimate codes. These codes can then be applied to evaluate the Emergency Core Cooling System (ECCS). The TRAC-PF1/MOD1 version was selected as the first code to undergo the CSAU analysis for LBLOCA applications. It was established through this methodology that break flow and pump models are among the top ranked models in the code affecting the peak clad temperature (PCT) prediction for LBLOCA.

The break flow model bias or discrepancy and the uncertainty were determined by modelling the test section near the break for 12 Marviken tests. It was observed that the TRAC-PF1/MOD1 code consistently underpredicts the break flow rate and that the prediction improved with increasing pipe length (larger L/D). This is true for both subcooled and two-phase critical flows.

A pump model was developed from Westinghouse (1/3 scale) data. The data represent the largest available test pump relevant to Westinghouse PWRs. It was then shown through the analysis of CE and CREARE pump data that larger pumps degrade less and also that pumps degrade less at higher pressures. Since the model developed here is based on the 1/3 scale pump and on low pressure data it is conservative and will overpredict the degradation when applied to PWRs.

1. INTRODUCTION

Appendix K of 10CFR50 provides the guidelines for evaluating the effectiveness of Emergency Core Cooling System (ECCS). However, it has been recognized from a decade of research in the area of thermal-hydraulics of the reactor system that these guidelines are very conservative and in some cases nonphysical, and a need exists to revise the ECCS evaluation methodology. One of the alternative acceptable methodologies, which emerged from the attempts to revise Appendix K, was the use of best estimate codes to analyze the accidents. It is required for such best estimate codes that a quantitative estimate for the uncertainty of important predicted safety parameters be made for a particular accident and for a given plant.

The USNRC has established a Code Scalability, Applicability and Uncertainty (CSAU) evaluation methodology [1] to quantify the uncertainty. TRAC-PF1/MOD1 version 14.3 has been selected to demonstrate the CSAU method for the Large Break Loss of Coolant Accident (LBLOCA). The CSAU methodology

*Work performed under the auspices of the U.S. Nuclear Regulatory Commission

requires identifying and ranking of all the important hydraulic processes and reactor components which affect the primary parameter(s) for the LBLOCA transients. The primary parameters are: the early (blowdown) peak clad temperature (PCT), and the late (reflood) peak clad temperature. The break flow and pump models were among the top-ranked components affecting the early peak.

In this paper the methods and results of the analysis forestimating the bias and the uncertainty in TRAC-PF1/MOD1 models [2] for the critical flow and for the pump performance are described.

2. UNCERTAINTY IN CRITICAL FLOW MODEL

The coolant inventory in the reactor system is controlled by the break flow rate. However, a more significant role of the break flow rate is its influence on the distribution of the liquid inventory during the blowdown phase. The fuel rod clad starts to heat up at the time of break as the flow stagnates in the core. However, around 2.3 seconds after break initiation, the break flow decreases below the flow through the pumps in the intact loops, after the break flow changes from subcooled to two-phase critical flow. This results in the restoration of some liquid flow into the core, in core-wide rewet, and in the occurrence of the first peak of the clad temperature in the blowdown phase.

2.1 The Critical Flow Model in TRAC-PF1

TRAC-PF1/MOD1 has three models for critical flow. One is for subcooled liquid, the second is for two-phase flow conditions and the third one is for single-phase vapor. This paper deals with the first and second models, because the third model is irrelevant for peak clad temperature predictions.

2.1.1 Subcooled Critical Flow is computed in TRAC from a modified Bernoulli equation, as described in Appendix D on page 530 of Reference [2]. This TRAC code document gives in Eq. (D-9) the critical velocity for subcooled liquid, calculated for the break plane location, as the velocity V_e:

$$V_e = \text{Max} \left\{ a_{HE} \sqrt{v_c^2 + 2\,(p_c - p_e)/\rho_m} \right\} , \qquad (2.1)$$

where a_{HE} is the sound speed of homogeneous two-phase mixtures, V_c and p_c are the velocity and pressure at the nearest upstream computational cell center, while p_e and ρ_m are the break plane pressure and the mixture density at a location not specified in the TRAC documentation. A number of questionable explanations are given to justify Eq. (2.1). They can be found in Section II-B of Appendix D, in Reference [2]. Particularly, the second argument of the maximizing function in Eq. (2.1) produces a velocity which is neither related to the pressure wave propagation velocity, nor does it satisfy a mass flux maximizing condition. Therefore, it is not clear why Eq. (2.1) should always produce a critical mass flow rate.

Equation (2.1) applies in TRAC, whenever the void fraction α_c at the upstream cell center nearest to the break satisfies $\alpha_c < 0.01$. The break plane

pressure p_e is computed in TRAC on the basis of the nonequilibrium flashing model by Jones [3] (who used Alamgir and Lienhard's earlier work). The pressure p_e is computed from Eq. (D-10) of Reference [2] according to:

$$p_e = p_s - \text{Max}\,\{0, \Delta p\}\ . \tag{2.2}$$

Here p_s is the saturation pressure (at unspecified location), and:

$$\Delta p = 0.258\ \frac{\sigma^{1.5}\,\left(\frac{T_\ell}{T_{crit}}\right)^{13.76}}{1 - \frac{\rho_g}{\rho_\ell}}\ \sqrt{\left[1 + 13.25\,\left(\frac{-Dp/Dt}{1.01325\times10^{11}}\right)\right]^{0.8}/(kT_{crit})}$$

$$-0.070\,\left(\frac{A_e}{A_c}\right)^2\,\rho_\ell\,V_e^2\ , \tag{2.3}$$

where σ, k, T and ρ designate surface tension, Boltzmann constant, temperature and density, respectively, all quantities being expressed in S.I. units. Subscripts g, ℓ and crit designate gas, liquid and thermodynamic critical, while subscripts e and c are, as before, designating break plane and upstream cell center locations. The locations associated with subscripts g and ℓ are also not specified in Reference [2].

Notice that Eq. (2.3) contains the limiting critical velocity V_e, that substitution of Eq. (2.3) first into Eq. (2.2) and then into Eq. (2.1) renders Eq. (2.1) implicit in the velocity V_e. The TRAC code document [2] fails to indicate the method by which V_e is computed from Eqs. (2.1, 2 and 3), with T_ℓ, ρ_ℓ snd p_s all dependent on V_e.

Notice also that Reference [2] fails to specify the method for computing the substantial derivative Dp/Dt. The RELAP5 code documentation shows the same model for critical flow of subcooled liquid* [22, p. 79] as TRAC and specifies:

$$Dp/Dt = \left(\rho_\ell V_e^3/A_e\right)\left(dA/dx\right)_e\ , \tag{2.4}$$

where $(dA/dx)_e$ is the variation of cross sectional area with respect to axial distance at the break. Obviously, Eq. (2.4) fails to produce nonequilibrium pressure undershoot for breaks in straight pipes.

---

*Aside from a factor of 2 discrepancy in the last term of Eq. (2.3).

Finally, it must be pointed out that Reference [2] fails to indicate how V_e , as computed from Eq. (2.1), limits the mass flux as computed from the field equations in TRAC.

2.1.2 Two-Phase Critical Flow is computed in TRAC from the condition that the maximum value of the real part of the characteristic roots λ_i, associated with the field equations:

$$\underset{\sim}{A}\partial\underset{\sim}{U}/\partial t + \underset{\sim}{B}\partial\underset{\sim}{U}/\partial x = \underset{\sim}{C} \qquad (2.5)$$

is zero [2, p. 528]. The field equations are the mass balances of an inert gas and the two-phase mixture, the phasic momentum balances and the mixture entropy balance for isentropic flow. $\underset{\sim}{A}$ and $\underset{\sim}{B}$ in Eq. (2.5) are 5x5 matrices and the state variable vector $\underset{\sim}{U}$ has the components of inert gas pressure p , vapor pressure p_v, void fraction α and phasic velocities v_ℓ and v_g. The source vector $\underset{\sim}{C}$ is unimportant for all but the entropy equation. In TRAC it is completely ignored.

The characteristic roots λ_i are computed numerically from the characteristic equation:

$$\det\left[\underset{\sim}{A}\lambda + \underset{\sim}{B}\right] = 0. \qquad (2.6)$$

The numerical scheme [2, p. 530] involves also the maximization of the mass flux at the location of the break plane. Thus, the two-phase critical flow model in TRAC contains two independent choking criteria, but not the standard compatibility criteria of quasi-steady critical flow (see Reocreux, NUREG-tr-0002, Vol. 1, p. 75).

The above two-phase flow choking criterion is imposed in TRAC for $\alpha_c > 0.1$ at the nearest upstream cell center. In the range of $0.01 \leq \alpha_c \leq 0.1$, a linear interpolation with respect to α_c is used between the critical flows calculated from Eq. (2.1) and from Eq. (2.6).

2.2 Purpose of Critical Flow Model Evaluation

The objective of the present study is to quantify the modeling deficiency and uncertainty in the TRAC-PF1/MOD1 critical flow model [2], as applied to PWR and LBLOCA conditions. The deficiency measure of the model is defined as the multiplier C_D, which is a ratio of measured over predicted critical flow rates:

$$C_D = \frac{\text{measured flow rate}}{\text{predicted flow rate}} .$$

The uncertainty in the model is represented by the standard deviation of C_D.

2.3 Procedure

Abdollahian et al. [4], in a study of Marviken Critical Flow tests, concluded that for large size pipes (D > 0.3m and L/D > 1.5), the subcooled

critical flow was independent of diameter (D) and length (L), and only depended on the inlet stagnation conditions as shown here:

$$G_c = f\ (P_o,\ T_o)$$

where G_c, P_o, T_o are critical mass flux, stagnation pressure and temperature at the inlet to the pipe. However, for small pipes, the subcooled critical mass flux does depend upon L/D. For PWRs, the cold leg diameter is around 0.7m and the distance between the RC pump discharge to the vessel is on the order of 8D (L/D ≈ 8). This implies that if the break is located anywhere between L/D = 1.5 to 6.5 from either the vessel or the pump, the break flow will only depend upon the conditions of the fluid entering the broken pipes and not on the pipe length or diameter, and C_D will reflect any dependence of TRAC-PF1 critical flow models on the pipe geometry (L,D).

As the purpose of the study is to quantify the uncertainty in the critical flow model of TRAC-PF1/MOD1 as applied to PWRs, it was decided to investigate the largest size tests which are available. The Marviken test matrix satisfied the requirement as it contained tests for diameters varying from 0.2m to 0.5m, nozzle lengths varying from 0.3D to 3.7D and inlet subcooling temperatures varying from 5K to 50K. Furthermore, these tests produced measurements of pressure and temperatures at 0.7m above the nozzle entrance, which makes it possible to model only the test section near the break. Then the break flow prediction will not be affected by phenomena taking place in the rest of the test facility. The mass flux data were obtained from a pitot-static method. The errors in the mass flux measurements were ± 3 to 10% for the subcooled flow and ± 8 to 15% for two-phase flow. For the current task, 12 tests [5-16] were selected and are listed in Table 1.

Separate TRAC-PF1/MOD1 models for each test were set up. These models consisted of two cells (0.35m each) in the discharge pipe, one cell for the converging section, a number of equal size cells in the straight section of the nozzle. The cell lengths in the straight section varied between 0.2 and 0.5 m. They were approximately equal to the test section diameter and also equal to the cell length used in standard PWR plant simulation.

Marviken Critical Flow tests are transient tests (blowdown) and the mass flow rate data are available at every 0.1 second interval up to 1.0 second, then at every 0.5 second up to 3.0 seconds, and at every second thereafter. The first ten seconds of these tests, for which the inlet fluid was subcooled, were predicted by the TRAC code. Comparisons between the predicted mass flow rates with the experimental mass flow rates were made for the times for which the void fraction in the last cell before the BREAK component was less than 0.03. This generated a number of C_D values per test for subcooled critical flow. A mean value for C_D and standard deviation were computed for each test from this set. Similarly, a set of C_Ds for two phase choking were computed for each test from the cases for which the void fraction in the last cell before the BREAK component was greater than 0.07. The mean value for C_D and the standard deviation were computed from each set of each test for two-phase choking. Only one-fourth to one-third of all data points fell into the two-phase choking regime. It should also be noted that some of the inlet temperature data were spurious and the corresponding data were omitted.

2.4 Results and Conclusions

As the purpose of this study is to provide a mean value of C_D and standard deviation for application to PWRs, the mean values for C_D were plotted as a function of D, inlet subcooling and L/D. It was observed from these plots that the mean C_D for subcooled choking and two phase choking had no discernable trend when plotted with D or subcooling, but it did show a trend with L/D. This can be verified from Table 1.

A curve fit was obtained for mean C_D for subcooled choking as shown in Figure 1.

$$\langle C_D \rangle = 0.696 \exp\left(0.649 \left(\frac{L}{D}\right)^{-0.168}\right)$$

The χ in all these expressions is L/D.

However, as this curve did not pass through all the data points, a new set of standard deviations was computed using the mean values from this curve and relevant data points at each L/D. These standard deviations have been plotted in Figure 2 as function of L/D and also show a distinct trend. A curve fit was generated for the standard deviation as given here:

$$\sigma = 0.9 \exp\left(-1.737 \left(\frac{L}{D}\right)^{0.227}\right)$$

A similar procedure was followed for two phase critical flow model and curve fit for C_D, 2Ø and standard deviation are shown in Figures 3 an 4 and are also described by the following expressions:

$$\langle C_{D,2\emptyset} \rangle = 0.778 \exp\left(0.679 \left(\frac{L}{D}\right)^{-0.25}\right)$$

$$\sigma_{2\emptyset} = 2.027 \exp\left(-2.16 \left(\frac{L}{D}\right)^{0.25}\right)$$

These $\langle C_D s \rangle$ must be used directly in the input deck through the options in the NAMELIST. Once the location of the break has been selected, L/D can be estimated from the distance of the break from the vessel and from the pump discharge, and C_Ds can be obtained from the curves provided. The perturbation or sensitivity study must be performed by adding to and subtracting one standard deviation and the measurement errors from C_D. The correction for the measurement errors of C_D in subcooled choking should be ± 0.1 and in the two-phase choking reqime it should be ± 0.15.

3. UNCERTAINTY IN PUMP MODEL

During a hypothetical large break LOCA in PWR, the reactor coolart pump plays an important role in determining the timing of restoring the core inlet

TABLE 1

Test #	L/D	D_m	ΔT_k	$C_{D,sub}$	$C_{D,2\emptyset}$
12	3.0	0.3	30	1.115	
13	3.0	0.2	30		1.111
15	3.6	0.5	30	1.219	
16	3.6	0.5	30	1.258	
17	3.7	0.3	30	1.146	
18	3.7	0.3	30	1.157	
19	3.7	0.3	5	1.11	1.309
20	1.5	0.5	5		1.54
21	1.5	0.5	30	1.364	
22	1.5	0.5	50	1.35	
24	0.3	0.5	30	1.533	1.92
25	1.7	0.3	5	1.18	1.485

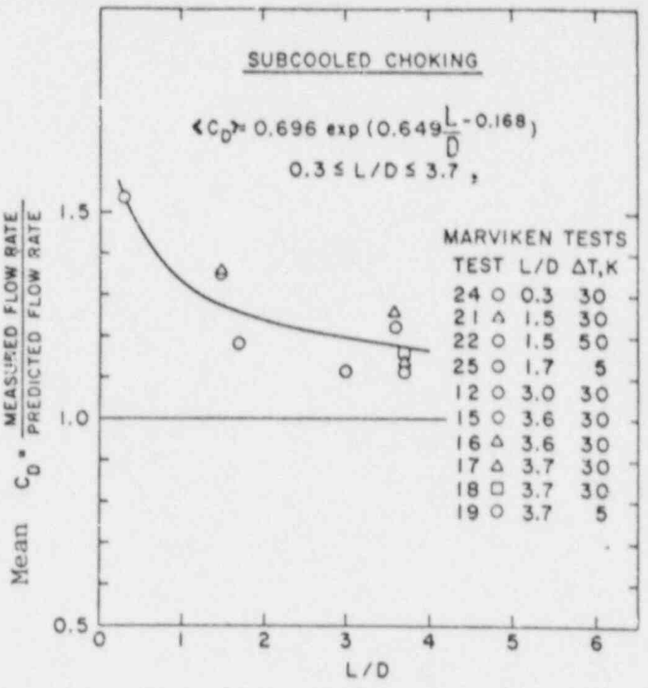

Figure 1 Mean C_D as Function of L/D for Subcooled Choking

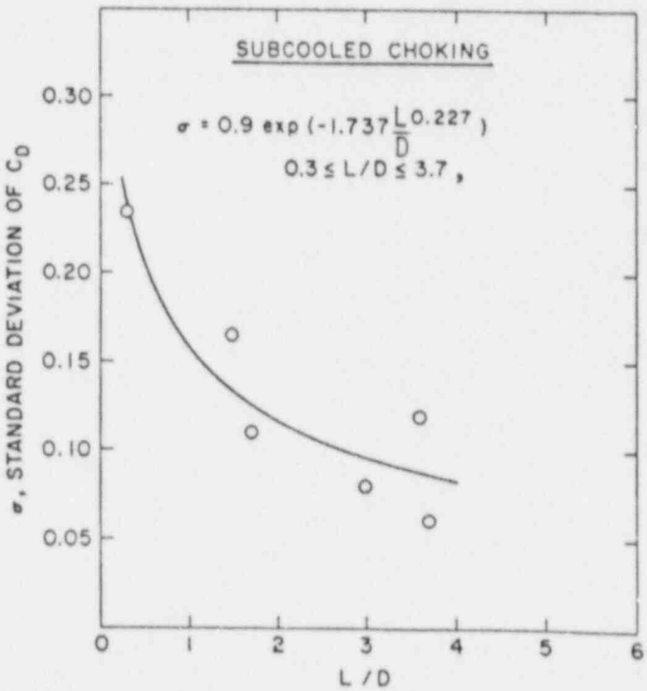

Figure 2 Standard Deviation of C_D as Function of L/D for Subcooled Choking

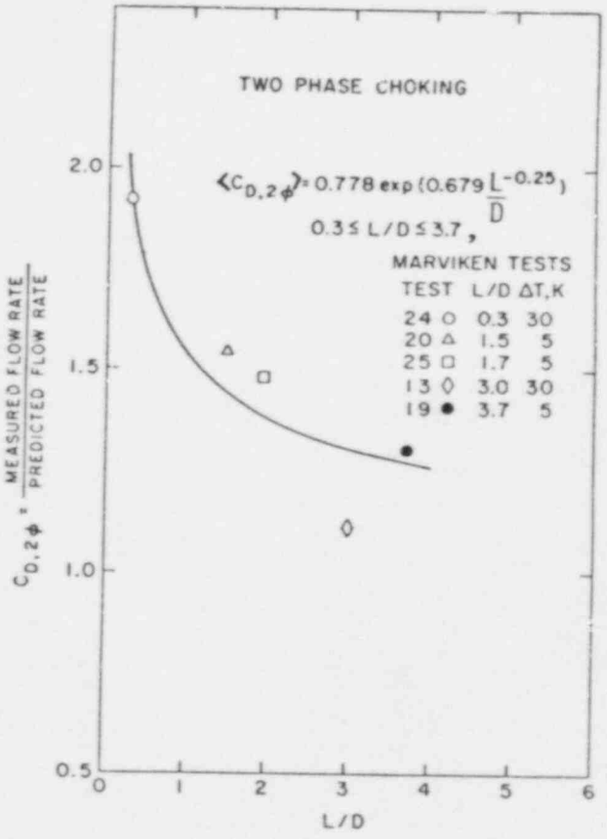

Figure 3 Mean C_D as Function of L/D for Two-Phase Choking

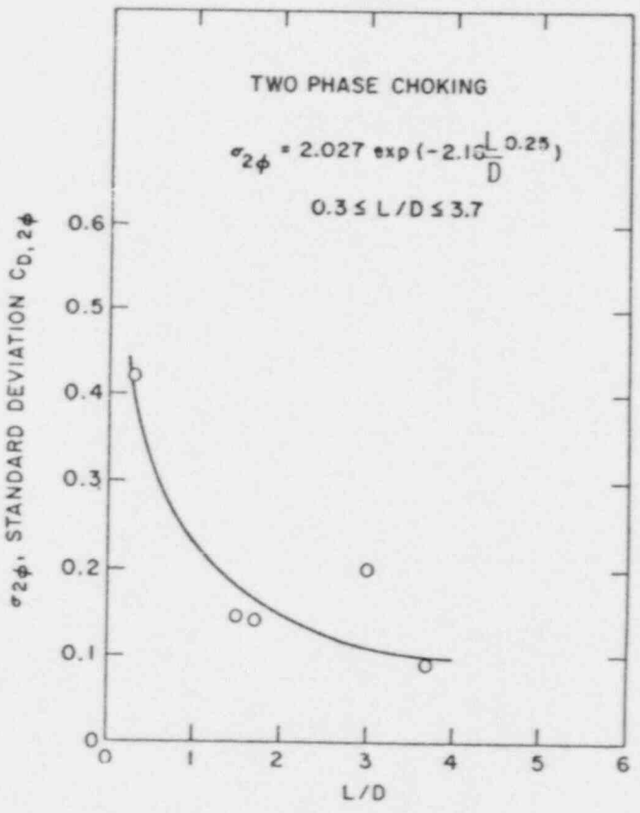

Figure 4 Standard Deviation of C_D as Function of L/D for Two-Phase Choking

flow after core flow reversal at the time of the pipe rupture. The flow into the downcomer and finally at the core inlet is a result of the competing influences of the vessel side cold leg break flow and intact loop cold leg flows into the downcomer due to the pumps in these loops. The core inlet flow is restored when the broken cold leg flow decreases below the total flow in the intact loops. The pump motor could be on or off depending upon the supply of AC power. In the case of loss of AC power, the pump will start to coast down. However, the pump has enough stored kinetic energy that it continues to transfer energy to the fluid, although at a decreasing rate. During the early part of the transient (up to first peak) the intact loop pump flows are close to single-phase flows and there will be no appreciable degradation in the pump performance. The situation changes as the transient proceeds; the primary system will have more voids leading to two phase flow through the pump and corresponding performance degradation.

3.1 Pump Model in TRAC

TRAC-PF1/MOD1 has a pump model [2] which is based on the model developed by Idaho National Engineering Laboratory (INEL) from the Semi-Scale test data. The model is general enough to apply to any other pump for which single phase homologous curves, two-phase fully degraded homologous curves and degradation multipliers as a function of void fraction (α) are available for the head and torque. The head across the pump is computed as follows:

$$H_{2\phi} = H_{1\phi} + M(\alpha)\,(H_{DEGRAD} - H_{1\phi}) \tag{3.1}$$

where $H_{2\phi}$, $H_{1\phi}$, H_{DEGRAD}, $M(\alpha)$ are two phase head, single phase head, fully degraded head and degradation multiplier respectively. The last three items in this list have to be supplied through input. The $M(\alpha)$ function is an interpolating function for interpolating between the single-phase head curve and the fully degraded or lowest two-phase head curve. The static pressure rise across the pump can be computed from the head, $H_{2\phi}$, and inlet density, ρ, as given here:

$$\Delta P = H_{2\phi}\rho_{in} \tag{3.2}$$

The head curves in the model are in the form of homologous curves with homologous variables as defined here:

$$(H/H_{ref})/(Q/Q_{ref})^2 \text{ vs. } (\Omega/\Omega_{ref})/(Q/Q_{ref}),\ (\Omega/\Omega_{ref})/(Q/Q_{ref}) \leq 1.0$$

$$(H/H_{ref})/(\Omega/\Omega_{ref})^2 \text{ vs. } (Q/Q_{ref})/(\Omega/\Omega_{ref}),\ (Q/Q_{ref})/(\Omega/\Omega_{ref}) \leq 1.0$$

A similar description is available for estimating the hydraulic torque for the pump and is given here:

$$T_{2\phi} = T_{1\phi} + N(\alpha)\,(T_{DEGRAD} - T_{1\phi}) \tag{3.3}$$

where $T_{2\phi}$, $T_{1\phi}$, T_{DEGRAD} and $N(\alpha)$ are two-phase, single-phase, two-phase fully degraded torques and torque degradation multiplier. $T_{1\phi}$ and T_{DEGRAD} are supplied through input tables or homologous curves. The homologous curves for torque are of the following form:

$$\beta = T/T_{ref}$$

$$\beta/(Q/Q_{ref}) \quad vs. \quad (\Omega/\Omega_{ref})/(Q/Q_{ref}),\ (\Omega/\Omega_{ref})/(Q/Q_{ref}) < 1.0$$

$$\beta/(\Omega/\Omega_{ref}) \quad vs. \quad (Q/Q_{ref})/(\Omega/\Omega_{ref}),\ (Q/Q_{ref})/(\Omega/\Omega_{ref}) \leq 1.0$$

The single-phase torque estimated from the homologous curves is corrected for the density if that is different from the rated density:

$$T = T_{ref}\ (\rho/\rho_{ref})\ (\beta)$$

The torque obtained from the homologous curves is used to compute the pump speed in case of loss of AC power.

The TRAC-PF1/MOD1 pump model is very simple and requires most of the information through the input. However, this model does not allow for the effect of many important parameters. In general the pump head for two phase flow is a function of the following variables:

$$H_{2\phi} = H_{2\phi}\ (Q/Q_{ref},\ \Omega/\Omega_{ref},\ \alpha,\ P,\ N_s,\ Geom)$$

where P, and N_S are pressure and pump specific speed.

Figure 5 shows homologous head curves as a function of void fraction for various pumps of different specific speeds and sizes at the rated condition of flow and speed. It can be seen from this figure that there is a significant effect of pump design. The RS111 pump, which has the highest specific speed and is closer to the axial flow pump design, undergoes the least degradation. However, the effect of the specific speed and geometry can be eliminated from the expression for the head if the data are available for the right type of pump:

$$H_{2\phi} = H_{2\phi}\ (Q/Q_{ref},\ \Omega/\Omega_{ref},\ \alpha,\ P)$$

The TRAC-PF1/MOD1 pump model also does not account for pressure effects. Figure 6 shows the effect of pressure on degradation for CE pump [17]. It is clear from this figure that degradation increases at low pressures.

The TRAC-PF1/MOD1 model as described earlier interpolates between single phase head curve and corresponding fully degraded head curve through a degradation multiplier which is only a function of void fraction. It has been observed that [18] the same degradation multiplier function cannot be used for all flows and the lack of accounting for all the influences in the model will lead to a larger uncertainty in the model.

In summary, the current TRAC model for reactor coolant pumps cannot account for effects of inlet pressure, specific pump speed and pump size.

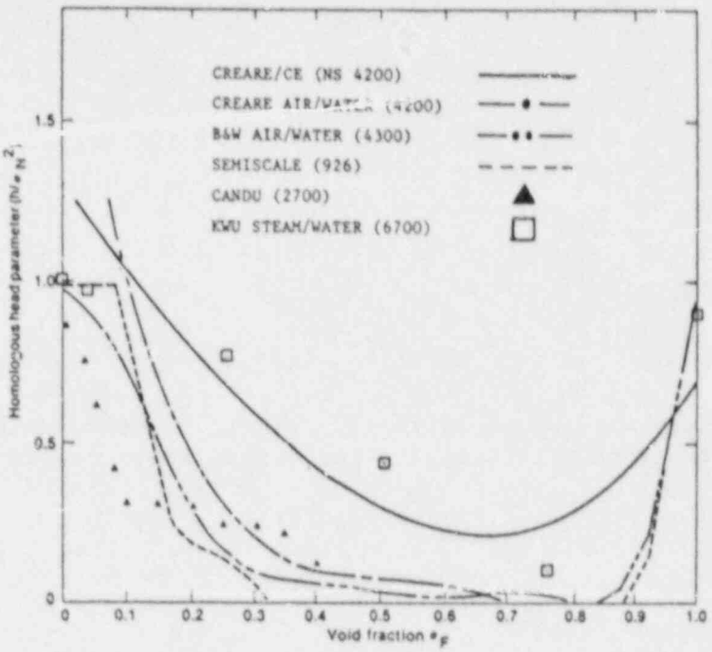

Figure 5 Comparison of Two-Phase Head for Various Pumps at Their Design Conditions

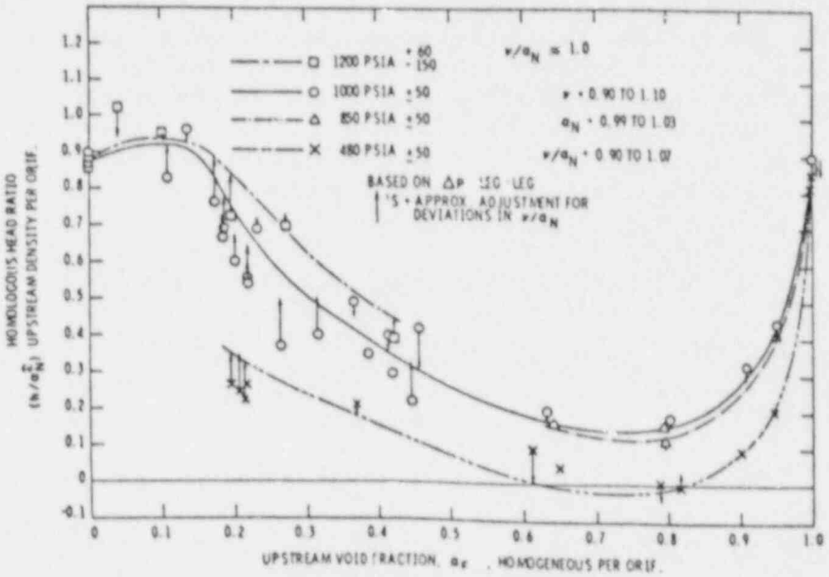

Figure 6 Effect of System Pressure on Two-Phase Flow Performance of CE Pump

3.2 Purpose of Pump Model Evaluation

The objective of this study is to provide single-phase and fully degraded two-phase homologous curves and the degradation multipliers for head and torque for the Westinghouse full-size pump (specific speed 5200 rpm $(gpm)^{0.5}/(ft)^{0.75}$) and their uncertainties as required for assessing the TRAC-PF1/MOD1 pump model.

3.3 Analysis

The single phase performance curves for the head and the torque for full size pumps or equivalent (same specific speed) small scale pumps are known with good accuracy (<2%). Also for pumps with the same specific speed, the effect of the size is negligible and the single phase curves from smaller size pumps could be used for larger size pumps. However, the two phase performance curves are dependent on many flow parameters and size. A model in the framework of TRAC-PF1/MOD1 does not account for all these variables adequately. Therefore, it leads to large uncertainties in the calculated results. All these uncertainties will be lumped in the degradation multipliers.

3.3.1 Available Pump Models

There are two semi-empirical models available in the literature; the EPRI model and the KWU model. The EPRI model [19] consists of a set of two-phase flow balance equations written in rotating coordinates for the impeller. The model uses available constitutive relationships for interfacial mass and momentum transfer, which were developed for the pipe flow. The model predicts the pump performance for various fluid conditions and pump speeds, but only near the design conditions for flow rate and pump speed. The EPRI model [19] has been applied to a variety of pumps and some of the predictions are shown in Figures 7 and 8 for CREARE and C-E pumps. There is a large spread in the experimental data for void fractions below 0.5. However, the EPRI model predicts the trends for head degradation correctly.

The EPRI model can be used to assess the uncertainty in the TRAC pump model by predicting the pump performance for various possible combinations of fluid and pump conditions. Each calculation provides one data set for checking out the TRAC-PF1/MOD1 pump model. The difference between the EPRI and TRAC models will be due to the uncertainties in the constitutive relationships used in the EPRI model and also due to the inability of properly accounting for pressure, flow rates and pump speed in TRAC. The difficulty in this approach is that it requires pump design data which are proprietary and generally not available.

The second semi-empirical model is the KWU model [18] which was developed for the Federal Ministry for Research and Technology, West Germany. Unlike the EPRI model, the KWU model does not imply integration of balance equations along the rotor channel, but does account for the important phenomena which cause the performance degradation. The model generates the degradation functions in terms of non-dimensional groups, using test data. The data are generally available only for small-scale pumps. The model has the potential to predict the performance of PWR pumps from subscale data. However, the KWU model does not account for condensation in the impeller, and there is some uncertainty about the allocation of head degradation among the three phenomena

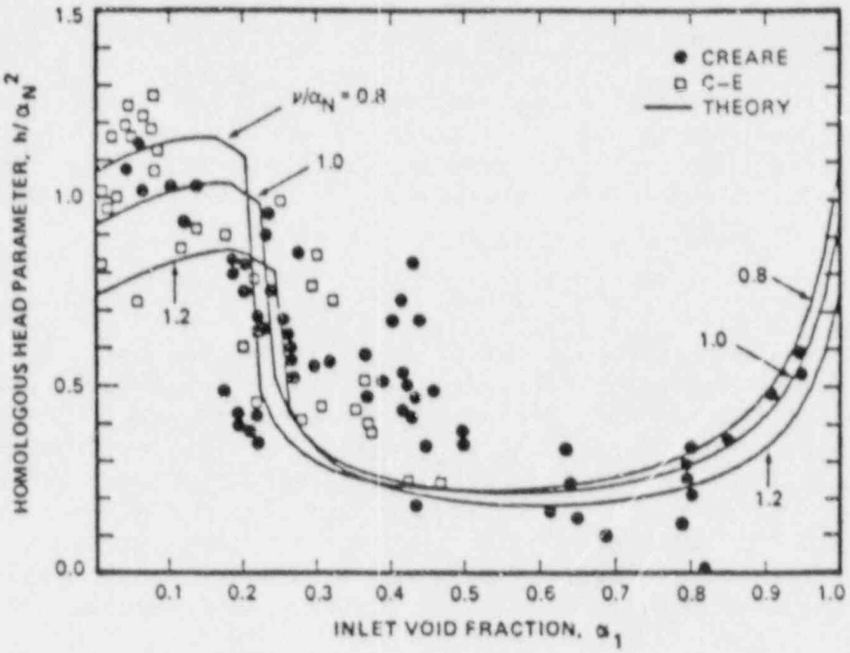

Figure 7 Comparison of the Head between the Theory and Experimental Data for a Mixed-Flow Pump for υ/α_N between 0.8 and 1.2 (steam/water case) (Furuya, 1987)

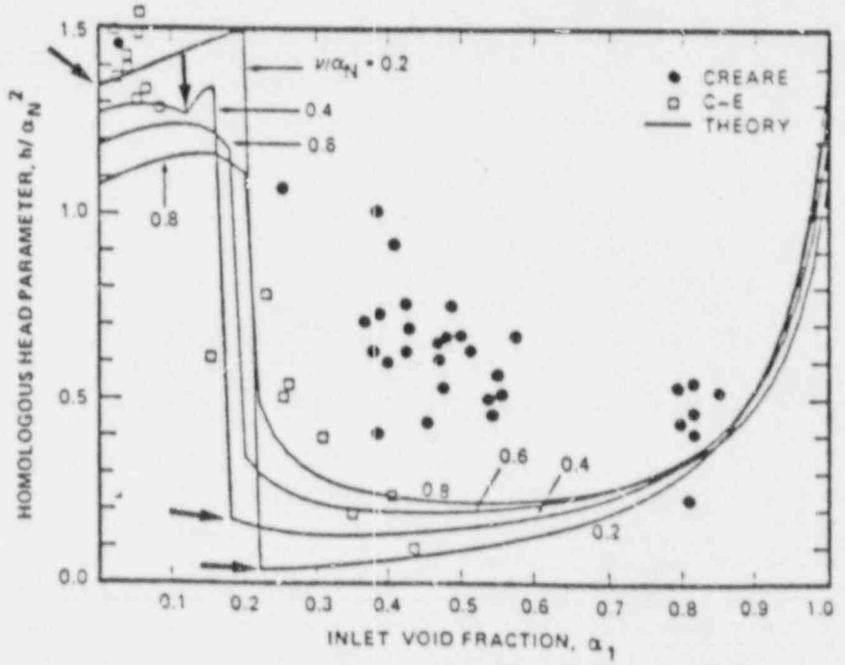

Figure 8 Comparison of the Head between the Theory with Inlet Pressure Variation and Experimental Data for Mixed-Flow Pump for υ/α_N between 0.0 and 0.8 (steam/water case) (Furuya, 1987)

of slip, phase separation and compressibility. This model is simple and requires only impeller diameter and the test data from subscale pumps.

The KWU model application requires test data directly in developing the TRAC-PF1 model parameters. The TRAC uncertainty will still be there because there is no accounting for pressure, flow rate and pump speed in the TRAC model. This resulting TRAC code uncertainty is reflected in the large spread of the computed degradation multipliers which are only functions of inlet void fraction.

There is an additional uncertainty as the test data are only available for small size pumps at specific pump speeds which differ from that of the full-scale PWR pump. Table 2 summarizes all the data available. There are two possible approaches to develop the KWU model; use the CE (1/5 scale, N_s = 4200) and KWU (1/5 scale, N_s = 6700) data to bracket the Westinghouse pump (N_s = 5200), or use the Westinghouse proprietary pump (1/3 scale, N_s = 5200) data directly. It was decided to follow the latter approach, as it produced data for the largest test pump available and at the correct specific speed. However, the data were taken at low pressure and some for air-water mixture, which implies that a model developed from these data will overpredict the degradation for PWR LBLOCA conditions and will be conservative.

3.3.2 Pump Model for TRAC Code Assessment

The model developed from the Westinghouse data consisted of single phase and fully degraded homologous curves for head and torque and, the mean value and the standard deviation of degradation multipliers.

The model developed from the Westinghouse pump data is for the correct specific speed, but it needs a correction for the size effect, before it can accurately represent the full size pump. In order to estimate the size effect, the data from CE (1/5 scale) [17] and CREARE (1/20 scale) [20] pumps were analyzed in the range of $0.0 \leq (Q/Q_R)/(N/N_R) \leq 2.0$. Here Q and N designate volumetric flow rate and rotational pump speed, respectively. Subscript R denotes the normal operating conditions (design conditions). In order to minimize the uncertainty in determining the size effect, the data were grouped in the increment of 0.25 for $(Q/Q_R)/(N/N_R)$. For each of these groups, least-square fit curves for $(H/H_R)/(N/N_R)^2$ or $(H/H_R)/(Q/Q_R)^2$ were obtained as a function of void fraction, for both the CE and CREARE pumps, as shown in Figures 9 through 12. The R value in these figures is the root-mean square value of the differences between the data and the best-fit curve. The number of data points considered in each curve fit are given in the bracket (#). The root mean square averages of the difference between the two curves for each group of $(Q/Q_R)/(N/N_R)$ were also obtained and the conclusion from these numbers is that the size effect is smallest near the design conditions ($(Q/Q_R)/(N/N_R)$ = 1.0), and that the larger pump degrades less. The difference between the curves would be less if CREARE data were available at the same higher pressure as CE data.

The CE and CREARE pump data were further analyzed by obtaining mean degradation functions which are shown in Figure 13. The CREARE data are available only for void fractions less than 0.5. This figure reconfirms our earlier conclusion that the larger size pump degrades less. Furthermore, it can also be hypothesized that the effect of size will be less for larger pumps

TABLE 2

RATED PUMP PARAMETERS AND OPERATING CONDITIONS AT FULL-SCALE AND IN VARIOUS TEST PROGRAMS

Parameter	Westinghouse PWR	PWR Primary Coolant Pump (Bingham-Williamette)	PWR Primary Coolant Pump (Byron-Jackson)	Westinghouse Pump	B&W Pump	C-E Pump	Creare Pumps	KWU Pump
Scale	1/1	1/1	1/1	1/3	1/3 of Bingham-Williamette Pump	1/5 of Byron Jackson Pump	1/20 of Byron-Jackson Pump	1/5, RS111
Rated Volumetric Flow Rate (gpm)	94,600	104,200	87,000	6210	11,200	3500	181 (219)	3148
Rated Total Head (ft)	290	397	252	64.4	390	252	252	293.7
Rated Speed (rpm)	1190	1190	900	1500	3580	4500	18,000	8480
Specific Speed rpm $(gpm)^{0.5}/(ft)^{0.75}$	5200	4319	4200	5190	4317	4200	4200	6700
Fluid*	S/W	S/W	S/W	A/W & S/W	A/W	S/W	A/W and S/W	S/W
Pressure (psia)	15-2250	15-2250	15-2250	15-420	20-120	15-1250	A/W at 90 S/W at 400	435-1305

* A/W is air/water mixture
S/W is steam/water mixture

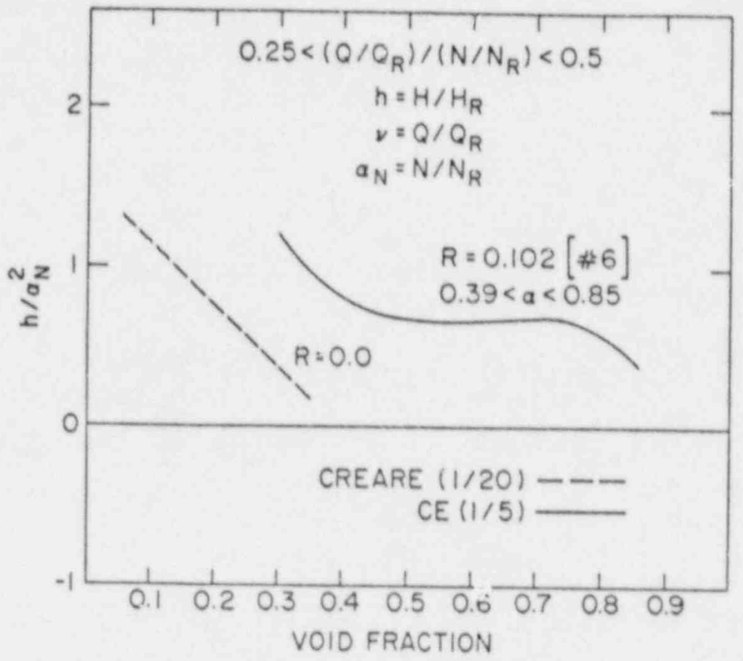

Figure 9 Comparison of CE and CREARE Pump Performance for $0.25 < (Q/Q_{ref})/(N/N_R) < 0.5$

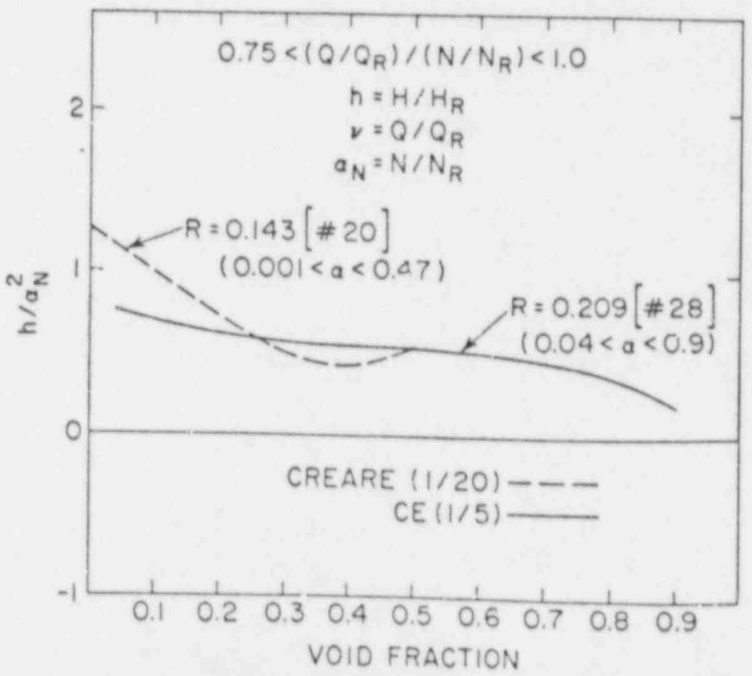

Figure 10 Comparison of CE and CREARE Pump Performance for $0.75 < (Q/Q_R)/(N/N_R) < 1.0$

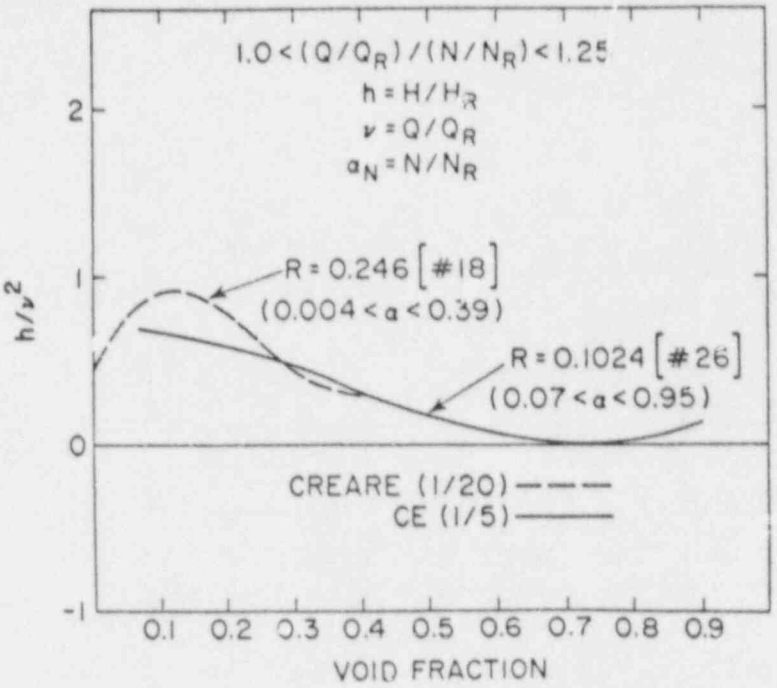

Figure 11 Comparison of CE and CREARE Pump Performance for $1.0 < (Q/Q_R)/(N/N_R) < 1.25$

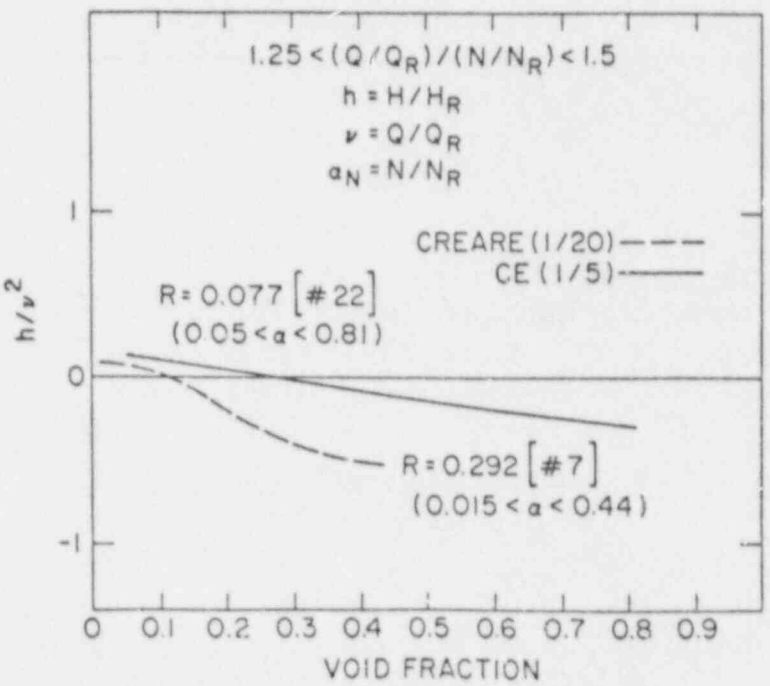

Figure 12 Comparison of CE and CREARE Pump Performance for $1.25 < (Q/Q_R)/(N/N_R) < 1.5$

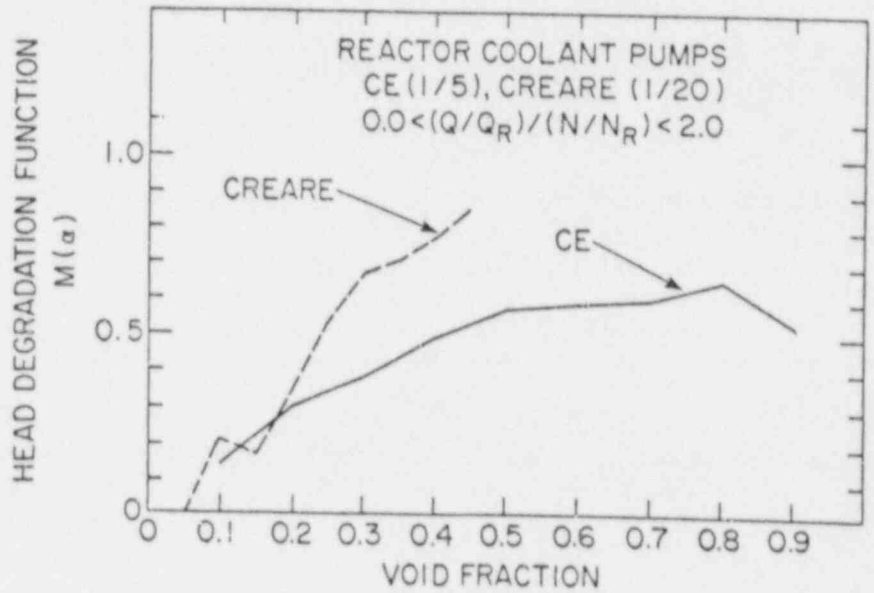

Figure 13 Comparison of Head Degradation Functions Developed from CREARE and CE Pump Data

because the length scale of two-phase flow structure will be much smaller than the pump dimensions. There is a definite lack of data at proper pressures and void fractions to make a quantitative estimate of the size effects to correct the model developed from the Westinghouse data.

A recent study was performed by Fujie and Yamanouchi [21], to investigate the similarity rules applicable to two phase flow through centrifugal pumps. They studied the flow regime transitions and the interfacial transfer functions in the blade channels. They concluded that for flow conditions near the design point, the single phase similarity laws also apply to two phase flows. This conclusion also agrees with the conclusion arrived at in the present study, namely that the effect of the pump size on the two-phase pump degradation decreases near the design conditions for similar pumps.

Based on the argument presented so far, it can be concluded that the pump model along with the uncertainties developed from the Westinghouse pump (1/3 scale) data can be used to represent the full-size pump and that the lack of correction for the size effect and pressure will tend to predict earlier pump degradation and higher peak clad temperature in LBLOCA.

3.4 Conclusions

A pump model and its uncertainties in the framework of TRAC-PF1/MOD1 were developed from the Westinghouse pump data (1/3). It was also shown that larger pumps will degrade less and that the model developed from low pressure data will over-predict pump degradation. The model developed here will predict early degradation for the pump in LBLOCA which will affect the thermal-hydraulic calculations for the reactor towards estimating higher peak clad temperatures.

A more realistic pump model is needed than the current TRAC pump model, which properly accounts for pressure, flow rate, pump speed and the pump size. The inability to account for these parameters is the largest contributor to the TRAC model uncertainty. There are data available for full-scale CANDU pumps and smaller scale KWU pumps (1/5 scale) which should be utilized. Furthermore, the EPRI model [19] and KWU semi-empirical [18] model should be utilized. The current TRAC model also does not account for the energy transfer from the impeller to the fluid in the energy equation and it assumes homogeneous fluid conditions at the pump discharge. These two model weaknesses should also be resolved.

4. ACKNOWLEDGEMENTS

The authors are grateful to Dr. Wolfgang Wulff for his very constructive suggestions during this work, and greatly appreciate the fine typing of Mrs. Linda Hanlon.

5. REFERENCES

1. Compendium of ECCS Research for Realistic LOCA Analysis, NUREG-1230, Chapter 4, April 1987.

2. Liles, D. R., et al., "TRAC-PF1/MOD1: An Advanced Best Estimate Computer Program for Pressurized Water Reactor Thermal-Hydraulics," NUREG/CR-3858, April 1987.

3. Jones, Jr., O. C., "Flashing Inception in Flowing Liquids," Brookhaven National Laboratory Report, BNL-NUREG-51221, 1980.

4. Abdollahian, D., "Critical Flow Data Review and Analysis," EPRI Report, NP-2192, January 1982.

5. "The Marviken Full Scale Critical Flow Tests, Results from Test 12," MXC-212, September 1979, Joint Reactor Safety Experiments in the Marviken Power Station, Sweden.

6. "The Marviken Full Scale Critical Flow Tests, Results from Test 13," MXC-213, September 1979, Joint Reactor Safety Experiments in the Marviken Power Station, Sweden.

7. "The Marviken Full Scale Critical Flow Tests, Results from Test 15," MXC-215, September 1979, Joint Reactor Safety Experiments in the Marviken Power Station, Sweden.

8. "The Marviken Full Scale Critical Flow Tests, Results from Test 16," MXC-216, September 1979, Joint Reactor Safety Experiments in the Marviken Power Station, Sweden.

9. "The Marviken Full Scale Critical Flow Tests, Results from Test 17," MXC-217, September 1979, Joint Reactor Safety Experiments in the Marviken Power Station, Sweden.

10. "The Marviken Full Scale Critical Flow Tests, Results from Test 18," MXC-218, September 1979, Joint Reactor Safety Experiments in the Marviken Power Station, Sweden.

11. "The Marviken Full Scale Critical Flow Tests, Results from Test 19," MXC-219, September 1979, Joint Reactor Safety Experiments in the Marviken Power Station, Sweden.

12. "The Marviken Full Scale Critical Flow Tests, Results from Test 20," MXC-220, September 1979, Joint Reactor Safety Experiments in the Marviken Power Station, Sweden.

13. "The Marviken Full Scale Critical Flow Tests, Results from Test 21," MXC-221, September 1979, Joint Reactor Safety Experiments in the Marviken Power Station, Sweden.

14. "The Marviken Full Scale Critical Flow Tests, Results from Test 22," MXC-222, September 1979, Joint Reactor Safety Experiments in the Marviken Power Station, Sweden.

15. "The Marviken Full Scale Critical Flow Tests, Results from Test 24," MXC-224, September 1979, Joint Reactor Safety Experiments in the Marviken Power Station, Sweden.

16. "The Marviken Full Scale Critical Flow Tests, Results from Test 25," MXC-225, September 1979, Joint Reactor Safety Experiments in the Marviken Power Station, Sweden.

17. Kennedy, W. C., et al., "Pump Two-Phase Performance Program," EPRI Reports, NP-1556 (Vol. 1-8), September 1980.

18. Seeberger, G. J. and Schneider, K., "Development of a Two-Phase Pump Model for the Main Coolant Pumps in Pressurized Water Reactors," Foreign Document I.D. R 917/85/003, NRC Translation 1821, May 1986.

19. Furuya, O. and Maekawa, S., "An Analytical Method for Prediction of Pump Performance Operating in Condensable Two-Phase Flows," Proc. of 1987 ASME/JSME Thermal Engineering Joint Conference, Hawaii, March 1987.

20. Swift, W. L., "Model Pump Performance Program - Data Report," EPRI NP-2379, May 1982.

21. Fujie, H. and Yamanouchi, A., "A Study on Applicability of Similarity Rule to Performances of Centrifugal Pumps Driven in Two-Phase Flow," Nuclear Engineering and Design, 85, 1985, pp. 345-352.

22. Ranson, V. H. "RELAP5/MOD 1 Manual, Volume 1: System Models and Numerical Methods," NUREG/CR-1826 (1981).

UNCERTAINTIES IN MODELING AND SCALING IN THE PREDICTION OF FUEL STORED ENERGY AND THERMAL RESPONSE*

by

Wolfgang Wulff
Department of Nuclear Energy
Brookhaven National Laboratory
Upton, New York USA 11973

Abstract

The steady-state temperature distribution and the stored energy in nuclear fuel elements are computed by analytical methods and used to rank, in the order of importance, the effects on stored energy from statistical uncertainties in modeling parameters, in boundary and in operating conditions. An integral technique is used to calculate the transient fuel temperature and to estimate the uncertainties in predicting the fuel thermal response and the peak clad temperature during a large-break loss of coolant accident.

The uncertainty analysis presented here is an important part of evaluating the applicability, the uncertainties and the scaling capabilities of computer codes for nuclear reactor safety analyses. The methods employed in this analysis merit general attention because of their simplicity.

It is shown that the blowdown peak is dominated by fuel stored energy alone or, equivalently, by linear heating rate. Gap conductance, peaking factors and fuel thermal conductivity are the three most important fuel modeling parameters affecting peak clad temperature uncertainty.

1. Introduction

Computer codes, such as TRAC-PF1 [1,2], play an important role in the assessment of nuclear reactor safety. The codes are used to predict many safety-related parameters during a variety of expected and postulated events, such as the peak clad temperature (PCT) during a large-break loss of coolant accident (LBLOCA). It is mandatory that reactor safety codes are quantitatively assessed concerning their applicability to a particular event, their ability to scale processes from test facility scales to full-scale power plants, and concerning their predictive uncertainties. The Nuclear Regulatory Commission has developed a new methodology for quantifying code uncertainties [3]. The analysis presented here is part of implementing this methodology, and of demonstrating its feasibility, for the TRAC-PF1/MOD1 computer code, as it is applied to LBLOCA analyses.

*Work performed under the auspices of the U.S. Nuclear Regulatory Commission.

The peak clad temperature (PCT) characterizes fuel integrity, i.e., the ability of the fuel cladding to retain fission products. Code uncertainties are quantified, therefore, on the basis of the code's ability to predict PCT accurately. During an LBLOCA, the clad temperature reaches, in general, two peaks; one during the earlier blowdown phase, the other one later, after the refill phase. Which one of the two peaks is higher depends on fuel design and coolant loop response characteristics. The clad temperature rises when the fuel element is suddenly surrounded by dry vapor. Then, more stored energy passes from the fuel pellets through the annular gas gap to the clad, then passes from the clad to the vapor, because the convective heat transfer is sharply reduced (dry-our or post-CHF*). The clad temperature reaches a peak when it decreases due to improved convective cooling after the arrival of liquid in the core or due to a decrease in pellet temperature. In either case, more heat is removed by convection from the clad than is supplied to the clad from the fuel pellet.

The PCT is the higher, the faster the clad temperature rises and the longer it rises. PCT uncertainty can therefore be decomposed into uncertainties of predicting the time rate of clad temperature rise and of predicting the time for liquid arrival in the core. The time rate of clad temperature change depends upon the energy initially stored in the fuel, primarily in the pellet, and upon the thermal response time of the fuel. The initially stored energy depends strongly on fuel parameters and on initial conditions. The thermal response of the fuel depends both on fuel parameters and on coolant conditions. The time for the reappearance of liquid in the core is dominated by break and pump flow characteristics for the first peak and by additional thermohydraulic loop phenomena for the second peak.

Thus, the energy stored initially in the fuel and the thermal response time of the fuel are key parameters affecting PCT. In fact, they will be shown to dominate PCT under the most plausible circumstances.

1.1 Purpose

The objective of the work presented here is to calculate the individual changes in initial fuel stored energy, associated with the known statistical uncertainties in input data specifications and with documented uncertainties of modeling fuel heat transfer in TRAC-PF1/MOD1. Specifically, the fuel stored energy variations are to be calculated for given 1σ-level uncertainties of:

(i) initial fission power,
(ii) local power peaking factors,
(iii) fuel thermal conductivity,
(iv) cladding thermal conductivity,
(v) gap conductance,
(vi) fuel heat capacity,
(vii) cladding heat capacity,
(viii) radial fission power distribution in pellet, and
(ix) convective film coefficient.

It is also the objective of the work presented here to calculate the variations of the peak clad temperature for the early or blowdown peak as they

*CHF stands for critical heat flux.

are caused by the uncertainties in the above nine parameters. The analysis is general in principle but evaluated for specific LBLOCA conditions in a Westinghouse plant with 17x17 fuel arrays. The analysis is evaluated for TRAC-PF1/MOD1 models and for reference conditions as computed by TRAC.

The effects from the above statistical uncertainties are to be ranked in the order of their relative importance on peak clad temperature predictions.

1.2 Approach

The energy stored in fuel pellet and clad is computed by integrating the steady-state temperature distributions in fuel pellet and clad. The temperature distributions are obtained by closed-form integration of the steady-state conduction equation, taking into account the temperature variation of thermal conductivities and the radial variation of fission power in the pellet. This is shown in Chapter 2 below.

An integral technique [4] is used to convert the partial differential equations of transient heat conduction in fuel pellet and clad into two ordinary differential equations for the volume-averaged temperatures in fuel pellet and clad [5]. The ordinary differential equations are numerically integrated to obtain the transient clad temperature under prescribed conditions for the coolant and for the fission power. The calculations are repeated, while changing the previously listed parameters by their respective 1σ-level uncertainties, to obtain the resultant changes in PCT. This is shown in Chapter 3 below.

2. Steady-State Analysis for Fuel Stored Energy

2.1 Problem Description

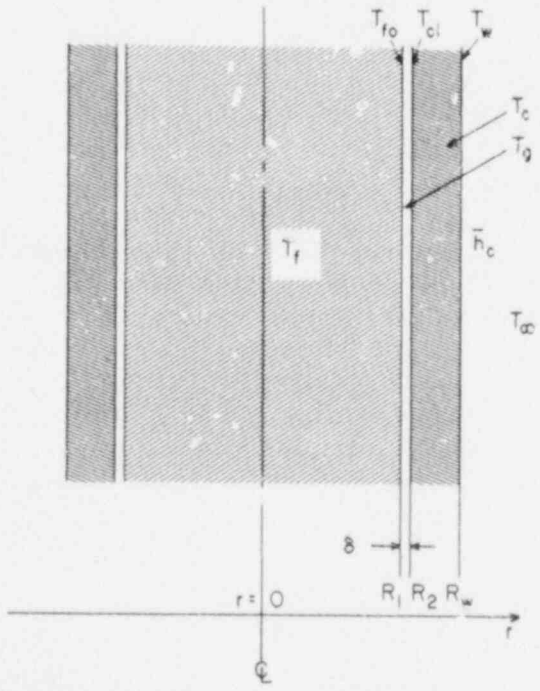

Figure 1 Geometry and Temperatures for Fuel Element

In order to compute the energy E stored in the fuel and in the clad, we determine first the temperature distributions $T_f(r)$, $0 \leq r \leq R_1$ and $T_c(r)$, $R_2 \leq r \leq R_w$ for the fuel and clad, respectively. Consider the right circular fuel pellet with the concentric clad, forming an annular gap of width δ, as shown in Figure 1.

We analyze steady radial conduction in pellet and in clad, convection and radiation between pellet and cladding, and convection between clad and the coolant at the known temperature T_∞. The convective heat transfer coefficient $\bar{h}_c$ is also known from hydraulics calculations.

The radii are computed from known specifications for cold conditions and from correlations for thermal expansion [6, p. 48d and p. 240]. Accordingly,

for the fuel pellet (UO_2), the relative radial expansion is

$$\Delta R_f/R_{of} = K_1(\langle T_f\rangle_f - T_o) + K_2 e^{-E_d/(k\langle T_f\rangle_f)} , \qquad (1)$$

where $\Delta R_f = R_1 - R_{of}$, radial pellet expansion
R_{of} = radius of cold pellet, at T_o
$K_1 = 1.0 \times 10^{-5}\ K^{-1}$ (linear expansion coefficient [7])
$K_2 = 4.0 \times 10^{-2}$
$T_o = 300$ K
$\langle T_f\rangle_f$ = area-averaged pellet temperature (see Ref. [7])
$E_d = 6.9 \times 10^{-20}$ J
$k = 1.38 \times 10^{-23}$ J/K ,

while for the cladding (zircaloy-2), the relative radial expansion is

$$\Delta R_c/R_{oc} = (6.72 \times 10^{-6})(\langle T_c\rangle_c - T_o) , \qquad (2)$$

where ΔR_c = expansion of inner or outer clad radii
R_{oc} = corresponding cold clad radii
$\langle T_c\rangle_c$ = area-averaged clad temperature.

The area averages in Eqs. (1) and (2) are defined as

$$\langle T_f\rangle_f = \frac{2}{R_{fo}^2}\int_o^{R_{fo}} T_f\, r\,dr \quad \text{and} \quad \langle T_c\rangle_c = \frac{2}{R_w^2 - R_{ci}^2}\int_{R_{ci}}^{R_w} T_c\, r\,dr , \qquad (3)$$

where R_{fo} = outer pellet radius
R_{ci} = inner clad radius
R_w = outer clad radius.

The equations in Reference [6] contain an additional constant each, from which the reference temperatures T_o in Eqs. (1) and (2) above have been inferred.

The steady-state temperature distributions are derived from the nonlinear conduction equation with temperature-dependent thermal conductivities. The gap conductance for the annular gap between pellet and clad is computed with temperature-dependent thermal conductivity for the helium fill gas, and with temperature-dependent radiative surface properties for pellet and clad.

Calculations of the stored energy take into account the variation of specific heat with temperature.

2.2 Thermal Conductivities and Radiative Emissivities

The temperature dependence of thermal conductivity k_f for UO_2 pellets is given in Reference [6, p. 23]. After the correction of typographical errors

in this reference, one finds for the range of temperatures encountered during normal operating conditions, that

$$k_f = \frac{D \cdot (1\ \mathrm{Wm^{-1}\,K})}{1+(6.5-4.69\times10^{-3}\mathrm{K^{-1}}\cdot T_f)(1-D)} \cdot \frac{c_v(T_f)\cdot(1\ \mathrm{kg\ m^{-1}s^{-1}})}{(0.339+0.06867\mathrm{K^{-1}}\cdot T_f)(1+3\Delta R_f/R_{of})}$$

$$+ 5.2997\times10^{-3}\ \mathrm{Wm^{-1}K^{-2}} \cdot T_f \cdot e^{-K_5/T_f}\left[1+\left(2+0.169\,\frac{K_5}{T_f}\right)^2\right], \qquad (4)$$

where D = fraction of theoretical density
T_f = fuel pellet temperature
c_v = fuel specific heat at constant volume for pellet
$\Delta R_f/R_{of}$ = thermal strain, Eq. (1) evaluated with T_f
K_5 = 13,358 K.

The specific heat c_v is found in Reference [6, p. 23]. For UO_2 pellets without plutonium, it is

$$c_v = 296.7\ \mathrm{J/(kgK)}\,x^2 e^x/(e^x-1)^2, \qquad (5)$$

where $x = 535.285\ \mathrm{K}/T_f$
T_f = fuel pellet temperature

Equation (4) is used in conjunction with Eqs. (1) and (5) to compute the fuel pellet thermal conductivity $(k_f)_{ref}$ for a reference temperature $(T_f)_{ref}$. For closed-form integration, the variation of thermal conductivity with temperature is then approximated by fitting results from Eq. (4), calculated in the temperature range $547\mathrm{K} \leq T \leq 1{,}330\mathrm{K}$ to an expression of this form:

$$k_f(T_f) = (k_f)_{ref}\left[\frac{T_f}{(T_f)_{ref}}\right]^{b_f}, \qquad (6)$$

where $(k_f)_{ref}$ = reference thermal conductivity, computed from Eq. (4)
b_f = 0.762 303

The maximum error of the curve fit in the above temperature range is $0.018\ \mathrm{Wm^{-1}\,k^{-1}}$ or 0.6%; the coefficient of determination is $r_d^2 = 0.999\,86$. The error of Eq. (6) is even less because $(k_f)_{ref}$ is exact, and the range of temperatures in the pellet is smaller than the range of the curve fit.

The temperature dependence of thermal conductivity k_c for zircaloy-2 cladding is given in Reference [6, p. 217] as

$$k_c = [7.51+(0.0209\ K^{-1})T - (1.45\times10^{-5}\ K^{-2})T^2 + (7.67\times10^{-9}\ K^{-3})T^3]Wm^{-1}\ K^{-1}\ . \tag{7}$$

Equation (7) is used to compute the thermal conductivity $(k_c)_{ref}$ of the clad at a reference temperature while the variation of thermal conductivity within the clad is taken to have the more convenient form

$$k_c = (k_c)_{ref} e^{b_c T}\ , \tag{8}$$

where $b_c = -7.71233\times10^{-4}\ K^{-1}$.

Equation (8) is suitable for closed form integration. It introduces an error of less than 0.3% and fits the results of Eq. (7) with the coefficient of determination, $r_d^2 = 0.9961$.

The thermal conductivity k_g of the fill gas in the gas gap between fuel pellet and cladding is needed for calculating the gap conductance. The calculations are performed here for helium gas. Reference [6, p. 485] gives for pure helium

$$k_g(\overline{T}) = A\left(\frac{\overline{T}}{1K}\right)^B\ , \tag{9}$$

where $\overline{T} = (T_{fo}+T_{ci})/2$, average gas temperature
T_{fo} = outer fuel pellet temperature
T_{ci} = inner clad temperature
$A = 2.639\times10^{-3}\ Wm^{-1}\ K^{-1}$
$B = 0.7085$.

Radiative emissitivies are also needed to compute the gap conductance. The emissivity for UO_2 pellets is found in Ref. [6, p.48] to be

$$\varepsilon_f = c_1 + c_2 T_{fo}\ , \tag{10}$$

where $c_1 = 0.7856$
$c_2 = 1.5263\times10^{-5}\ K^{-1}$,

while the emissivity of zircaloy-2 without oxide layer is, from Ref. [6, p. 250], a constant:

$$\varepsilon_c = 0.9151\ . \tag{11}$$

This completes the definition of all temperature-dependent properties required for computing the steady-state temperature distribution in fuel elements.

2.3 Fission Power Variation

The fission power varies radially within the pellet due to neutron flux depression. The variation increases with burnup. With the objectives in mind of assessing TRAC code uncertainties, the fuel conditions presented here are those used in the reference TRAC calculation.

The fission power varies radially in accordance with [5, Eq. 114]

$$q_f'''(\xi) = \frac{n+2}{n+2(1+m)} \langle q_f''' \rangle_f [1 + m\xi^n] \tag{12}$$

where q_f''' = local volumetric fission power density
$\langle q_f''' \rangle_f$ = area-averaged fission power density (see Eq. 3 for definition of $\langle \ \rangle_f$ operator)
ξ = r/R_1, normalized radius
R_1 = outer fuel pellet radius
r = radial coordinate
m,n = constants.

The form of Eq. (12) constitutes also the best type for fitting Westinghouse data as used in TRAC. The first coefficient on the right-hand side of Eq. (12) is needed to assure that averaging of Eq. (12) reduces to an identity. The coefficients m and n vary in the ranges of $0 \leq m \leq 3$ and $2 \leq n \leq 4$. Specified Westinghouse data require $m = 0.403$ and $n = 3.917$. This means that the fission power density is greater around the periphery of the pellet and that the temperature is more uniform than for constant fission power density.

2.4 Governing Equations for Steady Conduction

The combination of energy balance and Fourier's conduction law gives

$$\nabla \cdot (k \nabla T) + q''' = 0 , \tag{13}$$

where all symbols have been defined previously. Since k depends on temperature, one introduces a new temperature θ via the Kirchhoff transformation [8]

$$\theta = \frac{1}{k_{ref}} \int_{T_{ref}}^{T} k(T)dT , \tag{14}$$

where $k_{ref} = k(T_{ref})$ and T_{ref} is a known reference temperature. After substituting Eq. (14) into Eq. (13), one obtains this equation

$$k_{ref} \nabla^2 \theta + q'''(r) = 0 \tag{15}$$

which is linear and easy to integrate. Substitution of Eq. (6) into Eq. (14) gives for the fuel pellet temperature

$$T_f = (T_f)_{ref}\left[1 + \frac{b+1}{(T_f)_{ref}}\theta_f\right]^{\frac{1}{b+1}} , \tag{16}$$

where θ_f is the transformed fuel pellet temperature. Similarly, substituting Eq. (8) into Eq. (14) and solving for the cladding temperature, T_c, yields

$$T_c - (T_c)_{ref} = \frac{1}{b_c} \ln(1+b_c\theta_c) , \tag{17}$$

where θ_c is the transformed cladding temperature.

Equation (15) is written for radial conductance in the fuel pellet to give, in terms of the normalized radius $\xi_f = r/R_1$,

$$(k_f)_{ref} \frac{1}{\xi_f} \frac{d}{d\xi_f}\left(\xi_f \frac{d\theta_f}{d\xi_f}\right) + R_1^2 q_f'''(\xi_f) = 0 , \tag{18}$$

where R_1 is the outer radius of the pellet. Equation (12) defines $q_f'''(\xi_f)$ The appropriate boundary conditions for the fuel pellet are

$$\begin{aligned} &\text{at} \quad \xi_f = 0 \qquad d\theta_f/d\xi_f = 0 \\ &\text{at} \quad \xi_f = 1 \qquad \theta_f = 0 . \end{aligned} \tag{19}$$

From the last condition follows, by virtue of Eq. (14), that

$$(T_f)_{ref} = T_f(R_1) = T_{fo} \quad \text{and} \tag{20}$$

$$(k_f)_{ref} = k_f(T_{fo}) \tag{21}$$

Equation (15) reduces for the cladding to

$$\frac{1}{r} \frac{d}{dr}\left(r \frac{d\theta_c}{dr}\right) = 0 , \tag{22}$$

since there is no heat absorption in the cladding. Equation (14) and the boundary conditions for Eq. (22) require that, at the outer clad radius, i.e., at $r = R_w$:

$$\theta_c = 0 \qquad \text{and} \tag{23}$$

$$-k_c(T_w)dT_c/dr = -(k_c)_{ref}d\theta_c/dr = R_1^2\langle q_f'''\rangle_f/(2R_w) \ . \tag{24}$$

Equation (23) implies, similarly to the last of Eqs. (19), that

$$(T_c)_{ref} = T_c(R_w) = T_w \qquad \text{and} \tag{25}$$

$$(k_c)_{ref} = k_c(T_w) \ , \tag{26}$$

whence, Eq. (24) reduces to

$$\frac{d\theta_c}{dr} = -R_1^2\langle q_f'''\rangle_f/[2R_w k_c(T_w)] \ . \tag{27}$$

Equations (18) and (19) and Eqs. (22), (23) and (27) define, via Eqs. (16) and (17), the temperature distributions in fuel pellet and cladding, provided the outer temperatures T_{fo} in Eq. (20) and T_w in Eq. (25) of pellet and clad are known. These two temperatures are determined from the conditions of heat flux continuity at the outer pellet surface. First, at $r = R_1$:

$$T_{fo} - T_{ci} = R_1^2\langle q_f'''\rangle_f/[\pi(R_1 + R_2)h_{gp}] \ , \tag{28}$$

where T_{ci} = inner clad surface temperature
R_1 = outer fuel pellet radius
R_2 = inner clad radius and
$h_{gp} = h_{gas} + h_{rad}$ (29)

The gap conductance h_{gp} has a contribution from the conductance h_{gas} through the gas and a radiative contribution h_{rad}. For the gas conductance

$$h_{gas} = \frac{k_g(\bar{T})}{t} \ , \tag{30}$$

where $k_g(\bar{T})$ was defined earlier in Eq. (9), and t is the effective gap width, taken here to be uniform around the circumference. According to Siefken et al. [9], the effective gap width is

$$t = \delta + 3.2(\beta_f + \beta_c) + g_f + g_c \ , \tag{31}$$

where δ = $R_2 - R_1$, physical gap width
β = surface roughness
g = temperature jump distance

and subscripts f and c designate fuel and clad, respectively. The gap width δ is computed from radial thermal expansions according to Eqs. (1) and (2). Surface roughness β is known from measurements. The temperature jump distance g can be computed from temperature accommodation coefficients [9, p. 18], but it is normally derived from experiments to obtain measured fuel pellet temperatures. For the present analysis, $g_f + g_c$ are taken to be the same as the specified TRAC values [1, p. 69] (cf. Sec. 2.6).

The radiative conductance is

$$h_{rad} = \sigma \frac{(T_{fo}^2 + T_{ci})^2 (T_{fo} + T_{ci})}{\frac{1}{\varepsilon_f} + \frac{R_1}{R_2}\left(\frac{1}{\varepsilon_c} - 1\right)} \ , \tag{32}$$

where σ = 5.6697×10^{-8} W m^{-2} K^{-4}
T_{fo} = pellet outer surface temperature
T_{ci} = clad inner surface temperature
R_1 = pellet radius
R_2 = inner clad radius,

and ε_f and ε_f are specified by Eqs. (10) and (11). Thus, Eqs. (28) through (32) determine the pellet outer temperature T_{fo}.

Finally, the outer clad temperature T_w is given in terms of known coolant temperature T_∞ and convective film coefficient $\bar{h}_c$, averaged over the circumference of the clad. The energy balance for pellet and clad yields at $r = R_w$:

$$2R_w \bar{h}_c (T_w - T_\infty) = R_1^2 \langle q_f''' \rangle_f \ , \tag{33}$$

where all symbols have been previously defined. Equations (18), (27) and (33) suggest the simplification

$$R_1^2 \langle q_f''' \rangle_f = q_f'/\pi \ , \tag{34}$$

where q_f' = linear rate of fission power.

The linear heating rate q_f' is independent of R_1 and remains, in contrast to $\langle q_f''' \rangle_f$, fixed during radial expansion of the pellet.

Equations (13) through (33) define the temperature distribution in the fuel element. Their solutions are presented below.

2.5 Steady-State Temperatures

2.5.1 The Cladding Temperature $T_c(r)$ is found by computing first the outer wall temperature from Eq. (33). With Eq. (34), one finds

$$T_w = T_\infty + q_f' / [2\pi R_w \bar{h}_c] . \tag{35}$$

With T_w known, one can now compute the thermal conductivity $k_c(T_w)$ for Eq. (26), integrate Eq. (22), subject to Eqs. (23) and (27), to obtain first the solution for $\theta_c(r)$ and then from Eq. (17)

$$T_c(r) - T_w = \frac{1}{b_c} \ell n \left[1 + \frac{b_c \, q_f'}{2\pi k_c(T_w)} \ell n \frac{R_w}{r} \right] , \tag{36}$$

where b_c is given below Eq. (8). Equation (36) must be evaluated for $r = R_2$ to give the inner clad temperature

$$T_{ci} = T_w + \frac{1}{b_c} \ell n \left[1 + \frac{b_c \, q_f'}{2\pi k_c(T_w)} \ell n \frac{R_w}{R_2} \right] . \tag{37}$$

2.5.2 The Temperature Difference Across the Gap is computed by combining Eqs. (28) through (32) with Eqs. (9) and (10) to get

$$Y(\eta) = C_1(\eta - 1) \left(\frac{\eta+1}{2} \right)^B + \frac{C_2(\eta^4 - 1)}{\phi_1 + (c_1 + C_3\eta)^{-1}} - \phi_o = 0 , \tag{38}$$

where
$\eta = T_{fo}/T_{ci}$
$C_1 = k_g(T_{ci})/t$
$C_2 = \sigma T_{ci}^3$
$C_3 = c_2 T_{ci}$
$\phi_o = q_f'/(2\pi R_1 T_{ci})$
$\phi_1 = (R_1/R_2)(1/\varepsilon_c - 1)$

and the constants B, c_1 and c_2 are defined below Eqs. (9) and (10). All other symbols have been previously defined. Equation (38) is readily solved by Newton-Raphson iteration:

$$\eta^{\mu+1} = \eta^{\mu} - Y(\eta^{\mu})/Y'(\eta^{\mu}) , \tag{39}$$

where $Y'(\eta^{\mu})$ is the derivative $dY/d\eta$, evaluated with the μ-th iterate η^{μ}. The iteration is started with $\eta^{o} = 1.1$. When two successive iterates differ by less than 10^{-6}, then η for $Y(\eta) = 0$ is found and

$$T_{fo} = \eta\, T_{ci} \tag{40}$$

gives the outer pellet temperature.

2.5.3 The Fuel Pellet Temperature is obtained by substituting Eq. (12) into Eq. (18) and by integrating Eq. (18), subject to Eqs. (19). The result is $\theta_f(\xi_f)$, which must be substituted into Eq. (16) to yield the fuel pellet temperature

$$T_f(\xi_f) = T_{fo}\{1 + \frac{b_f + 1}{4T_{fo}k_f(T_{fo})}[R_1^2(q_f''')_{c\ell}][1 + \frac{4m}{(n+2)^2} - \xi_f^2(1 + \frac{4m}{(n+2)}\xi_f^n)]\}^{1/(b_f+1)} . \tag{41}$$

Here, $(q_f''')_{c\ell}$ is the fission power density at the centerline and given from Eq. (12) as

$$R_1^2(q_f''')_{c\ell} = (n+2)q_f'/\{\pi[n+2(1+m)]\} . \tag{42}$$

All other symbols have been defined in conjunction with Eqs. (6) and (12). The thermal conductivity $k_f(T_{fo})$ is evaluated from Eqs. (4) and (5).

2.6 Comparison of Analysis with TRAC Results

Even though the focus of this paper is on fuel stored energy, the results obtained so far provide an important assessment on fuel element simulations in TRAC. A conclusive assessment of TRAC modeling requires the output listing of important intermediate results which are not available from TRAC. Such results include radial expansions, gap width, thermophysical properties and the precise axial locations associated with listed temperatures and heat transfer coefficients. The comparison between TRAC results and this analysis is therefore limited to the comparisons of thermal conductivity and of temperature distribution.

The TRAC document [1, p. 501] claims that the fuel thermal conductivity is computed in TRAC in accordance with Reference [6, p. 23], but it is not. Evaluating the expressions in the TRAC document [1, pp. 501 and 502] for a fuel with 95% of theoretical density, one obtains the comparison with the MATPRO formulation [6, p. 23] as shown in Table 1 below. Also shown are the

results of an extremely simple correlation given by Malang [10], which is not only better than the TRAC formulation, but also produces results which are closer to the experimental data than the results from MATPRO [11, p. 3-33]. Table 1 shows that the values calculated by TRAC are too low and should result in higher fuel temperatures than those obtained with the MATPRO values. It will be shown below that this is not the case.

Table 1 Comparison of TRAC and MATPRO Results for Thermal Conductivity

Temperature K	Thermal Conductivity W/(mK)		
	MATPRO	TRAC	MALANG
300	8.28	7.56	8.91
500	6.09	5.42	6.08
750	4.47	4.03	4.38
1,000	3.58	3.23	3.45
1,250	3.03	2.73	2.89
1,500	2.68	2.39	2.55

Equations (35), (37), (40) and (41) were used to calculate the fuel temperature distribution in that rod and at that location, where TRAC computed the largest clad temperature at full power and under steady-state conditions in a Westinghouse PWR with 17x17 fuel arrays. It was the intent to have, for the reference calculation, the same conditions as in the TRAC-PF1/MOD1 calculation. These conditions are as follows:

linear heating rate, nominal		18.303 kWm^{-1}
local radial peaking factor		1.111
local axial peaking factor		1.050
hot rod peaking factor		1.215
linear heating rate, effective	q'_f =	25.942 $kWm^{-2}K^{-1}$
convective heat transfer coefficient	$\bar{h}_c$ =	40.05 $kWm^{-2}K^{-1}$
coolant temperature	T_∞ =	599.44 K
pellet radius, cold	R_{of} =	4.0960 mm
gap width, cold		0.0380 mm
outer clad radius, cold		4.750 mm
pellet radius, @ full power	R_1 =	4.11994 mm
inner clad radius, Eq. (2)	R_2 =	4.14058 mm
outer clad radius, Eq. (2)	R_w =	4.75756 mm
clad thickness (hot)		0.616981 mm

Since the convective heat transfer in TRAC is computed with the cold-value of outer clad radius, the heat transfer coefficient $\bar{h}_c$ had to be adjusted so that $(\bar{h}_c)_{TRAC}(R_w)_{COLD} = \bar{h}_c \cdot R_w$. The effective gap width t in Eqs. (31) and (38) was computed to produce the same gap conductance as produced in the TRAC code: h_{gp} = 10.960 $kWm^{-2}K^{-1}$. This was achieved by using first from TRAC [1, p. 69] for Eq. (31)

$$3.2(\beta_f + B_c) + g_f + g_c = 0.0044 \text{ mm},$$

by computing the cladding radii R_w and R_2 from Eq. (2), and then by computing the gap width δ so as to produce the TRAC-computed gap conductance from Eq. (38). The result is

$$\delta = 0.020\,639 \text{ mm}.$$

After substituting this gap width from R_2, the radius R_1 as shown above was obtained. Had Eq. (1) been used to compute R_1, then the hot-condition gap width would have been 13.801 μm instead of 20.639 μm.*

All the expressions for thermophysical properties and Eqs. (35), (36), (38) and (39), (40) and (41) were executed on an HP-41/CX programmable pocket calculator. Table 2 below shows the comparison between the results from closed-form integrations and from TRAC.

Table 2. Comparison Between Closed-Form Integration and TRAC-PF1 Solutions

Location	Temperature (K)		
	Closed-Form Int.	TRAC	Difference
Fluid (T_∞)	599.440	599.440	
Outer Clad Surf. (T_w)	621.109	620.174	-0.94
Inner Clad Surf. (T_{ci})	654.932	654.08	-0.85
Pellet Surface (T_{fo})	746.368	746.295	-0.07
In Fuel Pellet at			
$r/R_1=\sqrt{3}/2$	868.137	867.944	-0.19
$\sqrt{2}/2$	999.148	996.880	-2.27
1/2	1,140.99	1,137.60	-3.39
0	1,296.16	1,290.75	-5.41

The comparison reveals that the TRAC-computed centerline temperature is too low, even though the surface temperatures have been made to agree fairly well and even though the thermal conductivity k_f of the fuel is too low in TRAC as discussed above. Since the centerline temperature increases by approximately 16.4 K for a reduction in fuel thermal conductivity by 0.1 W/(mK),

*The gap width in TRAC was, in fact, increased to obtain fuel stored energy as provided by Westinghouse.

and since, according to Table 1 above, the mean difference between MATPRO and TRAC values of thermal conductivity is -0.46 W/mK), it appears as if TRAC had a total computational error of $-(4.6 \cdot 16.4 + 5.2)\ K \cong -80\ K$ for the center line temperature. Notice that if TRAC accounts for fuel cracking or other phenomena which reduce the thermal conductivity but are not accounted for in the closed-form integration, then the deficit of the centerline temperature can only be larger.

2.7 Stored Energy

The thermal energy stored in fuel pellet and cladding is computed with respect to the energy at the coolant temperature T_∞. It is the sum of energies stored in fuel pellet and in cladding, namely

$$E = E_f + E_c \quad , \tag{43}$$

where

$$E_f = 2\pi \int_0^{R_1} \rho_f \int_{T_\infty}^{T_f(r)} \left[c_p(T)\right]_f \, dT \, r\,dr \tag{44}$$

$$E_c = 2\pi \int_{R_2}^{R_W} \rho_c \int_{T_\infty}^{T_c(r)} \left[c_p(T)\right]_c \, dT \, r\,dr \tag{45}$$

and

ρ_f = 10,011.5 kg/m^3, fuel density [10]*)

ρ_c = 6,487/5 kg/m^3, clad density [10]

c_p = specific heat at const. pressure.

Subscripts f and c designate fuel and clad, respectively.

The specific heat for UO_2 pellets is given in Reference [6, p. 9]. For the oxygen to metal ratio of 2 for UO_2, it is

$$\left[c_p(T)\right]_f = c_v + K_6 T + \frac{K_7 E_D}{\mathcal{R} T^2} e^{-\frac{E_D}{\mathcal{R}T}} \quad , \tag{46}$$

where

$K_6 = 0.0243\ J/(kgK^2)$

$K_7 = 8.745 \times 10^7\ J/kg$

*) ρ_f and ρ_s are computed with $\langle T_f \rangle_f$ and $\langle T_c \rangle_c$, respecitvely and kept constant.

$$E_D = 1.577 \times 10^5 \text{ J/mol}$$

$$\mathcal{R} = 8.3143 \text{ J/(mol K)}$$

and c_v is given in Eq. (5). Figure A-1.1 on p. 14 of Ref. [6] shows that $(c_p)_f$ increases linearly between T = 650K and T = 1300 K. Thus, Eq. (46) is used to compute a reference value at $T = T_{fo}$, and the $[c_p(T)]_f$- variation within the pellet, as needed in Eq. (44), is approximated by

$$[c_p(T)]_f = [c_p(T_{fo})]_f [1 + K_8 (T_f - T_{fo}] , \qquad (47)$$

where $K_8 = 1.5299 \text{ K}^{-1}$.

Equation (47) introduces an error of less than 0.6% in the calculation of the energy stored in the pellet, but it facilitates greatly the evaluation of Eq. (44).

The specific heat for zircaloy in its alpha phase ($300 \leq T_c \leq 1090$ K) is given in Table B-1.1 of Reference [6, p. 206]. The data given in that table are represented best* by

$$[c_p(T)] \cong K_9 [T_c/(1K)]^{K_{10}} , \qquad (48)$$

where $K_9 = 80.20769$ J/(kg K)

$K_{10} = 0.220\,247.$

Equation (48) fits the tabulated data with the coefficient of determination $r_d^2 = 0.9983$ and a maximum error of 0.6%, having a maximum impact on E in Eq. (43) of 0.01%.

Equations (41) and (36) were substituted in Eqs. (47) and (48). The respective results were then substituted into Eqs. (44) and (45). The integrals of Eqs. (44) and (45) were numerically evaluated on an HP-41CX programmable pocket calculator, using its built-in quadrature algorithm. This algorithm was executed to guarantee six significant digits. With the conditions listed in Section 2.6 above, the following results were obtained:

$E_f = 66.5903$ kJ/m,

$E_c = 1.4005$ kJ/m and

$E = 67.9908$ kJ/m.

*Linear, exponential and power-law regressions were tried throughout this work. The regression with the largest r_d^2 value was selected.

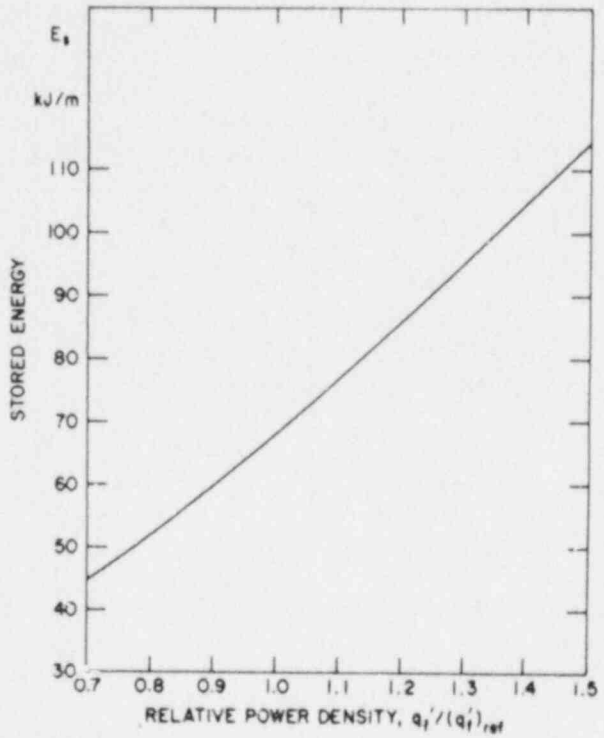

Figure 2. Stored Fuel Energy vs. Fission Power

Figure 2 shows the dependence of fuel stored energy E on normalized linear heating rate or fission power, the fission power being normalized by the value listed in Section 2.6 above.

It was indicated in Section 2.6 that the TRAC code appears to underpredict the fuel centerline temperature by 8)K. With Eq. (43), one can determine the corresponding deficiency in fuel stored energy. TRAC appears to underpredict fuel stored energy by 6.05 kJ/m or by 8.9% of its reference value relative to the coolant temperature (E = 0 for $\langle T_f \rangle_f = \langle T_c \rangle_c = T_\infty$).

2.8 Uncertainties in Predicting Fuel Stored Energy

Expressions for thermophysical properties and transfer laws are derived from experimental data with known random errors. Secondly, reactor and fuel conditions. are specified, but with statistical uncertainty. Thirdly, the mathematical models in TRAC-PF1/MOD1 were found to differ (cf. Table 1) from the documented models. The TRAC models have systematic errors because of such differences, because of parameter adjustments (cf. Sec. 2.6) and because of numerical approximations (computational errors). Parameter adjustments and computer errors are being assessed by comparison with data [3]. Their consequences are known, but only within statistical error bounds.

Thus, even though a computer code execution is deterministic, the statistical uncertainties in input data specifications and the often unpredictable consequences from systematic errors cause computer results to be afflic ed with essentially random errors, the magnitudes of which must be estimated with quantifiable confidence.

In this section are summarized the uncertainties in fuel-related parameter specifications. They were taken from previously published uncertainty analyses, from the available code documentation and from Reference [6].

2.8.1 Uncertainties of Input Data Specifications. In the category of input data are (i) the initial power level or linear heating rate, (ii) the power distribution, (iii) the fuel dimensions at cold conditions and (iv) the condition of the fuel (burn-up conditions). Table 3 below summarizes the fuel-

related input parameters, their 1-σ uncertainties, associated probability distributions and the references. Unknown probability distributions are specified as uniform because equal probabilities reflect the maximum of ignorance.

Table 3. Uncertainties in Input Data

Parameter	1-σ Uncertainty	Distribution	Reference
Fission Power	±2%	Normal	[12], Table 2
Peaking Factors			
Local Axial	±0.7%	Normal	[12], Table 2
Local Radial	±2.5%	Normal	[12], Table 2
Pellet Radius (cold)	±0.1%	Uniform	[13], Table 2
Clad Radii (cold)	±0.1%	Uniform	[13], Table 2
Neutron Flux Depression			
m (Eq. 12)	±0.05	Uniform	Estimated
n (Eq. 12)	±0.3	Uniform	Estimated

The uncertainty in fission power reflects the random error of matching the calorimetric balance of the plant with instrument readings. Even though it is not a code uncertainty, it must be part of the peak clad temperature uncertainty. Peaking factor uncertainties account for random errors in specifying power distributions in the core. B. W. Sheron [12] implied normal distributions for power and peaking factors. These have been adopted here also.

Errors in pellet and cladding dimensions are random fabrication errors. Since quality control eliminates large deviations, a uniform distribution is suggested here. However, for the purpose of this analysis, these size uncertainties and the uncertainties of surface roughness [13, Table 2] are combined later into the gap conductance uncertainty, to which is assigned also a uniform probability distribution.

Uncertainties for fission power variation within the fuel pellet are estimated. No data could be found.

2.8.2 Modeling Uncertainties. Modeling uncertainties arise from random differences between heat transfer and thermophysical property measurements and the correlations used to represent the measurements in the computer code. Systematic differences, however, between the mathematical models in the code and the experimental data are code-specific and presented later in Section 2.8.3. In the category of fuel-related modeling uncertainties are the uncertainties from (i) fuel pellet thermal conductivity, (ii) cladding thermal conductivity, (iii) fuel pellet heat capacity, (iv) cladding heat capacity, (v) filler gas thermal conductivity, (vi) thermal expansion or gap width, (vii) radiative surface properties and (viii) convective heat transfer coefficients. Table 4 below summarizes 1-σ level uncertainties, approximate distributions and source references for these parameters.

Table 4. Uncertainties of Fuel-Related Parameters

Parameter	1-σ Uncertainty	Distinction	Reference
Fuel thermal cond., k_f	±0.2 W/(mK)*	Uniform	[6], p. 24
Clad thermal cond., k_c	±1.01 W/(mK)	Normal	[6], p. 218
Fuel heat capacity, $(\rho c)_f$	±30.035 kJ/(m^{3}K)	Uniform	[6], p. 10†
Clad heat capacity, $(\rho c)_c$	±64.875 kJ/(m^{3}K)	Uniform	[6], p. 211
Gas thermal cond., k_g	±0.0131 W/(mK)	Uniform	[6], p. 485,† [14], p. 15
Effective gap width, t	±20.98 μm	Skewed	[15], pp. 31 & 92
Pellet emissivity, ε_f	±7%	Uniform	[6], p. 48.6
Clad emissivity, ε_c	±0.10	Uniform	[6], p. 237
Convective heat transf., single-phase, forced, turb.	-5% to +35%	Uniform	[16], p. 18; [17]

*Notice that Hobson's data listed in Table A-2.VII [6], are incorrectly plotted in Figure A-2.4 [6].
†Revision 8/81.

The probability distributions in Table 4 are specified as normal whenever they are unknown or known to be approximately normal.

The uncertainty of fuel thermal conductivity, k_f, is specified in Reference [6, p. 24] for all fractions of theoretical fuel density. For the fraction of 94.9%, Hobson's data as listed in Ref. [6] are (0.32 ± 0.09)W/(mK) higher than the MATPRO correlation, Eq. (4), in the temperature range between 547K and 1,330K. However, for this analysis we adopt the more universally applicable error range as specified in Reference [6].

Error brackets for heat capacities, (ρc_p), were computed from uncertainties specified for specific heats in Reference [6, pp. 10 (of 8/81 revision) and 211] and the densities given below Eq. (45). The uncertainty for density is trivial (±0.5% of theoretical density for fuel [13, Table 2]) and therefore ignored.

The uncertainties for important parameters affecting the gap conductance are combined into an overall gap conductance uncertainty, based on Eq. (3) and on the assumption of independence between the dominant gap width and gas conductivity uncertainties:

$$\Delta h_{gp} = \sqrt{\Delta_1^2 + \Delta_2^2} \, . \qquad (49)$$

Here, the uncertainty from gas conductance uncertainty, $\Delta k_g = 0.0131$ W/(mK), is

$$\Delta_1 = \Delta k_g / t = 634.7 \text{ W/(m}^2\text{K)} , \tag{50}$$

the effective gap width, t, being defined by Eq. (31) and computed with the values given in Section 2.6 to be t = 25.039 μm, and from gap width uncertainty,

$$\Delta_2 = h_{gp} - \frac{k_g}{t + \Delta t} = 4{,}992.0 \text{ W/(m}^2\text{K)} . \tag{51}$$

The gas thermal conductivity, k_g, is evaluated from Eq. (9), with the mean temperature computed from the values given in Table 2. The nominal gap conductance is $h_{gp} = 10.960$ kW/(m^{2}K) (cf. Sec. 2.6), as in the TRAC code. The gap width uncertainty, Δt, is taken from Reference [15] as shown there in Table 4. Uncertainties from radiative heat transfer (cf. Eq. (32)) are ignored because the entire contribution from radiative heat transfer to gap conductance is only 0.4% at normal full power conditions.

Substitution of Eqs. (50) and (51) into Eq. (49) yields the 1-σ uncertainty of gap conductance which is

$$\Delta h_{gp} = 5{,}032.2 \text{ kW/(m}^2\text{K)} \tag{52}$$

and amounts to 45.9% of the nominal gap conductance.

Gap conductance uncertainty is dominated by the uncertainty of effective gap width. The effective gap width uncertainty, Δt, is slightly smaller than the effective gap width t itself, but approximately as large as the physical gap width δ. There is no general agreement in the literature concerning gap width uncertainties; most error ranges have been assumed without basis. Sheron [12, Table 2] lists an "assumed RMS error" of 25% for gap conductance, which appears low. In contrast, Lassmann and Hohlefeld [18] more recently compared nearly a thousand gap conductance measurements with results from the URGAP computer code. The measurements were taken primarily from extremely well-controlled out-of-pile experiments, and URGAP "has been fitted to the data of Ross and Stoute [19], Dean [20] and Campbell et al. [21]." Under such rather ideal but atypical conditions, Lassmann and Hohlefeld obtained the gap conductance uncertainty of 33.4% (1-σ level). Cunningham et al. [22] concluded also from experiments that the gap width uncertainty is approximately 50% (p. C-2), based on an initial gap width of 229 μm (p. A-1) and a mean gap closure by 63% (p. C-2). This leaves, under normal full-power conditions (in a BWR fuel pin), a gap width of 108 μm with an uncertainty of 50 μm. Cunningham et al. add a 100% uncertainty (p. C-6) in temperature jump distance uncertainty (cf. Eq. (31)) and a 10% uncertainty in the gap width coefficient of their STORE computer code. This tends to support the uncertainty analysis by Steck et al. [15] for PWR conditions, i.e. the reference from which Eq. (52) was derived.

For uncertainties of convective film coefficients, it was pointed out by Lellouche [16] that when heat transfer coefficients appropriate for conditions inside circular tubes are used for heat transfer in tube bundles, then the heat transfer coefficients are consistently underestimated. This being the case in the TRAC code, the ±20% range of 1-σ level uncertainties suggested by the comparison of the Dittus-Boelter correlation with data [17], has been shifted to {-5%, +35%} to account for the above enhancement of heat transfer regimes with phase change. This is addressed in Section 3 later.

2.8.3 Systematic Modeling Errors in TRAC-PF1/MOD1. Based on presently available code documentation [1] and on the written responses [23] from Los Alamos National Laboratory to specific questions posed by the author, TRAC-PF1/MOD1 has four systematic errors related to its fuel modeling:

1. The thermal conductivity is too low as shown in Table 1 (cf. [1, p. 50]. The mean bias is -0.46 W/(mK) relative to the correlation given in MATPRO [6, p. 23]. The consequences should have been an excess of initial fuel stored energy of approximately 6 kJ/m or 9%, and a 13% increase in pellet thermal response time. As pointed out in Section 2.6, however, TRAC results show a slight deficit of 1% in fuel stored energy when compared with results from closed-form integration. The cause for this discrepancy might be computational error; the exact cause cannot be identified without additional code documentation. The increase in thermal response time, on the other hand, appears to be corroborated indirectly by comparing the thermal response of the cladding as computed by TRAC and by the analysis presented in Section 3.

2. The gap width is increased from approximately 14 μm to 21 μm (under hot conditions). The adjustment is suggested in the TRAC LBLOCA report [24, p. 17], to achieve vendor-specified initial fuel-stored energy. The magnitude of the adjustment given here is inferred from hand calculations (cf. Eqs. (1) and (2)) because the necessary documentation is lacking in TRAC output listings. It is possible, by gap width adjustments, to obtain the correct initial fuel stored energy, but not without changing the pellet and cladding response times. It will be shown in Section 3, that any increase in gap width, i.e. decrease in gap conductance, increases blowdown peak clad temperature. This is true only in the vicinity of the fuel conditions calculated in TRAC for full-power conditions, but it shows that stored energy and with it pellet temperature is more important for peak clad temperature than gap conductance. Whether TRAC results are conservative, however, can only be determined from calculations carried out with correct fuel thermal conductivity, without significant computational error and without gap width adjustments.

3. Thermal expansion in radial direction are computed incorrectly in TRAC [1, p. 70], because (i) the formula for radial displacements is evaluated with the absolute temperature instead of with the excess temperature above the temperature of the strain-free state and (ii) total radial displacements are added to radii from previous time steps, rather than to radii of cold conditions. One should suspect documentation errors here, but it was not possible to resolved this issue [23] without better documentation.

4. The calculation of two-phase flow heat transfer coefficients in TRAC-PF1/MOD1 [1, p. 81, Eq. (140), p. 83, top equation; p. 63] is incorrect because (i) the equation on page 63 is wrong and (ii) a mixture heat transfer coefficient is assigned to the liquid phase, while the vapor phase heat transfer coefficient is not zero.

   (i) Los Alamos National Laboratory claims [23], with unspecified references to M. Ishii and J. M. Delhaye, that the equation on page 63 of [1] for combining phasic heat transfer coefficients is derived by averaging. No reference for this averaging is offered. Since the equation contains neither a phasic perimeter fraction, nor a phasic wetted area fraction, nor a phasic wall residence time fraction, it is absolutely impossible to derive the equation on page 63, nor Eq. (98) on p. 58 (for solid structures) either by space or by time averaging.
   (ii) Los Alamos National Laboratory concedes [23], that mixture and vapor heat transfer coefficients should not be added as in the TRAC code, but they claim that it is permissible to add them because the liquid convective heat transfer coefficient $(\bar{h}_c)_\ell$ is at least 100 times greater than that for vapor, $(\bar{h}_c)_v$. This claim is wrong in principle (one does not introduce unnecessary errors, because they are small); it is also wrong because 25 randomly selected TRAC results, obtained from a PWR LBLOCA calculation, show that during the blowdown phase $(\bar{h}_c)_\ell/(\bar{h}_c)_v = 16 \pm 14$, $(1-\sigma)$.

This systematic error does not affect single-phase coolant conditions, whence it does not affect the initially stored energy but it will affect the transient calculations.

2.8.3 Resultant Uncertainties in Fuel Stored Energy. Table 5 summarizes the changes caused in fuel stored energy by varying the dominating fuel-related parameters, each one individually, by its 1-σ uncertainty. The second column shows the parameter values for normal conditions, as they were used to obtain the results in Table 2, and the stored energy given in Section 2.7. The third column shows the parameter changes which bring about an increase in fuel stored energy and which correspond to a 1-σ variation. Notice that the convective film coefficient was reduced by 20%, one-half of the total variation listed in Table 4. Column four shows the extreme values used to calculate the changes in stored energy, while column five lists the corresponding values for stored energy. The last column shows the changes in stored energy relative to the reference value of E = 67.991 kJ/m (cf. Section 2.7).

The values in Table 5 serve four purposes. Firstly, they serve to rank the parameters in their order of significance in affecting stored energy. Notice that, the convective film coefficient is in eighth place because it is assumed that its minimum value is only 5% below its computed reference value (on account of heat transfer enhancement in rod bundles, cf. Section 2.8.2), and because such a 5% decrease would increase the stored energy only by 0.313 kJ/m. Clearly, uncertainties in gap conductance, peaking factors and fuel thermal conductivity have the most serious influence on stored energy.

Table 5. Elements of Stored Energy Uncertainty

Parameter	Reference Value	1σ Change†	Max./Min. Values	E, Stored Energy kJ/m	$E - (E)_{ref}$ kJ/m
Gap Conductance	10.960 $kWm^{-2}K^{-1}$	-5.028 $kWm^{-2}K^{-1}$	5.932 $kWm^{-2}K^{-1}$	84.928	16.937
Peaking Factors	1.41736	x1.03218	1.46297	70.675	2.685
Fuel Thermal Cond.	4.392 $Wm^{-1}K^{-1}$	-0.2 $Wm^{-1}K^{-1}$	4.186 $Wm^{-1}K^{-1}$	70.475	2.484
Power	486.49 MW/m^3	+2%	496.22 MWm^{-3}	69.655	1.664
Fuel Heat Capacity	3.028 $MJm^{-3}K^{-1}$	+30.035 $kJm^{-3}K^{-1}$	3.059 MJ $m^{-3}K^{-1}$	68.651	0.661
Cladding Thermal Cond.	16.735 $Wm^{-1}K^{-1}$	-1.01 $Wm^{-1}K^{-1}$	15.728 $Wm^{-1}K^{-1}$	68.455	0.464
Burn-Up m n	0.4034 3.9167	-0.05 -0.30	0.3534 3.6167	68.346	0.355
Convective Film Coeff.	40.05 $kWm^{-2}K^{-1}$	-20%	32.04 $kWm^{-2}K^{-1}$	69.241	1.251
Cladding Heat Capacity	2.145 $MJm^{-3}K^{-1}$	+64.875 $kJm^{-3}K^{-1}$	2.210 MJ $m^{-3}K^{-1}$	68.033	0.042

†cf. Tables 3 and 4.

Secondly, the values listed in the third and last columns of Table 5 serve to estimate the sensitivity of fuel stored energy on modeling parameters. The ratio of listed stored energy change over a listed parameter change is an approximation to the partial derivative of stored energy with respect to that parameter and can be used to estimate the stored energy change for different parameter changes.

Thirdly, if one assumed that the conditions of linear error propagation are met, one could estimate the uncertainty in fuel stored energy from [25]

$$\sigma_E = \sqrt{\sum \sigma_i^2} = 17.7 \text{ kJ/m} , \qquad (53)$$

which is 26.1% of the reference value E = 67.991 kJ/m. The σ_i values in Eq. (53) are the values in the last column of Table 5, except that for convective heat transfer only 1/4 of the tabulated value is used (corresponding to the low range shown in Table 4). It must be pointed out, however, that Eq. (53) is only a rough estimate since the conditions of linear error propagation are not strictly met.

The fourth and last purpose served by Table 5 is to show that the effects of parameter variations on fuel stored energy can be simulated by simply varying the fission power or the power peaking factor. Since this is easy to carry out in the TRAC code for a large number of fuel elements, it is a powerful technique for developing response surfaces in support of statistical uncertainty analyses, because this technique saves computing resources. One needs to select from Table 5 the amount of needed change in stored energy for a given change of any of the listed parameters, and then to determine from Figure 2 the multiplier for peaking factor which is to be used for the steady-state calculations of initial conditions.

2.9 Conclusions Regarding Fuel Stored Energy Uncertainty

1. Initial fuel stored energy can be computed efficiently from closed-form integration of the steady-state conduction equation, taking into account the dependence of thermophysical properties on temperature and the radial variation of fission power due to neutron flux depression.

2. The uncertainty in fuel stored energy is dominated by uncertainties in gap conductance, peaking factors and fuel thermal conductivity.

3. The fuel stored energy per unit of length of fuel pin, in the fuel pin with the highest clad temperature at full-power conditions in a Westinghouse PWR core with 17 x 17 fuel arrays and 160,000 Md/t burnup is 68 kJ/m. The standard deviation of the stored energy is approximately 26%.

4. It is possible to approximate the effects on stored energy of all important uncertainties from fuel-related modeling parameters by corresponding variations in peaking factors.

3. Thermal Response of Fuel

It is recognized that peak clad temperatures are the higher the larger the initial fuel stored energy is and the more easily this stored energy can pass from the fuel pellet into the cladding. Also, one and the same change or uncertainty in important fuel modeling parameters can increase the stored energy while retarding the energy transfer from pellet to clad, thereby representing opposing mechanisms which determine peak clad temperature. Gap conductance and thermal conductivity of fuel pellets are two such important modeling parameters.

It is the purpose of this section to determine the effects which the parameters listed in Table 5 have on peak clad temperature. It is of particular interest to know which of these parameters have opposite effects on peak clad temperature and on fuel stored energy.

3.1 Problem Formulation

We seek the transient fuel and cladding temperature by integrating the transient conduction equation

$$\rho c_p \frac{\partial T}{\partial \tau} = \bar{k} \frac{1}{r} \frac{d}{dr} \left(r \frac{dT}{dr} \right) + q'''_f \tag{54}$$

in the two regions (subscripts f for fuel and c for clad), as shown in Figure 1. All symbols are defined as before, except

$\overline{\rho c}_p = \rho c(\langle T \rangle)$, mean volumetric heat capacity

$\bar{k} = k(\langle T \rangle)$, mean thermal conductivity,

both evaluated, respectively, for fuel and clad with the area-averaged temperatures defined in Eqs. (3) by using Eqs. (4) and (5) for $\bar{k}_f$, Eq. (7) for $\bar{k}_c$, Eq. (46) for $(\bar{c}_p)_f$ and Eq. (48) for $(\bar{c}_p)_c$. The densities ρ_f and ρ_c are kept constant as specified below Eq. (45). We impose as boundary conditions the same four heat flux conditions as in Section 2.4 for the steady-state analysis: zero flux at the center line and flux continuity at all three surfaces. We also impose continuity of temperature at three surfaces of pellet and clad, taking properly into account the temperature jump distances g_f and g_c (cf. Eq. (31)). The surface roughness is insignificant and ignored.

3.2 Solution Technique

Equation (54) is first converted, by area averaging (cf. Eq. 3), into one ordinary differential equation each for pellet and for clad, as shown in Reference [26]. The result is

$$\frac{d\langle T_f \rangle_f}{d\tau} = \frac{\langle q'''_f \rangle_f}{(\overline{\rho c}_p)_f} - \frac{2\bar{k}_g}{R_1^2 (\overline{\rho c}_p)_f} \frac{T_{fo} - T_{ci}}{\ln \frac{R_2 + g_c}{R_1 - g_f}} \tag{55}$$

$$\frac{d\langle T_c\rangle_c}{d\tau} = \frac{\bar{k}_g}{sR_m(\overline{\rho c_p})_c} \frac{T_{fo} - T_{ci}}{\frac{R_2+g_c}{R_1-g_f}} + \frac{R_w}{R_m} \frac{\bar{\alpha}_c}{s^2} N_{Bi} (T_\infty - T_w), \tag{56}$$

where $c = R_2 - R_1$, cladding thickness

$R_m = (R_1+R_2)/2$, mean radius of clad

$\bar{\alpha}_c = \bar{k}_c/(\overline{\rho C_p})_c$, thermal diffusivity of clad

$N_{Bi} = s\bar{h}_c/\bar{k}_c$, Biot number of clad

g = temperature jump distance

and all other symbols have been defined previously. The right-hand side of Eq. (55) represents clearly the balance between internal heat generation and heat transfer through the gap, while the right-hand side of Eq. (56) shows similarly the balance between heat supply from the pellet and heat loss to the coolant. Integration of Eqs. (55) and (56) yields the area-averaged temperatures defined in Eqs. (3) and needed to evaluate all properties. However, one needs to calculate the surface temperatures T_{fo}, T_{ci} and T_w, in order to integrate Eqs. (55) and (56).

These three temperatures are computed by approximating the transient temperature distributions in pellet and clad by two separate power polynomials in radius r. The polynomials have time-dependent coefficients which are computed to satisfy the above-mentioned seven boundary conditions of heat flux and temperature continuity, plus two requirements imposed by Eqs. (3). The total of nine conditions defines the three temperatures T_{fo}, T_{ci} and T_w, all in terms of $\langle T_f\rangle_f$, $\langle T_c\rangle_c$ and T_∞, and also six time-dependent polynomial coefficients [26]. The three surface temperatures are:

$$T_{fo} = F_1\langle T_f\rangle_f + F_2\langle T_c\rangle_c + F_3 T_\infty \tag{57}$$

$$T_{ci} = \langle T_f\rangle_f - \Omega_1(\langle T_f\rangle_f - T_{fo}) \tag{58}$$

$$T_w = [(\Omega_4-\Omega_3)T_\infty - T_{fo} + (\Omega_3+1)T_{ci}]/\Omega_4, \tag{59}$$

where $F_1 = (\Omega_1-1)[\Omega_4(\Omega_3-\Omega_2) - \Omega_5(\Omega_3+1)]/G$

$F_2 = \Omega_3\Omega_4/G$

$F_3 = -\Omega_3\Omega_5/G$

$$G = \Omega_1\Omega_3(\Omega_4-\Omega_5) + (1-\Omega_1)(\Omega_2\Omega_4+\Omega_5)$$

$$\Omega_1 = 4\lambda_f\gamma_3+1 \quad , \quad \Omega_4 = \Omega_3(N_{Bi}+2)/2$$

$$\Omega_2 = \gamma_6-2\gamma_5 \quad , \quad \Omega_5 = \gamma_6(\Omega_4-\Omega_3)$$

$$\Omega_3 = 2\lambda_c\gamma_4$$

$$\lambda_f = \overline{k}_f/\overline{k}_g \quad , \quad \lambda_c = \overline{k}_c/\overline{k}_g$$

$$\gamma_3 = \ln[(R_2+g_c)/(R_1-g_f)]$$

$$\gamma_4 = \gamma_3 R_2/s$$

$$\gamma_5 = (3R_2+2s)/[3(2R_2+s)]$$

$$\gamma_6 = (4R_2+3s)/[6(2R_2+s)] \ .$$

All γ-values are fixed for fixed geometry; λ-, Ω-, F- and G- values vary with temperature. One can integrate Eqs. (55) and (56) with Eqs. (57) through (58). The fuel center line temperature is given by

$$T_c = 2\langle T_f\rangle_f - T_{fo} \ . \tag{60}$$

The expressions for temperature distributions (parabolic in pellet and cladding, logarithmic in gap) can be found in Ref. [26]. They are not needed here. However, Eqs. (55) and (56) need initial values for $\tau = 0$. They are derived to render the derivatives in Eqs. (55) and (56) to be zero [26]. They are computed from:

$$\langle T_f(0)\rangle_f = (V_1U_{22} - V_2U_{12})/(U_{11}U_{22} - U_{12}U_{21}) \tag{61}$$

$$\langle T_c(0)\rangle_c = (V_2U_{11} - V_1U_{21})/(U_{11}U_{22} - U_{12}U_{21}), \tag{62}$$

where $V_1 = \dfrac{s/R_w}{N_{Bi}} \cdot \dfrac{R_1^2\langle q_f'''(0)\rangle_f}{2\overline{k}_f} + T_\infty \dfrac{\Omega_3-F_3[(1+\Omega_3)\Omega_1-1]}{\Omega_4}$

$$V_2 = \frac{R_1^2 \langle q'''_f(0) \rangle_f}{2\bar{k}_g} \gamma_3 - T_\infty F_3 (1-\Omega_1)$$

$$U_{11} = \{(1+\Omega_3)[1+\Omega_1(F_1-1)]-F_1\}/\Omega_4$$

$$U_{12} = F_2[(1+\Omega_3)\Omega_1-1]$$

$$U_{21} = (1-\Omega_1)(F_1-1)$$

$$U_{22} = F_2(1-\Omega_1),$$

and $\langle q'''_f(0) \rangle_f$ is the initial, area-averaged fission power; all other symbols are defined below Eq. (59).

The transient conduction model represented by Eqs. (55) through (62) was derived [5] on the basis of integral techniques described by Goodman [4]. The model applies to the thermally thin conduction regime. The criteria for its applicability are given by Wulff et al. [26]. Physically, the model implies thermal relaxation without delay; the results lead those of the exact solution by less than 12 milliseconds for the cladding and by less than 0.1 seconds for the pellet surface. This is deemed adequate for peak clad temperature calculations during LBLOCA simulations. See Reference [5] for more details concerning accuracy.

Equations (55) and (56) were integrated on an HP-41CX programmable pocket calculator, using a fourth-order Runge-Kutta integration algorithm†. The HP-41CX executes Eqs. (4), (5), (7), (9), (46) and (48) for properties, Eqs. (61) and (62) for initial conditions and Eqs. (57) through (60) for fuel and cladding temperatures. The integration step size of 50 milliseconds guarantees a computing accuracy of $\pm$0.05K; five significant digits remained unaltered during eighty integration steps or 4 second of a null transient which was started from Eqs. (61) and (61).

Results were computed for two sets of boundary conditions. One set approximates the fission power and coolant conditions as calculated by the TRAC code while simulating an LBLOCA for reference Westinghouse PWR plant conditions. The other set consists of limiting step changes in coolant conditions to show the effects from DNB delay (departure from nucleate boiling) or from dryout delay, and also with changes of time for scram initiation. The results are presented in the following two subsections.

†The Runge-Kutta algorithm was coded for the HP-41CX as part of this project. It needs 26 memory registers. The number of nonlinear ordinary differential equations, $\dot{Y} = f(x,Y)$, that can be integrated is free and depends only on the complexity of f and the number of available registers (max. 896).

3.3 Effect of Fuel Parameter Uncertainty on Peak Clad Temperature

Eighteen transient fuel temperature calculations have been performed to assess the effects of parameter variations on thermal response and on peak clad temperature. The results are shown in Table 6.

Table 6 Thermal Response of Fuel and Peak Clad Temperature Change

	Step Change		TRAC Blowdown B.C.	
Parameter	Initial Clad Temperature Rise K/s	Change of Initial Temp. Rise K/s	Peak Clad Temp. K	Change in Peak Clad Temp. K
Gap conductance	724.2	-7.2	884.8	52.4
Peaking factor	753.0	21.6	843.0	10.6
Fuel thermal conductivity	731.3	-0.1	847.5	15.1
Power	744.9	13.5	839.0	6.6
Fuel heat capacity	731.4	0	833.3	0.9
Cladding thermal cond.	732.0	0.6	833.9	1.5
Convective heat trans. coef.	722.0	-9.4	849.5	17.1
Cladding heat capacity	710.0	-21.4	833.5	1.1
Reference case	731.4	---	832.4	---

The first set of nine calculations was carried out to obtain the initial time rate of mean clad temperature rise from Eq. (56). Initial steady-state conditions were computed, according to Eqs. (61, (62) and (57) through (59), first with the parameters from TRAC-PF1/MOD1 as listed in Section 2.6, and then with all but the burn-up parameters (not modeled in Eqs. (55) and (56)) shown in Table 5 changed by the same 1-σ uncertainty as listed in Table 5. The transient was induced by changing the following three boundary conditions from initial values

$$\left.\begin{aligned} T_\infty &= 599.44\text{K} \\ \bar{h}_c &= 40.05\ \text{kW}/(\text{m}^2\text{K}) \end{aligned}\right\} \quad \text{for } \tau < \tau' = 0 \tag{63a}$$

$$\langle q'''_f \rangle_f = 486.49\ \text{MW/m}^3 \quad \text{for } \tau < \tau'' = 0 \tag{63b}$$

to

$$\left.\begin{aligned} T_\infty &= 666.80\text{K} \\ \bar{h}_c &= 0.8805\text{kW}/(\text{m}^2\text{K}) \end{aligned}\right\} \quad \text{for } \tau \geq \tau' = 0 \tag{64a}$$

$$\langle q'''_f \rangle_f = 27.24\ \text{MW/m}^3 \quad \text{for } \tau \geq \tau'' = 0, \tag{64b}$$

which are the highest vapor temperature, the lowest heat transfer coefficient, both as calculated by TRAC-PF1/MOD1 for an LBLOCA blow-down phase, and 5.6% of initial power, representing the mean fission power during the first two seconds. The results are shown in the second and third columns of Table 6. The second column shows the initial mean clad temperature rise, $d\langle T_c\rangle_c/dt$ at $\tau = 0$. The third column shows the effect of parameter variations on the thermal response of the cladding, relative to that of the reference calculation, which is shown in the last line. Indeed, gap conductance, fuel thermal conductivity, convective film coefficient and cladding heat capacity, when changed so as to increase fuel stored energy, decrease, as expected, the rate of thermal response by the cladding. This suggest that these four parameters have opposite effects on stored energy and peak clad temperature.

Figure 3 shows the transient outer cladding temperature, $T_w(\tau)$ under reference conditions and with boundary conditions as specified by Eqs. (63) and (64). This figure suggests that the initial slope might not dictate the peak of the clad temperature T_w. In fact, as shown in the first two columns of Table 6, the opposite effects suggested by the results in the second and third columns are unimportant with regard to peak clad temperature.

Far more importantly, Figure 3 shows that during the blowdown phase the clad temperature is limited by vapor cooling, without the arrival of droplets. The clad temperature peaks even when the pessimistic cooling conditions, Eqs. (64), prevail at once after scram and then remain. The blow-down peak clad temperature is unaffected by reactor pump degradation or by transition of critical break flow from subcooled to two-phase flow conditions, except in the highly unlikely event that liquid injection at core entrance should occur in less than approximately two seconds after dryout or departure from nuclear boiling (DNB). Aside from this exception, the blow-down peak clad temperature is dictated by fuel stored energy alone or, equivalently, by the linear heating rate (cf. Figure 2). Whence, blow-down peak clad temperature measurements are not affected by scale distortions outside the core in a test facility.

Turning now to the second set of transient fuel temperature calculations, we describe how the last two columns in Table 6 were obtained. Another reference and eight repeat calculations were carried out with the 1-σ parameter variations listed in Table 5, only one parameter being varied at a time, to show the effects of these parameter variations on blow-down peak clad temperature. These nine parametric calculations were carried out, however, with boundary conditions representative of the ones imposed by the TRAC-PF1/MOD1 code during blow-down, on the fuel pin segment which had the highest clad temperature at full-power steady-state conditions. Figures 4, 5, and 6 for cooling rate, liquid temperature and vapor temperature, respectively were generated by TRAC and used to derive these approximate boundary conditions for coolant temperature, T_∞, heat transfer coefficient, $\bar{h}_c$, and fission power, $\langle q_f''' \rangle_f$:

$$T_\infty(\tau) = 599.44K - (21.41K/s)\tau \qquad (65)$$

$$\bar{h}_c(\tau) = 40.05kW/(m^2K) \cdot f_1(\tau), \qquad (66)$$

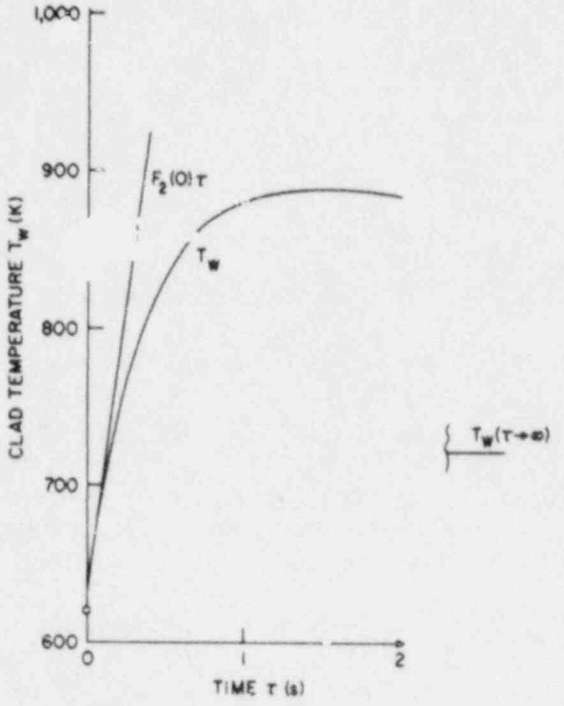

Figure 3. Transient Outer Clad Temperature for Step Change in Boundary Conditions at Time $\tau = 0$

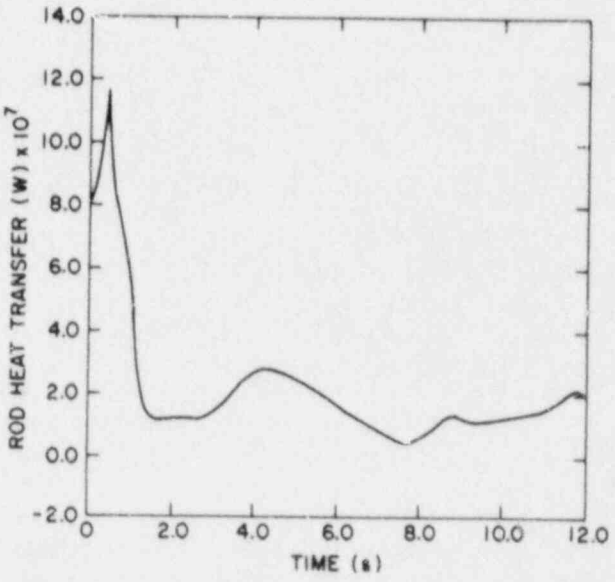

Figure 4. TRAC-Computed History of Heat Transfer Rate from Fuel Rod During LBLOCA for Rod Location With Greatest Initial Clad Temperature

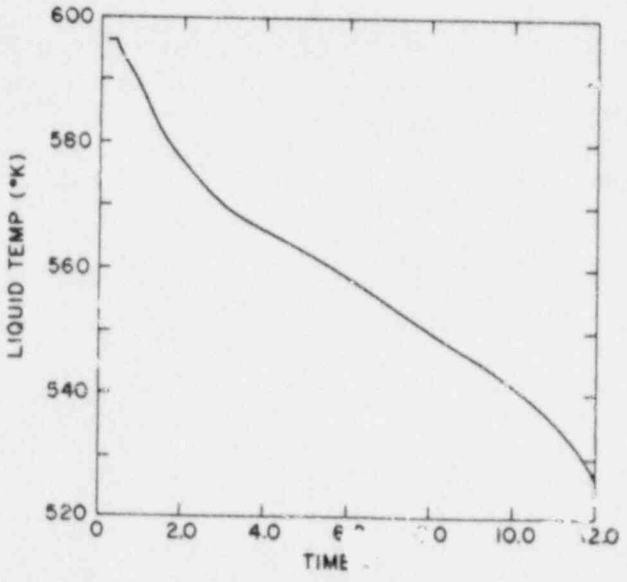

Figure 5. TRAC-Computed History of Liquid Temperature at Fuel Rod During LBLOCA for Rod Location With Greatest Initial Clad Temperature

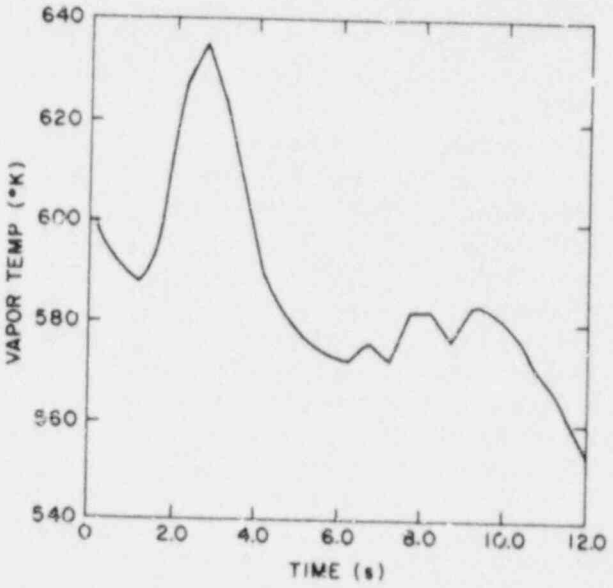

Figure 6. TRAC-Computed History of Vapor Temperature at Fuel Rod During LBLOCA for Rod Location With Greatest Initial Clad Temperature

where $f_1(\tau) = 1+(0.9812\ s^{-1})\tau$ for $0 \leq \tau \leq 0.47s$

$= \text{Max}\{0.022314,\ 2.13745-(1.43886\ s^{-1})\}$

for $0.47s \leq \tau$ 4s

and

$$\langle q'''_f \rangle_f = 486.49\ MW/m^3 \quad \text{for } 0 \leq \tau \leq t'' = 0.2s$$

$$= 486.49\ MW/m^3\ [1.236-(1.180\ s^{-1})\tau \quad \text{for } t'' \leq \tau \leq t'' + 0.8s$$

$$= 27.24\ MW/m^3 \quad \text{for } t'' + 0.8s \leq \tau \leq 4.0s \qquad (67)$$

All boundary conditions start out with steady-state initial conditions. The TRAC-computed cooling recovery at 2.81s after break initiation is intentionally omitted; the cooling rate is kept constant instead.

The outer clad temperature history, $T_w(\tau)$, obtained with these reference conditions and with all parameters in Table 5 at their nominal values is shown as the solid curve, marked REF, in Figure 7. The comparison with TRAC results shows that the TRAC-computed peak clad temperature is approximately 28K lower and appears 0.4 seconds later than shown in Figure 7. The shape of the curve from TRAC, however, is the same as that of the solid curve in Figure 7, except for a small reduction in slope at the time (1.47s) of a computer restart.

The fourth column in Table 6 shows the peak clad temperatures obtained by changing the listed parameters by the 1-σ uncertainties listed in Table 5. The last column shows the corresponding changes in peak clad temperature relative to the reference value of 832.4K, given in the last line. In contrast to the conclusion arrived at from the thermal response rate differences in the third column of Table 6, all parameter changes, which produce an increase in stored energy, produce also an increase in peak clad temperature. This shows clearly that energy storage is more important for peak clad temperature than are heat transfer rates.

After taking the square root of the sum of squares (cf. Eq. (53) for stored energy) of all the differences in the last column of Table 6, one obtains a rough estimate for the 1-σ uncertainty in peak clad temperature of 41.4K, as it results from the uncertainty of fuel-related parameters. This estimate is offered here with caution, because it is based on linear error propagation [25], of which the requirements can be met only approximately by the peak clad temperature modeling analysis. The dash-dot curve at the top in Figure 7 shows the expected peak clad temperature when all the 1-σ changes of fuel-related parameters combine statistically. The curve is drawn for the 1-σ uncertainty in gap conductance of 46%. The intermediate dash curve is drawn for the gap conductance uncertainty of 35% as proposed by Lassmann and Hohlefeld [18]. No attempt is made to assign confidence limits to these peak clad temperature uncertainties as these limits are the subject of an ongoing effort by the USNRC.

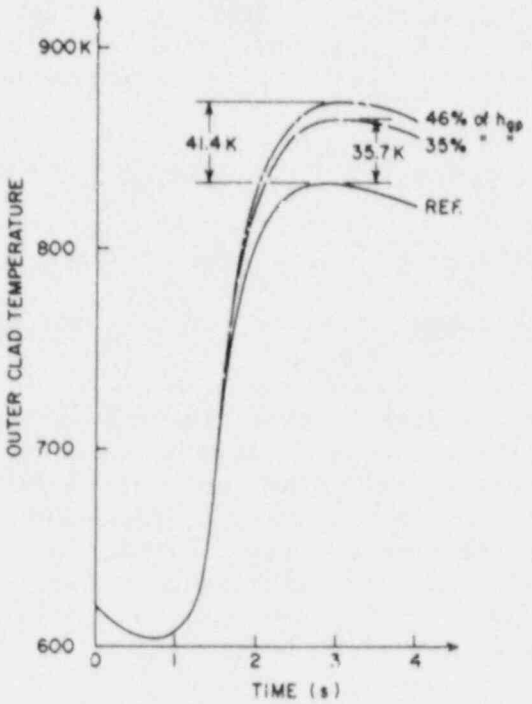

Figure 7. Peak Clad Temperature Change Due to Uncertainties in Fuel-Related Parameters

However, as before for stored energy, the peak clad temperature differences given in Table 6 can serve, along with their corresponding parameter changes listed in Table 5, to estimate the sensitivity of peak clad temperature on each of the fuel-related parameters. Finally, one can recognize the order of importance for the parameters concerning their effect on peak clad temperature; the order is the same as for fuel stored energy, as far as the three most important parameters are concerned. Notice that in this ordering the change of peak clad temperature due to a change in convective heat transfer coefficient should be divided by four because the coefficient is expected to change in the range from -5% to +35%, while the difference in peak clad temperature was obtained for -20%, as shown in Table 5.

Notice in Figure 7 that the clad temperature peaks without recovery of cooling due to droplet injection. This confirms the conclusions reached before for Figure 3, but now also for boundary conditions which approximate those computed by TRAC-PF1/MOD1.

3.4 Effect of Hydraulics Parameters on Peak Clad Temperature

In this section are presented the results from transient fuel temperature calculations carried out with limiting step changes in boundary conditions for the purpose of assessing the effects on peak clad temperature from (i) changes in heat transfer coefficients, (ii) delay of the time when DNB or dry-out occurs, and (iii) delay of the time when scram is initiated.

The Effect of Heat Transfer Coefficients can be seen by comparing the curves for outer clad temperature, $T_w(\tau)$, in Figures 8 and 9. These curves were computed with all parameters in Table 5 at their nominal values, with fission power as described by Eqs. (67), with the coolant temperature T_∞ as specified by the first of Eqs. (63a) and (64a) and with

$$\begin{aligned} \bar{h}_c &= 40.05 \text{ kW/(m}^2\text{K)} && \text{for } 0 \le \tau \le \tau' \\ \bar{h}_c &= 227.1 \text{ W/(m}^2\text{K)} && \text{for } t' \le \tau \le 4\text{s in Fig. 8} \\ &= 56.8 \text{ W/(m}^2\text{K)} && \text{for } t' \le \tau \le 4\text{s in Fig. 9} \end{aligned} \tag{68}$$

The lowest value of $\bar{h}_c$ computed during blowdown by TRAC-PF1/MOD1 is 880.5 W/(m^{2}K). This is for single-phase, turbulent vapor flow, with* the velocity of 4.62 m/s, at the pressure of 81 bar and the vapor temperature of 666.2K. Turbulent free convection by dry vapor would represent the pessimistic extreme in velocity calculation and produce 164 W/(m^{2}K). Thus, the heat transfer coefficient $\bar{h}_c$ used for Figure 8 is slightly more than 1/4 of the minimum TRAC-computed value; in Figure 9 it is ~1/15, and even only ~1/3 of the free convection value. This is extremely low.

The clad temperature peaks in Figures 3 and 8 reaches its asymptotic value $T_w(\infty)$ from above, in Figure 9 it approaches its asymptotic temperature from below. The clad temperature is limited by vapor cooling; a maximum occurs when the asymptotic wall temperature

$$T_w(\infty) = (T_v)_{max} + R_1^2 \langle q'''_{decay} \rangle_f / [2R_w(\bar{h}_c)_{min}] \tag{69}$$

is below the initial mean pellet temperature $\langle \bar{T}_f(o) \rangle_f$, where

$(T_v)_{max}$ = maximum vapor temperature
R_1 = pellet radius
R_w = outer clad radius
$\langle q'''_{decay} \rangle_f$ = decay power density in pellet
$(\bar{h}_c)_{min}$ = minimum heat transfer coefficient

Early arrival of liquid can turn down the clad temperature only if the heat transfer coefficient is unrealistically low or if the liquid arrives unrealistically early.

*Dittus-Boetter, $N_{Re} = 78{,}000$, $N_{pr} = 1.12$.

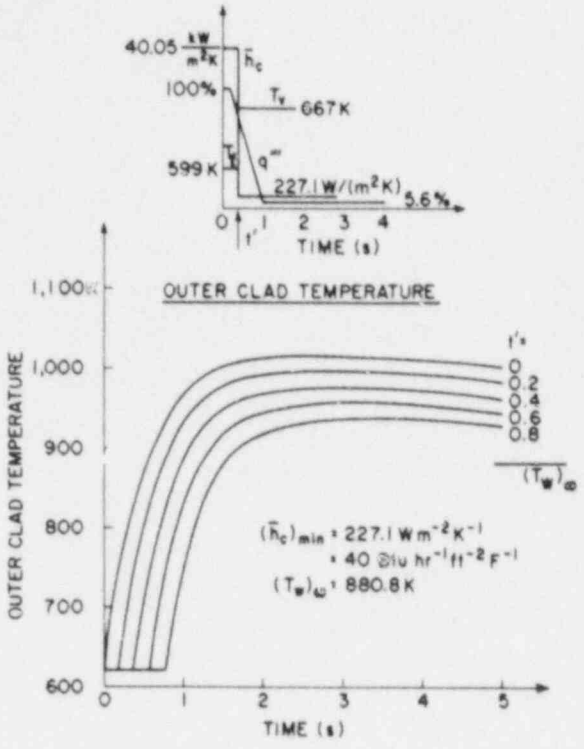

Fig. 8. Effect of DNB Delay Time t' on Peak Clad Temperature for Low Heat Transfer Coefficient, $\bar{h}_c$ = 227 $Wm^{-2}K^{-1}$

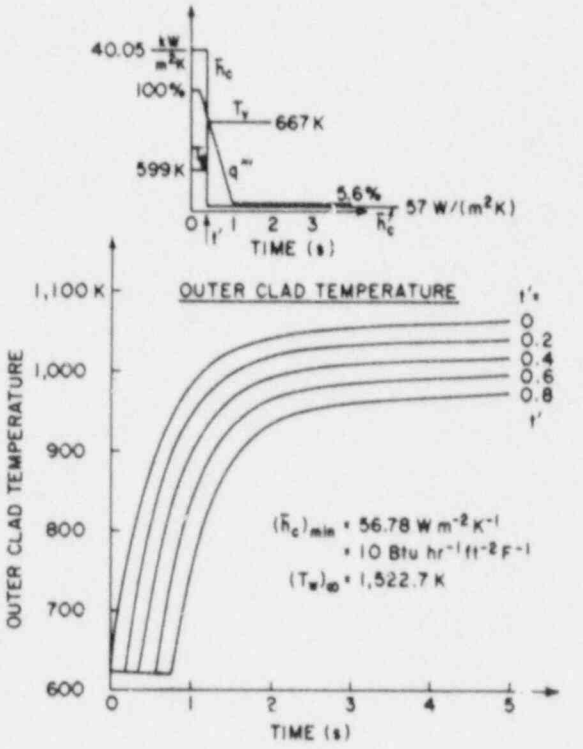

Fig. 9. Effect of DNB Delay Time t' on Peak Clad Temperature for Extremely Low Heat Transfer Coefficient, $\bar{h}_c$ = 56.8 $Wm^{-2}K^{-1}$

The Effect of DNB or Dry-Out Delay is shown also in Figures 8 and 9. The delay t' is measured from break initiation as shown in the top sketches of Figure 8 and 9.

Any delay in DNB or dry-out delays the temperature rise (horizontal shift of curves) and the peak by approximately the same amount t'. Moreover, any such delay reduces also the peak (vertical shift of curves), because extended cooling of the clad under pre-DNB conditions reduces the stored energy in the fuel prior to the temperature excursion.

The Effect of Scram Delay relative to the appearance of DNB or dry-out is shown in Figure 10. The three curves are obtained with t' = 0.2s in Eqs. (63a) and (64a). The middle curve is obtained with the fission and decay power history described by Eqs. (67) with t" = 0.2s, the top and bottom curves, respectively, with t" = 0.3s and 0.1s.

An advance in scram initiation reduces the peak clad temperature by approximately 300 K/s, while a delay of scram initiation increases the peak clad temperature by approximately 120 K/s.

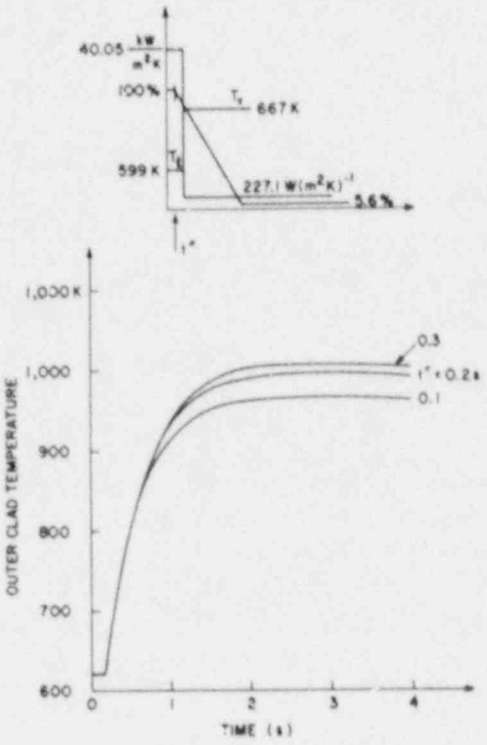

Figure 10. Effect of Scram Delay on Peak Clad Temperature

3.5 Concluding Remarks

The above effects from variations in heat transfer coefficient in DNB or dry-out delay and scram delay include all effects from hydraulic and system-related parameters on the blowdown peak clad temperature, because droplet cooling is unimportant under realistic blowdown conditions. The effects from systematic modeling errors (cf. Section 2.8.3) on peak clad temperature uncertainty is not quantified here, because the necessary modeling documentation for TRAC-PF1/MOD1 is not available at this time.

Confidence limits for peak clad temperature will be developed in an ongoing USNRC project. The work will be extended from blowdown to reflood peak clad temperature.

4. Conclusions

The analysis presented here leads to these major conclusions:

1. The peak clad temperature during blowdown is limited by effective single-phase vapor cooling to less than 880K.

2. The blowdown clad temperature peaks, under all credible circumstances, before the arrival of liquid droplets in the core. Therefore, the peak clad temperature during blowdown is not affected by reactor loop characteristics (break flow or pump degradation). It is governed instead by fuel stored energy or, equivalently, by linear heating rate. It depends only slightly on vapor velocity which affects the convective heat transfer coefficient after DNB or dry-out.

3. Fuel stored energy and peak clad temperature during blowdown depend primarily on three fuel-related modeling parameters, with this order of significance: gap conductance, power peaking factor and fuel thermal conductivity. Uncertaintites in stored energy and blowdown peaking factors are affected primarily by the uncertainties in these three parameters and potentially by systematic modeling errors in predicting these three parameters.

4. As a result of conclusions 2 and 3, blowdown peak clad temperature measurements are not affected by scaling distortions outside the reactor core (in downcomer, pumps, steam generators, etc.). Since test facilities with nuclear fuel (LOFT etc.) have full-scale fuel pins from the view point of transient radial conduction, it can be stated that blowdown experiments with nuclear fuel yield the blowdown peak clad temperature without scale distortion.

5. The expected uncertainty in fuel stored energy is found to be 26%, based on 1-σ uncertainties in all governing parameters. Based on the same parameter uncertainties, the blowdown peak clad temperature has an uncertainty of 42K (1-σ level).

6. Based on its published documentation, the TRAC-PF1/MOD1 computer code has systematic modeling errors in fuel thermal conductivity, gap conductance and convective film coefficients. The first two errors compensate during steady-state, but not during transient calculations. The third error applies only to two-phase flow and heat transfer conditions. Additional documentation is needed to quantify the effects on peak clad temperature from these errors.

References

1. Safety Code Development Group, "TRAC-PF1/MOD1: An Advanced Best Estimate Computer Program for Pressurized Water Reactor Thermal-Hydraulics Analysis," NUREG/CR-3858, LA-10157-MS, Los Alamos National Laboratory, Los Alamos, NM 87545 (1986).

2. B. E. Boyack et al., "TRAC User's Guide," NUREG/CR-4442, LA-10590-M, Los Alamos National Laboratory, Los Alamos, NM 87545 (1985).

3. "Compendium of ECCS Research for Realistic LOCA Analysis," Draft Report, NUREG-1230, Division of Reactor and Plant Systems, U.S. Nuclear Regulatory Commission, Washington, D.C. (1987). See Section 4.3.4.

4. T.R. Goodman, "Application of Integral Methods to Transient Nonlinear Heat Transfer," Advances in Heat Transfer, Vol. 1, Academic Press, New York (1964).

5. W. Wulff, "Lumped-Parameter Models for Transient Conduction in Nuclear Reactor Components," BNL-NUREG-51231, NUREG/CR-1540, Brookhaven National Laboratory, Upton, New York 11973 (1980).

6. D.L. Hagrman et al., "MATPRO-Version II (Revision 1), A Handbook of Materials Properties for Use in the Analysis of LWR Fuel Rod Behavior," NUREG/CR-0497, TREE-1280, Rev. 1, EG&G Idaho, Inc., Idaho Falls, ID (February 1980).

7. B.A. Boley and J.H. Winer, "Theory of Thermal Stress," John Wiley and Sons, Inc., New York, London, Sidney (1960). (See p. 290).

8. M. Jakob, Heat Transfer, Vol. 1, John Wiley and Sons, Inc., New York, London (1949). (See p. 192, Eq. 20-74).

9. L.J. Siefken, C.M. Allison, M.P. Bohn and S.O. Peck, "FRAP-T6: A Computer Code for the Transient Analysis of Oxide Fuel Rods," NUREG/CR-2148, EGG-2104, EG&G Idaho, Inc., Idaho Fall, ID 83415 (1981). (See p. 16, Eq. (2)).

10. S. Malang, "Simulation of Nuclear Fuel Pads by Using Process-Controlled Power for Indirect Electrically Heated Rods," ORNL-TM-4712 (GEMP-482), Oak Ridge National Laboratory (1975).

11. W. Wulff, H. S. Cheng, S. V. Lekach and A. N. Mallen, "The BWR Plant Analyzer," NUREG/CR-3943, BNL-NUREG-51812, Brookhaven National Laboratory, Upton, NY 11973 (1984).

12. B. W. Sheron, "Bases and Criteria for the Selection of Response Surface Parameters for the Statistical Assessment of LOCA," Enclosure 7, GEW-38-87, U.S. Nuclear Regulatory Commission, Division of Safety, Washington, DC 20555, (301) 492-7588 (1987).

13. E. T. Laats. "FRAPCON-2 Model Uncertainty Study," EGG-CAAD-5584, EG&G Idaho, Idaho National Engineering Laboratory, Idaho Falls, ID (1981).

14. R. Chambers, W. E. Driskell and S. C. Resch, "Assessment of FRAP-T6 Code Capabilities During Large Break Loss of Coolant Accidents," EGG-CAAD-5829, Idaho National Engineering Laboratory, Idaho Falls, ID (1982).

15. G. P. Steck, M. Berman, R. K. Byers, "Uncertainty Analysis for a PWR Loss-of-Coolant Accident: 1. Blowdown Phase Employing the RELAP4/MOD6 Computer Code," NUREG/CR-0940, SAND79-1206, Sandia Laboratories, Albuquerque, NM 87185 (1980).

16. G. S. Lellouche, "Considerations Relative to TRAC-PF1/MOD1 Uncertainty Analysis," distributed to members of the USNRC Technical Program Group, from S. Levy, Inc., 3425 S. Bascom Ave., Campbell, CA 95008-7006, Sept. 18, 1987.

17. F. W. Dittus and L. M. K. Boelter, "Heat Transfer in Automobile Radiators of Tubular Type," Publications in Engineering, University of California, Berkeley; p. 443 (1930).

18. K. Lassmann and F. Hohlefeld, "The Revised Urgap Model to Describe the Gap Conductance Between Fuel and Cladding," Nuclear Engineering and Design, 103 (1987), p. 215.

19. A. M. Ross and R. L. Stoute, "Heat Transfer Coefficient Between UO_2 and Zircaloy-2," CRFD-1075 (1962).

20. R. A. Dean, "Thermal Contact Conductance Between UO_2 and Zircaloy-2," CVNA-127, Westinghouse Electric Corporation (1962).

21. F. R. Campbell et al., "In-Reactor Measurement of Fuel-to-Sheath Heat Transfer Coefficients Between UO_2 and Stainless Steel," AECL-5400 (1977).

22. M. E. Cunningham et al., "Stored Energy Calculation: The State of the Art," PNL-2581, Pacific Northwest Laboratory, Richland, WA 99352, operated by Battelle Memorial Institute (1978).

23. B. E. Boyack, "Response to Questions of September 8, 1987," Letter dated September 15, 1987, from Los Alamos National Laboratory to U. S. Rohatgi, Brookhaven National Laboratory.

24. R. K. Fujita, F. R. Motley and K. A. Williams, "TRAC-PF1 Analysis of Best-Estimate Large-Break LOCA in a Westinghouse PWR with Four Loops and 17 x 17 Fuel," LA-2D/3D-TN-83-4, Los Alamos National Laboratory, Los Alamos, NM 87545 (1983).

25. M. E. Cunningham et al., "Application of Linear Propagation of Errors to Fuel Pad Temperature and Stored Energy Calculations," NUREG/CR-1753, PNL-3539, Pacific Northwest Laboratory, Richland, WA 99352, operated by Battelle Memorial Institute (1980).

26. W. Wulff, H. S. Cheng and A. N. Mallen, "Analytical Modeling Techniques for Efficient Heat Transfer Simulation in Nuclear Power Plants," 23rd ASME/AIChE/ANS National Heat Transfer Conference, Denver, CO, BNL-NUREG-35944 (1985). (See Eq. (9) for cladding and Eq. (12) for pellet).

WEAR IN CHECK VALVES DUE TO FLOW INDUCED MOTION

Peter Griffith
Professor of Mechanical Engineering

John C. Sununu
Former Research Assistant

Massachusetts Institute of Technology
Cambridge, Massachusetts 02139

ABSTRACT

Experiments showing the frequency and amplitude of the flow induced motion of the gate for a two and a four inch swing check valve have been performed. The gate motion is due to turbulence in approach flow. We have found the dominent turbulent frequency of the approach flow is about half the natural frequency of the valves. The valves appear to be almost critically damped. Because of this, the values respond almost as they would to a static force of the magnitude characteristic of the turbulent fluctuation in the flow.

Both the dimensionless exciting force and the damping ratio have been found to be independent of valve size so the above statements are true for larger valves also.

The valve oscillation amplitudes and frequencies are used to calculate the wear at the shaft and at the stop. For an unpegged check valve, such as one of the 10 inch valves which was used at San Onofre, we found that shaft wear would amount to .27 inches^3/ year and stop wear to .03 inches^3/ year.

INTRODUCTION

The check valves found in one of the feed water lines of the San Onofre plant leaked during a recent transient (1). The leakage allowed steam to enter the feed water lines so that when the feed water pump was turned on, steam was condensed very rapidly and a water hammer occurred. This has caused an extended outage for that plant.

The valves failed because the plant had operated at part load for more than a year and the gates on the check valves were swinging free or tapping. This caused the cotter pins holding nuts on the studs to break (See Figure 1) allowing the nuts holding the gate to the arm to back off resulting in several modes of failure. The modes of failure included the following:

1. The nut backed off completely and the disc fell to the bottom of the valve.

2. The nut backed off far enough so that one of the anti-rotation bars jams under the arm and the valve cocks. The valve then fails to seat properly.

3. The disc turned, wearing the stud off so the disc fell to the bottom of the valve.

All of these failures can, and should be eliminated by adopting an intregral disc and arm assembly, such as the Atwood-Morrill design illustrated in Reference 2, and operating the plant so that the valves are pegged as much of the time as possible. When a design of this kind is adopted the remaining kinds of valve failure are due to wear at the shaft and wear at the stop or gate where the gate impacts the stop.

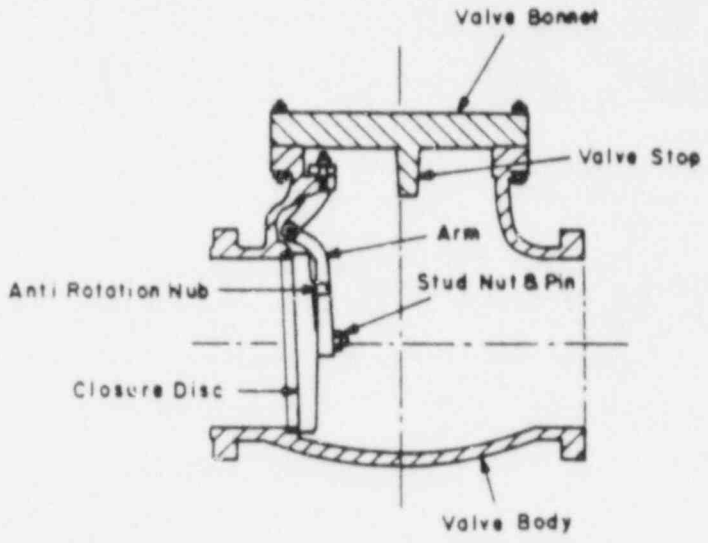

Figure 1 Typical swing check valve. Reference 1.

Some part load operation is inevitable during startup or during some transients. At this time we have no way of estimating how much valve wear occurs during part load operation, nor do we know how to set up an inspection program so we can rest assured that valves will not fail between inspections. The wear calculation procedure described in this paper addresses both these problems.

In this paper we shall start by giving the formulas used to calculate sliding wear (for the shaft/bearing surfaces) and impact wear (for the gate/stop surfaces). To evaluate both kinds of wear it will soon become evident that we will need a method of calculating the amplitude and frequency of the flow induced vibration of the gate. Experiments performed on the two and the four inch check valves will be described and the results presented. We will then show how these results can be used to calculate the frequency and amplitude of these oscillations. We shall also show that, in dimensionless terms the oscillations are independent of valve size so that we can use the results of these experiments to predict oscillations in larger valves. Finally a valve wear calculation procedure will be summarized.

CALCULATING SLIDING WEAR

Reference 3 gives a method of calculating adhesive wear which is the kind of wear which occurs when one surface slides over another. The formula is as follows:

$$\Delta V_s = K_s \frac{F}{3P} \Delta l \tag{1}$$

In this equation F is the normal force, Δl is the distance traveled, P is the penetration hardness (in units of pressure) and K_s is the adhesive wear coefficient. For clean, similar surfaces:

$$K_s = 5 \times 10^{-3} \quad (dimensionless) \tag{1a}$$

A force balance on the gate of a check valve (see Figure 1.) will allow us to estimate the normal force F. The distance traveled must be obtained by evaluating the angle traveled through and the frequency of oscillation. Doing this for an amplitude of ($\theta_{max} - \theta_{min}$) for the gate of a check valve, we obtain:

$$\frac{\Delta l}{\Delta t} = 2\left(\frac{(\theta_{max} - \theta_{min})}{360}\right) 2\pi r_s \omega \tag{2}$$

The factor two in equation (2) is there because the valve travels the full amplitude twice in each cycle. In equation 2, r_s is the shaft radius because this is the radius at which the contacting surfaces act.

Combining equations (1) and (2) we obtain:

$$\frac{\Delta V_s}{\Delta t} = K_s \frac{F}{3P}\left(\frac{2(\theta_{max} - \theta_{min})}{360}\right)2\pi r_s \omega$$

Let us now look at impact wear.

CALCULATING IMPACT WEAR

Reference 4 gives an expression for impact wear:

$$\frac{\Delta V_i}{\Delta t} = K_i \frac{I}{P}\omega \tag{4}$$

In this equation, I is the kinetic energy of impact, W is the rate at which impacts occur, P is the penetration hardness and K_i is the dimensionless wear coefficient. Its value is:

$$K_i = 1700 \times 10^{-6} \tag{4a}$$

We can estimate the kinetic energy of impact by using the average velocity of the center of mass of the gate over the cycle. In doing this we are slightly underestimating the kinetic energy by omitting the rotational component but slightly overestimating it by using the velocity of the center of mass of the disc rather than the disc and arm. The kinetic energy then is:

$$I = \frac{1}{2}\left(m - \frac{m_a}{2}\right)\left(2\frac{(\theta_{max} - \theta_{min})}{360}2\pi R\omega\right)^2 \tag{5}$$

Combining equations 4 and 5 we obtain:

$$\frac{\Delta V_i}{\Delta t} = \frac{K_i\left(m - \frac{m_a}{2}\right)}{2P}\left(2\frac{(\theta_{max} - \theta_{min})}{360}2\pi R\omega\right)^2 \tag{6}$$

The wear coefficient is given in reference (4). It is:

$$K_i = 1700 \times 10^{-6} \quad for\ steel \tag{6a}$$

$$K_i = 900 \times 10^{-6} \quad for\ brass \tag{6b}$$

It is clear from examining both equations (3) and (6) that to calculate the wear we need the angle through which the gate swings and the frequency of swinging. Determining these quantities is the main goal of this work.

EXPERIMENTS

A two inch and a four inch check valve were set up to determine the frequency and amplitude of the oscillations. The basic experiment is shown schematically in Figure 2. Light was shinned through the pipe and what was transmitted was picked up by the photo cell at the left of Figure 2. A length of pipe before the check valve which was greater than 8(L/D)'s was used to insure that the flow was fully developed. Reference 5 reports a figure (reproduced here as Figure 3) which shows the regions of operation of check valves. L/D greater than 6 is sufficient to give behavior typical of a fully developed flow. The details of the apparatus and running procedure used to develop this figure are available in reference 6. The apparatus was essentially the one illustrated in Figure 2.

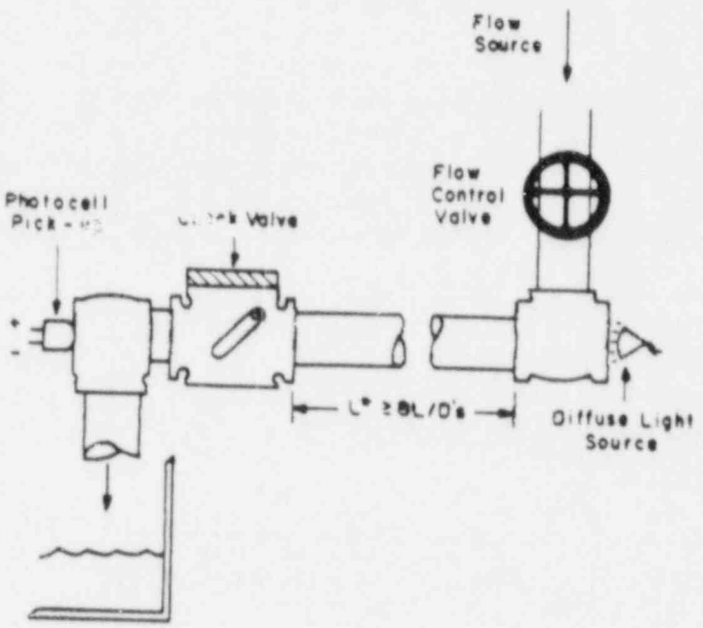

Figure 2 Schematic of the test setup.

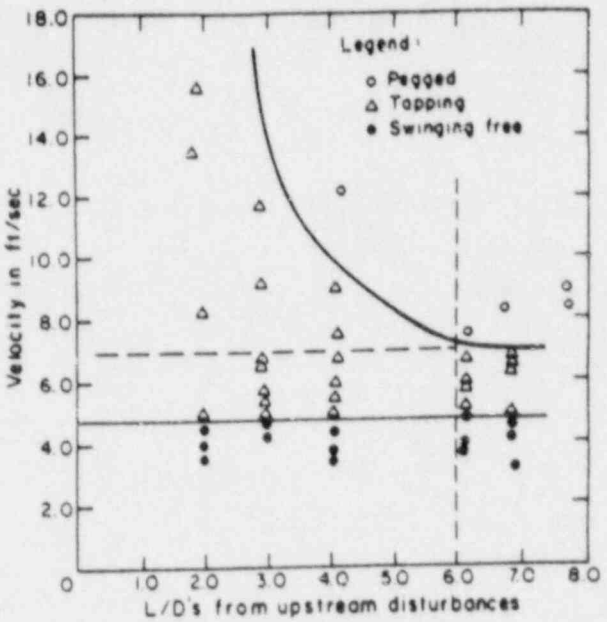

Figure 3 Regions of check valve operation. Reference 5.

A sample of the data as recorded digitally on an IBM PC AT with Unklescope softwear (6) is shown on Figure 4a. As recorded, it includes some 120 Hz noise due to flicker in the light source. When passed through a 15 Hz filter, the trace is as shown on Figure 4b.

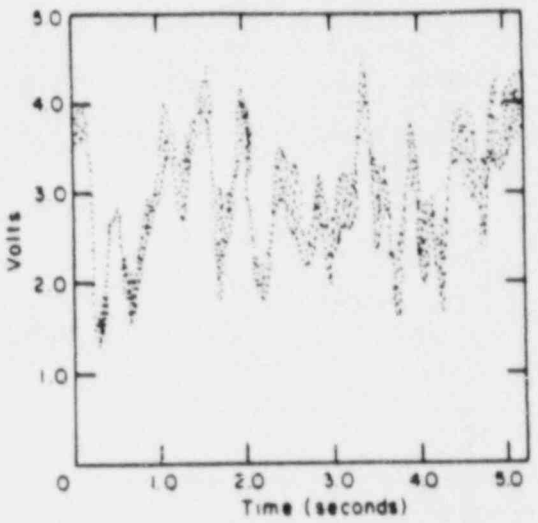

Figure 4a Raw data from photo-cell output as voltage. 4" valve at 6.6 ft/sec.

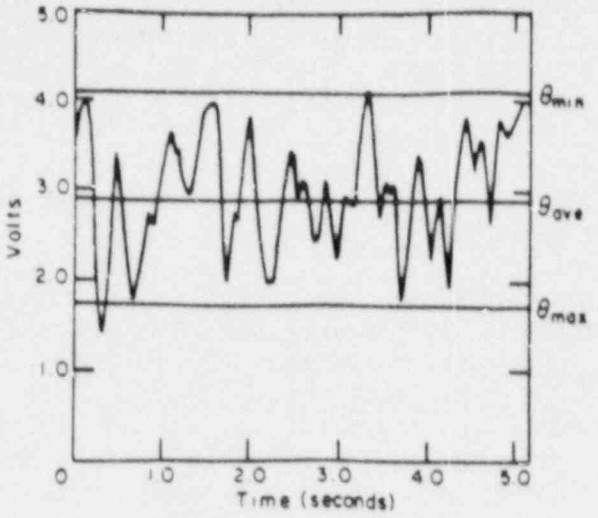

Figure 4b Filtered data showing average, maximum and minimum gate angles observed for this valve. 4" valve at 6.6 ft/sec.

We looked at a variety of methods of treating these data. We considered using a power spectral density and random vibration framework. We also looked at using a fast Fourier transform plus Hanning window to determine dominant frequency. We finally settled on using the measured distance traveled from a set of data, such as illustrated in Figure 4b, plus a frequency determined by counting the number of crossings of the average value over the time interval shown in Figure 4b. Conceptually the method chosen is the simplest. The results of all three methods were practically the same. The frequency data is shown in Figure 5.

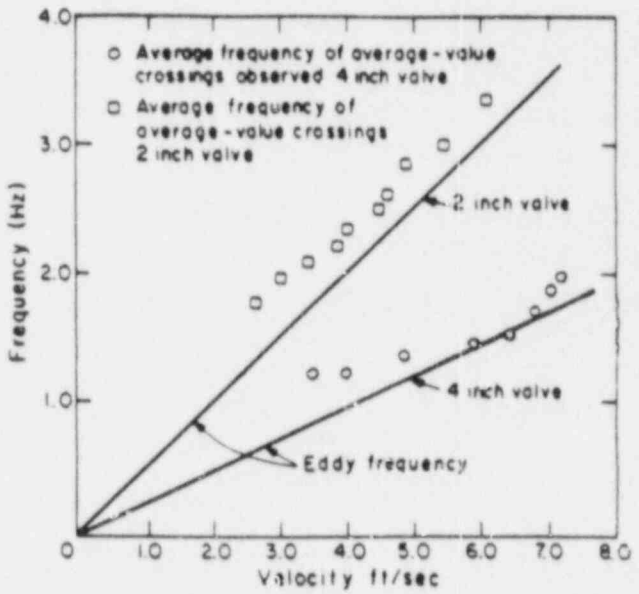

Figure 5 Valve natural frequency as a function of flow velocity.

In order to determine the amplitude of oscillation from Figure 4b, a calibration was needed. This was done by screwing a long bolt through a plastic bonnet (replacing the brass or steel one that came with the valve) and noting when the gate just cleared the bolt when it was oscillating, we then extended the bolt until the gate was just pegged. These positions were noted and the deflection angles θ_{max} and θ_{min} calculated from the geometry. The average value of the trace was determined from a subroutine accompanying the softwear used to take the data.

Another set of experiments was run to see if we could determine, experimentally, the dynamic properties of these valves when there was water running through them. We would need these to predict whether a resonance was present in the valve of interest over the operating range. This experiment consisted in partially forcing the valve shut with a wire inserted through a small hole in the plastic bonnet and then quickly withdrawing it. If the valve was underdamped there should have been a distinct overshoot. None was observed. The valve would go promptly to its approximate equilibrium position and start oscillating normally. The valve appeared heavily damped but not so heavily damped that a time period that was greated that one cycle in duration was needed to allow the valve to assume its fully developed oscillation.

EXPERIMENTAL RESULTS

Two quantities are needed to calculate wear, an amplitude and a frequency. The measurements of amplitude and frequency were made as described and are presented here in Figures 6, 7a and 7b. Figure 6 shows how the measured frequency increases with flow velocity while Figures 7a and 7b shows how the measured amplitude changes with flow velocity for both the 2 and the 4 inch valves. In the next section we will show how the theoretical lines on these figures were placed.

CALCULATING THE FREQUENCY OF GATE OSCILLATION USING A SIMPLE, LINEAR SPRING - MASS MODEL

The natural frequency can be calculated as:

$$\omega_n = \frac{1}{2\pi}\left(\frac{K_{stiff}}{m_{eff}}\right)^{\frac{1}{2}} \qquad (7)$$

$$m_{eff} = (m - \frac{m_a}{2}) + \frac{8}{3}\rho r_d^3 \tag{8}$$

The effective mass includes the mass of the gate itself plus the induced mass of water. Reference (8) suggests, for a translating disc in a large pool of water, the value give in equation (8). This is obviously not quite right as the disc is oscillating around a shaft while suspended in a pipe surrounded by flowing water. It is, however, a reasonable approximation.

The effective spring constant for a disc held at equilibrium by a jet of fluid is determined in reference 2. The hydraulic force on the disc is:

$$F = K\rho AV^2 sin^2\theta \tag{9}$$

The spring constant is obtained by differentiating (9) (the details are in appendix A) which results in:

$$K_{stiff} = \frac{K\rho AV^2 sin2\theta}{R} \tag{10}$$

where the recommended value for K is:

$$K = 2.21 \quad (dimensionless) \tag{10a}$$

As the velocity through the valve decreases, the angle θ increases and the valve's natural frequency approaches that of a pendulum. Valves are rarely operated for any length of time at such a low velocity. The extrapolated curves on Figure 6 show this extrapolation however.

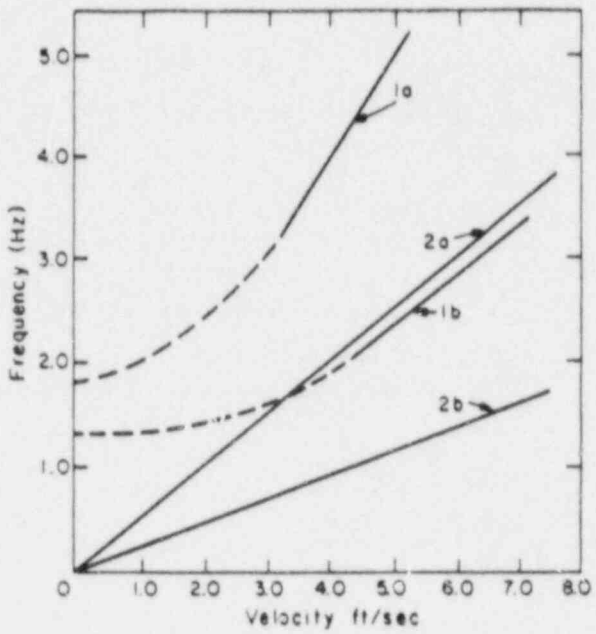

Figure 6 Comparison of natural and forcing frequencies.
1a - Natural frequency, 2" valve.
2a - Forcing frequency, 2" valve.
1b - Natural frequency, 4" valve.
2b - Forcing frequency, 4" valve.

FORCING FREQUENCIES AND AMPLITUDES

The turbulent fluctuations in the flow drive the oscillations of the valve. From an examination of these data and the information given in reference 10 the recommended equation for calculating the frequency is given in equation (11):

$$\omega_{eddy} = \frac{(0.04)V}{r_p} \tag{11}$$

The amplitude of these velocity fluctuations is about 6% of the velocity in the pipe. That is:

$$\Delta V = Velocity\ Fluctuation = (0.06)V \tag{12}$$

In order to convert this fluctuation velocity into a fluctuating gate angle, it is necessary to do a force balance on the gate. This has been done in reference (2) and the result is as follows:

$$\sin\theta = \left(\frac{(W - \frac{W_a}{2})bg}{K\rho AV^2}\right)^{\frac{1}{2}} \tag{13}$$

The range of angle swung through is determined by substituting the maximum and minimum values of the velocity:

$$\sin\theta_{max}^{min} = \left(\frac{(W - \frac{W_a}{2})bg}{K\rho A(V \pm \Delta V)^2}\right)^{\frac{1}{2}} \tag{14}$$

We are now in a position to calculate the natural frequency and fluctuation amplitude for the two values tested here. The results are shown as lines on Figures 6, 7a and 7b. In the higher velocity range where the valves are most likely to operate when the reactor is at part load, the natural frequency is about twice forcing frequency.

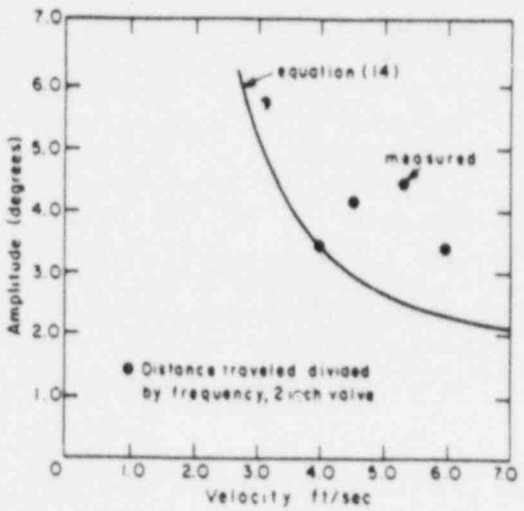

Figure 7a

Measured swing amplitude as a function of velocity for the 2" valve.

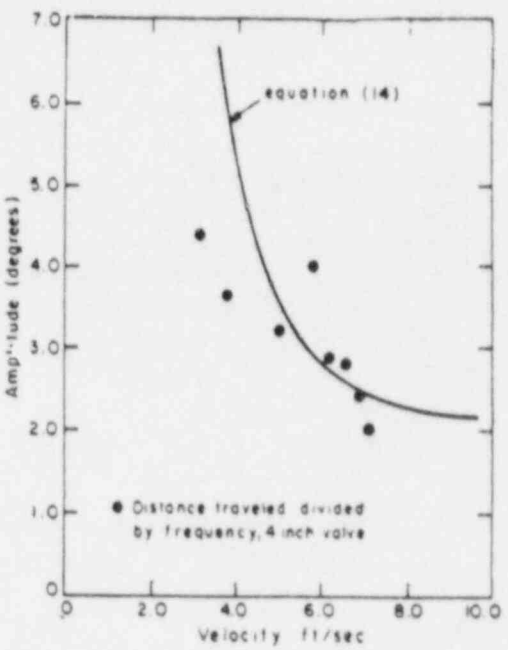

Figure 7b

Measured swing amplitude as a function of velocity for the 4" valve.

DISCUSSION OF VALVE DYNAMICS

Appendix A presents a scaling study of check valve dynamics. The result of this study is that, in dimensionless terms, the operation of small and large valves is the same. That is, if the dimensionless fluctuation amplitude for the gate on a small valve is plotted versus the dimensionless forcing frequency for the appropriate damping ratio, the operating point for a geometrically similar, large valve will plot on the same point as the small valve.

SUMMARY

Equations (3) and (6) allow us to calculate the wear on the shaft and the impact points respectively. The unknowns in these equations are the angle swept over by the gate ($\theta_{max} - \theta_{min}$), the frequency ω . The angle swept out by the gate can be calculated from equations (14) and (12). The frequency can be determined from equation (11).

Relating the amount of wear to a valve failure involves looking at a variety of possible failure modes and seeing whether the calculated amount of wear could have caused a failure to occur. For instance, shaft wear could allow the valve to drop far enough so it doesn't seat properly. Wear might so thin the shaft that it breaks. Both these failure modes are possible. However, we cannot check them here without further details on the valve geometry.

Similarly, wear at the stop could so change the geometry that the valve won't peg at the design velocities even though it is operating at its design velocity. Alternatively, for some designs, the tapping could thin the valve body so much that the body would be in danger of rupturing. Again more detail of the valve geometry is needed in order to check these possibilities. Reference 3 gives a recomendation on how to calculate the amount of material removed if the contacting materials do not have the same hardness.

APPENDIX A

SCALING THE DYNAMICS OF SWING CHECK VALVES

INTRODUCTION

The cost and complication of testing check valves increases very rapidly with size. There are, therefore, strong incentives to do testing on as small a scale as possible. In this Appendix we shall look at how the dimensionless amplitude and frequency of oscillation of the gate on a check valve varies with the size of the valve. We shall assume the valve is experiencing a small sinusoidal excitation due to the turbulent flow of a liquid passing through it.

The two variables we are concerned with are the dimensionless forcing frequency:

$$\omega^* = \frac{\omega}{\omega_n} \tag{A-1}$$

and the damping ratio:

$$\varsigma = \frac{b}{2\sqrt{Km}} \tag{A-2}$$

That is, if we specify these two variables on a plot such as figure A - 1, we can identify an operating point. The question we ask is how does that operating point move as we change the size of the valve?

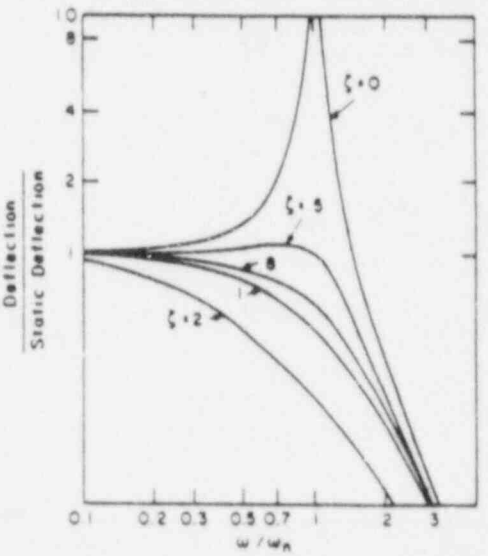

Figure A-1 Response curve for a linear, single degree of freedom oscillator, excited by a sinusoidally varying force.

DIMENSIONLESS FORCING FREQUENCY

The undamped natural frequency for a linear, single degree of freedom system is, from equation (7).

$$\omega_n = \frac{1}{2\pi}\left(\frac{K_{stiff}}{m_{eff}}\right)^{\frac{1}{2}} \tag{A-3}$$

From equation (9) we can determine the effectiveness by differentiating the force - deflection relation Equation (10), that is:

$$K_{stiff} = \frac{dF}{rd\theta} = \frac{K\rho AV^2 2sin\theta cos\theta}{R} \tag{A-4}$$

Recalling that the angle θ must be the same for two similar valves operating under hydraulically similar conditions, we can say (using " r " as a characteristic dimension) the stiffness varies as follows:

$$K_{stiff} \propto \frac{r^2V^2}{r} \tag{A-5}$$

because K , ρ , and θ are all constants.

The velocity in equation (A-5) varies with size. Solving equation (13) for V allows us to find out how it varies. The result is:

$$V = \left(\frac{(W - \frac{W_A}{2})bg}{K\rho A sin^2\theta}\right)^{\frac{1}{2}} \tag{A-6}$$

In equation (A-6), b , g , K , ρ , and θ are all constants so:

$$V \propto \left(\frac{r^3}{r^2}\right)^{\frac{1}{2}} \propto r^{\frac{1}{2}} \tag{A-7}$$

Substituting equation (A-7) into equation (A-5) we obtain:

$$K_{stiff} \propto \frac{r^2 r}{r} \propto r^2 \tag{A-8}$$

Now the mass is proportional to the density of the metal and the volume of the valve. However, as density is a constant, we can write:

$$m_{eff} \propto r^3 \tag{A-9}$$

Similarly, the forcing frequency is determined by the rate at which the large vortices shed upstream of the valve pass by the gate. From equation (11) this has been found to be:

$$\omega = (0.04)(\frac{V}{r_p}) \tag{A-10}$$

In other words:

$$\omega \propto \frac{V}{r} \propto \frac{1}{r^{\frac{1}{3}}} \tag{A-11}$$

Substituting equations (A-3), (A-5), (A-7), (A-8), and (A-10) into (A-1) yields the scaling law for the forcing frequency:

$$\omega^* \propto \frac{\omega}{\omega_n} \propto \omega(\frac{m_{eff}}{K_{stiff}})^{\frac{1}{2}} \propto \frac{1}{r^{\frac{1}{3}}}(\frac{r^3}{r^2})^{\frac{1}{2}} = 1 \tag{A-12}$$

That is, there is no effect of size on the dimensionless forcing frequency.

THE DAMPING RATIO

We extract the damping ratio from the relation for the fluid drag on a disc. For a disc moving back and forth in a check valve we can say:

$$F_b = C_D(\frac{\rho V^2}{2})A \tag{A-13}$$

By definition, the damping coefficient is obtained by differentiating this expression:

$$\frac{dF_b}{dV} = b = C_D \rho V A \tag{A-14}$$

C_D and ρ are constants so:

$$b \propto Vr^2 \propto r^{\frac{1}{3}} r^2 \propto r^{\frac{7}{3}} \tag{A-15}$$

From equation (A-2) we can say:

$$\zeta = \frac{b}{2(K_{stiff} m_{eff})^{\frac{1}{2}}} \propto \frac{r^{\frac{7}{3}}}{(r^2 r^3)^{\frac{1}{2}}} = 1 \tag{A-16}$$

So the damping ratio is also independent of valve size.

This is a very useful result. It says that, in dimensionless terms, the dynamic behavior of check valves is independent of their size. The check valves which we have looked at both have an operating angle which is given by equation (A-6). In adition, Reference (9) compares valves from a variety of manufacturers and finds a single value for K is sufficient to describe them so it appear this is a general result. As these valves are excited at about half their natural frequency, they respond as they would to a static force of the magnitude of the maximum of the fluctuative force. No resonance behavior is observed or expected. See figure A-1.

REFERENCES

(1) ----- "Loss of Power and Water Hammer Event at San Onofre, Unit 1 one 21st. November 1985. NUREG-1190, January 1986.

(2) Chiu, C. and M.S. Kalsi "Failure Analysis of Swing Check Valves." A report dated 4 April 1986, (version 2) from Southern California Edison Company.

(3) McClintock, R.A., A.S. Argon. "Mechanical Behavior of Materials." Addison - Wesley. Reading, Massachusetts. 1966. see page 669.

(4) Rabinowicz, E., K. Hozakai, "Impact Wear of Ductile Materials." International Tribology Conference, Tokyo, Japan. July 1985.

(5) Snopkowski, Jennifer., Peter Griffith. "Check Valve Dynamics." A report submitted to Dr. C. Nalezney, E.G. and G. Idaho, Inc. April 1, 1987, Available in the public document room at N.R.C. in Washington, D.C.

(6) Sununu, John. "Wear in Check Valves due to Flow induced Motion." M.S. thesis in Mechanical Engineering. May, 1987.

(7) Unklescope Softwear, Inc., Cambridge, Massachusetts. 1985.

(8) Patton, Kirk T. "Tables for Hydrodynamic Mass Factor for Translational Motion," ASME 65 - WA/UNT-2.

(9) Chiu, Chong, M.S. Kalsi. "Plant Availability Improvement by Eliminating Disc Vibrations in Swing Check Valves." ASME Paper. 86-JPGC-N-6

(10) Schlicting, Hermann. "Boundary Layer Theory." McGraw - Hill Book Company, New York. 1968. p. 523 -525.

RESULTS OF TWO-PHASE NATURAL CIRCULATION IN HOT-LEG U-BEND SIMULATION EXPERIMENTS

M. Ishii, S. Y. Lee and S. Abou El-Seoud

Reactor Analysis and Safety Division
Argonne National Laboratory
Argonne, Ill. 60439

ABSTRACT

In order to study the two-phase natural circulation and flow termination during a small break loss of coolant accident in LWR, simulation experiments have been performed using two different thermal-hydraulic loops. The main focus of the experiment was the two-phase flow behavior in the hot-leg U-bend typical of B&W LWR systems. The first group of experiments was carried out in the nitrogen gas-water adiabatic simulation loop and the second in the Freon 113 boiling and condensation loop. Both of the loops have been designed as a flow visualization facility and built according to the two-phase flow scaling criteria developed under this program. The nitrogen gas-water system has been used to isolate key hydrodynamic phenomena such as the phase distribution, relative velocity between phases, two-phase flow regimes and flow termination mechanisms, whereas the Freon loop has been used to study the effect of fluid properties, phase changes and coupling between hydrodynamic and heat transfer phenomena. Significantly different behaviors have been observed due to the non-equilibrium phase change phenomena such as the flashing and condensation in the Freon loop. The phenomena created much more unstable hydrodynamic conditions which lead to cyclic or oscillatory flow behaviors.

I. INTRODUCTION

In many cases, it is not practical to use full-scale testing for studying thermal-hydraulic phenomena. It is particularly so for analyzing the behaviors of nuclear reactor systems under abnormal operations or accident conditions due to safety reasons and high cost. The severity of the accident that occurred at Three Mile Island Unit-2 plant has increased interest in correct scaling of transient two-phase flow phenomena. In view of this, new scaling criteria for a two-phase system have been developed on a perturbation method applied to the system of governing equations by Ishii et al. [1,2]. This criteria has been used [3,4] to evaluate the design parameters of the new 2x4 simulation loop under the MIST program [5]. The extensions of the criteria to the pressure scaling as well as the fluid to fluid scaling have also been studied in detail [6]. In view of certain scaling difficulties and scaling distortions in the integral facilities [5,7], a supporting experimental study to investigate the two-phase natural circulation, hot-leg U-bend two-phase

flow behavior and associated scaling problems has been carried out at Argonne National Laboratory.

The major issues addressed under this program are as follows:

(1) Natural circulation interruption and resumption.
(2) Hot-leg two-phase flow regimes and regime transition.
(3) Void distribution and relative velocity between phases.
(4) Flow instability phenomena which may trigger loop-to-loop oscillations.
(5) Any particular thermal non-equilibrium phenomena which are important for natural circulation.
(6) Overall scaling effects in terms of geometries, pressure and fluid properties.

It is noted that in the prototype system, the diameter of the hot-legs is about 90 cm and the length to diameter ratio is relatively small at about 20. This indicates that the two-phase flow in the hot-leg can be quite different from the standard small scale experiments. There is a great uncertainty in describing the flow because the conventional two-phase flow models and correlations are developed based on small diameter and large length to diameter ratio system experiments. In view of this, the two-phase flow in a hot-leg is studied in detail through experiments in two different flow visualization loops in the present program.

II. NITROGEN-WATER HOT-LEG U-BEND SIMULATION EXPERIMENTS

A. Description of the Experimental Loop

Previously, the experimental results obtained from the nitrogen-water simulation loop using 5 cm (2") diameter glass pipe for the hot-leg have been reported [8,9]. Recently extensive experiments have been carried out in the loop with a new test section having a larger hot-leg diameter of 10 cm (4"). The loop was designed to simulate the part of the B&W 2 x 4 loop nuclear reactor system, see Figs. 1 and 2. The scaling criteria developed under the present program [3,4,6] have been used for this purpose. The basic scaling characteristic of the loop is given in Table I. As shown in Fig. 2, this two-phase flow loop consists of the bubble injection chamber simulating the core, 10 cm ID riser, inverted U-bend, gas separator simulating the once through steam generator, and cold-leg return. The bubble chamber, riser and U-bend section were made of Corning Pyrex glass tubes and fittings, whereas the gas separator was made of plexiglass. The riser (hot-leg) height was 5.13 m. The radius of the U-bend was 25 cm. However, the loop was designed such that the U-bend radius, hot-leg height and inlet geometry could be easily changed to study the parametric effects.

To model the steam/water flow in an actual LWR, in this experimental facility the tested fluids were nitrogen and water, working as the vapor phase and liquid phase, respectively. The gas was injected into the riser through nozzles which were made of stainless steel tubes, having a nominal 0.015 cm I.D. and 0.03 cm O.D. These 621 nozzles were molded into an epoxy plate which

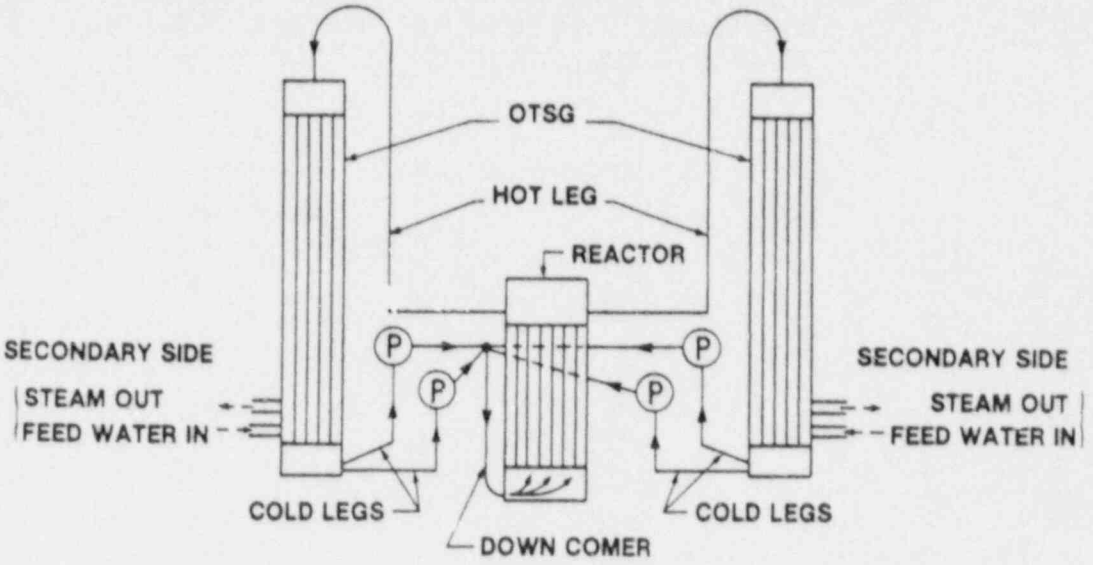

Fig. 1. Schematic of B&W 2x4 Loop Nuclear Reactor

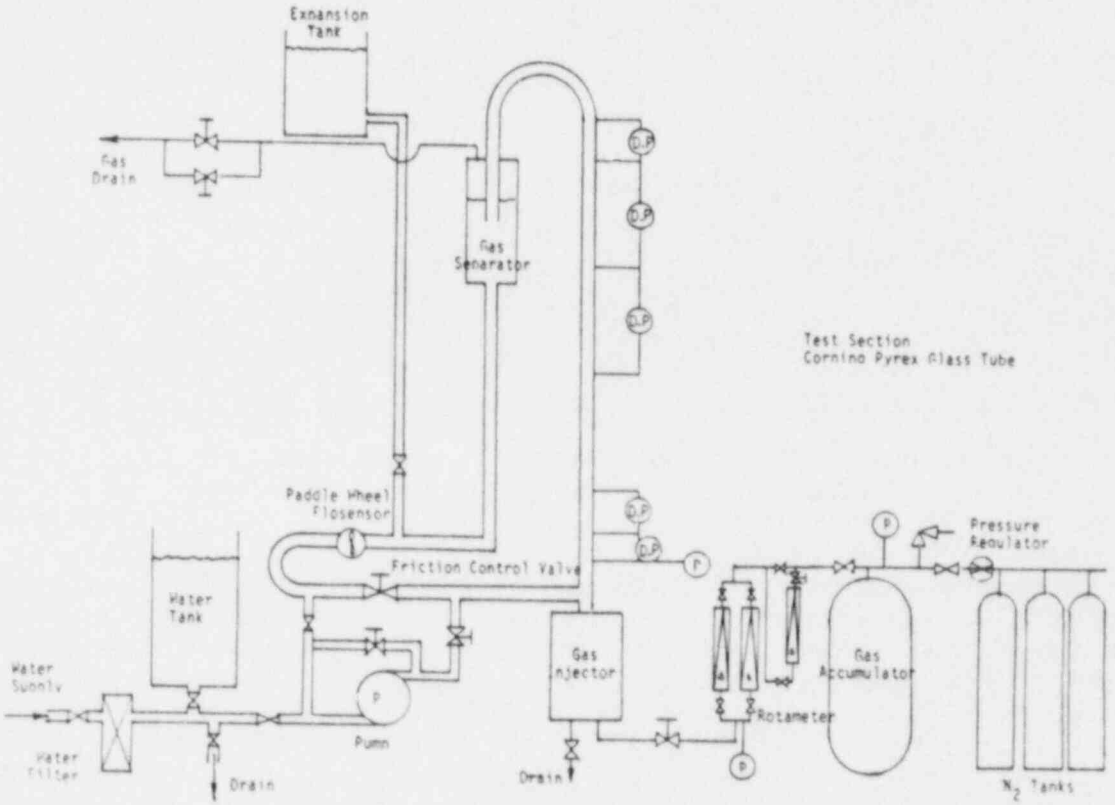

Fig. 2. Schematics of Hot-leg U-bend Simulation Loop for Nitrogen Gas-water Experiments

Table I. Typical Hot-Leg Natural Circulation Condition Corresponding to Prototype 2% Power at 4.7 MPa (680 psi) and 260°C (500°F)

	Prototype	N_2-Water Loop	Ratio
D(m)	0.915	0.102	1/9
A(m^2)	0.658	0.00817	1/81
L(m)	20.74	5.5	1/3.7
V(m^3)	13.65	0.0448	1/300
Single Phase			
u_f (m/sec)	0.88	0.45	1/1.93
τ (sec)	23.5	12.2	1/1.93
2 Phase Flow			
j_g (m/sec)	1.07*	0.55	1/1.93
j_f (m/sec)	1.95*	1.0	1/1.93
Quality	0.017	6.2×10^{-4}	1/27
Void Fraction	0.273	0.264	~1
ρ_g	0.0237	0.00114	1/21
ρ_f	0.786	1.0	1.27

*Depends on liquid subcooling and reactor core vent value bypass flow. No subcooling and no bypass flow case shown.

was held by a plenum at the bottom of the riser. The gas flowrate and pressure were measured between the plenum and the gas accumulator. Downstream of the U-bend, there was a separator where the gas was vented to the atmosphere from the loop through a valve. This separator, made of transparent plastic, was 91 cm high and 20 cm in diameter. Above the separator, a bellow type flexible coupling was used to reduce the stress on the glass test section. Beneath the separator, there was a 60 cm long glass tube through which entrainment of gas phase into the cold-leg was monitored. Beyond this point, a plastic tube of 5 cm in diameter was used instead of a glass tube since single phase flow could be expected. In the downcomer (cold-leg) section there was a

friction control valve which could be used to alter the loop frictional resistance. Furthermore, a liquid flow meter was installed in the horizontal section of the cold-leg with a sufficient straight entrance length. This flow meter is a paddle wheel type with magnetic pick-up and has special characteristics of very low pressure drops. In the riser section, six pressure taps were installed for measurement of the differential pressure at five locations. These pressure taps were made of brass plate. A small hole of approximately 0.4 mm in diameter was drilled to measure the pressure. At the low flowrates of interest to this experiment, these pressure taps give accurate void fraction measurements through differential pressure transducers because the frictional losses are negligibly small.

In order to study the effect of hot-leg inlet geometry on the two-phase flow regimes and flow interruption two different inlet sections were used, see Fig. 3. The first type had no horizontal hot-leg section to force the inlet flow to be in a bubbly flow. The latter had a short (50 cm) horizontal section.

B. Range of Flow Parameters

Generally, this experiment was conducted on the basis of three varying parameters; they were gas flowrate, friction valve opening and water level in the separator. Also, in order to study the effect of vapor phase at inlet section on the flow regimes and flow interruption, straight inlet and elbowed inlet sections were tested, see Fig. 3. The table below lists the ranges of parameters in this experiment.

Table II. Ranges of Parameters for N_2-Water Experiments

Gas Volumetric Flow	0 ~ 20 cm/sec
Friction Control Valve Opening	1, 1/4, 1/8
Separator Water Level	25 cm, 50 cm, 75 cm
Horizontal Section Length	0, 50 cm

C. Natural Circulation and Flow Interruption

In general, the induced liquid natural circulation rate decreases with the decreasing gas flow rate, see Figs. 4 and 5. As the gas flow rate decreases further, eventually the liquid circulation rate becomes zero corresponding to the flow interruption. When the permanent flow termination occurs, the two-phase level in the hot-leg stays at or below the lower surface of the top of the U-bend. Due to the insufficient hydrostatic head difference between the hot-leg and cold-leg, the two-phase level cannot rise to flow over

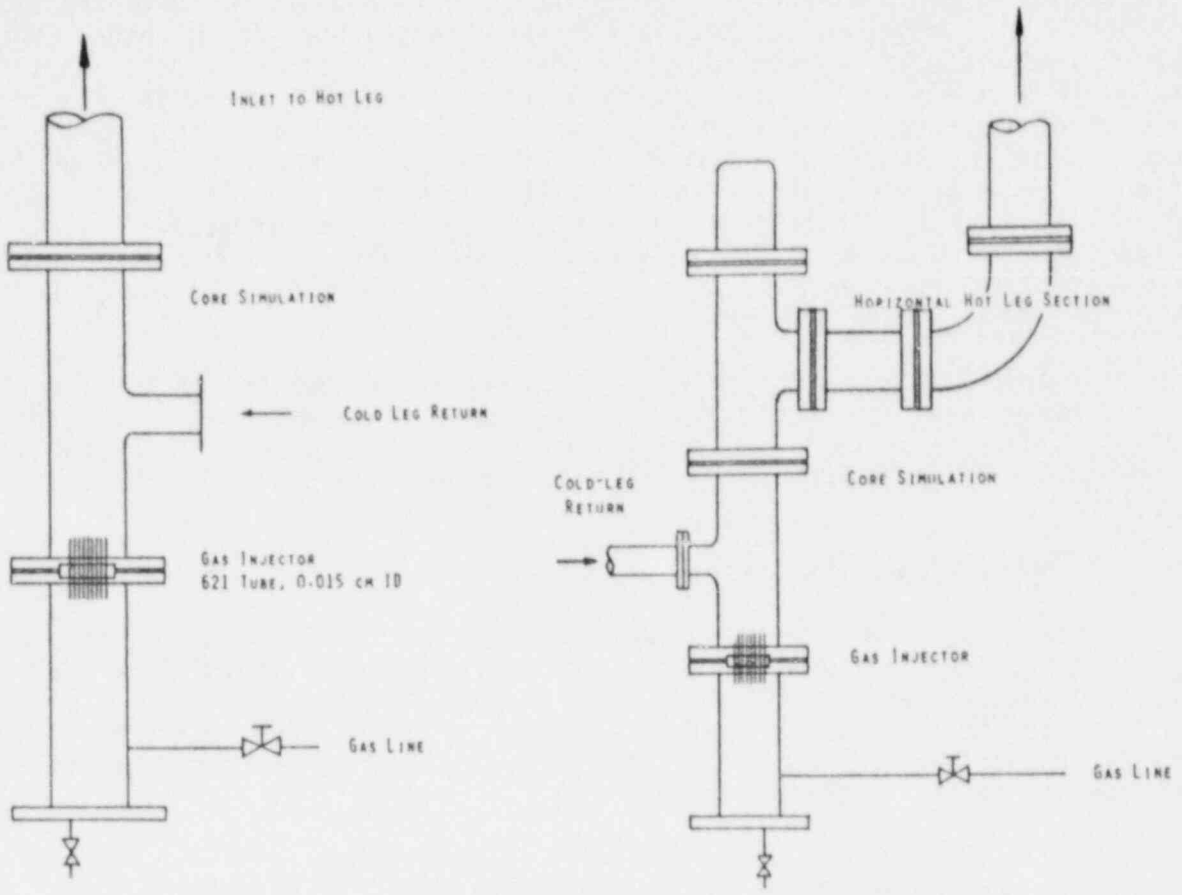

(a) Without Horizontal Section (b) With Horizontal Section

Fig. 3. Two Different Geometries of Hot-leg Inlet Portion

the U-bend section, thus there is no carry-over liquid flow. Only the gas phase is transported over the U-bend. Two-phase flow oscillations are relatively mild compared with the experiments with 5 cm I.D. hot-leg.

Besides the permanent flow interruption discussed above, intermittent flow interruptions have also been observed in the slug or churn turbulent flow regime. As a large slug bubble passes over the U-bend, the section is temporarily voided and the liquid carryover flow becomes very small. However, with the passing of a liquid slug, the carryover flow is fully recovered. The liquid natural circulation rate measured by the flow meter in the cold-leg return shows that the flow is quite steady and not much influenced by the intermittent carryover at the U-bend. It appears that the liquid mass has sufficient inertia, thus the total liquid flow is not sensitive to the disturbances caused by each slug bubble. The time scale of the intermittency is about 1 sec whereas the flow oscillations have a period of approximately 20 sec. Thus it can be concluded that these two phenomena are not related.

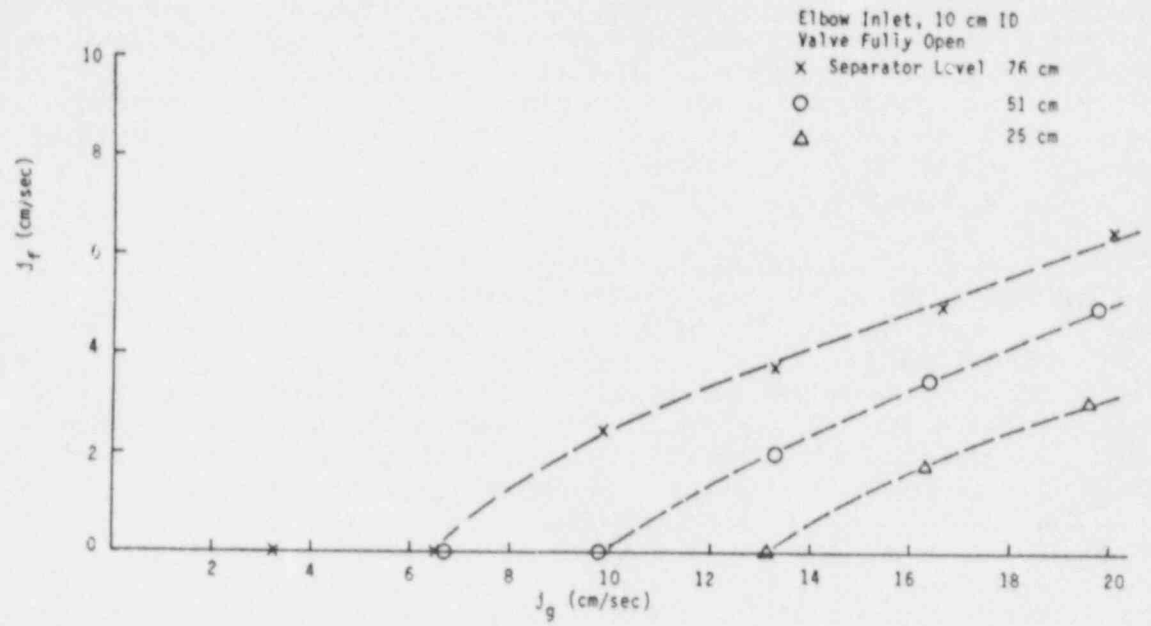

Fig. 4. Effect of Separator Water Level

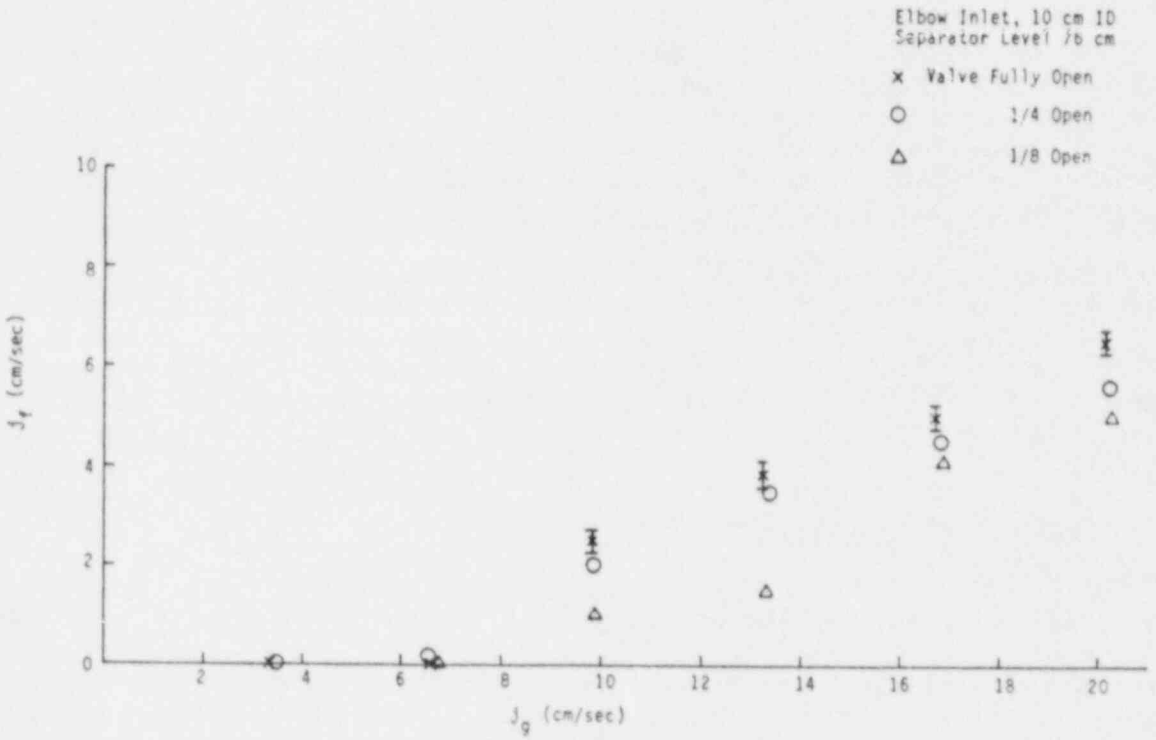

Fig. 5. Effect of Friction Control Valve Opening

The intermittent flow interruption does not lead to the permanent flow termination. This indicates that the phase separation in the U-bend is not the cause of the permanent flow termination. The present experiments have demonstrated that the natural circulation termination occurs when there is insufficient hydrostatic head in the downcomer side. As long as the two-phase flow continues, flow can be reestablished. This points to the importance of the thermal center in the once-through steam generator and the void fraction distribution in the hot-leg.

In the new 10 cm I.D. hot-leg experiments, the horizontal section also induced slugging phenomena due to the flow stratification and 90° turn. However, much more turbulent behaviors have been observed in the 10 cm I.D. case in comparison with 5 cm I.D. cases. The initial large slug bubbles tend to disintegrate into smaller cap bubbles. Thus the two-phase flow regime at the bottom of the vertical hot-leg is the churn turbulent flow with many cap bubbles. However, the disintegration of the slug bubbles is not complete and the hot-leg flow regime is strongly influenced by the inlet slugging. In the down stream, a transition to the slug flow has been observed. This transition occurred at the lower gas fluxes and at lower height in comparison with the straight inlet cases, see Figs. 6 and 7. Since the relative velocity between phases strongly depends on two-phase flow regimes, the inlet geometry has significant effect on the hot-leg void fraction and the natural circulation rate, see Fig. 8.

D. Effect of Separator Water Level (Thermal Center)

The induced liquid flow rate increases with the increasing water level in the separator at a fixed gas flowrate and fraction valve opening, see Fig. 4. The vertical distance between the U-bend and the bottom of the hot-leg is fixed, thus an increase of water level in the separator results in an increase of the hydrostatic head in the downcomer. Since the natural circulation is induced by the static head difference in the hot-leg and cold-leg downcomer, the circulation rate increases with the level.

The induced liquid flow rate depends on the separator water level, frictional loss along the loop and void fraction distribution in the hot-leg. The gas flow at the flow termination is reduced as the water level in the separator increases. Thus the flow termination condition conforms to the general parametric dependences of the natural circulation rate. This shows that at higher water levels, less gas rates are required to induce the same liquid flow rate.

E. Effect of Frictional Resistance

The changes in the frictional resistance of the test loop was achieved through adjusting the opening of the gate valve with a diameter of 5 cm. The openings of the gate valve was varied over fully, 1/2, 1/4, and 1/8 open in terms of the valve stem rotations. For each position, tests were run with three different water levels in the separator and two different geometries of the core exit section. It has been observed that as the friction valve opening decreases (implying increases in the single phase friction resistance)

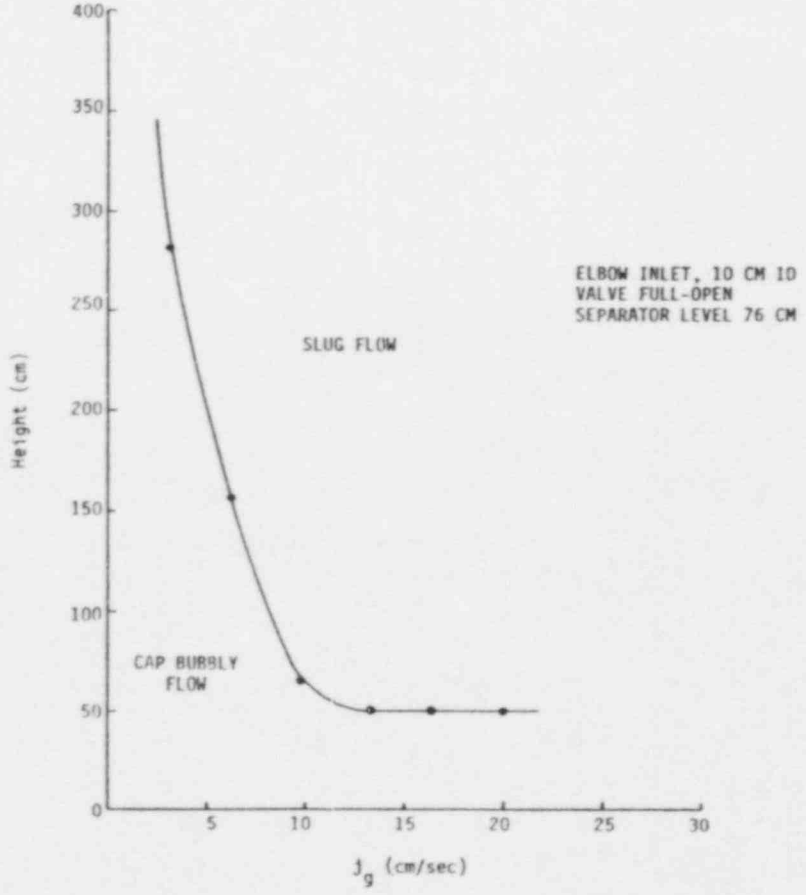

Fig. 6. Flow Regime Transition

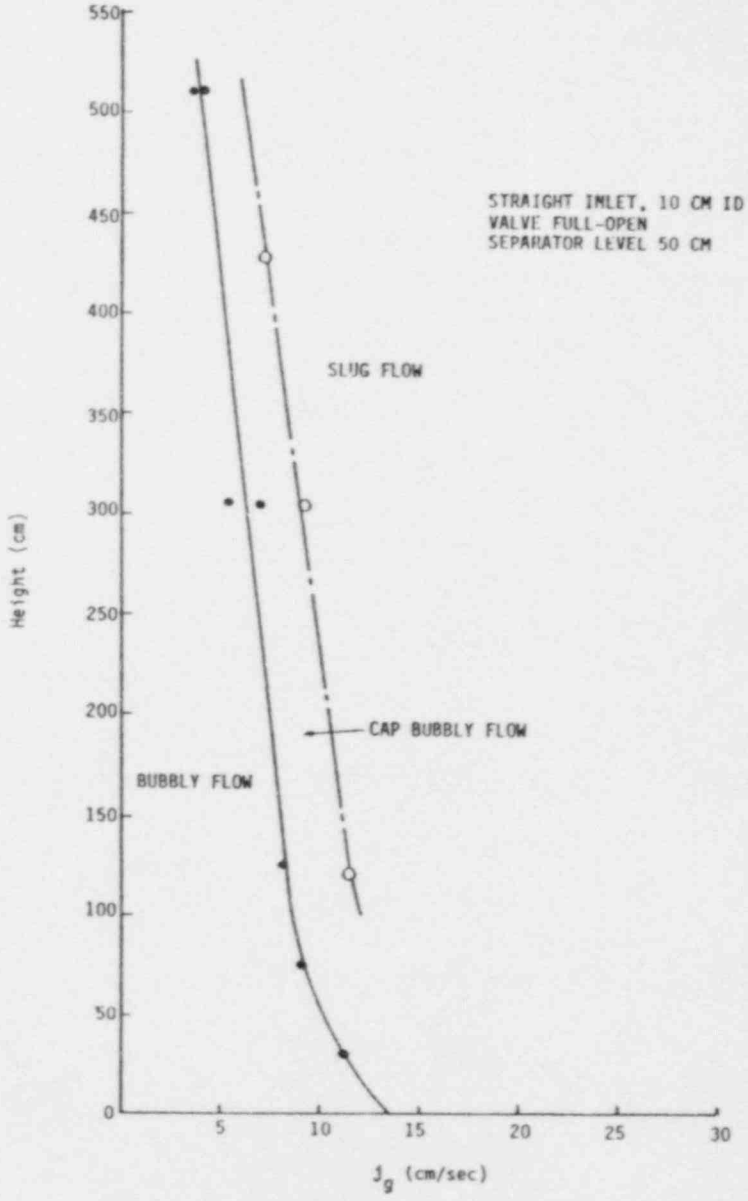

Fig. 7. Flow Regime Transition

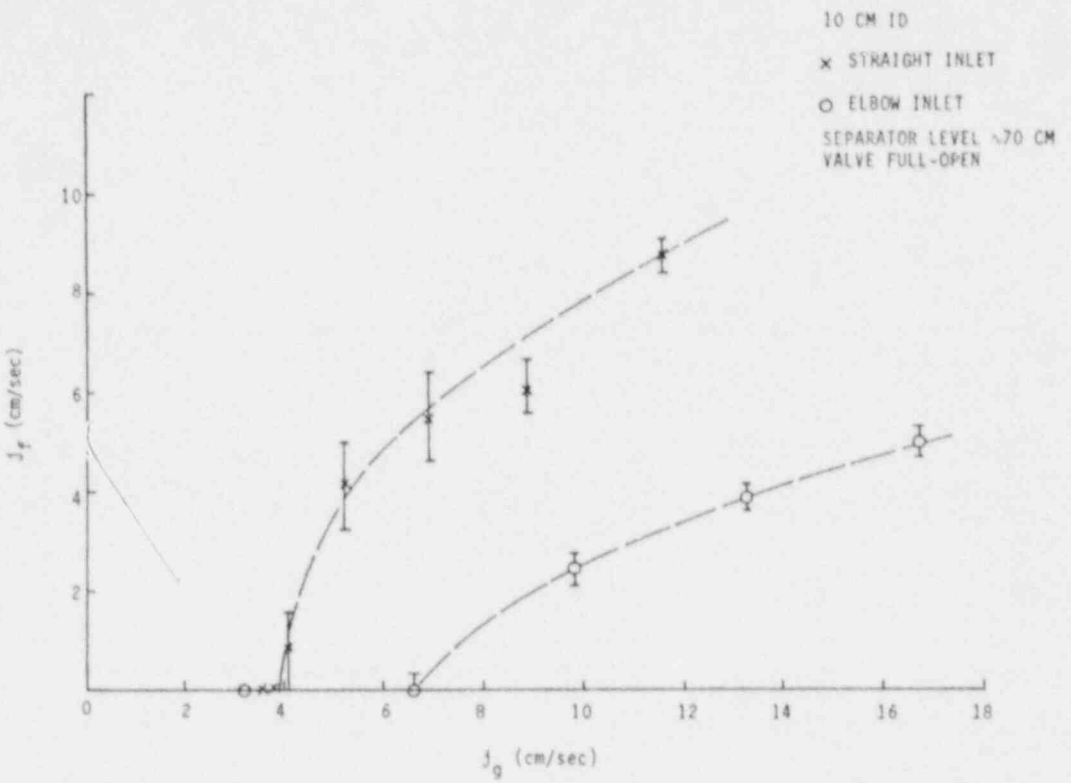

Fig. 8. Effect of Inlet Geometry

the induced liquid flowrate decreases, see Fig. 5. The extent of the effect of the friction valve opening on the induced liquid flowrate also depends on the separator water level.

F. Effect of Inlet Section Geometry

Two different geometries of a core exit section were tested to compare their effect on the flow interruption and induced liquid flowrate. One had a vertical inlet where the gas flowed vertically into the hot-leg as shown in Figs. 2 and 3(a). Another one had a simple mixing chamber, horizontal section and elbow, as shown in Fig. 3(b). The horizontal section had a length of 50 cm. An elbow of 90° was used between the vertical hot-leg and the horizontal section. The two-phase mixture of nitrogen and water flowed horizontally through this section before entering the vertical hot-leg.

In the previous 5 cm ID hot-leg experiments [8,9] the hot-leg flow with a horizontal section is always in the cap bubbly or slug flow regime. This is due to the flow stratification at the horizontal section. The flow regime in the horizontal section is either elongated bubbly flow or stratified flow with a propagating interfacial wave front. The stratification occurred within about one diameter of a pipe from the simulated core exit plane. However, in general this length depends on the bubble rise velocity and liquid flux. At the elbow the horizontal two-phase flow is turned 90° into a vertical flow.

At this point quasi-periodic slugging occurred. This slugging produced either cap bubbles or slug bubbles depending on the gas flux.

One of the most important effects of the inlet geometry is on the hot-leg void fraction. The cases with the horizontal section showed much lower void fraction than the straight inlet cases. This is because the bubbly flow tends to persist in the straight vertical inlet cases. It is noted that the relative velocity is higher in the slug flow regime than in the bubbly flow, thus at the same gas flux, the bubbly flow has higher void fraction than the slug flow. According to a recently developed theory by Kocamustafaogullari and Ishii [10], the maximum cap bubble size is about $40\sqrt{\sigma/g\Delta\rho}$. Thus for a vertical pipe much larger than this value (~10 cm), the stable slug flow cannot be sustained. Due to the instability, the initial large bubbles should disintegrate into smaller cap bubbles of stable sizes. Thus the 10 cm I.D. experiments corresponding to the boundary between stable and unstable slug flows. The experimental observation clearly showed this tendency of the instability of slug bubbles. It is also noted that, as the void fraction increases, the slug flow with relatively deformed large slug bubbles can be observed in the present 10 cm I.D. experiments. These results show that in the prototype system with a diameter of 91 cm the slug flow is unstable in the vertical hot-leg section. A typical flow regime should be a bubbly or dispersed cap bubble regime. On the other hand, in the integral test facilities, the slug flow is more stable. Thus both the diameter of the hot-leg and the inlet geometry have significant influence on the flow regimes, void distribution and flow behaviors.

III. FREON-113 BOILING AND CONDENSATION LOOP EXPERIMENTS

A. Description of the Experimental Loop

The overall loop schematic is shown in Fig. 9. This Freon-113 boiling and condensation loop was designed such that it could be operated either in a natural or in a forced circulation mode. The primary loop consists of the simulated core (heater section), hot-leg, U-bend, simulated steam generator (condenser), subcooler, loop friction control valve, expansion tank and a pump. The loop pressure is regulated by the pressure level applied to the free surface in the expansion tank. The pressure at this point is maintained close to the atmospheric pressure by two pressure relief valves for the positive and negative pressure cracking. Due to the hydrostatic head of the liquid Freon-113 in the connecting tube of the expansion tank, the pressure at the simulated core is always above the atmospheric pressure, up to 159 KPa (23 psia). Basically, the two phase flow is generated by boiling of Freon-113 in the simulated core and condensed in the simulated steam generator (condenser) by using secondary loop for cooling. Freon-113 has a low saturation temperature of about 47°C at 1 atm. Thus the loop is operated at relatively low pressures and temperatures. The components and sections involving two-phase flow are all transparent that a flow visualization is possible. At present, the loop is approximately 6 m in height with hot-leg inner diameter of 5 cm and length of about 5 m. The transparent sections were made of standard Corning Pyrex glass pipes and fittings. Other sections were made of copper tubes, brass fittings and stainless steel components.

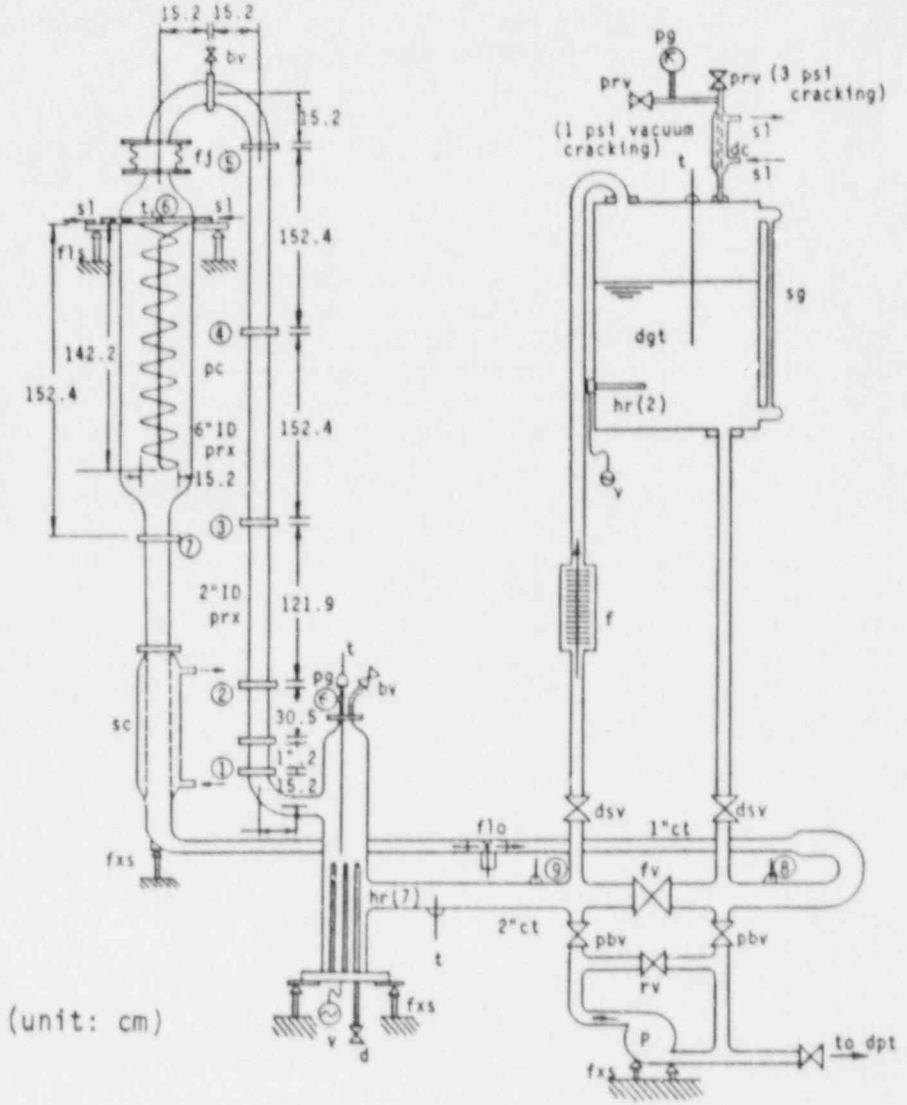

bv	bleed valve
ct	copper tube (nominal size)
d	drain
dc	dgt condenser (1" & 1¼" conc. ct)
dgt	degassing tank
dpt	dump tank
dsv	degassing tank shut-off valve
f	filter
fj	flexible joint
flo	flowmeter
fls	flexible support
fxs	fixed support
fv	friction control valve
hr	heating rod (7x600 W, 2x750 W)
P	pump (2 hp)
pbv	pump bypass valve
pc	primary condenser (40 coil/ ¼" ct)
pg	pressure gauge
prv	pressure relief valve
prx	pyrex test section
rv	recirculate valve
sc	subcooler (2" & 2½" conc. ct)
sg	sight glass
sl	flow to/from secondary loop
t	thermocouple
v	variable transformer (0-4 KVA)
①-⑨	pressure tap

Fig. 9. Schematic of Freon-113 Boiling and Condensation Loop for Hot-leg U-bend Natural Circulation Study

The heat sink to the primary loop is supplied by the secondary Freon-113 loop consisting of the circulation pump, condenser coil (divided into upper and lower sections to change the cooling conditions), heat exchanger cooled by cold tap water and coils submerged in cold baths of anti-freeze (ethylene-glycol) within a large chest-type freezer. The secondary loop is pressurized to 0.28 MPa (40 psig) and the coolant is always in the liquid state. Therefore, the thermal hydraulics of the secondary loop is not simulated in the present facility. The secondary side simply acts as a heat sink to the primary side in this design.

The simulated core is located at the bottom of the 5 cm I.D. hot-leg. It was made of two Corning Pyrex tees of 10x5 cm size and a reducer of 10x5 cm. The volume of the actual core, core internal geometry and vessel downcomer were not simulated in the present design. The subcooled Freon-113 enters through the lower tee branch and exits through the upper tee branch stretched to the opposite direction (see Fig. 9). Seven electrical rods (immersion type heaters) of 0.95 cm O.D. and 30.4 cm length with the maximum power of 600 Watts per rod are used as a heat source. This corresponds to the total power capacity of 4.2 KW. The AC power is applied with two variac transformers for the control of the power input. The loop reference absolute pressure is measured by a Bourdon type pressure gauge connected to the top of the heater section. A sheathed thermocouple measures the temperature of fluid (Freon-113) inside the heater section.

The riser section which corresponds to the hot-leg was made of Corning Pyrex glass pipes of 5 cm I.D. The total height of the hot-leg is 515 cm. The radius of the U-bend at the top of the loop is 15 cm. To measure the differential pressure, five pressure taps were installed along the hot-leg. The pressure tap plates of ring shape (5 cm I.D. and 8.9 cm O.D. with 1.3 cm thickness) was made of brass with a small hole of approximately 0.4 mm in diameter drilled in radial direction (i.e., perpendicular to the flow direction). Each plate was installed between glass pipes and sealed with Teflon gaskets (3.5 mm thickness). The end of the pressure taps were connected to the SENSOTEC differential pressure transducers which were of strain gauge wet/wet type with low sensitivity to liquid temperature changes. These differential pressure transducers given accurate measurements of the void fractions in the hot-leg provided that the frictional pressure drop is negligible.

The steam generator is simulated by a simple coil condenser in a 15.2 cm I.D. and 152.4 cm long Pyrex glass pipe. The condenser was made of nominal 1/4" copper tube with 40 turns of 13 cm coil O.D. and 142.2 cm coil length. The condenser is divided into lower and upper sections to use either the entire coil or the upper half of the coil for condensation by simple valve operations. The primary coolant flows outside the condenser tube. The secondary loop Freon-113 fluid flows inside the tube and cools the primary fluid. Two pressure taps were installed at inlet and outlet of the primary side of the simulated steam generator to measure the void fraction (i.e., liquid level). Below the simulated steam generator, there is a Pyrex glass pipe of 5 cm I.D. and 152.4 cm length. Downstream of the pipe, there is a subcooler made of concentric copper tubes of 2.5" (6.4 cm) and 2" (5 cm) I.D., respectively. The effective length of the subcooler is 117 cm. This subcooler is also connected to the secondary loop for cooling.

The horizontal section of the loop was made of 1" (2.5 cm) and 2" (5 cm) nominal I.D. copper tubes connected in series as shown in Fig. 9. The above mentioned subcooler is followed by a 1" I.D. section. A paddle wheel type turbine flow meter (SIGNET, MK515-P0) was installed to measure the liquid circulation rate of the primary side at the 1" I.D. horizontal section. It covers 0~1.89 liter/sec (0~30 gpm) with an accuracy of ±1% of the full scale. This corresponds to a range of the hot-leg liquid volumetric flux from 0 to 96 cm/sec. This paddle wheel type turbine flow meter is designed to have very little pressure loss and the accuracy is increased by reducing the flow area to one-fourth of the hot-leg section. The 1" I.D. section is followed by a 2" I.D. copper tube section. This section has a friction control valve (2" full port ball valve) to change the overall loop frictional resistance. In parallel to this valve, the primary circulation pump with a bypass and the expansion tank are connected.

The expansion tank of approximately 114 liters (30 gal.) is located near the top of the loop and connected to the pump section side. This tank acts as a pressure regulating device and absorbs the volume changes of the coolant due to boiling and condensation. It can be also used as a degassing tank to eliminate dissolved gases and moisture from the Freon-113 inside the primary loop. For this purpose, two immersion type electric heaters (750 Watts per rod) were installed near the bottom of the tank. This heater is used to boil Freon-113 in the tank, whereas the condenser at the top of the tank condenses back the vapor of Freon-113. The air and moisture can be purged to the outside of the loop through the relief valve. The top of the expansion tank is connected to the discharge side of the primary pump. A filter is located in the line. By using the primary pump, the coolant can be circulated through this filter and the expansion tank to eliminate impurity from the primary coolant. The primary side fluid temperature is measured at various key locations (i.e., heater section, inlets of heater section and simulated steam generator) by the immersion type sheathed thermocouples (T-type, Copper-Constantan). The temperatures of the secondary loop Freon-113 at the two inlets (for upper section and lower section respectively) and the exit of the condenser coil are also measured by the immersion type sheathed thermocouples (Type-T, Copper-Constantan). All the analog signals from the thermocouples, pressure transducers and turbine type flow meters are read through the DASH-8 A/D board with two EXP-16 multiplexer boards and a STA-08 screw termination accessory board into the IBM-PC/XT using LTN (Labtech Notebook) software.

B. Experimental Procedures

Experimental measurements were performed using the Freon-113 loop with experimental parameters chosen as Table III. The initial conditions of the experiments for the primary side were

(1) the single phase liquid state throughout the loop,
(2) no initial flow,
(3) an uniform temperature throughout the loop,
(4) no cooling in the condenser (simulated steam generator).

Table III. Experimental Conditions

Experimental Parameters	Conditions
Friction Control Valve	Full-open, 1/4-open
Heat (Power) Input	1.3 KW, 2.2 KW
Secondary Loop Cooling	High, Medium, Low and No Cooling

At the start of an experiment, a predetermined constant power was supplied to the simulated core, then it was kept until to the end of the experiment. The secondary loop was kept in the shutdown mode with no cooling to the primary loop until the U-bend portion at the top of the loop is filled by a substantial amount of the vapor. Then the subcooled liquid flow was initiated in the secondary loop with constant flow rate to activate the heat sink to the primary side. In the present test runs, the lower condenser coil and liquid subcooler were not used by closing the corresponding valves.

C. Global (Overall) Phenomena

As explained in the experimental procedure, the loop operation was started by heating the liquid Freon-113 in the heater section with no initial flow and secondary cooling. The secondary loop circulation pump was then turned on when the primary loop was sufficiently heated, i.e., when a substantial amount of the vapor was accumulated at the top of the loop. During the experiments, several different loop-wise phenomena were observed as in Fig. 10; the phenomena appeared to be very complicated, and depend very much on the experimental conditions. Here the typical loop-wise phenomena are going to be explained with the corresponding figures.

At the beginning of the initial stage no loop-wise natural circulation of liquid was observed. The hot liquid from the core simply built up the hot liquid column in the hot-leg by natural convections within it. This state continues for a couple of minutes followed by the stable single (liquid) phase natural circulation over a fairly long period (7-39 minutes depending on the conditions, Region A-B in Fig. 10(a) and 10(d)). The loop-wise natural circulation started when a sufficient head difference was established between the hot-leg (riser section) and the cold-leg (downcomer section) return. When the single phase natural circulation starts, the heater section temperature drops temporarily (Point A of Fig. 10(a)) and increases gradually until the boiling starts. It was observed that the liquid flow rate was nearly constant (Region A-B in Fig. 10(d)). During this natural circulation, the vapor was slowly accumulated at the top of the loop which led to the termination of the single phase natural circulation.

The termination of the single phase natural circulation was followed by the boiling in the heater section, and the vapor started to accumulate at the

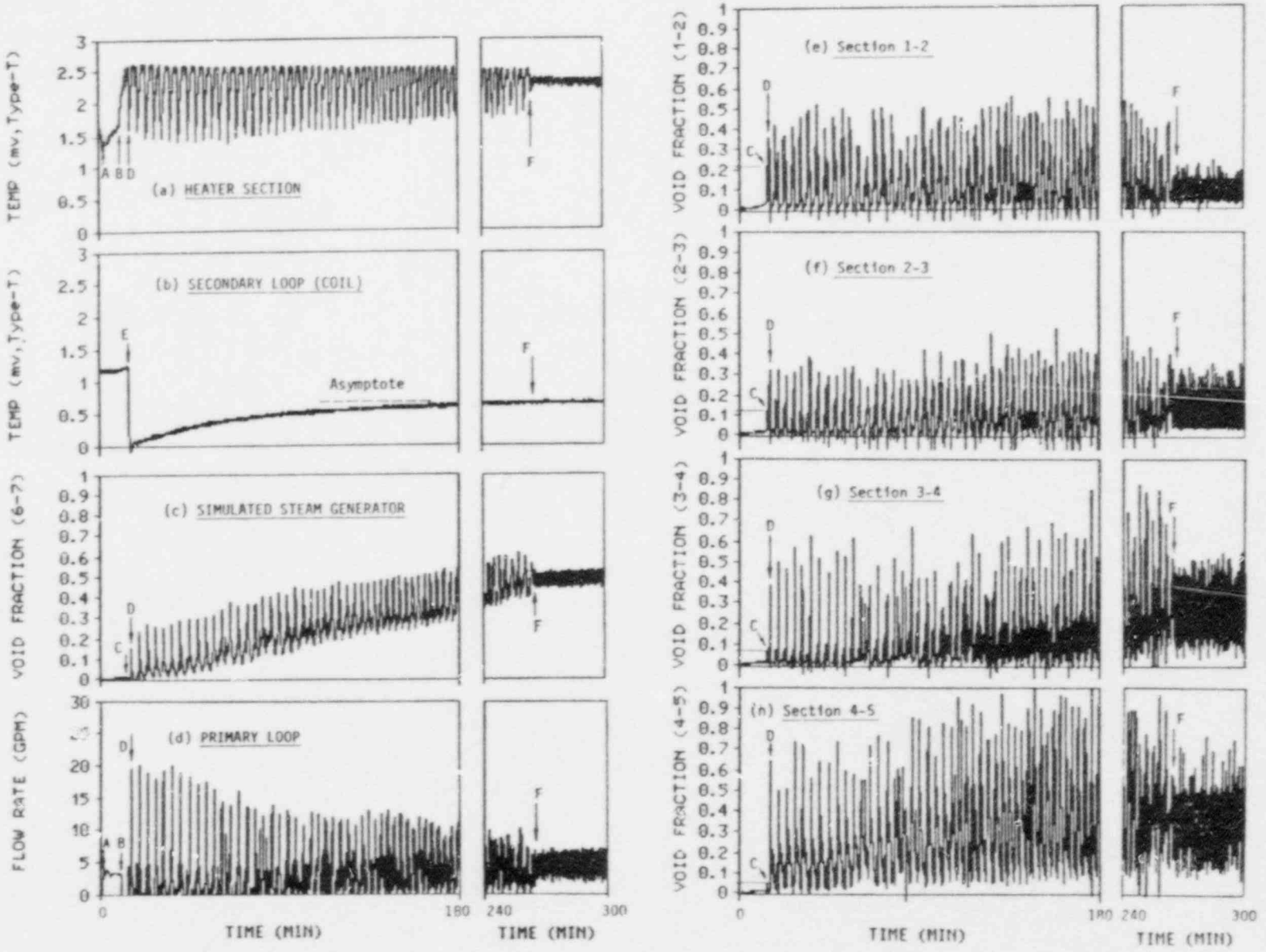

Fig. 10. Initial Stage (Friction Control Valve Full-open, Heater 2.2 KW, High Cooling)

space above the simulated core (heater section), which resulted in decrease of the liquid level in it. Once the liquid level reached the horizontal outlet of the heater section connected to the vertical rise of the hot-leg, the two-phase flow was established in the hot-leg, and eventually led to the two-phase natural circulation. Most of the vapor came from the vapor space above the simulated core. At the bottom of the vertical hot-leg, slugging occurred due to the flow stratification in the horizontal outlet of the heater section. However, the slug or cup bubbles immediately disintegrated into the bubbly flow. Initially, strong turbulent motions were observed and the bubble rise velocity was relatively small due to strong coupling between the liquid and vapor. Near the bottom of the vertical hot-leg, the void fraction appeared to be higher than the section above. (Compare the void fraction at Point C in Fig. 10(e) ~ Fig. 10(h).) Here the numbering of the axial sections corresponds to the pressure taps in the hot-leg shown in Fig. 9. Thus at this section, the flow regime was churn turbulent flow. Above this quite turbulent section, a typical bubbly flow was established up to the U-bend section. During this stage, a substantial amount of the vapor phase accumulated at the U-bend section, which might cause temporal flow terminations. The bubbly flow in the vertical hot-leg was maintained and the liquid level at condenser gradually came down (Fig. 10(c)). At certain instances during this stage, occurrence of sudden flashing at the upper part of the hot-leg were observed; the main cause of this flashing appear to be the hydrostatic pressure decrease along the hot-leg which results in superheating of liquid and pressure fluctuations due to condensation in the simulated steam generator. Once the flashing started, the two-phase flow regime changed from bubbly to slug flow very rapidly, with the length of the slug bubble up to ~70 cm (Point D of Fig. 10(e) ~ Fig. 10(h)). A slug bubble was generated by very rapid growth of a nucleated bubble. Often, the bubble growth was so rapid that the flow could not be accelerated sufficiently and the motion of the slug bubble slowed down considerably. Several cycles of the slug bubble generation led to a very much increased natural circulation rate (see Point D of Fig. 10(d)). Due to this increased flow rate, a considerable amount of subcooled liquid flowed into the heater section, and resulted in complete suppression of the boiling (Point D of Fig. 10(a)); also the liquid level in simulated steam generator temporarily decreases considerably (Point D of Fig. 10(c)). This led to the termination of natural circulation and the stagnant liquid was observed in the hot-leg and the heater section. The vapor filled the upper part of the hot-leg and U-bend section. The subcooled boiling started during this period and the whole process repeated within a period of 4-15 minutes depending on the condition imposed.

Cooling by the secondary loop can be started any time during the experiment (Point E of Fig. 10(b)). The condensation of the vapor accumulated at the upper part of the condenser (simulated steam generator) results in reduction of the pressure in the hot-leg; thus promotes the flashing phenomena. However, as pointed out earlier, the main cause of the flashing phenomena appears to be the decrease of the hydrostatic pressure along the upward direction inside the hot-leg.

As the cycles of the flashing continue (mostly for 3-6 hours), the whole flow phenomena may reach a certain quasi-steady state (Point F in Fig.

10(a)~(h)); the secondary loop coil temperature reached a certain constant asymptote (Fig. 10(b) and Fig. 11(b)) and the amplitudes of the peak values at the primary side became smaller. Once this state is reached, the flashing with large flow carry-over was not observed any longer, instead, the bubbly flow, churn turbulent flow or small-scale slug flow maintained small intermittent flow carry-over through the inverted U-bend at the top of the loop. During this stage, the temperature of the fluid (Freon-113) in the heater section remained at almost constant due to the saturation condition (Fig. 10(a) or Fig. 11(a)). However, certain regular patterns of flow oscillation were observed. Two different types of oscillations were observed; here, they are named as Type 1 and Type 2 respectively. Along with those two different types of oscillations, two dominant ranges of oscillatory periods were detected; they are 8~35 sec. and 2.4~4 min. respectively.

In Fig. 11(c)~(h), Type 1 oscillation with a period of ~20 sec. is clearly observed. At the beginning of each cycle of Type 1 oscillation, the liquid level in the heater section is slightly higher than the horizontal outlet of the heater section connected to the riser section of the hot-leg. Due to the regular oscillation of the liquid level with continuous boiling inside the heater section, the liquid level approaches the horizontal outlet, and the vapor begins to flow into the riser section. Since the temperature of the fluid in the riser section remains almost in saturated condition, the vapor introduced into the riser section becomes a small-sized slug bubble by flashing phenomenon. This oscillation with a period of ~20 sec. turned out to be a manometer type oscillation.

In Type 2 oscillation, though not shown in the figures of this paper, the liquid level in the heater section remains almost stationary with continuous flow of vapor into the riser section. The flow carry-over is maintained by bubbly flow generated by continuous micro-flashing; thus the void fraction becomes relatively steady with longer period (2.5~4 min.) of oscillation. This long-period signal comes from the density wave oscillation. Along with the longer period of oscillation, the ~35 second-period oscillation is also observed though not very regular, which is also a manometer type oscillation.

Large flow carry-over with flashing (unsteady behavior) shown in the initial stage seems to be triggered by the density wave oscillations if the system is in unstable flow conditions. Once the temperature of the fluid in the heater section reaches close to the saturation temperature, density wave causes flow oscillations and triggers large flow carry-over. However, as the cycle continues, the overall loop temperature reaches a certain quasi-steady state, and the peak flow rate and temperature fluctuation by large flow carry-over decrease; this eventually leads the two oscillations indistinguishable, and in a sense of long-period oscillation, the density wave oscillation is detected only.

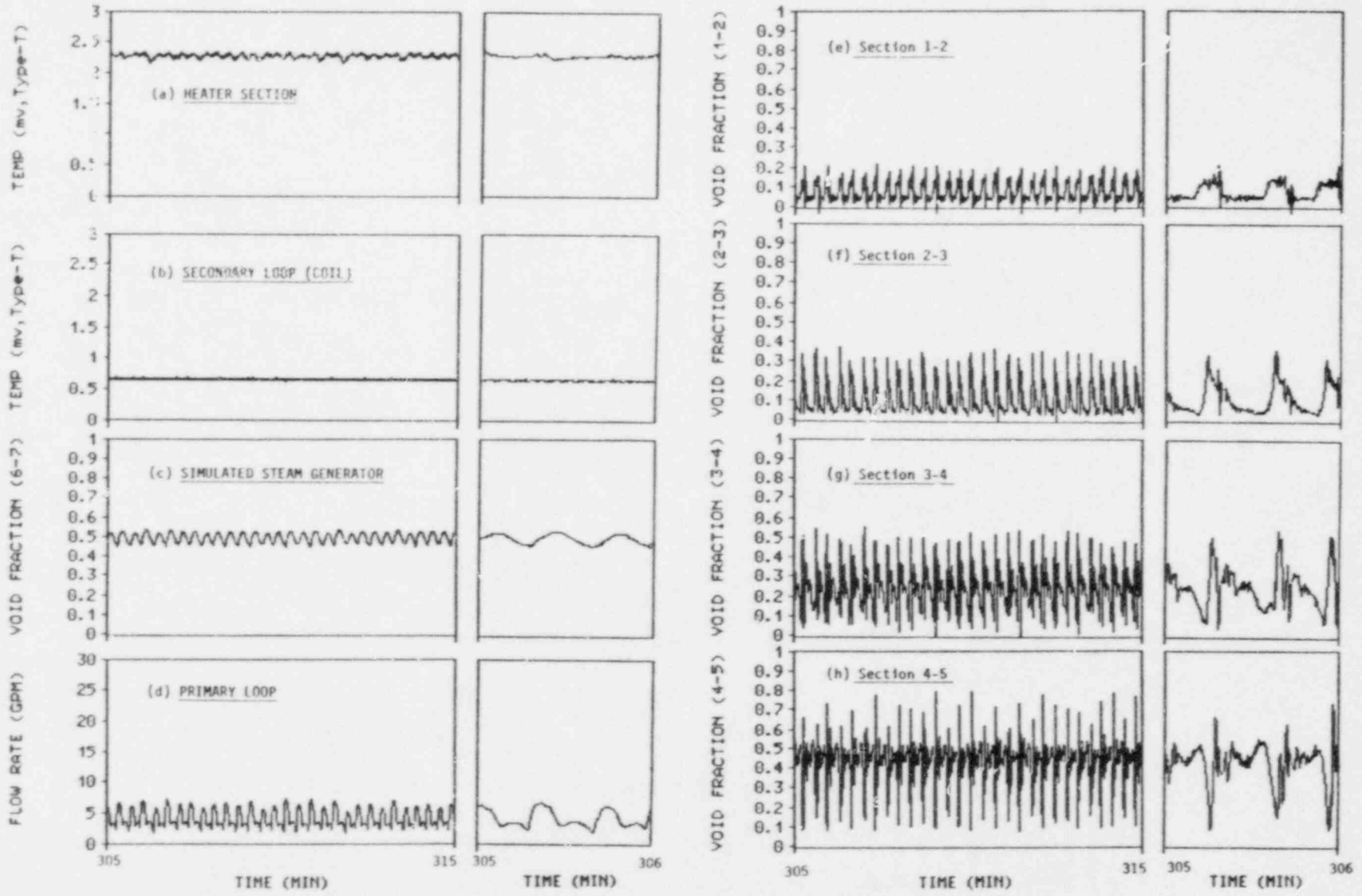

Fig. 11. Quasi-steady State, Type 1 Oscillation (Friction Control Valve Full-open, Heater 2.2 KW, High Cooling)

D. Analysis of Experimental Data

1. Single-phase Natural Circulation and Flashing (Initial Stage)

As mentioned earlier, at the beginning of the initial stage, the single phase natural circulation was observed. Table IV shows the effects of the heat (power) input and friction control valve openings on the single phase natural circulation. The durations and flow rates shown in Table IV are the averaged value of several trials for each experimental conditions. The single phase natural circulation flow rate increases as the heat (power) input and the opening of the friction control valve increases. However, the duration of the circulation decreases as increase of heat (power) input since overall temperature rises rapidly in case of higher heat input which leads the earlier incipience of boiling phenomena. The effect of the opening of the friction control valve on the duration of this single phase flow seems to be minor; however, if the loop friction increases, the flow rate decreases, which results in build-up of higher temperature locally at the heater section and eventually the boiling starts earlier.

After the termination of single phase natural circulation, the subcooled and saturated boiling occurred and then flashing with large flow carry-over followed. And then subcooled boiling started again and the whole process repeated with certain period. The period of this cyclic behavior also depends on the experimental conditions (Table V).

Little difference is observed between the periods with different cooling rates. However, the effect of the heat (power) input was significant; the period of this cyclic behavior decreases considerably with the increase of heat (power) input. That can be explained as follows. The flashing (and large flow carry-over) occurs when the two phase bubble column is fully established in the hot-leg portion with its density low enough (compared with the liquid density in the cold-leg portion) to induce the natural circulation. Also, the maximum flow rate depends on the density difference between bubble column and liquid column inside the hot-leg and the cold-leg respectively. Once the pressure of the system is fixed to a certain value, the density difference required for the flashing tends to be constant regardless of heat (power) input and the peak flow rates appear to be about the same. However, the time required for heating up to the saturated condition depends on the heat (power) input significantly, and the period of flashing becomes shorter with high heat input. The effect of the friction control valve opening on the period of flashing seems to be relatively minor. At low heat input, the peak flow rate appears to be smaller with smaller valve-opening, and from the viewpoint of the overall energy balance, flashing should occur more frequently in order to transfer same amount of heat from the heater section to the condenser by natural circulation. On the other hand, in case of high heat input, the primary flow rate depends much on the small-scale flow carry-over, and the decrease of peak flow rate by reducing the friction control valve opening does not affect much on the period of flashing.

Table IV. Single Phase Natural Circulation

Power Input \ Friction Control Valve	Full-Open		1/4-Open	
	Duration	Flow Rate	Duration	Flow Rate
1.3 KW	26.5 min	2.5 gpm	23.0 min	1.1 gpm
2.2 KW	12.1 min	3.4 gpm	10.3 min	1.4 gpm

Table V. Cyclic Period of Flashing/Large Flow Carry-Over

Friction Control Valve Opening	Heat (Power) Input \ Cooling Rate	High Cooling	Med. Cooling	Low Cooling
Full-Open	1.3 KW	14.0 min	13.0 min	15.2 min
	2.2 KW	4.0 min	3.8 min	3.7 min
1/4-Open	1.3 KW	11.5 min	10.6 min	12.2 min
	2.2 KW	4.2 min	4.5 min	4.1 min

2. Void Fraction

At initial stage with the friction control valve full-open, the bottom section (1-2) shows higher average void fraction than the average void fraction at the next two sections (2-3 and 3-4). (See Fig. 9 for the locations of each section.) This is due to high-void churn turbulent flow in section 1-2 generated by the 90° elbow connected between the section 1-2 and the heater section compared with the low-void bubbly flow in the next two sections. However, in section 3-4, occurrence of slug bubble with flashing causes large peak void fraction. This behavior is more pronounced at the top section (4-5) which has the highest peak void fraction, and also highest average void fraction is detected at this section (see Fig. 10(e)-(h)). Similar behavior was observed in case of friction control valve 1/4-open except for the occurrence of higher peak void fraction at the second lowest section (2-3) than at the bottom section (1-2); in case of small valve-opening, slug bubble rapidly grew at lower section of the hot-leg. This seems to be due to the lower velocity of fluid passing through the heater section, which leads to slightly higher (superheated) fluid temperature at the lower part of the hot-leg than the case of the friction control valve full-open.

Figure 11 shows the void fractions of each riser section at quasi-steady state. Figure 11(e)-(h) shows the trend of increasing of void fraction as the fluid rises up through the riser section of the hot-leg. This is due to the decrease of saturation temperature corresponding to hydrostatic pressure at each riser section. For the case of high power (heat) input with friction control valve full-open, the void fractions of each riser section suddenly change at certain liquid level of the simulated steam generator (condenser). That is, as the liquid level at the condenser (simulated steam generator) decreases, the flow behavior changes from one mode (Type 1) to another (Type 2); and the void fractions of the first three sections from the bottom (1-2, 2-3, 3-4) increase whereas the void fraction at the top section (4-5) decreases. This is because, as explained earlier, slug bubble forms inside the hot-leg in Type 1 flow, which leads to higher-void flow at the top section. If the opening of the friction valve decreases, only Type 2 oscillation is detected, which indicates the system is more stabilized. When the heat input is reduced, the void fraction inside the entire riser section decreases with low primary flow rate, and Type 2 oscillation was detected only.

3. Average Flow Rate at Quasi-Steady State

The primary loop flow rate changes with variation of liquid level inside the condenser (simulated steam generator). For the case of high power (heat) input with friction control valve full-open, flow rate suddenly changes at certain liquid levels of the simulated steam generator by the changes of the flow behavior from Type 1 to Type 2. Type 1 flow is mostly induced by the flashing with slug bubble, and the flow rate is several times higher than the Type 2 flow in which the flow carry-over is maintained by the bubbly flow. If the opening of the friction control valve decreases, Type 1 flow did not appear and only Type 2 flow was observed; similar flow behavior was observed with the low power (heat) input. This again indicates that the flow rate considerably depends on the liquid level inside the condenser in present experimental range. If the experiment continues longer, the liquid level inside the condenser decreases further (since it is not exactly steady-state) with the temperature of the fluid inside the loop increasing gradually; this leads to the higher-void two-phase flow inside the riser section with higher flow rate.

IV. SUMMARY AND CONCLUSIONS

In order to study two-phase natural circulation behaviors during a small break loss of coolant accident in LWR, simulation experiments have been performed in two different thermal-hydraulic loops. The focus of these experiments was the scale effects on the natural circulation, flow termination and hot-leg flow regime. Both of the loops have been designed as a flow visualization facility and built according to the two-phase flow scaling criteria developed previously under this program. The first group of experiments was carried out in the nitrogen gas-water adiabatic simulation loop and the second in the Freon-113 boiling and condensation loop.

The nitrogen gas-water loop has been used to isolate key hydrodynamic phenomena from heat transfer coupled phenomena. In particular, the effects of

the inlet geometry, gas flux, loop frictional resistance, and water level in the gas separator have been studied in detail. Two different geometries of a core exit section were tested to compare their effect on the flow interruption, induced natural circulation, hot-leg two-phase flow regimes and void distribution. One had a vertical straight inlet where the gas flowed vertically into the hot-leg. Another one had a simple mixing chamber, a short horizontal section and an elbow at the bottom of the vertical section of the hot-leg. The two-phase flow regimes, void distribution, natural circulation rate and flow termination point were considerably different between these two systems.

However, in general the induced natural circulation rate decreased with the decreasing gas flow rate. As the gas flow rate decreased further, eventually the flow termination occurred. The induced natural circulation rate depended on the separator water level, frictional loss and void distribution in the hot-leg. The gas flow at the flow termination was reduced as the water level in the separator increased, however the frictional resistance did not affect the flow termination point.

The straight inlet cases showed much higher natural circulation rates than the corresponding cases with the inlet elbow. This was mainly due to the differences in the two-phase flow regimes and hot-leg void distributions. The transition to cup bubble or slug flow from bubbly flow was induced by the stratification and slugging at the elbow. Since the rise velocity of cap or slug bubbles is higher than that of smaller bubbles, the void fraction is smaller in the elbowed inlet cases than the straight inlet cases.

These observations indicate that the hot-leg flow regime in a small diameter facility tends to be cup bubble or slug flow. However, as the theoretical study has shown, the slug bubbles are unstable in a large diameter pipe typical of a protctype system. Thus it can be concluded that the cap bubbly flow with the maximum bubble diameter given by $40\sqrt{\sigma/g\Delta\rho}$ should be the predominant flow regime for a prototype system.

Experimental results from the Freon-113 flow visualization loop showed significant effects of heat transfer and phase changes on overall flow behaviors. They are summarized as follows:

1. At the beginning of heating-up of the loop, the single-phase natural circulation is observed for a fairly long period. This is followed by the cyclic behavior of two-phase flow (bubbly and churn-turbulent flow at the upper and lower parts of the hot-leg respectively), sudden flashing, and suppression of boiling with flow termination. Those unsteady behaviors usually continue for three to six hours from the beginning of the heating-up depending on the experimental conditions.

2. Unsteady flow behavior is followed by the quasi-steady state; in this stage the flow becomes stabilized, and no large-scale flow carry-over through the inverted U-bend with flashing was observed. Here, certain regular patterns of flow oscillation are detected; one mode is the manometer type oscillation with a range of period of 8-35 sec, and another

mode seems to be density wave oscillation with a range of period of 2.5-4 minutes and close to the residence time of a fluid particle flow around the loop. Along with a manometer type oscillation, two different types of flow are observed. In one type of oscillation (Type 1), a periodic small-scale flashing with formation of a small-sized slug bubble was observed with sizable amount of flow carry-over through the inverted U-bend. In another type of oscillation (Type 2), a continuous micro-flashing along the riser section of the hot-leg with bubbly flow causes small flow carry-over through the inverted U-bend. Appearance of those types of oscillations depends strongly on the liquid level in condenser (simulated steam generator), as well as the heat (power) input and friction valve openings.

3. Each riser section along the hot-leg shows different void fractions. At the initial stage, the bottom section shows higher void fraction than the second bottom section due to high-void churn-turbulent flow generated by 90° elbow connections between the heater section and the riser section of the hot-leg. However, at the following downstream section along the hot-leg, void fractions become larger due to the occurrence of slug bubble with large periodic flashing. At the quasi-steady state, the void fraction increases along the riser section of the hot-leg. This implies that, at the quasi-steady state, the heat transfer effect (i.e., flashing phenomenon) is more important than the hydrodynamic effect (i.e., the slugging effect by the 90° elbow at the bottom of the hot-leg).

4. Average flow rate inside the primary loop at quasi-steady state depends strongly on the liquid level inside the condenser which also changes the types of oscillations explained above. Type 1 oscillation induces relatively larger flow rate due to formation of a slug bubble with flashing, though in small scale.

Through the Freon-113 loop experiments, an understanding of the basic mechanism of the natural circulation and flow termination with heat transfer and phase changes has been established. The power (heat) input, loop friction (by controlling friction control valve opening) and the liquid level inside the condenser (thermal center) play key roles in determining natural circulation rate and flow behavior including flow oscillations inside the loop.

ACKNOWLEDGMENTS

The authors would like to express their sincere appreciation to Drs. Novak Zuber and Richard Lee of NRC for valuable discussions and support on the subject. This work was performed under the auspices of the U.S. Nuclear Regulatory Commission.

REFERENCES

1. Ishii, M. and Kataoka, I., "Similarity Analysis and Scaling Criteria for LWR's under Single-phase and Two-phase Natural Circulation, NUREG/CR-3267, ANL-83-32 (1983).

2. Ishii, M. and Kataoka, I., "Scaling Laws for Thermal-hydraulic System under Single Phase and Two-phase Natural Circulation," Nucl. Eng. & Design, Vol. 81, pp. 411-425 (1984).

3. Kocamustafaogullari, G. and Ishii, M., "Scaling Criteria for Two-phase Flow Natural and Forced Convection Loop and Their Application to Conceptual 2x4 Simulation Loop Design," NUREG/CR-3420, ANL-83-61 (1983).

4. Kocamustafaogullari, G. and Ishii, M., "Scaling Criteria for Two-phase Flow Loop and Their Application to Conceptual 2x4 Simulation Loop Design," Nucl. Tech., Vol. 65, pp. 146-160 (1984).

5. Carter, H. R., "MIST Facility Status," Proc. 13th Water Reactor Safety Research Information Meeting, NUREG/CP-0072, Vol. 4, pp. 83-100 (1985).

6. Kocamustafaogullari, G. and Ishii, M., "Reduced Pressure and Fluid to Fluid Scaling Laws for Two-phase Flow Loop," NUREG/CR-4584, ANL-86-19 (1986).

7. Wang, Z., Popp, M., DiMarzo, M., et al., "University of Maryland Test Facility Results," Proc. 13th Water Reactor Safety Research Information Meeting, NUREG/CP-0072, Vol. 4, pp. 47-82 (1985).

8. Kim, S. B. and Ishii, M., "Flow Visualization Experiment on Hot-Leg U-Bend Two-phase Natural Circulation Phenomena," NUREG/CR-4621, ANL-86-27 (1986).

9. Hsu, J. T. and Ishii, M., "Experimental Study on Two-phase Natural Circulation and Flow Termination in a Loop," NUREG/CR-4682, ANL-86-32 (1986).

10. Kocamustafaogullari, G. and Ishii, M., "Maximum Fluid Particle Size for Bubbles and Drops," ASME Winter Annual Meeting, Miami Beach, Nov. 17-22, Proc. Fundamental Aspects of Gas-Liquid Flow, FED-Vol. 29, pp. 99-109 (1985).

B&W ONCE-THROUGH STEAM GENERATOR SINGLE TUBE EXPERIMENT RESULTS*

G. E. McCreery, K. G. Condie, and M. P. Plessinger
Idaho National Engineering Laboratory, EG&G Idaho, Inc.

1. INTRODUCTION

Experiments are being conducted in an air-water facility that model B&W Once Through Steam Generator (OTSG) heat transfer and fluid flow behavior during auxiliary feedwater (AFW) injection. The OTSG is a single-pass counterflow tube-in-shell heat exchanger (Figure 1) in which decay heat removal capability is provided by injection of AFW into the steam generator boiler region. AFW is injected near the top of the bundle, typically through seven penetrating nozzles at the periphery of the bundle. Injection of AFW results in a complex steam-water counterflow situation within the boiler. As AFW is injected it tends to fall downward due to gravity and flow inward due to momentum. Fluid flow is impeded and redistributed by tube support plates (TSP's) spaced along the bundle and by steam flow up the bundle.

The single tube experiments described in this paper are the first in a series that examine the basic phenomena of AFW radial and axial flow distribution, tube support plate (TSP) flooding, and tube heat transfer. The succeeding experiments, which are presently underway, address the AFW behavior in an unheated multi-tube (625 tubes) full scale 1/8 sector of the OTSG that includes the top three TSP's. The overall objective of the experiment series is to obtain observations and data of steam generator fluid flow and heat transfer phenomena for the development of RELAP5 and TRAC code models capable of improved predictions.

The apparatus consists of a single tube and associated tube support plate (TSP) enclosed in a cylindrical lexan shroud (Figures 2 and 3). A controlled flow of feedwater is injected above the TSP. Steam flow from the evaporation of AFW is simulated by air, which is drawn through the TSP by a suction fan connected to the outlet of the shroud. Heated primary water is pumped through the tube and its bulk temperature measured with thermocouples spaced along the tube axis.

The specific objectives of the single tube experiments are:

1. Determine the flooding curve for the single tube TSP with broached hole.

2. Investigate steam generator tube wetting phenomena.

3. Obtain heat transfer data for typical AFW and primary flow conditions.

---

* Work prepared for the U.S. Nuclear Regulatory Commission under DOE Contract No. DE-AC07-76ID01570

4. Investigate heat transfer regimes and heat transfer rates for these data.

5. Investigate methods to determine liquid level above the TSP in the multi-tube experiments where much of the TSP's are not visible (e.g., a borescope in a clear plastic tube)

Additional single tube experiments are planned. The experiments will investigate heat transfer with raised primary temperature, heat transfer and fluid flow above and within the TSP, and the effects of condensation on heat transfer. Condensation effects will be investigated by employing steam flow rather than air flow up the tube.

This paper describes data obtained in the single tube experiments conducted to date. The relevant phenomena observed is described and the data analyzed. The analysis is preliminary for the heat transfer data since its analysis employs a computer program that is presently under development.

2. DESCRIPTION OF APPARATUS

The apparatus is configured in two forms, one for the adiabatic experiments (flooding and pressure loss), and the other for the heat transfer experiments.

The adiabatic experimental apparatus employs a clear 5/8" O.D. Lexan tube, which passes through the TSP. The TSP is a 1-1/2" thick aluminum plate with accurately duplicated broached hole geometry (Figure 4). The tube and TSP are enclosed by a 4" O.D. clear lexan shroud. AFW is supplied by a header that penetrates the shroud approximately 3 ft above the TSP. The AFW falls down the inside of the shroud and accumulates on the TSP, where it may then flow through the broached hole and down the outside of the tube and eventually to a catch tank measuring system.

Steam generated by the evaporation of AFW flowing down the steam generator tubes and from the liquid pool on the bottom of the steam generator is simulated by air flow. The air is driven through the holes by an air suction fan. The fluid passed through a phase separator upstream of the fan and flow measurement station and removes any entrained liquid. Air flow rate is regulated by means of a bypass valve

Recorded parameters include temperature, pressure, air flow rate, water flow rate, and water head above the TSP. A standpipe is employed to maintain the water height above the TSP at a fixed level during flooding experiments. Direct observations of water level on the TSP are made using a borescope which slips inside the clear Lexan tube. The device is being used successfully in these experiments and in the multi-tube experiments.

The heated tube apparatus employs an actual 5/8" O.D. inconel steam generator tube provided by B&W. The primary fluid is pressurized and heated [typically 1.38 MPa (200 psi), and 420 K (296 F)]. The AFW is heated to 370 K (205 F) maximum before injection. The inside of the tube is instrumented with 36 thermocouples (Figure 5), which measure primary bulk fluid temperature. In addition to temperature and flow measurements, video

and still photography is used to record flow phenomena on the outside of the tube. A typical photograph of rivulet flow down the outside of the tube is shown in Figure 4.

3. FLOODING AND PRESSURE LOSS EXPERIMENTS

The downward flow of AFW injected into the steam generator secondary side is limited by the upward flow of steam generated by the water evaporating and boiling if the steam velocity through the tie plate holes is sufficiently high. This counter-current flow limiting (CCFL) or "flooding" phenomena is described by semi-empirical correlations, usually either the Wallis or Kutateladze correlations (Bankoff, et al., 1981).

Experiments were performed to characterize the flooding of the single tube TSP hole. The broached TSP hole consists of three equally spaced lobes. In the experiments the air flow rate was varied until the liquid head above the TSP was maintained constant (as determined by standpipe level) for a constant liquid injection rate. The measured air and water flow rates then determine a point on the flooding curve (Figure 6).

The CCFL data may be represented by a Wallis correlation

$$j_g^{*1/2} + j_l^{*1/2} = 1.735$$

where

$$j_i^* = j_i \left(\frac{\rho_i}{gD\ \rho_{fg}} \right)^{1/2}$$

or a Kutateladze correlation:

$$K_g^{1/2} + K_l^{1/2} = 1.83$$

$$K_i = j_i \left(\rho_i^2 / \sigma g \rho_{fg} \right)^{1/4}$$

j_i = volumetric flux or phase i

ρ_i = phase density

i = g = gas

i = l = liquid

$\rho_{fg} = \rho_l - \rho_g$

σ = surface tension

The critical superficial air velocity for flooding, the air velocity that completely prevents liquid penetration, is considerably larger than that for a long tube of the same hydraulic diameter (0.1627 in.), (Figure 7). Flooding in a long tube occurs when liquid waves build in amplitude and bridge the tube diameter. The broached hole length is insufficient for this to occur at low liquid superficial velocity.

When flooding first occurs in the broached holes, one or two holes flood, rather than all three simultaneously. The hole or holes that first flood are random and do not necessarily repeat with similar flow conditions.

An experiment was performed to examine the influence of surface tension forces, which it was postulated, draw the water into the thin gap adjacent to the rod and cause flooding to occur at higher j_g^* than without the gap. This was tested by running a flooding experiment in which flooding was just barely achieved, and then adding wetting agent (Kodak Photoflo) to the secondary water inlet flow in sufficient quantity to reduce the surface tension by a factor of three. The wetting agent did not terminate flooding, and the effect on flooding of surface tension forces drawing water into the gap is therefore small.

The critical j_g^* for the broached hole is similar to that for a round hole multi-hole plate with slightly larger hydraulic diameter (0.19 in.) reported by Bankoff et al., 1981. The authors investigated the effects on flooding of plate thickness/hydraulic diameter and the fraction of plate area occupied by holes. The effect of increasing the number of holes is to increase j_g^*. This is observed for the flooding data for our multi-tube experiments (Figure 6), which floods with a critical $j_g^{*1/2}$ of approximately 20% higher than for the single tube data.

The critical gas Kutateladze number (4.04 for the single tube, and 4.81 for the multi-tube TSP) is typical for a BWR bundle tie plate ($K_{g\ crit}$ = 4.3, Sun, 1979), even though the hydraulic diameter is smaller than for these tie-plates or for that which the Kutateladze correlation is typically applied.

Experiments were performed to determine the loss coefficient for for the single tube broached hole. Water at a given flow rate was input above the tie-plate and the steady state head from the bottom of the plate measured. The loss coefficient is calculated to be

$$K_{loss} = 0.94$$

where the loss coefficient is based on broached hole average velocity (K_{loss} = 401 based on 3.5 in. I.D. shroud). This compares with a K_{loss} = 1.6 for a square edged orifice of the same hydraulic diameter and without the tube, and again based on hole average velocity.

4. HEAT TRANSFER EXPERIMENTS

Experiments are being performed to determine the heat transfer characteristics of the steam generator tube under typical AFW flow conditions. 52 experiments have been conducted to date with varying primary and secondary flow rates and inlet temperatures. Primary flow rate was

varied between 20 g/s to 70 g/s, and secondary flow between 1.6 g/s to 41 g/s. A primary flow rate of 22 g/s corresponds to a typical natural circulation velocity of 0.5 m/s in the hot leg. A secondary flow rate of 6.5 g/s on the single tube corresponds to a typical AFW injection rate of 757 l/s (200 gpm) per nozzle spread over a 1/8 sector of the steam generator (the AFW does not spread evenly, but varies from a high flow rate close to the nozzles to zero within 5 to 15 tube rows away from the outside wall containing the injection nozzles). Primary fluid inlet temperature is maintained at approximately 420 K (296 F), and secondary inlet temperature is varied between 296 K (73 F) and 369 K (205 F). In addition, two experiments were repeated with the surface tension of the secondary water reduced to approximately that of water at 1,000 psi. This was achieved by the addition of a wetting agent (Kodak Photoflo, diluted approximately 1 ml per liter of water).

Measurements consist of primary and secondary inlet flow rates, temperatures and pressures, and primary bulk fluid temperatures as described in Section 2.

4.1 Sample Heat Transfer Data, and Phenomena Observed

Data from representative experiments is plotted in Figures 7, 8, and 9. The first figure shows data from a high secondary flow (30 g/s) experiment, the second from a medium flow (12 g/s) experiment, and the third from a low flow (1.6 g/s) experiment. In addition, Figure 8 plots data from a similar experiment, with the exception of initial temperature, in which surface tension was reduced by the addition of a wetting agent.

The secondary water in the high flow experiment fully coats the outside of the tube and flows as a thin film. The secondary water in the medium and low flow experiments initially breaks into 3 rivulets and snakes down the periphery of the tube (Figure 5 shows rivulets for a medium flow experiment). The rivulet flow thus provides reduced heat transfer area to the secondary liquid compared with the fully wet tube.

Rivulet flow heat transfer is complicated by azimuthally varying wall temperatures and heat transfer rates. It is observed that a rivulet at one axial position may flow with no boiling, while another rivulet at the same axial position will simultaneously boil. The tube wall temperature is uneven since the wall is thin in comparison with its radius, and wall conduction heat transfer in the azimuthal direction is therefore small compared with that in the radial direction (this is confirmed by a simplified heat transfer analysis which treats the wall as rectangular cooling fin).

The heat transfer regimes observed in the experiments are (a) convection to low velocity subcooled water pool above the TSP, (b) convection to subcooled or saturated water within the TSP holes (augmented by conduction to the TSP at points of contact), (c) convection to falling film or rivulets below the TSP, transitioning to, (d) nucleate boiling, transitioning back to (e) falling film or rivulet convection. If the nucleate boiling is sufficiently intense, the secondary fluid is observed to "sputter" from the tube, and is thereby prevented from further

cooling the tube (however, in a tube bundle the majority of the sputtered water drops will impact other tubes, including tubes which would otherwise be dry).

The effect of reduced surface tension on rivulet flow is to enhance heat transfer (Figure 8). This occurs because the rivulets spread out and thin and cover a wider area if the surface tension is reduced. The height of a liquid rivulet varies approximately with the square root of surface tension (for the same contact angle) (this assumes that the height varies with surface tension the same as for a quiescent sesile drop, e.g., Matijevic, 1969). In our comparative experiments the surface tension was reduced by a factor or approximately 3, thereby providing a wetted area increase of approximately 1.7. This is close to the ratio of overall heat transfer rates in the two experiments (equal to the ratio of primary bulk fluid inlet temperature minus outlet temperature changes = (11 K)/(7 K) = 1.6. This neglects the small subcooled heat transfer in the comparative experiments).

Both surface tension and viscosity of the secondary fluid decrease with temperature. The result is increased rivulet spreading with increased temperature. The transition between rivulet flow and a falling film which fully covers the tube below the TSP (the water is initially channeled into three rivulets which then join to coat the tube) occurs at approximately 18 g/s secondary flow rate for an inlet temperature of 296 K (70 F). The transition flow rate decreases to approximately 11 g/s at 369 K (205 F), and will be lower yet at full temperature and pressure steam generator conditions. Simplified models exist for the rivulet/film flow transition, such as that of Hartley and Murgatroyd (1964) which formulates the transition flow rate per unit perimeter (Γ) as a function of liquid density (ρ_l), surface tension (σ), dynamic viscosity (μ), and surface contact angle (θ). Their equation based on a force criterion is

$$\Gamma = 1.69\ (\mu\rho/g)^{1/5}\ [\sigma(1 - \cos\theta)]^{3/5}$$

The model assumes that the film flows isothermally, which is not the case. The initial channeling of flow below the TSP into rivulets and the elevated temperatures of dry patches on the tube result in an actual transition flow rate higher by at least a factor of four than calculated by the equation (using estimated contact angles of between 45^{o} and 75^{o}). The isothermal model predicts the correct trend of wetting rate decrease with secondary temperature increase for these experiments. The influence of wall heat flux is to increase the transition flow rate, as shown by Hsu et. al. (1965). The effects of heat flux on on the transition flow rate will be investigated by varying the primary flow inlet temperature.

5.2 Heat Transfer Analysis Using Computer Program "TUBEHT"

A computer program which models steam generator tube heat transfer is presently being developed. The program, named TUBEHT, is being used in a preliminary form to analyze these experiments and to thereby test the applicability of various heat transfer models. The work is directed toward the ultimate goal of developing fluid flow and heat transfer models for inclusion in the RELAP5 or TRAC systems codes.

The program models the tube heat transfer as one dimensional and the flow as steady state. The model subdivides the tube, primary fluid, and secondary fluid into evenly spaced axial increments represented by nodes (typically with node spacing = 1 in. along the 36 in. length). At each node the local primary and secondary heat convection coefficients, primary and secondary bulk fluid temperatures, secondary liquid flow rate and evaporated steam flow rate, conduction heat transfer in the radial direction, and wall superheat are calculated. Heat transfer models used in the program include Dittus-Boelter (1936) for the primary flow, and for falling film convection, Labuntsov (1957) for film Reynolds' number less than 1280, and Chen (1985) for Re > 1280 (the transition recommended by Chen).

For nucleate boiling a primary side thermal entry length solution (Kays, 1966) is used and is necessary to account for the sudden increase in heat transfer rate (note that the temperature slope in the boiling region is steeper than the slope for the infinite secondary heat transfer, but well developed primary temperature profiles). The initial position of nucleate boiling is specified as that at which the secondary fluid reaches saturation.

For rivulet flow, the overall thermal conductance, defined as the reciprocal of the sum of primary convection resistance plus conduction resistance, plus secondary convection resistance (calculated on the basis of a fully wet periphery) is multiplied by an estimated fraction of rod periphery wetted below the TSP (0.4 for the example calculation in Figure 8). Heat transfer per unit perimeter (q) is then given by

$$q = U\,(T_{primary} - T_{secondary})$$

$$U = \frac{1}{\frac{D_o}{D_i h_i} + \frac{D_o}{2k} \ln \frac{D_o}{D_i} + \frac{1}{h_o}} \frac{P_{wet}}{P}$$

where,

U	=	thermal conductance
T	=	fluid temperature
D_i	=	tube inside diameter
D_o	=	tube outside diameter
k	=	tube wall conduction coefficient
h_i	=	tube inside wall convection coefficient
h_o	=	tube outside wall convection coefficient
P_{wet}	=	perimeter wet
P	=	tube outside perimeter

If wall to gas heat transfer proves important at high temperature and pressure, this may easily be added to the above equation.

The preliminary calculations shown in Figure 8 show good agreement with the data. The agreement is achieved, however, by varying the wetted flow area ratio until agreement is reached (the ratio chosen, 0.4, is, however, a reasonable estimate). Further development is necessary before the program is capable of calculating heat transfer over the wide ranges of conditions encountered in these experiments and in an actual steam generator.

This heat transfer analysis suggests that a three region model of OTSG heat transfer is appropriate and reasonable for inclusion in RELAP5 or TRAC. The three regions would describe steam generator tubes which are (a) fully wet with falling film, (b) partially wet with rivulet flow, and (c) completely dry.

6. CONCLUSIONS

Fluid flow and heat transfer experiments are being successfully run in a single tube air-water apparatus which model OTSG behavior during AFW injection.

The experiments are one part of a series which also includes the study of AFW distribution in a multi-tube apparatus. The results of the experiments performed to date are:

A flooding curve for the single tube broached hole TSP was determined. The critical gas superficial velocity for flooding is lower than that for a multi-tube TSP. The data is consistent with that of other researchers for small hydraulic diameter perforated plates.

Pressure drops were measured across the TSP and a loss coefficient calculated (K_{loss} = 0.94, based on average velocity within the hole).

A borescope slipped into a clear Lexan tube was successfully used to determine liquid level above the TSP, and is being used in the multi-tube experiments where the TSP is only partially visible.

Tube wetting phenomena is being investigated and described. Of primary interest is the formation of rivulets rather than a thin film at lower flow rates. The rivulet/falling film transition is being quantified.

Heat transfer data for typical primary flow and AFW flow conditions is being obtained and the heat transfer regimes identified.

The heat transfer data is analyzed by use of a computer program which is presently in development. Preliminary calculations show that a one-dimensional model of steam generator tubes, such as employed in RELAP5 or TRAC, is capable of reasonable heat transfer calculations if appropriate models are employed. Modeling rivulet flow heat transfer may be accomplished by multiplying the overall thermal conductance calculated for a fully wet tube by the fraction of the tube perimeter wet.

REFERENCES

1. Bankoff, S. G., et. al., "Countercurrent Flow of Air/Water and Steam/Water Through a Horizontal Perforated Plate", Int. J. Heat and Mass Transfer, 24, 1981.

2. Chen, S. J., "Turbulent Film Condensation on a Vertical Plate", Proceedings of the Eighth International Heat Transfer Conference, 1986, Hemesphere, New York.

3. Dittus, F. W., and Boelter, L. M. K., Univ. Calif. Publs. Engr., 2:443, 1930.

4. Hsu, Y. Y., Simon, F. F., and Lad, J. F., "Destruction of a Thin Liquid Film Flowing Over a Heating Surface", Chemical Engineering Progress Series, 61, 57, 1965.

5. Kays, W. M., Convective Heat and Mass Transfer, New York, McGraw-Hill, 1966.

6. Labuntsov, D. A., "Heat Transfer in Condensation of Pure Steam on Vertical Surface and Horizontal Tubes", Teploenergetika, 4, 1957.

7. Matijevic, E., Surface and Colloid Science, New York, Wiley-Interscience, 1969.

8. Sun, K. H., "Flooding Correlations for BWR Bundle Upper Tie-Plates and Bottom Side-Entry Orifices", Proceedings Second Multi-Phase Flow and Heat Transfer Symposium-Workshop, Hemesphere, New York, 1979.

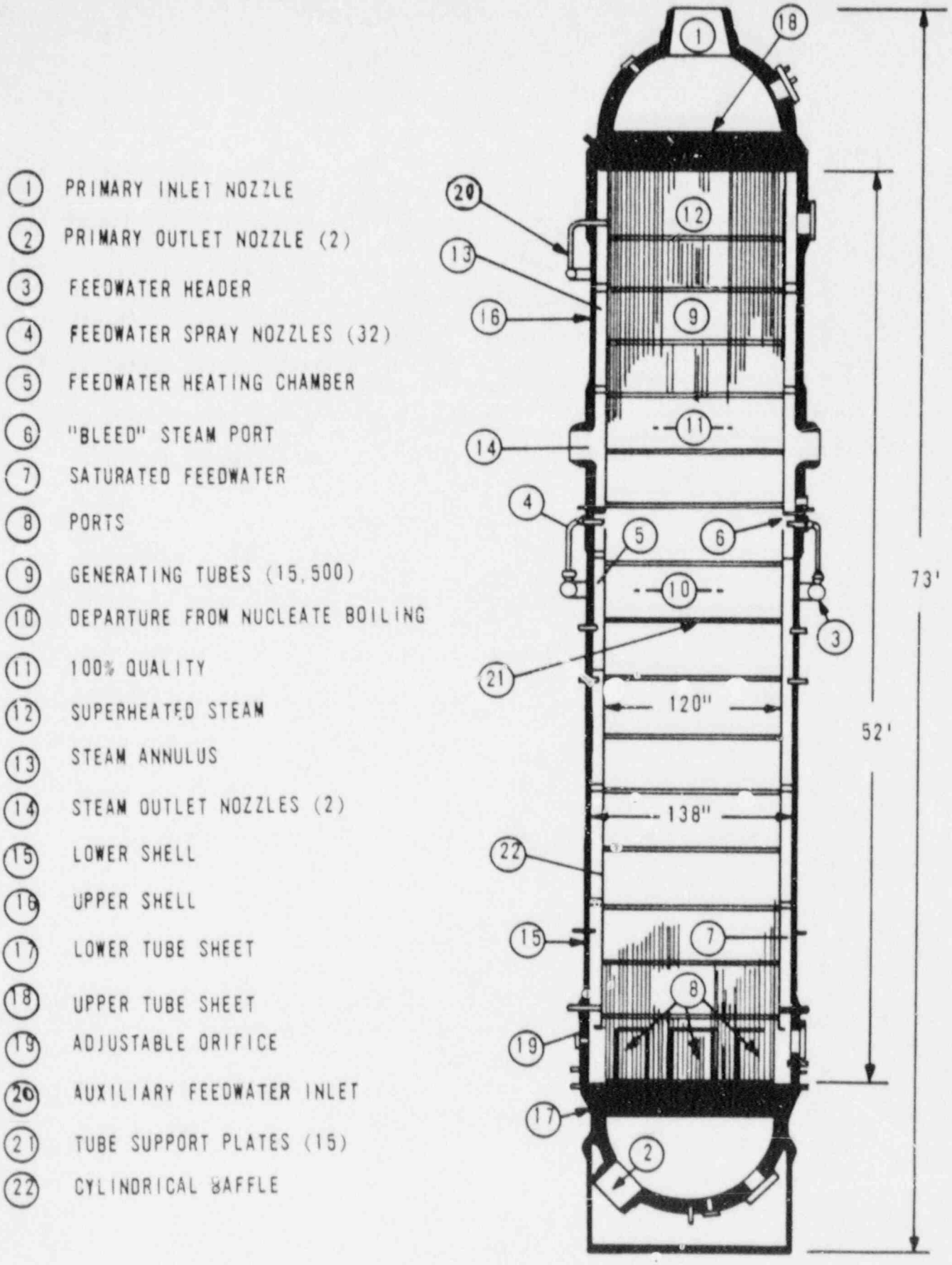

Figure 1. Once Through Steam Generator.

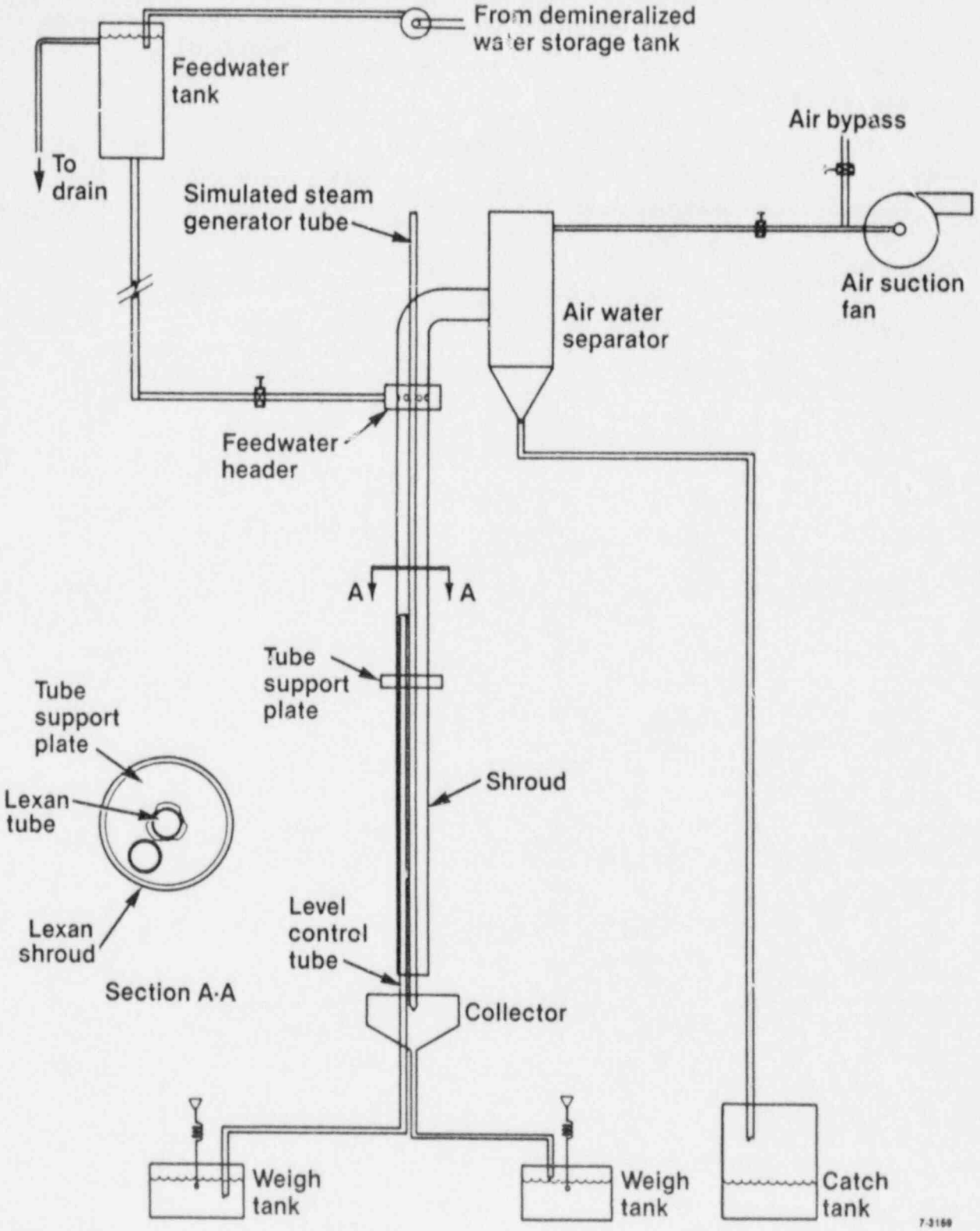

Figure 2. Single tube adiabatic air-water OTSG apparatus.

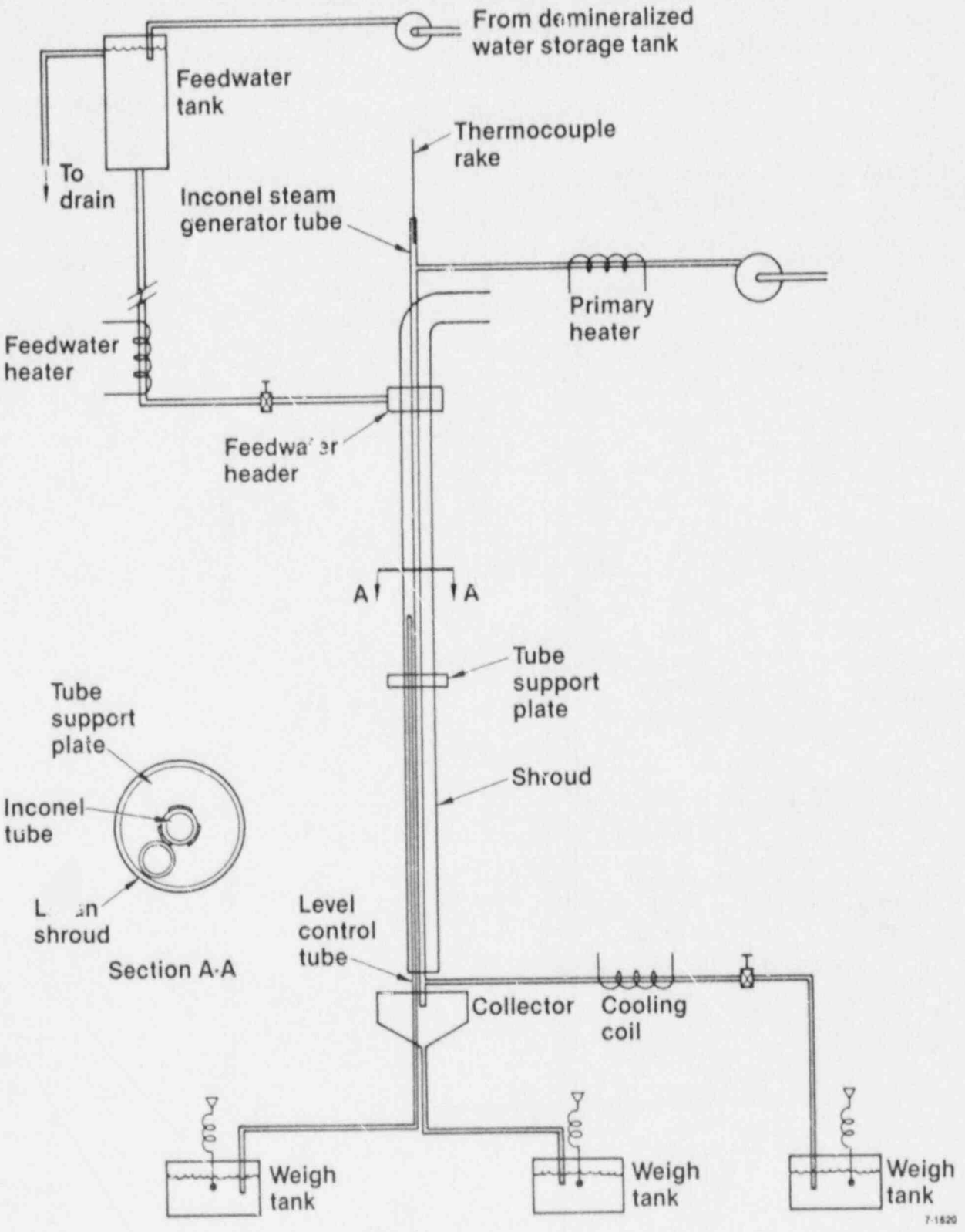

Figure 3. Single tube heated OTSG apparatus.

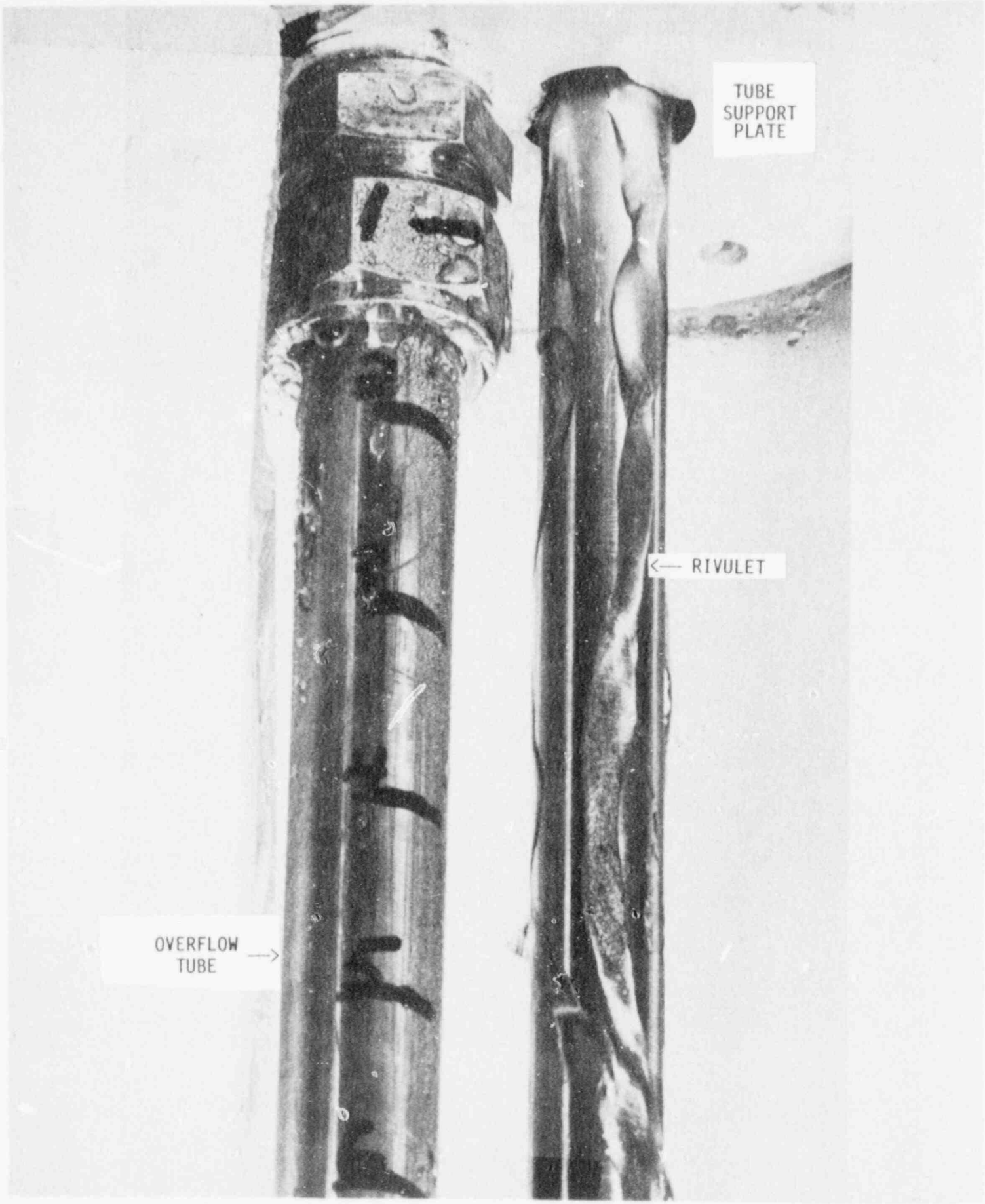

Figure 4. Rivulet flow down steam generator tube.

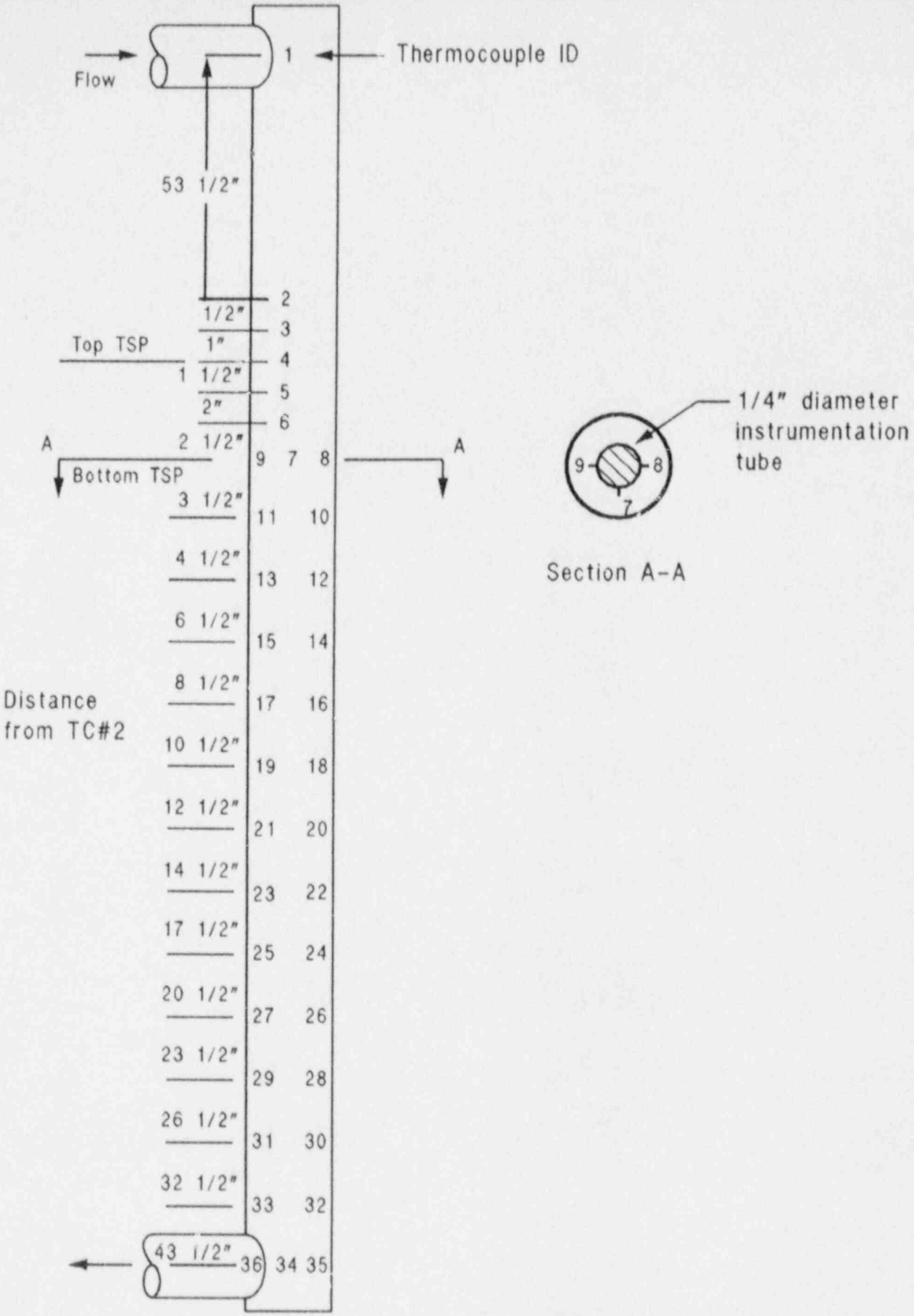

Figure 5. Thermocouple locations.

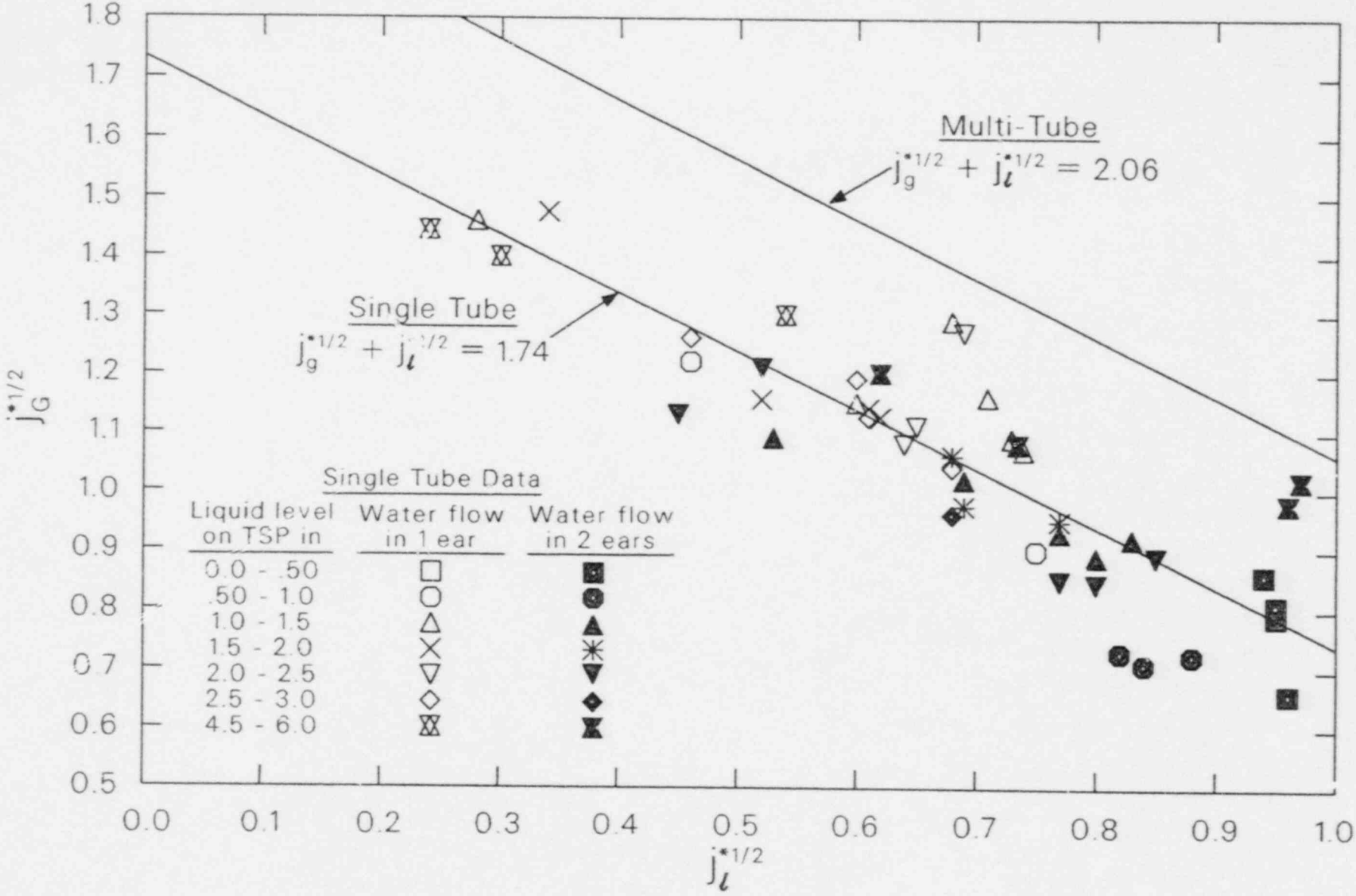

Figure 6. CCFL data on $j^{*1/2}$ plot.

WRR8714-1

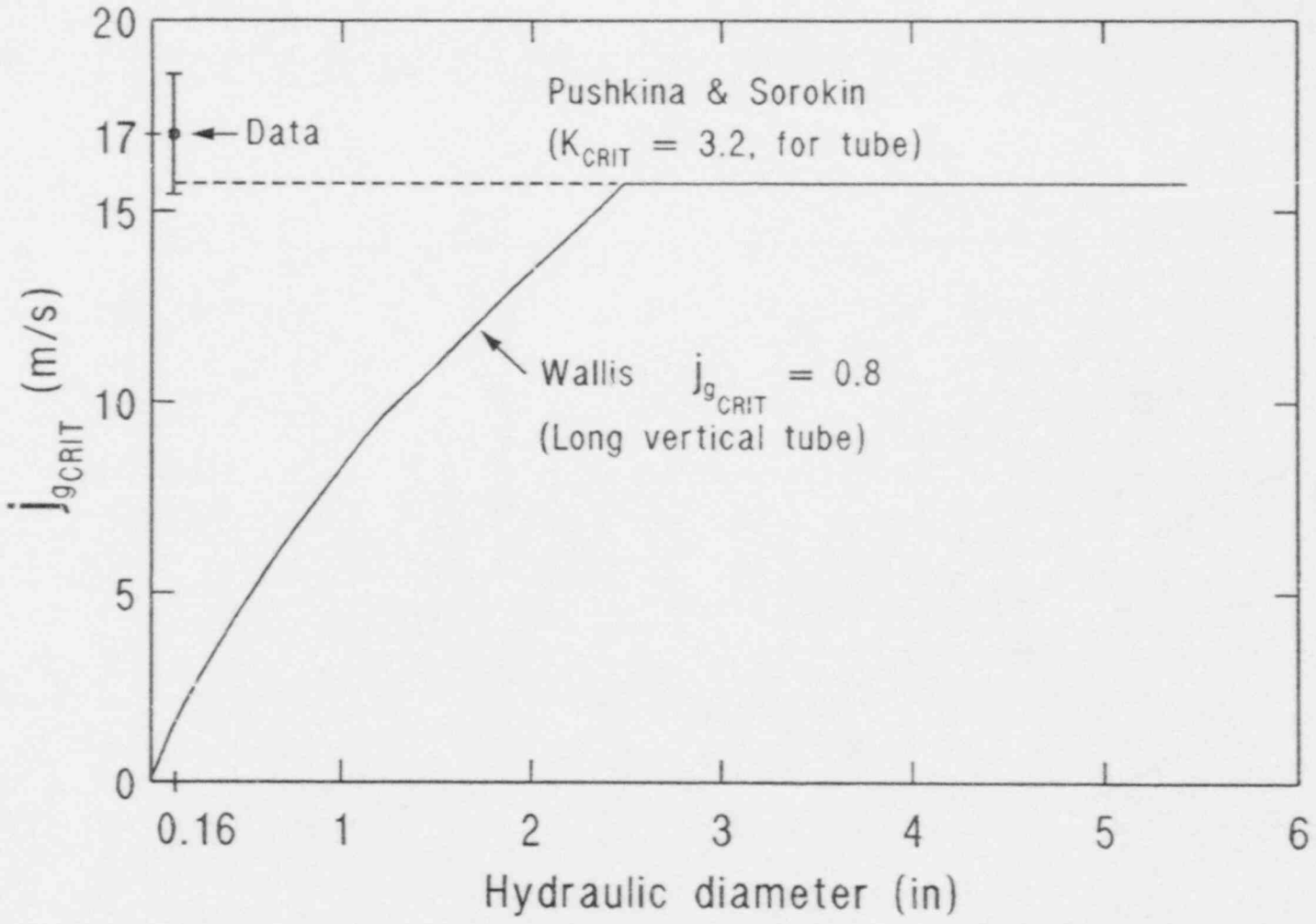

Figure 7. Critical superficial air velocity for water at standard temperature and pressure.

CCK00631

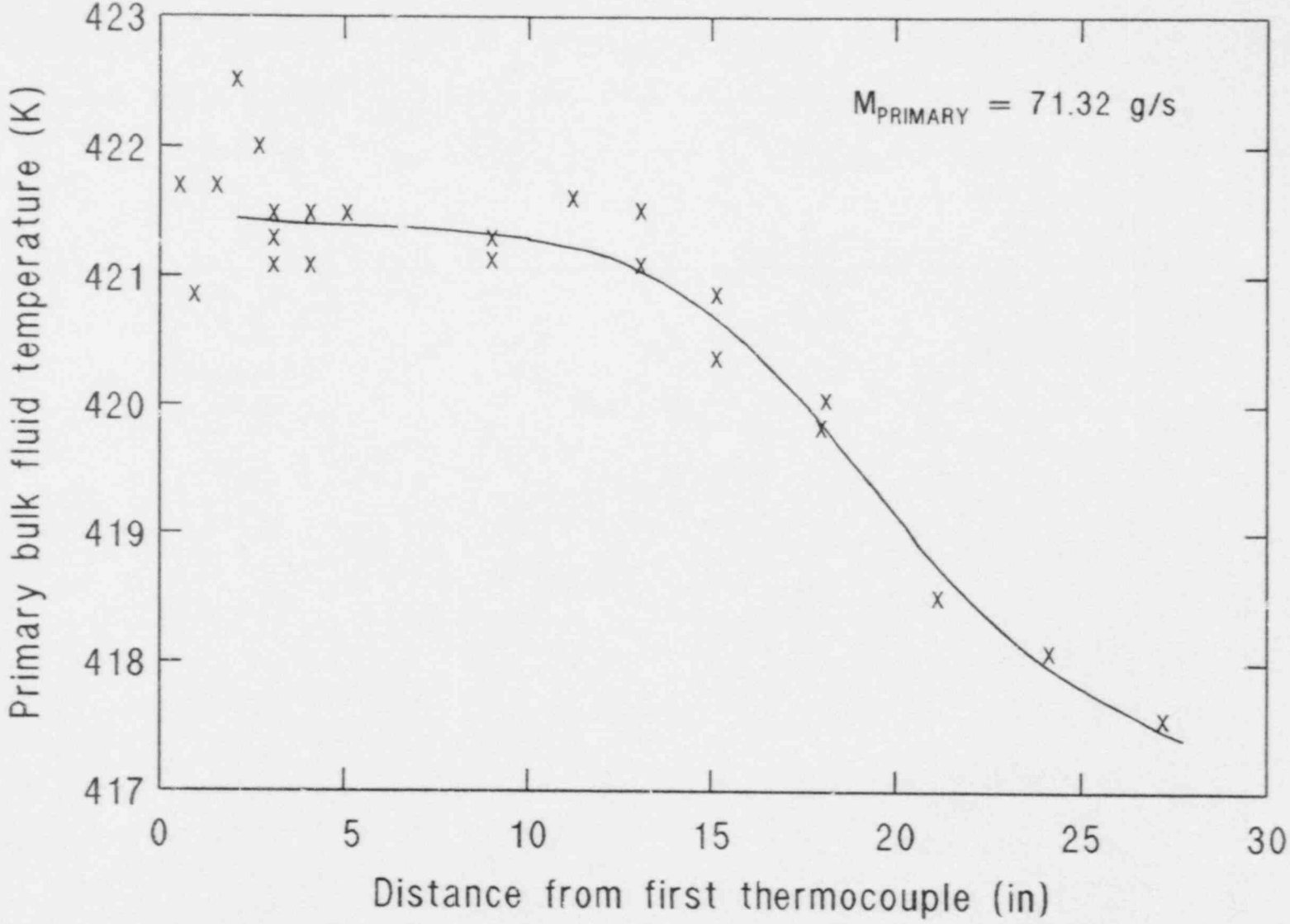

Figure 8. Primary fluid temperature, low secondary flow rate (1.67 g/s).

CCK00637

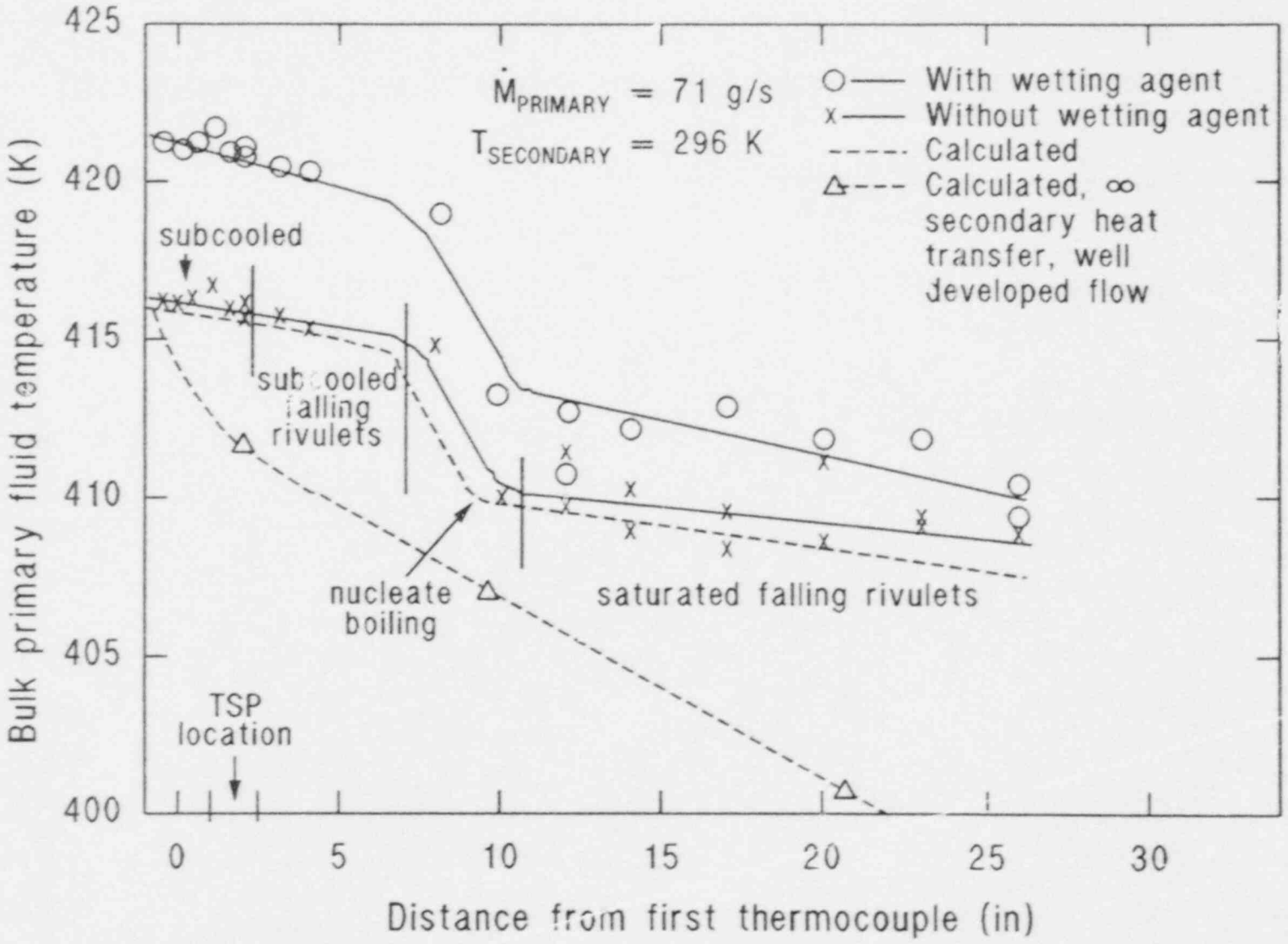

Figure 9. Primary fluid temperature, measured and calculated. Medium secondary flow rate (12 g/s).

CCK00636

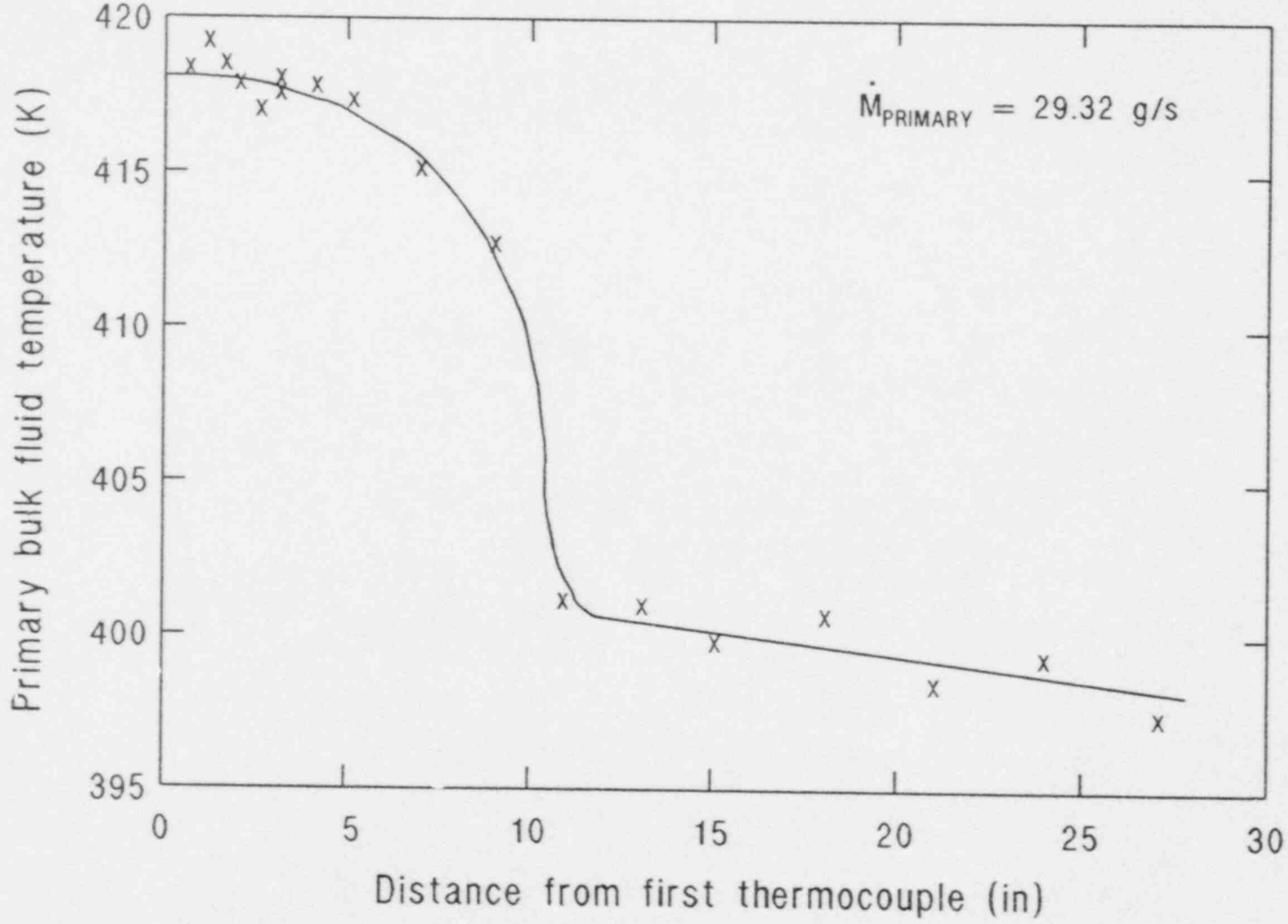

Figure 10. Primary fluid temperature, high secondary flow rate (30.35 g/s).

CCK00632

NON-EQUILIBRIUM VAPORIZATION IN THE POST-CHF HEAT TRANSFER REGIME*

by

C. Unal,** K. Tuzla, S. Neti, and J. C. Chen
Institute of Thermo-Fluids Engineering and Science
Whitaker Lab #5
Lehigh University
Bethlehem, PA 18015

ABSTRACT

An experimental study of convective film boiling (post-CHF) was carried out for low pressure steam and water flow in a nine-rod bundle with heated shroud. Measurements of wall heat flux, wall superheat, and vapor superheat were obtained as a function of axial distance from the CHF quench front for a range of flow rates and flow qualities. Three series of tests were carried out: a) fixed quench front with the CHF dryout point stabilized at test section inlet, b) reflood with advancing quench front propagating upward through the test section, c) dryout with the quench front retreating upstream downwards through the test section. A total of 467 data points were generated from 144 experimental runs which were executed in the following range of conditions.

Coolant Mass Flux	0.1 to 26 kg/m^2s
Inlet Quality	$40^{\circ}C$ subcooled to 0.40
Pressure	105 to 120 kPa
Heat Flux	5 to 43 kW/m^2

INTRODUCTION

Convective boiling after exceeding the critical heat flux (CHF) can be encountered in steam generators, refrigeration systems, cryogenic systems, nuclear reactors and other applications. This regime of boiling is sometimes referred to as "convective film boiling," "post-CHF heat transfer," "post-dryout boiling," or "flow-film boiling." The flow pattern

*This work was performed under the auspices of the U.S. Nuclear Regulatory Commission, Office of Nuclear Regulatory Research, Division of Reactor Systems Safety.

**Presently with University of Maryland, Department of Chemical and Nuclear Engineering, College Park, MD 20742

is either inverted annular flow (liquid core surrounded by a vapor annulus) or fully dispersed flow (liquid drops dispersed in a vapor continuum). In either case, superheating of the vapor above the saturation temperature can occur, resulting in thermodynamic nonequilibrium between the two phases [1-7]. This state is characterized by a superheating bulk vapor and an actual flow quality (X_a) less than the thermodynamic equilibrium quality (X_e). Energy balance requires that

$$X_e h_{fg} = X_a[h_{fg} + C_{pv}(T_v - T_s)] \tag{1}$$

and if

$$T_v > T_s \ , \tag{2}$$

then

$$X_a < X_e \ .$$

Analysis of convective film boiling requires knowledge of the degree of vapor superheating and the resultant degree of thermodynamic nonequilibrium. Of particular importance is the axial variation of vapor superheat (in the direction of flow) since the intensity of vaporization (Γ) is characterized by the axial derivative of the bulk vapor temperature,

$$\begin{aligned} \Gamma &= \frac{(\text{Mass of liquid vaporized})}{(\text{Time}) \cdot (\text{Volume})} \\ &= G \frac{dX_a}{dz} \\ &= G \frac{d}{dz} \left[\frac{X_e h_{fg}}{h_{fg} + C_{pv}(T_v - T_s)} \right] \end{aligned} \tag{3}$$

Finally, since only a fraction of the heat transfer to the fluid effects vaporization of the liquid phase (the balance going toward superheating of the vapor), one is concerned with the "evaporation ratio," defined as

$$\begin{aligned} R_E &\equiv \left(\frac{\text{Latent heat of vaporization}}{\text{Time} \cdot \text{Volume}} \right) \div \left(\frac{\text{Total heat input}}{\text{Time} \cdot \text{Volume}} \right) \\ &= \frac{h_{fg} \cdot \Gamma}{Q/V} \end{aligned} \tag{4}$$

Due to the difficulty of measuring vapor superheat in the presence of dispersed liquid, only a few attempts to quantify the degree of thermodynamic nonequilibrium have been reported. Mueller [8], Polomik [9], Nijhawan, et al. [10], Annunziato [11], Gottula, et al. [12] and Evans, et al. [13] were successful in obtaining measurements of nonequilibrium vapor superheats for post-CHF boiling in vertical tubes. Of these, only the latter two studies [12,13] obtained information on the axial variation of the vapor superheats. There is also concern that the thermodynamic behavior may be affected by channel geometry; and since many applications involve flow in rod or tube bundle geometries, there is a need to characterize the nonequilibrium behavior in bundles.

The objective of the present study was to obtain experimental measurements of post-CHF boiling in a rod bundle geometry, including information on the axial variation of vapor superheats. The aspirated probe technique of Nijhawan, Chen, et al. [10] was modified to permit measurement of vapor superheats in the flow channels of the rod bundle.

EXPERIMENT

The experiments were carried out in a two-phase loop with a vertical rod bundle test section. The loop provided a metered flow of known flow rate, pressure, and vapor/liquid quality to the inlet of the test section. The test section consisted of a heated shroud containing a 3 x 3 rod bundle assembly, as illustrated in Figure 1. Dimensions of the rods and the shroud were selected to have equal hydraulic diameters in all flow subchannels (e.g. cells I and II). Figure 2 shows a schematic diagram of the test section and its inlet and exit connections. The inlet section provided a flow length with an internal strainer to obtain good mixing between the vapor and liquid phases. A hot patch was also available to condition the thermal state of the inlet two-phase flow and to stabilize the quench front for those tests where a fixed CHF point was desired. The test section had a length of 1.2 meters and incorporated four ports for vapor temperature and pressure probes and a rod spacer, as indicated in Figure 2. The vapor superheat probes were similar to those used by Nijhawan [10] and Evans [13], modified to permit traversing across the rod bundle width. The nine test rods were electrically heated with uniform heat flux. The test section shroud was heated by a radiant furnace with multi-zone control. Thermocouples mounted on the external wall of the shroud permitted determination of shroud temperatures along its axial length. Each of the nine internal rods were equipped with 12 thermocouples imbedded in grooves near the rod surface for measurement of wall temperatures at various axial locations. In addition to rod's and shroud's power and temperature measurements, the fluid flow rate, inlet enthalpy, inlet pressure, and bulk vapor superheats were determined and recorded for each run. Details of the test facility and instrumentation are given in Reference [14].

In a typical fixed-quench-front run, the test section would be preheated to a selected post-CHF state with the inlet hot-patch, the shroud and rods at substantial superheats. A steady two-phase flow, with desired flow rate, pressure, and inlet mixture enthalpy would be established, using a bypass around the test section during the prehating stage. Upon

obtaining the desired initial condition, data acquisition was started and the two-phase fluid would be switched from the bypass line to the test section. Ninety channels of experimental data would be recorded on a 7-second time cycle through the duration of each test run. As the two-phase fluid passed through the test section, steady-state post-CHF boiling occurred along the length of the test section downstream of the CHF point which is arrested at the inlet of the hot-patch.

For advancing-quench-front runs the procedure was similar to the one described above for fixed-quench-front runs, except the inlet hot-patch was maintained as an adiabatic section at the fluid saturation temperature. By adjustment of the power input to the test rods and shroud, it was possible to attain a steady upward movement of the CHF location (propagating quench front) as the test section slowly cooled. Because the quench front velocity was orders of magnitude less than the fluid flow velocity, sufficient time was obtained to establish thermal-hydraulic quasi-steady state downstream from the quench front through the course of each run. In this manner, measurements of vapor superheats at the probe location could be analyzed to obtain axial variations of the degree of nonequilibrium as a function of distance from the CHF point. In a typical run, the quench front would propagate with a velocity of the order of 1 mm per second, and single run would last approximately 10 minutes (time for the quench front to reach the vapor probe station).

For a typical retreating-quench-front run the test section was filled with fluid at saturation temperature, and test rods and the shroud were powered for the desired heat flux. Post-CHF conditions, starting from the top, were obtained above a dry-off point. When the dry-off point reached the vapor probe elevations, the probes were activated for vapor temperature measurements, and the experiment was terminated when the dry-off point reached the bottom of the test section.

All experiments were carried out with water/steam as the test fluid. The two-phase mass flux ranged from 0.1 to 26 kg/m^2s, the inlet enthalpy varied from 40°C subcooled to 50 percent net quality and the test pressure was between 105 to 120 kPa. A total of 467 data points were generated from 144 experimental runs. The distribution of the data points among the fixed-quench-front, advancing-quench-front and retreating-quench-front data was 97, 278 and 92 respectively.

RESULTS

The primary information recorded was temperatures of the heater rods and two-phase vapor. Figures 3-5 show representative plots of the rod and vapor temperatures measured along the length of the test section during the three different modes of tests. Figure 3 shows the conditions obtained during a typical fixed-quench-front test. Wall superheats at 44 axial locations and vapor superheats at two axial locations are indicated together with the axial variation of equilibrium quality, and calculated actual qualities at the two probe elevations. The wall superheat temperatures mainly belong to three representative rods which are indicated as 1, 2 and 3 in Figure 1. The axial variation of the rod temperatures shown in Figure 3 is typical for all fixed-quench-front tests; the rod's surface superheats are between 400-500°C at the test section inlet, and

rise to about 650°C in a distance of about 0.3 m. At the grid spacer, as indicated by the symbol S in Figure 3, the rods experience a sharp decrease in wall superheat, requiring an axial distance of approximately 0.2 m before recovering to the pre-spacer temperatures. This desuperheating effect of the grid spacer was consistently found in all experiments, regardless of the mode of the experiment, indicating the promotion of enhanced two-phase cooling by the spacer obstruction. During these experiments, only two of the vapor probe stations, those indicated by the symbol P in Figure 3, were mounted with vapor probes; the measured vapor temperatures are indicated by the dark symbols in Figure 3. For the conditions of this test, it is seen that the vapor attains a very significant level of superheat (~ 500°C) at the first vapor probe elevation. The downstream measurement indicated less vapor superheat due to desuperheating effects of the grid spacer on the two-phase fluid.

During an advancing-quench-front test the lower hot-patch is kept at fluids saturation temperature and as a result the CHF point will propagate into the test section with slow velocities, leading to pseudo-steady-state conditions in the test section. Figure 4 shows "snapshots" of the rod and vapor temperatures measured during such an experiment, at two particular times (70 and 280 seconds) after initiation of two-phase flow. For the time A (70 seconds) the open circles represent surface temperatures measured on the nine rods in the test section at the various elevations indicated. The uniformity and smoothness of this composite curve confirms the similarities of thermal hydraulic conditions in all flow subchannels of the rod bundle. Upstream of CHF (quench front), the rods' surface superheats were essentially zero; immediately downstream of the quench front, the rods experienced a rapid rise in temperature to several hundred degrees centigrade in a distance of approximately 0.3 m. Further downstream, the rods were found to have a fairly uniform superheat (of approximately 600°C for this run), with the exception of the region near the grid spacer. The measured vapor temperatures are indicated by the dark symbols in Figure 4. For the conditions of this test, it is seen that the vapor attains a very significant level of superheat (400°C) just half a meter downstream from the CHF (quench front). The downstream measurement did not indicate any significant further increase, due primarily to the desuperheating effects of the grid spacer on the two-phase fluid. The run progressed, the CHF quench front propagated upward in the test section as indicated by the two snapshots in Figure 4. The general characteristics of the downstream wall temperatures remained similar, although there is a discernible decrease in the magnitude of the local wall superheat upon approach of the quench front. The vapor superheats were more significantly affected by the advancing quench front; at the first probe station, the vapor superheat was observed to decrease from 420°C to 200°C as the quench front advanced by a distance of approximately 0.25 m in that experiment.

A retreating-quench-front experiment starts by filling the test section with fluid at saturation temperature. As the fluid is evaporated by the heat from heated rods and the shroud, the liquid level in the test section retreats with post-CHF conditions at downstream. Figure 5 shows a plot of axial variation of rod and vapor temperatures at a particular time (258 seconds) after the initiation of the test. Quench front is located

around 20 cm elevation. Axial variation of rods' surface temperatures are similar to the variations observed in advancing-quench-front tests.

The axial variations of rod and vapor superheats shown in Figures 3-5 are illustrative of behavior found in these experiments. Reproducibility was checked by carrying out two or more runs with similar entrance and boundary conditions. It was found that derivations in wall and vapor superheats were of the order of only 3 percent for similar runs.

Lateral Variation of Vapor Superheat

Steady-state post-CHF conditions, obtained with fixed-quench-front tests, allowed ample time for repeated vapor superheat measurements. Under steady-state conditions, the vapor probe was moved in the cross-sectional plane (between points B and C in Figure 1) and vapor superheats were measured. Typical measurements from the first vapor probe port are shown in Figure 6 for three different inlet qualities. Significant temperature differences, up to 120°C, were measured in the cross-sectional plane of the test bundle for low inlet quality conditions. The lateral temperature profile has a bell shape with its maximum value obtained at the minimum channel width (point A), and its minimum values at the centers of inner and outer flow cells (points B and C). The symmetric behavior of the vapor temperature profile, between AB and AC, is evidence of even thermal hydraulic conditions in the inner and outer cells. Though the vapor temperature profile is influenced by the flow conditions in the channel, the locations of maxima and minima of the vapor temperatures do not appear to be affected. Also shown in Figure 6 is the effect of inlet quality on the vapor temperature that indicates a flatter profile with increasing inlet quality. For the conditions of Figure 6, the maximum lateral variation in vapor temperature (ΔT_{max}) is reduced from 120°C to 40°C when the inlet quality is increased from 0.04 to 0.40.

Axial Variation of Vapor Superheat

In order to obtain the variation of vapor superheat with axial position, it is necessary to collect experimental measurements for a given set of inlet conditions and downstream boundary conditions. Since the post-CHF regime starts at the CHF (quench front) location it is therefore necessary to use data for equal values of mass flux (G), pressure (p), and equilibrium quality at the CHF point (X_{CHF}). Similarity of downstream boundary conditions require given values of the wall temperature and wall heat flux. These requirements are not easily satisfied in a single experimental run. As illustrated in Figures 3-5, the equilibrium quality increases along the test section; thus the quality at the CHF point changes as the quench front propagates along the test section in an advancing-quench-front run. To satisfy the requirement for similar initial and boundary conditions, it was necessary to search the complete data base of all runs for subsets having similar boundary conditions and initial inlet conditions at the CHF location. Figure 7 shows a composite plot of the data for such a subset of measurements obtained at similar entrance and boundary conditions. It is seen that both the wall superheat and the vapor superheat data do delineate axial curves for such a composite set of test

conditions. Within the range of conditions indicated, these data give a true indication of the variations of the nonequilibrium thermodynamic conditions as a function of axial position from the quench (CHF) point.

Several important observations can be made from the data shown in Figure 7. First, it is seen that the axial variation of vapor superheat shows an S-shaped profile. Thus the derivative of vapor superheat with axial distance (slope of the curves) are small near the CHF point and at far distances from the CHF point, with a higher value at intermediate distances. The slope of the axial profile of vapor temperature measures the rate of specific heat addition to the vapor. A steeper slope implies greater heat addition to the vapor and correspondingly lesser heat contribution to evaporative phase change; conversely, a shallower slope of the vapor temperature profile indicates a larger amount of heat input going to evaporation and thus a tendency for the two-phase fluid to approach thermodynamic equilibrium. The results obtained from plots similar to Figure 7 indicate a region of approximately 20-30 cm immediately downstream from the quench front with relatively low values of vapor superheat and having a fairly shallow slope in the axial variation of vapor superheat. This implies that the vaporization process is relatively efficient in this region near to the quench front location. Evaporation of the liquid phase can be caused by either heat transfer from the superheated vapor to the entrained liquid or from heat transfer from the superheated wall to the liquid. The corresponding driving forces for these two mechanisms are the vapor superheat ($T_v - T_s$) and the wall superheat ($T_w - T_s$), respectively. In this near-distance region, the wall superheats are seen to be quite significant while the vapor superheats are relatively low. Thus the data similar to Figure 7 implies that there is an effective mechanism for vaporization in the near region due to direct heat transfer from the wall to the liquid phase. This hypothesis is qualitatively consistent with the observations reported by Hewitt, et al. [15] and by Ishii [16] which indicate a near-zone region with relatively large amount of liquid present in a fairly agitated flow pattern which could cause significant liquid splashing on the channel walls.

At greater distances downstream from the quench front, the axial gradient of vapor superheat first increases and then decreases with increasing axial distance. It is our belief that the middle region with the high axial gradient indicate that the evaporation process diminishes in intensity due to a diminishment of wall-to-liquid heat transfer, as the two-phase flow passes out of the near-region splash zone. This effect continues into the far zone but at these downstream positions the cumulative evaporation has increased the absolute mass flux of vapor flow such that the rate of increase in specific vapor sensible heat (per unit mass of vapor) is decreased even though most of the heat addition still goes toward vapor superheating rather than evaporation. This point can be more easily observed by comparing the axial gradient of vapor superheat to the gradient that would be obtained for the limiting case of "frozen quality" conditions where all the heat input goes toward vapor superheating. In Figure 7, a frozen quality line is drawn from point A to indicate the axial profile if no further evaporation were to occur after point A. It is seen that the measured vapor temperature profile lies

fairly close to this limiting condition, indicating a relatively ineffective evaporation process in this downstream region.

The experimental results of this study permit an evaluation of the net evaporation process as a function of axial distance. Since bulk vapor superheat is observed in this post-CHF heat transfer process, it is obvious that only a fraction of the total heat input to the two-phase fluid results in vapor formation, the balance being absorbed as sensible superheat of the vapor. To improve our ability for mechanistic modeling of the process one would like to know the division of heat input between evaporation and sensible heating.

The evaporation ratio defined by equation (4), represents the fraction of total heat input that is utilized in vaporization. The local evaporation ratio can be expressed,

$$R_E = h_{fg} \frac{\Gamma}{(Q/V)} = (dX_a/dz) \div (dX_e/dz) = \frac{dX_a}{dX_e} \qquad (5)$$

Axial gradients of actual and equilibrium qualities are required for calculation of the local evaporation ratio. A sample case is calculated for the conditions of Figure 7 and plotted in Figure 8. The scatter of the data in this figure is partly due to slightly different operating conditions for the various runs that are included, and partly due to experimental accuracy. The data obviously show a decreasing trend in R_E with increasing axial distance. It is seen that the local evaporation ratio approaches unity at the CHF (quench front), decreasing to approximately 0.3 at about 20 cm. This decrease continues with increasing axial distance, approaching magnitudes of less than 0.1 after 60 cm.

It is clear that post-CHF heat transfer downstream from the CHF quench front involves a "near region" with reasonably effective evaporation and a "far region" where the evaporation process is relatively ineffective and almost all the heat input goes toward sensible superheating of the vapor phase.

The experimental information represented in Figures 6-8, showing lateral variation of vapor superheats and axial variations of heat flux, wall superheats, vapor superheats, and evaporation ratios, are the final results of this study. Clearly, such detailed experimental information is needed to assess and improve models for analysis of the post-CHF heat transfer process. An initial attempt to compare existing models [4,5,7] with these data showed unsatisfactory agreement [17]. A few models were reasonably close in prediction of heat fluxes, but essentially all the models did not satisfactorily predict the axial variation of vapor superheating or the evaporation ratio. Clearly, one can have confidence in a phenomenological model only if it can satisfactorily describe the total interacting mechanisms. These experimental findings are being presented in this paper in hopes of aiding future developments of improved mechanistic models for the post-CHF heat transfer process. Detailed documentation and tabulation of the data will be available in a separate reference report [18].

REFERENCES

1. Forslund, R. P. and W. M. Rohsenow, "Dispersed Flow Film Boiling," Journal of Heat Transfer, Trans. ASME, Series C, vol. 90, pp. 399-407.

2. Groeneveld, D. C., "The Thermal Behavior of a Heated Surface at Beyond Dryout," AECL-4309, 1972.

3. Bennett, A. W., et al., "Heat Transfer to Steam-Water Mixtures Flowing in Uniformly Heated Tubes in Which the Critical Heat Flux has been Exceeded," UKAEA Research Group Report AERE-R5373, 1967.

4. Saha, P., B. S. Shiralkar and G. E. Dix, "A Post-Dryout Heat Transfer Model Based on Actual Vapor Generation Rate in Dispersed Droplet Regime," ASME Paper No. 77-HT-80, 1977.

5. Webb, S. W., J. C. Chen and R. K. Sundaram, "Vapor Generation Rate in Non-equilibrium Convective Film Boiling," 7th Int. Heat Transfer Conf., September 6-10d, Munich, 1982.

6. Webb, S. W., and J. C. Chen, "A Nonequilibrium Model for Post-CHF Heat Transfer," Proc. OECD(NEA) CSNI Third Spec. Meet. on Trans. Two-Phase Flow, Pasadena, CA (USA), CSNI, Report No. 61, March 1981.

7. Webb, S. W. and J. C. Chen, "A Two-Region Vapor Generation Rate Model for Convective Film Boiling," International Workshop on Fundamental Aspects of Post-Dryout Heat Transfer," Salt Lake City, Utah, April 1-4, 1984.

8. Mueller, R. E., "Film Boiling Heat Transfer Measurements in a Tubular Test Section," EURAEC-1971/ GEAP-5423, 1967.

9. Polomik, E. E., "Transition Boiling Heat Transfer Program - Final Summary Report for Feb/63 - Oct/67," GEAP-5563, 1967.

10. Nijhawan, S., J. C. Chen, R. K. Sundaram, and E. J. London, "Measurements of Vapor Superheat in Post-Critical-Heat Flux Boiling," ASME Journal of Heat Transfer, vol. 102, 1980, pp. 465-570.

11. Annunziato, A. M. Cumo and G. Palazzi, "Post-Dryout Heat Transfer in Uncovered Core Accidents," ANS 2nd Nuclear Reactor Thermal-Hydraulics Conference, Santa Barbara, January 1983.

12. Gottula, R. C., R. A. Nelson, J. C. Chen, S. Neti and R. K. Sundaram, "Forced Convective Nonequilibrium Post-CHF Heat Transfer Experiments in a Vertical Tube," ASME-JSME Thermal Engineering Conference, Honolulu, March 1983.

13. Evans, D., S. W. Webb and J. C. Chen, "Axially Varying Vapor Superheats in Convective Film Boiling," ASME Journal of Heat Transfer, vol. 107, pp. 663-669, August 1985.

14. Tuzla, K., C. Unal, O. A. Badr, S. Neti and J. C. Chen, "Two-Phase 3 x 3 Rod Bundle Test Facility for Post-CHF Boiling," NUREG/CR-3849, 1984.

15. Hewitt, G. F., G. Costigan and D. Lee, "UK Studies of Post Dryout Heat Tranfer," Trans. of the Twelfth Water Reactor Safety Research Inf. Meeting, Gaithersburg, Maryland, October 22-26, 1984.

16. Ishii, M., Inverted Annular Flow Experiment at ANL," Priviate communications, Lehigh University, 21 January 1986.

17. Unal, C., "An Experimental Study of Thermal Nonequilibrium Convective Boiling in Post-Critical-Heat-Flux Region in Rod Bundles," PhD Thesis, Lehigh University, Bethlehem, PA, 1986.

18. Tuzla, K., C. Unal, O. Badr, S. Neti and J. C. Chen, "Post-Critical Heat Flux Boiling; Rod Bundle Test Data Report," to be printed as a NUREG Report, 1987.

NOMENCLATURE

G	:	Mass Flux	Kg/m^2s
P	:	Pressure	KPa
R_E	:	Evaporation ratio	--
T	:	Temperature	^oC
X	:	Vapor mass quality	Kg/Kg
Z	:	Axial distance	m
	:	Vapor generation rate	Kg/m^3s

SUBSCRIPTS

a	:	Actual
CHF	:	Critical heat flux
e	:	Equilibrium
in	:	Inlet
r	:	Rod
s	:	Saturation
v	:	Vapor
W	:	Wall

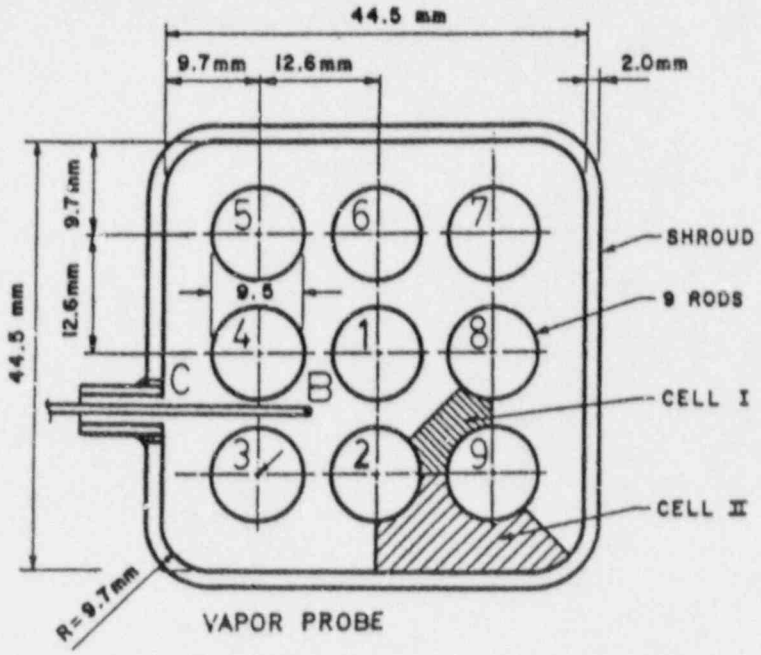

Figure 1 Cross-sectional view of the test section

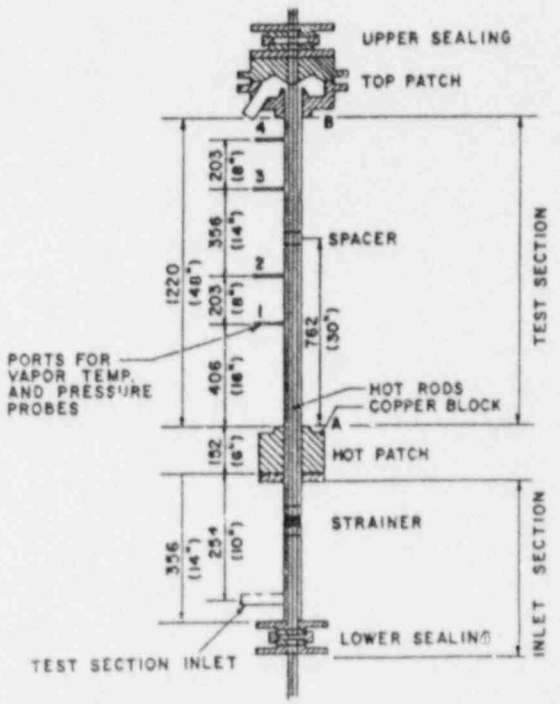

Figure 2 Schematic of the vertical view of the test section

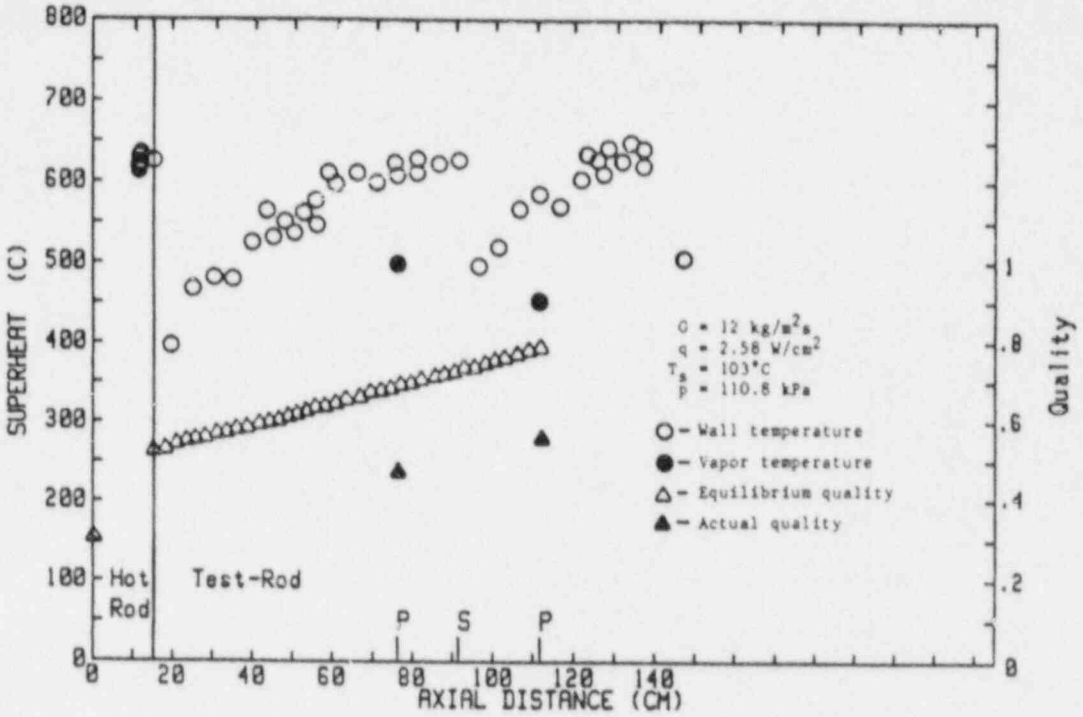

Figure 3 Wall and vapor superheats versus axial distance for a fixed-quench-front run

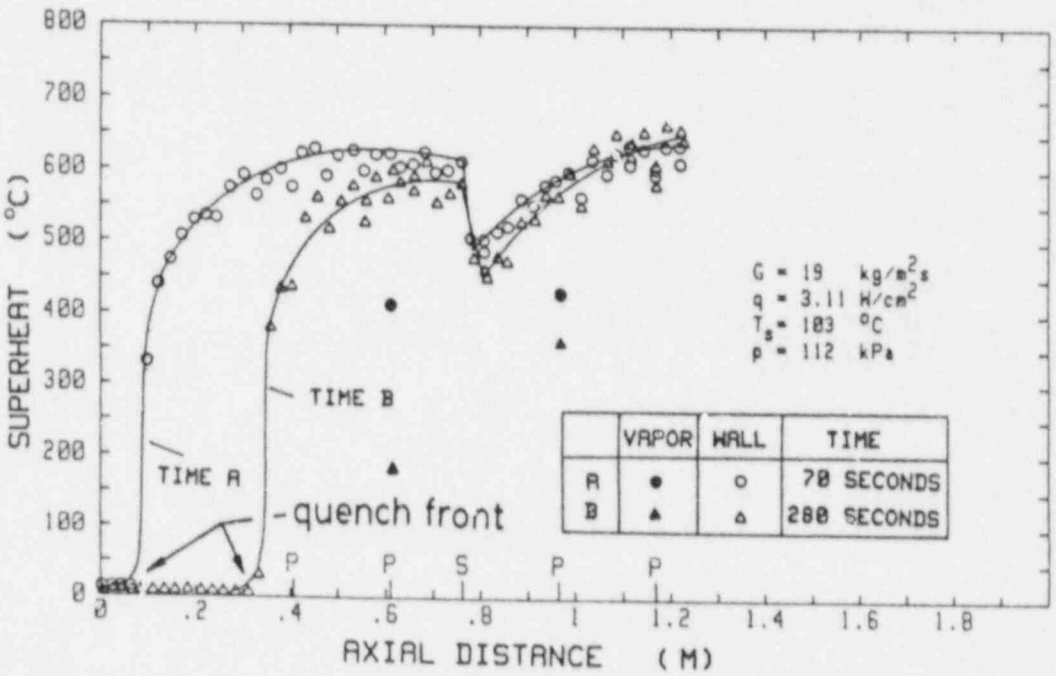

Figure 4 Wall and vapor superheats versus axial distance for an advancing-quench-front run

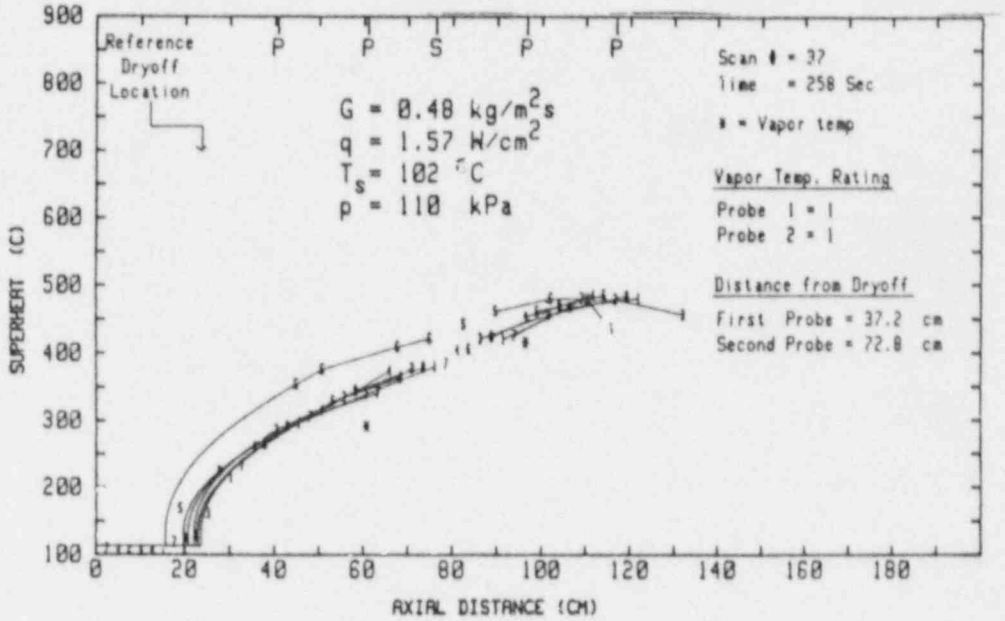

Figure 5 Wall and vapor superheats versus axial distance for a retreating-quench-front run

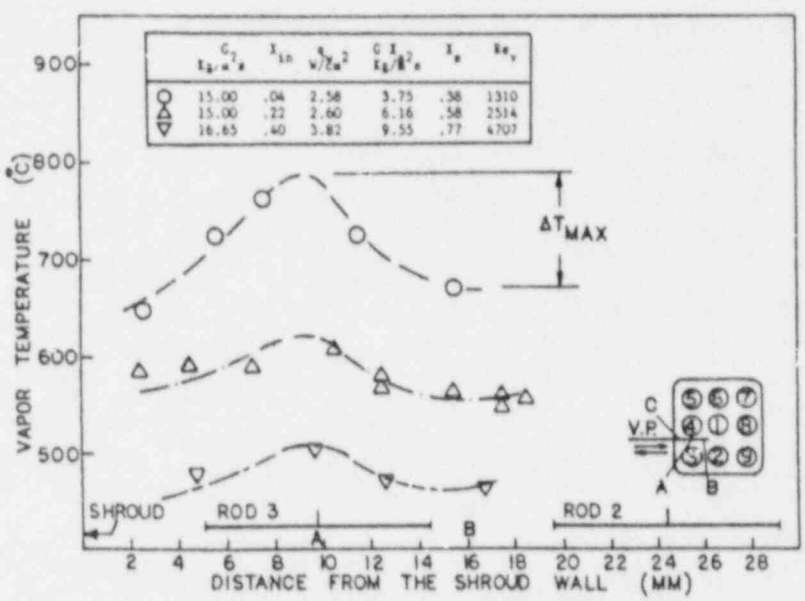

Figure 6 Typical lateral vapor temperature profiles

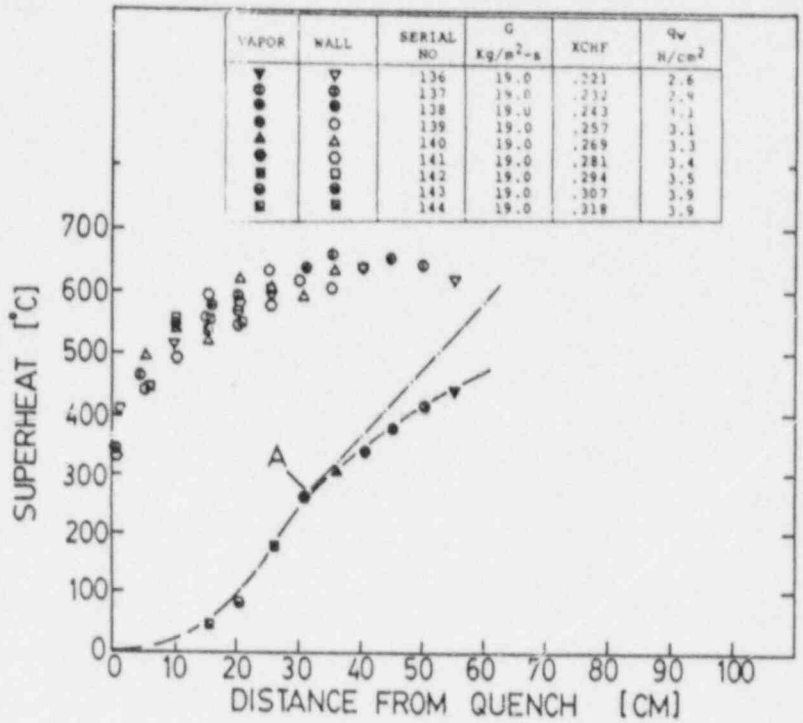

Figure 7 Vapor superheats and distributions of wall superheat between the CHF point and the first vapor probe for comparable runs

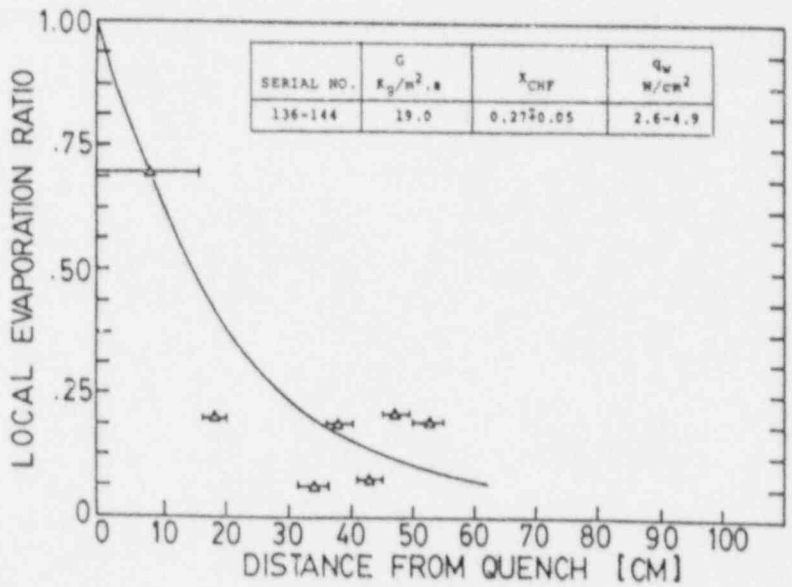

Figure 8 Evaporation ratio versus distance calculated from comparable runs

USE OF FULL-SCALE UPTF DATA TO EVALUATE SCALING OF DOWNCOMER (ECC BYPASS) AND HOT LEG TWO-PHASE FLOW PHENOMENA

P. S. Damerell
N. E. Ehrich
K. A. Wolfe

MPR Associates, Inc.

Abstract

The first UPTF Downcomer Separate Effects Test and the UPTF Hot Leg Separate Effects Test provide full-scale data useful for evaluating scaling effects. The downcomer test showed that subcooled ECC penetration down the downcomer at one steam flow was greater than would be predicted from several correlations using the largest available subscale data (1/5 scale by length). This is a favorable result from a licensing standpoint, i.e., actual full-scale performance is better than thought. The multidimensional flow in a large downcomer appears to be a key factor in the better delivery at large scale. The hot leg test showed that saturated water runback to the vessel in a hot leg under CCFL conditions is very close (±5%) to that predicted from the largest subscale tests (1/13 scale by area). This is an encouraging result from the standpoint of scaling. Further, this test shows there is a large margin between typical small break LOCA reflux condensation conditions and CCFL, and that the major scaled small break LOCA scaled integral facilities (PKL, Semiscale, ROSA-IV, FLECHT-SEASET) operated within the hot leg CCFL boundary, even though not necessarily at ideally scaled PWR conditions. Finally, evaluation of these data show that runback of de-entrained water in a hot leg during large break LOCA reflood is likely to occur in typical US PWRs, and the data successfully explain the observation of runback in SCTF (full-height oval hot leg) and the lack of runback in CCTF (scaled height hot leg).

Introduction

Research on the effectiveness of the emergency core cooling system (ECCS) in a pressurized water reactor (PWR) has involved a large number of separate effects and integral tests, essentially all at scaled geometry. The large number of tests have provided useful data for models and correlations of various pheonemena, and for assessment of integrated

computer codes for loss-of-coolant accident (LOCA) evaluation. One of the residual issues with regard to the accuracy of nuclear power plant calculations is the uncertainty introduced by calculating at full-scale while testing and assessing at subscale.

One of the major effects of scale is the impact of flow channel size on flow patterns and flow regimes in two-phase flow. Particularly during portions of a LOCA in which velocities are lower and gravitational forces play a much stronger role, it is known that the size of the flow section has a significant effect on the flow pattern, on the transport and retention of water in key areas, and thus on the overall course of a transient. The latter portion of a large break LOCA and a small break LOCA are examples of scenarios where gravitational (and hence size) effects are important.

Recently, separate effects tests in the Upper Plenum Test Facility (UPTF) have provided the first full-scale data on two key two-phase flow scenarios in PWR LOCA evaluation. These UPTF data provide a unique opportunity to evaluate the effect of scaling up to full-scale and to assess the scale-up capability of analytical and empirical models. Also, evaluation of these data provide improved insight and assurance about expected PWR behavior. Accordingly, it is appropriate to evaluate the data from these tests in this regard and the purpose of this paper is to describe the results of initial scaling evaluations from these tests.

The two UPTF tests discussed herein and the overall reactor safety scenarios to which they relate are as follows:

1. Downcomer Separate Effects Test -- This UPTF test investigated ECC delivery/bypass in the downcomer of a PWR. It is related to the reactor safety question of how soon and how quickly the vessel refills with ECC water at the end of the blowdown phase in a large break LOCA. The key phenomenon is the countercurrent flow limitation (CCFL) in the downcomer (i.e., downflowing water in the face of an upflowing steam/water mixture) which is strongly affected by condensation and by the multidimensionality of the downcomer. This scenario has long been considered to be scale-dependent. US licensing rules (10 CFR 50 Appendix K) artificially require no ECC delivery down the downcomer until blowdown is concluded. Scale test results from the NRC ECC Bypass Program (up to 1/5 scale by length) showed ECC does penetrate, and empirical correlations to quantify penetration were developed in that program. These correlations were generally thought to be conservative if applied to a full-scale PWR. Accordingly, this UPTF test (which was the first of four downcomer separate effects tests) helps to accurately quantify full-scale behavior.

2. Hot Leg Separate Effects Test -- This UPTF test investigated steam/water countercurrent flows in the hot leg of a PWR. It is related to the reactor safety question of how readily the drain-back of water occurs in the hot legs during a small break LOCA (e.g., during reflux condensation cooling) and also to how readily de-entrained water might drain back during the reflood portion of a large break LOCA. This issue has been previously addressed with separate effects tests up to 1/13-scale (area). Accordingly, the UPTF data provide the first full-scale glimpse at this phenomenon.

This report presents brief overviews of UPTF and of the two tests (all of which have been presented elsewhere) and discusses the scaling evaluation of downcomer and hot leg phenomena.

Summary Description of UPTF

The UPTF has been previously described (References 1 and 2) and is briefly discussed here with emphasis on the downcomer and hot legs.

UPTF simulates a 4-loop German PWR which is similar to a US 4-loop Westinghouse PWR (Figure 1). A full-size reactor vessel and piping (four hot legs and four cold legs) are included in UPTF. ECC can be injected in the hot and/or cold legs of all four loops, or in the downcomer. One of the four loops contains break valves which are piped to a large containment simulator tank. The four steam generators are simulated by four steam/water separators and the four reactor coolant pumps are simulated by four passive, adjustable resistances. The reactor vessel upper plenum internals and top-of-core are full-scale replicas. The core

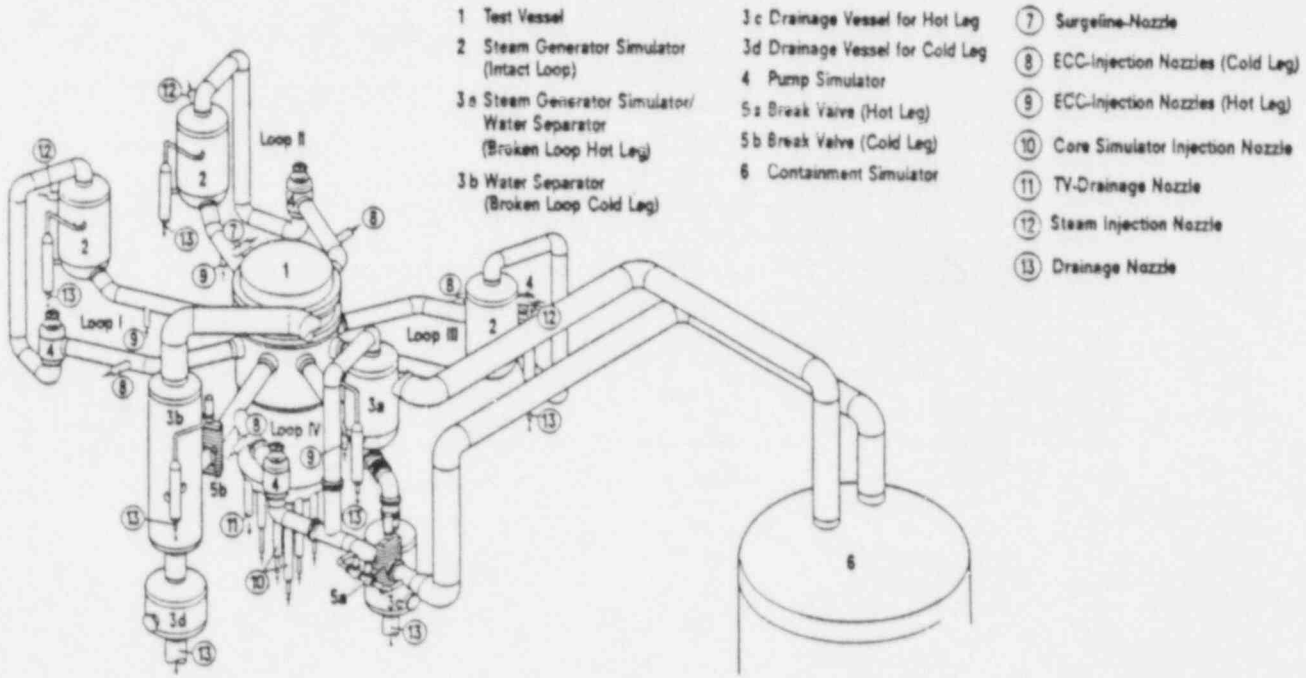

OVERALL VIEW OF UPTF (FROM REFERENCE 4)

FIGURE 1

is simulated by a steam/water injection system with 193 nozzles, one for each active fuel assembly which would be present in a PWR. UPTF was originally designed as an integral system test facility covering the end-of-blowdown, refill and reflood phases of a large break LOCA; as discussed in this paper it has also proven very useful as a full-scale separate effects facility covering both large and small break LOCA phenomena. UPTF can operate at up to 18 bar (260 psia) pressure and 220°C (428°F) temperature.

The UPTF vessel downcomer (Figure 2) has an inner diameter of 4.370 m (14.3 ft) and an outer diameter of 4.870 m (16.0 ft), giving a gap of 250 mm (9.8 in). The height of the downcomer from the lower edge of the downcomer skirt to the cold leg centerline is 6.64 m (21.8 ft). The four 750 mm (29.5 in) cold leg nozzles are spaced around the downcomer as shown in Figure 2. The lower plenum is 2.48 m (8.14 ft) high from vessel bottom dead-center to the lower edge of the downcomer skirt and has a volume of 24.9 m^3 (880 ft^3). This volume is slightly less than that of a Westinghouse PWR due to the presence of core simulator piping in the UPTF lower plenum. Table 1 compares UPTF downcomer and lower plenum configuration with that of typical Westinghouse and Combustion Engineering (CE) US PWRs*.

---

* Babcock & Wilcox (B&W) PWRs are not discussed herein because these UPTF tests are relevant mainly to Westinghouse and CE PWRs. Future UPTF tests will cover conditions relevant to B&W PWRs.

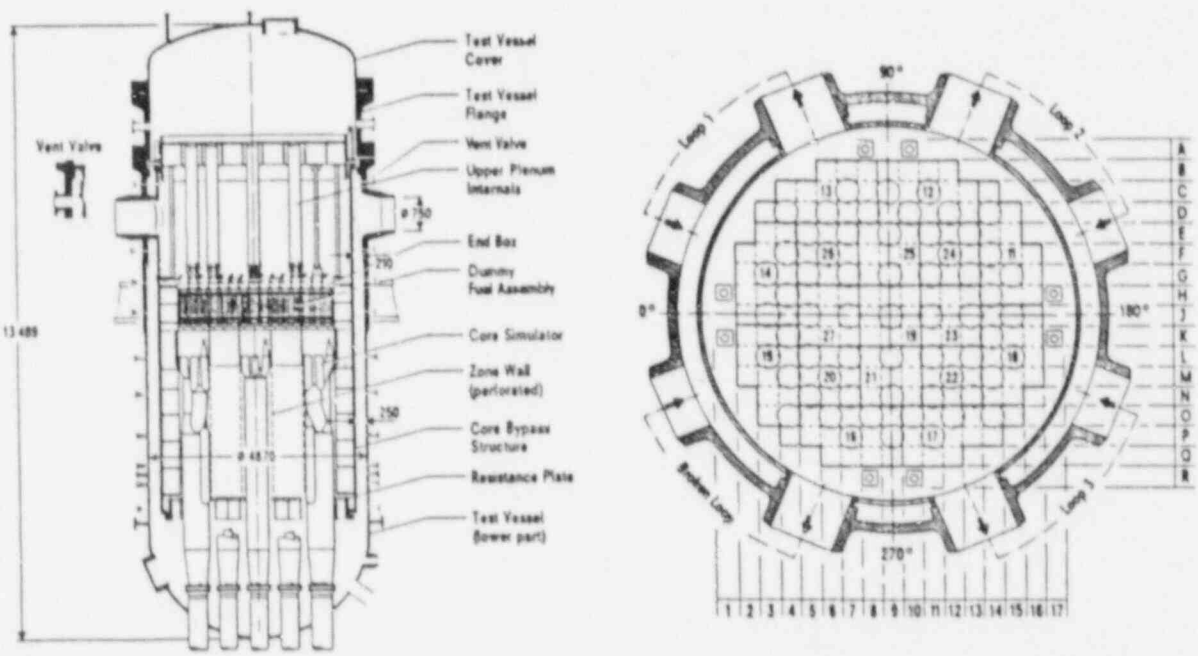

UPTF PRIMARY VESSEL (FROM REFERENCE 2)

FIGURE 2

TABLE 1

COMPARISON OF UPTF DOWNCOMER AND LOWER PLENUM CONFIGURATION WITH TYPICAL WESTINGHOUSE AND COMBUSTION ENGINEERING (CE) PWR'S

Parameter	UPTF Value	Westinghouse PWR Value	CE PWR Value
Downcomer OD m (ft)	4.87 (16.0)	4.39 (14.4)	4.63 (15.2)
Downcomer Gap mm (in)	250 (9.8)	260 (10.2)	254 (10.0)
Downcomer Height, Skirt to Cold Leg Center m (ft)	6.64 (21.8)	5.33 (17.5)	6.46 (21.2)
Lower Plenum Volume m^3 (ft^3)	24.9 (880)	29.7 (1049)	22.5 (794)

Each UPTF hot leg (Figure 3) is 750 mm (29.5 in) inner diameter and has a total lateral run from the vessel to the steam generator simulator of about 8 m (26 ft). A 50° riser section rises 0.91 m (3.0 ft) at the end of the hot leg attached to the steam generator simulator. In the horizontal section of hot leg, an internal ECC injection pipe ("Hutze") is located along the bottom edge of the pipe (Figure 4). There was no injection through the Hutze in the tests discussed in this report, i.e., it is a dead space in the hot leg. The Hutze blocks an area of 0.0444 m^2 (0.478 ft^2), about 10 percent of the total pipe area. A Hutze is present in German PWRs but not in US PWRs. Table 2 compares UPTF hot leg configuration with that of typical Westinghouse and CE US PWRs.

TABLE 2

COMPARISON OF UPTF HOT LEG CONFIGURATION WITH TYPICAL WESTINGHOUSE AND COMBUSTION ENGINEERING (CE) PWR'S

Parameter	UPTF Value	Westinghouse PWR Value	CE PWR Value
Diameter, m (in)	0.750 (29.5)	0.737 (29)	1.07 (42)
Hydraulic Diameter, m (in)	0.639 (25.2)	0.737 (29)	1.07 (42)
Flow Area, m^2 (ft^2)	0.397 (4.28)*	0.427 (4.59)	0.894 (9.62)

* 0.4418 m^2 within diameter minus 0.0444 m^2 blocked by "Hutze".

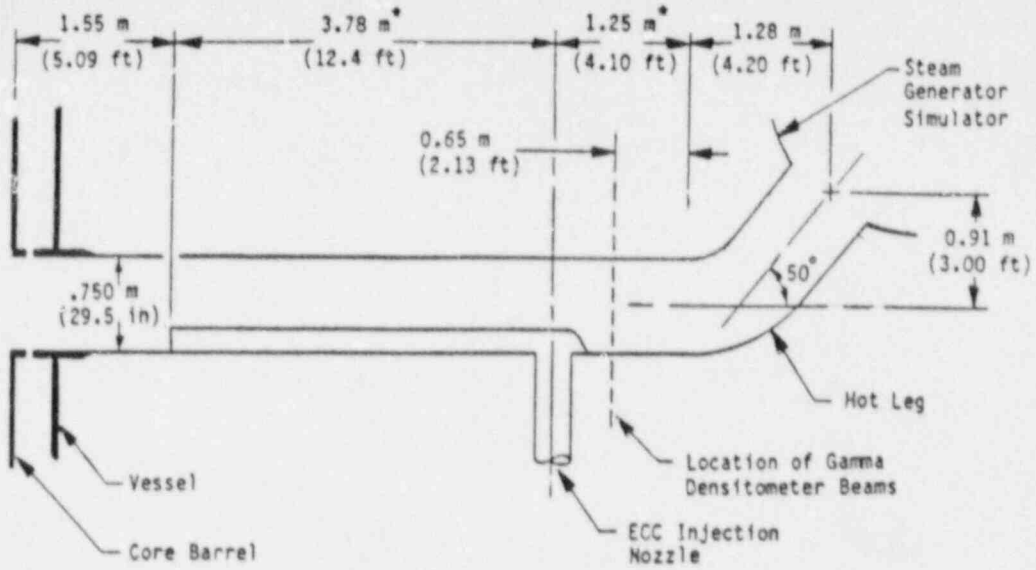

* Note: These dimensions are for the UPTF broken loop hot leg, which was the only hot leg used in the Hot Leg Separate Effects Test. In the intact loops, these two dimensions are slightly larger (3.86 m and 1.34 m).

UPTF HOT LEG CONFIGURATION

FIGURE 3

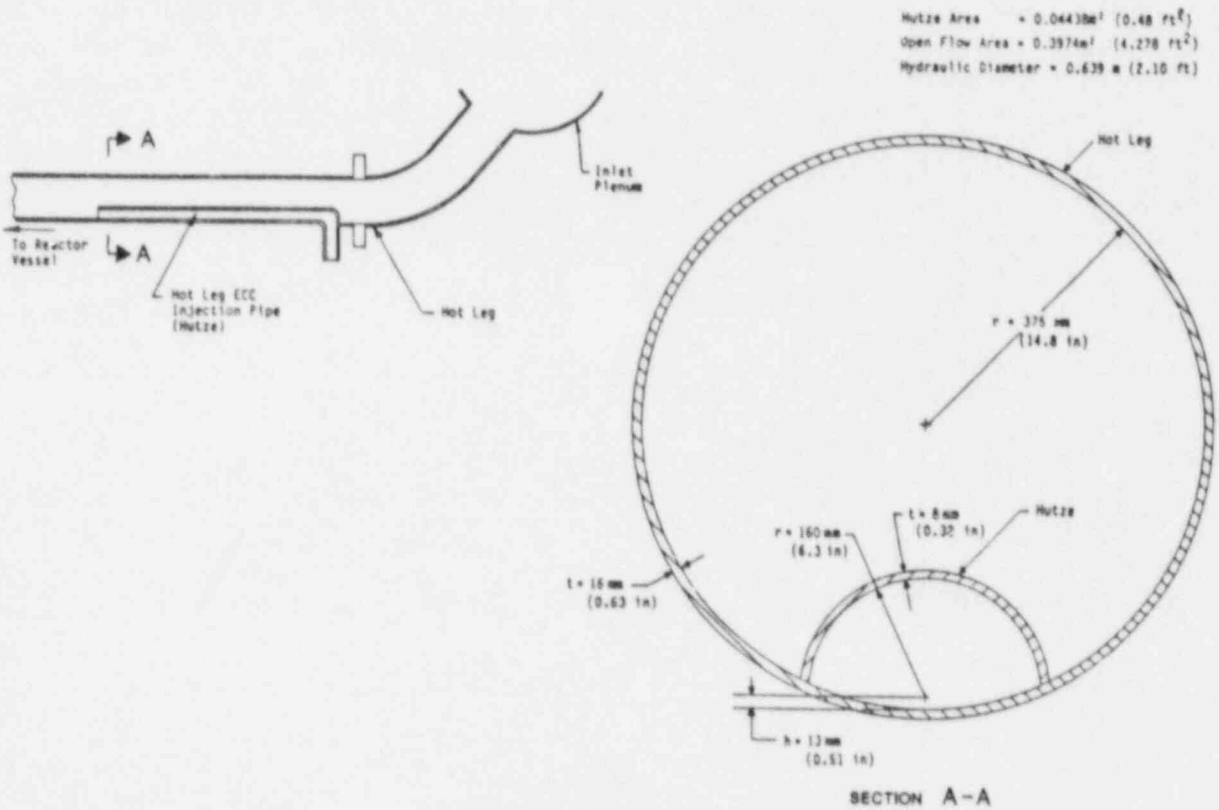

CONFIGURATION OF INTERNAL ECC INJECTION
PIPE (HUTZE) IN UPTF HOT LEG

FIGURE 4

Overview of UPTF Downcomer Separate Effects Test

The test conditions and results from the first UPTF Downcomer Separate Effects test are described elsewhere (Reference 3) and are briefly reviewed here. The test was run in two phases: transient and steady. In both phases the loops were blocked at the pump simulators, and the cold leg break valve was used to allow flow to discharge from the system. Also in both phases, 30°C (86°F) ECC was injected into the three intact cold legs at a rate of 500 kg/sec/loop (1100 lb/sec/loop). A small amount of nitrogen (about 0.15 kg/sec/loop or 0.33 lb/sec/loop) was injected with the ECC to simulate the nitrogen coming out of solution in a PWR accumulator.

In the transient phase, the facility was initialized at 18 bar (260 psia) with the cold leg break valve closed and the containment at 2.5 bar (37 psia). The lower plenum was approximately half full of saturated water. The test was initiated by starting ECC flow to the cold legs and opening the break valve to full-open at about the same time. This produced a depressurization transient with steam (from expansion and flashing) and entrained water escaping up the downcomer and out the break, and subcooled ECC water entering the top of the downcomer from the three intact legs (Figure 5). The transient lasted about 25 seconds.

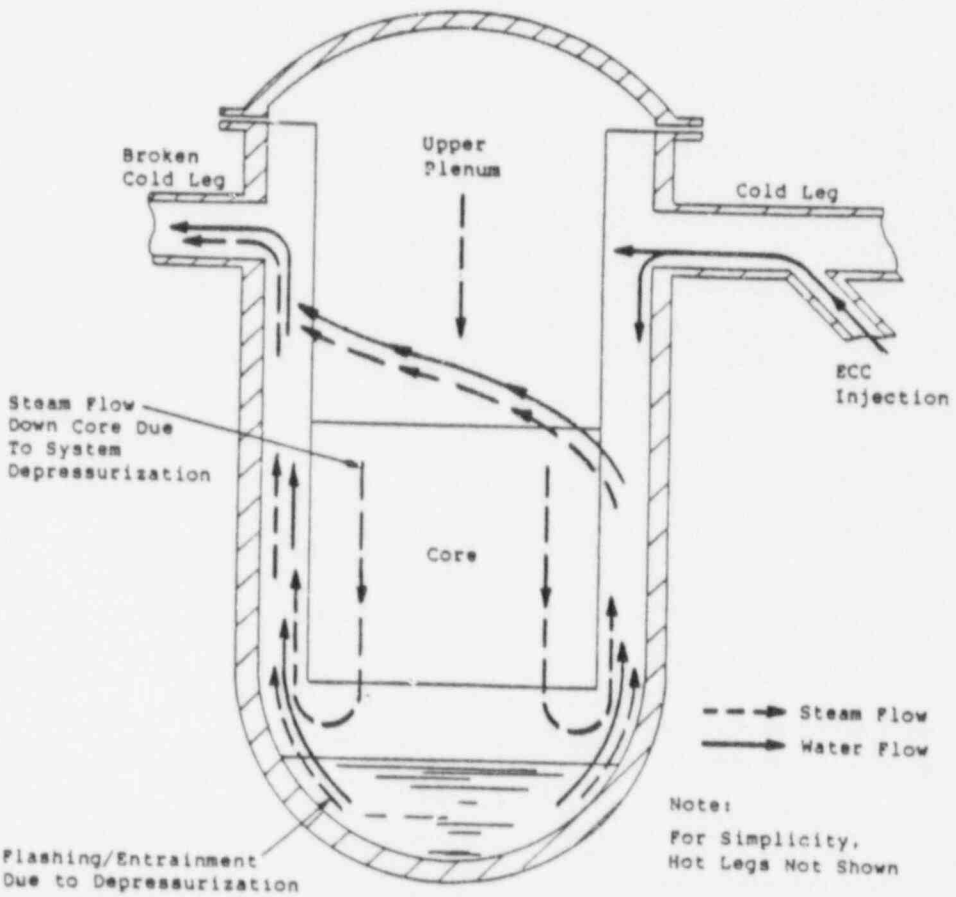

DIAGRAM OF FLOW CONDITIONS DURING TRANSIENT PHASE OF UPTF DOWNCOMER SEPARATE EFFECTS TEST

FIGURE 5

In the steady phase, the facility and containment were initialized at 2.5 bar (37 psia) with the cold leg break valve fully open. There was a small initial saturated water inventory in the lower plenum. To start the test, a preprogrammed steam flow of about 320 kg/sec (705 lbm/sec) was injected in the core which flowed to the lower plenum, up the downcomer and out the break. After a few seconds, ECC injection in the cold legs was initiated (Figure 6). The downcomer test was over in about 20 seconds at which time the lower plenum filled to nearly the bottom of the core.

As discussed in Reference 3, the transient phase showed a mixture of ECC bypass (out the break) and delivery down the downcomer. At the conclusion of the blowdown the lower plenum was nearly full, i.e., the inventory increased during the transient. Local downcomer measurements showed a strong asymmetry in the flow, with ECC delivery preferentially occuring on the side of the downcomer away from the break. The steady phase showed nearly complete penetration (about 80 percent) of ECC down the downcomer against the upward steam flow. Once again, local downcomer measurements showed strongly asymmetric flow with ECC penetration favoring the side of the downcomer away from the break.

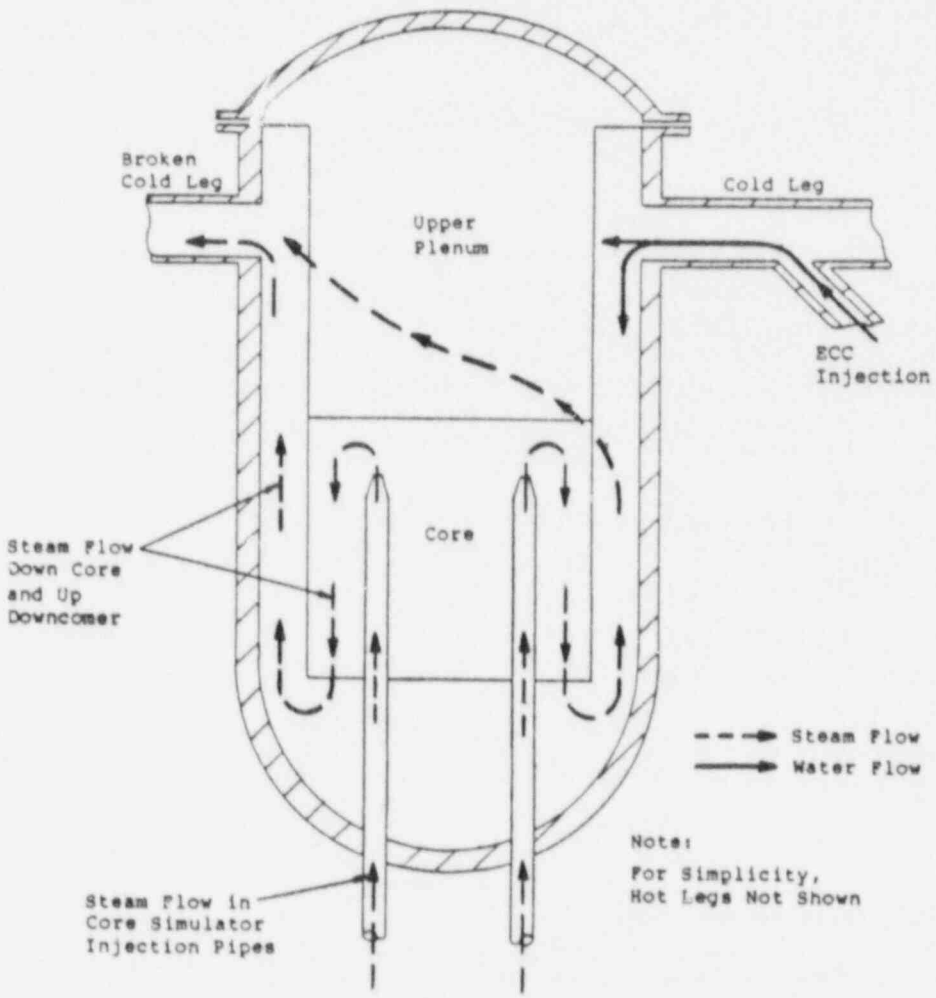

DIAGRAM OF FLOW CONDITIONS DURING PSEUDO-STEADY PHASE OF UPTF DOWNCOMER SEPARATE EFFECTS TEST

FIGURE 6

Evaluation of ECC Delivery/Bypass Scaling

To best quantify the results of the UPTF downcomer separate effects test for evaluation of scaling, mass balances were performed for each test phase. The results of the mass balance are shown in Figure 7 for the transient phase and in Figure 8 for the steady phase.

Figure 7 shows that when the transient started there was a period during which ECC was stored in the intact cold legs. This storage was inferred from thermocouple rakes in one cold leg which showed subcooling appearing at all locations over this time frame. There were no direct measurements of the amount of mass stored; the curve shown assumes the closed end pipes filled according to the injection rate. Vessel inventory decreased slightly while the legs were filling due to flashing.

When the cold legs filled and water was being delivered to the downcomer, vessel inventory rapidly increased, indicating ECC delivery. Small indications of bypass out the broken cold leg first appeared at this time as well. Over a period of about 15 seconds, delivery and bypass both occurred. The "spike" in delivery is apparently attributable to a brief emptying of the cold leg inventory -- a corresponding decrease does not appear in the cold leg curve because cold leg inventory was inferred rather than measured, as discussed above. At the end of the depressurization (about 25 seconds), the lower plenum was essentially full and less than half the injected water had been bypassed out the broken cold leg.

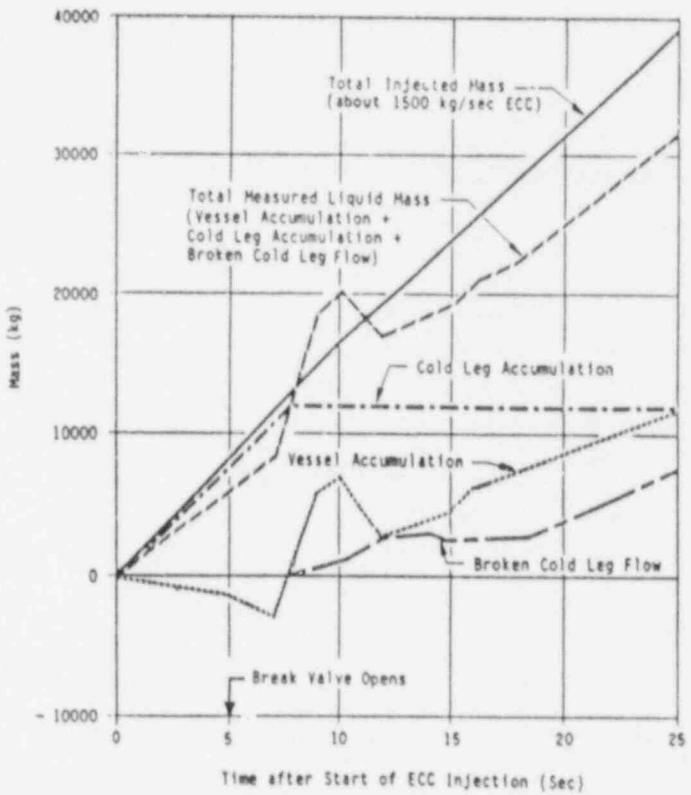

UPTF DOWNCOMER SEPARATE EFFECTS TEST
MASS BALANCE FOR TRANSIENT PHASE

FIGURE 7

Figure 8 shows that during the steady test there was also an initial period during which the cold legs filled, followed by substantial delivery to the vessel with limited bypass out the broken cold leg. At approximately 20 seconds after the start of ECC injection, the lower plenum was essentially full, and only 20 percent of the ECC had been bypassed out the broken cold leg.

The evaluation of scaling using the UPTF test results was found to be most useful using the steady phase test results; accordingly, they are discussed first below. Figure 9 shows a downcomer dimensionless flow plot using the parameters j_g^* and j_f^* where

$$j_g^* = M_g (\rho_g)^{1/2} / \rho_g A ((\rho_f - \rho_g) gW)^{1/2}$$

$$j_f^* = M_f (\rho_f)^{1/2} / \rho_f A ((\rho_f - \rho_g) gW)^{1/2}$$

where M = mass flow rate of gas or liquid

A = downcomer area (3.62 m^2 or 39 ft^2 for UPTF)

ρ = density of gas or liquid

g = gravity

W = downcomer circumference (14.5 m or 47.6 ft for UPTF)

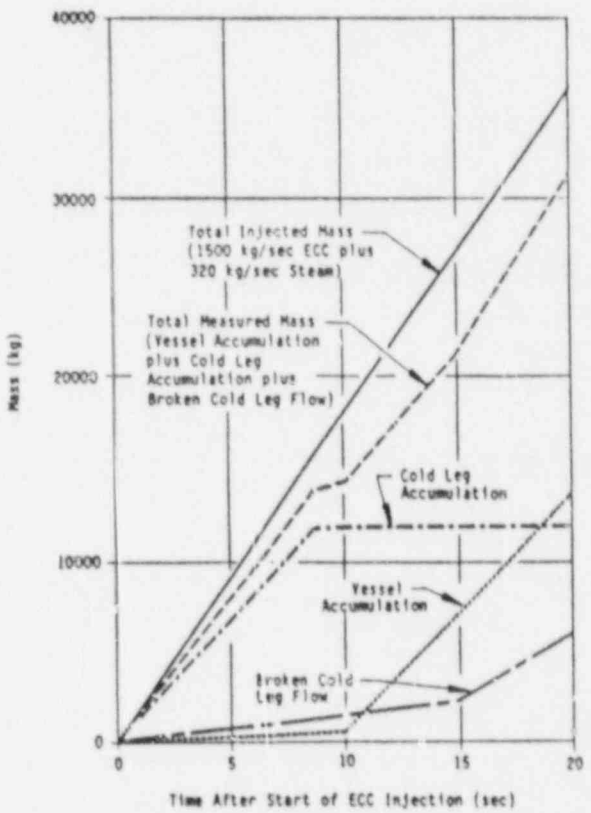

UPTF DOWNCOMER SEPARATE EFFECTS TEST
MASS BALANCE FOR STEADY PHASE

FIGURE 8

MPR ASSOCIATES
F-73-26-1309
9/21/87

Correlation 1: $(j_g^* - F\, j_{g,\,Tcond}^*)^{1/2} + M\, j_f^{*1/2} = C$

Correlation 2: $j_g^{*1/2} - F\, j_{g,\,Tcond}^{1/2} + M\, j_f^{*1/2} = C$

$$j_g^* = \frac{\dot{M}_g}{\rho_g A}\sqrt{\frac{\rho_g}{\Delta\rho g W}} \qquad j_f^* = \frac{\dot{M}_f}{\rho_f A}\sqrt{\frac{\rho_f}{\Delta\rho g W}} \qquad j_{g,\,Tcond}^* = j_{f,in}^* \frac{C_p\,(T_{sat} - T_\ell)}{h_{fg}}\sqrt{\frac{\rho_f}{\rho_g}}$$

Parameter	Momentum Flux Scaling		j* Scaling	
	Correlation 1	Correlation 2	Correlation 1	Correlation 2
F	0.281	0.209	0.281	0.209
M	0.896	0.822	0.896	0.822
C	0.250	0.230	0.369	0.344

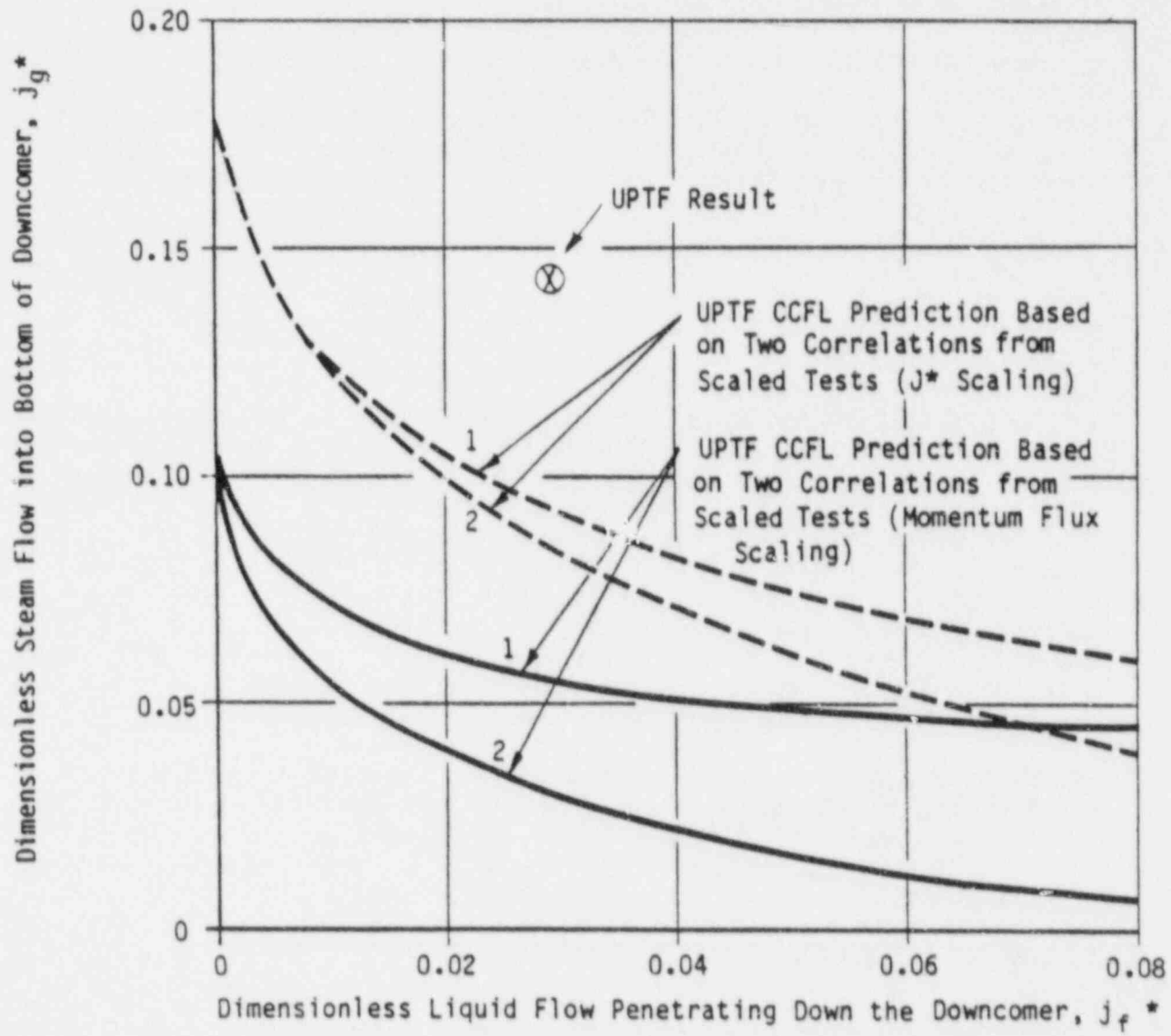

COMPARISON OF UPTF DOWNCOMER TEST RESULT WITH PREDICTIONS BASED ON 1/5 SCALE TESTS

FIGURE 9

From previous scaled tests in the NRC ECC Bypass Program (References 4 - 8), j* correlations were developed using data from 1/30, 1/15, 2/15 and 1/5 scale (by length). A convenient summary of the correlations is in Reference 4.

The curves shown on Figure 9 represent the CCFL boundary calculated for UPTF based on the largest scale data available from the previous scaled tests (1/5-scale). The four lines show four possible approaches for calculating the UPTF boundary: the two lower curves represent a "constant momentum flux" scaling approach with two different forms of correlating the 1/5-scale data; and the two upper curves represent a "constant j*" scaling approach with two different forms of correlating the 1/5-scale data. The two correlation forms (labeled 1 and 2 on Figure 9) each correlated some of the subscale data more favorably -- there is no clear basis for recommending one over the other. The lower curves are the NRC-recommended approach for downcomer CCFL based on the scaled tests in the NRC ECC Bypass Program. The upper curves represented a more "realistic" approach which was not recommended by the NRC because it could not be demonstrated to be conservative at full-scale based on the scaled tests. The main result of the UPTF downcomer separate effects test is that the full-scale test shows more ECC penetration than would be predicted by either the NRC-recommended or realistic approaches at full-scale. Hence, there appears to be a beneficial effect of large scale, which may be related to improved condensation, to large channel hydraulics, or to both. The observation of the strong asymmetry in the downcomer, i.e., preferential ECC downflow on the side away from the break (see Reference 3), indicates that the large channel effect is probably significant.

The main result of the transient phase of the downcomer separate effects test is that it showed that ECC penetrates the downcomer and refills the lower plenum even while the primary system is continuing to depressurize. Although scaled tests suggested this would occur, this full-scale test provides the best direct evidence. The UPTF test was reasonably PWR-typical with regard to lower plenum inventory and ECC subcooling. The ECC injection rate was somewhat low and the depressurization somewhat prolonged in comparison to a typical PWR LOCA, but these differences do not affect the validity of the overall result discussed above. The main use of the transient case is as a full-scale benchmark analysis case for computer codes.

It is not feasible to run in UPTF a direct counterpart transient test to previous scaled ECC bypass tests, due to some particular choices (non-PWR-typical) made in plenum volume and containment pressure in the previous scaled facilities. Accordingly, future downcomer separate effects tests will focus on steady-state downcomer CCFL conditions, in an attempt to further evaluate scaling by comparing UPTF results with CCFL curves derived from previous scaled tests.

Overview of the Hot Leg Separate Effects Test

The test conditions and results from the UPTF Hot Leg Separate Effects Test are described elsewhere (Reference 9) and are briefly reviewed here. The test was run using only the broken loop hot leg of the UPTF. The test was performed as several steady phases, each consisting of steam injection into the primary vessel which flowed out the broken loop hot leg, and saturated water injection in the steam generator simulator plenum which could either flow back down the hot leg toward the vessel or out of the system through the steam generator simulator (Figure 10). Six separate steady flows were obtained at 3 bar (44 psia) system pressure and 10 flows were obtained at 15 bar (218 psia) system pressure. In all cases water flow was established prior to steam flow. The intent of obtaining several flows at each pressure was to "map out" the CCFL boundary. Also, one of the flows at 15 bar simulated conditions in a Westinghouse 4-loop PWR during the reflux condensation mode, which can occur during an SBLOCA.

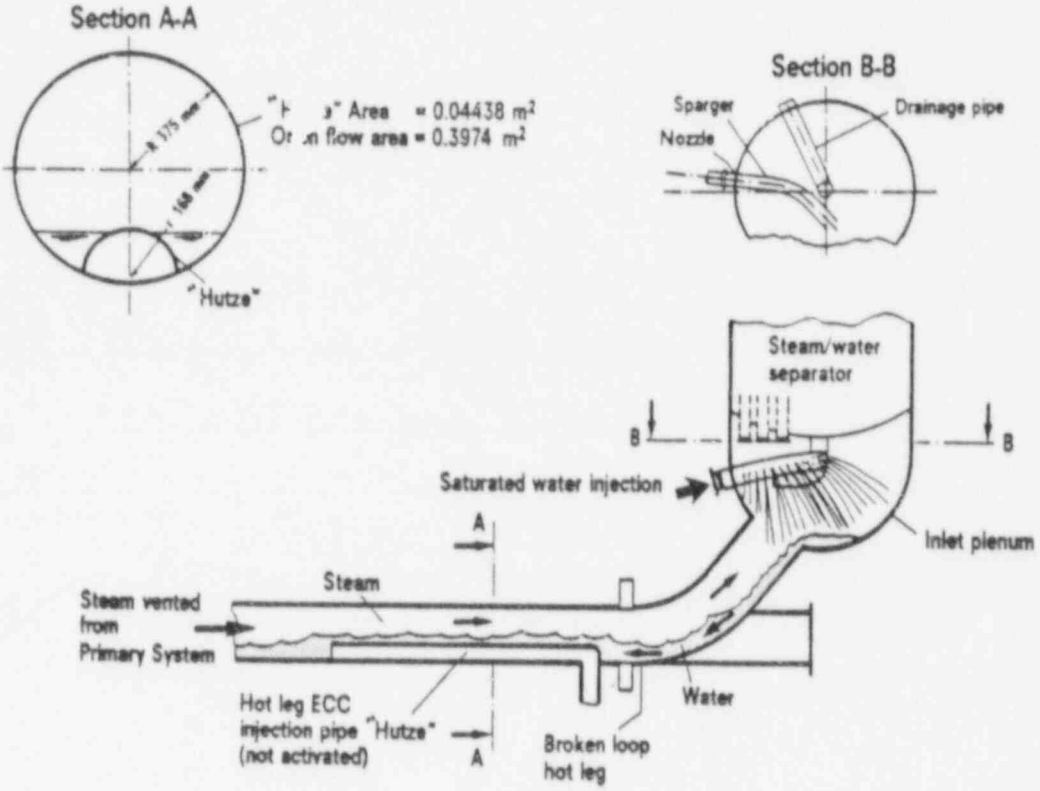

UPTF HOT LEG SEPARATE EFFECTS TEST
OVERALL FLOW CONDITIONS
(FROM REFERENCE 4)

FIGURE 10

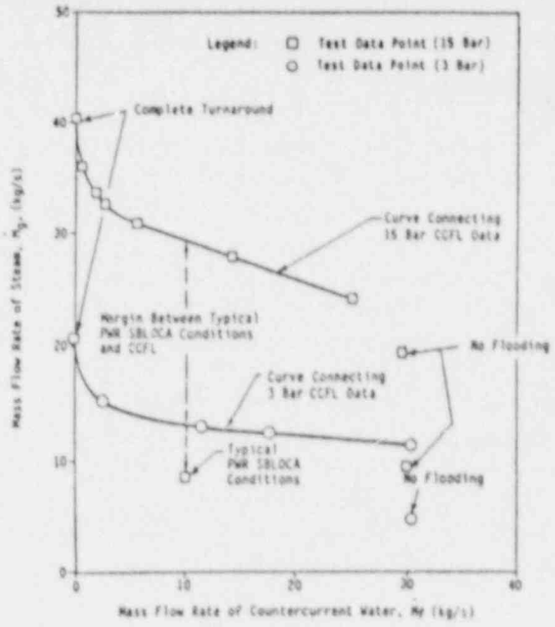

UPTF HOT LEG SEPARATE EFFECTS TEST
SUMMARY OF DATA

FIGURE 11

Figure 11 shows the measured flows at the two test pressures, and Figure 12 shows the data on a dimensionless j* plot, where

$$j_g^* = M_g (\rho_g)^{1/2} / \rho_g A (\rho_f - \rho_g) g D_h)^{1/2}$$

$$j_f^* = M_f (\rho_f)^{1/2} / \rho_f A (\rho_f - \rho_g) g D_h)^{1/2}$$

The variables are as defined previously and D_h is the hydraulic diameter, which is .639 m (2.10 ft) for the UPTF hot leg at the "Hutze".

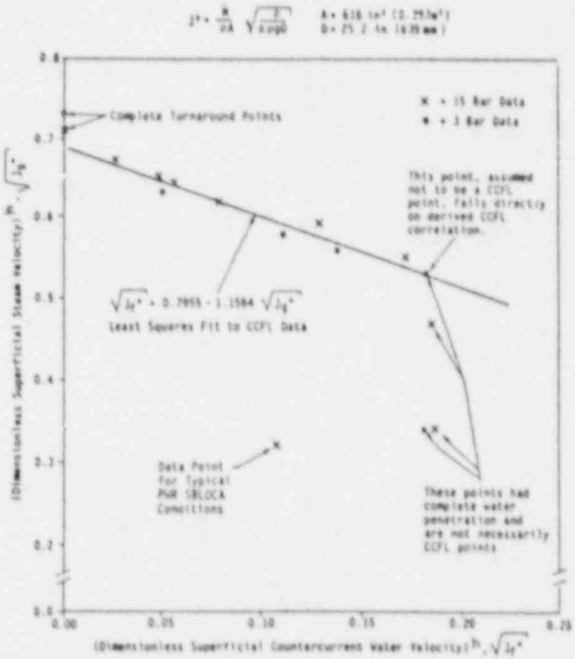

UPTF HOT LEG SEPARATE EFFECTS TEST
RESULTS SHOWN ON j* PLOT

FIGURE 12

On the j* plot, the 3 bar (44 psia) and 15 bar (218 psia) data correlate favorably. The line drawn through the data on Figure 12 is the "best-fit" experimental correlation to the UPTF data.

The results of this test provided direct demonstration that there is significant margin against hot leg CCFL during the reflux condensation phase of an SBLOCA. This is shown in Figure 12 by the fact that the "typical" point is substantially below the CCFL boundary. This point was chosen based on conservative assumptions such as relatively high power and one steam generator inactive, etc. Accordingly, this result provides direct and convincing evidence that substantial margin exists.

Figure 13 shows the measured hot leg level and void fraction for all of the tests, plotted against j_g^*, the dimensionless gas flow. These data are from a three-beam gamma densitometer located just on the vessel side of the hot leg riser bend, as shown on the figure. There is no "Hutze" obstructing the bottom of the hot leg in this short section of hot leg. The data clearly indicated a stratified regime and show significant water presence in this region of the hot leg. These data appear to show that CCFL is being controlled by the hot leg (i.e., CCFL is not occurring in the riser or steam generator simulator), since water is not absent from the hot leg when there is zero net penetration to the vessel.

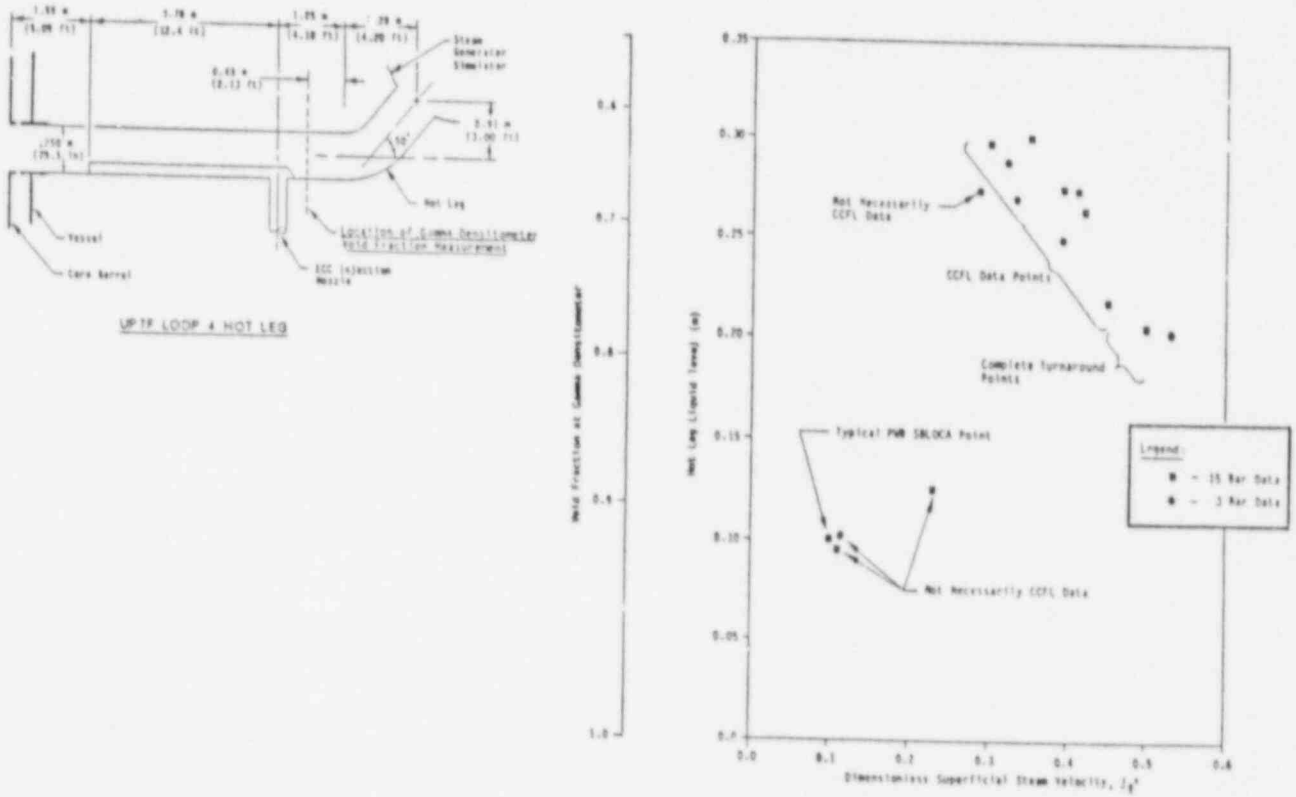

UPTF LOOP 4 HOT LEG

UPTF HOT LEG SEPARATE EFFECTS TEST
MEASURED HOT LEG LEVEL AND VOID FRACTION AS
A FUNCTION OF DIMENSIONLESS STEAM VELOCITY

FIGURE 13

Evaluation of Hot Leg CCFL Scaling

Several theoretical and scaled, separate effects studies of hot leg CCFL or generalized horizontal channel CCFL have been carried out, including:

- Richter, et al (Reference 10) -- 1/13 scale by area compared to Westinghouse PWR
- Gardner (Reference 11) -- Theoretical
- Wallis (Reference 12) -- .0254 m (1-inch) square channel (approx. 1/660 scale by area compared to Westinghouse PWR)
- Ohnuki (Reference 13) -- 1/840 scale to 1/93 scale by area compared to Westinghouse PWR
- Krolewski (Reference 14) -- 1/210 scale by area compared to Westinghouse PWR

Also, Transient Reactor Analysis Code (TRAC) predictions of the UPTF test were performed. Each of these previous studies provides a way to predict full-scale hot leg CCFL behavior. In all cases, j^* is the key parameter in scaling.

Figure 14 shows the UPTF data compared to the full-scale predictions based on five of the six studies mentioned above, on a j^* plot. In the

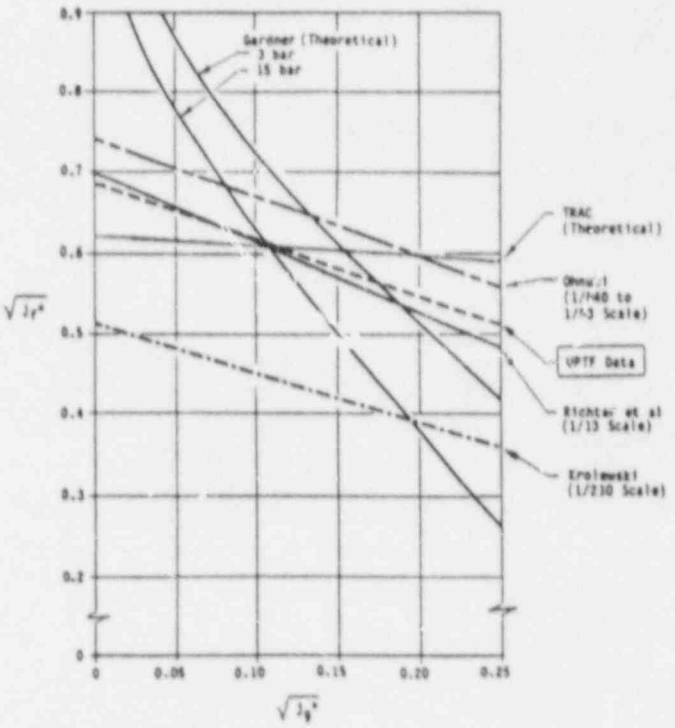

UPTF HOT LEG SEPARATE EFFECTS TEST
COMPARISON OF DATA TO THEORETICAL MODELS AND CORRELATIONS
FROM SMALL SCALE TESTS

FIGURE 14

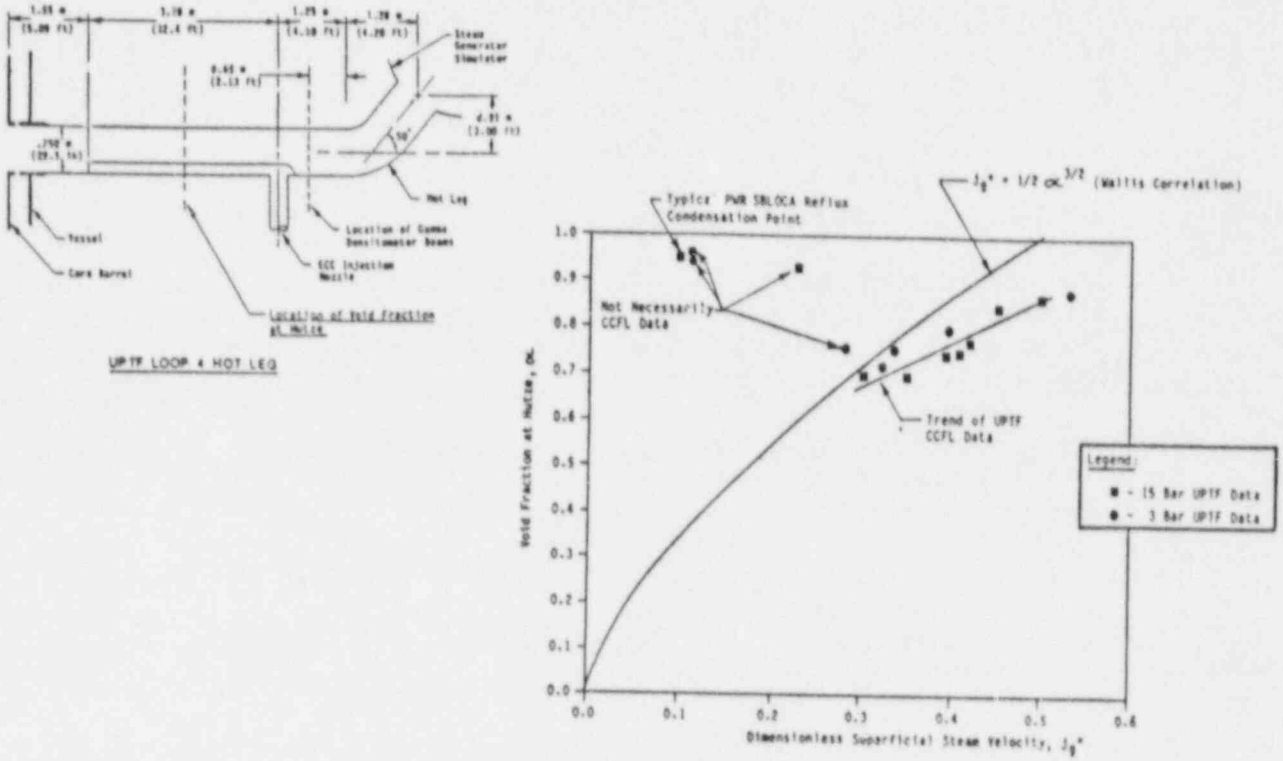

UPTF HOT LEG SEPARATE EFFECTS TEST
COMPARISON OF UPTF HOT LEG VOID FRACTIONS TO
WALLIS CORRELATION

FIGURE 15

case of the Wallis correlation, which is a j*/void fraction correlation, the comparison is on Figure 15. The results of the comparisons shown on Figures 14 and 15 are as follows:

- Very close agreement is obtained between the UPTF data and the Richter, et al correlation, which is the largest subscale data previously available. The agreement is ±5 percent. This agreement confirms that the j* correlation approach appears to be valid. The close comparison indicates that scaling up across an order of magnitude (based on pipe area) is successful and is therefore an encouraging result.

- Close agreement is obtained between the UPTF data and the Wallis correlation which is based on void fraction rather than liquid flow. This indicates that the basic approach of this correlation (once again, a j* correlation) appears correct for scaling, but that implementing this model to calculate liquid flows is dependent on knowing an accurate void fraction.

- Significant deviation is observed in the case of the Ohnuki and Krolewski correlations. This is considered to be due to the small scale of the underlying tests and the strong effect of the riser bend in the previcus tests. The Ohnuki tests, for example, showed that changes in the geometry of the riser section (e.g., length and angle) could significantly affect the flooding. It is not known if this sensitivity is PWR-typical; this makes it difficult to "scale-up" these small-scale results.

- The predictions using the Gardner theoretical model do not agree favorably with the UPTF data. The flooding mechanism presumed in the model (i.e., unstable stationary disturbance) does not appear to realistically reflect the true flow behavior in a PWR hot leg.

- The predictions from TRAC show a nearly "bi-stable" behavior with changing gas flow rather than the gradual CCFL boundary. The reasons are still being investigated.

Overall, the comparison with previous theoretical and scaled results is very favorable in that the results from simulated hot leg separate effects tests with one order of magnitude lower area were sufficient to accurately predict full-scale behavior.

In addition to these separate effects comparisons discussed above, several PWR integral tests of small and large break LOCAs have been conducted. In the small break case, these facilities demonstrated reflux condensation occurs without apparent hold-up due to hot leg CCFL. The major small break facilities investigating reflux condensation are:

- Semiscale (References 15 and 16) -- 1/1705 scale

- FLECHT-SEASET (Reference 17) -- 1/307 scale

- PKL (References 18 and 19) -- 1/134 scale

- ROSA-IV LSTF (Reference 20) -- 1/48 scale

The conditions achieved in reflux condensation tests in the four subscale SBLOCA facilities are plotted on a j* graph along with the correlation of UPTF results in Figure 16. Also shown in this figure is a band of "PWR conditions" which roughly envelope SBLOCA reflux condensation conditions. This figure shows that although the scaled facility conditions tend to be scattered about the graph, they are all well within the CCFL boundary, as are the PWR conditions. The PKL points, which deviate most from PWR conditions, tend to be a result of the hot leg area scaling used in these tests, which did not seek to preserve j* as in the other tests. The major conclusions, though, are that for all of the

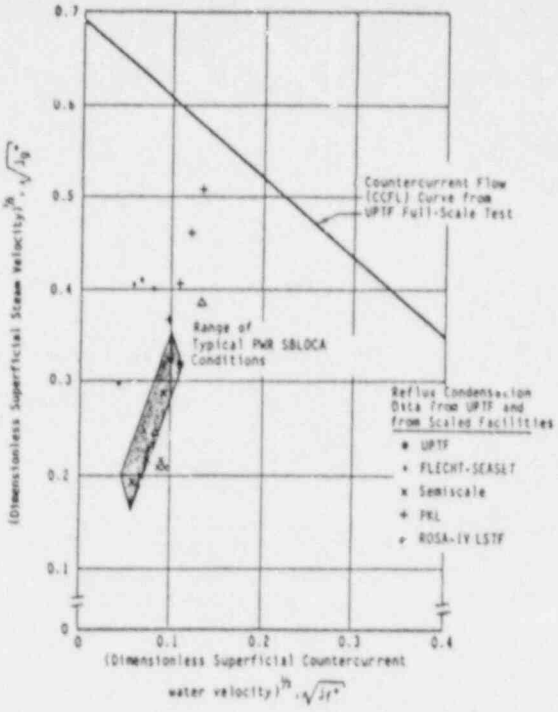

COMPARISON OF SMALL-SCALE FACILITY
REFLUX CONDENSATION EXPERIMENTAL CONDITIONS
TO UPTF TEST RESULTS

FIGURE 16

facilities, the observation of reflux condensation without hold-up from hot leg CCFL is consistent with the UPTF data, and that the scale facilities did not distort PWR hot leg behavior in a major phenomenological way.

The reflux condensation results are applied to US PWR's on Figure 17. This figure shows hot leg CCFL curves calculated for the most limiting Westinghouse and CE plants (3800 MW(t) in both cases) at 80 bar (1160 psia). Also shown are conservatively calculated SBLOCA reflux condensation conditions for both plants. The large margin is evident in both cases.

In the large break case, hot leg CCFL is only an important consideration during the reflood phase of the transient. The major, large scale reflood facilities which allow a detailed evaluation of hot leg effects are:

- Cylindrical Core Test Facility (CCTF) -- 1/21 scale
- Slab Core Test Facility (SCTF) -- 1/21 scale with full-height hot leg

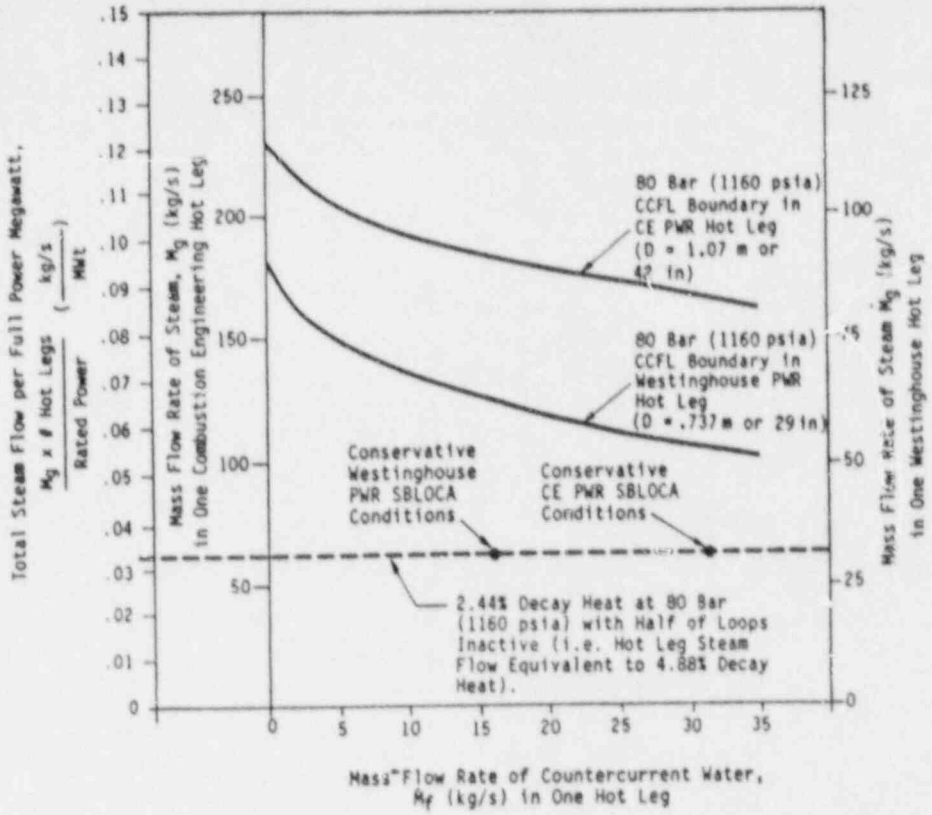

PREDICTED HOT LEG CCFL BEHAVIOR IN U.S. PWRs COMPARED WITH SBLOCA REFLUX CONDENSATION FLOW CONDITIONS

FIGURE 17

In CCTF, no evidence of counterflowing water during reflood was observed, i.e., any water reaching the hot legs tended to be swept through the primary coolant loops by the steam flow. In SCTF, though, hot leg water runback to the vessel by countercurrent flow was observed and directly measured. It is noted that due to the unique cross-section of the SCTF hot leg (oval) there may have been greater de-entrainment and more water available for runback in the hot leg.

The conditions achieved in the CCTF and SCTF large break reflood tests are indicated on a j* graph along with the correlation of UPTF results in Figure 18. The steam flow j_g^* associated with typical PWR reflood conditions is also shown on this graph. As indicated on the graph, counterflowing water during reflood would be expected in SCTF but not in CCTF, i.e., consistent with observations. The CCTF/SCTF difference is due to the height of the hot leg (full-scale in SCTF but not in CCTF). The figure shows the SCTF results, in this regard, are closer to PWR-typical. As Figure 18 shows, counterflowing water would be expected in both Westinghouse and CE PWR's.

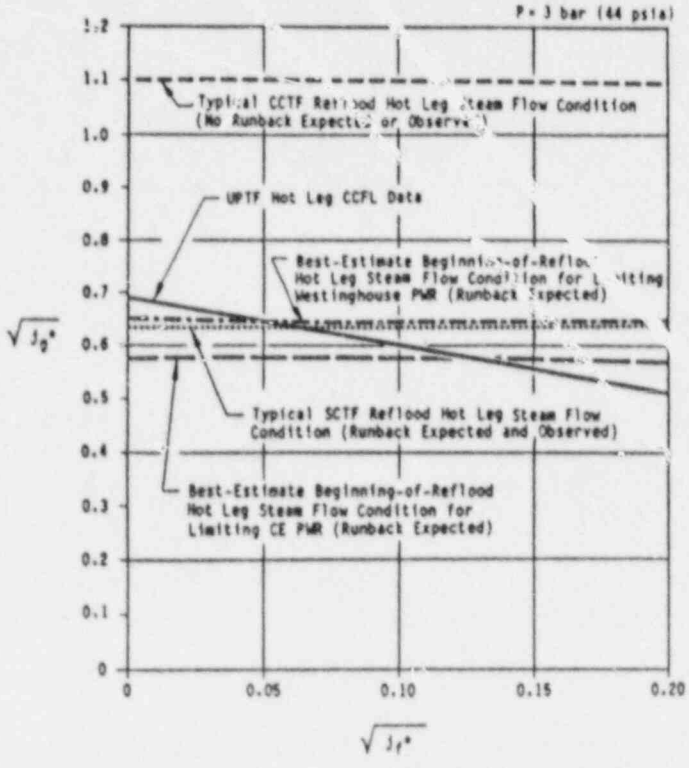

EVALUATION OF HOT LEG RUNBACK
DURING LARGE BREAK LOCA REFLOOD IN CCTF, SCTF
AND A PWR BASED ON UPTF HOT LEG TEST RESULTS

FIGURE 18

Conclusion

The UTPF Downcomer Separate Effects Test and Hot Leg Separate Effects Test have provided useful information for evaluation of scaling. For both tests the direct results convey favorable and encouraging conclusions, i.e., water penetrates to the reactor vessel through a downcomer or a hot leg as well as or better than would be predicted from subscale results. For the downcomer situation, the present test data do not provide a broad enough base to evaluate the accuracy of scaling CCFL up from previous tests. The UPTF results presently available though, do suggest that j^* scaling from previous scales provides at least a conservative approach, and that determination of a precise realistic approach will have to await upcoming UPTF test results. In the hot leg, the UPTF data show that predictions from the largest subscale tests (Richter, et al at 1/13 scale based on area) are quite accurate (±5 percent). The correlation which gives this successful scaling is based on the j^* parameter, indicating it appears to be the correct approach. Application of the UPTF hot leg results to US PWR's indicates that: (1) during SBLOCA reflux condensation, there is a significant margin between actual flows and the CCFL boundary, as expected; and (2) during large break LOCA reflood runback is likely for water de-entrained in the hot legs.

References

1. Hofmann, K., "Status of the German UPTF Program," presented at the 13th Water Reactor Safety Information Meeting, October 22 - 25, 1985.

2. Weiss, P., Sawitzki M. and Winkler, F.; "UPTF, a Full-Scale PWR Loss-of-Coolant Accident Program," Atomkern-Energie Kerntechnik, Vol.49, 1986.

3. Hertlein, R. and Weiss, P.; "UPTF Experiment: PWR ECC Downcomer Countercurrent Flow Under Steam and Two-Phase Upflow Condition," presented at the 15th Water Reactor Safety Information Meeting, October 26 - 29, 1987.

4. "1/5-Scale Countercurrent Flow Data Presentation and Discussion," NUREG/CR-2106, November, 1981.

5. "Analysis of ECC Bypass Data," NUREG-0573, July, 1979.

6. "Application of Battelle's Mechanistic Model to Lower Plenum Refill," NUREG/CR-2030, March, 1981.

7. "Analysis of Flashing Transient Effects During Refill," NUREG/CR-1765, March, 1981.

8. "Summary of Refill Effects Studies with Flashing and ECC Interactions," NUREG/CR-2058, November, 1981.

9. Weiss, P. A. and Hertlein, R. J.; "UPTF Test Results - First 3 Separate Effects Tests," presented at the 14th Water Reactor Safety Information Meeting, October 27 - 31, 1986.

10. Richter, Horst J.; Wallis, Graham B; Carter, Kelly H. and Murphy, Stephen L.; "Deentrainment and Countercurrent Air-water Flow in Model PWR Hot Leg," Thayer School of Engineering, September, 1978

11. Gardner, G. C., "Flooded Countercurrent Two-phase Flow in Horizontal Tubes and Channels," Int. J. Multiphase Flow, Vol. 9, No. 4, 1983, pp. 367 through 382.

12. Wallis, G. B., "Flooding in Stratified Gas-liquid Flow," Dartmouth College Report No. 27327-9, August, 1970.

13. Ohnuki, A., "Experimental Study of Countercurrent Two-phase Flow in Horizontal Tube Connected to Inclined Riser," Journal of Nuclear Science and Technology, March, 1986, pp. 219 through 232.

14. Krolewski, S. M., "Flooding Limits in a Simulated Nuclear reactor Hot Leg," Massachusetts Institute of Technology, Submission as Part of Requirement for a B.Sc. (1980).

15. "Experiment Data Report for Semiscale Mod-2A Natural Circulation Tests S-NC-2B, S-NC-3, and SNC-4B," NUREG/CR-2454, prepared by EG&G Idaho, December 1981.

16. "Experiment Data Report for Semiscale Mod-2A Natural Circulation Tests S-NC-5 and S-NC-6," NUREG/CR-2501, prepared by EG&G Idaho, January 1982.

17. "PWR FLECHT-SEASET Systems Effects, Natural Circulation and Reflux Condensation," NUREG/CR-3654, EPRI NP-3497, WCAP-10415, prepared by Westinghouse Electric Corporation, August 1984.

18. Mandl, R. M., and Weiss, P. A., "PKL Tests on Energy Transfer Mechanisms during Small-break LOCAs," Nuclear Safety, Vol. 23, No. 2, March-April 1982.

19. Thompson, S. L., Kmetyk, L. N., "RELAP5 Assessment: PKL Natural Circulation Tests," prepared by Sandia National Laboratories, NUREG/CR-3100, SAND82-2902, January 1983.

20. Tasaka, K., et. al., "The Results of 5% Small-Break LOCA Tests and Natural Circulation tests at the ROSA-IV LSTF," presented at the Fourteenth Water Reactor Safety Information Meeting, October 27-31, 1986, NUREG/CP-0082, Volume 4.

THE COOLDOWN ASPECTS OF THE TMI-2 ACCIDENT

by

T.G. Theofanous
Department of Chemical and Nuclear Engineering
University of California
Santa Barbara, CA 93106

The cooldown of the TMI-2 reactor vessel due to high pressure injection that occurred at 200 minutes into the accident is re-examined. Flow regimes and condensation heat transfer in the cold legs and downcomer are considered. The presence of noncondensibles (hydrogen) and a mechanism leading to its accumulation around the condensation interfaces lead to conclusions that are materially different from those of a previous study that did not consider these effects.

1. INTRODUCTION

Previous studies on the Thermal-Hydraulics of the TMI-2 accident have focused on phenomena leading to core uncovery, associated heatup and eventual degradation. With the recent interest in the Pressurized Thermal Shock (PTS) issue [1] it would be interesting to consider, also, the cooldown behavior, particularly that associated with the actuation of the High Pressure safety Injection (HPI) system [2].

In fact, the B&W Owner's Group (OG) task force on PTS considered this problem soon after the accident [3]. The phenomenology invoked in this assessment is schematically illustrated in Figure 1. The basic idea is that the vent valves allowed steam from the rest of the primary system to flow towards the HPI stream and to condense on it, thus heating it from the rather low initial temperature of $T_i \sim 10°C$ (50°F) to a considerably higher level before it reached the cold leg exit into the downcomer. Based on condensation rates alone this exit temperature, T_e, was estimated at 207°C (406° F). On the other hand, neglecting (conservatively) the quantity of steam already stored within the voided portions of the primary system, an estimate based on available decay heat (i.e., steaming rate) of 141°C (286°F) was given. The fracture mechanics analysis for the TMI-2 vessel was carried out at 141°C (286°F).

In fact within the assumptions of the OG analysis the limit based on condensation rates is conservative, while that based on the decay heat is irrelevant. Each part of this statement is clarified, in turn, below.

The condensation rates were based on the stratified regime (Figure 1), and did not consider the jetting/splashing phenomena (Figure 2) at the point of injection. We have estimated that just over the jet length a heatup to 115°C (249°F) can be expected [4].

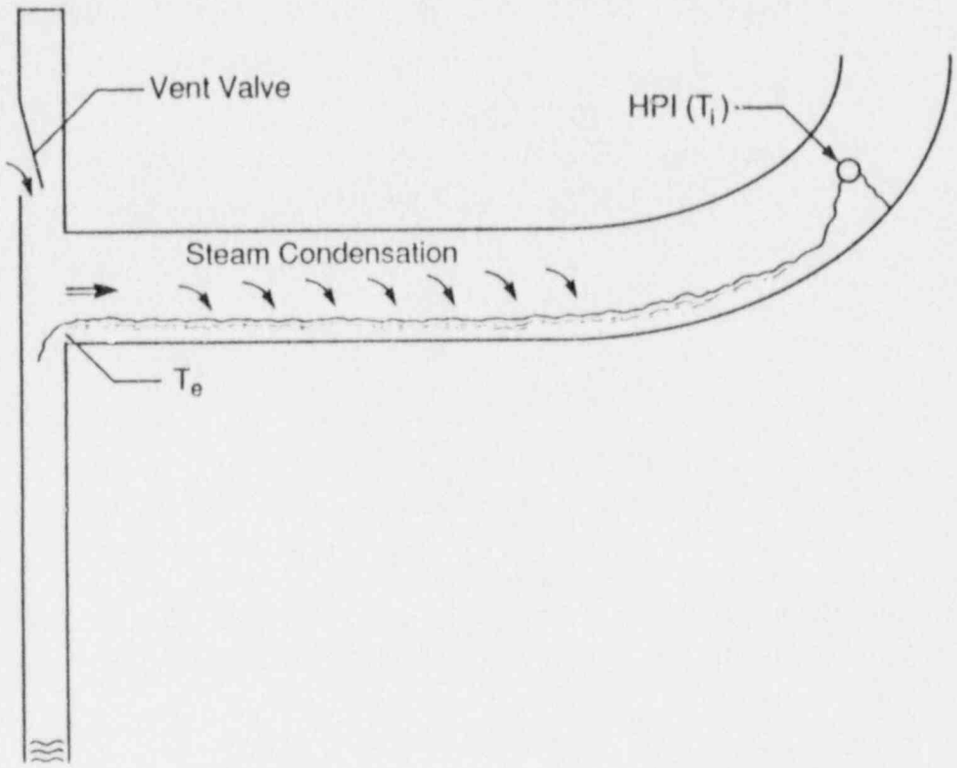

Fig. 1. *Owner's Group evaluation model*

Considering the increased interfacial area (wall films, entrainment of drops into the vapor space) generated as the jet splashes against the opposite wall, most of the heatup should have occurred prior to the flow's entering the stratified regime. It does not appear, therefore, that condensation rates could have imposed any limitations on achieving near saturation temperatures at the cold leg exit (i.e., 284°C or 543°F at 1,000 psia).

The decay heat is available to generate steam for only so long as the core remains covered. The fact that a voided cold leg condition is being addressed implies a core already uncovered or well on its way to being so. Thus a portion of the decay heat, equal (roughly) to the portion of the core that still is in contact with liquid coolant should be utilized. In fact, at TMI-2 at the time the HPI was turned on, essentially the whole core was uncovered and severely damaged. Any steaming estimates must, therefore, be based upon fuel quenching and water availability to this process, rather than decay power levels. On the other hand, the steam content of the various voided parts of the primary system could be significant but was neglected in the OG analysis. Even the liquid still present in the lower elevations could have been activated into steaming if the already existing steam inventory continued to deplete and system pressure decreased. This flashing process could further be aided by energy stored in structures still wetted.

There is another aspect to this problem, however, that dominates the heat-up process to such an extent that any uncertainities associated with the above mentioned complex

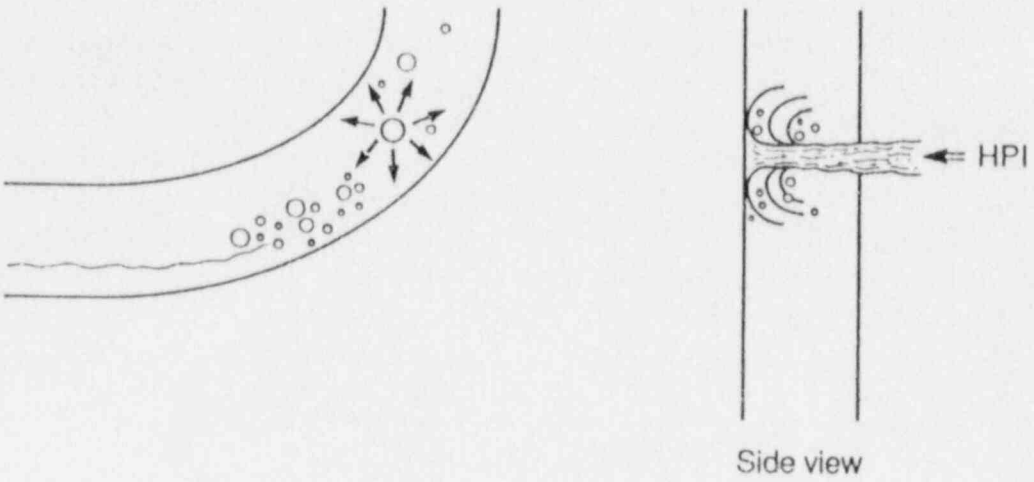

Fig. 2. *Flow regime at the injection point*

phenomena affecting steam availability are negligible by comparison. This aspect arises because of the presence of noncondensibles, that is, hydrogen and fission product gases, in mixture with the steam. Noncondensibles are notorious in degrading the performance of process condensers. They impose an additional, diffusional, resistance to the condensation process, and because they tend to collect in the immediate vicinity of the condensing interfaces, they can be detrimental even in trace quantities. Even more importantly, in the present case, we will demonstrate a mechanism which leads to continuing accumulation of noncondensibles within the cold leg and eventually to shutting off the condensation process. The rate of accumulation is proportional to the heatup of the HPI (i.e., proportional to the condensation rate), yielding a self-regulating behavior whereby condensation shut-off is rapidly obtained independently of the details used in the calculation.

The purpose of this paper is to reassess the TMI-2 vessel wall temperature transient, due to HPI, in the light of the phenomena introduced above. The assessment proceeds in two steps. In the first, a simple analytical model is used to quantify the condensation transient, as affected by the accumulation of noncondensibles, and hence to arrive at the temperature transient of the HPI water entering the downcomer. In the second step, these results are used in conjunction with methods adapted from past PTS thermal mixing analyses [5] to determine the vessel wall temperature.

2. THE CONDENSATION TRANSIENT

Formulation of the Analytical Model

Consider the cold leg/HPI-stream configuration of Figure 3. The cold leg is horizontal, its length is L, its volume is V, and it is initially filled with saturated steam at a pressure P_∞. The HPI water enters at time $t = 0$ with a mass flow rate $\dot{m}_{HPI}$ and a temperature T_i which is well below the saturation temperature corresponding to the system pressure, $T^*(P_\infty)$. It forms a stream along the bottom of the cold leg and exits at the other end with

a temperature T_e. The cold leg is assumed to comunicate with an *inexhaustible* supply of a steam/hydrogen mixture such that any mass loss from volume V, due to condensation, is perfectly compensated to maintain a constant pressure level P_∞, throughout the system. The mass flow rate of this supply is denoted by $\dot{m}_T$ and its hydrogen content is expressed by the mass fraction $w_{i\infty}$. The condensation rate over the whole of the liquid/vapor interface (area $S = \ell \times L$) is $\dot{m}_s^c$. The removal of hydrogen, from volume V, by absorption into the water stream may be assumed to be negligible (see Appendix A). As a consequence the hydrogen density, ρ_i, within the cold leg will increase with time, yielding corresponding transients on $\dot{m}_T$, $\dot{m}_s^c$ and T_e. Our task is to relate these quantities through the relevant flow and condensation processes.

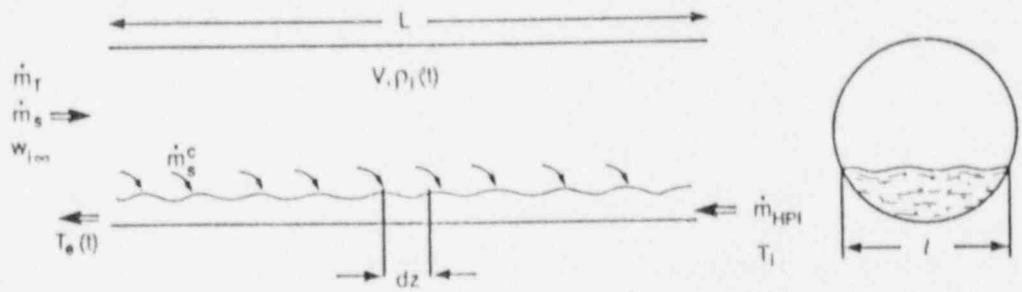

Fig. 3. *Transient condensation model*

As the liquid heats up from T_i to T_e, along its flow path, the potential for condensation decreases. Condensation rates are, therefore, functions of both time and position, z, and as a consequence we would expect the composition within the gaseous space to vary as well. We believe that the essence of the physical behavior may be captured without having to consider this detail. That is, the whole steam/hydrogen space within the cold leg is assumed to be well mixed, and ρ_i is taken to be a function of time only.

A hydrogen mass balance, over the gaseous volume of the cold leg (without loss of generality taken as V), yields:

$$\frac{d}{dt}(V\rho_i) = \dot{m}_T \; w_{i\infty} \tag{1}$$

It is convenient to work with mole fractions, x_i, instead of densities, and steam mass flow rates, $\dot{m}_s$, instead of total flow rates. The transformations can be carried out as follows: We use

$$\rho_i = M_i \; c_i = M_i \; c_T \; x_i \tag{2}$$

and

$$c_T = c_i + c_s = \frac{P_i}{RT} + \frac{P_s}{RT} = \frac{P_i + P_s}{RT} = \frac{P_\infty}{RT} = const. \tag{3}$$

to express the left hand side of Equation (1), as:

$$\frac{d}{d}(V\rho_i) = V \; M_i c_T \frac{dx_i}{dt} \tag{4}$$

For the right hand side of Equation (1) we use

$$w_i = \frac{\rho_i}{\rho_T}, \quad \rho_i = \frac{P_i M_i}{RT}, \quad \rho_s = \frac{P_s M_s}{RT}, \quad P_i + P_s = P_\infty \tag{5}$$

$$x_i = \frac{P_i}{P_\infty}, \quad x_s = \frac{P_s}{P_\infty}, \quad M_R \equiv \frac{M_s}{M_i}, \quad \text{and } x_s + x_i = 1 \tag{6}$$

to obtain

$$w_{i\infty} = \frac{x_{i\infty}}{M_R + (1 - M_R)x_{i\infty}} \tag{7}$$

Clearly,

$$\dot{m}_T = \dot{m}_i + \dot{m}_s \tag{8}$$

and since steam and hydrogen enter the cold leg with the same velocity:

$$\frac{\dot{m}_i}{\dot{m}_s} = \frac{\rho_i}{\rho_s} = \frac{c_i M_i}{c_s M_s} = \frac{x_{i\infty}}{x_s M_R} = \frac{x_{i\infty}}{(1 - x_{i\infty})M_R} \tag{9}$$

therefore,

$$\dot{m}_T = \dot{m}_s \left[1 + \frac{\dot{m}_i}{\dot{m}_s}\right] = \dot{m}_s \frac{M_R + (1 - M_R)x_{i\infty}}{(1 - x_{i\infty})M_R} \tag{10}$$

Thus, Equation (1) becomes:

$$\frac{dx_i}{dt} = \frac{\dot{m}_s}{V\ M_s c_T} \left\{ \frac{x_{i\infty}}{1 - x_{i\infty}} \right\} \tag{11}$$

The steam flow rate entering the cold leg, $\dot{m}_s$, together with the rate of mass depletion of steam within the cold leg, must constitute the rate of condensation, $\dot{m}_s^c$. That is:

$$\dot{m}_s - \frac{dx_s}{dt} c_T\ M_s\ V = \dot{m}_s^c \tag{12}$$

But $dx_i = -dx_s$ and together with Equation (11), Equation (12) becomes

$$\dot{m}_s = \dot{m}_s^c (1 - x_{i\infty}) \tag{13}$$

This result is used in Equation (11) to obtain the final form:

$$\frac{dx_i}{dt} = \frac{\dot{m}_s^c}{V\ M_s\ c_T} x_{i\infty} \tag{14}$$

Next we must relate $\dot{m}_s^c$ to the appropriate temperatures and heat transfer coefficients. The role of hydrogen in the condensation process is illlustrated in Figure 4. The steam is assumed to be in thermodynamic equilibrium with the liquid at the interface. If there

had been no diffusional resistance on the vapor side of the interface the concentration distribution would have been uniform, at x_i; the interface temperature would have been

$$T_i = T^*[(1 - x_i)P_\infty] \tag{15}$$

and the condensation rate would have been controlled by the turbulence in the liquid and a corresponding heat transfer coefficient, h_o, i.e.,

$$q^0 = h_o\{T^*[(1 - x_i)P_\infty] - T_{HPI}(z,t)\} \tag{16}$$

In fact, diffusional resistance of steam against the hydrogen molecules is extremely important. It gives rise to a buildup of noncondensibles at the interface and a corresponding decrease of the interfacial temperature, as shown in Figure 4. That is,

$$T_i = T^*[(1 - x_{ii})P_\infty] \tag{17}$$

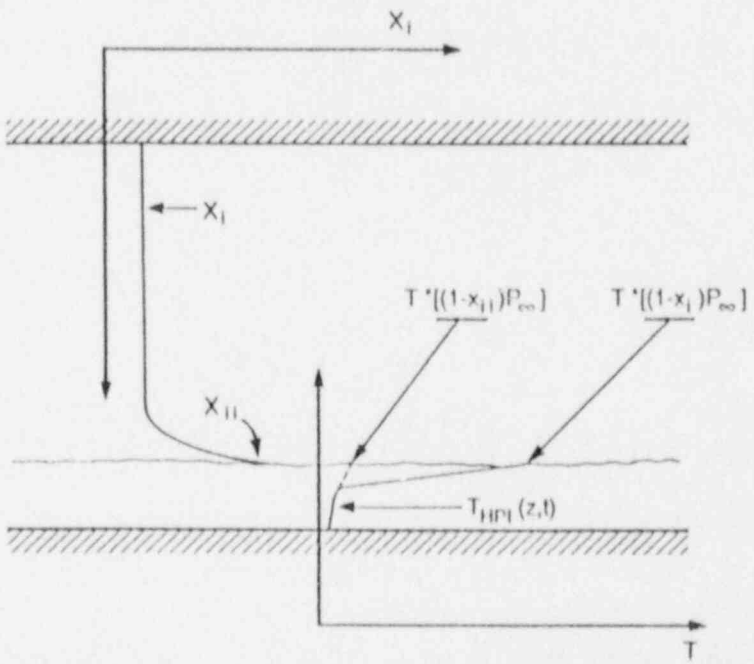

Fig. 4. *Mechanism of condensation in the presence of noncondensibles*

Now the heat flux is

$$q = h_o\{T^*[(1 - x_{ii})P_\infty] - T_{HPI}(z,t)\} \tag{18}$$

and a significant degradation in heat transfer is seen if x_{ii} is significantly higher than x_i. The quantities x_{ii} and T_i can be determined by coupling the mass diffusion process on the vapor side to the heat transfer process on the liquid side of the interface. For laminar flow this can be done exactly [6], but for turbulent flow the process remains poorly understood. The experimental data are scarce and highly non-prototypic (steam-air system, low pressures, film condensation on cooled walls). Our approach is to express

the degradation in heat transfer as an exponential function of the hydrogen mole fraction as follows:

$$\frac{q}{q^0} = \frac{T^*[(1-x_{ii})P_\infty] - T_{HPI}(z,t)}{T^*[(1-x_i)P_\infty] - T_{HPI}(z,t)} = \exp\left\{-\frac{x_i}{x_{1/2}}\right\} \tag{19}$$

And in combination with Equation (18) we have

$$q = h_o \exp\left\{-\frac{x_i}{x_{1/2}}\right\} \{T^*[(1-x_i)P] - T_{HPI}(z,t)\} \tag{20}$$

The basis for Equation (19) is given in Appendix B.

The heatup of the HPI stream can be obtained from an energy balance over a differential element, dz, as shown in Figure 3. That is,

$$\dot{m}_{HPI}\, c_p \frac{dT_{HPI}}{dz} = \ell h_o \exp\left\{-\frac{x_i}{x_{1/2}}\right\} \{T^*[(1-x_i)P_\infty] - T_{HPI}\} \tag{21}$$

which upon integration yields,

$$T_e - T_i = \{T^*[(1-x_i)P_\infty] - T_i\} \left\{1 - \exp\left[-\frac{h_o S \exp\left\{-\frac{x_i}{x_{1/2}}\right\}}{\dot{m}_{HPI} c_p}\right]\right\} \tag{22}$$

This heatup may also be related to the latent heat of condensation by:

$$\dot{m}_{HPI} c_p (T_e - T_i) = h_{fg} \dot{m}_s^c \tag{23}$$

Thus the condensation rate may be written as,

$$\dot{m}_s^c = \frac{\dot{m}_{HPI} c_p}{h_{fg}} \{T^*[(1-x_i)P_\infty] - T_i\} \left\{1 - \exp\left[-\frac{h_o S \exp\left\{-\frac{x_i}{x_{1/2}}\right\}}{\dot{m}_{HPI} c_p}\right]\right\} \tag{24}$$

and the exit temperature as,

$$T_e = T_i + \frac{h_{fg} \dot{m}_s^c}{c_p \dot{m}_{HPI}} \tag{25}$$

The solution, $x_i(t)$, is obtained by integrating Equation (14) with $x_i(o) = 0$, in conjunction with Equation (24). This ignores some initial accumulation due to condensation already occurring on the makeup flow but does not affect the conclusions of the study. The quantities $\dot{m}_s^c(t)$ and $T_e(t)$ can then be readily calculated from the last two equations.

The Choice of Parameters for the TMI-2 Case

The relevant geometric dimensions were taken from the design information from Oconee, which is a B&W reactor similar to TMI-2. From the cold leg diameter of $0.7m$ and its length of $8.15m$, between the reactor vessel and the pump, a volume of $3.1m^3$ is

obtained. The volume of the upper $1m$ of the downcomer corresponding to each one of the four cold legs is $\sim 1m^3$. Considering that a good fraction of the inclined portion of the cold leg volume may not participate in the mixing process a value of $V = 3.5m^3$ was chosen for the calculations. The sensivity to this parameter was examined by also considering a value of $V = 2.5m^3$.

The high pressure injection in TMI is believed to have occurred with $\sim 15kg/s$ [7]. We bracket this value by choosing $\dot{m}_{HPI} = 10kg/s$ for the base case and $\dot{m}_{HPI} = 20kg/s$ for a sensitivity case. The inlet water temperature is taken at $T_i = 10°C(50°F)$. Assuming critical open channel flow at the cold leg exit, the water stream is estimated to attain a depth of $8cm$, a width $\ell \sim 20cm$, and a velocity of $u \sim 1m/s$ (for the 15 kg/s injection rate). The minimum value of the vapor/liquid interfacial area is thus estimated at $S \sim 1m^2$.

As seen in Equation (24) the interfacial area, S, appears only in product with the heat transfer coefficient, h_o. The effect of higher areas, likely to exist due to splashing and entrainment as shown in Figure 2, was covered by considering a generous range in the sensitivity analysis for h_o. As discussed in Appendix C a realistic estimate for this quantity is $h_o \sim$ 1,300 BTU/hr ft^2°F. Accounting for a moderate increase in interfacial area due to splashing and associated enhancement of h_o (jet condensation, etc.) the low end of the range for h_o considered in the calculation was set at 5,000 BTU/hr ft^2°F (i.e., nearly a factor of four higher). The base case value was taken nearly as one order of magnitude higher at $h_o \sim 10,000$ BTU/hr ft^2°F. The upper end, at $h_o \sim$50,000 BTU/hr ft^2°F represents an enhancement by a factor of x37 and is judged to adequately cover the most extreme behavior.

For the base case the liquid heat capacity was taken at $c_p \sim$1.3 BTU/lb°F. Because of the wide temperature range present the sensitivity to this parameter was examined by considering also the case of $c_p \sim$1 BTU/lb°F. The saturation temperatures and latent heat of condensation (h_{fg}) were obtained from the steam tables. The system pressure, P_∞, was taken as 1,000 psia. Sensitivity to this parameter was examined by considering the case of $P_\infty \sim 2,000$ psia. The molecular weight of steam is $M_s = 18$ g/g-mole.

As discussed in Appendix B for $x_{1/2}$ a value of 0.05 is deemed appropriate. To generously cover for uncertainities and not to overestimate the degradation in heat transfer, a base case value of $x_{1/2} \sim 0.1$ was selected. The upper end of the range was set at $x_{1/2} \sim 0.2$.

Finally, the choice of $x_{i\infty}$, must be made on the basis of core steaming and oxidation rates at the time of high pressure injection (around 200 minutes after the start of the accident). It is now known that by this time the TMI-2 core had already been severely oxidized and partially molten. There seems to be some indication that the molten material relocated in the lower portion of the core where it froze forming substanital blockages [8]. Eventually some 20 to 30 tons of core material made it into the lower plenum where it was found in a solidified debris form. At 174 minutes the "B" loop primary coolant pumps were actuated for a short period of time. As a result some loop seal water was displaced into the reactor vessel yielding a vigorous steaming process as verified by the rapid pressurization to 2,000 psia seen around that time. The details of this process will remain

highly uncertain; however, there should be little doubt that the renewed steam availability reactivated the oxidation processes (hydrogen production). On the other hand, at 142 minutes the pressurizer block valves were closed, they were opened briefly (~5 minutes) at 192 minutes and remained closed until 220 minutes. All indications are that the pressurizer remained more than 3/4 full throughout the accident; it is unlikely, therefore, that any venting of steam (and non-condensible gases) occurred during this brief opening of the pressurizer block valve. Thus at the time of HPI operation (200 to 217 minutes) the major fraction of hydrogen already produced and of the fission products released from the disrupted fuel rods, were still present within the primary system volume. The total amounts of gases released in the accident are estimated at [9]: Kr ~ 3.5 kg, $Xe \sim 40.6kg$ and $H_2 \sim 510kg$.* The total primary system volume is ~10,000 ft^3. Assuming that loop seals ($\sim 2,700ft^3$) and lower plenum ($\sim 685ft^3$) were still full with water the total steam mass, saturated at 2,000 psia, is estimated at 18,976 kg. A low bound of noncondensibles mass fraction may be obtained by assuming a homogenous distribution throughout the steam volume. For Kr, Xe, and H_2 we obtain 0.018%, 0.214%, and 2.68% respectively. Clearly, only the hydrogen is significant. Its concentration may be obtained on a mole fraction basis as $x_{i\infty} \sim 29.7\%$. On this basis we chose the values $x_{i\infty} = 0.05, 0.1, 0.2, 0.3$ and 0.4 to parametrically cover a broad range around the above estimated value. For the base case we chose $x_{i\infty} = 0.2$.

Numerical Results and Discussion

The solution for the base case is shown in Figures 5 to 7. A rapid buildup of hydrogen in the cold leg and a concomitant decrease in steam condensation rate are predicted. As a result, the HPI water heat up is drastically reduced with cold leg exit temperatures approaching inlet values within a matter of 1 to 2 minutes. All parameter sensitivity results lead to the same conclusion. The $x_{i\infty}$ and $x_{1/2}$ parametrics are summarized in Figures 8 and 9. The results of the $x_{i\infty} = 0.4$ parametric calculation are given in Appendix B. All other parametric results are presented elsewhere [11] and lead to the same conclusion.

3. THE DOWNCOMER COOLDOWN TRANSIENT

From the above analysis we expect that cold HPI water, nearly at the injection temperature of ~50 F, entered the TMI-2 downcomer for the major portion of the injection period. Our task here is to determine the resulting vessel wall cooldown.

We will attempt to look at the problem from two complementary perspectives. First, we examine whether any portion of the HPI stream entering the downcomer could have come in contact directly with the reactor vessel wall. Second, we consider the downcomer fluid temperature transient as it fills with the HPI.

Direct Contact Mechanisms

The first critical consideration is whether the HPI cold stream comes directly into contact with the vessel wall. An experimental run at the UCSB 1/2-Scale integral thermal

* A quantity of only 25.6 kg of hydrogen would be sufficient to obtain a mole fraction of 0.4 in all four cold legs.

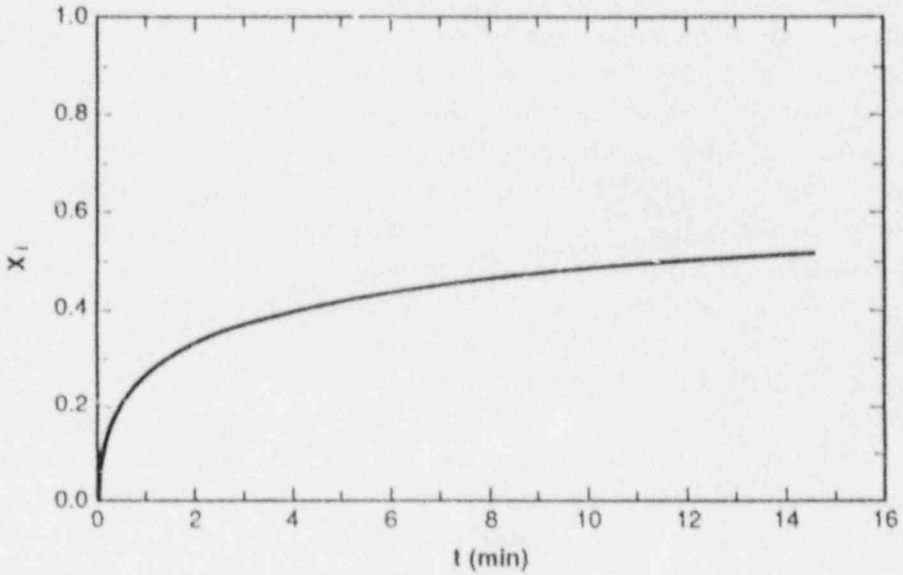

Fig. 5. *Predicted hydrogen concentration transient for base case*

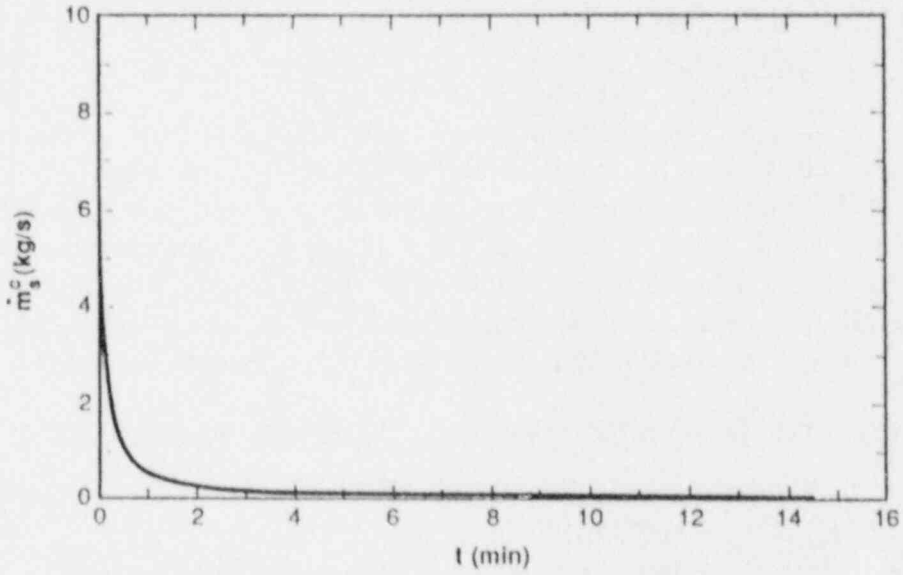

Fig. 6. *Predicted condensation rate transient for base case.*

mixing facility with an injection flow rate of 1.2 kg/s revealed the flow regime indicated in Figure 10. That is, the stream impinged upon the core barrel side of the downcomer and fell along it as a well-defined attached film. It is our judgment that this flow pattern should also have prevailed at full scale under the 15 kg/s flow rate. If there were no obstacles along the path of this film the flow would have continued smoothly until it reached the water level within the downcomer. Unfortunately, such obstacles did exist and very likely caused an abrupt deflection, of the downwards flow, laterally, towards the reactor vessel wall as illustrated in Figure 11.

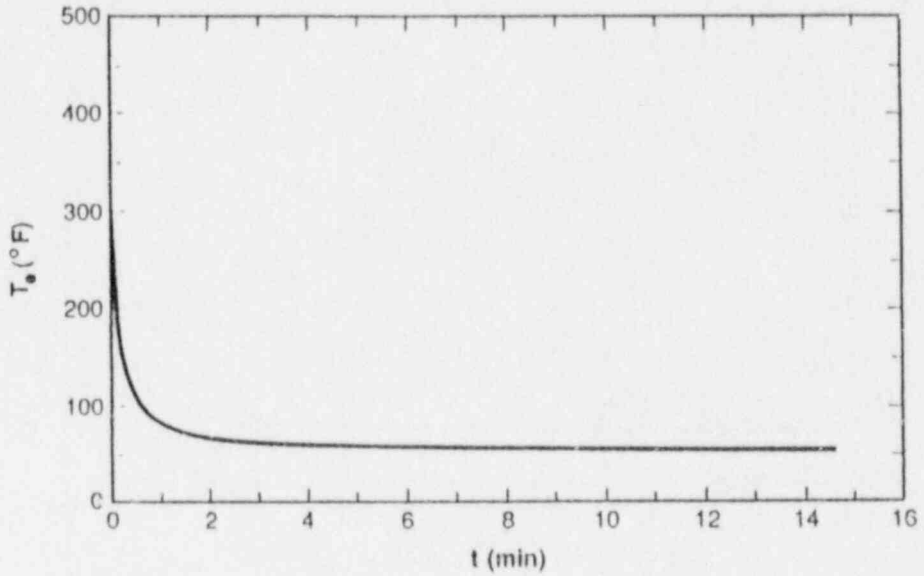

Fig. 7. *HPI temperature at the cold leg exit for base case*

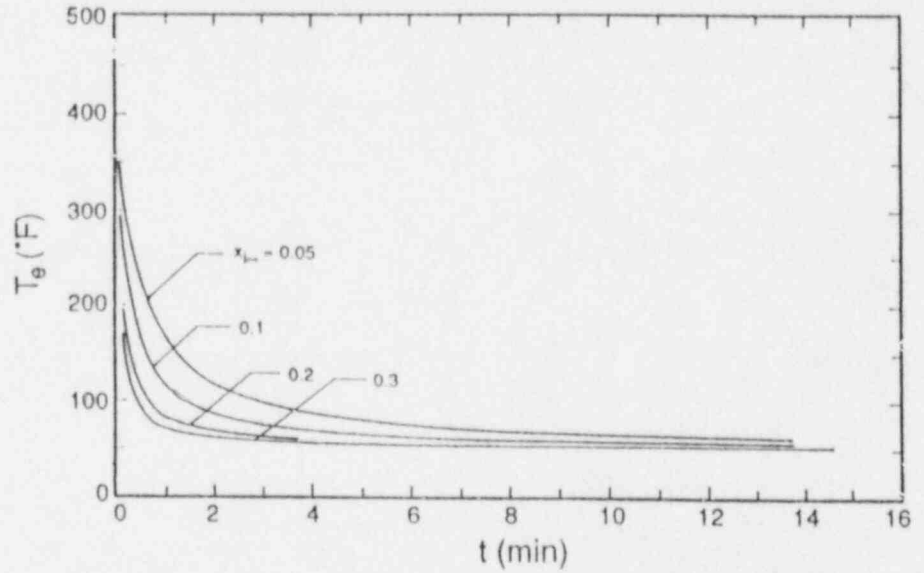

Fig. 8. *HPI temperature transient at cold leg exit for a variety of inlet hydrogen concentrations ($x_{i\infty}$ parametric)*

The detailed geometry of those obstacles is illustrated in Figure 12. The obstacles are called clips. Twenty of them are attached to the core barrel to support the upper end of the thermal shield. From the design information provided [10], their positions relative to the cold legs could be determined as illustrated in Figure 13. Clearly, nearly one-half of the flow must have impinged upon the upper surfaces of those clips causing it to splash upon the reactor vessel wall. The other half must have continued undisturbed and been confined between the core barrel and the thermal shield space.

This behavior was actually demonstrated by means of a simple model experiment. The open air arrangement involved a horizontal acrylic tube positioned opposite a vertical

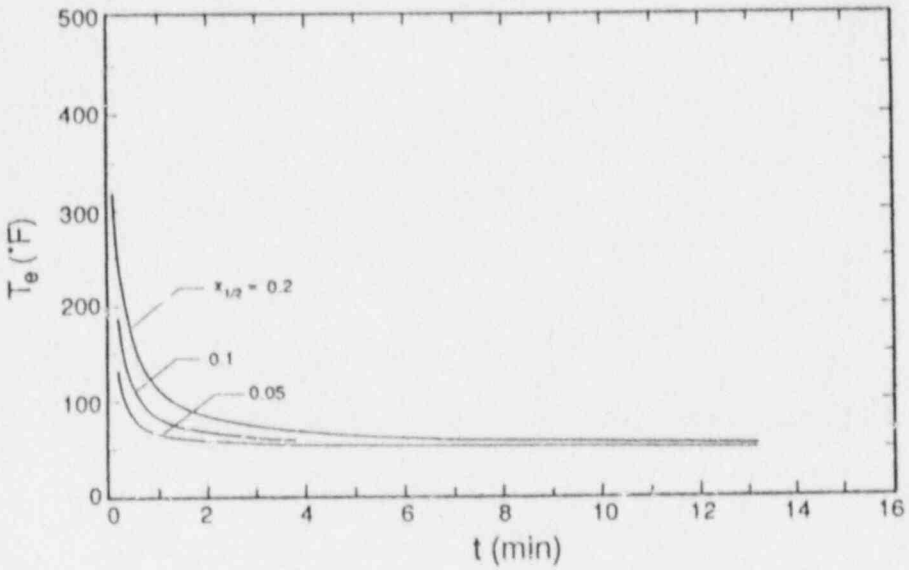

Fig. 9. *HPI temperature transient at cold leg exit for a variety of condensation degradation assumptions ($x_{1/2}$ parametric)*

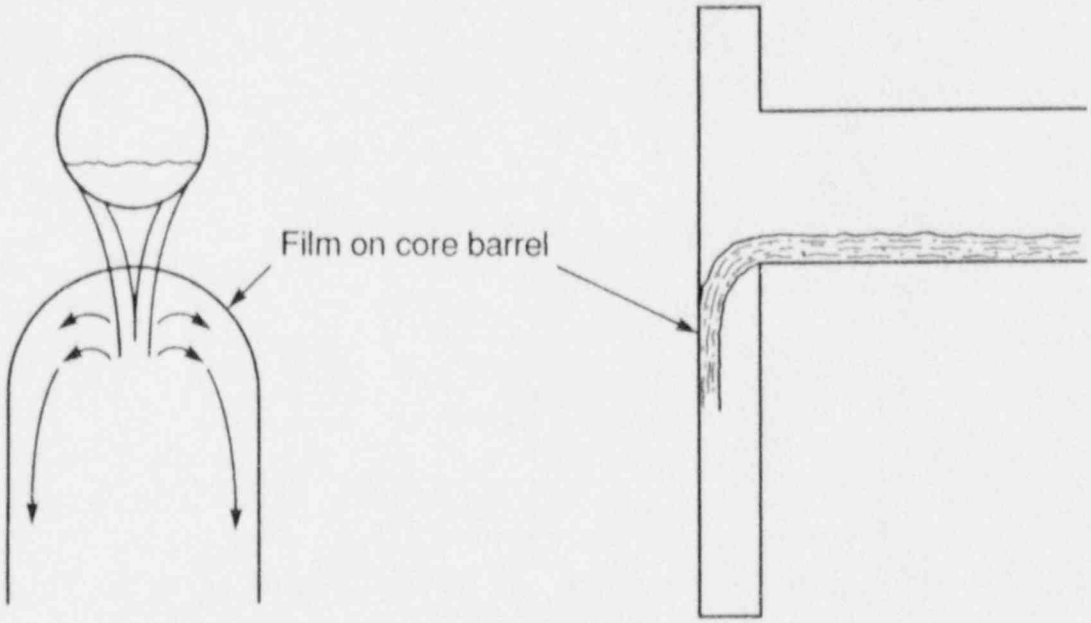

Fig. 10. *Flow regime at 1/2-scale and 1.2 kg/s*

wooden wall fitted with a model clip as illustrated in Figure 14. The relative positions, dimensions (except for the tube diameter), and flow rates of tap water were at 1:1 (full) scale. The flow regime is illustrated, from several perspectives in Figure 14. The vigorous splashing and flow diversion away from the core barrel observed in this experiment leave no doubt that the areas of the TMI-2 vessel under the cold leg nozzles were exposed directly to near 50°F water.

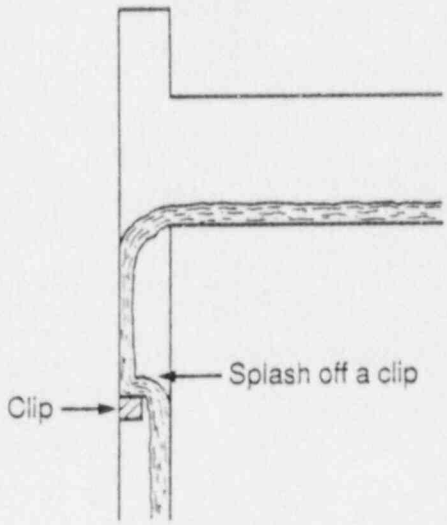

Fig. 11. *Mechanism for contact with vessel wall*

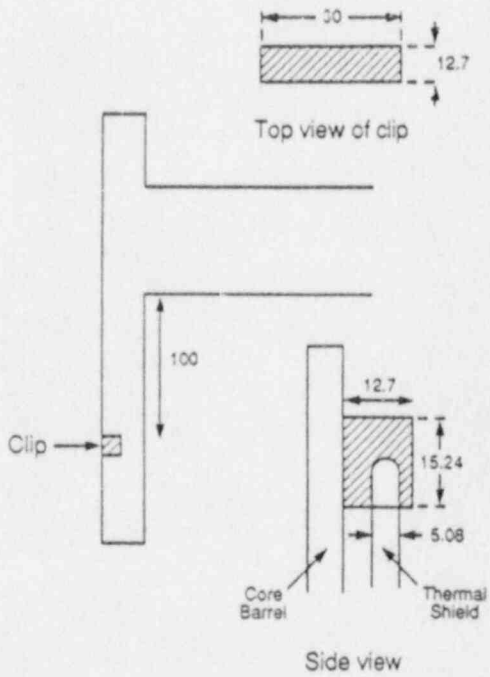

Fig. 12. *Representation of clip position and geometry (all dimensions in cm.)*

A REMIX-Type Cooldown Analysis

In addition to the direct contact of cold water discussed above the TMI-2 vessel wall was gradually exposed to the fluid filling up the downcomer. The situation is illustrated in Figure 15. Except for the thin thermal plumes (created as the falling films enter the fluid volume) which mix quickly as they descend, the rest of the fluid volume would be well mixed. This situation is very similar to that of a portion of the REMIX procedure utilized in the usual HPI thermal-mixing analyses dealing with a liquid-full cold leg situation [5].

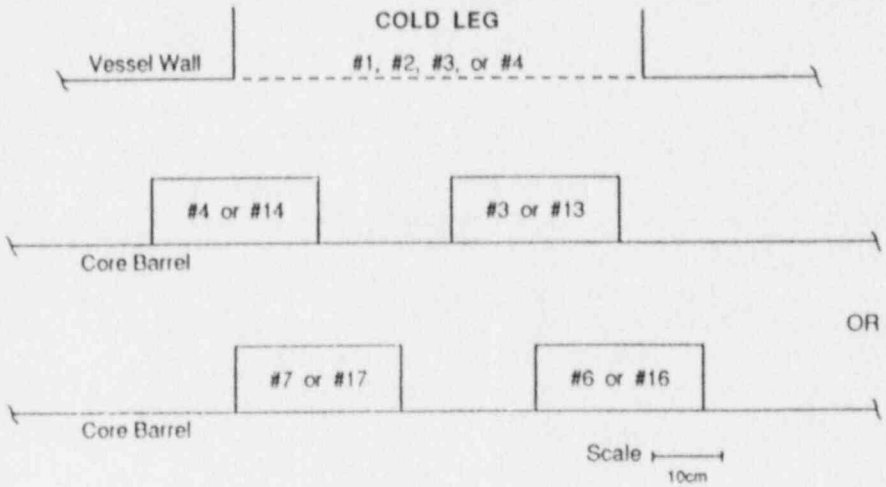

Fig. 13. *Top view of clips in relation to cold legs and downcomer (clip #1 is under hot leg)*

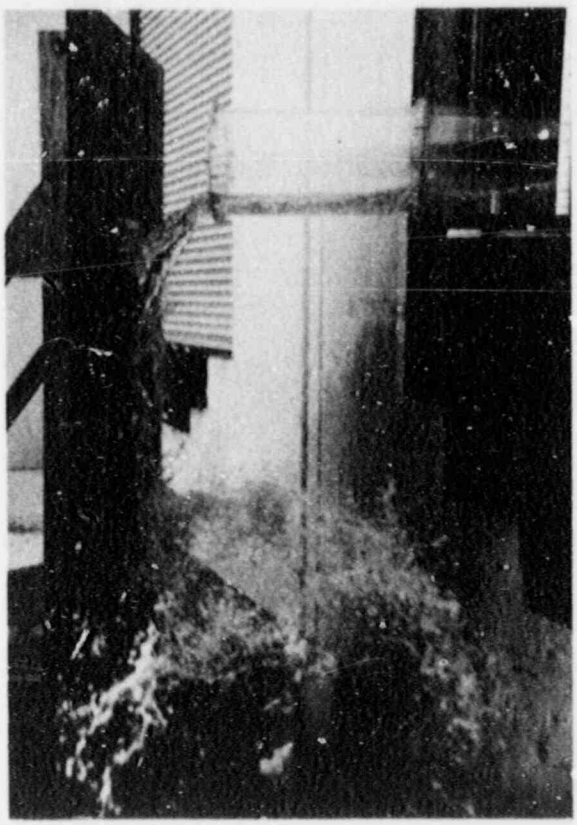

Fig. 14. *Full-scale demonstration of the off clip splashing*

Let $V_f(t)$ be the volume of the fluid within the lower plenum and the downcomer corresponding to each of the four cold legs as shown in Figure 15. The density of this fluid is denoted by ρ_m. The cold stream enters at a volumetric flow rate Q_e and a density ρ_e.

A fraction, α, of the flow, Q_o, which would have to exit if the control volume was fixed in time is assumed to enter the core, while the remaining, $(1-\alpha)Q_o$, is utilized to increase the fluid volume within the downcomer. Based on available flow areas within the core and the downcomer, the maximum value of α is 0.6. For a fully obstructed core $\alpha = 0$. In the presence of vent valves any steam binding would be insignificant. Since the degree of lower core blockage in TMI is not known, the quantity α is treated as a parameter within the above range.

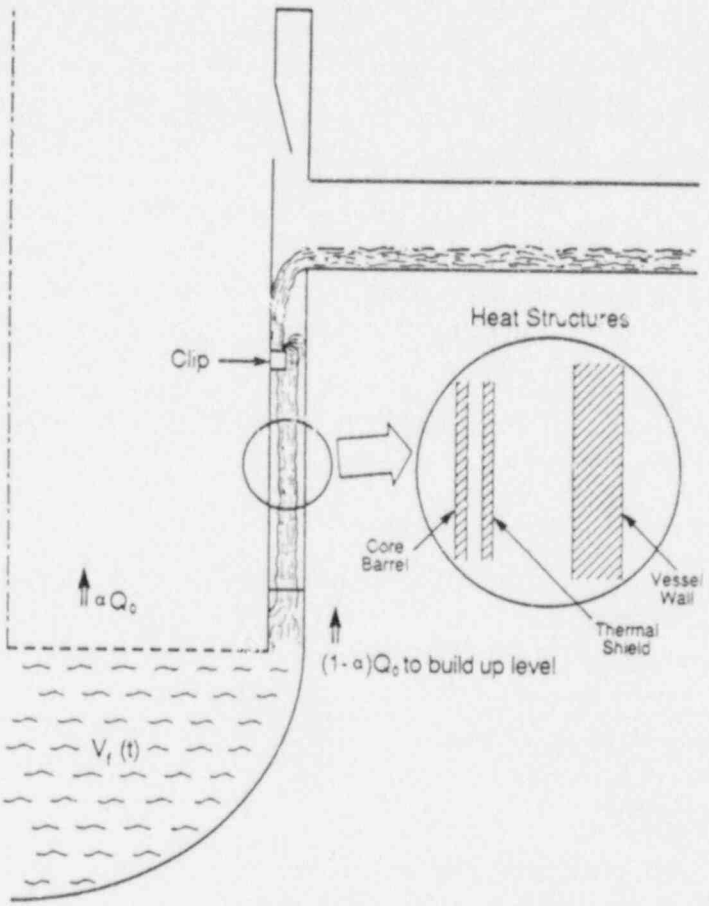

Fig. 15. *Cooldown model*

An overall mass balance may be written as

$$\frac{d}{dt}(V_f \rho_m) = Q_e \rho_e - \alpha Q_o \rho_m \tag{26}$$

The rate of change of the control volume is given by

$$\frac{dV_f}{dt} = (1-\alpha)Q_o \tag{27}$$

The energy balance accounting for the thermal energy conducted out of the metal structural components as they become submerged, $\dot{Q}_w$, is written as

$$\frac{d}{dt}(V_f \rho_m h_m) = Q_e \rho_e h_e - \alpha Q_o \rho_m h_m + \dot{Q}_w \tag{28}$$

Together with the equations of state

$$\rho = f(h) \quad \text{and} \quad \mathrm{T = g(h)} \tag{29}$$

we have a closed system of five equations in the five unknowns, namely, ρ_m, h_m, T_m, Q_o and V_f.

For an approximate estimation of $\dot{Q}_w$ the downcomer was discretized axially into four equal segments. When the level of fluid volume V_f reached the lower end of each axial segment, the conduction calculation for that segment was initiated and continued to the end of the calculation. The total heating was obtained by summing up the contribution of all the thus-activated segments.

Solutions were obtained by marching out, numerically, in time for specified initial conditions.

Choice of Parameters and Numerical Results

With the exception of the initial fluid volume, $V_f(o)$, and of the initial temperature of the non-submerged portion of the structures, the choice of parameters in this rather basic analytical model is straightforward. The relevant geometric quantities were taken to be those of the Oconee reactor (see Table 1). The cold water was taken to enter at $T_e = 50°\mathrm{F}$ with a mass flow rate of $Q_e \rho_e = 15 kg/s$. Parametric calculations with $T_e = 60°\mathrm{F}$ and $70°\mathrm{F}$ also were performed. As mentioned earlier the value of α was considered parametrically within the 0.0 to 0.6 range.

The possibility that additional condensation upon the core barrel film which would increase T_e prior to contact with the downcomer water level should also be mentioned here. From the thermal shield length (Table 1) and an assumed lateral spread of ~ 1 m we obtained an additional condensation surface area of ~ 5.3 m^2. The downcomer volume is ~ 6.3 m^3. Employing the results of the condensation parametrics we see that the additional area (a factor x5.3 from base case) is amply covered by the $h_o \sim 50{,}000$ BTU/hr $\mathrm{ft}^{2°} F$ parametric caculation (factor of x37). Also as we can see from Equation (14) the increased volume (a factor of x1.8 from the base case) may be thought of as compensated by the $x_{i\infty} \sim 0.4$ parametric (i.e., a factor of x2 from the base case). Thus, again, unless an unforseen phenomenon strongly mitigates the condensation inhibiting effect of noncondensibles the values of T_e utilized in this analysis would not be materially altered.

The initial fluid volume within the downcomer/lower-plenum region is uncertain. Prior to the "B" loop pump actuation the downcomer was essentially empty. There have been some estimates, however, that the pumps displaced nearly 1,000 ft^3 of water from the cold

Table 1 - GEOMETRIC CONFIGURATION OF OCONEE

Injector diameter: 0.177 ft

	Cold leg	Vessel/ downcomer	Lower plenum	Pump	Loop seal	Core barrel	Thermal shield
Inner diameter/ width (ft)	2.33	14.22	14.22	---	---	---	---
Length (ft)	24.5	18.6	---	---	---	18.6	16.0
Base metal wall thickness (ft)	0.21[a]	0.703	0.36[a]	---	---	0.19[a]	0.167
Clad thickness (ft)	0.01[a]	0.016	0.016	---	---	---	---
Insulation thickness (ft)	0.30	0.30	0.30	---	---	---	---
Wall heat tr. area to water (ft^2)	179.3	207.7	69.2	---	---	176.8	304.1[b]
Internal structures: heat tr. area (ft^2)	---	---	---	---	---	---	---
Thickness (ft)	---	---	---	---	---	---	---
Fluid Volume (ft^3)[c]	104.5	176.3	153.3	---	---	---	---

[a] Assumed
[b] Both sides
[c] Per cold leg

leg piping into the reactor vessel. This would have been sufficient to fill the downcomer completely if the core had been completely blocked, or to fill one-half of the core and downcomer volumes if free flow into the core had been possible. However, the HPI occurred nearly one-half hour later, and in all likelihood this was adequate time to allow, again, downcomer depletion. The value of $V_f(o)$ was, therefore, taken equal to the lower plenum volume (divided by four to account for the four cold legs). The effect of any larger initial fluid volume would have been to decrease, somewhat, the cooldown rate.

The initial temperature of the downcomer structures is also uncertain. The water displaced, by the "B" pumps, from the cold leg piping (loop seal volumes principally) had been stagnant for a considerable length of time and it could have cooled somewhat from its normal operating temperature of $\sim 530°F$. We ignore this effect and take all structures (core barrel, thermal shield, vessel wall) as well as the fluid within V_f to be initially at $530°F$. In addition, a parametric calculation was run assuming a core barrel temperature of $1,000°F$ to reflect, approximately, consistency with the highly degraded core conditions at that time.

The results are shown in Figures 16 to 18. The sensitivity to parameter α is seen to be rather small. The effect of the overheated core barrel is also seen to be small. For the maximum duration of high pressure injection quoted [7], temperatures of $\sim 200°F$ are being predicted. The breaks in the curves are due to the discretization of the structural heat input. They are useful in indicating the time-wise progression of the water level in the downcomer. In particular the last break, which has been marked in the Figures, indicates the time that the downcomer is 100% full.

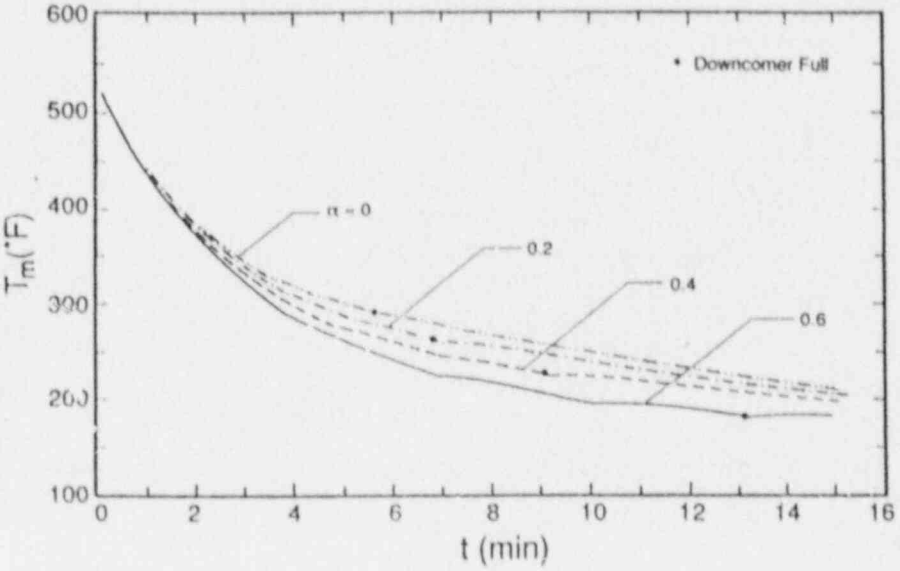

Fig. 16. *Downcomer fluid temperature transients for base case*

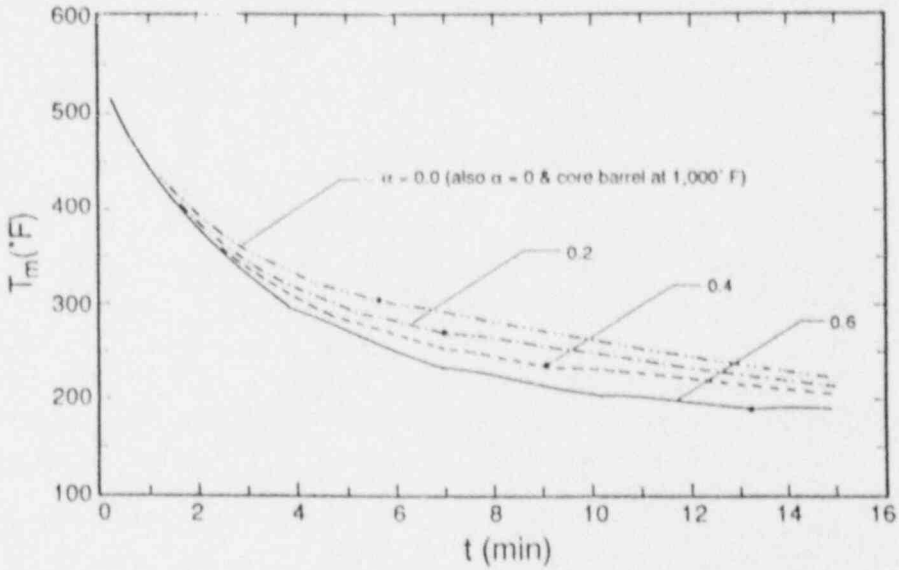

Fig. 17. *Downcomer fluid temperature transients for* $T_e = 60^\circ\ F$

4. CONCLUSIONS

If the high pressure safety injection that was initiated at ~ 200 minutes took place for ~ 15 minutes at 15 kg/s, the TMI-2 vessel wall temperatures reached levels well below $200^\circ F$. The principal factor in this conclusion is degradation of heat transfer due to the presence of noncondensibles (hydrogen, fission product gases). A mechanism leading to the accumulation of noncondensibles within the TMI-2 cold legs has been described and indicates that the above conclusion would be true even if the noncondensible concentration in the upper plenum area was rather low. The HPI water is predicted to have entered the empty downcomer at $\sim 60^\circ\ F$ and a mechanism for direct contact of a portion of this flow with restricted areas of the reactor vessel wall has been demonstrated. On the other

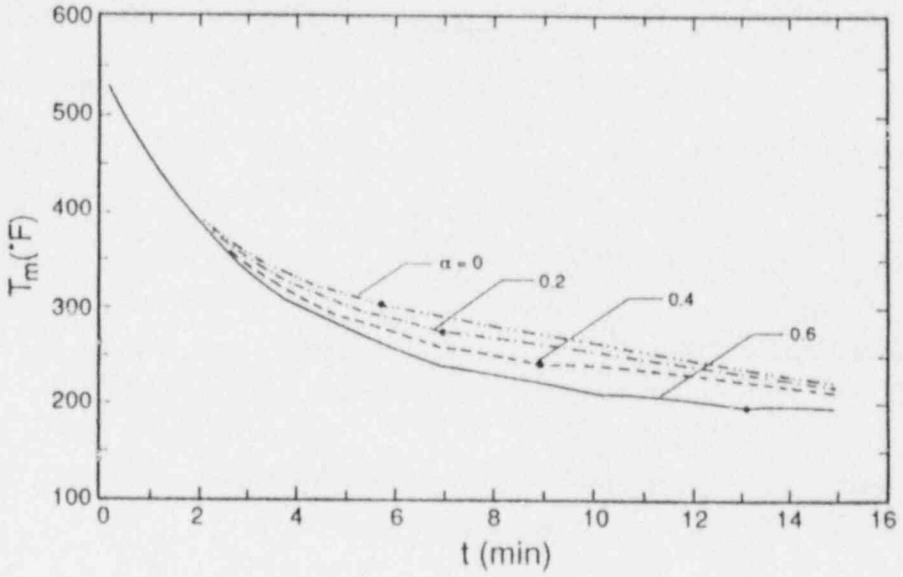

Fig. 18. *Downcomer fluid temperature transients for* $T_e = 60^\circ\ F$

hand thermal mixing with lower plenum fluid and structural heat limited the cooldown of downcomer fluid and global exposure of the vessel was to $\sim 200^\circ\ F$.

Appendix A

Hydrogen Absorption in the HPI

The mass flux of hydrogen into the turbulent HPI stream may be estimated from [A.1]

$$\dot{m} \approx C M_i \left\{ \frac{Du'}{\lambda} \right\}^{1/2} \tag{A.1}$$

where D is the molecular diffusivity of hydrogen in water, u' and λ are the velocity and length scales of the turbulence energy-containing eddies, C is the solubility of hydrogen in water, and M is the molecular weight of hydrogen.

The diffusivity, D_o in $20°C$ water is given [A.2] as $5 \times 10^{-5} cm^2/s$. For any other temperature, T, the diffusivity may be obtained by

$$D = D_o \frac{T}{T_o} \frac{\mu_o}{\mu} \tag{A.2}$$

where μ is the viscosity of water at T. For example at 160°C the viscosity is 0.174 cp [A.3] and $D \sim 4.2 \times 10^{-4} cm^2/s$.

The solubility may be related to the partial pressure of hydrogen, P_i, through Henry's law by

$$x = \frac{P_i}{K} \tag{A.3}$$

For 100°C water the Henry's law constant K is given [A.3] as $K = 5.73 \times 10^7 mmHg$. At a hydrogen partial pressure of 1 bar we can thus calculate an equilibrium hydrogen mole fraction of 1.32×10^{-5}. For a partial pressure of ~100 bar (assuming a high value of x_i) we have $x \sim 1.32 \times 10^{-3}$, which corresponds roughly to $C \sim 7.3 \times 10^{-5}$ g-moles $H_2/cm^3 H_2O$.

The turbulence length and velocity scales are chosen as 8 cm and 30 cm/s respectively (see Appendix C).

With the above estimates Equation (A.1) yields $\dot{m} = 5.76 \times 10^{-6} g/cm^2 s$. The exposed area within the cold leg is of the order of $1 m^2$. Thus a hydrogen mass of $\sim 3.5g$ could be absorbed per minute, or $\sim 52g$ for the 15 minute duration of the high pressure injection. On the other hand, a steam volume of $3.5 m^3$ at 105 bar at hydrogen mole fractions of 0.2 and 0.4 would contain $\sim 3,200$ and $\sim 6,400g$, respectively. Clearly the dissolution of H_2 into the water cannot provide an effective mechanism for countering the hydrogen accumulation caused by condensation.

Appendix B

Degradation of Condensation Rates Due to Noncondensibles

No directly applicable experimental data could be located in this area. Our approach is, therefore, based on cautious utilization of available data, in low pressure steam/air systems.

First, let us consider how the binary diffusivity in the hydrogen/steam system compares with that of the air/steam system. At low pressures the diffusivisity may be related to the critical pressures, temperatures and molecular weights of the components [B.1]

$$P^0 D^0_{1\ 2} = 3.64 \times 10^{-4} \left\{ \frac{T}{\sqrt{T_{c1} T_{c2}}} \right\}^{2.334} (P_{c1} P_{c2})^{1/3} (T_{c1} T_{c2})^{5/12} \left\{ \frac{1}{M_1} + \frac{1}{M_2} \right\}^{1/2} \qquad (B.1)$$

At 533°K this yields $P^0 D^0_{1\ 2} \sim 4.91$ atm cm^2/s. This value may be converted to high pressure using the critical properties of the mixture

$$P'_c = \sum_j x_j P_{cj} \quad \text{and} \quad T'_c = \sum_j x_j T_{cj}$$

and a graphical representation of the ratio

$$\frac{P\ D}{P^0\ D^0} = K$$

given by Bird et al. [B.1]. For example for $x_i = 0.1$ we have $T'_c = 585.3°$ K and $P'_c = 197.3$ bar. Thus K = 0.6 and with the previously obtained value of $P^0 D^0_{1\ 2}$ we obtain, for $P =$ 102 bar, $D \sim 2.9 \times 10^{-2} cm^2/s$. At 373 K the same procedure yields $D \sim 1 \times 10^{-2} cm2/s$. Very similar results are obtained also for $x_i = 0.2$. At the other extreme of $x_i = 0.8$ we have $T'_c = 155.8° K$, $P'_c = 54$ bar, and $K \sim 1$. Thus the $D \sim 4.8 \times 10^{-2} cm^2/s$ and $2 \times 10^{-2} cm^2/s$ values are obtained for the high and low temperature cases respectively. These values are to be contrasted with a value of $D \sim 0.239 cm^2/s$ for an 8°C air/steam system and a value of $D = 0.634 cm^2/s$ for the hydrogen/air system at 0°C and 1 bar. At 100°C the above values are multiplied by a factor of ×2. It is clear, therefore, that the high pressure steam/hydrogen system (present application) would give rise to considerably higher diffusional resistance to condensation than the low pressure steam/air systems which have been previously studied experimentally.

Stein et al. [B.2] carried out experiments of steam condensation in the presence of air. Condensation took place in the underside of a horizontal cooled copper plate, at system pressures of 3.1, 6.2 and 12.4 bar. We have correlated these data in the manner shown in Figure B.1. An exponential decay with $x_{1/2} = 0.05$ is indicated. This is consistent with much older data obtained in vertical condensing plate geometries [B.3].

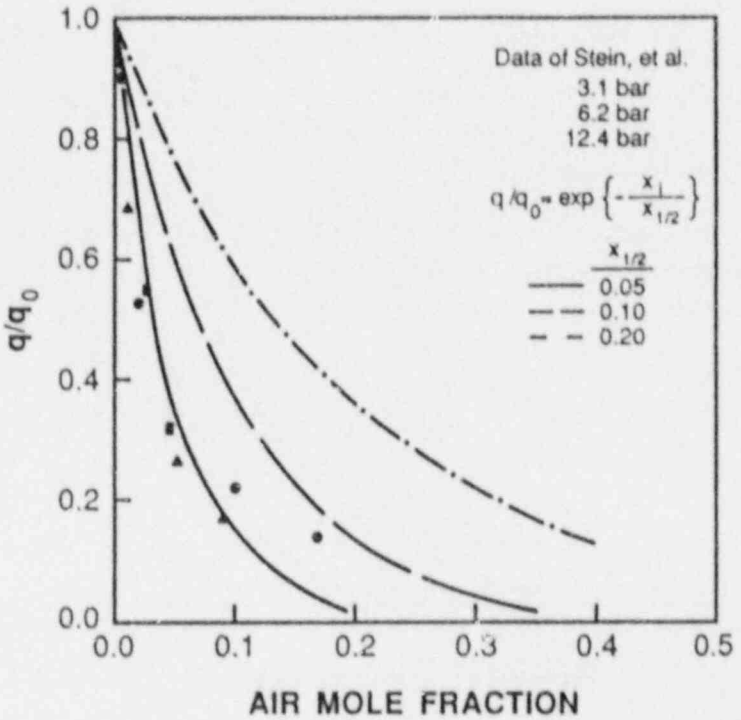

Fig. B.1. *Correlation of the Stein, et al. data [B.2] in terms of more fraction of noncondensibles*

On the other hand, Stein et al. [B.2] have argued that natural convection effects were important in mitigating some of the condensation inhibition efffects of the noncondensibles. If this were true in the air/steam system it would be even more important in the hydrogen/steam system. Unfortunately, the information available does not allow the reliable evaluation of such effects, which are, therefore, left outside the scope of the present study.

In an effort to cover such uncertainties the slower exponential decays of $x_{1/2} = 0.1$ and 0.2, as shown in Figure B.1 were also considered in the parametric evaluations. Furthermore, if natural convection effects are important their onset should take place at low enough condensation rates where the suction due to condensation is somewhat diminished. Indeed the deviation seen in the data at $q/q_o \sim 0.1$ may be due to this type of behavior. To cover this possibility and acknowledging the absence of data for $q/q_o < 0.1$ we have also carried out additional parametric calculations whereby for $x_i > x_L$ (where x_L in some specified, limiting value) the q/q_o decay is specified to linearly approach zero at $x_i = 1$. Except for using $x_{i\infty} = 0.3$ or 0.4 all other parameters were fixed at the base case values. The condensation transient for this kind of behavior is shown in Figures B.2 to B.7. Again a rapid shut-off of condensation is observed, although in this case the hydrogen mole fraction continues to increase approaching values close to unity.

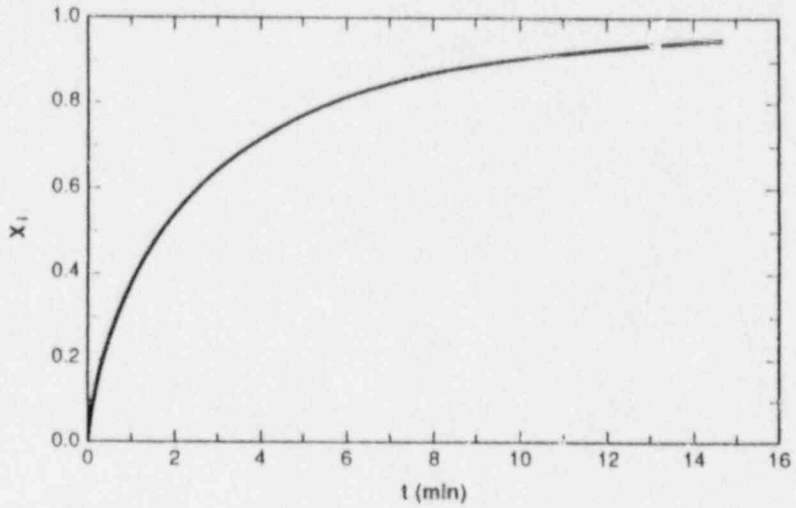

Fig. B.2. *Hydrogen concentration transient,* $x_{i\infty} = 0.3$, $x_L = 2x_{1/2}$

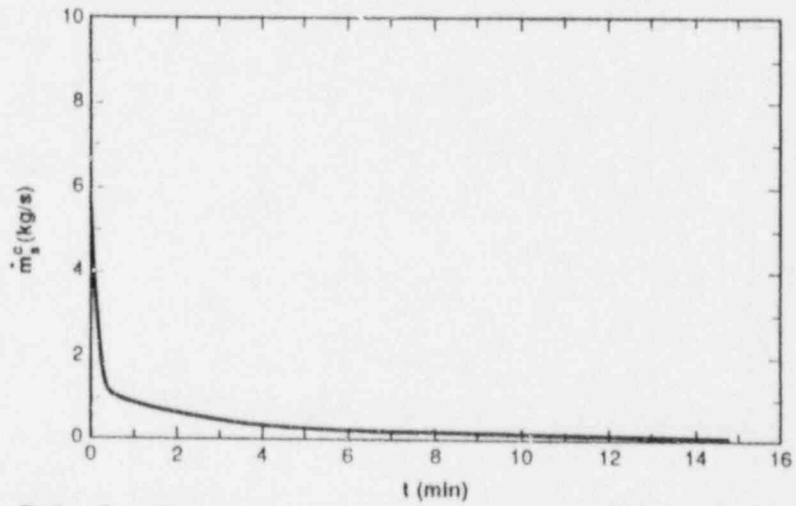

Fig. B.3. *Condensation rate transient,* $x_{i\infty} = 0.3$, $x_L = 2x_{1/2}$

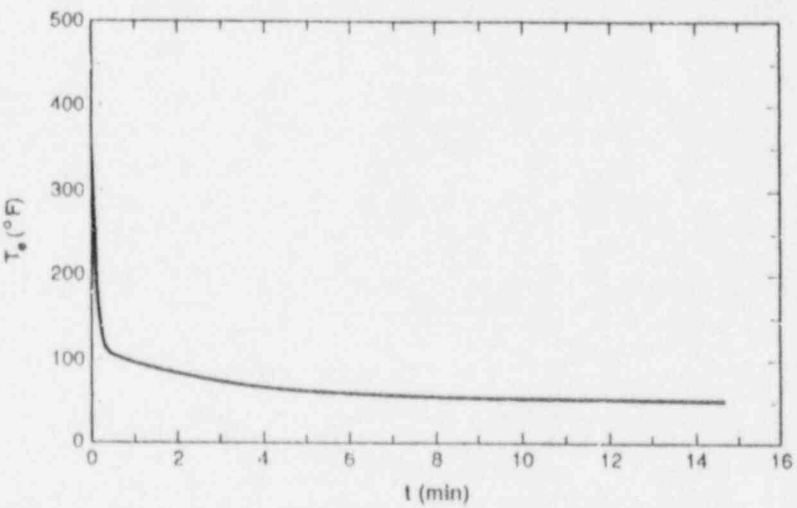

Fig. B.4. *HPI temperature transient,* $x_{i\infty} = 0.3$, $x_L = 2x_{1/2}$

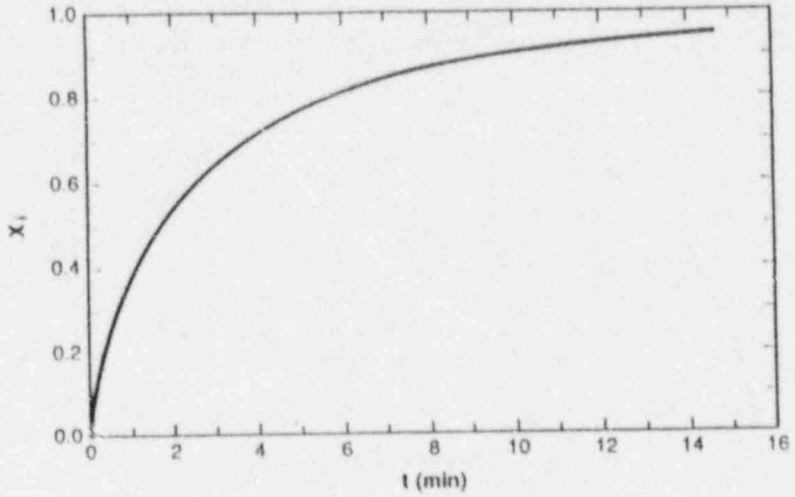

Fig. B.5. *Hydrogen concentration transient,* $x_{i\infty} = 0.4$, $x_L = 2x_{1/2}$

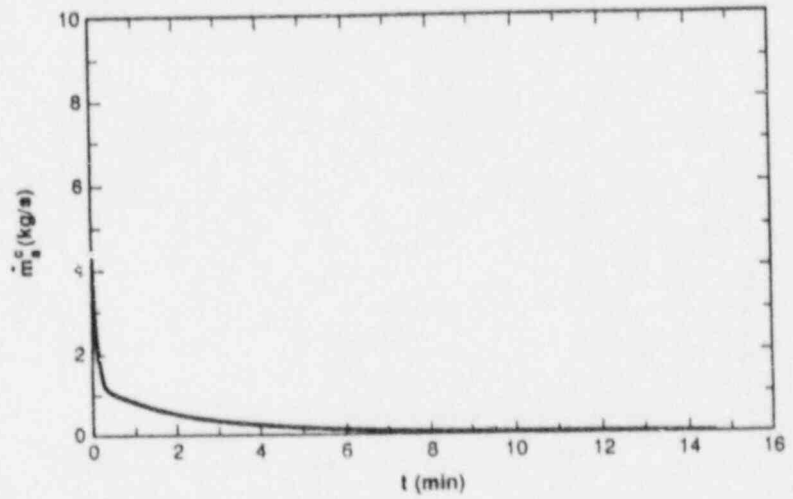

Fig. B.6. *Concentration rate transient,* $x_{i\infty} = 0.4$, $x_L = 2x_{1/2}$

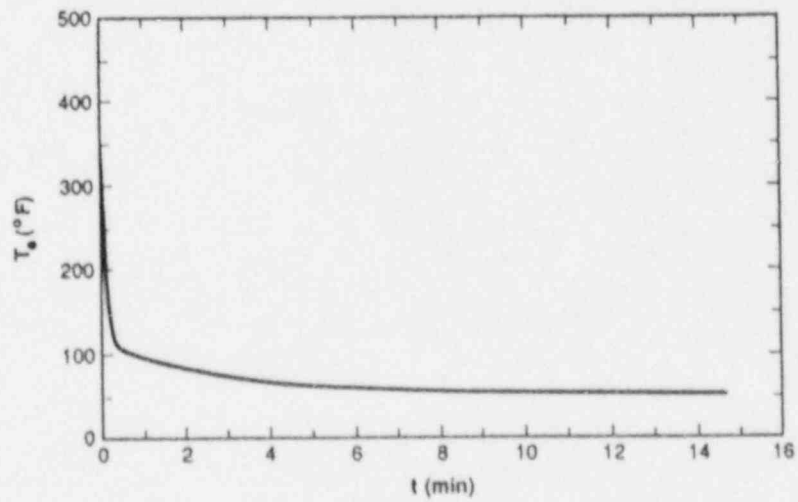

Fig. B.7. *HPI temperature transient,* $x_{i\infty} = 0.4$, $x_L = 2x_{1/2}$

Appendix C

The Heat Transfer Coefficient in the Absence of Noncondensibles

In the absence of noncondensibles heat transfer is controlled by the turbulence in the liquid stream. A formulation developed for mass absorption by Theofanous et al. [C.1] about 10 years ago was found also appropriate for condensation by the experimental work of Bankoff [C.2] and Thomas [C.3]. For heat transfer, using $Pr \sim 1$, the equations are

$$St_t = 0.25 Re_t^{-1/4} \quad \text{for} \quad \mathrm{Re}_t > 500 \tag{C.1}$$

$$St_t = 0.70 Re_t^{-1/2} \quad \text{for} \quad \mathrm{Re}_t < 500 \tag{C.2}$$

The turbulence Stanton and Reynolds numbers are given by:

$$St_t = \frac{h_o}{U' \rho c} \quad \text{and} \quad \mathrm{Re}_t = \frac{\mathrm{u}' \lambda}{\nu} \tag{C.3}$$

The u' and λ, also called integral velocity and length scales have been related to the mean flow velocity, U, and hydraulic diameter, D, in a couple of different ways. Theofanous et al. [C.1] used the relations known to apply for pipe flow: $u' \sim 0.05U$ and $\lambda \sim 0.03 D_h$. Bankoff [C.2] suggested that for stratified flow of depth δ: $u' = 0.3U$ and $\lambda \sim \delta$.

Assuming open channel critical flow at the cold leg exit (Fr $\sim$ 1) we can estimate a liquid depth $\delta \sim 8cm$ and a velocity $U \sim 1m/s$. With the Theofanous et al. choices for u' and λ and for 100°C water ($\nu = 0.0029 cm^2/s$) we obtain $Re_t \sim 826$. The choice of Bankoff yields even higher values. Thus, the regime of Equation (C.1) is applicable. We will first show that both choices for u' and λ lead to very similar results.

We can define a mean flow Stanton number by

$$St = \frac{h_o}{U \rho} \equiv \frac{Nu}{RePr} \sim \frac{Nu}{Re} \tag{C.4}$$

and in combination with Equations (C.1) and (C.3) we obtain

$$St = St_t \frac{U'}{U} = 0.25 Re_t^{-1/4} \frac{u'}{U} \tag{C.5}$$

or

$$h_o = 0.25 \rho \frac{\nu^{1/4} u'^{3/4}}{\lambda^{1/4}} \tag{C.6}$$

Denoting by h_o^T and h_o^B the heat transfer coefficients based on the Theofanous and Bankoff choices of turbulence parameters respectively we have:

$$\frac{h_o^T}{h_o^B} = \left[\frac{5}{30}\right]^{3/4} \left[\frac{100}{3}\right]^{1/4} = 0.62 \tag{C.7}$$

That is a difference between the two predictions of only 38%.

Using $Re_t = 826$ in Equations (C.1) and (C.2) we obtain $St_t \sim 4.66 \times 10^{-2}$ and 2.43×10^{-2}, respectively. Let us choose the value $St_t \sim 3 \times 10^{-2}$. In combination with Equation (C.5) we obtain $St \sim 1.5 \times 10^{-3}$ which utilized in Equation (C.4) finally yields $h_o^T \sim 1,004$ BTU/hr ft2°F. The Bankoff prediction would then be $h_o^B \sim 1,620$ BTU/hr ft2°F. An in-between value of $h_o \sim 1,300$ BTU/hr ft2°F will be considered as a best estimate.

These predictions should be viewed, however, with a certain degree of reservation. The reason is that the limited experimental data available in this area were obtained at low pressures. The concern is that at the high pressures, high subcoolings and high heat fluxes of interest here the condensate fluid may be difficult to dissipate by turbulent mixing, yielding stratification and hence a significant reduction of the heat transfer coefficients from the values predicted above.

NOMENCLATURE

c	concentration
c_p	heat capacity
C	solubility
d	diameter
D	mass diffusivity (molecular)
h	heat transfer coefficient, or enthalpy
K	Henry's constant
ℓ	width of liquid layer
$\dot{m}$	mass flow rate
M	molecular weight
P	pressure
q	heat flux
$\dot{Q}$	heat flow rate
Q	volumetric flow rate
R	gas constant
S	surface area
t	time
T	temperature
T^*	saturation temperature
U	velocity
V	volume
w	mass fraction
x	mole fraction
z	axial coordinate

Subscripts

c	critical
e	exit condition

fg	liquid-to-vapor
HPI	high pressure injection
i	inlet condition or hydrogen
o	reference state
R	ratio (of molecular weights)
s	steam
t	turbulent
T	total
$1/2$	defines a constant–see Appendix B
∞	condition in the reactor vessel

Superscripts

c	condensation

Greek

α	thermal diffusivity or flow fraction entering core, Eq (26)
λ	length scale of turbulence
μ	viscosity
ρ	density
ν	kinematic viscosity

ACKNOWLEDGMENTS

This work was performed under NRC Grant No. NRC-03-003 under the supervision of Dr. J. Reyes. The continuing encouragement of Dr. N. Zuber and Dr. D. Ross also is gratefully acknowledged. The author is indebted to Mr. K. Iyer for helping with the numerical calculations and to Mr. M. Vandenbroek for carrying out the experiments. We also appreciate the cooperation of Drs. S. Behling and B. Tollman (EG&G) in supplying information and documents relevant to the TMI-2 accident scenario.

REFERENCES

1. PTS Rule, 10CFR50.61, U. S. Nuclear Regulatory Commission.

2. J. Reyes, Ltr. to T.G. Theofanous, Subject: HPI Mixing in Steam, February 25, 1985.

3. B&W Owner's Group Report on TMI-2 PTS.

4. T.G. Theofanous, Ltr. to J. Reyes on "TMI-2 Downcomer Temperatures with HPI," April 1, 1985.

5. K. Iyer and T.G. Theofanous, "Decay of Buoyancy Driven Stratified Layers with Applications to PTS: Reactor Predictions," ANS Proceedings of the National Heat Transfer Conference of 1985 held in Denver, Colorado, August 4-7, 1985.

6. T.G. Theofanous and H.K. Fauske, "The Effects of noncondensibles on the Rate of Sodium Vapor Condensation from a Single-Rising HCDA Bubble," *Nuclear Technology*, **19**, 132 (1973).

7. S.R. Behling, "Computer Code Calculations on the TMI-2 Accident: Initial and Boundary Conditions," EGG-TMI-6859, May 1985.

8. B. Tollman, "Thermal Hydraulic Features of the TMI Accident," Draft EG&G Report, June 1985.

9. S. Behling, EG&G, Private Communication, August 9, 1985.

10. G. Skillman, Metropolitan Edison Co., Private Communication, August 4, 1985.

11. T.G. Theofanous, "The Cooldown Aspects of the TMI-2 Accident," NUREG/CR-4978, July 1987.

A.1 T.G. Theofanous, et al., "Turbulent Mass Transfer at Free Gas-Liquid Interfaces, with Applications to Open-Channel, Bubble and Jet Flows," *Int. J. Heat Mass Transfer*, **19**, pp. 613-614 (1976).

A.2 F. Kreith, *Principles of Heat Transfer*, Int. Textbook Co. 1966.

A.3 *Handbook of Chemistry and Physics*, 47th Edition, Chemical Rubber Publishing Co., Cleveland, Ohio (1961).

B.1 R. Bird R., *Transport Phenomena*, Wiley Publishing Co. 1961.

B.2 R.P. Stein, et al., "Condensation on the Underside of a Horizontal Surface in a Closed Vessel," HTD-Vol. **47**, ASME 1985.

B.3 E. Langen, Forschung a.d. Geb. d. Ingenieurwes, 2:359 (1931).

C.1 T.G. Theofanous, et al., "Turbulent Mass Transfer at Free, Gas-Liquid Interfaces, with Applications to Open-Channel, Bubble and Jet Flows," *Int. J. Heat Mass Transfer* **19**, pp. 613-624 (1976).

C.2 L. Lee, R. Jensen, S.G. Bankoff, M.C. Yuen and R.S. Zankin, "Local Condensation Rates in Cocurrent Steam-Water Flow," in Non-equilibrium Interfacial Transient Processes, Ed. J.C. Chen and S.G. Bankoff, ASME 1979.

C.3 R.M. Thomas, "Condensation of Steam on Water in Turbulent Motion," *Int. J. Multiphase Flow* **5**, 1-15 (1979).

BORON MIXING IN THE LOWER PLENUM OF A BWR

by

T.G. Theofanous, E.S. Shabana, and M. Vandenbroek
Department of Chemical and Nuclear Engineering
University of California
Santa Barbara, CA 93106

Current ATWS procedures are rather complicated because of uncertainties regarding the flow behavior of the liquid poison injected into the lower plenum for control. The concern, supported by some old small scale experiments (at General Electric Co.), is that due to strong buoyancy forces the natural circulation flow (less than 30% of rated) would be insufficient to entrain and convect the cold boric acid solution upwards and into the core area. On the other hand, the applicability of these experimental results is also in doubt. This is because Froude number scaling becomes problematic at small scales. The purpose of this work is to bypass such concerns by carrying out a set of experimental simulations at full scale.

Such full-scale simulations are practical because of the high degree of compartmentalization of a BWR lower plenum by the control rod guides and the nearly longitudinal flow of coolant in the interstitial spaces. The experimental facility represents a lower plenum slice corresponding to 9 guide tubes in the neighborhood of the injection standpipe (also included at full scale). The structural material is acrylic, allowing full visualization. The base flow is created by recirculating from a 2,000 gal. capacity (water) tank at velocities up to the full natural circulation strength expected in the reactor. The injection flow consists of a $NaC\ell$ solution. In addition to visualization the facility is instrumented for mapping out the local/instantaneous concentration (conductivity probes) and velocity (fibre optic laser doppler anemometer)fields.

Data from the first round of experiments will be presented and initial conclusions regarding stratification potential will be drawn.

BORON MIXING IN ATWS

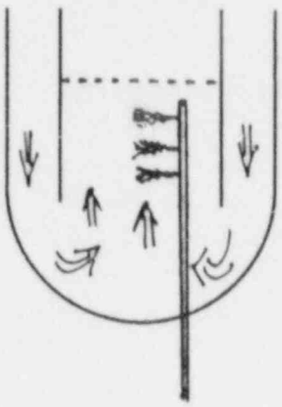

- NATURAL CIRCULATION FLOW
- 1/6-SCALE EXPERIMENTS (GE) SHOW STRATIFICATION
- COMPLICATED ATWS PROCEDURES
- CODE DEVELOPMENT EFFORTS

Slide 1

Many boiling water reactors rely on liquid poison, injected into the lower plenum, to achieve shutdown from postulate ATWS (Anticipated Transients Without Scram) events. Due to the combination of solute and temperature effects, the injected solution is ~60% heavier than the primary fluid, and the potential for its stratification (settling) into the lower plenum under the relatively low natural circulation flow velocities has been recognized long ago. The General Electric Company has obtained mixing data in a 1/6-scale simulation facility. Their data remain unavailable (proprietary), although indications are that they exhibit a strong tendency to stratify for recirculation flows less than ~20% of rated. This lead to complicated operator procedures and an interest to model the mixing process in a form appropriate for use in system's codes (i.e., TRAC-BWR).

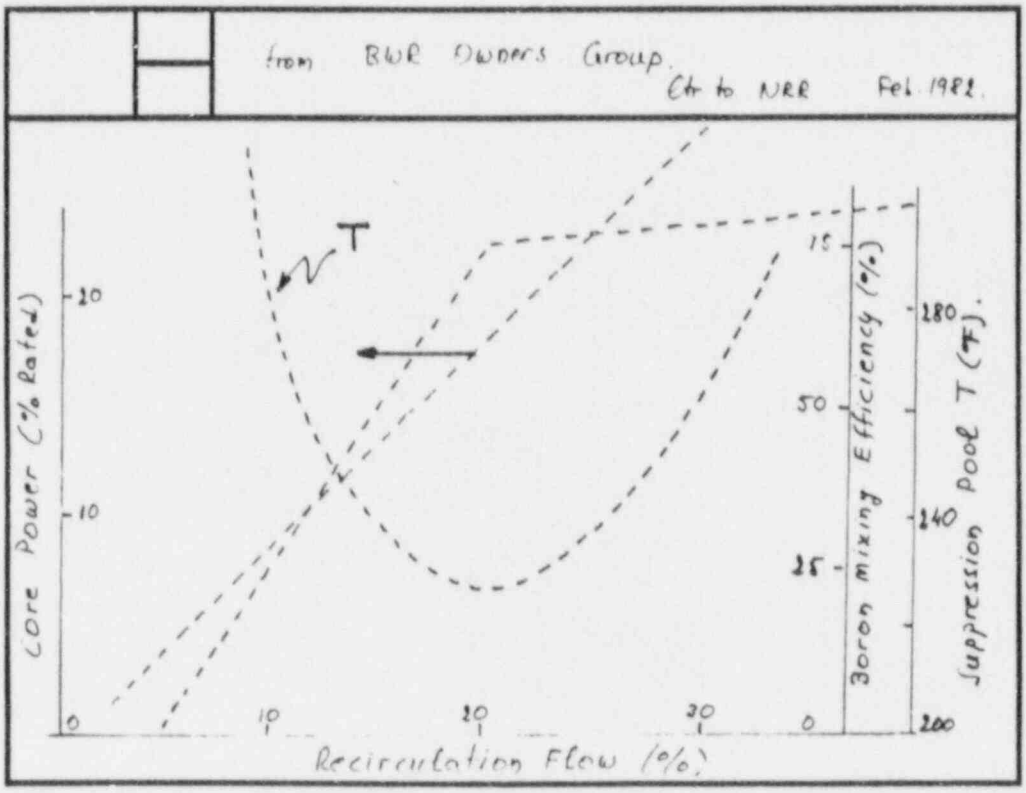

Slide 2

The complications arising from inadequate mixing can be understood in terms of this slide, obtained from a 1982 BWR Owner's Group letter to the NRC. As seen, the mixing efficiency approaches zero at ~5% of rated flow, while it seems to reach a nearly constant upper value of ~75% for flows higher than ~20%. On the other hand, the core power shows a linear decrease with recirculation flow, due to a corresponding increase in core void fraction. The combined effect on an ATWS transient is to produce the strongly upwards concave curve of suppression pool temperature, as shown above. That is, at high flows the suppression pool overheats as the boron mixing cannot keep up with the steam production. At very low flows, on the other hand, the whole transient is prolonged such that even at the low power levels suppression pool overheating is obtained. According to this figure the operators should maintain reactor water level such as to produce the 20% flow required for the minimum in pool temperature rise. At present there is a proposal made to the NRC that the water level be dropped below the top of the active core in order to achieve an acceptable performance under such conditions. Clearly, such procedures are not particularly condusive to safety and provide the motivation for the closer examination of the boron mixing phenomena that is the subject of this study.

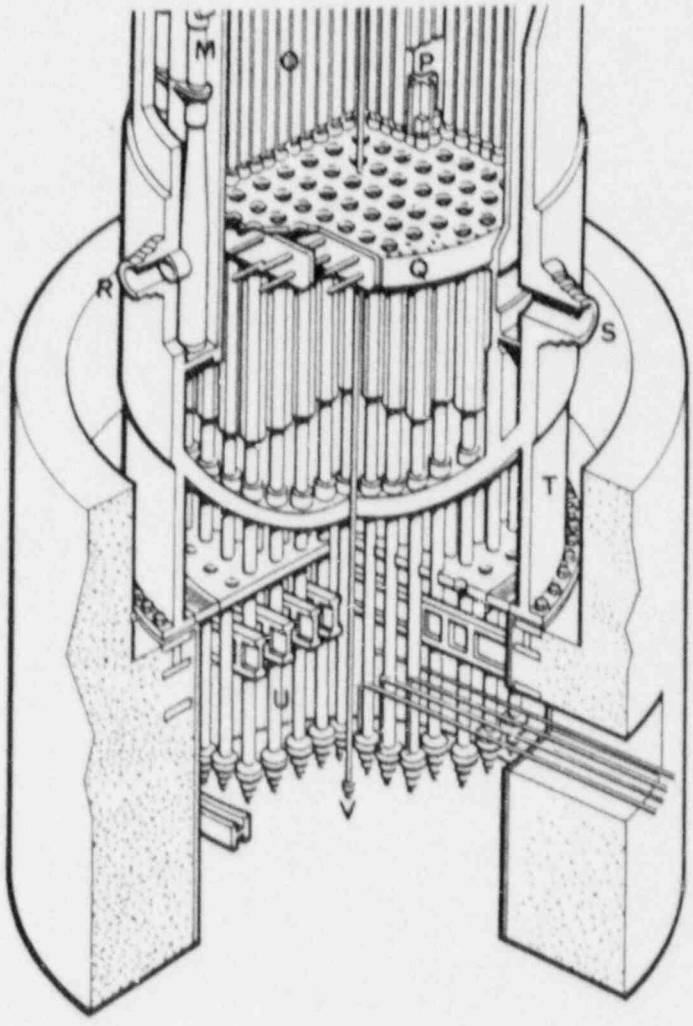

Slide 3

The lower plenum geometry of interest has been schematically illustrated in Slide 1. A more realistic perspective of the actual geometry is shown above. We can identify two potential mixing regimes. The first (or vertical mixing regime) is obtained as the mean flow streams along the control rod guides while the injected solution jets in a direction cross to it, impinging upon the nearest control rod guide tube. The second (or horizontal mixing regime) may be obtained in case some solution settles downwards having escaped mixing in the vertical regime (i.e., the fraction that was not entrained during the mixing process described above). It is characterized by the mean flow streaming cross to the guide tubes and the solution settling through it. This presentation is focused on the first mixing regime. We have also examined the second one and found it to be rather effective.

SCALING CONSIDERATIONS

FROUDE SCALING

$$Fr = \frac{U}{\sqrt{gD\frac{\Delta\rho}{\rho}}}$$

AT SMALL SCALES FORCES

LARGE DISSIMILARITY IN

$$Re \sim U\,D/\nu$$

AND MOMENTUM FLUX

Slide 4

The GE data were obtained in a 1/6-scale geometrically-scaled facility using Froude number similarity. This approach is rather limited because, as seen above, at small scales Froude number similarity causes large Reynold's number and momentum flux dissimilarities. This is particularly important in the present geometry that involves high Froude number injections (i.e., strong momentum effects) and an impinging jet geometry. These considerations led us to the decision to study this problem, experimentally, at full scale (i.e., 1:1).

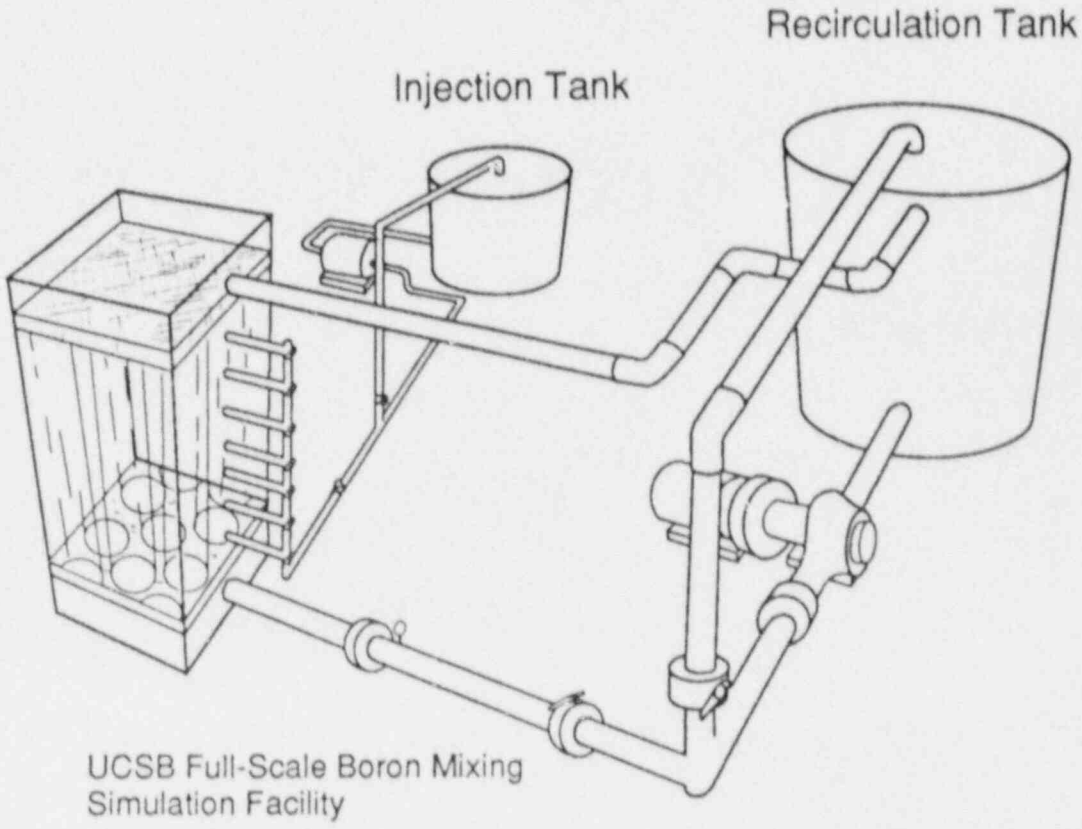

Slide 5

As shown, the UCSB facility simulates a 3×3 array of control rod guides. The injection line, also at full scale, is shown to take suction from the injection tank. In the experiments reported herein the injection consisted of a sugar/salt solution with a density of 1.3 g/cm^3 ($\sim$16% sugar and 14% salt). A positive displacement pump can provide up to $\sim$10 gpm per nozzle, and four-nozzle injections were employed in the present set of experiments. The recirculation tank (1,000 gal. capacity) holds, initially, fresh water at room temperature. The recirculation pumps can provide up to 2,300 gpm, which is more than adequate to provide simulations of up to 30% of rated flow recirculation. The recirculation flow is measured by a venturi, the injection flow by an orifice, and the salinity of inlet and outlet flows by conductivity probes. Dye injection and video records are also used to determine mixing regimes and the onset of stratification. Baffles placed within the lower plenum help even out the flow and preliminary subchannel flows measured by a dye injection technique indicate a uniform flow within $\pm$10%.

CONCLUSIONS

- ALL BORON INJECTED WITH NATURAL CIRCULATION STRONGER THAN ~ 5% OF RATED IS ENTRAINED AND CONVECTED INTO THE CORE

- CURRENT ATWS PROCEDURES COULD BE BENEFICIALLY REVISED

WORK IS CONTINUING
TO BETTER QUANTIFY RELEVANT PHENOMENA

Slide 6

The first round of visualization experiments (videos shown in the presentation) were conducted at recirculating flow rates equivalent to 15%, 10%, and 5% of rated flow. At the first two levels the injection flow was fully mixed and entrained with the recirculation flow. The 5% flow level exhibited the onset of stratification (settleing). The demarcation seems to be rather abrupt, although it would appear that the settled flow from this last case could be easily dispersed in the horizontal mixing regime mentioned in Slide 3. Future work will employ $CaC\ell_2$ solutions (up to $\Delta\rho/\rho$ of ~30%, which is considered close enough to the 40% value applicable in the reactor case) and conductivity probes as well as local velocity measurement by a Laser Doppler Anemometer (in the fibre optic mode–FOLDA). With reference to Slide 2, it is expected that, on the basis of these results, ATWS procedures could be beneficially revised. Work along these lines is also underway.

ACKNOWLEDGMENT

This work was supported by the U.S. Nuclear Regulatory Commission.

MULTI-DIMENSIONAL RCS NATURAL CIRCULATION DURING A PWR SEVERE ACCIDENT

James T. Han

Office of Nuclear Regulatory Research
U.S. Nuclear Regulatory Commission

ABSTRACT

This paper summarizes the scope, status, and the preliminary findings of the NRC-sponsored research programs addressing multi-dimensional natural circulation in the reactor coolant system (RCS) during a PWR station blackout accident in which the auxiliary feedwater to steam generators is also lost (the TMLB'accident).

1. INTRODUCTION

Multi-dimensional RCS natural circulation is buoyancy-driven coolant circulation in the steam-filled space above the water level in a PWR core. It consists of circulation flows between the uncovered core and the upper plenum (in-vessel circulation) and counter-current flows in the hot legs and steam generators (ex-vessel circulation), as shown in Fig. 1. This kind of natural circulation serves as a means of transferring the heat from the uncovered core to the upper plenum structures, hot leg piping, and steam generator tubes. As a result, the reactor coolant system (RCS) pressure boundaries may be heated to high temperature at which the structural integrity is challenged.

The multi-dimensional RCS natural circulation is likely to occur during the core uncovery period of a PWR station blackout accident in which the auxiliary feedwater to steam generators is also lost (the TMLB' accident). We are currently studying the assumed TMLB' accident in the Surry Plant, which is a Westinghouse three-loop plant. Effects being addressed are the RCS structural integrity, initial conditions and likelihood for high-pressure melt ejection that may lead to direct containment heating (DCH) and challenge containment integrity, and the release of fission products and hydrogen to the containment.

An extensive review of this issue was presented in NUREG-1265 (Ref. 1) and also in Appendix J of NUREG-1150 (Ref. 2). An independent panel of experts has reviewed the NRC-sponsored research programs addressing the issue, and the panel endorses the overall approach adopted by NRC (Ref. 3).

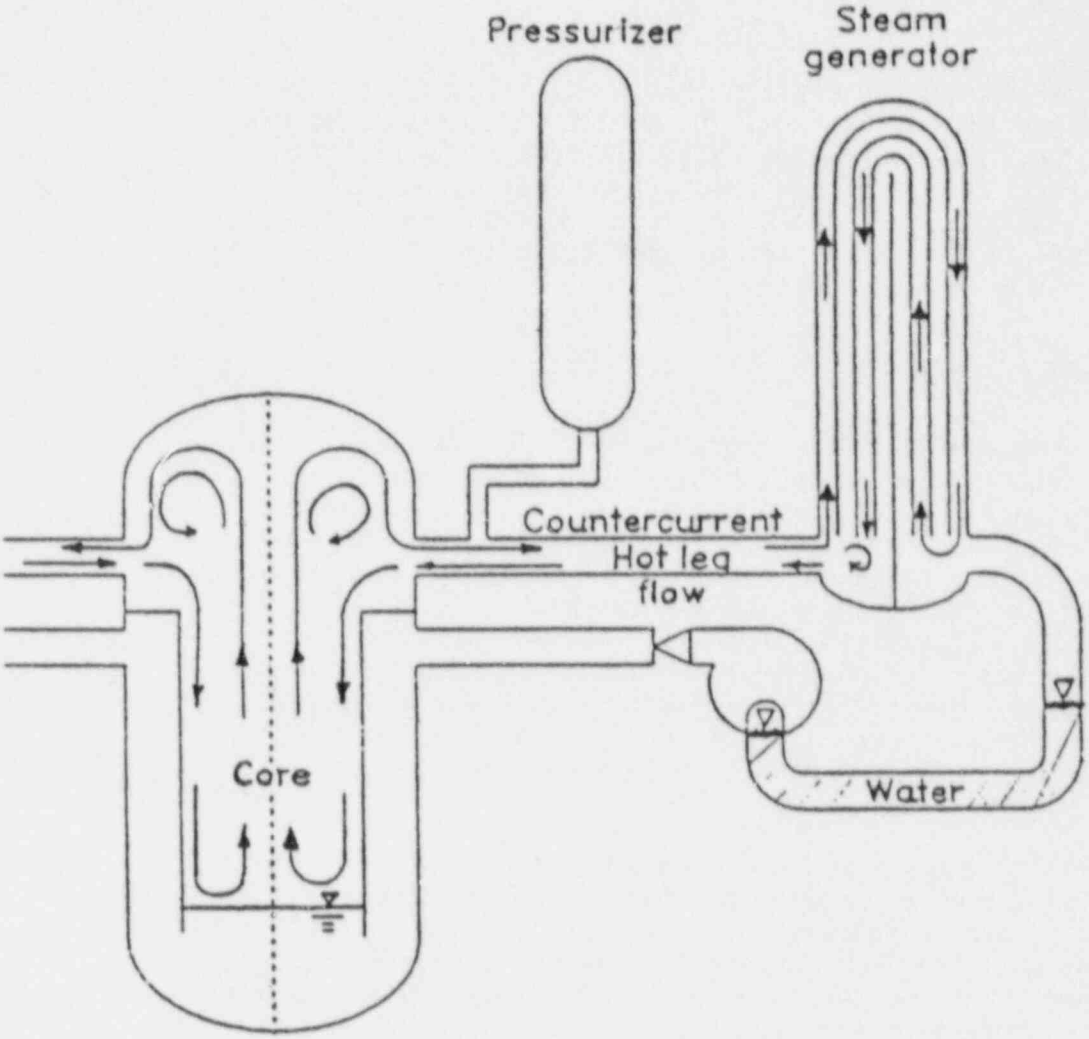

FIG. 1. A SKETCH OF MULTI-DIMENSIONAL NATURAL CIRCULATION IN THE STEAM-FILLED SPACE IN THE VESSEL, HOT LEG, AND STEAM GENERATOR TUBES OF A PWR.

2. SCOPE AND STATUS OF THE NRC-SPONSORED RESEARCH PROGRAMS

- OVERALL APPROACH: DEVELOPING INTEGRATED MECHANISTIC CODES BY USING THE STATE-OF-THE-ART GOVERNING EQUATIONS AND MODELS, VALIDATING AND IMPROVING THE CODES AGAINST RELEVANT DATA, AND USING THE CODES FOR ANALYSIS. THE PROCESS IS ITERATIVE AND IT INVOLVES THE MELPROG/TRAC AND SCDAP/RELAP5 CODES.

- COMPLETED WORK

  - O MELPROG CALCULATIONS INVESTIGATING IN-VESSEL NATURAL CIRCULATION WITH NO FISSION PRODUCT DEPOSITION HEATING OF STRUCTURES (SNL/LANL - REF. 4)

  - O SCDAP/RELAP5 CALCULATIONS ANALYZING RCS NATURAL CIRCULATION IN VESSEL/HOT LEGS/STEAM GENERATORS WITH NO FISSION PRODUCT DEPOSITION HEATING OF STRUCTURES (INEL - REF. 5)

  - O SUPPORTIVE COMMIX CALCULATIONS PROVIDING INSIGHTS ON COUNTER-CURRENT FLOWS IN HOT LEGS AND STEAM GENERATOR TUBES (ANL - REF. 6)

  - O CODE VALIDATION AGAINST DATA SIMULATING SEVERE CORE DAMAGE (INEL - REFS. 7-8)

  - O STRUCTURAL FAILURE STUDIES FOR HOT LEG NOZZLE AND PIPING, AND FOR STEAM GENERATOR TUBES OF A WESTINGHOUSE PWR (INEL - REF. 9)

- ONGOING AND FUTURE WORK

  - O MELPROG/TRAC CALCULATIONS ANALYZING RCS NATURAL CIRCULATION IN SURRY INCLUDING FISSION PRODUCT DEPOSITION HEATING OF PIPING AND STRUCTURE SURFACES (LANL/SNL)

  - O SCDAP/RELAP5 CALCULATIONS ANALYZING RCS BEHAVIOR IN SURRY FOLLOWING THE FAILURE OF RCS PRESSURE BOUNDARIES, WHICH IS CALCULATED TO OCCUR BEFORE THE FAILURE OF VESSEL LOWER HEAD (INEL)

  - O INVESTIGATION OF MEANS TO PREVENT HEGH-PRESSURE MELT EJECTION WHICH MAY CHALLENGE CONTAINMENT INTEGRITY (E.G., LATE RECOVERY OF AUXILIARY FEEDWATER AND EMERGENCY CORE COOLING SYSTEM INJECTION)

  - O SUPPORTIVE COMMIX CALCULATIONS (ANL)

  - O TMI-2 STANDARD PROBLEM EXERCISE

- SUPPORTIVE MODEL DEVELOPMENT FOR THE COUNTER-CURRENT FLOW IN A HOT LEG AND MIXING PROCESS IN STEAM GENERATOR INLET PLENUM (FLUID PHYSICS IND/SAI, OCT. 1987 - MARCH 1988)

- CODE VALIDATION AGAINST SEVERE CORE DAMAGE DATA FROM NRU, CORA, PBF, ACRR, TMI-2 ACCIDENT, ETC. (INEL, LANL/SNL)

- COMPARISON WITH EPRI-SPONSORED NATURAL CIRCULATION EXPERIMENTS (REF. 10) AND ANALYSIS (REF. 11: CORMLT CALCULATIONS FOR RCS NATURAL CIRCULATION WITH NO FISSION PRODUCT DEPOSITION HEATING OF SURFACES)

3. PRELIMINARY FINDINGS AND RECOMMENDATIONS

BASED ON THE PREDICTION OF THE TMLB' CALCULATIONS FOR THE SURRY PLANT OR FOR A SIMILAR WESTINGHOUSE PWR WITHOUT MODELING FISSION PRODUCT DEPOSITION HEATING OF PIPING AND STRUCTURE SURFACES, THE SURGE LINE (CONNECTING THE PRESSURIZER TO A HOT LEG) OR THE HOT LEG CONNECTION AT THE REACTOR VESSEL IS LIKELY TO FAIL BEFORE THE VESSEL LOWER HEAD FAILURE (REFS. 1, 2, 4, 5, AND 11). HOWEVER, UNCERTAINTIES IN THE CALCULATIONS ARE STILL UNKNOWN AND SHOULD BE DETERMINED. FURTHERMORE, THE LACK OF EVIDENCE FOR THIS KIND OF NATURAL CIRCULATION IN THE TMI-2 PLANT NEEDS TO BE RESOLVED.

THE ONGOING AND FUTURE WORK DISCUSSED EARLIER IS NEEDED TO IMPROVE OUR UNDERSTANDING ON THE ISSUE, TO ESTIMATE UNCERTAINTIES IN THE CALCULATIONS, AND TO DEVELOP A STRATEGY FOR PREVENTING HIGH-PRESSURE MELT EJECTION WHICH MAY CHALLENGE CONTAINMENT INTEGRITY.

4. REFERENCES

1. U.S. NUCLEAR REGULATORY COMMISSION, "UNCERTAINTY PAPERS ON SEVERE ACCIDENT SOURCE TERMS," NUREG-1265, CHAPTER 2, MAY 1987.

2. U.S. NUCLEAR REGULATORY COMMISSION, "REACTOR RISK REFERENCE DOCUMENT (DRAFT)," NUREG-1150, APPENDIX J.3, FEBRUARY 1987.

3. H. KOUTS, "REVIEW OF RESEARCH ON UNCERTAINTIES IN ESTIMATES OF SOURCE TERMS FROM SEVERE ACCIDENTS IN NUCLEAR POWER PLANTS," NUREG/CR-4883, PP. 26-36, APRIL 1987.

4. J. E. KELLY, R. J. HENNINGER, AND J. F. DEARING, "MELPROG-PWR/MOD1 ANALYSIS OF A TMLB' ACCIDENT SEQUENCE," NUREG/CR-4742, JANUARY 1987.

5. P. D. BAYLESS, "NATURAL CIRCULATION DURING A SEVERE ACCIDENT: SURRY STATION BLACKOUT," IDAHO NATIONAL ENGINEERING LABORATORY, EGG-SSRE-7858, SEPTEMBER 1987.

6. H. M. DOMANUS ET AL., "COMMIX ANALYSIS OF NATURAL CONVECTION PHENOMENA IN A THREE-LOOP PWR DURING A TMLB' TRANSIENT," ARGONNE NATIONAL LABORATORY, ATHRP-32, MAY 1987.

7. L. J. SIEFKEN ET AL.,"ASSESSMENT OF SCDAP AND SCDAP/RELAP5 USING THE PBF SFD TESTS," IDAHO NATIONAL ENGINEERING LABORATORY, INFORMAL REPORT, JANUARY 1986.

8. G. A. BERNA, INEL, LETTER TO J. T. HAN, USNRC, "POSTTEST ANALYSIS OF OECD LOFT EXPERIMENT LP-FP-2 USING THE SCDAP/RELAP5 CODE, GAB-27-86, JUNE 27, 1986.

9. B. L. HARRIS, V. N. SHAH, AND G. E. KORTH, "CREEP RUPTURE OF THREE COMPONENTS OF THE REACTOR PRIMARY COOLANT SYSTEM DURING THE TMLB' ACCIDENT," IDAHO NATIONAL ENGINEERING LABORATORY, EGG-EA-7431, NOVEMBER 1986.

10. W. A. STEWART, A. T. PIECZYNSKI, AND V. SRINIVAS, "EXPERIMENTS ON NATURAL CIRCULATION FLOW IN A SCALE MODEL PWR REACTOR COOLANT SYSTEM DURING POSTULATED DEGRADED CORE ACCIDENTS," PROCEEDINGS OF THIRD INTERNATIONAL TOPICAL MEETING ON REACTOR THERMAL HYDRAULICS, AMERICAN NUCLEAR SOCIETY, VOL. I, P. 10.C-1, OCTOBER 1985.

11. B. R. SEHGAL ET AL., "EFFECTS OF NATURAL CIRCULATION FLOWS ON PWR SYSTEM TEMPERATURES DURING SEVERE ACCIDENTS," PROCEEDINGS OF 23RD ASME/AICHE/ANS NATIONAL HEAT TRANSFER CONFERENCE (DENVER, COLORADO), AMERICAN NUCLEAR SOCIETY, AUGUST 1985.

DIRECT CONTAINMENT HEATING: IS THE HAZARD REAL?

Tim M. Lee

U.S. Nuclear Regulatory Commission

Abstract

The state of understanding of the DCH issue is reviewed. It appears that neither the analytical tools nor the experimental data that are currently available are adequate to quantify the effects of direct containment heating in a severe reactor accident. It is, therefore, difficult to estimate the hazard of DCH at this time. An estimate of the probable range of containment pressurization due to DCH has been made and discussed here. The NRC research programs are also discussed.

Introduction

A severe reactor accident may involve core melting while the reactor coolant system remains pressurized. If the bottom head of the reactor vessel is breached by molten core materials in such a sequence, a high pressure melt ejection would result. The ejected materials are likely to be dispersed out of the reactor cavity into surrounding containment volumes as fine particles transferring thermal energy to heat the containment atmosphere. In addition, metallic components of the core debris can react with oxygen and steam in the atmosphere to generate a large amount of chemical energy to heat and pressurize the containment still further. This complicated physical and chemical process is known as direct containment heating (DCH). The peak containment pressure is normally attained within seconds after the melt ejection. A large amount of aerosols that are likely to contain refractory fission products could be generated in a high-pressure melt ejection. If the containment should fail from the DCH loading, radiological consequences could be serious.

The possibility that core debris could be dispersed out of the reactor cavity in the event of a pressurized ejection of core melt from the reactor vessel was first identified in Zion Probabilistic Safety Study.[1] While conducting tests[2,3] to confirm such debris dispersal, Sandia National Laboratories (SNL) became aware that the dispersed debris is likely to be sprayed into the containment atmosphere resulting in DCH. The Containment Loads Working Group expressed concern over this possibility and formed the DCH Subcommittee to investigate the potential importance of DCH effects.[4] The committee reached a consensus that the DCH effects would not be large if the reactor vessel failed under low pressure. On the potential importance of DCH effects in high pressure scenarios, the subcommittee was divided in its opinion. A group of analysts, including experts from Electric Power Research Institute (EPRI) and Argonne National Laboratory (ANL), estimated, from the results of EPRI sponsored tests at ANL, that thermal energy no greater than that stored in 2% of

the initial melt would enter into DCH; the bulk of the ejected melt would be trapped by structures and quenched by water in the containment. However, a larger number of the subcommittee members, including experts from SNL, believed that DCH involving a substantial fraction of the ejected melt (16 to 50%) cannot be ruled out. This group argued that the effectiveness of water as the quenching medium had not been demonstrated, that a debris particle of the expected size (less than 1 mm) could release its thermal and chemical energy on a time scale of just a few seconds, and that metal-steam reactions followed by hydrogen recombination could not be precluded.

Clearly, an integrated research program that coordinates analytical and experimental activities is needed, and planned, to resolve this highly complex and potentially hazardous issue.

Analyses

As a part of a standard problem exercise for the Containment Loads Working Group, SNL used CONTAIN and DHEAT codes to analyze DCH effects for standard problems SP-1 (Zion) and SP-2 (Surry).[4] The SP-2 results are reproduced in Figure 1. The method of analyses was basically a lumped parameter approach; chemical reactions and heat transfer between core debris and the containment atmosphere were assumed to be completed, and thermal equilibrium attained, instantaneously. Effects of heat losses to containment heat sinks were not included. Figure 1 shows that participation of approximately 25% of the core inventory in DCH could raise the pressure in Surry containment to 9.2 bars, which was estimated by the Containment Performance Working Group to be the ultimate pressure capacity for the Surry containment. These results are believed to be close to an upper bound because of conservative assumptions made in the calculations. While preparing for NUREG-1150, the Reactor Risk Reference Document,[5] SNL recalculated SP-2 using a modified version of the CONTAIN code[6] that included rate equations for heat transfer and chemical reactions. Ex-vessel metal-steam reactions were calculated with a single droplet model. Results of these revised calculations[6] generally showed more moderate pressure rises compared with Figure 1. Nevertheless, the possibility remains that, in the event of a high pressure melt ejection, the integrity of the containment could be challenged. Uncertainties involved in these calculations are large, however.

How well a computer code can predict DCH effects depends on how well relevant phenomena are modeled. Unfortunately, many phenomena that strongly affect the outcome of DCH are not yet included in the codes used to analyze DCH. For example, none of the presently available computer codes model the intricate process of debris transport, including phenomena inside the reactor cavity and debris-structure interactions. This shortcoming can best be illustrated when we compare the CONTAIN calculations of DCH-1[7] and DCH-2[8] tests. Figure 2 provides results of the post-test calculation of DCH-1 that matched the test data remarkably well, yet when the same code was used to predict the results of DCH-2, it over-predicted the peak pressure by about 55% (Figure 3),[8,9] although there was only a minor difference in the test configurations (Figure 4). The recent finding that extensive metal-steam reactions can take place in, and around, the reactor cavity[4,6,10] may moderate the need for a detailed debris transport analysis because hydrogen generated in such reactions can migrate relatively freely to other parts of the containment and reacts with available

oxygen to release the remaining chemical energy. However, the expert panel assembled by the Brookhaven National Laboratory (BNL) to review NRC research programs in major source term uncertainty areas pointed out in its report[11] that they believe the single droplet model used in the CONTAIN code substantially over-predicts the chemical reaction rates. Moreover, the relative velocity between the debris particle and interacting gases, which is an important parameter in both thermal and chemical interactions, is a user supplied parameter in the CONTAIN analyses.

Experimental Data

Results of experiments are no more conclusive. Available test data are limited to start with, but a bigger problem is the lack of a scaling law that can be used to interpret the test data and extrapolate them for evaluation of risk associated with DCH in severe reactor accidents. SNL has proposed an alternative to develop analytical models of phenomena important to DCH from the test data to be incorporated in a containment code for DCH analyses.

ANL has completed a series of tests (CWTI) that were sponsored by EPRI. SNL, under NRC funding, has completed the System Pressure Injection tests (SPIT) and the High Pressure Streaming tests (HIPS), and is continuing with the Surtsey/DCH tests. BNL is conducting studies of debris transport with low temperature simulant tests. These activities are discussed below. In addition, the United Kingdom Atomic Energy Authority (UKAEA) is embarking on a program similar to that at BNL, and Fauske and Associates, Inc. are reported to have conducted small scale debris transport tests. Reports on neither of these tests are available so that we are unable to include these activities in this review.

ANL Experiments

ANL experiments as reported by the Industry Degraded Core Rulemaking Program (IDCOR)[12] used an apparatus that included a thermite vessel representing the reactor pressure vessel, an interaction chamber to represent a reactor cavity, a pipeway simulating an instrument tunnel, and an expansion vessel simulating the containment. The interaction chamber, the pipeway, and the expansion chamber were all of steel construction. A partial partition was provided in the expansion chamber to simulate a containment structure. The experiments used molten materials composed of uranium dioxide, zirconium dioxide, and stainless steel to simulate the core melt. The melt were ejected into the interaction chamber by gas that was pressurized to a level ranging from 0.21 MPa (30.5 psia) to 5.7 MPa (826.5 psia). The facility was approximately a 1/30th linear scale of the Zion plant configuration, but no attempt was made to maintain geometric similarity.

A separate series of tests using Wood's metal as the melt simulant was also conducted to investigate the characteristics of core debris dispersal. Wood's metal has a melting point of 73°C. The injection pressure used in this series of tests ranged from 0.25 MPa (36 psia) to 1.4 MPa (200 psia).

The corium tests showed a sweepout fraction of 1 to 60 percent and a peak pressure rise from 0.12 MPa (17.5 psi) to 0.38 MPa (55 psi). The temperature rise ranged from -4 to 50°C. These results do not include a contribution from oxidation of metallic components since the tests were conducted in an inerted expansion chamber atmosphere. The Wood's metal tests showed that the fraction dispersed out of the test cavity ranged from 10 to 90 percent.

More recently, ANL has conducted some more tests with regular air in the expansion chamber and with the partition that simulated containment structure removed. Significantly higher pressure rises resulted. In CWTI-13,[13] the most severe test conducted to date at the facility, a maximum pressure of 0.31 MPa (45.5 psia) was measured in the expansion chamber although only 8.7% of the ejected melt was dispersed into the chamber.

SNL Experiments

Nineteen tests were conducted in the SPIT series and eight in the HIPS series[2].

Most of the SPIT tests were for scoping and technology development; only the last two provided useful data. Molten materials produced by a thermite reaction between iron oxide and aluminum were used to simulate the core melt. The melt generator was pressurized to a level ranging from 3.3 MPa (480 psia) to 11 MPa (1600 psia) by air, nitrogen, or carbon-dioxide. All except the last two SPIT tests were conducted outdoors.

SPIT-18 and SPIT-19[3] were conducted with an interaction chamber that simulated a containment volume; the apparatus was placed in a metal shed that had an estimated pressure rating of 3 psig. A concrete cavity simulating a 1/20th linear scale model of the Zion reactor cavity was used in SPIT-19 while an alumina cavity was used in SPIT-18.

In SPIT-19, 95 percent of the ejected melt was dispersed out of the test cavity, while only 58 percent was dispersed in SPIT-18. The lower dispersal in SPIT-18 was attributed to higher heat loss, and consequently higher freezeup of the debris, in the alumina cavity. Measured pressure rises of 3.5 and 2 psi were not considered meaningful because the interaction chamber suffered substantial damages in both tests that resulted in large leakage. It was estimated that 1 to 5 percent of the ejected melt was aerosolized.

The HIPS test apparatus included a 1/10th linear scale model of the Zion reactor cavity. The mass of the melt was scaled to that of the reactor core, but the volume and geometry of the melt generator were not scaled to those of the reactor vessel.

A total of eight tests were conducted in the HIPS series. HIPS-4W and HIPS-6W[14] were conducted with a water-filled test cavity while in HIPS-7C[15] structure was added at the exit of the test cavity to simulate the instrument shaft and the seal table area of the Zion plant. In HIPS-8C,[15] the annular gap around the reactor vessel of Zion Unit 1 was simulated to investigate the potential for core debris dispersal directly into the upper containment dome via this gap.

In all tests, practically all molten materials ejected from the melt generator were dispersed out of the test cavity even at a pressure as low as 3.3 MPa (480 psia). The presence of water in the test cavity did not appreciably affect the fraction of dispersal. High-speed movies showed that a slug of water was expelled ahead of dispersing debris in both HIPS-4W and HIPS-6W. A pressure spike on the order of a 1,000 psi was measured in the cavity following the melt ejection. The reinforced concrete test cavity was destroyed in both tests, and in HIPS-6W the whole test facility was lifted 6 feet in the air.

No appreciable retention of debris was observed in HIPS-7C where the additional structure was expected to trap dispersing debris. In HIPS-8C, approximately one-third of the dispersed debris escaped through the annular gap. This fraction is roughly equal to the ratio of the flow area through the gap to the total outflow area, supporting the theory that the predominant mechanism for debris dispersal is entrainment by a high-velocity gas flow. A large cloud of aerosols was observed in each HIPS test.

Surtsey is a steel vessel approximately 12 feet in diameter and 40 feet high. Its volume is approximately that of a 1/10th linear scale of a large, dry containment. The pressure rating of the Surtsey vessel is 150 psig and the maximum operating temperature is 650°F. The facility became operational in 1986 and three tests have been completed to date (DCH-3 test results have not been published yet); the fourth test will be conducted in October 1987. A total of eleven Surtsey/DCH tests are currently planned. The test matrix is provided in Table 1.

In all completed DCH tests, the melt generator and the test cavity were placed inside the Surtsey vessel. A 1/10th scale model of the Zion reactor cavity was used. 20 kg of an iron oxide, aluminum thermite melt were involved in DCH-1[7] versus 80 kg in DCH-2.[8] In DCH-1 a chute at the exit of the cavity directed the dispersing debris vertically upward while in DCH-2 the debris jet is allowed to impinge on the side wall of the vessel at an angle approximately 26° from the vertical without a chute. 11.6 kg of the debris were collected in the Surtsey vessel following the DCH-1 test where a maximum pressure rise of 0.133 MPa (19.4 psi) was measured. The corresponding values for DCH-2 are 91.3 kg and 0.31 MPa (45 psi). The total mass of debris collected after each test was greater than the initial thermite charge because of materials eroded by the melt, oxygen uptake from the chamber atmosphere in the chemical reactions, and materials adhered to the debris removed from the cavity and the chamber walls. The fraction of the ejected mass aerosolized was estimated to be 2 to 16% in DCH-1 and 1 to 6.6% in DCH-2.

BNL Experiments

BNL is using low temperature melt simulants to investigate the hydrodynamics of the debris dispersal during a high pressure melt ejection. Apparatus used consists of 1/42nd scale models of operating plants. Water and Wood's metal are being used to simulate the core melt. The plan is to study several plant configurations to characterize the effect of containment structures on the flow fields of gas and debris.

Tests in three different reactor cavities, Zion, Surry, and Watts Barr, have been completed. These tests results appear to show that the fraction of the ejected "melt" dispersed out of the reactor cavity is insensitive to the cavity design. It is interesting to note that the Surry and the Watts Bar cavities are classified by IDCOR as non-dispersive. BNL is continuing with tests on containment models that include major structures. A high speed movie taken during a test in the Zion containment model, using water as the melt simulant, recorded some fascinating aspects of the process of debris dispersal; notably among them is re-entrainment of debris deposited on the containment floor.

BNL's program also includes a scaling study[16] that identifys a set of dimensionless parameters whose values must be held constant to preserve physical similarities between the test and the plant conditions under investigation. The number of similarity parameters identified is now eleven. It is not possible to match all eleven parameters in designing tests so that BNL must exercise engineering judgment in matching those that were considered important.

A major limitation in BNL's program is the use of low temperature melt simulants. This would be an excellent program for the study of debris transport if the hydrodynamic phenomena are independent. Unfortunately, for the process of debris dispersal and DCH, heat transfer, chemical reactions, and hydrodynamics of the gas flow and debris transport are all interrelated; they affect one another. BNL attempted to partially compensate for this shortcoming by matching the Mach number of the blowdown flow in its tests. Many other effects that are important to DCH are not addressed; for example, melt-structure interactions and change in transport properties of the molten core materials with temperature are the more important ones among them.

Estimate of Hazard

It is evident from the above discussion that neither the analytical tools, nor the experimental data currently available, are adequate to quantify the DCH effects in a severe reactor plant accident. To estimate the hazard associated with this complicated phenomenon with the present state of understanding therefore involves a high degree of uncertainty. Attempts have been made previously by the Containment Loads Working Group DCH subcommittee[4] and in the Severe Accident Risk Rebaseline Program[17] to estimate the peak containment pressure, using subjective judgment of the experts.

A more systematic approach was adopted for such estimation in NUREG-1265, Uncertainty Papers on Severe Accident Source Terms.[18] Parameters that affect the containment heating were identified. A likely range of the value for each parameter was determined from available information, and degrees-of-belief, or the probability distribution over the range, assigned. Sensitivities of the containment pressure rise to variations in these parameters were established from results of available code calculations. Random sampling was made of combinations of these parameters, and the containment pressure rises and associated probabilities, corresponding to chosen combinations, were calculated using the relationship discussed above. This approach still required engineering judgment where the state-of-understanding lags, but it has an advantage

that areas of uncertainties and their contributions to the overall uncertainty are clearly identified. It is possible, therefore, to program the research tasks to address areas of uncertainties in preferential order that will reduce the overall issue uncertainty most effectively.

Input and results of such calculations in NUREG-1265 are reproduced in Appendix A as an example to illustrate the method. Ranges and degrees-of-belief used for the input represent the judgment only of the author and the result should be considered in that context. For simplicity, it was assumed in the calculations that all the parameters are non-interacting and that sensitivities of the containment pressure rise to variations in these parameters are linear, but the method works as well without these constraints.

NRC Research Plan

Much progress was made in the last couple of years regarding the understanding of DCH phenomenon. Among the major findings are the ex-vessel metal steam reactions and the effect of the geometrical scale of the facility. Both BNL and SNL predicted from their calculations that metallic Zr and Fe in the melt could rapidly be oxidized by steam in the vicinity of the reactor cavity. Because hydrogen generated in such reactions can be transported through the containment much easier than core debris particles, transport of the debris particles to open containment volumes no longer is a prerequisite for DCH. Also, many experts now agree that the larger the scale of the facility, the more extensive the containment heating is likely to be because of the longer debris flight times and hence reaction times. Experimental data are needed to confirm and quantify these effects. The on-going NRC programs at SNL and at BNL are expected to address such needs and enhance our phenomenological understanding to reduce the uncertainty of the issue.

Ongoing and planned NRC research activities are summarized below. How much research can be performed, and how soon, depends on the available funding level.

On-Going Research

Surtsey/DCH Tests

This program is being relied on to generate a large scale test data base for analytical modeling of processes important to DCH. Currently, the tests are being performed at a rate of one test per quarter. Eleven tests are planned (Table 1).

BNL Program

This program includes small scale simulant tests, scaling studies, and analytical modeling of separate effects mostly related to core debris transport. Currently, the experimental effort is concentrated on investigation of the effect of containment structures on the debris transport.

Low Pressure DCH Cut-off

SNL will conduct several HIPS type tests at variable ejection pressure to investigate a possible low pressure cut-off for the core debris dispersal and DCH. This task is a part of the larger NRC program to determine if depressurizing the RCS to preclude high pressure melt ejection is feasible and practicable.

Analyses

Analytical activities are being consolidated at SNL who will use CONTAIN for the DCH analyses.

Planned Research

Tests for Geometrical Scaling

As discussed above, there is evidence that the DCH effects will be more extensive in a larger facility. Experimental data are needed to quantify this effect. It appears that the ANL facility at 1/30th scale and the SNL facility at 1/10th scale are most appropriate for such an investigation.

Tests with Prototypical Melts

Neither SNL tests, nor the BNL tests used a melt that is representative of molten reactor core materials. Tests with prototypical melts are needed to resolve controversies regarding the melt temperature, heat content, reaction rates, etc. A pressurized melt generator, possibly utilizing induction heating, is needed for such tests.

Tests for Chemical Reaction Rates

The expert panel[11] that reviewed the DCH research programs indicated that the single droplet model currently used to calculate metal-steam reactions in DCH analyses may significantly over-predict the rate of hydrogen generation. Test data are needed to assess the adequacy of the model.

TABLE 1

DCH TEST MATRIX
SURTSEY DIRECT HEATING FACILITY

Test	Characteristic
1	Small mass (20 kg)
2	Large mass (80 kg)
3	Surry cavity
4	In-containment structures
5	Defined flow paths
6	Inert atmosphere
7	Air, steam, & H_2
8	Water sprays
9	Corium melt
10	Water-filled cavity
11	Shallow water pool

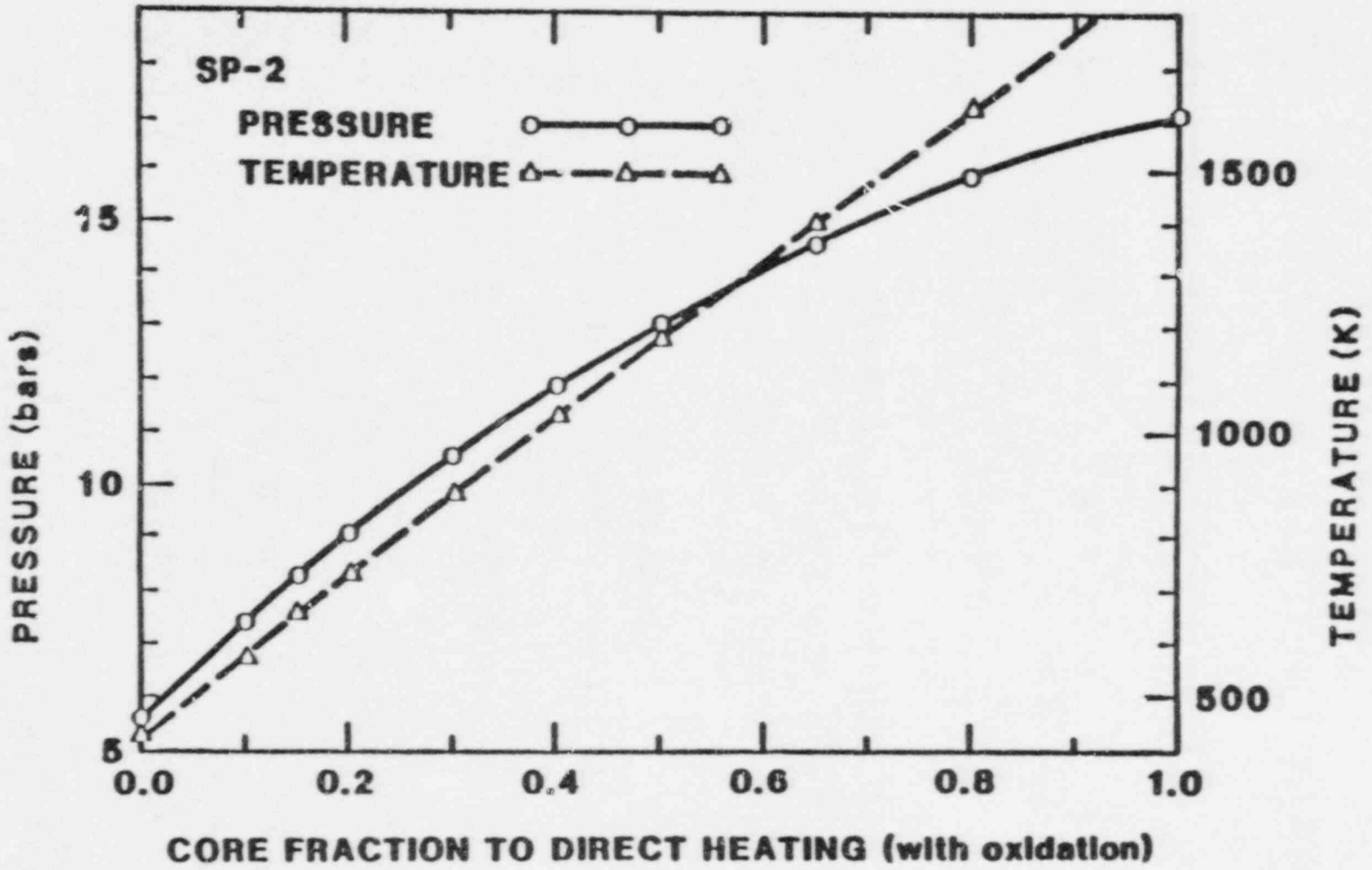

Figure 1 SP-2 pressure and temperature as a function of core fraction involved in direct heating (with metal oxidation)

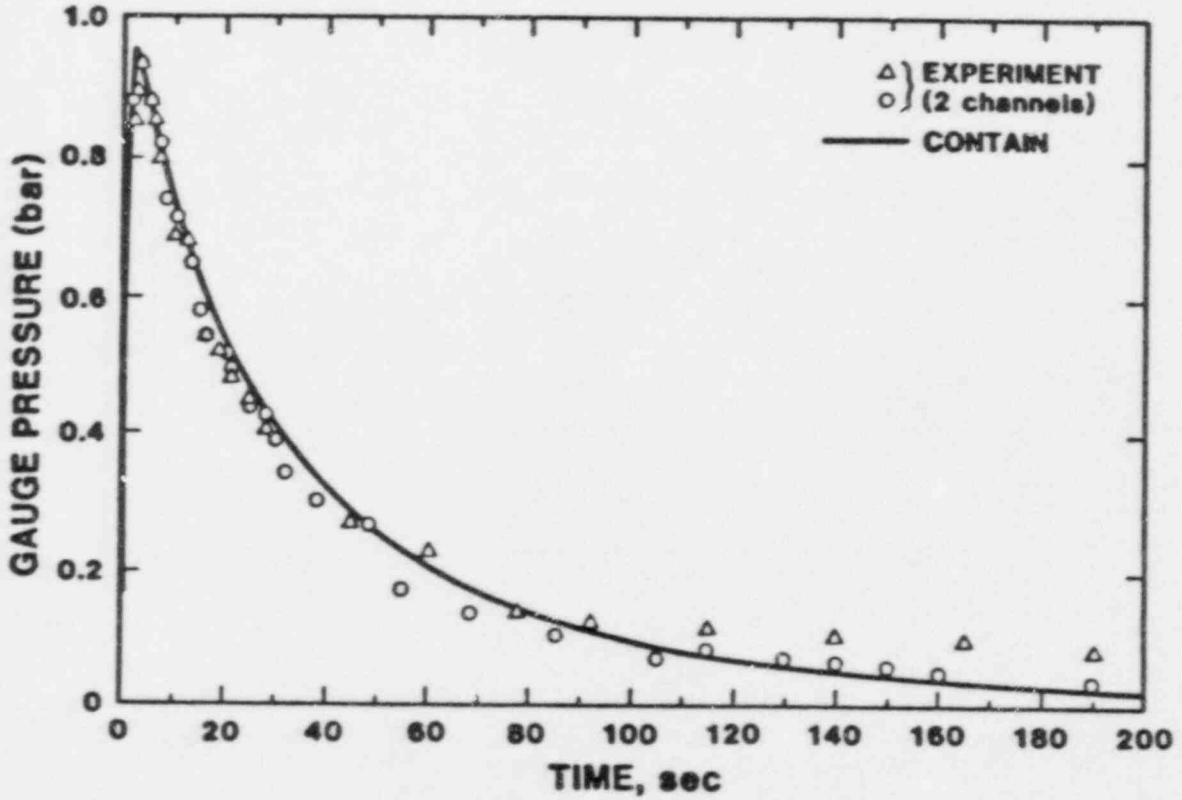

Fig. 2 Comparison of experimental results and CONTAIN predictions for the first Surtsey direct containment heating test, DCH-1.

FIGURE 3

DCH-2 TEST DATA VERSUS CONTAIN PREDICTION

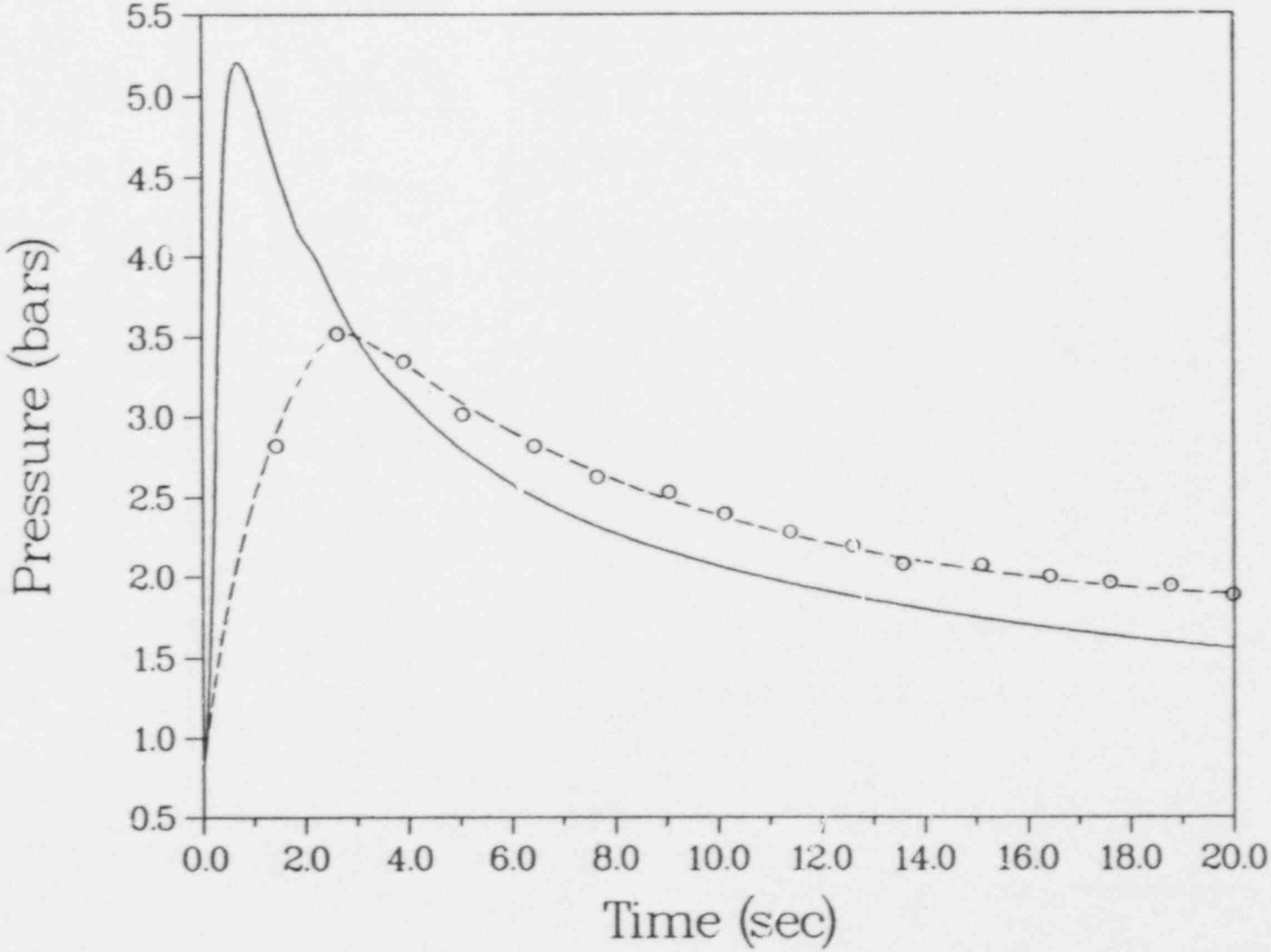

FIGURE 4 -- DCH TEST CONFIGURATIONS

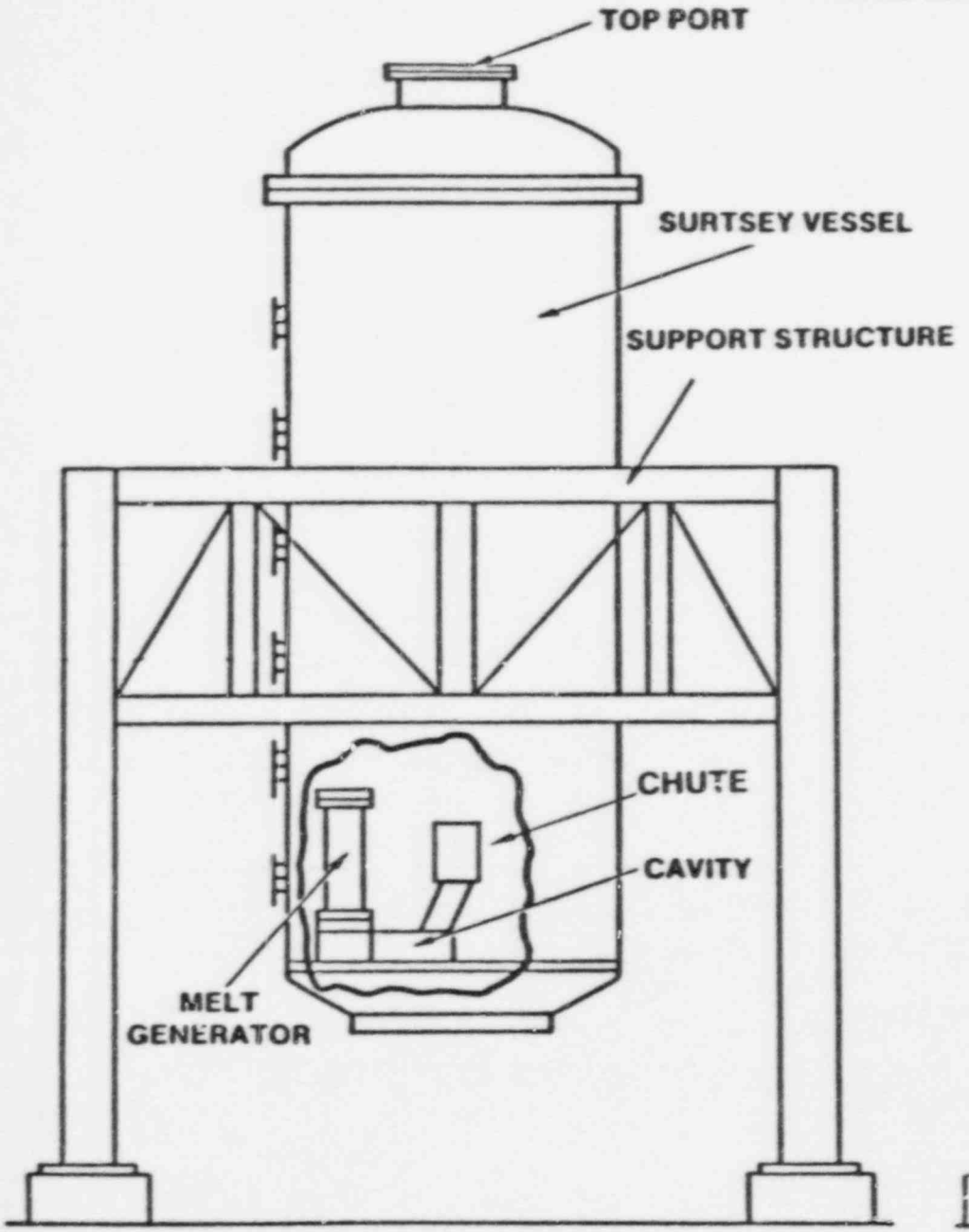

DCH-1

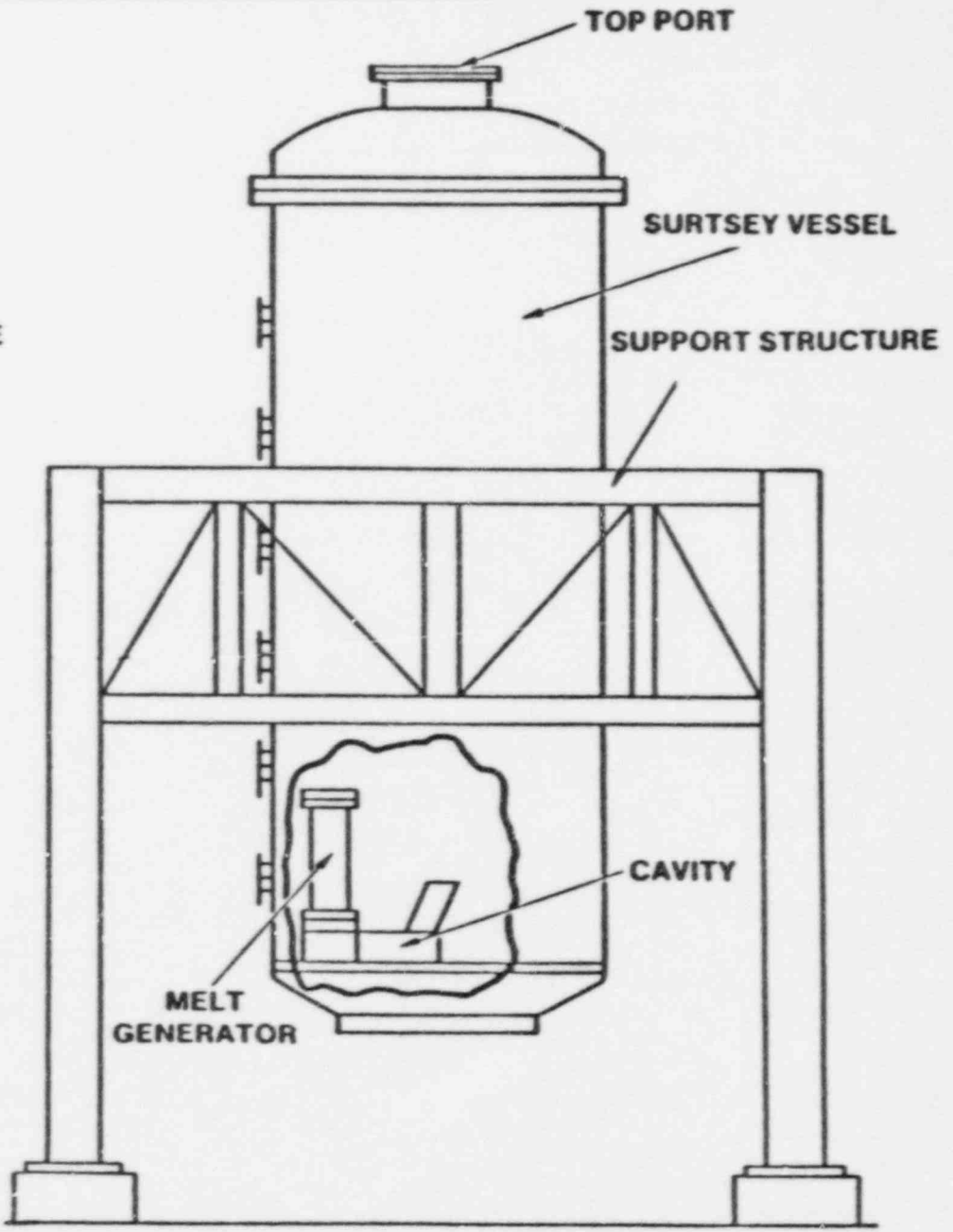

DCH-2

APPENDIX

UNCERTAINTIES ESTIMATE

Figure A.1 is a revised result of DHEAT code analyses for the Containment Load Working Group (CLWG) Standard Problem SP-2 that excluded the effect of the steam spike. It will be used as the basis for our estimation of uncertainties in the pressure rise in Surry Containment due to DCH. Sensitivities of the pressure rise to changes in the value of various parameters suggested in Table A.1 are an approximation from results of later DHEAT analyses. Ranges, degrees-of-belief, and sensitivities provided in Table A.1 were then sampled by a Latin hypercube procedure[19,20,21] to compile a composite peak containment pressure versus probability curve that is shown on Figure A.2.

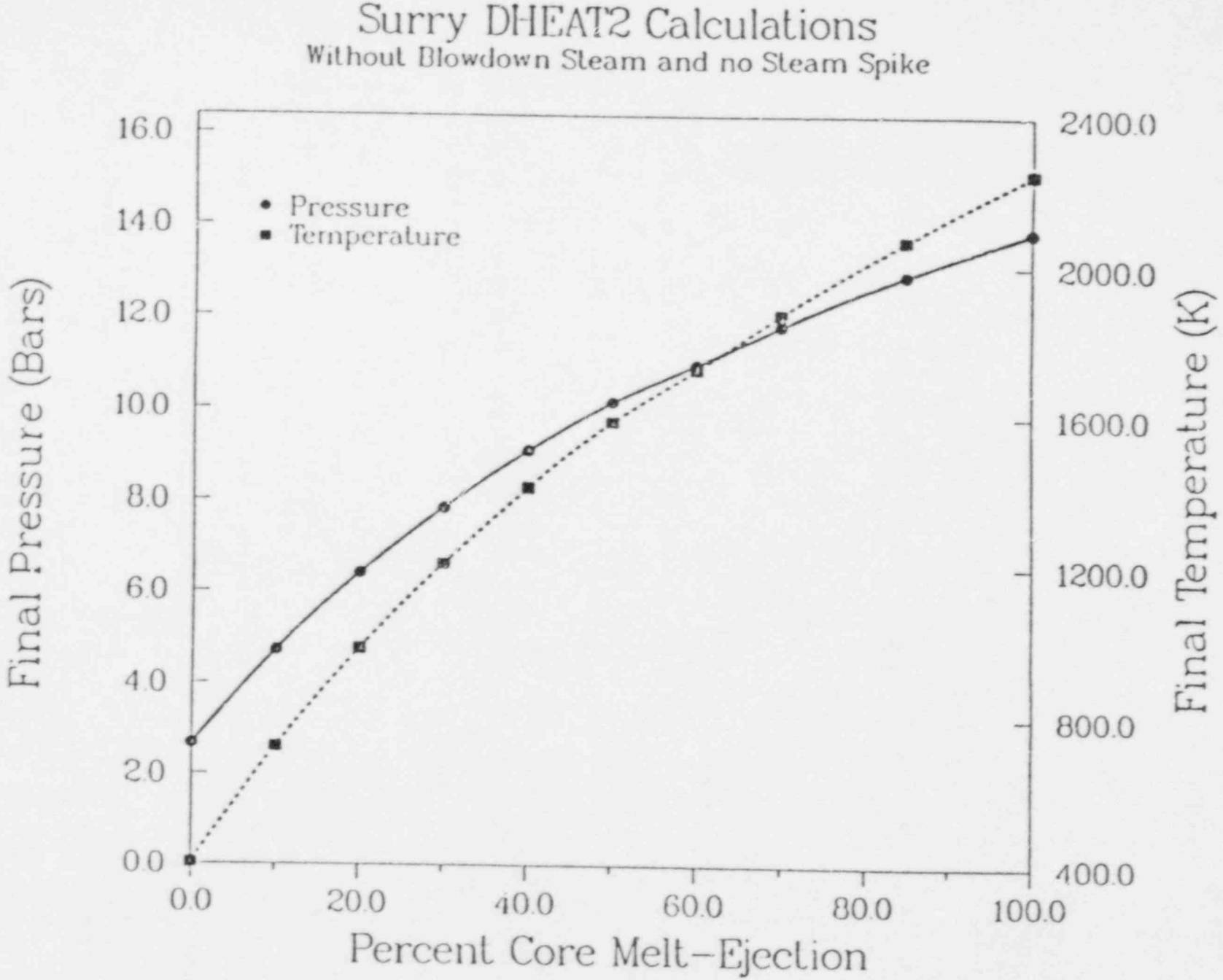

Figure A.1 Surry DHEAT2 calculations.

Table A.1 Surry direct containment heating (input for statistical analysis of pressure rise versus probability).

1. Reactor Coolant System Pressure (0-2400 psig)

Range	Degree-of-Belief (DOB)
1,000 psig and up	0.1
600 - 1,000 psig	0.2
below 600 psig	0.7

Sensitivity: Considered here is only the effect of the reactor coolant system steam inventory on containment pressurization. Linear interpolation has been used for intermediate values.

Add for the range	(+)	18 - 25 psi 0 - 2,400 psig	$= F_1$

2. Melt Temperature (1,800 - 3,100 K)

Range	DOB
2,500 - 3,100 K	0.2
2,300 - 2,500 K	0.65
1,800 - 2,300 K	0.15

Sensitivity

Multiply for the range	(x)	0.85 - 1.10 1,800 - 3,100 K	$= F_2$

3. Fraction of Core Melted and Ejected (20 - 80%)

Range	DOB
60 - 80%	0.3
50 - 60%	0.5
20 - 50%	0.2

Sensitivity

No correction from Figure A.1. Value read from Figure A.1 = P_3

Table A.1 (continued)

4. Unoxidized Metal Contents in Melt (20 - 70%)

Range	DOB
55 - 70%	0.25
40 - 55%	0.5
20 - 40%	0.25

Sensitivity

Multiply for the range (x) 0.8 - 1.0 (20 - 70%) = F_4

5. Effect of Water (0 - 50% quenched)

Range	DOB
0 - 15%	.3
15 - 30%	0.4
30 - 50%	0.3

Sensitivity

Multiply for the range (x) 1.0 - 0.85 (0 - 50%) = F_5

6. Effect of Structure (75 - 100% dispersed)

Range	DOB
90% and up	0.85
75 - 90%	0.1
below 75%	0.05

Sensitivity

Multiply for the range (x) 0.85 - 1.00 (75 - 100%) = F_6

7. Completeness of Thermal and Chemical Interactions (50 - 95%)

Range	DOB
85 - 95%	0.25
70 - 85%	0.6
50 - 70%	0.15

Table A.1 (continued)

Sensitivity

Multiply	(x)	0.63 - 0.97 50 - 95%	= F_7

8. Hydrogen Recombination (0 - 6% H_2 by volume)

Range	DOB
5 - 6%	0.2
2 - 5%	0.6
0 - 2%	0.2

Sensitivity

Multiply for the range	(x)	1.0 - 1.23 0 - 6% H_2	= F_8

Estimated Peak Pressure

$P_{max} = P_3 \times F_2 \times F_4 \times F_5 \times F_6 \times F_7 = F_1 = P_o (F_8-1)$

$P_o = P_3$ at 0% core fraction = 2.67 bars (Fig. A.1)

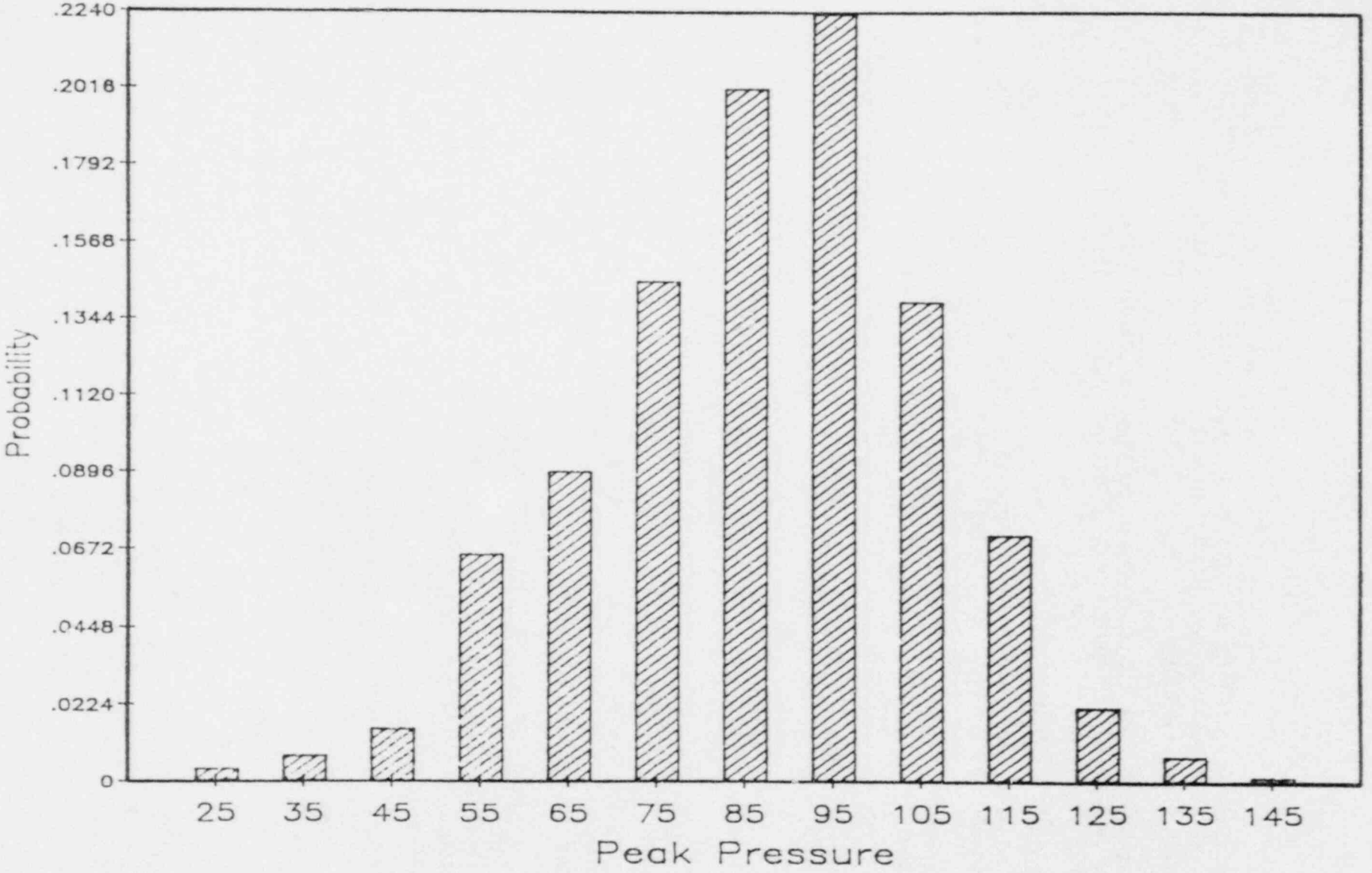

Figure A.2 Estimated peak pressure in direct containment heating for Surry.

REFERENCES

1. Commonwealth Edison Company, "Zion Probabilistic Safety Study," September 1981.

2. W. W. Tarbell, J. E. Brockman, and M. Pilch, "High Pressure Melt Streaming (HIPS) Program Plan," Sandia National Laboratories, NUREG/CR-3025, December 1984.

3. W. W. Tarbell, et al., "Pressurized Melt Ejection into Reactor Cavities," Sandia National Laboratories, NUREG/CR-4512, October 1986.

4. C. L. Allen and Containment Loads Working Group, "Estimates of Early Containment Loads from Core Melt Accidents," NUREG-1079, December 1985.

5. USNRC, "Reactor Risk Reference Document," NUREG-1150, Draft for Comment. February 1987.

6. D. C. Williams, et al., "Containment Loads Due to Direct Containment Heating and Associated Hydrogen Behavior," NUREG/CR-4896, May 1987.

7. W. W. Tarbel, et al., "Results from the DCH-1 Experiment," NUREG/CR-4871, June 1987.

8. W. W. Tarbell et al., "Results from the Second Experiment Performed in the Surtsey Direct Heating Test Facility," NUREG/CR-4917, October 1987.

9. K. D. Bergeron, Sandia, Letter to T. M. Lee, USNRC, dated October 20, 1986.

10. Brookhaven National Laboratory, "Safety Research Programs Sponsored by Office of Nuclear Regulatory Research," Quarterly Progress Report, July-September 1985, NUREG/CR-2331, Vol. 5, No. 3, March 1986.

11. H. Kouts, "Review of Research on Uncertainties in Estimates of Source Terms from Severe Accidents in Nuclear Power Plants," NUREG/CR-4883, April 1987.

12. Fauske and Associates, Inc., "IDCOR Technical Report 85.2: Technical Support for Issue Resolution," Atomic Industrial Forum, July 1985.

13. C. A. Blomquist, B. W. Spencer and others, "Data Report for Corium/Water Thermal Interaction Test CWT I-13," Argonne National Laboratory, October 1985.

14. W. W. Tarbell, et al., "Behavior of Core Debris Ejected from a Pressurized Vessel into Scaled Reactor Cavities," Proceedings of Twelfth Water Reactor Safety Research Information Meeting, NUREG/CP-0058, Vol. 3, January 1985.

15. W. W. Tarbell, et al., "Melt Expulsion and Direct Containment Heating in Realistic Plant Geometries," Proceedings of the International ANS/ENS Topical Meeting on Thermal Reactor Safety (San Diego, CA), American Nuclear Society, February 1986.

16. T. Ginsberg and N. Tutu, "Recent Experimental and Analytical Results of BNL Direct Containment Heating Programs," Proceedings of USNRC Fourteenth Water Reactor Safety Information Meeting, NUREG/CP-0082, Vol. 6, February 1987.

17. M. Ernst, RES, Note to T. Speis, NRR, "Initial SARRP Information of Direct Heating Surry," dated April 19, 1986.

18. USNRC, "Uncertainty Papers on Severe Accident Source Terms," NUREG-1265, May 1987.

19. R. Iman and W. Conover, "Sensitivity Analysis Techniques: Self-Teaching Curriculum," Sandia National Laboratories, NUREG/CR-2350, SAND81-1978, June 1982.

20. M. McKay, W. Conover, and R. Beckman, "A Comparison of Three Methods for Selecting Values of Input Variables on the Analysis of Output From a Computer Code," Technometrics, Vol. 21, pp. 239-245, 1975.

21. R. Iman and W. Conover, "The Use of the Rank Transform in Regression," Technometrics, Vol. 21, No. 4, pp. 499-509, 1979.

UNITED STATES NUCLEAR REGULATORY COMMISSION RESEARCH PROGRAM ON MOLTEN CORE DEBRIS INTERACTIONS IN THE REACTOR CAVITY

S. B. BURSON, OFFICE OF RESEARCH,
U.S. NUCLEAR REGULATORY COMMISSION
D. BRADLEY, J. BROCKMAN, E. COPUS, D. POWERS,
SANDIA NATIONAL LABORATORIES
G. GREENE, BROOKHAVEN NATIONAL LABORATORY
C. ALEXANDER, BATTELLE COLUMBUS LABORATORY

ABSTRACT

The NRC research program on Core-Debris/Cavity Interactions comprises two principle elements: (1) An analytical effort focused principally on the development of computer codes needed to predict the potential consequences of risk-significant severe-accident scenarios; and (2) an experimental component to provide insights into the relevant phenomenological processes and to develop the data base necessary for validation of the codes. The analytical activities at Sandia National Laboratories focus primarily on refinement and validation of the CORCON and VANESA codes. Two major experimental activities are also based at SNL: The large scale SURC tests address the thermal-hydraulic phenomena as well as aerosol release associated with prototypical core-melt materials in various types of concrete crucibles, while the WITCH and GHOST experiments are concerned with aerosol generation and radionuclide release phenomena. A program of small scale special-effects tests at Brookhaven National Laboratory is coupled to a concomitant model-development and code-validation activity. In addition, measurements are being made at Battelle Columbus Laboratory to augment the thermochemical data base needed in the VANESA code to permit refined radiological source-term predictions. The current scope and status of this research is reviewed.

1.0 INTRODUCTION

Potential exposure of the public to radioactive materials inadvertently released during an accident is considered to be the most significant risk associated with nuclear power generation. To enable regulatory decision making intended to minimize the risk of such an environmental release, a thorough knowledge of the accident-related phenomena is indispensable. In the following discussion, it is assumed that a postulated accident has advanced to the point

where the reactor core has been disrupted so that radioactive materials mixed with fuel and structural components escape the primary pressure boundary and relocate into the reactor cavity below the vessel. It is further assumed that the radioactive gases and volatile fission product species such as xenon and iodine are released to the containment atmosphere at the time of vessel failure while the more refractory materials, such as strontium and cerium remain with the core debris. The aspect of the NRC research program described here is concerned with the phenomena expected to occur in the reactor cavity at the time of, and following vessel failure.

The only barrier that remains between the radioactive inventory and the outside environment is the reactor containment system. It is therefore essential to understand and evaluate the abnormal loads imposed on the containment by the accident-related phenomena and to quantify the radionuclide inventory so that the radiological source term can be assessed in the event of containment failure. The purpose of the NRC Research Program on Molten Core Debris Interactions in the Reactor Cavity is to develop and validate computational tools to calculate the physical and thermal-hydraulic variables needed to characterize containment loading and ex-vessel source-term phenomena. This information is essential in NRC licensing and regulatory decision-making functions related to containment integrity and environmental radiological source-term assessment.

1.1 Potential Contributions to Risk

The most significant potential consequences that may result when high temperature core debris finds its way into the reactor cavity are summarized in table 1.

Table 1. Potential Consequences of Molten Core Interactions in the Reactor Cavity

Containment Loading Effects CORCON Code

- Containment Overpressurization
  - Combustible gas generation (H_2 and CO)
  - Noncondensable gas generation (H_2, CO and CO_2)
  - Containment atmosphere heating from debris pool surface, released aerosols, and gases
- Structural Damage
  - Basemat penetration, erosion of reactor pedestal
  - Thermal attack on upper structures
  - Degradation of engineered safety features

Refractory Radionuclide Release and Aerosol Generation VANESA Code

- Radioactive and nonradioactive aerosols from core debris
- Containment atmosphere heating
- Plugging of filters/vents
- Aerosol decontamination by overlying water

If containment integrity can be maintained, immediate public risk is virtually eliminated. To make credible structural-response predictions, the abnormal

loadings must be quantified. Thermal decomposition of concrete releases water vapor, carbon dioxide and other gases. Some of these gases react chemically with molten metals in the debris pool to produce the combustible gases, hydrogen and carbon monoxide. The aerosols and gaseous components enter the containment atmosphere at high temperature; the pressure loading of the containment increases from the addition of heat, noncondensable gases, and the possible burning of H_2 and CO. The CORCON code computes these phenomena and provides quantitative output data from which the concrete attack and containment loading can be computed.

The issues of basemat penetration and containment overpressurization have been under consideration for quite some time, however, a number of other potential consequences of core-debris interactions in the cavity have only come into focus more recently; for example, the direct attack by core debris on engineered safety features such as the BWR Mark-I steel containment liner. These transient effects are presently being more closely studied.

If the containment does fail, it is necessary to know the radionuclide burden in the atmosphere in order to compute the ultimate radiological source term. The bubbling of concrete decomposition gases through the molten debris has two effects; (1) the sparging of the more refractory fission product elements dissolved in the molten materials, and (2), the generation of aerosols at the debris pool surface. Although the radioactive aerosols are the most significant, it is important to note that the nonradioactive particulates (primarily composed of concrete decomposition products) can contribute significantly to reduction of the source term because of their scavaging effect in the atmosphere. The VANESA code computes the sparging process within the debris as well as the aerosol generation at the pool surface. Finally, if overlying water is present, the surface aerosols may be significantly attenuated by decontamination in the water.

It cannot be emphasized too strongly that the possible consequences outlined in table 1 do not apply with equal significance to all accidents. Their relative importance is determined by many factors, eg, the type of reactor, the structural details of the containment system, and the initial and boundary conditions related to the particular accident scenario.

1.2 Uncertainties Associated With the Prediction of Risk-Related Accident Consequences

As indicated in the opening of this section, the estimation of public risk accompanying a postulated nuclear accident is predicated primarily upon assessment of the probable radiological source term accompanying the event. During the preparation of NUREG-0956 "Reassessment of the Technical Bases for Estimating Source Terms," (Ref. 1), a cadre of computer codes (known as the NRC Source Term Code Package) was assembled to permit the best possible radiological source term predictions for selected hypothetical accident scenarios. Since no error propagation is conducted in the codes themselves, only point estimates derived from the input assumptions made by the analysts were possible. Efforts to address the issue of uncertainty bands have been made in NUREG-1150 "Reactor Risk Reference Document," (Ref. 2). In addition,

more extensive treatment of predictive uncertainties is to be found in NUREG-1265 "Uncertainty Papers on Severe Accident Source Terms," (Ref. 3.)

Application of even the most mechanistic computer codes (those based on the fundamental laws of physics, chemistry and engineering, rather than empirical correlations and models) still retain (and possibly introduce) uncertainties in the calculations. The principle possible contributors to uncertainties in code predictions are outlined in table 2.

Table 2. Sources of Uncertainties Associated With Code Predictions

1. Uncertainties in the phenomenological models
2. Computational uncertainties
3. Uncertainties in the physical/chemcial data base
4. Uncertainties in input variables derived from other analysis codes used to compute earlier stages in the accident sequence
5. Uncertainties attributable to the exercise of user options

The relevance of these five sources of uncertainty in code predictions is not limited to CORCON and VANESA, they are generic to all computer codes. The first three items, phenomenological modelling, computational precision and accuracy in the data base fall within the purview and responsibility of the code developers. The last two items, uncertainties and the input data and possible idiosyncrasies exercised by the users are outside the control of the code developers. Awareness of these uncertainties plays an important role in the formulation and execution of both the analytical and experimental aspects of the NRC research program on core-debris/cavity interactions.

1.3 Scope of the Program

The CORCON MOD 2 code, used to compute thermal-hydraulic containment-loading phenomena, and the VANESA code used to calculate the ex-vessel radiological source term are acknowledged by the world-wide reactor-safety research community to be state-of-the-art computational tools. At the same time, their deficiencies and limitations are acknowledged. The refinement and experimental validation of these codes constitute the principle motivation and guidance for the research program described in this report.

2.0 Analytical Program — Codes Development and Validation

The physical, thermal, and chemical processes that occur when high-temperature reactor core debris comes into contact with concrete are extremely complex. The reactions that occur depend strongly upon (1) the composition of the debris, (2) its initial temperature, (3) the rate at which the debris is deposited onto the concrete, (4) the composition of the concrete, (5) the geometric configuration of the concrete cavity in which the reactions occur, and (6) the properties of the atmosphere and surroundings above the debris.

There has been a prevailing tendency to oversimplify the mechanisms involved; this disposition is reflected in such simple-minded questions as "will the core debris penetrate the basemat and contaminate the groundwater?" This type of question, without extensive qualification reflects a disturbing naivete. This

point is made in order to emphasize the importance of having adequate knowledge of the initial and boundary conditions listed above.

There are three principle sources of heat available to drive the interactions: (1) Sensible and latent heat present in the debris when it exits the vessel, (2) heat released from radioactive decay of the fission products accumulated in the fuel during reactor operation, and (3) energy from chemical reactions that occur when concrete decomposition products begin to enter the molten core materials. The relative importance of the roles played by these various energy sources shifts with time and depends critically upon the composition of the debris as well as the concrete. For example, BWR cores contain a much higher proportion of zirconium metal than do PWR cores so that chemical reactions may dominate the energy considerations for some period of time.

2.1 The CORCON Code — Thermal Hydraulic Effects

The CORCON Code developed at Sandia is designed to compute the significant variables needed to answer such specific safety related questions as basemat penetration, containment overpressurization, or reactor pedestal degradation resulting from thermal ablation of the concrete. CORCON MOD2 (Ref. 4) was released in August 1984 and is now being implemented in seventeen major research establishments throughout the United States and a number of foreign countries. The code development group at SNL provides periodic code-update sets and ongoing support to the users. Principle features of the CORCON Code are outlined in table 3.

Table 3. CORCON-MOD2 Code Features

- Obtains Input Data From Melt-Progression Codes, e.g., MELPROG, MARCH, etc.
  - Mass flow rate and core-debris composition
  - Initial debris temperature
- Core Debris/Concrete Interactions Modelled
  - Concrete ablation rate and cavity geometry
  - Gas release rate and composition
  - Debris temperature distribution
  - Debris pool chemistry including metal oxidation
  - Heat and mass transfer
- CORCON Output Provides Input For
  - VANESA Code to calculate fission-product aerosol release
  - CONTAIN Code to compute loading effects
- Areas of Application
  - Actively used in 17 research facilities
  - Adopted for use in: MELCOR, CONTAIN, NRC Source Term Code Package

During 1987 two additional update sets to CORCON MOD2 (No. 3 and No. 4) were distributed to the users. The nature of the four revisions made are summarized in table 4.

Table 4. CORCON-MOD2 Correction Sets

VERSION	PURPOSE	EFFECT ON CALCULATIONS
2.01	Correct Minor Bugs	Not Significant
2.02	Improve Decay-Heat Calculation	Significant Only for $T < 1$-2 Hours
2.03	Improve Chemistry Package	Not Usually Significant
2.04	Allows Addition of Debris Mass and Coolant	Can be Significant-depends on Mass Addition Rate, Temperature, and Timing

The two most recent revisions to CORCON (1) improve the treatment of chemical phenomena, and (2) provide for time-dependent addition of core materials to the debris pool. Test calculations show CORCON results to be sensitive to the rate and temperature of material added to the debris pool. A new axial heat transfer model has been developed for CORCON which brings calculated downward concrete ablation into better agreement with experimental results. Comparison of a CORCON calculation made using the new model with experimental data from the KfK BETA test V3.3 is shown in Fig. 1.

FIGURE 1

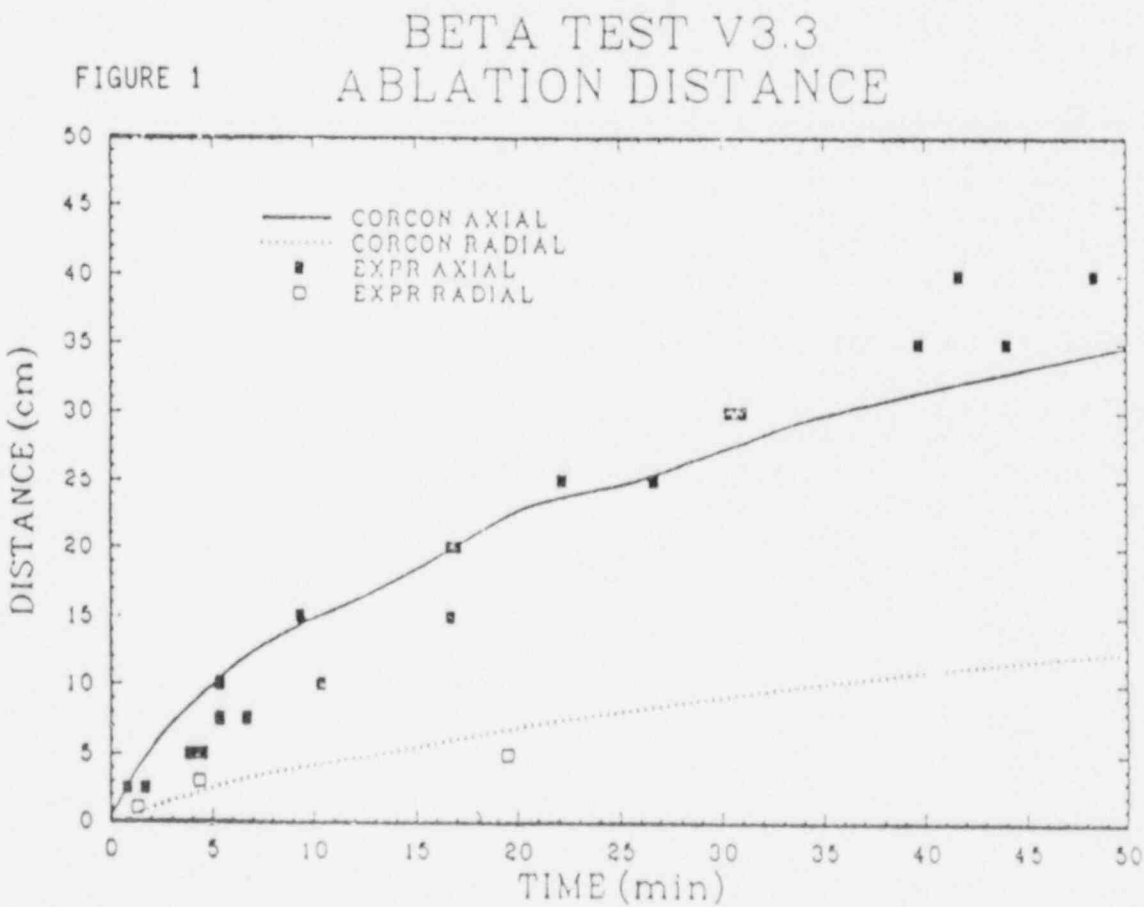

A number of deficiencies remain in the current version of CORCON; specific efforts to remedy these shortcomings are in progress. Some of these areas are: (1) Transient heat transfer to concrete is not treated; water vapor and gas release prior to reaching the ablation temperature needs to be modelled, (2) the treatment of radial heat transfer to vertical concrete surfaces is not yet considered adequate (this matter is intimately involved in the question of reactor pedestal degradation), and (3) the question of heat transfer to overlying water is not yet adequately understood or modelled; this issue is intimately involved with the question of debris coolability.

2.2 The VANESA Code — Aerosol Generation and Radionuclide Release

The first implementation of the VANESA model for radionuclide release from molten core debris was published in July 1986 (Ref. 5). The calculation considers the sparging of the important radioactive chemical species from molten debris by the bubbling of concrete decomposition gases through the debris pool. The vapor phases, of the pool constituents are assumed to attain thermodynamic equilibrium within the bubbles; these vapors then condense to form aerosols when the bubbles break at the pool surface. Mechanical aerosol formation is also computed, i.e., when the film formed at the surface fragments into fine particles. In addition, the model considers the trapping (decontamination) of the aerosols if an overlying layer of water is present. The general features of the VANESA code are summarized in table 5.

Table 5. Vanesa Code Features

- Obtains Input Data from CORCON
  - Mass flow rate and composition of debris
  - Debris pool temperature
  - Gas composition and flow rate
- Aerosol Generation Phenomena Modelled
  - Vapor condensation
  - Bubble film fragmentation (entrainment)
  - Aerosol decontamination by overlying water layer
- Output Variables
  - Aerosol composition and release rate (includes radiological source-term data)
  - Aerosol decontamination factor
- Areas of Applications
  - Adopted for use in MELCOR, CONTAIN NRC Source Term Code Package
  - Used in national, private, a. foreign research laboratories

The first revision to the VANESA code was distributed to the users; the refinements are shown in table 6.

Table 6. Revisions to VANESA

VERSION	REVISIONS	COMMENTS
1.00	-Original version	Used in early source-term code-package calculations
1.01	-Improved treatment of thermodynamic data	Released September 14, 1987. Revisions have minor impact on calculated results.
	- More mechanistic mechanical aerosol model	
	- Explicit treatment of coking	

The improvements include: (1) A more accurate representation of the temperature-dependent free energies of the chemical species considered by the code, (2) the capability for an explicit treatment of carburization reactions to the chemistry solution and, (3) a more mechanistic model for mechanical aerosol generation. The VANESA code was developed independently from the CORCON code, however, it has been recognized for some time that the intimate interrelationship between these two codes renders their integration into a single computational tool highly desirable. Significant progress has already been made toward consolidation of the CORCON and VANESA codes into a single integrated code.

3.0 Experimental Programs

The purpose of the experimental research activities is often given as code validation. Indeed, to achieve a sufficient level of predictive credibility, code calculations must be tested against real data. However, experiments serve another extremely important purpose; they frequently provide new and unexpected technical insights into phenomena that have been virtually unexplored previously. For example, the observation of energetic thermal interactions (steam explosions) during the small-scale BNL experiments intended to study heat transfer from molten metals to overlying water was totally unancticipated. This inadvertent observation led to significant redirection of the activities and thinking with respect to the major steam-explosion research. The experimental research program on core-debris/cavity interactions continues to serve both of these purposes, i.e., (1) to augment the validation data base and (2) to provide new technical insight into phenomenology where a paucity of understanding continues to exist.

3.1 Large-scale Integral Experiments on Prototypical Reactor Materials Interacting with Concrete – SURC Tests.

A large number of experiments have been conducted at SNL and at the Kernforschungszentrum, Karlsruhe, FRG (KfK) with molten steel interacting with various types of concrete. This research has yielded important data and provided insights into the phenomena. However, virtually no studies have been made that are truly representative of reactor core debris. The SURC series of tests (Sustained Urania Reacting with Concrete) is being conducted at SNL to fill this gap. The purpose and orientation of the research are summarized in table 7.

Table 7. Sandia-Integral-Core-Concrete Interaction Experiment Program SURC Test Series (Sustained Urania Reacting with Concrete)

- Purpose of the Large-Scale Sustained-Heating Integral Tests
  - Provide thermal-hydraulic data for CORCON validation
  - Provide data to validate VANESA aerosol-generation and chemistry models.

- Phenomena Observed
  - Concrete ablation, rate and direction
  - Gas generation, rate and composition
  - Aerosol generation and properties

- Input Parameters Varies
  - Concrete composition, e.g. limestone, silicious, etc.
  - Melt composition, e.g. metals, oxides, mixtures
  - Input power level

Induction heating is used to prepare the melts as well as sustain the temperature after experimental conditions are reached. This approach permits certain studies (such as the addition of Zr metal) which may be precluded when thermitically prepared melts are used. The experimental facility is schematically outlined in figure 2. The external water-cooled aluminum containment shell permits the acquisition of more accurate gas-production data as well as a more precise determination of side-wall heat losses from the test vehicle. The plan matrix of experiments is shown in table 8.

Table 8 SURC Test Matrix

TEST	CHARGE	MASS	CONCRETE	H_2O
1	UO_2-ZRO_2	250KG	Limestone	No
2	UO_2-ZRO_2	250KG	Basaltic	No
		Completed		
3	Steel-ZR	50KG	Limestone	No
3A	Steel-ZR	50KG	Limestone	No
4	Steel-ZR	200KG	Basaltic	No
5	UO_2-ZRO_2-ZR	250KG	Limestone	Yes
6	UO_2-ZRO_2-ZR	250KG	Basaltic	Yes
7	Steel-B_4C	200KG	Limestone	No
8	Steel-B_4C	200KG	Basaltic	No

The anticipated measurements involving metallic Zr and boron carbide (B_4C) are of particular importance with respect to BWR accidents. Three tests have been performed; the current status of the project is summarized in table 9.

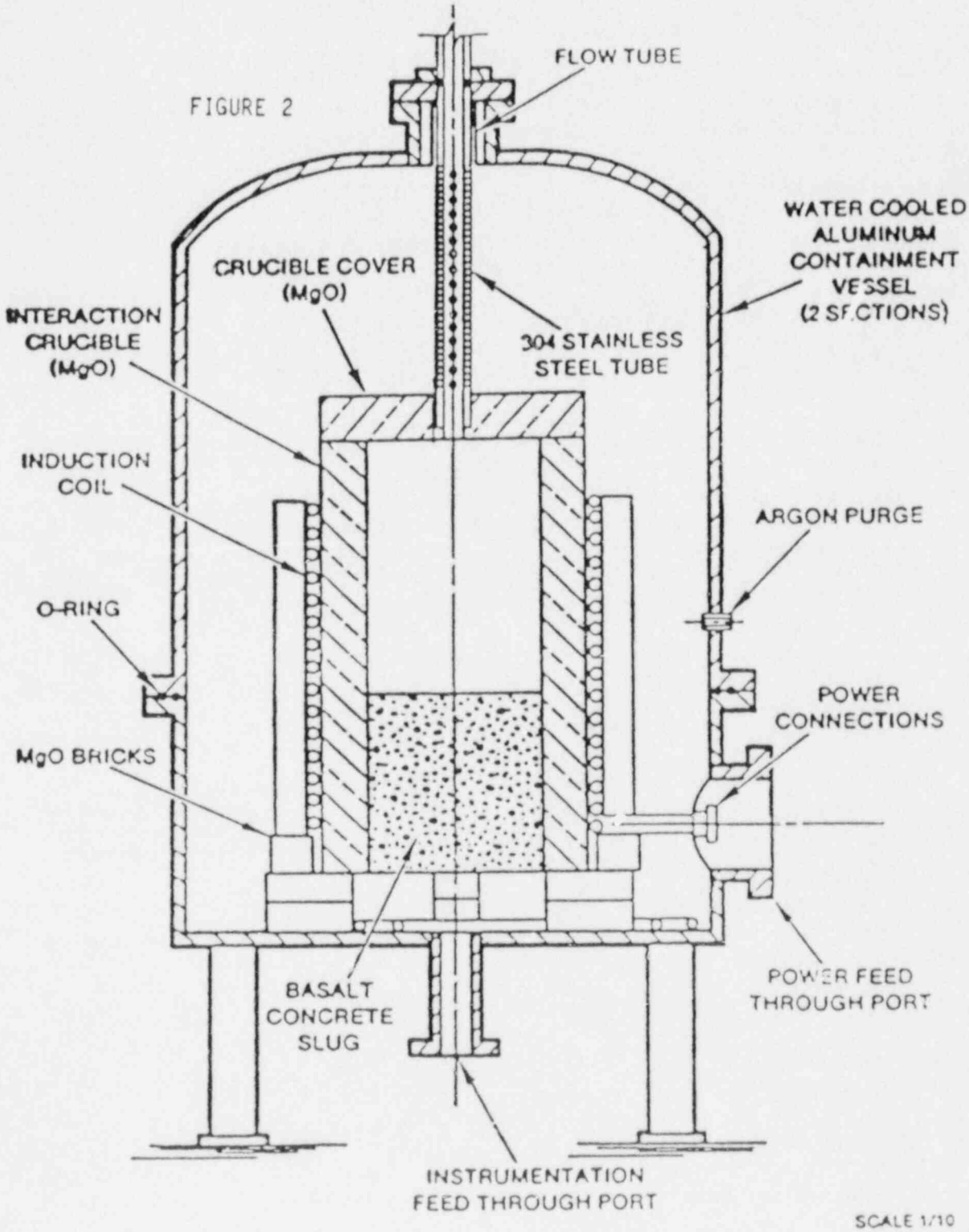

Figure 3.1 SURC-4 Experimental Apparatus

Table 9. SURC Program Status and Results

- Apparatus Operational - Techniques Demonstrated

- SURC 3 and 3A Completed - General Observations:
  - Copeous aerosol generation with limestone concrete (strong tellurium component)
  - Addition of Zr metal increases ablation rates:
  - SURC 3 (one-D crucible) 0.20 to 0.45 cm/min axial only
  - SURC 3A (two-D crucible) 0.19 to 0.35 cm/min axial
  - 0.15 to 0.75 cm/min radial
  - Melt temperatures fairly stable about 1900K
  - CO_2 and H_2O mostly reduced but no clear evidence of carburization (coking)

- SURC-4 Results Test Are Sequestered For Use in CSNI PWG-2 Blind Code-Comparison Project

The important parameters involved in these tests are shown in table 10.

Table 10. SURC 3, 3A and SURC 4 Parameters

- SURC-3: One-D, Limestone Concrete (20 CM I.D.)
  SURC-3A: Two-D, Limestone Concrete (20 CM I.D.)
  - 50 KG stainless steel + 2 KG F.P. simulants
  - Inductively heated ($\sim$ 35KW)
  - 2KG Zr metal added after steady state achieved

- SURC 4: One-D, Silicious Concrete (40 CM I.D.)
  - 200 KG stainless steel + 6 KG F.P. simulants
  - Inductively heated ($\sim$ 70KW)
  - 20 Kg Zr added after steady state achieved

Three tests (SURC 3, 3A and 4) have been conducted; the primary objective was to study the influence of metallic Zr present in the melt. This is a vital issue with respect to BWR safety because of the high inventory of Zr in the core. All three tests involved the addition of Zr metal to molten stainless steel in the crucible after quasi-steady-state ablation had been achieved. All of the tests incorporated nonradioactive representative fission-product elements in the melt. The first two tests were conducted with limestone concrete; the first (SURC 3) was one-dimensional, while the second (SURC 3A) was a 2-dimensional test. Figure 3 compares a pretest CORCON calculation with the SURC 3 experimental data. The inflection at approximately 130 minutes reflects the augmented concrete attack resulting from the increased power from chemical reactions when the Zr metal was added. Results of the third test, (SURC 4) have been sequestered and will be used in an international code-comparison exercise sponsored by the CSNI Working Group 2.

SURC3 ABLATION FRONT FIGURE 3

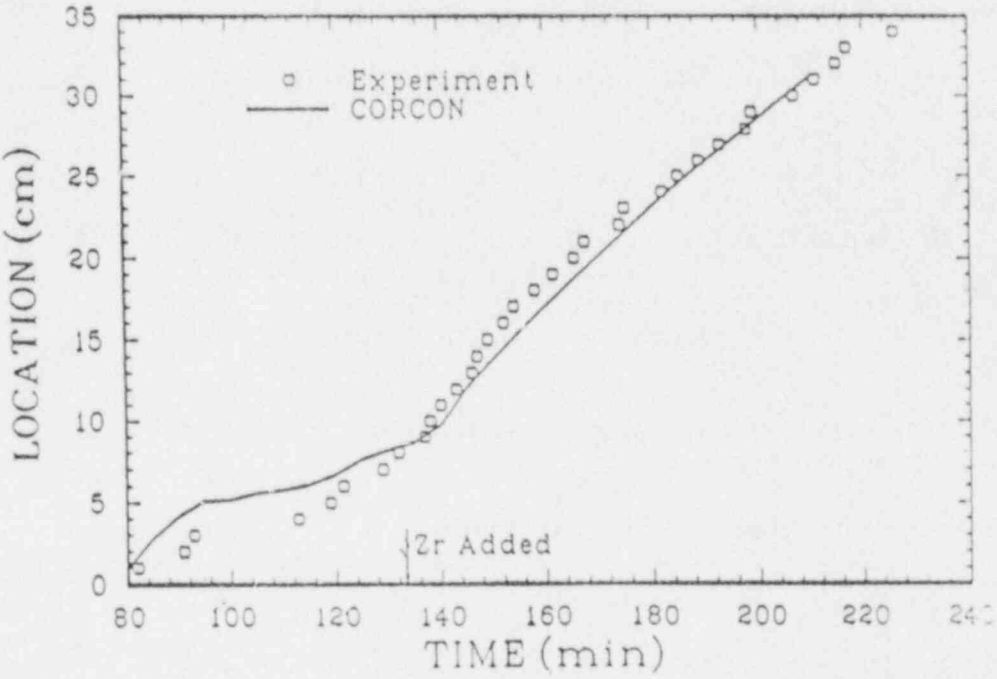

3.2 Sandia Core-Concrete Aerosol Research Program - WITCH/GHOST Experiments

To evaluate the public risk associated with possible exposure to nuclear radiation, it is necessary to understand the mechanisms by which radionuclides might be transported from their source (the reactor core). Probably the most significant mode is the transport of airborne particulates (aerosols). Once airborne, the behavior of aerosols is relatively well understood and modelled. By contrast, the generation and release to the atmosphere of refractory fission products from high-temperature core debris is poorly understood. The aerosol generation process is modelled by the VANESA code, but there is very little experimental data to validate and lend credibility to the code predictions. This problem is being addressed by the WITCH/GHOST series of experiments at SNL. The thrust of the research is outlined in table 11.

In these studies, controlled gas bubbling through selected metallic and oxidic melts permit the delineation of mechanical and condensation aerosol-generation processes. This information is necessary to develop and test the aerosol-generation and release models in the VANESA code. The apparatus is complete and the effectiveness of the x-ray diagnostic system to measure gas hold-up time has been demonstrated. The gas residence time influences the degree to which fission-product vapors may reach equilibrium within the bubbles during their transit through the molten debris. A schematic outline of the WITCH/GHOST experimental apparatus is shown in figure 4. The system is operational and tested, however, none of the early experimental results are yet ready for reporting.

Table 11. Sandia Core-Concrete Aerosol Research Program

- Purpose of the WITCH/GHOST separate-effects tests
- Provide validation data base for CORCON and VANESA
- Study Properties of aerosols generated by
  A) WITCH - Bubble film rupture (Melt-pool mass entrainment)
  B) GHOST - Vapor condensation after bubble rupture
- Study chemical properties of prototypic core-debris materials (affects debris-to-concrete heat transfer correlation in CORCON, and chemical vapor equilibrium in VANESA)
- Experimental Conditions
- Temperature controlled by sustained induction heating
- One-dimensional refractory crucible (to eliminate actual core-concrete interaction)
- Bottom gas injection with controlled composition, temperature and flow rate
- Prototypic reactor-material melts doped with nonradioactive fission-product chemical species
- Fully instrumented to measure aerosol properties and system conditions including x-ray diasnostic system to determine level swell

3.3 Separate-Effects Simulant Experiments and Modelling at Brookhaven National Laboratory

At Brookhaven National Laboratory, a research program of separate-effects experiments and modelling is closely coordinated with the CORCON code development work at SNL. Certain CORCON output variables depend critically upon the heat-transfer processes that occur within the debris pool as well as between the debris and the concrete cavity. Whether or not the immiscible metallic and oxidic components of the debris are stratified into layers or become well mixed depends upon many factors and the same debris pool may take on either configuration at various times. The BNL research is concerned specifically with the CORCON models that treat these heat transfer processes; the areas being studied include: (1) Interlayer heat and mass transfer in two-liquid immiscible systems, (2) liquid-liquid boiling coolant-layer phenomena, and (3) the influence of bubble-induced mass entrainment between immiscible layers. The current status of the BNL program is summarized in table 12.

Table 12. Brookhaven Core-Concrete Program Status and Results

- Bubble-Induced Mass Transfer in Stratified Liquid-Liquid Core Debris (Liquid Metallic and Liquid Oxidic Components)
- Onset and rates of entrainment and de-entrainment function of liquid-liquid density ratio and surface tension
- Measured entrainment onset for eight simulant fluid pairs
- Measured entrainment rate — function of liquid densities, surface tension, bubble size, and gas flow rate
- Entrainment vs. de-entrainment rates determines degree of pool mixing (destratification)
- Gas-Bubble Enhanced Heat Transfer
- Interfacial heat transfer enhanced without entrainment
- Liquid-liquid thermal equilibrium approached with increased entrainment
- Heat-Transfer Models are Being Incorporated into CORCON

FIGURE 4

WITCH/GHOST TEST ARTICLE

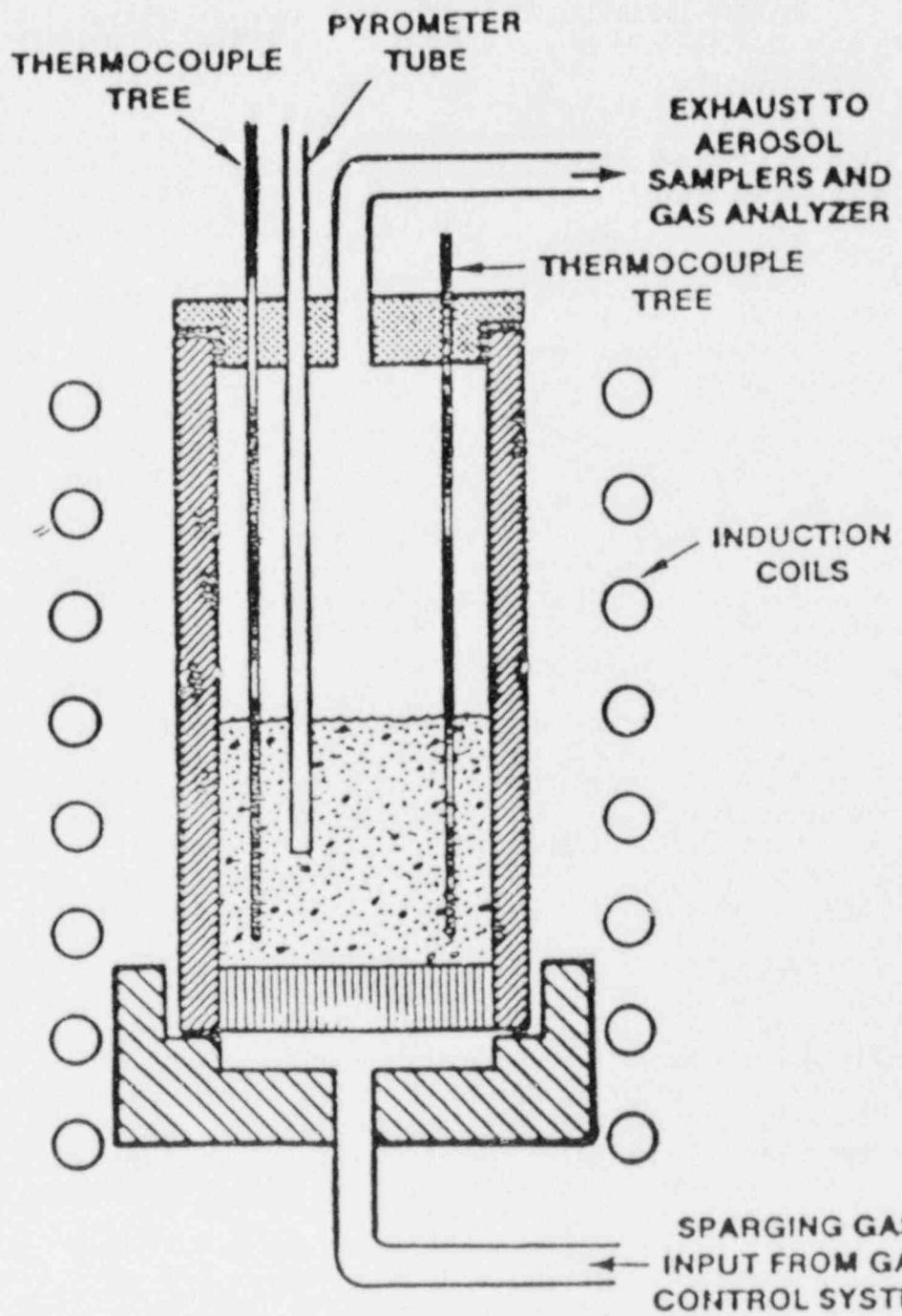

Sandia National Laboratories

Models have been developed to describe the influence of mass entrainment on the heat transfer between immiscible layers as well as the influence of gas bubbling across the surface of the debris pool and overlying water. The latter studies have shown that film-boiling heat transfer may be enhanced by as much as a factor of 3-5. The improved models are being prepared for incorporation into CORCON.

3.4 Chemical Activity Coefficient Measurements at Battelle Columbus Laboratory

The rates at which refractory fission-product elements are sparged from molten debris by decomposition-gas bubbling depend critically upon the characteristics of the various species and the surrounding chemical environment. Mass spectrometric measurements of the oxygen potential and activity coefficients of particularly important systems are being conducted at Battelle. Small sample mixtures (mg amounts) of core-debris materials are elevated in tungsten crucibles to temperatures at which the vapor pressures can be measured.

These data are needed to reduce the uncertainties associated with VANESA predictions which depend on a knowledge of the high-temperature chemical properties. The scope of the program is summarized in table 13. The completed experiments will be described.

Table 13 Battelle Columbus Laboratories Program to Measure Thermochemical Properties of Molten Core Debris

- Purpose-Provide a Data Base of High-Temperature Thermochemical Material Properties Needed for the VANESA Chemistry Model: DATA are Essential to Quantify the Ex-Vessel Refrectory Fission-Product Raiological Source Term

- Methodology-High-Temperature Mass Spectometry
  - Single-crystal tungsten crucibles used to inhibit chemical degradation
  - Melt mixtures selected to represent typical core-melt regimes, e.g. UO_2 +ZrO_2 + Zr Metal + Surrogate Fission-Product Elements
  - Measure vapor pressures to determine chemical activity coefficients and system oxygen potential

References

1. R. Meyer, J. Mitchell, C. Ryder, M. Silberburg, Reassessment of the Technical Bases for Estimating Source Terms, USNRC, NUREG-0956, July 1986

2. USNRC, Reactor Risk Reference Document, (DRAFT) NUREG-1150, Vol. 1-3, February,1987

3. B. Burson, L. ChaN. J. Han. T. Lee, P. Worthington, Uncertainty Papers on Severe Accident Source Terms, NUREG-1265, May 1987

4. R. Cole, M. Ellis, D. Kelly, CORCON MOD 2, A Computer Program for Analysis of Molten-Core Concrete Interactions, NUREG/CR-3920 SAND 84-1246, August 1984

5. J. Brockmann, D. Powers, A. Shiver, VANESA: A Mechanistic Model of Radionuclide Release and Aerosol Generation During Core Debris Interactions with Concrete, NRUEG/CR-4308, SAND 85-1370, July 1986

UNCERTAINTIES IN HYDROGEN COMBUSTION

D. W. Stamps, C. C. Wong, and L. S. Nelson
Sandia National Laboratories
Albuquerque, New Mexico 87185

ABSTRACT

Three important areas of hydrogen combustion with uncertainties are identified: high-temperature combustion, flame acceleration and deflagration-to-detonation transition, and aerosol resuspension during hydrogen combustion. The uncertainties associated with high-temperature combustion may affect at least three different accident scenarios: the in-cavity oxidation of combustible gases produced by core-concrete interactions, the direct containment heating hydrogen problem, and the possibility of local detonations. How these uncertainties may affect the sequence of various accident scenarios is discussed and recommendations are made to reduce these uncertainties.

1. Introduction

Uncertainties are identified and their consequences are discussed for three areas of hydrogen combustion: high temperature combustion, flame acceleration and deflagration-to-detonation transition (DDT), and aerosol resuspension during hydrogen combustion. Many other areas of hydrogen combustion contain uncertainties that have not been quantified. A review by the National Academy of Sciences [1] on hydrogen combustion as it pertains to severe light-water reactor accidents recommends areas of research to reduce some of these uncertainties. The three areas of hydrogen combustion discussed in the present paper were identified as important areas from research conducted primarily since the National Academy of Sciences review. The purpose of this paper is to identify the uncertainties in these three important areas of hydrogen combustion. The consequences of these uncertainties are discussed with respect to various accident scenarios and recommendations are made to reduce these uncertainties.

2. High-Temperature Combustion

The uncertainties associated with high-temperature combustion may affect at least three different accident scenarios: the in-cavity oxidation of combustible gases produced by core-concrete interactions, the direct containment heating (DCH) hydrogen problem, and the possibility of local detonations.

2.a In-Cavity Oxidation

In a severe accident involving core meltdown, the molten core will slump onto the floor of the reactor cavity after the vessel breach, Fig. 1. If the reactor cavity is dry, the temperature of the reactor cavity atmosphere and structures may be sufficiently high to promote oxidation of combustible gases produced by core-concrete interactions. Specifically, hydrogen and carbon monoxide may react with available oxygen near the heated structures in the reactor cavity to form steam and carbon dioxide. Complete in-cavity oxidation

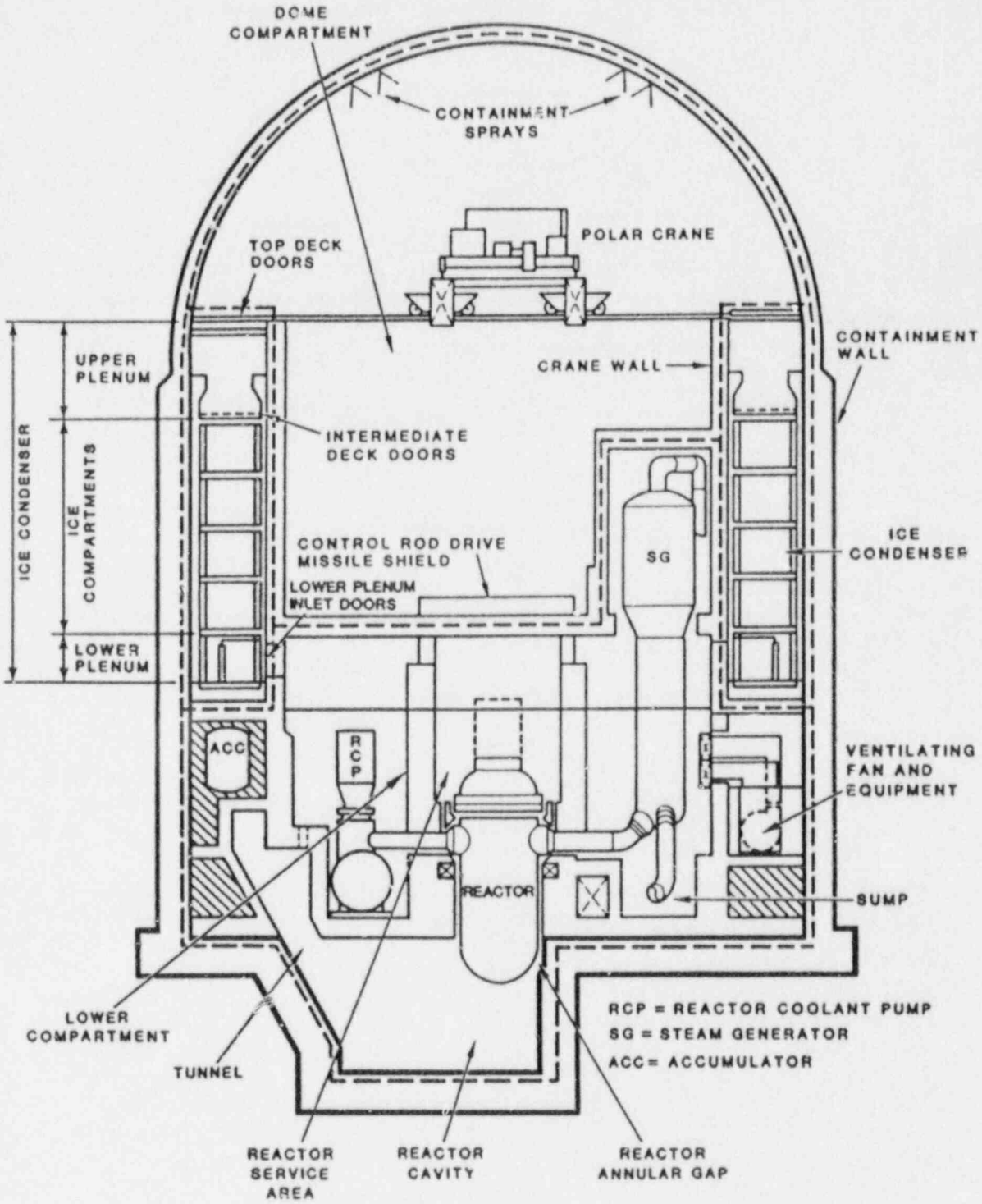

Figure 1. Simplified Diagram of Ice-Condenser Containment

would prevent any accumulation and combustion of hydrogen and carbon monoxide in the lower and upper compartments, and the probability of early containment failure caused by combustion would be minimal. However, the ability to predict the degree of in-cavity oxidation is severely limited by the lack of high-temperature data for autoignition and flammability limits. The degree of uncertainty is illustrated by the different results obtained for the amount of in-cavity oxidation calculated for an S2HF (small-break loss-of-coolant accident with failure of both emergency core-coolant system and containment sprays upon switch-over from injection to recirculation) drain-closed accident in an ice-condenser containment using the HECTR code [2].

HECTR analyses of the problem show that the degree of in-cavity oxidation depends strongly on the extent of natural convection, the flammability criteria for steam-inerted conditions, and the characteristics of the diffusion flame in the cavity [3, 4]. Assuming an unconditionally complete in-cavity oxidation would prevent any accumulation and combustion of hydrogen and carbon monoxide in the lower and upper compartments. No sharp pressure rise is predicted, as shown in Fig. 2. However, assuming an incomplete in-cavity oxidation because of various factors such as the steam inerting effect or insufficient oxygen transport for oxidation will lead to accumulation and combustion of hydrogen and carbon monoxide in the lower and upper compartments. This produces a sharp increase in pressure. In the case shown in Fig. 2, the peak pressure rise was 384 Pa (56 psig) at 7.4 hours into the accident.

The ability to accurately predict the degree of in-cavity oxidation is a difficult task because a variety of phenomena that take place in the cavity at the same time can have substantial influence on the process. Three key phenomena that contribute substantial uncertainties associated with high-temperature combustion will be addressed here: (1) autoignition, (2) flammability limits at high temperature, and (3) characteristics of the diffusion flame in the cavity.

Autoignition of a combustible mixture without any ignition source requires a high gas temperature [5]. If one assumes a well-mixed environment in the cavity, the bulk gas temperature in the cavity has to be above a critical temperature, known as the autoignition temperature, above which molecules possess sufficient energy for the chemical reaction to become self-propagating and lead to flaming combustion [6]. A self-propagating combustion is a thermal runaway process when the rate of energy gain due to the chemical exothermic reaction is greater than the combined rate of energy loss to energize more fuel and oxygen molecules to form activated complexes plus the heat loss to the surroundings including the nonreactive molecules. For hydrogen and carbon monoxide in dry air at normal atmospheric pressure, the lowest autoignition temperatures measured are 833 and 878 K, respectively [5]. Autoignition temperature, however, depends on many parameters such as pressure, catalysts, oxygen, fuel and diluent gas concentrations.

During a severe accident such as an S2HF and with a dry cavity, heat released from the molten core, which has slumped onto the floor of the reactor cavity after the vessel breach, and heat from molten metal-water and molten metal-carbon dioxide reactions may be sufficient to initiate an autoignition, depending on the initial and boundary conditions [7]. However, in other cases such as a wet cavity without any hot surface, the temperature of the combustible mixture in the cavity may not be sufficiently high to autoignite. In

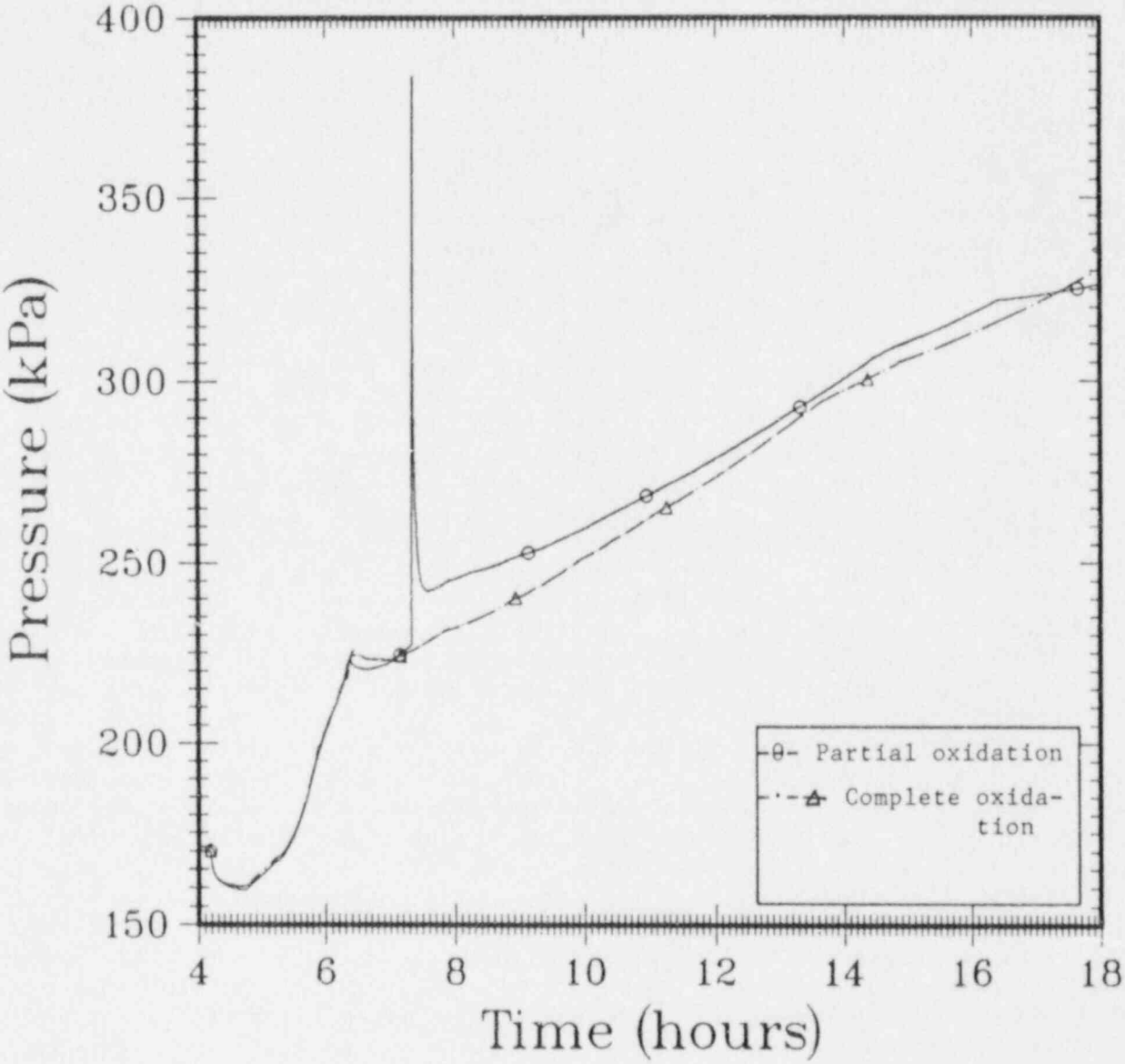

Figure 2. Pressure Response in the Upper Compartment Predicted by HECTR (Partial vs. Complete In-Cavity Oxidation).

order to determine whether autoignition will occur in the cavity, the autoignition temperature of the combustible mixture composed of hydrogen, air, steam, carbon monoxide, and carbon dioxide needs to be established.

Once the ignition occurs in the cavity, either by autoignition or by some accidental source such as a hot surface, it is very difficult to determine whether this flame will be stable as a continuous combustion process. Substantial amounts of steam and carbon dioxide are also generated during core-concrete interactions. This provides a significant heat sink capacity such that the standing flame may be highly unstable or may even be extinguished. Hence complete in-cavity oxidation may not occur. Figure 3 shows the pressure responses in an ice-condenser containment during an S2HF accident for two cases; one including the steam-inerting effect on in-cavity oxidation based on the existing flammability data of the mixture at 400 K, which is far below the calculated gas temperature in the cavity, and the other case excluding the steam-inerting effect. This demonstrates that in order to achieve a better understanding of in-cavity oxidation, the steam-inerting effect on a combustible mixture at an elevated temperature needs to be studied. At present, the flammability limits of a hydrogen:air:steam:carbon monoxide:carbon dioxide mixture at high temperatures have not been well established because of insufficient experimental data [8, 9].

Once the in-cavity oxidation begins, most computer codes for containment analysis, including HECTR, assume an instantaneous one-step chemical reaction. The comprehensive structure and characteristics of the diffusion flame are not modeled. Hydrogen and carbon monoxide molecules are assumed to react with oxygen molecules to form steam and carbon dioxide molecules, respectively, as soon as they are released to the environment. In reality, the gas mixture released from core-concrete interactions will rise up as a plume. The oxidation of combustible gases will carry on in the outer mixing-layer of the plume as a diffusive type of flame, and its rate will be controlled by the relative rate of diffusion of oxygen into the flame. Insufficient supply of oxygen for reaction or adding steam to the atmosphere will elongate the flame [10]. A high steam-content environment is very likely to occur during core-concrete interactions. Hence the flame will probably be longer, and may exceed the height of the cavity, and extend out into the tunnel, Fig. 4. If there is not sufficient oxygen for reaction, the flame will probably be extinguished at the tip of the plume. This will result in an incomplete in-cavity oxidation of hydrogen and carbon monoxide. Other considerations, like the instability of the flame, which may also prevent a complete in-cavity oxidation, will not be discussed in detail here; a general review can be found in Reference 11.

2.b Direct Containment Heating Hydrogen Problem

Direct containment heating is a postulated phenomenon that occurs during a severe core-melt accident like TLMB' when the primary vessel fails with the reactor coolant system still at high pressure. Then as the vessel breaches, the molten corium will be ejected under high pressure from the reactor vessel and dispersed into the containment atmosphere, thereby causing sufficient heating and pressurization to threaten containment integrity, Fig. 5. This DCH problem is a complex phenomenon involving many physical and chemical processes that are not well understood and also are extremely difficult to model. Recent analyses using the CONTAIN code indicate that one of the most dominant uncertainties is the hydrogen combustion phenomena in the extreme environments

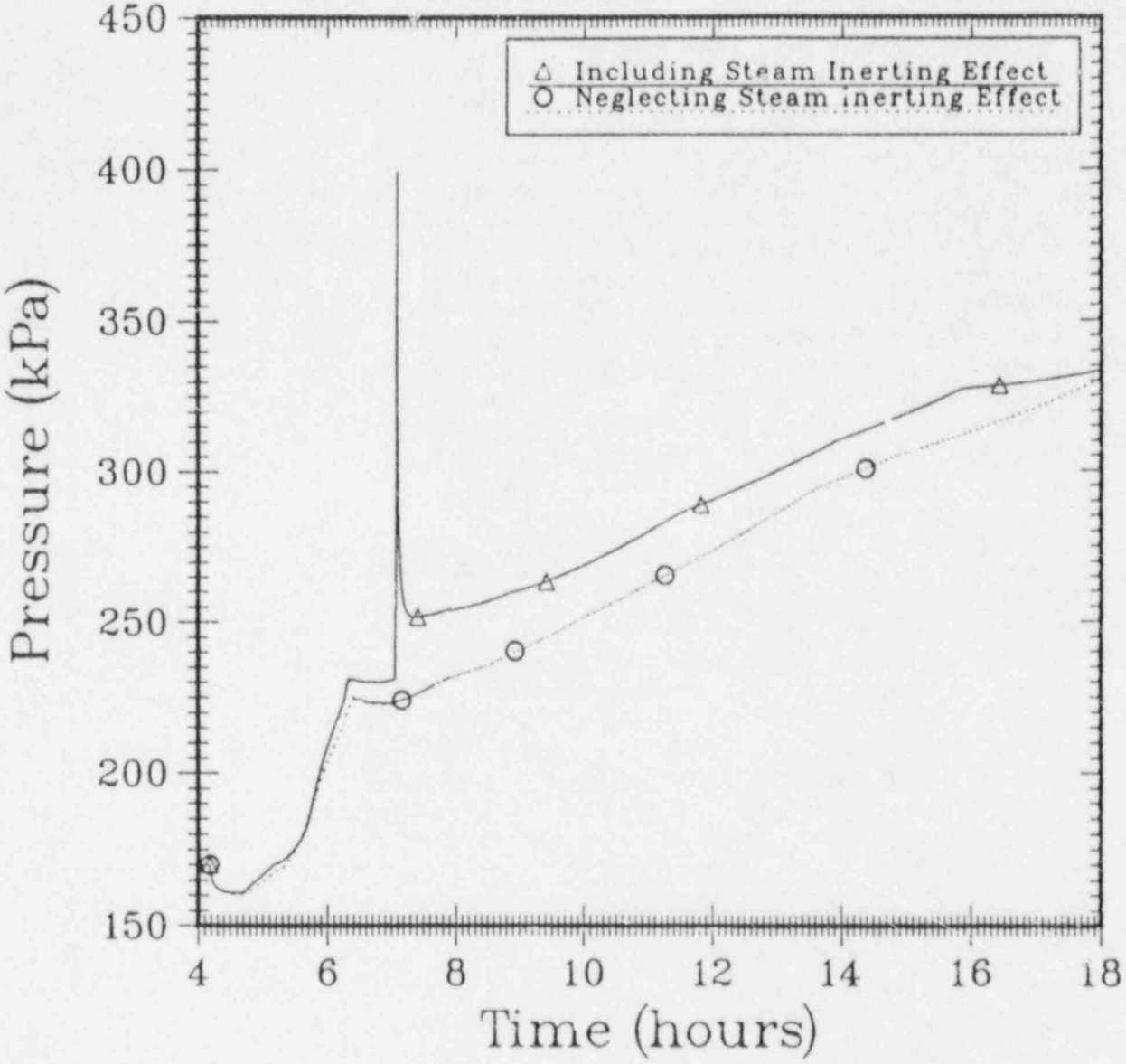

Figure 3. Pressure Response in the Upper Compartment Predicted by HECTR (6-Compartment Model; Excluding vs. Including Steam Inerting Effect)

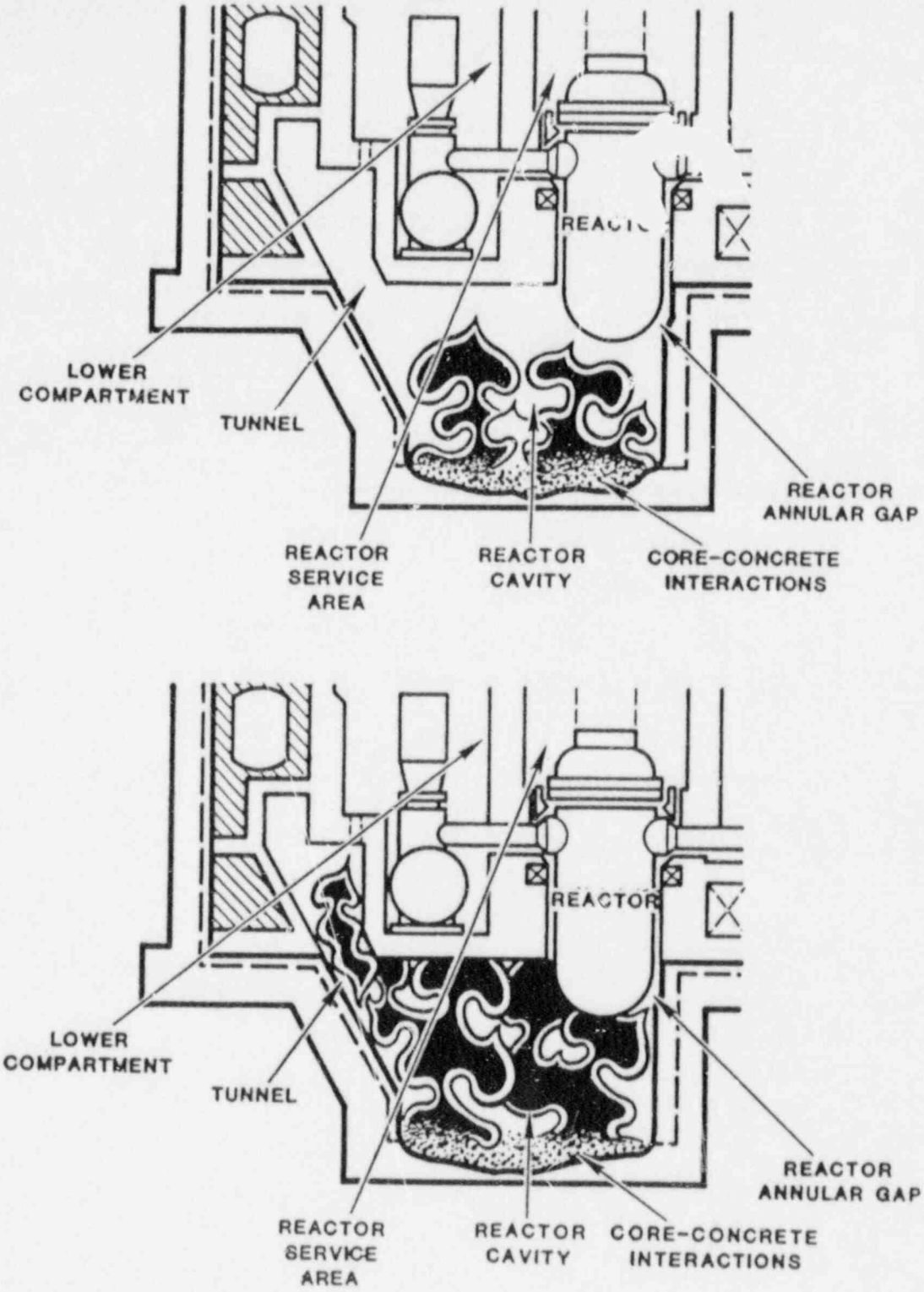

Figure 4. Schematic of In-Cavity Oxidation; (Top) Complete Oxidation, (Bottom) Incomplete Oxidation

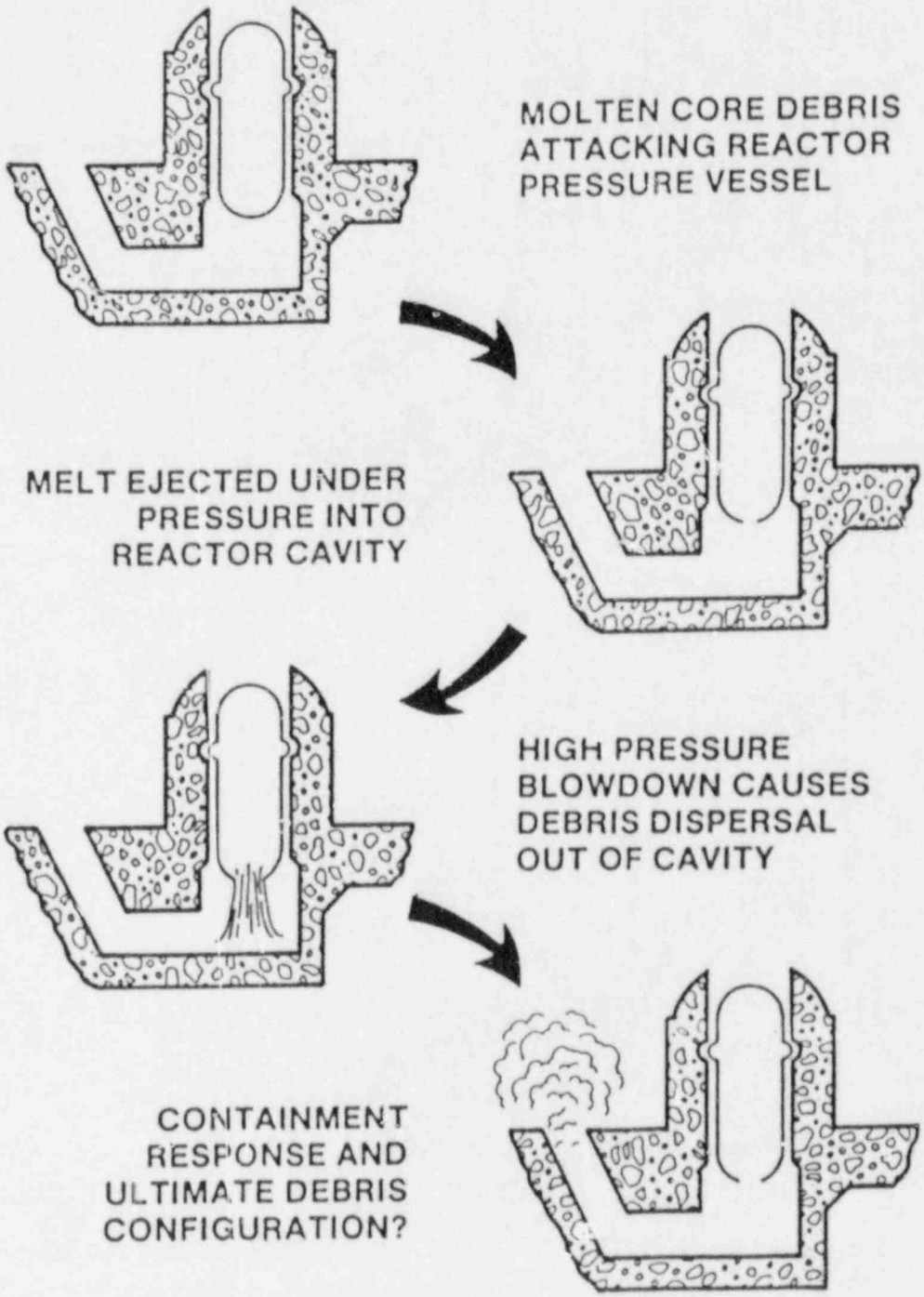

Figure 5. High-Pressure Melt Ejection and Direct Containment Accident Sequences

produced by DCH scenarios [12-14]. Some of these uncertainties are a result of the poorly known effect of high-temperature on spontaneous combustion temperatures (or autoignition temperature) and flammability limits as in the case of the in-cavity oxidation problem in section 2.a. Other uncertainties are due to dynamic conditions such as the transport and mixing of high-temperature gases promoted by the high pressure injection of the melt.

During high-pressure melt ejection, large quantities of hydrogen at temperatures up to 2000 K could be produced in the reactor cavity and lower compartment due to rapid metal-steam reactions. Since oxygen is almost immediately depleted in these regions during this ejection period, substantial amount of hydrogen will not be combusted and ultimately will enter into the upper compartment. The threat from containment overpressurization can increase significantly for some plants if the hydrogen were to burn in this ostensibly inert environment in the upper compartment, i.e. more than 55 percent of steam and at a temperature up to 900 K. Because of the uncertainties associated with the inerting criterion, or alternately the flammability limits of hydrogen-air-steam mixtures at elevated temperatures, a parametric study was performed. The parametric study consisted of two cases in an attempt to bound the hydrogen deflagration effect. The first case, identified as the default burn, is based on the existing flammability data of the mixture at a temperature of about 400 K. That is, a deflagration is precluded in a compartment if the concentration of steam is above 55 percent. The second case, identified as the unconditional burn, neglects any inerting effect; all hydrogen combusts regardless of the concentrations of hydrogen, oxygen, or steam. As shown in Table 1, a wide range of peak pressures may result between these two cases in the parametric study. In many of the runs, the assumed failure pressure of 9.3 bar for Surry and 4.45 bar for Sequoyah lie between the two cases.

The uncertainties associated with the flammability limits of hydrogen-air-steam mixtures are not the only ones for the DCH problem. Deflagrations are the only mode of combustion considered by the combustion models in CONTAIN. At temperatures that are high, but below spontaneous combustion temperatures, the likelihood of other modes of combustion may increase. For example, the effect of elevated temperature on the likelihood of hydrogen-air-steam mixtures to detonate is discussed in section 2c. For the DCH problem, if the mixture of hydrogen, air, and steam is uniformly mixed, will the mixture spontaneously combust, deflagrate, or detonate? If the mixture is not uniformly mixed, at what rate can combustion occur at the boundaries of the hot hydrogen jet or plume as it enters the relatively cooler upper containment atmosphere? It is also clear that these questions involve dynamic conditions including transport, mixing, and the presence of hot solid or liquid particles moving with the gases.

In order to better understand the combustion phenomenon in such an extreme environment produced by the DCH scenario and to reduce the uncertainties for risk assessment, it is necessary to conduct experiments to address questions regarding combustion at elevated temperatures. Questions such as flammability limits of a hydrogen:air:steam mixture and the characteristics of the jet/plume flame are difficult to answer theoretically because of the complexity of the problem. Experimental work at small scale could provide importan-

Case	Variation	Surry Plant		Sequoyah Plant	
		Default Burn	Unconditional Burn	Default Burn	Unconditional Burn
		P_{max}	P_{max}	P_{max}	P_{max}
1	Base case	7.2	9.3	7.6	6.6
2	No trapping: $\lambda_{tr} = 0$	7.9	9.8	7.4	7.4
3	Fast trapping: $\lambda_{tr} = 10\lambda_{tr}$ (base)	6.4	8.5	6.4	5.5
4	Change drop diam. from 0.5 to 1.0 mm	6.9	9.0	6.4	5.8
5	Change steam blowdown from 30 to 10 sec.	9.5	12.3	8.5	8.8
6	Change core injection fraction from 0.75 to 0.25	5.9	7.7	3.4	4.6
7	Change Zr oxidation from 0.5 to 0.30	7.4	9.1	7.6	6.6
8	Add 2.0E4 kg co-dispersed water	8.8	11.6	8.1	7.7
9	Add 1.0E5 kg co-dispersed water	6.9	9.5	3.6	4.2

Table 1. Comparison of sensitivity study results for Surry and Sequoyah [9]. Peak pressures are given in bars (10^5 Pa).

information on flammability limits, detonability limits, spontaneous combustion temperatures, and the dynamic conditions associated with the DCH problem. Scaling laws would also be necessary to apply these results to reactor geometry. Once the experimental data base is developed, hydrogen combustion correlations derived from this data base may be incorporated into predictive codes such as CONTAIN.

2.c Local Detonations

Another area of hydrogen combustion affected by high temperature is the possibility of local detonations in the vicinity of hot hydrogen-steam releases from the primary system. Two accident scenarios are examined: a TMLB', or station blackout, accident sequence and an S2D, or small-diameter break in the reactor coolant system, LOCA. For the first accident scenario, a MELPROG-PWR/MOD1 computer code analysis [15] of a TMLB' accident sequence for the Surry Unit 1 power unit indicates hydrogen-steam gas temperatures at the vessel outlet gradually increase from about 600 K to 1400 K over a time period of approximately one hour. Therefore, depending on the location of the release, the temperature of the hydrogen-steam mixture in the pipe at the release point may be up to 1400 K. For the second accident scenario, an analysis of a small break LOCA for the Bellefonte plant was made with the SCDAP/RELAPS computer code [16]. For an S2D accident sequence with a small break at the pump in the cold leg, calculations show average cold leg pipe temperatures gradually increase during a three hour time period from about 600 K to 1050 K. In general, the gas temperature is about 150 K higher [17] than the average cold leg pipe temperature indicating the hydrogen-steam gas temperature in the pipe may be up to 1200 K depending on the location of the release. For both accident scenarios, because of the gradual increase in gas temperature, hydrogen may be released before the hydrogen-steam mixture autoignites and potentially burn as a diffusion flame at the release. A hydrogen-steam release that is burning as a diffusion flame, therefore, can be an ignition source for hydrogen that may have accumulated previously in the vicinity of the release.

As the hot hydrogen and steam gases that are released mix with the cooler surrounding air, it is possible that local areas will contain detonable mixtures. These detonable mixtures will contain high-temperature off-stoichiometric hydrogen-air mixtures that are fuel rich and diluted with large amounts of steam. It is important that safety-related equipment and the containment survive a local detonation in these areas. Some safety-related equipment that is used to reduce containment pressure, however, is located at some distance away from the release. The likelihood of a local detonation depends on the effect that elevated initial temperature has on the detonability of hydrogen-air-steam mixtures. Based on recent theoretical predictions that will be discussed later in this section, the possibility of local detonations at elevated initial temperatures may be more likely than previously thought, particularly for the off-stoichiometric mixtures and mixtures with large steam concentrations that are likely to exist near the hydrogen-steam release. Although the theoretical predictions have been partially supported experimentally, uncertainties in the predictions at elevated initial temperatures cannot be quantified due to lack of experimental evidence.

The theoretical predictions are obtained from a Zeldovich-von Neumann-Doering (ZND) chemical kinetics model [18]. The model uses a set of 23 reac-

tions and 11 species for hydrogen oxidation. The one-dimensional ZND model of a detonation is used to calculate the reaction zone structure. Reaction zone length, to first order, may be proportional to an intrinsic chemical length scale of a detonation called the detonation cell width. The reaction zone length used to predict the detonation cell width is arbitrary. Theoretical predictions compare well with existing experimental data when the reaction zone is based on the location of Mach number 0.75. Other reaction zone lengths, such as one based on the maximum rate of energy release in the reaction zone, may also be used.

The limited experimental data are obtained from a heated detonation tube that is 0.43 m in internal diameter and 13.1 m long [19]. The temperature of the tube can be raised to approximately 375 K. The detonation is initiated by a sheet of high explosive and detonation cells are recorded on a 3.66 m long by 1.22 m wide smoked aluminum sheet formed into a cylinder that lines the opposite end of the tube.

The possibility of local detonations near the hot hydrogen-steam release should be considered based on theoretical predictions at elevated initial temperatures. As shown in Figure 6, a large decrease in the detonation cell width for fuel-lean hydrogen-air mixtures is predicted as the initial temperature increases from about 300 K to 500 K. Similar results are obtained for fuel-rich hydrogen-air mixtures with equivalence ratios larger than the example in Figure 6. Since the critical initiation energy depends on the cube of the detonation cell width, the decrease in the detonation cell width, or alternately the decrease in the critical initiation energy, represents an increased detonability of lean or rich mixtures with elevated temperatures. Above 500-600 K, the detonation cell width increases and is of the same order for all mixtures, from lean to rich. Unlike mixtures at ambient temperatures, this means there is essentially no difference in the detonability of mixtures from lean to rich at elevated temperatures.

A decreasing detonation cell width is predicted initially for stoichiometric hydrogen-air-steam mixtures with increasing initial temperatures as shown in Figure 7. The effect is most pronounced for hydrogen-air mixtures containing large amounts of steam that would typically exist near the hydrogen-steam release. Additionally the effectiveness of steam to inhibit detonations decreases with increasing temperature. The addition of 40% steam increases the detonation cell width for a stoichiometric mixture by about a factor of 200 at 380 K compared to no steam, but only by a factor of 2 at 800 K. Above 700-800 K, the detonation cell width is of the same order for all stoichiometric mixtures with 0-40% steam. Unlike mixtures at ambient temperatures, this means there is essentially no difference in the detonability of stoichiometric mixtures regardless of the steam content up to at least 40% at elevated temperatures.

The uncertainty in the theoretical predictions for the effect of temperature on the detonability of hydrogen-air-steam mixtures is not quantifiable in temperature ranges that are not supported with experimental data. Additionally, because different reaction zone lengths may be used in the theoretical predictions, additional uncertainty exists between theoretical predictions of the detonation cell width for the same mixture and temperature. For example, all predictions illustrated in Figures 6 and 7 are made using a reaction zone length denoted Z.75 based on the location of Mach number 0.75. When the theo-

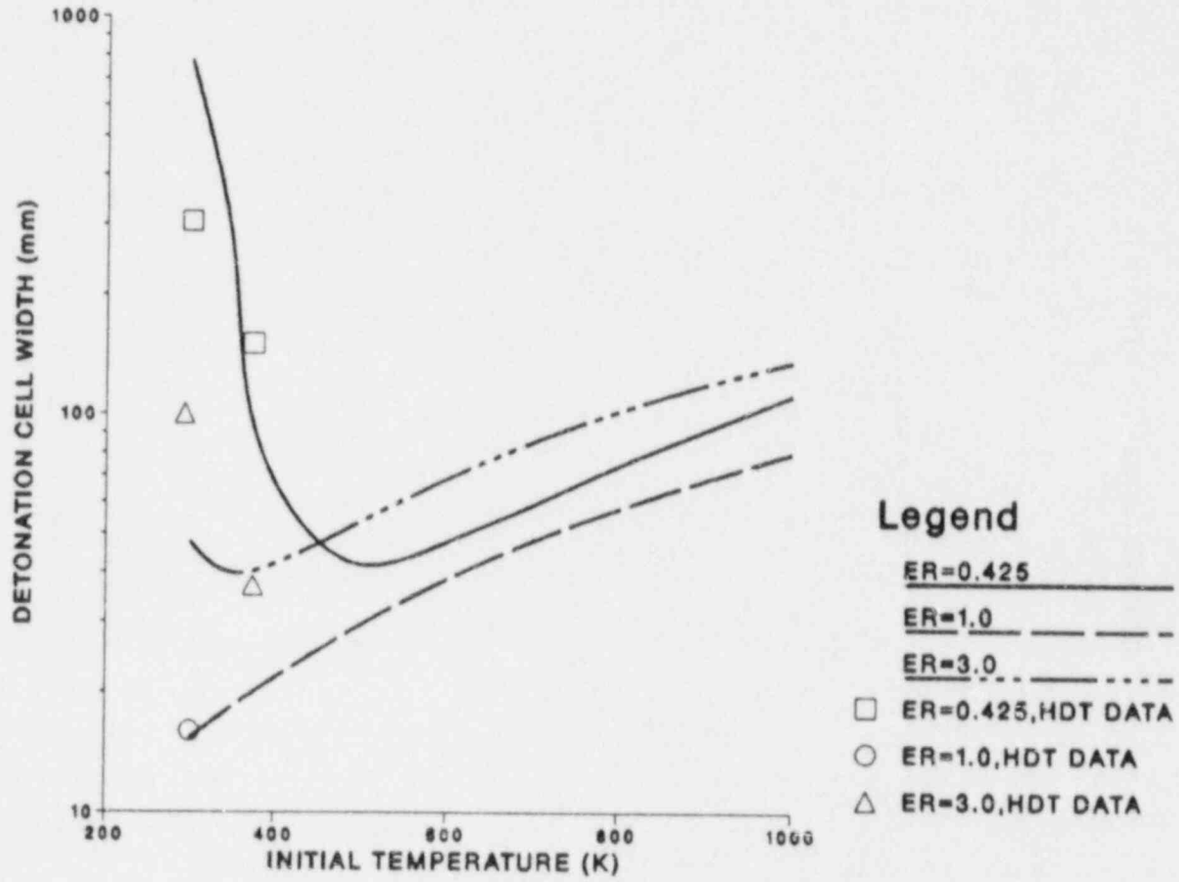

Figure 6. Effect of temperature and stoichiometry on hydrogen-air mixtures.

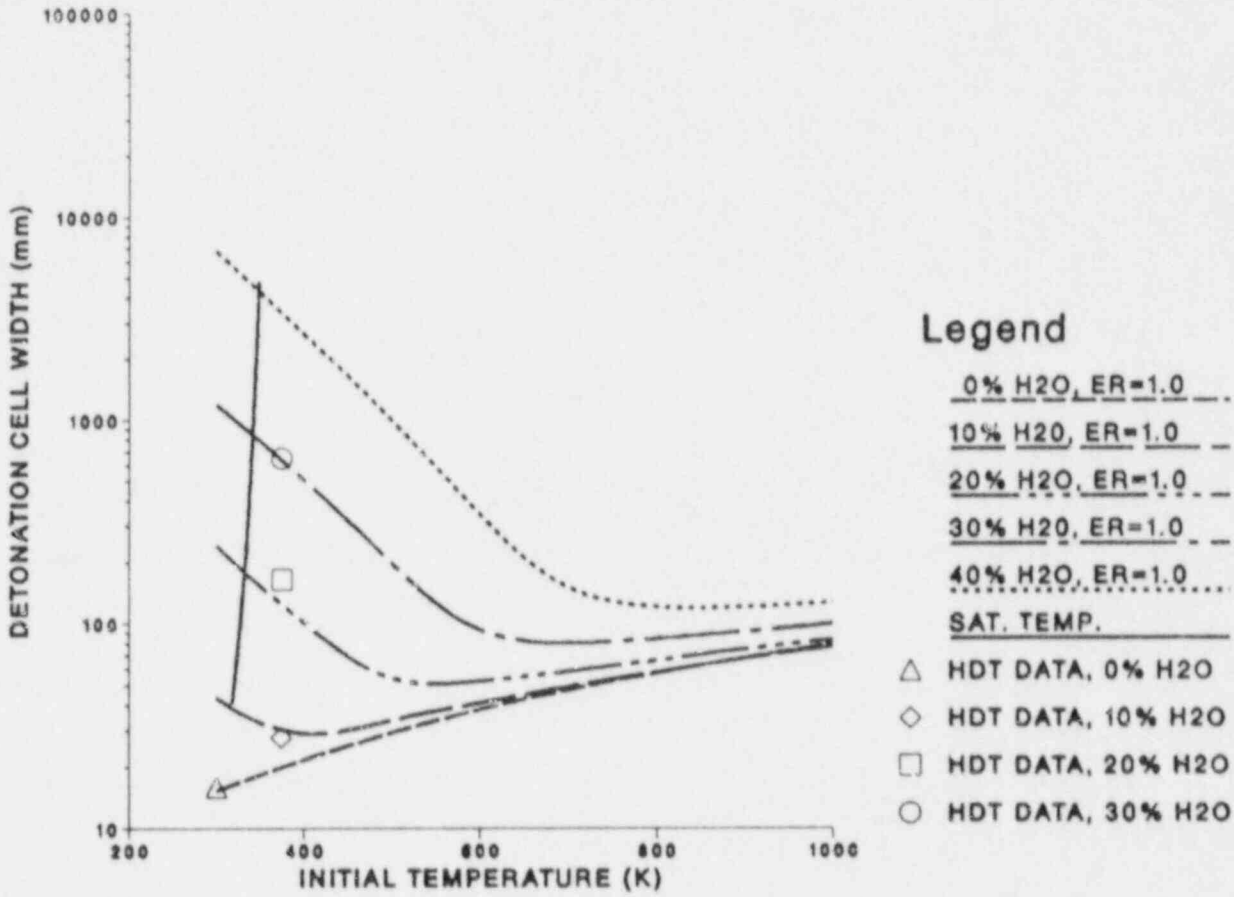

Figure 7. Effect of temperature and steam concentration on stoichiometric hydrogen-air mixtures. The reaction zone length Z.75, based on the location of the Mach number equal to 0.75, is used in the theoretical predictions.

retical predictions for the conditions in Figure 7 are made using a different reaction zone length denoted ZSIGMA (based on the maximum rate of energy release in the reaction zone) the trends are qualitatively the same in Figure 8 as in Figure 7 but differences are observed in the detonation cell width prediction. The reaction zone length Z.75 is currently used since it provides the best comparison between the predictions and the data available at lower initial temperatures. The reaction zone length that provides the best predictions of the detonation cell width for temperature ranges in which an experimental data base does not exist cannot be chosen a priori.

The increased detonability of hot hydrogen-air-steam mixtures predicted theoretically could influence several aspects of severe accidents that involve high gas temperatures. Hot hydrogen-steam release from a small break has been used as an example. Gas temperatures from a release could be up to 1400 K and in this temperature range a wide range of mixture concentrations will have similar detonabilities. As the hydrogen and steam from the release mix with the surrounding air, the potential for a detonation could increase dramatically based on theoretical predictions with increasing gas temperatures, even for off-stoichiometric mixtures and mixtures with large steam concentrations. The model's predictions have been supported experimentally only for hydrogen-air-diluent mixtures up to approximately 375 K. If the model is supported experimentally at higher temperatures, its predictions indicate that detonations may be significantly more probable than previously considered in the vicinity of hot hydrogen and steam released from the vessel or wherever the temperature is high.

3. Flame Acceleration and Deflagration-to-Detonation Transition

The uncertainty in the area of flame acceleration and DDT has increased importance due to recent experimental results presented later in this section that show the detonability limit is nominally at or near the flammability limit for some mixtures. For these mixtures, it is important to predict which mode of combustion, either a deflagration or a detonation, is more likely. The ability to make this prediction, however, depends on the likelihood of the mode of initiation of a detonation in a reactor accident. Since the direct initiation of a detonation in mixtures near the limits may be unlikely in a severe accident due to the large energy requirements, a more likely mode of initiation would be through flame acceleration and DDT. Direct initiation at the limits may be more likely at higher temperatures, however, based on the theoretical predictions discussed in Section 2.c. for the effect of elevated temperatures on the detonability of hydrogen-air-steam mixtures. Although past research on flame acceleration and DDT indicates the important effects of fuel concentration, obstacles, and venting, current uncertainties in the area of flame acceleration and DDT preclude the prediction of whether a deflagration or detonation is a more likely mode of combustion for certain severe accident conditions. These uncertainties are due to a lack of information on flame acceleration and DDT for conditions prototypical of severe accidents including the effects of steam dilution, elevated temperature, large scale, and prototypical obstacle types and spacings.

A comparison of the flammability, flame acceleration, and detonability limits is shown in Table 2. The detonability limits are not intrinsic but depend on scale, geometry, and initiation charge strength. The flame acceleration limit is defined as the point where the flow is choked. The flame ac-

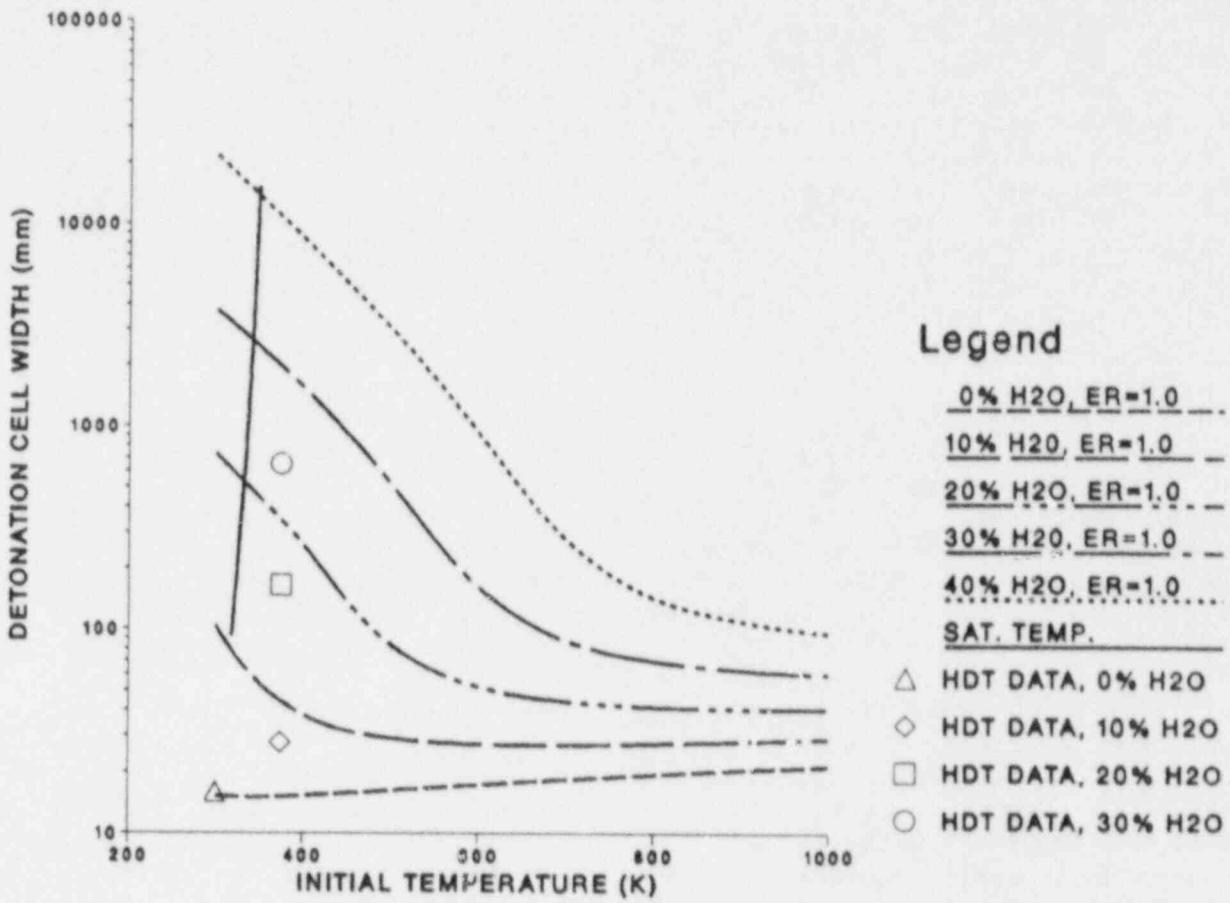

Figure 8. Effect of temperature and steam concentration on stoichiometric hydrogen-air mixtures. The reaction zone length ZSIGMA, based on the location of maximum energy release, is used in the theoretical predictions.

COMPOSITION	THERMODYNAMIC STATE	FLAMMABILITY LIMITS	FLAME ACCELERATION LIMITS +	DETONATION LIMITS *
Lean H_2-Air	T-20°C, P-1 atm	4-9% H_2[25]#	10% H_2[22]	11.7% H_2
Lean H_2-Air	T-100°C, P-1 atm	4.5% H_2[8]		9.5% H_2
Rich H_2-Air	T-20°C, P-1 atm	74.2% H_2[25]	73% H_2[22]	75% H_2
Rich H_2-Air	T-100°C, P-1 atm	78.5% H_2[8] (extrapol.)		77% H_2
Steam-Diluted Stoichiometric H_2-Air	T-100°C, P-1 atm	>52% H_2O[8]	>35% H_2O[26] (to inert)	>35% H_2O (to inert)
Helium-Diluted Stoichiometric H_2-O_2	T-22°C, P-1 atm	>86.5% He[27] (to inert)		>86.5% He[28] (to inert)

+ Acceleration of flame to the isobaric sound speed.

4% H_2 is the upward propagation limit and 9% H_2 is the downward propagation limit.

* The detonability limits are based on preliminary data and are subject to change.

Table 2. A Comparison of the Limits of Various Combustion Modes.

celeration limits are also not intrinsic and depend not only on scale, geometry, and initiation strength as with the detonability limits but also on other parameters such as obstacle type, spacing, and blockage ratio.

Several important points can be made from the comparison of the various combustion limits. First, a comparison of the detonability limits for hydrogen-air mixtures shows the important effect of increasing initial temperature. The detonable range of hydrogen in a hydrogen-air mixtures at 20°C in the HDT for a planar initiating charge of approximately 100 grams of high explosive is between 11.7 and 75 percent by volume. This range is much wider than the range of 18 and 59 percent reported earlier [20]. At 100°C initial temperature, the range of detonable concentrations expands to 9.5 and 77 percent. The widening of the limits from 20°C to 100°C by approximately 2 percent hydrogen on a volume basis on both the lean and rich limits illustrates the important sensitizing effect of increasing initial temperature discussed in the section on local detonations. Second, a comparison of the flame acceleration and detonability limits indicates the limits are similar for all mixtures tested. And finally, a comparison of the flammability and detonability limits for the mixtures in Table 2 shows that the limits are similar for some mixtures and, while there is a discrepancy between the limits for the other mixtures, the limits are much closer than previously thought. For those mixtures in which the limits are similar, if the mixture can deflagrate, it can detonate. The ability to determine which mode of combustion is most likely to occur will depend largely on our understanding of flame acceleration and DDT.

While a fundamental understanding of the mechanisms of flame acceleration and DDT is not available currently, recent reviews [21, 22] have summarized the important roles of geometry, scale, mixture concentrations, obstacles, venting, and ignition characteristics. The lowest concentration of hydrogen that has been observed to undergo a DDT is 15% by volume in the FLAME facility [23]. This is not necessarily the minimum concentration of hydrogen that may undergo a DDT. As shown in Table 2, flames have been observed to accelerate down to hydrogen concentrations of 10% by volume. It may be possible that mixtures in which flame acceleration has been observed may undergo a DDT given a sufficiently large scale and "run up" distance.

A qualitative methodology has been developed based on the present experimental data base for flame acceleration, DDT, and detonations to estimate the likelihood of a DDT in a reactor during degraded-core accidents [24]. Because most of the data, however, were obtained for dry hydrogen-air mixtures at ambient initial temperatures in facilities with small and intermediate scale, extrapolations of the present data were necessary to apply the methodology to reactor accidents. To reduce the uncertainty in the qualitative methodology, additional data on flame acceleration and DDT is necessary for conditions prototypical of severe reactor accidents. These conditions must include the effects of steam dilution, elevated temperature, scale, and prototypical obstacles and spacings.

4. Resuspension of Aerosols

In a nuclear reactor accident in which severe fuel damage occurs, aerosols containing fission products may be released into the containment building. Such a phenomenon was observed in the case of the Three Mile Island-2 accident in which numerous fission product radionuclides were found on the

walls, ceiling and floor of the reactor containment building. This process is sometimes referred to as plateout or deposition. Various accident scenarios predict the generation and deposition of aerosols on surfaces in the containment building. For example, calculations of the TMLB' sequence for the Surry plant suggest that on the order of 1 kg per square meter of aerosols will be deposited on floors and other horizontal surfaces [29]. This corresponds to an approximately 1 mm-thick layer of precipitated materials containing both structural and fission product particulates. Another important source of aerosol deposition in containment might be high pressure melt ejection [30].

It is usually assumed that the normal coagulation and settling processes associated with aerosols will tend to mitigate the volumetric concentration of aerosols in the containment progressively with time. It is also assumed that when these aerosols are removed from the containment volume by these deposition processes, they are no longer available for participation in the source term should the containment fail or somehow be circumvented at a late time. Additionally, it is assumed that steam or high humidity in the containment building will tend to cause efficient adhesion of the sedimented aerosols to the surfaces once deposited.

Recently, however, concern has arisen over the possibility that these once-sedimented aerosols might be placed back into gaseous suspension by various events that might happen in the containment [31]. One of these involves the catastrophic failure and depressurization of a containment building overpressurized by steam. Other gas dynamic processes such as the V-sequence [32] are also considered. Significant studies along these lines have been made in the LACE program [33].

Relatively little attention has been given to the possible ability of hydrogen combustion to resuspend once-sedimented aerosols. This may have occurred in the Three Mile Island-2 accident, for example, in which several global hydrogen deflagrations occurred. The effect of these burns on the sedimented aerosols has not been studied extensively to our knowledge.

Hydrogen combustion in containment might assume a variety of forms ranging from the mildest of deflagrations through accelerated flames and eventually to detonations, depending on such parameters as concentrations of hydrogen, the geometry of the system and the presence of turbulence-producing obstacles or mechanical agitation [34]. It seems likely that hydrogen burns could produce a variety of gas-dynamic processes that might affect the deposited aerosols. Moreover, it is also possible that energy transfer mechanisms unique to hydrogen burns might also participate in manners other than gas dynamic.

In order to study these phenomena in a preliminary way, Nelson and coworkers have taken advantage of an ongoing large scale hydrogen combustion program at Sandia National Laboratories to examine the removal and presumably resuspension of aerosols from prototypical reactor surfaces exposed to the burn environment [35]. Experiments were performed in the FLAME facility [36], which is an open-ended, linear channel in which the approach to and achievement of detonations under various circumstances are being studied. One experiment was also performed in a 5.1 m^3 inclined, open-ended cylindrical chamber called VGES-II [37]. Several experiments have also been performed recently in the 5.6 cubic meter FITS facility [8] to examine the possible effects of deflagrations in closed volumes compared to the open linear format of the FLAME facility.

Nelson, et al. [35] performed scoping experiments in which bare metal disks, or planchets, were exposed to the various combustion environments in the FLAME and VGES-II facilities. These planchets had been exposed to aerosols of CsI and MgO before the shots. The planchets were made of stainless steel and carbon steel. The planchets were analyzed pre- and post-shot by x-ray fluorescence to determine loss of the aerosols components. Salient features of their results with bare metal planchets were:

- For the more vigorous burns, there was removal of over 60% of Cs, I and Mg.
- For the milder burns, the amounts of Cs and I removed were lower, but still substantial, in the range 15-55%.
- The amounts of both CsI and MgO aerosols removed from stainless steel surfaces were somewhat greater than for carbon steel surfaces.
- A flowing, wet steam atmosphere locally enveloping two stainless steel planchets, one coated with CsI and the other with MgO, seemed to do little to reduce the aerosols removal compared to analogous, neighboring planchets exposed to the burn in the absence of steam. In fact, there is an indication that the removal might even have been enhanced in the presence of steam.

The preliminary experiments performed in the closed FITS chamber indicate aerosol removals on the same order as those observed in the experiments performed in FITS and VGES II.

In three FLAME experiments, stainless steel and carbon steel planchets were first coated with a phenolic finish and then exposed to a combined CsOH and MnO_x aerosol produced in experiment LA-2 of the LACE program [33]. Comparison of pre- and post-shot analyses of these planchets suggested:

- Trends in aerosol removal similar to those observed in the earlier experiments with bare metallic planchets.
- Greater removals of Cs than Mn.
- Poorer reproducibility of x-ray fluorescence measurements for some of the coated planchets caused by cracking and chipping of the phenolic finish coating during exposure to the LACE experimental environment.
- Little effect of a wet steam atmosphere to enhance adherence of either CsOH or MnO_x aerosols during the hydrogen burns.

Although there has been significant work done on resuspension of aerosols and the effect of moisture thereon in both nuclear [33] and non-nuclear [38] applications, there has been little effort devoted to highly energetic situations, as might be encountered in the hydrogen combustion situation. Most of the quantitative work on aerosol resuspension has been done in the presence of hydrodynamic flows only.

There are many uncertainties associated with the work of Nelson, et al. [35]. In none of their experiments was resuspension of aerosols studied directly. This was mainly a practical matter because of the scoping nature of the experiments. However, serious personnel, safety and environmental questions arise when a resuspension of aerosols experiment is attempted in a facility as large as the FLAME facility. It was estimated that to deposit a representative coating of aerosols on the floor of the FLAME facility it would

have been necessary to use 66 kg of aerosol. Since cesium iodide was one of the major materials of interest, the health and environmental impact of discharging this amount of material into ambient atmosphere was seriously questioned. Moreover in facilities as large as FLAME and VGES-II, the sampling of aerosols directly becomes as complex and costly operation. Furthermore, the interpretation of the data in a rapidly changing, pulsed flow becomes difficult. The experiments in the FITS facility, because it is a closed volume, should be more amenable to careful sampling and meaningful data analysis.

Nelson, et al. [35] have hypothesized that several unique properties of hydrogen burns may cause effective and efficient removal of aerosols deposited on surfaces. For example, the instantaneous presence of energetic short lived species such as free atoms and radicals and possibly ionic species may well provide a surface cleaning mechanism somewhat analogous to the commercially available plasma cleaning devices. Moreover the presence of rapid pressurizations and, in some cases, rarefactions, may cause the aerosol to efficiently leave the surface as the burn progresses. Nelson, et al. have also hypothesized that the most effective means of resuspending aerosols caused by the hydrogen burn might be related to the intense infra-red radiation produced during the burn. This would tend to give localized surface heating in the vicinity of the aerosols. It is also hypothesized by these workers that the discrete vibrational and rotational radiation emitted by excited water molecules may be selectively and efficiently absorbed by adsorbed water at surfaces which normally causes adherence of the aerosol to the surface. It is possible that the adhering film may virtually "explode" and drive aerosol from the surface. Nothing in their scoping experiments contradicted this observation.

In light of the possible containment-threatening nature of some hydrogen burns, and the apparently efficient removal of aerosols from surfaces in the presence of hydrogen burns, it would seem very important to study in careful detail the phenomena that would arise from exposure of deposited aerosols to hydrogen combustion. Not only should the removal experiments be extended, but also full scale resuspension experiments should be performed in which aerosols are sampled in the gas phase during and after the hydrogen burn. Many techniques are available for these latter studies. One that has been carefully worked on for use in atmospheric tracer experiments is the fluorescent dye particle technique which has been used to observe air motion over long distances (many kilometers) [39]. This might be considered as a scheme to study the aerosol resuspension produced in a large open combustion chamber such as FLAME. Also, the hypothesized selective absorption of discrete radiation emitted by excited water molecules might be tested by studying the combustion of CO in air. Since the products of this reaction do not contain water, the discrete emission from CO burns would definitely be at different wave lengths than the absorption of the water molecules at the surface. Thus a distinction might be made between the purely thermal (black or gray body) absorption of the radiation and this discrete absorption at specific molecular resonances. Another procedure for studying removal from surfaces would be to use optical methods [40].

5. Discussion of Uncertainties and Recommendations

Important uncertainties are identified for the areas of high-temperature

combustion, flame acceleration and DDT, and aerosol resuspension during hydrogen combustion. The impact of these uncertainties on various accident scenarios and recommendations to reduce these uncertainties are discussed. The uncertainties associated with high-temperature combustion may affect at least three different accident scenarios: the in-cavity oxidation of combustible gases produced by core-concrete interactions, the DCH hydrogen problem, and the possibility of local detonations. Uncertainties in the inerting criterion at elevated temperatures preclude the ability to accurately predict the degree of in-cavity oxidation. As a result of this, a parametric study using HECTR yields a wide range of peak pressures in the lower and upper compartment due to either steam pressurization or a hydrogen burn coupled with steam pressurization depending on the inerting criterion. The uncertainties may be reduced by obtaining high-temperature data for autoignition temperatures and flammability limits for hydrogen- arbon monoxide-air-diluent mixtures. Similar to the in-cavity oxidation problem, the peak pressure in the DCH problem cannot be predicted accurately due to uncertainties in the inerting criterion at high temperatures. An accurate prediction of the peak pressure may be important in determining containment integrity. Autoignition temperatures and flammability limits for hydrogen-air-steam mixtures at elevated temperatures will reduce these uncertainties. Additional uncertainties exist for the dynamic processes associated with the DCH problem. Determining what modes of combustion are possible and the different rates of combustion associated with the transport and mixing of combustible gases at elevated temperatures will reduce these uncertainties. The uncertainty in the theoretical predictions for the effect of initial temperature on the detonability of hydrogen-air-steam mixtures increases as the predictions are extrapolated farther from the existing database which is between approximately 300 K and 400 K. It is important to reduce these uncertainties to determine the likelihood of a local detonation at elevated temperatures. This can be accomplished by developing an experimental database for the detonability of hydrogen-air-steam mixtures at temperatures greater than 400 K, particularly for off-stoichiometric mixtures and mixtures with large steam concentrations. The ability to determine which mode of combustion, either a deflagration or a detonation, is most likely is not presently possible due to uncertainties in the areas of flame acceleration and DDT. These uncertainties impact the qualitative methodology that is currently used to estimate the likelihood of a DDT in a reactor during degraded-core accidents. To reduce the uncertainty in the qualitative methodology, additional data are necessary for conditions prototypical of severe reactor accidents including the effects of steam dilution, elevated temperature, scale, and prototypical obstacles and spacings on flame acceleration and DDT. Uncertainties associated with the removal mechanism of aerosols containing fission products, especially with respect to deposited aerosols in the presence of condensing steam, limit our ability to determine the effect that resuspension has on the radiological source term. The resuspension and dispersion of aerosols may have important radiological consequences if containment failed as a result of hydrogen combustion at some relatively late time. Because of the possible serious consequences, it seems important to be able to confidently model the effects of resuspension of aerosols by hydrogen burns on the source term under various accident scenarios. To validate the models, it is necessary to investigate experimentally on large and small scales the resuspension of aerosols both by direct sampling of the aerosols and by the removal of aerosols from surfaces.

References

1. "Technical Aspects of Hydrogen Control and Combustion in Severe Light-Water Reactor Accident," a report prepared by the Committee on Hydrogen Combustion, Energy Engineering Board, Commission on Engineering and Technical Systems, National Research Council, National Academy Press, Washington, DC, 1987.
2. S.E. Dingman, A.L. Camp, C.C. Wong, D.B. King, R.D. Gasser, HECTR Version 1.5 User's Manual, Sandia National Laboratories, Albuquerque, N.M., NUREG/CR-4507, SAND86-0101, February 1986.
3. C. C. Wong, A Standard Problem for HECTR-MAAP Comparison - In-Cavity Oxidation, Sandia National Laboratories, Albuquerque, N.M., to be published.
4. C. C. Wong, "Natural Convection and In-Cavity Oxidation of Combustible Gases," ANS Proceedings of the 1987 National Heat Transfer Conference, Pittsburgh, PA, August 9-12, 1987, p. 194-200.
5. G.G. DeSoete, "The Flammability of Hydrogen-Oxygen-Nitrogen Mixtures at High Temperature," La Rivista dei Combustibili, Vol. XXIX, No. 5-6, P. 166-172, May-June 1975.
6. M. Sheldon, "Understanding Auto-ignition Temperature," Fire Engineers Journal, Vol. 43, No. 133, P. 27 - 32, June 1984.
7. D.A. Powers, Sustained Molten Steel/Concrete Interactions Tests, Sandia National Laboratories, Albuquerque, N.M., NUREG/CR-1066, SAND77-1423, June 1978.
8. B. Marshall, Hydrogen:Air:Steam Flammability Limits and Combustion Characteristics in the FITS Vessel, Sandia National Laboratories, Albuquerque, N.M., NUREG/CR-3468, SAND84-0383, December 1986.
9. M.G. Zabetakis, Research on the Combustion and Explosion Hazards of Hydrogen-Water Vapor-Air Mixtures, Bureau of Mines, Division of Explosives Technology, Pittsburgh, PA., NTIS, USAEC Report AECU-3327, September 1957.
10. J.E. Shepherd, Hydrogen-Steam Jet-Flame Facility and Experiments, Sandia National Laboratories, Albuquerque, N.M., NUREG/CR-3638, SAND84-0060, February 1985.
11. B. Lewis and G. Von Elbe, Combustion, Flames and Explosions of Gases, P. 259, 2nd Edition, Academic Press, New York (1961).
12. D. C. Williams et al., Containment Loads Due to Direct Containment Heating and Associated Hydrogen Behavior: Analysis and Calculations With the CONTAIN Code, NUREG/CR-4896, SAND87-0633, Sandia National Laboratories, Albuquerque, NM, May 1987.
13. D. C. Williams, "Hydrogen Behavior in DCH Scenarios," memo to M.Berman, Sandia National Laboratories, March 31, 1987.
14. K. D. Bergeron, "Considerations for Experimental Research on Hot Hydrogen Jet Combustion," memo to M. Berman, Sandia National Laboratories, April 1, 1987.
15. J. E. Kelly, R. J. Henninger, and J. F. Dearing, MELPROG-PWR/MOD1 Analysis of a TMLB' Accident Sequence, Sandia National Laboratories, NUREG/CR-4742, SAND86-2175, January 1987.
16. P. D. Bayless, C. A. Dobbe, and R. Chambers, Feedwater Transient and Small Break Loss of Coolant Accident Analysis for the Bellefonte Nuclear Plant, E.G.&G. Idaho, Inc., NUREG/CR-4741, March 1987.

17. P. D. Bayless, E.G.&G. Idaho, Inc., personal communication, October, 1987.
18. J. E. Shepherd, "Chemical Kinetics of Hydrogen-Air-Diluent Detonations," Progress in Astronautics and Aeronautics, Vol. 106, p. 263, 1985.
19. S. R. Tieszen, et al., "Detonation Cell Size Measurements in Hydrogen-Air-Steam Mixtures," Progress in Astronautics and Aeronautics, Vol. 106, p. 205, 1985.
20. Z. M. Shapiro and T. R. Moffette, "Hydrogen Flammability Data and Application to PWR Loss-of-Coolant Accident," WAPD-SC-545, Reactors-Power, TID-4500, 13th Edition, September, 1957.
21. M. Berman, "A Critical Review of Recent Large-Scale Experiments on Hydrogen-Air Detonations," Nuclear Science and Engineering, Vol. 93, pp. 321-347, 1986.
22. J. H. Lee and R. Knystautas, Flame Acceleration Due to Obstacles and Transition to Detonation in Tubes, Final Report on Joint McGill-SNL Studies of Hydrogen Explosion and Threat to Nuclear Reactors, to be published.
23. M. P. Sherman, S. R. Tieszen, and W. B. Benedick, Flame Acceleration and Transition to Detonation in Channels, Fall 1987 Joint Meeting of the Western States and Japanese Sections of the Combustion Institute, Hawaii, November, 1987.
24. M. P. Sherman and M. Berman, The Possibility of Local Detonations During Degraded-Core Accidents in the Bellefonte Nuclear Power Plant, Sandia National Labs, NUREG/CR-4803, SAND86-1180, January 1987.
25. H. F. Coward and G. W. Jones, "Limits of Flammability of Gases and Vapor," U. S. Bureau of Mines Bulletin 503, 1952.
26. N. Brehm, DDT-Limits Under Blow Down Conditions, Technical University Munich, BMFT/NRC Core Melt Meeting, Cologne, West Germany, 1986.
27. R. K. Kumar, "Flammability Limits of Hydrogen-Oxygen-Diluent Mixtures," J. Fire Sciences, Vol. 3, pp. 245-262, 1985.
28. R. K. Kumar, Whiteshell Nuclear Research Establishment, personal communications, October, 1987.
29. K. D. Bergeron, Sandia National Laboratories, Albuquerque, NM, personal communication, 1986.
30. J. E. Brockmann and W. W. Tarbell, "Aerosol Source Term in High Pressure Melt Ejection," Nuclear Science and Engineering, 88, 342-356 (1984).
31. D. A. Powers, "Fission Product Release and Aerosol Generation within the Reactor Containment," Chapter 4 in Fission Product Behavior During Severe LWR Accidents - Modeling Recommendations for the MELCOR Code System, Sandia National Laboratories, Albuquerque, NM, SAND85-2743, NUREG/CR-4481, 1986.
32. A. Drozd, F. A. Elia, Jr., and J. E. Metcalf, "The V Sequence: An Engineering Viewpoint," Proceedings: American Nuclear Society Meeting on Fission-Product Behavior and Source Term Research, Snowbird, Utah, July 15-19, 1984, NP-4113-SR, Electric Power Research Institute, Palo Alto, CA, pp. 70-1 through 70-9, 1985.
33. G. R. Bloom, D. R. Dickinson, R. K. Hilliard, J. D. McCormack, L. D. Muhlestein, and F. J. Rahn, "Status of the LWR Aerosol Containment Experiments (LACE) Program" Proceedings of the Thirteenth Water Reactor Safety Research Information Meeting, Gaithersburg, MD, October 22-25, 1985, NUREG/CP0072, U.S. Nuclear Regulatory Commission, Washington, DC, v. 6, pp. 27-40, 1986.

34. M. Berman, "Hydrogen Behavior and Nuclear Reactor Safety," Chapter 2 in Recent Developments in Hydrogen Technology, Volume II, Editors, K. D. Williamson, Jr. and F. J. Edeskuty, CRC Press, Inc., Boca Raton, FL, pp. 35-67, 1986.
35. L. S. Nelson and K. P. Guay, "Experiments Related to the Resuspension of Aerosols During Hydrogen Burns," Proc. 24th Nat'l. Heat Transfer Conf., AIChE Symposium Series, Volume 83, Number 257, American Institute of Chemical Engineers, New York, pp. 369-374, 1987.
36. M. Berman, M. P. Sherman, and C. C. Wong, "Recent Results in Hydrogen Research," Proceedings of the Fourteenth Water Reactor Safety Research Information Meeting, Gaithersburg, MD, October 27-31, 1986, in press.
37. J. C. Cummings, J. R. Torczynski, and W. B. Benedick, Flame Acceleration in Mixtures of Hydrogen and Air, Sandia National Laboratories, Albuquerque, NM, SAND86-0173, in preparation.
38. M. Corn and F. Stein, "Re-entrainment of Particles from a Plane Surface," J. Amer. Indust. Hygiene Assn. 26, 325-336 (1965).
39. A. Leighton, A. Perkins, W. Grinnell, and F. X. Webster, "The Fluorescent Particle Atmospheric Tracer," J. Appl. Meteorology, 4, 334-348 (1965).
40. D. J. Holve and G. W. Davis, Analysis of a Single Particle Counter for Application to General Aerosol Measurements, Sandia National Laboratories, Livermore, CA, SAND82-8815, 1982.

*This work was supported by the U.S. Nuclear Regulatory Commission and performed at Sandia National Laboratories, which is operated for the U.S. Department of Energy under contract number DE-AC04-76DP00789.

QUANTIFICATION OF UNCERTAINTIES IN SOURCE TERM ESTIMATES FOR A BWR WITH MARK I CONTAINMENT*

M. Khatib-Rahbar, E. Cazzoli, R. Davis, T. Ishigami**, M. Lee
H. Nourbakhsh, E. Schmidt, S. Unwin

Department of Nuclear Energy
Brookhaven National Laboratory
Upton, NY 11973

1. INTRODUCTION

Over the last decade, substantial development and progress has been made in the understanding of the nature of severe accidents and associated fission product release and transport. As part of this continuing effort, the United States Nuclear Regulatory Commission (USNRC) sponsored the development of the Source Term Code Package (STCP), which models core degradation, fission product release from the damaged fuel, and the subsequent migration of the fission products from the primary system to the containment and finally to the environment.

In order to better establish the validity and potential applications of source term predictions from these phenomenological models, quantification of the uncertainties associated with the STCP calculated source terms is essential.

A methodology for Quantification and Uncertainty Analysis of Source Terms for Severe Accident in Light Water Reactors (QUASAR) has been developed and discussed in References [1] and [2]. The objectives of the QUASAR program are (1) to develop a framework for performing an uncertainty evaluation of the input parameters of the phenomenological models used in the Source Term Code Package[3] (STCP), and (2) to quantify the uncertainties in certain phenomenological aspects of source terms (that are not modelled by STCP) using state-of-the-art methods.

The QUASAR methodology consists of (1) screening sensitivity analysis, where the most sensitive input variables are selected for detailed uncertainty analysis, (2) uncertainty analysis, where probability density functions (PDFs) are established for the parameters identified by the screening stage and propagated through the codes to obtain PDFs for the outputs (i.e., release fractions to the environment), and (3) distribution sensitivity analysis, which is performed to determine the sensitivity of the output PDFs to the input PDFs.

*Work performed under the auspices of the U.S. Nuclear Regulatory Commission. Views expressed are not necessarily those of the Nuclear Regulatory Commission.

**Visiting Scientist from Japan Atomic Energy Research Institute.

In this paper attention is limited to a single accident progression sequence, namely; a station blackout accident in a BWR with a Mark I containment building. Identified as an important accident in the draft NUREG-1150[4] a station blackout involves loss of both off-site power and DC power resulting in failure of the diesels to start and in the unavailability of the high pressure injection and core isolation coding systems.

2. SCREENING SENSITIVITY ANALYSIS

The screening sensitivity analysis is necessary in order to reduce the number of input variables to a manageable level.

The general problem addressed by screening is one that is basic to the analysis of most large and complex computer codes. One is faced with solving a large system of equations requiring a vast amount of input data whose importance to the calculated results are not often quantitatively understood. Screening is thus designed to determine which data elements are important for a given calculated result. This will reduce the number of model parameters for which an extensive uncertainty analysis is needed.

Each constituent code in the STCP has been used for detailed sensitivity analysis. In this approach, a stratified Monte Carlo technique (i.e. the Latin Hypercube Sampling (LHS)) has been used to generate input vectors for each computer code. The response of the examined codes to these input variations were analyzed by regression. Importance measures based on Partial Correlation Coefficients (PCC's) and Standardized Regression Coefficients (SRC's) were calculated on the raw and ranked data as reported in References [5] through [8]. The choice of using the rank regression results (Partial and Standardized Rank Correlation Coefficients, PRCC and SRCC, respectively), rather than the results of the regression on the actual input variability, was based on the desire to avoid the adverse effects of nonlinear correlations of input and output variables[9]. In many cases, the functional dependencies of input and output variables may be complex and not be amiable to a priori specification. Also based upon the guidance provided in Reference [1], a threshold criterion for screening correlations was employed. If the absolute value of the PRCC exceeded 0.60 the paired variables were considered to be correlated to an extent worthy of further consideration, otherwise they were considered to be insensitive and thus eliminated as candidates for further uncertainty evaluation. Figure 1 shows a typical scatterplot and time dependent PRCC and SRCC for Sr release versus its activity coefficient, showing a very strong correlation.

Using this approach, the most sensitive input parameters to the STCP listed in Table 1 were screened and selected for further uncertainty analysis.

3. FORMULATION OF PROBABILITY DISTRIBUTIONS

The QUASAR program utilizes probabilisitic characterizations of STCP input parameter uncertainties. Care is taken, however, to address many of the concerns expressed on occasions regarding the formulation of probability distributions in the nuclear safety assessment context. Typical of such concerns are: (1) the spareseness of relevant data precludes reliance upon notions of experimental population variability in the construction of distributions, and (2) the subjective approach to formulating distributions

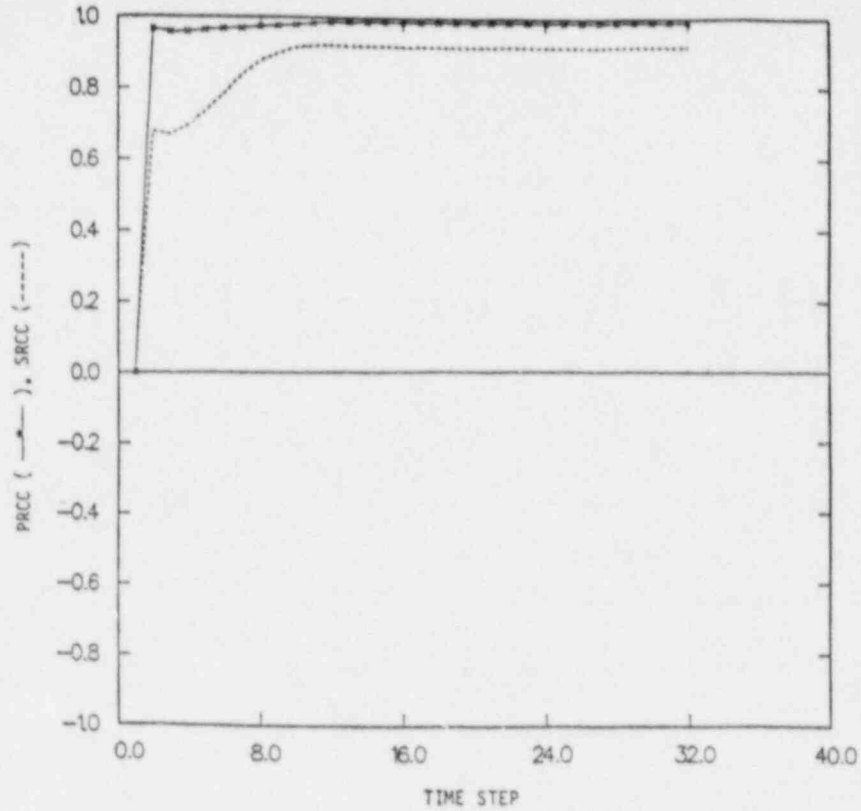

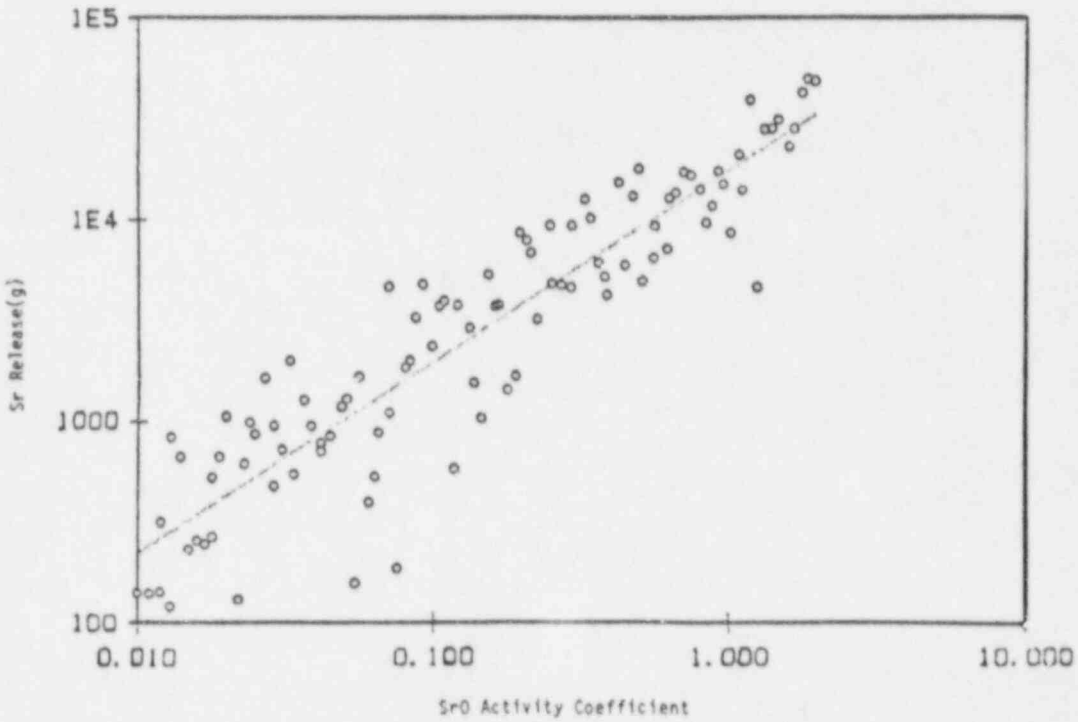

Figure 1 Typical scatterplot, PRCC and SRCC for Sr Release vs SrO Activity Coefficient.

Table 1 Most Sensitive Input Parameters for STCP Together With Their Respective Ranges and Probability Density Functions (Uncertainty Distributions)

Code	Parameter	Definition	Range (Percentile)				Coordinate Basis
			Min.	5th	95th	Max.	
MARCH	DPART (m)	Debris particle size (in-vessel)	10^{-3}	10^{-3}	0.2	0.2	Log-Uniform
	FHEAD	Fraction of bottom head CCI	0	0.01	1.0	1.0	Uniform
	FDROP	Core slump criterion	0	0.01	0.75	0.75	Uniform
	$\Delta H_f^{(1)}$ (MJ/m^3)	Volumetric latent heat of fuel	410	410	2420	2420	Uniform
	RHOCU ($MJ/m^3 °K$)	Volumetric heat capacity of fuel	2.96	2.96	4.44	4.44	Uniform
	TMELT (°K)	Fuel melting temperature	2120	2200	2980	3110	Uniform
	WGRID (kg)	Mass of grid plate	3.4×10^4	3.4×10^4	4.8×10^4	3.4×10^4	Uniform
	P_1(Pa)	Containment leakage pressure threshold	1.0×10^5	4.1×10^5	1.4x10	1.5×10^6	Uniform
	P_r(Pa)	Containment rupture pressure threshold	4.9×10^5	8.9×10^5	1.6x10	2.5×10^6	Uniform
	$C^{(2)}$(mm^2/Pa)	Proportionality constant between Drywell leakage area and drywell pressure	4.7×10^{-2}	4.7×10^{-2}	6.1×10^{-2}	6.1×10^{-2}	Uniform
CORSOR-M	Cs, I, Te(3)	Multiplier for the pre-exponential factor	10^{-3}	10^{-2}	2	10	Log-Uniform
	Ba, Sr(3)	" " " "	10^{-3}	10^{-2}	10	10^2	Log-Uniform
	Ru, Rh, Pd(3)	" " " "	10^{-1}	1	10^2	10^3	Log-Uniform
	Mn, Cr(3)	" " " "	10^{-3}	10^{-2}	10	10^2	Log-Uniform
TRAPMELT	GAMMA	Collision shape factor	1.0	1.2	10	15	Uniform
	VTE (mm/sec)	Te deposition velocity	0	0.1	90	100	Uniform
	PDEN (kg/m^3)	Aerosol Density	1000	1000	8000	8000	Uniform
SPARC	DIAM (mm)	Mean bubble diameter	3	4	12	20	Uniform
	RATIO	Bubble aspect ratio	1	1.25	1.5	4	Uniform
	VSWARM (m/sec)	Bubble swarm rise velocity	0.2	0.25	1.0	1.2	Uniform
CORCON	RW (m)	Corium spread (radius of corium pool)	3	3	6.5	6.5	Uniform
	TDC (°K)	Concrete decomposition temperature	1200	1690	1875	1950	Uniform
	EVAP	Weight % of concrete evaporable water	2.3	3.9	7.8	3.0	Uniform
	EM	Metal phase emmissivity	0.2	0.5	1.0	1.0	Uniform
	ES	Emmissivity of Surroundings	0.1	0.1	1.0	1.0	Uniform
VANESA	SIGMA	Aerosol size distribution parameter	1.5	1.5	3.2	3.2	Uniform
	NC	Number concentration of condensed aerosol	10^7	10^7	10^9	10^9	Log-Uniform
	Mo, Te, CsI	Activity coefficient	10^{-4}	10^{-3}	1	10	Log-Uniform
	BaO, SrO(2)	" "	10^{-4}	10^{-3}	1	10	Log-Uniform
	La_2O_3, CeO_2(2)	" "	10^{-4}	10^{-3}	1	10	Log-Uniform
NAUA	GAMMA	Collision shape factor	1.0	1.0	10	10	Uniform
	CHI	Dynamic shape factor	1.0	1.0	5.0	10	Uniform

(1) With a correlation coefficient of 0.9 with TMELT
(2) $A=C(P-P_1)$
(3) With a correlation coefficient of 0.9

gives an unwarranted impression of precision, thus understating the true degree of uncertainty.

The QUASAR approach to formulating distributions is a new one in the Probabilistic Risk Assessment (PRA) context and places reliance upon principles of information theory.[8] Given the absence of a relevant data base, the utilization of expert opinion in characterizing uncertainties is a necessity. The approach utilized, however, is one in which the information elicited from the experts does not exceed that of which each individual is legitimately capable of providing. In particular, the experts were not asked to provide entire probability distributions, but, rather, to provide a minimal number of constraints, relative to each uncertain parameter, that the corresponding distribution must satisfy. A measure characterizing the uncertainty reflected by each probability distribution, was then maximized subject to whatever expert-provided constraints were available. In this way, the resultant distributions are those that reflect the greatest degree of uncertainty consistent with the finite, individually defensible constraints furnished by the experts.

Details of the technique for formulating probability distributions in the QUASAR program are contained in Reference [8]. In brief, the approach is one in which the constraints upon any one distribution is in the form of uncertainty bands: a credibility band and a reasonable uncertainty band. The former is the narrowest band that encompasses all 'credible' values of the parameter under consideration. Hence, it determines the region of the parameter space over which the distribution is to be constructed. Clearly, where Monte Carlo methods are to be utilized to propagate distributions, all approaches require the establishment of such bands. The latter type of band is the narrowest such that there is 'reasonable' certainty that the true value of the parameter does not lie outside the band. For this less restrictive band definition, the convention used was one in which the band edges are interpreted, generally, as 0.05 and 0.95 quantile levels of the distribution to be constructed. The basis for this convention is discussed in References [8] and [10].

Extremization of a distribution subject to these constraints is effected relative to the Kullback-Leibler information-difference measure D:

$$D = \int P(x) \ln \left[\frac{P(x)}{P_o(x)} \right] dx$$

Here, x is the parameter of uncertain magnitude, P(x) is the distribution to be formulated and $P_o(x)$, the pre-prior, is the distribution adopted to reflect maximal ignorance in the absence of constraints. D, a measure of the difference between the information inherent in P(x) and the information inherent in $P_o(x)$, is closely related to the notion of information-theoretic entropy, although somewhat refined. Hence, to maximize the uncertainty reflected by P(x), subject to constraints, is to minimize D subject to those same constraints. Given, the reasonable uncertainty band constraints described earlier, the distribution that minimizes D is generally of a simple piecewise uniform or piecewise loguniform nature.

With regard to the aggregation of the opinions rendered by individual members of any one expert group, two options were available: (1) distributions could have been formulated on an expert-specific basis and then aggregated via some probabilistic algorithm, or (2) the uncertainty band information provided by each expert could have been aggregated by the analysts into net uncertainty bands and a single distribution then formulated by use of the information-theoretic principles described. The latter option was selected for both practical and conceptual reasons. The practical reason is that not all experts provided appropriate constraints by which to implement the information theoretic principles. The conceptual reason is that aggregation of distributions utilizing some selected probabilistic algorithm would not in general preserve the simple scrutable nature of the input piecewise uniform distributions. Given that scrutability and defensibility are prime objectives of the distribution formulation procedure, aggregation of the raw expert-provided information, by reference to the underlying physical and chemical principles, was the preferred approach.

4. PROPAGATION OF UNCERTAINTIES

The uncertainties associated with each input variable quantified in the previous section and listed in Table 1 are propagated through the STCP using the LHS approach. The various dependencies between the variables is taken into account during the sampling process.

The choice of the sample size n depends on a number of considerations but will be dominated by the cost of carrying the calculations and the number of the input variables k. Though it is not an absolute rule, it is suggested that n be greater or equal to 4/3k for moderate k. For the present analysis, this requires a sample size of about 60 (k=43; n=4(43/3)=57); however, in order to minimize possible statistical errors, a sample size of 100 was adopted.

The 100 LHS input vectors were propagated through the STCP and detailed thermal-hydraulics and fission product release information were stored for future evaluation.

5. OUTPUT IMPORTANCE AND SENSITIVITY ANALYSIS

Following the completion of the uncertainty propagtion, the sizeable number of STCP generated samples are used to determine the importance measures based on the time-dependent PRCC and SRCC for all of the relevant variable to establish an importance ranking. Furthermore, the sensitivity of the calculated radiological release uncertainty distributions to the assigned input uncertainties (input PDFs) is also established as described in Reference [12].

6. RESULTS

Figure 2 illustrates the calculated uncertainties (PDFs) associated with the radiological releases into the environment for the nine fission product groups at 10 hours following the initiation of corium-concrete interactions. Also shown are the results of the STCP base case simulation. It is seen that the uncertainties in the calculated releases are significant.

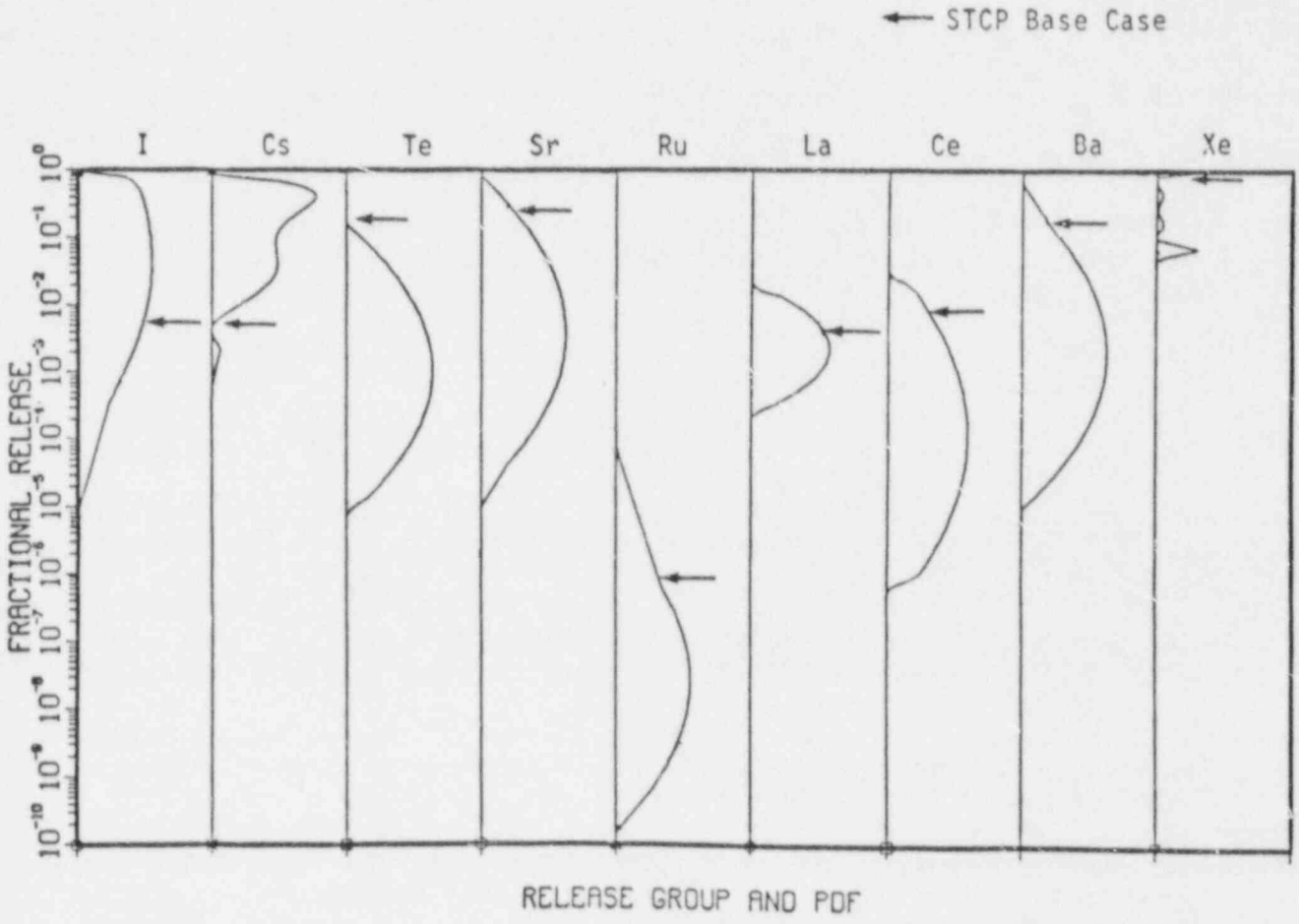

Figure 2 Calculated uncertainties in radiological releases into the environment for a station blackout sequence in a BWR with Mark I containment.

The calculated uncertainties in Iodine and Cesium releases are for the most part governed by the uncertainties in the transient release during core meltdown and in the CsI chemical activity coefficient during corium-concrete interactions, and to a lesser degree by the core slump criterion and the containment leakage pressure threshold.

The uncertainties in Te, Sr, Ru, La, Ce, and Ba releases are governed by the uncertainties in the chemical activity coefficients and the containment rupture pressure threshold. The apparent reduced uncertainty for the La group in comparison to other refractory groups is due to the assumed reference state of Nb in the STCP/Mod1 version of VANESA code, which has been corrected in more recent versions of the VANESA code. On the other hand, the uncertainty in the release of noble gases is only governed by the containment rupture pressure threshold.

REFERENCES

1. C. Park and M. Khatib-Rahbar, "Quantification and Uncertainty Analysis of Source Terms for Severe Accidents in LWRs (QUASAR), Part 1: Methodology and Program Plan", NUREG/CR-4688 (June 1986).

2. M. Khatib-Rahbar, et al., "QUASAR: A Methodology for Quantification of Uncertainties in Severe Accident Source Terms", Trans. Am. Nucl. Soc. 53, 354 (1986).

3. J.A. Gieseke, et al., "Source Term Code Package: A User's Guide (Mod 1)", NUREG/CR-4587 (July 1986).

4. "Reactor Risk Reference Document", NUREG-1150, Draft (February 1987).

5. C.K. Park and E.G. Cazzoli, "QUASAR Screening Sensitivity Analysis: Application to the NAUA Aerosol Transport Code", BNL Technical Report A-3286 (March, 1987).

6. R.E. Davis, et al., "QUASAR Screening Sensitivity Analysis: Application to the CORCON and VANESA Codes", BNL Technical Report A-3286 (June 1987).

7. H.P. Nourbakhsh, et al., "QUASAR Screening Sensitivity Analysis: Application to the Suppression Pool Aerosol Removal Code (SPARC)", BNL Technical Report A-3286 (July 1987).

8. S.D. Unwin, et al., " The Formulation of Probability Distributions for the QUASAR Program", BNL Technical Report A-3286 (September 1987).

9. R.L. Iman, et al., "A FORTRAN77 Program and User's Guide for the Generation of Latin Hypercube and Random Samples for Use With Computer Models", NUREG/CR-3624 (1984).

10. I. Cook and S.D. Unwin, "Controlling Principles for Prior Probability Assignments in Nuclear Risk Assessment", NUREG/CR-4514 (1986).

PRELIMINARY RESULTS OF AEROSOL DEPOSITION EXPERIMENTS IN AN ENGINEERING-SCALE ICE CONDENSER

L. D. Kannberg, M. W. Ligotke, E. J. Eschbach, and B. A. Ross
Pacific Northwest Laboratory(a)
Richland, Washington 99352

ABSTRACT

Initial data are reported from engineering-scale tests of aerosol deposition in a small section of an ice condenser typical of that used in certain pressurized water reactors (PWRs). The data will be used to validate a computer code (ICEDF) that predicts aerosol deposition in PWR ice condensers. The code was developed to assess the effectiveness of one type of engineered safety feature (ESF). Such assessment is part of a high-priority U.S. Nuclear Regulatory Commission effort to reassess and update analytical procedures for estimating accident source terms for nuclear power plants.

The engineering-scale test facility designed and constructed for the testing has the capability of passing steam/air mixtures through a test section containing the equivalent of four full-height (48-ft) ice baskets. Flows ranging from 0.03 to 0.38 m^3/s at temperatures up to 200°C are possible. Aerosols to be mixed with the gas flow are generated by dispersion of powders in fluid energy mills or by atmoization of liquids in two-fluid spray nozzles.

Results of the three tests completed show that decontamination factors (DF = aerosol mass flux entering divided by aerosol mass flux leaving) from 1 to 3 are achieved in the test section depending on aerosol, gas flow, and ice conditions. A measured DF of 1.0 was obtained when no ice was present in the test section, the aerosol aerodynamic mass median diameter (AMMD) was 6 μm, and gas flow rate was low, 0.03 m^3/s. The computer code, ICEDF, calculated a DF of 1.4 for similar conditions. When ice was present in the system and the same aerosol and gas flow conditions were used, the measured DF increased to 2.1 while the ICEDF computed DF ranged from 2.6 to 1.9. The DF increased dramatically when the gas flow rate was increased to 0.23 m^3/s and had a steam mole fraction of 0.44. Including the zone upstream of the test section where considerable cooling occurs, a measured DF of 10 or more was observed. The test section DF declined during this test from 3.6 to less than 1.0, as ice was melted out. Particle growth from 2.4 μm (AMMD) to 9.1 μm (AMMD) was observed in the test section during this test, probably due to steam condensation. Test temperature data and flow visualization studies indicate complex gas flow with stable large-scale flow recirculation.

(a) Operated for the U.S. Department of Energy by Battelle Memorial Institute under Contract DE-AC06-76RLO 1830.

INTRODUCTION

The U.S. Nuclear Regulatory Commission (NRC) is undertaking numerous studies to refine earlier estimates of radioactive emissions from nuclear power plants during severe accidents. This effort to define source terms includes the evaluation of various engineered safety features (ESFs) as a means of reducing the postulated airborne concentrations of radioactive aerosols within a power reactor containment system following a severe reactor core accident.

One ESF in certain pressurized water reactor (PWR) containment buildings is an ice condenser. The primary function of this ESF is to condense steam that would otherwise contribute to a buildup of pressure in the containment shell. A typical ice condenser is illustrated in Figure 1. The ice condenser is composed of 1,944 baskets, each 48-ft (14.6-m) tall and 1-ft (30.5-cm) in diameter. Each basket contains flaked, borated ice. The amount of ice typically present during reactor operation is in excess of 1.1 million kg (2.4 million lb).

Results of an earlier examination of the ice condenser suggest that it could serve as a very effective aerosol trap during severe nuclear accidents (Winegardner, Postma, and Jankowski 1983). A computer program, ICEDF, was developed to estimate the extent of aerosol deposit in the ice condenser (Owczarski, Schreck, and Winegardner 1985). However, the code developers found inadequate data for code validation.

To help validate the ICEDF code, researchers at Pacific Northwest Laboratory (PNL) have initiated a program to obtain data on the deposition of aerosols in a representative section of an ice condenser. In the test section, all pertinent thermohydraulic and aerosol deposition processes anticipated during reactor accidents are represented as closely as feasible.

The program was initiated in 1985. This paper provides an update on information presented a year ago (Kannberg et al. 1986). Discussion focuses on the completion of test facility construction and on initial test results.

Before initiating design and construction of the test facility, a review of the available information on severe accident sequences was conducted for PWRs having ice condensers. Information on thermohydraulic and aerosol conditions at the inlet to the ice condenser was used to develop functional design criteria for the test facility and to help design a matrix of conditions at which testing would be conducted. This test matrix is shown in Table 1. The underlined tests have been completed.

This work was supported by the U.S. Nuclear Regulatory Commission under Contract DE-AC06-76RLO 1830, NRC FIN B2444.

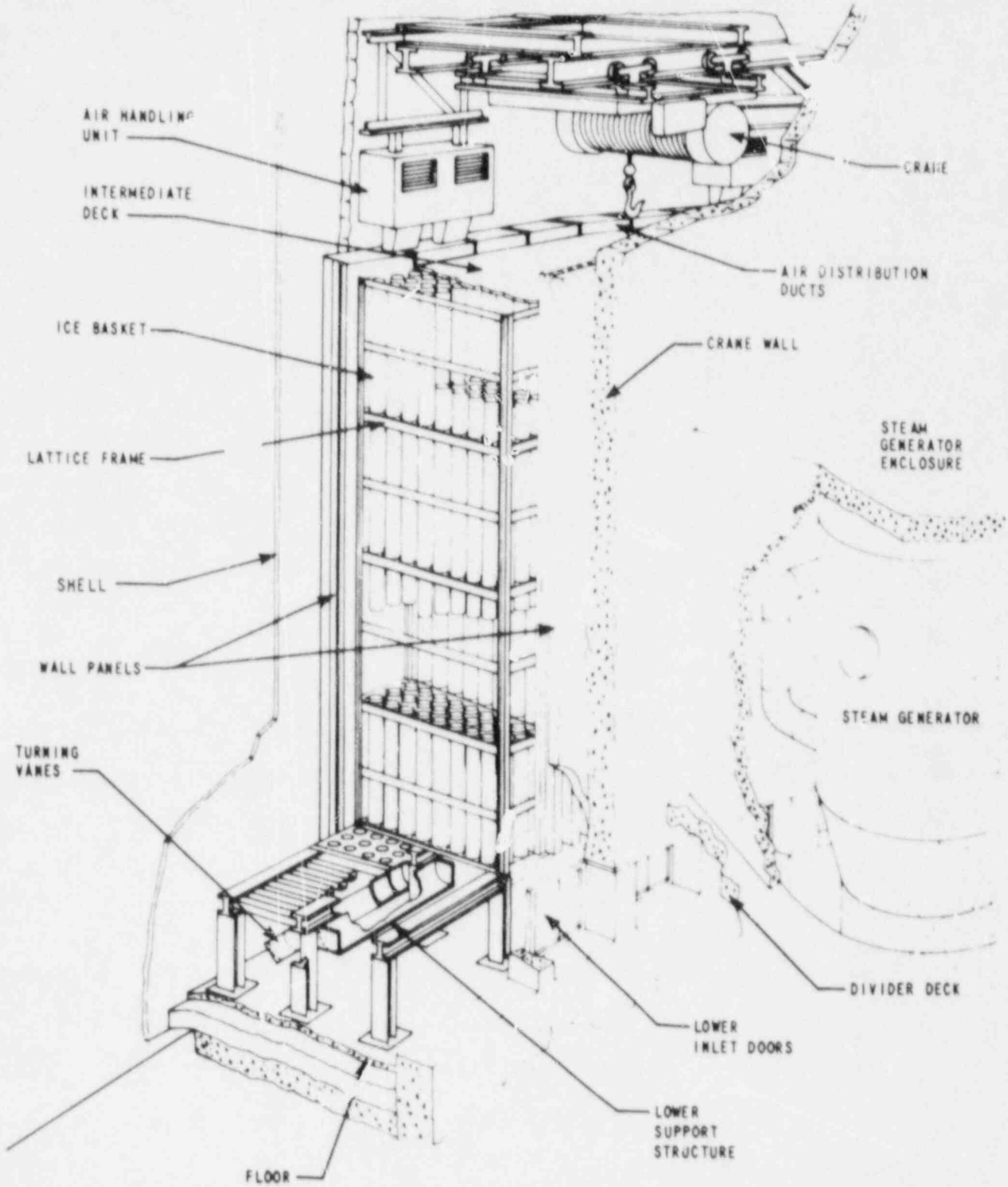

FIGURE 1. Isometric Diagram of Ice Condenser

TABLE 1. Text Matrix

Test No.	Particulate Characteristics: AMMD m	Density g/cc	Mass Conc. g/m^3	Material Solubility	Test Section Inlet Stream Parameters: Temperature °C	Volume Flow Rate m^3/s	Steam Mole Fraction	Test Section: Ice Fraction
1	12.00	4.5	7.0	1	60	0.15	0.20	1
2	12.00	2.0	0.74	-1	60	0.030	0.04	1
3	0.70	2.0	0.0037	-1	60	0.15	0.04	1
4	12.00	2.0	20.0	-1	105	0.033	0.90	1
5	4.22	2.0	7.0	1	105	0.380	0.90	1
6	12.00	2.0	1.8	1	200	0.030	0.04	1
7	4.98	4.5	7.0	-1	200	0.15	0.04	1
8	12.00	2.0	0.74	-1	200	0.380	0.90	1
9	1.25	4.5	0.0037	1	200	0.030	0.90	1
10	6.00	2.0	4.0	1	125	0.220	0.42	1
11	2.00	4.5	0.025	-1	125	0.220	0.60	1
Replicate 12 (4)	12.00	2.0	20.0	-1	105	0.033	0.90	1
13 (5)	4.22	2.0	7.0	1	105	0.380	0.90	1
14 (10)	6.00	2.0	4.0	1	125	0.220	0.42	1
No ice 15 (2)	12.00	2.0	0.74	-1	60	0.030	0.04	0

Notes:
Material solubility: 1 = soluble, -1 = insoluble
Ice fraction: 1 = full ice baskets, 0 = empty ice baskets
AMMD = aerodynamic mass median diameter
Underlined tests completed as of 10/01/87

FACILITY DESCRIPTION

The purpose of testing conducted in the ICEDF test facility is to measure the retention of airborne particles that would occur under prototypic conditions in a nuclear power plant ice condenser. A number of testing capabilities have been developed:

- generation of uniformly-mixed steady-state streams of heated air, superheated steam, and various aerosols
- introduction of gas/aerosol mixtures into a representative full-height ice condenser test section
- measurement of gas temperature, steam content, and aerosol concentration and size distribution at the entrance, exit, and various locations within the ice condenser test section
- measurement of the test section temperature and rate of liquid draining from the test section
- filtration of particulate matter from the exhaust gas stream.

Construction of the test facility was completed in April 1987. An isometric view of the facility is presented in Figure 2.

The inlet stream to the ice condenser test section is composed of steam, hot air, and various aerosols as required for each individual test. A total inlet gas flow rate range of 0.03 to 0.38 m^3/s corresponds to prototypic plant flow rates of approximately 16 to 200 m^3/s. Steam is generated for most of the testing in a 150-kW electric boiler and can be superheated to 200°C. Steam for high flow tests (0.38 m^3/s), scheduled for late in FY 1988 and FY 1989, will be provided by a rented, gas-fired boiler capable of providing 910 kg/hr (2000 lb/hr). Filtered compressed air is used for tests requiring low noncondensible flow rates. Higher noncondensible flow rates are provided by a 45-kW (60-hp) blower. A heater is used to heat the air stream to 200°C.

The test section has a square cross section and contains the equivalent of four full-height [48-ft (14.6-m)] ice baskets. The cross section has one whole basket (graciously provided by Duke Power Co.) and four each of half- and quarter-section baskets. A lattice work of support members matching the plant arrangement is provided every 6 ft of elevation in the test section. Turning vanes are provided in the 90° corner ducts above and below the ice baskets to reduce nonuniform gas flows that may be caused by flow redirection. The test section contains 11 access doors (including one for ice loading), 11 4-in. (10.2-cm) windows, and 12 instrument probe panels. A valved bypass is provided to permit operation of fluid and aerosol streams while maintaining the ice condenser test section in isolation.

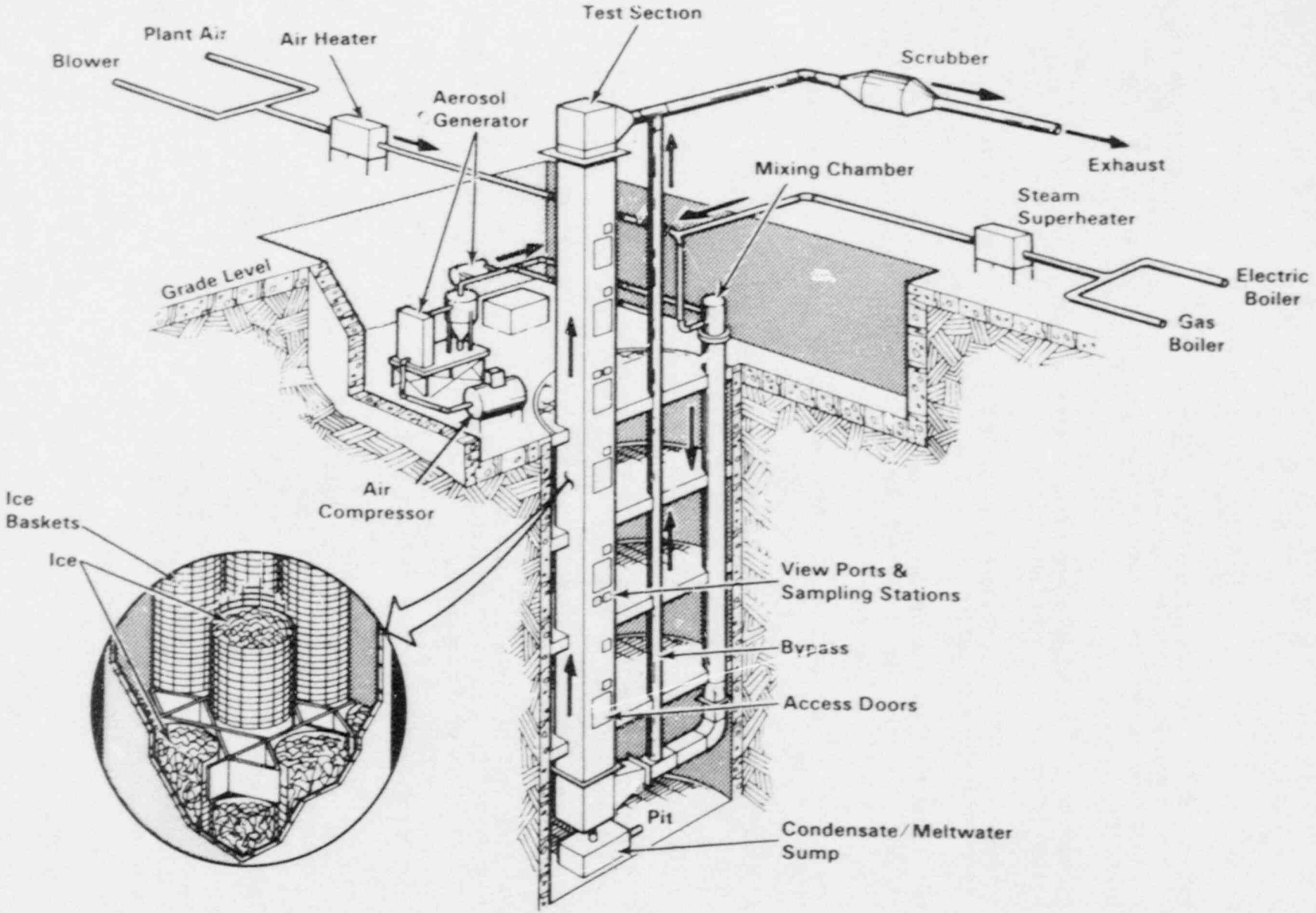

FIGURE 2. Ice Condenser Aerosol Deposition Test Assembly

All fluid streams supplied to the test section inlet are characterized with variable area flowmeters, with the exception of the high flow air supply, which is monitored with a vortex meter. The exit gas flow rate is measured with a pitot-static tube.

Liquid drained from the test section is measured in a sump and periodically pumped to waste. Liquid collected in the sump is sampled periodically during the test to evaluate particulate matter concentration in the meltwater.

Temperatures and pressures are monitored for all fluid streams entering and exiting the test section and at various locations in the test section. The measurements of temperature in the test section are made in the channels between the baskets where the primary gas flows occur when ice is present. During a test, thermohydraulic data are gathered and stored automatically by a computer data acquisition system (DAS). The DAS records output from 80 temperature sensors, 8 pressure transducers, 7 flowmeters, 2 load cells, and a laser transmissometer.

Aerosol mass concentration is measured with filters at five locations including the inlet to the test section and at four elevations. Aerosol size distribution is measured with cascade impactors at three locations including the inlet and two test section elevations. In both cases, isokinetic probes are used to withdraw the sample from the test section. The sampling probes are heat traced to prevent condensation in the sampling lines or on the collection substrate. Critical orifices are used to control sample flow rates. Chilled condensate traps are used to condense water to determine the steam mole fraction in the test section gas periodically during the test.

The parameter ranges were selected because they span the majority of conditions occurring during postulated accidents. However, the entire range of accident conditions could not be accommodated within a reasonable design. Aerosol solubility is considered an important factor because of its possible affect on the particle growth, which is due to steam condensation and ice melt. The size distribution of the aerosol particles is also important because anticipated processes of deposition are strongly affected by particle size. For testing purposes, two distinct particle densities were selected, 2 and 4.5 g/cm^3. The combinations of parameters, probable generation methods, and primary aerosol materials are given in Table 2. Cesium iodide, a likely actual accident aerosol material, will be used during tests involving dense, soluble particles. Complex aerosols, having particles consisting of several different materials will not be addressed in this phase of ICEDF code validation experimentation. A two-fluid atomizing nozzle system was selected to generate most of the aerosols with aerodynamic mass median diameters (AMMD) less than approximately 2 μm and an energy mill was selected to generate the remaining large-particle aerosols.

TABLE 2. Aerosol Generation Techniques and Materials for ICEDF Tests

Test No.	Generator	Primary/Backup Material
1	EM	CsI/-
2	EM	SiO_2/Fluorescein
3	AN	Fluorescein/SiO_2
4	EM	SiO_2/Fluorescein
5	EM/AN	NaCl/KCl
6	EM	KCl/NaCl/Uranine
7	EM/AN	ZnS/TiO_2/Al_2O_3
8	EM	SiO_2/Fluorescein
9	AN	CsI/-
10	EM/AN	KCl/NaCl
11	AN	ZnS/TiO_2/Al_2O_3

Material	Formula	Material	Formula
Primary		Secondary	
Alumina	Al_2O_3	Calcium carbonate	$CaCO_3$
Cesium iodide	CsI	Cesium hydroxide	CsOH
Potassium chloride	KCl	Magnesium oxide	MgO
Silica	SiO_2	Tellurium dioxide	TeO_2
Sodium chloride	NaCl	Tin	Sn
Titanium dioxide	TiO_2	Zinc chloride	ZnCl
Zinc sulfide	ZnS		
Fluorescein	$C_{20}H_{12}O_5$		

EM = Energy mill
AN = Atomizing nozzle

COMPLETED TESTS AND PRELIMINARY RESULTS

During FY87, one facility acceptance test and three "matrix" tests were conducted. The acceptance test employed the same target conditions as Test 10-4 listed above in Table 1. In addition to tests of equipment and procedures, the potential for ice condensers to work as aerosol scrubbers was demonstrated. The subsequent "matrix" tests conducted in FY87 were Test 15-2[a] (the only planned test without ice), Test 2-3[a] (counterpart of Test 15-2 with ice) and Test 10-4[a] (the same as the acceptance test), in that order. During Test 2-3 and Test 10-4, the effects of initial steam blowdown were simulated by injecting steam into the ice condenser until 20% to 30% of the initial ice inventory was melted. This was done because computer simulations of severe accidents indicate that in most of the accident sequences, about 30% of the initial ice inventory is melted prior to release of aerosols (Gieseke et al. 1984).

The acceptance test provided the first opportunity to test steam and air supply systems simultaneously, as well as aerosol generation and measurement systems and steam measuring devices. Problems with aerosol sampler heating, condensate collection, and the power supply to the computer system were identified and subsequently corrected.

Thermohydraulic and aerosol conditions and particle deposition measured during Tests 15-2, 2-3, and 10-4 are summarized in Table 3. The thermohydraulic data include average measured inlet gas flows and temperatures and the initial ice fraction. All tests were conducted at near atmospheric pressure. In the case of Test 2-3, very little ice was melted during the test because there was relatively little energy in the inlet gas stream. During Test 10-4, essentially all of the ice was melted.

The primary measure of validation for ICEDF model is the decontamination factor (DF); the ratio of aerosol mass flux at the inlet to that at the outlet of the test section. The inlet conditions were measured at Station 6 located upstream of the expansion duct leading to the lower turning vanes below the ice condenser test section (see Figure 3). The DF values listed in Table 3, based on aerosol flux data shown in Figures 4 and 5, were determined between Station 6 and Station 5 located about 1 m above the bottom of the ice condenser, and between Station 5 and Station 1 located 2 m below the top of the ice condenser. These two DF values are given for two reasons. First, there was a considerable amount of settling in the zone between Stations 6 and 5 for the conditions employed in Test 15-2 and 2-3 (i.e., slow gas flow and large aerodynamic particle sizes). This was evident in the DF measured between these stations. Second, during Test 10-4 (and as observed during the acceptance test), there was considerable change in thermohydraulic conditions between Stations 6 and 5 as a result of gas cooling and steam condensation on water draining from the melting ice and on structural elements.

(a) The test mnemonic calls out the matrix test number followed by the chronologic sequence of performance (i.e., 15-2, 2-3, 10-4).

TABLE 3. Summary of Conditions Measured During Initial Tests

	Thermohydraulic[a]					Aerosol						
						Inlet[a]	Test Section Aerosol Observations					
Test	Initial Ice Fraction	Average Gas Flow Rate m^3/s	Average Temperature °C	Average Steam Mole Fraction	Material	Mass Concentration mg/m^3	Sta 6 AMMD/GSD μm/-	Sta 5[b] PSD AMMD/GSD μm/-	Sta 1[b] PSD AMMD/GSD μm/-	Inlet[c] DF Sta 6-Sta 5	Test Section[c] DF Sta 5-Sta 1	ICEDF Predicted DF Sta 5-Sta 1
15-2	0	0.031	91	~0	KCl	1150 ± 220	NA	6.1/2.7	6.3/2.6	2.4 ± 0.5	1.0 ± 0.03	1.4
2-3	0.79	0.031	89	~0	SiO_2	500 ± 30	>12[d]	9.7/3.7	5.2/3.0	4.4 ± 1.0	2.1 ± 0.1	2.50 to 1.94[e]
18-4	0.61	0.231	125	0.44	KCl	1830 ± 340	9.8/3.6	2.4/3.2	9.1/2.4	5.0 → 13.4[f]	3.6 → 0.9[f]	NA

(a) Inlet (Station 6) conditions

(b) Averaged values. See Tables 4, 5, and 6 for more information. PSD = particle size distribution, AMMD = aerodynamic mass median diameter, GSD = geometric standard deviation.

(c) Averaged values. See Figures 4 and 5 for aerosol mass flux at various sampling stations. Listed variance is observed range from average value.

(d) Measurements do not have sufficient resolution for accurate estimates. Considerable settling occurred in inlet duct.

(e) Computed for conditions occurring at two different instances. Values are preliminary, see text.

(f) These values are estimated, final values may be changed. Observed DF between Station 5 and Station 1 is less than 1.0 near end of test when ice is nearly depleted (see text)

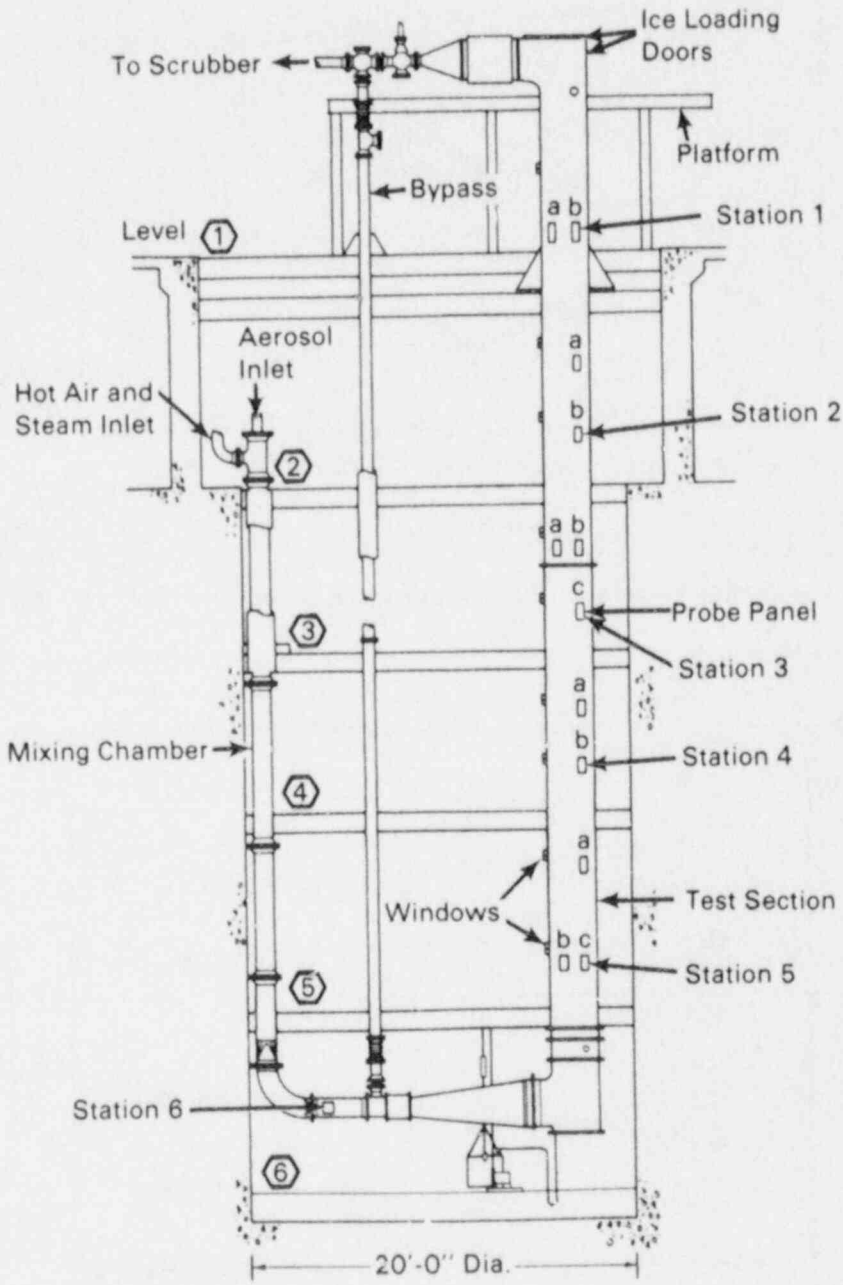

FIGURE 3. Elevation View of Test Facility

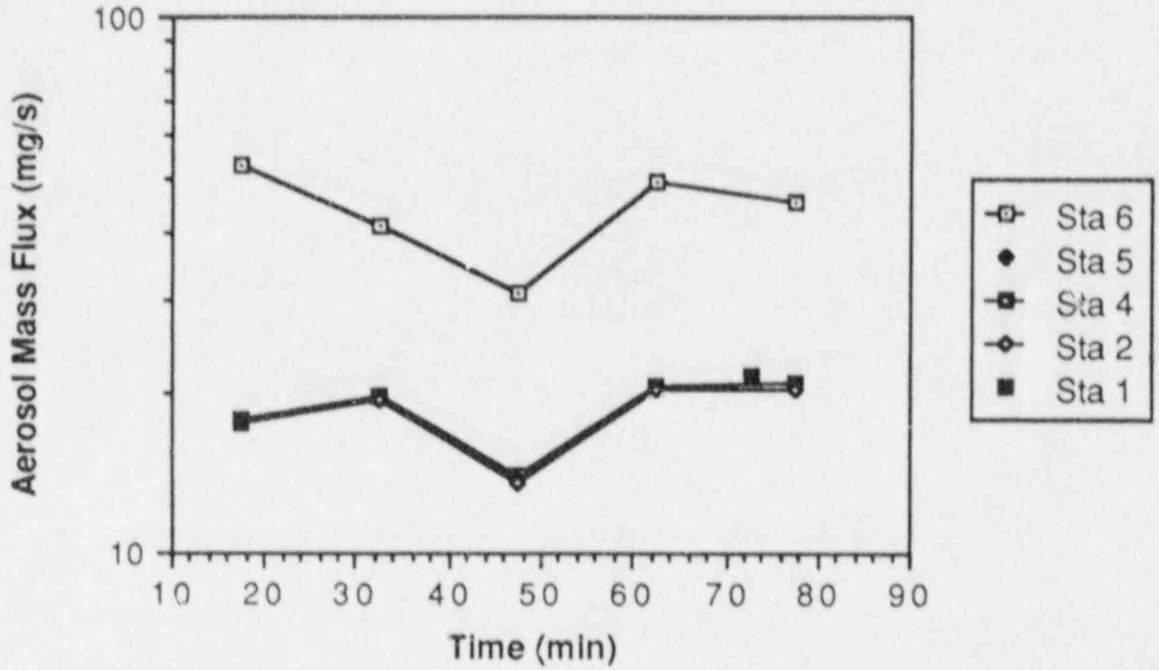

FIGURE 4. Aerosol Mass Flux at Various Stations During Test 15-2

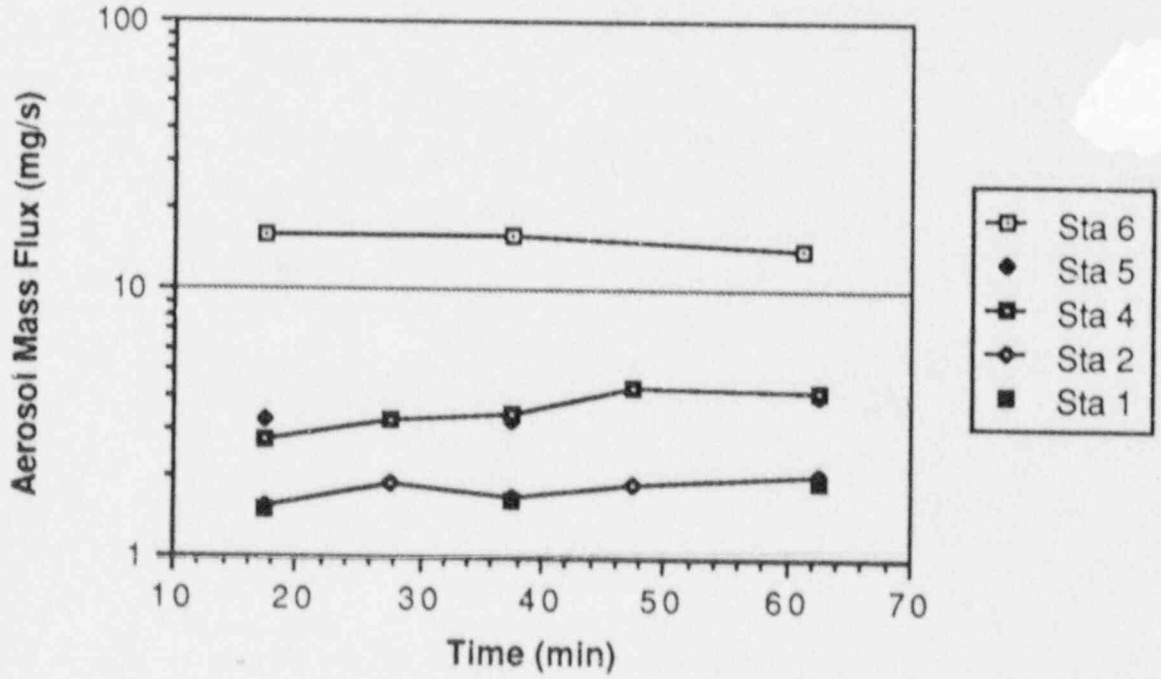

FIGURE 5. Aerosol Mass Flux at Various Stations During Test 2-3

Table 3 also provides the DFs predicted with the ICEDF code for the first two of these cases. These predictions were done "blind"; i.e., the modeler did not have access to experimental measurements, except inlet conditions, prior to performing the simulation. The code addresses most of the thermohydraulic processes in a locally-mixed fashion and, therefore, is somewhat unsophisticated in this regard. Furthermore, because the code does not consider the zone between Stations 6 and 5, it is difficult to interpret some comparisons between these results. For Test 15-2 and Test 2-3 the model input used aerosol conditions measured at Station 5 and thermohydraulic conditions measured at Station 6. This input had little impact on comparison of predictions and data on Test 15-2 because there was little change in thermohydraulic conditions between Stations 5 and 6 (there was no ice). Whereas, for Test 2-3, the temperature dropped from approximately 90°C to 10°C in that same zone. The measured DFs from Stations 6 to 5 and from Stations 5 to 1 are given to provide some perspective on the relative magnitudes of the observed and predicted DF values.

The first "matrix" test conducted, Test 15-2, was performed to provide information on the degree of aerosol scrubbing when no ice exists in the test section. A soluble aerosol, KCl, was used rather than insoluble SiO_2, as planned, because of aerosol generation problems. The absence of steam and ice was anticipated to negate any affect of particle solubility. Data from the test at two different time intervals at measurement Stations 5 and 1 are given in Table 4.

As can be seen, there was virtually no change in the characteristics of the aerosol as it passed through the ice condenser test section. The aerosol flux passing each station is presented as a function of time in Figure 4. It indicates that no appreciable scrubbing occurred between Stations 5 and 1 in the ice condenser test section. This was consistent with expectations because the primary processes available for aerosol deposition were settling, impaction, and interception. Most settling took place in the upstream ductwork leading to the ice condenser--and because of the very slow gas velocities, impaction and interception were likely of less importance. The measured DF value of 1.0 indicates the ice condenser was a poor scrubber for slow gas flows after the ice has been depleted.

TABLE 4. Aerosol Measurements at Stations 5 and 1 for Test 15-2

Time (min)	Station	AMMD (μm)	Geometric Standard Deviation
32	5	6.2	2.8
32	1	6.1	2.6
62	5	6.0	2.7
62	1	6.5	2.6

Test 2-3 was similar to Test 15-2 except that ice was present in the ice condenser and an insoluble aerosol (SiO_2) was used. Table 5 provides data on aerosol conditions at two stations for two instances during the test. As can be seen, particle size decreased somewhat as the aerosol passed from Station 5 to Station 1. The aerosol mass flux at the various sampling stations as a function of time is shown in Table 5. Because a portion of the ice was melted prior to the test to simulate blowdown effects, Stations 4 and 5 were located below the ice front (i.e., in a zone where ice presence was substantially reduced) in the ice condenser. Stations 2 and 1 were located higher in the test section, where ice had not melted significantly. There was a change in aerosol mass flux across that zone indicating that exposure to the ice increases particle scrubbing. The active scrubbing processes may have included diffusiophoresis in the condensing steam flow, settling on the exposed ice surfaces or impaction/interception on the ice and baskets as velocities increased (due to reduced flow area around the ice) and as gas recirculation zones developed. Data are insufficient to identify the specific relative importance of contributions by the aforementioned processes other than to conclude that diffusiophoresis was likely limited due to the near absence of steam in the 90°C inlet flow. The DF between Stations 6 and 5 was approximately 4.4 and between Stations 5 and 1 was approximately 2.1.

Preliminary data are available for Test 10-4, the last test conducted in FY 1987. Test 10-4 involved mid-range flow rates of steam and air. Because of the presence of the steam, ice meltout proceeded over the entire period of the test until, after about 2 hours, the ice was depleted. The steam condensation was expected to have significant effect on aerosol deposition, primarily because of diffusiophoresis. Particle growth was also expected as condensation occurred. Aerosol characteristics for Stations 5 and 1 are given for two times during Test 10 in Table 6. As can be seen, there was substantial particle growth in the ice condenser, with particles growing from 2.4 μm (AMMD) to about 9.1 μm (AMMD). Preliminary analysis of aerosol mass flux indicates a DF of ~10 occurred between Stations 6 and 5, and that the DF between Stations 5 and 1 may have decreased from ~3.6 to ~0.9 during the test. Two possible explanations of the "negative DF" include flow channeling and flow reversals, discussed below, and probable lower relative aerosol sampling probe efficiency in Station 1 due to the large aerosol AMMD (9 μm). We plan to do additional characterization of sampling losses to resolve the latter.

TABLE 5. Aerosol Measurements at Stations 5 and 1 for Test 2-3

Time (min)	Station	AMMD (μm)	Geometric Standard Deviation
28	5	12.0	4.5
28	1	5.5	2.7
46	5	7.2	3.0
46	1	4.6	3.1

TABLE 6. Aerosol Measurements at Stations 5 and 1 for Test 10-4

Time (min)	Station	AMMD (μm)	Geometric Standard Deviation
32	5	2.9	2.4
32	1	9.3	2.6
72	5	1.9	4.1
72	1	9.0	2.2

Temperature measurements were made within the test section during Test 15-2 and 10-4, as well as during the acceptance test. As expected, the temperatures within the test section were essentially uniform during Test 15-2 because there was no ice in the system. However, for the acceptance test and for Test 10-4, the temperatures were far from uniform. In certain flow channels between baskets within the ice condenser, temperatures during Test 10-4 were as much as 10°C cooler than in neighboring flow channels at the same elevation. Such temperature differentials alerted us to the high probability that recirculation was occurring; that is, that gas was passing up one or more channels of the ice condenser and down another channel. Because of the condensing environment, velocity measurements could not be made.

Flow visualization with titanium dioxide smoke was conducted at several elevations after "blowdown" preconditioning but prior to aerosol and steam injection. Air flow into the system was varied from 0.094 to 0.188 m^3/s during these visualization tests. At the low air flow rate, the direction of flow in the three accessible flow channels was up in one, down in another, and unstable in the third. Upon increasing the flow rate to 0.188 m^3/s, the downflow persisted for several minutes before reversing, at which time flow was upward in the three accessible channels. It should be noted that when scaled to plant conditions, the low flow rate is approximately 20% greater than that achieved with both recirculation fans (80,000 cmf). Additional access ports are being installed to provide access to the fourth open-flow channel. It was also observed that the ice did not melt uniformly. Zones of ice about 1 to 5 ft in length remained at a few random locations in the upper third of the test section. This is a further indication of the potential for complex flow conditions in the ice condenser.

CONCLUSIONS

A test facility has been constructed to obtain data on aerosol deposition in an ice condenser for validation of the computer code ICEDF. The facility includes a test section housing the equivalent of four full-scale ice baskets, typical of the 1,944 used in certain PWR power plants. The geometry of the baskets and of all structural support members is similar to a prototype ice condenser. The facility mixes air, steam, and aerosols at temperatures up to 200°C for flow into the bottom (inlet) of the simulated ice condenser. Gas

flow rates between 0.03 and 0.38 m^3/s are possible in the test facility, comparable to prototype gas flows of approximately 16 to 200 m^3/s. Aerosols are generated in the test facility by dispersion of powders in fluid energy mills or by atomization of liquids in two-fluid spray nozzles.

Four tests have been conducted including an acceptance test and 3 of 15 planned "matrix" tests. Results show that decontamination factors (DF = aerosol mass flux entering divided by aerosol mass flux leaving) from 1 to 3 are achieved in the test section depending on aerosol, gas flow, and ice conditions.

A measured DF of 1.0 was obtained for the first matrix test when no ice was present in the test section; the aerosol mass median diameter (AMMD) was 6 μm; and the gas flow rate was low, 0.03 m^3/s. The computer code, ICEDF, predicted a DF of 1.4 in the test section for comparable conditions. Substantial settling (DF = 2.4) occurred upstream of the test section during this test as a result of the relatively large particle size ducted to the test section and because of the very low gas flow rate.

Ice was present during the second test and similar gas flow and aerosol conditions were achieved as when no ice was present. The measured test section DF was approximately 2.1 while the comparable ICEDF-computed DF ranged from 2.6 to 1.9, depending upon amount of ice in the ice condenser. The deposition in the test section appeared to occur entirely in the zone where the gas first encountered ice. Again significant settling occurred in the inlet ductwork accounting for a DF of approximately 4.4.

For the latest test, the gas flow rate was increased to 0.23 m^3/s and steam mixed with the air (steam mole fraction = 0.44). The measured DF in the test section decreased from approximately 3.6 to less than 1.0 as ice was almost completely melted from the test section. No comparable ICEDF calculation of DF is available yet. Considerable steam condensation occurred upstream of the ice baskets during the period of the test contributing to a DF ranging from 5.0 to approximately 13 in the upstream ductwork. Substantial particle growth was observed in the test section with the aerosol AMMD changing from 2.4 μm to 9.1 μm as it flowed past the ice baskets. Particle growth was attributed to steam condensation.

Thermohydraulic behavior in the test section is very complex when ice is present. Temperature data from the "matrix" tests and flow visualization studies without steam in the inlet gas indicate complex flow patterns with stable large-scale flow recirculation.

REFERENCES

Gieseke, J. A., P. Cybulskis, R. S. Denning, M. R. Kuhlman, K. W. Lee, and H. Chen. 1984. Radionuclide Release Under Specific LWR Accident Conditions. Volume IV: PWR, Ice Condenser Containment Design. BMI-2104, Battelle Columbus Laboratory, Columbus, Ohio.

Kannberg, L. D., B. A. Ross, E. J. Eschbach, and M. W. Ligotke. 1986. "Ice Condenser Testing Facility and Plans." PNL-SA-14273, Pacific Northwest Laboratory, Richland, Washington. Presented at the Fourteenth Water Reactor Safety Research Information Meeting, Gaithersburg, Maryland, October 28, 1986.

Owczarski, P. C., R. I. Schreck, and W. K. Winegardner. 1985. A Code for Aerosol Particle Capture in Ice Compartments. NUREG/CR-5130, U.S. Nuclear Regulatory Commission, Washington, D.C.

Winegardner, W. K., A. K. Postma, and M. W. Jankowski. 1983. Studies of Fission Product Scrubbing Within Ice Compartments. NUREG/CR-3248, U.S. Nuclear Regulatory Commission, Washington, D.C.

RESULTS OF THE FOUR PBF SEVERE FUEL DAMAGE TESTS[a]

Daniel J. Osetek

Idaho National Engineering Laboratory
Idaho Falls, Idaho 83415

ABSTRACT

Four in-pile severe fuel damage tests have been conducted in the Power Burst Facility as part of the United States Nuclear Regulatory Commission's (USNRC) Severe Accident and Source Term Research Program. The tests included 1-m long bundles of PWR fuel pins and simulated the thermal-hydraulic and fuel damage conditions of a severe core damage accident. Tests were run with both low and high burnup fuel, low and high coolant flow and with slow and rapid cooldown. One test included Ag-In-Cd control rods. The various types of fuel damage that occurred in the four tests are presented and the measured hydrogen generation, fission product release, and aerosol behavior are described. The principal benefits of the test program have been to improve the USNRC's severe accident analysis capability. Some of the computer models affected by the test results are discussed in the paper.

Introduction

The U.S. Nuclear Regulatory Commission (USNRC) is conducting an internationally sponsored[b] Severe Accident and Source Team research program. The principal objective of this program is to develop a technical basis to support anticipated regulatory changes that may be necessary to implement the USNRC's Severe Accident Policy[1] and achieve the Commission's published Safety Goals.[2] A major part of the program is a series of four in-pile experiments that were conducted at the Idaho National Engineering Laboratory in the Power Burst Facility (PBF).

These four tests, termed the Severe Fuel Damage or SFD tests, were designed to study the understanding of fuel and core material behavior during severe accidents including fission product release, transport and deposition; hydrogen generation; and aerosol behavior. The results of these tests are being used to assess and improve detailed mechanistic models used in the USNRC's Severe Accident and Source Terms computer codes.[3]

---

a. The Severe Fuel Damage Program is sponsored by the U.S. Nuclear Regulatory Commission and its international partners and is performed at INEL under DOE Contract No. DE-AC07-76ID01570.

b. Partners of the program include Belgium, Canada, Federal Republic of Germany, Italy, Japan, Netherlands, Republic of Korea, Spain, Sweden, United Kingdom, American Institute of Taiwan, and the United States Nuclear Regulatory Commission.

One of these codes, the combined SCDAP/RELAP5 computer code,[4] has been under development at INEL and, therefore, has allowed a close working relationship between the SFD test program and the code development program. The SCDAP/RELAP5 code includes models to calculate the coupled thermal-hydraulic, fuel and fission product behavior during a severe fuel damage event including the influences of structural components and control materials. The SFD test results have provided a severe accident data base for code development and assessment. Together the test data and computer codes have allowed early application of research results to important safety questions for the USNRC.

This paper provides a summary of the PBF SFD tests, highlighting the principal fuel and fission product behavior results and their impact on the important safety issues. The design and conduct of the four tests are described followed by an illustrated description of the posttest conditions of the test bundles as determined by detailed destructive examinations. The measured behavior of fission products, hydrogen and aerosols is presented, and the importance of the measurement results on detailed code models is described. The major lessons learned in the testing program and some resulting model improvements are discussed in the conclusion.

The test-specific objectives developed for the SFD Test Series were defined to envelop a wide range of core damage phenomena including zircaloy melting and oxidation, fuel dissolution, debris formation and flow blockage. Each experiment consisted of a bundle of UO_2 fuel pins driven to severe accident conditions by fission heat while monitored by a variety of specialized instruments. Table 1 lists the various parameters that were used in each of the four tests.

The transients were initiated by controlling the inlet coolant to the test bundles and increasing the nuclear power. Water in each test was allowed to boil down to the lower regions of the fuel rods while pressure was kept constant at ~7 MPa (1000 psi). Fuel rod temperatures were increased slowly in the first test and more rapidly in the other three tests. As the fuel rod cladding temperature approached 1700 K, oxidation of the zircaloy cladding increased rapidly, resulting in higher heating rates (>10 K/s). This exothermic reaction, limited only by the availability of steam and zirconium, rapidly increased fuel and cladding temperatures. The differences in coolant flow rate affected the degree and rate of zircaloy oxidation. Since the melting temperature of ZrO_2 is much higher than metallic zircaloy, the degree of oxidation affected the timing and amount of molten material formation and thus the melt progression and flow blockage behavior. The high steam flow rate used in the SFD-ST allowed nearly complete oxidation of the zircaloy and some oxidation of the UO_2 fuel. Steam limited conditions in the SFD 1-1, 1-3 and 1-4 bundles reduced the degree of oxidation that could occur before temperatures reached the melting point of the zircaloy cladding (~2150 K). Peak temperatures in each test approached fuel melting (3100 K) in some small regions of the bundles, and the average temperature of large bundle regions exceeded 2600 K.

Other parameters varied in the four tests were cooldown rate, fuel rod burnup and the presence of control rods. The more rapid cooldown rate was

TABLE 1. SUMMARY OF PBF SFD TEST CONDITIONS

Test Date	Heating Rate[a]	Number Rods	Fuel Burnup (MWd/tU)	Nominal Coolant Flow (g/s)	Cooling Mode	Test Characteristics
SFD-ST Oct 1982	0.13 K/s to 1700 K	32	90	16.0	Water reflood	Steam rich, 72% zircaloy oxidation, partial fuel liquefaction
SFD 1-1 Sept 1983	0.45 K/s to 1300 K 1.3 K/s to 1700 K	32	30	0.7	Slow steam	Steam starved, 39% zircaloy oxidation, extensive UO_2 liquefaction
SFD 1-3 Aug 1984	1.9 K/s to 1700 K	26 2 4	36,000 80 empty Zr guide tubes	0.7	Slow argon	Similar to SFD 1-1, but less UO_2 liquefaction
SFD 1-4 Feb 1985	0.5 K/s to 1200 K 1.8 K/s to 1700 K	26 2 4	36,000 80 Ag-In-Cd control rods in Zr guide tubes	0.9-1.5	Slow argon	Large molten mass of control and fuel rod material

[a]Above 1700 K, heating rates are driven by rapid oxidation and are typically >10 K/s.

expected to generate greater fragmentation than slow cooling. The high burnup fuel provided smaller fuel particle sizes and a larger fission product inventory than the low burnup fuel. The Ag-In-Cd control rods provided low melting point materials that changed the melt progression behavior of the last test and increased the aerosol generation rate.

Test Design and Conduct

The PBF has been used by the USNRC for several years to conduct fuel behavior tests for design basis accident and other off-normal reactor transients. Since the facility's unique capabilities were well suited to the needs of a severe fuel damage program, only minor modifications were necessary to meet the operational objectives of the SFD tests.

The PBF uses a 30-MW pool-type reactor that consists of a ternary fuel (urania-zirconia-calcia) driver core and a central flux trap contained in an open tank reactor vessel. An independent, pressurized-water coolant loop provides a wide range of thermal-hydraulic test conditions in an in-pile tube located within the flux trap test space.

Experiment test trains are designed to fit into the in-pile tube and use the pressurized-water coolant loop for control of the thermal-hydraulic test conditions. For the SFD tests the loop was used to supply bypass coolant flow for cooling of the in-pile tube and the outer shroud of the test assembly. A separate bundle inlet line provided controlled coolant flow to the test fuel within the test train assembly.

The SFD test trains used in the four SFD tests are illustrated in Figures 1 and 2. The test trains used in the first two tests were designed and built by the Pacific Northwest Laboratory (PNL) and assembled at INEL.

The fuel bundles for the first two tests consisted of 32 unirradiated zircaloy-clad UO_2 fuel rods arranged in a 6 x 6 array without the four corner rods. The fuel rods were of typical PWR 17 x 17 design with a fuel length of 0.914 m. The fuel bundles were assembled using three Inconel grid spacers to maintain a typical PWR fuel rod pitch of 12.75 ± 0.25 mm. The rods were fixed to a lower support plate but were free to expand upwards. A ZrO_2 bypass tube (4.75-mm ID) extended over the length of the fuel rods in the SFD 1-1, 1-3 and 1-4 bundles. The tube provided a flow path in case the bundle became completely blocked.

The fuel bundle was contained within an insulating shroud constructed from a zirconia insulator sandwiched between zircaloy structural components. A separate coolant line provided inlet flow to the test bundle region, and the entire bundle effluent was routed out through a pipe to a sampling and monitoring system. The test trains were instrumented with fuel rod centerline thermocouples, inside cladding thermocouples, shroud thermocouples, and flow channel thermocouples. Several other instruments provided bundle pressure and flow data, and a shroud penetration detector was included for indication of radial meltthrough.

The effluent sampling and monitoring system is diagramed in Figure 3. This system directed the bundle effluent to several fission product and

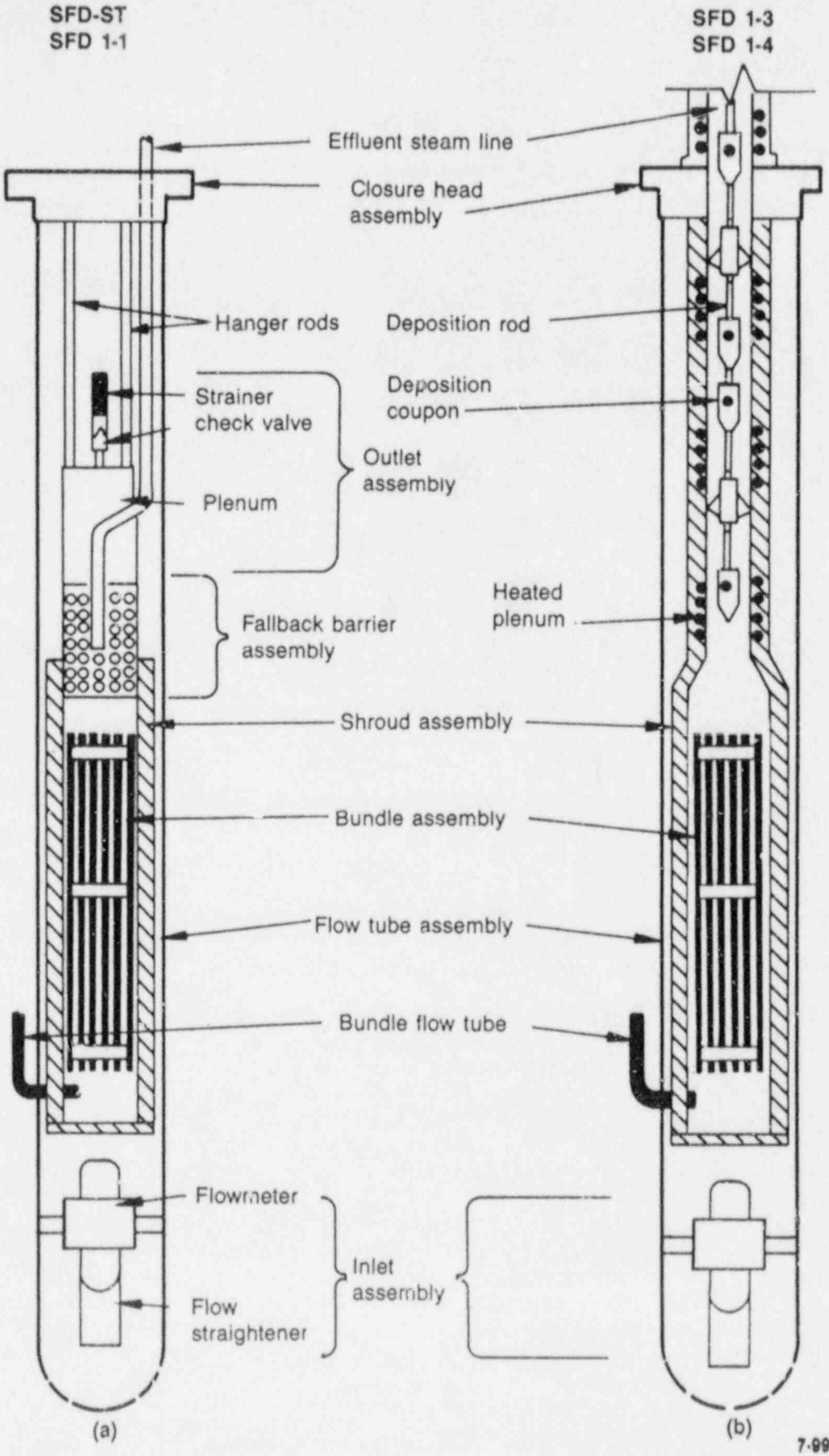

Figure 1. Diagram of PBF SFD test trains used for the SFD-ST and 1-1 test (a), and for the SFD 1-3 and 1-4 tests (b).

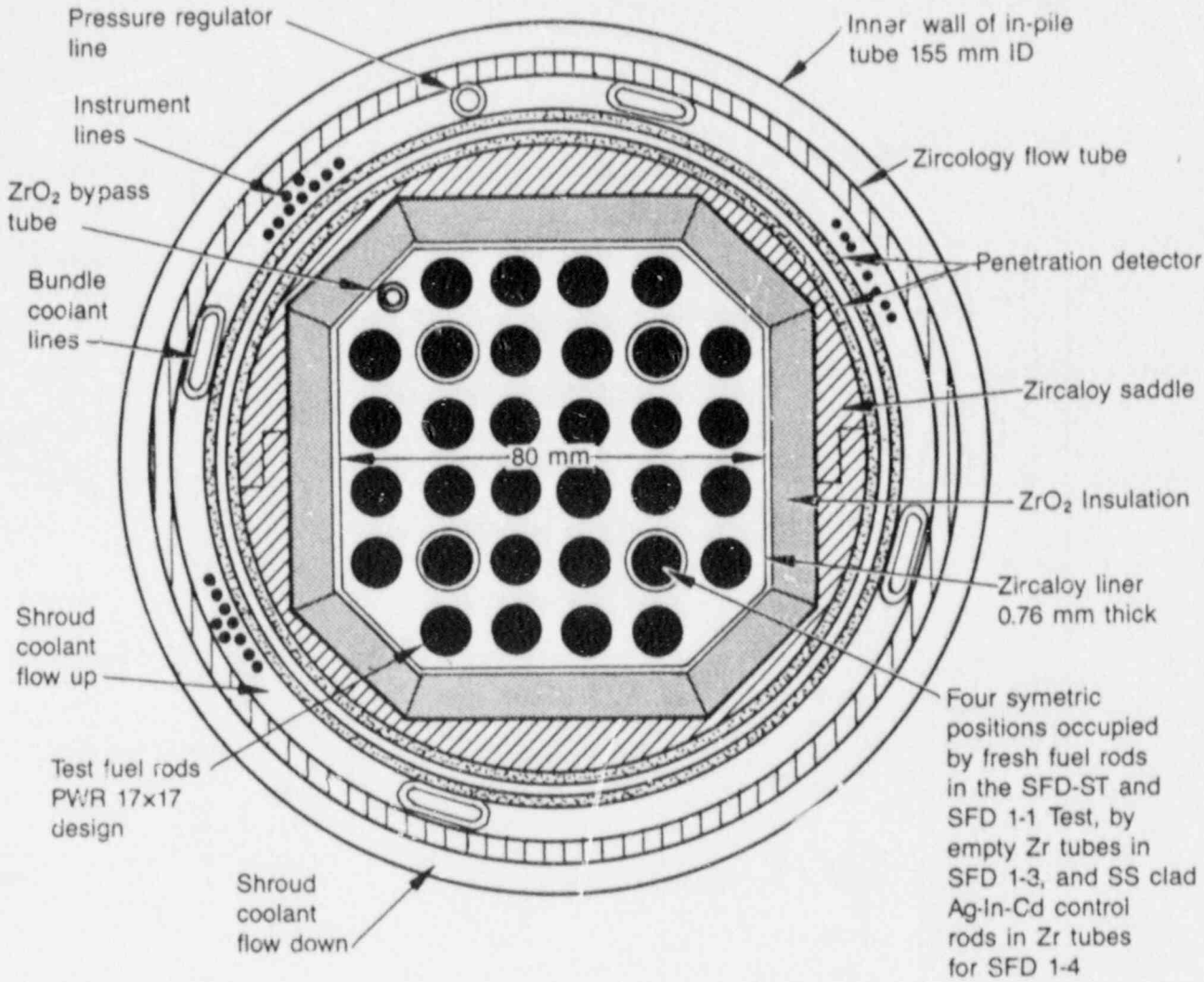

Figure 2. Cross-sectional diagram of SFD test train at the fuel bundle region.

hydrogen monitors and included separate gas and liquid streams and sequentially operated grab samples. The entire effluent was collected in a tank that was sampled posttest to define the integral gas and liquid content.

The test trains used in the 3rd and 4th tests included design modifications to accommodate the 1-m long high-burnup fuel rods, four control rod positions and a removable deposition rod mounted above the fuel bundle to collect effluent deposition samples. Twenty-six uninstrumented fuel rods with a burnup of ~36000 MWd/MtU were used in each of these two tests. Two fresh fuel rods with temperature and plenum pressure instruments were also included. The SFD 1-3 bundle had four control rod guide tubes made of zircaloy included in the array of fuel rods. The SFD 1-4 test included four Ag-In-Cd control rods with stainless steel cladding inserted into the zircaloy guide tubes.

An on-line aerosol monitor, an additional gamma spectrometer, and a bank of six filtered grab samples were added to the effluent sampling and

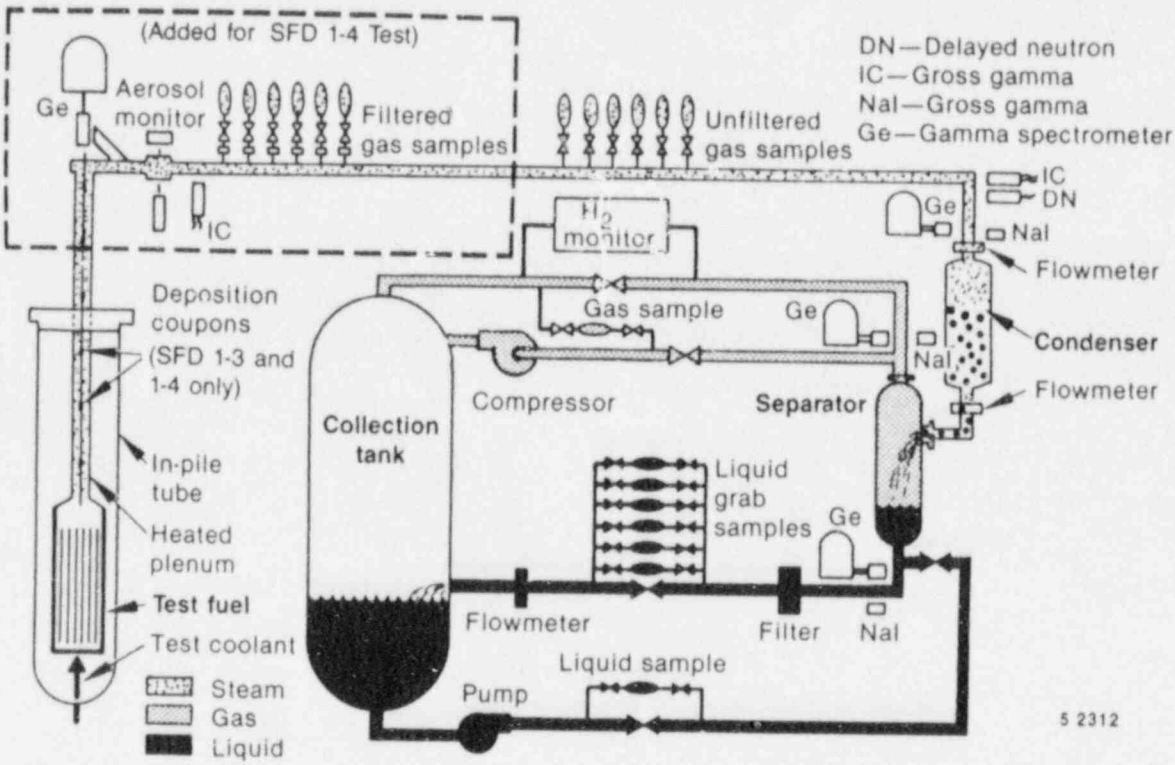

Figure 3. Schematic diagram of the PBF SFD Test Effluent Sampling and Monitoring System.

monitoring system for the SFD 1-4 test to characterize aerosol and fission product concentrations close to the test bundle.

Before each of the severe fuel damage transients the fuel bundles were preconditioned in a similar manner to promote fuel pellet cracking and to generate a short-lived fission product inventory. The high temperature transient of the SFD-ST was initiated by a long slow heatup in a high flow of steam and was terminated by a reactor scram and reflood with cooling water. The high temperature transients of the SFD 1-1, 1-3 and 1-4 tests were each run with a more rapid heatup, a lower coolant flow rate and a slow power-controlled cooldown. The SFD 1-1 test bundle was reflooded immediately upon cooldown. Figure 4 compares the peak temperature histories of the SFD-ST and the SFD 1-1 test to illustrate the different thermal transients. Because thermocouples fail at temperatures above 2100 K, best-estimate peak temperature histories were determined from shroud instrumentation and detailed thermal-hydraulic calculations. The detailed calculations are still ongoing for the SFD 1-3 and 1-4 test, so the best estimate temperature histories for these two tests are not yet available. Current estimates suggest that the SFD 1-3 test realized a temperature history very similar to the SFD 1-1 test, and Test SFD 1-4 may have achieved slightly longer time at high temperature.

The SFD 1-3 and 1-4 tests were cooled down from high temperature using a flow of argon gas. This technique maintained dry surfaces on the removable deposition rod in these two tests. After the rods were removed from

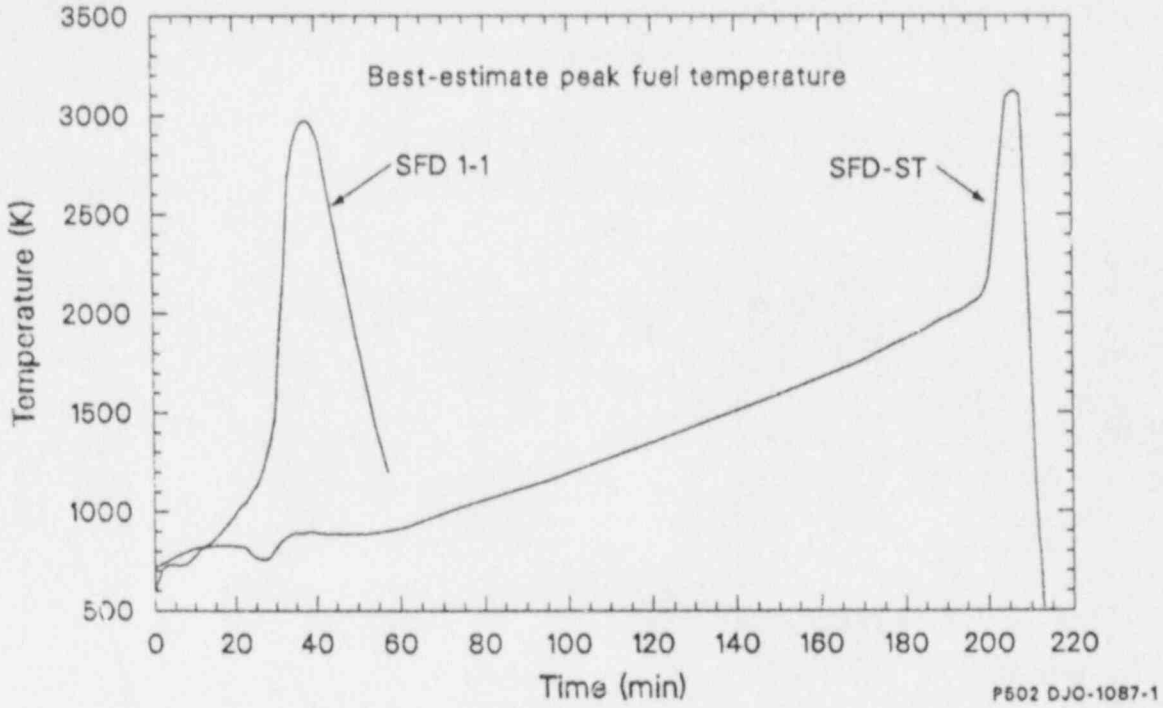

Figure 4. Comparison of best estimate peak fuel temperature histories for the SFD-ST and SFD 1-1 test.

the test trains, the fuel bundles and effluent lines were washed with reflood water. Measurements taken before and after the washing operation gave indications of fission product deposition on the effluent line surfaces and the effects of reflood water on the deposits.

Posttest Bundle Configuration

Each of the four SFD test bundles were radiographed after the experiments. Figure 5 is a comparison of the four radiographs, which illustrates the different damage characteristics. Detailed posttest examination of each bundle also included cross-sectioning and photographic documentation. Figure 6 shows photographs of bundle cross sections from each of the four tests at the maximum flow blockage region.

Posttest examination of the SFD-ST bundle indicated extensive fragmentation of the fuel rods. Of the zircaloy associated with the fuel rod cladding ~72% was oxidized and this bundle-average value included essentially complete conversion to ZrO_2 in the upper regions. A large, cohesive, previously-molten mass of U-Zr-O accumulated near the bottom of the bundle, cementing an array of partially dissolved fuel pellets. Posttest analysis of the SFD-ST bundle geometry indicated a 26% reduction of the original bundle flow area resulted from blockage by the relocated material. Fuel fragments in the debris above the blockage region ranged from approximately millimeter size to quarter pellet (cm) size. A rod-like geometry remained in the upper region of the bundle in the form of rod segments mixed with oxidized cladding fragments and partial fuel pellets. Complete details of the SFD-ST are given in Reference 5.

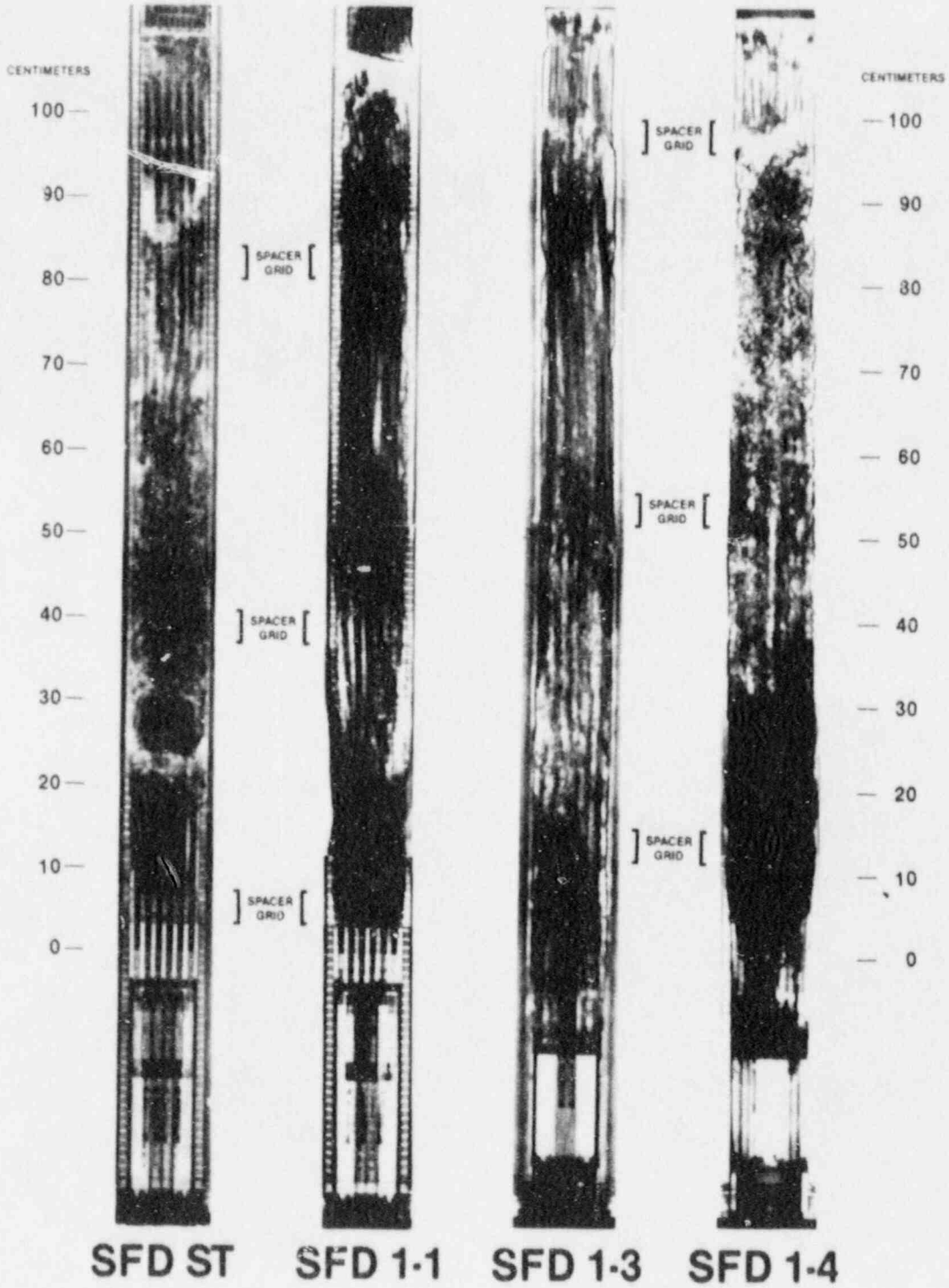

Figure 5. Composite posttest neutron radiographs of the four PBF SFD test bundles.

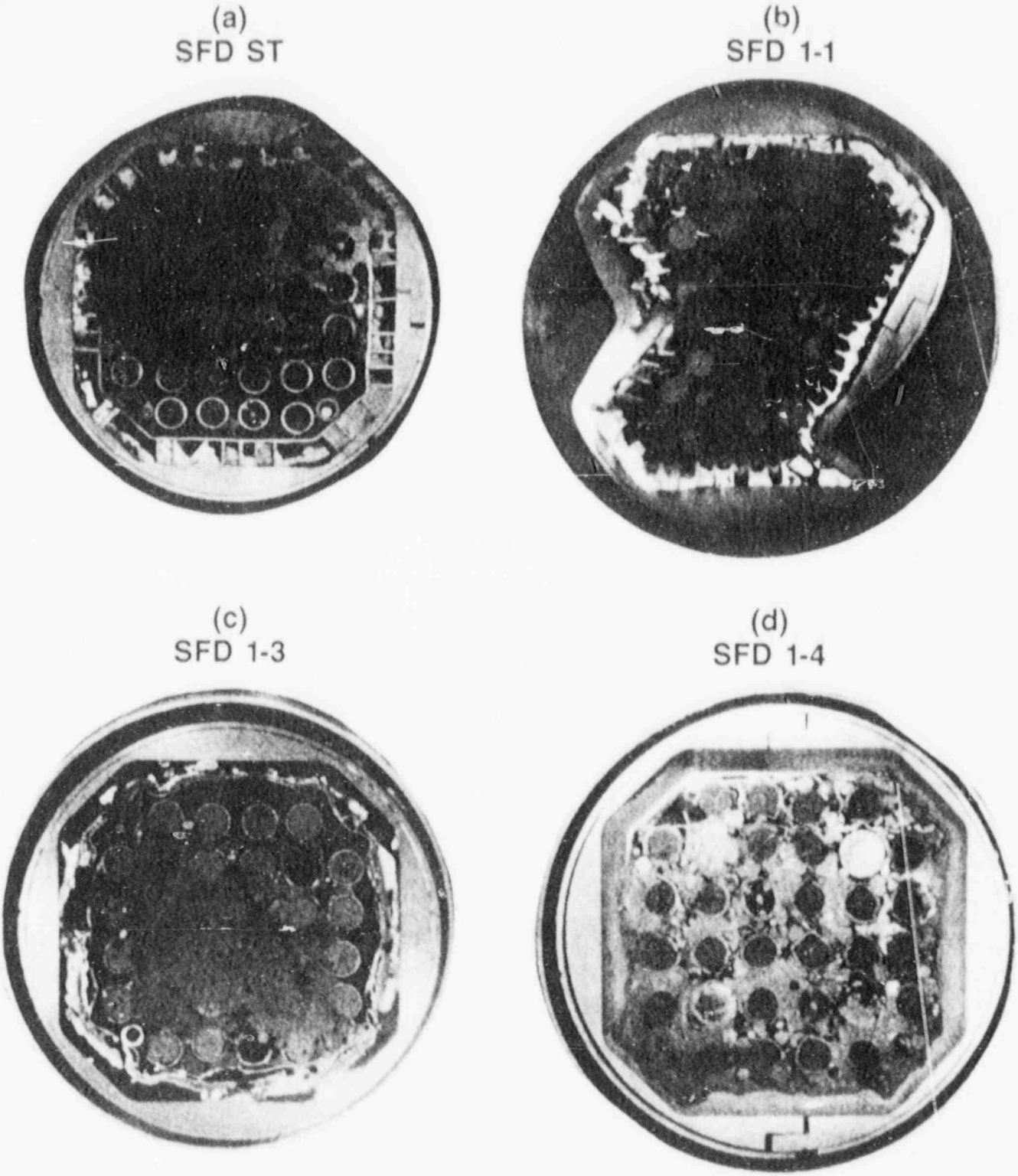

Figure 6. Photographs of SFD test bundle cross-sections taken near regions of maximum flow blockage.

The SFD 1-1 bundle experienced less oxidation (39%) during the transient, resulting in greater zircaloy melting and fuel liquefaction. The fuel rods in the upper regions of the bundle were highly fragmented,

but a rod-like geometry was still partially retained. A large cohesive mass accumulated in the lower bundle region, resulting in significant blockage of flow channels with approximately a 95% reduction in total flow area. The posttest metallographic and chemical examination of the prior molten region indicates nearly complete dissolution of the UO_2 fuel pellets in the central region of the melt. Extensive cracking of the prior molten mass occurred as the bundle was cooled. Figure 7 is a photograph of material from this region showing the cracking. Thermal stresses and shrinkage apparently caused the cracking after the mixture froze and began to cool down. Complete details of the SFD 1-1 test are provided in Reference 6.

The SFD 1-3 Test, which used higher burnup fuel (~36 GWD/tU) differed from the SFD 1-1 Test in overall fuel damage in that less dissolution of fuel occurred in the lower one-third of the bundle. More dissolution of the surface of the fuel pellets occurred higher in the bundle, and some rod-like structure remained in the upper bundle region. Although hydrogen production in the SFD 1-3 Test was about equal to that in the SFD 1-1 Test, indications are that less zircaloy oxidation and more UO_2 fuel oxidation occurred. Flow area blockage in the SFD 1-3 Test was less than that developed in the SFD 1-1 Test and approximately the same as in the SFD-ST. The particle size of the debris formed during the SFD 1-3 Test was smaller than that in the tests with fresh fuel as a result of the fracturing that occurred in the fuel pellets during irradiation to 36 GWD/tU. Some fine debris was found below the fuel bundle region. The empty control rod guide tubes in the bundle provided a flow path for material relocation. Relocated fuel and zircaloy material was found inside these tubes at low bundle regions.

Four Ag-In-Cd control rods were included in the SFD 1-4 test bundle along with the higher-burnup fuel rods. Control rod melting added significantly to the axial extent of the previously molten cohesive mass that developed in the lower region, although the amount of dissolved fuel was about equal to that in the SFD 1-3 Test. Hydrogen production during the SFD 1-4 Test appears to be greater than that in either the SFD 1-1 or 1-3 Test, but the relative amounts of fuel and zircaloy oxidation have not yet been fully evaluated. The fuel in the upper regions appears more fragmented than in previous tests. No rod-like geometry was obvious from the neutron radiographs, and essentially no cladding remains on the rods in the upper regions. Figure 8 is a composite photograph of bundle cross sections from the upper regions of the SFD 1-1 and 1-4 test bundles. The difference in fuel particle size is evident in the photographs. The contrast in cladding remnants is also clear; the SFD 1-4 test produced complete melting and relocation of the cladding possibly assisted by interactions of the stainless steel in the bundle. Nearly complete obstruction of the original flow area was estimated from the visual examination of the bundle sections.

The relocated material in the lower region of the SFD 1-4 bundle developed in 3 distinct regions. The first material to melt and relocate was the control rod alloy. Some of this material moved down completely through the fuel region and into the lower plenum. The second layer of debris (Figure 6d) was composed of partially oxidized Zr-Fe and Zr-Ni material mixed with control rod alloy. The stainless steel control rod

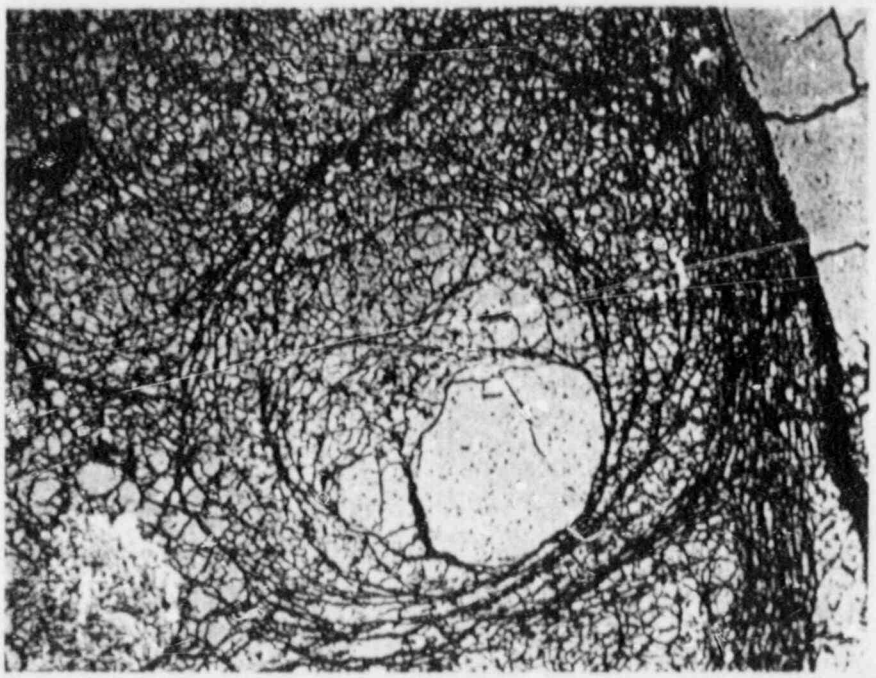

Figure 7. Photograph of prior molten debris from lower flow blockage region of the SFD 1-1 fuel bundle illustrating extensive cracking.

cladding and Inconel spacer grids interacted quite extensively with the zircaloy material in the bundle. The control rod positions in this region contained prior molten control rod alloy and stainless steel materials. In two of the four control rod positions a mixture of fuel and cladding materials was found. The third or upper layer of debris in the melt region was

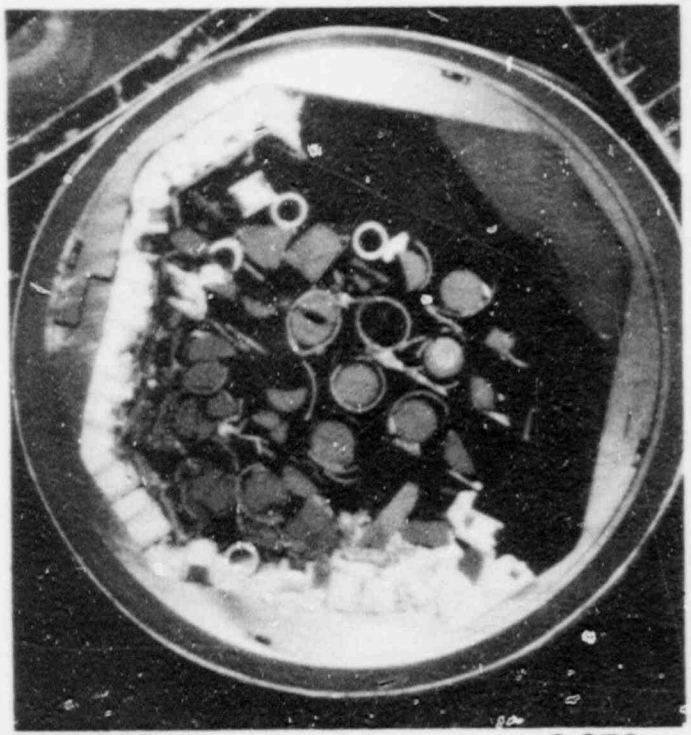

84M-523 0.879 m

SFD 1-1

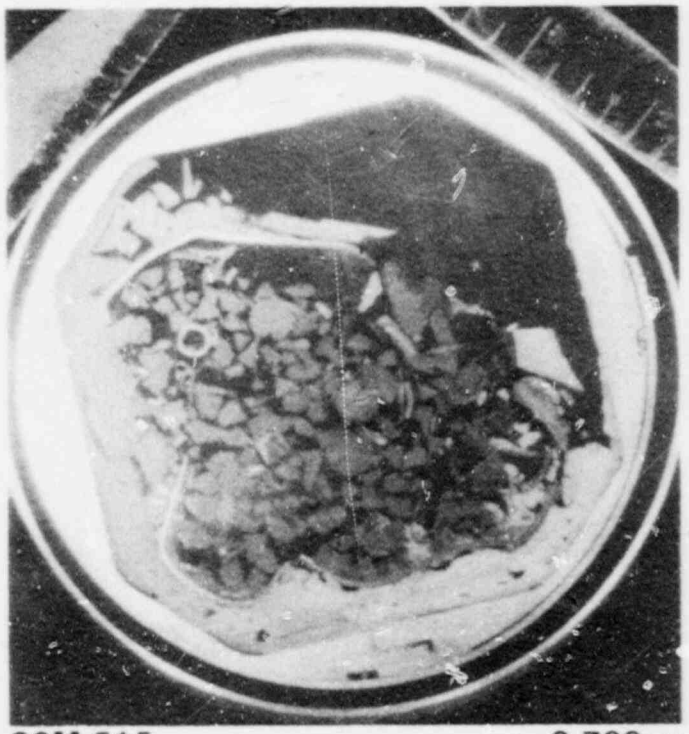

86M-515 0.783 m

SFD 1-4

Figure 8. Photograph of cross-sections from upper regions of the SFD 1-1 and 1-4 fuel bundles.

rich in uranium. The bulk material was a matrix containing U-Zr-O with Zr-Fe and Zr-Ni inclusions and traces of control rod alloy.

Fission Product Release

Total fission product releases during each SFD test were determined by summing the measured quantities found in various locations throughout the effluent system. Thus, these numbers represent movement of material out of the bundle region; and except for noble gases, these numbers should not be considered representative of accident source terms. Significant deposition occurred of all fission products except noble gases on surfaces in the effluent system. Most of the deposition was easily removed by water flushing and was measured in the collection tank after the flushing operations. Some small quantities of certain fission products remained fixed to system surfaces. These deposits were quantified by sampling and assay of the effluent system piping and components. Table 2 lists the total release fraction results of the principal fission product groups for each test.

The range of values given for some of the release fractions represents data for different isotopes of the same element. The SFD-ST, which was highly oxidized and rapidly cooled, produced the highest releases of noble gas and iodine. The SFD 1-1 and 1-3 tests both produced quite low release fractions, although the high burnup fuel in the SFD 1-3 tests produced release fractions of volatile species about twice those of the fresh fuel in Test SFD 1-1. Tellurium showed a remarkable difference in release fraction between the SFD-ST and the other three tests. This observation is consistent with the current theory that tellurium reacts with zirconium and tin in the zircaloy cladding preventing its release from the bundle region until nearly complete oxidation liberates the fission product in some less reactive form, perhaps SnTe. Release fractions of less volatile species Ba, La, Sr, Ru, and Ce were also measured and found to be 1% or less in all cases. Actinides released from the high burnup fuel in the SFD 1-3 and 1-4 test were measured; release fractions were very small, the order of 10^{-6} and lower. Traces of uranium were found in the regions just above the fuel bundle suggesting some fuel movement, probably as particulate. These fuel release fraction determinations are complicated by the presence of plutonium isotopes, but estimates are in the range of 10^{-5} to 10^{-6}.

On-line gamma spectroscopy measurements made during the SFD tests allow evaluation of fractional release rates of certain noble gas isotopes. The measured concentrations can be compared to calculated bundle inventories to generate fractional release rate histories of noble gas isotopes versus time. To be useful for model assessment, these data should be compared to the principal controlling parameters affecting fuel behavior in the test bundle throughout the time of the measurements. Fuel temperature is only one of these principal parameters; fuel morphology changes during the test must also be included in the analyses to properly understand the release behavior.

The fractional release rate history for noble gas measured during the SFD 1-1 test is provided in Figure 9; best-estimate average bundle temperature is also plotted and key bundle events that may have affected fuel morphology or the fission product behavior are also noted. Inspection

TABLE 2. FISSION PRODUCT RELEASE FRACTIONS MEASURED DURING THE SFD TESTS

Element	SFD-ST	SFD 1-1	SFD 1-3	SFD 1-4
Noble Gas	~0.50	0.026 to 0.093	0.08 to 0.19	0.23 to 0.44
Iodine	0.51	0.12	0.18	0.26
Cesium	0.32	0.09	0.18	0.44 to 0.56
Tellurium	0.40	0.01	0.01 to 0.09	0.03
Barium	0.01	0.006	0.004	0.008

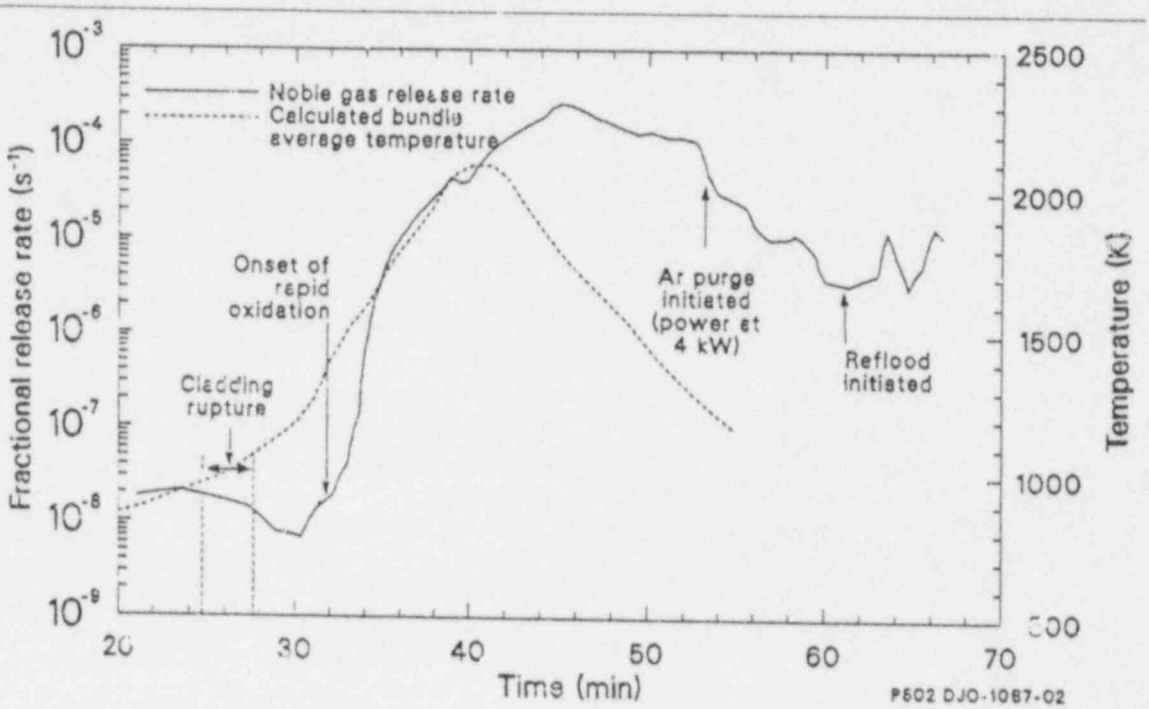

Figure 9. Fraction release rate of noble gas measured during the SFD 1-1 test compared to the temperature history and key events.

of Figure 9 illustrates that the fission product release in this severe fuel damage test of low burnup fuel is controlled by fuel morphology changes in addition to the fuel temperature. The peak release period occurs after the peak temperature period, and release rates remain significantly high after temperature dropped late in the test.

Just before initiation of the Ar purge system at 3200 s, when bundle temperatures were below 1450 K, the fractional release rates were ~3 orders of magnitude higher than those measured at comparable temperatures during heatup of the bundle (at ~1800 s). This enhanced fuel release on cooldown is believed related to fuel morphology changes that occurred during the transient such as cracking and grain boundary separation

Similar release measurements were taken during the SFD tests with high burnup fuel, however the data have not been fully analyzed at this time. Preliminary results suggest that during heatup the release rates of noble gas from the high burnup fuel are greater than those for the low burnup fuel; but releases are still strongly coupled to fuel morphology changes, and release rates during cooldown exceed those at similar temperature during heatup.

Models of fission product release based on temperature alone consistently overpredict the measured release rates during the heatup phases of all the SFD tests. These same models underpredict the measured releases late in the tests when significant fuel dissolution and cracking has occurred. Figure 10 illustrates this discrepancy for the temperature dependent model given in NUREG-0772.[7] A further discussion of fuel morphology effects on fission product release is given in Reference 8.

Fission Product Transport and Deposition

No significant amount of volatile fission products was transported to the collection tank in any of the SFD tests until the bundles and effluent lines were flushed with water. Prior to reflood in each test, <1% of the iodine and cesium and negligible quantities of less volatile species were measured in the collection tank prior to reflood in each test. Fission products deposited readily on effluent line surfaces, being concentrated in regions close to the fuel bundle. Figure 11 is a plot of the surface concentrations of iodine and cesium measured on the horizontal and vertical surfaces of the deposition rod from the SFD 1-3 test. The deposition patterns of the two species are remarkably similar suggesting similar deposition mechanisms or chemical association. Both species also displayed greatly enhanced concentrations on horizontal surfaces, suggesting a strong association with aerosol particles and settling or impaction as a dominant deposition mechanism.

The horizontal deposition that occurred during the SFD 1-4 test was extremely heavy. A photograph of part of the deposition rod as shown in Figure 12. Analysis of these heavy horizontal deposits showed that cadmium was the overwhelming constituent. The iodine and cesium inventories in both the SFD 1-3 and 1-4 tests were nearly identical, and the activity of iodine and cesium isotopes measured on the horizontal surfaces after both tests were similar (within a factor 2). At downstream locations, the aerosol deposits were found to contain large fractions of tin and zirconium in addition to cadmium.

Control Rod Behavior

As noted from the posttest bundle examinations, the Ag-In-Cd control rods with their stainless steel cladding added substantially to the amount of molten material that relocated and developed blockage. The control rod alloy has a melting point of 1073 K, and the cadmium has a very high vapor pressure under these accident conditions; therefore, when the control rod cladding is breached the liquid alloy begins to relocate giving off cadmium vapors. However, the relocation downward is so rapid that little cadmium can escape before the alloy reaches a cooler region and freezes. Thus, the silver and indium as well as much of the cadmium can remain in the lower

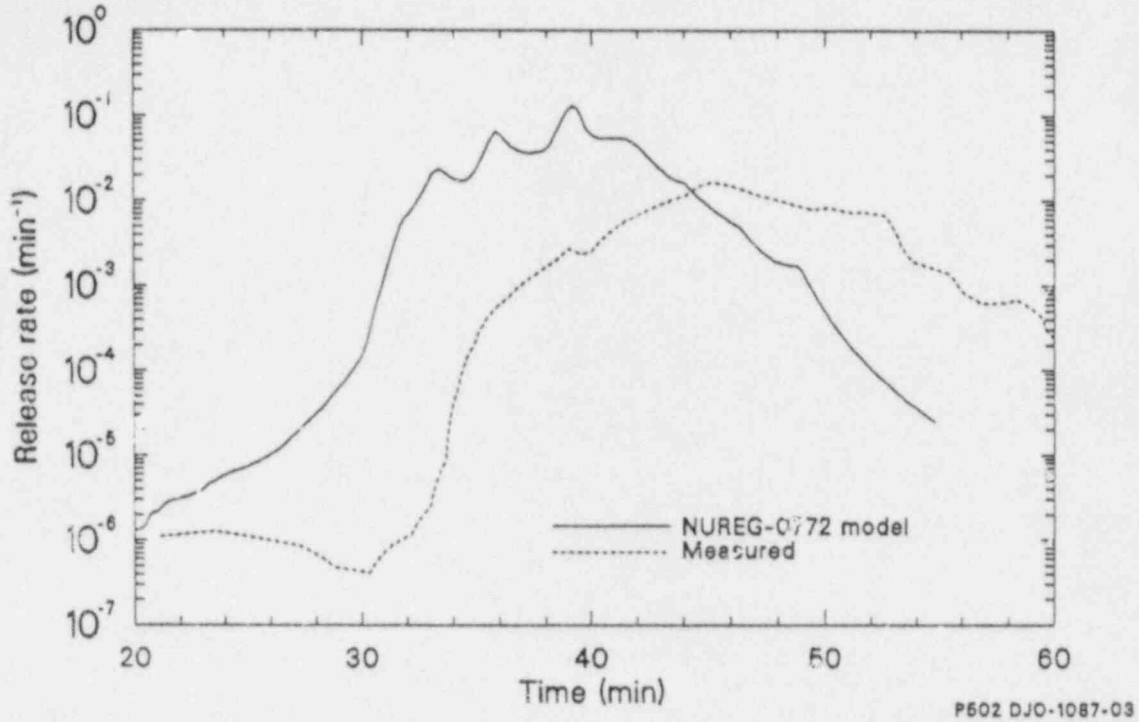

Figure 10. Comparison of noble gas fractional release rates measured during the SFD 1-1 test and calculated using the fuel temperature correlation from NUREG-0772.

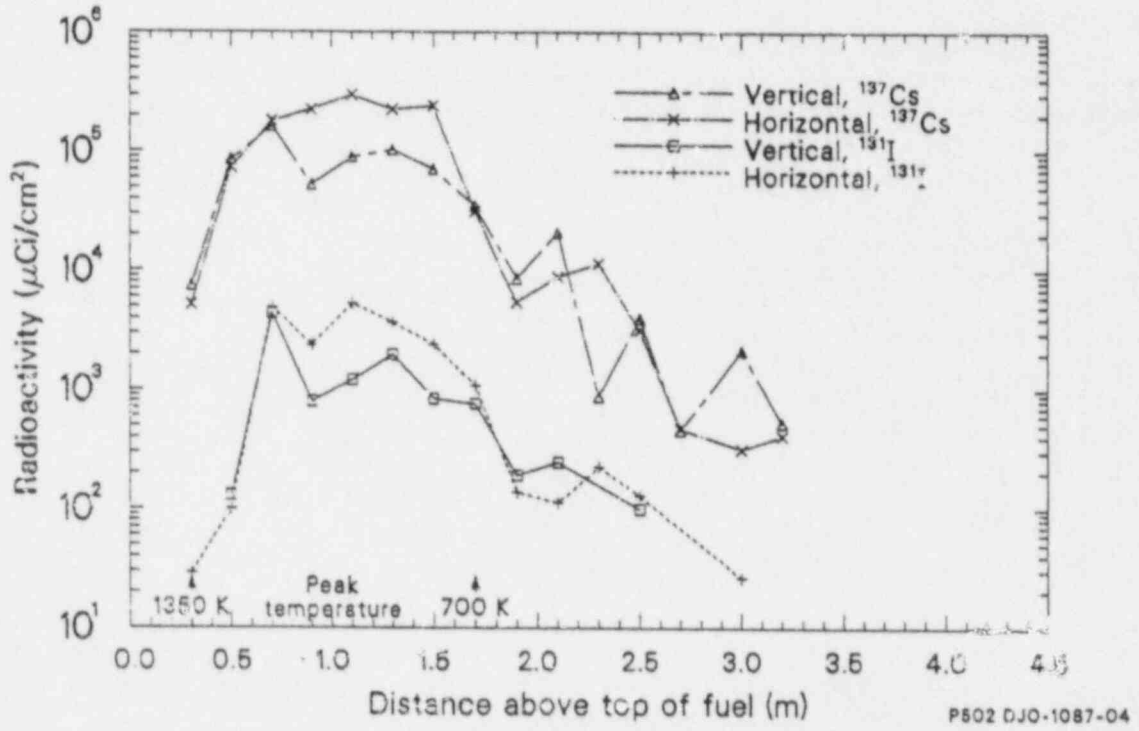

Figure 11. Deposition of iodine and cesium measured on horizontal and vertical surfaces above fuel bundle after Test SFD 1-3.

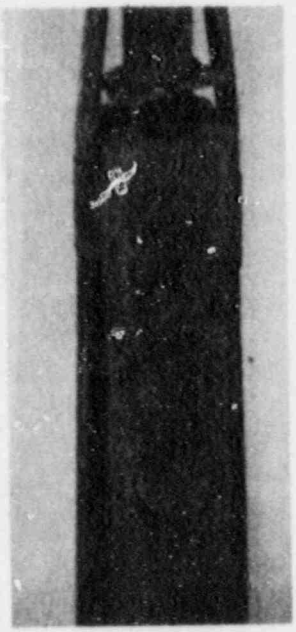

Figure 12. Photograph of heavy deposit observed on horizontal surface above fuel bundle after Test SFD 1-4.

fuel regions until later in the accident sequence when it can be reheated. The total fraction of cadmium found outside the fuel bundle region was <5%, and <0.1% of the silver and indium was measured outside the bundle.

Aerosol Generation

Vapors generated in the SFD test bundles can from aerosol as they transport through the effluent line and cool. Fission products can interact with the aerosols affecting transport and thus source terms. The large increase in vapors expected from the control rod materials in the SFD 1-4 test stimulated the addition of an on-line aerosol concentration monitor to the last experiment. Dense aerosols will promote particle agglomeration and settling leading to a diminishing aerosol concentration and smaller particle sizes in the downstream sections of the effluent system. Therefore a goal of the aerosol measurements designed for the SFD 1-4 test was to position the monitoring device as close as possible to the source in the fuel bundle. The measurement was achieved by a combination of an on-line light attenuation measurement and a series of filtered grab samples for posttest analysis. Figure 3 illustrates the relative locations of the equipment. Design details will be published in the final SFD 1-4 Test Results Report, and a good description of the design and operation of the instrument is given in Reference 9.

The aerosol measurement taken with the on-line monitor is shown in Figure 13 with the estimated average bundle temperature. The aerosol concentration is proportional to the indicated light attenuation and ranges from ~10^6 to 10^9 particles per cm^3 (equivalent 1.0 μm diameter).

The first response of the aerosol monitor at 1740 s corresponds to the failure of the first control rod in the SFD 1-4 test. Beginning at 2050 s a

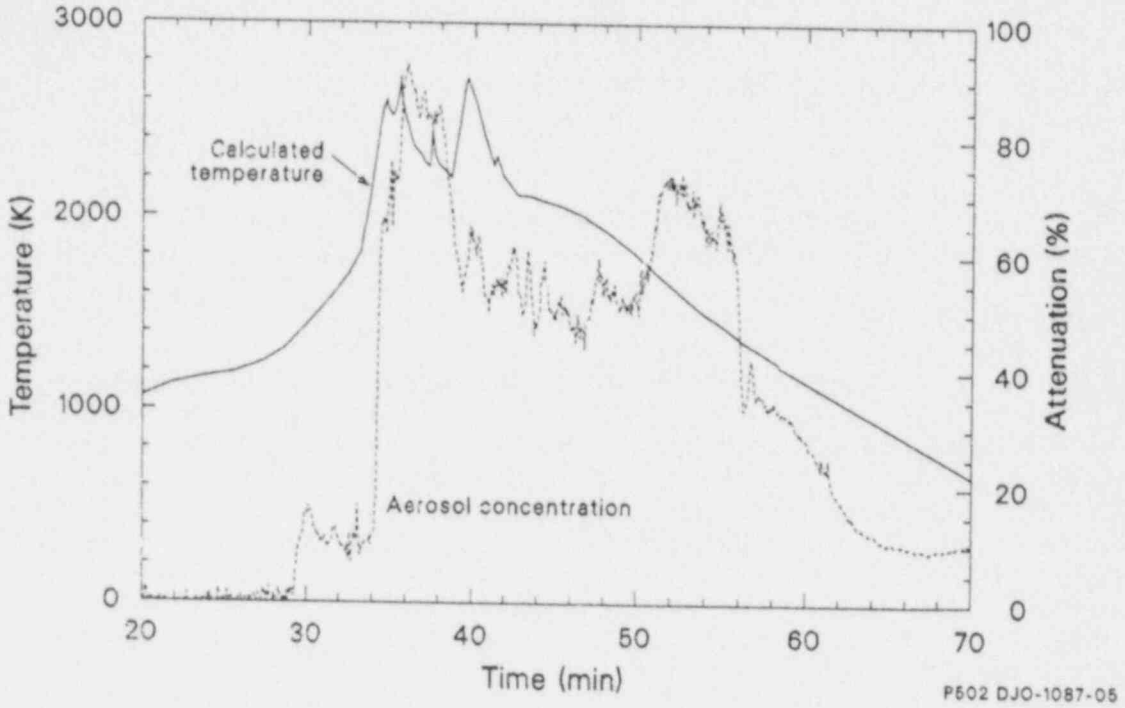

Figure 13. Comparison of aerosol monitor signal recorded during Test SFD 1-4 with temperature history.

large increase in aerosol generation was indicated that achieved the highest concentration measured during the test. This dense aerosol lasted ~250 s which corresponds to the high-temperature period of the test when the three uninstrumented control rods failed and when rapid oxidation of the zircaloy cladding began. The aerosol generation diminished slightly but continued at a significant high concentration throughout the remainder of the test. Analysis of the aerosol grab samples collected at six times during the transient shows that tin, cadmium and other materials were responsible for the aerosol source at this location in the effluent line. Zr, Ag and Cs were also found in relatively large quantities in the aerosol samples. The zircaloy in the bundle includes over 800 grams of tin which can be driven out of the metal at high temperatures. Some of the zirconium found in the samples may have been aerosolized by oxidation of the zircaloy or may be from ZrO_2 that was liberated from shroud insulation during the test.

A comparison of fission product transport behavior in the SFD 1-3 and 1-4 tests indicates an important difference that may be attributable to aerosol effects. The fractions of bundle inventory of iodine, cesium, and tellurium were measured at several locations in the effluent system after the tests. These data indicate that most of the released cesium and tellurium deposited within the first few meters in both tests. However, iodine showed a distinct difference in behavior in the two tests. Following the SFD 1-3 test released iodine was found deposited predominantly in the first few meters along with the cesium and very little iodine was found deposited in downstream sections of the effluent line or in the collection tank. Following the SFD 1-4 test released iodine was found deposited over greater distances in the effluent line, and the largest fraction of deposited iodine

was noted in the ex-vessel effluent lines ~20 m downstream of the test bundle.

The presence of greater amounts of reactive aerosols in the SFD 1-4 test apparently carried more of the iodine farther downstream than was possible in the SFD 1-3 test. The basic difference was the presence of Ag-In-Cd control rods in the SFD 1-4 test. Perhaps a chemical interaction of the iodine with silver in the aerosols or a physical interaction with the greater aeroso' surface area was responsible for this change in behavior.

Hydrogen Generation

The amount of hydrogen generated by oxidation processes during severe accidents and the timing of the hydrogen generation is very important for assessment of containment challenges. Containment overpressurization can occur if large amounts of noncondensible gas are generated during an accident, and large pressure spikes can occur if some or all of the hydrogen is burned. One of the principal issues regarding hydrogen generation in severe accidents is how melt progression and flow blockage formation changes hydrogen generation. Changes in the surface area, oxide thickness and availability of steam to the metals in the hot regions of the core will all affect hydrogen generation.

Hydrogen released from the SFD test bundles was measured in the effluent of each test using a thermal conductivity analyzer. In each test varying amounts of hydrogen were generated by oxidation of the zircaloy. Some small amounts of fuel, iron and nickel were also oxidized producing hydrogen. The hydrogen generation rates did vary significantly during some phases of the first three SFD tests. However, in the SFD 1-4 test, which actually produced the greatest amount of material melting and relocation, the hydrogen source was relatively constant. Figure 14 shows the hydrogen generation history for the SFD 1-4 test. The magnitude of hydrogen generation during the high temperature phase of the test is nearly equivalent to complete consumption of steam at the inlet flow rate. The major melt relocation and test termination times are labeled on the figure, and the final flow blockage was measured in the posttest examination and found to be ~98%. Further, posttest examinations of the SFD 1-1 test bundle indicated that some of the cladding located in the melt region oxidized during and following relocation. This evidence strongly suggests that under certain severe accident conditions hydrogen generation will be uninhibited by the various melting and flow blockage processes.

The availability of steam and metallic zircaloy strongly influence the rate of oxidation and hydrogen production. An oxide layer on the zircaloy will slow, but not terminate, the reaction. The oxide can be breached by thermal and mechanical processes exposing the hot metals to steam. The amount of metallic surface area that can be exposed to steam is an important parameter in the detailed analyzes of the tests. Another lesson learned from the analysis of the SFD tests was that the inside surface of ballooned and ruptured zircaloy cladding and the two sided surface of the zircaloy guide tubes for control rods greatly increase the available surface area for oxidation and affect the oxidation process. Such geometries were required in the models before detailed calculations agreed with measured results.

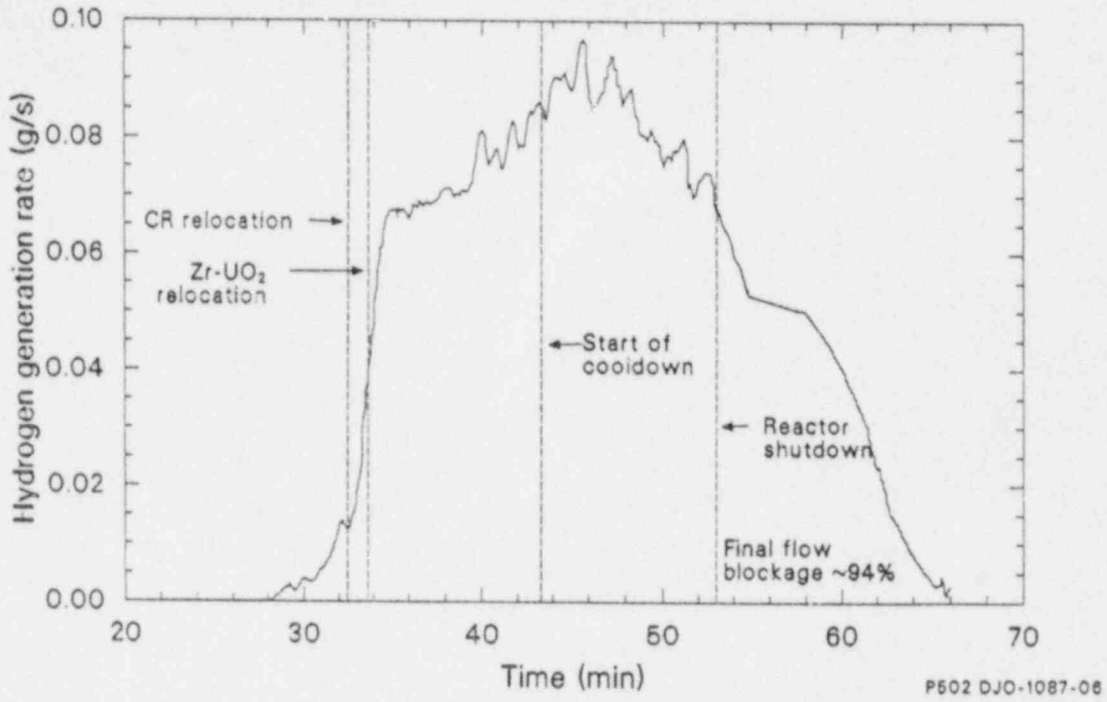

Figure 14. Hydrogen generation measured during the SFD 1-4 test compared with key events.

The high steam flow used during the SFD-ST resulted in some additional hydrogen generation by oxidation of the UO_2 fuel. Posttest examination identified some local regions of elevated fuel stoichiometry. This phenomena, in addition to the oxidation of other core materials such as iron and nickel, must be considered when evaluating total hydrogen sources.

Principal Observations and Conclusions

All four PBF SFD tests, and the detailed posttest examinations of all four test bundles, have been completed. However, only the first two tests have been fully analyzed using the detailed thermal hydraulic, fuel behavior and fission product models in the RELAP5, SCDAP, TRAP-MELT family of codes. INEL is continuing such detailed analyses for the SFD 1-3 and 1-4 tests, and other USNRC contractors are beginning similar analyses with other codes (e.g. TRAC, MELPROG). Final conclusions must await the results of these important remaining tasks, but several preliminary findings can be presented and used to guide future research and regulatory planning. The following highlights summarize these important findings from the PBF SFD test program, and Table 3 gives a synopsis of these highlights.

One of the first lessons learned from conducting these severe accident tests is that rapid, uncontrolled oxidation occurs in such events and neither reduction of steam flow nor slow heatup conditions will prevent the rapid rise in temperatures above 1700 K. Peak temperatures can reach 3000 K in localized regions, and large sections of the bundles can attain temperatures above 2670 K. Hydrogen generation was found to peak during the rapid oxidation phase of each test, and hydrogen generation was never completely terminated at any time during the high temperature periods of any of the

TABLE 3. HIGHLIGHTS OF PBF SFD TEST RESULTS

Phenomena	Observation
Initial Heatup	o Rapid uncontrolled oxidation occurs at ~1700 K in both high and low steam flows.
	o Oxidation propagates rapidly raising temperatures to ~2400 K in a few minutes.
	o Peak temperatures can reach 3000 K in local regions.
	o Average temperatures can exceed 2670 K over large regions.
Oxidation/H_2 Production	o Ballooned and ruptured cladding and control rod guide tubes allow two-sided oxidation.
	o Fuel oxidation can occur in steam-rich environments and stainless steel materials can oxidize adding to the H_2 source.
	o H_2 generation continues during melt progression and after debris beds form.
Melting/Liquefaction	o Melt can accumulate in localized regions and form flow blockages (hard pan) with trapped gas.
	o A significant fraction of fuel can be dissolved by molten zircaloy and add to the blockage.
	o Complete loss of cladding in upper bundle (core) regions can occur and result in loss of rod-like geometry.
	o Material interactions can generate low-melting-point eutectics.
Debris/Blockage	o Both metallic and ceramic materials can relocate and form flow blockages up to 98%.
	o Control rod guide tubes provide a flow path for material relocation.
	o Oxidation and dissolution continue in the flow blockage material.
	o Fuel fragments from HBU fuel are smaller than those from LBU fuel.
	o Stainless steel and Inconel materials react with zircaloy to change composition of debris.
	o Relocated material can develop layers: - Lower: Control rod alloy, - Middle: Oxidized Zr-Fe and Zr-Ni with control material. - Upper: U-Zr-O matrix with Zr-Fe, Zr-Ni and control rod materials.
Ag-In-Cd Control Rods and Aerosol Production	o Low melting point eutectics (Zr-Fe, Zr-Ni) may initiate early control rod failure.
	o Control rods add significantly to the amount of melt and relocation of materials.
	o Aerosol generation is continuous during the high temperature transient.
	o Control material relocation can reduce (or at least delay) vaporization of Ag-In-Cd from the bundle (core).
Cooldown/Quench	o Extensive cracking can occur in melt region on cooldown and release gases and fission products.
	o Large fractions of H_2 generation and fission product release were measured during cooldown.
Fission Product Release	o Fission product release is strongly dependent on fuel morphology.
	o Release rates can be significantly lower during heatup than during cooldown at the same temperature.
	o Except for noble gases, all fission products deposit readily on cool downstream surfaces.
	o Iodine and cesium generally deposit similarly and resuspend in reflood water.
	o Iodine transport can be affected by the chemical or physical action of aerosols.
	o Tellurium can be retained in the bundle (core) until liberated by thorough oxidation.
	o Tellurium deposits are not easily resuspended in reflood water.

tests. Continuous hydrogen production was measured during the SFD 1-4 test although extensive zircaloy melting and relocation occurred and ~94% flow blockage developed. Hydrogen generation models in the SCDAP/RELAP computer code were adjusted to include physical processes such as two sided oxidation of ballooned cladding which achieved better agreement between calculations and measurements.

Debris beds can develop from the relocation of both solid and liquid material. These debris beds may include small internal steam channels and extend over a large axial region. In the SFD tests the debris beds held relocated material in a zone hot enough to sustain oxidation and melting. Models of these processes had to be carefully designed to avoid unrealistic reduction in the oxidation process and to achieve good agreement with the measured data.

When debris beds heat sufficiently to attain melting temperature, they can form self-sealing hard-surface regions. Once molten, the debris beds can dissolve a large amount of UO_2 fuel in the zircaloy, and portions of this mixture of U, Zr, and O may not freeze on cooling until temperatures are below ~1600 K. Upon cooling these molten regions may develop shrinkage or thermal stress cracks and trapped gases may be released.

A critical consideration in modeling severe accidents is the timing and mechanisms for the change in core geometry from rods to a particle bed. The complete loss of cladding from the upper regions of the SFD 1-4 test bundle and the existence of a large particle bed region can be contrasted to the rod like geometries of the other tests to help understand when and how this transition occurs. The interaction of stainless steel with zircaloy in regions that include control rods may be the key to this process. The smaller particle size observed from the high burnup fuel may also be an important influence. The factor of 2-4 difference in particle size can mean the difference in achieving a coolable debris bed or continued heating and melting.

The presence of several kinds of materials in a core allow the development of debris beds and blockages in stages. The lowest melting point material relocates first and, in the case of Ag-In-Cd, may move completely down to the water level near the bottom of the fuel or even below the fuel region. The development of low melting point eutectic materials can be the initiators for the first material relocation. Interaction of iron and nickel in the stainless steel cladding of control rods with the zircaloy guide tubes can occur if the rods balloon, and the chemical interdiffusion can result in melt through. Since the Ag-In-Cd alloy is liquid at these temperatures, the material quickly runs out through the breach and down to cooler regions. The presence of the control rods added significantly to the extent of the debris bed and blockage region in the SFD 1-4 Test. Fuel assemblies without control rods may form smaller blockages at later times because of the lack of these materials. Following the melting of the control rods, larger passages became available for material relocation. Fuel and zircaloy materials were found in the control rod positions at points low in both the SFD 1-3 and 1-4 bundles. The bulk of material that relocates during the later phases remains above the control rod and stainless steel materials. The upper region of relocated material in the SFD 1-4 test were rich in fuel material, and only

small amounts of control rod materials were found intermixed. The middle region of the bed contained greater amounts of oxidized Zr-Fe and Zr-Ni and control rod alloy. This layering effect delays the heating and continued vaporization of the low melting point materials and contributes to the continuous generation of aerosols as was observed in the SFD 1-4 test.

Volatile fission product release in the SFD tests varied from a low of ~10% in the fresh fuel SFD 1-1 test to a high of ~50% in the SFD-ST and 1-4 test. The iodine and cesium, however, did not transport far from the fuel bundle unless it was carried by a high flow rate of steam of reflood water. Some iodine was found ~20 m from the fuel in the SFD 1-4 test apparently carried downstream by the enhanced aerosol in that test. Tellurium was restricted to the fuel bundle and nearby locations, except in the SFD-ST that produced extensive oxidation of the zircaloy.

Iodine and cesium deposition patterns were found to be similar on dry surfaces examined after the SFD 1-3 test. Post test analyses of samples indicated that these fission products were highly soluble in water, and transport analyses using the SFD test conditions suggest that CsI and CsOH were the probable chemical forms that deposited in the effluent line during the SFD-ST, 1-1 test and 1-3 test. Analysis of the SFD 1-4 test is complicated by the presence of the control rod materials, and ongoing analysis will evaluate the potential effects of these materials on the fission product behavior for that test.

Noble gas release rates were found to be significantly lower during heatup in the fresh fuel tests than current temperature correlations would predict. Release rates during cooldown, however, exceeded those measured during heatup at equivalent temperatures. This observation, together with the preliminary results from the high burnup tests showing higher release rates during heatup, suggest that fuel morphology has a strong influence on volatile fission product release.

Aerosol generation and transport effects were found to be significant in the test with Ag-In-Cd control rods. Cadmium contributed the principal mass for aerosol found deposited in regions above the fuel bundle. Tin and zirconium were found in addition to cadmium in aerosol samples from downstream regions. The continuous generation of aerosols measured during the SFD 1-4 test indicates that fission product transport analysis must include aerosol processes in addition to vapor chemistry.

The PBF SFD tests were, of necessity, terminated before many of the later-phase melt progression processes could take place. Nevertheless analysis of these tests led to significant modeling improvements and better understanding of severe accident phenomena. Additional experimentation is needed to extend the models and understanding of severe accidents through melt progression to the lower vessel structures, attack of the lower vessel head and instrument penetrations, and to melt ejection and ex-vessel phenomena. The need for the later phase phenomenology is understandably of lesser urgency, since the probability of such occurrences diminishes as more and more time for corrective actions becomes part of the accident progression. The most important data base, that impacting the early in-vessel processes, is now partly in place because of the PBF SFD test program. The completion of the detailed analysis of the last two tests

will add an important part of the needed information to the data base and to the computer codes that embody what has been learned. Similar analyses ongoing in other USNRC programs will further enhance the data base and the computer programs, giving the USNRC a powerful tool for regulating the nuclear power industry and guiding reactor operator actions during severe off-normal events.

References

1. U.S. Nuclear Regulatory Commission, "USNRC Policy on Future Reactor Designs: Decisions on Severe Accident Issues in Nuclear Power Plant Regulation," NUREG-1070, July 1985.

2. U.S. Nuclear Regulatory Commission, "Policy Statement on Safety Goals for the Operation of Nuclear Power Plants," Federal Register, Vol. 51, p. 28044, August 4, 1986.

3. M. Silberberg et al., "Reassessment of the Technical Bases for Estimating Source Terms," NUREG-0956, July 1986.

4. C. M. Allison, et al., "Capabilities of the Integrated SCDAP/RELAP5/TRAP-MELT Severe Accident Computer Code," Proceedings of the IAEA International Symposium on Source Term Evaluation for Accident Conditions, Columbus, OH, October 1985.

5. A. D. Knipe, S. A. Ploger, and D. J. Osetek, "PBF Severe Fuel Damage Scoping Test--Test Results Report", NUREG/CR-4683, EG&G-2413, August 1986.

6. Z. R. Martinson, et al., "PBF Severe Fuel Damage Test 1-1 Test Results Report, NUREG/CR-4684, EG&G-2463, October 1986.

7. U.S. Nuclear Regulatory Commission, "Technical Bases for Estimating Fission Product Behavior During LWR Accidents", NUREG-0772, June 1981.

8. D. J. Osetek, et al., "Fuel Morphology Effects on Fission Product Release," Proceedings of the International ANS/ENS Topical Meetings on Thermal Reactor Safety, Volume 5, page IX.2-1, San Diego, California, February 2-6, 1986.

9. J. P. Adams, et al., "Development and Calibration of an Aerosol Monitor Used for the PBF Test SFD 1-4," Proceedings: Miami International Symposium on Multiphase Transport and Particulate Phenomena, CONF-861204-8, December 1986.

MIST TEST RESULTS

J. R. Gloudemans
Nuclear Power Division
The Babcock & Wilcox Company
Lynchburg, VA

D. P. Birmingham
Alliance Research Center
The Babcock & Wilcox Company
Alliance, OH

ABSTRACT

The multiloop integral system test facility (MIST) was part of a jointly-sponsored program to generate integral system data for code benchmarking. The MIST facility, a scaled model of a B&W-designed lowered-loop plant, was extensively instrumented. Small-Break Loss of Coolant Accidents (SBLOCA), HPI-PORV cooling, steam generator tube ruptures, and the effects of non-condensible gases and pump operation were tested. A number of noteworthy interactions that occurred during the SBLOCA tests are summarized herein. The results of three SBLOCA tests that demonstrate an important system response, the ability of the system to adjust to imbalanced boundary conditions, are presented.

INTRODUCTION

The multiloop integral system test (MIST) is part of a multiphase program started in 1983 to address small-break loss-of-coolant accidents (SBLOCAs) specific to Babcock & Wilcox-designed plants. MIST is sponsored by the U.S. Nuclear Regulatory Commission, the Babcock & Wilcox Owners Group, the Electric Power Research Institute, and Babcock & Wilcox. The unique features of the Babcock & Wilcox design, specifically the hot leg U-bends and steam generators, prevented the use of existing integral system data or existing integral system facilities to address the thermal-hydraulic SBLOCA questions. MIST and two other supporting facilities were specifically designed and constructed for this program, and an existing facility -- the once-through integral system (OTIS)-- was also used. Data from MIST and the other facilities will be used to benchmark the adequacy of system codes, such as RELAP-5 and TRAC, for predicting abnormal plant transients. The results of the MIST SBLOCA tests are described.

FACILITY

The multiloop integral system test (MIST) facility was a scaled 2-by-4 (2 hot legs and 4 cold legs) physical model of a Babcock & Wilcox (B&W), lowered-loop, nuclear steam supply system (NSSS). MIST was designed to operate at typical plant pressures and temperatures. Experimental data obtained from this facility during post-small-break loss-of-coolant accident (SBLOCA) testing are used for computer code benchmarking.

MIST consisted of two 19-tube, once-through steam generators, an electrically-heated core, a pressurizer, 2 hot legs, and 4 cold legs with scaled reactor coolant pumps. Other loop components included a closed secondary system, simulated reactor vessel vent valves, a pressurizer power-operated relief valve (PORV), hot leg and reactor vessel upper head vents, high-pressure injection (HPI), a core flood system, and critical flow orifices for leak simulation. Guard heaters, used in conjunction with passive insulation to reduce model heat losses, were used on all primary system components as well as the steam generator secondaries. MIST is illustrated in Figure 1.

Boundary Systems

The MIST boundary systems were sized to power-scale the plant boundary conditions. HPI and auxiliary feedwater (AFW) characteristics were based on composite plant characteristics. Scaled vents were included in both hot legs and in the reactor vessel upper head. Leaks were located in the cold leg suction and discharge piping, and the upper and lower elevations of steam generator B (for tube rupture simulation). The desired vent and leak flows were obtained using power-scaled restrictors.

Heat Losses and Guard Heaters

MIST was designed to minimize heat losses from the reactor coolant system. Fin effects (instrument penetrations through the insulation) were minimized by using 1/4-inch penetrations for most of the instrumentation. Heat losses due to conduction through component supports were minimized by designing the supports to reduce the cross-sectional area and by placing insulating blocks between load-bearing surfaces. The reactor coolant system piping and vessels were covered with passive insulation, guard heaters, and an outer-sealed jacket (to prevent chimney effects). The guard heaters were divided into 42 zones, each controlled by a zonal temperature difference and a pipe metal temperature.

Instrumentation

MIST had approximately 850 instruments. These instruments were interfaced to a computer-controlled, high-speed data acquisition system. MIST instrumentation consisted of measurements of temperature, pressure, and differential pressure. Fluid level and phase indications were provided by optical viewports, conductivity probes, differential pressures, and gamma densitometers. Mass flow rates at the system boundaries were measured using Corioles flowmeters and weigh scales. Loop mass flow rates were measured using venturis and turbines.

TRANSIENT TEST PROGRAM

The MIST transient tests were defined to generate integral system data for code benchmarking. The transient test series was divided into the following seven groups:

- Mapping
- Boundary systems

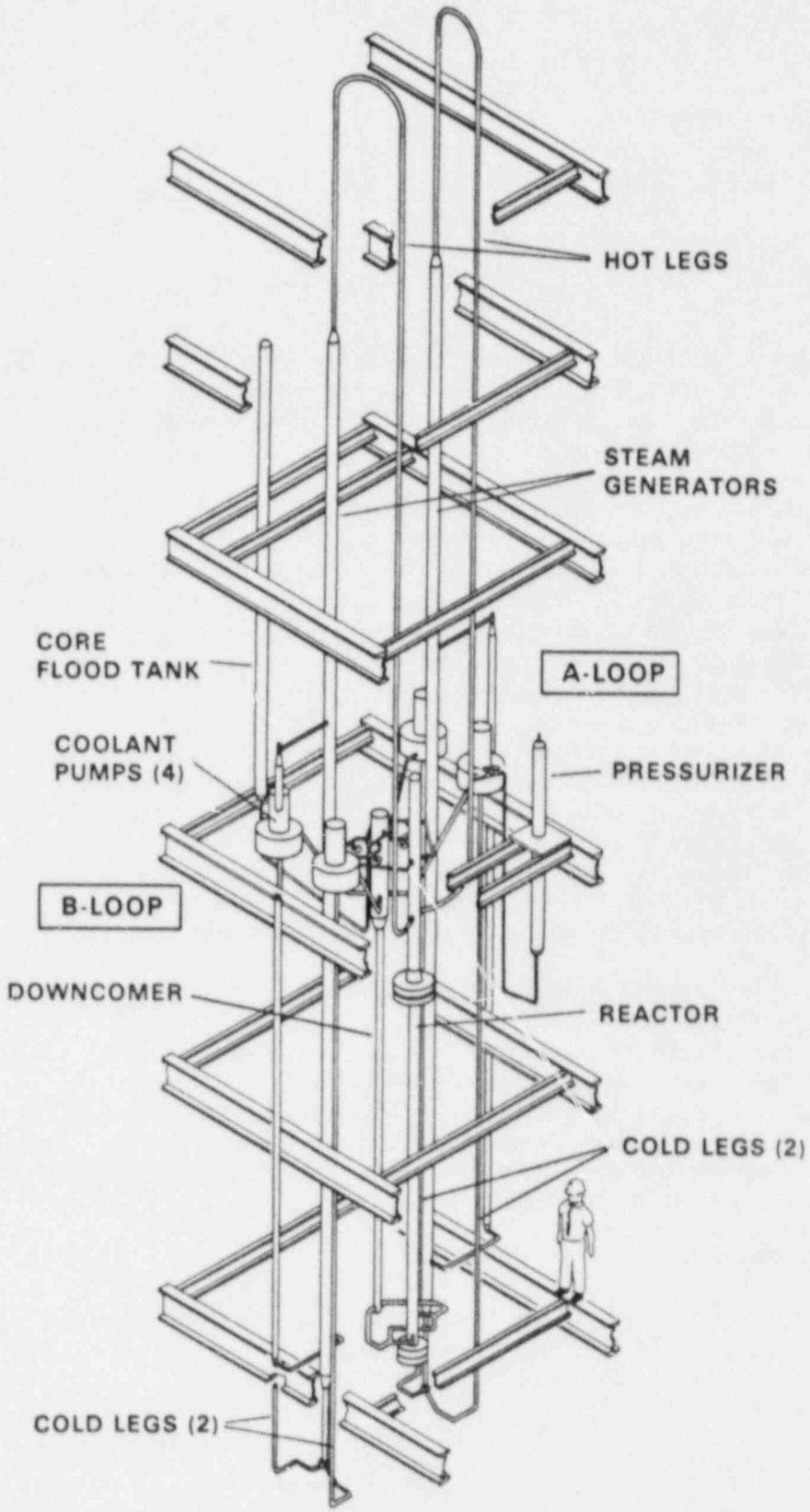

Figure 1. Reactor Coolant System -- Multiloop Integral System Test (MIST)

- Leak and HPI configuration
- HPI-PORV cooling (feed and bleed)
- Steam generator tube rupture
- Noncondensible gas and venting
- Reactor coolant pump operation

The mapping tests were intended to examine the initial post-SBLOCA transient interactions. In these tests, the primary system inventory was carefully controlled and slowly varied to allow the examination of the normally rapid and overlapping post-SBLOCA events.

The boundary system tests examined the adequacy and impact of the major boundary system simulations of MIST; namely, the reactor vessel vent valves (RVVVs), guard heating, level controls of the steam generators, and auxiliary feedwater (AFW) wetting. These tests were the first to be conducted after mapping to ensure that the boundary system simulations were understood and that the proper simulation had been selected before most of the transient tests were performed. One test with a plant-versed operator was also scheduled early to permit revision of the subsequent tests, if required. The base test conditions for the group included a scaled, 10-cm^2, cold leg discharge leak; automatic RVVV actuation on differential pressure; automatic guard heater control; constant steam generator level control (after refill); and symmetric steam generator cooldown. The inter-test variations included RVVVs manually closed, RVVVs manually opened, no guard heating, band control of the steam generator secondary level, asymmetric steam generator cooldown, maximum feed wetting, and use of abnormal transient operating guidelines. The base test was also repeated.

The SBLOCA interactions were also examined in the third group of tests, the Leak and HPI Configuration Group. The leak size and location as well as the HPI capacity were varied singly among the tests, while maintaining the other boundary conditions at their nominal settings. Whereas the nominal leak size was 10 cm^2, leak flow areas of 5 and 50 cm^2 (scaled to MIST) were also tested. A cold leg suction and a PORV break were used, in addition to the nominal cold leg discharge break. Also, the capacity of the high-pressure injection system was reduced by roughly one-half in one SBLOCA test.

NOTEWORTHY INTERACTIONS

The interactions summarized herein were noteworthy for one or both of the following two reasons: The MIST interaction was inherently of interest, or the interaction had implications for code modelling and the interpretation of code predictions.

Initial Interruption

The initial asymmetric interruption of one loop was quite sensitive to the test initial conditions and to the actuation and performance of the boundary

systems. The initial interruption strongly influenced subsequent events, such as occurred in Nominal Test 9 versus Nominal Repeat Test 10. This sensitivity of early events was apparently peculiar to the use of natural circulation rather than forced flow in this MIST test group. This sensitivity is thus of interest primarily to the code analysts modelling these MIST transients.

Counterflow

Liquid-liquid counterflow was generally observed. Based on repeated observations of its occurrence in MIST, the necessary conditions for counterflow included low or stagnating loop flow and relatively warm fluid at a lower elevation (such as warm upper-downcomer fluid versus HPI-cooled fluid). Counterflow permitted leak fluid heating and, hence, augmented HPI-leak cooling. Because system codes generally have no provision for liquid-liquid counterflow, code predictions of transients may diverge from observations except as mitigated by modelling adjustments.

Hot Leg Level Differences

Hot leg levels generally differed both across the U-bends (riser versus stub) and between loops. These level differences were of inherent interest for several reasons. The differences influenced the level range over which both BCM and spillover circulation were precluded; they varied (within a loop) with the natural circulation driving head and, between loops, in response to the amount of excess energy in the U-bend steam and adjacent metal.

RVVV Effects

The primary system generally depressurized, even with the steam generators inactive, after the downcomer liquid level had descended to the elevation of the cold leg nozzles. In this configuration, the RVVVs discharged core-generated steam into the downcomer whereupon it condensed on the relatively cold HPI. The RVVVs were thus observed to enhance primary system depressurization. With the RVVVs kept closed, the primary system first depressurized readily through sustained circulation in one loop, but then repressurized and began a prolonged period of variations of pressure, levels, and total fluid mass.

Inter-Cold Leg Flow

Periods of inter-cold leg (intra-loop) flow were observed in most SBLOCA tests. The HPI-cooled cold leg fluid would backflow down the cold leg suction piping to the cold leg junction near the steam generator primary outlet. Here, the fluid was heated slightly by the steam generator fluid. The somewhat warmer fluid flowed forward, upward through the adjacent cold leg suction piping, and down the discharge piping to the common point in the downcomer. The slight temperature difference between the fluid in the adjacent cold leg suctions sustained the inter-cold leg flow. This flow circuit tended to equalize the cold leg fluid temperatures, but had little apparent impact on the ongoing system events.

BCM

The boiler-condenser mode (BCM) was repeatedly observed to provide an effective mechanism for primary-to-secondary heat transfer, condensation of primary system vapor, and hence primary system depressurization. AFW-BCM rather than pool BCM was generally observed. The AFW-BCMs occurred singly, alternating between loops, and in tandem.

Equilibrium

Primary and secondary system conditions generally stabilized when the hot leg (riser and stub) levels attained intermediate values. The primary system pressure stabilized after an initial increase. The core exit fluid remained saturated whereas the core inlet (and lower downcomer) fluid temperatures slowly decreased due to HPI cooling. The temperature rise across the core thus increased, exceeding 200F.

Spillover

The quiescent primary and secondary systems abruptly reactivated when a hot leg riser level reattained the U-bend spillover elevation. The accompanying displacement of fluid throughout the primary system caused rapid temperature changes, most notably within the core. The relatively cold core-inlet fluid, upon its displacement through the core, caused the subcooling margin (SCM) to jump from 0 to more than 100F. Several such spillover events generally occurred before a hot leg remained full.

Band Steam Generator Control

Band rather than constant control of the steam generator secondary levels had a remarkable effect. With band control (feeding from a lower level setpoint to a higher setpoint, then interrupting feed), there were no periods of lingering or slight steam generator heat transfer activity. The steam generators were either dormant or active -- sometimes unusually so. Upon the first spillover event, after several hours of primary-to-secondary decoupling, the ensuing steam generator activity resulted in the bulk diversion of feed into the steam lines.

Operator Effects

The operator-controlled transient resembled the rest of the transients, but primary system refill and depressurization were more quickly accomplished. The operator employed a wide variety and relatively extensive set of actions to sustain primary-to-secondary heat transfer, control the SCM, and hasten refill. Unlike the usual MIST SBLOCA tests, the operator manually opened the PORV.

Restart of Natural Circulation

Natural circulation generally restarted upon hot leg spillover and remained active, provided that a hot leg riser level remained at the U-bend spillover elevation. The natural circulation restart was rapid and smooth. The primary system was then cooled and depressurized regularly through primary-to-secondary heat transfer.

Core Cooling

Core cooling was maintained throughout each of the MIST SBLOCA tests. The core region collapsed liquid level generally remained well above the top of the core.

System Resiliency

Because the RVVVs linked the core steam generation to the subcooled HPI and to the cold leg break site, the system conditions changed inherently toward depressurization and fluid mass equilibrium. With an increased break size, for example, the saturation of the break site fluid caused the break mass flow rate to decrease toward the HPI flow rate. As another example, the decreased condensing capacity with a reduced HPI flow rate was offset by an increased break volumetric discharge rate when the break site voided. Following a small break, the RVVV-equipped system thus has an inherent tendency to depressurize and to attain mass equilibrium.

This system resiliency is illustrated further by examining the results from three tests in which the imposed boundary conditions were significantly different. The three tests include the Nominal Repeat Test, 3110AA, a 10 square centimeter cold leg pump discharge break with full capacity HPI; the Increased Break Size, Test 320201, a 50 square centimeter cold leg pump discharge break with full capacity HPI; and Reduced HPI Capacity, Test 320604, a 10 square centimeter cold leg pump discharge break with approximately half-capacity HPI. The remaining initial and boundary conditions were the same for these three tests. A brief description of the results from each test will be presented.

Test Facility Initial Conditions

The test facility was initialized in steady-state natural circulation with a scaled core power of 3.9%. Primary pressure was adjusted to obtain a core exist subcooling of about 23F. The secondary side of the steam generators was controlled to 1010 psia steam pressure, the secondary level was maintained at 5 feet. The initial conditions for the three tests are summarized in Table 1.

Table 1

Initial Conditions

Parameter	Test 3110AA	Test 320201	Test 320604
Primary Loop			
Pressure, psia	1729	1730	1730
Core Exist Sub-cooling, F	23.2	23.6	23.9
Core Power, kW	127.8	128.1	127.9
Pressurizer Level, feet(1)	23.0	22.9	22.8
Secondary Loop			
Steam Pressure, psia			
Generator A	1013	1014	1013
Generator B	1013	1014	1015
Collapsed Level, feet			
Generator A	5.1	4.7	5.1
Generator B	5.1	5.0	4.8
Feedwater Temperature, F			
Generator A	113.3	116.6	112.5
Generator B	114.5	117.5	113.1

---

(1) All levels are reported relative to the steam generator secondary face of the lower tubesheet.

Each test was initiated by opening a scaled leak in the cold leg discharge piping. The leak was located downstream of the B1 reactor coolant pump, just beyond the HPI nozzle, on the bottom side of the pipe. Following leak actuation, the operator performed the following actions when the pressurizer level reached the 19 feet.

- Initiated refill of the steam generators to 31.6 feet using full auxiliary feedwater head-flow capability

- Activated HPI to each cold leg using either full capacity (Test 3110AA and 320201), or approximately half capacity (Test 320604)

- Started the simulated decay core power ramp

- Transferred reactor vessel vent valve control to allow valve actuation based on the differential pressure between the vessel and downcomer

- Actuated the steam pressure controls

After steam generator refill to 31.6 feet, the generators were controlled to maintain a constant level. Steam pressure was controlled to maintain a 50F temperature difference between core exist temperature and secondary saturation temperature by steaming the generator at a cooldown rate of 100F/hour. If this primary-to-secondary temperature difference becomes negative (reverse heat transfer), then steam pressure was reduced at 50 psi/minute until the desired 50F primary-to-secondary temperature difference was obtained. When the difference between core exist temperature and secondary saturation exceeded 50F, steam pressure was maintained constant. HPI was controlled to maintain the desired head-flow characteristic (either full or half capacity), unless a core exit subcooling of 70F was reached. HPI flow was then proportionally throttled as the core exit subcooling increased from 70 to 80F. In each test the Core Flood Tank (CFT) was available and charged to 600 psia. For this phase of MIST testing a low pressure injection simulation was not available.

Nominal Repeat, Test 3110AA

Upon initiating the 10 square centimeter leak the primary system began to depressurize at 115 psi per minute from 1730 psia (Figure 2a). The pressurizer outsurge accompanying leak actuation first displaced the relatively cold surge line fluid into the hot leg A riser, then reheated the A riser as the initially saturated pressurizer fluid entered the hot leg. The hot leg B riser temperatures increased to 596F at 1 minute in response to the decreasing core flow, and the subsequent core exit temperature rise. At about 2.1 minutes (relative to leak opening) the hot leg A U-bend fluid saturated. The hot leg A U-bend voiding increased and the spillover elevation became uncovered, resulting in a reduction of the loop A flow (Figure 3) and a rapid decrease in the level beyond the U-bend (Figure 4a). The loop A flow rates remained virtually stagnated beyond 3.6 minutes. The hot leg B U-bend first saturated at 2.4 minutes, however intermittent loop B flow continued until 15 minutes (Figure 3). Primary pressure stabilized around 1400 psia flowing loop saturation, then continued to gradually depressurize due to primary-to-steam generator B heat transfer. Primary pressure began to slowly increase from 1350 psia following com-

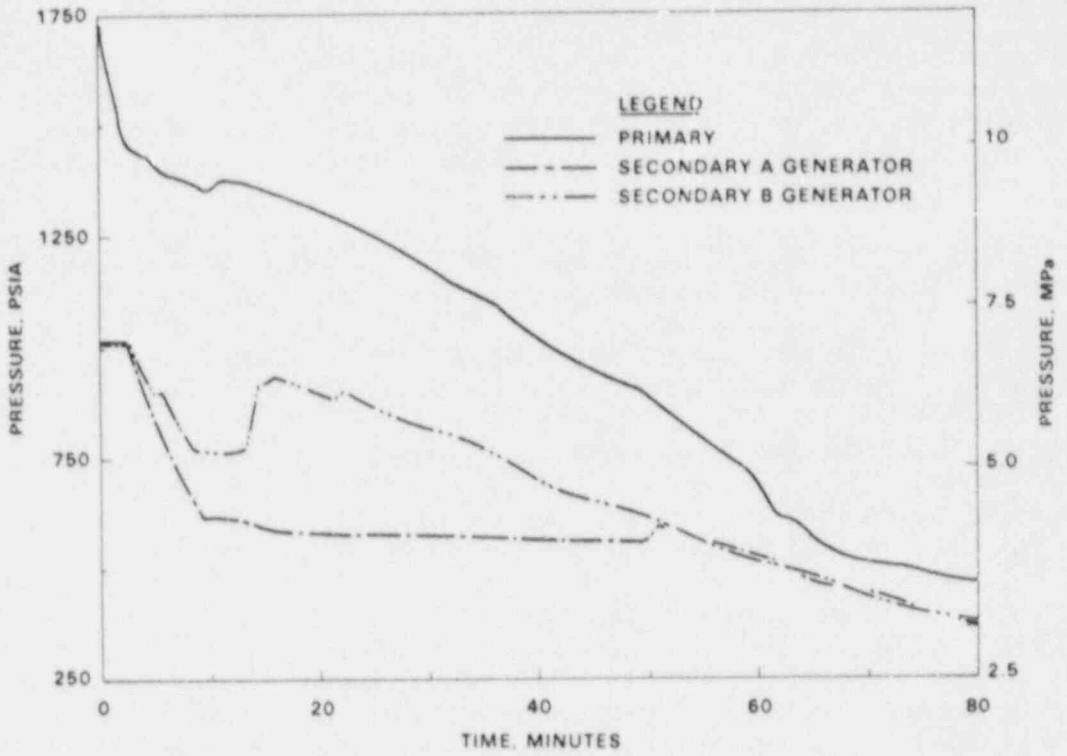

Figure 2a. Test 3110AA -- Primary and Secondary System Pressures

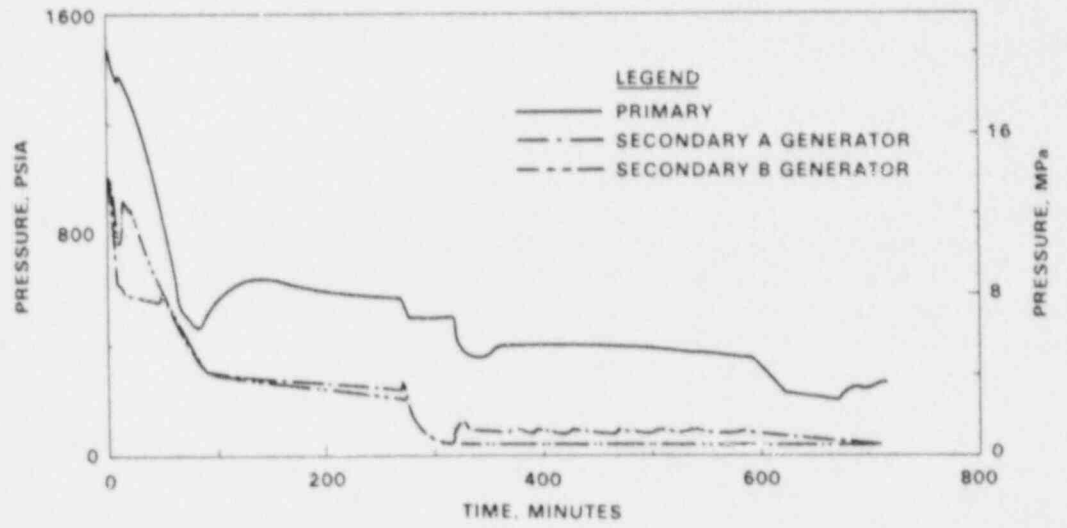

Figure 2b. Test 3110AA -- Primary and Secondary System Pressures

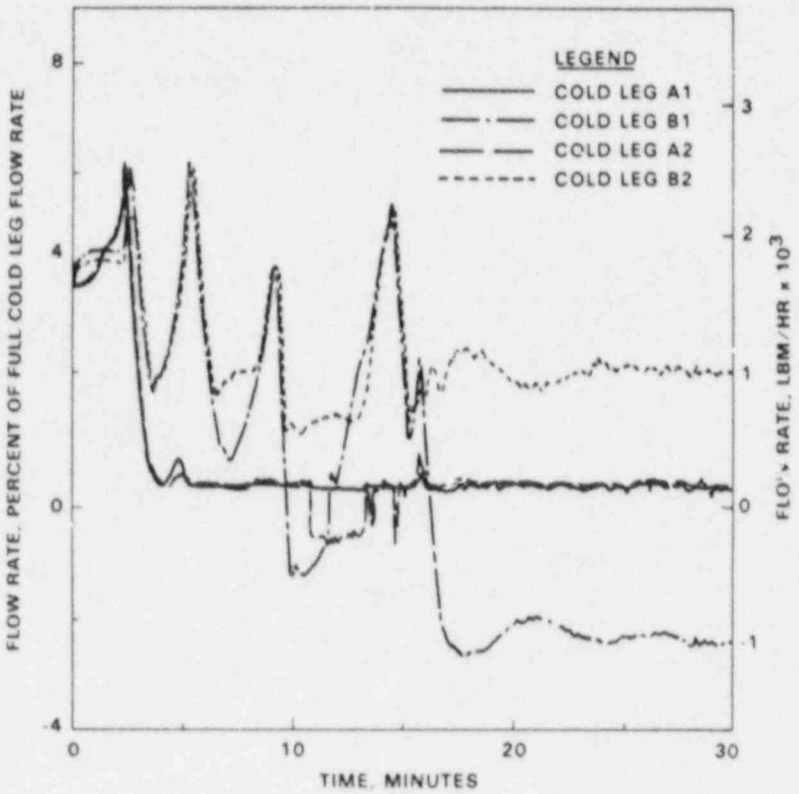

Figure 3. Test 3110AA -- Cold Leg Flow Rates

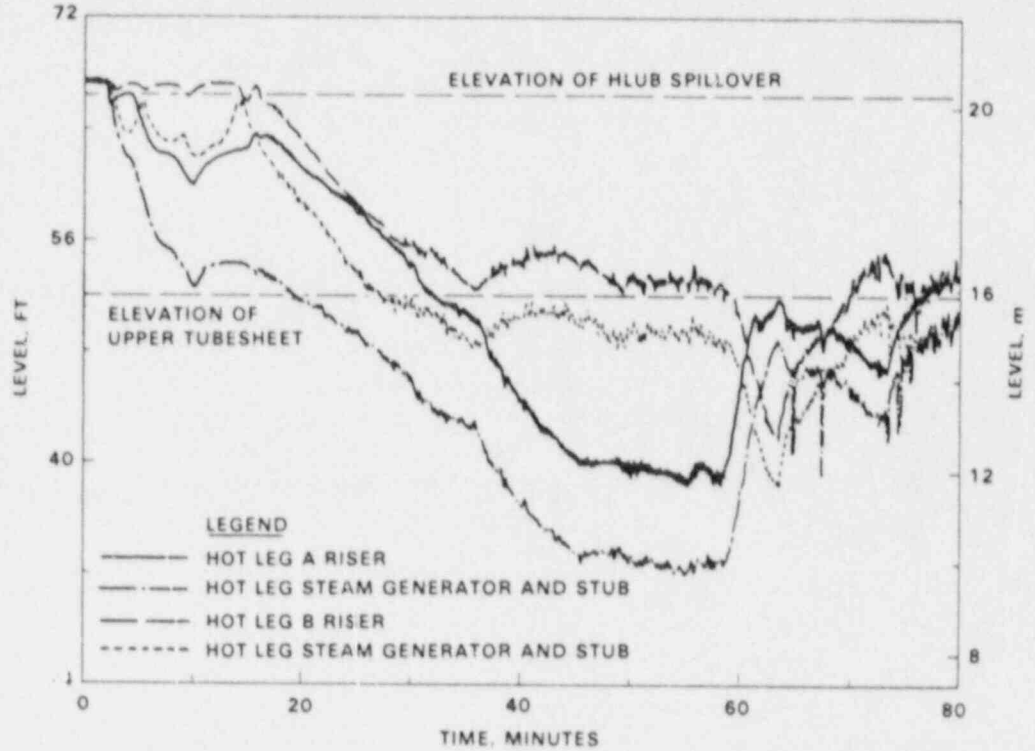

Figure 4a. Test 3110AA -- Hot Leg Riser and Stub Collapsed Liquid Levels

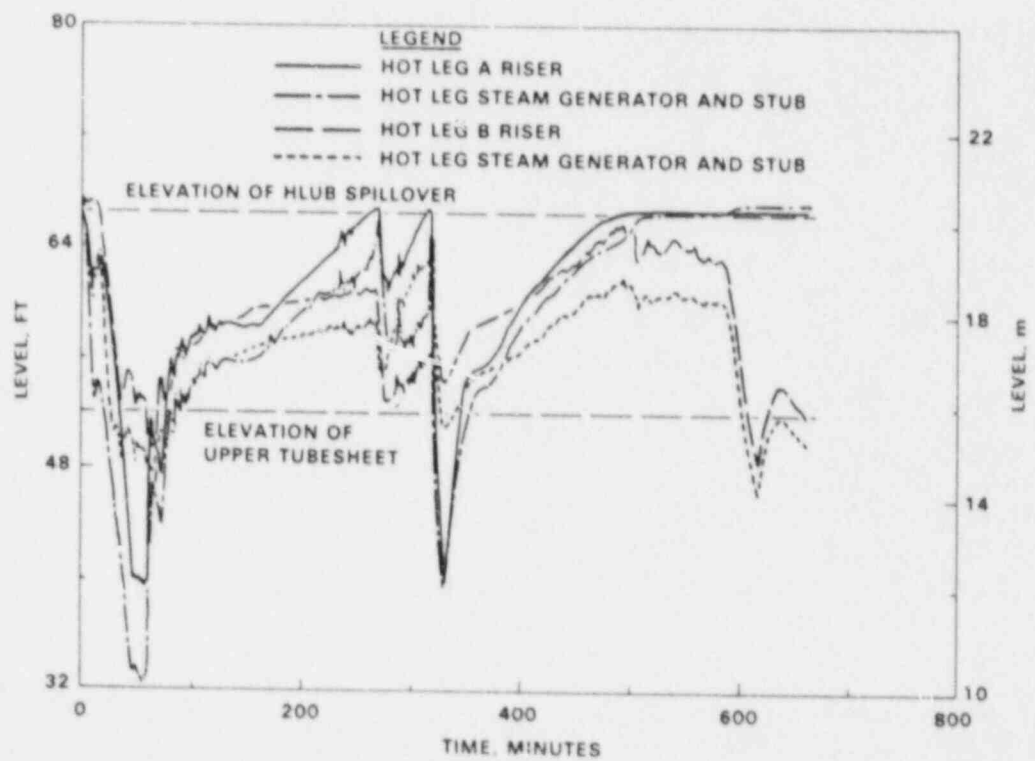

Figure 4b. Test 3110AA -- Hot Leg Riser and Stub Collapsed Liquid Levels

increased effects of HPI cooling. The leak flow rate thus increased dramatically and approached the diminished HPI flow rate at 130 minutes. The rate of hot leg level rise thus slowed with the riser and stub levels between 55 and 58 feet, that is, above the steam generators but well below the U-bend spillover (Figure 4b).

During the next several hours the hot leg levels slowly increased. The reactor vessel vent valves began to actuate intermittently as the core vapor generation rate became insufficient to continuously maintain the vent valve differential pressures above the closing setpoint. The core exit fluid remained saturated during the slow refill of the hot legs, but the temperature difference across the core rose as the lower downcomer and core inlet fluid cooled. This cooling occurred as the HPI capacity exceeded the core vapor generation rate.

At 270 minutes the hot leg A riser level achieved the U-bend spillover. The test was terminated at 663 minutes with loop A full, whereas the loop B hot leg riser and steam generator primary levels remained in the vicinity of the upper tubesheet (Figure 4b).

Increased Leak Size, Test 320201

A 50 square centimeter cold leg B1 discharge leak was used in test 320201. The initial conditions for this test were similar to those of the previous test as shown in Table 1. Upon leak actuation the primary depressurized at about 1700 psi/minute (Figure 5). The enhanced initial primary system mass depletion rate with the 50 square centimeter break caused (broken) loop B, rather than (intact and pressurizer) loop A, to interrupt first. The levels in both hot legs began to decrease around 1 minute (Figure 6). The primary pressure briefly stabilized near 1400 psia as the primary fluid saturated. During this time, the core region collapsed liquid level descended through the elevation of the reactor vessel vent valves and down to the hot leg nozzles, then the downcomer level descended to the same elevation. The core region and downcomer voiding propagated to the cold legs beyond 2 minutes. The (broken) cold leg B1 discharge level began to decrease, followed by the other three cold leg levels at 4 minutes (Figure 7). The leak site fluid saturated at 3.2 minutes, and the leak flow rate abruptly decreased as the leak site fluid state changed from subcooled to two-phase. The leak site conditions approached saturated vapor beyond 4 minutes. The voiding of the leak site slowed the rate of primary system fluid mass depletion to approximately 500 lb/hour beyond 5 minutes (Figure 8).

The hot leg levels of both loops descended rapidly beyond 2 minutes (Figure 6). Both steam generator primary levels descended below the elevation of the upper tubesheet, exposing primary system vapor to the feed injection site. The rate of primary system depressurization approached 200 psi/minute at 3 minutes (Figure 5). The combination of the continuing vent valve discharge of core-generated steam and the decreasing primary system saturation temperature caused the core region liquid to saturate. At 6 minutes the steam generator primary levels rose slightly to the vicinity of the upper tubesheet (Figure 6), thus slowing the rate of primary system depressurization. The steam generators were refilled to 31.6 feet at 8 minutes. Feed was thus interrupted and the steam generator A and B pressures stabilized at 710 and 630 psia (Figure 5). The primary depressurization rate increased slightly between 10 and 15 minutes as both

pletion of the steam generator refill to 31.6 feet. Following the final loop B spillover at 15 minutes, the steam generator B secondary repressurized to the control setpoint and began steaming to obtain a cooldown rate of 100F per hour, and primary system pressure began to slowly decrease (Figure 2a).

From 15 to 45 minutes steam generator B was gradually depressurized with the primary system to maintain the control temperature difference of 50F (between core exit and secondary saturation). At 36 minutes the B hot leg level beyond the U-bend reached the elevation of the auxiliary feedwater (AFW) injection (Figure 4a). Since this generator was feeding and steaming to maintain the primary-to-secondary control temperature difference of 50F, "AFW induced boiler-condenser mode (BCM)" heat transfer occurred. In this mode of cooling, primary vapor was condensed within the steam generator, in the region cooled by the injection of relatively cold feed. This event resulted in a slight increase in the primary depressurization rate (Figure 2a) and a realignment of hot leg levels (Figure 4a). Primary depressurization continued through heat transfer to the B generator. At 45 minutes the loop A steam generator primary level descended to the elevation of the secondary pool, thus activating a "pool BCM", the condensation of primary vapor within the steam generator in the vicinity of the liquid level overlap, with the secondary level at or above the primary level. The steam generator A secondary pressure (Figure 2a), which had remained constant since secondary refill, now repressurized to the control value, then began to be steamed at 50 minutes. The primary depressurization rate, which had decreased since the earlier generator B event, now stabilized at 20 psi/minute.

This enhanced rate of primary depressurization reduced the core exit-to-steam generator saturation temperature difference at a rate sufficient to activate the 100F/hour cooldown on both generators. The reactivation of steam generator A feedwater at 58 minutes obtained sufficient condensation heat transfer from the loop A primary fluid to alter the inter-loop levels (Figure 4a). The loop A hot leg levels rose, and the B levels dropped. Thus, the steam generator A "pool BCM" was supplanted by (steam generator A) "AFW induced BCM". The primary system depressurization rate approached 40 psi/minute, reducing the primary system pressure to within 100 psi of the steam generator secondary pressure (Figure 2a). This steam generator activity reversed the primary system mass depletion. The leak fluid subcooling, which had been 50F, decreased to less than 20F subcooling at 60 minutes. As a result of the reduction in both leak subcooling and primary pressure, the leak mass flow rate decreased while the HPI flow rate increased. Beyond 55 minutes the HPI flow exceeded the leak flow and primary system refill began.

The primary system depressurized below the CFT pressure of 600 psia at 63 minutes. The effects of the CFT discharge were overshadowed by the ongoing steam generator activity. The rate of gain of the primary system total fluid mass (HPI minus leak flow) approached 200 lb/hour between 70 and 95 minutes. The primary system fluid mass increase quickly precluded steam generator heat transfer, however, as the primary levels in both generators exceeded the upper tubesheet elevation at 85 minutes (Figure 4b). The controlled depressurization of the steam generator secondaries ceased at 90 minutes. The secondary pressures stabilized at 300 psia, whereas the primary system repressurized as rapidly as 7 psi/minute from a minimum value of 470 psia (Figure 2b). The leak fluid subcooling increased due to the primary system repressurization and due to the

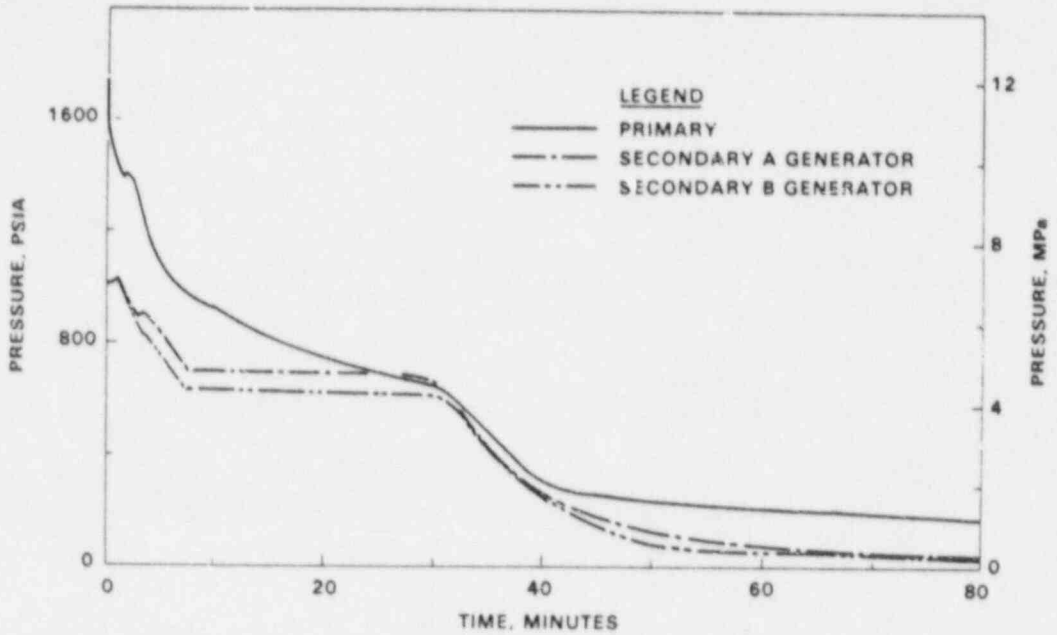

Figure 5. Test 320201 -- Primary and Secondary System Pressures

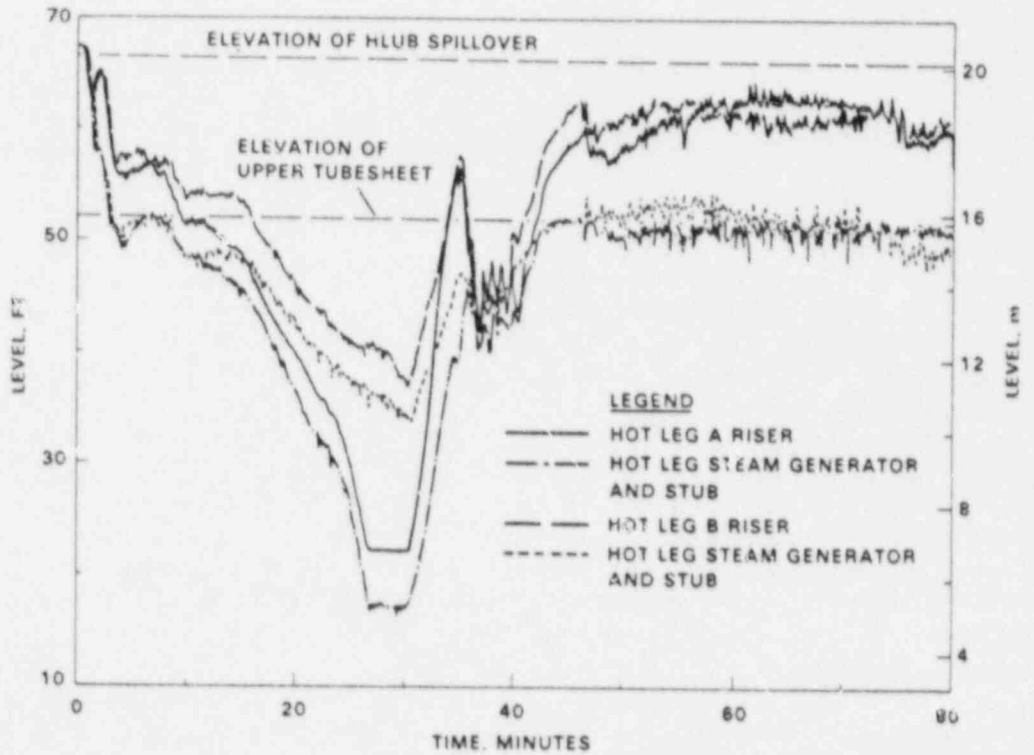

Figure 6. Test 320201 -- Hot Leg Riser and Stub Collapsed Liquid Levels

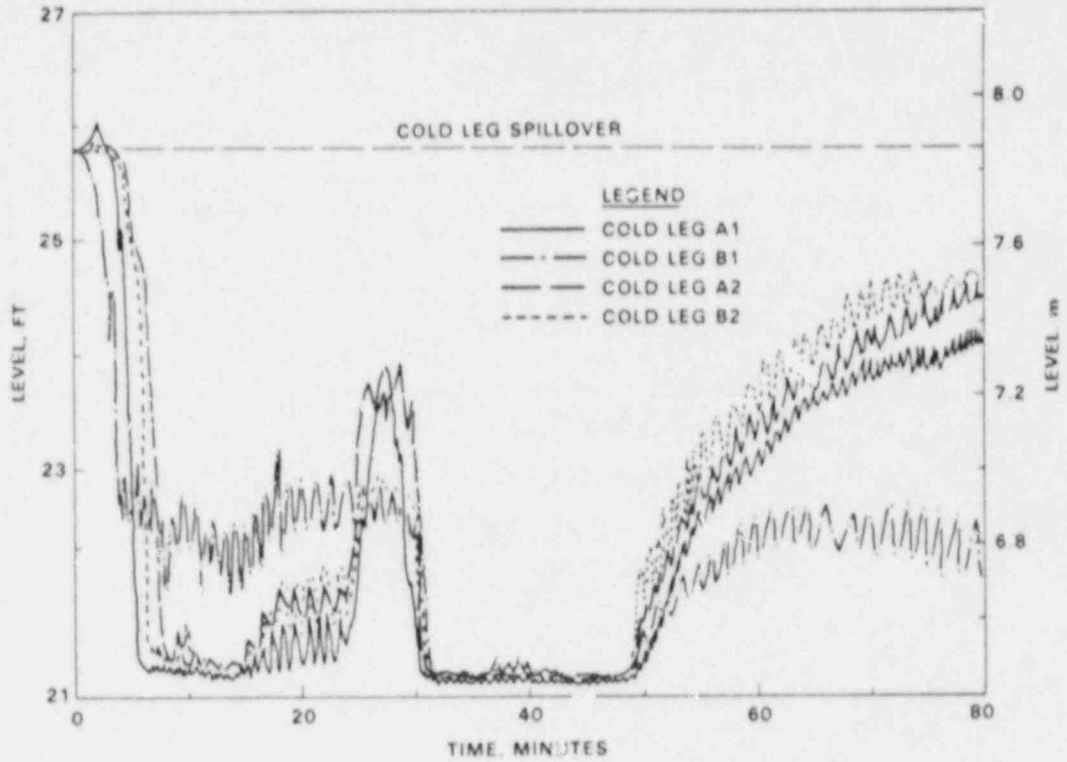

Figure 7. Test 320201 -- Cold Leg Discharge Collapsed Liquid Levels

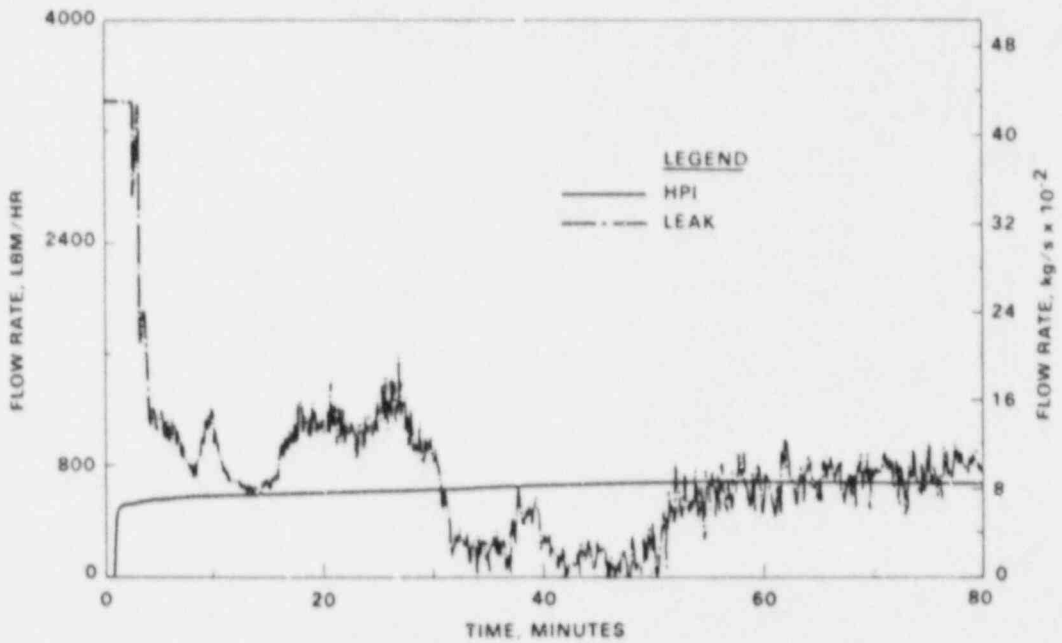

Figure 8. Test 320201 -- Primary System Boundary Flow Rates

generators began feeding, following the transition from AFW head-flow control (to refill the generators) to a constant SG level control. The temperature differences between the core exit fluid and the steam generator saturation temperatures remained less than the controlled value of 50F, due to the continuing primary depressurization with the core exit fluid saturated. Thus, the secondary control pressure was continually reduced at a rate equivalent to 100F/hour. The decreasing control pressure finally reached the current steam pressure at 28.5 minutes. However, before the controlled steaming could take effect, the primary system depressurization overtook that of the steam generator secondaries. The core exit-to-steam generator A saturation temperature difference became negative and the rapid mode of steam generator depressurization was activated. Both generators were depressurized at approximately 50 psi/minute from 30 to 35 minutes.

The reactivation of the steam generators under these circumstances produced strong primary-to-secondary coupling. The primary system depressurized in parallel with the secondaries, from 650 psia at 30 minutes to 300 psia at 40 minutes. The leak flow rate abruptly decreased (Figure 8) and the core flood tank actuated, both due to the primary system depressurization. The primary system began to refill. As the steam generator secondary pressures approached their minimum values, the rate of secondary depressurization gradually diminished beyond 35 minutes (Figure 5).

Beyond 50 minutes the HPI and leak mass flow rates remained approximately equal (Figure 8), the steam generator primary levels remained near the elevation of the upper tubesheets (Figure 6), and the primary system gradually depressurized towards the 25 psia secondaries (Figure 5). The core flood tank was isolated at 90 minutes upon satisfying the low level isolation criteria. The test was terminated at 187 minutes at a primary pressure of 100 psia. The core exit and upper elevation loop fluid remained saturated, the hot leg U-bends remained voided, and the core region levels remained in the vicinity of the nozzles.

Reduced HPI Capacity, Test 320604

The Reduced HPI Capacity Test (320604) was initialized in the same fashion as the two previously-discussed tests. The variation of this test was the use of half-capacity HPI as opposed to full capacity in the two previous tests. The initial conditions are summarized in Table 1.

With the reduced HPI capacity the initial hot leg voiding and flow interruption were rapid and quite symmetric. The hot leg riser and stub levels in both loops receded from the U-bend spillover elevation at 2 minutes after leak actuation (Figure 9). After two subsequent spillovers, both hot leg levels continually subsided from the spillover elevation beyond 8.6 minutes. Both steam generator secondary pressures (Figure 10) decreased with secondary refill, although the steam generator B secondary repressurized slightly after 4 minutes due to a brief period of primary-to-secondary heat transfer. The reactor vessel and downcomer levels reached the vicinity of the cold leg and hot leg nozzles by 9 minutes. Following steam generator refill to 31.6 feet at 9.2 minutes, the steam pressures remained quite constant, indicating negligible primary-to-secondary heat transfer. During the succeeding 4 hours, the steam generator sec-

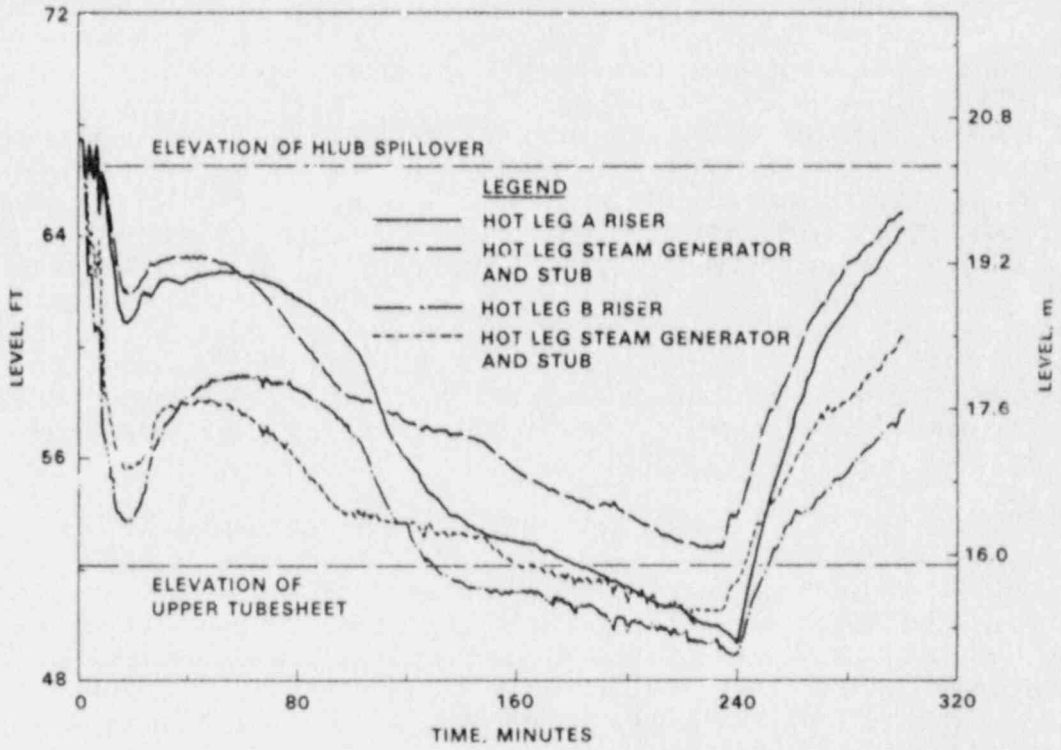

Figure 9. Test 320604 -- Hot Leg and Stub Collapsed Liquid Levels

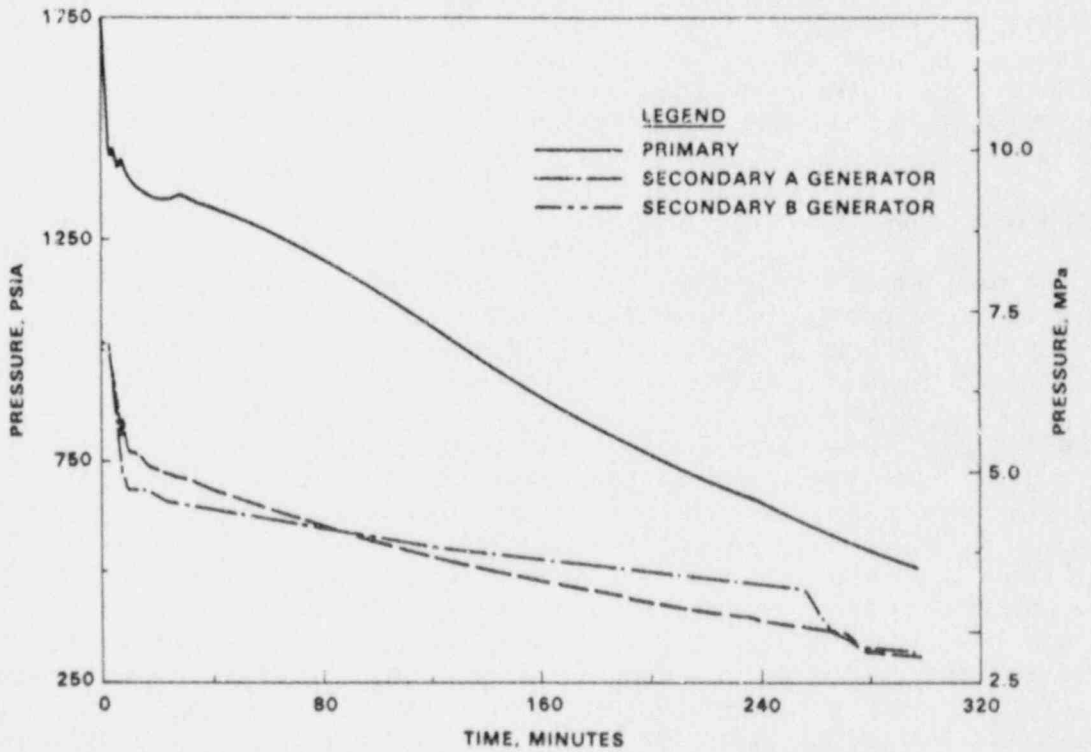

Figure 10. Test 320604 — Primary and Secondary System Pressures

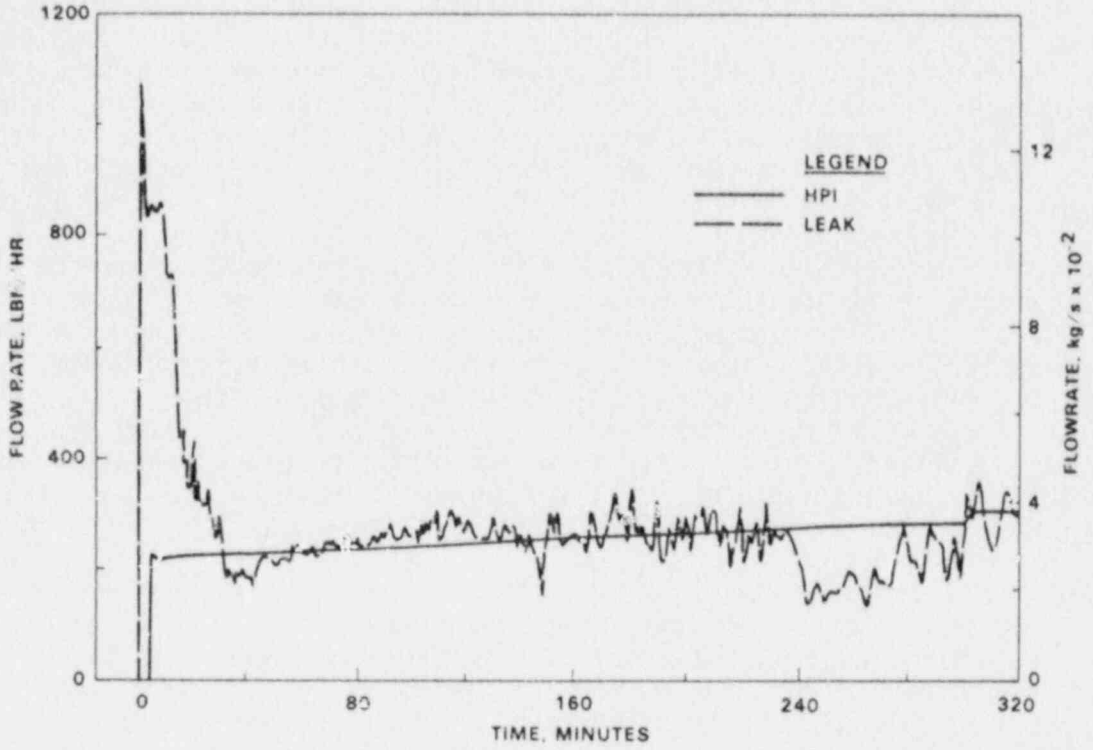

Figure 11. Test 320604 -- Primary System Boundary Flow Rates

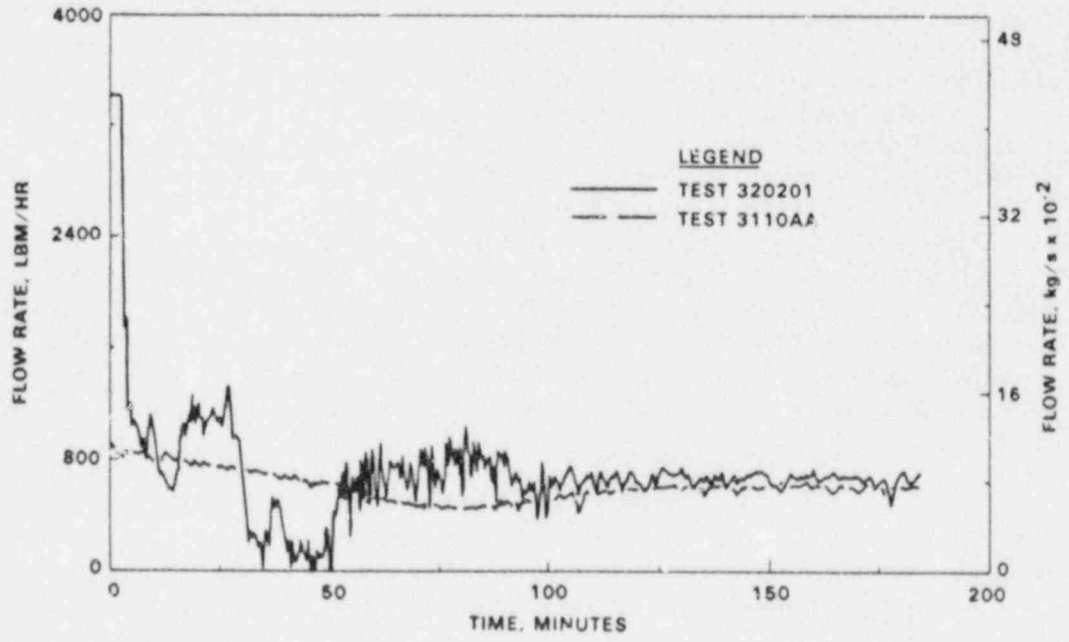

Figure 12. Tests 3110AA and 320201 -- Comparison of Leak Flow Rates

ondaries depressurized somewhat due to steam leakage through the control valves. The temperature difference between the core exit fluid and secondary saturation stabilized at about 80F, well above the control value of 50F at which the generators would be steamed. The generators thus became relatively inactive for a prolonged period.

The continuing excess of the leak flow rate over the HPI flow rate caused the hot leg levels to decrease toward the steam generators (Figure 9). The (broken) cold leg B1 discharge piping began to void at 11.6 minutes, the leak fluid temperature abruptly increased and, at 12.3 minutes, the leak flow rate decreased (Figure 11), indicating saturated conditions at the leak site. The excess of leak over HPI flow rate was thus reduced and the primary system total fluid mass stabilized. The hot leg levels stabilized before reaching the upper tubesheet elevation, then began to slowly increase, thus precluding primary-to-secondary heat transfer through condensation of primary vapor.

Whereas the hot leg levels stabilized, the cold leg suction and discharge piping voided sporadically between 12 and 29 minutes. At 30 minutes, the leak quality apparently increased, causing the leak mass flow rate to decrease further and to approximately equal the (reduced capacity) HPI flow rate. The primary system pressure (Figure 10), which had been nearly constant at 1350 psia, began to diminish slowly in response to the enhanced volumetric flow out the break. The resulting gradual primary system depressurization with negligible primary-to-secondary heat transfer was of long duration.

During the next 3.5 hours the primary system pressure (Figure 10) decreased steadily at about 200 psi/hour. The hot leg levels (Figure 9) in both loops declined slowly. The levels beyond the U-bends entered steam generators A and B at 123 and 165 minutes, but with no dramatic system response. The hot leg high-point vents were opened at 240 minutes. The vents apparently had little effect on the system conditions, although certain interactions occurred near the time at which the vents were opened. Steam generator B feeding began at 235 minutes, and the leak flow rate decreased noticeably (Figure 11), indicating increased leak fluid quality. The cold leg suction piping in all the loops began to lose liquid at this time, and both hot leg levels began to increase (Figure 9).

The concurrent translation of loop fluid apparently caused the steam generator pressure control to activate. Steam generator A was steamed beginning at 255 minutes, reducing its pressure (Figure 10) from 455 to 365 psia at 266 minutes. The gradual primary system depressurization continued from 660 psia at 240 minutes to 510 psia upon test termination at 300 minutes. The core flood tank became weakly active at 270 minutes as the primary system depressurized below 575 psia.

At test termination the system was relatively quiescent. The reactor vessel and downcomer collapsed liquid levels remained near the nozzle elevation, the reactor vessel vent valves remained open, and the hot leg levels had virtually stabilized below the U-bends but above the steam generators.

Comparisons

The comparison of the Nominal Repeat test to the Increased Break Size and

Reduced HPI Capacity tests demonstrates an important system response--the ability to adjust to imbalanced boundary conditions.

The primary system conditions equilibrated with the 50 square centimeter break much as they did with the 10 square centimeter break. The HPI flow rate and core power input of the two tests were virtually identical. The key to this seeming contradiction was the break fluid conditions. The core region level increased toward the elevation of the reactor vessel vent valves in the Nominal Repeat test, while it remained near the top of the core in the Increased Break Size test. The break site fluid remained saturated with the 50 square centimeter leak whereas the break fluid was slightly subcooled with the 10 square centimeter leak. The break mass flow rates thus remained approximately equal beyond 90 minutes (Figure 12). The higher volumetric flow rate with two-phase conditions at the break obtained a lower sustained pressure with the larger break (Figure 13). The lower pressure in the Increased Break Size test also contributed to its lower break mass flux. Near-equilibrium conditions of mass and energy were obtained with both the 10 and 50 square centimeter breaks, but at a lower pressure with the larger break.

The ability of the system to adjust to imbalanced boundary conditions was again demonstrated with reduced HPI capacity. In the Nominal Repeat test, the heat capacity of the injected fluid was sufficient to condense core-generated steam, offsetting the tendency of core steaming to pressurize the system. Furthermore, the transport of condensation-heated fluid to the break site obtained HPI-leak cooling sufficient to offset the core energy deposition. However, with reduced capacity HPI, the HPI heat capacity was initially insufficient to condense the entire core steam production. The reactor vessel vent valves continued to discharge steam in excess of the HPI condensation capacity, thus the downcomer and cold leg discharge piping continued to void until the leak fluid saturated. In response to the strong dependence of leak (critical) flow on fluid conditions, the leak mass flow rate then decreased and the leak volumetric flow rate increased. In addition, the increased leak fluid enthalpy augmented leak-HPI cooling. These inherent adjustments occurred early in the Reduced HPI Capacity test, at approximately 9 minutes. The leak fluid saturated (Figure 14), the measured leak fluid enthalpy indicated two-phase flow (Figure 15) and, at 30 minutes, the leak fluid enthalpy increased toward that of saturated vapor. Upon the latter fluid state transition, the primary system pressure began to decrease continuously from 1350 psia. In the Nominal Repeat test, with full-capacity HPI, the primary system depressurized up to 80 minutes, primarily through boiler--condenser mode heat transfer, then repressurized and stabilized when the hot leg levels attained intermediate elevations between the top of the generators and the U-bends. In this manner the primary system pressures in the two tests became approximately equal beyond 4 hours (Figure 16).

In summary, the Reduced HPI Capacity test, much like the Increased Break Size test, demonstrated the inherent responsiveness of the system due primarily to the reactor vessel vent valves. In both tests, the leak site fluid saturated, thus altering the system mass, energy, and volume balances toward equilibrium.

SUMMARY

The Boundary Systems tests permitted the evaluation of the major MIST bound-

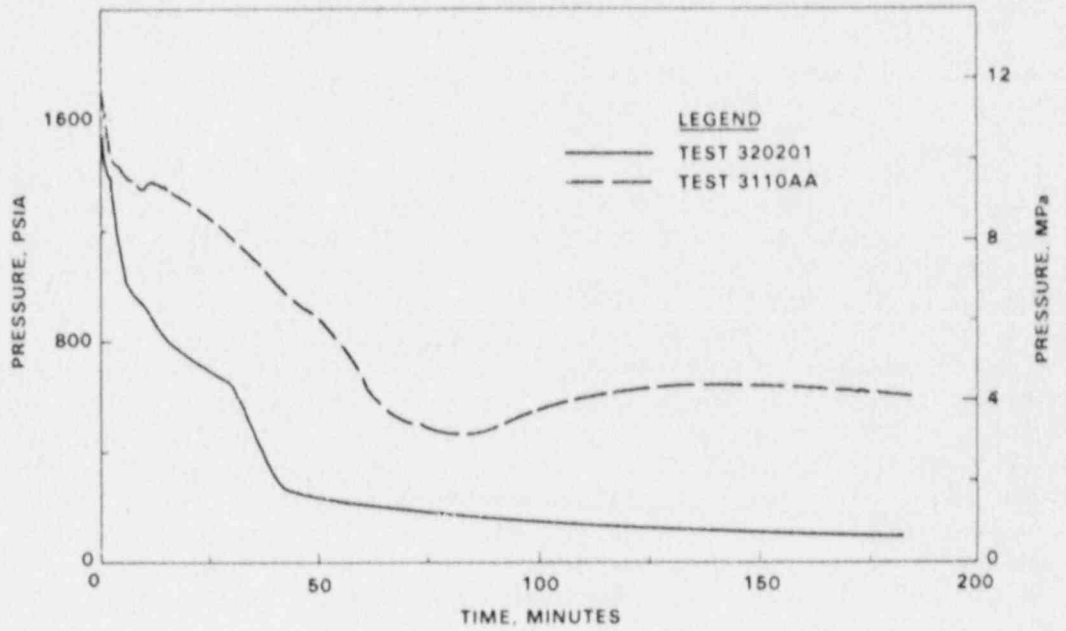

Figure 13. Tests 3110AA and 320201 -- Comparison of Primary System Pressure

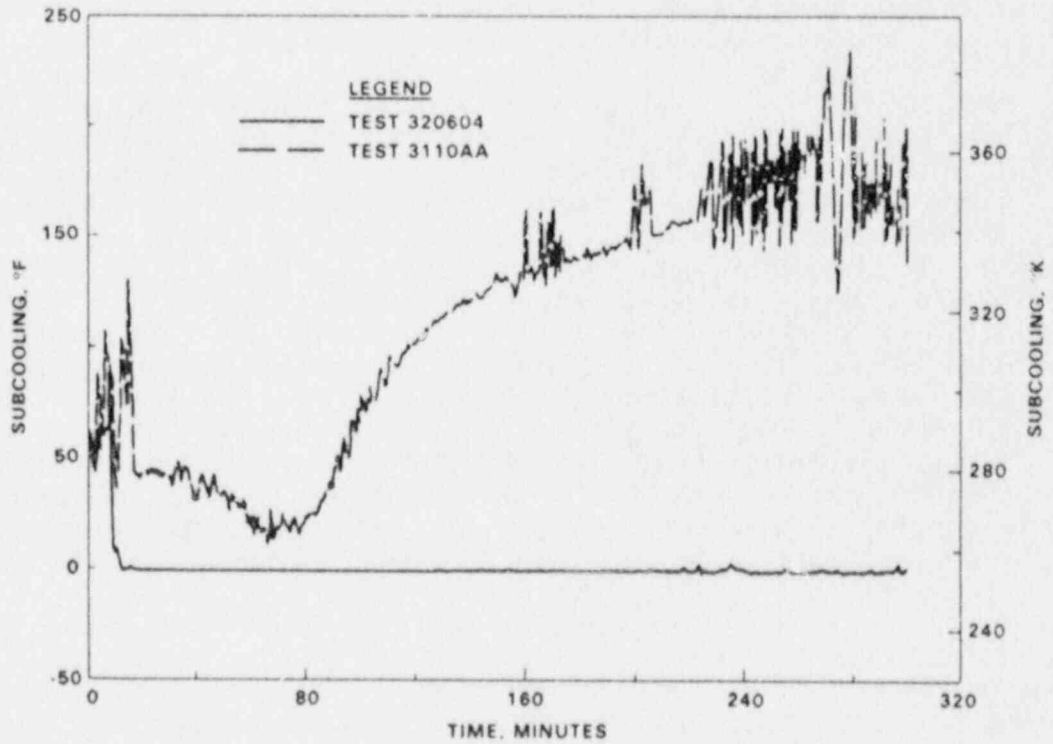

Figure 14. Tests 3110AA and 320604 -- Comparison of Leak Fluid Subcooling

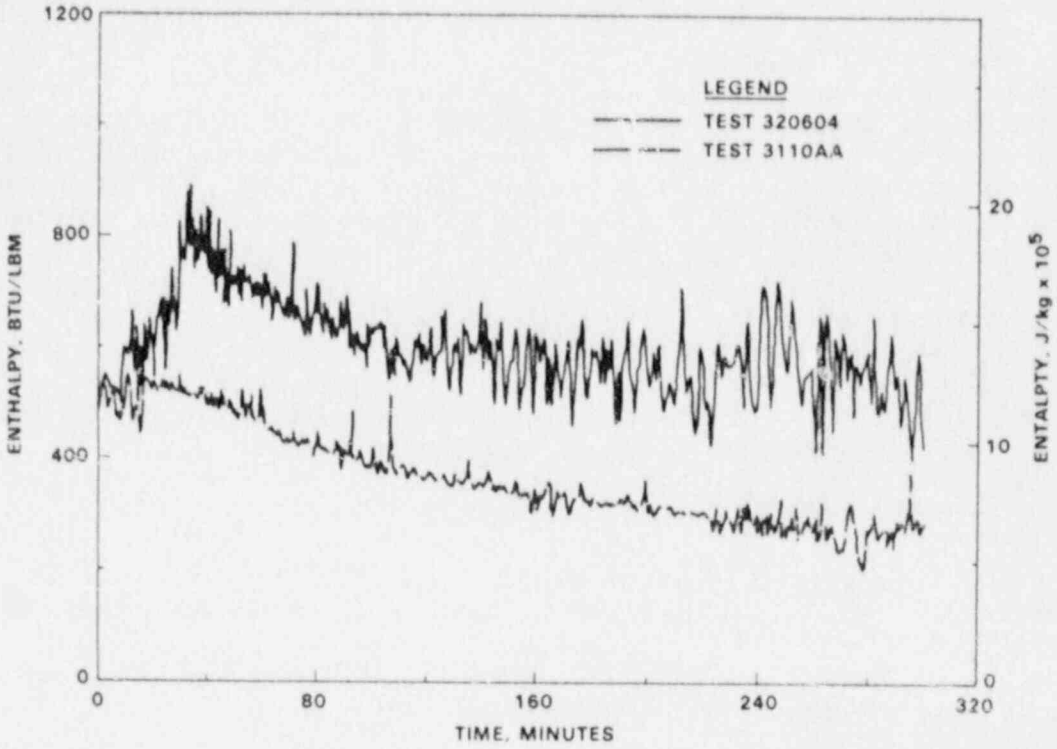

Figure 15. Tests 3110AA and 320604 -- Comparison of Leak Fluid Enthalpy

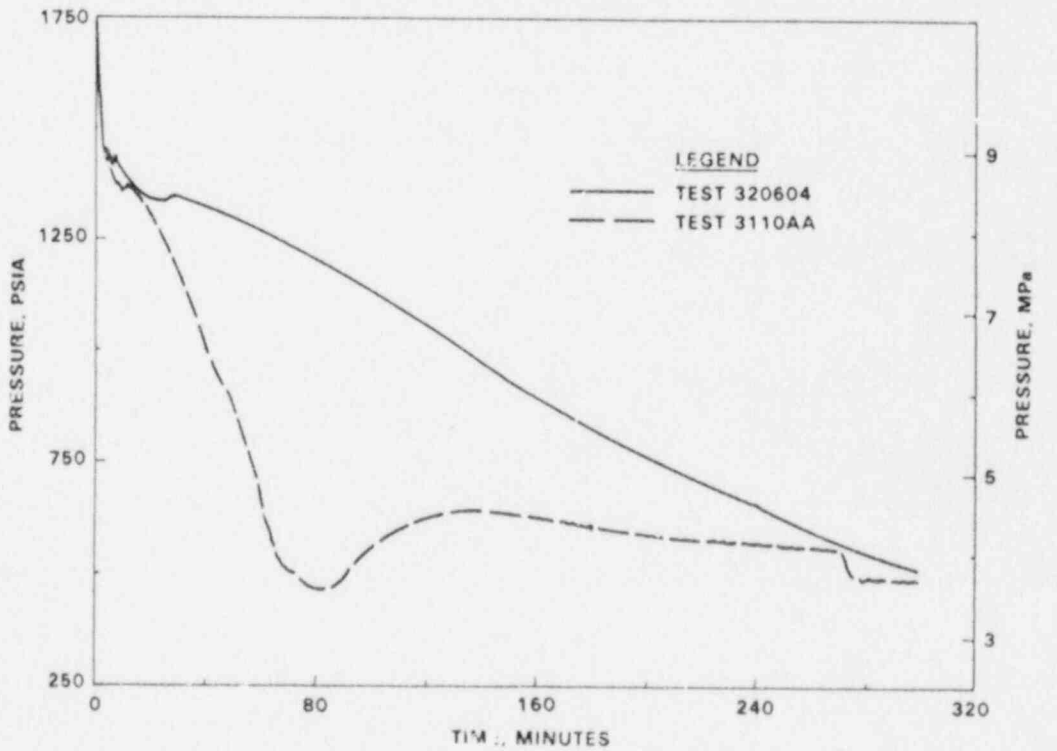

Figure 16. Tests 3110AA and 320604 -- Comparison of Primary System Pressure

ary system simulations and thus fulfilled their purpose. The Leak and HPI Configuration tests provided integral-system data with differing conditions and interactions. The test initial conditions, initiating actions, and control during testing were generally as specified. The several indications of the MIST events, often using completely independent indications, repeatedly attested to the consistency of the MIST measurements.

The three tests presented, Nominal Repeat, Increased Break Size, and Reduced HPI Capacity, demonstrated the inherent responsiveness of the system due primarily to the reactor vessel vent valves. In these tests, the state of the leak site fluid adapted to the imposed boundary conditions, thus altering the system mass, energy, and volume balances toward equilibrium.

Observations of UMCP 2x4 Loop Test Result Simulating B&W Power Plants Behavior

Y.Y. Hsu, K. Almenas, M. Di Marzo*, C. Unal, Z.Y. Wang

Chemical & Nuclear Engr. Dept.
*Mechanical Engineering Dept.
University of Maryland
College Park, MD

Abstract

Three areas are covered in this report. Namely a) the thermal-hydraulics behavior of the loop during liquid inventory depletion transients as a result of SBLOCA; b) the integral and global approach to the facility scaling; and c) the repeatability of the tests.

Phenomenological description of the thermal-hydraulic events that take place during a simulated Small Break Loss Of Coolant Accident is presented. Two types of conditions are present. The process was found to be controlled by inventory. Thus inventory scaling can be used as an alternative to time scaling in describing the event sequence. Such scaling is much simpler than the conventional hydrodynamic scaling. The causes producing variability between the test data of identical test runs in a multi-loop thermal-hydraulic system can be divided into two categories. The categories can be distinguished by the distribution of the experimental variation, namely:

1. Gaussian
2. Bifurcation

The first category encompasses that could be called the `standard´ variations of experimental data. The second category of deviations to arise when a system under certain conditions can be in two alternate but energetically equivalent states.

1. Introduction

The UMCP 2x4 Loop Project is a part of NRC Integral System Test Program to provide data on tests simulating the B&W power plant behavior. The loop facility is 1/500 of the proto-type by volume scale, and operates at low pressure (up to 400 psia (see Fig. 1)). The height is about 1/4 of the proto-type with cross-sectional areas proportionally "fatter" than the linear scaling. Such scaling is necessitated by the requirement that the friction loss be properly balanced by the static head for natural circulation. However, due to its low operating pressure, under which there exists larger ratio of liquid density to vapor density than that at proto-type pressure range of 1600 - 2200 psi, questions have been raised as to the adequacy of low pressure system to model the high-pressure plant. The strategy we take are three folds:

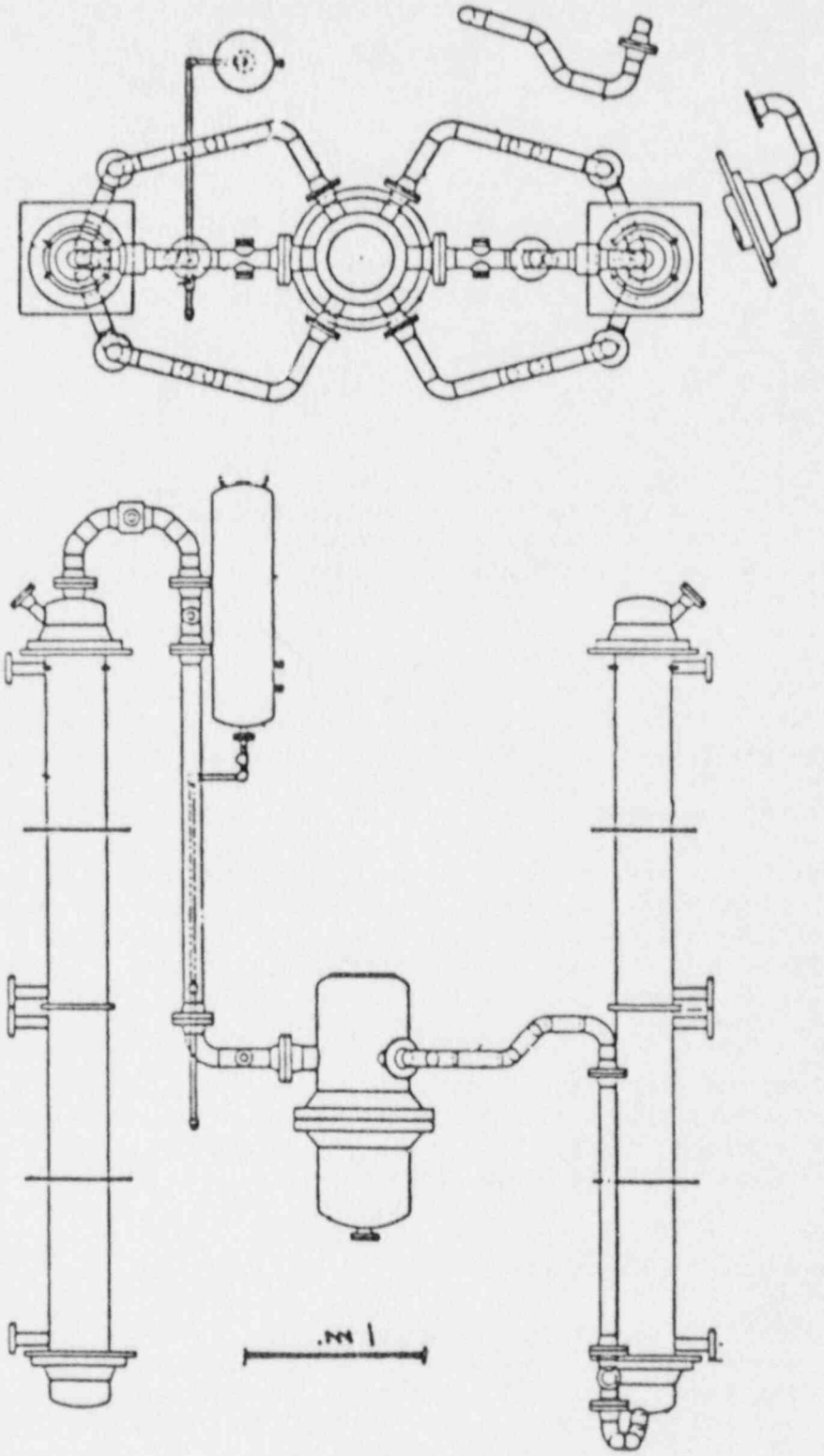

Figure 1: System Layout

(1) Regardless of the pressure level, the physical phenomena encountered should be basically the same although time scale might be altered. Thus, the UMCP facility can produce thermal-hydraulic data of a 2x4 Loop for code assessment.

(2) Since the SB-LOCA process is slower than that of LB-LOCA, the system can approach closer to the thermal equilibrium. Thus, a global scaling based upon inventory, enthalpy and pressure (akin to PVT-relation in gas-state) can be used to describe state of the system. In such global scaling, inventory of the system (or components) can be used as a substitute to time-scale.

(3) For code assessment, it is important to establish the uncertainty of the data base. In the past, due to the cost of operation of the large integral test facilities, the uncertainties can only be determined from the repeatability of two (or at most three) runs. UMCP Loop, being a small facility, can be used to run many repeated runs to establish the band of uncertainty and the sensitivity of test results to variation in test boundary/initial conditions.

In this report, we will address the above three issues based upon the observations of test results that we have obtained in the past year.

2. Test Scope

Three categories of tests were performed:

(1) Single-phase natural circulation.

(2) Two-phase natural circulation, i.e. start the run after the saturation condition is reached and vapor appears.

(3) Integral test, i.e., the run was started with subcooled condition so that the depressurization period precedes the two-phase period.

The test conditions of various runs are shown in Table 1. All of them were without HPI. In addition to the above listed runs, a few runs with HPI were conducted, but they are not listed since test results are still undergoing data qualification procedures.

3. Test Results

3.1 Single-Phase Natural Circulation Run Series

The objective of this series of runs is to determine the effect of unbalanced load between loops in the secondary side on the interloop distribution of flow rates in the primary side.

3.1.1 Response of the Primary System to Asymmetric Conditions

Asymmetric distribution of secondary-side flow rates results in similar primary-side response. Higher secondary-side flow rate extracts more energy from the corresponding heat exchanger, enhancing the rate of

Table 1: Test Conditions

TEST COMPLETED AS OF SEPTEMBER 1987

Test no.	Power	Break size	Sec. Level	Initial cond.	Comments
ITL031287	130 kw	1/8"	75%	ASYMMETRIC	Scoping test
ITL031387	130 kw	1/8"	75%	ASYMMETRIC	Repeat of ITL031287
BCM071587		1/8"	50%	SYMMETRIC	Power drop test
BCM071687	"	"	"	"	Repeat of BCM071587
SNC072987	160 KW	N/A	50%	ASYMMETRIC	ASYMMETRIC TO SYMMETRIC
BCM(old)	140 KW	1/8"	75%	ASYMMETRIC	
• BCM073187	141kw	1/8"	50%	Symmetric	
• ITL080587	168kw	1/8"	50%	Symmetric	
ITL080787	168 kw	1/8"	50%	Symmetric	Repeat of ITL080587
• ITL081487	168 - 80 kw	1/8"	50%	Symmetric	Power drop test
BCM091587	141 kw	1/8"	75%	Symmetric	
BCM091787	141 kw	1/8"	50%	Asymmetric	
• BCM092287	141 kw	1/16"	50%	Symmetric	
• BCM092487	141 kw	1/16"	50%	Asymmetric	

heat transfer which in turn increases the rate of primary-side flow rate and lowers primary-side temperature gradient. However, the magnitude of primary-side flow redistribution is much less drastic as compared with that of the secondary (Figs. 2 and 3). This is due to the fact that the thermal length of the loop with higher secondary-side flow rate increases while the friction head loss increases. The reverse is true with lower secondary-side flow rate. The net result would be a milder response to the imposed asymmetry.

3.1.2 Stability of the Primary System Flow during Imposed Transient

Flow instability resulting in cessation of circulation was not observed either in the asymmetry or during two-to-one loop operation transients. However, flow and temperature fluctuations existed in the loops with lower secondary-side flow rates. However, primary system temperature increases due to asymmetric operation. The system average temperature rose during a symmetric to asymmetric transient while the total secondary-side flow rate was maintained. This is due to the fact that the asymmetric secondary load degrades the efficiency of total heat removal.

3.2 Two-Phase Natural Circulation Test Series

The series of tests described in this paper were performed to characterize the phenomena occurring during a small break LOCA. The initial conditions are different from the actual small break LOCA. However, there is reason to believe that similar phenomena should be observed in the more complex integral tests. The most important difference between the tests described here and the integral test is the thermal-hydraulic interaction of the pressurizer with the primary loop. For these currently analyzed tests the pressurizer surge line is isolated from the system.

The initial condition is characterized by a steady-state single-phase natural circulation in the primary loop. The secondary loop liquid inventory is kept at a constant level (25%, 50%, 75% of the steam generator height) during each test. Note that when the secondary liquid level is held at 25%, single-phase natural circulation is not established. Furthermore, due to the asymmetric feed of the secondary-side coolant and/or due to the initial enthalpic content of the primary-side, asymmetric behavior could easily be encountered in single-phase natural circulation for the 50% and 75% liquid level cases. The asymmetries are such that only one cold leg of each steam generator pair is flowing while the other is stagnant.

The tests, for which the secondary-side liquid level is kept at 25% of the steam generator height, are not of great interest. The primary loop remains stagnant and the reactor core heats the reactor vessel inventory and could, if permitted, raise the loop pressure well beyond the system design pressure. The thermal center location is such that flow is not possible hence the volume of fluid involved in the heating process is limited to the reactor core and its immediate surroundings.

The test is initiated when the break is opened. During the beginning of inventory loss, some voidage is observed at the candy canes and two-phase natural circulation effectively performs in all similarly to the single-phase steady-state natural circulation present prior to the break

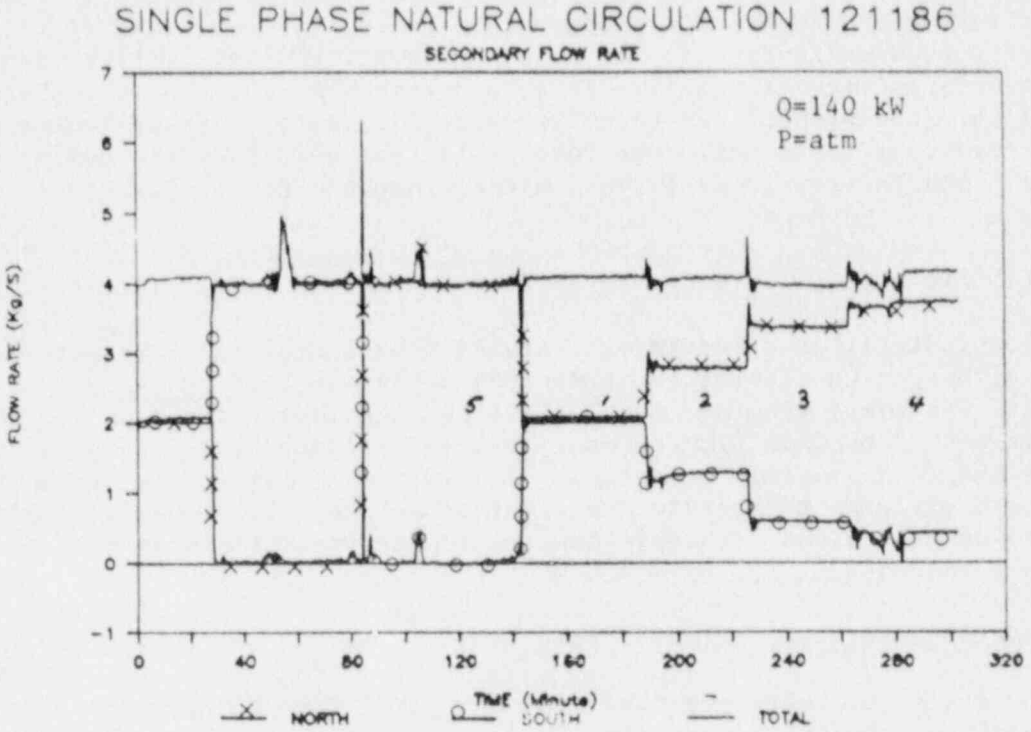

Figure 2: Unbalance of Flow in Secondary-Side of Steam Generator

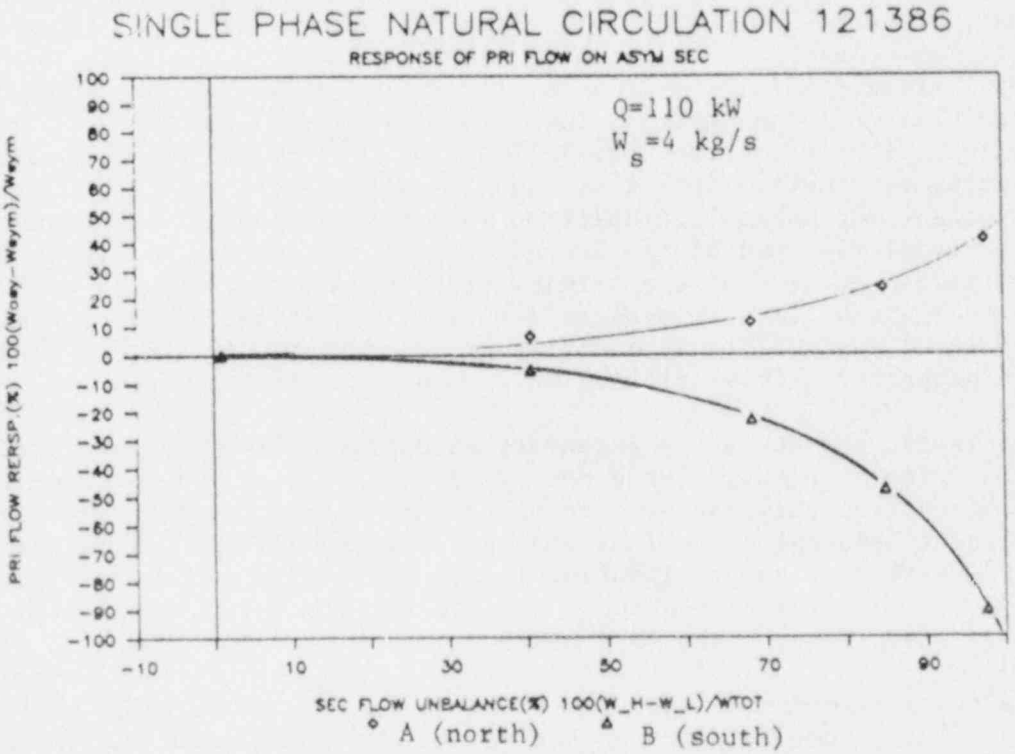

Figure 3: Flow Distribution in Primary Side in Response to Unbalance in Secondary-Side Flow

activation.

As the primary liquid inventory is depleted, the void becomes more important and the two-phase natural circulation is interrupted in one and then both candy canes. During the flow interruption, heat is not removed from the vessel core at sufficient rate and the pressure rises. The vapor generated in the vessel core fills the upper plenum and overflows in the hot legs. The two-phase mixture in the vertical section of the hot legs swells and spills over the candy canes thus causing a brief but intense flow resumption. The pressure falls. The two-phase mixture that has passed over the candy-cane reaches the steam generator and an equal volume of liquid is spilled over the top of the cold legs loop seal. Note that the phenomena takes place in one hot leg at the time, hence in one steam generator at the same time. Furthermore, only one cold leg is flowing. Obviously the cold leg with higher enthalpic content carries the flow because its vertical portion leading to the loop seal is lighter. The subsequent spill-over of relatively cold water over the cold leg loop seal generates a flow of cold water in the downcomer.

At this point a very important phenomenon takes place. The vapor present in the upper plenum of the reactor vessel is brought in contact with this cold water. There is still speculation concerning the path of the cold water and of the vapor which brings both in direct contact. The fact is that a sudden, violent condensation is observed in the upper plenum. Pressure drops substantially and there is evidence that water is drawn to the vessel from the cold legs and from the hot legs. This substantial condensation pull subsides and a new warming trend takes place, leading to flow resumption in the candy canes. This oscillatory behavior is evident in Fig. 4. The RVVV open briefly when the pressure in the reactor upper plenum reaches its minimum and is in its early portion of its subsequent upward transient.

The liquid inventory keeps depleting and the system reaches a condition where the resumption phenomenon can not occur because the liquid-vapor mixture in the hot leg swells to the level lower than the candy cane elevation. Pressure then rapidly rises and depending on the secondary level action must be taken to keep the pressure within the system design boundaries. The power level is reduced in the test shown in Fig. 5. In Figure 6, the power was fixed but the PORV was open to relieve the pressure. The power versus time curve is superimposed in the figure, while the PORV cycling is evident.

Further depletion of the primary liquid inventory drops the liquid level in the primary side of one steam generator bellow the fixed secondary level. A cold condensing surface then becomes available for the vapor to be collapsed and quickly an intense heat transfer recovery from the reactor core to the activated steam generator is observed. The heat is transferred into Boiler Condenser Mode and a strong vapor flow is observed throughout the hot leg of the loop containing the activated steam generator. In the test performed up to date, one steam generator is sufficient to carry the entire cooling load. The primary pressure is brought down to a level lower or similar to the one reached in single-phase natural circulation. This is a clear evidence of the BCM heat transfer effectiveness (Fig. 7.)

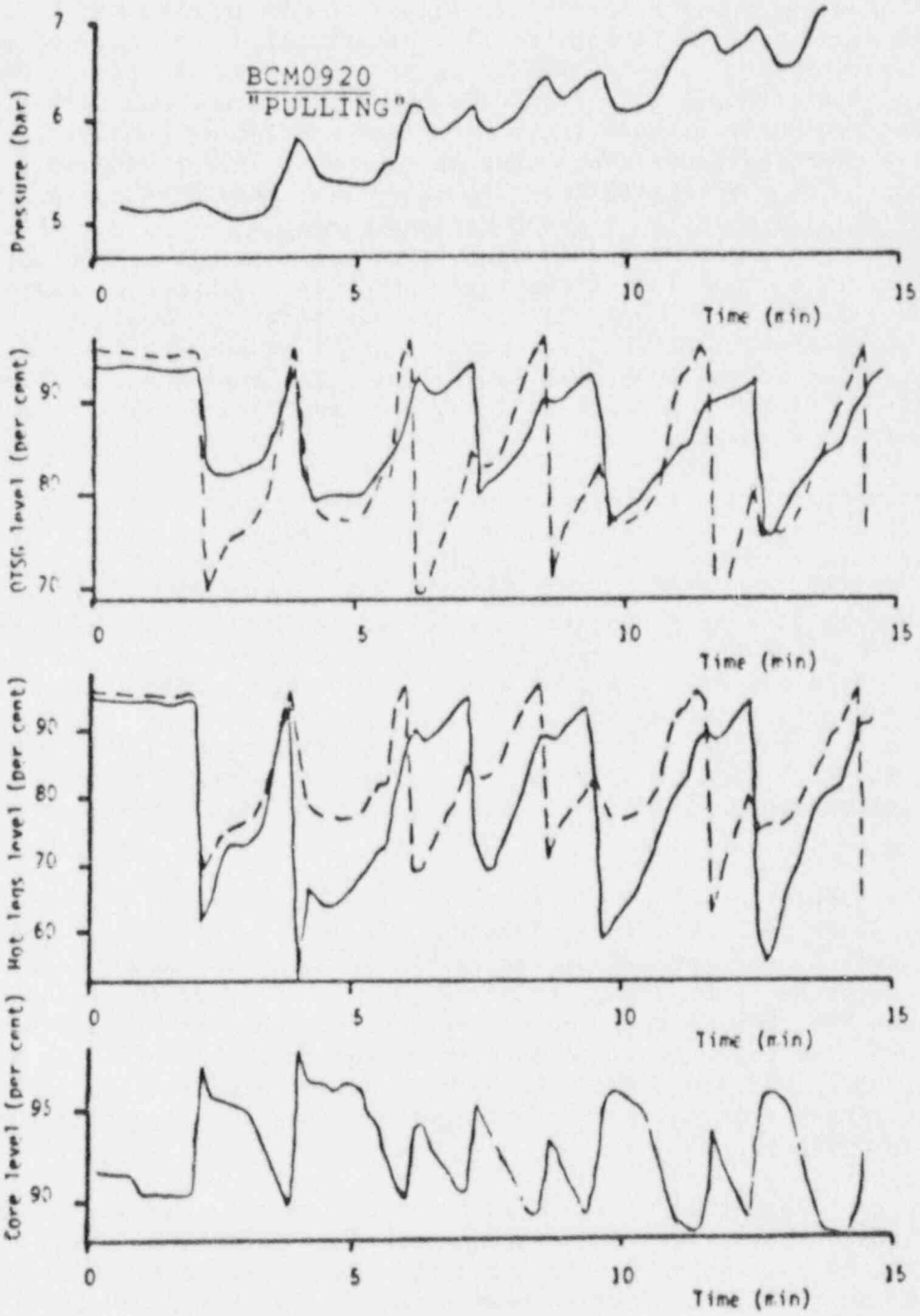

Figure 4: "Condensation Pull." Notice the Change of Level at 4 sec.

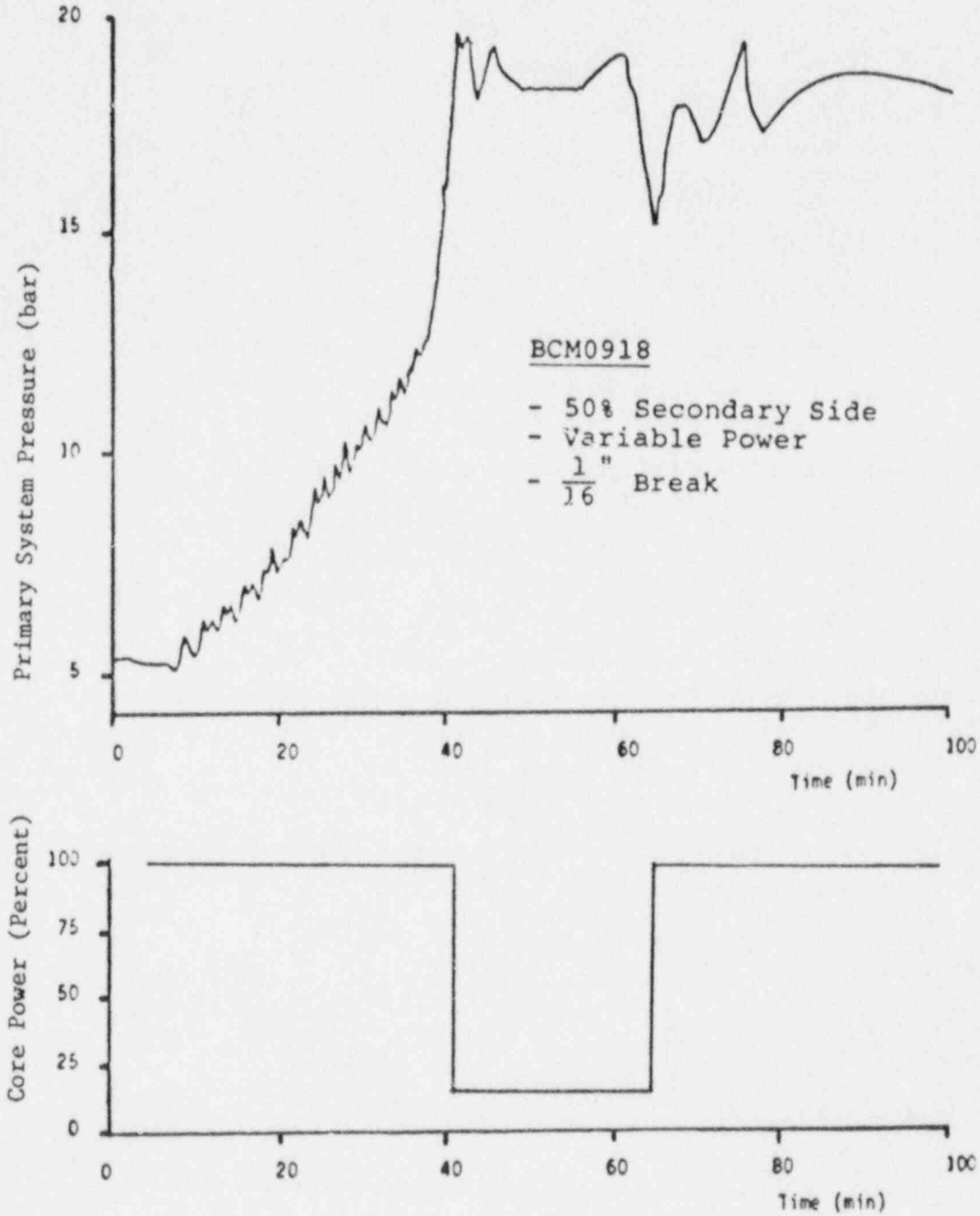

Figure 5: Relieve of Pressure but Reduction of Power during Flow Interruption

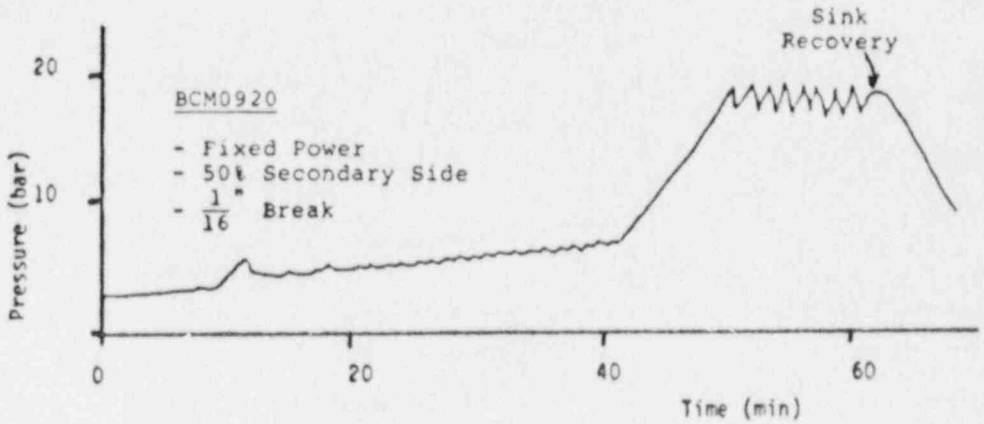

Figure 6: Two-Phase Natural Circulation (with PORV)

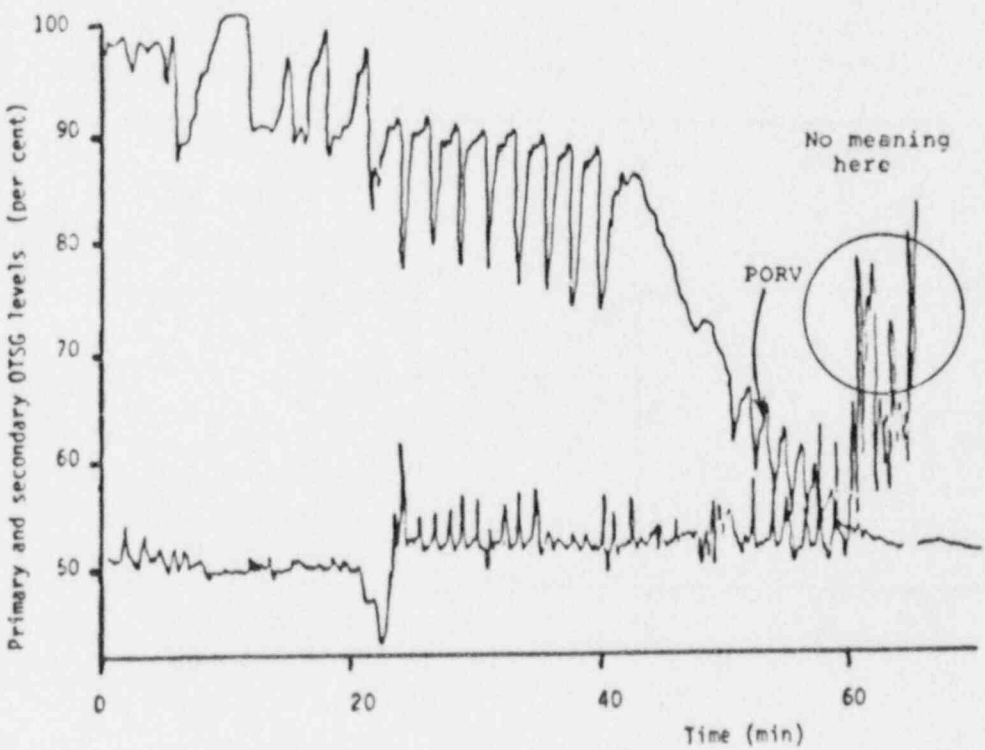

Figure 7: Resumption of Flow where the level in 1st and 2nd Sides of Steam Generator Meet

The test is terminated when heat transfer resumption is clearly achieved, or when liquid level indicates the impending danger of core uncovery.

3.3 Integral Test Series

In this series, the operation procedure is similar to that for the two-phase natural circulation, with the only difference being the initial conditions. The initial conditions were set at a pressure which was about 1.4 times of the vapor pressure of the temperature in the vessel. Such subcooling could be maintained by proper operation of heaters in the pressurizer. Once the desired steady-state initial conditions were reached, the break was initiated. The pressure curve (Fig. 8) shows the similar trends for the two-phase natural circulation, except a depressurization period preceded the two-phase region. Although the pressure levels for those runs were different, the essential similarity in phenomena indicates that the integral test can be synthesized by connecting the segments of thermal-hydraulic modes such as depressurization period and two-phase period.

4. Inventory Scaling

In Ref. 1, it was shown that the equation of state in the pressurizer can be scaled so that p/p_o can be expressed as a function of α/α_o, where subscript o indicates the condition. As shown in Fig. 9, the three runs for three different break sizes can all be collapsed into one line in term of $p/p_o = f(\alpha/\alpha_o)$, which each would be of different lines in terms of $p/p_o = f(t)$. The basic premise of scaling by equation of state is that during small break LOCA, the process is slow and thermal - equilibrium can be approached and thermodynamic states are of concern, while in Large Break LOCA, the process is very fast and the dynamics and thermal transport rates are of concern. From such consideration, thermodynamic equation of states can be used to scale the major parts of SB-LOCA process, considering only the energy and mass balances. This approach is much simpler than the conventional scaling approach based upon the matching of many dimensionless groups obtained from the coefficients of each terms in the basic field equations for momentum and energy transport (Ref. 2). Thus, if the thermodynamic scaling is correct, the pressure of the system can be correlated to the inventory of system as a first approximation and to the inventory of the pressure controlling component of system at each phase of the process, if a finer correlation is desired. If the inventory scaling is correct, the transient pressure histories for various runs can be plotted against corresponding inventory history so that p can be shown as a function of inventory. Since total loss of coolant through the break are readily calculated, p can also be plotted against cumulative loss of inventory from the break, which is equivalent to $V_{total} \cdot \alpha \cdot \rho_l$, or is an indication of α. Such plots are shown in Figs. 11 to 13. Notice that Fig. 10 is for two p-curves for the break flow rates. If p were plotted against time, they would be off in time scale by a factor of about 3-4, while in inventory scale, the sequence of events coincides in the same inventory frames (Fig. 11.)

If we take the inventory level at the point of transition between the various phases of events (from two-phase circulation, to intermittent flow, to flow interruption "frozen" state; to flow resumption, or BCM mode), the

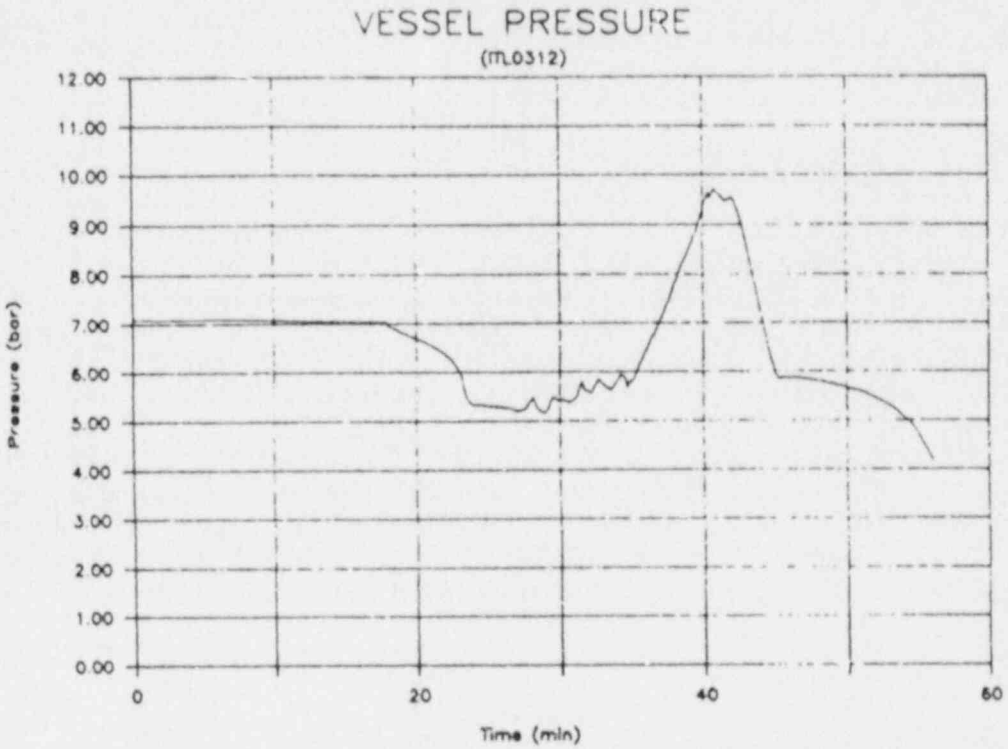

Figure 8: P(t) for Integral Test

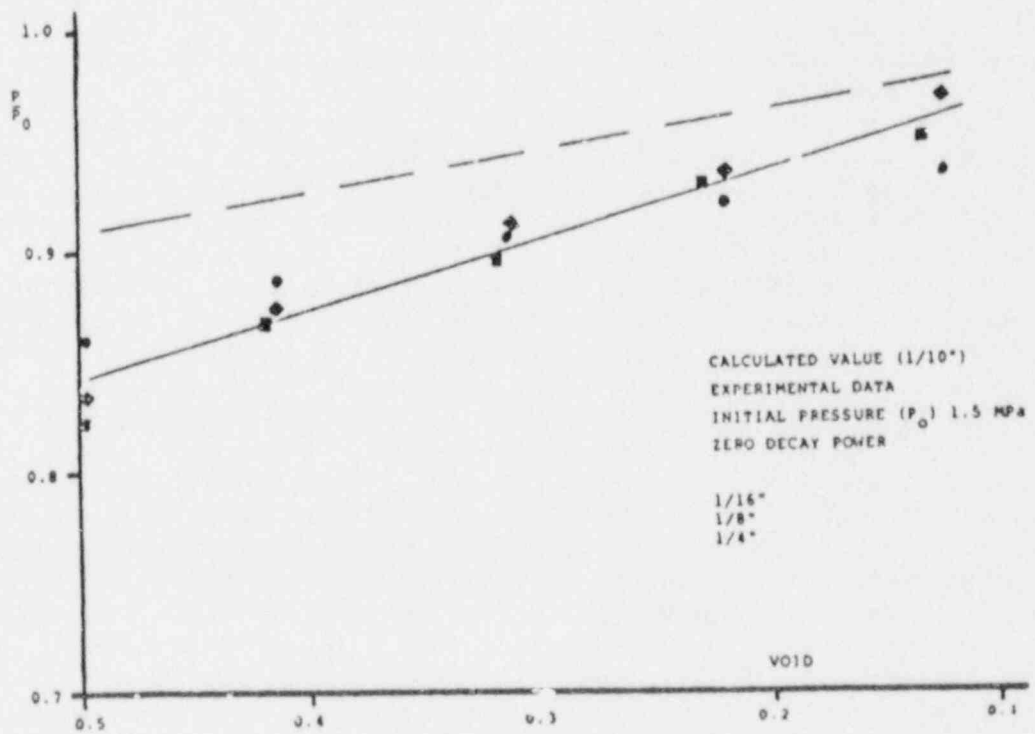

Figure 9: Pressure Ratio vs. Void

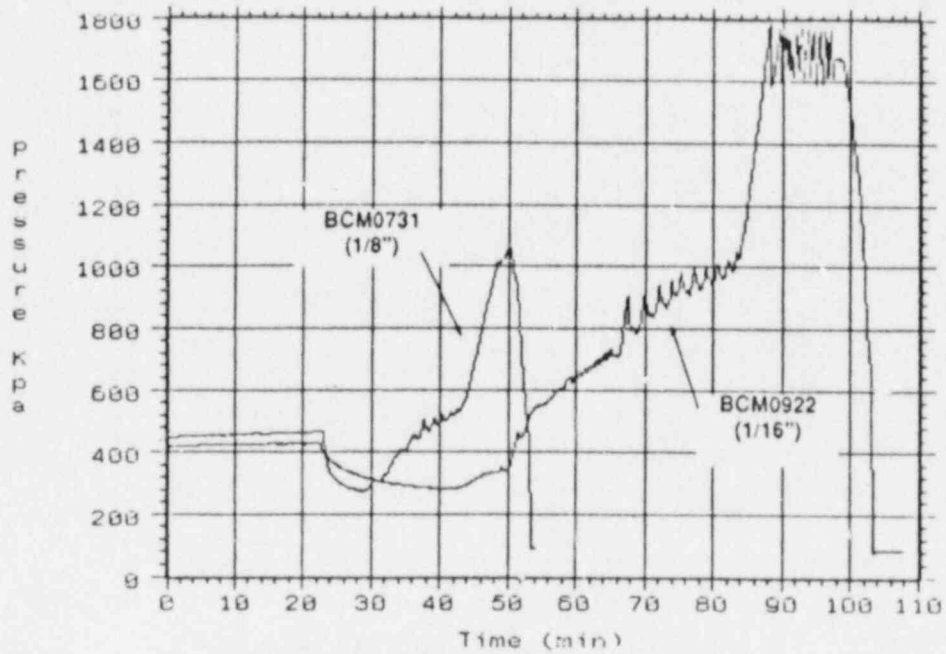

Figure 10: Pressure v.s. Time
(1/8" v.s. 1/16")

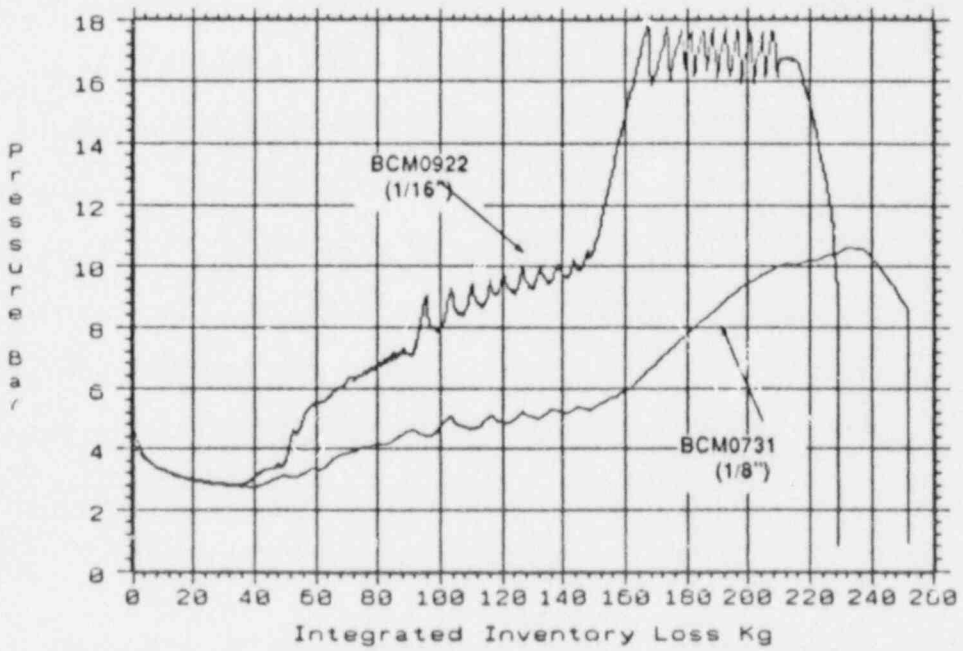

Figure 11: Pressure v.s. Integrated Inventory Loss
(1/8" v.s. 1/16")

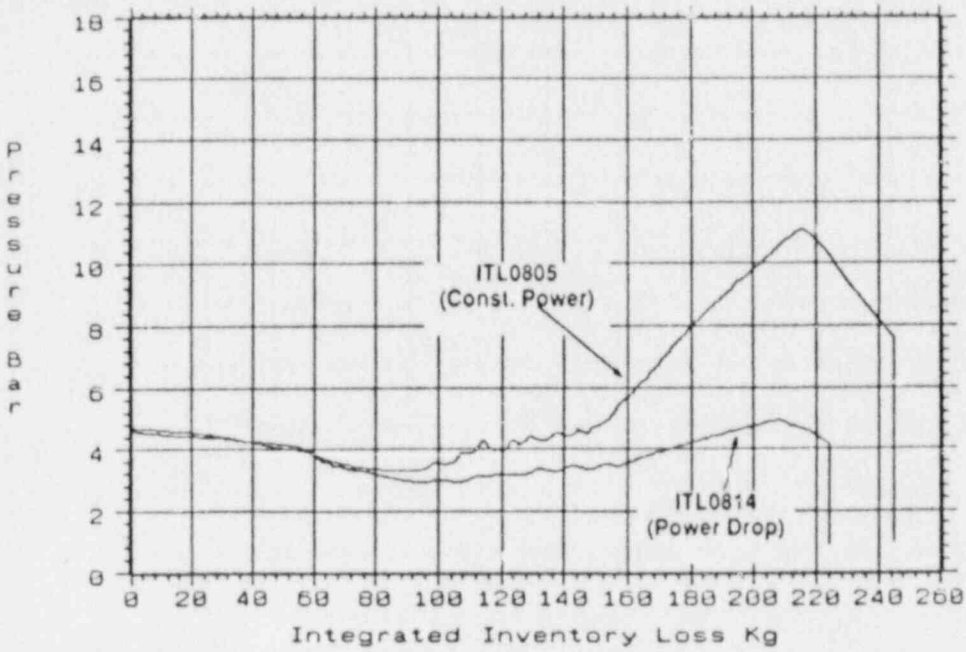

Figure 12: Pressure v.s. Integrated Inventory Loss
(Const. Power v.s. Reduced Power)

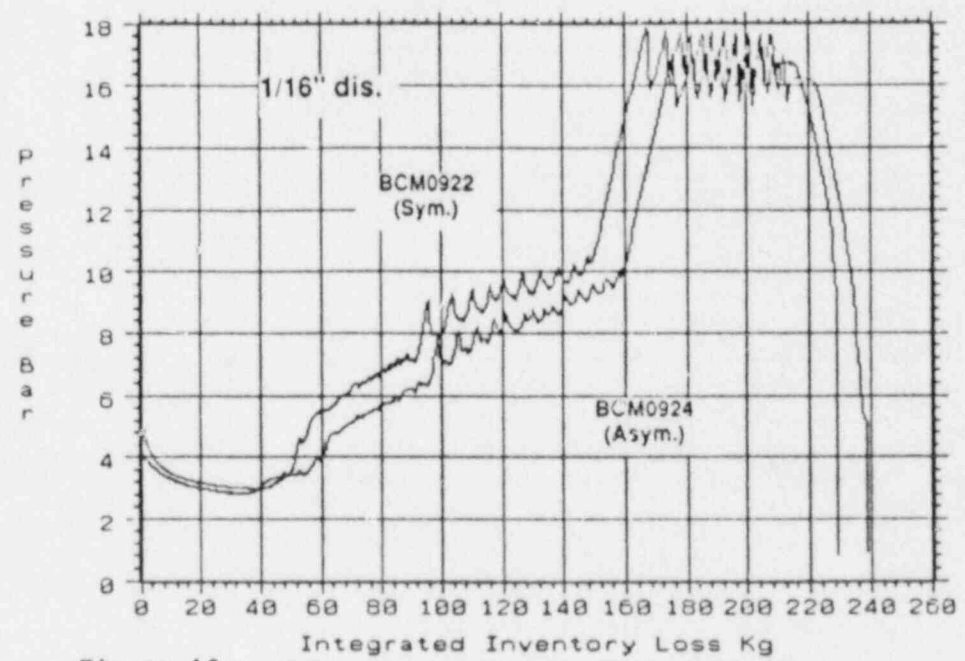

Figure 13: Pressure v.s. Integrated Inventory Loss
(Symmetric v.s. Asymmetric)

transition inventory for various events can be shown to be closely clustered (Fig. 14). From physical consideration, each event transition is controlled by the state of a specific component; as shown in the following table:

From:	to:	transition is controlled by
Natural Circulation	Intermittent Flow	level in the vessel
Intermittent Flow	Flow Interruption	level in the hot leg
Flow Interruption	Flow Resumption (or BCM)	matching of levels on primary and secondary sides in the steam generator

The specific transition inventories are plotted in Fig. 15. Thus from the above discussions, it can be concluded that the inventory scaling based upon thermodynamic state is a promising alternative to the conventional and more difficult hydrodynamic scaling.

5. Repeatability

5.1 Objectives of Repeatability Study

The reproducibility of experimental data is a longstanding, fundamental concern. Traditionally the experimenter seeks to achieve the minimum possible variance between successive experimental measurements. The inevitable interexperiment deviations are considered to be `errors´ which obscure the picture of reality as `it really is´. They should therefore be eliminated, or, failing that, at least minimized by precise control of initial and boundary conditions. For experimental data obtained from multi-loop thermal hydraulic test facilities this traditional view is inadequate. Such question is of fundamental concern to code assessment.

The first step in a code assessment process thus must quantify the reproducibility of the experimental data used in the verification. Note, that this issue has similarities but also that it is different from the important on-going subject of code-experiment comparisons. The later subject area is also not resolved to date, but it has received appreciable attention and its scope has been defined. Thus Boyack (Ref. 3) has proposed a systematic terminology which should make code-experiment comparisons at least qualitatively consistent. Two studies have appeared (Refs. 4,5) which attempt to quantify code-experiment comparison by statistical methods. In the noted studies the question of experimental reproducibility (or accuracy) was not addressed. The implicit assumption being made then is that the experimental uncertainty is small in comparison to the expected code-experiment differences. This assumption is probably correct for most cases where the experimental data is obtained from separate effect measurements which usually concentrate on single physical mechanisms with externally controlled boundary conditions. For experimental data obtained from integral multi-loop facilities this assumption has to be reexamined. In fact, it appears to be possible that for certain transients the experiment-to-experiment (rather than the code-to-experiment) deviation can be larger and will therefore set quantitative limits to the verification procedure. It will then also set the limits of precision for the mathematical models.

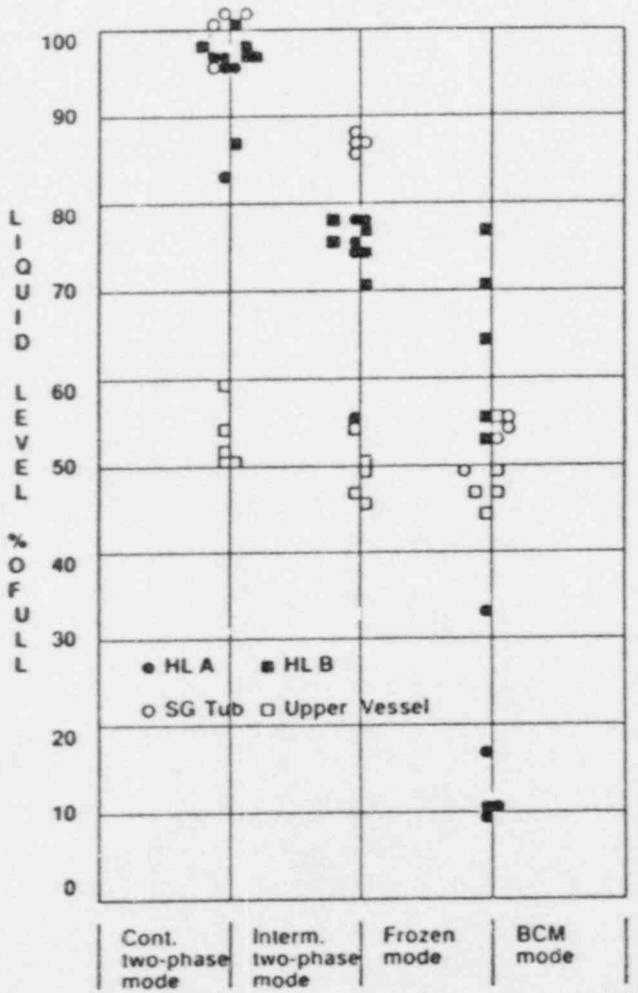

Figure 14: The Transition between Heat Removal Modes (Component Inventory v.s. Transition Point)

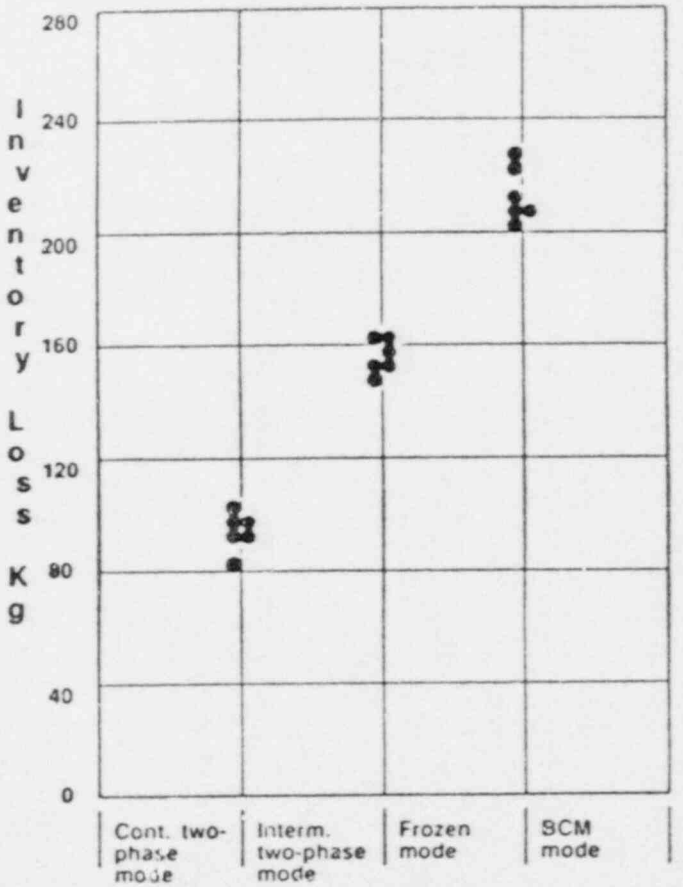

Figure 15: The Transition Between Heat Removal Modes (Integrated Inventory Loss v.s. Transition Point)

This study provides an overview and analysis of the variability of thermal-hydraulic phenomena observed in the U. of Md. 2x4 Loop (Refs. 1,6,7). Because of reasonably fast turnaround times of the facility, it has been possible to conduct a range of experiments. The number is still limited. However, for the first time a data base is being accumulated for integral multi-loop facilities which will allow, not just comparisons of specific repeat tests, but also broader generalizations. The observations reported in this study are lent further credence by qualitatively similar experimental phenomena reported by the SRI (Ref. 8) and MIST (Ref. 9) test facilities.

One of the features which complicates the analysis of test data variability for multi-loop thermal-hydraulic systems is that this variability can be generated by several qualitatively different phenomena. Therefore, before presentation and analysis of the test data, the nature of these potential phenomena is reviewed.

5.2 Causes of Variability in Multi-Loop Systems

An integral thermal-hydraulic multi-loop system differs from an open separate effect test facility in several important aspects. These distinctions can lead to qualitatively different behavior during tests which attempt to reproduce measurements. The differences encompass both steady-state and transient behavior. Let's consider steady-state first.

5.2.1 Existence of Alternative States.

For a range of source-sink conditions a multi-loop facility can be in alternate steady flow states. For example, consider the four cold legs of the U. of Md. facility. Any one of the cold legs or any combination of cold legs acting in concern can provide a complete path for coolant flow. Thus at least theoretically a total of 15 (i.e. 2^4-1) equivalent steady-state operations based on flow distribution in the cold legs flow are possible. The flow geometry in the core and downcomer and through the steam generator tubes also provides opportunities for less clearly defined multiple flow paths. It thus is apparent that theoretically the number of potential flow paths and thus the number of possible steady-states is very large.

Not all of the states are equally probable, furthermore the probability distribution of the states will change with core power, with sink configuration, and with prehistory (that is the path by which the steady-state is approached). For example, for the power levels at which the tests have been conducted so far no cases have occurred where all of the flows were carried by a single cold leg, though various two and three cold leg combinations have been observed. The probability of multi cold leg operation increases with power and at the maximum power level usually all four cold legs are active. Furthermore, once established, all flow states tend to become stabilized. This is the consequence of the loop seal geometry of the cold legs which stabilize with the accumulation of colder water. The existence of alternate flow paths within the core and downcomer is not verified as readily, though indirect evidence indicates that they are present.

From the point of view of steady state operation, the existence of multiple flow states does not have significant consequences. If they are indeed stable alternate states, this implies that their energy carrying capability is equivalent. The overall performance of the system therefore does not depend on which of the alternate state is active. However, this situation can change for the case of a transient which takes the system through a scenario of sequential events. The path (or `trajectory´) to be followed by the transient can potentially be influenced by a given alternate flow state.

5.2.2 Amplification of Phenomena

Another important characteristic of integral systems is that for certain conditions they are able to amplify (or dampen) imposed perturbations. To a degree `amplification´ has similarities with what is traditionally called parametric `sensitivity´. That is, some parameters like, for example, temperature in a two-phase system can produce larger consequences than others. In such cases perturbation of the `sensitive´ parameters must be controlled more tightly in order to achieve acceptable reproducibility between tests. This is true also for separate effects experiments, however, separate effect tests continuously control boundary conditions and this in turn keeps the amplification of phenomena produced by perturbation of sensitive parameters within finite bounds. This is not necessarily true for an integral facility. In an integral loop the state of the fluid in one component at time t becomes the boundary condition for the fluid in another component at time t+dt. Thus true amplification during which a local perturbation grows with time to encompass the entire system becomes possible. Such phenomena are observed whenever a two-phase stratified temperature condition develops. The temperature difference (at times of up to ~100 C) between the `hot´ partly vaporized upper regions and the `cold´ lower regions represents a large energy potential. If local turbulence succeed in transferring even small amounts of mass between the two temperature gradients, they can initiate condensation implosions which can effect the entire system.

Note that for a number of phenomena and perturbations the integral natured of the facility can also exert a dampening influence. As matter of fact, for an adequately designed natural circulation system damping effects predominate.

The perturbation amplification is even more dramatic if it coincides with the transition mechanism when a thermal-hydraulic process is about to enter a new phase and the transition is delayed or promoted.

5.2.3 Distribution of Deviations

The presence of alternate operational states in multi-loop thermal-hydraulic systems and the tendency of integral facilities to `amplify´ perturbations under some conditions influence test repeatability. If the noted physical mechanisms are not damped, a new type of test to test deviation will be present. Test repeatability can now be divided into two categories which are distinguished by the distribution of the experimental variations.

The two types of distribution are:

a. Gaussian
b. Bifurcation

The first category encompasses what could be called the `standard´ variations of experimental data. The causes of these variations are the inevitable imprecisions of initial and boundary conditions which are coupled with the imprecision of measuring instruments. If all of these imprecisions can be assumed to be random, then the measurements of repeat experiments will have a Gaussian distribution about some statistical mean. The task seeking to quantify a lower limit for the code-experiment agreement margin would then be reduced to the determination of standard deviations of such distributions. An example of repeat tests which appear to fit this category is shown in Figs. 16 and 17.

The second category of deviations to be considered is less familiar. They arise when the trajectory of a transient is deflected into an alternate path. This can happen if the transient scenario passes through an operating region where alternate states are possible or through operation conditions which can amplify small perturbations. In either case it is possible that a new trajectory completely outside the expected margin of two standard deviations is generated. An example of two duplicate tests which follow qualitatively different paths is given in Figs. 18 and 19.

The definitions noted above are made primarily for classification purposes. Actually in multi-loop thermal-hydraulic facilities usually both deviation causing mechanisms (random errors and bifurcations) are present. The circumstance that at time very similar test trajectories for duplicate experiments are obtained is due to the strong `damping´ mechanism that characterizes most operating regimes of an integral facility.

6. Conclusion

Based upon the results of tests obtained from UMCP 2x4 Loop the following conclusions can be drawn:

6.1 For Parametric Effects

6.1.1 One-phase natural circulation - The flow distributions between the primary loops are only weakly dependent upon the unbalance of loads or the secondary-side; but only become significant when loads were almost completely tilted to one loop.

6.1.2 Two-phase natural circulation, including BCM, exhibits consistent behavior for various conditions. The sequence of events are the same and the transitions between events seemed to be mostly controlled by inventory.

6.1.3 Integral test - The scenario of integral test can be synthesized by combining the segments of thermal-hydraulic modes observed in one-phase and two-phase natural circulations.

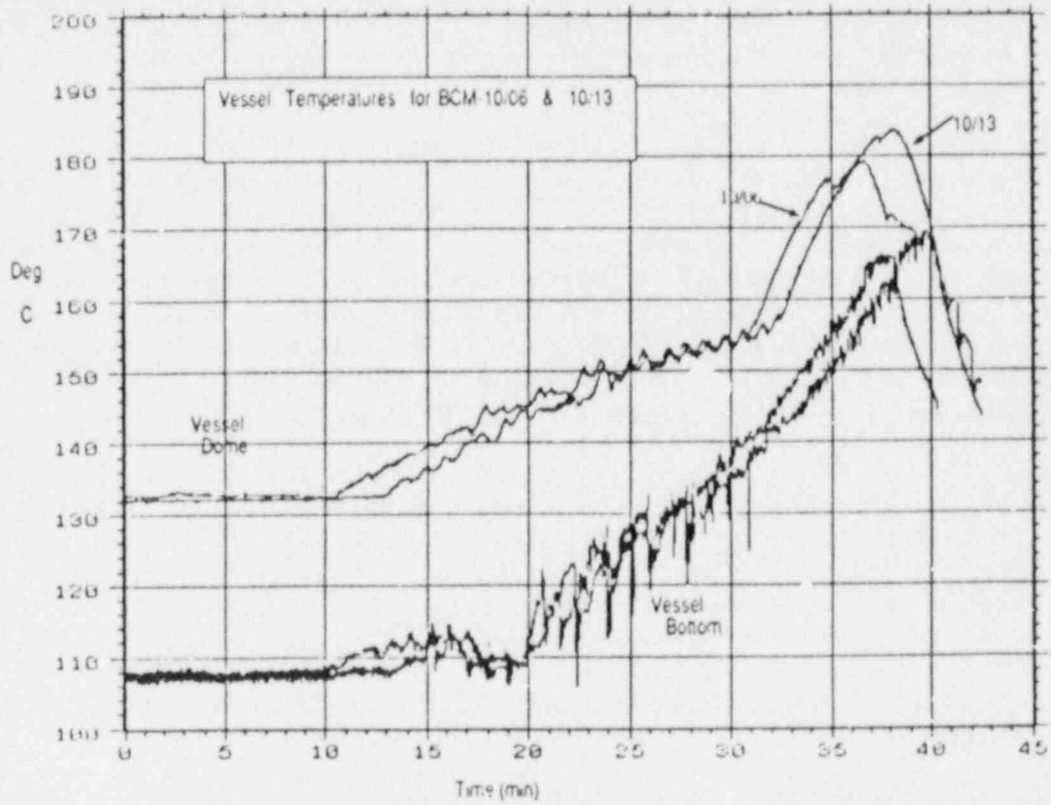

Figure 16: Repeated Runs (Gaussian Type)

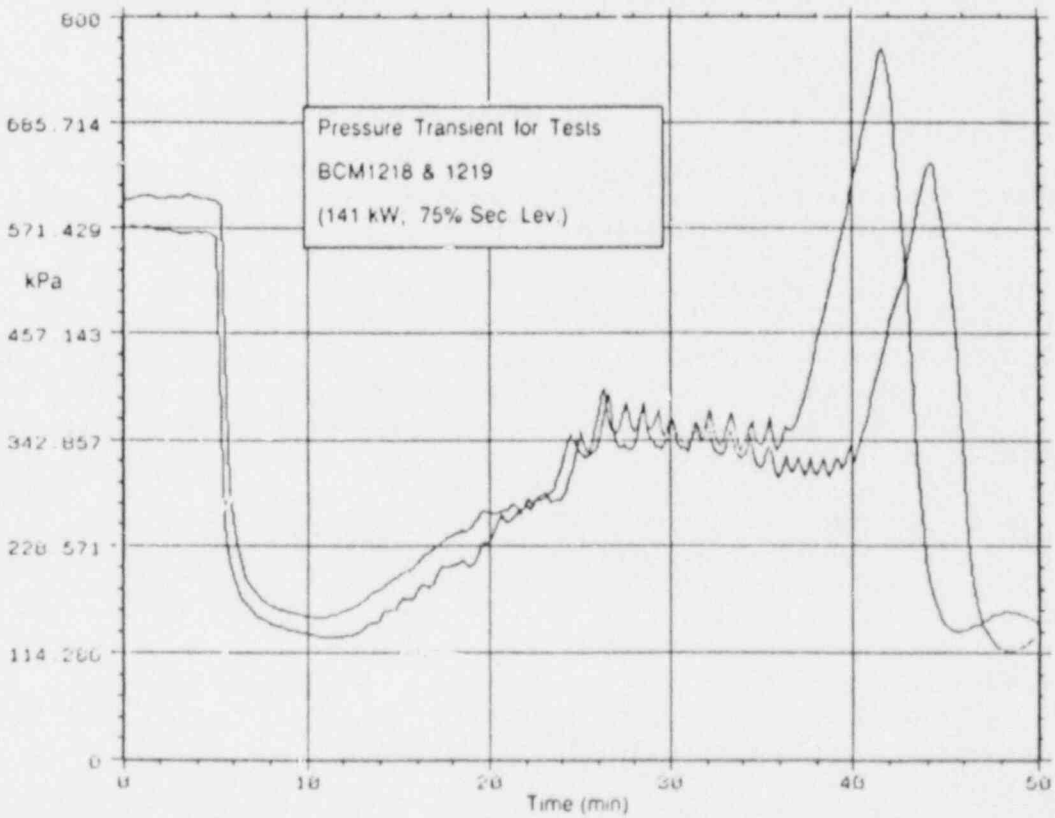

Figure 17: Repeated Runs (Gaussian Type)

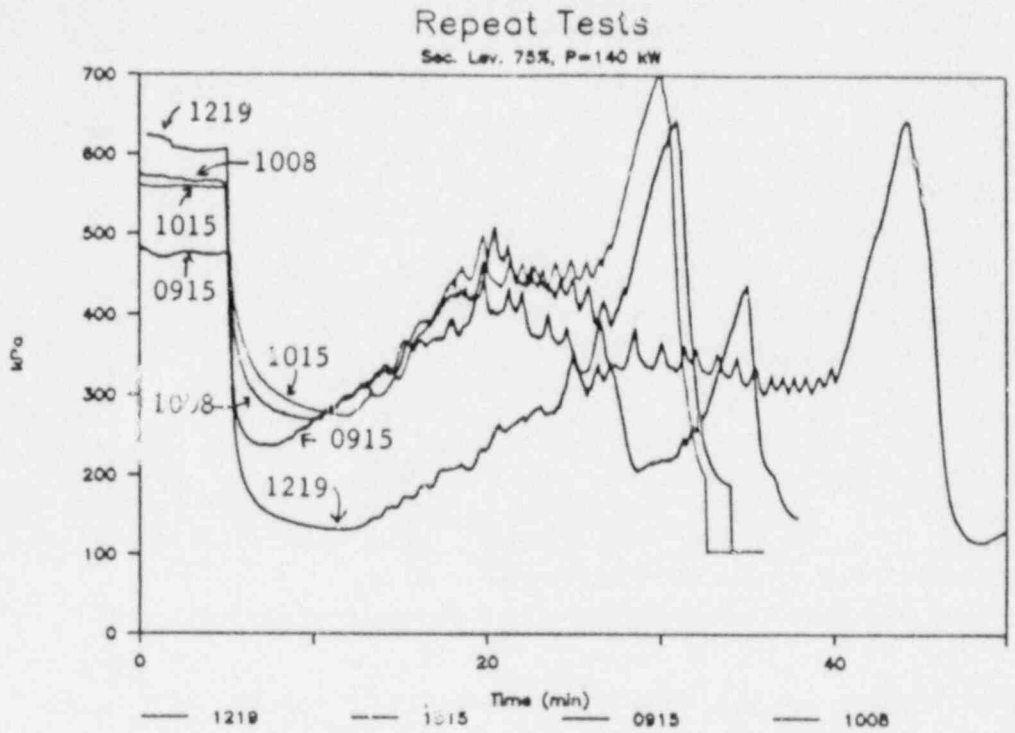

Figure 18: Repeated Runs (Bifurcation Type)

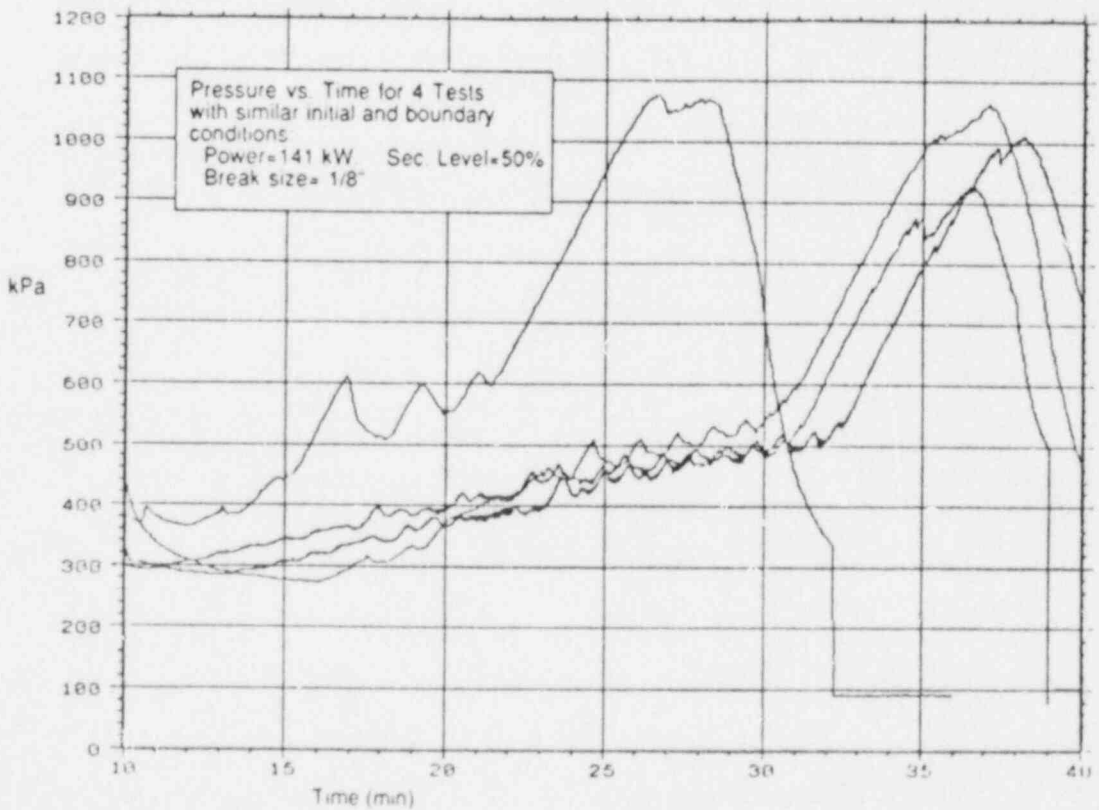

Figure 19: Repeated Runs (Bifurcation Type)

6.2 Inventory Scaling

The inventory scale shows as a promising alternative to time scale. The major events can be plotted on a global inventory scale, with transition between modes be more finely correlated to the inventory of the respective dominating components.

6.3 Repeatability

The loop provides a vehicle to carry out many repeated runs with the same initial conditions. The test results show that although many runs can be clustered together in Gaussian type distribution, there are occasional "out-layers", which are quite dissimilar to the other clustered runs. These runs should also be considered as legitimate data, and were due to the amplification of some small unaccounted disturbance which were propagated due to the feed-back mechanism of the loop. Such type of runs can be call "bifurcation" runs. Both types of runs can provide a realistic data base for the code assessor for comparison against codes.

References

[1] Di Marzo, M., Y.Y. Hsu, W.K. Lin, M. Massoud, C.J. Munno, F.J. Munno, G.A. Pertmer, M. Popp, D.W. Sallet, Z.Y. Wang, "UMCP 2x4 Loop Test Facility - Annual Report," NUREG/CR-4843 (1986)

[2] Ishii, M., Kataoka, I., "Similarity Analysis Scaling Criteria for LWR's under Single-Phase & Two-Phase Natural Circulation," US NRC May 1983. NUREG/CR3267

[3] Boyack, B. "Descriptors for Characterizing Agreement between Test and TRAC Results," given in `Compendium of ECCS Research for Realistic LOCA Analysis' Fig. 4-58. NUREG-1230 (April 1987)

[4] Kmetyk L. N., M.G. Elrick, R.K. Byers and L. d. Buxton, "Independent Code Assessment: Sandia - Proposed Accuracy Quantification Methodology," NUREG/CR-3969 (Aug. 1986)

[5] Hanson, R.G., C.L. Atwood, J.J. Eiverson, G.E. Wilson and N.D. Cox, "Development and Testing of Methods to Characterize the Uncertainty of Computer Codes," NUREG/CR-3006 (Feb. 1986)

[6] Almenas, K., M. Di Marzo, Y.Y. Hsu, M. Massoud, S.L. Shieh, Z.Y. Wang, C.J. Munno, H. Hper G.A. Pertmer, "One- and Two-Phase Natural Circulation in Multi-Loop Systems," Proc. of 14th Reactor Safety Research Information Meeting NUREG/CP-0082 Vol. 4, pp 133-149, NBS-Gaithersburg, Md., 1986

[7] Di Marzo, M., K. Almenas, Y.Y. Hsu, Z. Wang, "Thermal Hydraulics in a Complex Loop Subjected to Liquid Inventory Depletion." Submitted to Nuclear Science and Engineering

[8] Gloudemans, J.R., "MIST Highlights" ACRS ECCS Subcommittee Meeting (June 18, 1987)

[9] Sursock, J., "SRI-2 Integral Test Project" Presentation to ACRS (June 16-18, 1987)

LOBI-MOD2 Small Break LOCA and Special Transients Experimental Programme - Status and Future Plans

L. Piplies, C. Addabbo

Commission of the European Communities
Joint Research Centre, Ispra Establishment
I-21020 Ispra, Italy

ABSTRACT

The LOBI-MOD2 experimental programme is outlined with emphasis on specific programme objectives, significant achievements and future plans. The general structure of and the framework in which the research programme is carried out are firstly described. The status of the experimental programme and short term plans are then presented; within this context the methodology underlying the establishment of the LOCA and Special Transients Test Matrices is discussed. Finally, system code assessment and improvement activities which complement the experimental programme are briefly highlighted.

INTRODUCTION

The LOBI-MOD2 (LWR Off-normal Behaviour Investigations) experimental programme represents an important contribution to the Light Water Reactor (LWR) Safety Research Programme of the Commission of the European Communities (CEC). It is being conducted in the Ispra Establishment of the Joint Research Centre (JRC) and its primary objective is to provide experimental data for the assessment of system codes used in the LWR safety analysis. Within this context, experiments are conducted in a 2-loop, 1/700 scaled high pressure integral system test facility for a range of conditions relevant to small break Loss-Of-Coolant Accident (LOCA) and Special Transients in Pressurized Water Reactors (PWRs).

Originally, the research programme was mainly conceived for the parametric investigation of large break LOCAs in PWRs with emphasis on the performance of the Emergency-Core-Cooling Systems (ECCS). As the perception of priorities in water reactor safety changed early in 1980, the programme was redirected towards the investigation of small break LOCA and Special Transients phenomenology requiring the modification of the test facility from the MOD1 to the present MOD2 configuration.

The LOBI-MOD1 test facility was operated until June 1982; 25 LOCA experiments were performed covering the large to intermediate break size spectrum. In addition, 3 small break LOCA scoping tests were performed to assess the adequacy of the MOD1 configuration in representing the governing physical phenomena for this class of accidents. The LOBI-MOD2 test facility which incorporates extensive modifications with respect to the MOD1 configuration, became operational in April 1984. To date, 23 experiments have been performed. They comprise 14 small break LOCA tests, 5 Special Transients tests, 1 natural circulation test and 3 steam generators secondary side performance and characterization tests.

The general structure of the overall research programme and the international context in which is carried out, provide the basis for a close collaboration among the various European Community Member Countries. Such a collaboration which is formalized in the LOBI Working Group B (WG-B) and in the LOCA and Transients Programme Task Forces (LPTF and TPTF), encompasses the elaboration of the experimental programme, the definition of test profiles and pre- as well as post-test analysis with large system codes.

The experimental programme is complemented by a comprehensive code assessment and improvement programme. RELAP5/MOD1-EUR and RELAP5/MOD2 are currently being used within the LOBI Project as main analytical tools; CATHARE, DRUFAN, ATHLET, TRAC and RETRAN are being used by outside organisations for test design and prediction calculations.

THE LOBI-MOD2 TEST FACILITY

The LOBI-MOD2 test facility / 1 / is a high pressure, full power integral system test facility representing an approximately 1 : 700 scale model of a 4-loop, 1300 MWe PWR, Fig. 1. It has two primary loops, the intact or triple loop representing three loops and the single or broken loop representing one loop of the reference PWR. Each primary loop contains a main coolant circulation pump (MCP) and a steam generator (SG). The simulated core consists of an electricly heated 64 rod bundle arranged in an 8 x 8 square matrix inside the pressure vessel model; nominal heating power is 5.3 MW. Lower plenum, upper plenum, an annular downcomer and an externally mounted upper head simulator are additional major components of the reactor model assembly. The primary cooling system operates at normal PWR conditions: approximately 158 bar and 294 - 326 °C pressure and temperatures, respectively.

Heat is removed from the primary loops by the secondary cooling circuit containing a condenser and a cooler, the main feedwater pump, and the auxiliary feedwater system. The normal operating conditions of the secondary cooling circuit are 210 °C feedwater temperature and 64.5 bar pressure. The secondary cooling circuit is, however, designed for pressure and temperature of up to 100 bar and 310 °C, respectively.

The measurement system currently consists of a total of about 700 measurement channel. It allows the measurement of all relevant thermo-hydraulic quantities at the boundaries (inlet and outlet) of each individual loop component and within the reactor pressure vessel model and steam generators.

The whole LOBI-MOD2 test facility and individual components were scaled to preserve, insofar as possible or practical, similarity of thermo-hydraulic behaviour with respect to the reference plant during normal and off-normal conditions. A process control system allows the simulation of both the reactor pump hydraulic behaviour and the thermal behaviour of an equivalent fuel rod bundle.

THE LOBI-MOD2 EXPERIMENTAL PROGRAMME

The LOBI-MOD2 experimental programme is basically oriented towards the generation of experimental data to support the development of analytical models and the assessment of large system codes used in water reactor safety analysis. The experimental programme comprises the A-Test Matrix which is being performed in the framework of a R&D contract between the Bundesminister für Forschung und Technologie (BMFT) of the Federal Republic of Germany and the Commission of the European Communities and the small break LOCA and the Special Transients test matrices of the Community- or B-Programme. A summary review on the status of the overall experimental programme is given in Table 1.

A-Programme:

The LOBI-MOD2 A-Programme Test Matrix consists of a total of 15 tests of which 11 have been already performed. It includes small break LOCA tests covering a range of test conditions of interest to PWR of German design. In the test matrix is included also a loss of offsite and normal onsite electrical power ATWS (LONOP-ATWS) event and performance/-characterization tests. A number of tests are defined as counterpart or complementary tests to the Kraftwerk Union Primärkreislauf III (PKL-III) test facility.

B-Programme:

As previously mentioned, the B-Programme is the result of an international cooperation in the field of water reactor safety reseach. Within this framework, a small break LOCA and a Special Transients test matrix have been established by experts of the member states assembled in the LOCA and Transients Programme Task Forces which are sub-units of the Research Programme Working Group B, a consultative body of the JRC Directorate.

The terms of reference of the Task Forces is to elaborate and propose to the Working Group B an experimental programme on PWR LOCA and anticipated as well as abnormal transients which could be performed with the LOBI-MOD2 test facility. The mandate also includes to advise, taking into account theoretical needs and safety concerns, on test priorities and to allocate for each test a Partner Country (PC): that is, an EC member state organisation having the task to collaborate, on behalf of all participating countries, with the LOBI staff in the detailed test specification as well as in the pre- and post-test analysis of the results with large system codes.

The methodology used in the definition of each test case and in the establishment of the corresponding test profile, is to reproduce governing physical phenomena rather than test reference plant specific conditions. To this end, a common set of test initial and boundary conditions is agreed upon taking into account differences in the design of PWRs of current interest to the participating EC member states. The ultimate goal is to establish for each test case a common profile which would allow the investigation of the relevant phenomena and eventual parametric studies in variant tests.

The LOBI-MOD2 small break LOCA B-Test Matrix at present contains 32 test cases which cover a wide range of parametric variations. The break size spectrum ranges from 0.4 % to 25 % including the Steam Generator Tube Rupture (SGTR) scenario. Other major parametric variations include the break location, the configuration and setpoints of the engineered safety systems, the operation of the main coolant pumps and the cooldown rate of the secondary system; 5 small break LOCA tests of the B-Matrix have been so far performed.

The LOBI-MOD2 Special Transients B-Test Matrix comprises at present 15 test cases spanning a variety of anticipated and abnormal PWR conditions caused by intact circuit faults such as loss of main and/or auxiliary feedwater, station blackout, steam line break and feedline break events. Accident mitigation and recovery procedures are generally considered in the definition of the transient profile; 5 Special Transients tests of the B-Matrix have been so far performed.

Performance and characterization tests are integral part of the overall experimental programme. They include steam generator performance and secondary side mass inventory tests as well as primary and secondary system heat loss tests. The general objective is to reduce uncertainties in predicted results which may originate from potential plant state modelling inaccuracies.

COUNTERPART TEST PROGRAMME

System codes adopted in LWR safety analysis are generally developed and assessed on the basis of experimental data acquired in scaled test facilities. To verify the scalability of such codes to full-size plants, JRC-Ispra is advocating the establishment of a data base in which scaling is the main parametric variation. To this end, JRC-Ispra is in favour of a counterpart test programme to be carried out among the differently volume-scaled LOBI-MOD2 (1 : 700), SPES (1 : 425) and BETHSY (1 : 100) test facilities. Perceived practical consideration have suggested to use the above test facilities in the feasibility assessment of such a test programme which could, however, be expanded to the Japanese LSTF (1 : 50) and, where appropriate, to the German PKL III (1 : 145) test facility.

The ultimate objective of such a programme is to contribute to the quantification of the expected predictive accuracy of system code calculation for full-size PWRs. In this framework proper strategies for counterpart testing in integral loop systems should be applied, see / 2, 3 /.

CODE ASSESSMENT

RELAP5/MOD1 and RELAP5/MOD2 converted into an IBM compatible form are the main analytical tools used within the LOBI Project for test design as well as for pre- and post-test prediction calculations / 4 /. RELAP5/MOD1-EUR, the JRC-Ispra version of the original Idaho National Engineering Laboratory (INEL) version, includes several model improvements with respect to the latter.

JRC-Ispra, on behalf of the Commission of the European Communities is promoting the participation of EC member state national organisations in system code assessment. This activity is carried out within the Shared Cost Action Programme in the form of research contracts between the Commission and national laboratories or organisations of EC member states. The Commission funding of these contracts amounts to about

50 %. This activity is devoted in particular to the assessment of CATHARE, DRUFAN and RELAP5/MOD2 with LOBI-MOD1 and LOBI-MOD2 experimental data. The organisations participating in this activity and the test matrix are given in Table 2.

Extensive use of LOBI data is made in the code assessment test matrices of the OECD-CNSI (Organisation for Economic Cooperation and Development - Committee on the Safety of Nuclear Installations) and USNRC-ICAP (International Code Assessment Programme).

PLANS

Short term plans are focussed on the execution of already defined tests as shown in the provisional '88 test matrix, Table 3. Tests of proven relevance to system code assessment have been already identified for inclusion in the '89-90 experimental programme; test priorities and test partner countries are, however, not yet finally allocated.

The use of the LOBI-MOD2 test facility for the systematic validation/-verification of PWR accident management strategies is being assessed; also, the potential use of the MOD2 configuration for the investigation of advanced light water reactor safety problems is under consideration.

Assessment and improvement of RELAP5/MOD1-EUR and RELAP5/MOD2 will be a continuing activity in support of the experimental programme and as part of the USNRC ICAP Programme.

The IBM version of the RELAP5/MOD2 code will be maintained. Development work on a Plant Analyser System and on methodologies for diagnostic/prognostic systems will be pursued.

Considerable effort will be devoted to the maintenance of the measurement system, to the improvement of existing measurement techniques and to the development of new ones, especially in two-phase flow regimes.

CONCLUSIONS

Small Break LOCA tests and Special Transients are being performed in the LOBI-MOD2 test facility. Testing strategy is focussed on governing physical phenomena of relevance to code development and assessment rather than on reproducing full-size plant specific conditions.

As structured, the LOBI overall research programme represents a effective approach to international collaboration in the field of reactor safety research and development. Such a collaboration provides also the opportunity for the exchange of national views and expertise among the participating delegations of the European Community member states.

The experimental programme is complemented by an extensive code application and improvement programme. Within this context the LOBI-Project intends to provide a relevant contribution to the international effort in system code assessment.

REFERENCE

/ 1 / C. Addabbo, L. Piplies, W. L. Riebold:
"LOBI-MOD2: Geometrical Configuration of the Test Facility"
Com. No. 4010, CEC-JRC, July 1983

/ 2 / H. Karwat:
"Elaboration of a Guideline for Counterpart Testing of Integral Loop Systems", Final Report on Study Contract between the Commission of the European Communities and TU-München, EUR 6540 EN, 1987

/ 3 / N. Zuber:
"Code Scaling, Applicability and Uncertainty Evaluation Methodology", Meeting of the CSNI PWG-2 Task Group on Codes, Paris, June 1 - 3, 1987

/ 4 / H. Städtke, W. Kolar:
"JRC Ispra Results from Assessment of RELAP5/MOD2 on the Basis of LOBI Test Data", 15th USNRC Water Reactor Safety Information Meeting, October 26 - 29, 1987, Gaithersburg, MD/USA

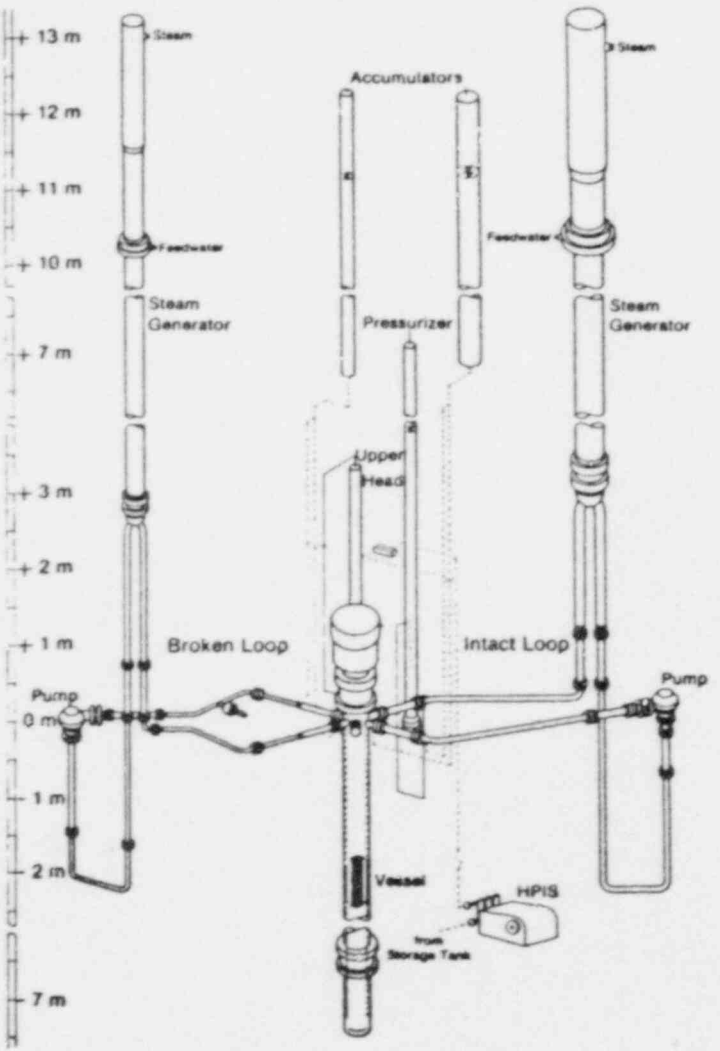

System	loops	2 (1 :3)
Volume	total - m^3	0.6
	scale reduction	700
Core	power - MWth	5.28
	length - m	3.9
	no. rods	64
	matrix	8 x 8
	heating	electrical
Downcomer	configuration	annular
	gap width -mm	12
SGs	type	U - tube
	no. tubes: 1-loop	8
	3-loop	24
MCPs	type	centrifugal
	n_q	29.2
Operation	pressure - MPa	15.8
	temperature - C	294/326
Organisation		CEC - JRC
Place		Ispra (Italy)

Fig. 1: The LOBI-MOD2 Test Facility and Main Characteristics

Table 1: LOBI-MOD2 EXPERIMENTAL PROGRAMME

Test Matrix for 1984 - 1987 (Status: October 1987)

Test Date	Definition	Partner Country	Test Design/ Prediction Calculations	Phenomenology
A1-76 12.04.84	SG Performance at 100 %, 50 % and 10 % power	Germany BMFT (GRS)	DRUFAN RELAP5/MOD1-EUR	Separator efficiency at high SCS inventory SG heat transfer degradation at low SCS inventory
A2-81 27.09.84	1 % CL break LOCA 2 x 4 HPIS into CL Accu off 100 K/h SCS cooldown	Germany BMFT (GRS) ISP-18	ATHENA CATHARE DRUFAN-MOD2(3) FRACAS NOTRUMP RELAP4/MOD6(2) RELAP5/MOD1(10) RELAP5/MOD2(4) TRAC-PF1(3)	Primary system depressurization governed by secondary system cooldown rate 2 Ø natural circulation and reflux condenser heat transport No core uncovery and no loop seal clearout
A1-82 28.09.84	1 % CL break LOCA 2 x 4 HPIS into HL Accu off 100 K/h SCS cooldown	Germany BMFT (GRS)	DRUFAN RELAP5/MOD1-EUR	Counterpart to test A2-81 with respect to HPIS connection Primary and secondary system strongly coupled Reduced ECC bypass and mitigation of subcooling in the vessel downcomer No core uncovery and no loop seal clearout
A1-78 24.10.84	2 % CL break LOCA 2 x 4 HPIS into HL ACCU on at 27 bar 100 K/h SCS cooldown	Germany BMFT (GRS)	DRUFAN RELAP5/MOD1-EUR	Primary system depressurization decoupled from secondary system cooldown Potential for reverse SG heat transfer Voiding in SG U-tubes No core uncovery and no loop seal clearout
A2-77A 28.11.84	Natural circulation and reflux condenser at 90 and 75 bar Power 3.5 %	Germany BMFT (GRS) (90 bar) France CEA (75 bar)	DRUFAN	1 Ø - 2 Ø Natural circulation and reflux condenser heat transport modes characterized as function of primary system mass inventory and secondary system pressure
A1-83 14.12.84	10 % CL break LOCA 2 x 4 HPIS into HL Accu on at 27 bar 100 K/h SCS cooldown	Germany BMFT (GRS)	DRUFAN RELAP5/MOD1-EUR	Primary system depressurization decoupled from secondary system cooldown Early voiding of SG U-tubes and vessel uppermost elevations Initial core dryout-rewet controlled by loop seal formation and clearout Second core dryout-rewet controlled by boiloff and accumulator ECC injection

Table 1: cont.d

Test Date	Definition	Partner Country	Test Design/ Prediction Calculations	Phenomenology
A2-90 27.03.85	A2-90-1: LONOP-ATWS, Loss of offsite and normal-onsite electrical power - anticipated transient without SCRAM	Germany BMFT (GRS-KWU)	ALMOD4 RELAP5/MOD1-EUR	Pressure increase and fluid discharge from primary and secondary system Pressurizer insurge-outsurge SG heat-transfer degradation
	A2-90-2: SG secondaries boiloff down to c. 1 m above tube plate		RELAP5/MOD1-EUR	Reestablishment of primary to secondary heat transfer and long term plant cool-down
	A2-90-3: SG secondaries refill and cooldown at a rate of 100 K/h		RELAP5/MOD1-EUR	Primary system 1 Ø, 2 Ø natural circulation
A1-85 07.05.85	0.4 % Pressurizer break 2 x 4 HPIS into HL Accu off 100 K/h SCS cooldown	Germany BMFT (GRS)	DRUFAN	Primary system depressurization coupled to secondary system cooldown Pressurizer insurge Primary system overfeed No core uncovery and no loop seal clearout
BL-00 03.07.85	0.4 % CL break LOCA 2 x 4 HPIS into CL Accu on at 41 bar 56 K/h SCS cooldown	France CEA	TRAC RELAP5/MOD1-EUR	SG heat transfer Fluid stratification Holdup in hot legs Primary system overfeed No core uncovery and no loop seal clearout Thermal non-equilibrium
A1-84 14.10.85	10 % HL break LOCA 2 x 4 HPIS into HL Accu on at 27 bar 100 K/h SCS cooldown	Germany BMFT (GRS)	DRUFAN	Primary system depressurization decoupled from secondary system cooldown Early voiding of SG U-tubes and vessel uppermost elevations No core uncovery and no loop seal clearout
BT-00 30.11.85	BT-00-1: LOFW, Loss of main feedwater SCRAM on low SG level	England CEGB	RETRAN RELAP5/MOD1-EUR	Primary and secondary system pressure increase pressurizer insurge-outsurge SG heat transfer degradation and loss of heat sink Primary system cooldown PORV discharge HPIS inflow and primary system inventory recovery
	BT-00-2: LOAF, Loss of auxiliary feedwater			
	BT-00-3: Bleed and feed of primary cooling system			

Table 1: cont.d

Test Date	Definition	Partner Country	Test Design/ Prediction Calculations	Phenomenology
BT-01 24.01.86	BT-01-1: SLB 10 % Steam line break Hot standby BT-01-2: PTS scenario MCP off, HPIS on BT-01-3: Mitigation of PTS consequences	Belgium TRACTEBEL	RELAP5/MOD1-EUR	Blowdown of affected SG Primary system cooldown Pressurizer behaviour Subcooling and thermal stratification in RPVM downcomer Recovery of adequate subcooling margin
BL-02 22.03.86	3 % CL break LOCA 2 x 4 HPIS into HL Accu on at 41 bar 56 K/h cooldown	England CEGB	RELAP5/MOD2 RELAP5/MOD1-EUR	Primary system depressurisation decoupled from secondary system cooldown Voiding in SG U-tubes and upper vessel internals Mixing of HPIS and Accu flow with main loop flow Condensation, non equilibrium at ECC injection points, no core uncovery Intact and broken loop seals clearout
A1-79 15.05.86	1 % CL break LOCA 4 x 4 HPIS into HL Accu off 100 K/h SCS cooldown	Germany BMFT (GRS)	DRUFAN	Overfeeding of primary cooling system Influence of HPIS capacity on fluid flow distribution No core uncovery and no loop seal clearout
A1-88 11.06.86	0.4 % CL break LOCA 2 x 4 HPIS into HL Accu off Asymmetric SCS cooldown: 100 K/h in intact loop 0 K/h in broken loop	Germany BMFT (GRS)	DRUFAN	Hydraulics Test Asymmetry in intact and broken loop behaviour Depressurization rate controlled by isolated SG
BL-01 20.09.86	5 % CL break LOCA 2 x 4 HPIS into HL Accu on at 27 bar 100 K/h SCS cooldown	Germany GRS-KWU	DRUFAN RELAP5/MOD1-EUR	Primary system depressurization decoupled from secondary system cooldown SG reverse heat transfer No core uncovery Intact loop seal clearout Holdup of fluid in the vessel upper internals
BC-01 18.10.86	SG Inventory Test	-	RELAP5/MOD1-EUR	SGs mass inventory and recirculation characteristics established as function of secondary system downcomer level
BC-02 26.11.86	SG Heat Loss Test	-	-	Characterization of SGs secondary side heat losses

Table 1: cont.d

Test Date	Definition	Partner Country	Test Design/ Prediction Calculations	Phenomenology
BL-21 24.01.87	BL-21-1: 0.4 % SGTR HPIS off BL-21-2: Accident Recovery Procedure	Italy ENEA-Univ.Pisa	RELAP5/MOD1-EUR	Primary to secondary mass and energy transfer Filling of affected SG Behaviour of isolated SG Core uncovery and dryout Primary system depressurization from top of pressurizer and ECC injection from Accu system
BL-12 19.02.87	1 % CL break LOCA HPIS off Accu on at 41 bar No SCS cooldown	France CEA	TRAC RELAP5/MOD1-EUR RELAP5/MOD2 DRUFAN	Core uncovery and dryout at high pressure Heater rod temperature excursion
BT-02 09.05.87	BT-01-1: LOAF, Loss of all feedwater BT-02-2: Primary system Feed and bleed	France CEA	TRAC	Primary and secondary system pressure increase Safety valves discharge SG heat transfer degradation Pressurizer insurge-outsurge Loss of heat sink Primary system cooldown
BT-12 17.06.87	100 % SLB Orifice limited Hot standby	England CEGB	RETRAN RELAP5/MOD1-EUR	Blowdown of affected SG Separator efficiency and carryover Reverse heat transfer in isolated SG Pressurizer outsurge Thermal asymmetry in primary cooling system
A1-91 26.09.87	1 % CL break LOCA 1 x 4 HPIS into HL Accu off 100 K/h SCS cooldown	Germany BMFT (GRS)	ATHLET RELAP5/MOD1-EUR	Influence of minimum HPIS capacity configuration on overall system response No core uncovery and no loop seal clearout
BT-03* xx.10.87	BT-03-1: LOFW-ATWS Loss of main feedwater - Anticipated transient without SCRAM BT-03-2: Accident recovery procedure	Italy ENEA-Univ.Pisa	FASTRAP RELAP5/MOD2	Pressure increase in primary and secondary system safety valves relief capacity Pressurizer insurge-outsurge SG heat transfer degradation Passive recovery procedure via depressurization from pressurizer and Accu injection
A1-92* xx.11.87	Natural circulation and reflux condenser at 40 bar	Germany BMFT (GRS-KWU)		Counterpart Test to PKL-III 2.1 Test

A - Tests from the German Matrix

BL - B-Programme LOCA tests

BT - B-Programme Transient tests

* scheduled for execution

Table 2: JRC-ISPRA CODE ASSESSMENT TEST MATRIX

Shared Cost Action Programme (1984 - 87)

Test	Definition	Organisation	Code
A1-76	SG Performance	GRS-Garching, D	DRUFAN
		Univ. of Pisa, I	RELAP5/MOD2, CATHARE
		Univ. of Bologna, I	RELAP5/MOD2
A2-81	1 % CL Break LOCA	GRS-Garching, D	DRUFAN
		Univ. of Pisa, I	RELAP4, RELAP5/MOD2
A2-77A	Natural Circulation and Reflux Condenser	GRS-Garching, D	DRUFAN
		CEN-Grenoble, F	CATHARE
		Univ. of Pisa, I	RELAP5/MOD2
A1-83	10 % CL Break LOCA	Univ. of Stuttgart, D	RELAP5/MOD1, RELAP5/MOD1-EUR, RELAP5/MOD2, DRUFAN
		Univ. of Pisa, I	CATHARE
A2-90	LONOP-ATWS	Univ. of Stuttgart, D	RELAP5/MOD2, DRUFAN
		Univ. of Rome, I	RELAP5/MOD1-EUR
BT-00	LOFW	Turin Polytecnic, I	RELAP5/MOD2
BT-01	SLB (10 %)	Univ. of Palermo, I	RELAP5/MOD1-EUR
BL-01	5 % CL Break LOCA	GRS-Garching, D	DRUFAN
B-101*	2 x 50 % CL Break LOCA	CEN-Grenoble, F	CATHARE
B-302*	2 x 50 % HL Break LOCA	CEN-Grenoble, F	CATHARE

* LOBI-MOD1 tests

Table 3: LOBI-MOD2 EXPERIMENTAL PROGRAMME:

Test Matrix for 1988 (Status: October 1987)

Test	Definition	Partner Country	Remarks
BL-16	0.4 % Cold Leg Break LOCA . asymmetric cooldown of SG secondary side with 100 K/h . delayed restart of MCP . HPIS on . Accu off	Germany GRS	To investigate pressurizing effect of isolated SG and depressurization after delayed restart of MCP
BL-22	0.4 % SGTR . initiation, no operator intervention . depressurization and . cooldown with operator intervention	Belgium TRACTEBEL	To represent as close as possible a real SGTR scenario and to qualify proposed plant recovery procedures
BT-04	Cooldown Transient with MCP on . asymmetric cooldwon with single loop SG isolated	France CEA	To investigate phenomenologies relevant to post accident (e.g. SGTR) recovery procedures
BT-05	Cooldown Transient with MCP off . asymmetric cooldown with single loop SG isolated	Germany GRS-KWU	as above
A1-87	Cooldown Transient with MCP off . natural circulation under saturated condition and with steam bubble in upper-head	Germany BMFT (GRS-KWU)	LOBI-PKL counterpart-complementary test; to complement PKL III 2.1 test results in the high pressure range (> 40 bar)
A1-93	SBLOCA test . HPIS off	Germany BMFT (GRS-KWU)	LOBI-PKL counterpart-complementary test; to verify scaling rationales adopted in PKL III SBLOCA tests
A1-94	0.4 % SBLOCA . HPIS off	Germany BMFT (GRS-KWU)	To verify Transient management procedures; effectiveness of secondary system cooldown for the mitigation of small SBLOCA consequences in absence of HPIS

BL - B-Programme LOCA tests

BT - B-Programme Transients tests

TRAC-PF1/MOD1 CALCULATIONS AND DATA COMPARISONS FOR MIST SMALL-BREAK LOSS-OF-COOLANT ACCIDENTS WITH SCALED 10 cm^2 AND 50 cm^2 BREAKS*

by

J. L. Steiner, D. A. Siebe, and J. E. Boyack

Safety Code Development Group
Nuclear Technology and Engineering Division
Los Alamos National Laboratory
Los Alamos, New Mexico 87545

ABSTRACT

Los Alamos National Laboratory is a participant in the Integral System Test (IST) program initiated in June 1983 for the purpose of providing integral system test data on specific issues/phenomena relevant to post-small-break loss-of-coolant accidents (SBLOCAs), loss of feedwater and other transients in Babcock & Wilcox (B&W) plant designs. The Multi-Loop Integral System Test (MIST) facility is the largest single component in the IST program. MIST is a 2×4 (2 hot legs and steam generators, 4 cold legs and reactor-coolant pumps) representation of lowered-loop reactor systems of the B&W design. It is a full-height, full-pressure facility with 1/817 power and volume scaling. Two other experimental facilities are included in the IST program: test loops at the University of Maryland, College Park and at Stanford Research Institute. The objective of the IST tests is to generate high-quality experimental data to be used for assessing thermal-hydraulic safety computer codes. Efforts are underway at Los Alamos to assess TRAC-PF1/MOD1 against data from each of the IST facilities.

Calculations and data comparisons for TRAC-PF1/MOD1 assessment have been completed for two transients run in the MIST facility. These are the MIST nominal test, Test 3109AA, a scaled 10 cm^2 SBLOCA and Test 320201, a scaled 50 cm^2 SBLOCA. Only MIST assessment results are presented in this paper.

INTRODUCTION

Los Alamos is currently providing analytical support to the Integral System Test (IST) program; the largest part of our analytical efforts involve the use of the TRAC-PF1/MOD1 code. There are three applications where TRAC is, or has been, used as a complement to the Multi-Loop Integral System Test (MIST) experimental program. The first application is related to test specification or design. During fiscal year 1986, Los Alamos performed five MIST pretest analyses. The five experiments were chosen on the basis of their potential either to approach the facility limits or to challenge the predictive capability of the TRAC-PF1/MOD1 code. Three small-break loss-of-coolant accident (SBLOCA) tests were examined that included nominal test conditions, throttled auxiliary feedwater (AFW) and asymmetric steam-generator (SG) cooldown, and reduced high-pressure-injection (HPI) capacity, respectively. Also analyzed were two "feed-and-bleed" cooling tests with reduced HPI and delayed HPI initiation. Results of the tests showed that the MIST facility limits would not be approached in the five tests considered. The second application is related to test evaluation. It is impossible to include all the desired instrumentation in a facility. Constraints of cost, complexity, space, etc., are rapidly reached. If one has sufficient confidence that TRAC will correctly predict the dominant test phenomena, calculations can be used to fill in gaps about quantities that are not measured in the facility. The third application is related to TRAC assessment. The ability of a thermal-hydraulic code to accurately calculate experimental behavior in scaled facilities is an important link in demonstrating that the code can be used to predict how an operating pressurized water reactor would perform under accident conditions. During fiscal year 1987, Los Alamos performed two MIST posttest analyses. The two experiments were chosen on the basis of their potential to challenge the predictive capability of the TRAC code. These tests are identified and briefly discussed in the following paragraphs.

* This work was funded by the US Nuclear Regulatory Commission, Office of Nuclear Regulatory Research, Division of Accident Evaluation.

Test 3109AA. MIST test 3109AA was the nominal test for the MIST program. During the early test program, several repeats of the specified nominal test were run. The test selected for the nominal, Test 3109AA, differs from the pretest specification for 310000 in the initial pressurizer liquid level and efforts to warm the surge line and maintain the pressurizer liquid at saturation until test initiation. The nominal conditions include a scaled 10-cm^2 cold-leg (CL) discharge leak, full HPI and AFW, reactor-coolant pumps (RCPs) not available, no noncondensible gas injection, automatic reactor vessel vent valve (RVVV) actuation on differential pressure, automatic guard heater control, constant steam generator (SG) secondary level control after SG refill, and symmetric SG cooldown.

Test 320201. This test differed from the nominal in that the scaled leak size was increased from 10 cm^2 to 50 cm^2. Other specified conditions and procedures for the test were the same.

Most experiments scheduled for the first year of operation of the MIST facility have been completed. Tests 3109AA and 320201 are from test groups 31 and 32 for which formal test reports have been submitted to IST program participants for review. Data tapes for the posttest analyses of tests 3109AA and 320201 were obtained in a preliminary form prior to the completion of final data qualification by Babcock & Wilcox (B&W).

CODE VERSIONS

We used updated versions of the TRAC-PF1/MOD1 code (Ref. 1). The TRAC-PF1/MOD1 code was developed at Los Alamos National Laboratory to provide advanced best-estimate predictions of postulated accidents in light-water reactors. The code features a two-phase, two-fluid nonequilibrium hydrodynamics model with a noncondensible gas field; flow-regime-dependent constitutive equation treatment; either one- or three-dimensional treatment of the reactor vessel; complete control-systems modeling capability; a turbine component model; and a generalized steam-generator component model.

Code versions 12.7 and 14.3 were used for the analysis of tests 3109AA and 320201 respectively. Code modifications were necessary for this application. Initialization of the MIST facility in natural circulation rather than pumped flow caused modeling difficulties unique to this facility. An accurate prediction of SG heat-transfer distribution is necessary to correctly predict steady-state loop flows and hence initial system pressure and temperatures. Code and model modifications were necessary to achieve this. These are expected to be applicable only to the MIST facility and are used only with the model for it.

PLANT MODEL

Figure 1 is a MIST facility arrangement drawing. Figures 2 and 3 provide an overview of the TRAC MIST facility model. The TRAC model of the MIST facility has evolved over a period of time. The model was initially based on preliminary information provided in the MIST Facility Specification. It has progressed to its present form as available as-built facility information was received from B&W. The model consists of 77 components that have been subdivided into 251 fluid cells. Only one-dimensional components are used in this model. The model is considered to be rather finely noded and is expected to predict the dominant phenomena during MIST experiments.

CALCULATION RESULTS

During analysis of our calculations, we found that many of the predicted phenomena occurred in each of the calculations. Therefore, we have chosen to provide a detailed description of nominal MIST Test 3109AA and a less detailed description for the posttest prediction for Test 320201. The discussion in this case focuses on the important phenomena that differ from those in the nominal case. We note that for each test calculation, at time zero, the primary was liquid full and coolant was being driven by natural circulation.

TEST 3109AA CALCULATION

The TRAC-PF1/MOD1 posttest calculation for Test 3109AA was performed for the first 7000 s of the experiment. During this time period, all of the major phenomena took place and the automatic safety systems and emergency operating procedures were activated. At the end of the 7000 s calculational period, the HPI flow exceeded the leak flow and refilling of the primary system was well underway.

Steady-State Calculation

The TRAC-PF1/MOD1 steady-state calculation for Test 3109AA was performed for 2000 s, corresponding to approximately five loop transients. At the end of the steady-state calculation, the primary- and secondary-system fluid conditions had stabilized within the uncertainties of the measured values.

Transient Calculation

The observed and calculated thermal hydraulic phenomena and system interactions are discussed in detail in this section. The discussion is divided into four transient phases; these phases are defined with reference to Fig. 4, the primary and secondary pressure response. Data is denoted by a dashed line and calculated values by a solid line.

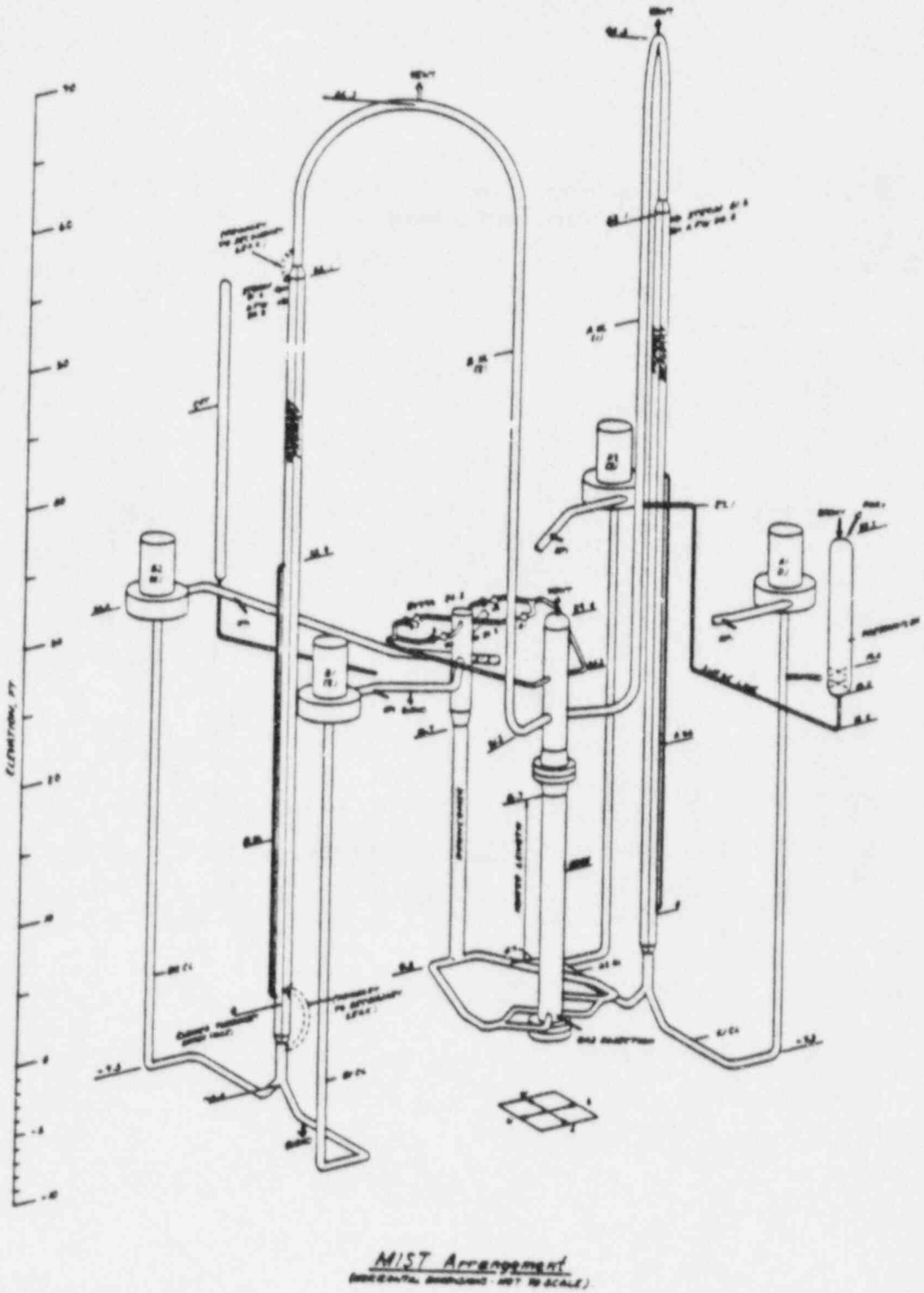

Fig. 1.
MIST facility isometric.

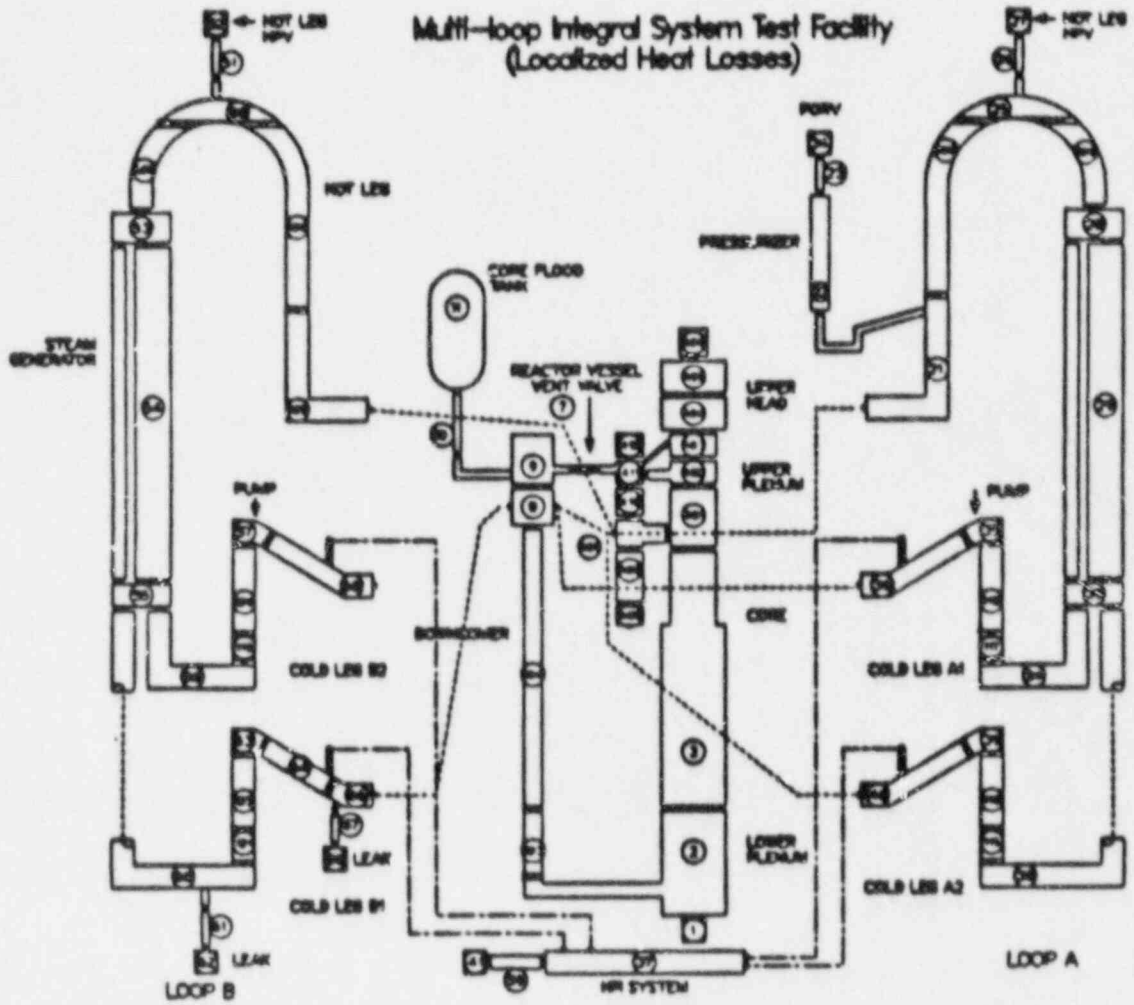

Fig. 2.
TRAC component noding schematic of MIST facility.

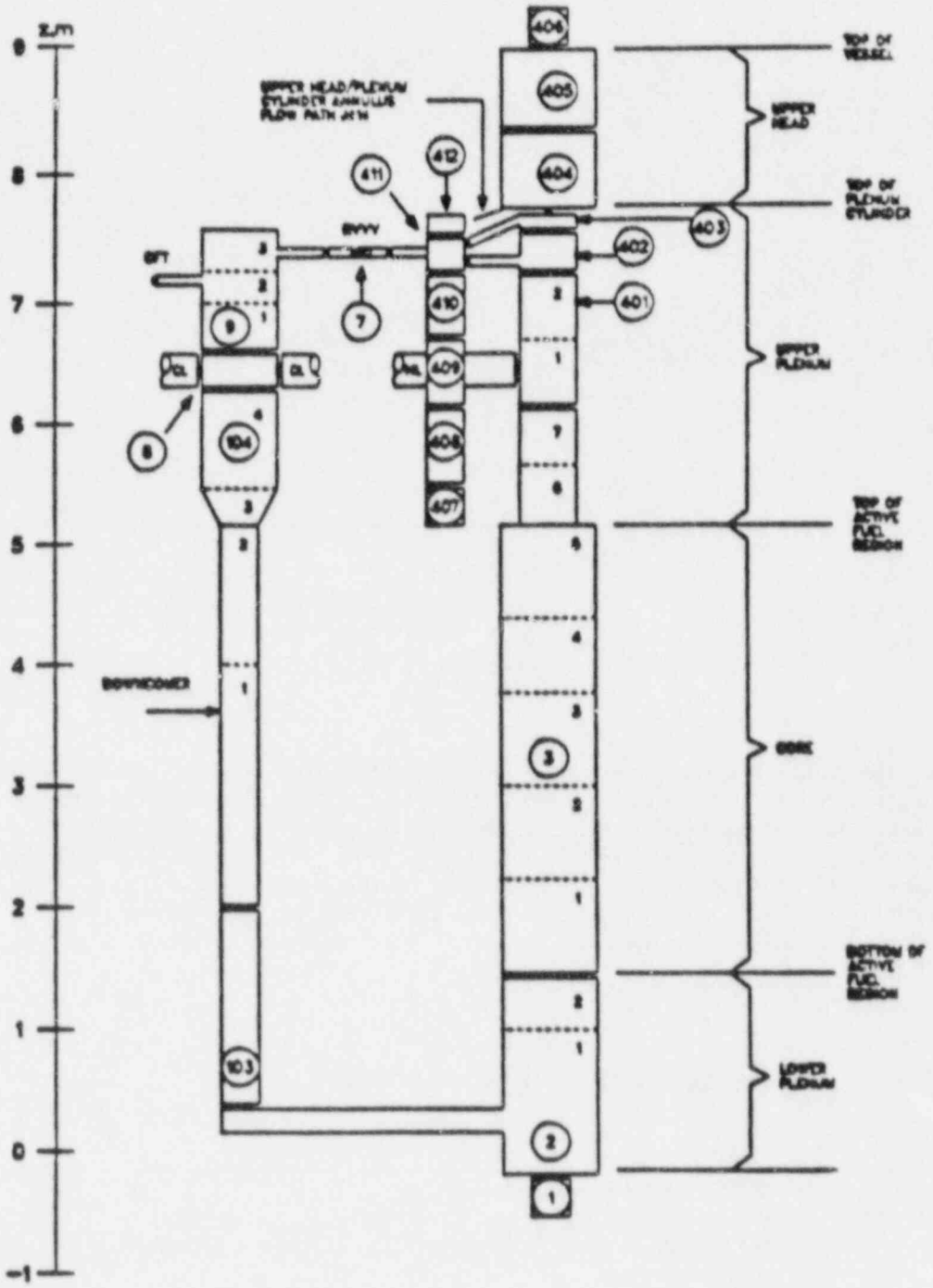

Fig. 3.
TRAC reactor-vessel noding schematic of MIST facility.

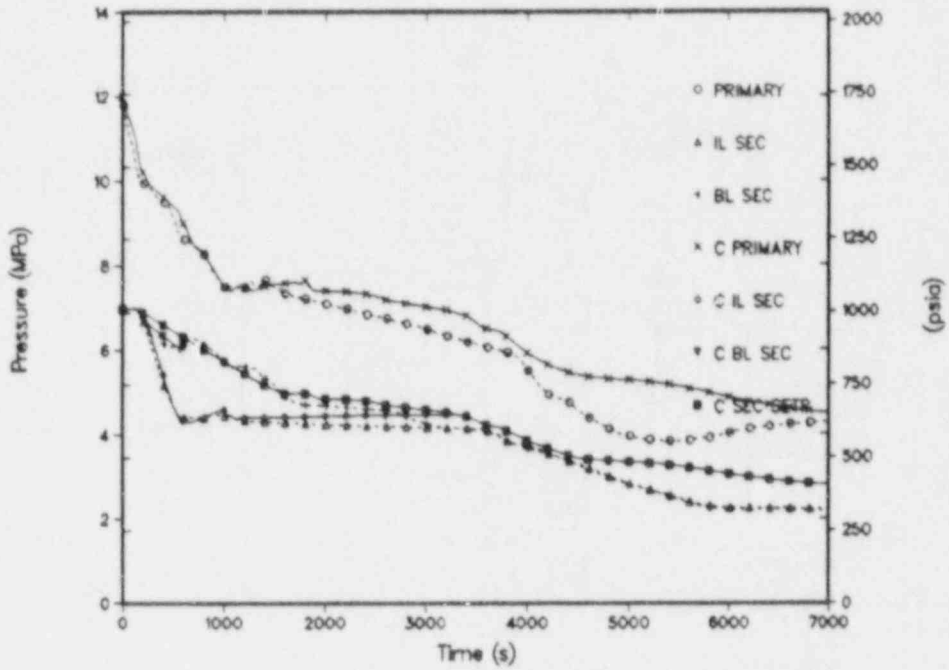

Fig. 4.
Test 3109AA primary and secondary pressures.

A "C" as the first letter in the curve label denotes a calculated value. Phase one, subcooled decompression, covers the period from the start of the transient to 185 s when the intact-loop hot leg saturates and the depressurization rate is reduced. Phase two, intermittent circulation, covers the period of continued depressurization, repressurization, and termination of repressurization from 185 s to 1870 s when natural circulation is terminated in the loops. Phase three, loop stagnation, covers the period of gradual depressurization from 1875 s to approximately 4000 s when primary-system refill begins. Phase four, refill, extends from the beginning of refill at 4000 s to the end of the calculation at 7000 s. A summary of the major events for Test 3109AA is presented in Table I.

TABLE I
EVENT TABLE FOR TEST 3109AA

Test Time (s)	Calculation Time (s)	Event Description
0.0	0.0	Start transient—break initiation.
150.0	160.0	Pressurizer level drops to 0.3048 m (1.0 ft), core power ramp, HPI RVVV automatic control initiated, RVVV first opens, SG secondary level reset.
185.0	185.0	Intac-loop hot leg saturates.
240.0	310.0	Intact-loop flow ends.
1575.0	1840.0	Intermittent broken-loop flow ends.
4000.0	3400.0	Beginning of refill.
	7000.0	Calculation terminated.

Phase One, Subcooled Decompression. Phase one is the first part of the transient from leak initiation until the saturation pressure was reached in the hot legs at 185 s. During phase one, the fluid in the primary system was subcooled liquid, and the primary-system pressure decreased rapidly as the liquid expanded due to the leak flow. At the end of phase one, the primary-system depressurization rate was reduced by flashing of the liquid in the hot legs.

At the beginning of the transient, the primary system was in steady-state single-phase natural circulation. The driving force for natural circulation was the density difference between the hot fluid in the hot legs and vessel and colder fluid in the SG tubes, CLs, and downcomer. The test was initiated at time zero by opening a scaled 10-cm^2 leak in the B1 CL just downstream of the HPI port. This caused an immediate reduction in the calculated primary-system pressure (Fig. 4) and pressurizer level as a result of the flow of liquid through the leak. The liquid initially in the pressurizer was near saturation temperature, and as this liquid was discharged into the intact-loop hot leg, it mixed with the hot-leg fluid resulting in a higher fluid temperature in the intact-loop hot leg relative to the broken-loop hot leg. Since the density of the liquid in the intact-loop hot leg was thereby reduced, the intact-loop natural-circulation flow increased at the beginning of the transient as shown in Fig. 5.

The level in the pressurizer drained down to the 0.3048 m (1-ft) level at 150 s in the test and at 160 s in the calculation. At these times the following control actions were taken: core power decay was started, HPI flow was started, the RVVVs were transferred to automatic control, the AFW level control set point was changed from 1.52 m (5 ft) to 9.63 m (31.6 ft), and the abnormal transient operator guidelines (ATOG)-based pressure-control logic was initiated for the SG secondaries. This automated SG secondary pressure control was used to archive modelable and reproducable boundary conditions while approximating plant ATOG control. The pressurizer low-level trip was reached 10 s earlier in the test because of the higher measured leak flow at the beginning of the transient (Fig. 6).

The effect of the core power decay after the pressurizer low-level trip was to increase the measured and calculated primary depressurization rates as shown in Fig. 4. The depressurization rate was high at this time because all of the primary fluid was still subcooled and expanding because of the leak flow. Also at the time of the low-level trip, the RVVVs were switched from manually closed to automatic control based on differential pressure. Figures 7 and 8 show that the vent valves opened immediately, causing a brief reduction in both loop flows at 150 s in the calculation and 160 s in the test. The reduction in the loop flows was then followed by a recovery in both loops (Figs. 5 and 9) with the sharpest recovery in the intact loop. This increase in the loop flows was a result of the increased AFW flow (Figs. 10 and 11) in response to the AFW set-point change at 150 s in the calculation and 160 s in the test. The loop flows were increased by the AFW flow because the AFW raised the thermal center in the SG; the intact-loop flow was increased more since the pressurizer was still discharging hot fluid into the intact loop at this time.

Figure 5 shows that the increase in the intact-loop flow was abruptly terminated at approximately 185 s in both the calculation and the experiment. At this time the primary-system pressure (Fig. 4) had decreased to the saturation pressure of the intact-loop hot-leg fluid. Flashing of the hot-leg fluid then created a vapor bubble in the intact-loop hot leg U-bend (Fig. 12) and the natural-circulation flow in the intact loop was interrupted as shown in Fig. 5. The intact-loop saturation marked the end of phase one at 185 s. Subsequent depressurization of the primary system was then inhibited by flashing of the fluid in the intact-loop hot leg, as shown in Fig. 4, which indicates a reduction in the measured and calculated primary-system depressurization rates at 185 s.

Differences between the calculation and the experiment during phase one resulted primarily from the higher measured leak flow (Fig. 6). This caused a slightly higher depressurization rate (Fig. 4) and an earlier occurrence of the pressurizer low-level trip in the test.

Phase Two, Intermittent Circulation. Phase two covers the period of intermittent circulation in the loops after the first saturation of loop fluid occurs in the intact-loop hot leg. During phase two, the natural circulation flow in each loop was governed by the liquid level in the hot leg in that loop. As the hot leg liquid level receded, the U-bend was uncovered and the loop flow was quickly terminated. Also during phase two, the SG AFW and steam flows responded to the control procedures started during phase one when the pressurizer level decreased to 0.3048 m (1 ft). At the beginning of phase two the AFW was on in both SGs as the levels were being raised to the 9.36 m (31.6 ft) set point, and throughout phase two, the secondary pressures were controlled to a variable set point based on ATOG. The ATOG set point is determined from the core exit temperature and the saturation temperatures corresponding to the SG secondary pressures as described in Ref. 2. Depending on these three temperatures, the set point pressure may be (1) held constant, (2) reduced by 5.746×10^{-3} MPa/s (50 psi/min), or (3) reduced such that the corresponding saturation temperature is reduced by 55.56 K/h (100°F/h). The logic for determining which of these pressure-control modes is to be used is explained in detail in Ref. 2. Phase two extends to 157[illegible] s in the test and 1870 s in the calculation, when the flow in the broken loop is terminated by the uncovery of the broken-loop hot-leg U-bend.

After the saturation of the intact-loop hot-leg fluid at the end of phase one, the liquid level in the intact-loop hot leg decreased rapidly (Fig. 12) as a result of continued flashing. Figure 5 shows that as a result, the intact-loop

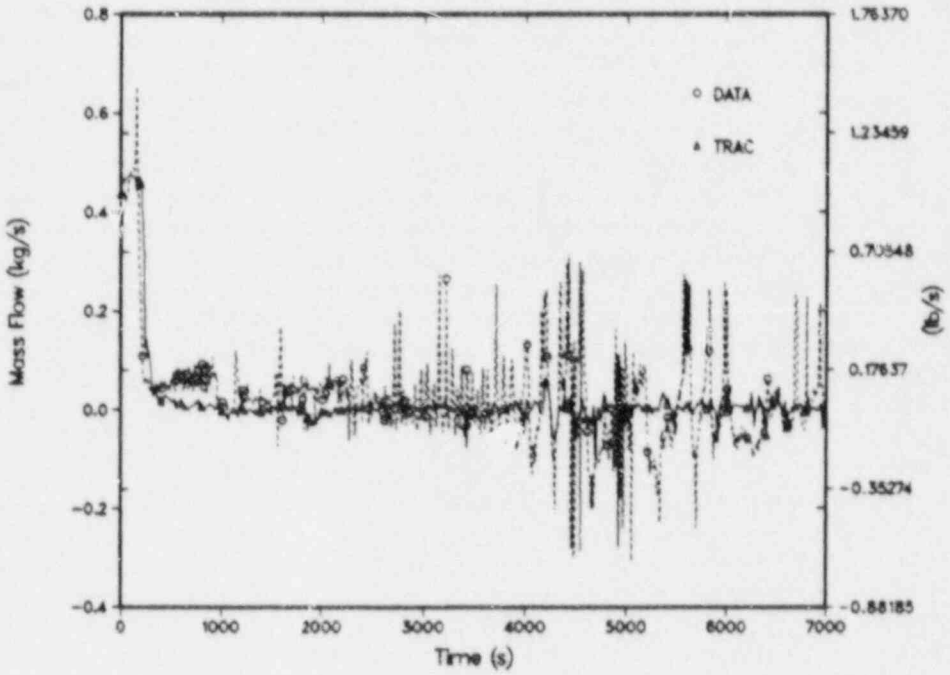

Fig. 5.
Test 3109AA total intact-loop CL flow.

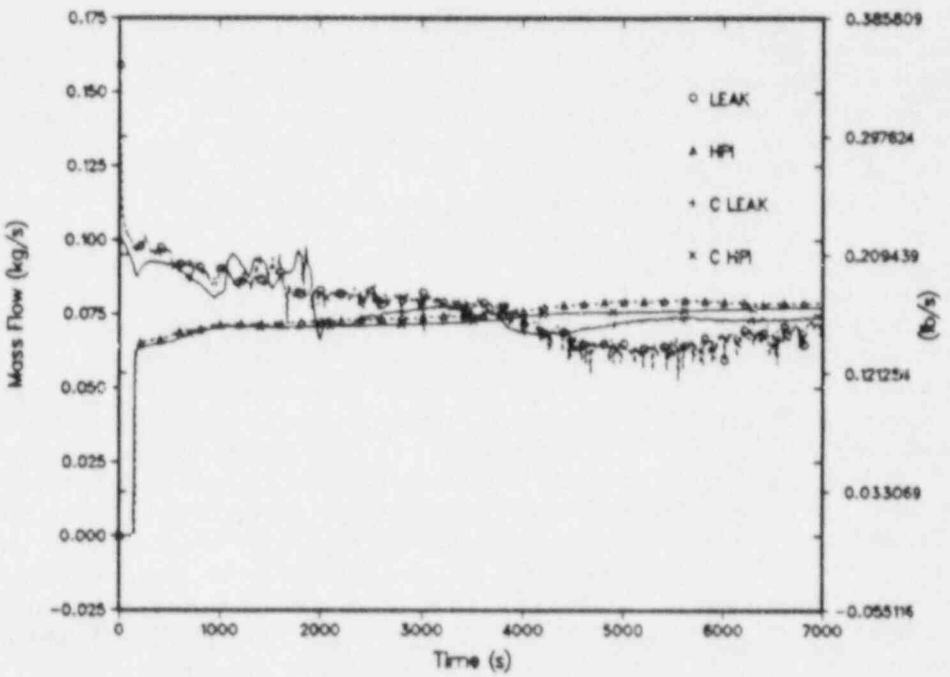

Fig. 6.
Test 3109AA CL leak and HPI flows.

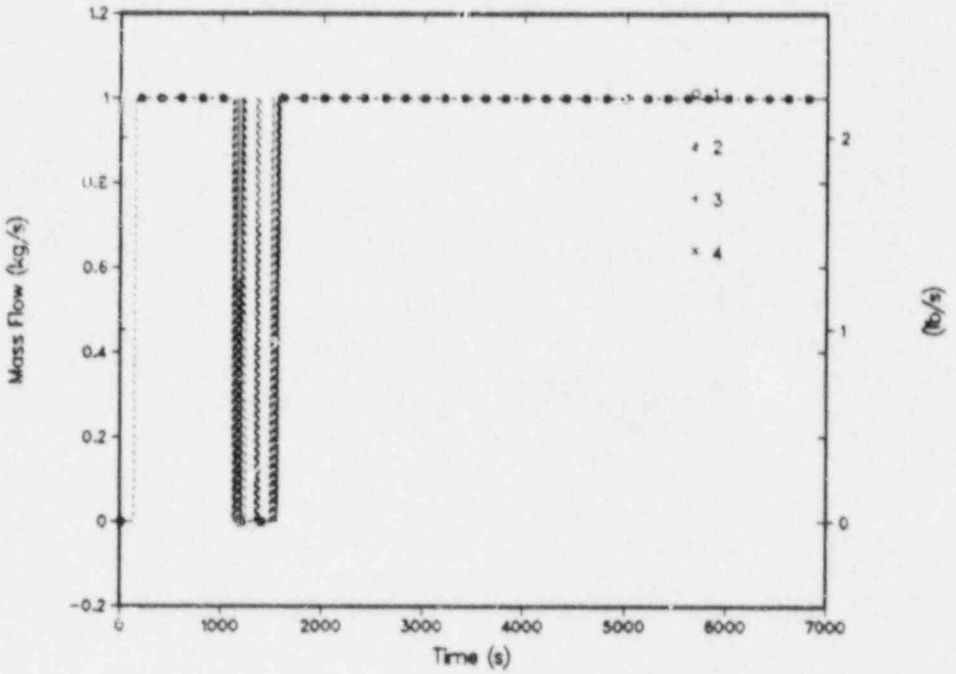

Fig. 7.
Test 3109AA MIST vent valve full closed indicator (test).

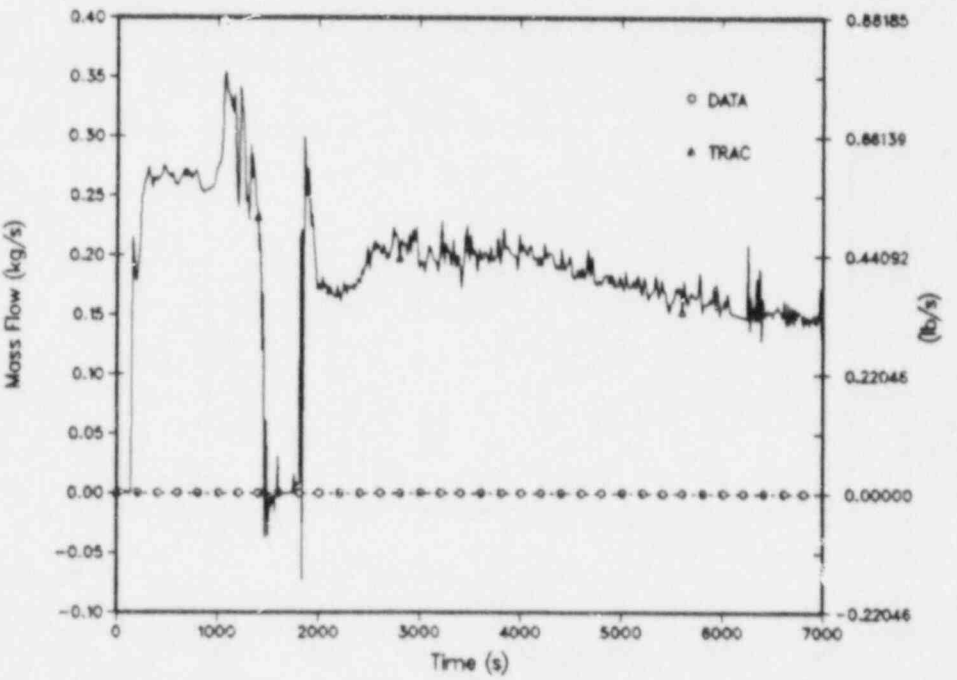

Fig. 8.
Test 3109AA RV'VV flows.

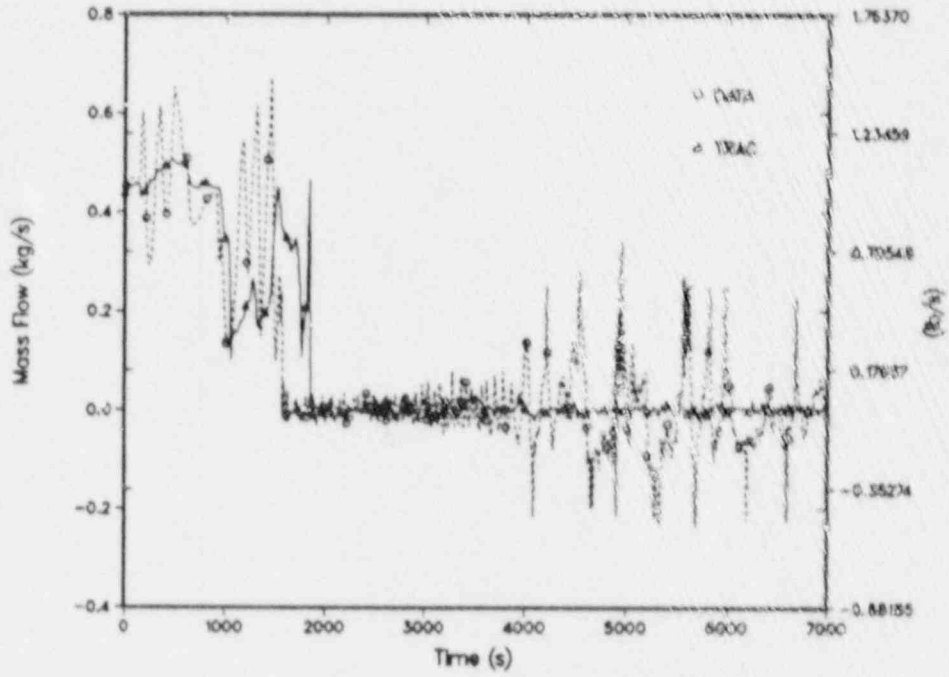

Fig. 9.
Test 3109AA total broken-loop CL flow.

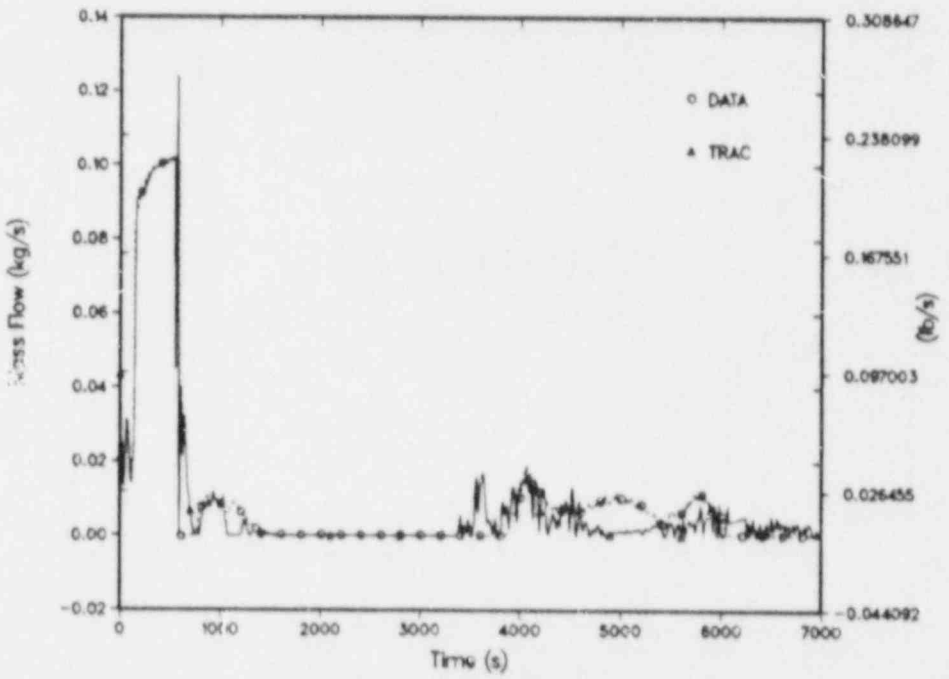

Fig. 10.
Test 3109AA intact-loop SG AFW flow

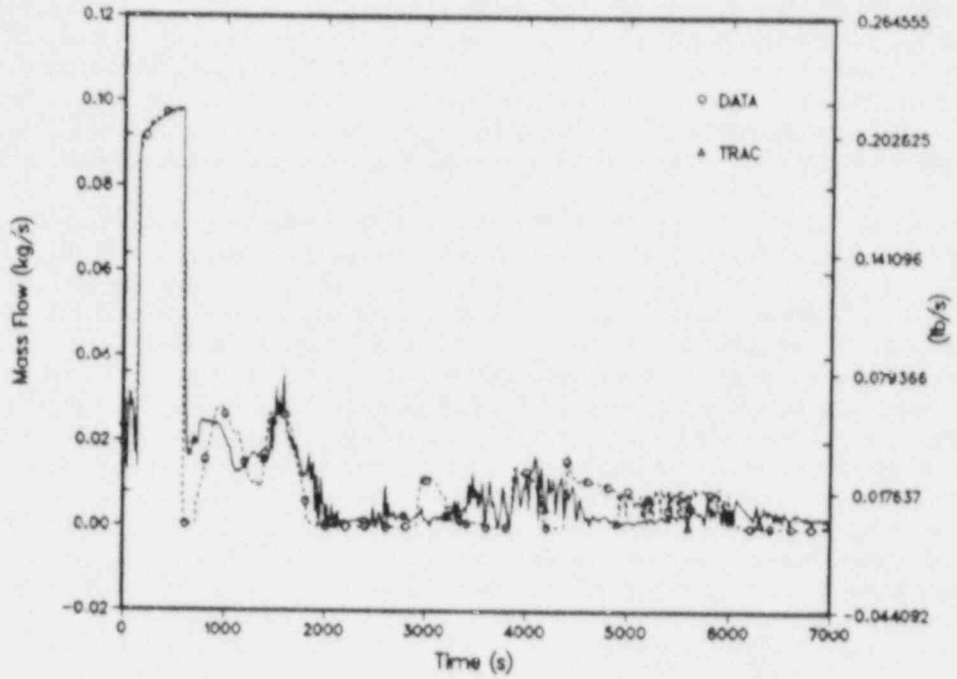

Fig. 11.
Test 3109AA broken-loop SG AFW flow.

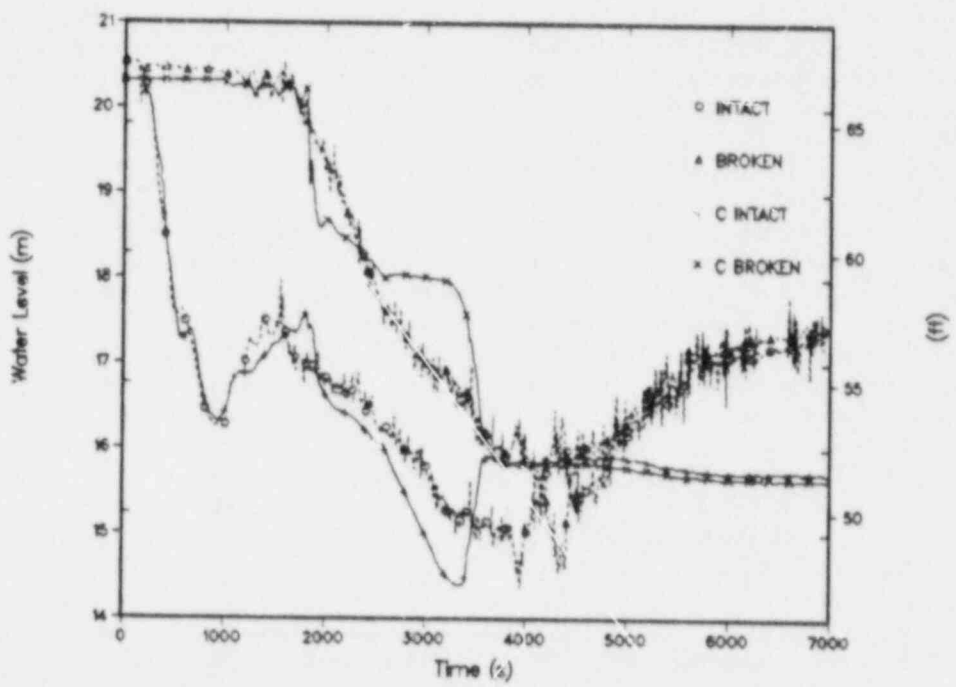

Fig. 12.
Test 3109AA hot-leg collapsed liquid levels.

natural-circulation flow was terminated by 240 s in the test and 310 s in the calculation and was not reestablished. Heat transfer in the intact-loop SG then ceased because of the loss of natural circulation in the intact loop. In the absence of heat transfer from the primary, the intact-loop SG secondary pressure decreased from the ATOG set point in both the test (at 240 s) and in the calculation (at 310 s) as shown in Fig. 4. This decrease, caused by the AFW flow into the intact-loop SG (Fig. 10), continued until the level (Fig. 13) reached the 9.63 m (31.6 ft) set point at 565 s in both the test and the calculation and the AFW flow decreased (Fig. 10). After the intact-loop SG secondary pressure fell below the ATOG set point, the steam flow in the intact-loop secondary was terminated (Fig. 14) by the pressure controller.

When the intact-loop SG secondary was refilled to the 9.63-m (31.6-ft) level in the experiment, the AFW controller was switched into a constant-level control mode and a proportional-integral controller was used to maintain the SG level at the 9.63-m (31.6-ft) set point. This control mode change affected the AFW flow after the intact loop SG was refilled at 565 s. Figure 10 shows that after 565 s, the AFW flow was briefly terminated and then restarted from 800 to 1500 s while the SG level settled in on the 31.6 ft set point. When the AFW was restarted in the intact-loop SG, vapor was present in the primary side of the tubes at the 15.48 m (50.8 ft) AFW elevation (Fig. 13) and condensation heat transfer began immediately. This boiler condenser mode (BCM) heat transfer began in both the test and the calculation at 565 s resulting in a more rapid primary depressurization (Fig. 4). The BCM was terminated at 1000 s in both the test and the calculation when the intact-loop SG primary level (Fig. 13) increased to the AFW elevation and condensation in the primary was terminated.

Without steam flow, AFW flow was not required to maintain the level in the intact-loop SG after the 31.6 ft set point was achieved and Fig. 10 shows that the AFW flow was completely terminated in the intact loop after 1500 s in both the test and the calculation. The intact-loop SG therefore remained inactive after 1500 s while its pressure was below the ATOG set point.

The system interactions in the broken loop during phase two were similar to those just described in the intact loop. However, the timing of events in the broken loop was delayed because the broken loop hot leg fluid was cooler than the fluid in the intact-loop hot leg at the beginning of phase two. Figure 12 shows that the broken-loop hot leg was maintained liquid full until 1000 s as the intact-loop hot-leg level receded as a result of local flashing. Beginning at approximately 850 s, however, the intact-loop level fell at a slower rate as it approached the liquid level in the primary side of the intact-loop SG (Fig. 12). With the slower draining in the intact-loop hot leg, the broken-loop hot leg level eventually began to recede at 1000 s as indicated in Fig. 12. The natural-circulation flow in the broken loop (Fig. 9) then began to decrease rapidly at approximately 1000 s, in both the test and the calculation, in response to the decrease in the broken-loop hot-leg level. This reduction of flow in the broken loop had two effects. First, the heat transfer in the broken-loop SG started to decrease, leading to an increase in the primary-system pressure and corresponding decrease in broken-loop secondary pressure beginning at 1000 s (Fig. 4). Second, the core-outlet flow was diverted into the upper head and through the RVVVs as shown in Fig. 8. The repressurization of the primary system retarded the flashing in both the intact and broken loops and, at the same time, flashing increased in the upper head due to the diverted core outlet flow. As a consequence, both the measured and calculated intact-loop hot-leg levels started to increase at 1000 s while the vessel level decreased more rapidly, as shown in Figs. 12 and 15.

The final sequence of events in phase two started at 1000 s with the intact-loop hot-leg levels increasing and the vessel levels decreasing as described above. The increased rate of upper head voiding in both the test and the calculation at 1000 s was sufficient to terminate the reduction in the broken-loop natural-circulation flow (Fig. 9), which then began to increase. As flashing continued in the upper head, the vessel level receded, as shown in Fig. 15, and at 1250 s in the test (1385 s in the calculation) the RVVV nozzles were uncovered. As a result, the RVVV flow began to decrease rapidly at this time and was completely terminated at 1150 s in the test and at 1480 s in the calculation as shown in Figs. 7 and 8. The broken-loop spillover flows (Fig. 9) were sharply increased by the RVVV closures at these times in both the test and the calculation. Shortly afterward, however, the broken-loop U-bend uncovered (Fig. 12) as the primary system continued to drain and the natural-circulation flow in the broken loop started to decrease rapidly, as shown in Fig. 9. The broken-loop natural-circulation flow then continued to decrease and was completely interrupted at 1575 s in the test and at 1870 s in the calculation. During this final decrease in broken-loop natural-circulation flow, Figs. 7 and 8 show that the RVVVs reopened at 1575 s in the test and at 1840 s in the calculation when the downcomer drained to the RVVV elevation (Fig. 16) and remained open thereafter.

During the period when the RVVVs were closed, Fig. 9 shows a strong natural-circulation flow in the broken loop. The effect of this flow was to increase the heat transfer in the broken-loop SG and also to mix cold HPI fluid with hotter fluid in the primary system. As a result, the primary-system repressurization which began at 1000 s was terminated at 1575 s in the test and 1875 s in the calculation.

The termination of spillover circulation in the broken loop at 1575 s in the test and 1870 s in the calculation marks the end of phase two. Major events during phase two occurred slightly earlier in the test than in the calculation

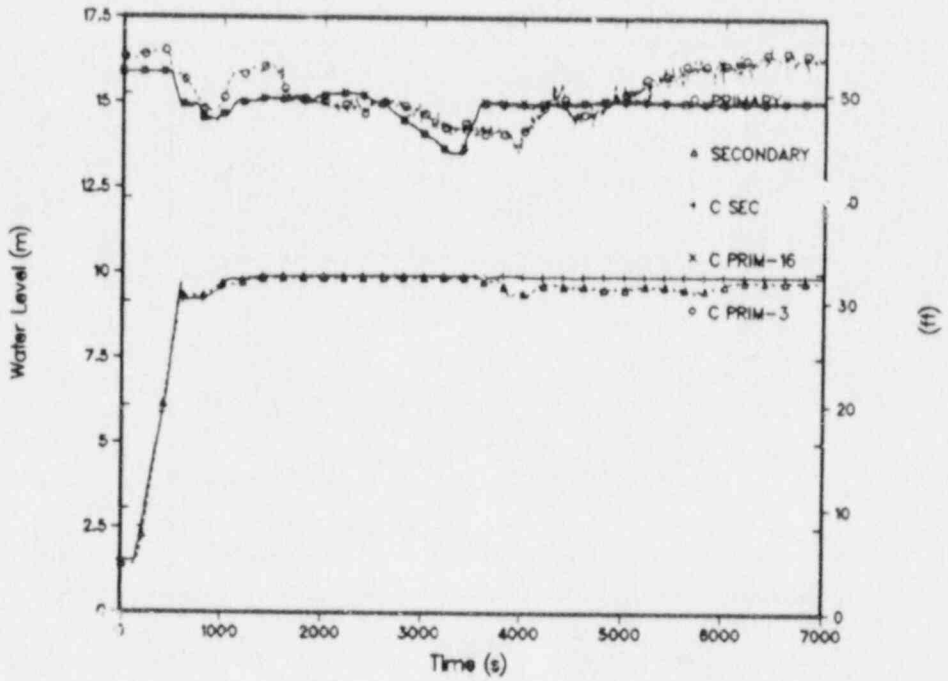

Fig. 13.
Test 3109AA intact-loop SG collapsed liquid levels.

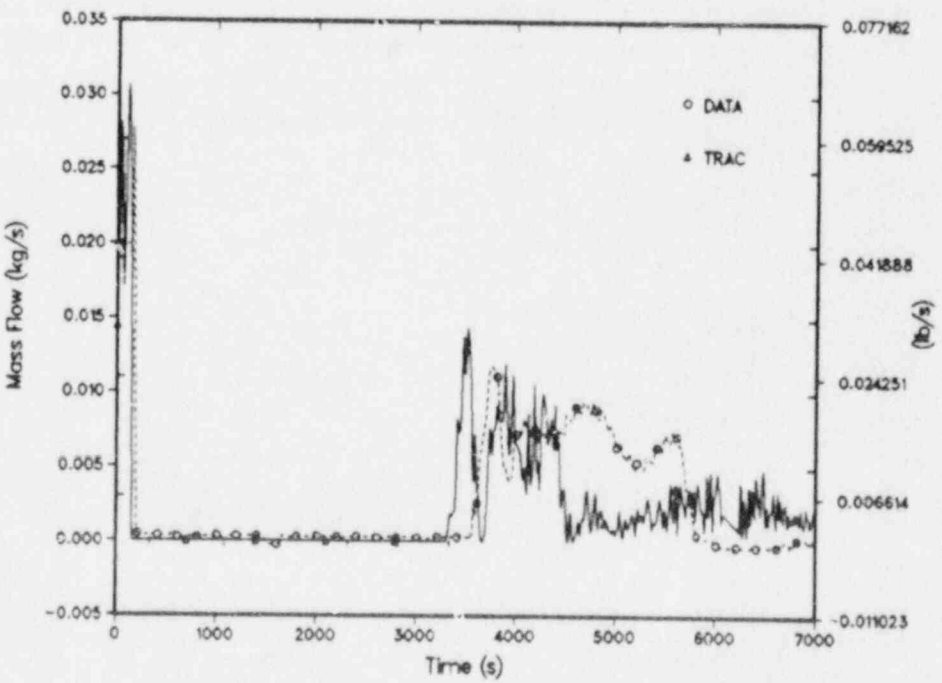

Fig. 14.
Test 3109AA intact-loop SG secondary steam flow.

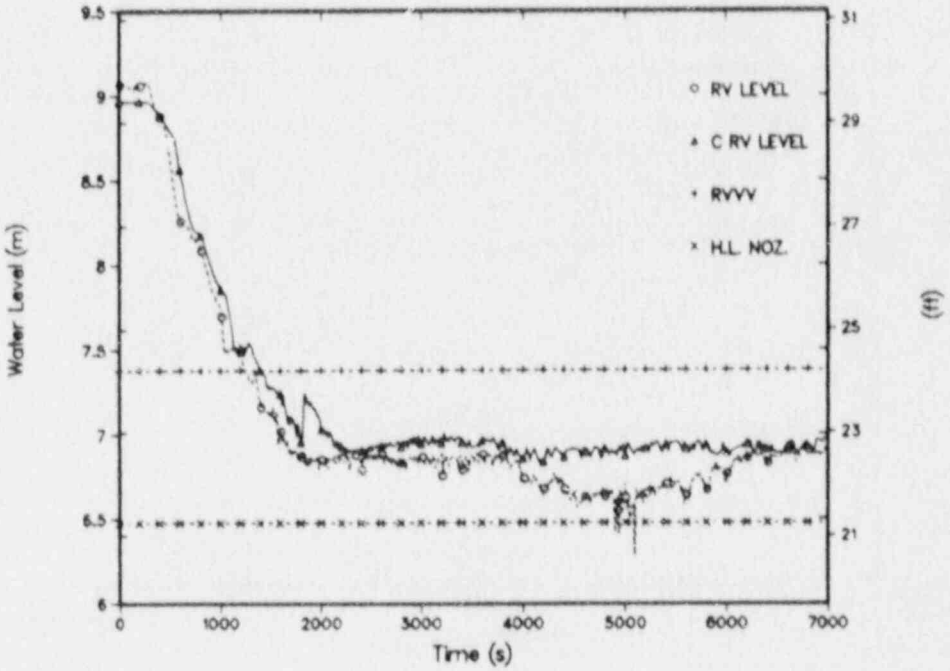

Fig. 15.
Test 3109AA reactor vessel collapsed liquid level.

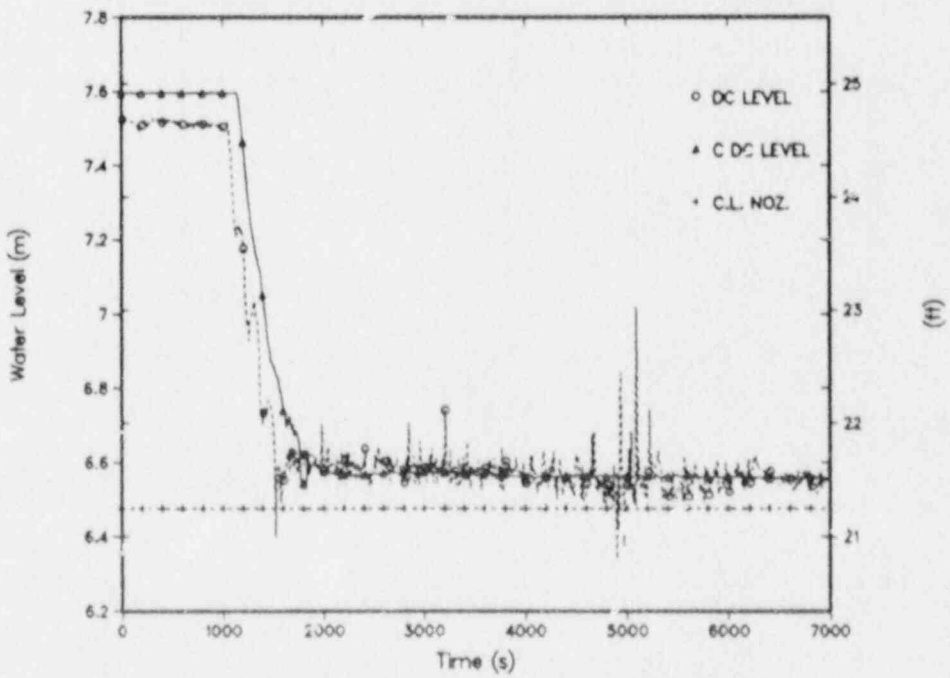

Fig. 16.
Test 3109AA downcomer collapsed liquid level.

because of the higher leak flow in the test from test initiation to 1080 s. At the end of phase two, in both the test and the calculation, the primary system was depressurizing, the broken-loop SG secondary pressure was being controlled to the decreasing ATOG set point, and AFW was controlling the SG level in the broken loop. The intact-loop SG was inactive at the end of phase two since its pressure was below the ATOG set point.

Phase Three, Loop Stagnation. Phase three is the period of stagnated natural-circulation flow in the loops after the final spillover in the broken loop. During phase three the primary system was cooled by the leak/HPI feed and bleed and by AFW in the broken loop SG. The primary-system pressure decreased during phase three as a result of core power decay and the leak/HPI cooling. Phase three ended at 4000 s in the test and 3400 s in the calculation when AFW was restarted in the intact loop and the primary-system depressurization rate was increased.

During most of phase three, the primary was cooled by the leak/HPI feed and bleed and by AFW in the broken loop (Fig. 11). Most of the cooling was done by the feed and bleed: at 3000 s, for example, Fig. 6 shows that in the test, the HPI flow was approximately 0.074 kg/s (0.1628 lb/s) and the leak upstream temperature (Fig. 17) was 524.9 K. The energy required to heat this HPI flow to the temperature at the leaksite, 72 kW, was greater than the 59 kW core power at this time. In the calculation at 3000 s, the HPI flow was slightly lower (0.0716 kg/s), 71 kW was needed to heat this flow to the leak upstream temperature in the calculation, and the core power was also 59 kW at 3000 s. The primary-system pressure decreased during phase three as a result of the decreasing core power and excess energy removal of the leak/HPI cooling.

At the beginning of phase three, a circulation flow developed in the broken-loop CLs in both the test and the calculation. The CL circulation flow began immediately after the broken-loop U-bend spillover flow was terminated at the end of phase two. At this time, fluid from the downcomer was drawn toward the leak site and the flow in the B1 CL reversed. The CL circulation flow was then maintained by the density difference between the B1 and B2 CLs resulting from the flow of warmer fluid from the downcomer into the B1 CL. The circulation flow was important because it affected the leak upstream temperature (Fig. 17) in both the test and the calculation.

Figure 17 shows that the broken loop CL circulation flow caused a reduction of approximately 30 K in the fluid subcooling upstream of the leak in the test as well as in the calculation. The corresponding reduction in the leak flow (Fig. 6) at 1930 s in the calculation, however, was larger than the reduction observed in the test at 1660 s. This difference apparently indicates that the TRAC-PF1/MOD1 critical flow model did not properly account for the change in leak upstream subcooling in the calculation. After the initial decrease in leak flow at the beginning of phase three, Figs. 6 and 17 show that the calculated leak flow gradually recovered toward the measured value as the subcooling increased in the calculation.

The lower calculated leak flow during phase three resulted in a lower depressurization rate in the calculation (Fig. 4) and slower loop draining (Fig. 12). Figure 12 shows that after the broken loop interrupted in the test, the broken-loop hot-leg level remained above the intact-loop level, and both loops drained at approximately the same rate. The difference in hot-leg levels resulted from a temperature difference between the intact and broken loop the hot leg piping. After the flow in each U-bend voided and the loop flow interrupted, the U-bend piping temperature was maintained by the guard heaters at approximately the saturation temperature at the time of the interruption. Since the intact loop interrupted earlier when the saturation temperature was higher, the intact-loop U-bend piping temperature stayed higher after both loops had interrupted. The higher piping temperature created a higher vapor pressure in the intact-loop U-bend relative to the broken-loop U-bend; and because of this pressure difference, the intact-loop hot-leg level remained below the broken-loop hot-leg level during phase three.

The same draining behavior, with the higher level in the broken-loop hot leg, occurred in the calculation during phase three. However, after 2600 s in the calculation, the draining in the broken loop was halted and the leak was then fed by accelerated draining of the intact loop (Fig. 12). This transition at 2600 s in the calculation is currently under further study; it appears that a change occurred in the calculation at this time which affected the heat transfer from the piping to the vapor in one of the U-bends. The difference in the observed and calculated hot-leg draining rates after 2600 s, however, did not cause other calculated parameters to diverge from the measured values. Figures 4, 6, and 17 show no change in the calculated leak upstream temperature, leak flow, or primary-system pressure at 2600 s.

During phase three, the primary and secondary conditions were such that the ATOG set-point pressure was approximately equal to the saturation pressure corresponding to a temperature 27.78 k (50°F) below the core-exit temperature. This is evidenced in Fig. 4, which shows that during phase three, the calculated ATOG pressure decreased at the same rate as the primary pressure. The difference in the corresponding saturation temperatures during this decrease was approximately 27.78 K (50°F). Fig. 4 shows that the difference between the primary and ATOG pressures was nearly constant during phase three in the test and in the calculation.

The SG secondary pressure control is important because it affects the AFW flow in each SG. The AFW flow depends on the pressure control because AFW is used to control the secondary levels: if the secondary pressure is being reduced then AFW will be required to maintain the secondary level. During phase three, the broken-loop AFW

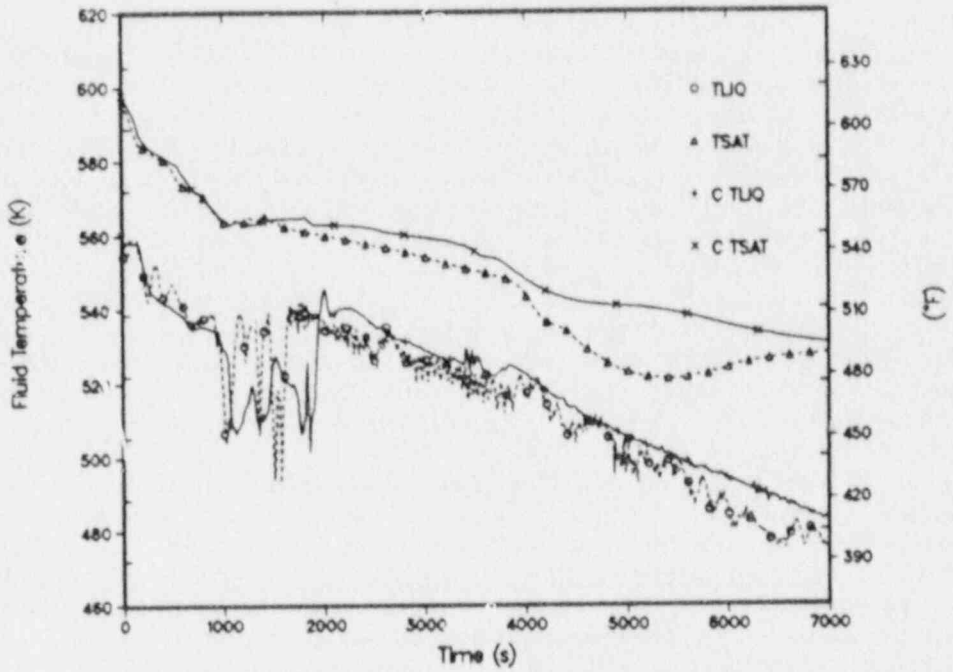

Fig. 17.
Test 3109AA leak upstream fluid temperatures.

was on (Fig. 11) in both the test and the calculation because the broken loop SG secondary pressure was controlled to the decreasing ATOG set point (Fig. 4). The intact-loop AFW was off (Fig. 10), however, since the intact-loop SG secondary pressure was below the ATOG set point (Fig. 4), and therefore the intact-loop steam flow was controlled to zero (Fig. 14).

Figure 4 shows that in the test, the intact-loop SG pressure remained constant during phase three when the AFW and steam flows were off. The calculated intact-loop SG pressure, however, increased slightly during phase three. This may have occurred because the steam-line heat losses modeled (1.5 kW per steam line) were too low. The test may have also had other losses, such as leakage of steam through the control valve, that contributed to the stability of the secondary pressures that were not modeled. The increase in the intact-loop SG pressure during phase three caused the decreasing ATOG set-point pressure to be reached at 3400 s in the calculation (4000 s in the test) as shown in Fig. 4. At these respective times, AFW was restarted in the intact loop leading to BCM which marked the end of phase three in both the test and the calculation.

Phase Four, Refill. Phase four covers the period from the beginning of the BCM in the intact loop until the end of the calculation at 7000 s. During phase four, the primary-system pressure was reduced by AFW boiler condenser mode heat transfer in the intact-loop SG causing the HPI flow to exceed the leak flow. The calculation was terminated at 7000 s, since at this time it was evident that the point of minimum primary system inventory had been reached.

At the end of phase three, the ATOG set-point pressure decreased to the intact-loop SG secondary pressure (Fig. 4), causing the steam and AFW flows to be restarted in the intact-loop at 4000 s in the test and at 3400 s in the calculation. This caused extensive condensation heat transfer in the primary side of the intact-loop SG tubes since the level in the tubes was well below the 15.48 m (50.8 ft) AFW-injection elevation (Fig. 13) at this time. As a result, the primary to secondary heat transfer in the intact-loop SG was increased at these times and the primary system began to depressurize rapidly in the test and the calculation (Fig. 4).

When the AFW was restarted in the intact loop, the pressure of the vapor inside the SG tubes was reduced by condensation. The liquid level in the intact-loop SG and hot leg then rose rapidly while the levels in the broken loop fell. This occurred in both the test and in the calculation, as shown in Fig. 12. However, the level in the broken-loop

SG (Fig. 18) fell below the 15.48 m (50.8-ft) AFW elevation in the test but not in the calculation. Therefore, the intact-loop BCM in the test was immediately followed by a BCM in the broken loop and the overall reduction in the primary pressure (Fig. 4) was greater in the test than in the calculation.

The effect of the primary-system depressurization at 4000 s in the test and 3400 s in the calculation was to increase the HPI flow above the leak flow as shown in Fig. 6. This event marks the beginning of the refill period. After the start of refill, the levels in the intact and broken loops started to increase as shown in Figs. 13 and 18. The refill rate (excess of HPI flow over leak flow) was higher in the test because of the larger BCM depressurization in the test (Fig. 4). The higher refill rate in the test resulted in correspondingly higher primary-system level increases after refill began in the test as shown in Figs. 6 and 4. The primary system continued to depressurize rapidly in the test (Fig. 4) until the SG primaries were filled above the upper tube sheets (Figs. 13 and 18) and the condensation heat transfer was terminated at approximately 5200 s. This event still had not been reached by the end of the calculation at 7000 s because of the lower refill rate in the calculation.

The differences between the test and the calculation discussed above involved three separate phenomena. First, the critical flow model in TRAC apparently did not properly account for the changes in the leak upstream temperature. Consequently, the calculated leak flow and primary depressurization rates were too low during phase three. Second, the TRAC input model did not include enough heat or steam losses for the secondary side. This allowed the intact-loop SG to pressurize slightly during phase three in the calculation and thereby reach the ATOG set point too soon. Phase three was therefore terminated 600 s early in the calculation. Third, the magnitude of the BCM heat transfer was apparently too low at the beginning of phase four in the calculation. Even though the condensation surface area and AFW flow during this BCM in the calculation matched the data, the primary-system depressurization during the BCM was too low in the calculation. This then caused a lower refill rate during phase four in the calculation.

The overall comparison of the TRAC-PF1/MOD1 calculation for Test 3019AA with measured data from the test was reasonable; this means that the major trends were predicted correctly in the calculation, although TRAC values were frequently outside the range of data uncertainty because of minor code/model deficiencies. With reasonable agreement, correct conclusions will still be reached when the code is used in similar applications.

TEST 320201 CALCULATION

The TRAC-PF1/MOD1 posttest calculation for Test 320201 was performed for the first 2800 s of the experiment. During this period, all of the major events occurred and the automatic safety systems and emergency operating procedures were activated. At the end of the 2800 s calculational period, the HPI and accumulator flows exceeded the leak flow and refilling of the primary system was well underway.

Steady-State Calculation

The TRAC-PF1/MOD1 steady-state calculation for Test 320201 was also performed for 2000 s (approximately 5 loop transits). At the end of the steady-state calculation, the primary and secondary system fluid conditions had stabilized within the uncertainties of the measured values.

Transient Calculation

The comparison of the observed and calculated thermal hydraulic phenomena and system interactions is discussed in this section. Test 320201 was exactly like Test 3109AA except that a (scaled) 50-cm^2 leak orifice was used instead of a 10-cm^2 orifice. The purpose of the test was to investigate the effects of increased leak size on the SBLOCA behavior. Many of the same phenomena occurred during Test 320201 as occurred in Test 3109AA; however, the magnitude of the phenomena and the timing of major events were altered by the larger leak size. In the following discussion, the phenomena are explained in less detail than for Test 3109AA and the emphasis is placed on the analysis of the differences between the calculation and the test. The analysis is somewhat limited, however, by the fact that measured mass flow rates in the loops and downcomer are not available for this test. The discussion of this SBLOCA transient is again divided into four phases; these phases are defined with reference to Fig. 19, the primary and secondary pressure response. Phase one, subcooled decompression, covers the period from the start of the transient to approximately 20 s when the loop hot-leg fluid saturated and the depressurization rate was reduced. Phase two, spillover circulation, covers the period of continued depressurization and brief pressure stabilization from 20 s to 100 s when natural circulation was terminated in the loops. Phase three, loop stagnation, covers the period of depressurization from 100 s to approximately 1760 s in the test (1650 s in the calculation) when primary-system refill began. Phase four, refill, then extends to the end of the calculation at 2800 s. A summary of the major events for Test 3109AA is presented in Table II.

Phase One, Subcooled Decompression. Phase one is the first part of the transient from leak initiation until the saturation pressure was reached in the hot legs at 20 s. During phase one, the fluid in the primary system was subcooled liquid, and the primary-system pressure decreased rapidly as the liquid expanded as a result of the leak

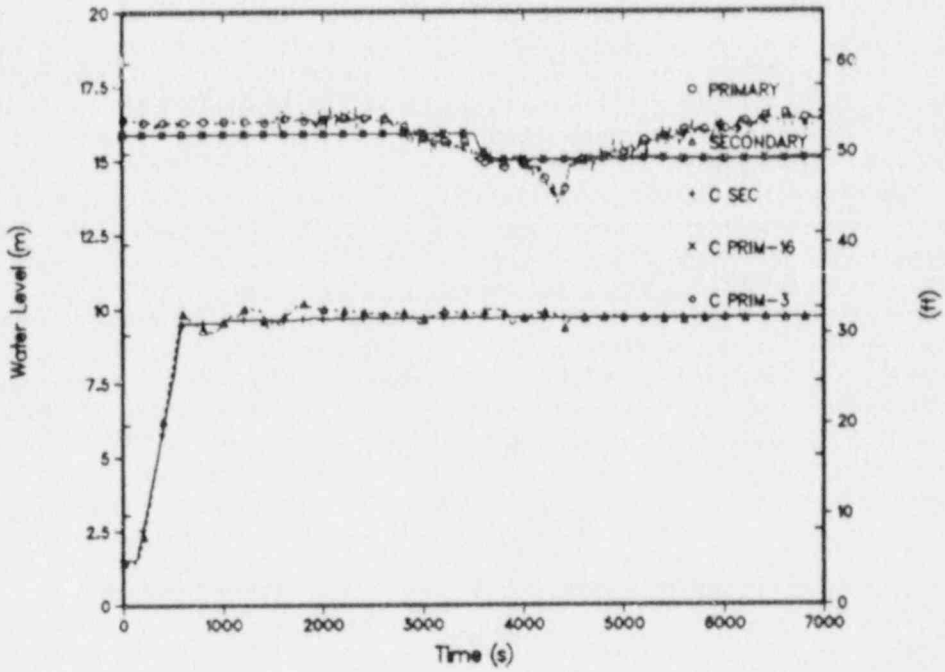

Fig. 18.
Test 3109AA broken looop SG collapsed liquid levels.

TABLE II
EVENT TABLE FOR TEST 20201

Test Time (s)	Calculation Time (s)	Event Description
0.0	0.0	Start transient break initiation.
20.0	20.0	Hot legs saturate.
40.0	38.0	Pressurizer level drops to 0.3048 m (1.0 ft), core power ramp, HPI RVVV automatic control initiated, RVVV first opens, SG secondary level reset.
100.0	100.0	Loop flows terminate.
1760.0	1650.0	Beginning of refill.
	2800.0	Calculation terminated.

flow. At the end of phase one, the primary-system depressurization rate was reduced by flashing of the liquid in the hot legs.

At the beginning of the transient, the primary system was in steady state single phase natural circulation, and the test was initiated at time zero by opening a scaled 50 cm^2 leak in the B1 CL just downstream of the HPI injection port. This caused a sharp reduction in the primary-system pressure (Fig. 19) and a rapid increase in the leak flow (Fig. 20). The leak flow in the experiment exceeded the capacity of the leak flow meter for the first 170 s (Ref. 3); Fig. 20 indicates a constant measured value of 0.43 kg/s during this period. Figure 21, however, shows good agreement between the measured and calculated primary-system mass inventories during phase one.

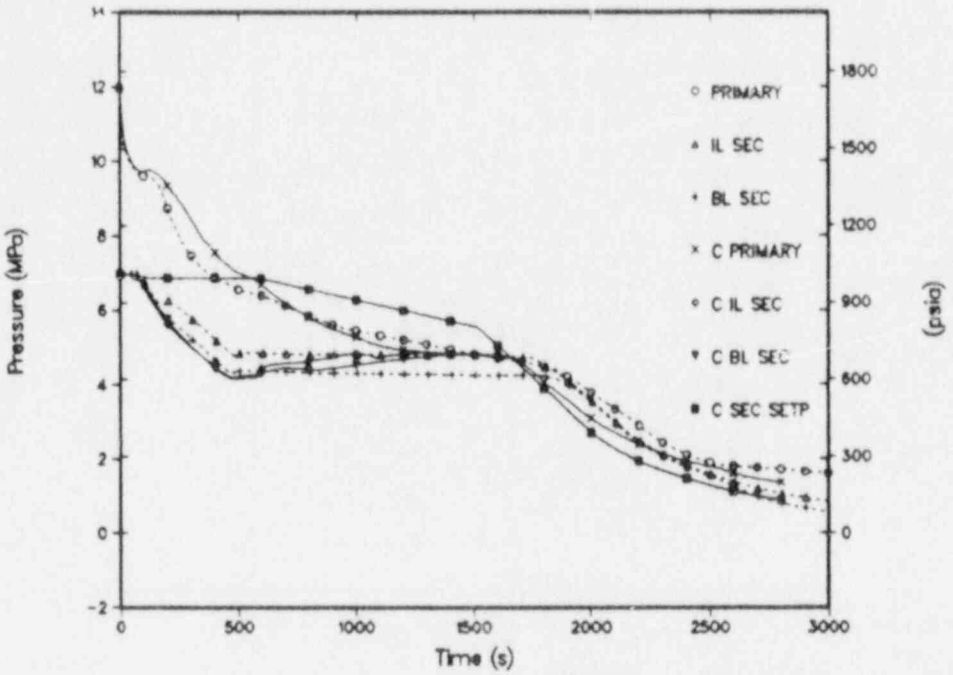

Fig. 19.
Test 320201 primary and secondary pressures.

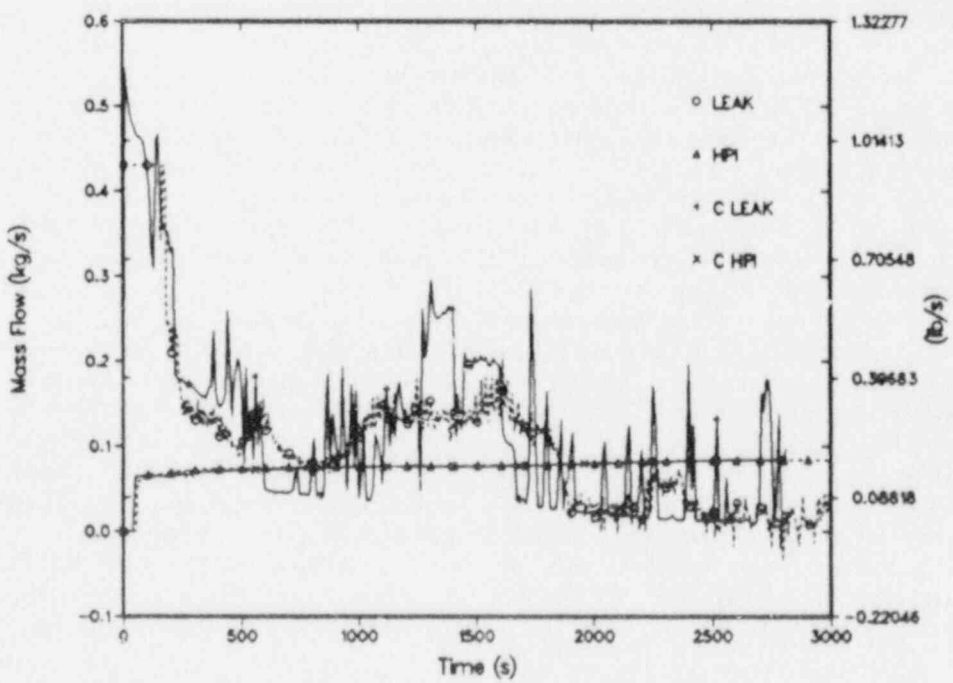

Fig. 20.
Test 320201 CL leak and HPI flows.

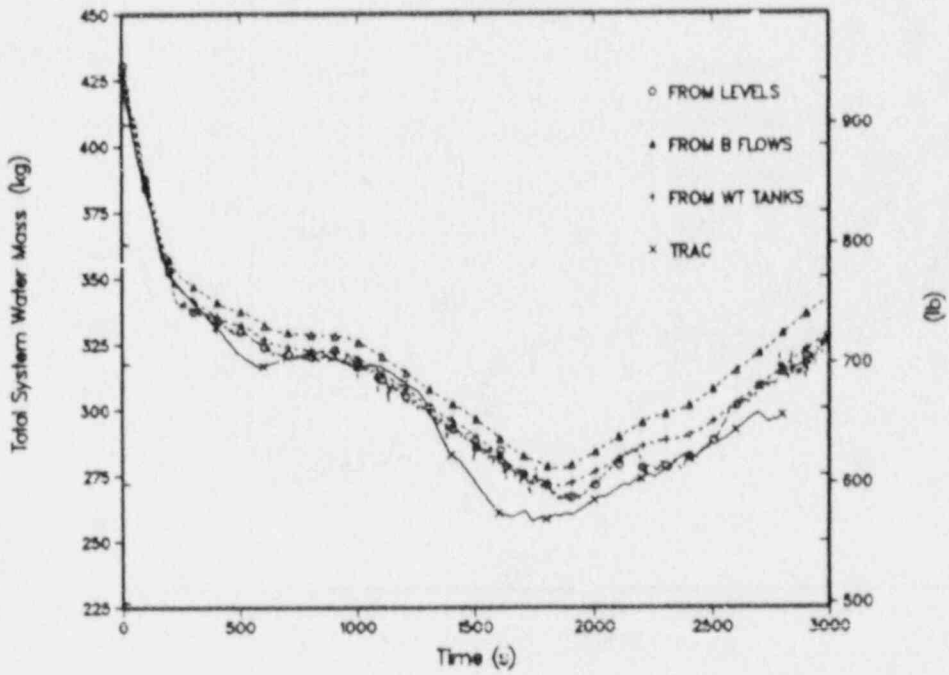

Fig. 21.
Test 320201 primary system water mass.

Phase one was terminated at approximately 20 s in both the test and in the calculation when the saturation pressure was reached in the hot legs. Figure 19 shows that the primary-system depressurization rate was reduced at this time as a result of flashing in the hot legs. Because of the increased leak size in Test 320201, phase one ended before the 0.3048 m (1 ft) pressurizer low-level trip had occurred in either the test or the calculation.

Phase Two, Spillover Circulation. Phase two covers the brief period of spillover circulation in the loops after the first saturation of loop fluid occurred in the hot legs. During phase two, the natural-circulation flow in each loop quickly coasted down as the hot-leg levels receded from the U-bends. Also during phase two, the pressurizer level decreased to 0.3048 m (1 ft) and the control procedures for the core power, SG level and pressure control, and RVVVs were reset as described previously. Phase two extends to 100 s, when the flow in each loop was completely terminated by the uncovery of the hot-leg U-bends.

After the saturation of the intact-loop hot-leg fluid at the end of phase one, the liquid level in the intact-loop hot legs decreased (Fig. 22) because of continued flashing and the loop flows began to subside. In the calculation, the U-bend flows (Fig. 23) were approximately the same during phase two and both decreased to zero at 100 s. This same behavior apparently took place in the test, although the measured flows are not available. The AFW was started at 40 s in the test (38 s in the calculation) on pressurizer low-level trip. Figure 19 shows that after 40 s in the test, the SG pressures both fell at the same rate due to the AFW flow. The symmetric secondary response to the AFW flow in the test during phase two indicates that the loop flows were also symmetric in the test. Therefore, it is concluded that the spillover flows in the test were in good agreement with the calculated spillover flows.

When the loop flows were interrupted at the end of phase three at 100 s, SG heat transfer was lost and Fig. 19 shows that the primary-system pressure briefly stabilized in both the test and the calculation. The agreement between the measured and calculated primary pressures during phase two is further evidence that the spillover loop flows were calculated correctly.

Phase Three, Loop Stagnation. Phase three is the period of stagnated natural-circulation flow in the loops after the final spillover in the U-bends. During phase three, the primary was depressurized by BCM heat transfer which began in both loops during the SG refill. Also during phase three, heat transfer in the broken-loop SG affected the draining rate of liquid through the primary side of the broken loop SG. This draining then influenced the leak site

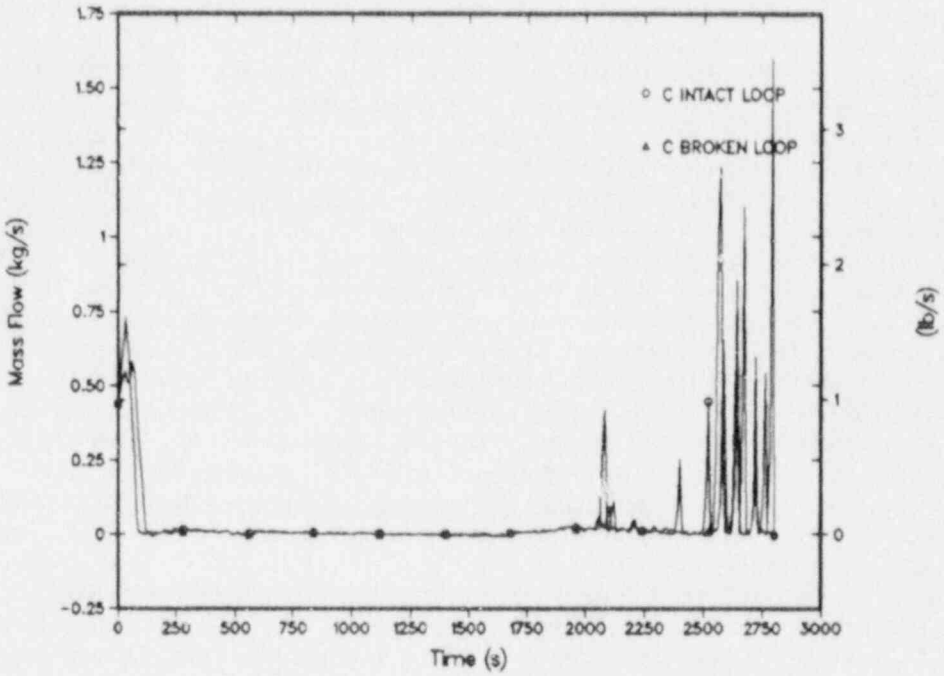

Fig. 22.
Test 320201 hot leg collapsed liquid levels.

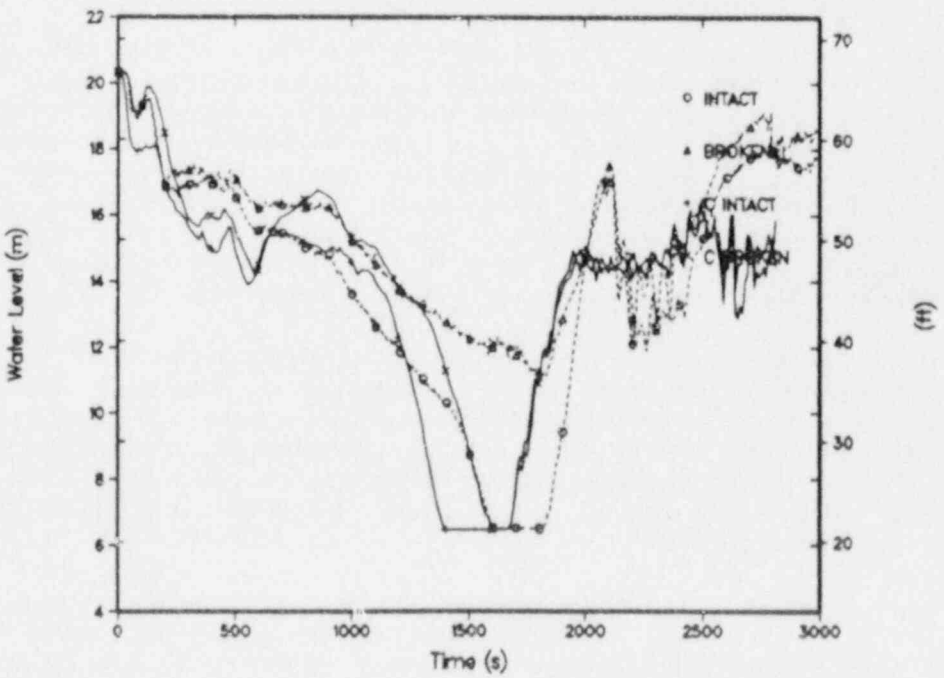

Fig. 23.
Test 320201 calculated hot leg U-bend mass flows.

which began in both loops during the SG refill. Also during phase three, heat transfer in the broken-loop SG affected the draining rate of liquid through the primary side of the broken loop SG. This draining then influenced the leak site fluid conditions and the leak flow rate. Phase three ended at 1760 s in the test and 1650 s in the calculation when AFW was restarted in the intact loop and the primary-system depressurization rate was increased.

At the beginning of phase three, the SG refill which was started on the low-level pressurizer trip in phase two, was still in progress. Figures 24 and 25 show that in both the test and the calculation the SG primary levels fell below the 15.48 m (50.8 ft) AFW elevation before the secondaries were refilled. This occurred at approximately 170 s in the intact loop and 190 s in the broken loop. At these times condensation (BCM) began in the SG primaries. The BCM heat transfer was relatively large because of the high AFW flows during the SG refill. Fig. 19 shows that the primary system depressurized rapidly in both the test and the calculation.

The magnitude of the BCM heat transfer in the calculation was apparently too low in the intact loop. Figure 19 shows that after BCM started in the intact loop at 170 s, the calculated secondary pressure in the intact loop continued to decrease whereas the measured value briefly increased. Figure 19 also shows that the primary depressurization rate at this time was too low in the calculation, further evidence of insufficient primary-to-secondary heat transfer. At the same time, Fig. 24 shows that the calculated primary-side level was below the measured level in the intact-loop SG indicating that the condensing surface area at the inner tube surfaces was greater in the calculation. This indicates that the BCM heat transfer in the intact loop was underpredicted because the effects of the BCM were less pronounced in the calculation while the condensation surface area available was greater in the calculation.

The BCM during phase three was briefly interrupted at the end of SG refill when the AFW in each loop was terminated to transfer the AFW controllers to the constant-level-control mode as described previously. The duration of the AFW termination and the subsequent measured AFW flow until the constant SG levels were achieved in the test were used as boundary conditions in the calculation. Figure 19 shows that when the AFW flow was off from 490 to 575 s, the depressurization rate was reduced in both the test and the calculation. When the AFW flow was restarted and the BCM resumed at 575 s, the subsequent depressurization (Fig. 19) was more rapid in the calculation because the SG primary levels (Figs. 24 and 25) were lower in the calculation at this time. These levels were lower in the calculation because the calculated leak flow (Fig. 20) was generally higher than in the test before 575 s and the primary system inventory (Fig. 21) was lower in the calculation.

The AFW termination from 490 s to 575 s affected other system parameters both in the test and in the calculation. Figure 25 shows that when the AFW was off, the liquid receded faster in the broken-loop SG primary because the vapor above was not being cooled by the AFW. The increased liquid flow from the broken-loop SG primary then fed the leak with colder fluid causing an increase in the measured and calculated leak flows (Fig. 20) during this period.

The draining of liquid from the SG primaries was also affected by the primary-to-secondary heat transfer after AFW flow was terminated at approximately 1200 s when the 9.63 m (31.6 ft) level set point was achieved (Figs. 24 and 25). The draining behavior after this time differed between the test and the calculation because of differences between the measured and calculated SG secondary pressures. In the test, the intact-loop SG pressure increased at 170 s during the BCM as described above, and afterward, the intact-loop SG pressure was higher than the broken-loop SG pressure. Consequently, the saturation temperature difference between the primary and SG secondary was higher in the broken loop, and there was more heat transfer from the primary to the broken loop SG during phase three in the test. Since the fluid in the intact-loop SG primary had less heat loss to the secondary, flashing and draining occurred faster in the intact-loop SG primary in the test, and Fig. 24 shows that the intact-loop SG primary drained faster after 1200 s.

In the calculation, the SG secondary pressures (Fig. 19) increased gradually during phase three as a result of the insufficient heat or steam losses in the model secondary discussed earlier. The intact-loop SG secondary pressure increased slightly faster than the broken loop because of small differences in the primary levels and primary-to-secondary heat transfer. After 1200 s in the calculation, both SG primary levels fell rapidly with the intact-loop SG level falling slightly. The SG primary-level decrease was more uniform in the calculation than in the test because the SG secondary pressures were closer to each other in the calculation. In both the test and the calculation, the draining of the SG primaries supplied the leak with cold fluid, resulting in increased leak flow after 1200 s (Fig. 20).

Phase three was terminated at 1760 s in the test and at 1650 s in the calculation when the primary pressure decreased to the highest SG secondary pressure and the blowdown mode of secondary pressure control was started. Phase three ended earlier in the calculation because of the gradual secondary pressure increase after AFW was terminated in the calculation, and because the primary-system depressurized more rapidly in the calculation after AFW was restarted at the end of SG refill.

Phase Four, Refill. Phase four covers the period beginning with the SG secondary blowdown until the end of the calculation at 2800 s. BCM heat transfer was reestablished in both SGs at the beginning of phase four, and

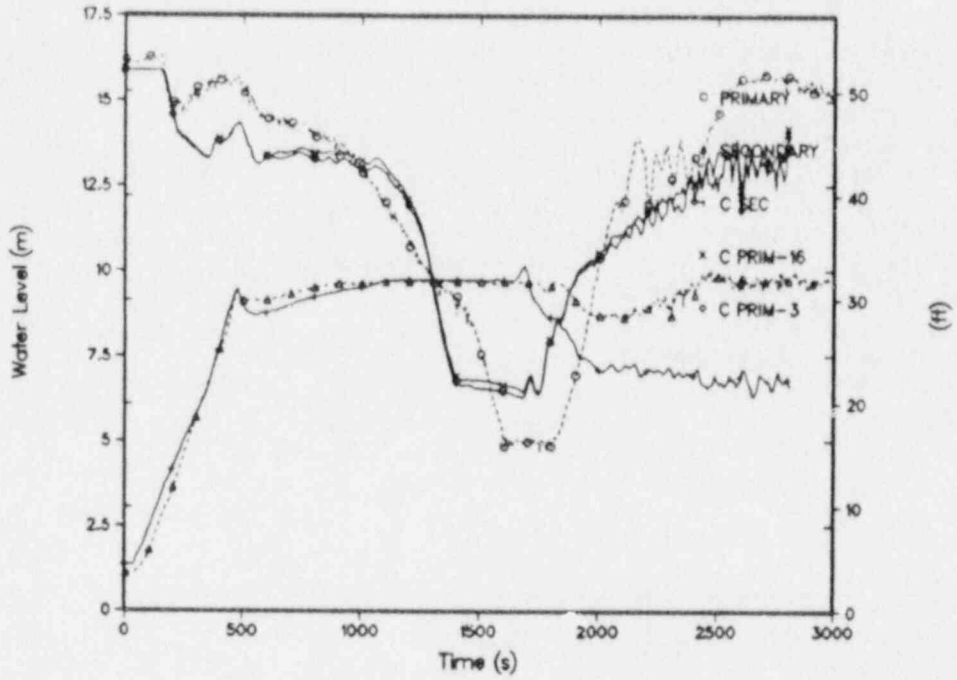

Fig. 24.
Test 320201 intact loop SG collapsed liquid levels.

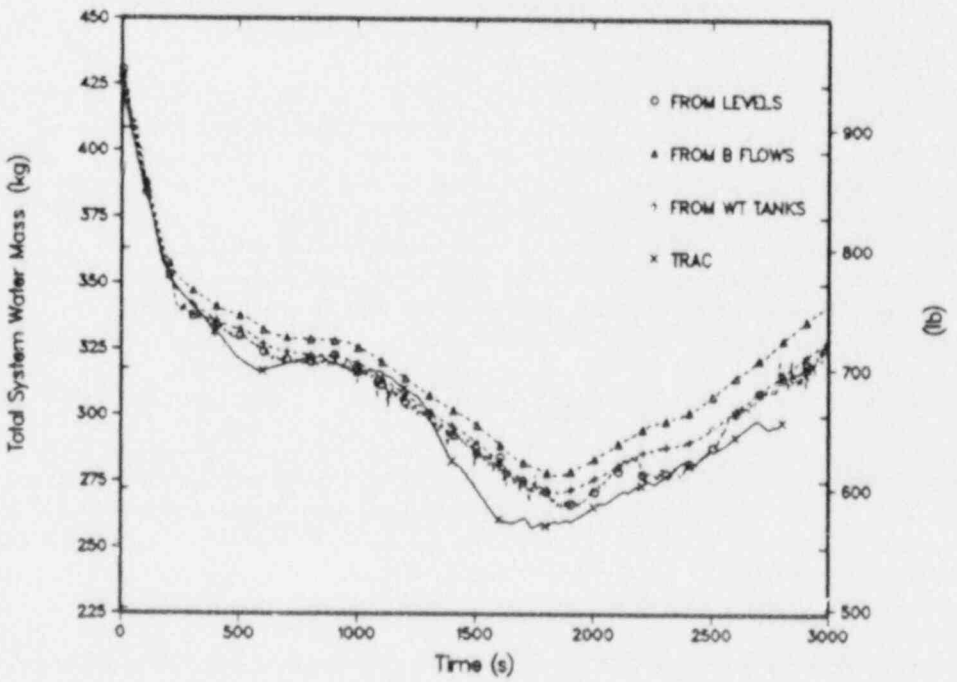

Fig. 25.
Test 320201 broken loop SG collapsed liquid levels.

CFT was actuated on low pressure and fluid was discharged from the CFT into the upper downcomer. The calculation was terminated at 2800 s because at this time it was evident that the point of minimum primary system inventory had been surpassed.

Phase four began at 1760 s in the test and 1650 s in the calculation when the primary-system pressure (Fig. 19) decreased to the highest SG secondary pressure and the pressure control for both secondaries was switched into the 5.246×10^{-3} MPa/s (50 psi/min) blowdown mode. AFW flow was then restarted in both SGs to maintain the secondary level at the 9.63 m (31.6 ft) set point, and BCM heat transfer was reestablished since the SG primary levels (Figs. 24 and 25) were well below the AFW injection elevation. The primary depressurization rates were increased at these times in the test and the calculation (Fig. 19), causing the measured and calculated leak flows to fall below the HPI flows (Fig. 20). The calculated leak flow in Fig. 20 showed oscillations; the peaks of these oscillations corresponded to brief periods when the fluid at the leak site was subcooled. This difference between the measured and calculated leak flows probably resulted from differences in the CL flows. The integrated leak flow comparison was reasonable, however, as indicated by Fig. 21, which shows that the calculated refill rate during phase four compared well with the observed refill rate.

Figures 24 and 25 show that the measured and calculated SG secondary levels decreased from the 9.63 m (31.6 ft) set point at the beginning of phase four. The level decrease was caused by entrainment of the AFW liquid by the upward steam flow in the secondaries. The entrainment of the AFW while the secondaries were in the blowdown mode prevented the AFW from effectively controlling the secondary levels. This three-dimensional phenomenon was modeled with one-dimensional components in the calculation. Differences between the magnitude of the phenomenon the test and in the calculation are difficult to isolate because the steam flow measurements did not provide reliable data after the AFW was entrained into the steam lines (Ref. 3).

As the secondary pressures continued to decrease during phase four in the test, the SG blowdown depressurization was limited by the relief capacity of the secondary pressure control valves. Figure 19 shows that when the secondary pressures decreased below approximately 2.758 MPa (400 psi), the 5.246×10^{-3} MPa/s (50 psi/min) depressurization rate was no longer achieved. This behavior was modeled in the calculation by using the measured SG depressurization rate for the ATOG set point when the secondary pressure was below 2.758 MPa (400 psi). Figure 19 shows that the primary pressure followed the decreasing secondary pressures during phase four in both the test and the calculation.

Figure 26 shows that the CFT was actuated at 1865 s in the test and at 1755 s in the calculation when the primary system pressure decreased to 4.48 MPa (650 psia). The injection of liquid from the CFT into the upper downcomer enhanced the refilling of the primary (Fig. 21) which was already in progress at these respective times in the test and the calculation. The measured and calculated CFT levels were approximately the same since the primary depressurization rates were nearly the same below 4.48 MPa (650 psi).

The differences between Test 320201 and the posttest calculation discussed above were very similar to the differences noted for Test 3109AA. Again, there was evidence that the BCM heat transfer was too low in the calculation. This difference occurred during phase three in the intact-loop SG. Differences between the measured and calculated leak flows occurred over most of the 3000-s calculational period. These differences could be caused by deficiencies in the TRAC-PF1/MOD1 critical flow model, or by differences in the measured and calculated leak upstream conditions. To further isolate the cause of the leak flow differences would require measured data for the leak upstream pressure and the broken loop CL flow rates. The primary-system mass inventory comparison, however, indicates that the integrated leak flow was calculated correctly when the primary pressure was calculated correctly. Finally, the results for Test 320201 also indicate that the secondary heat or steam losses were too low in the TRAC-PF1/MOD1 input model. This shortened the duration of phase three in the calculation. Despite these differences, the overall comparison of the measured and calculated parameters for Test 320201 was reasonable.

CONCLUSIONS

The comparison of measured and calculated parameters for MIST Tests 3109AA and 320201 has shown that the physical phenomena which governed the course of these transients were also predicted in the calculations. The overall agreement between the tests and the calculations was reasonable: the major trends of the data were predicted correctly, although TRAC values were frequently outside the range of data uncertainty because of minor code/model deficiencies. With reasonable agreement, valid conclusions should still be reached if the code is used in similar applications.

Specific differences between measured and calculated parameters can be attributed to one of three categories of factors that can affect the calculated results. First, uncertainty in the data necessary to fully describe the facility and test operation can lead to uncertainty in the calculated results. Second, approximations in the code input model such as the resolution of the nodalization, time-step size, or the selection of a one-dimensional component vs a

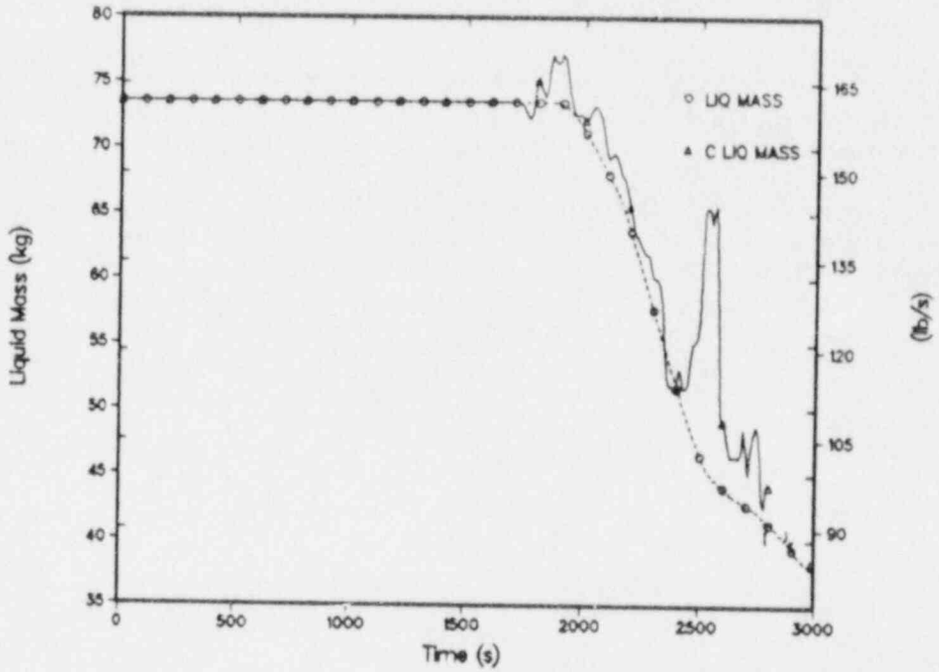

Fig. 26.
CFT mass.

three-dimensional component can affect calculated parameters. Third, the validity of the correlations and models in the code may affect the code calculations. Before conclusions can be drawn from code/data comparisons about the third category, code correlations and models, factors in the first two categories must be ruled out as possible causes for the differences between measured and calculated parameters.

Differences between MIST Tests 3109AA and 320201 were caused by factors from each category. Uncertainty in the secondary heat and steam losses in the MIST facility led to the inaccurate modeling of these losses. The losses were estimated to be 1.5 kW per steam line, which was not sufficient energy loss. This caused the secondary pressures in both calculations to increase when the measured remained constant. As a result, the duration of phase three was too short in each calculation and the phase four phenomena were shifted forward in time. Since both the 10-cm^2 calculation and the 50-cm^2 calculation were affected, it can be concluded that steam line heat-loss modeling is important for a wide range of SBLOCA leak sizes in the MIST facility. In general, if BCM is calculated to occur at the wrong time, the magnitude of the calculated BCM can be affected since the calculated SG primary levels generally vary with time. This, however, does not appear to be the case for the Test 3109AA and 320201 calculations.

The calculated results for both experiments were found to be very sensitive to the representation of the boundary conditions in the TRAC-PF1/MOD1 input model. In order to calculate the BCM phenomena as closely as possible, it was necessary to input the measured AFW flow for a period of several hundred seconds after SG refill. In the calculation for Test 3109AA, it was found that a subcooled leak flow multiplier of 0.87 was needed to accurately calculate the subcooled leak flow and phenomena that occurred before BCM.

Correlations and models in the code that cause differences between the test and calculation are often difficult to identify among the many factors that can affect the calculated parameters. The results of the Test 3109AA calculation, however, indicated that the TRAC-PF1/MOD1 critical flow model does not properly account for changes in upstream subcooling. Conclusions about the critical flow model cannot be drawn from Test 320201 because, with the higher leak flow, uncertainty in the frictional pressure losses upstream of the leak creates uncertainty in the leak upstream pressure during the test. Finally, the results indicated that the calculated BCM heat transfer was too low for both experiments. This could be caused by a heat-transfer correlation error, SG nodalization that was too coarse, or by an incorrectly determined flow regime during the calculation.

The code/data analyses presented herein constitute part of an assessment matrix for the performance of the TRAC-PF1/MOD1 code, which will ultimately be used to extrapolate data from the MIST facility to full-scale plant behavior.

REFERENCES

1. Safety Code Development Group, "TRAC-PF1/MOD1: An Advanced Best-Estimate Computer Program for Pressurized Water Reactor Thermal-Hydraulic Analysis," Los Alamos National Laboratory report LA-10157-MS, NUREG/CR-3858 (July 1986).
2. "MIST Test Specifications," Babcock & Wilcox document BAW-1894 (October 1985).
3. J. R. Gloudemans, *et al.*, "Group Report, MIST Test Group 32, Leak-HPI Configuration," Babcock and Wilcox document BAW-1964 (June 1987).

Two-Phase Scaling Distortions

Z.Y. Wang and K. Almenas
Chemical & Nuclear Engineering Department
University of Maryland
College Park, Maryland 20742

ABSTRACT

A methodology is developed to evaluate the limitations of the similarity laws currently used for reactor thermal-hydraulics. It is shown that the currently used similarity laws should be used with caution. On the other hand, although the scalability of the system simulation code remains to be investigated, the code is a scaling methodology that has much more potential than the similarity laws. In the paper, the distortions generated by scaling laws are called Scaling Law Distortions (SLD). It is argued that the SLD may not be equal to the actually existing Total Distortions (TD). The difference between the SLD and TD represent the limitations of the similarity laws in scaling application. Because in reality the TD cannot be experimentally obtained, the TD is approximated by employing the system simulation code calculations. This is because the system simulation code is the only analytical tool that can best simulate a system characterized by complex cause-and-effect interrelationships between flow phenomena, whereas the similarity laws (based on only a single set of dimensionless numbers) do not consider these interrelationships. It is shown that an analysis regarding scaling adequacy based on TD's can at times reverse the analysis based on SLD's. The vertical hot leg of a B&W type Pressurized Water Reactor is chosen as the demonstration problem. The current RELAP5/MOD2 code is used to calculate the TD's.

I. INTRODUCTION

Over the past two decades of thermal-hydraulic research related to water reactor safety, two independent approaches for the study of scaling have evolved: the similarity laws and the system thermal-hydraulic simulation codes. The similarity laws are scaling criteria which provide direct extrapolation of the small-scale test results to the prototype. The similarity laws which have wide influence include those developed by Carbiener[1], Nahavan-

di[2] and Ishii[3]. Currently, Ishii's similarity laws represent the 'state-of-the-art' similarity laws. In general, they are developed on the basis of a single set of similarity parameters which are derived by non-dimensionalizing the governing mathematical equations at a chosen location of the system. Therefore, they are single values and are known 'a priori'. On the other hand, the system simulation codes are computer programs which predict the scenario (trajectory) of a sequence of thermal-hydraulic phenomena (events) after some controllable actions. The computer code incorporates a set of mathematical equations and a large number of empirical correlations. The 'state-of-the-art' system codes include RELAP5, TRAC, RETRAN2 and etc.

Although the similarity laws have been widely used in thermal-hydraulic transient, their limitations have also been recognized[4.5]. It is understood that the similarity laws cannot provide a satisfactory and quantitative prediction of the prototypical reactor thermal-hydraulic transients. That is the case because the similarity laws have a crucial limitation. They do not consider the complex cause-and-effect inter-relationship of the phenomena which are governed by local conditions in a two-phase flow system. The code does consider this interrelationship since the conditions in one segment of the thermal-hydraulic system become boundary conditions for the adjoining segments. In this manner, local conditions exert an integral influence. Consequently, the code is a promising scaling method which has the potential for satisfactorily predicting the prototypical reactor thermal-hydraulic transients.

The above observations lead to the following two questions:

1. What are the limitations of the similarity laws?
2. What is the potential of the system code to predict the complex cause-and-effect inter-relationship of flow phenomena in a two-phase fluid system?

Currently, these two questions have been discussed and analyzed extensively. For many years, the code assessment program[6,7] has been trying to answer the second question. Notwithstanding large efforts, only qualitative measures of accuracy have been proposed[8]. On the other hand, because of the simplicity of the similarity laws (i.e. only a single set of dimensionless parameters is needed), they continue to be used[9.10], despite the already recognized limitations of the similarity laws.

Recently, Larson and Dimenna[11] attempted to answer the second question (still in a qualitative manner) by first applying the code to a simplified problem 'for which similitude criteria can be established' and then examining the code results 'to determine the ability of the code to preserve the expected scaling relationships for different scales of the same problem.' The underlying hypothesis of this approach, though it is not stated, is that the similarity laws are capable of preserving thermal-hydraulic phenomena in a scaled-down system. This hypothesis is questionable.

Wang[12] has also investigated this important subject in a quantitative manner. The distortions (called the Scaling Law Distortions, SLD) are evaluated for four potential sets of similarity laws. It is then argued that the SLD can not be equal to the actually existing Total Distortion (TD). The difference between the SLD and TD represent the limitations of the

similarity laws in scaling application. Because in reality the TD cannot be experimentally obtained, a methodology is therefore developed to evaluate the TD. The essence of this methodology is to approximate the TD by employing the system simulation code calculations, i.e., RELAP5 and TRAC codes. It is shown that an analysis regarding scaling adequacy based on TD's can at times reverse the analysis based on SLD's. Consequently, the currently used similarity laws should be used with caution. On the other hand, although the scalability of the system simulation code remains to be investigated, the code is a scaling methodology that has much more potential than the similarity laws.

In the following sections, the scaling methodology and its relevant concepts proposed in Reference 12 are presented. A sample problem is used to illustrate the difference between the SLD's and TD's.

II. SCALING CONCEPTS AND METHODOLOGY

In order to perform a systematic mathematical analysis of scaling, it is first necessary to define a consistent terminology. This includes already familiar concepts and terms with new shades of meaning to cope with the methodology adopted in this study. The scaling concepts described include:

1. Scaling scheme
   1.1 Assumption
   1.2 Requirement
2. Distortion
   2.1 Scaling Law distortion (SLD)
   2.2 Total distortion (TD)
3. Scaling Approach
   3.1 Geometric-Scaling approach
   3.2 Pressure-Scaling approach
   3.3 Combined-Scaling approach
4. Similarity Parameter
   4.1 Dimensionless Variable
   4.2 Reference Similarity Parameter
   4.3 Local Similarity Parameter

A scaling scheme represents a set of similarity laws which, in the literature, are also called requirements. A scaling scheme includes "Assumptions" and "Requirements". These two concepts distinguish "controllable" from "uncontrollable" conditions. An "Assumption" is a condition of a dependent variable which is assumed to be true in the model, but which is beyond our control (e.g. time and local thermodynamic conditions). A "Requirement" is a condition which can be imposed on the model (e.g. geometric scale factors and reference conditions).

"Distortion" is a deviation from "Similarity". Two terms are required to quantify distortions. These terms are based upon the distinction of imposed and assumed conditions.

The Scaling Law Distortion (SLD) is the distortion quantified by the classical single parameter similarity laws. Note, by definition, SLD requires that "Assumptions" defining a scaling scheme be accurate. The Total Distortion (TD) is the distortion that is present in an actual scaling situation and thus the "Assumptions" might not be accurate..

An important distinction between the SLD and the TD should be noted. The SLD is evaluated on the basis of fluid conditions which are determined locally and in an isolated fashion. The TD can not be evaluated in this manner, since it includes distortions contributed from phenomena which occur simultaneously in other locations of the flow system (i.e., the inter-dependent effect). Another way of phrasing it would be: the SLD is evaluated for boundary conditions which are assumed to be known, the TD recognizes that, in a complex flow system, boundary conditions for isolated region of the flow system can not be rigorously established.

Note that the distortions evaluated by using a system simulation code can approximate the TD for actual scaling situation. The system simulation code has the potential for calculating the non-controllable conditions within a two-phase fluid system. The currently used reactor transient scaling approach evaluates distortion which are identical to the definition of SLD.

Differences of geometry and fluid properties existing between the model and prototype define three possible scaling approaches. The Geometric-Scaling approach employs the Requirement and Assumption that the fluid properties are preserved. Models employing this approach will have aspect ratios different from those of the prototype but will strive to have identical fluid conditions. This is the conventional full pressure scaling approach in which the distortions are generated only by the scaled-hardware. In the Pressure-Scaling approach, the model and the prototype have identical geometric dimensions but different operating conditions. The Combined-Scaling approach, as the name implies, employs both different geometry and fluid properties in the model and prototype. The individual distortion resulting either from the Geometry- or the Pressure-scaling approach may compensate or amplify each other in the Combined-Scaling approach.

A "Similarity Parameter" is a nondimensional product of dimensional variables[13]. In Ref. [12], it is shown that the Similarity Parameter includes three types of nondimensional parameters (See Table 1). These are:

The Dimensionless Variable - A Similarity Parameter which is the ratio of a dependent variable to its reference value

The Reference Similarity Parameter - A Similarity Parameter which contains only reference variables.

The Local Similarity Parameter - A Similarity Parameter which contains reference variables as well as coefficients of the constitutive correlations (i.e. f_f, f_g, C_D, a_{gf}, Γ_g and etc.). Constitutive correlations are functions of dependent variables.

From the above definitions, it follows that since Reference Similarity Parameters can be rigorously specified, they will incorporate only SLD, while other groups can have both SLD and TD. The goal of a scaling scheme is to achieve similarity of the Dimensionless Variables by imposing the controllable requirements on the Reference Similarity Parameters. The similarity of Local Similarity Parameters can only be approximated as much as possible, however, cannot be accurately controlled. Mathematically, both the SLD and TD are defined as:

$$\text{SLD or TD} = \frac{[\text{Similarity Parameter}]^m}{[\text{Similarity parameter}]^p} \qquad (1)$$

METHODOLOGY

The purpose of this study is to demonstrate the significant differences between SLD's and TD's. The approach used includes the following steps:

1. A set of similarity parameters including dimensionless variables, reference and local similarity parameters are derived. The two-fluid momentum equations used in the RELAP5/MOD2 code are employed for this step
2. A set of scaling laws including 'Assumptions' and 'Requirements' of time, geometry and thermodynamic conditions are chosen.
3. A range of scaled-models and the SLD's are evaluated by assuming the 'Assumptions' are accurate.
4. RELAP5/MOD2 models are developed for each of the scaled-model.
5. The TD's of the dimensionless variables are quantified for each of the hypothetical models. This is done by performing RELAP5 calculations for the geometric-, pressure- and the combined-scaling approaches.
6. The calculated SLD's and TD's are compared.

III. SIMILARITY PARAMETERS

The Similarity Parameters are derived from the two-fluid continuity and momentum equations used in the RELAP5/MOD2 code. The two-fluid equations are complex, therefore, several different forms of Similarity Parameters can be derived. The primary criteria guiding the derivations are: to reduce the number of constituent variables without loosing physical information; to introduce those Similarity Parameters which dominate the complex phenomena being studied, and to obtain similarity parameters in such a form that contributions of system distortion from various constitutive correlations are readily distinguished.

A description of the two-fluid equations and the derivation steps is presented in the RELAP5/MOD2 code manual[14] and Ref. [12] respectively. Table 1 lists the derived Similarity Parameters in three groups.

Table 1: List of Similarity Parameters

Similarity Parameters		Equations
Dimensionless Variables		v_g^*, ρ_g^*, ρ_f^*, ρ^* v_f^*, α_g^*
Reference Similarity Parameter	Vapor inertia No. (N_{gm})	$\frac{\alpha_{go}\rho_{go}v_{go}^2}{F_{mo}}$
	Liquid inertia No. (N_{fm})	$\frac{\alpha_{fo}\rho_{fo}v_{fo}^2}{F_{mo}}$
	Mixture Froude No. (F_{rm})	$\frac{\rho_o g L_o}{F_{mo}}$
	Slip Ratio (S_o)	$\frac{v_{go}}{v_{fo}}$
	Density Ratio ($C_{\rho o}$)	$\frac{\rho_{go}}{\rho_{fo}}$
	Void Ratio ($C_{\alpha o}$)	$\frac{\alpha_{go}}{\alpha_{fo}}$

Local Similarity Parameter	Phase Change No. (N_{pch})	$\frac{(1-\alpha_{go})\Gamma_g L_o}{v_f \rho_g}$
	Liquid Wall Friction No. (F_{wf})	$\frac{f_\ell}{2}\frac{\alpha_{fo}\rho_{fo}v_{fo}^2}{F_{mo}}$
	Vapor Wall Friction No. (F_{wg})	$\frac{f_g}{2}\frac{\alpha_{go}\rho_{go}v_{go}^2}{F_{mo}}$
	Interface Drag No. (F_{id})	$\frac{a_{gf}C_D L_o v_{gfo}^2 \rho_{co}}{8F_{mo}}$
	Pressure Drop (N_{pd})	$\frac{\Delta P_o}{F_{mo}}$
	Interface Momentum Transfer No. (N_{im})	$\frac{\Gamma_g v_{gfo} L_o}{F_{mo}}$

* $F_{mo} = \alpha_{go}\rho_{go}v_{go}^2 + \alpha_{fo}\rho_{fo}v_{fo}^2$

The Reference Similarity Parameter includes two phasic Inertia Numbers (N_{fm}, N_{gm}), Mixture Froude Number (F_{rm}), Slip Ratio (S_0), Density Ratio ($C_{\rho 0}$) and Void Ratio ($C_{\alpha 0}$). They are related to Dynamic (N_{fm}, N_{gm}, F_{rm}), kinematic (S_0) and thermodynamic ($C_{\rho 0}$, $C_{\alpha 0}$) similarities of the reference conditions of the scaled system. The Phasic Inertia Numbers are the ratios of a phasic inertia force to the mixture inertia force and characterize the dynamic response of the two-fluid system. For transient conditions, they represent the important parameters which should be scaled. The Mixture Froude Number takes into account the effect of gravity. It is the ratio of the gravity force to the mixture inertia force.

The Local Similarity Parameter includes the Phase Change Number (N_{pch}), two Phasic Wall Friction Numbers (F_{wf}, F_{wg}), Interface Drag Number (F_{id}), Pressure Drop Number (N_{pd}) and Interface Momentum Transfer Number (N_{im}). The Phase Change Number is roughly equal to the void fraction change within a certain flow length. The F_{wf}, F_{wg} and F_{id} take into account the effects of the liquid, vapor wall friction and the interface drag respectively. They are equivalent to a correlation-determined factor multiplied by an inertia number. The correlation-determined factor can be a nonlinear or discontinuous function of the flow conditions. Thus, these factors can generate substantial distortions. The impact of these distortions on the overall two-phase flow system are then determined by their respective inertia numbers. The Pressure Drop Number (N_{pd}) takes into account the effect of pressure drop. It is not an independent parameter. Rather, it is a function of several similarity parameters. At steady state, N_{pd} can be approximated by a direct summation of F_{wf}, F_{wg}, F_{rm} and N_{im}.

IV. SCALING LAWS

Four types of potential scaling schemes are proposed. The definitions are based on the varying Assumptions or Requirements imposed on a) time and b) fluid property (i.e., pressure). They are:

1. The 'Time-Preserving, Property-Preserving' scheme (TPPP)
2. The 'Time-Scaled, Property-Preserving' scheme (TSPP)
3. The 'Time-Preserving, Property-Scaled' scheme (TPPS), and
4. The 'Time-Scaled, Property-Scaled' scheme (TSPS).

Table 2 lists the "Assumptions" and "Requirements" employed in the above four schemes respectively. Note that the characteristics of the two-phase flow system will change drastically in a "void-scaled" model. Therefore, the void fraction should be preserved for all schemes. In the two-phase flow system, the property of the (saturated) fluid is defined by two variables: the void fraction and pressure. Since the void fraction is preserved, the term "Property-Scaled" implies that only the pressure is scaled.

Table 2: Assumptions and Requirements for Four Scaling Schemes

Similarity Laws	Scheme param.	TPPP	TSPP	TPPS	TSPS
Requirements	L_0^R	λ	λ	λ	λ
	A_0^R	σ	σ	σ	σ
	p_0^R	1	1	p_0^R	p_0^R
	a_{g0}^R	1	1	1	1
	v_{f0}^R,	λ	$\sqrt{\lambda}$	λ	$\sqrt{\lambda}$
	v_{g0}^R	λ	$\sqrt{\lambda}$	λ	$\sqrt{\lambda}$
Assumptions	τ	1	$\sqrt{\lambda}$	1	$\sqrt{\lambda}$
	p^R	λ	1	p_0^R	p_0^R
	a_g^R	1	1	1	1
	v_f^R	λ	$\sqrt{\lambda}$	λ	$\sqrt{\lambda}$
	v_g^R	λ	$\sqrt{\lambda}$	λ	$\sqrt{\lambda}$

When the concept of geometric similarity is employed, both the length and area scale factors should be constant at homologous points of the model, i.e., $A_0^R = \sigma$, $L_0^R = \lambda$. When the kinematic similarity concept is employed, both the local and reference phasic velocity scale factors of the two-phase fluid should be constant at homologous points of the model, i.e., $v^R_{f0} = v^R_{g0} = v^R_f = v^R_g = \lambda / \tau$.

To satisfy the dynamic similarity concept, in addition to the kinematic and geometric similarity, the inventory distribution should be preserved. Thus, both the Density Ratio and Void ratio have to be preserved. This implies that the "Property-Scaled" schemes cannot achieve dynamic similarity because, by definition, the Density Ratio is distorted in the "Property-Scaled" schemes. However, it can be argued that at steady state the requirements of dynamic similarity concept can be relaxed, and thus this shortcoming can be overlooked.

V. THE SCALING LAW DISTORTIONS

The SLD's of Dimensionless Variables and Reference Similarity Parameters for each scaling scheme are listed in Table 3 and those of Local Similarity Parameters are presented in Table 4. They are obtained by assuming that the Assumptions of a scaling scheme are accurate and by imposing the Requirements on the similarity parameter. Detailed derivations and the analysis of their trends and magnitudes as functions of flow conditions are referred to Ref. [12]. A brief summary of the results are presented here.

The SLD's of all the Dimensionless Variables are equal to 1.0. This implies that by simply imposing certain scaled boundary conditions on the model the objective of the two-phase flow scaling can be met (i.e., similarities of the Dimensionless Variables can be achieved.). However, such a conclusion is not based on the TD's and is therefore premature.

The SLD's of Reference Similarity Parameters are generated by known differences between the model and prototype in the flow geometry and fluid pressure. The SLD's produced by geometry can be eliminated by reducing the model time scale (i.e., $t^R = \sqrt{\lambda}$). That is done in the two "Time-Scaled" schemes. On the other hand, the SLD's produced by pressure can be eliminated by preserving the fluid pressure at a location. This defines the two "Property- Preserving" schemes. As a result, the "Time-Scaled, Property-Preserving" scheme (TSPP) preserves all of the Reference Similarity Parameters, while the other three schemes retain SLD's.

The SLD's of Local Similarity Parameters include factors which are determined by constitutive correlations for all four scaling schemes except for the Pressure Drop Number. These factors include the phasic wall friction factors (f_f and f_g), interface area and drag (a_{gf} and C_D) and the vapor generation rate (Γ_g). In general, their contributions to the SLD's is

Table 3: The Scaling Law Distortions of Reference Similarity Parameters for Four Scaling Schemes

Similarity Parameter		Scaling Law Distortion			
		TSPS	TSPP	TPPS	TPPP
Dimensionless Variable	v_g^*, v_f^*, a_g^*	1.0	1.0	1.0	1.0
	ρ_g^*, ρ_f^*	1.0	1.0	1.0	1.0
Reference Similarity Parameter	N_{fm}	$\frac{E_{So}^*}{[1+C_{ao}C_{\rho o}]^R}$	1.0	$\frac{E_{So}}{[1+C_{ao}C_{\rho o}]^R}$	1.0
	N_{gm}	$\frac{C_{\rho o}^R E_{So}}{[1+C_{ao}C_{\rho o}]^R}$	1.0	$\frac{C_{\rho o}^R E_{So}}{[1+C_{ao}C_{\rho o}]^R}$	1.0
	Fr_m	$*\ E_{So}$	$**$ 1.0	$\frac{E_{So}}{\lambda}$	$\frac{1}{\lambda}$
	S_o	1.0	1.0	1.0	1.0
	$C_{\rho o}$	$(\frac{\rho_{go}}{\rho_{fo}})^R$	1.0	$(\frac{\rho_{go}}{\rho_{fo}})^R$	1.0
	C_{ao}	1.0	1.0	1.0	1.0

Note: * $E_{So} = (1 + C_{ao}C_{\rho o})^R/(1 + C_{ao}C_{\rho o}S_o^2)^R$

** $\tau = \sqrt{\lambda}$

Table 4: The Scaling Law Distortion of Local Similarity Parameters for Four Scaling Schemes

Similarity Parameters		Scaling Law Distortion			
		TSPS	TSPP	TPPS	TPPP
Local Similarity Parameter	N_{pch}	$\frac{\sqrt{\chi}\,\Gamma_g^R}{\rho_{go}^R}$	$\sqrt{\lambda}\ \Gamma_g^R$	$\frac{\Gamma_g^R}{\rho_{go}^R}$	Γ_g^R
	F_{wf}	$f_f^R\ SLD(N_{fm})$	f_f^R	$f_f^R\ SLD(N_{fm})$	f_f^R
	F_{wg}	$f_g^R\ SLD(N_{gm})$	f_g^R	$f_g^R\ SLD(N_{fm})$	f_g^R
	F_{id}	$(a_{gf}C_D)^R\lambda^2\ (\frac{\rho_{co}}{\rho_{fo}})^R\ SLD(N_{fm})$	$\lambda^2(a_{gf}C_D)^R$	$(a_{gf}C_D)^R\chi\ (\frac{\rho_{co}}{\rho_{fo}})^R\ SLD(N_{fm})$	$\lambda^2(a_{gf}C_D)^R$
	N_{pd}	$\frac{\Delta P_o^R\ SLD(N_{fm})}{\rho_{fo}^R\ \lambda}$	$\frac{1}{\lambda}$	$\frac{\Delta P_c^R\ SLD(N_{fm})}{\rho_{fo}^R\ \lambda}$	$\frac{1}{\lambda^2}$
	N_{im}	$\frac{\Gamma_g^R\sqrt{\lambda}\ SLD(N_{fm})}{\rho_{fo}^R}$	$\Gamma_g^R\sqrt{\lambda}$	$\frac{\Gamma_g^R\ SLD(N_{fm})}{\rho_{fo}^R}$	Γ_g^R

substantial.

The differences of pressure and geometry existing between the model and prototype both contribute SLD's to the correlation-determined factors (i.e., f_f, f_g, Γ_g). The "Time-Scaled" schemes cannot eliminate the SLD's produced by geometric differences by reducing the model time scale, although they can eliminate the SLD's for the Reference Similarity Parameters. The "Property- Preserving" schemes cannot eliminate the correlation-determined SLD's by preserving the model pressure.

Consequently, even when the "Assumptions" are accurate, none of the schemes can preserve the Local Similarity Parameters for any of the four schemes. For the most part, these SLD's are generated by the correlation-determined factors. They are in fact substantially larger than the SLD's of the Reference Similarity Parameters. A detailed evaluation of the SLD's presented in Ref. [12] shows that the "Time-Preserving, Property-Preserving" scheme yields the smallest range of SLD's of Local Similarity Parameters.

VI. SAMPLE PROBLEM FOR ANALYZING TOTAL DISTORTION USING THE RELAP5/MOD2 CODE

The sample problem chosen for this study represents the vertical hot leg of a B&W type Pressurized Water Reactor. The modeled vertical hot leg includes a vertical pipe and an inverted U-bend. This hot leg geometry is an open system which has two boundaries. The major task of the analysis is the determination of the TD of Dimensionless Variable at two locations (i.e., the top of the vertical pipe and the exit of the inverted U-bend) while imposing the scaled 'Requirements' at the two boundaries (i.e., inlet- and outlet-boundary). The TD's are evaluated on the basis of steady state calculations for the four potential scaling schemes (i.e., TPPP, TSPP, TPPS and TSPS). The RELAP5/MOD2 code is used.

The noding scheme employed for the RELAP5/MOD2 calculations shown in Fig. 1 consists of 12 control volumes. It includes the following features: 1. ten 'pipe volumes' (PIPE) for the vertical hot leg pipe, 2. three 'single volumes' (SNGLVOL) for the inverted U-bend, 3. two 'pipe volumes' (PIPE) for the downward pipe, 4. two 'time-dependent volumes' (TMDPVOL) for the vessel (source of fluid) and the steam generator (sink of fluid) respectively.

The two TMDPVOL-volumes are used to simulate a constant source of fluid (vessel) and a constant sink for the fluid (steam generator) respectively. The fluid conditions in a TMDPVOL are user-specified. The incoming or outgoing fluid is determined by the difference in the pressure between the TMDPVOL and the adjacent volume.

In the calculations, the reference pressure and void fraction of a system are specified in the source-TMDPVOL. A reference fluid velocity at the inlet of the pipe is determined by the difference in pressure between the source- and sink-volumes. Therefore, one pressure is specified in the sink-TMDPVOL in order to obtain a reference liquid velocity at the inlet of

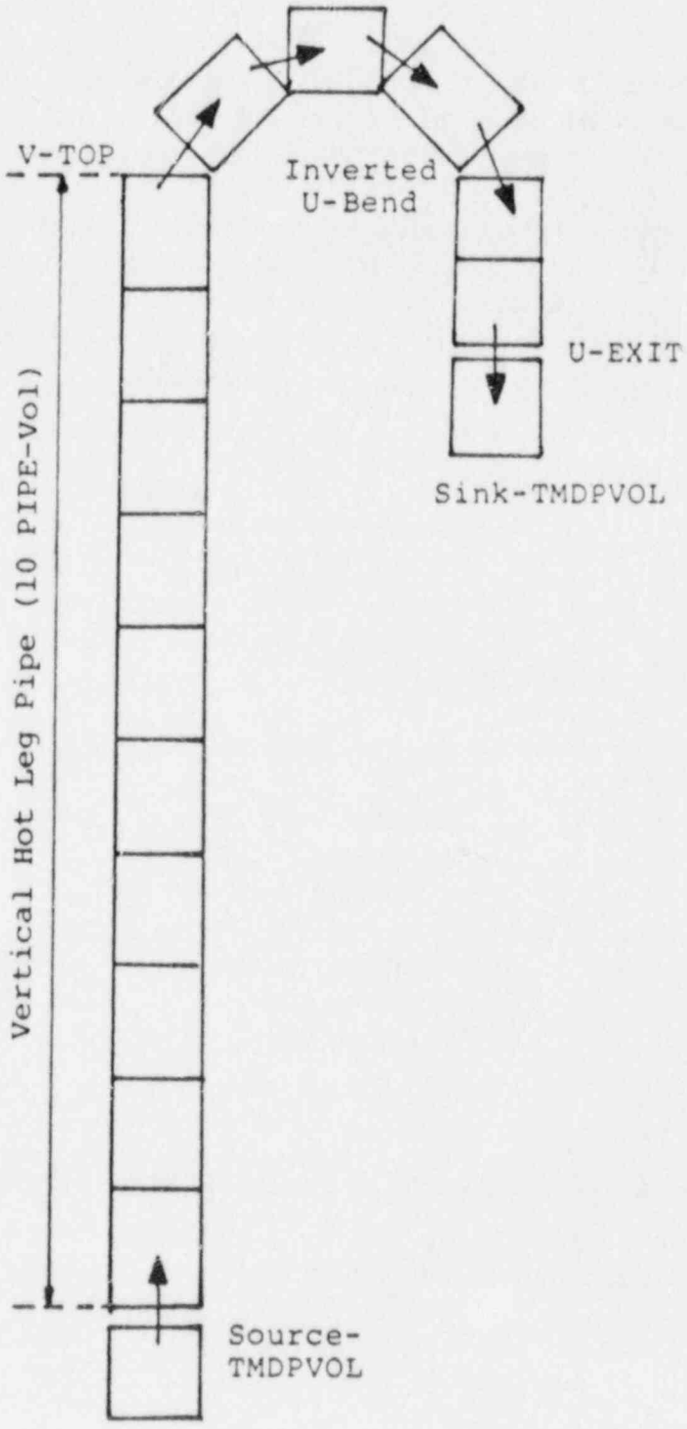

Figure 1: The RELAP5/MOD2 Code Numerical Scheme For the Vertical Hot Leg Problem

the vertical pipe. For a reference pressure in the source-TMDPVOL, several reference liquid velocities are obtained. The void fraction in the sink-TMDPVOL is always specified as 1.0 (pure steam).

The reference pressures in the models are taken to be 20 Bar, for the prototype, two sets of calculations are performed at 20 and 60 Bar. The reference void fraction is 0.2. The reference liquid velocities are varied from 0.5 to 14 m/s.

One prototype and three models are chosen. The prototype represents the vertical hot leg of the Three-Mile-Island (TMI) nuclear power plant. The height is 14 m and the diameter is 0.9 m. The volumes are scaled by a factor of 1/500 for all the three models. The models thus differ in their aspect ratios. The TL Model represents the 'thinnest' and 'longest' (full-length) model hot leg ($(L/D)^R = 22.36$). The LN Model represents a model closest to the linearly-scaled model ($(L/D)^R = 2.0$) and the FS model represents the 'fattest' and 'shortest' model ($(L/D)^R = 0.25$). Figure 2 illustrates the geometrical scales of the prototype and these three scaled-down models. Table 5 summarizes the geometrical dimensions of the prototype and three models.

VII. THE TOTAL DISTORTIONS

The TD's are evaluated using the following equation on the basis of its definition:

$$TD = \frac{\text{Similarity Parameter for a model Calculated by the RELAP5 code}}{\text{Similarity Parameter for the prototype Calculated by the RELAP5 code at } v^p_{f0}} \qquad (2)$$

At a homologous reference liquid velocity of the prototype (v^p_{f0}), the TD is equal to the ratio of the calculated Similarity Parameter for the model to that of the corresponding prototype. The homologous reference liquid velocity for the prototype is determined by a scaling scheme; that is,

$$v^p_{f0} = v^m_{f0} / \sqrt{\lambda}$$

where $\lambda = 1$ for the 'Time-Preserving' Schemes,

$= \sqrt{L_0^R}$ for the 'Time-Scaled' Schemes.

Table 5: Geometric Scales for the Prototype and Three Models

	Prototype	Model TL	Model LN	Model FS
L (m)	13.86	13.86	2.772	0.693
D (m)	0.9	0.04	0.09	0.18
L/D	15.4	346.5	30.8	3.85
$(L/D)^R$	1.0	22.36	2.0	0.25
L^R (λ)	1.0	1.0	0.2	0.05

Table 6: Summary of Various Scaling Approaches

Scaling Approach	Pressure-Scaling Approach	Geometric-Scaling Approach	
Model - Prototype	Prot.(20 Bar) - Prot.(60 Bar)	Model TL - Prot.(20 Bar)	Model LN,FS - Prot.(20 Bar)
Dominating Mechanism	Liquid Flashing	Liquid Flashing	Liquid Flashing
Key Parameter	Vapor Dendity -higher in the Proto.(20 Bar)	Aspect Ratio	
		Wall Friction -larger in Model TL	Elevation -lower in Model LN,FS
Dimension-less Variables	Higher in the Prot.(20 Bar)	Higher in the Model TL	Higher in the Prot.(20 Bar)
System Distortion	> 1	> 1	< 1
Combined-Scaling Approach	Amplifying		
	Compensating		

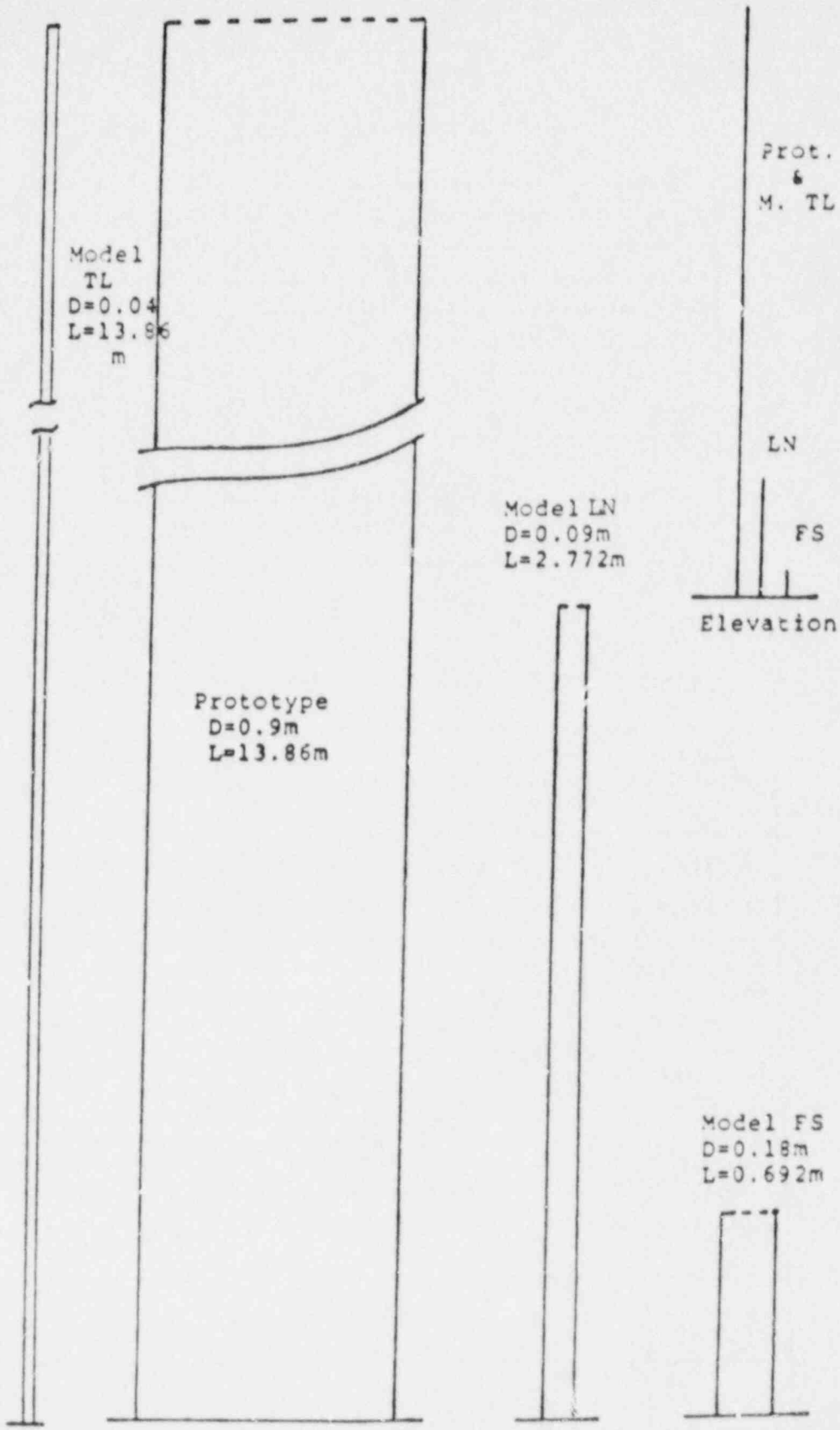

Fig 2: Geometric Scales of the Prototype and Three Models

The magnitude of TD's is illustrated by using the dimensionless liquid velocity (v_f') as an example. Figure 3 shows three monotonically increasing v_f' curves which are calculated at the top of the vertical pipe (V-TOP): The dotted curve represents the v_f' as a function of reference liquid velocities for the prototype operating at 20 Bar. The two solid curves represent the v_f' for the TL and LN models plotted against a shifted velocity scale, i.e., $v^P_{f0} = v^m_{f0} / \sqrt{\lambda}$.

It is seen that these three v_f' curves are increasing monotonically. This implies that, an increase of the inlet liquid velocity produces an amplified increase of the liquid velocity at V-TOP. The higher liquid velocity at V-Top is caused by vapor generation in the vertical pipe. A larger vapor generation rate produces a larger void fraction and, thus, a smaller liquid volume fraction. For steady-state conditions the liquid volumetric flow rate ($\alpha_f v_f$) is approximately constant, therefore, the smaller liquid volume fraction induces a higher liquid velocity. Vapor generation occurs primarily because the liquid flashes as pressure is reduced. The liquid flashing is governed by the depressurization rate and the fluid thermodynamic properties. When the depressurization rate is larger, the degree of superheat of the liquid is higher and consequently, more liquid flashes. On the other hand, a larger depressurization rate is caused by a higher inlet liquid velocity. Therefore, when the liquid inlet velocity is higher, the acceleration of the liquid is larger as well.

In Fig 3, the v_f' of the TL model is shown to have higher values than for the prototype which in turn is higher than that of the LN model. This observation can also be explained by the mechanism discussed above. The thin-and-long model (TL) produces a larger depressurization rate than the prototype due to a higher wall friction effect; whereas the linearly-scaled model (LN) generates a smaller depressurization rate than the prototype due to a lower elevation.

The effect of scaled-properties is analyzed in Fig 4 which shows the v_f' for the Prototype at 20 (dotted curve) and 60 Bar (solid curve). It is seen that at 60 Bar the curve is substantially lower. This is also predominantly caused by the liquid flashing mechanism. At the two prototypical pressures (20 and 60 Bar), most parameters are similar except for the vapor density. The vapor density at 20 Bar is smaller than that at 60 Bar by a factor of three. The larger vapor void at 20 Bar produced by the flashing of an equivalent amount of liquid then induces a higher v_f'.

Consequently, as shown in Fig 5, the TD's resulting from the TL model and the Pressure-scaling approach are similar and larger than 1.0. On the other hand, the TD's resulting from the LN model are predominantly smaller than 1.0. The corresponding SLD's are also shown in Fig 5 for comparison. They are very close to 1.0 for the entire range and thus are much smaller than the TD's.

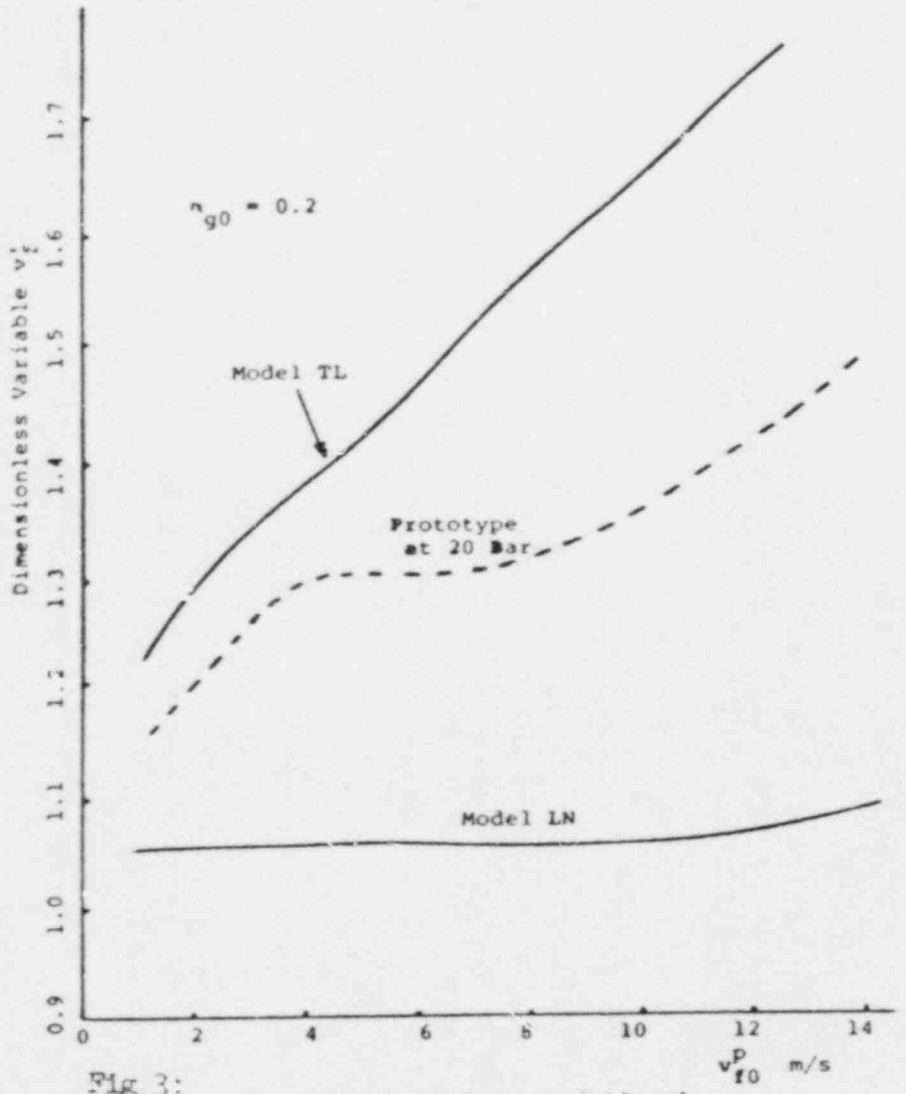

Fig 3: Comparison of Dimensionless Variable v'_f At the Top of the Vertical Pipe

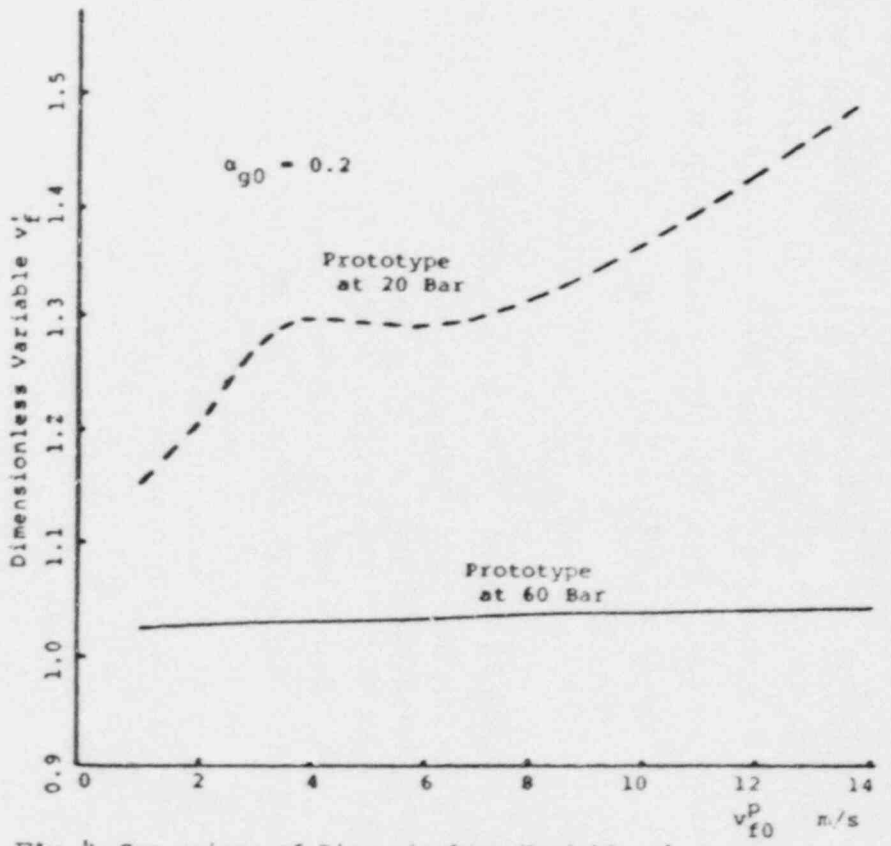

Fig 4: Comparison of Dimensionless Variable v'_f At the Top of the Vertical Pipe

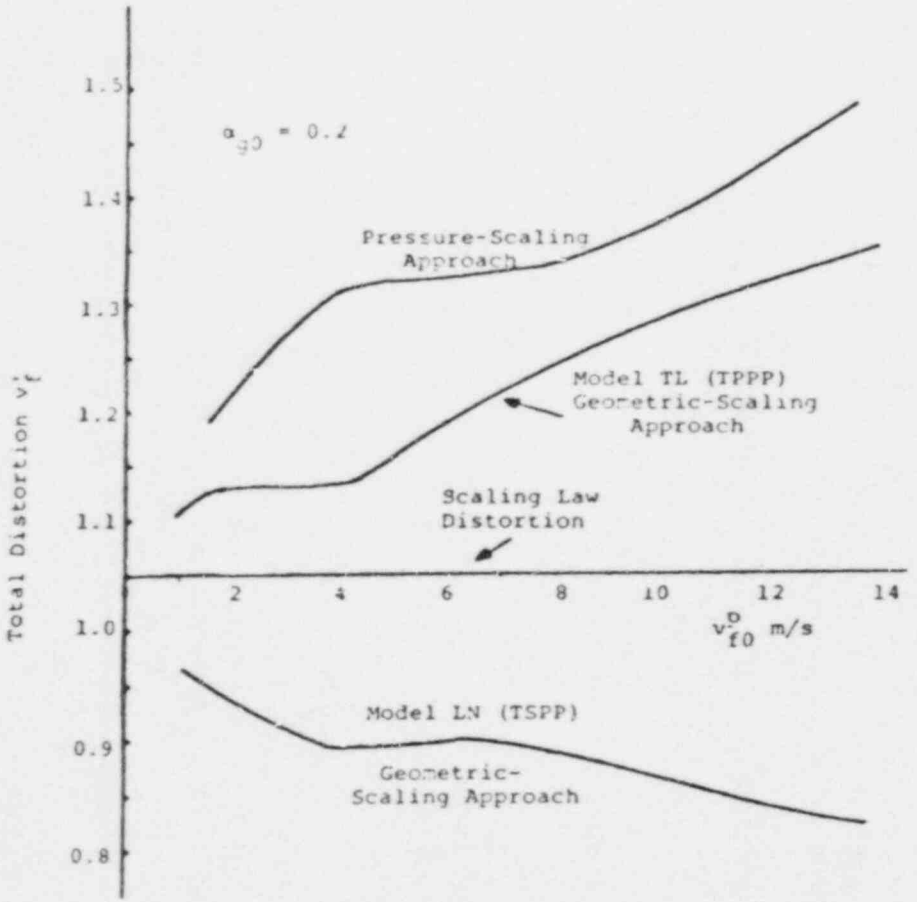

Figure 5: Total Distortions of v_f' Evaluated at the Top of the Vertical Pipe

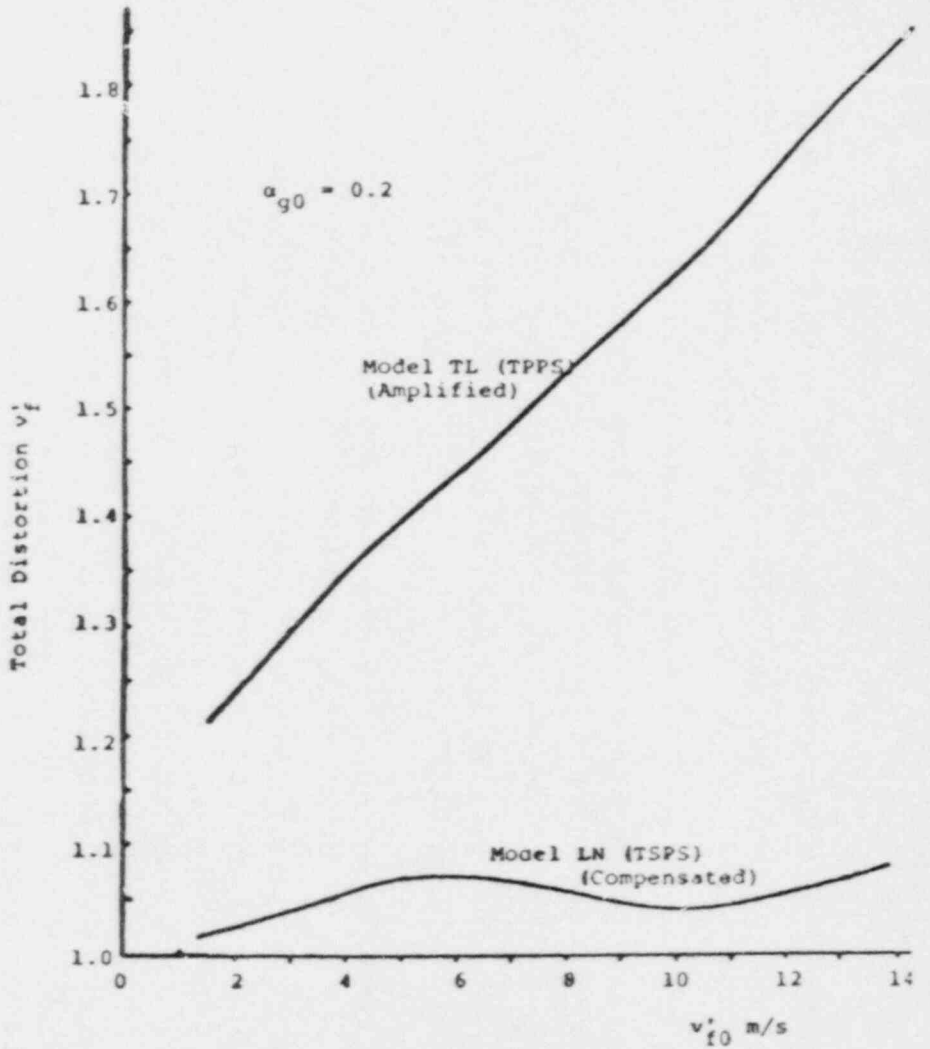

Figure 6: Total Distortions of v_f' Produced by the Combined-Scaling Approach (At the Top of the Vertical Pipe)

The effect of combining both scaling approaches can be analyzed by comparing the v_f' curves for the LN and TL models at 20 Bar (Fig 3) with those for the Prototype at 60 Bar (Fig 4). The v_f' curve for the LN model at 20 Bar is close to the one for the Prototype at 60 Bar. On the other hand, the v_f' curve for TL model is much higher than that for the Prototype at 60 Bar. Consequently, when both scaling approaches combine, the TD's of the LN model are smaller than those obtained by the individual scaling approach. In fact, for most of the v^P_{f0} range, the TD's are confined within 10% (i.e. $1.0 < TD < 1.1$) (See Fig 6). On the other hand, the TD's of the TL model is higher using the combined-scaling approach than those for the individual scaling approaches.

Table 6 summaries the dominating mechanisms and the key parameters which determine the TD's for various scaling approaches. For the geometric-scaling approach, the aspect ratio $(L/D)^2$ exerts a decisive influence on the functional dependence of TD's. A model (i.e., TL model) having a high aspect ratio (substantially larger than 1.0) has an elevation close to that of the prototype and a pipe diameter considerably smaller than that of the prototype. The gravitational pressure drop occurring in the model is close to that for the prototype, but the wall frictional pressure drop is larger. Accordingly, the model has a larger pressure gradient and the flowing fluid experiences more depressurization than is the case for the prototype. On the other hand, if a model (i.e., LN model) has a low aspect ratio (close to 1.0 or smaller than 1.0), the gravitational pressure drop is low (considerably lower than that of the prototype) and since the diameter is relatively large (close to that of the prototype), frictional pressure drop cannot compensate the difference. Hence, fluid in the model experiences a smaller depressurization than it does in the prototype.

The stronger depressurization effect observed in the TL model produces more flashing of liquid and, thus, generates a bigger vapor void in the pipe. Under the steady-state conditions, the higher vapor void produces faster fluid velocities. Consequently, the TD's of the dimensionless velocities and void ratio are larger than 1.0. On the other hand, the TD's associated with the LN model are smaller than 1.0.

To sum up: for $\alpha_{g0} = 0.2$, the Total Distortions generated by:

1. the pressure-scaling approach > 1.0
2. the geometric-scaling approach
   associated with the TL model > 1.0
   associated with the LN & FS model < 1.0

When a combined-scaling approach is used, the flashing of liquid in the geometric-scaling approach for the LN model compensates that in the pressure-scaling approach. On the other hand, for the TL model, the liquid flashing in the geometric-scaling approach amplifies that in the pressure-scaling approach. These conclusions are different from those obtained from SLD's analysis.

VIII. CONCLUSIONS

The most important conclusion obtained in this study is that the SLD's cannot be equal to the TD's. In fact, the analyses of SLD's and TD's can lead to different results. It is shown that, an analysis based only on SLD's leads to the conclusion that the geometric-scaling approach produces more accurate results. However the analysis of the actually occurring distortions (the TD's), shows that the combined-scaling approach is preferable. This can be attributed to the fact that the SLD does not (,but TD does) consider the complex cause-and-effect inter-relationship of flow phenomena within the flow system. Therefore, the currently used similarity method should be used with caution. On the other hand, although the scalability of the system simulation code needs to be investigated, the code is a scaling methodology which has much more potential than the similarity laws. This conclusion is based on the analysis of an open system (i.e. the vertical hot leg of a B&W type Pressurized Water Reactor) and it is a reasonable speculation that the same conclusion will hold for a closed system.

The analysis of the SLD's indicates that different scaling schemes may be required in order to preserve different similarity parameters. For example, judged on the basis of the Reference Similarity Parameters, the 'Time-scaled, Property-preserving' (TSPP) scheme is preferable to the other three schemes. On the other hand, in terms of the Local Similarity Parameters, the 'Time-preserving, Property-preserving' (TPPP) scheme is favored. Thus, the choice of an appropriate scaling scheme requires engineering judgement. This of course is a qualitative judgment and cannot provide the actual scaling distortions.

The analysis of the TD's indicates that the distortions resulting from the scaled-hardware may be amplified or compensated by those generated by different operating conditions in the model. Futhermore, the compensating or amplifying effect can be large. Consequently, models having different aspect ratios may need different scaling schemes to produce the least TD's. For example, when a 'thin-and-long' model is used, the 'Property-preserving' schemes are preferable. When a 'fat-and-short' or a 'linearly-scaled' model is used, the Property-scaled' scheme are favored. In general, when a 'linearly-scaled' model and the 'Property-scaled' schemes are both used, the generated TD's are the smallest among all the scaling approaches.

NOMENCLATURE

a_{gf}	Interfacial area concentration, (m^{-1})
A	Flow cross sectional area (m^2)
C_D	Interfacial drag coefficient
$C_{\alpha 0}$	Void Ratio

$C_{\rho 0}$	Density Ratio
D	Diameter (m)
f_f	Liquid wall friction factor
f_g	Vapor wall friction factor
F_{id}	Interface drag number
F_{rm}	Mixture froude number
F_{wf}	Liquid wall friction number
F_{wg}	Vapor wall friction number
FS	Fat-and-short model
g	Gravitational constant (m / s^2)
LN	Linear-scaled model
N_{fm}	Liquid inertia number
N_{gm}	Vapor inertia number
N_{im}	Interface momentum transfer number
N_{pch}	Phase change number
P	Pressure
SLD	Scaling Law Distortion
S	Slip ratio
TD	Total Distortion
t	Time
TL	Thin-and-long Model
TPPP	Time-preserving, property-preserving scheme
TSPP	Time-scaled, property-preserving scheme
TPPS	Time-preserving, property-scaled scheme
TSPS	Time-scaled, property-scaled scheme
U-EXIT	The exit of the inverted U-bend
V-TOP	The top of the vertical pipe
v_f	Phasic liquid velocity (m/s)
v_g	Phasic vapor velocity (m/s)
x	x-coordinate

GREEK

α_g	Void fraction
α_f	Liquid volume fraction
λ	Length scale factor
ρ_g	Vapor density (kg/m^3)
ρ_f	Liquid density (kg/m^3)
τ	Time scale factor

SUPERSCRIPT

m	Model
p	Prototype
R	Ratio of model value to prototype value
'	Dimensionless variable

SUBSCRIPT

0	Reference value
f	Liquid phase
g	Vapor phase

ACKNOWLEDGMENT

The authors gratefully acknowledge the support of Dr. Y.Y. Hsu who is in charge of the University of Maryland College Park 2x4 simulation loop project. Our gratitude also goes to Dr. Richard Lee for many valuable references that he provided.

REFERENCES

1. W.A. Carbiener and R.A. Cudnik, 'Similitude Considerations for Modeling Nuclear Reactor Blowdown', Trans. Am. Nucl. Soc., 12, 1969.

2. A.N. Navahandi, et. al.. 'Scaling Laws for Modeling Nuclear Reactor Systems', Nuclear Science and Engineering 72. 75-83, 1979.

3. M. Ishii and I. Kataok, 'Scaling Criteria for LWR's Under Single-Phase and Two-Phase Natural Circulation,' ANL-83-32, NUREG/CR-3267, Argonne National Laboratory, March 1983.

4. R.L. Kiang, 'Scaling Criteria for Nuclear Reactor Thermal-Hydraulic,' Nuclear Science and Engineering, 89, 207-216

5. T.k. Larson, 'Scaling Criteria and an Assessment of Semi-scale MOD3 Scaling for Small Break LOCA Transients', EGG/SEMI 5121, March 1980.

6. L.N. Kmetyk., 'RELAP5 Assessment: Conclusions and User Guidelines', NUREG/CR-3936, SAND84-1122, October, 1984.

7. P. Saha, et. al., 'Independent Assessment of TRAC-PF1 (Version 7.0), RELAP5/MOD1 (Cycle 14) and TRAC-BD1 (Version 12.0) Codes Using Separate Effect Experiments', NUREG/CR-4359, BNL-NUREG-51919, August, 1985.

8. B.E. Boyack, 'Descriptors for Characterizing Agreement Between Test and TRAC Results', PMG meeting 15, June 16-17, 1987, Washington, DC.

9. T.K. Larson, 'An Investigation of Integral Facility Scaling and Data Relation Methods (Integral System Test Program)', NUREG/CR-4531, EGG-2440, February, 1987.

10. Y. Zvirin and J.P. Sursock, 'Scaling of Natural Circulation Experiments', ANS Proceedings, 1987 National Heat Transfer Conference, August, 1987.

11. T.K. Larson and R.A. Dimenna, 'Preservation of Natural Circulation Similarity Criteria in Mathematical Models', ANS Proceeding, 1987 National Heat Transfer Conference, August, 1987.

12. Z.Y. Wang, 'A Comparison of The Similarity Laws and The System Thermal-Hydraulic Code For Scaling Applications', NUREG/CR-5027, 1987.

13. V.J. Skoglund, 'Similitude, Theory and Applications', Pennsylvania: International Textbook Company, 1967.

14. V.H. Ransom et al., 'RELAP5/MOD2 Code Manual, Volume 1: Code Structure, System Models, and Solution Methods', NUREG/CR-4312, EGG-2396, August, 1985.

THE RESULTS OF 0.5% PWR SMALL BREAK LOCA TESTS IN ROSA-IV

LSTF BREAK LOCATION PARAMETER TEST SERIES

K. Tasaka, Y. Kukita, H. Kumamaru, T. Yonomoto
M. Suzuki and Y. Koizumi

Japan Atomic Energy Research Institute
Tokai, Ibaraki, 319-11 Japan

ABSTRACT

The effects of break location on a PWR small-break LOCA with failure of the high pressure injection (HPI) system were studied experimentally using the Large Scale Test Facility of the ROSA-IV Program. The LSTF is a 1/48 volumetrically-scaled simulator of a Westinghouse-type 4-loop (3423 MWt) PWR. Five tests were conducted for a break area of 0.5% of the volumetrically-scaled PWR cold leg cross-sectional area (equivalent approximately to a 2-in. diameter break in a PWR). In these tests the break was located at the pressure vessel lower plenum, cold leg, hot leg, pressure vessel upper head, and the top of the pressurizer. HPI and the auxiliary feedwater were assumed unavailable. In all of these tests the core was uncovered and heated up at a primary pressure higher than the secondary pressure. The heatup was terminated when the core level was recovered by initiating HPI manually. The break location had a significant influence on the time available before the initiation of the core uncovery.

I. INTRODUCTION

The ROSA-IV Program of the Japan Atomic Energy Research Institute (JAERI) is conducting large-scale integral experiments on small-break loss-of-coolant accidents (SBLOCAs) and transients in a pressurized water reactor (PWR) using the Large Scale Test Facility (LSTF) located at the JAERI Tokai Research Establishment. The LSTF (1) is a 1/48 volumetrically-scaled simulator of a Westinghouse-type 4-loop (3423 MWt) PWR.

This paper presents results from five LSTF tests which investigated the effects of break location on a SPLOCA with failure of the high pressure injection (HPI) system. These tests were conducted for a break area of 0.5% of the 1/48-scaled PWR cold leg cross-sectional area (equivalent approximately to a 2-in. diameter break in a PWR). The break was located at the pressure vessel lower plenum (SB-PV-01), cold leg (SB-CL-11), hot leg (SB-HL-03), pressure vessel upper head (SB-PV-02) and the top of the pressurizer (AT-SB-03). HPI and the auxiliary feedwater were assumed unavailable, but HPI was turned on manually when a core temperature excursion was detected.

II. CHARACTERISTICS OF SBLOCA WITHOUT HPI

Slow depressurization of the primary system is one of the characteristic features of a SBLOCA. The system mass and energy balance determines the depressurization rate, and this is dependent on the mass and energy release rate out of the break, the core power generation rate, the primary-to-secondary heat transfer rate at the steam generators, the emergency core coolant flow rates and temperature, etc.

For relatively-large small breaks the primary depressurization will be fairly fast, and a crossover of the primary and secondary pressures may occur early in the transient. For instance, in the 5% break tests conducted so far in the LSTF, this crossover of pressures occurred as soon as the break became uncovered and the break flow turned to vapor or high-quality two-phase flow (2). However, for smaller small breaks, the energy release out of the break may be insufficient, even after vapor discharge initiates, to cause the primary system to depressurize without cooling by the secondary system. Thus, if HPI should fail following such a smaller small break, the primary pressure will remain higher than the accumulator injection pressure (typically 4.5 MPa) until late in the transient. Meanwhile the primary coolant continue to decrease, and it is likely that core ucovery initiates at a relatively high primary pressure.

It is of interest to define the minimum break area required to depressurize the primary system below the secondary pressure (about 8 MPa) without HPI, and the minimum area required to depressurize the primary system below the accumulator injection pressure (4.5 MPa) without either HPI or cooling by the secondary system. These break areas can be calculated from the balance between the vapor generation in the core and the vapor discharge out of the break. The calculated break areas are shown in Fig. 1, in percentage of the cold leg flow area, as a function of core power. These values were calculated for a break flow quality of unity (pure vapor discharge) and a discharge coefficient of 0.6.

Also shown in this figure are the timings of core heatup initiation recorded in the LSTF no-HPI tests which have been conducted for various break locations and break areas. These data points do not include either those temporary core heatups which were caused by a core level depression during the loop seal clearing phase in cold-leg break tests, or caused by condensation depressurization following the accumulator injection. The observations in these tests, summarized in the following paragraph, are consistent with the energy balance calculation results shown in Fig. 1.

Figure 1 shows core heatup initiation timings for two 5% break tests, three 2.5% break tests, one 1.3% break test and five 0.5% break tests. The 5% break tests (2) were conducted for a cold leg horizontal break. In these tests the core started to uncover at primary pressures of about 5 MPa, i.e., shortly before the accumulator injection pressure was reached. Thus the core heatup was terminated soon, as the accumulator initiated, without reaching exessively high temperatures. A no-HPI 5% break test was conducted

also for a hot leg break (2). however, this test indicated only minimal core temperature excursions before the accumulator injection initiated. The 2.5% break tests were conducted for cold leg breaks with different break orientations (upward, downward and horizontal). In these tests the core became uncovered at a primarty pressure of about 6.5 MPa irrespective of the break orientation. The heater rod temperature reached the 900 K setpoint temperature of the core protection circuit before the accumulator injection started and thus the core power was tripped off. The 1.3% break test was conducted for a pressurizer top break. The core became uncovered in this test at a primary pressure of 7.5 MPa, shortly after the crossover of the primary and secondary pressures had occurred. HPI was initiated manually in this test to quench the core by recovering the water level. Finally, in the 0.5% break tests, which were conducted for five different break locations, the core started to uncover at primary pressures higher than the secondary pressure irrespective of the break location.

In summary, these test results show that there is a bounding break area of about 1% below which the core starts to uncover, if HPI is unavailable, at a primary pressure higher than the secondary pressure.

III. TEST FACILITY

The LSTF (1) is a 1/48 volumetrically-scaled simulator of a Westinghouse-type 4-loop (3423 MWt) PWR. The schematic view of the LSTF is shown in Fig. 2 and its design characteristics are summarized in Table 1. The LSTF represents the four loops of the reference PWR with two equal-volume loops each one containing an active steam generator and a pump. The elevations of the major components are preserved full-scale to simulate the natural circulation phenomena peculiar to SBLOCAs and transients. The hot legs and cold legs are sized to conserve the volume scaling (2/48) and the ratio of the length to the square root of the diameter, $L/\sqrt{D}$, to simulate the flow regime transitions in the horizontal legs.

The LSTF represents the reference PWR bypasses at the upper head spray nozzles (UHSN) and at the hot leg nozzle leakage (HLNL). The UHSN bypass is simulated by nozzles connecting the upper head to the upper downcomer. The reference PWR nozzle geometry is preserved approximately and the total nozzle area is scaled by scaling the number of the nozzles. The HLNL bypass is simulated by a piping which connects each hot leg to the downcomer. During the steady state UHSN allows a bypass flow of about 0.3% of the core flow. The HLNL bypass area can be changed by adjusting the valve flow area in the line, and was set for the present tests to allow 0.1% bypass flow for each loop. In addition to these simulated bypasses, there existed unintended leakage between the top of the upper plenum and the downcomer. The flow through this leakage during the steady state is estimated to be about 0.1% of the core flow.

IV. TEST CONDITIONS

All the tests, except the presurizer top break test, AT-SB-03, were

conducted for the same break area of 0.5%. The break area for Run AT-SB-03 was 0.43%. The break was simulated using a sharp edged orifice in all the tests. The break locations are shown in Fig. 3.

All the tests were conducted for the same boundary conditions except that the core power decay curve used for Run AT-SB-03 provided less power to the core than in other four tests for the first 400 seconds after the scram. These core power curves are shown in Fig. 4.

All the tests were started from the same initial conditions which included the reference PWR nominal operating pressure (15.5 MPa) and hot leg and cold leg fluid temperatures (598 and 562 K). Since the maximum core power available in the LSTF is limited at 10 MW, which is 14% of the volumetrically-scaled PWR rated power, because of the power supply limitations, the above fluid temperatures were obtained by operating the facility at a core flow rate of 14% of the scaled PWR flow rate. The primary-to-secondary heat transfer rate also needed to be limited to 14% of the scaled value to obtain a steady state with 14% core power. Since the steam generator heat transfer areas are scaled volumetrically, this was done by operating the secondary system at a higher pressure (7.3 MPa) than the reference PWR secondary pressure of 6.2 MPa.

The tests were initiated by opening a valve at the simulated break. Then the primary pressure started to decrease. At a pressurizer pressure of 12.97 MPa the scram signal was generated. This signal closed the steam valves and the feedwater valves on the steam generator, initiated the simulated core power decay, and also initiated the pump coastdown.

V. TEST RESULTS

V.1 Break Location Effects on Integrated Break Flow

Figure 5 compares integrated break flow rates measured in the present tests. These were calculated from the level rise in a tank where the break flow was injected into subcooled water to condense the vapor. This measurement was unavailable for the pressurizer break test, AT-SB-03. In each experiment the break flow rate decreased with time, as the upstream break condition changed from subcooled liquid to two-phase, and then to single-phase vapor. These break flow quality transitions are seen in Fig. 5 as inflections in the increase of the integrated break flow with time. The primary pressure was maintained slightly above the secondary pressure for most of the period shown in this figure, and affected the break flow only during the initial depressurization phase which ended at about 500 s and after HPI was initiated manually which caused the primary system to depressurize.

This figure indicates that the break flow rate and the break flow quality were strongly dependent on the break location. The general tendency was, as expected, that the increase in the break flow quality, i.e., the decrease in the break flow rate, occurred earlier for breaks located at higher elevation in the primary system. This is reasonable because in these tests the draining of the primary

system was controlled by the gravity. The primary system emptied from the higher portions to the lower. However, analyses of the test results have indicated that the break upstream conditions in each test were affected by complicated phenomena which may not be predicted easily by existing LOCA thermal-hydraulic computer codes. The analyses were done using the computer codes RELAP5/MOD2, CATHARE-1 and TRAC-PF1/MOD1, and were not always successful in predicting the core heatup initiation timings, particularly for the tests in which two-phase discharge continued. Such disagreement between the experimental and analytical results occurred since the predictive ability of these codes (either some or all of them) was unsatisfactory in several areas, for instance, the subcooled and saturated critical flow at the break orifice, the interactions between the mixture level and the break flow (the liquid entrainment and vapor pullthrough phenomena) and the countercurrent flow limiting (CCFL) phenomena at various locations in the primary system. The timings of major events in these tests are listed in Table 2.

V.2 Lower Plenum Break Test (SB-PV-01)

In this test the break was located on the vessel wall 0.626 m above the bottom of the lower plenum. The break orientation was horizontal.

Figure 6 shows the primary and secondary pressures during this test. After the steam and feedwater valves were closed by the scram signal, the secondary pressure cycled between the atmospheric relief valve opening and closing setpoints of 8.2 and 7.8 MPa, respectively, as long as there was heat transfer from the primary to the secondary systems. The primary pressure closely followed this variation of the secondary pressure, except during the first 400 s into the transient, as shown in this figure. The difference between the primary and secondary pressures (i.e., the temperature difference between the primary and secondary systems after the primary system saturated) decreased as the core power decayed and the core was uncovered following the primary mass inventory decrease.

The natural circulation ceased in this test at about 800 s. Thereafter, only intermittent flows occurred in the loops. The flow occurred when the secondary pressure dropped as the relief valve opened as shown in Fig. 6. The steam generator U-tubes and plenums became empty of liquid at about 1200 s.

Figure 7 shown the major transient parameters during this test. The top of the core started to uncover at 1490 s. Shortly after this, the primary pressure became lower than the secondary pressure at 1550 s (Fig. 6) when the break flow was still single-phase liquid. This occurred because the core uncovery progressed rapidly causing a sharp decrease in the core vapor generation rate.

The break flow remained single-phase liquid until after the core became entirely uncovered. The core uncovery initiated earliest of the five tests (1490 s) because of the largest break flow rates (Fig. 5). The entire core was uncovered within about 160 s after the incipient core uncovery, and then the level penetrated into the

lower plenum as shown in Fig. 7.

HPI was initiated manually at 1670 s. At this time the peak rod cladding temperature had reached 820 K. The HPI flow rates represented the volumetrically-scaled reference PWR injection rate. Both two HPI pumps in the PWR were assumed to be operative. However, the inititation of HPI did not cause the vessel level to recover immediately, and the level stayed at the elevation of the path between the lower plenum and the downcomer as shown in Fig. 7.

The coolant distribution immediately after the HPI initiation is shown schematically in Fig. 8 A large vapor space had formed in the cold legs and the downcomer before HPI was started. This vapor space formed because the fluid in these regions saturated and flashed as the primary pressure started to decrease after the core uncovery initiation (Fig. 6). This vapor space was isolated from the hot leg/upper plenum vapor space by loop seals in the crossover legs and by the water in the lower plenum. Therefore, when HPI injected cold water into the cold legs, condensation of vapor caused a depressurization in the cold legs and the downcomer. This depressurization tended to retard the increase of the vessel riser level until the loop seals cleared.

It is also important to note that the break flow was still single phase and was comparable to the HPI flow rate. This large break flow rate slowed the accumulation in the vessel bottom of the accumulator water which drained from the cold legs into the downcomer.

V.3 Cold Leg Break Test (SB-CL-11)

In this test the break was located at the cold leg of the loop without the pressurizer (Loop B). The break orientation was horizontal. The break orifice was located in a horizontal branch piping which was about 440 mm in length and 87 mm in diameter.

The major transient parameters during this test are shown in Fig. 9. In this test the break flow became two-phase at about 900 s (Fig. 5) when liquid level formed in the cold legs. This occurred approximately at the same time as the natural circulation in the primary loops ceased. The mixture level in the cold legs formed as vapor entered the cold legs from the upper plenum through the bypasses driven by the pressure difference across the bypasses. During this phase of the transient, the UHSN bypass was still covered by liquid in the upper head, and thus the vapor enetred the cold legs only through the simulated HLNL bypasses. During the two-phase discharge the vapor component of the break flow balanced with this bypass flow. Since the effective (uncovered) bypass area in this test was relatively small (corresponding to a steady-state bypass flow of 0.3% of the core flow rate), the break flow quality was relatively small. The cold leg mixture level was maintained at about the cold leg centerline elevation where the break was located.

The bypasses have a large influence on the two-phase break flow and the cold leg behavior. Different cold leg behavior may occur when

the bypass areas are larger. For instance, in the Semiscale Experiment S-NH-1 which was conducted for a UHSN bypass of 3.16%, the bypass uncovered early in the transient and this caused the cold leg level to drop. Consequently, the loop seals did not clear in Experiment S-NH-1 (3).

The break flow became single-phase vapor in Run SB-CL-11 as the loop seals cleared at 1880 s. The loop seals cleared in both the broken and intact loops at the same time. The level behavior in the two loops was symmetrical until the loop seal clearing as shown in Fig. 9, however, the intact loop was sealed again by water immediately after the clearing whereas the broken loop remained cleared.

During the loop seal clearing the core level was depressed by a differential pressure which developed between the upper plenum and the downcomer. The core level was determined by the static head balance in the lower portions of the primary system as shown in Fig. 10a. The steam generators were empty of liquid at this time and did not contribute to the static head balance in the primary system. The core was uncovered shortly until this differential pressure was relieved by the completion of loop seal clearing.

The loss of coolant continued thereafter due to vapor discharge through the break (Fig. 10b), and resulted in a second core uncovery, which started at 2180 s and continued until the core level recovered after HPI was initiated manually at 2540 s.

This second core uncovery was promoted by a development of differential pressure in the broken loop crossover leg due to accumulation of water in this region. This water came from the steam generator primary side (U-tube downflow side in the broken loop steam generator) where condensation of vapor continued as the primary pressure remained higher than the secondary pressure. This accumulated water formed a column of two-phase mixture in the pump suction (upflow) side of the broken loop crossover leg, through which the vapor entered the broken cold leg and reached the break. This situation is shown schematically in Fig. 10c. The differential pressure caused by this water accumulation can be seen in the upper trace in Fig. 11, the differential pressure between the upper plenum and the downcomer, and is clearly responsible for the core level drop after 2180 s.

The rate of condensate accumulation in the crossover leg should be dependent on the heat transfer rate in the broken loop steam generator. Then this heat transfer rate may be affected by the differences among the secondary side pressures of the steam generators, because at this stage of the transient the primary-to-secondary pressure difference is very small. For the present test, Run SB-CL-11, the steam generator pressures suggest that the heat transfer rate in the broken loop steam generator was smaller than that in the intact loop steam generator. This occurred because there was slight difference between the relief valve opening setpoints for the two steam generators. However, the condensate accumulation had an important influence on the core uncovery. Thus the present test results may have an interesting implication related to the use of the steam-and-feed procedure for

depressurization of the primary system; if the broken loop steam generator is used for this procedure, the heat transfer rate in this steam generator will increase and thus the increase of the crossover leg differential pressure will be accelerated.

HPI was initiated manually at 2540 s, and then the core level recovered quickly.

V.4 Hot Leg Break Test (SB-HL-03)

The break in this test was located at the Loop B hot leg. The break orientation was horizontal. The break orifice was mounted flush to the inner wall of the hot leg piping. Thus the break geometry was different from that in the cold leg break test, SB-CL-11.

This test was conducted very recently, and no qualified data were available at the writing of this paper. However, preliminary data indicate that large break flow (i.e., discharge of liquid or low-quality two-phase) continued for about 1600 s, almost as long as that in the cold leg break test, SB-CL-11, as shown in Fig. 5. The core started to uncover at about 2400 s, again almost at the same timing as in the cold leg break test.

V.5 Upper Head Break Test (SB-PV-02)

The major transient parameters and typical coolant distribution during this tests are shown in Figs. 12 and 13 respectively. The flow out of the break, located at the top of the pressure vessel (Fig. 13) became two phase early in the transient (170 s), however, it remained two-phase for a relatively long period, until it became single-phase vapor at 2500 s (Fig. 5). This long duration of two-phase discharge occurred since liquid was held up in the upper head as long as the holes on the control rod guide tubes (CRGTs), located slightly above the upper core plate, were covered by two-phase mixture in the upper plenum (Fig. 13). The break flow was two-phase probably because two-phase mixture entered CRGTs from the upper plenum. In addition to this, it is probable that vapor entered the upper head also from the upper downcomer through the UHSN bypasses. Conduction probe signals indicated that a mixture level formed in the upper downcomer. This may have occurred since the vapor entered the downcomer from the upper plenum through the HLNL bypasses. Thus, it is likely that for this break location the break flow quality was highly dependent on the pressure differences between the upper head, the upper plenum and the downcomer.

The upper plenum level dropped to the CRGT hole elevation at 2180 s (Fig. 12), and the holes were uncovered at about 2500 s. The break flow was vapor after this point and the pressure vessel level continued to decrease due to boiloff.

The core became uncovered at 3460 s and HPI was initiated manually at 3930 s. The injection of cold water from HPI resulted in a temporary depressurization in the cold leg, and this caused a core level depression as shown in Fig. 12, however, the core level recoverd quickly and mixture covered the entire core.

V.6 Pressurizer PORV Break Test (AT-SB-03)

This test (4) simulated a SBLOCA caused by a stuck-oper power operated relief valve (PORV) on the pressurizer. The break area (0.43%) was scaled to the PORV flow area in the reference PWR, and thus was different from that in the other four tests. Liquid holdup in the pressurizer, as occurred in the Three-Mile Island Unit 2 (TMI-2) accident, was observed in this test (Figs. 14 and 15). Because of this liquid holdup, the break, located at the top of the presurizer, continued to be covered by two-phase mixture. The break was uncovered at 4300 s, as the surge line inlet in the hot leg was uncovered, before the initiation of core uncovery at 5510 s. After HPI was initiated manually at 6600 s, the core level indicated a temporary depression as in the upper head break test.

VI. CONCLUDING REMARKS

Core uncovery was observed in all of the five 0.5% break test conducted in the LSTF for different break locations with an assumed failure of HPI. In all the tests the core uncovery initiated at a primary pressure higher than the secondary pressure.

The change of break flow quality with time was dependent on the break location. This resulted in significant differences in the primary mass decrease rate and thus in the core uncovery timings.

The coolant distribution at the initiation of core uncovery was different between the cold leg break test and other four tests. In the cold leg break test, the first core uncovery occurred during the loop seal clearing, however, in the other four tests core uncovery initiated before the loop seal clearing.

Continued core uncovery, irrecoverable without initiation of HPI or some other appropriate operator actions, occurred after the initiation of vapor discharge from the break in all the test except the lower plenum break test.

When the core uncovery occurred, the cold legs were empty or nearly empty of liquid in all the tests, and there was loop seals in the crossover leg except for the cold leg break test. Thus when HPI was initiated manually in these tests, after the detection of core temperature excursion, condensation depressurization occurred in the cold legs and this retarded the recovery of the core level. However, generally the core was quenched quickly after HPI was initiated.

VII. REFERENCES

1. ROSA-IV Group, "ROSA-IV Program Large Scale Test Facility (LSTF) System Description", JAERI-M 84-237 (1985).
2. Tasaka, K. et al., "The Results of 5% Small-Break LOCA Tests and Natural Circulation Tests at the ROSA-IV LSTF", Proc. 14th Water Reactor Safety Information Meeting, Gaithersburg, Maryland, Oct. 27-31, 1986.
3. Streit, J.E., "Results of Semiscale Mod-2C Small-Break

Loss-of-Coolant Accident Without HPI (S-NH) Experiment Series", NUREG/CR-4793, EGG-2482 (1987).
4. Tasaka, K. et al., "The ROSA-IV Program TMI-2 Type Scenario Experiments : A Multifaceted Investigation", Proc. Specialists Meeting on Small Break LOCA Analyses in LWRs, Pisa, Italy, June 23-27, 1985.

Table 1 LSTF Design Characteristics

		LSTF	PWR	PWR/LSTF
Pressure	(MPa)	16	16	1
Temperature	(K)	598	598	1
No. of fuel rods		1064	50952	48
Core height	(m)	3.66	3.66	1
Fluid volume V	(m^3)	7.23	347	48
Core power P	(MW)	10	3423(t)	342
P/V	(MW/m^3)	1.4	9.9	7.1
Core inlet flow	(t/s)	0.0488	16.7	342
Downcomer gap	(m)	0.053	0.260	4.91
Hot leg D	(m)	0.207	0.737	3.56
L	(m)	3.69	6.99	1.89
$L/\sqrt{D}$	($m^{1/2}$)	8.15	8.15	1.0
$\frac{\pi}{4}D^2L$	(m^3)	0.124	2.98	24.0
No. of loops		2	4	2
No. of tubes in steam generator		141	3382	24
Length of steam generator tube (average)	(m)	20.2	20.2	1.0

Table 2 Chronology of Major Events

Test ID	SB-PV-01	SB-CL-11	SB-PV-02	AT-SB-03
Break Location	Lower Plenum	Cold Leg	Upper Head	Pressurizer PORV
Chronology of Events				
Break flow becomes two phase		900 s	170 s	?
Break flow becomes vapor		1880 s	2180 s	4300 s
Core uncovery starts	1490 s	1880, 2180 s	3520 s	5510 s
HPI is initiated manually	1670 s	2540 s	3930 s	6600 s

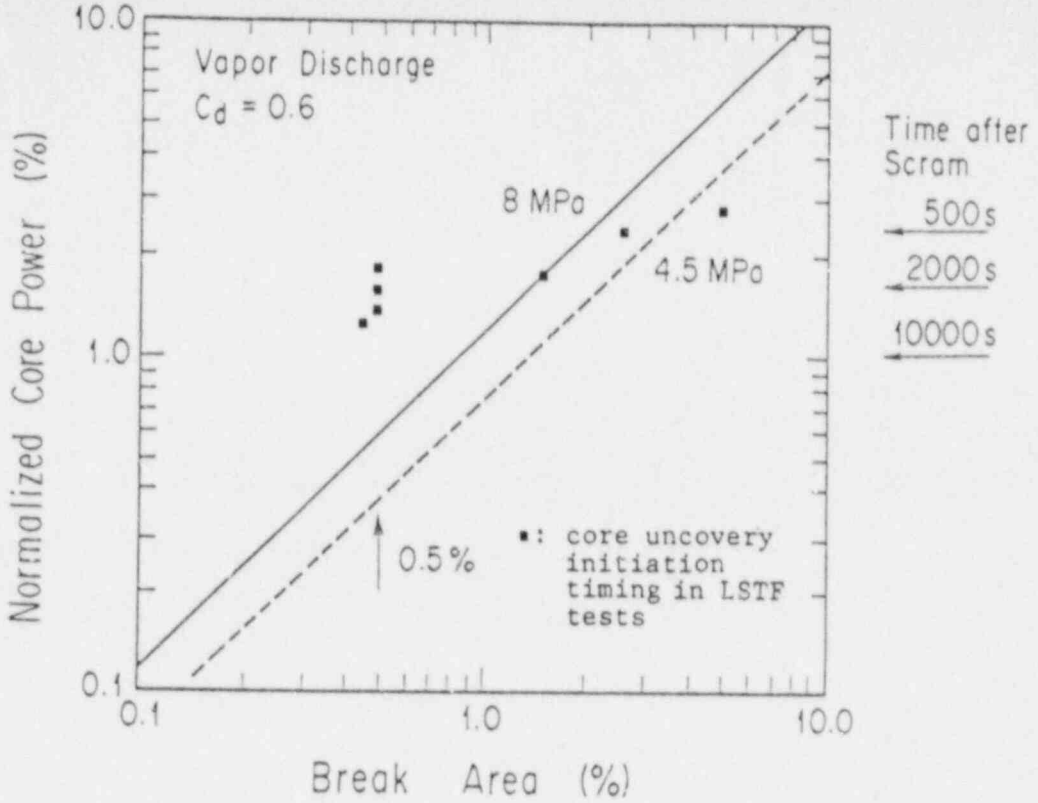

Fig. 1 Break Area Required for Depressurization of Primary Pressure

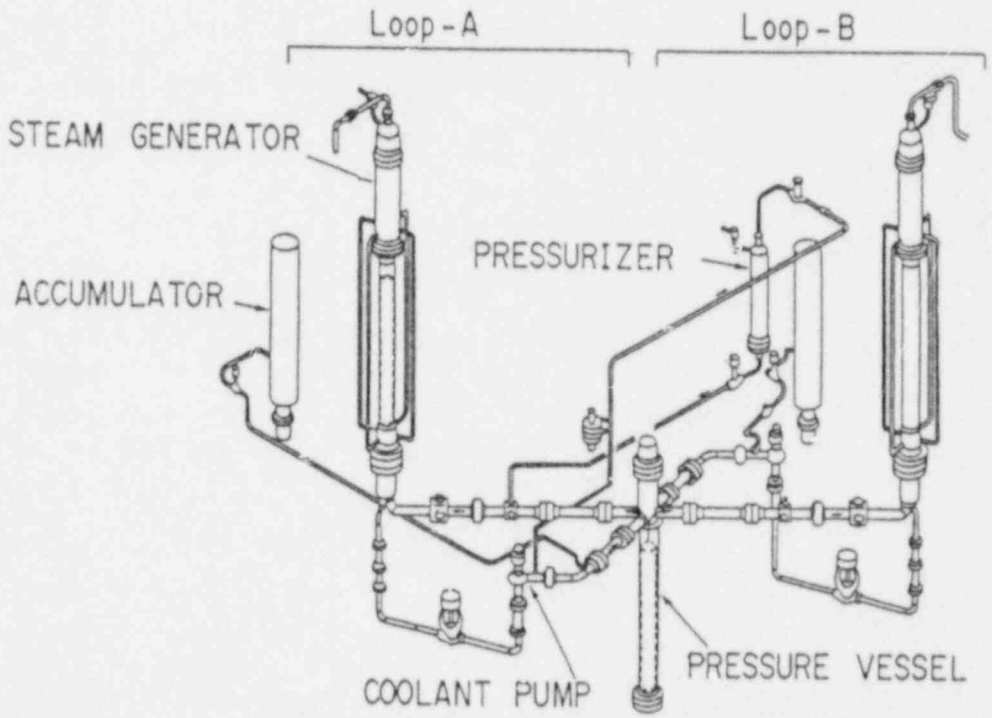

Fig. 2 ROSA-IV Large Scale Test Facility

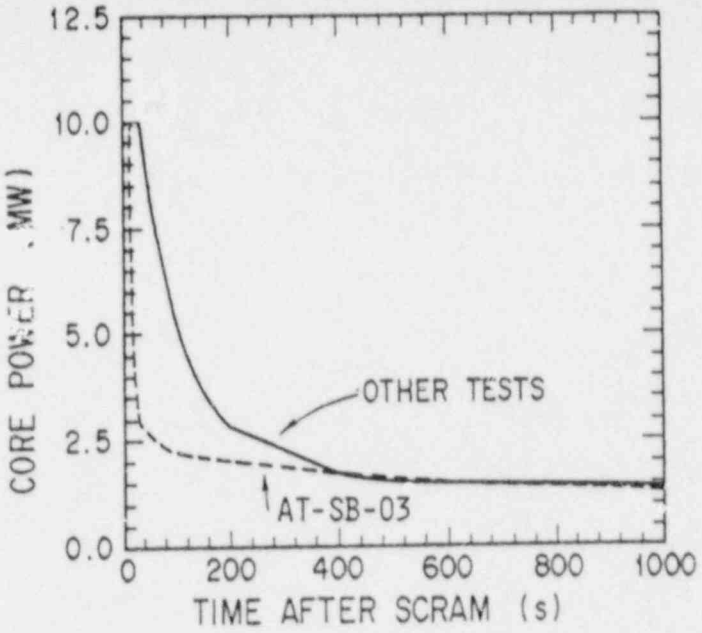

Fig. 3 Core Power Decay Curve

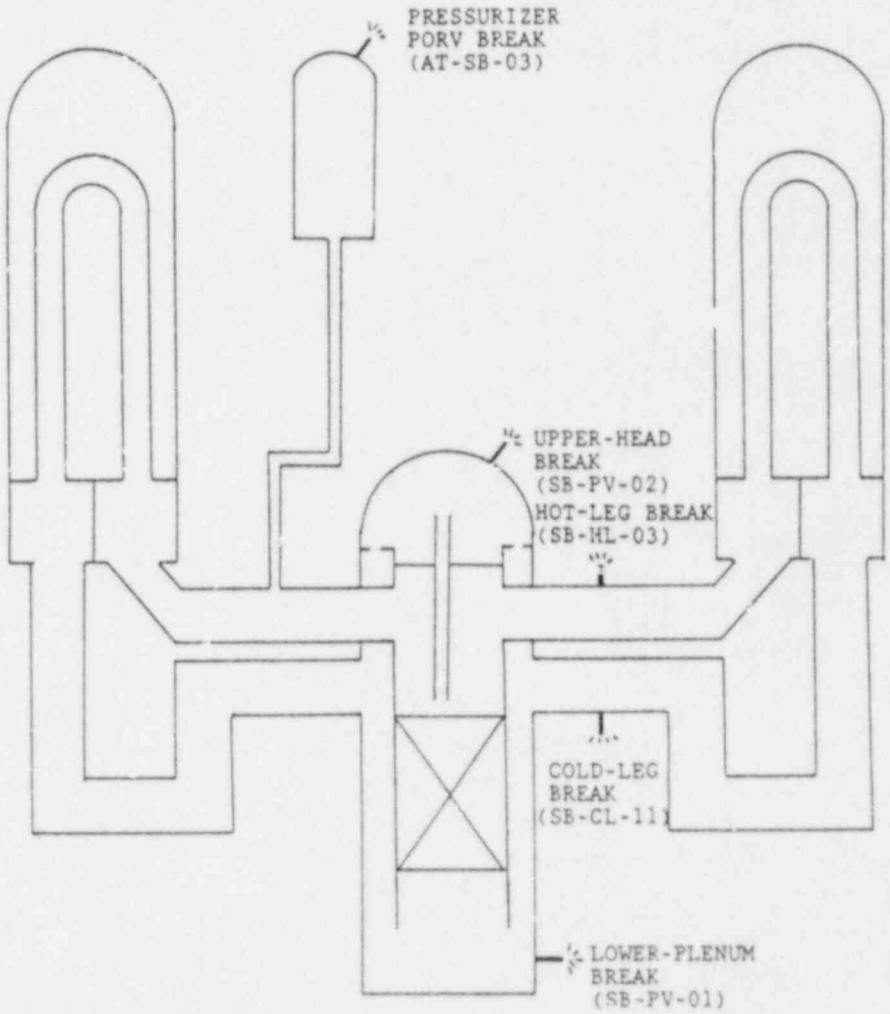

Fig. 4 Break Locations

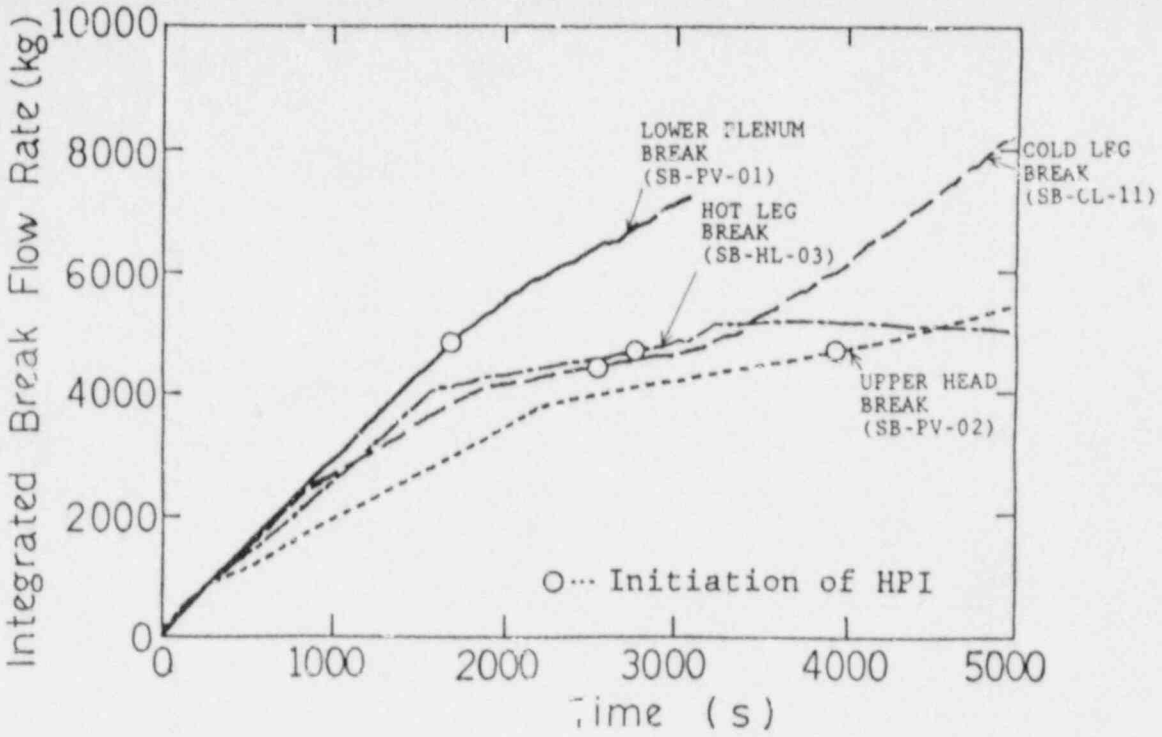

Fig. 5 Break Location Effects on Integrated Break Flow

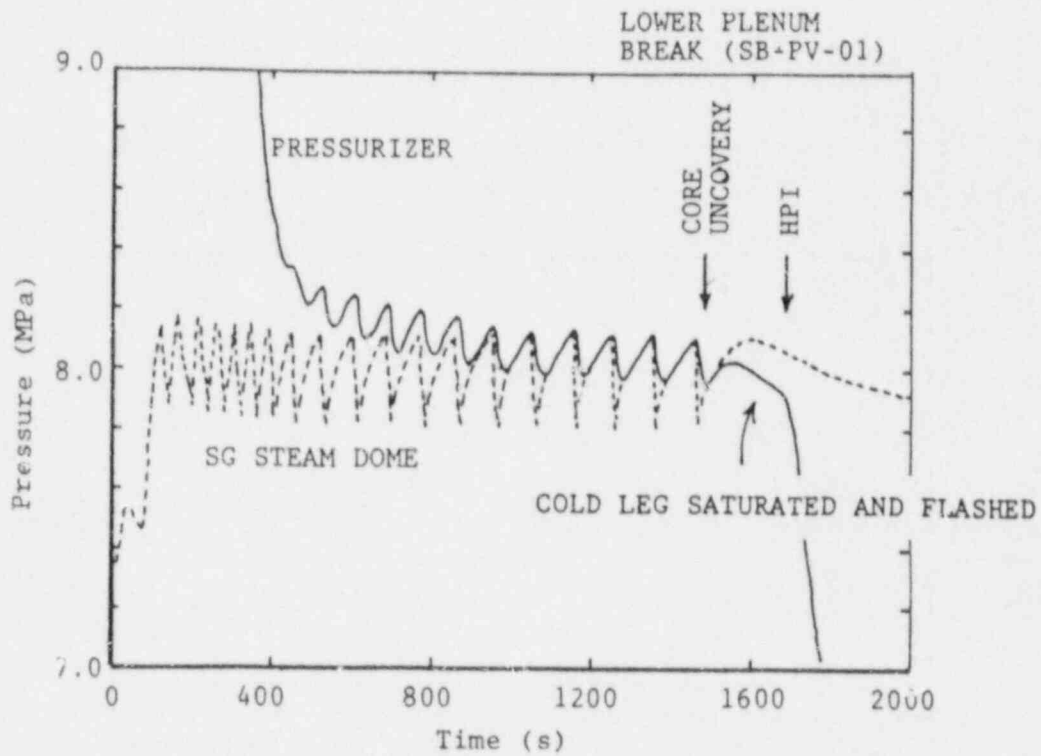

Fig. 6 Primary and Secondary Pressures during Lower Plenum Break Test, SB-PV-01

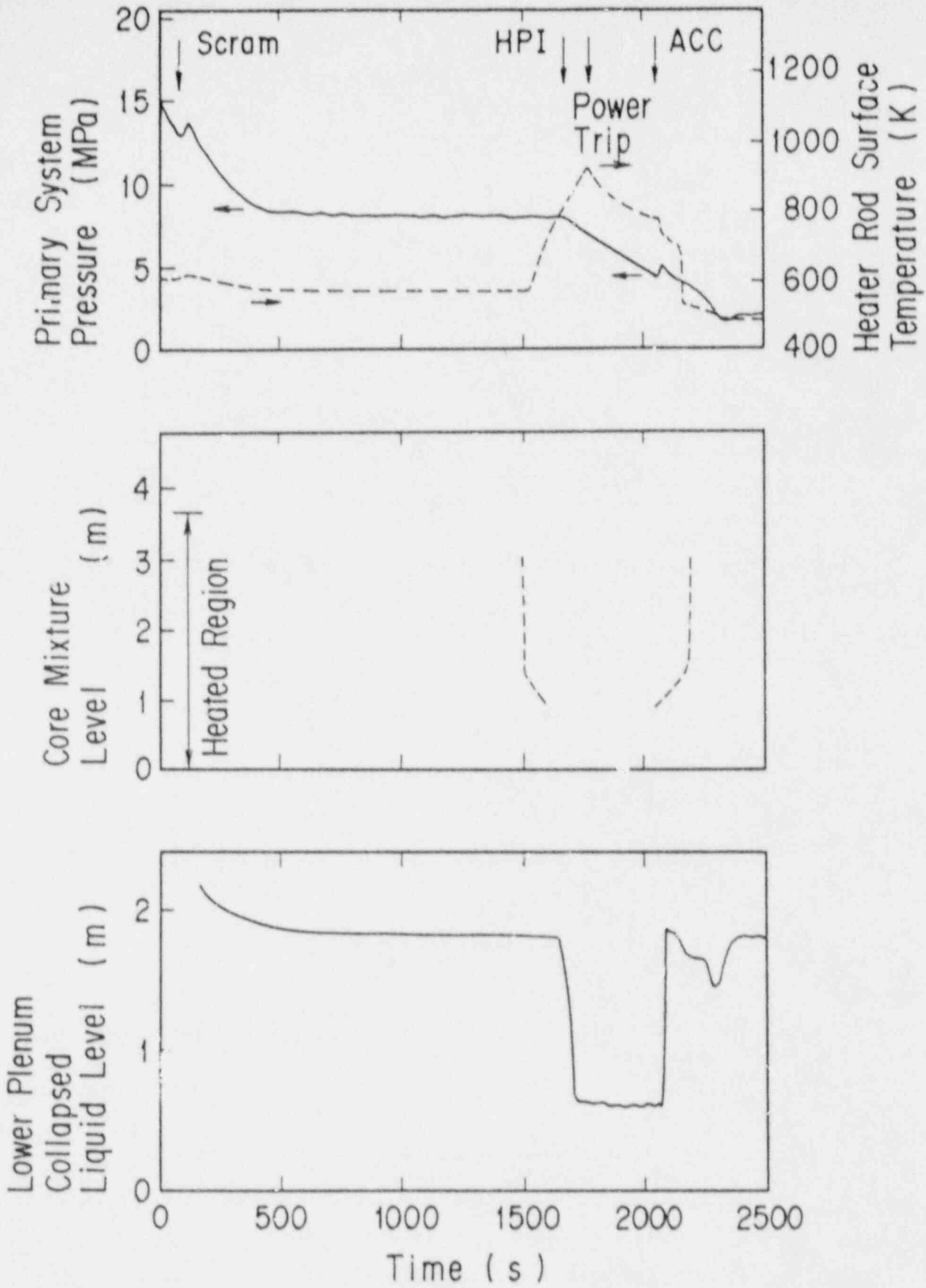

Fig. 7 Major Transient Parameters During Lower Plenum Break Test, SB-PV-01

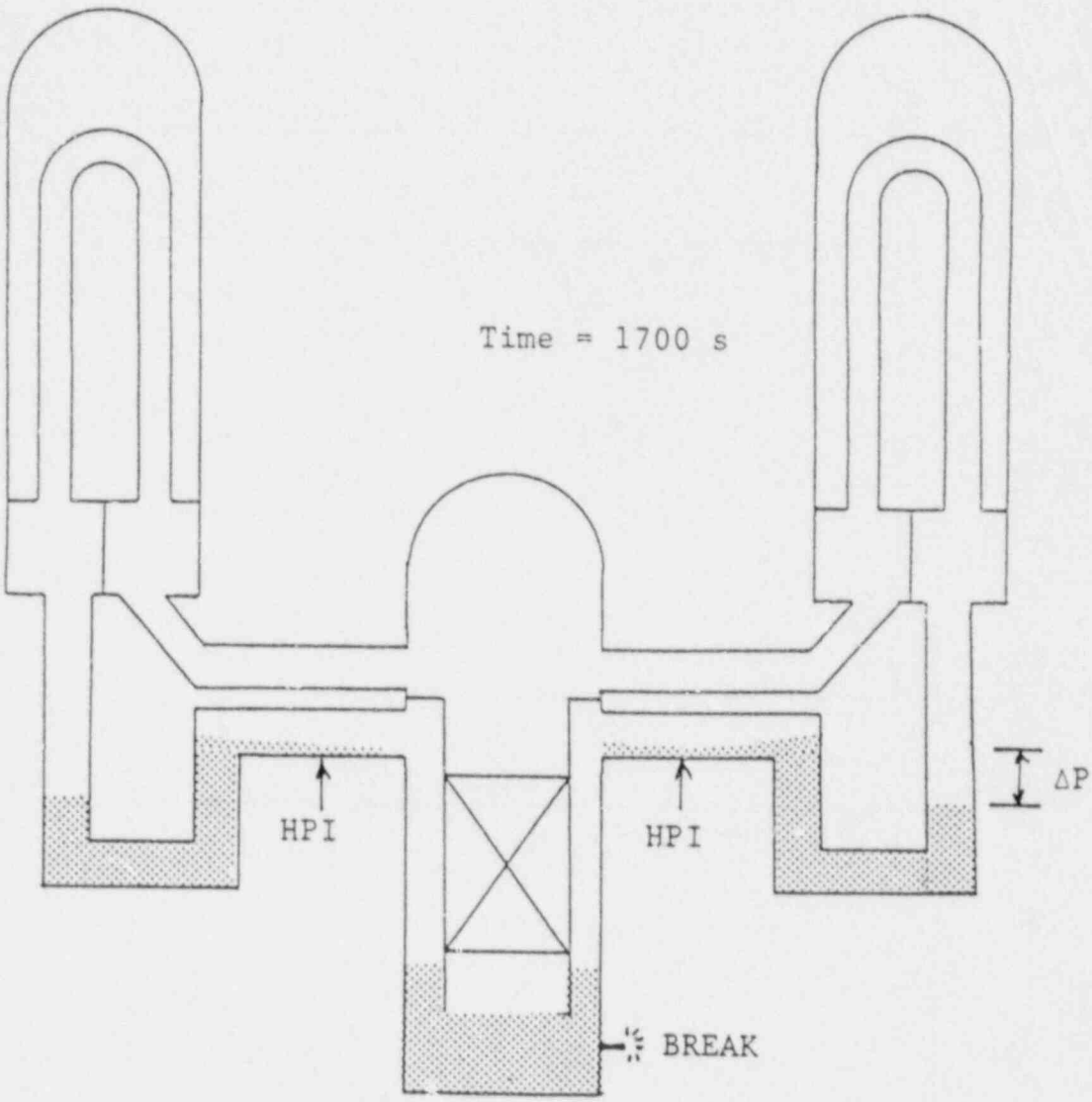

Fig. 8 Coolant Distribution Immediately after HPI Initiation in Lower Plenum Break Test, SB-PV-C1

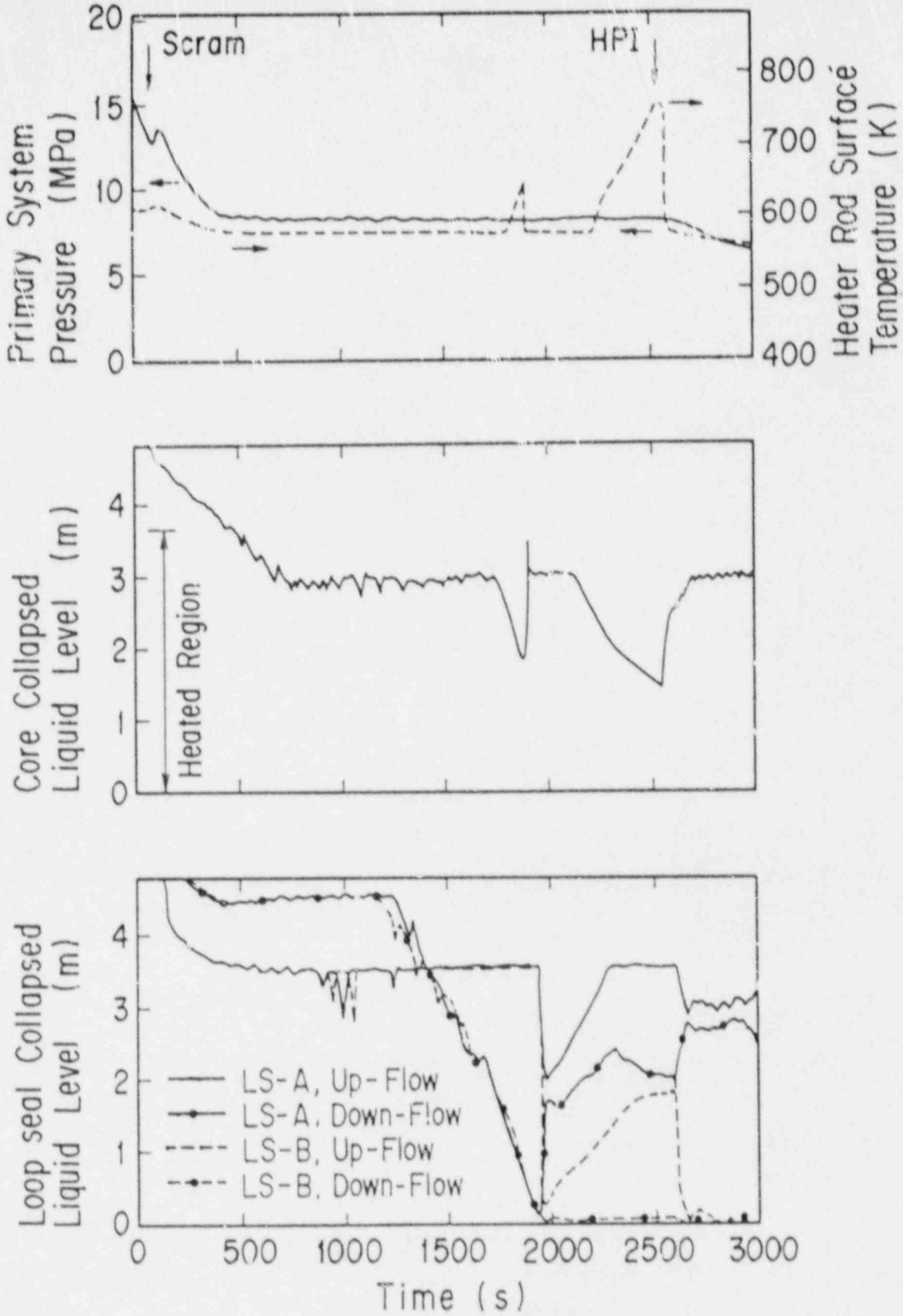

Fig. 9 Results of Cold Leg Break Test, SB-CL-11

a)

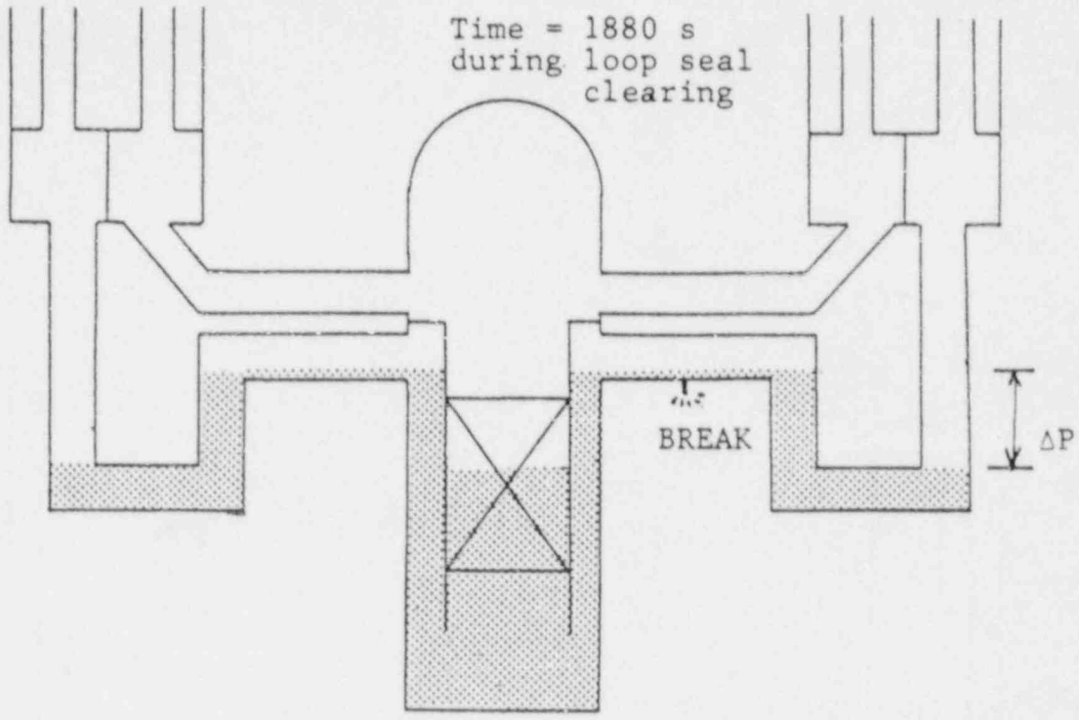

b)

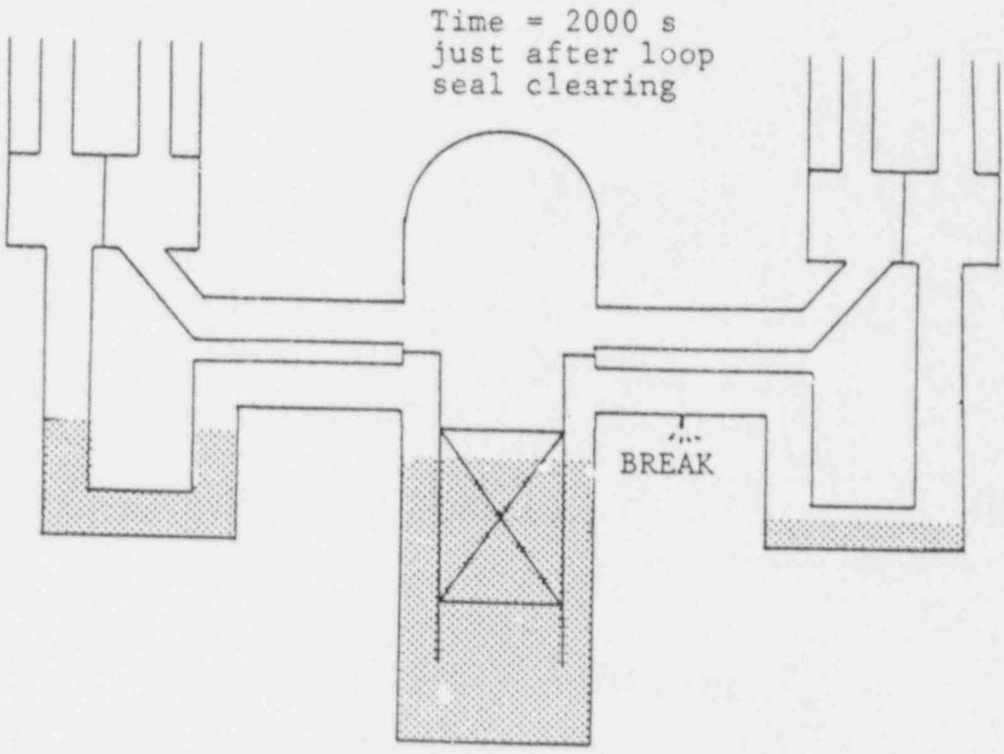

Fig. 10 Primary System Coolant Distribution during Cold Leg Break Test, SB-CL-11

c)

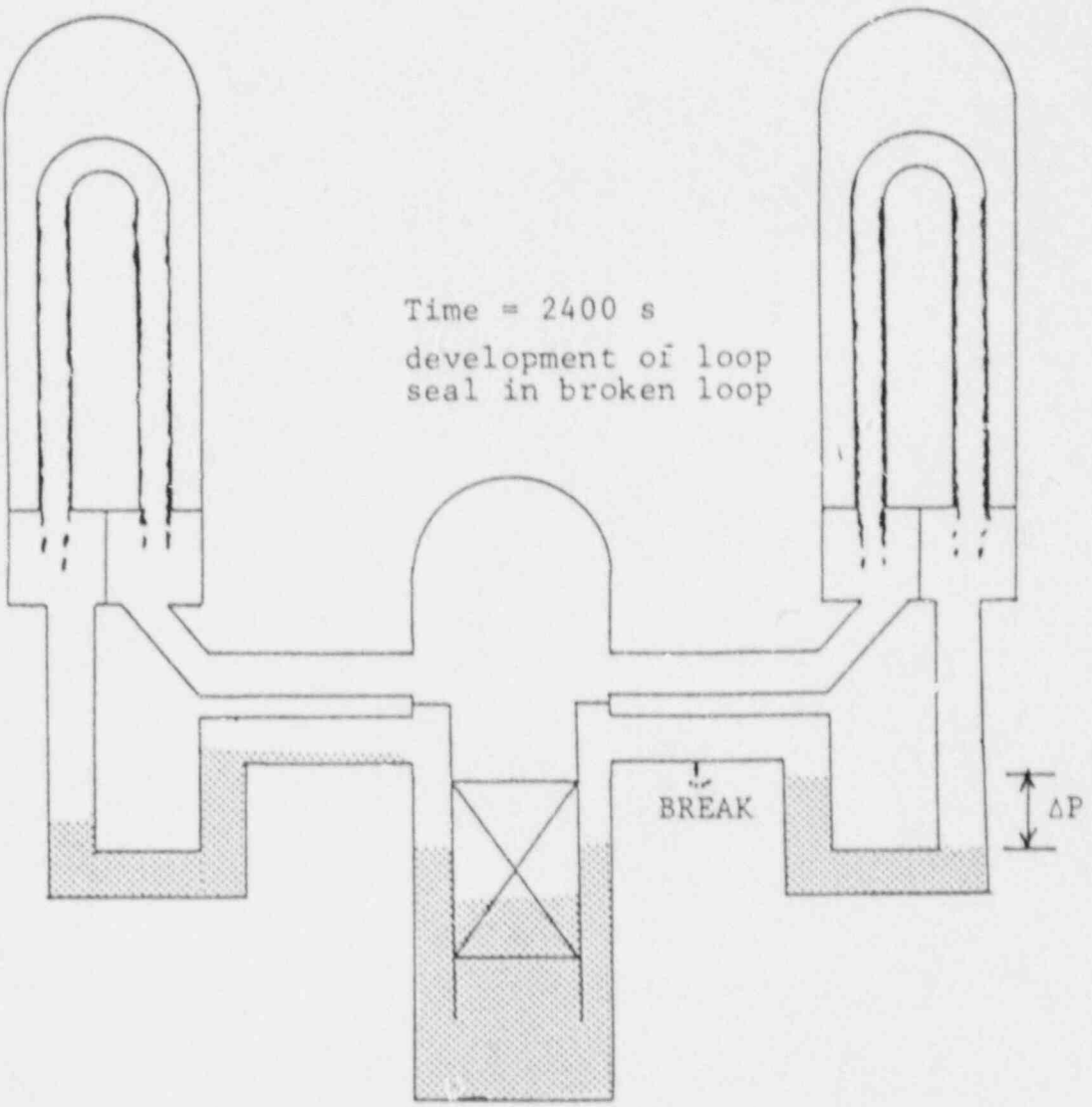

Fig. 10 (continued)

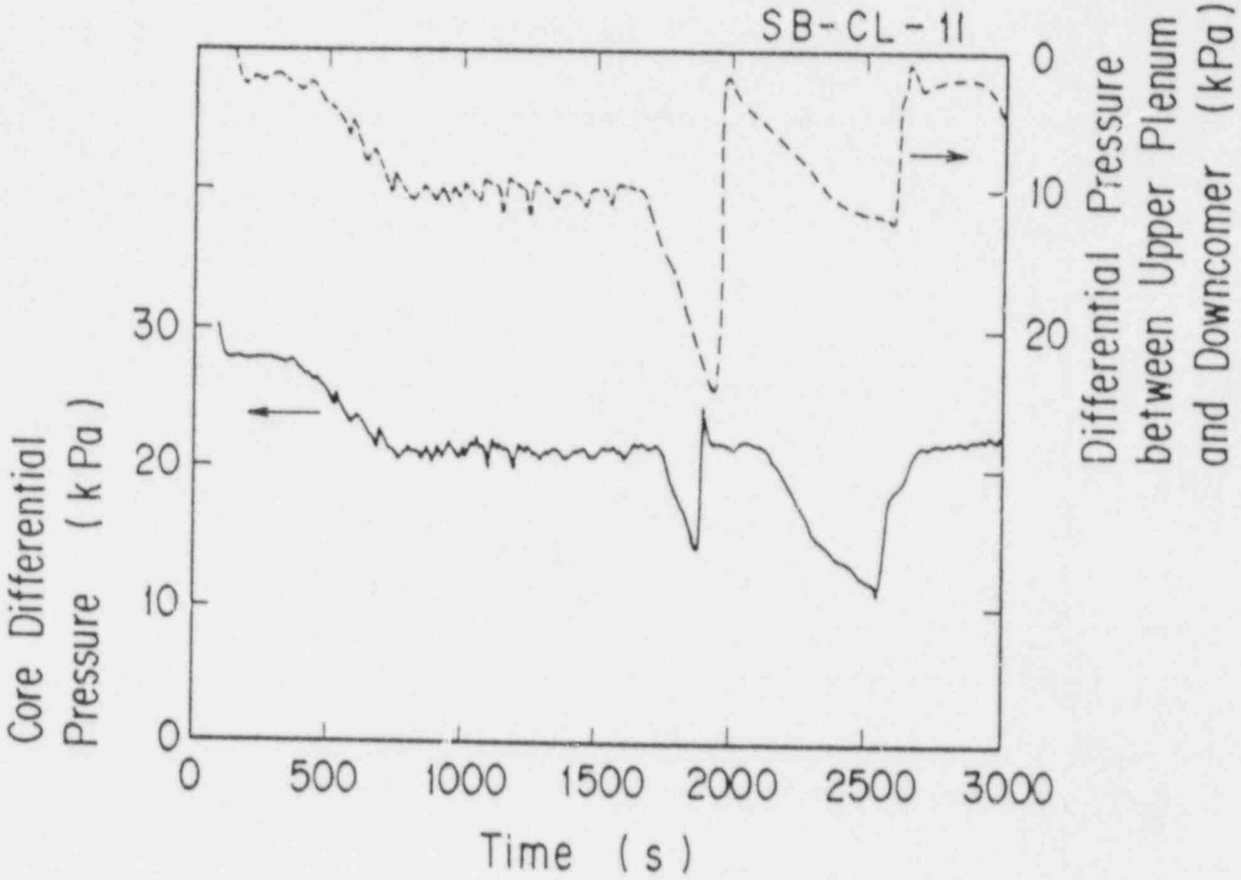

Fig. 11 Contribution of Loop Differential Pressure to Core Level Depression during Cold Leg Break Tests, SB-CL-11

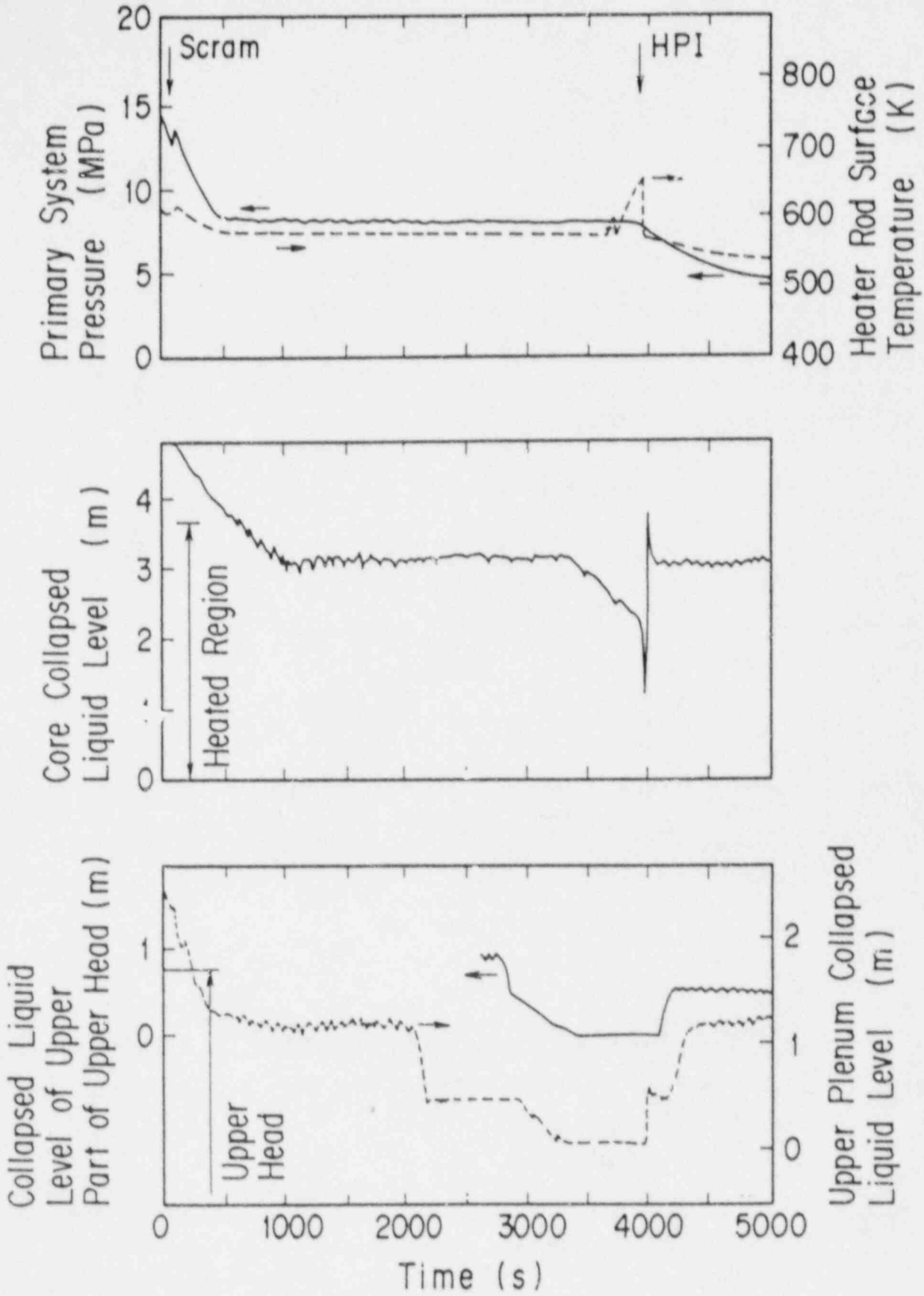

Fig. 12 Results of Upper Head Break Test, SB-PV-02

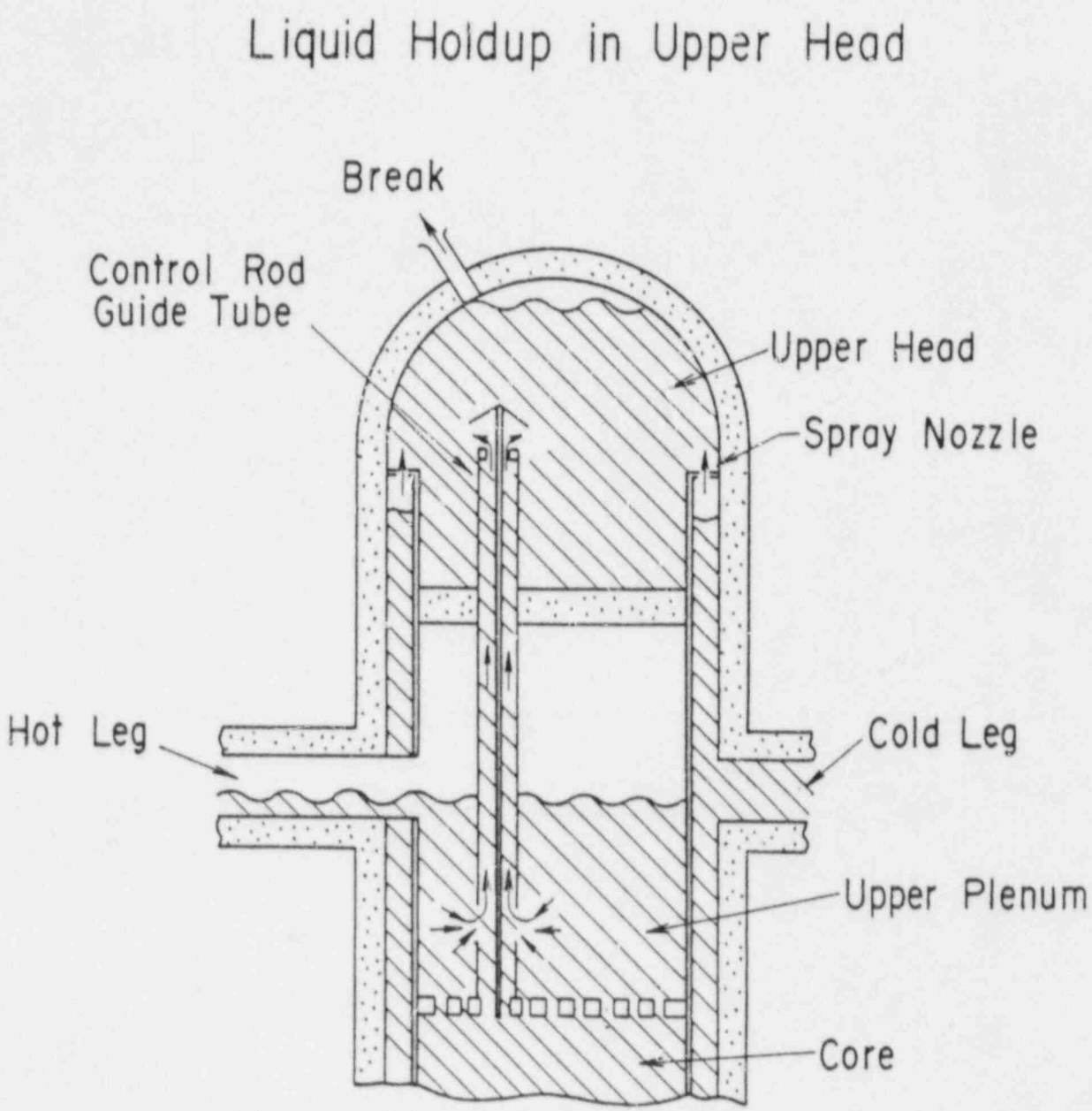

Fig. 13 Coolant Distribution in Upper Part of Pressure Vessel during Upper Head Break Test, SB-CL-11

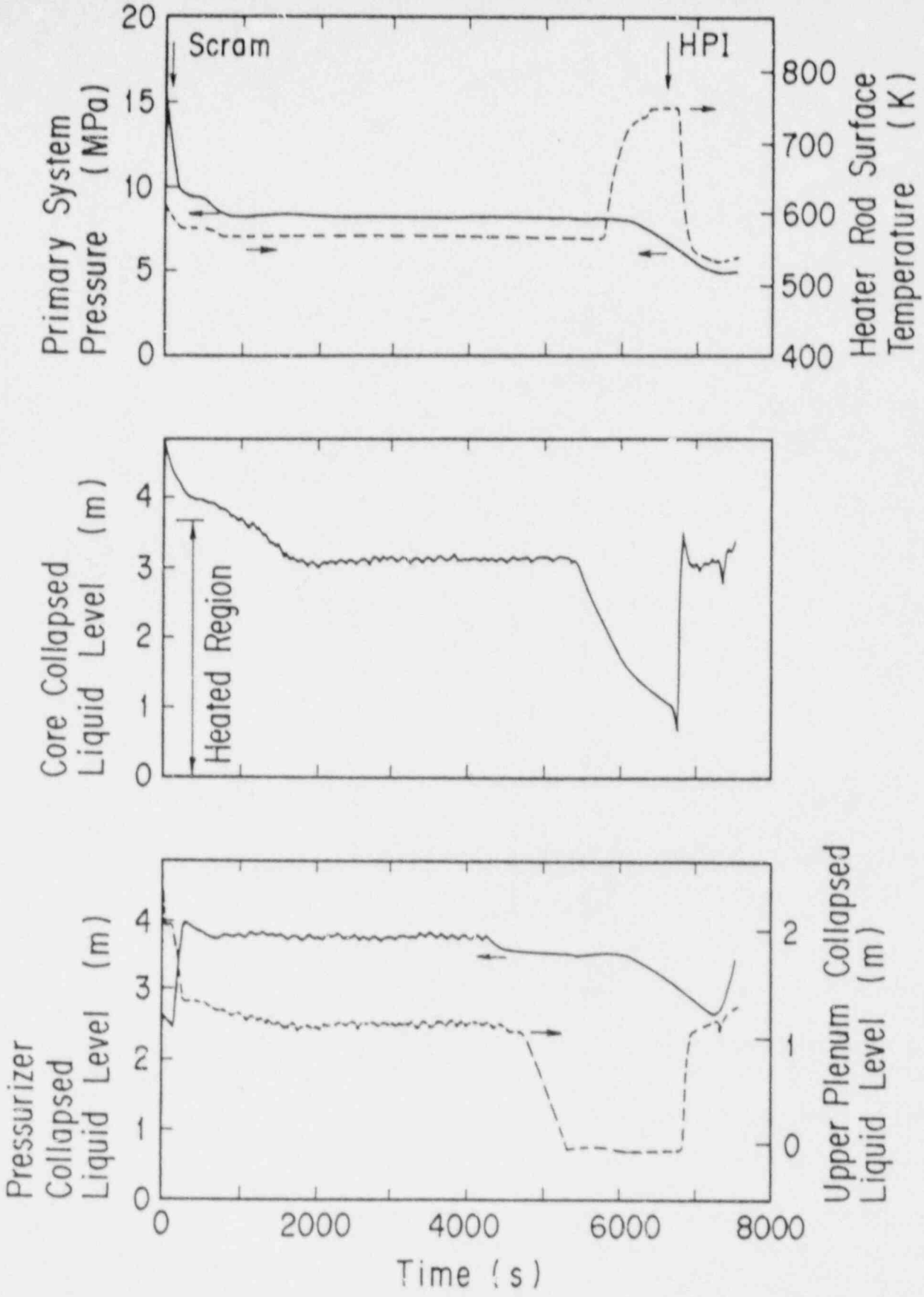

Fig. 14 Results of Pressurizer PORV Break Test, AT-SB-03

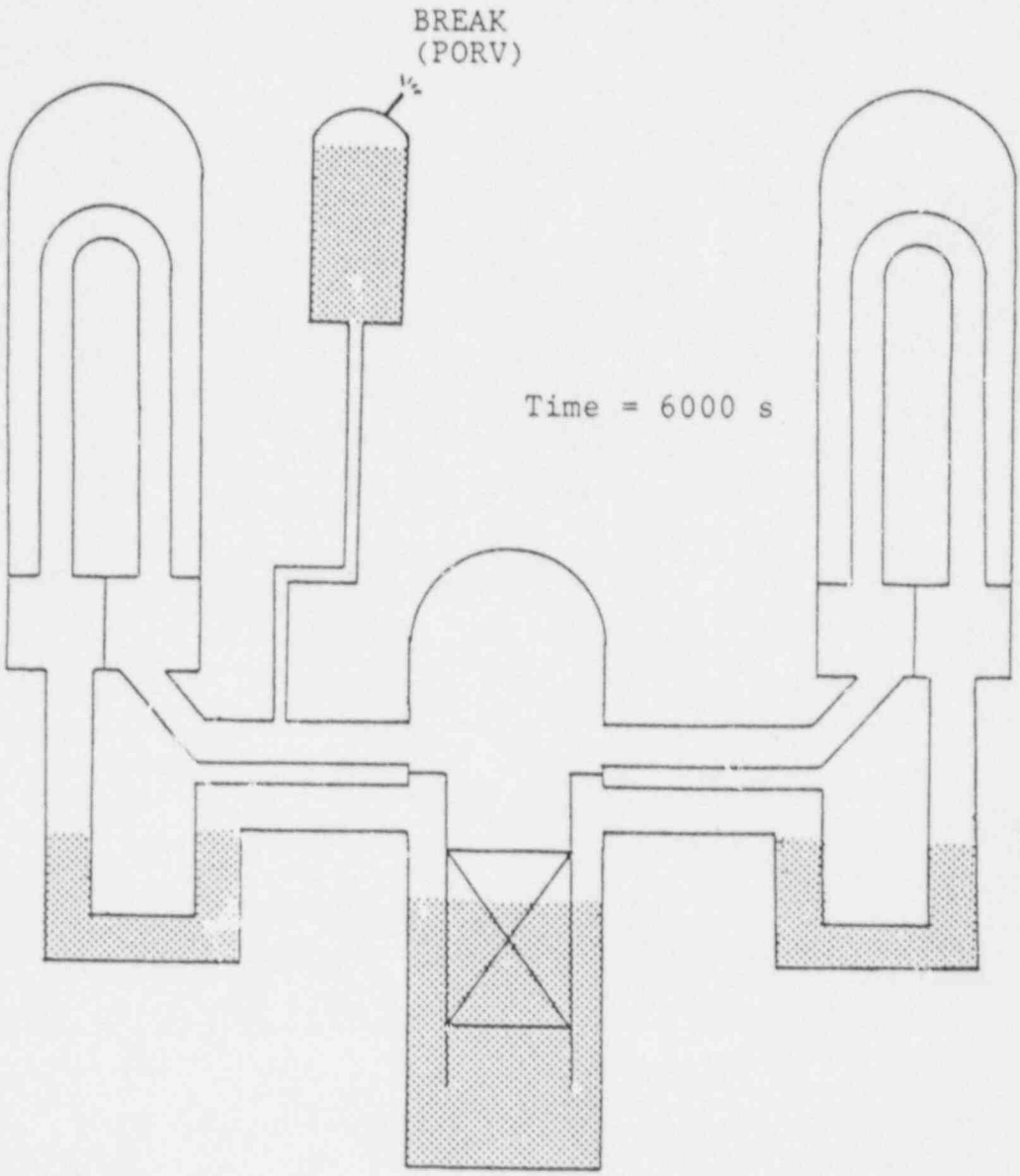

Fig. 15 Coolant Distribution in Pressurizer PORV Break Test, AT-SB-03

CORE LIQUID LEVEL DEPRESSION IN 5% SMALL BREAK LOCAS: AN INVESTIGATION USING SUBSCALE DATA[a]

R. R. Schultz[b], F. E. Motley[c], H. Stumpf[c], J. C. Watkins[b], and Y. S. Chen[d]

ABSTRACT

Core heatup has been shown to be possible, during the course of small break loss-of-coolant accidents (SBLOCAs), even when sufficient inventory is present to fully cover the rods with a two-phase mixture. Such behavior occurs when steam, trapped between the loop seal and the core inventory, moves coolant out of the core barrel region and uncovers the rod upper elevations. The net result is core liquid level depression.

Core liquid level depression and subsequent core heatups are investigated using subscale data from the ROSA-IV Program's 1/48-scale Large Scale Test Facility (LSTF) and the 1/1705-scale Semiscale facility. The depression phenomena and factors which influence the minimum core level are described and illustrated using examples from the data. Analyses conducted using the TRAC-PF1/MOD1 version 12.7 thermal-hydraulic code are also described and summarized.

INTRODUCTION

Several subscale experiments conducted over the past few years have demonstrated that core uncovery and heatup can occur during a small break loss-of-coolant-accident (SBLOCA), even when sufficient vessel liquid inventory is available to completely cover the core with a two-phase mixture level. Such a situation was observed when simulating 5% cold leg SBLOCAs in two Westinghouse (W) plant simulators: the Semiscale facility (1/1705-scale) and the Japan Atomic Energy Research Institute's (JAERI) 1/48-scale Large Scale Test Facility (LSTF). Core uncovery occurred, prior to 300 s in the transient, when steam generated by core decay power, flashing, and metal mass stored energy, expanded against vessel and loop liquid inventory while enroute to the simulated cold leg break. Core liquid inventory was moved out of the core shroud region (core liquid level depression) into the vessel lower plenum and downcomer regions by the expanding steam. As the core heater rods uncovered subsequent heatup occurred. The core heatup was mitigated when steam moved through the loop

---

a. Work supported by the U.S. Nuclear Regulatory Commission, Office of Nuclear Regulatory Research under DOE Contract No. DE-AC07-76ID01570. Note: The data contained herein, from the ROSA-IV Program, were provided by the Japan Atomic Energy Research Institute (JAERI).
b. EG&G Idaho, Inc., Idaho National Engineering Laboratory (INEL).
c. Los Alamos National Laboratory (LANL).
d. United States Nuclear Regulatory Commission (USNRC).

seal and reached the break. During the subsequent depressurization, the vessel liquid inventory flowed back into the core shroud volume.

The following subsections describe the major factors contributing to core liquid level depression and the subsequent core heatup. To support the description of the core liquid level depression sequence, data from two LSTF experiments are described in some detail. Finally, the ability of the USNRC's TRAC-PF1/MOD1 thermal-hydraulic analysis code to calculate core liquid level depression phenomena is briefly summarized by comparing code calculations to data from four experiments. The following subsections are organized as follows:

1. The subscale facilities are briefly described.

2. The 5% SBLOCA experiments are summarized.

3. The SBLOCA behavior in general and the core liquid level depression behavior in particular are discussed in detail. Data from two of the LSTF experiments are used to support the described behavior. Finally, factors which influence the core liquid level behavior are described and results from parametric changes are compared.

4. The overall results of code assessment calculations of the above experiments are presented and discussed. The calculations were done using the TRAC-PF1/MOD1 version 12.7 code.

5. Conclusions and observations are summarized.

EXPERIMENTAL FACILITY DESCRIPTIONS

The two facilities which are compared herein, are different from one another not only from a scaling perspective, but also in other ways as well. The LSTF and Semiscale facilities are each described briefly in the following paragraphs to establish the discussion basis for the remainder of the paper.

Large Scale Test Facility

The LSTF is a nonnuclear model of a W four loop pressurized water reactor (PWR) such as the Trojan plant (hereinafter called the reference PWR). The LSTF was designed to simulate SBLOCAs (up to 10%) and operational transients. The LSTF has two equally sized loops (see Fig. 1) that differ only in the possible break geometries and in the presence of a pressurizer in one of the loops. Each loop contains all the components of the reference plant. The hot and cold legs were scaled based on $L/\sqrt{D}$, where L is the piping length and D the piping diameter, to properly simulate flow regime transition. Each LSTF steam generator (SG) represents two SGs in the reference PWR and has 141 full-sized U-tubes. Six of the U-tubes in each SG are fully instrumented and can be used to analyze the system behavior. Of the instrumented U-tubes, two each are representative of the short, medium and long SG U-tube lengths of the reference plant. The vessel, built with internal downcomers and housing 1064 electrical heater rods (simulating 17 x 17 rod bundles), also models

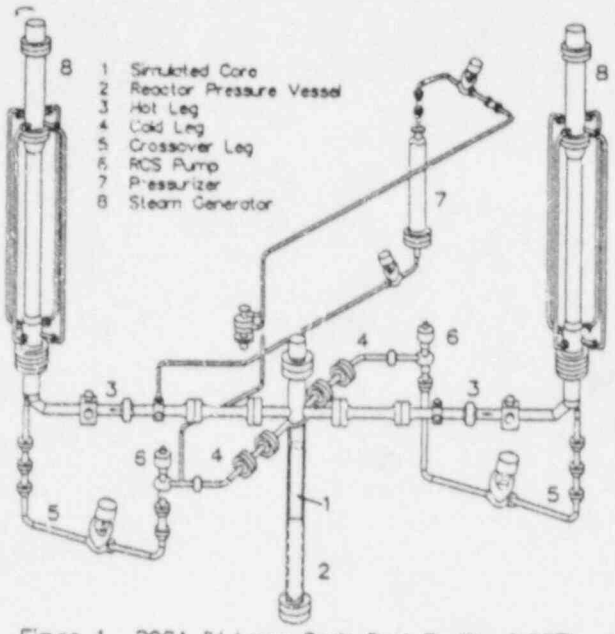

Figure 1. ROSA IV Large Scale Test Facility (LSTF).

the various reference PWR vessel leakage paths. The primary volume is 8.2 m^3 and the standard operational primary conditions are 15.6 MPa and 600 K. The LSTF can operate at a maximum power of only 10 MW, i.e. 14% of rated scaled power.

Semiscale Test Facility

The Semiscale (sponsored by the USNRC through the Department of Energy) Mod-2C configuration is a small-scale non-nuclear model of the reference PWR. The scaling basis is a modified volume scaling using a scaling factor of 1/1705. The relative elevations and sizes of the facility components and the dynamic pressure heads around the loop are maintained as prototypical as practical. The primary coolant volume of the facility is about 0.21 m^3, and the design operating pressure and temperature are 15.2 MPa and 600 K. The facility consists of a pressure vessel housing the simulated reactor core, a pressurizer, and two primary coolant loops each containing an active steam generator and a primary coolant pump. The vessel downcomer is an external pipe. The reactor core was simulated with a 5 x 5 array of electrically heated rods. Support plates, guide tubes, support columns, and an annular input plenum are also simulated in the Mod-2C vessel. The "intact" loop represents three PWR loops, and the "broken" loop represents the remaining PWR loop. The steam generators are inverted U-tube and shell boilers. The intact loop steam generator has six inverted U-tubes paired into three representative heights. The broken loop generator has two inverted U-tubes corresponding to the longest and the shortest tubes in the intact loop generator.

SBLOCA EXPERIMENT DESCRIPTIONS

Three experiments were conducted in the LSTF to examine the core liquid level depression phenomenon, i.e., SB-CL-05, -08, and -10. Of these, SB-CL-10 was a LSTF counterpart experiment to the Semiscale LH-1 experiment. The three LSTF experiments and the Semiscale experiment were 5% SBLOCAs that were simulated by opening break valves in the cold leg at the beginning of the test. The programmed initial and boundary conditions were as listed in Table 1. All the experiments were initiated with typical reference PWR primary thermodynamic conditions. However, the experiments differed in the upper head bypass flow and the core decay power curve.

The SB-CL-05 experiment, originally scheduled to be done with only a 0.5% bypass, was found to have 2.3% bypass since unanticipated leakage paths were located in the pressure vessel upper head and plenum. Consequently, following repair, SB-CL-08 was conducted with the same initial conditions as SB-CL-05, but with a greatly reduced upper head bypass flow, i.e., 0.3%. Later, the SB-CL-10 experiment was conducted as a counterpart test to the

Semiscale-LH-1 experiment to provide a means of comparing the scale differences between the two facilities. SB-CL-10 had 0.5% upper head bypass (Note: Due to thermal fatigue, the weld repairs to the vessel upper head between SB-CL-05 and -08 had partially failed such that the upper head leakage increased by the time SB-CL-10 was conducted.) and the Semiscale LH-1 test had 0.9% bypass.

A significant difference between the three LSTF experiments was in the core power decay curves. JAERI defined a power decay curve early in the ROSA-IV Program based on conservative assumptions[1] including the contribution of neutron fission power (see Table 2). The JAERI power decay curve gives markedly larger core decay power during the first 300s of SBLOCA transients (exactly the period of time when core liquid level depression occurs during a 5% SBLOCA) than the Semiscale power decay curve. However, the Semiscale power decay curve[2] was based on the 1979 American Nuclear Society's decay heat curve for an equilibrium core plus the core typical stored energy and is thus more representative of the reference PWR decay power.

Test Procedures - LSTF

All of the LSTF tests compared herein were conducted in a similar manner. Since the LSTF is only capable of maintaining 14% of rated scaled core power at steady-state initial conditions, the coolant pumps and the secondary system conditions were changed accordingly. Thus, the pumps were operated to deliver 14% of rated scaled primary mass flow and the secondary system pressure was held at 7.4 MPa (Note: The normal reference PWR condition is 5.7 MPa.) to limit the primary to secondary energy transfer rate to 14% of the rated scaled value. Immediately after the transient began, the coolant pumps were accelerated to their maximum speed to deliver approximately 30% of rated scaled mass flow such that the primary to secondary energy transfer was increased as much as possible to approach the reference PWR behavior. Thereafter, equipment tripped on or off at the conditions listed in Table 3. A summary of the test procedures is given in the SB-CL-10 Quick Look Note[3]. A summary of the hardware design requirements and compromises is given in the LSTF System Description[4].

Test Procedures - Semiscale

The Semiscale facility had power and pump capabilities sufficient to simulate 100% rated scaled conditions in a reference PWR. However, the facility surface area to volume ratio was so large that the facility had uncharacteristically large system power losses. Consequently, "guard" heaters attached to the outer facility walls were used throughout the experiment to compensate for system heat losses.

Trips used to switch equipment on or off are summarized in Table 3. A more detailed description of the facility characteristics and operational characteristics are given in the Semiscale LH-1 experimental results report[5].

Table 1 - 5% SBLOCA Experiments: Initial and Boundary Conditions

Parameter	LSTF SB-CL-05	LSTF SB-CL-08	LSTF SB-CL-10	Semiscale S-LH-1
Primary pressure (MPa)	15.6	15.4		15.5
Cold leg fluid temp (K)	565.	565.		562.[1]
Core temperature rise (K)	34.	35.4		37.8
Total primary mass flow (kg/s)	49.3	48.8		9.48
Total bypass flow (%)[2]	2.3	0.3		0.9
Power decay curve[3]	JPD	JPD		SPD

1. Intact loop values given.
2. Percent of total mass flow rate.
3. JPD = JAERI power decay; SPD = Semiscale power decay - see Table 2.

Table 2 - Comparison of JAERI and Semiscale Power Decay Curves

Time (s)[1]	JAERI[2]	Semiscale used by JAERI[2]	Semiscale[2]
0.	0.14	0.14	1.00
15.4	0.14	0.14[3]	1.00
19.6	0.14	0.13	1.00[3]
20.0	0.14	0.13	0.99
40.0	0.139[3]	0.063	0.056
60.0	0.12	0.043	0.041
80.0	0.10	0.036	0.037
100.0	0.086	0.033	0.035
150.0	0.059	0.030	0.032
200.0	0.044	0.029	0.032
300.0	0.034	0.027	0.030

1. Time after break.
2. Normalized power, i.e., (Core power)/(Rated scaled power).
3. Beginning of power decrease.

CORE LIQUID LEVEL DEPRESSION PHENOMENA

SBLOCA transients, with the initial and boundary conditions described in the previous sections, can be summarized as consisting of nine important event groups (see Ref. 6 - Section 4.2), as outlined in Table 4. It should be noted that the Table 4 event group timings overlap in some cases.

The following four subsections discuss the first 300s of 5% cold leg SBLOCAs in the LSTF and Semiscale. The first subsection outlines the events occurring in the LSTF SB-CL-10 experiment to serve as an example of such transients. The next subsection addresses the core liquid level depression observed during SB-CL-10 exclusively. The third subsection discusses parameters which affect core depression, especially those which exacerbate

Table 3 - Equipment Trips and Setpoints: LSTF and Semiscale First 300s of Transient[1]

Parameter	LSTF			Semiscale
	SB-CL-05	SB-CL-08	SB-CL-10	S-LH-1
Reactor scram[2]	12.97MPa	12.97MPa	12.6MPa	12.6MPa+4.6s
Initiation of pump coastdown[3]	——— at reactor scram ———			
High pressure injection	[4]	None		12.6MPa+27.s
Main feedwater termination	Scram+28.s	Scram		12.6MPa
Auxiliary feed initiation	Scram+28.s	None		None
Main steam valve closure	Scram	Scram		12.6MPa
Secondary relief valve[6]				
Open - 1st cycle	8.03MPa	8.03MPa		Not used
Close	7.82MPa	7.82MPa		
Open - Subsequent cycles	8.03MPa	8.03MPa		

1. All listed pressures are in the pressurizer unless otherwise noted.
2. Scram occurred at pressure indicated plus time delay if listed.
3. The coolant pump coastdowns were the same for SB-CL-05 and -08. The coolant pump coastdown used in SB-CL-10 was programmed to match that of Semiscale LH-1.
4. High pressure charging pump trip signal given at 12 s after 12.27 MPa reached. Safety injection pump trip signal given at 17 s after 12.27 MPa reached.
5. High pressure injection signal generated 25 s after scram.
6. Reference pressure in secondary.

Table 4 - SBLOCA Scenario: Important Events

Event Group	Description of Event Group
1.	Break initiation and the resulting coolant discharge.
2.	Rapid depressurization of the primary coolant system until flashing occurs, and subsequent decreases in the primary depressurization rate as core flashing/boiling occurs and the break coolant discharge becomes two-phase.
3.	Rapid decrease in pressurizer water level, continued core inventory flashing, and development of steam volumes in the upper core region and vessel top.
4.	Change in character of primary to secondary energy exchange. Such behavior is caused by isolation of the secondary due to closure of the turbine stop valve and the incidence of a two-phase primary mixture entering the steam generator's (SG) U-tubes. A continuous vapor phase at the top of the SG U-tubes is established.
5.	Initiation of high pressure (HP) emergency core cooling (ECC) system injection, stabilization of the primary pressure at a relatively high level, e.g., 8 MPa, and the beginning of core uncovery.
6.	Core liquid level depression and loop seal clearing.
7.	Following loop seal clearing and a subsequent increase in the core liquid level, an increased primary depressurization rate occurs. During this phase of the transient, the primary pressure may decrease to a value less than the secondary pressure.
8.	The core remains well-cooled, i.e., submerged, by either a single or two-phase mixture level until core boil-off begins, with the possible exception of the core liquid level depression phase (see items 6 and 7).
9.	Possible core heatup phase resulting from primary inventory boil-off. Whether boil-off results in core heatup is tied to the system's depressurization and the ECC system's characteristics.

core uncovery and heatup. Finally, the results are summarized. Although the overall behavior of the SBLOCA transient for the first 300s will be briefly discussed, i.e., items 1 through 8 - Table 4, the discussion focuses on items 6 through 8, i.e., core liquid level depression, subsequent core heatup, and loop seal clearing.

The 5% SBLOCA Transient: The First 300s

NOTE: The discussion concerning the SB-CL-10 experiment is JAERI PROPRIETARY until JAERI has first published their initial results. After their publication, please contact R. R. Schultz for complete copies of the text.

Factors Exacerbating Core Depression

Data from three other experiments were also examined to gain insight into the factors which worsen core depression, i.e., give a lower core liquid level during the loop seal clearing phase of the SBLOCA transient. The other tests are briefly compared in Table 1 and will be discussed individually in the following paragraphs.

SB-CL-08 Experiment[9]

The major difference between the SB-CL-08 and -10 experiments was the core power decay boundary condition. CL-08 was conducted using the JAERI power decay while CL-10 used the Semiscale power decay (see Table 2). Thus, during most of the transient, CL-08 had at least twice the core decay power that was input to CL-10.

The SB-CL-08 transient followed the same sequence of events observed in CL-10 and outlined in Table 4. However, the time of each event was earlier. As summarized in Fig. 8, the loop seal clearing phase of the transient began at 106 s, the minimum core level was reached at 138 s and the loop seal clearing phase was completed at 216 s.

An important difference between the CL-08 and -10 experiments was in the net core steaming rates. Because of the larger power in CL-08, the vapor fluxes at the SG U-tubes were such that the countercurrent liquid flux was probably in the CCFL or flooding mode prior to the minimum core level time (see Fig. 7). Consequently, when the loop seal clearing phase of the transient began, a substantial collapsed liquid level was present in the upflow side of the U-tubes. In addition, larger collapsed liquid levels were also present in the hot leg and the SG downflow sides. As the loop seal clearing process occurred and the steam volume increased to fill the loop seal downflow side, the core level was depressed to 0.64 m, i.e., 1.2 m below the loop seal bottom, causing core heatup in a large portion of the core.

An important factor in causing the core level to be so much lower in CL-08 than in CL-10, was the presence of a significant amount of liquid in the SG, particularly the upflow sides of the U-tubes during CL-08. The primary mass inventory was as shown in Fig. 8. Thus, the mass present in the hot side, balanced against the cold side mass, was located not just in

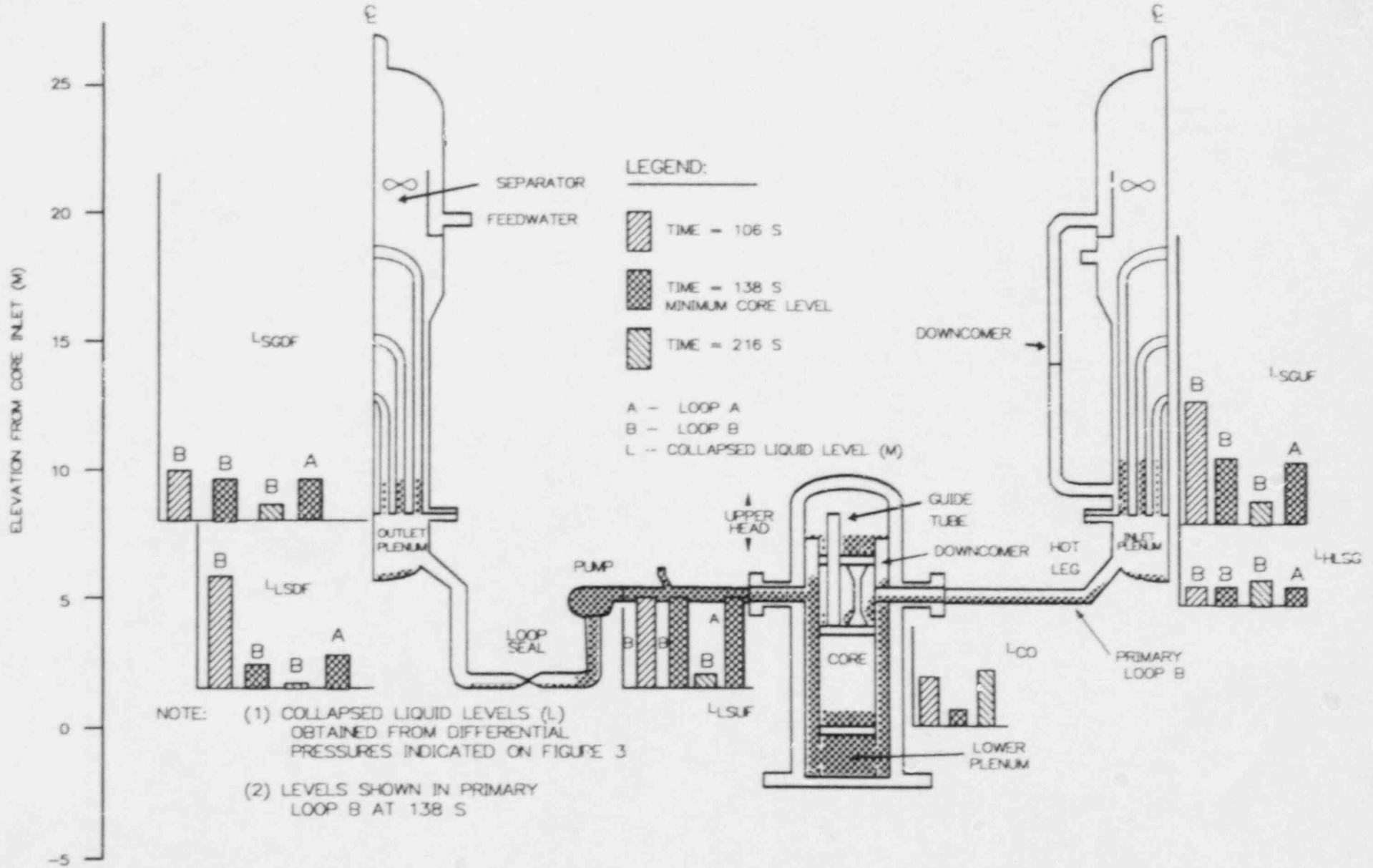

Figure 8. Primary system mass distribution during core depression SB-CL-08.

NSL00744

the core (as in the CL-10 experiment), but instead the SG U-tubes as well. Consequently, the core collapsed liquid level was reduced. These results are summarized in Table 5.

SB-CL-05 Experiment[10]

The SB-CL-05 experiment was very similar to the CL-08 experiment; the major difference being the core bypass. CL-08 was in fact a rerun of the CL-05 experiment that was conducted after the upper head bypass leakage path welds were repaired. Consequently, the two experiments differed in that CL-05 had 2.3% bypass flow and CL-08 had only 0.3%.

Although the bypass flow differed by a factor of seven, no significant differences were seen between the two tests (see Fig. 5). As summarized in Table 5, the loop seal clearing phase occurred over the same time period, the minimum core level was nearly the same, and the core heatup began at the same times.

These results indicate that core bypass is not a significant factor in the extent and timing of the core liquid level depression and are the opposite of the Semiscale results (see Ref. 5). Further analysis is necessary to assess these apparent differences.

S-LH-1 Experiment

The Semiscale LH-1 experiment was the baseline for the initial and boundary conditions used in the SB-CL-10 experiment.

S-LH-1 also followed the same sequence of events as CL-10 and as outlined in Table 4. The loop seal clearing phase began at 125 s (see Fig. 9), 17 s prior to CL-10. However, the core was depressed to it's

Table 5 - Comparison of Core Depression Data:

LSTF and Semiscale Experiments

Event	SB-CL-10	SB-CL-05	SB-CL-08	S-LH-1
Beginning of core heatup (s)		125.	120.	150.
Minimum core level				
Time (s)		137.	138.	173.
Level (m)		0.53	0.64	1.2
Core level recovery (s)		165.	160.	275.
Normalized core power at minimum core level (%)		6.5	6.4	3.3
Core bypass (%)		2.3	0.3	0.9

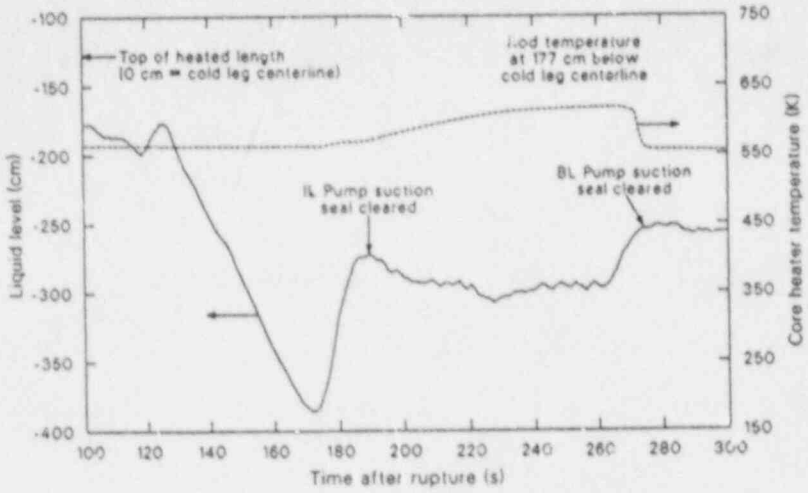

Figure 9. Core liquid level and heater rod temperature during the Semiscale test S-LH-1.

minimum level by 170 s, 30 s earlier than in CL-10. Further, full core level recovery was not experienced in LH-1 until 262 s, when the broken loop seal finally cleared (nearly 91 s after the intact loop seal cleared).

The loop seal clearing process in S-LH-1 was unsymmetrical, as opposed to SB-CL-10 (see Figs. 4 and 10). The core collapsed liquid level was at minimum in response to the intact loop seal being depressed to the minimum level. Liquid present in the broken loop SG upflow side, in particular, was partially responsible for lowering the core level to 1.2 m.

It is believed that the loop seal clearing process, observed in the LH-1 test, reached the core minimum level at an earlier time than in CL-10 due to the asymmetry of the Semiscale facility. However, exactly how the mechanism differs in the Semiscale facility from the LSTF will have to be analyzed further. For example, why didn't the broken loop in Semiscale clear first?

The Semiscale LH-1 core depression data are compared to the three LSTF experiments in Table 5.

Summary

The above discussion clearly shows the importance of core power in determining the magnitude and timing of the core liquid level depression. The difference in timing of the minimum core level between CL-08 and -10 was due to the greater power input in the former test. In addition, the larger steaming rate in CL-08 caused liquid holdup in the SG U-tubes and thus directly increased the portion of the core heater rods that were uncovered and that experienced temperature excursions from those of the lower powered CL-10 test.

The small range of bypass flows simulated in the LSTF does not seem to have an influence on the severity of the core liquid level depression. Further study of this result is needed.

TRAC-PF1/MOD1 VERSION 12.7 CALCULATIONS

All the experiments discussed above were analyzed using TRAC-PF1/MOD1 version 12.7[11]. The following discussion is divided into two major sections. First the LSTF TRAC model is discussed together with the calculational results from the three LSTF experiments. Finally, the Semiscale TRAC model is described and the resulting S-LH-1 calculation summarized.

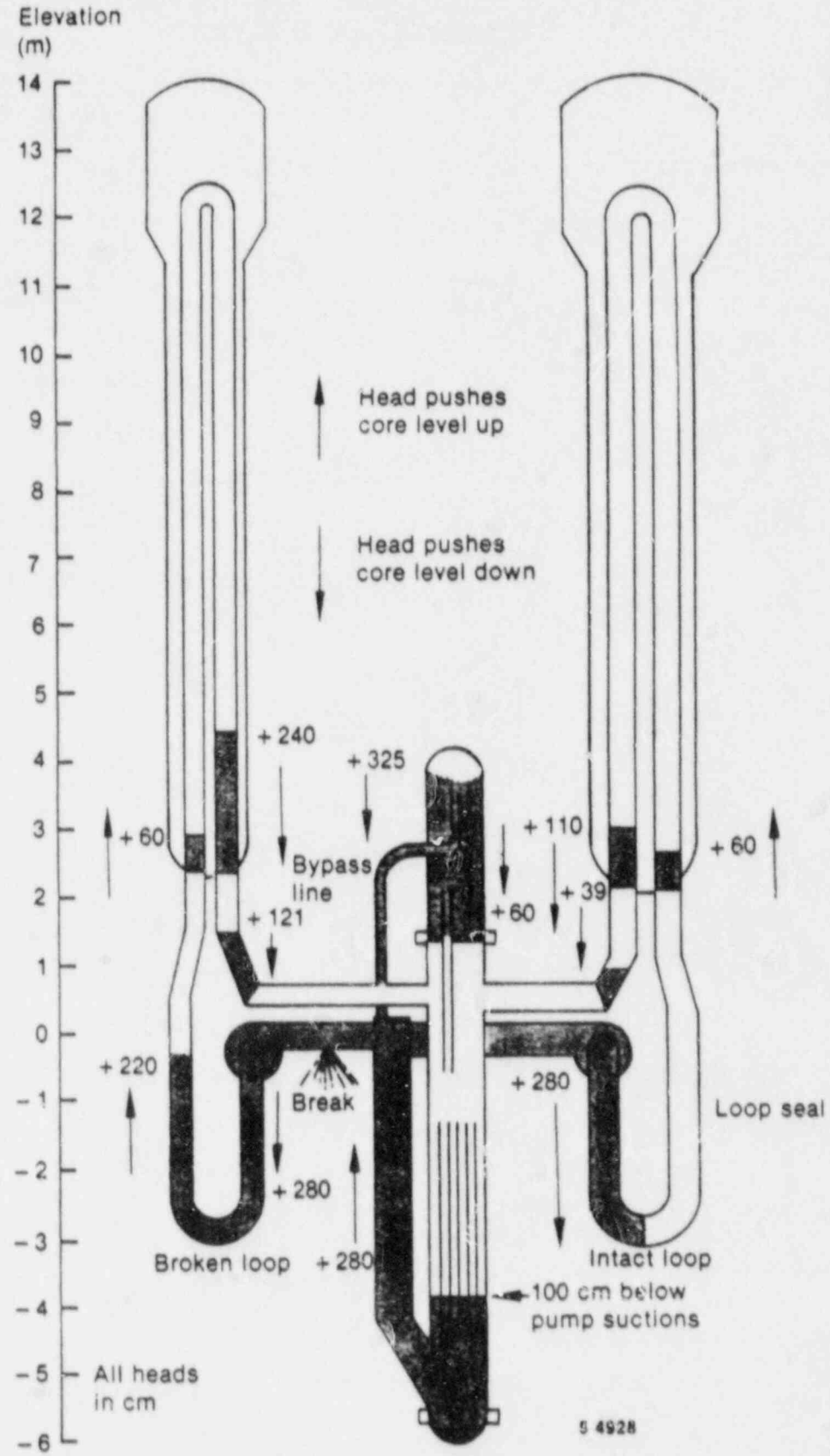

Figure 10. Manometric fluid head balance prior to intact loop pump suction seal clearing during 5% SBLOCA experiment S-LH-1.

LSTF Model and Calculations

The LSTF model was constructed to be economical and yet provide a sufficient amount of detail to adequately simulate all phases of the SBLOCA transients. The model nodalization was defined not only by the system geometry restrictions, but also the instrumentation locations.

The model has 41 components and 50 junctions with a total of 325 computational cells. The vessel has 15 levels, 4 rings and 2 azimuthal sections (see Fig. 11). The model, initial conditions and boundary conditions are described in more detail in the SB-CL-05 analysis paper presented at the 14th Water Reactor Safety Information Meeting[12].

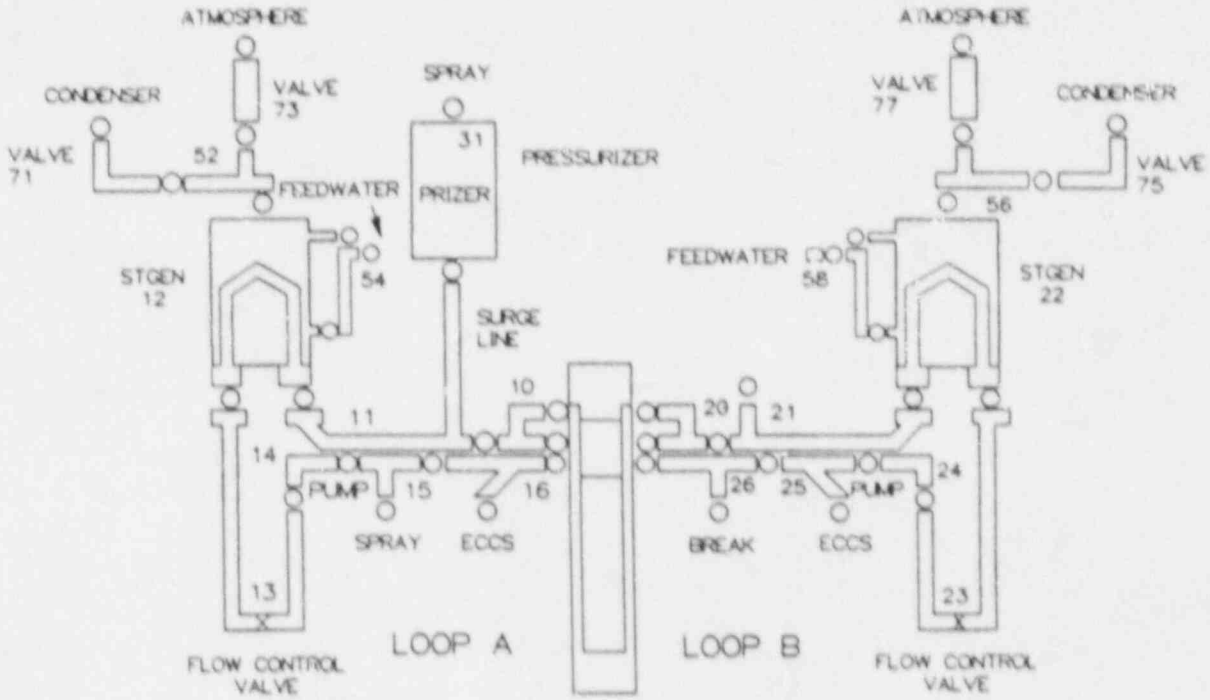

Figure 11. TRAC-PF1 nodalization of the Large Scale Test Facility.

SB-CL-10 Calculation

SB-CL-05 and -08 Calculations

The calculations of the SB-CL-05 and -08 experiments had the same basic characteristics as the SB-CL-10 calculation. The calculated break mass flow rates for the SB-CL-05 and -08 experiments appeared too low with respect to the data. Consequently, the calculated transient events occurred at later times than observed in the data.

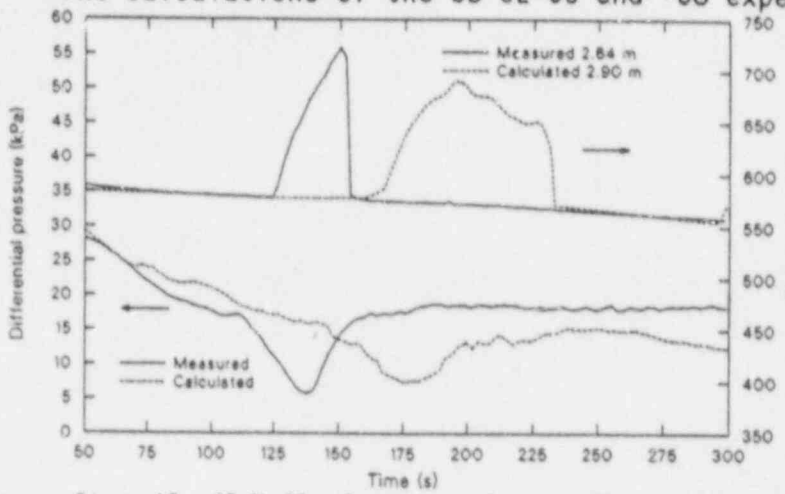

Figure 15. SB-CL-08: Comparison of core differential pressure - and heater rod temperature - measured and calculated.

The predicted core differential pressures and typical core heater rod temperatures for the SB-CL-05 and -08 experiments are shown in Figs. 14 and 15 respectively. Relatively good agreement was obtained between the calculated and measured core differential pressure in part because the calculation predicted liquid holdup in the SG U-tubes much like the data. As in the SB-CL-10 calculation, the predicted core minimum levels were not as severe as the data. However, the predicted core heatups were comparable to the data.

Semiscale LH-1 Model and Calculation

The TRAC-PF1 model of the Semiscale MOD-2C facility was constructed using all one-dimensional components (see Fig. 16). A vessel component was not used since external heaters cannot be simulated in the current code configuration and external heaters were used extensively during the Semiscale SBLOCA experiments.

The model has 55 components and 59 junctions with a total of 218 computational cells. The presence of external heaters was simulated in every component that had such hardware mounted in the experiment. The power to the external heaters was programmed to behave as input to the facility during the LH-1 experiment.

The results of the calculation are summarized using comparisons of the calculated to measured primary pressure, core differential pressure, and a typical heater rod temperature response (see Figs. 17 and 18).

The calculated primary pressure matched the data very closely for the first 35 s of the transient. Thereafter the calculated pressure was greater than the data. The mismatch between the data and the calculation is attributed to (1) a mismatch between the calculated and measured secondary pressure and (2) a calculated saturated break mass flow rate that was 10% less than measured.

The data shows a continually decreasing secondary pressure, after 50 s,

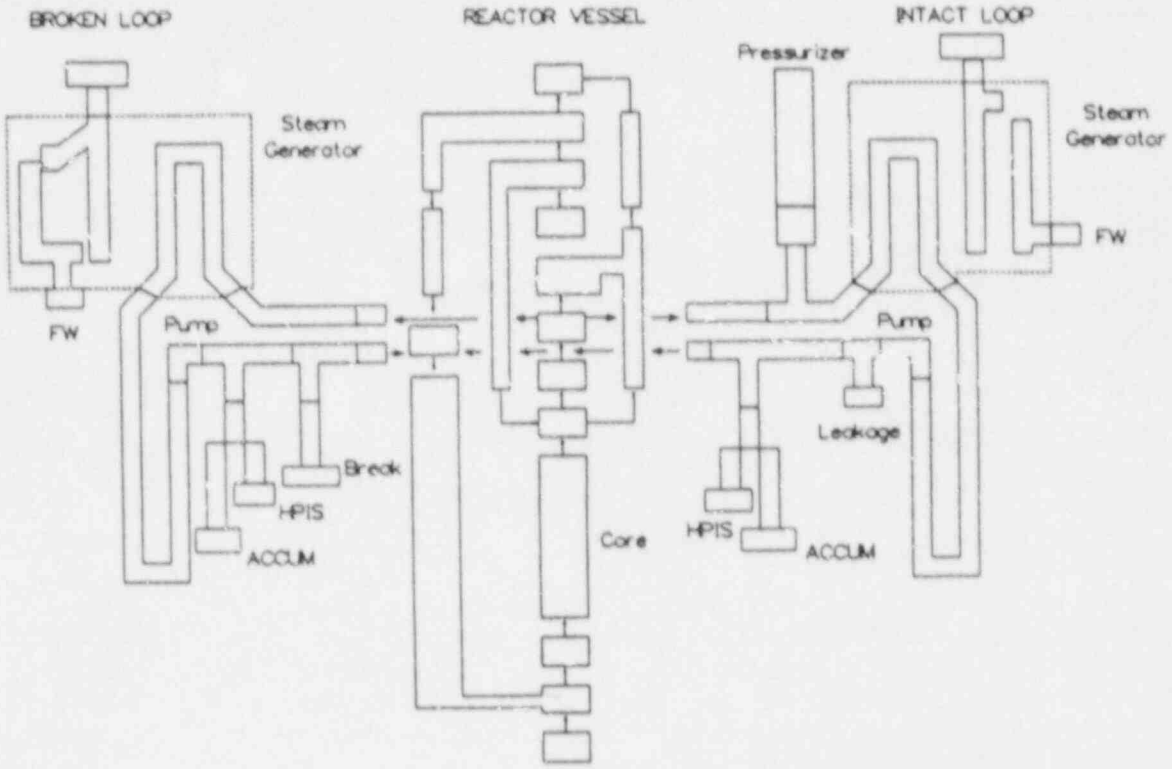

Figure 16. TRAC-PF1 nodalization of Semiscale.

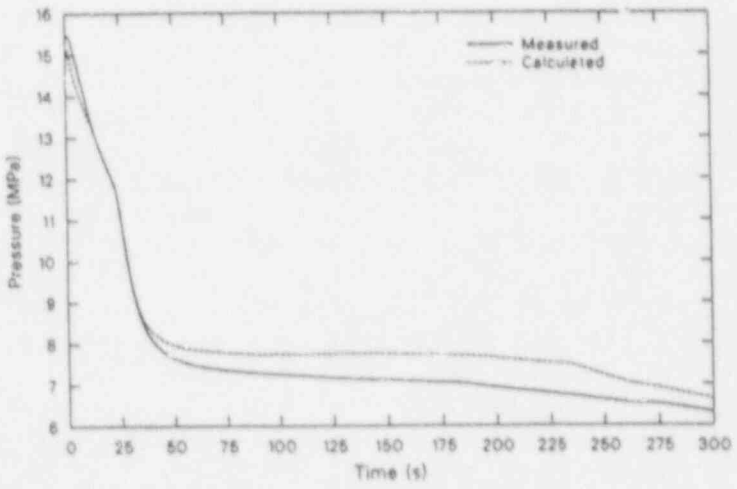

Figure 17. S-LH-1: Comparison of primary pressure - measured and calculated.

that implies a system heat loss. The calculation, even including the best-known information concerning the heat structures and external heater power input, was unable to duplicate the secondary behavior. The decreasing measured secondary pressure was in part responsible for the lower primary pressure than calculated by TRAC.

The core depression calculated by the code compared quite favorably to the data. The calculated minimum core level occurred at 188 s, only 15 s later than shown in the data. The calculated minimum core DP was -25 kPa versus -28 kPa shown by the data. Corresponding to the minimum core level, the calculation predicted a

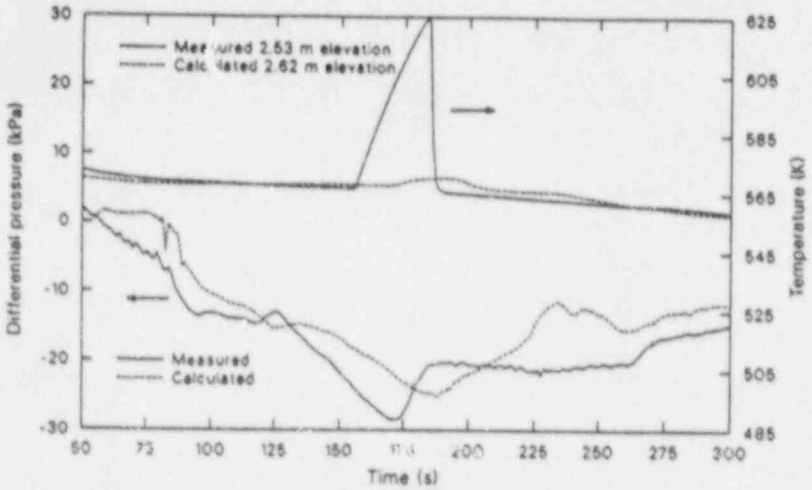

Figure 18. S-LH-1: Comparison of core differential pressure - and heater rod temperature - measured and calculated.

heatup, but to a much lesser degree than shown in the data.

Summary

The four calculations briefly summarized above show TRAC-PF1/MOD1 version 12.7 to have the ability to predict the thermal-hydraulic events and phenomena of importance during a core liquid level depression for 5% SBLOCAs. In general, the code predicts a lesser core liquid level depression, more extensive core heatup, and later times for the loop seal clearing phase of the transients. However, the code predicts the data trends qualitatively and gives reasonable agreement as defined earlier.

OBSERVATIONS AND CONCLUSIONS

1. The core power level, during a given size of SBLOCA, is instrumental in determining the extent and timing of core liquid level depression and the associated core heatup.

2. Based on the LSTF 5% SBLOCA experiments, flooding and CCFL does not appear to be a factor in exacerbating the core liquid level depression and core heatup at core power decay levels representative of operational PWRs.

3. Further analysis is required to resolve the apparent discrepancy between the effect of vessel bypass on core depression and heatup that exists between the Semiscale and the LSTF experiments.

4. The TRAC-PF1/MOD1 version 12.7 thermal-hydraulic code has be shown to have the ability to predict important phenomena pres during the loop seal clearing phase of the 5% SBLOCA transien including core liquid level depression and core heatup. Agree between the calculations and the data are considered reasonabl

REFERENCES

1. K. Tasaka ltr to Y. S. Chen, "Power Decay Curve for LSTF Tests," February 4, 1987.

2. R. R. Schultz ltr to Y. S. Chen, "The Semiscale MOD-2 Power Decay Curve - Background and Assumptions," January 30, 1987.

3. R. R. Rohrdanz ltr to Distribution, "Transmittal of SB-CL-09 and SB-CL-10 Quick Look Notes," October, 1986.

4. ROSA-IV Large Scale Test Facility (LSTF) System Description, JAERI-M 84-237, January, 1985.

5. G. G. Loomis and J. E. Streit, Results of Semiscale Mod-2C Small-Break (5%) Loss-of-Coolant Accident Experiments S-LH-1 and S-LH-2, NUREG/CR-4438 EGG-2424, November, 1985.

6. Compendium of ECCS Research for Realistic LOCA Analysis, (Draft Report for Comment), NUREG-1230, April, 1987.

7. G. G. Loomis and K. Soda, Results of the Semiscale MOD-2A Natural Circulation Experiments, p. 28, NUREG/CR-2335, EGG-2200, September, 1982.

8. Graham B. Wallis, One-dimensional Two-phase Flow, p. 339, McGraw-Hill, Inc., 1969.

9. M. Osakabe, C. Chauliac, T. Yonomoto, Y. Koizumi, M. Kawaji, and K. Tasaka, "Core Liquid Level Depression Due to Manometric Effect During PWR Small Break LOCA," Journal of Nuclear Science and Technology, Vol.24, No. 2, February, 1987.

10. K. Tasaka, Y. Kukita, Y. Koizumi, M. Osakabe, and H. Nakamura, "The Results of 5% Small-Break LOCA Test and Natural Circulation Test at the ROSA-IV LSTF," Proceedings of the 14th Water Reactor Safety Information Meeting, NUREG/CR-0082, Vol. 4, 1987.

11. Safety Code Analysis Group, TRAC-PF1/MOD1: An Advanced Best-Estimate Computer Program for Pressurized Water Reactor Thermal-Hydraulic Analysis, Los Alamos National Laboratory Report NUREG/CR-3858, LA-10157-MS, July, 1986.

12. F. E. Motley and R. R. Schultz, "Comparison of a TRAC Calculation to the Data From LSTF Run SB-CL-05," LA-UR-86-3692, 14th Water Reactor Safety Information Meeting, October 27-31, 1986.

EVALUATION OF OPERATIONAL SAFETY AT BABCOCK AND WILCOX PLANTS[a]

D. J. Hanson
H. S. Blackman
P. D. Wheatley
O. R. Meyer
W. R. Nelson
C. B. Davis

Idaho National Engineering Laboratory
EG&G Idaho, Inc.

ABSTRACT

A methodology was developed to assess the operational performance of nuclear power plants through an integration of thermal-hydraulic, human factors, and risk analysis techniques. This methodology was applied to evaluate the effectiveness of plant systems and operator actions in lessening the severity of selected transients for Babcock and Wilcox (B&W) plants. Comparisons were also performed to assess differences in operational performance capabilities and limitations between selected Combustion Engineering, Westinghouse, and B&W plants. For the selected B&W plant, the results show the probability that an operating crew would not respond within the times available (the non-response probability) is estimated to be relatively small for the three transients studied. Results also show a strong correlation between operator performance and the influence of eight performance shaping factors (PSFs). Comparison of results from the Oconee, Calvert Cliffs, and H. B. Robinson plants indicate that the likelihood operators would take the proper actions to return Oconee to a safe stable state is not judged to be significantly different than the likelihood operators at Calvert Cliffs or H. B. Robinson would recover their plants for the transients investigated. The validity of this conclusion depends on the assumption that the performance shaping factors at all three plants are essentially equivalent. Recommendations are made that influence performance shaping factors positively and thereby influence operator performance positively.

INTRODUCTION

The sensitivity of Babcock and Wilcox (B&W) nuclear power plants to operational transients has been a concern since the core damage accident at Three Mile Island Unit 2. Recent events at some B&W plants have reinforced this concern and lead the Nuclear Regulatory Commission (NRC) to "conclude that there is a need to reexamine the basic design requirements for B&W reactors.[1]" Although the B&W Owners' Group is taking the lead in this reexamination, the NRC has sponsored a research program to develop a methodology to assess the operational performance of B&W plants and to apply this methodology on a trial basis. Results from this NRC research program are reported herein.

a. Work sponsored by the Division of Reactor and Plant Systems, Office of Nuclear Regulatory Research, U. S. Nuclear Regulatory Commission, Washington D. C. 20555, Under DOE Contract No. DE-AC07-76ID01570, FIN No. A6328.

A methodology was developed to evaluate certain aspects of the operational safety of nuclear power plants through an integrated assessment of plant phenomenological behavior, performance of plant operators, and plant risk information. This methodology was applied to aid in the assessment of the operational performance capabilities and limitations of B&W plants and provide a basis for judging the results from programs sponsored by the B&W Owner's Group. Specifically, the objectives of this application are as follows:

1. Evaluate the effectiveness of the plant systems and/or operator actions in lessening the severity of transients in B&W plants as defined by

   - o The timing and severity of thermal-hydraulic behavior
   - o The reliance on safety systems and components for transient mitigation and the defense-in-depth of these safety systems
   - o The degree of dependence on operator performance (performance demands vs performance capability).

2. Compare the operational performance capabilities and limitations of a representative Combustion Engineering and Westinghouse plant with a B&W plant.

3. Evaluate the significance of the findings in terms of the risk currently identified in existing PRAs for the selected plants.

The program objectives were achieved in two steps, progressing from specific plant findings to more general plant results. The first step was to investigate the operational performance of a representative plant for each of the three pressurized water reactor (PWR) vendors during selected transients. This step provided detailed information leading to understanding the complex interactions that occur between the various elements that influence operational safety. The second step was to generalize, to the extent possible, the applicability of the individual plant findings to the appropriate population of plants, with emphasis on the findings directed toward B&W plants. A detailed description of the results from this two-step approach are presented in a two-volume NUREG report [2,3].

METHODOLOGY

The response of a nuclear power plant during operational upsets is influenced by the complex interactions between plant phenomena, plant hardware, and operator actions. To account for the influence of these complex interactions, the methodology developed for this study integrated analysis techniques from the areas of thermal-hydraulics, systems analysis, and human factors. The approach adopted was to develop plant specific results for selected plant transients, and then generalize these specific results, to the extent possible, for the appropriate population of plants. The plant-specific portion of the methodology was developed to include the contributions of the plant thermal-hydraulic behavior and the timing of this behavior, the capability of the plant systems to control the plant behavior within acceptable bounds, and the ability of the plant operators to use their procedures to return the plant to a safe stable state once a plant transient

had occurred. Extension of the plant specific results to the appropriate plant populations was made primarily for the B&W plants. This extension relied heavily on evaluation of operator behavior during actual transient events and on plant hardware similarities.

Owing to limitations in both the time and resources available for application of the methodology, the results are not intended to provide a comprehensive assessment of all aspects of operational safety for each of the plants. However, by assessing plant and operator performance during a limited number of transients that can have a major influence on plant operational behavior, it can be determined with reasonable confidence where a plant has strong and weak points from an operational safety viewpoint.

Figure 1 provides an overview of the plant specific approach used for the operational safety analysis. The rectangles represent the inputs to the program and the results derived from the evaluation. The oval shapes represent the different analyses performed. The arrows between the ovals are labeled to show examples of the products from the analysis steps that served as inputs to subsequent analysis. The individual analyses include the following:

Plant Model - A major goal of the method was to provide consistent thermal-hydraulic results that could be compared between different plants. This consistency of the results was obtained through use of a standardized set of plant thermal-hydraulic modeling techniques and assumptions on boundary conditions, and use of the same computer code for all the thermal-hydraulic calculations. The RELAP5/MOD2 computer code [4] was selected and used to perform the thermal-hydraulic calculations described in this study.

Critical Safety Function Analysis - Critical safety function (CSF) response trees are graphical representations depicting how the operator and plant hardware combine to implement the safety functions used for maintaining plant safety. Since critical safety functions can be defined in several different ways, selection of a common set of CSFs was made so the functional characteristics could be more easily compared between plants. The selected CSFs included reactor coolant system (RCS) inventory control, RCS pressure control, RCS heat removal, core heat removal, reactivity control, and vital auxiliaries. The CSF response tree logic was then developed for each CSF, using design information and emergency procedures. Based on this information, the manual and automatic success paths for providing relevant critical safety functions were identified.

Transient Selection - Based on plant operational and plant risk information and input from a preliminary evaluation of the CSF response trees, three transients were selected for evaluation. A description of the transient selection process, together with the three transients selected, is contained in a following section.

Operational Sequence Analysis - Operational sequence diagrams (OSDs) were developed for each plant to identify the functional interface between the plant hardware and the control room crew as a function of time during the transients selected. Operator tasks that are required were determined by

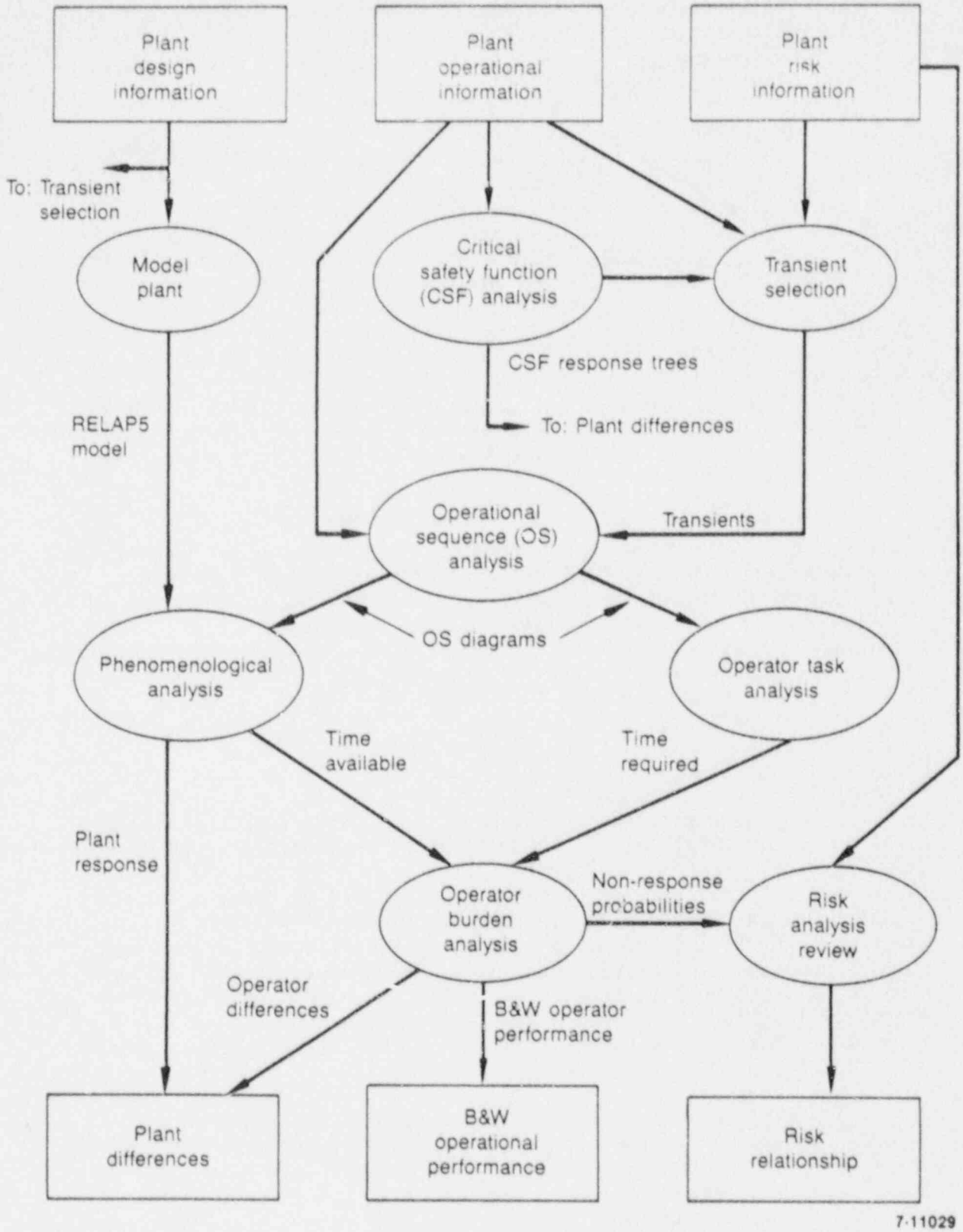

Figure 1. B&W program methodology

assessing the status of the CSFs and applying the emergency operating procedures. The operators were considered to have "regained control" when the safety function dynamics were no longer the direct, immediate determinant of the operators' tasks.

Phenomenological Analysis - Calculations were performed for each plant for the selected transients using the RELAP5/MOD2 computer code, Cycle 36.04. Baseline transients were initially calculated using conservative assumptions concerning hardware failure and minimal operator actions. These calculations were used to provide information on the timing of the events that occurred during the transient, with minimal operator or hardware intervention. Based on the results from the baseline calculations and the OSDs, sensitivity calculations were performed to investigate the influence of actions that were specified to restore the plant to a safe, stable state.

Operator Task Analysis - A task analysis provided detailed descriptions of the operator response during each of the transients for each of the selected plants. The OSDs were used during visits to the H. B. Robinson and Calvert Cliffs plants as guidelines for conduct of a table top exercise form of task analysis. For the B&W plant, a series of simulator runs were performed for each transient using four different crews. The effect of variables such as crew differences, different trials, and special challenges to operator performance were defined. A survey was used to assess the influence of the following important performance-shaping factors (PSFs): procedures, man-machine interface, operator workload, stress, use of plant simulators, and training.

Operator Burden Analysis - Results from the Task Analysis and Phenomenological Analysis were combined to aid in assessing the operator burden at the selected plants. Important operator actions were classified according to cognitive content as being skill, rule, or knowledge based and were also categorized as being involved in actions requiring verification or checking of displays, use of controls, communications, or decisions. This information was displayed on a time line, and the density of operator actions was determined for each plant. The PSFs were analyzed and correlated with the performance of the crews to indicate which PSFs play an important role. Non-response probabilities were calculated to estimate the likelihood the operator would successfully execute certain important actions.

Risk Analysis Review - The risk analysis review was restricted to only the B&W plant, since the other plants either did not have a probabilistic risk assessment (PRA) or the existing PRA was significantly out of date. An assessment was made of how well the human actions were incorporated in the PRA fault/event trees. A review was made of the method of calculating the human error probabilities (HEPs) for certain actions. A comparison of the HEPs with the non-response probabilities was made to determine the influence of the current findings on the risk represented in the PRA.

Extending results from the plant-specific application of the methodology to the general population of plants was done primarily for the B&W plants. This extension was made on a general basis since recent detailed information on the plant hardware, operations, or the capabilities of the operators was not readily available. Results relating to thermal-hydraulic behavior were extended using relationships primarily based on parameters derived from the basic configuration of the plant or from the system hardware. The hardware differences are based on recent hardware descriptions but may not represent changes. However, the parameters that describe operator performance are not normally documented and disclosed to the same degree as hardware information. Operator information was primarily derived from records of the response of the operators to plant transient as documented by the B&W Owners Group Transient Assessment Program (TAP).

PLANT SELECTION

One plant was selected for study from each of the three major vendors of PWRs to allow vendor-to-vendor comparisons of plant performance in terms of system and operational performance. The plants were selected based on a weighting of five criteria. These criteria included (1) the availability of thermal-hydraulic code input models, (2) the availability of plant information to support human factors and thermal-hydraulic analysis needs, (3) the availability of a suitable PRA, (4) the typicality of the plant relative to other plants designed by the same vendor, and (5) similarities in plant volume, power rating, and loop configuration between a selected plant and plants selected for other reactor vendors. Based on these criteria, the plants selected for study were Oconee Unit 1 (B&W), H. B. Robinson Unit 2 (Westinghouse), and Calvert Cliffs Unit 1 (Combustion Engineering).

TRANSIENT SELECTION

Based on the study objectives, time, and resource constraints, three transients were judged to be sufficient to provide significant results from the outlined methodology. Selection of the transients was based on several criteria. Each transient selected should (1) severely challenge the operators and/or safety systems of the plants, (2) highlight differences in the response of the operators and/or safety systems for each of the three plants selected, (3) be expected to occur at a reasonably high frequency based on plant operating histories, (4) be estimated to make a reasonable contribution to core melt frequency for one or more plants, and (5) have the potential to be successfully analyzed within the time and resource constraints using available human factors methods and thermal-hydraulic models.

A review of risk-dominant sequences was performed initially to identify those transients that severely challenge the plant or the operator. Sixteen classes of risk-significant sequences were identified as part of the Accident Sequence Evaluation Program [5]. To aid in the selection process, these sixteen classes of sequences were grouped into three general types of transients based on thermal-hydraulic phenomena. These general transient types included total loss of heat sink (including feed and bleed), loss-of-coolant accidents with failure of the emergency core cooling (ECC)

system, and anticipated transients without scram. Transients falling into one of these three broad categories were rated as more desirable than those not doing so.

Data from the B&W Owners' Group Transient Assessment Program (TAP) were reviewed to identify the most common transients that have occurred in B&W plants. All of the TAP Category C transients, those which have most severely challenged the plant safety systems, were reviewed together with about 50% of the less severe Category B events. The results of these reviews indicated that the most common sequences occurring at B&W plants are overcooling transients initiated by either a stuck-open steam line valve, an overfill of the steam generators, or a combination of both. Examples of these types of overcooling transients are presented in References 6 and 7. Transients involving loss, or near loss, of heat sink owing to loss of feedwater or insufficient feedwater also were found to occur relatively frequently. Note that only a few transients reported in the TAPs data actually resulted in overheating of the RCS such as occurred at Davis-Besse [8]. The majority of these transients simply resulted in lower than normal steam generator water levels.

The selection criteria were applied to candidate transients identified from the reviews of the risk-dominant accidents and the TAPs data. The three transients selected by this process were (1) a total loss of all feedwater (LOFW), (2) a small-break loss-of-coolant accident (SBLOCA) with degraded high-pressure injection (HPI), and (3) a steam generator overfill transient with full auxiliary feedwater (AFW). These transients, which involved undercooling, overcooling, and loss of reactor coolant, would challenge the operator and plant safety systems over a wide range of conditions, thus satisfying the first two selection criteria. The three transients also satisfy the fourth selection criterion associated with risk significance. The total LOFW transient was identified directly as a risk-dominant sequence. The SBLOCA was closely related to the LOCA with total loss of ECC, a risk dominant sequence. The steam generator overfill transient was similar to a transient described by Oak Ridge National Laboratory, [9] with potentially significant implications to safety.

B&W PLANT RESULTS

The results presented in this section are intended to address the first objective identified for the program, i.e., evaluation of the operational performance of B&W plants. The methodology was initially applied to the Oconee plant. Results from this application fell into four major categories: plant operational performance, degree of reliance on safety systems (defense in depth), operator burden, and effect of performance shaping factors on operator performance. An assessment of the degree to which the Oconee results could be extended to other B&W plants followed.

Oconee Plant Operational Response

As discussed earlier, the response of the plant during a transient is influenced by a combination of factors, including the thermal-hydraulic phenomena and the behavior of the operator. Since the operator may have a dominant role in mitigating the effects of certain transients, it is

important to understand the likelihood that the operator will not respond in a manner that will successfully return the plant to a safe stable state. A recently developed model, the Human Cognitive Reliability (HCR) Model [10], has the capability to estimate the non-response probability of an operator action or group of actions. This model is based on crew response data taken from a large number of simulator trials and uses plots of the non-response probabilities versus a normalized elapsed time. These plots provide a consistent basis for predicting the non-response of a future crew as a function of the time available for operator action.

Results from the thermal-hydraulic analysis were combined with results from the Oconee simulator runs as input to the HCR Model, to provide an assessment of the plant operational response in terms of the non-response probability for plant operating crews.

Loss-of-Feedwater Transient. Bounding information on event timing for the LOFW transient was determined from the baseline thermal-hydraulic calculation. This baseline transient simulated a main feedwater pump (MFP) trip and included the failure of all emergency feedwater. The only operator action modeled was the trip of the reactor coolant pump following the directions contained in the emergency operating procedures. Results from this calculation show that the steam generators would dry out relatively early in the transient, at 4.3 minutes; the primary system would reach saturation temperature at 31 minutes; and core uncovery would begin 57 minutes after the main feed pump trip. Initiation of core uncovery was selected as the limiting case for the operator to mitigate rather than the more extreme case of unacceptably high fuel rod temperature.

For a total loss of feedwater at Oconee, the emergency operating procedures call for operator actions that result in the initiation of primary system feed and bleed or use of alternate sources of feedwater to return the plant to a safe stable state. Results from the simulator runs show that either feed and bleed, or the use of the condensate booster pumps as the alternate feedwater source, had the capability to mitigate the LOFW transient. Primary system feed and bleed was chosen for calculation of non-response probabilities since it can be initiated later than condensate booster pump flow and still be effective.

Results from the plant task analysis and simulator runs indicate that the operators would complete the initiation of feed and bleed at about 9 minutes following initiation of the LOFW. Thermal-hydraulic sensitivity calculations, performed to determine the latest time that feed and bleed could be initiated and keep the core covered, demonstrated that feed and bleed could successfully cool the core if initiated at about 50 minutes after the loss of feedwater (within about 7 minutes of core uncovery).

An additional thermal-hydraulic calculation was performed to estimate the event timing under the extreme case of degraded flow capacity for both the feed and the bleed systems. The results showed that feed-and-bleed cooling can successfully keep the core covered even if the power-operated relief valve (PORV) and high-point vent valves (HPVVs) are failed and only one of the three HPI pumps are available. Successful performance is possible under these adverse conditions because the shutoff head of the Oconee HPI pumps is higher than the Reactor Coolant System (RCS) safety relief valve (SRV)

setpoint, and these pumps have a relatively high flow capacity. In this situation, the results indicate that the single HPI pump would need to be started within 40 minutes after loss of feedwater to prevent core uncovery.

Estimation of the desired plant-specific LOFW transient non-response probabilities was accomplished by plotting the simulator results over curves that represent data disclosed from a number of operator response tests described in the referenced HCR Model. Figure 2 shows these curves, labeled "skill," "rule," and "knowledge," together with the four data points that correspond to the response of each of the four Oconee crews. The following example shows how the simulator data were plotted. The first crew completed the task of restoring RCS heat removal at approximately 0.66 of the normal, or median, time of the four crews' responses. Therefore, at a time corresponding to 0.66, the non-response probability for the four crews is shown as decreasing from 1.0 to 0.75 to reflect the fact that one of the four crew has responded and three of the four have yet to respond. (Note the height of the bar represents the change from 1.0 to 0.75.) The change in non-response as each of 3 remaining crews responded is similarly illustrated. The final bar is not shown dropping to zero, since the log scale would distort its position and make observation of the trends on the graph more difficult.

Comparison of the Oconee simulator results for the LOFW with the referenced HCR Model curves shows that the distribution of responses for the four Oconee crews is bounded by the general trend of the rule-based distribution and appears to correspond most closely with a mixture of skill-based and rule based operator actions. This correspondence is expected since the crew actions for loss of feedwater are delineated in the Emergency Operating Procedures, i.e., "rules" are well-established, and are well-practiced by the crews during simulator training, which is a classic method of establishing a basis for skill- and rule-based behavior.

The latest time at which the operator can take action and still prevent core uncovery (50 minutes after loss of feedwater) is shown by the dashed vertical line on Figure 2. The non-response probability that corresponds to that time, i.e., the probability that a future crew would not respond by this latest calculated time for action to prevent core uncovery, based on either skill or rule behavior, is seen to be approximately 10^{-3}, or less. Also shown is the latest time at which the operator can take action with degraded feed- and bleed-capabilities (40 minutes after loss of feedwater). The non-response probability that a future crew would not take action to prevent core uncovery by this time is seen to be less than about 5×10^{-2}, using rule based behavior as the upper bound. Therefore, based on HCR Model results, there is a relatively high probability that the Oconee crews would make a successful response to the combination of faults caused by a loss of both the main and emergency feedwater, even with degraded feed- and bleed-capabilities.

Small Break Loss-of-Coolant Accident. The thermal-hydraulic baseline results indicate that a SBLOCA in Oconee initiated by a 0.01 ft^2 break in the cold leg, and with only one HPI pump operating, did not result in a calculated core uncovery. The only operator actions represented in the baseline SBLOCA calculation were to trip the reactor coolant pumps according to emergency operating procedures. The calculated results indicate that the reactor coolant system experienced a net loss-of-fluid mass for 37 minutes

after the initiation of the break. The net mass loss was terminated when vapor flow from the upper plenum reached the break through the reactor vessel vent valves, thus reducing the break mass flow. No dryout or heatup of the core occurred. The reactor coolant system was in a stable condition at the termination of the calculation with the core covered. However, the system pressure remained well above the entry conditions for long-term decay heat removal. Since significant heat transfer to the steam generators was not possible, owing to voiding in the candy cane, the operator could not use the steam generators to reduce system temperatures and pressures to the point where long-term cooling could be initiated. For this situation, the emergency operating procedures call for the operator to "bump" the reactor coolant pumps in order remove the void in the candy cane and allow the steam generators to be used to cool down and depressurize the RCS. Simulator data for this operator action was not available because the Oconee simulator does not have the capability to adequately simulate voiding in the candy cane. Since this was the only major operator action identified for the SBLOCA, calculation of non-response probabilities was not possible.

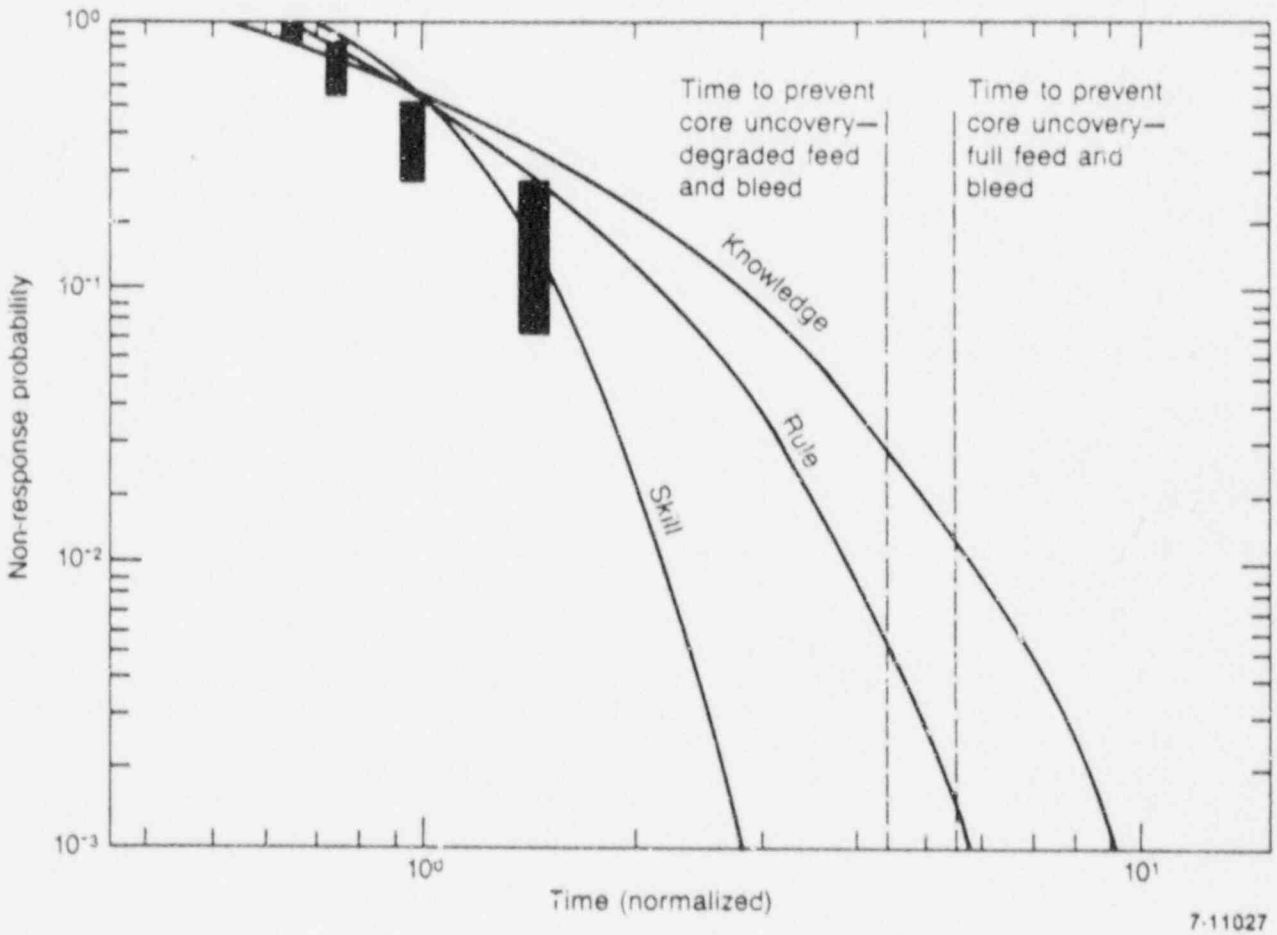

Figure 2. Restoration of the RCS heat removal after loss of main and emergency feedwater

Steam Generator Overfill Transient. Timing for the steam generator overfill calculation was determined from the baseline thermal-hydraulic calculation. This calculation was initiated by a main feed pump trip and was followed by an overfill of the steam generators with emergency feedwater (EFW). No operator actions were modeled, and it was assumed that the automatic control systems designed to throttle EFW failed. Refill of the steam generators began at about 2.5 minutes after main feed pump trip, when the steam generator levels reached the EFW initiation setpoint. At 21 minutes after initiation of the transient, the generators were calculated to be full to the point that a significant amount of liquid would begin entering the steam lines. The calculation was terminated at this point. This overfill transient caused an overcooling of the reactor coolant system at a rate of about 256^{0}F/hr which is considered to be a relatively rapid cooldown rate. At the end of the calculation, the minimum reactor coolant system temperature was about 490^{0}F and still decreasing. If the plant equipment or operator actions were successful in terminating EFW prior to 21 minutes, the severity of the overfill transient in terms of overall cooldown rate, total amount of cooldown, or potential for damage to the steam line would be lessened.

Using the same approach as described for the LOFW transient, results from the baseline transient were used in conjunction with results obtained from the Oconee simulator to estimate the operator non-response probability for the overfill transient. The four data points corresponding to the response of each of the four crews during the overfill transient are shown in Figure 3. Again, the curves labeled "skill," "rule," and "knowledge" represent data disclosed from a large number of operator response data described in the referenced HCR Model.

The distribution of responses of the four Oconee crews would be bounded by the general trend of the knowledge based distribution derived for the referenced HCR Model although the non-response probabilities at the larger normalized times appear to be trending toward rule based behavior. This tendency toward knowledge or possibly rule based actions rather than skill based may have been influenced by opposing goals imposed by this particular transient. Since loss of feedwater initiates the transient, the initial goal, which is stressed very heavily in Oconee plant procedures, is to restore steam generator inventory. The goal of reducing the inventory only becomes important once the high level setpoint had been exceeded. In addition, the simulator did not model the EFW spraying directly on to the steam generator tubes. It was necessary to include additional equipment failures in the transient representation so that the primary to secondary heat transfer would be increased to approximately represent the effects of this spray. Since the operator had to overcome these additional failures, additional time and thought were required which is reflected in the data.

The time at which water is calculated to enter the steam line from the baseline calculation, which does not include major operator actions, is shown by the dashed vertical line on Figure 3. The non-response probability that corresponds to that time, i.e., the probability that a future crew would not respond by the calculated time of water entering the steam line, based on either rule or knowledge based behavior is seen to be in the range of about 10^{-2} to $5x10^{-2}$. Therefore, based on HCR Model results, there is a reasonable probability that the Oconee crews would make a successful response to the combination of faults causing a loss of both the main and emergency

feedwater. Since the probability that the operator will not successfully terminate this transient is approaching an appreciable value, further study of the implications of the steam generator overfill transient may be warranted to determine if the consequences are risk significant.

Defense in Depth for Oconee. The adequacy of Oconee's defense in depth for the selected transients was assessed using the Oconee critical safety function response trees to characterize the plant's overall functional response to the transients, i.e., to determine the expected response of both plant systems and operators to challenges to the critical safety functions. Using the critical safety function response trees, the details of the plant's response (including hardware and operator actions) to safety function challenges can be laid out in a concise format, and the number of success paths that are being used and that remain available at any point in the transient can be identified. The number of success paths that remain available for use is an indication of the plant's defense in depth for that transient. Defense in depth is considered adequate for a given transient if sufficient success paths are available for providing each relevant critical safety function during the course of the transient. Of course, it is also important to consider how many additional success paths are available after the minimum requirements for responding to the transient are satisfied.

Based on the Oconee CSF response trees, defense in depth was judged to be adequate for all three transients analyzed. The functional response assessments show that the Oconee crews were able to successfully select and implement a success path for each safety function during the three transients. With only one exception, which was shown to be inconsequential,

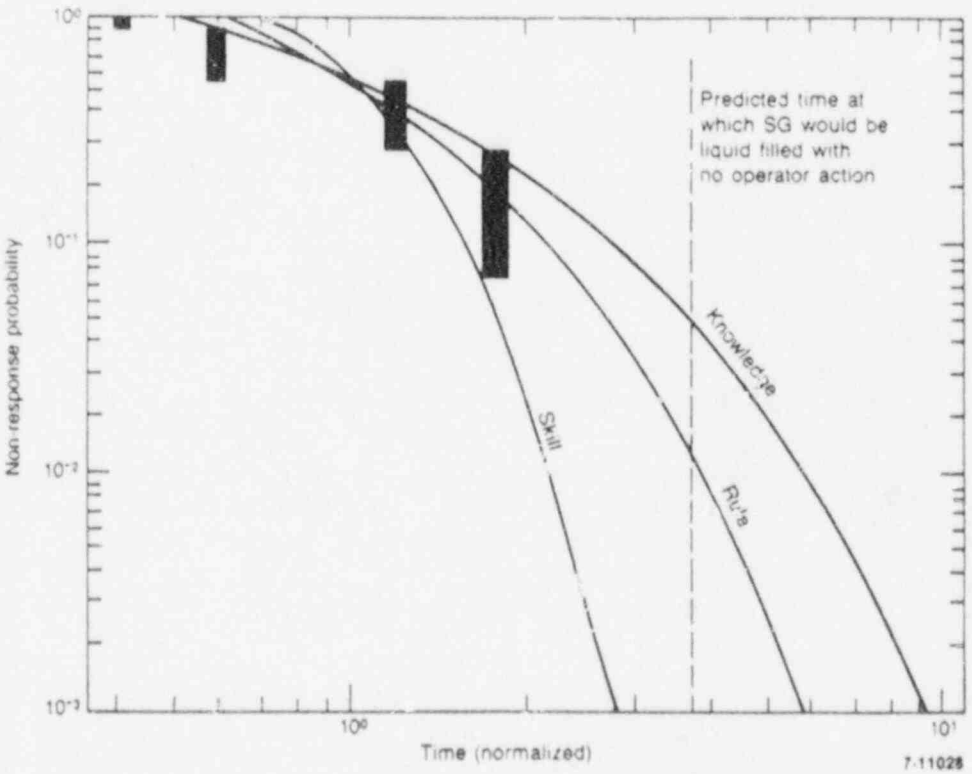

Figure 3. Mitigation of steam generator overfill event

additional success paths (beyond those actually used) remained available after the adverse transient conditions had been mitigated.

Analysis of Operator Burden for Oconee. The tasks taken from the simulator runs at Oconee were tabulated in a time line format to provide a simple means to examine operator burden. The time lines and tasks within these time lines were then analyzed. The number of operator tasks that occurred during blocks of time were determined for each transient, and a task density calculation (number of tasks per unit time) was performed. As would be expected, the task density was higher in the early part of the transients, reflecting the immediate actions taken by the crew at the onset of a transient condition. However, the numbers of tasks per time period were not considered to be excessive nor outside the capability of a well trained crew, as they are comparable to task densities of other types of plants that are similar to nuclear reactors in complexity.

In addition to determining task densities, two different task classification systems were applied to evaluate the types of tasks being performed by the crews during the transients. The first system was based upon Rasmussens' classification [11] of cognitive tasks into three categories: skill, rule, and knowledge-based behavior. In this context, skill based behaviors are those more reflexive and mechanistic in nature, and also depend upon the level of training and the degree of practice of the operators performing the activity. Rule-based behaviors are those which are directed by a set of procedures or rules. Knowledge-based behaviors are those which require the operators to rely upon their own knowledge and problem solving ability to resolve problems. Each operator task in the timeline was classified according to this system. The second classification system was based upon the behavior required by the type of interaction being carried out between the operator and the plant system with which he was interfacing, or between the crew members. Each task was categorized as to whether it required taking a reading, taking a control action, communicating, or making a decision.

Results from the classification of tasks, did not suggest problems in terms of operator burden for any of the three transients. The distribution of tasks across the categories of the classification systems revealed no trends or patterns. In general, the LOFW scenario appeared to be the most difficult transient for the Oconee crews in that more rule- and knowledge-based activities were required. The increased difficulty was also reflected in higher levels of communication and decision in the second classification system. Increased difficulty for this transient was also reflected by the higher task densities in the early portion of the transient.

Performance Shaping Factors for Oconee

Performance shaping factors (PSFs) for nuclear power plants are generally defined as factors that can influence the performance of the operator. A set of eight performance-shaping factors were selected for this study, factors that experience has shown to have important effects on reliable human performance during plant operation: (1) training, (2) procedures, (3) information available, (4) system feedback, (5) instrumentation, control, and layout, (6) environment, (7) stress, and (8) workload.

To assess the influence of performance-shaping factors on the Oconee operators, members of each of the four crews filled out a survey designed to assess their perceptions of the influence of PSFs following completion of the simulator runs. The operators were asked to rate the PSFs on a scale of one to five, according to whether the PSFs hindered or helped performance. Since these factors could influence the operators differently during each of the three transients, an identical PSF survey was filled out for each transient. A detailed evaluation of the survey results was performed to assess the impact of the PSFs on performance as perceived by the operator, to identify relationships among the PSFs, and to identify correspondence between the PSFs and other measures of crew performance taken in the survey.

Based on results from the PSF ratings, the Oconee operators considered their training, procedures, information available, and system feedback to be positive contributors to their performance. Instrumentation, control and layout, and environment were generally not ranked as either helping or hindering performance. Stress and workload were considered definite hindrances to performance, because they add to and complicate the operator's tasks.

The survey results were analyzed further to determine the extent to which the ratings of PSFs correlate with are predict crew performance. For the first analysis, operator performance as measured by the time required by the crews to mitigate the transients was correlated with the rankings of the PSFs. This analysis identified a high degree of correlation between the PSF ratings and time needed for transient mitigation. In addition to time, four additional crew performance measures were evaluated, including selection of the proper mitigation path, control of the plant, crew communications, and confidence in mitigating the transient. Each of these measures were created through a careful evaluation of the crew performance by a licensed operator examiner using a rating scale. The results show that the PSFs also correlate strongly with these four measures. The strong correlations of PSFs with the selected performance measures indicate their capability to evaluate and predict operator performance.

Because strong correlations were shown to exist among the PSF ratings and the various performance measures, a regression model was developed based on the PSF ratings and time required by the crews to mitigate the transients. This model was used to perform a set of sensitivity calculations for each transient to predict changes in the time taken to mitigate the transients, given changes in the PSF ratings. That is, the PSFs were systematically set to their highest and then lowest ratings to evaluate the effect that PSFs could have on the time required for the operator to complete a task for best- and worst-case situations. Results from these sensitivity calculations indicate that when the PSF ratings are decreased from their highest rating to their lowest rating, the time taken to mitigate a transient may increase by between a factor of 6 to 16, depending on the type of transient. The factor of 6 applied to the steam generator overfill transient and the factor of 16 applied to the loss-of-feedwater transient. Assuming that an operator's perception of the PSFs accurately reflect the real PSFs, then these results indicate that substantial decreases in the quality of the identified PSFs will be accompanied by substantial decreases in operator performance.

Relation of Oconee Findings to Other B&W Plants

The degree to which the Oconee results could be extended to other B&W plants was evaluated based on similarity to the Oconee hardware and operations. This extension was intended to provide a general overview of how the calculated results could be applied to other plants. A rigorous extension one considering the many detailed plant differences, would require a comprehensive program well beyond the scope of the current program. The discussion has been grouped according to relationships of the plant responses, relationships of the defense in depth, and the expected relationship of the performance-shaping factors for the operators.

Relation of Plant Response

Plant response relationships were based primarily on an assessment of hardware similarities and differences among the B&W plants. Using this approach, the thermal-hydraulic results for the three Oconee Unit 1 transients are believed to be generally applicable to all the other B&W lowered-loop plants. Differences in core power and PORV size between Oconee and these other lowered-loop plants should result in only relatively minor differences in the timing of events. Differences in the design of the ICS and the balance of plant should have an insignificant effect on plant response because the transients selected for this study do not rely on the functions performed by the ICS system. Plant response differences become more significant for transients in which the ICS or the balance of plant plays an important role. The steam line break detection system present in some plants could influence the course of the overfill transient by automatically terminating EFW and preventing the continued overfilling of the steam generators. The calculated results for Oconee are not as applicable for Davis-Besse, the raised-loop plant, primarily because of differences in plant configuration and the HPI system design.

Analysis of Oconee Response Trees for Selected TAPS Transients

The B&W Transient Assessment Program (TAP) Reports provide useful information on actual events that have occurred at B&W plants. These reports included a detailed discussion of the sequence of events, including the operator actions for these events. It is, thus, possible to evaluate the actual events using the Oconee critical safety function response trees to evaluate the functional response of the plant. This application of the Oconee response trees to actual transients allows the actions of crews from other plants to be evaluated in terms of the adequacy of the functional response as if the events had occurred at Oconee. It is recognized that there may be design differences between Oconee and the other plants that may influence the response of the systems or operators. Where these differences would significantly impact the functional response, their influence was evaluated.

Three actual events were selected for response tree analysis because of their challenge to the operating crew and the safety functions. These events are as follows:

1. Davis Besse Loss of Feedwater, June 9, 1985 (information regarding this transient was taken from NUREG-1154)

2. Rancho Seco Overcooling Event, October 2, 1985 (TAP Report RS-86-05)

3. Rancho Seco Loss of ICS Power, December 26, 1985 (TAP Report RS-86-01).

Results from the functional response evaluation show that, although the three transients challenged some of the plant safety functions, there were always several success paths remaining with the capability of returning the plant to a safe stable state. However, even though the operating crews were able to successfully mitigate the three TAP transients analyzed, they did so with a certain amount of difficulty. Results from the functional response evaluation indicated that, in some cases, the response could have been significantly improved if proper maintenance had been performed for equipment important to the implementation of success paths. In other cases the response, although ultimately successful, could have been much more effective in the use of the plant's resources if a focused safety function perspective had been maintained by the operating crews.

Relation of Oconee PSF Findings.

An evaluation of B&W plants other than Oconee was performed to demonstrate use of the PSF results. The objective of this effort is to show how performance-shaping factors might be assessed and how they affect overall operator performance. The approach taken was to select a small number of TAP transients from different plants and combine estimated PSFs for these transients into a single composite plant, because it is recognized that selected plants would have made modifications since the transients occurred and, thus, a plant-specific assessment of the performance shaping factors would no longer be applicable or meaningful. The transients selected for evaluation were the Rancho Seco loss-of-feedwater, the Rancho Seco loss of Integrated Control System, and the Davis-Besse loss-of-feedwater.

Based on the information from the TAP reports, expert judgement was used to estimate PSF ratings for the composite plant, using the scales previously developed for the Oconee operator survey. The estimated PSFs were in all cases determined to be lower than those determined for Oconee. The ratings of the performance-shaping factors were applied in the Human Cognitive Reliability Model (HCR) model to demonstrate how they affect the human error probabilities associated with specific operator tasks. As required by the model, the performance-shaping factors were grouped to fit the HCR taxonomy and, using engineering judgement, to identify the appropriate HCR weights. The next step was to take the median task performance time obtained in the Oconee simulator runs and use it as a baseline to apply the PSF weights to calculate a failure probability for the composite plant. The resultant probabilities show a minimum of an order of magnitude of difference between the plants for two tasks selected as important to the potential risk from the LOFW and steam generator overfill transients. It is expected that similar differences would occur for other tasks of equal duration and complexity.

Even without further detailed plant evaluations, the high degree of correlation between crew performance and the PSFs provides significant insight into what could be monitored at plants to aid in evaluating the expected performance of crews. The operator performance at some B&W plants could be improved. by either establishing standards or monitoring programs for training, procedures, information available, system feedback, instrumentation control and layout, environment, stress, and workload.

PLANT COMPARISONS

These results are intended to address the second objective identified for the program, i.e., comparison of the operational performance capabilities of a representative Combustion Engineering, Westinghouse, and B&W plant, using the approach and general results from Oconee.

Plant Response Comparisons

The plant response comparisons have been made both on the basis of thermal-hydraulic results and the capability of the operator to respond and control the transients. Results from the thermal-hydraulic comparisons are summarized to provide insights into the timing and severity of the transients. Comparisons of the capability of the operator to respond were found to be more difficult than had originally been anticipated, owing to differences in the levels of information available for each of the different vendor plants.

The thermal-hydraulic responses of Oconee, H. B. Robinson, and Calvert Cliffs were generally similar for the three transients analyzed. Observed differences in plant responses were primarily related to design differences between the once-through and U-tube steam generators, and the vent valves in the Oconee reactor vessel. Comparison of the LOFW, SBLOCA, and steam generator overfill transient thermal-hydraulic results follow.

Loss-of-Feedwater Transient. Operator actions are required to prevent core uncovery and heatup in a total LOFW transient at each of the plants studied. For the baseline calculation, i.e., without initiation of feed and bleed cooling and substantial operator actions, the responses of all three plants were similar except for the timing of events. Significant thermal-hydraulic events generally occurred first in Oconee, then in Calvert Cliffs, and finally in H. B. Robinson. For example, the steam generators dried out about 4 minutes after MFP trip in Oconee, about 20 minutes in Calvert Cliffs, and at about 62 minutes in H. B. Robinson. Core uncovery and heatup began at 57 minutes after MFP trip in Oconee, at 101 minutes in Calvert Cliffs, and at 126 minutes in H. B. Robinson. The calculated differences in plant responses are primarily attributed to the smaller initial liquid inventory in the Oconee steam generators and differences in the reactor trip parameters that delayed reactor trip in Calvert Cliffs, compared to the other two plants.

Results from the calculations indicate that feed and bleed can be successfully used to cool the core in all three plants if initiated early enough following a total LOFW transient. Feed and bleed was calculated to prevent core heatup if initiated at 31 minutes following MFP trip in Calvert

Cliffs (70 minutes prior to core uncovery), 50 minutes in Oconee (7 minutes prior to core uncovery), and 104 minutes in H. B. Robinson (22 minutes prior to core uncovery). Estimates indicate that if the start of feed and bleed had been delayed by more than about 5 minutes from the times given above, core heatup would have begun in each plant.

Oconee has the capability to feed and bleed the primary system, even with degraded conditions in both the HPI and power operated relief valve systems. A sensitivity calculation shows that with only one of three HPI pumps operating and complete failure of the power-operated relief valve system (HPI flow was delivered against the setpoint pressure of the pressurizer safety relief valves), core uncovery could be prevented if HPI was initiated within 40 minutes of MFP trip. Both the H. B. Robinson and the Calvert Cliffs plants are more restricted in their capability to prevent core uncovery with degraded capacity in the feed and bleed systems. The primary difference in the capability to successfully feed and bleed with degraded systems is associated with the lower pressure shutoff head of the HPI pumps for H. B. Robinson and Calvert Cliffs.

Condensate pumps can be used to prevent steam generator dryout in H. B. Robinson and Calvert Cliffs if the operators act to depressurize the steam generators during a LOFW transient. Although the condensate booster pumps can not be used to prevent steam generator dryout at Oconee, the simulator runs indicate they can be used to feed the dry steam generators and provide RCS cooling thereby eliminating the need for feed and bleed cooling. By passing the condensate booster pump flow through the emergency feedwater system, which would spray the water on the upper portion of the tubes, it is believed that a relatively less significant thermal impact would occur for the dry steam generator tubesheet. This belief appears to be reasonable but analysis should be made available to confirm that thermal stresses are not excessive.

Small-Break Loss-of-Coolant Accident. Oconee, H. B. Robinson, and Calvert Cliffs remained in a safe condition during a SBLOCA initiated by a 0.01 ft^2 break with degraded HPI. No critical operator action was determined necessary to maintain the safety of the plants for this transient. The thermal-hydraulic responses of the three plants were similar early in the SBLOCA. However, one significant difference in behavior was related to the time that the break flow transitioned from single-phase liquid to a high-quality two-phase mixture. This transition occurred between 29 and 43 minutes earlier in Oconee than in the other two plants because the reactor vessel vent valves, present in B&W plants, allowed steam to enter the cold leg piping before the reactor coolant pump loop seal had cleared. The earlier transition to two-phase flow at the break in Oconee resulted in less depletion of the RCS liquid inventory and a more rapid depressurization occurred earlier in time compared to the other two plants.

Differences between plants were also observed relative to the ability of the operators to recover from the SBLOCA. As discussed earlier, the Oconee operators could not depressurize the RCS (a step necessary to reach residual heat removal entry conditions) by depressurizing the steam generator unless the reactor coolant pumps were "bumped." However, the capability for heat removal from the reactor coolant system by the steam generators was still present in both H. B. Robinson and Calvert Cliffs at the end of the SBLOCA, so the operators could depressurize the RCS using the steam generators

without "bumping" pumps. Thus, H. B. Robinson and Calvert Cliffs have an RCS depressurization mechanism for certain break sizes that is not available at Oconee without additional operator actions and hardware operation.

Steam Generator Overfill Transient. The overfill transients investigated were initiated by a trip of the MFPs followed by an overfill with auxiliary feedwater (AFW). The maximum AFW flow rate was used for the Oconee calculation because overfill would not occur unless the systems controlling the steam generator level had failed and it was assumed that this failure would result in a worst case (maximum) AFW flow. The AFW rates at Calvert Cliffs and H. B. Robinson were assumed to be the nominal AFW flow rates, since no failures in the AFW flow control systems were required to have an overfill transient.

Because of their relatively small size, the steam generators filled rapidly at Oconee. The steam generators were liquid full at 21 minutes after MFP trip in Oconee, at 45 minutes in H. B. Robinson, and at 106 minutes Calvert Cliffs. The steam generator overfill caused a more rapid cooldown in Oconee than in the other two plants. This more rapid cooldown is caused by enhanced heat transfer from the spray of emergency feedwater (EFW) directly on the upper portion of the tube bundle, together with the more rapid coverage of the tubes. The cooldown rate of the average RCS temperature from the time of reactor trip to the time the steam generators filled with liquid was 256^{o}F/hr in Oconee, 93^{o}F/hr in H. B. Robinson, and 41^{o}F/hr in Calvert Cliffs. The only critical operator action identified for this transient was to terminate AFW or EFW before liquid entered the steam lines. Liquid in the steam lines could possibly cause a steam line failure due to water hammer induced hydrostatic loading. A steam line failure has the potential to result in a more severe overcooling transient.

An assessment of the difference in assumptions on rate of AFW flow shows that the conclusions drawn from the results would not change significantly if the maximum flow rate was used for all plants rather than just for Oconee.

Operator Response Comparisons

A direct comparison of the operator response for Oconee, Calvert Cliffs, and H. B. Robinson during the three transients was difficult owing to differences in the amount of detail contained in the available information. The Oconee simulator runs provide significant detail concerning the response of the operator during a variety of conditions. However, the table top discussions at both Calvert Cliffs and H. B. Robinson not only provided less detail, but the information is somewhat lower in quality since there was no way to easily assess the influence of the performance-shaping factors.

To aid in comparisons of operator response, the time available for the operator to respond before serious consequences occur during a transient can be considered to comprise two broad time frames. In the first time frame, the operator is attempting to overcome the affects of the initial fault or faults while minimizing challenges to the major plant safety functions or damage to plant hardware. If the operator can bring the plant to a safe stable state during this time frame, the importance of the transient is usually considered minor. The second time frame begins when multiple challenges to the plant safety functions occur as a result of the operator's

inability to correct the initial fault or faults. A transient that progresses into the second time frame is usually considered to be relatively serious, since several plant safety functions are generally challenged and the potential for risk-significant consequences are larger.

A comparison of the transient timing results presented in the previous portion of this subsection for the three plants indicates that the Oconee plant progresses more rapidly through the first time frame than the Calvert Cliffs and H. B. Robinson plants for the two feedwater flow upsets evaluated. For example, during the complete loss of feedwater transient, the step in the procedures that directs the operator to initiate feed and bleed cooling is reached at about 7 minutes at Oconee, 16 minutes at Calvert Cliffs, and 64 minutes at H. B. Robinson. Obviously the operators at Calvert Cliffs and H. B. Robinson have significantly more time to attempt to recover feedwater before initiating feed and bleed cooling. A similar situation exists for the overfill transient where the Oconee operator has significantly less time to terminate the overfeed condition before water enters the steam line. Based on these results, the Oconee operators would have less time to mitigate these two transients before the transition was made from what is considered to be a less serious to a more serious situation. The shorter available for response could also reduce the capability of the operator to deal with additional equipment failures or complex operating situations.

An assessment of the effect of shorter time available to recover from the two feedwater related transient initiators must rely on comparison of non-response probabilities among the three plants. The non-response probability for an operator to perform an action or series of related actions, as determined using the HCR Model, depends on three parameters: the time available, median response time, and a series of weighting factors to account for the effect of performance shaping factors. The time available to prevent initiation of feed and bleed was less at Oconee by a factor of between two and nine; whereas, while the time for termination of the overfeed condition was less at Oconee by a factor of between two and five. An assessment of the median time required for the operator to correct the initial fault was not available from the table-top task analysis or simulator trial. However, based on an evaluation of the Emergency Operating Procedures and the complexity of the equipment involved in the transient initiator recovery, there is nothing to indicate that the median response time for the operators at the three plants would vary by as much as a factor of two. Therefore, the ratio of time available to median operator response time would be somewhat higher for Oconee than for the other two plants. If performance-shaping factors were equivalent at each of the three plants, this higher ratio of time available to median operator response time would translate into a somewhat higher probability that the operator would not respond in sufficient time to correct the initial fault for the two feedwater transient initiators investigated. Based on an assumption of equivalent performance shaping factors and the known similarities between Oconee and other B&W plants, the somewhat lower probability of recovering the initial fault for the two transients analyzed may help to explain the perception that transients tend to progress to a more serious state in B&W plants than in other vendor plants. However, this result does not carry with it the implication that progressing to a more serious plant state necessarily translates into higher plant risk.

Transition to the second time phase caused by an inability to recover the initial fault and challenges to multiple safety functions is generally perceived to be serious. In fact, entry into this time phase may not be serious if there is a relatively high probability that the operator can return the plant to a safe stable state without incurring plant damage. It was not possible to determining non-response probabilities for this time period based on the HCR Model owing to the lack of data from Calvert Cliffs and H. B. Robinson. However, the non-response probability for Oconee was determined to be relatively low, less than about 10^{-2} and 10^{-3}, for the loss-of-feedwater and steam generator overfill transients.

To further compare the potential for the operators of the three plants to prevent plant damage during this time period, estimates were made of the probability that the operator would carry out certain critical mitigative tasks for each of the three transients. Selection of the types of tasks was limited to a relatively narrow set of actions by the type of analysis being performed. Initially, fault trees were developed to reflect the operator actions identified in the plant EOPs for each of the three selected tasks. Using these fault trees, the operator action failure probabilities were then quantified using THERP [12] to provide task failure probabilities. Comparison of these failure probabilities for each of the tasks showed that they are very similar, well within the uncertainties of the method. Based on the fact the differences are small, no one plant appears to have a greater overall potential for the operator to fail to mitigate the transient based on these tasks.

Although there are other critical tasks that are important for the three transients, comparison of the procedures indicates that similar results, i.e., equivalent failure probabilities, are likely for these other tasks. The results, therefore, indicate that although it may be more likely that a transient in the Oconee plant may progress to a more severe plant condition, the likelihood that the operators could return Oconee to a safe stable state is not significantly different than the likelihood that the Calvert Cliffs or H. B. Robinson operators would recover their plants for the transients investigated. The validity of this conclusion depends on the assumption that the performance-shaping factors at all three plants are essentially equivalent.

Comparison of Defense In-Depth

The defense-in-depth for the three plants can be compared by looking at the functional response summaries for the three plants based on the current procedures and plant configuration. The results for the complete-loss-of-feedwater transient indicate that Oconee provides explicit direction for use of more success paths and therefore would be more likely to provide additional defense in depth for the total loss of feedwater transient. For the LOCA transient, there does not appear to be a distinguishable difference in the defense in depth for the small break loss-of-coolant accident. In addition. the plants appear to have the same degree of defense in depth for the steam generator overfill transient.

Comparison CSF Strategies

The resources available for maintaining the critical safety functions during transients are quite comparable for the three plants analyzed. There are some differences in how the resources are prioritized to respond to safety function challenges. However, these differences in resource prioritization are not large enough to cause significant differences in the capability of the operator to provide and maintain needed safety functions for the three plants.

The primary difference in the operators' means for providing the safety functions for the three plants lies in the focus and organization of the procedures. The H.B. Robinson and Calvert Cliffs procedures are organized around clearly defined safety functions. In addition, the operators of both of these plants are periodically directed to assess the status of the safety functions using clearly specified measures. Thus, the H.B. Robinson and Calvert Cliffs operators should always have a clear picture of plant state and why they are performing the actions specified. The same may not be true for the Oconee operators. It was apparent from the response tree analyses that the actions specified in the Oconee procedures are adequate for maintaining the safety functions for the transients analyzed. The individual Oconee procedures specifically address maintenance of the critical safety functions. However, each action appears to be specified in isolation from the overall objectives of the procedure. The procedural steps are followed based on the outcome of previous steps. When high-level safety function parameters are checked, the procedures do not always make it clear why the parameter is being checked, and what the significance of the outcome is. Without a clear view of safety function status, it may be possible to become lost in the procedural logic. A clear definition of the objectives of transient response, that is, maintenance of the critical safety functions, can help ensure that reactor operators successfully mitigate accidents.

Operator Burden Comparisons

An approach was designed to compare operator burden based upon the density of tasks required of the operating crew. The success of this approach requires that a consistent set of data be collected among the plants through task analyses conducted in table-top exercises and from observations gathered during simulator exercises. However, owing to time constraints and administrative constraints at some of the plants, it was not possible to collect both types of data at each plant.

Data collection on operator performance included simulator runs at Oconee; whereas, H. B. Robinson and Calvert Cliffs data were collected from table-top exercises. Upon comparison of these data it became apparent that the level of detail was sufficiently different between the simulator data and the table top task analysis data that detailed comparisons of operator burden could not be made across the plant types. In an effort to make general comparisons, operator actions for each transient were compiled from the simulator runs at Oconee and the table-top task analysis at H. B. Robinson, and Calvert Cliffs. These actions were then tabulated in a time line format to provide a simple means to examine operator burden in terms of task density. The times and tasks in the time lines were further analyzed by calculating task density (number of tasks per unit time) for each scenario

and plant combination. Results from compilation of the task densities show differences among the plants within specific time intervals. For example, within the first two minutes, for the loss of feedwater event, Oconee and Calvert Cliffs have significantly fewer actions that H. B. Robinson. While later in that same event, within the first ten minutes, Oconee and Robinson have significantly more actions than Calvert Cliffs. These types of fluctuations are present throughout the data, that is, no consistent, discrenable trend is apparent. It appears that some combination of task frequency, task difficulty, and, perhaps, task duration is necessary to be able to reliably compare operator burden among a group of plants. To determine that optimal combination and perform the desired comparisons would require far more detailed data than was available for this study.

RELATION TO OCONEE RISK

The results presented in this section are intended to address the third objective identified for the program, i.e., evaluation of the significance of the finding in terms of the risk currently identified in existing probabilistic risk assessments (PRAs) for the selected plants. PRAs were available for two of the plants, Oconee and Calvert Cliffs. Evaluation of these PRAs indicate that the operator was not modeled in sufficient detail in the Calvert Cliffs PRA to make reasonable comparisons with the program findings. Modeling of the operator in the Oconee PRA was judged to be adequate for further evaluation.

A review of the Human Reliability Analyses used in the Oconee PRA found no major shortcomings. In fact, many of the major shortcomings of past PRAs in terms of proper inclusion of the human element were recognized and adequately addressed in this PRA. The HRA process used by Oconee was well-planned and well carried-out by the analysts. The human elements were included at appropriate levels in the PRA, and diagnostic behavior on the part of the operator was also included. Performance-shaping factors and dependencies were also considered in the Oconee PRA in an appropriate manner.

To further assess the Oconee PRA methods and results, three actions considered important were quantified using HCR and/or THERP for each transient used in this study. The quantification was done to facilitate a direct comparison of the values found in the PRA and those estimated based on this study, and also to provide a direct comparison of fault trees for operator actions found in the PRA and those that would be generated during the quantification process. Differences identified were shown to be well within the uncertainty bounds associated with the calculated core melt frequency.

CONCLUSIONS AND RECOMMENDATIONS

The conclusions have been grouped according to the objectives. Recommendations were formulated as based on program results and conclusions.

Conclusions

Conclusions relating to the operational performance of B&W plants first considers the specific Oconee results and then generalize these findings to other B&W plants. The results relating to Oconee indicate that the times required for the operator to return the plant to a safe stable state for the three transients evaluated are well within the times available. The relatively small probability that an operating crew would not respond within the times available, plus the results of operator task density studies, indicate that operator burden is not excessive for the transients studied. Based on these results and the fact that the defense in depth of the hardware and operations was judged to be adequate for Oconee, it is concluded that the Oconee operators have a high likelihood of returning the plant to a safe stable state if confronted with the three transients analyzed.

Results from simulator testing at Oconee show that a strong correlation exists between operator performance in terms of such variables as time required to mitigate transients, and the influence of the performance-shaping factors as perceived by the operator. This close correlation is an indicator of the major influence the performance-shaping factors can have on the ability of the operator to properly respond to plant transients. The correlation was sufficiently strong that a statistical model of the effect of PSF ratings on the time required for the operators to mitigate transients could be developed. This statistical model predicts that the mitigation time could theoretically be decreased by up to one order of magnitude, if the PSFs were improved from worst case to best case.

Generalization of Oconee results to other B&W plants was difficult, owing to differences in both hardware and operations. The timing of the phenomena and general thermal-hydraulic response at Oconee are expected to be reasonably represent other B&W lower loop plants for the transients analyzed. For Davis Besse, owing to the raised loops and other hardware differences, the Oconee thermal-hydraulic results are much less representative.

The strong correlation between performance-shaping factors and operator performance identified in the Oconee studies makes extrapolation of Oconee results highly dependant on an understanding of performance shaping factors at other plants. However, an accurate determination of a wide range of PSFs is not possible owing to the limited amount of data related to operator performance contained in the TAP reports. Therefore, an accurate estimation of the operational performance at B&W plants other than Oconee would require proper collection and analysis of performance-shaping factor data from these plants. It can be concluded from the Oconee results that if other B&W plants had equivalent performance-shaping factors, the likelihood that these plants can be returned to a safe stable state for the three transients analyzed is high.

Based on the comparisons between results from Oconee, Calvert Cliffs, and H. B. Robinson, the following conclusions can be drawn. Although it may be more likely that a transient in the Oconee plant could progress to a more severe plant state prior to recovery, the likelihood that the operators could return Oconee to a safe stable state is not significantly different than the likelihood that the Calvert Cliffs or H. B. Robinson operators would recover

their plants for the transients investigated. The validity of this conclusion depends on the assumption that the performance shaping factors at all three plants are essentially equivalent.

Results from the evaluation of the operation of plants show that both Calvert Cliffs' and H. B. Robinson's procedures explicitly address the maintenance and monitoring of critical safety functions. The Oconee procedures do not provide explicit guidance for monitoring the status of the critical safety functions as a transient progresses. It is concluded that this lack of continual guidance for monitoring may cause, in extreme cases, the operator to have problems in overcoming the effects of multiple failures or previous operator errors.

Based on the evaluation of the Oconee PRA, it is concluded that the human reliability analysis is systematic and rigorous. Some improvements would be possible, owing to changes in human reliability analysis over the past several years, but even with these improvements it is not expected that major changes in core melt frequencies would result.

Recommendations

Recommendations have been developed based on the results and conclusions of this program and are considered to be applicable to reactors in general rather than specific only to B&W plants. Implementation of these recommendations would positively influence performance-shaping factors and thereby positively influence plant safety. The recommendations are as follows:

1. Ensure that a plant-specific simulator, which represents the current plant, both in terms of physical behavior and configuration, is available for each plant.

2. Ensure that the simulator is used for procedure validation and operator training, using a variety of severe, risk-significant and novel events.

3. Ensure that all operators are given practice in dealing with stressful, high workload events.

4. Ensure that a feedback loop is in place, from training to procedure writers and plant engineers, to implement modifications discovered in training and plant operations.

5. Ensure that Licensee Event Reports are monitored for performance shaping factors as a performance indicator.

These recommendations, if used, would provide operations personnel with the opportunity to implement all of their procedures during severe risk-significant transients so that they would have practical experience in the use of the procedures and plant equipment should an actual transient occur. This type of training also provides them the necessary exposure during stressful events to help reduce the stress and perceived workload during an actual event. Measurements of the operators perception of the

important performance shaping factors can also be made to provide and indication of the expected performance of the operating crews during a future transient.

REFERENCES

1. V. Stello, Jr., Executive Director for Operations, United States Nuclear Regulatory Commission, letter to H. Tucker, Chairman, Babcock and Wilcox Owners Group, January 24, 1987.

2. D. J. Hanson et al, Evaluation of Operational Safety at Babcock and Wilcox Plants Volume 1 - Results Overview, NUREG/CR-4966, EGG-2515, October, 1987.

3. P. D. Wheatley et al, Evaluation of Operational Safety at Babcock and Wilcox Plants Volume 2 - Thermal Hydraulic Results, NUREG/CR-4966, EGG-2515, December, 1987.

4. V. H. Ransom et al, RELAP5/MOD2 Code Manual, NUREG/CR-4312, EGG-2369, EGG-SAAM-6377, August, 1985.

5. N. G. Cathey et al, Catalog of PRA Dominant Accident Sequence Information (draft), NUREG/CR-3301 EGG-2259, August 1984.

6. Sacramento Municipal Utility District, Transient Assessment Program Report for Rancho Seco Reactor Trip on June 17, 1981, TAP Number RS-82-04.

7. Florida Power Corporation, Transient Assessment Pr m Report for Crystal River Unit 3 Reactor Trip On October 9, 1 TAP Number CR-85-01.

8. U. S. Nuclear Regulatory Commission, Loss of Main and Auxiliary Feedwater Event at the Davis-Besse Plant on June 9, 1985, NUREG-1154, July 1985.

9. R. S. Stone et al, An Assessment of the Safety Implications of Control at the Oconee 1 Nuclear Plant Final Report, NUREG/CR-4047 ORNL/TM-9444, March 1986.

10. G. R. Crane and G. W. Hannaman, Realistic Operator Response Measurement, ANS Topical Meeting on Reactor Safety, San Diego, CA, April 1986.

11. J. Rasmussen, "Skills, rules, and knowledge; signals, signs, and symbols; and other distinctions in human performance models", IEEE Transactions on Systems, Man, and Cybernetics SMC-12:257-266, 1983.

12. A. D. Swain and H. E. Guttman, Handbook of Human Reliability Analysis with Emphasis on Nuclear Power Plant Applications, NUREG/CR-1278, (1983).

UPTF EXPERIMENT

FIRST INTEGRAL TEST WITH COMBINED

ECC INJECTION

BY

P.A. WEISS, R.J. HERTLEIN

SIEMENS AG

UB K W U

8520 ERLANGEN (FRG)

Abstract

The first integral test was run in the Upper Plenum Test Facility (UPTF) - a 1:1 representation of a PWR primary system. A double-ended cold leg break under evaluation model-type (EM) conditions with combined ECC injection was simulated in this test. The focus was on the thermohydraulic phenomena in the upper plenum and downcomer as well as in the cold and hot legs under transient conditions. Of special interest were the thermohydraulic interactions between the above mentioned regions.

1. Introduction

The Upper Plenum Test Facility (UPTF) Experimental Program, sponsored by the Ministry for Research and Technology (BMTF) is the German contribution to the trilateral 2D/3D Project, and is performed within international cooperation among Japan (JAERI), USA (USNRC) and the Federal Republic of Germany (BMFT).

The UPTF simulates the primary cooling system of a KWU 1300 MW PWR. The system configuration of UPTF is shown in Figure 1, and major dimensions of the facility are depicted in Figure 2. The upper plenum including internals, the downcomer and the four connected loops are represented in 1:1 scale. The core is simulated with controlled injection of steam and water supplied from external sources.

The three intact loops are equipped with flow restrictors to simulate the reactor coolant pumps, and with steam/water separators representing the steam generators. The hot and cold legs of the broken loop lead through steam water separators and break valves into the containment simulator. Breaks of variable sizes can be simulated in the hot and in the cold leg respectively. A first integral test with combined ECC injection was performed in December 1986, according to the internationally agreed upon test matrix.

2. Test Objectives

The first UPTF-integral test was a transient test with combined ECC injection simulating a double-ended cold leg break of the main coolant line between pump and reactor pressure vessel. This test was run under EM (evaluation model) boundary conditions. The goal of this test was to investigate in a full-scale facility the overall system thermohydraulic behaviour and the thermohydraulic phenomena in the upper plenum, tie plate region, downcomer and loops during end-of-blowdown, refill and reflood phases following a LOCA, with a simulated double-ended cold leg break.

The following thermohydraulic phenomena and data were of special interest in the Downcomer and Cold Legs Area :

- Occurence of water plugging, its time history and plug oscillations in the cold legs

- Rate of effective ECC delivery to downcomer and rate of ECC bypass out of the downcomer via the broken loop

- Location of water downflow paths in the downcomer

The focus of the test in the Upper Plenum, Tie Plate and Hot Leg Area was on the:

- Water plug formation, its time history and plug movement in the hot legs
- Rate of effective ECC delivery to the upper plenum for hot side ECC injection
- Spatial and temporal relation between ECC delivery from the hot legs and the water breakthrough events detected at the tie plate.
- Steam and water mass flow distribution at the tie plate

Integral tests with combined ECC injection have been performed in several scaled-down test facilities. Of special importance are the tests performed in the PKL test facility at KWU (PKL II scaling factor 1:145) and the tests performed at JAERI within the 2D/3D Program in the CCTF and SCTF facilities (scaling factor 1:24). The experimental data from these test facilities show a quick core quench for the combined ECC injection mode, when intermediate size up to double-ended breaks are simulated. It can be expected that the core quench time decreases when the geometrical radial scaling factor of the test facility approaches unity. Subsequently the water penetration through the tie plate and the downcomer into the core region is less affected by simultaneously upflowing steam than in scaled-down test facilities. For that reason the focus of the first UPTF integral test was on water breakthrough phenomena in the PWR primary system. As there were no water breakthrough data related to full-scale PWR geometries available before UPTF, in the past the scaling laws for water breakthrough limitation were derived from experimental results obtained in scaled-down separate effect test facilities.

3. Initial and Boundary Conditions of the Test, Test Procedure

All relevant initial and boundary conditions applied to the first integral test are depicted in Figure 3 and 4.

Initial conditions

The pressure in the primary system before the test was 18 bar and in the containment - 4 bar with the two systems separated by closed break valves.

An initial amount of 8900 kg of saturated water, stored in the test vessel, was intended to cause flashing during the depressurization phase and to contribute to the test conditioning during the first stage of the test transient.
The pump simulators in the intact loops were set to a flow resistance factor of K = 12 (related to 750 mm loop diameter) to simulate a running pump. A factor K = 18.2 was used for the simulation of a blocked pump in the broken loop.

Boundary conditions

The configuration of the ECC injection was based on the assumption of an evaluation model concept simulating a hot side single failure, one hot side accumulator in repair and no ECC injection into the broken cold leg.
The nitrogen injection into the ECC water was in operation to simulate the nitrogen dissolved in the ECC water. The break valves were opened within 4 s after activation.
To simulate the steam generator response during the transient the steam injection into the steam generator simulators was activated.
Steam injection into hot loop 2 was active to simulate the pressurizer.
The core simulator feedback and correction system (CSFS) was activated to simulate the core response, whenever a massive breakthrough of subcooled water from the upper plenum into the core region occured, and to correct the base steam injection, when the water level in the core region, measured during the test, deviated substantially from the water level corresponding to the base steam injection.
Water breakthrough from the upper plenum into the core simulator region of UPTF is measured by means of 94 Break Through Detectors and 36 Drag Bodies installed in the tie plate area. When water breakthrough occurs in a PWR fuel assembly the heat transfer from the unquenched fuel rods to the surrounding fluid increases rapidly. To simulate such an assembly response, the core simulator steam injection rate into a UPTF core simulator zone affected by water breakthrough was increased according to the increased heat transfer in the real reactor fuel assembly. In this test the CSFS was activated in the event of water breakthrough when the measured water downflow rate exceeded 13 kg/s per fuel assembly.

In addition to the core simulator feedback system injecting additional core steam as a function of tie plate water breakthrough rates, a core simulator correction system was used to compensate for the deviation of core collapsed level measured

during the test from the water level determined by a GPWR-TRAC pretest calculation. The core simulator base steam flow rate corresponded to the precalculated core collapsed water level.

Consequently the total steam injection rate $M_{STEAM, TOTAL}$ via the core simulator was the sum of three components

$$M_{STEAM, TOTAL} = M_{BASE} + M_{BT} + M_{\Delta H}$$

where

M_{BASE} - core simulator base steam flow rate determined by the GPWR-TRAC pretest calculation

M_{BT} - additional steam injection rate whenever massive water breakthrough occured

$M_{\Delta H}$ - base steam flow rate correction to compensate for core collapsed water level deviations.

The water injection rate $M_{WATER,TOTAL}$ via the core simulator was proportional to the base steam flow rate to simulate the water entrainment in the core during the test transient

$$M_{WATER, TOTAL} = K^{*}M_{BASE}$$

The time series plots of the relevant boundary conditions are depicted in Figure 4.

Test procedure

To establish the conditions in the UPTF primary system similar to those expected in a reactor primary system during a LOCA transient, a conditioning phase preceded the actual test phase. The following parameters were optimized by means of UPTF-TRAC calculations to reach the thermohydraulic conditions in the primary system expected at 10.5 bar:

- Activation and opening time of the break valves

- Initial saturated water mass stored in the lower plenum

- Steam injection rate through the core, steam generator and pressurizer simulators

- ECC water injection rate into the primary system

A list of significant events during the test transient is given in Table 1. It shows, that the conditioning phase (18 to 10.5 bar) lasted for 5 s.

4. Test results

4.1 Overall system behavior

During the end-of-blowdown phase (28 to 40 s), following the conditioning phase, the pressure in the test vessel decreased from 10.5 bar to the actual pressure in the containment simulator dry well (3.8 bar), see Figure 5. The water level in the lower plenum started increasing after initiation of the transient phase and reached the lower end of core barrel at 38 s.

The refill phase ended at 49 s when the water level reached the elevation in the core simulator equivalent to the lower edge of the active fuel length. The water injection into the core simulator started at 53 s (see Figure 4).

At 54 s the main drainage system started to drain water from the lower plenum of the test vessel to maintain the mass balance. The reference value of the drainage rate corresponded to the steam and water mass flow rates injected through the core simulator plus the steam mass flow rates injected into the steam generator simulators.

The collapsed water level in the downcomer increased sharply at 40 s (see Figure 5) At 58 s the downcomer was filled and water flowed through the cold leg of broken loop.

The test was terminated at 65 s by the Fast-Automatic-Shutdown-System (FASS), to avoid water penetration into the core simulator steam injection pipes. At this

time the collapsed water level in the core reached approximately 5 m (see Figure 5).

4.2 Thermohydraulic Phenomena Observed in the Hot Leg and Upper Plenum Region

Water breakthrough events at the tie plate, typical for hot leg ECC injection, are depicted in Figure 6. The subcooled ECC water flowing out of the hot leg broke through the tie plate into the core region. The breakthrough locations and areas are indicated by the Break Through Detectors forces. The hot leg ECC injection into intact loops 2 and 3 started at 26 s. Figure 6 shows that the first water breakthrough occurred near hot legs 2 and 3 immediately after the start of ECC injection.
The location of water breakthrough was always near the injecting hot legs only. The change in breakthrough location with time was because of the discontinuous ECC delivery from the injecting hot legs 2, 3 and 4. It should be pointed out that ECC injection into hot leg 4 was delayed (start at 34 s).

The histogram representing the duration of upflow and downflow of fluid across the tie plate near the hot leg is depicted in Figure 7. Using this histogram the downflow periods through the tie plate near the injecting hot legs can be compared with the ECC delivery period. For example in the period from 47 to 57 s there was no water breakthrough at the tie plate near hot leg 2 because of no water delivery out of this hot leg.

The data for injection zone 21 near loop 3, shown in Figure 8, indicated a massive water breakthrough at 36 s which was not stopped by the sharply increasing steam mass flow rate injected into this core simulation zone as a core feedback response. The fluid temperature measured 10 mm below the tie plate indicated subcooling during water downflow.

A comparison of the core simulator steam injection rate with the Flow Module Turbine velocity also shows that the change from water downflow to cocurrent upflow of steam and water droplets was not caused by the core simulator steam and water injection.

The signals from the wide range differential pressure measurements indicated a rapid change of water distribution on the tie plate. The wide range differential

pressure decreased during increasing void fraction on the tie plate, when the vertical Flow Module Turbine indicated upward flow.

The characteristic of the data for injection zone 25 near loop 2, as shown in Figure 9, is similar to that of zone 21. Both zones are near ECC delivery hot legs.

The cocurrent upflow period between 47 and 57 s in front of loop 2, accompanied by discontinuous ECC delivery out of the hot leg, was well indicated by the Break Through Detectors signals. Figure 10 shows the existence of a water plug in hot leg 2 and the movement of this water plug which is the reason for the discontinuous ECC delivery. At 47 s the differential pressure between the upper plenum and hot leg 2 increased indicating an increased two-phase flow in hot leg 2. This two-phase flow led to a reversal of the ECC water flowing out of the deflector nozzle between 47 and 57 s. At 50 s the fluid density measured by the Gamma Densitometer (PFM) showed a quick increase indicating a completely water-filled pipe cross section. Also the Pipe Flow Meter drag paddles measured increased positive fluid force which indicated that the water plug was flowing towards the steam generator simulator between 49 and 56 s.

From 55 s to 56 s the PFM forces changed their direction indicating that the plug was moving towards the upper plenum leading to a massive water breakthrough at the tie plate near loop 2 at 57 s.
The Gamma Densitometer (PFM) showed high fluid density in the hot leg, and there was also an indication of a water level in the SG inlet chamber till the end of the test (65 s).

4.3 Thermohydraulic Phenomena Observed in the Cold Leg and Downcomer Region

The distribution of subcooled ECC water along cold leg 2 is indicated by the fluid temperature measurements shown in Figure 11. ECC water injection into the intact loops cold legs was started at 26 s. TC stalk 3 measured subcooled water immediately after the start of ECC injection showing water flow towards the downcomer. After a short delay the TC stalks 3,4 and 5 indicated subcooled water at all TC positions. This indicates, that a water plug was quickly formed covering the locations of TC stalks 3, 4 and 5. This water plug filled the loop cross section completely and existed till the end of test, moving to and fro in the cold leg with a frequency of about 0.3 Hz. The fluid temperatures of stalk 6 near the pump simulator showed saturation temperature till 30 s. Thereafter the fluid temperatures measured at the lower positions of the TC stalk decreased in an oscillatory manner indicating that a subcooled water wedge was approaching the pump simulator causing the filling of the pump seal.

The water flow paths in the downcomer can be studied by means of the fluid temperatures. In Figure 12 the fluid isotherms are plotted in the unwrapped downcomer for particular instants during the test transient. The axial fluid velocities measured by means of the turbines located at the lower end of the downcomer are also indicated in these figures. The cold leg ECC injection started at 26 s. At 30 s subcooled water out of loop 2 reached the downcomer. At the same time the fluid density in the broken cold leg began to increase. The downcomer fluid temperature distribution at 34 s and 36 s show that ECC water coming out of loops 1, 2 and 3 was bypassed partially to the broken cold leg. The first water breakthrough of subcooled water into lower plenum occured at 38 s. During the period from 40 to 58 s no water discharged from the broken cold leg.

The delivery of ECC water to the downcomer was discontinuous due to oscillations of water plugs in the cold legs. This discontinuous delivery resulted in rather complex fluid temperature distributions in the downcomer during the refill and the reflood phases. Significant water delivery to the lower plenum started at 42 s. At 58 s the downcomer was filled with subcooled water and the measured data in the broken cold leg showed unsteady overflow.

The oscillatory fluid velocities with occasional flow reversal, measured by the turbine meters in the downcomer near the lower end of the core barrel, indicated

unsteady water mass delivery to the lower plenum during the transient. The fluid temperature in the downcomer below the centerline of loop 2 is depicted in Figure 13 for several vertical positions. It is quite evident from this figure that the sharp drop of fluid temperature in different vertical positions at different instants indicated the flow path of the water plug through the downcomer. The water plug needed approximately 8 s to reach the lower plenum.

5. Major Findings and Conclusions

The main findings from the first UPTF-integral test can be summarized as follows:

- Almost immediately after the start of the ECC injection the collapsed water level in the lower plenum started to increase continuously indicating a remarkably effective delivery of ECC water to the lower plenum and core region.

- During the end-of-blowdown phase this collapsed water level increase was caused mainly by the hot side injected water

- During this phase a fraction of the cold side injected water was bypassed via the broken loop nozzle and did not contribute to the refill process in the lower plenum.

Regarding the Cold Leg and Downcomer Region it was observed, that

- After the start of the cold side ECC injection the pipe between injection nozzle and downcomer is filled completely with subcooled water. The ECC water enters the downcomer approximately 7 s after start of the ECC injection

- Due to oscillations of the water plugs in the cold legs the water delivery into the downcomer was intermittent

- The water flow in the downcomer can be characterized by the following three phases

- The ECC bypass phase, which lasted for appr. 8 s after the first water had entered the upper part of the downcomer

- The complete delivery phase lasting for 20 s, when the total cold side injected ECC water contributed to the refill process

- The downcomer overflow phase, which started 35 s after start of the test.

With respect to the Hot Leg and Upper Plenum Region it was observed, that

- The breakthrough zones were located in front of the injecting loops

- The water breakthrough events at the upper tie plate occured intermittently because of the unsteady ECC delivery from the hot legs

- The pressure difference between upper plenum and downcomer combined with condensation effects at the injection ports caused steam/water countercurrent flow in the intact loop hot legs when ECC water was injected in both legs. Countercurrent flow led to water flow reversal and plug formation in the hot leg. The ECC delivery into the upper plenum was temporarily stopped when the water plug was formed and/or moved towards the steam generator simulator. After the plug formation was completed a substantial ECC delivery into the upper plenum occurred causing extensive breakthrough phenomena at the tie plate.

- These breakthrough processes were not stopped even when the core simulator feedback system increased the steam injection substantially.

Action (in order of occurence)	Time on Plots
• Start-up of the data acquisition system	0
• Opening of the cold leg break valve	23
• Start of the steam injection through the core, steam generator and pressurizer simulator	25
• Start of ECC injection	26
• Opening of the hot leg break valve	27
• Pressure of primary system p = 1050 kPa; start of actual test phase	29
• Activation of core simulator feedback system	32
• Water level reached lower edge of core barrel	38
• End-of-blowdown	40
• Water level reached a value corresponding to lower edge of active core	49
• Start of core simulator water injection	53
• Activation of Fast Automated Shutdown System (FASS)	65

Table 1: LIST OF EVENTS DURING TEST TRANSIENT

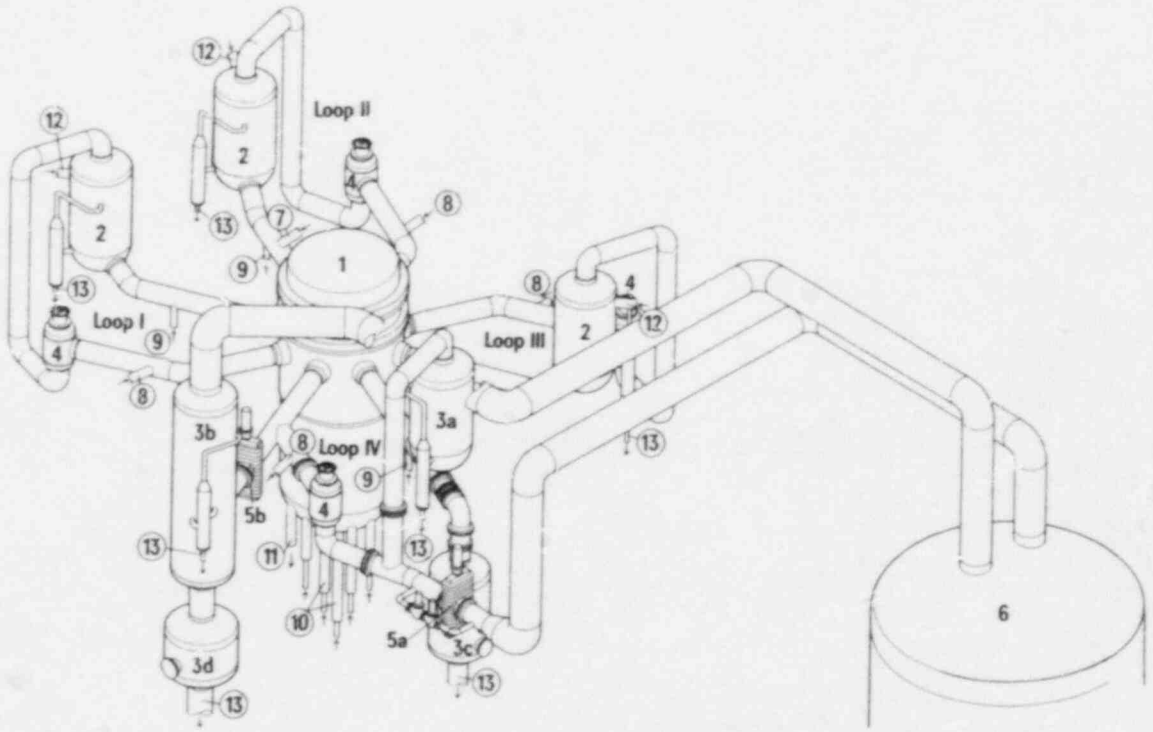

1 Test Vessel
2 Steam Generator Simulator (Intact Loop)
3a Steam Generator Simulator/ Water Separator (Broken Loop Hot Leg)
3b Water Separator (Broken Loop Cold Leg)
3c Drainage Vessel for Hot Leg
3d Drainage Vessel for Cold Leg
4 Pump Simulator
5a Break Valve (Hot Leg)
5b Break Valve (Cold Leg)
6 Containment Simulator

(7) Surgeline-Nozzle
(8) ECC-Injection Nozzles (Cold Leg)
(9) ECC-Injection Nozzles (Hot Leg)
(10) Core Simulator Injection Nozzle
(11) TV-Drainage Nozzle
(12) Steam Injection Nozzle
(13) Drainage Nozzle

Fig. 1: Upper Plenum Test Facility-Primary System

86 PWR 039e
UB KWU

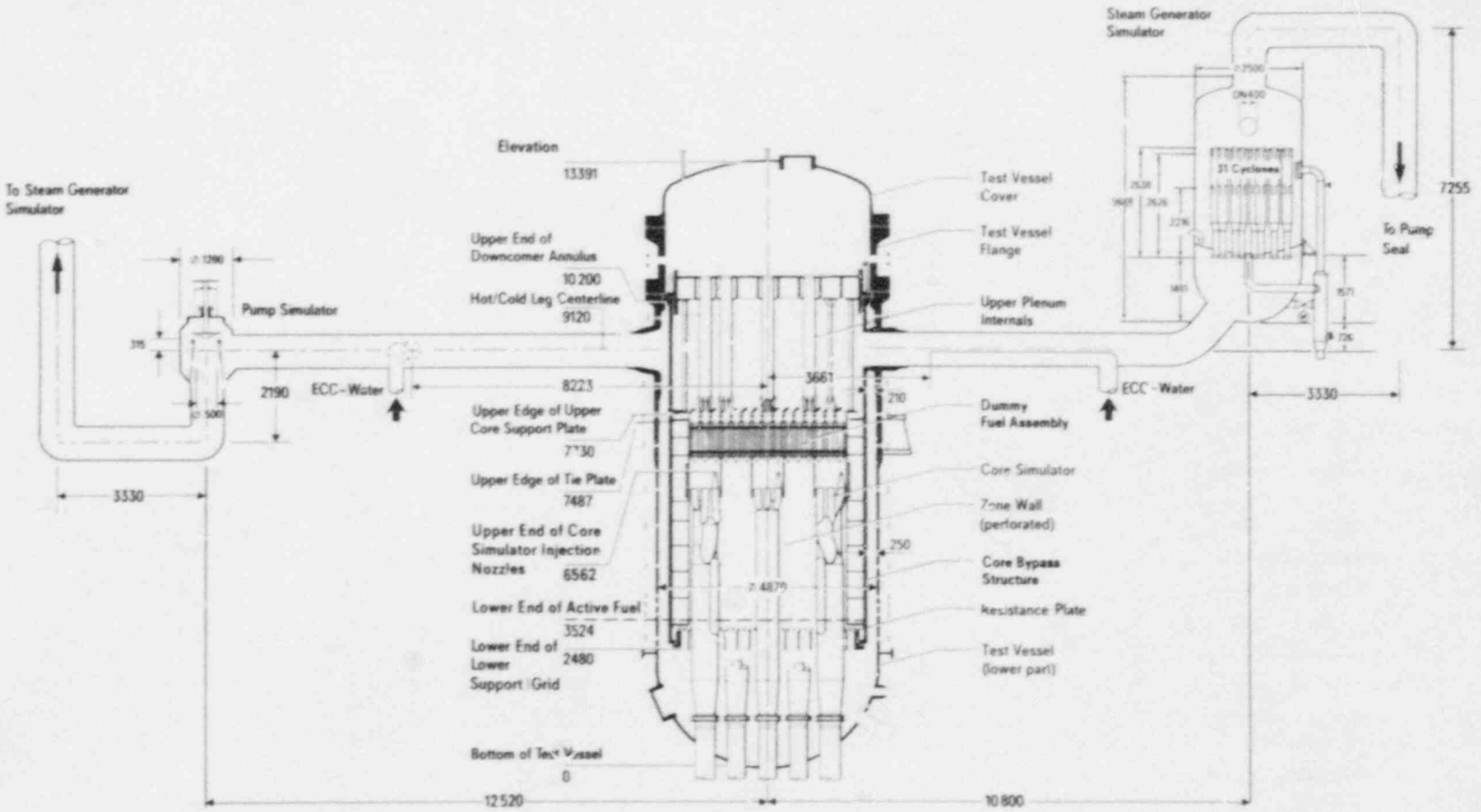

Fig. 2: Major Dimensions of UPTF-Primary System

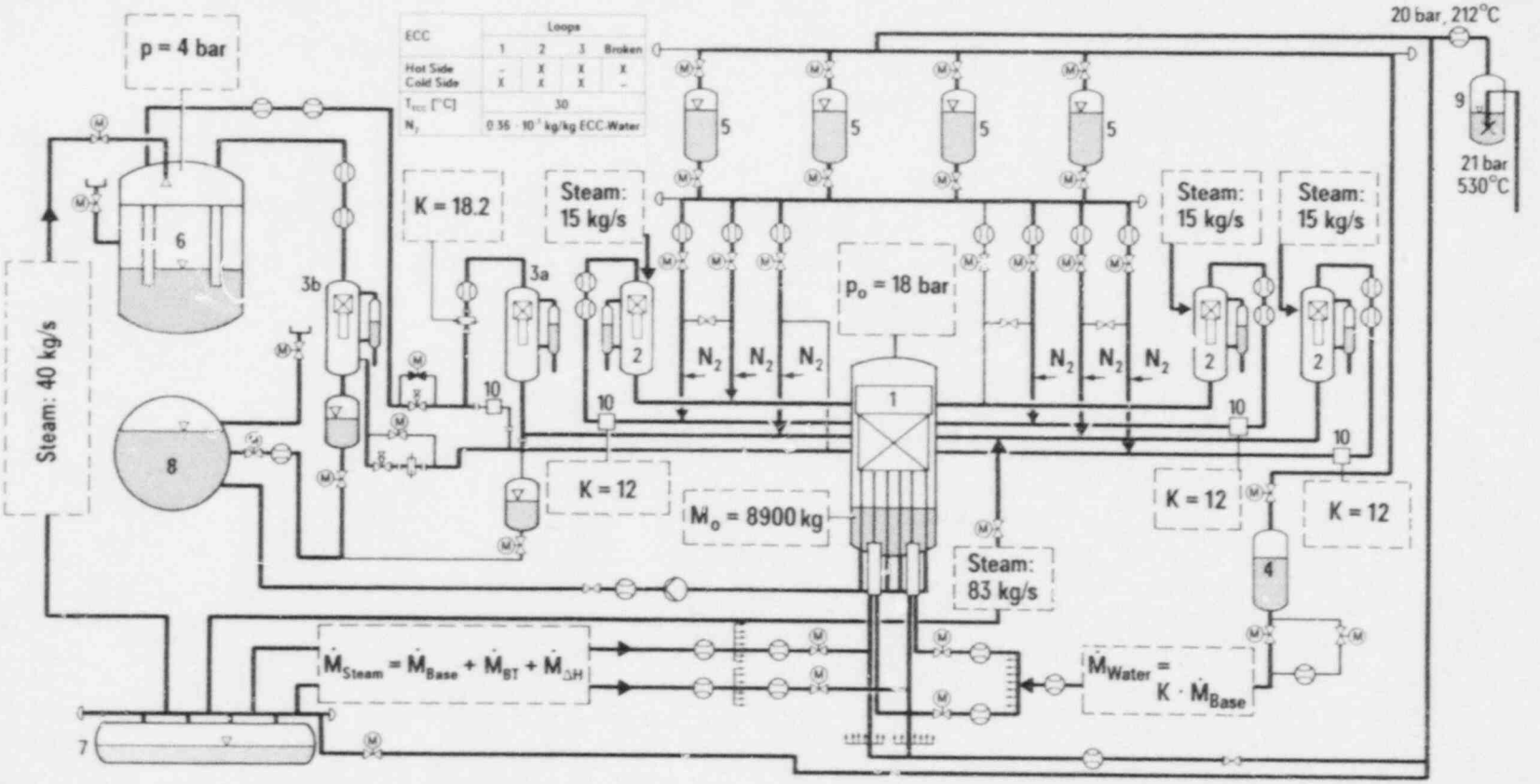

1 Test Vessel
2 Steam Generator Simulator
3a Water Separator (HL) (Steam Generator Simulator)
3b Water Separator (CL)
4 Hot Water Storage Tank
5 Accumulator
6 Containment Simulator
7 Steam Storage Tank
8 Water Collection Tank
9 Steam Cooler
10 Pump Simulator

Flow Path
Filled with Water
Not Activated

Fig. 3: System Configuration for Test No. 3

UB KWU

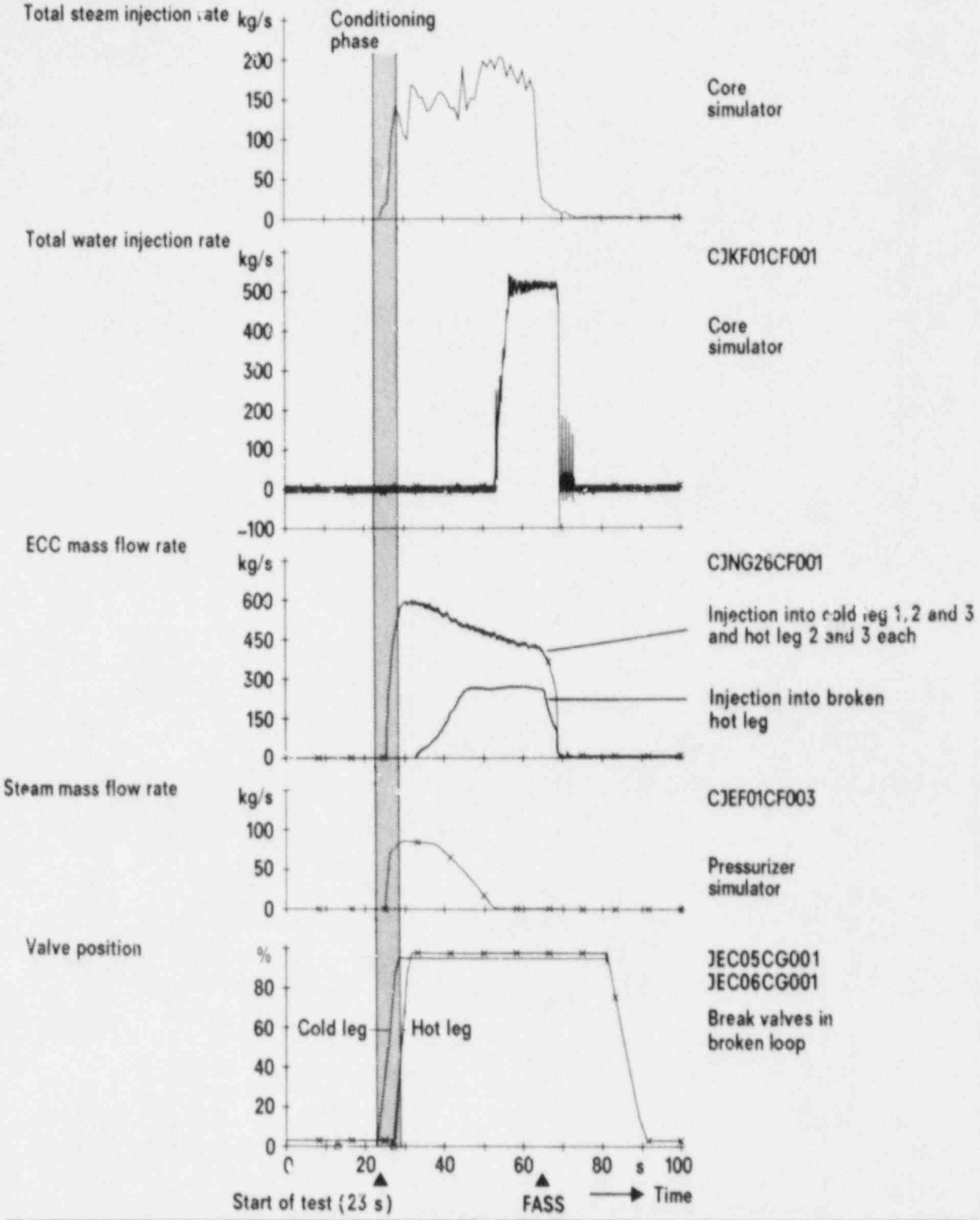

Figure 4: Test Boundary Conditions

UB KWU

SIEMENS

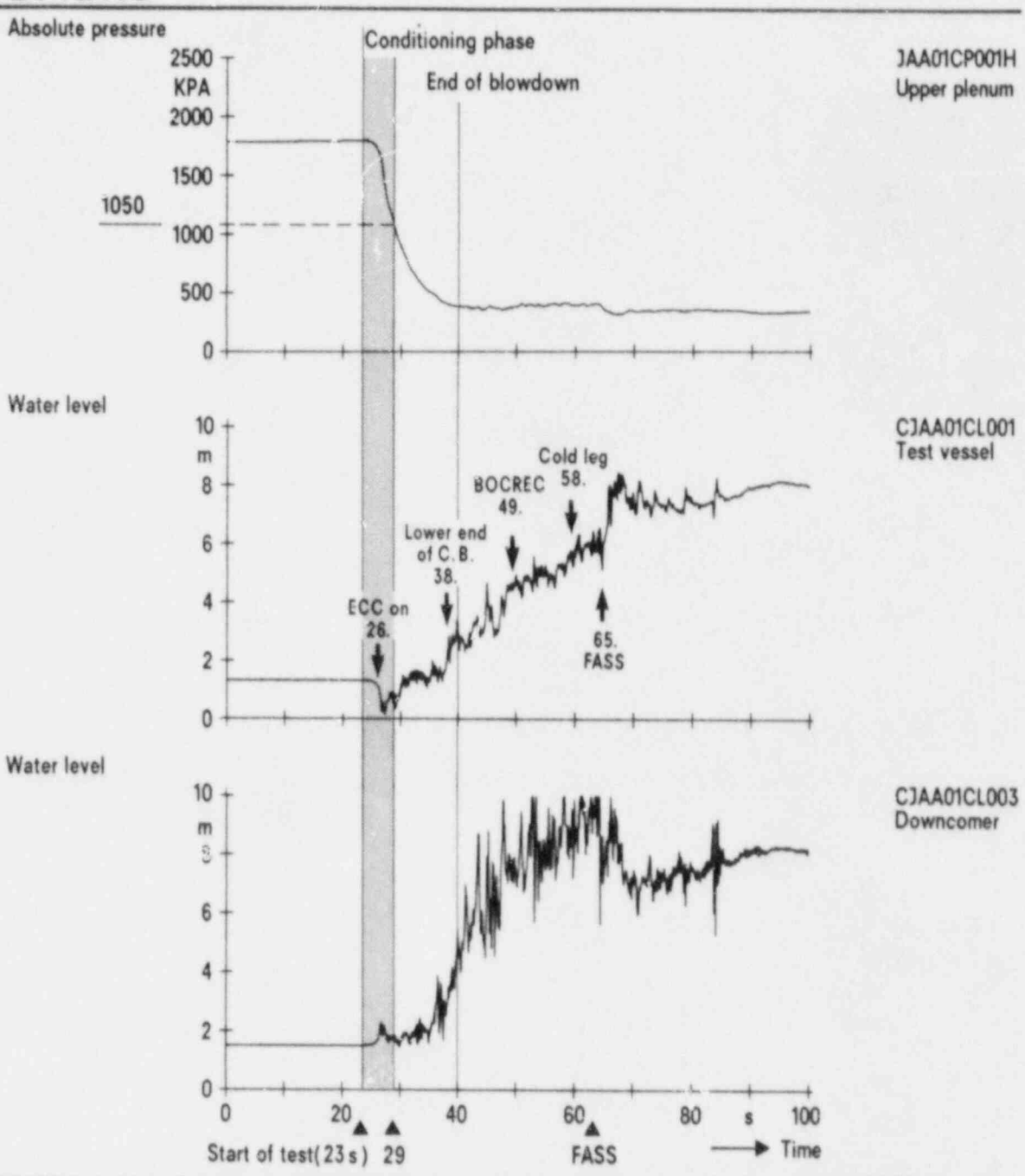

UB KWU

Figure 5: Overall System Behavior

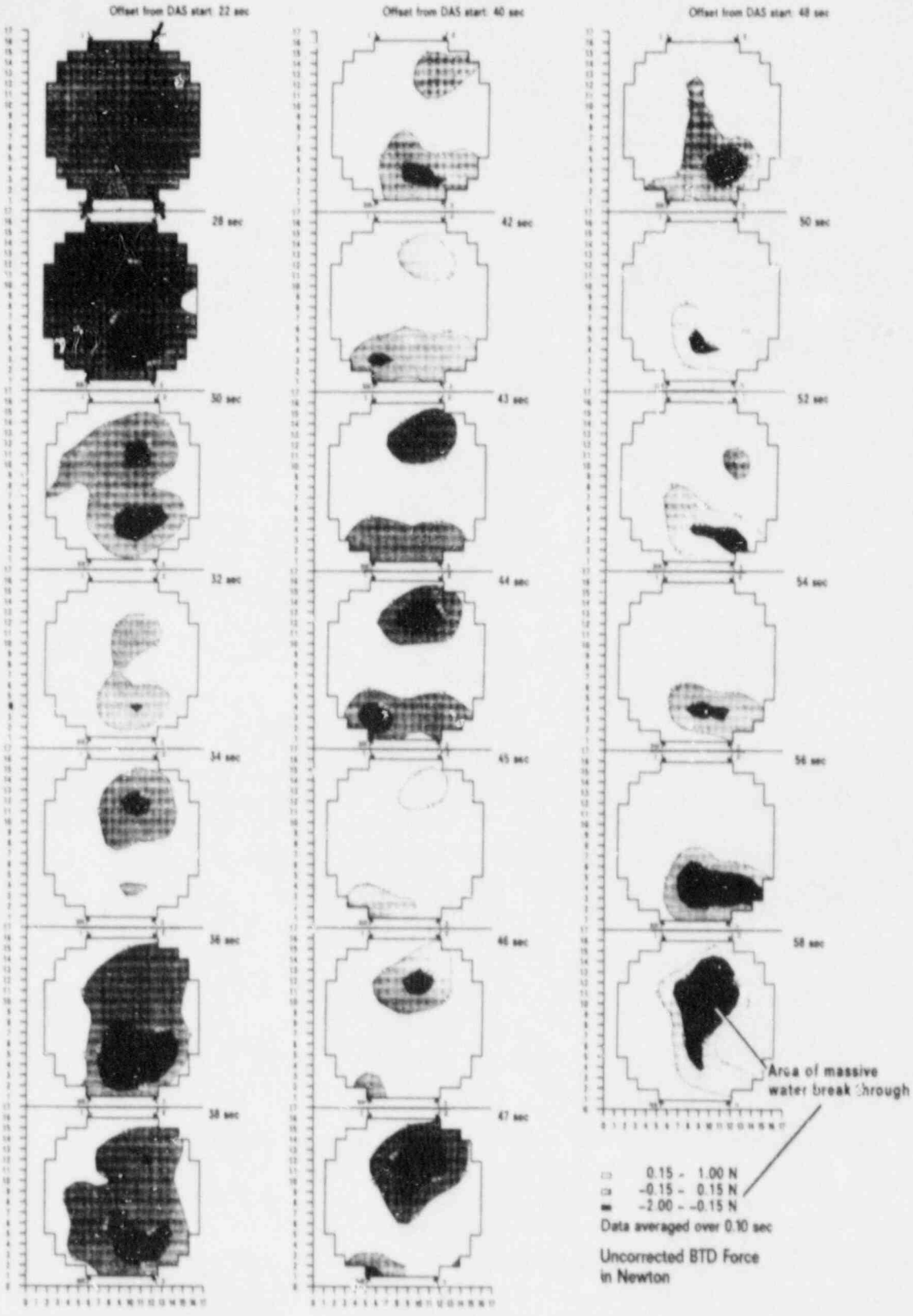

Fig. 6 Contour Plots of Water Breakthrough Areas at Tie Plate

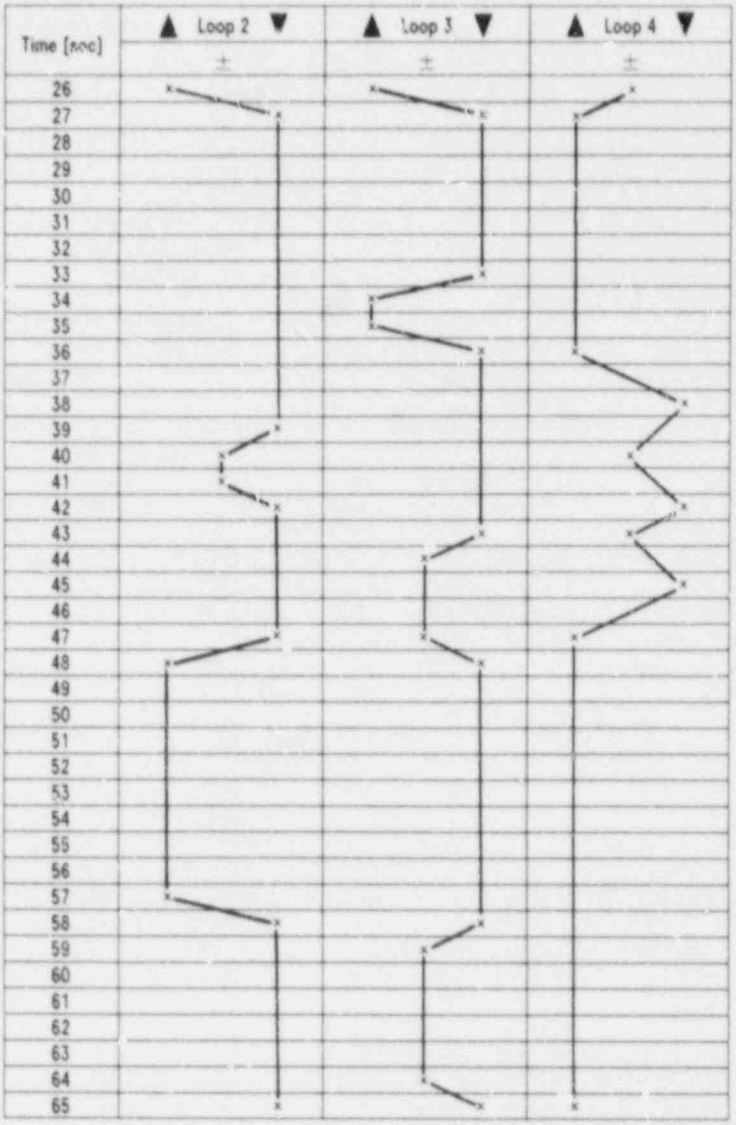

Fig. 7: Up and Down Flow Periods through Tie Plate near Injecting Hot Legs

87 PWR 261e
UB KWU

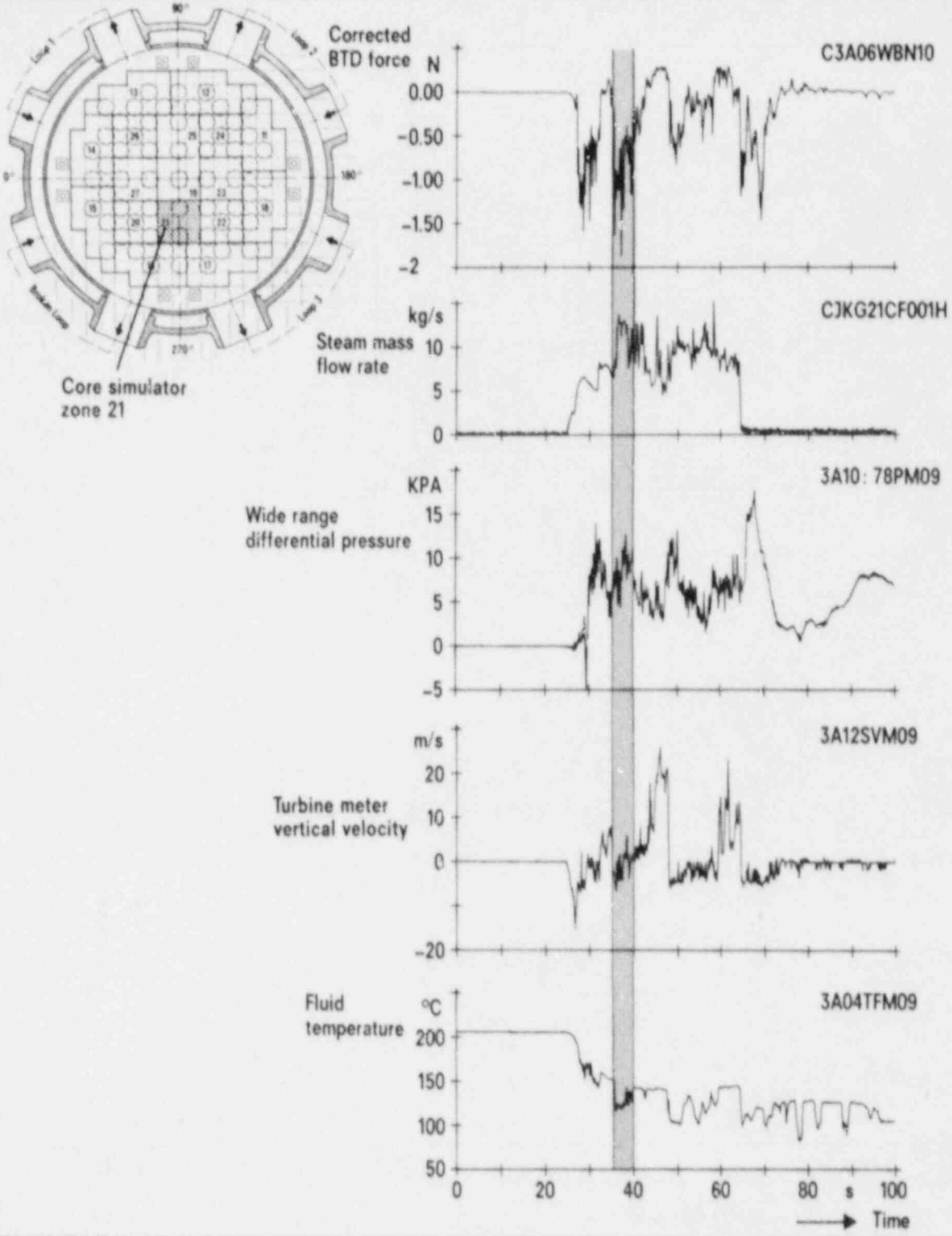

Figure 8: Core Simulator Zone 21; Signals of Instruments at Tie Plate

UB KWU

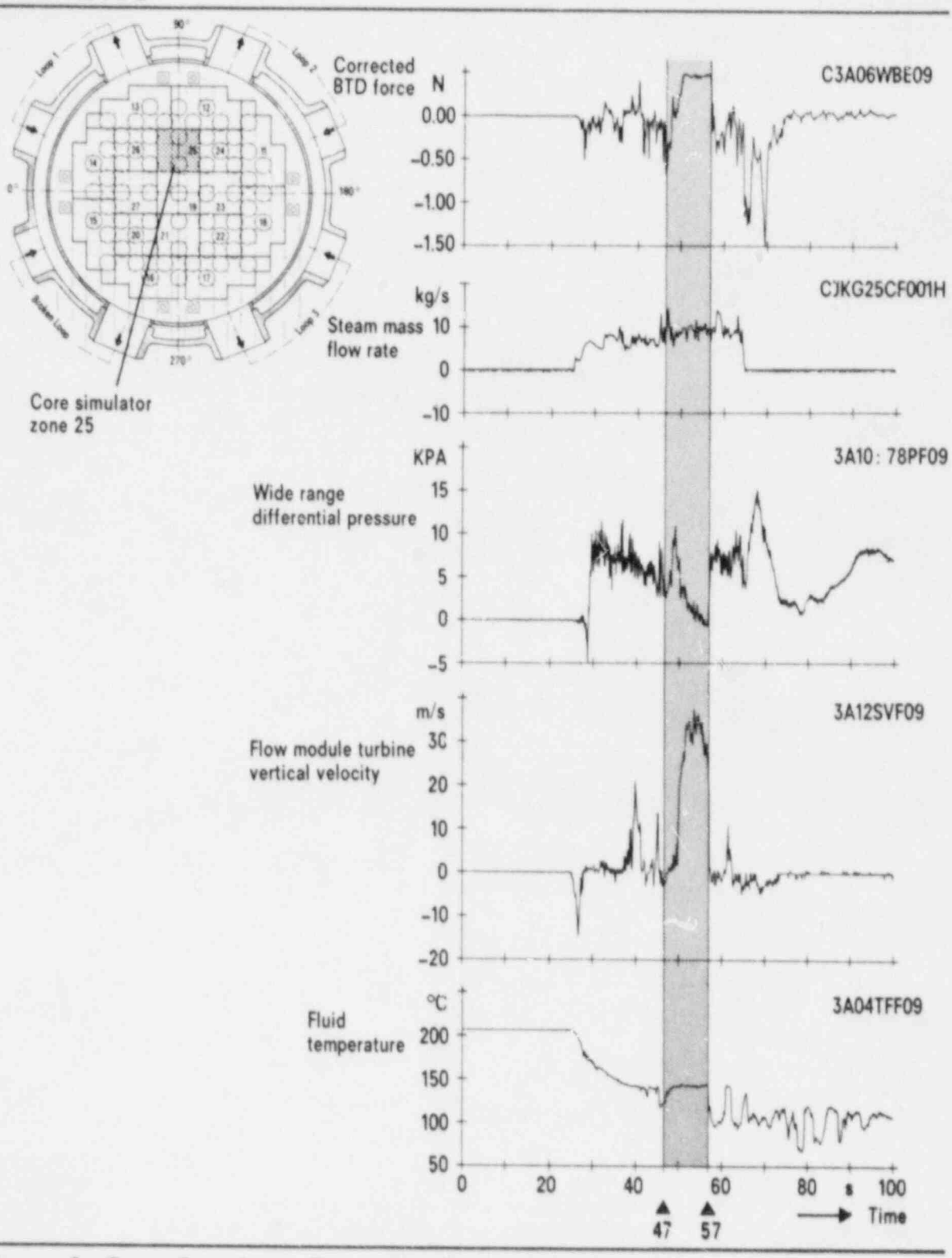

Figure 9: Core Simulator Zone 25; Signals of Instruments at Tie Plate

UB KWU

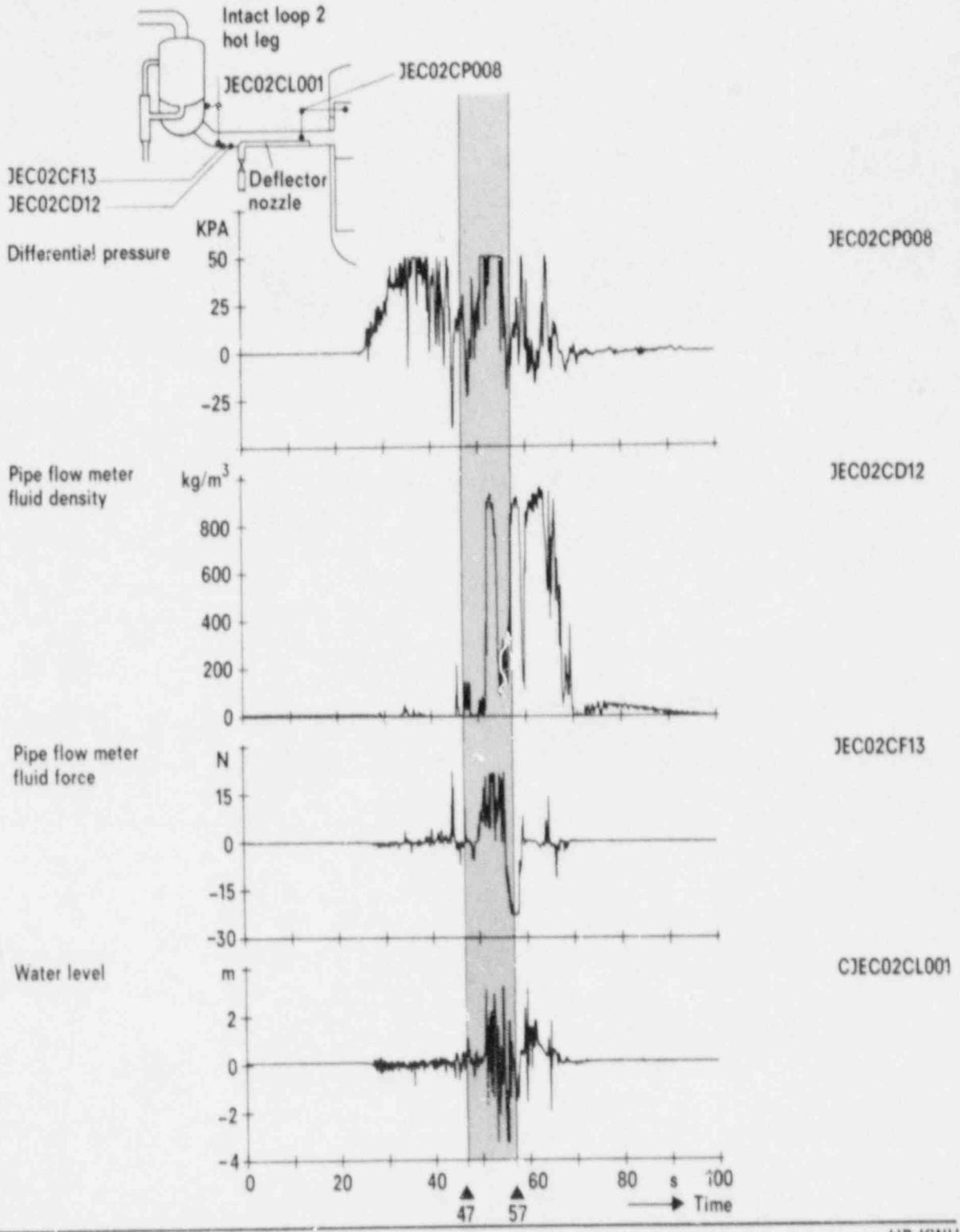

Figure 10: Water Plug Formation Indicated by Data of Hot Leg 2

UB KWU

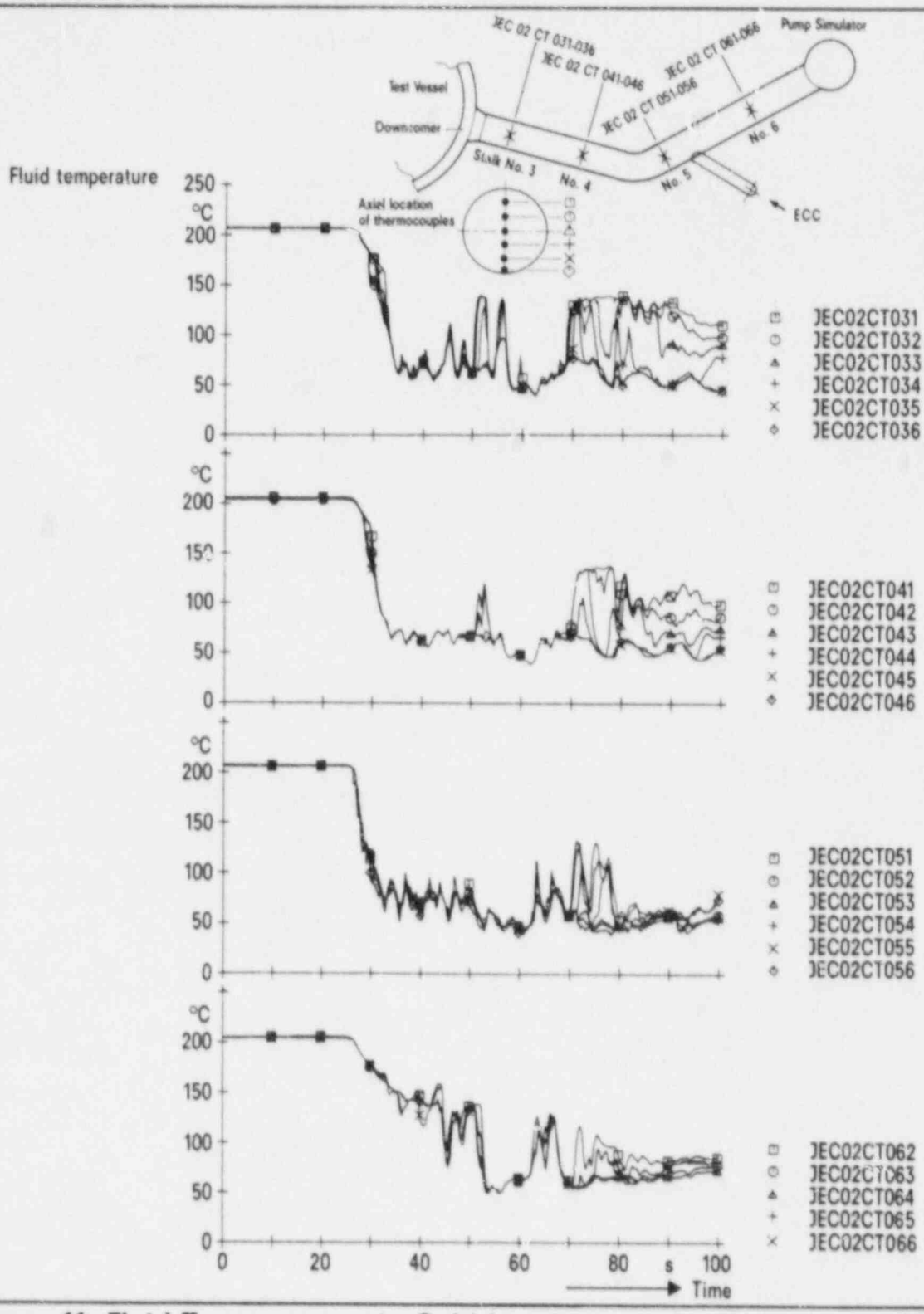

Figure 11: Fluid Temperatures in Cold Leg 2

UB KWU

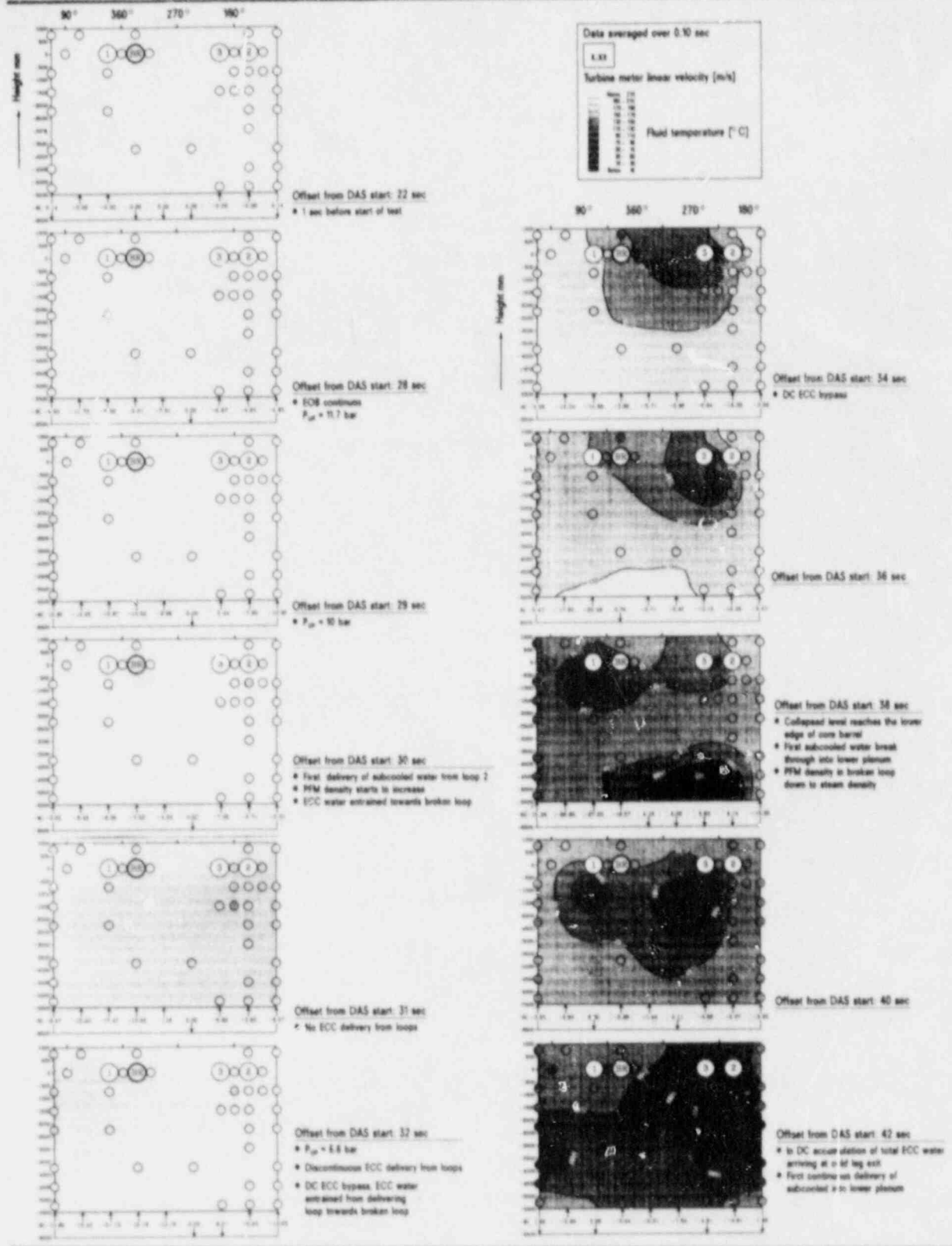

Fig. 12 a: Contour Plots of Fluid Temperature Distribution and Turbine Meter Readings in Downcomer

UB KWU

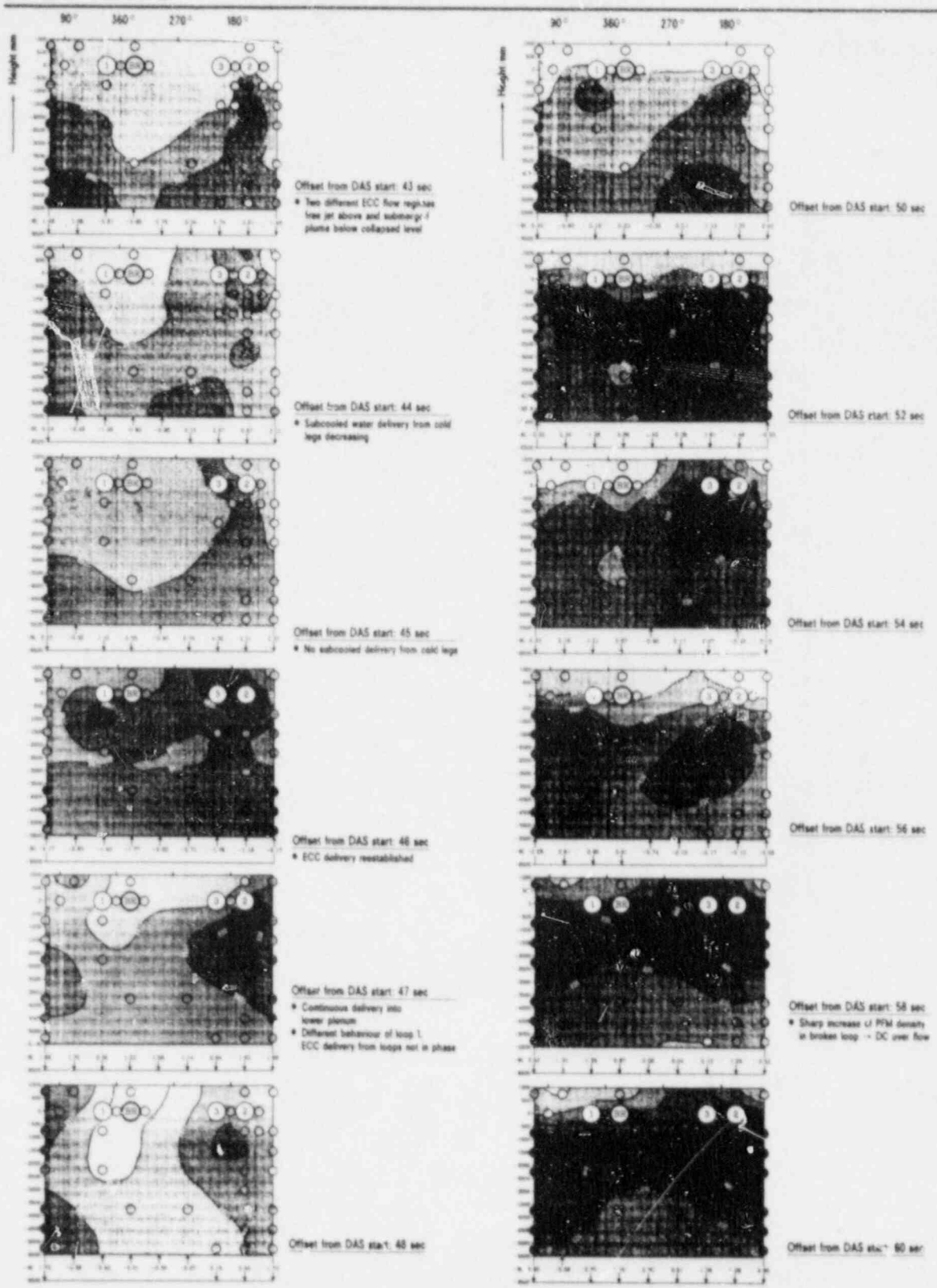

Fig. 12 b: Contour Plots of Fluid Temperature Distribution and Turbine Meter Readings in Downcomer

UB KWU

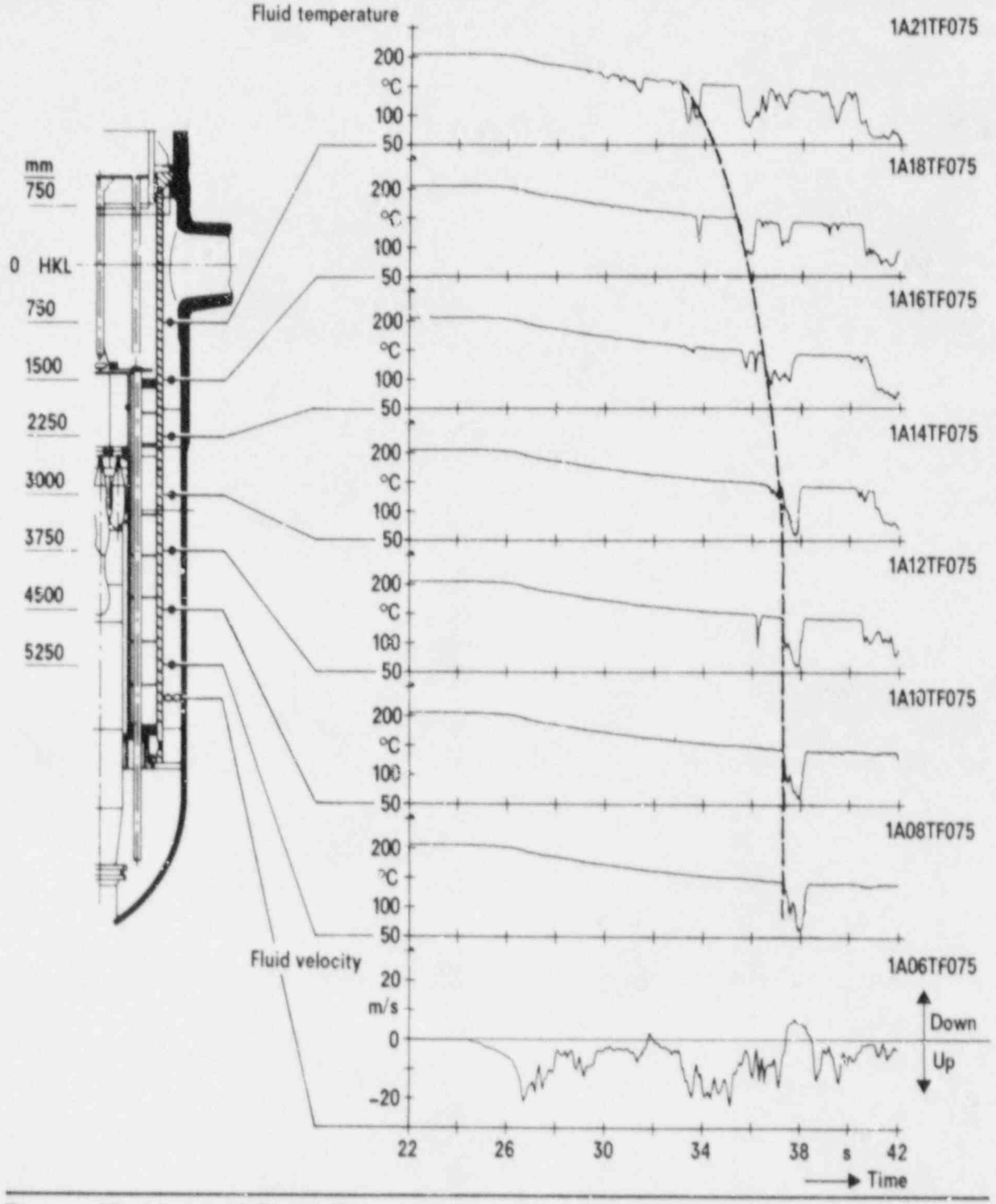

Figure 13: Vertical Fluid Temperature Distribution and Turbine Meter Readings in Downcomer below Cold Leg 2

UB KWU

UPTF TEST RESULTS

FIRST DOWNCOMER CCF TEST

BY

R.J. HERTLEIN, P.A. WEISS

SIEMENS AG

UB K W U

8520 ERLANGEN (FRG)

Abstract

The first downcomer countercurrent flow test was run in the Upper Plenum Test Facility - a 1:1 representation of a PWR primary system. In this downcomer separate effect test the simultaneous steam up or two-phase mixture up and water downflow phenomena were investigated.

1. INTRODUCTION

The Upper Plenum Test Facility (UPTF) Experimental Program, sponsored by the Ministry for Research and Technology (BMFT) is the German contribution to the trilateral 2D/3D Project, and is performed within international cooperation among Japan (JAERI), USA (USNRC) and the Federal Republic of Germany (BMFT).

A short description of the UPTF is given in the presentation "UPTF Test Results-First Integral Test with Combined ECC Injection" included in these Proceedings of the Meeting. The separate effect test No. 5, focusing the simultaneous steam up or two-phase mixture up and water downflow in a PWR downcomer, was performed during January 1987 according to an internationally agreed upon test matrix.

In the following a summary of the test objectives, initial and boundary conditions, test results and major findings is given.

2. TEST OBJECTIVES

The objective of test no. 5 was to investigate the three dimensional simultaneous steam or two-phase mixture up flow and water downflow in the downcomer of a pressurized water reactor (PWR). In test no. 5 subcooled water was injected into three intact loop cold legs via the ECC injection nozzles. The goal of test no. 5 was to investigate which part of the injected ECC water penetrates to the lower plenum. Of special interest were the location of water breakthrough areas in the downcomer relative to the injecting cold legs and the broken cold leg nozzle, the water accumulation in the lower plenum, the duration of ECC bypass via the broken cold leg nozzle and the beginning of local water breakthrough related to the start of ECC injection.

3. INITIAL AND BOUNDARY CONDITIONS, TEST PROCEDURE

The test was performed in two phases, a transient phase (phase A, RUN 063) starting from 18 bar and decreasing to containment pressure and a pseudo-steady test phase (phase B, RUN 062) starting with broken cold leg break valve open.

At start of test phase A the break valve simulating the vessel side of the cold leg break was opened over a 4 s time period. Two-phase mixture upflow in the downcomer was produced in test phase A by flashing of 13 200 kg of saturated water initially stored in the lower plenum.

In the pseudo-steady phase B steam upflow was established in the downcomer by steam injection into the core simulator system. The steam mass flow rate was ramped down from 322 kg/s to 309 kg/s during the test period. No water was initially stored in the lower plenum in test phase B.

In both test phases the pump simulators in the intact loops were blocked and the broken hot leg break valve was closed, so as to force steam or two-phase mixture to flow around lower edge of core barrel.

During both test phases a containment simulator pressure of 2.5 bar was used and an ECC mass flow rate of 500 kg/s was injected into each of the three intact loop cold legs. The ECC temperature was 30°C.

According to the test concept in test phase A the ECC injection could be activated only, when two-phase mixture upflow had been fully established.

For that reason the delay between start of ECC injection and first water penetration into the downcomer was studied in a pretest. Based on this pretest results in test phase A the ECC injection into the three intact loop cold legs was initiated 5 s prior to the break valve opening.

In test phase B core simulator steam injection started 8 s before start of ECC injection such, that the downcomer steam upflow rate was at maximum when the ECC entered the downcomer.

To simulate the dissolved nitrogen in the ECC water a mass flow rate of 0.31 kg/s nitrogen was specified to be injected into the ECC line upstream of each activated injection port.

4. TEST RESULTS

4.1 TEST PHASE A

In the transient test phase A the ECC injection started at 24 s plot time (time = 0 is arbitrary). Due to steam condensation on the cold ECC water the test vessel pressure started to decrease at the same time as shown in Figure 1. At 29 s when the break valve began to open, the test vessel pressure reached 14.3 bar.

Figure 3 shows fluid temperature data measured by the TC stalks of cold leg 2. Immediately after start of ECC injection a subcooled water plug was formed. As indicated by the TC stalks the water plug first formed near the ECC injection port (near stalks No. 5 and 6) and filled the cross section of the pipe completely. As the fluid temperatures measured by one stalk were close together the water plug had

relatively steep fronts. At 28 s (4.5 after start of ECC injection) the subcooled water plug had grown until it covered stalks No. 4, 5 and 6.

The fluid temperatures measured by stalk 6 between ECC port and pump simulator increased again at 30 s, indicating that the plug moved towards the downcomer at this time. TC stalk No. 3 and the fluid TC in the downcomer below cold leg 2 measured subcooling at 31 s, indicating that the water plug had reached the downcomer.

An analysis of the TC stalk temperatures in cold leg 2 indicated a change in flow direction at 33 s. In the period 34 to 37 s almost no ECC was delivered to the downcomer by cold leg 2. Delivery to the downcomer out of this cold leg was reestablished at 38 s and lasted till the end of this test phase (50 s).

Similar water plug formation and oscillations were indicated by the fluid temperatures measured in intact loop cold leg 1 and 3.

ECC water injected into cold legs 2 and 3 entered the downcomer at 31 s. The fluid TC's in the downcomer at elevation 5.25 m below cold leg center line measured water subcooling at 32 s below cold leg 2 and at 39 s below cold leg No. 3. Also the turbines located near the lower end of the core barrel in the downcomer showed a flow direction corresponding to water downflow at 32 s below cold leg 2 and at 39 s below cold leg 3.

These TC and turbine data lead to the conclusion that the cold water plume originating from cold leg 2 and 3 fell to the lower plenum without being strongly affected by the upflowing two-phase mixture.

A different flow direction of the cold water plume originating from cold leg 1 was indicated by the temperature and velocity measurements below this cold leg. No water subcooling was measured below cold leg 1 before 42 s.

The Pipe Flow Meter densitometer (see Figure 2) and the fluid temperatures in the broken loop cold leg indicated subcooled water flowing out via the broken cold leg immediately after ECC injected into cold leg 1 had reached the downcomer. Also the fluid temperature measurement between cold leg 1 and the broken cold leg showed subcooled temperatures at 31 s.

The downcomer measurement positions around cold leg 1 indicated that the upflowing two phase mixture prevented the subcooled ECC out of cold leg 1 from flowing directly to the lower plenum. At least part of this ECC mass flow rate was bypassed via the broken cold leg nozzle out of the test vessel.

The development of the cold water plumes in the downcomer during the transient can be followed by means of the contour plots shown in Figure 4 and 5 for a series of times. Lines of constant fluid temperatures are shown in the unwrapped downcomer in these figures. These contour lines can only be interpreted qualitatively due to the limited number of downcomer thermocouples from which they were developed, but they are useful for showing an overall picture of downcomer penetration. Fluid temperatures measured in the intact loop cold legs implied that no ECC was delivered to the downcomer in the period 34 to 38 s. This finding is in agreement with the broken cold leg Pipe Flow Meter fluid density data shown in Figure 2.

The collapsed water level in the lower plenum based on DP measurements is depicted in Figure 6.

An estimation of the total amount of coolant leaving the primary system through the broken loop cold leg nozzle during the test period from 20 to 55 s results in approximately 18 000 kg of water.

4.2 TEST PHASE B

The core simulator steam flow started at 22 s, eight seconds before start of ECC injection (see Figure 11).

The ECC injection started at 30 s. Fluid temperature measurements in the intact loop cold legs indicated that a subcooled water plug was formed immediately after start of ECC injection in each intact loop cold leg. The water plug moved to and fro. This oscillatory movement was clearly shown by TC stalk 6 in cold leg 2. Plug formation and movement observed in this test phase were similar to that measured in the transient test phase A.

ECC entered the downcomer at 36 s. Measured fluid temperature distributions plotted in the unwrapped downcomer shown in Figure 8 and 9 indicated that the

cold water plumes originating from cold leg 2 and 3 fell to the lower plenum without being strongly affected by the upflowing steam.

The cold water plume originating from cold leg 1 (next to broken cold leg) was forced by the upflowing steam not to take the shortest way to the lower plenum. The same behaviour was observed in test phase A.

A smoothed mean value of the water mass collected in the lower plenum versus time is depicted in Figure 10. The increase of the collected water mass was almost the same as the injected ECC water mass. This was possible because the steam mass condensed by the subcooled ECC increased the downflowing water mass.

A small but increasing fraction of the injected ECC water was carried out of the broken cold leg nozzle after 42 s, by the steam leaving the primary system. The test vessel pressure in test phase B is depicted in Figure 7.

5. MAJOR FINDINGS

- The test results show a marked immediate local breakthrough and downflow of the subcooled ECC water delivered by cold legs No. 2 and 3 for both steam and two-phase mixture upflow.

- The upflowing two phase mixture and also the upflowing steam prevented the subcooled ECC flowing out of cold leg 1, which is next to the broken cold leg, from flowing over the shortest path to the lower plenum. For the steam only case it took a curved path but reached the lower plenum.

- Water bypass via the broken cold leg was observed for two-phase upflow. Almost no water bypass occurred when 320 kg/s of steam were flowing upwards in the downcomer in test phase B.

- Water plugs were formed in all intact loop cold legs immediately after start of ECC injection. The water plugs existed throughout the ECC injection period and moved back and forth.

- ECC delivery to the downcomer was consistent with the water plug movement. Also the ECC delivery appeared to be intermittend and the water

bypass periods measured in test phase A are consistent with periods of ECC delivery to the downcomer.

- The boundary condition of no intact loop flow chosen in this test caused the high two-phase upflow necessary for water downflow limitation. This boundary condition is untypical for the end-of-blowdown phase of a pressurized water reactor. For that reason, the bypassed water mass flow rate measured in this test can not be transferred directly to a pressurized water reactor analysis.

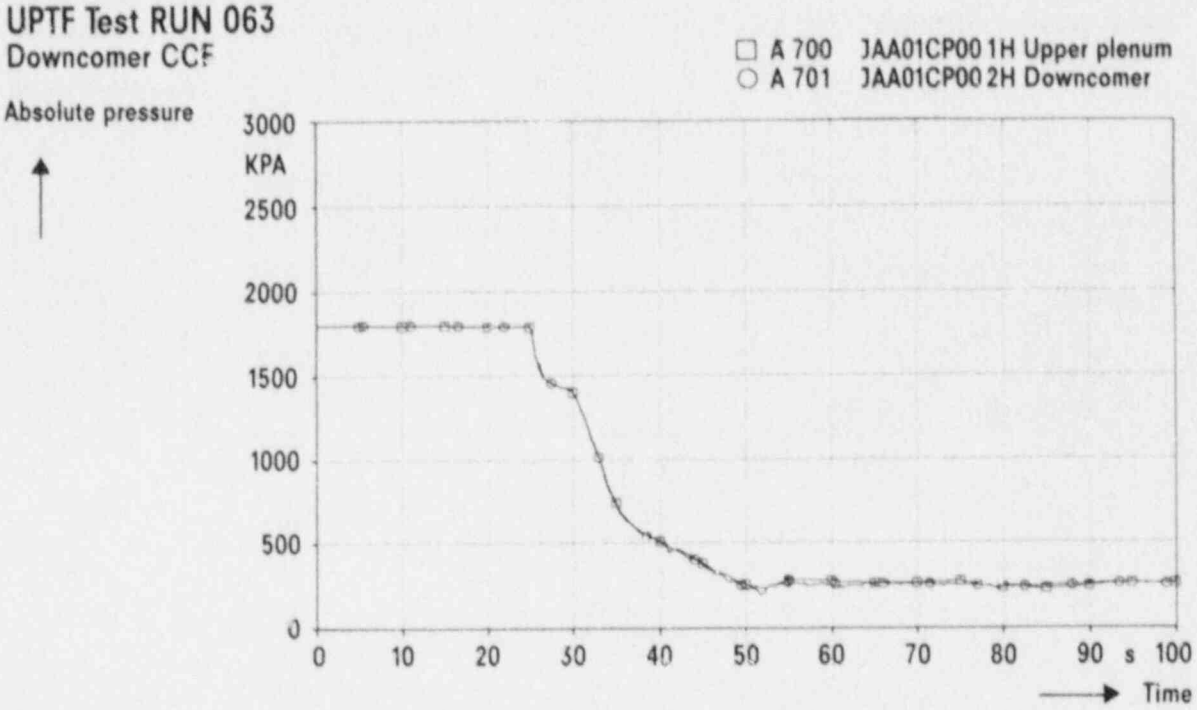

Fig. 1: Pressure in Upper Plenum and Downcomer

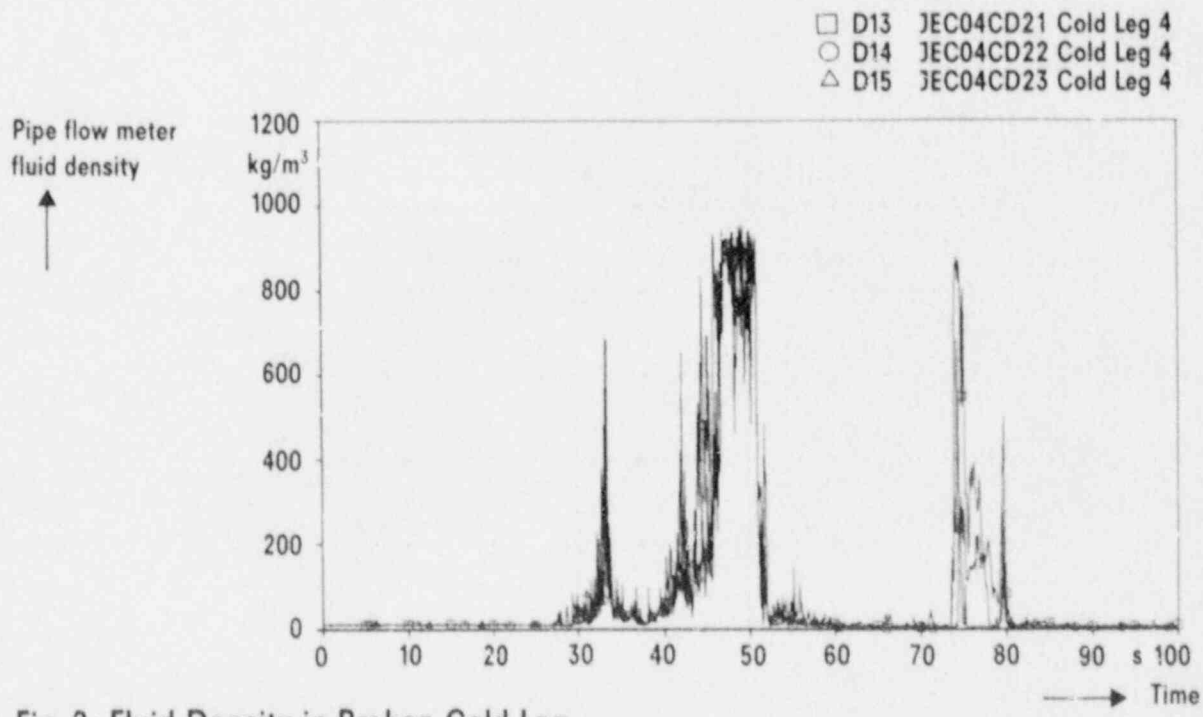

Fig. 2: Fluid Density in Broken Cold Leg

UB KWU

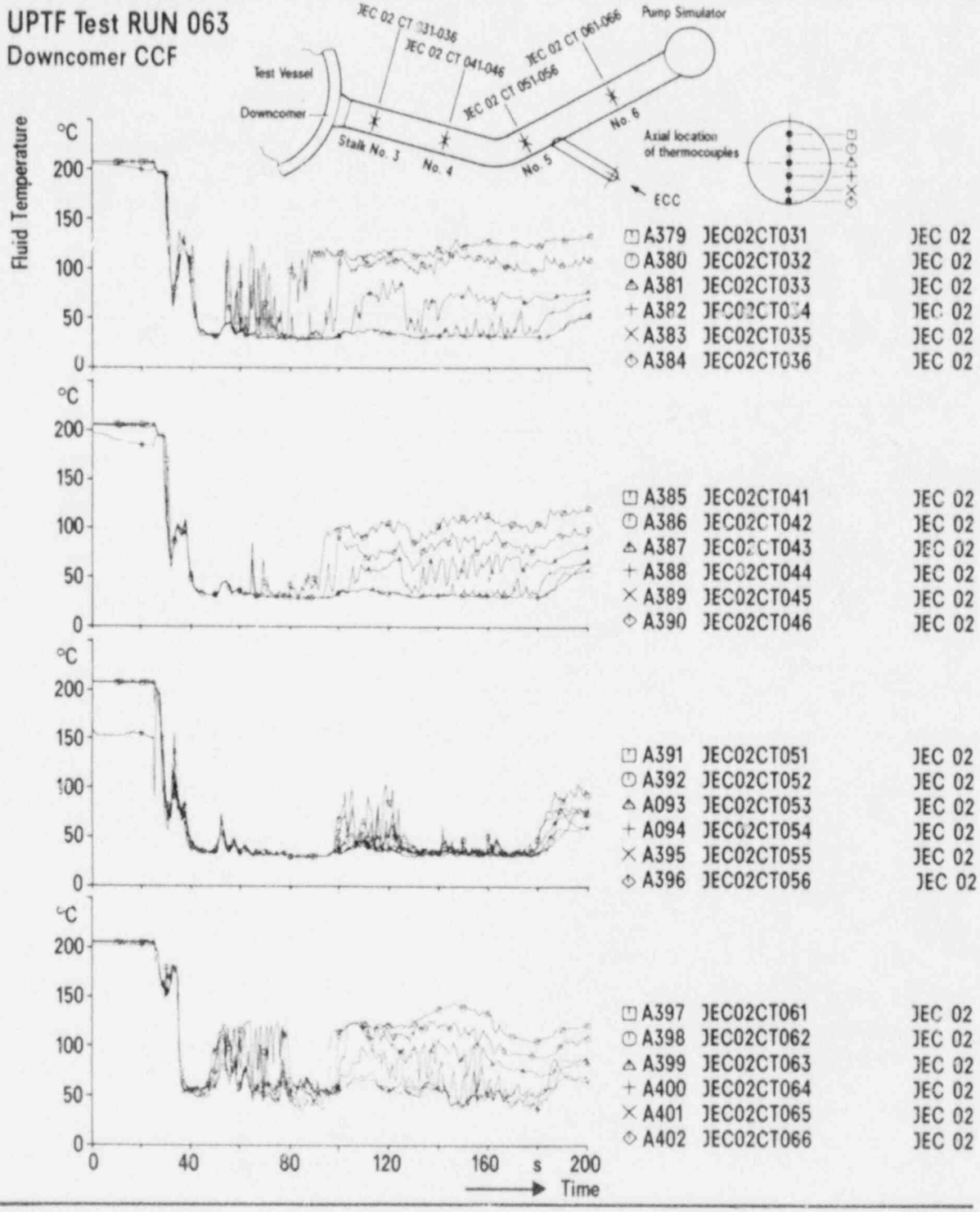

Figure 3: Fluid Temperature in Cold Leg 2

UB KWU

SIEMENS

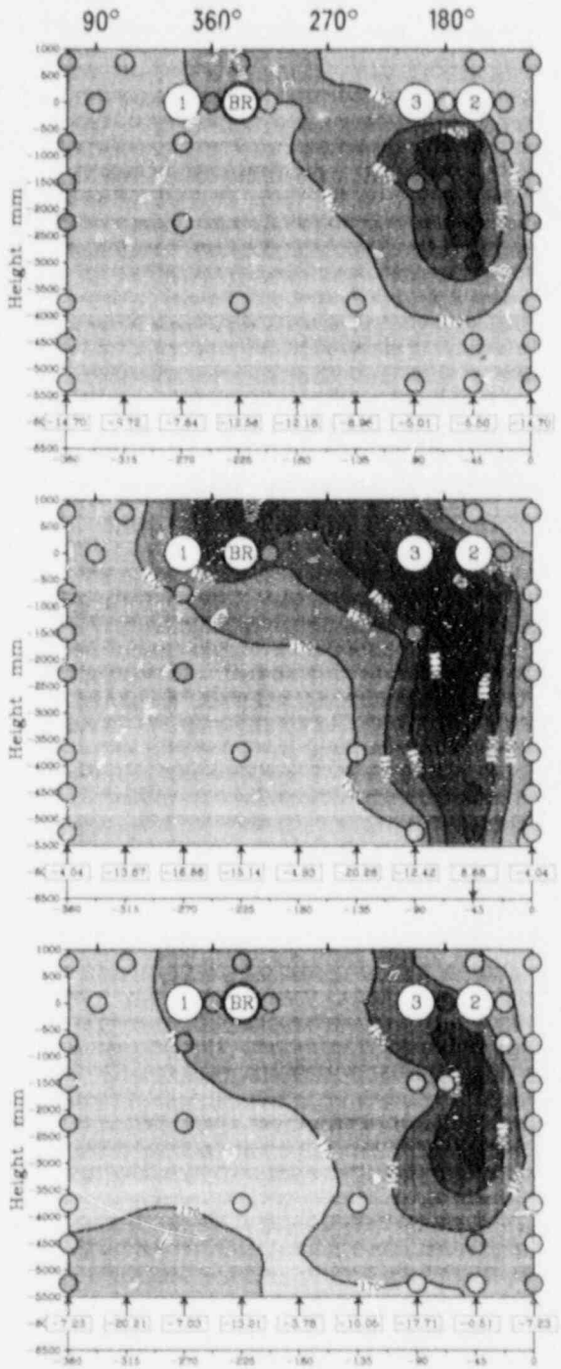

UPTF Test RUN 063 Downcomer CCF

Data averaged over 0.10 sec

X.XX

Turbine meter linear velocity [m/s]

Fluid temperature [°C]

Offset from DAS start: 32 sec

- Water downflow below cold legs 2 and 3

Offset from DAS start: 33 sec

Offset from DAS start: 34 sec

- No ECC delivery out of cold legs

Fig. 4: Contour Plots of Fluid Temperature Distribution in Downcomer (Test Phase A)

UB KWU

SIEMENS

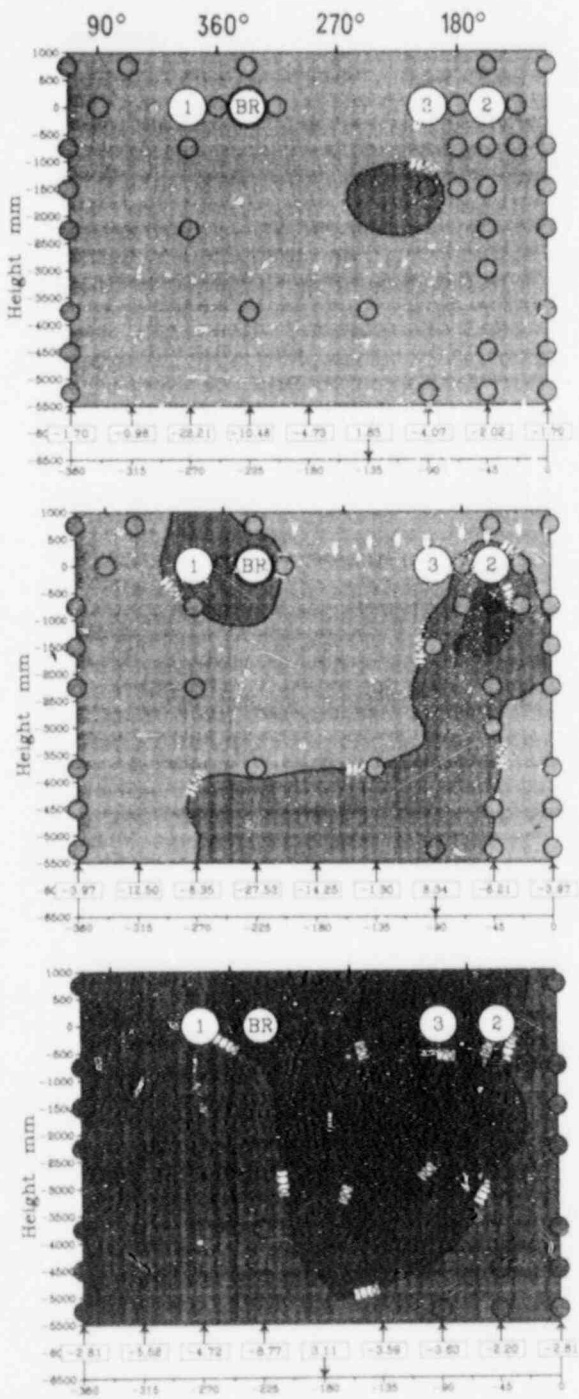

UPTF Test RUN 063 Downcomer CCF

Data averaged over 0.10 sec

X.XX

Turbine meter linear velocity (m/s)

Above 210
190 - 210
170 - 190
150 - 170
130 - 150
110 - 130
90 - 110
70 - 90
50 - 70
30 - 50
10 - 30
Below 10

Fluid temperature [°C]

Offset from DAS start: 37 sec

- No ECC delivery out of cold legs

Offset from DAS start: 40 sec

- ECC delivery out of cold legs reestablished
- Water downflow below cold leg 2 and 3

Offset from DAS start: 50 sec

- Massive water downflow

Fig. 5: Contour Plots of Fluid Temperature Distribution in Downcomer (Test Phase A)

UB KWU

UPTF Test RUN 063
Downcomer CCF

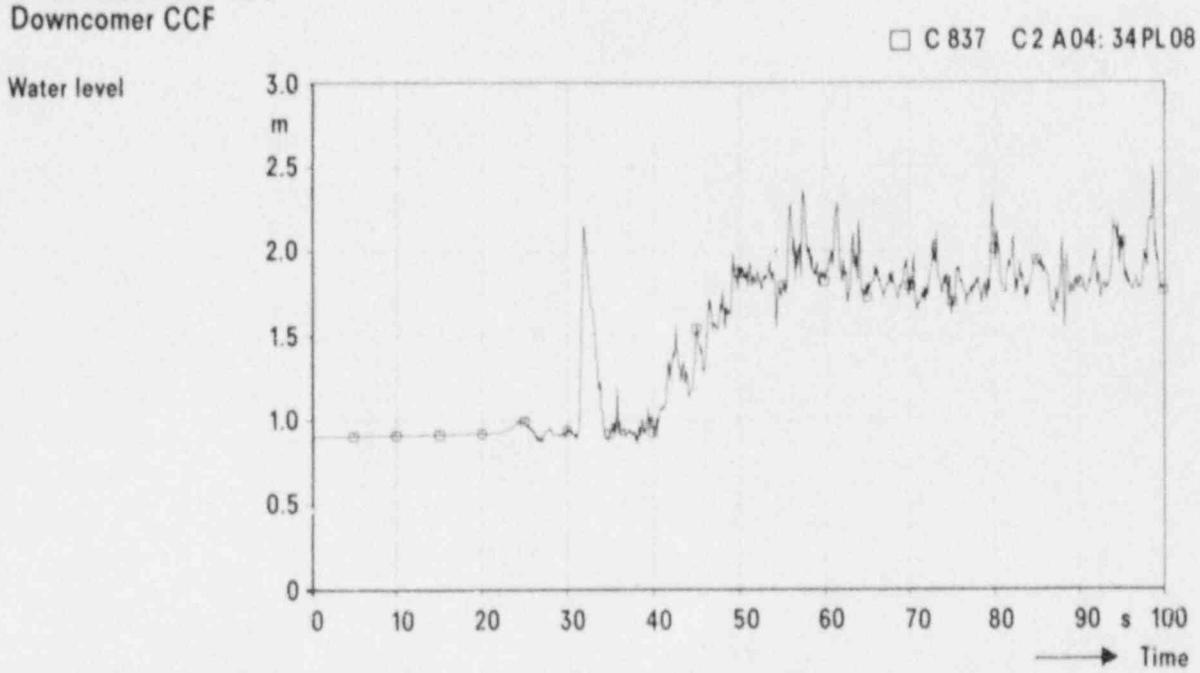

Fig. 6: Collapsed Water Level in Lower Plenum

UPTF Test RUN 062
Downcomer CCF

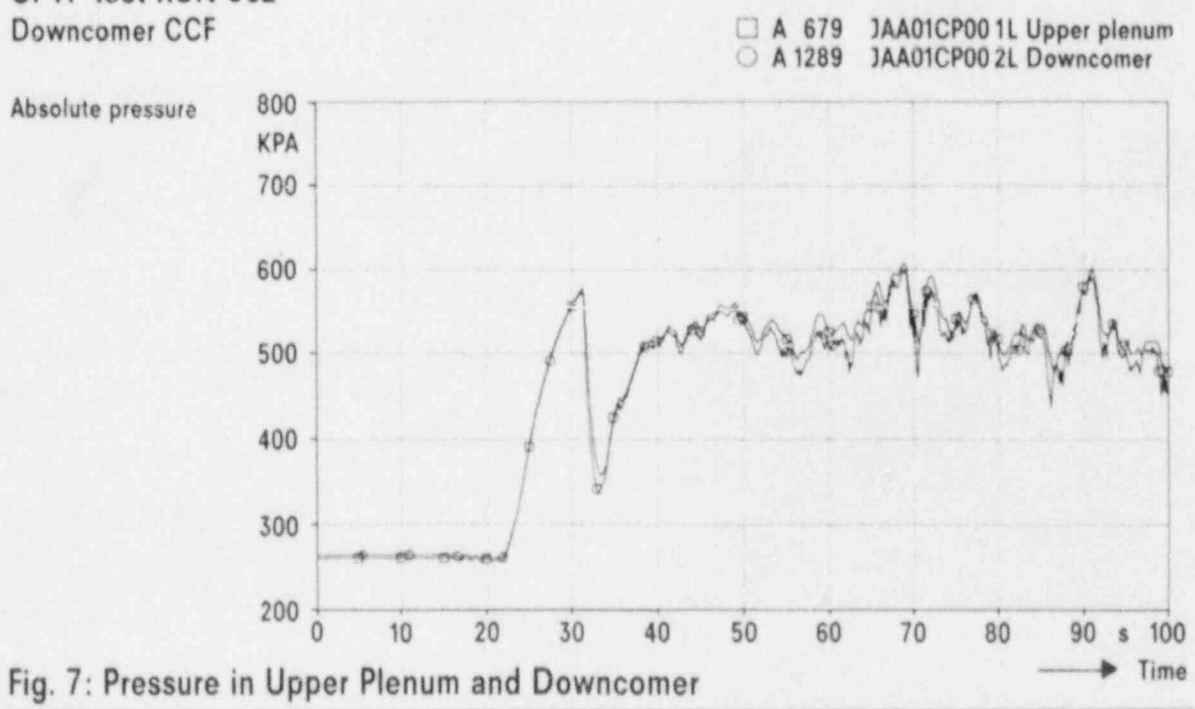

Fig. 7: Pressure in Upper Plenum and Downcomer

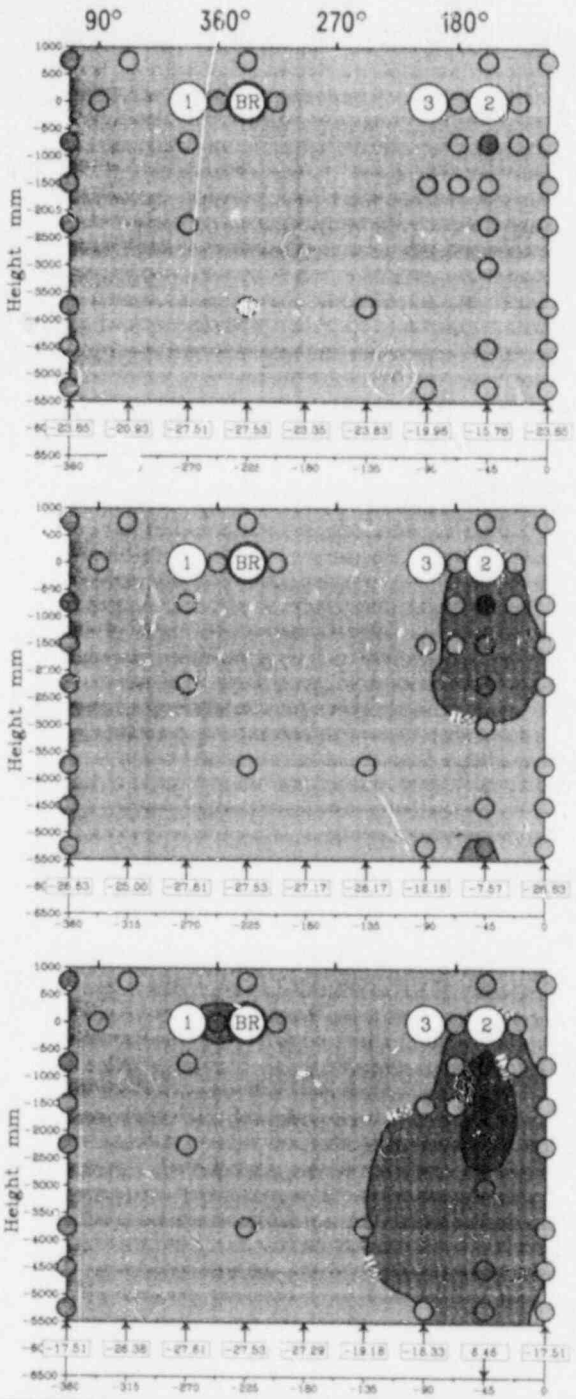

UPTF Test RUN 062 Downcomer CCF

Data averaged over 0.10 sec

x.xx

Turbine meter linear velocity [m/s]

Above 210
190 - 210
170 - 190
150 - 170
130 - 150
110 - 130
90 - 110
70 - 90
50 - 70
30 - 50
10 - 30
Below 10

Fluid temperature [°C]

Offset from DAS start: 38 sec

Offset from DAS start: 39 sec

- Cold water plume below cold leg 2

Offset from DAS start: 40 sec

- Water out of cold leg 1 enters downcomer

Fig. 8: Contour Plots of Fluid Temperature Distribution in Downcomer (Test Phase B)

UB KWU

SIEMENS

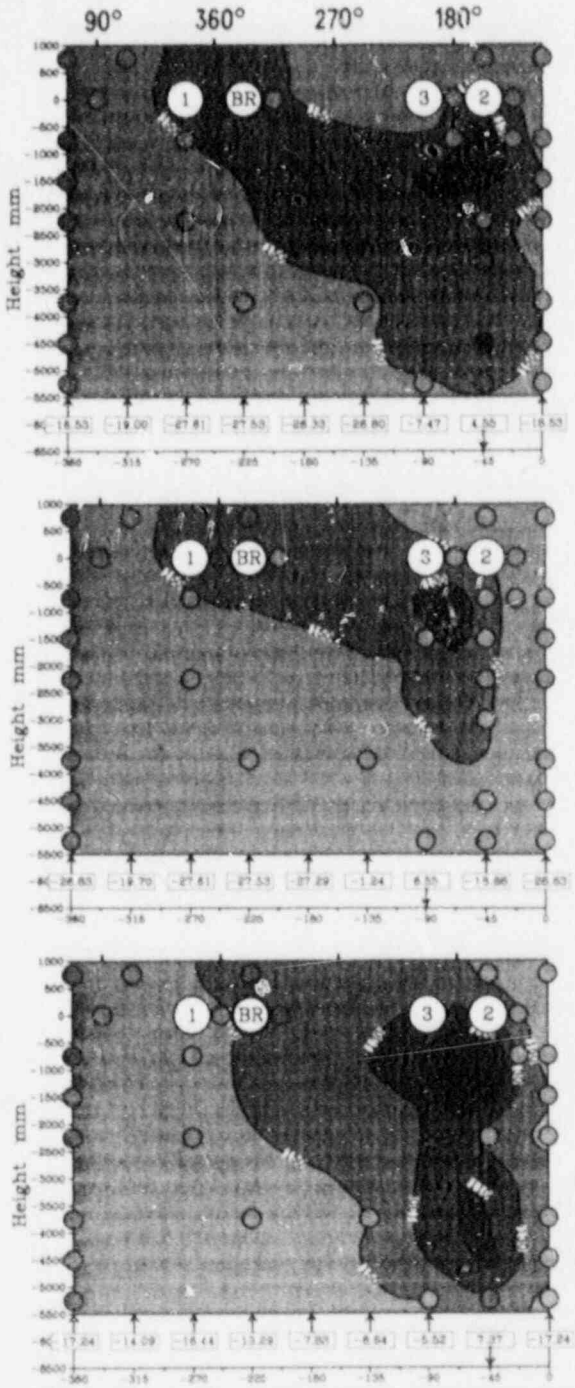

UPTF Test RUN 062 Downcomer CCF

Data averaged over 0.10 sec

X.XX

Turbine meter linear velocity [m/s]

Above 210
190 - 210
170 - 190
150 - 170
130 - 150
110 - 130
90 - 110
70 - 90
50 - 70
30 - 50
10 - 30
Below 10

Fluid temperature [°C]

Offset from DAS start: 41 sec

- Water out of cold leg 1 is affected by the upflowing steam

Offset from DAS start: 42 sec

- No ECC delivery out of cold legs

Offset from DAS start: 50 sec

- Downflow reestablished

Fig. 9: Contour Plots of Fluid Temperature Distribution in Downcomer (Test Phase B)

UB KWU

UPTF Test RUN 062 Downcomer CCF

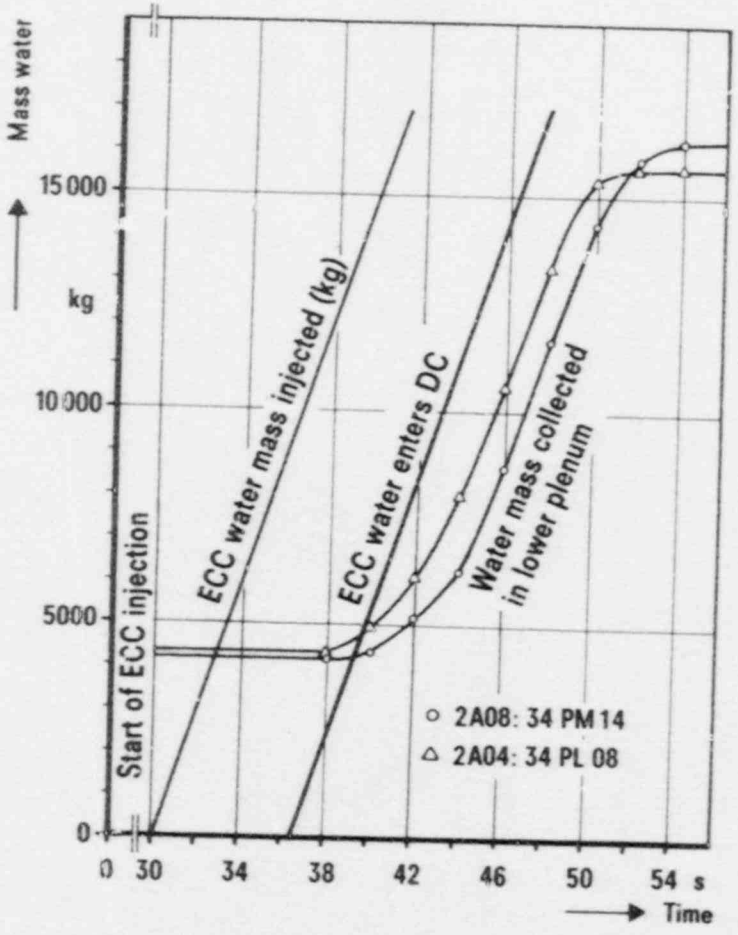

Fig. 10: Water Mass Collected in Lower Plenum

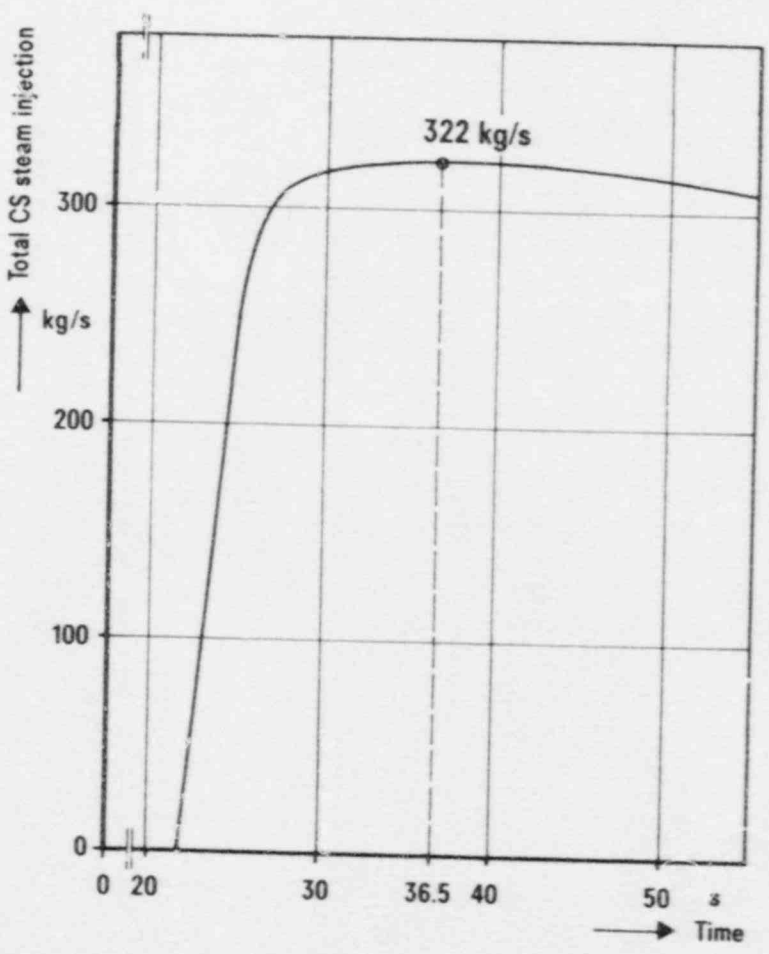

Fig. 11: Total Core Simulator Steam Injection

UB KWU

Multi-Dimensional Effect Found in SCTF Reflood Tests for US/J PWR*

Hiromichi ADACHI, Tadashi IGUCHI, Takamichi IWAMURA,
Akira OHNUKI, Yutaka ABE, Hajime AKIMOTO,
Tsutomu OKUBO and Yoshio MURAO
(Japan Atomic Energy Research Institute)

Abstract---Multi-dimensional core thermal-hydraulic behavior in the reflooding process of a large break loss-of-coolant accident was studied with Slab Core Test Facility (SCTF) for pressurized water reactors with cold leg injection type emergency core cooling system, which are operated mainly in the United States and Japan.
The most remarkable finding is enhancement of heat transfer in the high power bundles due to radial power distribution effect. The effect always reduces the turnaround temperature of the high power bundles. Increase in heat transfer coefficient in the high power bundles can be predicted with an empirical correlation proposed in this paper as function of local radial power ratio and radial peaking factor.

1. Introduction

Slab Core Test Facility (SCTF) Test Program (Ref.1) is a part of the large trilateral research program called 2D/3D Program on reflooding thermal-hydraulics among the United States (US), Federal Republic of Germany (FRG) and Japan together with Cylindrical Core Test Facility (CCTF) Test Program.
Multi-dimensional core thermal-hydraulic behavior during reflooding process was studied for pressurized water reactor (PWR) with cold leg injection type emergency core cooling system (ECCS) by using mainly SCTF Core-I and Core-II (Refs. 3-9) and partially Core-III. Since this type PWR is operated mainly in the US and Japan, it shall be called US/J PWR in this paper.
Described in this paper is summary of SCTF test results on multi-dimensional thermal-hydraulic behavior in a US/J PWR core.

2. Test Facility

SCTF core simulates the slab shaped part of full height×full radius×one bundle width which is extracted from 1,100 MWe class PWR core as shown in Fig.1. It consists of eight full scale, electrically heated simulated fuel bundles. Bundles 1 is designated central bundle and Bundle 8 is designated peripheral bundle. Heating power for each bundle can be controled independently.
SCTF has accumulator injection system (Acc) and low pressure coolant injection system (LPCI) as ECCS.
On the other hand, primary system of SCTF is, as shown in Fig.2, simply designed one without active steam generator. More detailed information for SCTF is given in Ref.2.

---

* The work was performed under contract with the Atomic Energy Bureau of Science and Technology Agency of Japan.

3. Types of Multi-Dimensionality

Two types of multi-dimensional thermal-hydraulic behavior were observed (Ref.7) in the reflooding core as illustrated in Fig.3.

One is caused by radial power distribution in the core. Heat transfer coefficient is increased in the high power bundles and decreased in the low power bundles by the effect, as shown in Fig.4, for given distance from the approaching quench front. Nominal water fraction calculated from differential pressure data without pressure loss correction is, on the other hand, larger in the high power bundles and smaller in the low power bundles. As the reslult, heat transfer coefficient data and nominal water fraction data fall on a line within only a small error band, although some effect of spacers seems to exist. SCTF Core-I data (Ref.5) are shown in Fig.5 as an example. This relationship between heat trasfer cofficient and nominal water fraction suggests that converging of water flow to the high power bundles results in the excellent cooling of the bundles (Refs.5,8).

The other kind of multi-dimensional core behavior is caused by non-uniform water distribution on the UCSP as illustrated in Fig.3(b). Higher upper plenum collapsed water level in the peripheral side restricts the discharge of core fluid and then two-phase flow in the core converges to the central side. As the result, quench front propagation in the upper part of the peripheral bundles delays, as seen in Fig.6, not only in a flat power distribution test but also in a steep power distribution test of which bundle power is the minimum at the periphery. However, peak clad temperature (PCT) is not affected by the effect becasuse the non-uniform water distribution is developed after appearance of PCT.

4. Parameter Effects

Effects of various test parameters on multi-dimensional core thermal-hydraulic behavior due to radial power distribution effect were studied.

Studied test parameters are system pressure, flooding velocity, core inlet subcooling, total power and initial stored energy in the core (Ref.5).

Each test parmeter shows only little effect on the difference in heat transfer coefficient between the high power bundles and the low power bundles for given distance from the approaching quench front. For example, Fig.7 compares heat transfer coefficients in the highest and the lowest power bundles between two tests with different system pressure.

Both tests show almost the same difference in heat transfer coefficient between the highest and the lowest power bundles, indicating almost the same degree of multi-dimensionality.

Multi-dimensionality of core heat transfer is also almost the same between SCTF and CCTF tests with the same radial power ratios as shown in Fig.8. Core cross section is circular in CCTF and slab in SCTF. Representative core radius of CCTF is only about 1/4.5 times that of SCTF. However, degree of multi-dimensionality in core heat transfer is almost the same between the two tests, indicating that multi-dimensional fluid behavior is not affected so much by geometrical shape and size of the core cross section in a relatively large core such as SCTF and CCTF. This is considered due to very small horizontal flow resistance (Ref.5) of slanting two-phase flow in rod bundles. From this fact, slab shape of SCTF core is justified and also scale of the CCTF is considered

enough even from the view point of multi-dimensionality simulation.

5. Reduction of PCT

Clad temperature is decreased in the high power bundles (Ref.6) and increased in the low power bundles due to the radial power distribution effect. Shown in Fig.9 is calculated clad temperatures for the common power and initial stored energy condition by using the heat transfer coefficients measured in steep power distribution test (Test S2-06) and flat power distribution test (S2-SH2), indicating an evident reduction of clad temperature in the high power bundle. In this case, reduction of turnaround temperature at the elevation of 2.760 m of the high power bundle with local radial power ratio of 1.2 is 89 K. Reduction of clad temperature and that of the turnaround temperature are shown with respect to bundle number in Figs.10 and 11, respectively, based on similar calculations.

Reduction of the turnaround temperature of T/C elevations 4 through 8 (1.730 through 2.760 m from the heated length bottom) of the bundles with local radial power ratio of 1.2 in the various SCTF tests is summarized in Fig.12. Each bundle shows a convex characteristics on the graph, indicating that large reduction of the turnaround temperature is realized in the upper half of the core although at low elevations reduction of the turnaround temperature is small. Since PCT appears in the upper half of core, this characteristics is quite desirable from the view point of reactor safety. In most cases, the maximum turnaround temperature in each bundle appeared at T/C elevation 6 (1.905 m from the heated length bottom) although the predicted elevation based on heat transfer coefficient data from the corresponding flat power distribution test was T/C elevation 7 (2.330 m). Taking this movement of the maximum turnaround temperature point into account, reduction of the maximum turnaround temperature in each bundle reached upto 130 K.

As seen in Fig.12, turnaround temperatures in the bundles with local radial power ratio of 1.2 always reduced, except only two data which were considered to be affected by top-down cooling. Therefore, if radial power distribution effect is ignored as in the current licensing procedure, a potential conservatism can be expected. Larger additonal safety margin due to radial power distribution effect can be expected under more severe core cooling condition, because delayed turnaround of clad temperature due to poor core cooling gives long integration time for the effect of increased heat transfer coefficient until the turnaround. Difference in turnaround temperature reduction between Test S2-06 and S2-12 in Fig.12 is a good example of such fact because difference in initial flooding velocity resulted in the different turnaround characteristics in these two tests.

6. Effect of Radial Power Ratio

As described in Section 4, radial power distribution effect is not affected so significantly by various test parameters but determined by radial power distribution only. To make the characteristics of radial power distribution effect more clear, two SCTF Core-III tests with different radial power distribution shape were performed: one is Test S3-15 with inclined power distribution and the other is Test S3-16 with convex power distribution as illustrated in Fig.13. Based on the relationship between increase or decrease

in heat transfer coefficient from the value for flat power distribution test (Test S3-14) and distance from the approaching quench front shown in Fig.14, average increase or decrease in heat transfer coefficient was evaluated as shown in Fig.15 with respect to local radial power ratio which is corresponding to each bundle. CCTF data are also shown in this figure for reference. Since radial power distribution shape is different in these two tests, only one circulational flow was observed in Test S3-15, on the other hand, two circulational flows in Test S3-16 as illustrated in Fig.13. However, the same increase or decrease in heat transfer coefficient is realized in the same local radial power ratio as shown in Fig.15. This means power distribution shape is not important but local radial power ratio is essential. The fact that CCTF data showed almost the same degree of multi-dimensionality as SCTF data under the same radial power ratios as described in Section 4 supports this understanding, because difference in geometrical shape and size of the core cross sections of these two test facilities gave almost no effect on multi-dimensionality of core thermal-hydraulic behavior.

Actually speaking, increase or decrease in heat transfer coefficient is affected also by the maximum local radial power ratio, i.e., the radial peaking factor as shown in Fig.16. That is, in the larger peaking factor, the larger increase in heat transfer coefficient can be expected. From this fact, even average power bundles show some enhancement in cooling.

By assuming function form and applying the least square method, increase or decrease in heat transfer coefficient can be formulated, based on the data from Tests S3-15 and S3-16 for T/C elevations 6 and 7, as:

$$\Delta h = -16.8+275.9\ Fr-97.7\ Fr^2-(43.4-31.9\ Fp) \qquad (1)$$

Here, Δh is difference in heat transfer coefficient from the value for flat power distribution (W/m^2K), Fr is local radial power ratio and Fp is radial peaking factor. By using this empirical correlation, heat transfer coefficient in any bundle can be estimated based on that for flat power distribution. Fig. 17 shows verification result for this method. Clad temperature transient is well predicted with this method especially in the early portion of reflooding period when PCT is anticipated to appear.

Predicted turnaround temperatures for T/C elevation 6 of the bundles with local radial power ratio larger than or equal to 1.0 in various SCTF tests are compared with the respective measured values in Fig.18. Some CCTF data (T/C elevation is 1.83 m from the heated length bottom) are also shown in this figure for reference. From this result, Δh is considered to be predicted well with the above empirical correlation.

Conservatism of current licensing procedure was examined with REFLA code developed by JAERI by applying Eq.(1) in addition to complete fluid mixing assumption between bundles. The results shown in Fig.19 indicates that the licensing calculation for the bundle with radial power ratio of 1.5, for example, has 57K of additional safety margin due to radial power distribution effect.

7. Conclusions

For multi-dimensional core thermal-hydraulics during reflooding period of PWR with cold leg injection type ECCS, the following conclusions were obtained

experimentally through the SCTF tests:

(1) Radial power distribution effect enhances heat transfer in the high power bundles and degrades in the low power bundles.

(2) Radial power distribution effect is not affected so signicantly by parameters such as system pressure, flooding velocity, core inlet subcooling, total power and initial stored energy in the core.

(3) Radial power distribution effect is not affected so significantly by geometrical shape and size of the core cross section in relatively large scale core such as SCTF and CCTF.

(4) Clad temperature in the high power bundles is reduced especially in the upper core under severe core cooling condition.

(5) Since radial power distribution effect always reduces clad temperature of the high power bundles, a potential conservatism is expected if the effect is ignored in safety assessment of PWR.

(6) Increase in heat transfer coefficient in the high power bundles can be predicted well with the proposed empirical correlation.

(7) Non-uniform water distribution on the UCSP results in a delay of quench propagation in the upper part of peripheral bundles. However, PCT is not affected by this phenomenon because non-uniform water distribution is developed after appearance of PCT.

References:

1. K. Hirano and Y. Murao, "Large Scale Reflood Test", J. At. Energy Soc. Japan, Vol. 22, No. 10, 681~686 (1980).
2. H. Adachi, et. al., "Design of Slab Core Test Facility (SCTF) in Large Scale Reflood Test Program, Part I: Core-I", JAERI-M 83-080 (1983).
3. H. Adachi, et. al., "SCTF Core-I Test Results (System Pressure Effects on Reflooding Phenomena)", 9th Water Reactor Safety Research Information Meeting, Maryland, USA (1981).
4. H. Adachi, et. al., "SCTF Core-I Reflood Test Results", Proc. 10th Water Reactor Safety Reaearch Information Meeting, Vol. 1, 287 (1983).
5. H. Adachi, et. al., "SCTF Core-I Reflood Test Results", Proc. 11th Water Reactor Safety Reaearch Information Meeting, Vol. 2, 277 (1984).
6. Y. Murao, et. al., "Status of CCTF/SCTF Test Program", Proc. 12th Water Reactor Safety Research Information Meeting, Vol. 2, 342 (1985).
7. T. Iwamura, et. al., "Results of SCTF Reflood Tests", Proc. 13th Water Reactor Safety Research Information Meeting, Vol.4, 315 (1986)
8. T. Iwamura, et. al., "Heat Transfer Enhancement In SCTF Tests", Proc. 14th Water Reactor Safety Information Meeting, Vol.4, 429 (1987)
9. H. Adachi, et. al., "Recent study on Two-Dimensional Thermal-Hydraulic Behavior in PWR Core during the Reflood Phase of LOCA with the Slab Core Test Facility (SCTF)", Proc. 2nd International Topical Mtg. on Nucl Power Plant Thermal Hydraulics and Operations, 2-104 (1986).

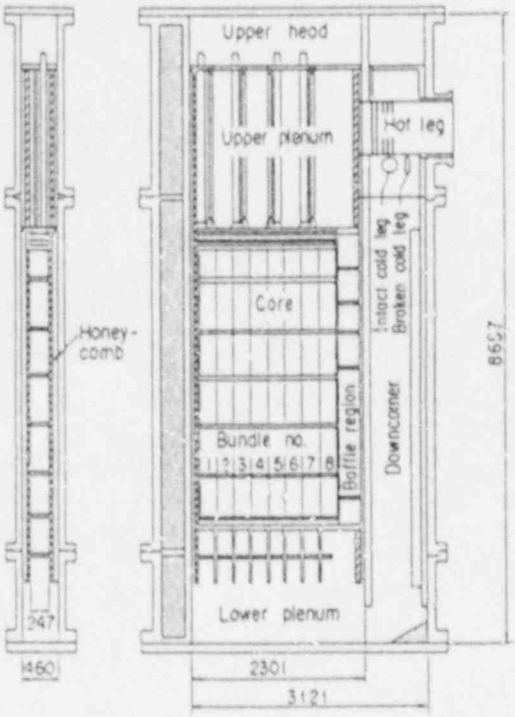

Fig. 1 Pressure vessel of SCTF

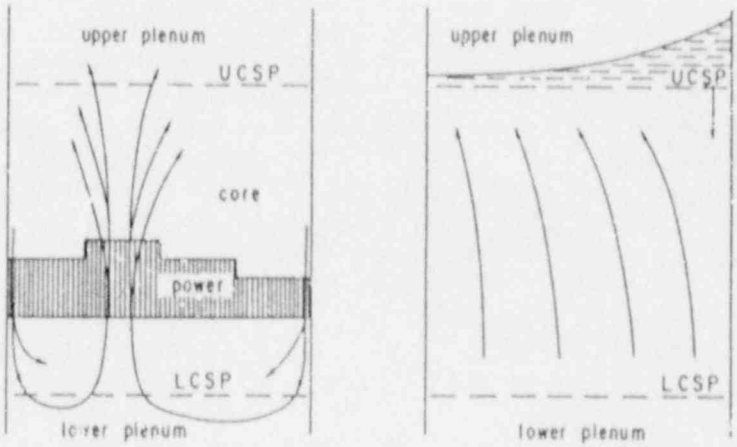

Fig. 3 Two-dimensional flow patterns

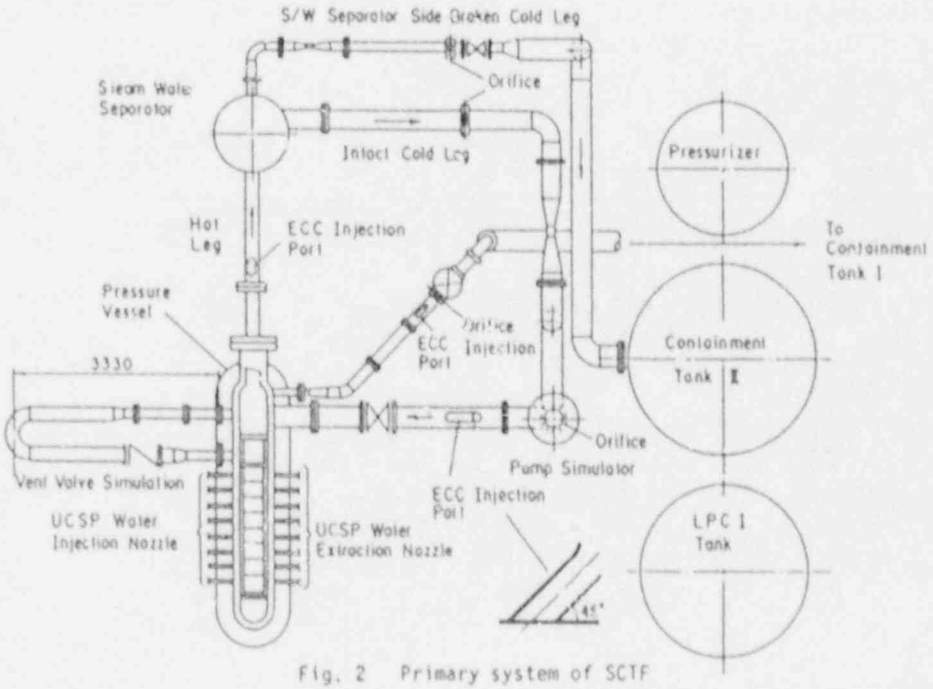

Fig. 2 Primary system of SCTF

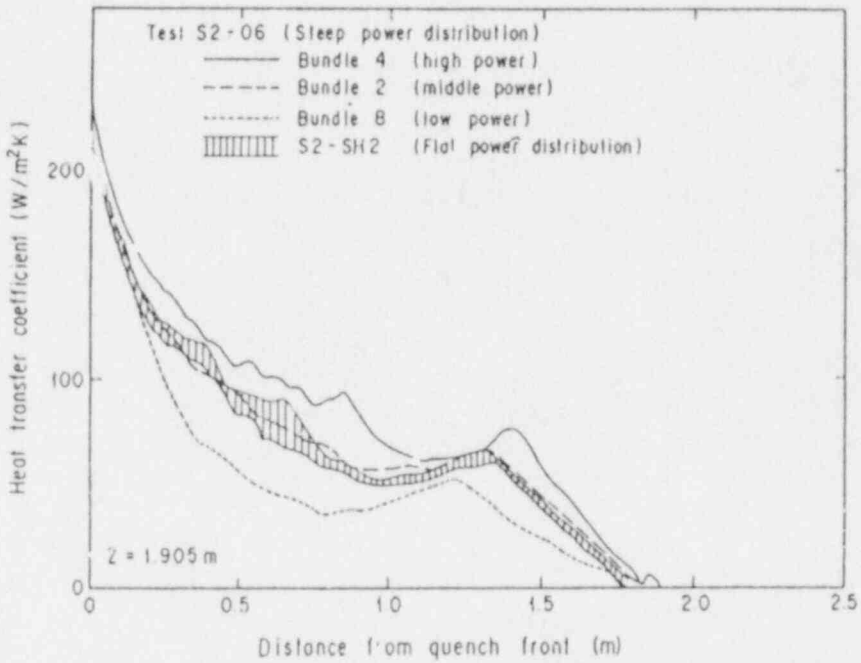

Fig. 4 Two-dimensionality in heat transfer due to radial power distribution

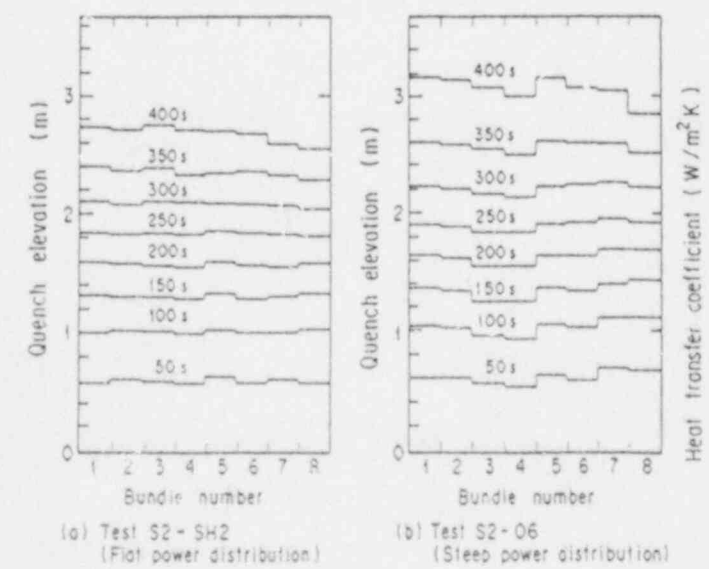

Fig. 6 Quench delay due to upper plenum water distribution

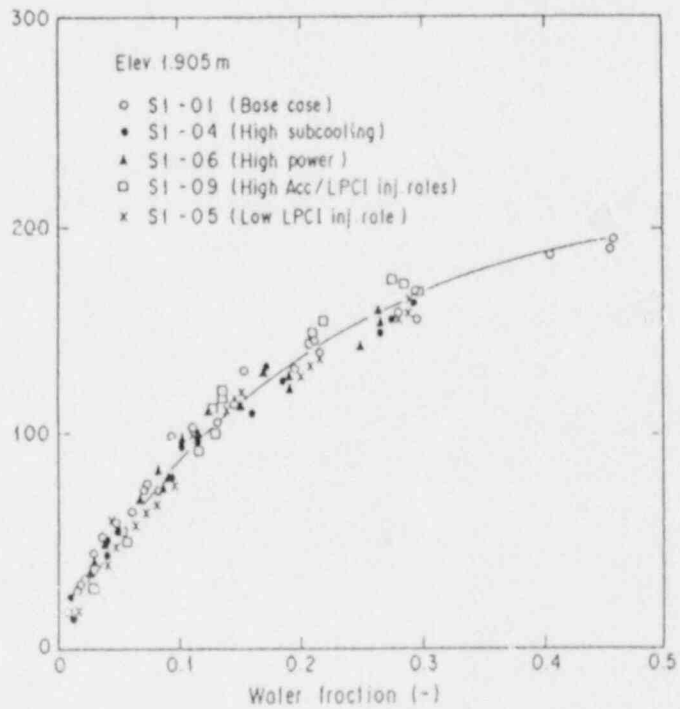

Fig. 5 Heat transfer coefficient vs. nominal water fraction

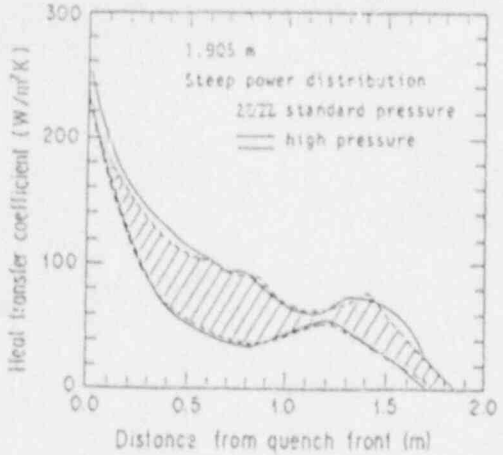

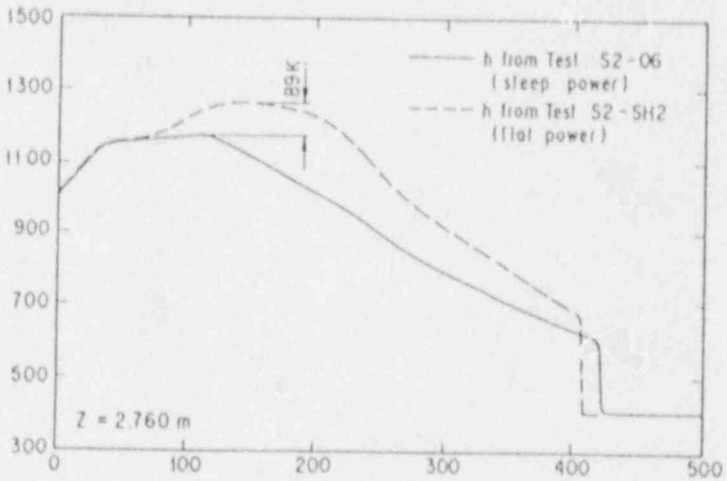

Fig. 7 Comparison in two-dimensional heat transfer between high and standard pressure tests

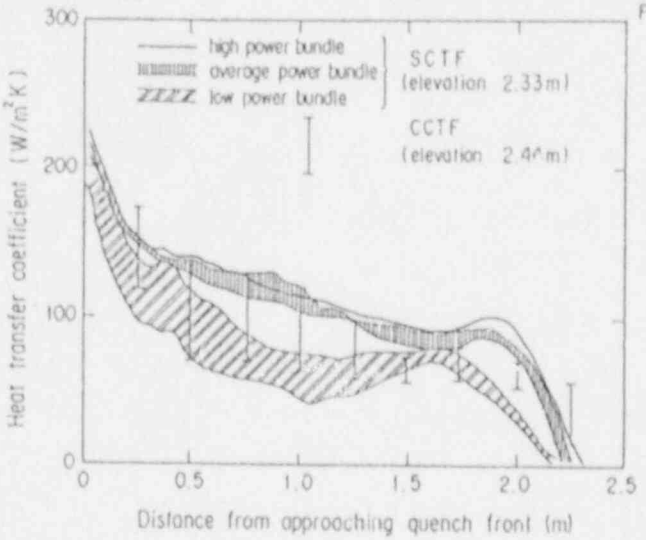

Fig. 8 Comparison in two-dimensional heat transfer between SCTF and CCTF

Fig. 9 Effect of two-dimensional heat transfer on temperature transient

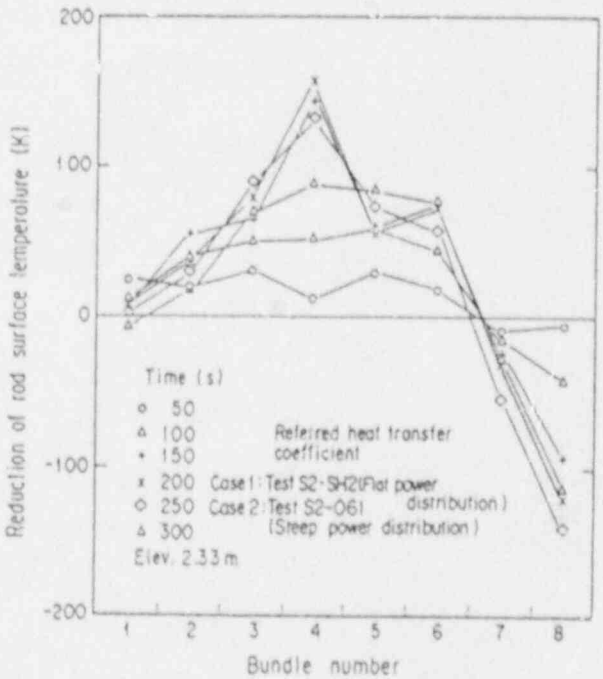

Fig. 10 Temperature reduction due to two-dimensional effect

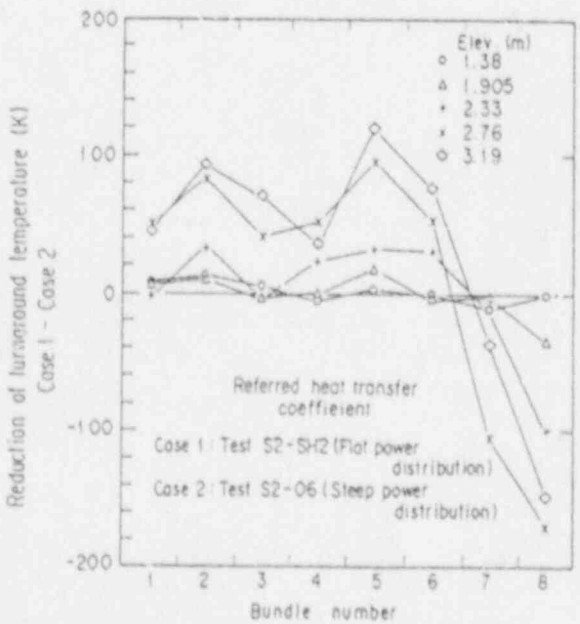

Fig. 11 Turnaround temperature reduction due to two-dimensional effect

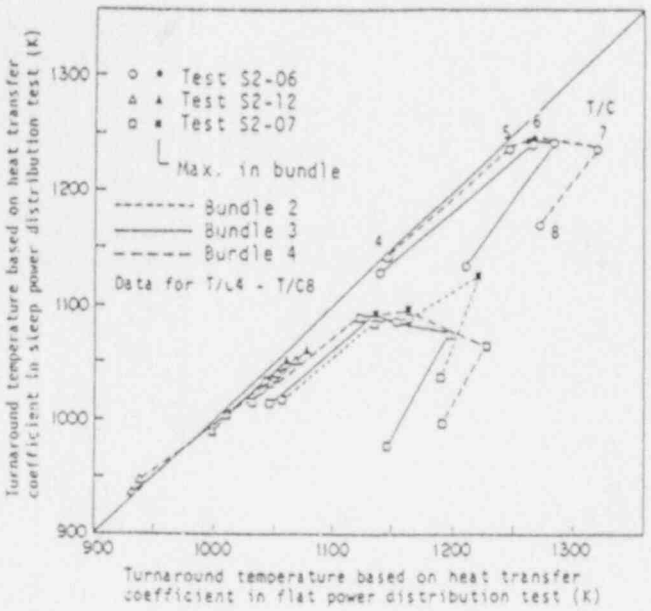

Fig. 12 Turnaround temperature reduction in bundles with power ratio of 1.2

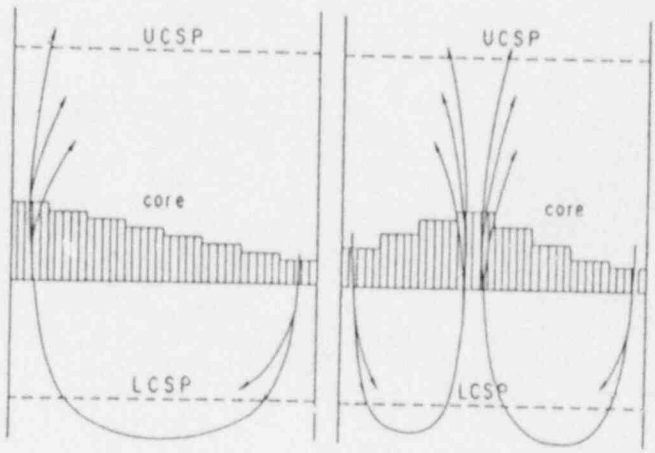

Fig. 13 Two water circulation patterns depending on power shape

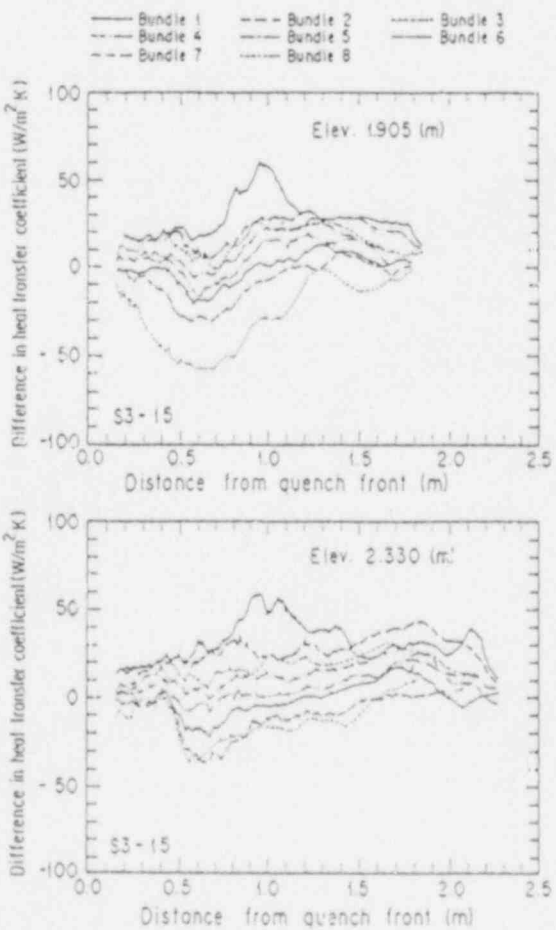

Fig. 14 Difference in heat transfer coefficient between inclined and flat power distribution tests

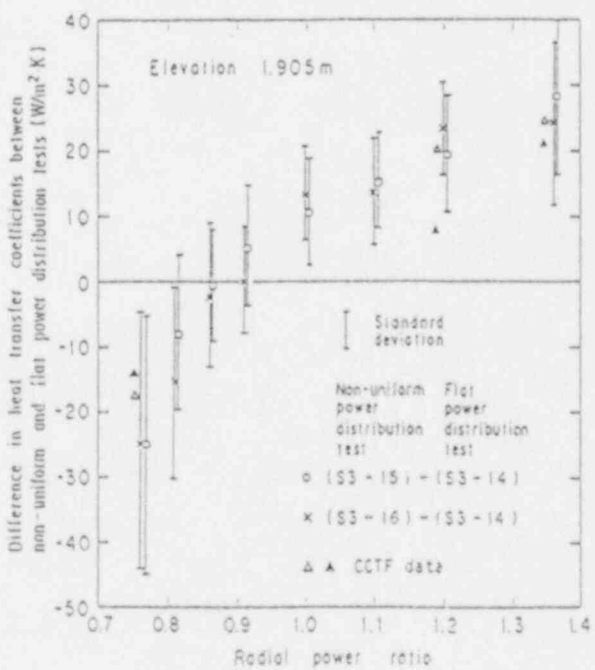

Fig. 15 Difference in heat transfer coefficient vs. bundle power ratio

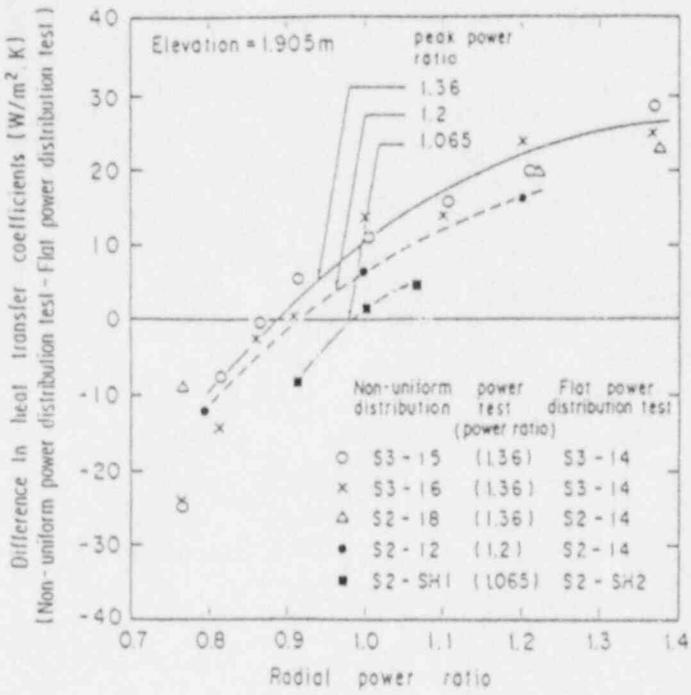

Fig. 16 Effect of radial peaking factor on two-dimensionality

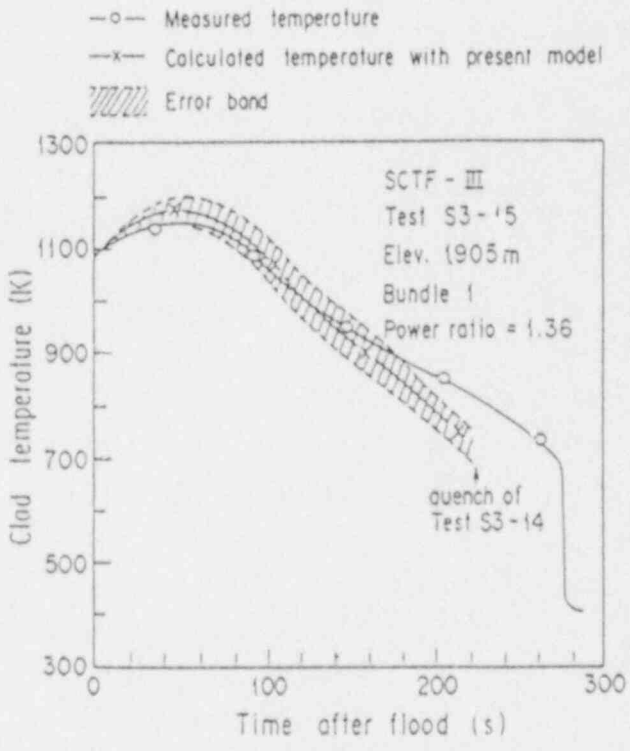

Fig. 17 Temperature transient evaluated with Eq.(1)

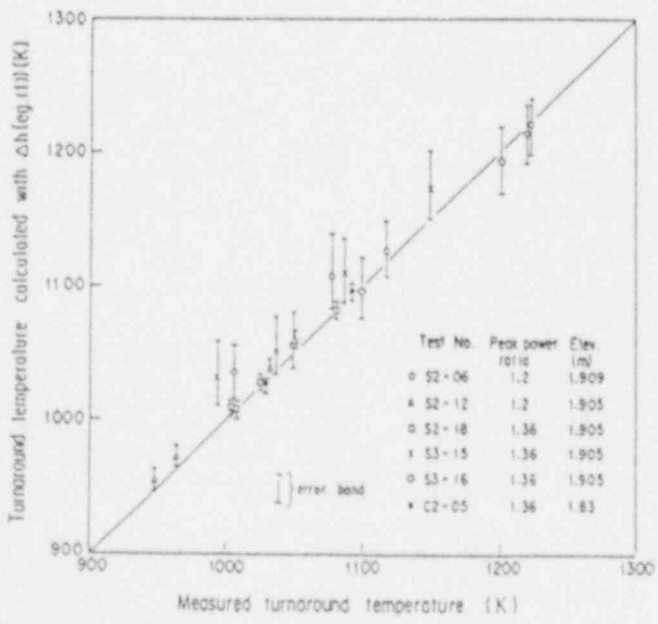

Fig. 18 Turnaround temperature evaluated with Eq.(1)

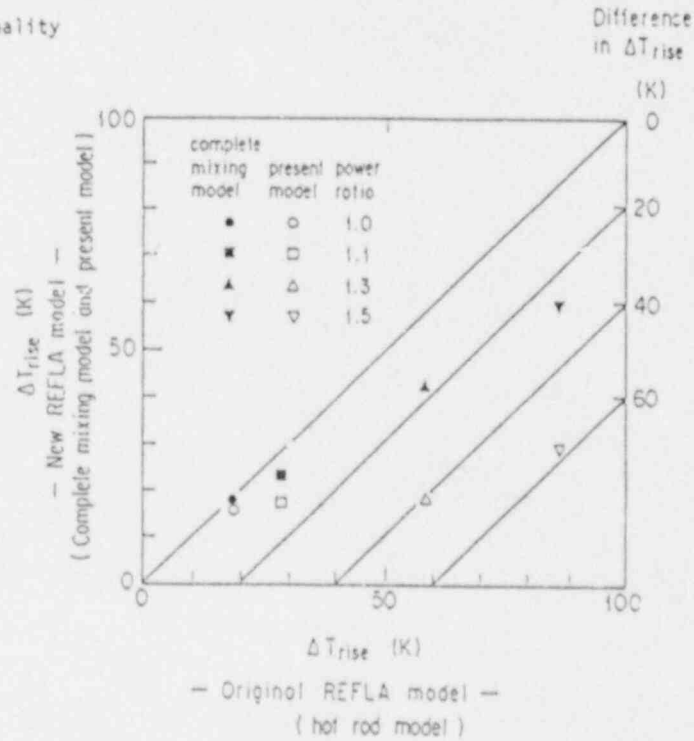

Fig. 19 Safety margin expected in licensing calculation (evaluated with REFLA)

Reflooding Phenomena of German PWR Estimated from CCTF and SCTF Test Results

Y. Murao, T. Iguchi, J. Sugimoto, H. Akimoto,
T. Iwamura, T. Okubo, A. Ohnuki, I. Sakaki,
M. Kikuta and H. Adachi

Japan Atomic Energy Research Institute

(TO BE PUBLISHED AT A LATER DATE.)

ANALYSIS RESULTS FROM THE LOS ALAMOS 2D/3D PROGRAM*

by

B. E. Boyack, M. W. Cappiello,
S. C. Harmony, P. R. Shire, and D. A. Siebe

Safety Code Development
Nuclear Technology and Engineering Division
Los Alamos National Laboratory
Los Alamos, New Mexico 87545

ABSTRACT

Los Alamos National Laboratory is a participant in the 2D/3D program. Activities conducted at Los Alamos National Laboratory in support of 2D/3D program goals include analysis support of facility design, construction, and operation; provision of boundary and initial conditions for test-facility operations based on analysis of pressurized water reactors; performance of pretest and posttest predictions and analyses; and use of experimental results to validate and assess the single- and multi-dimensional, nonequilibrium features in the Transient Reactor Analysis Code (TRAC). During fiscal year 1987, Los Alamos conducted analytical assessment activities using data from the Slab Core Test Facility, the Cylindrical Core Test Facility, and the Upper Plenum Test Facility. Finally, Los Alamos continued work to provide TRAC improvements. In this paper, Los Alamos activities during fiscal year 1987 will be summarized; several significant accomplishments will be described in more detail to illustrate the work activities at Los Alamos.

INTRODUCTION

The 2D/3D program is sponsored jointly by Japan, the Federal Republic of Germany, and the United States (US). The safety related objectives of the 2D/3D program are as follows: first, to provide an improved understanding of the effectiveness of various emergency core-cooling (ECC) systems in limiting peak fuel rod cladding temperatures during vessel refill and core reflood for medium- to large-break loss-of-coolant accidents (LOCAs) in pressurized water reactors (PWRs); second, to reveal core-coolant inventory and system flow characteristics during the refill and reflood phases of a medium to large-break LOCA; third, to study convective flow and temperature distributions inside a heated core during reflood for a medium- to large-break LOCA; fourth, to assess the predictive capability of best-estimate computer codes and the conservatisms of evaluation-model computer codes; and fifth, to obtain information which

* Work performed under the auspices of the US Nuclear Regulatory Commission.

may be used to improve thermal-hydraulic models in best-estimate, evaluation-model and other computer codes.

Activities conducted at Los Alamos National Laboratory in support of 2D/3D program goals include analysis support of facility design, construction, and operation; provision of boundary and initial conditions for test facility operations based on analysis of PWRs; performance of pretest and posttest predictions and analyses; and use of experimental results to validate and assess the single- and multidimensional, nonequilibrium features in the Transient Reactor Analysis Code (TRAC).

Three experimental facilities provide data to 2D/3D program participants. The Slab Core Test Facility (SCTF) is a separate-effects reflood facility located in Japan. It models a full-height 1/21-scale section of the core, one fuel element wide from core centerline to outer periphery. This facility began testing with its third electrically heated core during 1986; Los Alamos will continue analysis of Core-III tests in FY-1988. The Cylindrical Core Test Facility (CCTF) is an approximately 1/21-scale facility, also located in Japan; this facility has completed its test program and the Los Alamos counterpart analysis program is nearing completion. The Upper Plenum Test Facility (UPTF), located in the Federal Republic of Germany, is a 1/1-scale integral test facility focusing on phenomena in the downcomer, lower plenum, upper plenum, and primary-system loops of a PWR. Los Alamos analytical efforts to date have largely supported test design and specification; posttest analyses of UPTF experiments have started and will be emphasized during FY-1988; in part because of the importance of these efforts in supporting an effort to quantify the uncertainty associated with TRAC predictions of peak cladding temperatures for large-break LOCAs.

During FY-1987, Los Alamos conducted analytical assessment activities using data from the SCTF, CCTF, and UPTF facilities. Finally, Los Alamos continued efforts to provide improvements to the TRAC code. This paper summarizes Los Alamos activities during FY-1987; several significant accomplishments are described in more detail to illustrate the work activities at Los Alamos.

TRAC ASSESSMENT ACTIVITIES

A few comments are appropriate to introduce the summary comments that will be provided to describe our TRAC-PF1/MOD1 (Ref. 1) assessment activities. When performing a code assessment, understanding must be developed, catalogued, and reported in three vital areas. These three areas are (1) sufficiency of knowledge about the as-built and as-operated state of the facility providing the data to be used for assessment, (2) the adequacy of the input model prepared to describe the facility, and (3) the adequacy of the closure models and correlations within the code.

Now consider a situation in which some significant feature of the plant configuration or operation is either unknown or undetected by the individual performing a posttest assessment. This deficiency of knowledge will be reflected in the input model and in the calculated result. Lacking knowledge that the deficiency exists, the analyst will tend to assign fault incorrectly to either the adequacy of the input model or the adequacy of the closure models and correlations within the code. Consider, for example, a second example in which the overall knowledge of the facility and its operation is good; *i.e.*, the perception of the plant configuration and operation is accurate, but the calculated and measured results do not agree in significant respects. The cause for the disagreement(s) can lie with either the adequacy of the input model or the

adequacy of the code closure models and correlations or with some combination of the two. Care must be taken to determine the cause. Problems associated with the input model can frequently be remedied and user guidelines issued to alert others to the problem. Problems associated with the code closure models and correlations frequently require more effort to correct. A decision must be reached as to whether code model and correlation improvement should be attempted or whether the deficiency should be accepted as part of the quantified code uncertainty for related transients.

As we summarize our CCTF, SCTF, and UPTF posttest assessment activities, we will attempt to use the framework identified above. It is hoped that this will provide a cohesive structure for identifying the "lessons learned" during these assessment activities.

SCTF PROGRAM SUPPORT

We will summarize results for three SCTF posttest assessment activities at Los Alamos, Runs 704, 713, and 714. The versions of TRAC-PF1/MOD1 used for these analyses were version 13.1 for Run 704, 13.0 for Run 713, and 13.1 for Run 714. A detailed analysis discussion is provided for Run 704, with more concise discussions for Runs 713 and 714. For all figures in this paper comparing calculated and test results, the calculated results are shown as a solid line and the data as a dashed line. In addition, the figures frequently carry a legend identifying the JAERI identification number for that data item. In the legend, the corresponding TRAC calculated value carries the prefix "C."

SCTF Run 704 (Ref. 2) is a German PWR (GPWR) evaluation-model integral orientation test. Run 704 was one of the first GPWR tests. Important features of the test specification included a blowdown of the initial primary pressure from 0.6 MPa to 0.3 MPa and multiple ECC-system injections into the cold leg, four locations in the upper plenum and two locations above the upper core support plate. Many interesting phenomena occurred during the test. The posttest calculation and analysis effort for Run 704 are also interesting because information was obtained in each of the three assessment areas identified above. Figure 1 displays the measured and calculated differential pressure in bundle 5 over the full core height. The differential pressure can also be considered as a direct measure of the liquid level in the bundle. During the test, the liquid level in the bundle generally increased until about 200 s, when the liquid level in the core was severely depressed. The liquid level subsequently began to recover at about 245 s. The TRAC-calculated liquid level trace showed a similar trend but was noticeably different in magnitude. In particular, the increase in liquid level stalled at about 170 s and the calculated depression in liquid level occurred later (at about 220 s) and was deeper than measured. In fact, liquid displaced from the core passed into the lower plenum, up the downcomer, and out the broken cold leg on the pressure vessel side. This liquid was lost from the system and not available for subsequent core cooling. One consequence of the greater liquid-level depression and loss of core coolant calculated by TRAC was a dryout and heating of the high-elevation cladding not seen in the test, as shown in Fig. 2. A number of lessons were learned during the course of the posttest analysis. These are summarized below using the categories previously discussed.

Overall, our knowledge of the facility configuration and operation is very good. However, the GPWR integral orientation test Run 704 was among the first in a new test series having conditions markedly different than tests previously analyzed. In particular, the quantity of ECC liquid injected into the upper plenum was large; much of this liquid was carried out

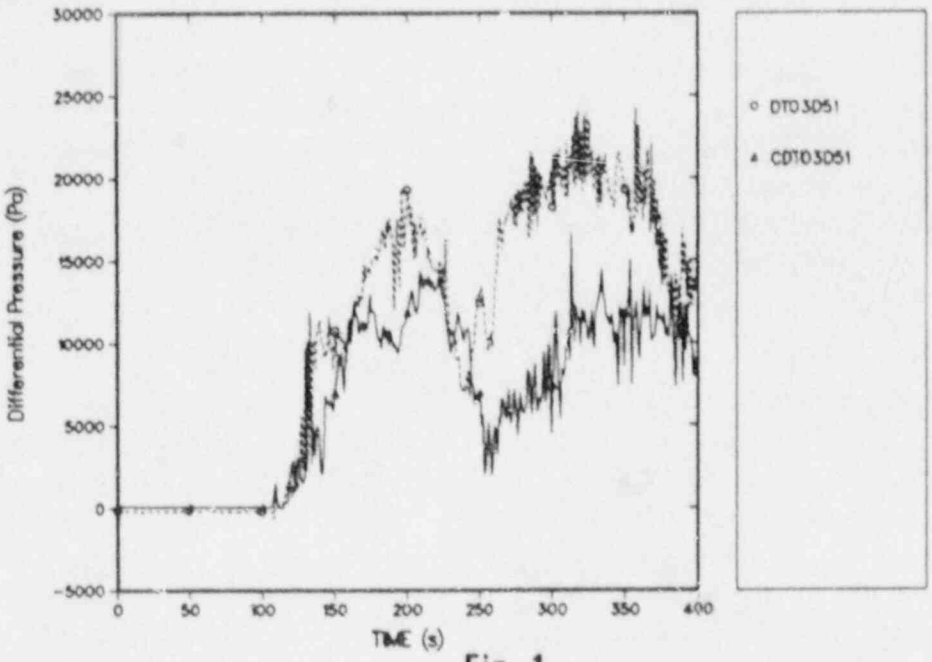

Fig. 1.
Bundle 5 liquid levels for SCTF Run 704.

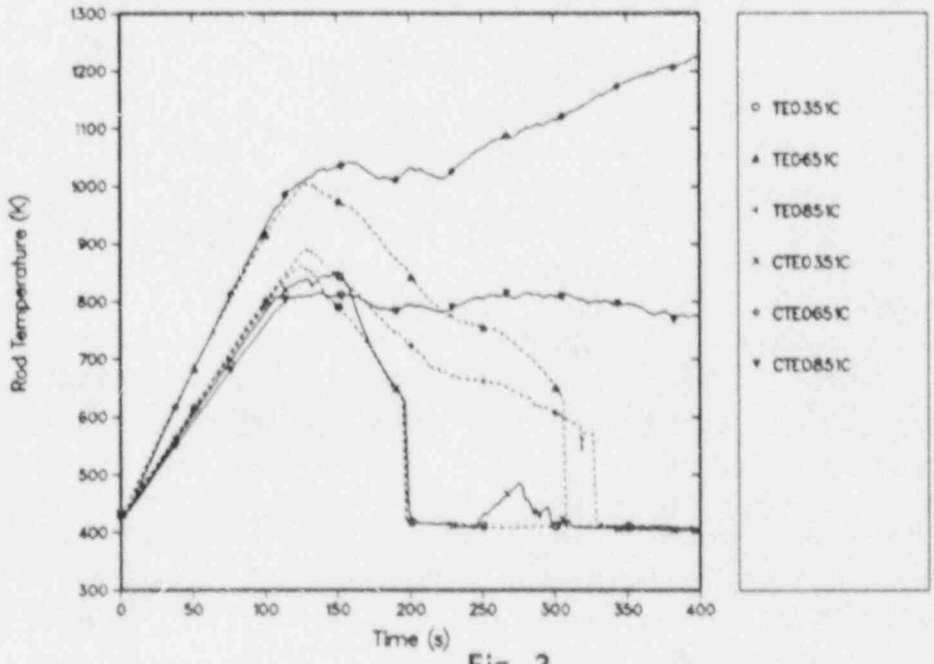

Fig. 2.
Bundle 5 cladding temperatures for SCTF Run 704.

of the upper plenum, through the hot leg, and into the steam/water (S/W) separator. The facility is equipped with a trip-activated drain line that is activated when the liquid level in the S/W separator reaches 1 m. During the test, the trip level was activated at 190 s and the drain line removed between 5.5 and 7.5 kg/s thereafter. Nevertheless, the S/W separator continued to fill, and by 200 s liquid in the S/W separator was being entrained and carried from the S/W separator to containment tank II. The increased pressure drop associated with two-phase flow increased the S/W separator, hot-leg, and upper-plenum pressures and caused the core liquid level depression seen in Fig. 1. The same phenomena were calculated in TRAC; however, there were some important differences. To our knowledge, Run 704 was the first test analyzed by Los Alamos in which the drain line was activated; thus, we had not considered it in our previous SCTF analyses. Therefore, the TRAC calculation did not model the liquid removed from the S/W separator by the drain line. This example illustrates a case in which the analyst's knowledge of the facility configuration and operation was inadequate.

We gained important information about our SCTF Core-III input model during our posttest calculation and analysis of SCTF Run 704. This input model had been recently created for the SCTF Core-III configuration. Relative to the earlier Core-II input model, it featured finer axial noding in the region of the upper plenum because modification of the upper plenum internals to model the GPWR was the primary difference between the SCTF Core-II and Core-III configurations. This finer axial noding extended into the downcomer region because axial noding is preserved at all radial nodes in the VESSEL component. The calculation of SCTF Run 704 was the second application of a newly developed input model created for the recently installed SCTF Core III. The first application of the new Core-III input model was for SCTF Run 714, which was a relatively simple test in that the only ECC injection was directly into the lower plenum and there was no primary-system blowdown.

No input model problems were identified during the analysis of SCTF Run 714. However, use of the finely noded SCTF Core-III input model produced a calculated result in which there was insufficient agreement between the calculated result and the data. In the calculation, essentially all ECC liquid injected into the cold leg bypassed the core through the broken cold leg on the pressure-vessel side. The lower plenum did not refill during the calculated transient as in the test. It was determined that the small axial downcomer noding below the level of the loop cold-leg nozzles caused the TRAC cell-based constitutive package to predict that the liquid flowing into the downcomer from the intact cold leg was in the slug flow regime, a regime of high drag. Rather than penetrating the downcomer to the lower plenum, the liquid remained suspended in the downcomer until it was entrained by steam flowing up one side of the downcomer and out the broken cold leg. Because the cell-based calculation structure is inherent to the TRAC code, the immediate remedy was to revise the VESSEL noding. A reduced number of nodes was used in the downcomer below the intact cold leg. With the reduced noding, a more nearly correct flow regime was predicted by TRAC and the downcomer penetration observed in the test was calculated. A more extensive discussion of this problem is found in the posttest analysis report.[3]

Additional information about the input model was obtained from the calculation using the reduced noding just described. In our discussion of the predicted core liquid level (Fig. 1), we noted that the predicted core liquid-level increase stalled at about 160 s. We determined that this was the time at which the calculated S/W separator liquid level exceeded the height

of the lowest cell, or level one in the S/W separator model. The next cell, or level two above, included the junction of the broken cold leg on the S/W separator side to containment tank II. We should note that the TRAC model prepared for the S/W separator does not maintain a sharp liquid-level interface. Thus, as liquid enters a cell, a two-phase mixture is predicted and donor-celled into the broken cold leg. The pressure drop through the line increases, elevating the S/W separator, hot-leg, and upper-plenum pressures. The two phase flow was sufficient to stall the refilling of the core as seen in Fig. 1 beginning at about 160 s. The calculated sharp liquid-level depression beginning at about 225 s corresponds to the time when the cells at level two are about half full, *i.e.*, full to the nozzle, and the pressure drop through the line from the S/W separator to containment tank II further increases.

Two modifications that should be made to the reduced-noding SCTF Run 704 model are evident. First, the S/W separator noding should be modified. Although there are several approaches for doing so, it would seem that several additional levels should be included below the nozzle level in the S/W separator. In addition, a S/W separator drainline model should be added as the S/W separator liquid level is reduced by approximately 1 m during every 150-s period in the test. This corresponds to a drain rate of 5.5 to 7.5 Kg/s.

We now consider the question usually asked in a posttest assessment activity. How well did the code do in predicting the transient and what was learned about deficiencies in the code constitutive models and correlations? We must first note that inadequacies in our knowledge of the facility configuration and operation resulted in failure to model a significant component in the transient, the S/W separator line. In addition, the S/W separator noding was too coarse. These understandings are important in and of themselves to the assessment analyst and prospective code users. However, these defects strongly affected the course of the calculation beginning early in the transient [about 60 s after bottom-of-core recovery (BOCREC)] and limited our ability to assess how well the code was able to simulate SCTF Run 704. We did determine that over the limited time in which useful results for code assessment were generated, the interfacial shear in the upper plenum was too high. Details of this code deficiency have been documented in Ref. 4.

SCTF Run 713 (Ref. 5) is a United States/Japan (US/J) evaluation-model test. Important features of the test specification included a steep power profile (bundles 1–2 at a relative power of 1.0, bundles 3–4 at 1.2, bundles 5–6 at 1.0, and bundles 7–8 at 0.8), and ECC injection into the lower plenum only. The peak rate of accumulator injection was 37 kg/s beginning at 74 s after transient initiation; low-pressure coolant injection (LPCI) of 3.75 kg/s began at 180 s. Several interesting phenomena were observed and calculated in this test. Figure 3 is a display of the integrated core-exit liquid flow calculated by TRAC for each of the eight heater-rod bundles in the SCTF facility. Flow is greatest in the high-powered bundles 3 and 4 and smallest in the low-powered bundles 7 and 8; there was reverse flow in bundle 8 after 450 s. This overall behavior is consistent with two-dimensional core flow and is caused by the sharply varying radial power profile. The enhanced heat transfer in high-powered bundles has been studied by JAERI for SCTF Core-II and results in a greater steam-generation rate and increased liquid entrainment.[6] As shown in Fig. 3, TRAC also predicts increased liquid flow above the high-powered bundles 3 and 4.

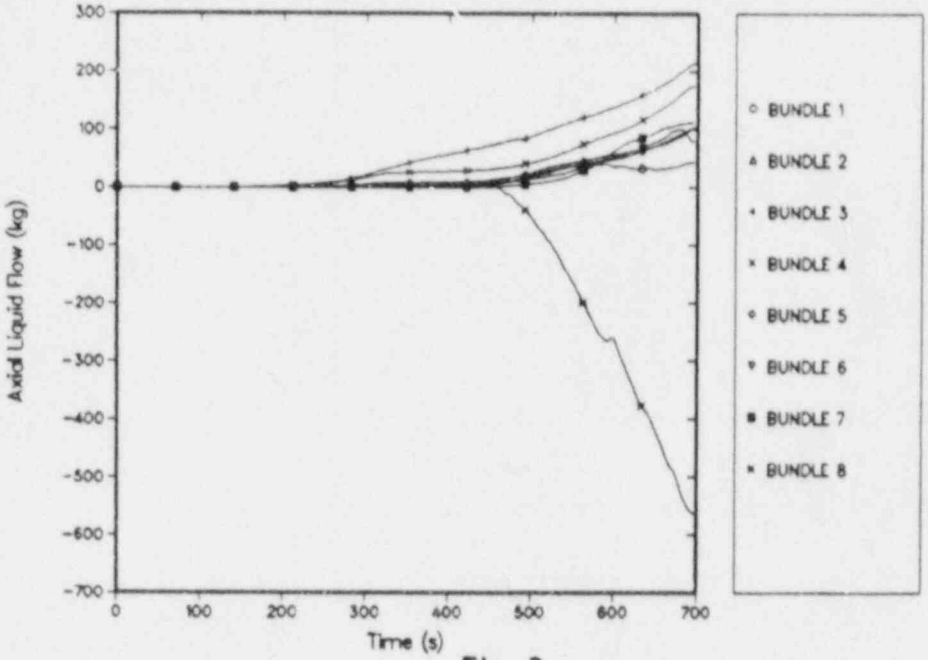

Fig. 3.
Integrated core-outlet liquid flow for SCTF Run 713.

Calculated and measured cladding temperatures in high-powered bundle 4 are presented in Fig. 4. Both the calculated peak cladding temperatures and time of quench are judged to be in reasonable agreement with the data. One trend calculated to occur and not evident in the data is a reheat at the three-quarter plane (about 200 s) and midplane (about 325 s) positions. This reheat is due to a sudden decrease in the heat-transfer coefficient resulting from the TRAC interface-sharpener model. The action of the interface-sharpener is illustrated in Fig. 5 at a position just above the core midplane (core elevation 1.905 m). Calculated void fractions remain at or near pure vapor longer than observed in the test and then suddenly decrease to a value much lower than that observed in the test. Efforts are in progress to remedy this deficiency in the TRAC-PF1/MOD2 code. Preliminary results describing this effort are presented later in the paper. Calculated and measured cladding temperatures in bundle 2 are presented in Fig. 6 as typical of the cladding temperature behavior calculated in all the moderately powered bundles 1, 2, 5, and 6. Compared with the data, too little cooling is calculated above the quench front as shown by the calculated cladding temperature behavior at the midplane and three-quarter-plane levels. From the information available, we infer that the calculated chimney effect above the high-powered bundles 3 and 4 is too strong. That is, the moderately powered bundles adjacent to the high-powered bundles are starved as liquid is entrained by the more rapidly upflowing vapor stream above the high-powered bundles 3 and 4 (see Fig. 3 for the calculated liquid exiting the core above each bundle). Passage of the quench front calculated by the interface sharpener can be observed at the midplane in Fig. 6.

We summarize our conclusions related to the posttest analysis of SCTF Run 713 using the categories previously discussed. We feel that our overall knowledge of the SCTF facility

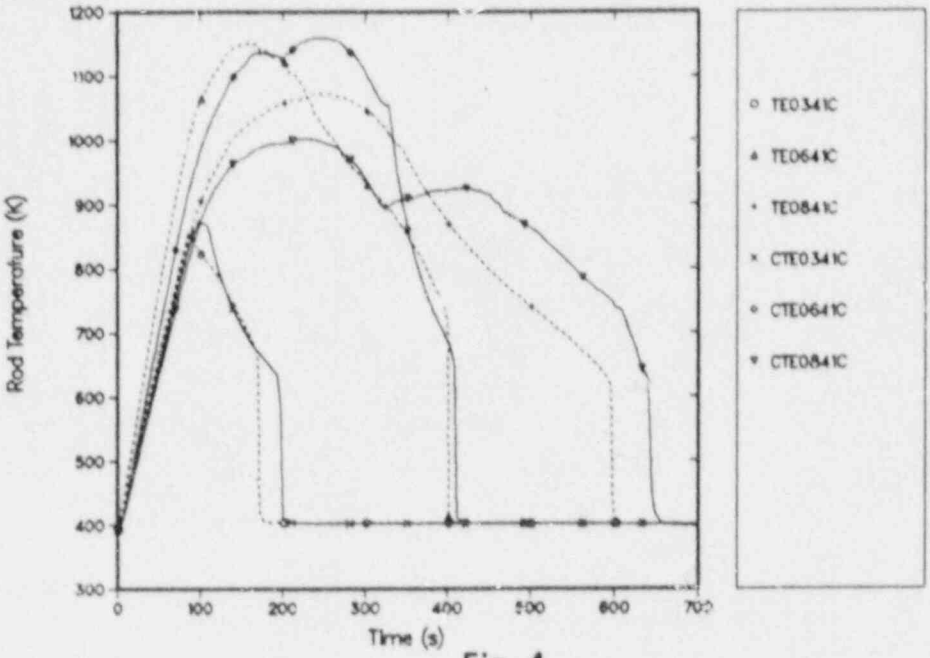

Fig. 4.
Bundle 4 cladding temperatures for SCTF Run 713.

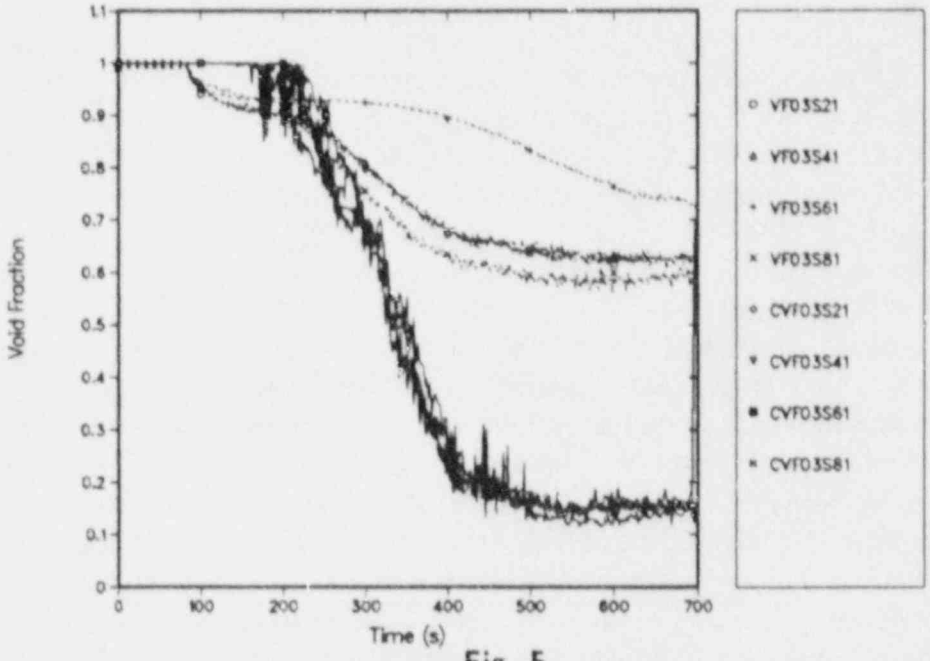

Fig. 5.
Bundles 2, 4, 6, and 8 void fractions at the 1905-mm level for SCTF Run 713.

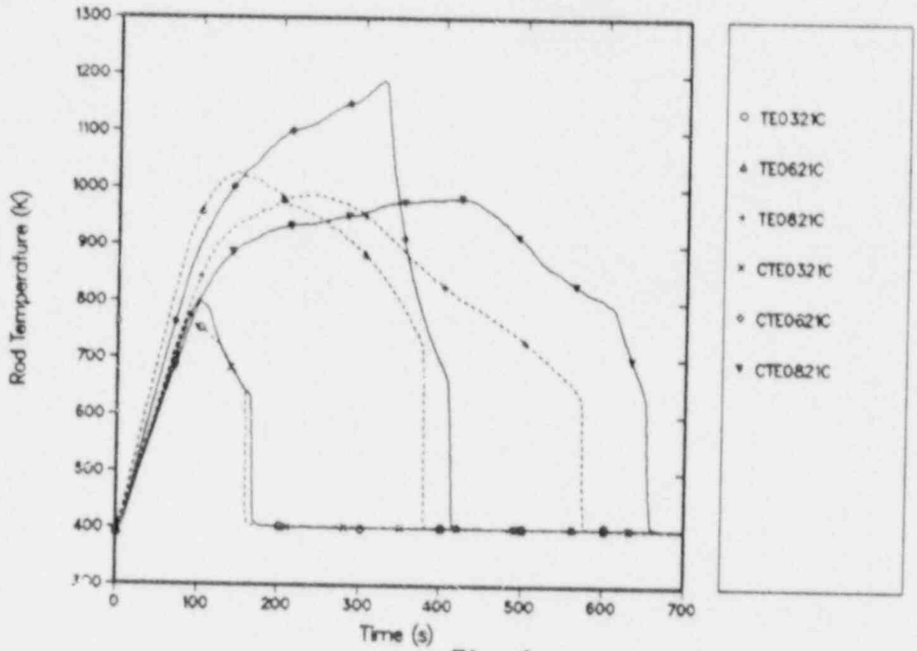

Fig. 6.
Bundle 2 cladding temperatures for SCTF Run 713.

configuration and operation is good. We could identify no deficiencies in our knowledge about either facility configuration or operation for SCTF Run 713. No input model deficiencies were identified during the analysis of SCTF Run 713. However, we remind the reader that this same finely noded model was found to be inadequate when used for the calculation of SCTF Run 704. With regard to the adequacy of the code constitutive models and correlations we draw the following conclusions: (1) TRAC generally calculates the major trends of the test, (2) the calculated two-dimensional flow pattern predicted is consistent with that inferred to exist in the test facility, (3) it appears that the calculated chimney effect above the high-powered bundles is too intense and that adjoining moderately powered bundles are starved of coolant, and (4) the interface sharpener further reduced cooling in the starved bundles. Posttest assessment results for SCTF Run 713 are summarized in Ref. 7.

SCTF Run 714 (Ref. 8) is a US/J best-estimate test. Important features of the test specification included a two-step power profile (bundles 1–4 at a relative power of 1.1 and bundles 5–8 at 0.9) and ECC injection into the lower plenum only. The peak rate of accumulator injection was 100 kg/s beginning at 67 s after transient initiation and LPCI at 5.3 kg/s beginning at 84 s. Relative to evaluation-model test Run 713, the ECC injections occurred earlier and were at a higher rate. Overall, the agreement between the calculated and measured results was reasonable with the exception of the time of core quench, which was predicted to occur too early. This means that the calculated phenomena generally were as in the test. However, assessment analyses tend to emphasize those phenomena which were not precisely calculated, even if the effect is second order on key parameters such as cladding temperature. Figure 7 displays the calculated and measured upper-plenum measured pressures. The system

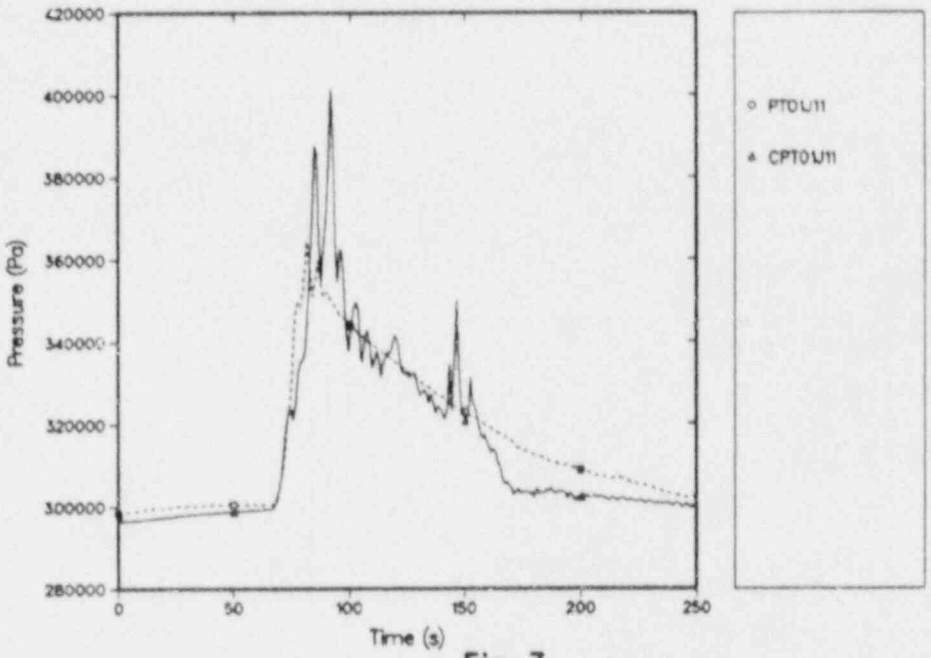

Fig. 7.
Upper plenum average pressures for SCTF Run 714.

pressure increases sharply as liquid enters the core beginning at about 70 s at the time of BOCREC. However, the calculated pressure is too high, indicating too much steam generation in the core. The core reflooding is illustrated in Fig. 8, which compares the differential pressures (liquid levels) in bundle 3. Following BOCREC, large oscillations in liquid level are both observed and calculated. However, the measured oscillations damp out more rapidly than those calculated. The calculated oscillations appear to be of greater magnitude, as shown by a higher calculated downcomer liquid level in Fig. 9. One consequence of the higher liquid level is the calculated loss of system inventory through the broken cold leg on the pressure-vessel side, as shown in Fig. 10; this did not occur in the test. A second consequence is that large amounts of liquid are carried into the upper plenum as shown in Fig. 11. As this liquid passes through the core, it cools the upper portions of the cladding at a faster rate than measured in the test, as shown in Fig. 12. This excess calculated heat transfer results in a calculated quench of the core about 80 s earlier than measured. A careful examination of the calculated results indicates that the excessive core heat transfer and steam generation calculated may be related to the limited number of thermal-hydraulic nodes in the core; *i.e.*, the problem may be noding related. The bursts of steam generation and related liquid pulses into the upper plenum and downcomer result from near simultaneous quenching in several sections of the core. This is most evident for the final core quench at about 155 s but can also be related to earlier core quenches shortly following BOCREC. Clearly, there is a physical basis for this phenomenon as the measured core behavior is similar. However, increased noding may lead to an earlier end to the oscillations in the calculation and a result that more nearly simulates the test.

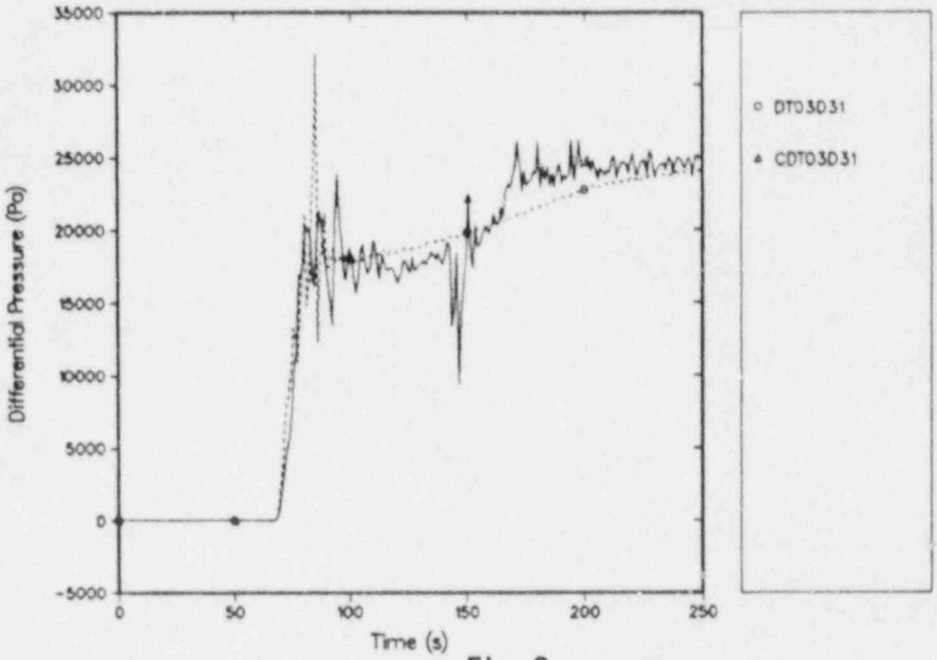

Fig. 8.
Bundle 3 liquid levels for SCTF Run 714.

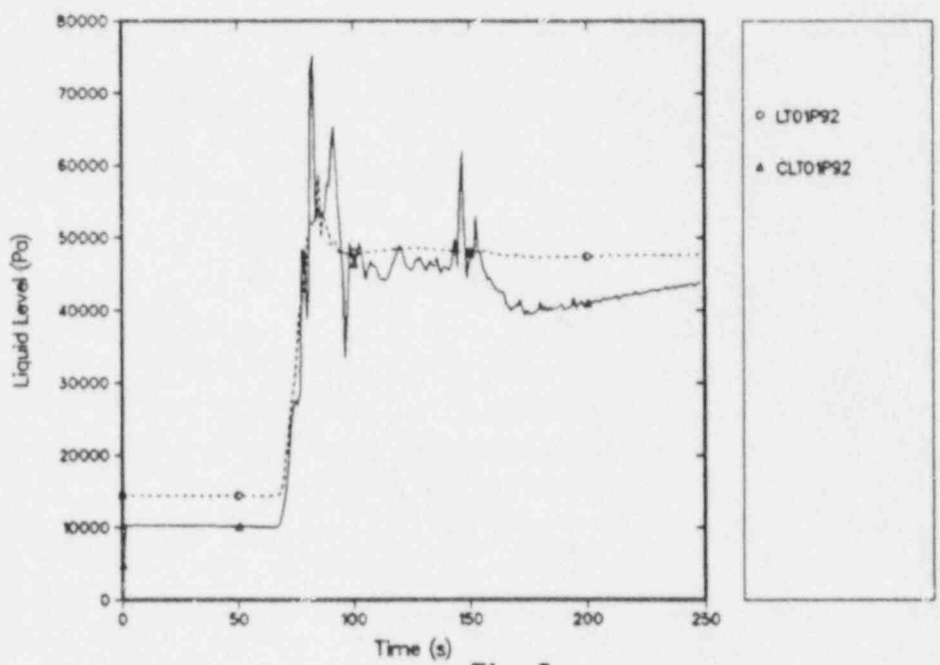

Fig. 9.
Downc- ner liquid levels for SCTF Run 714.

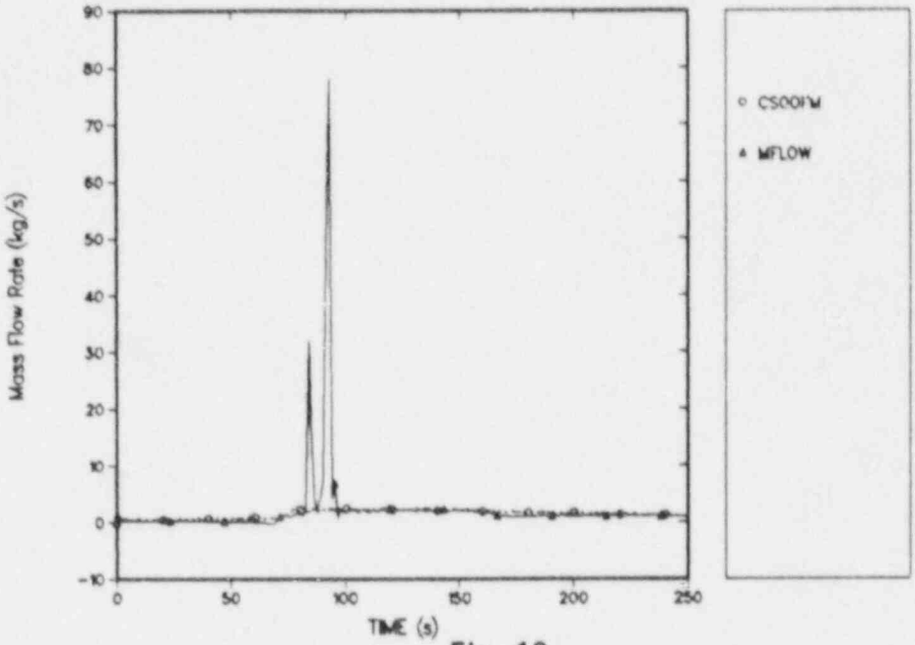

Fig. 10.
Mass flows in the broken cold leg pressure-vessel side for SCTF Run 714.

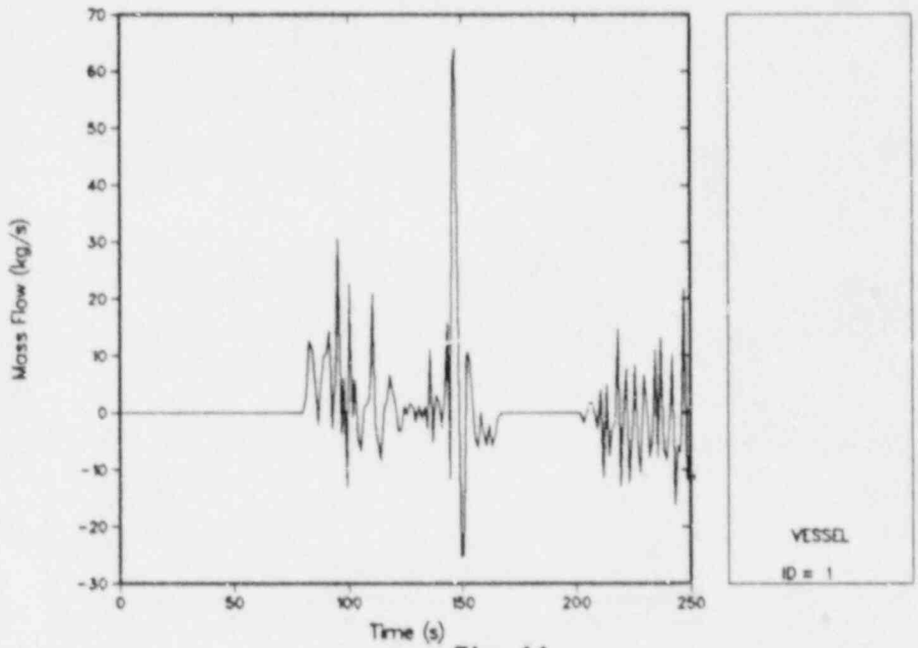

Fig. 11.
Core-outlet liquid mass flows for SCTF Run 714.

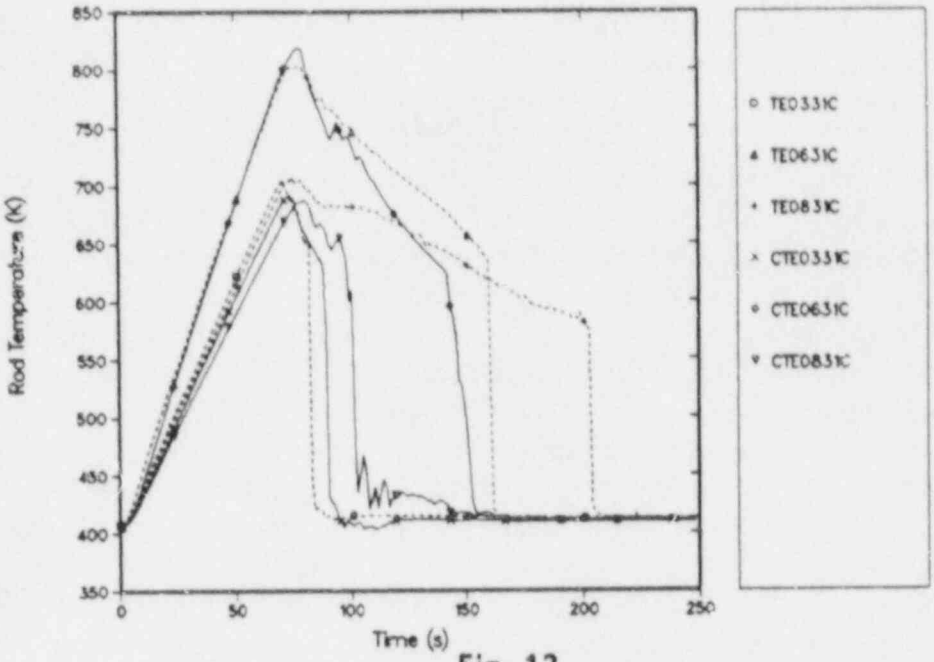

Fig. 12.
Bundle 3 cladding temperatures for SCTF Run 714.

We summarize our conclusions related to the posttest analysis of SCTF Run 714 using the categories previously discussed. We feel that our overall knowledge of the SCTF facility configuration and operation is good. We could identify no deficiencies in our knowledge about either facility configuration or operation for SCTF Run 714. No major input model deficiencies were identified during the analysis of SCTF Run 714. However, the excessive heat transfer occurring following BOCREC does have the appearance of being noding sensitive. We believe that an additional noding study could prove whether the calculation has a sensitivity to the number of core thermal-hydraulic nodes and quantify the effect if it existed. Finally, we remind the reader that this same finely noded model was found to be inadequate when used for the calculation of SCTF Run 704. With regard to the adequacy of the code constitutive models and correlations we draw the following conclusions: (1) TRAC generally calculates the major trends of the test, (2) the excessive steam generation in the core may be related to the code constitutive models and correlations (however, the noding study discussed above would be a prerequisite to evaluating whether or not a code deficiency exists), and (3) too little liquid is carried into the upper plenum following BOCREC. This is related to the interface-sharpener model in the core which generally retains too much liquid below the interface and allows too little above the interface. Posttest assessment results for SCTF Run 714 are summarized in Ref. 9.

CCTF PROGRAM SUPPORT

CCTF Run 58 (Ref. 10) is a combined downcomer and cold-leg injection test. Test initiation began with the primary steam filled except for the downcomer, which contained 0.86 m water. Downcomer injection began at 85.5 s and continued to 100.8 s at about 8.5 kg/s. ECC injection into the lower plenum simulated accumulator injection at the rate of approximately 92 kg/s and lasted from 85.5 s to 97.0 s when ECC injection was switched to the cold leg. The ECC injection into the cold leg first continued the simulation of accumulator injection at 78 kg/s until 111 s then switched to the LPCI rate of approximately 2.1 kg/s which continued until 1008 s. The test was characterized by a long-term manometric-type oscillation that occurred between the downcomer and the core.

After a close examination of the test results, JAERI concluded that when subcooled water in the downcomer rose to the level of the cold-leg nozzles, some of the water was entrained by steam flowing from the intact cold legs, through the downcomer, and into the broken cold leg. This cold water condensed steam in the downcomer and broken cold leg, causing a decrease in the pressure at the top of the downcomer. The pressure difference between the upper plenum and the vessel, which provides the driving potential for flow through the intact loops, increased and caused a surge of fluid, mostly steam, to flow into the downcomer. This in turn caused the pressure in the downcomer to rise and the liquid level in the core to fall, with liquid forced into the core. As some of this liquid vaporized, the pressure in the core increased and reversed the inflow. This forced the water to rise again in the downcomer, leading to the start of the next cycle. The oscillation occurred at the manometric frequency and seemed to be a resonant condition. Every second oscillation, sufficient water from the ECC injection had accumulated in the downcomer to allow the level to reach the cold-leg nozzle elevation.

A comparison of calculated and measured downcomer liquid level (Ref. 11) is presented in Fig. 13. It can be seen that a slightly higher average downcomer liquid level was calculated but that the magnitude of the calculated oscillation was much less than measured. It appears that TRAC underpredicts the entrainment of downcomer liquid by vapor passing from the intact loops into the broken cold leg. As a consequence, too little condensation is predicted to occur in the broken cold leg. A related outcome of too little condensation is that the pressure differences driving the oscillations are underpredicted. Thus, TRAC shows a smaller oscillation than in the test. Because liquid is repeatedly carried into the broken cold leg during the level oscillations and this phenomenon is not calculated, more liquid is calculated to remain in the vessel. The presence of additional liquid above that measured in the test can be seen in Fig. 14, which compares the calculated and measured liquid levels in the upper half of the core. After about 200 s, excess liquid is calculated. As previously discussed, TRAC consistently predicts too little liquid above the quench front because of its interface-sharpener model. Thus, the excess calculated liquid indicates a higher calculated liquid level than measured.

We summarize our conclusions related to the posttest analysis of CCTF Run 58 using the categories previously discussed. We feel that our overall knowledge of the CCTF facility configuration and operation is good because many tests have been conducted and analyzed. However, some deficiencies in our knowledge about the configuration and operation of the facility for Run 58 were identified. First, the open/shut status of the reactor vent valves (RVVs) was unclear when the first posttest calculation and analysis were performed. The actual status of the RVVs was shut; Los Alamos assumed the valves were open. Second, the

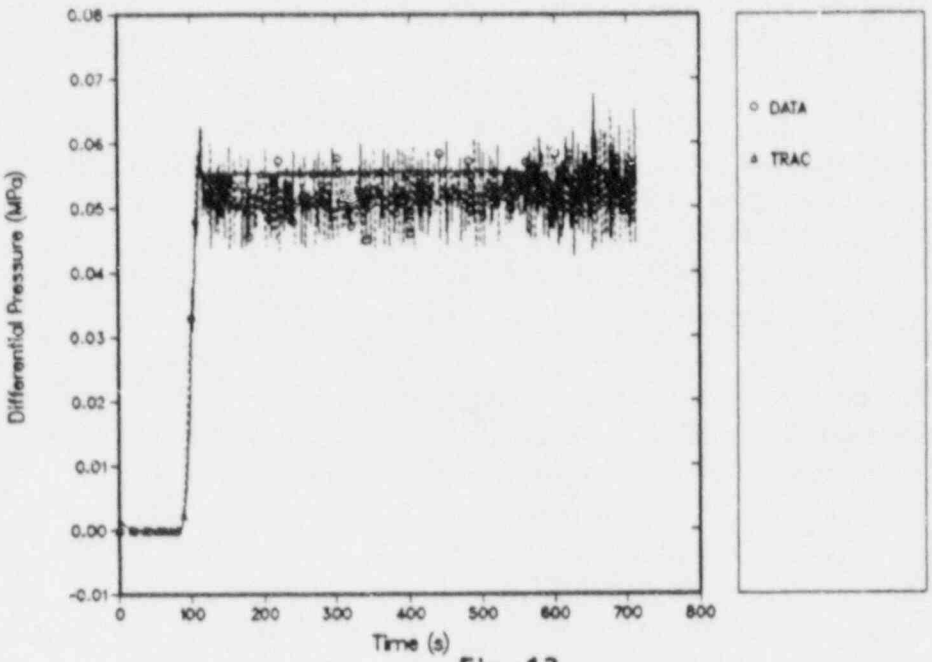

Fig. 13.
Downcomer liquid levels for CCTF Run 58.

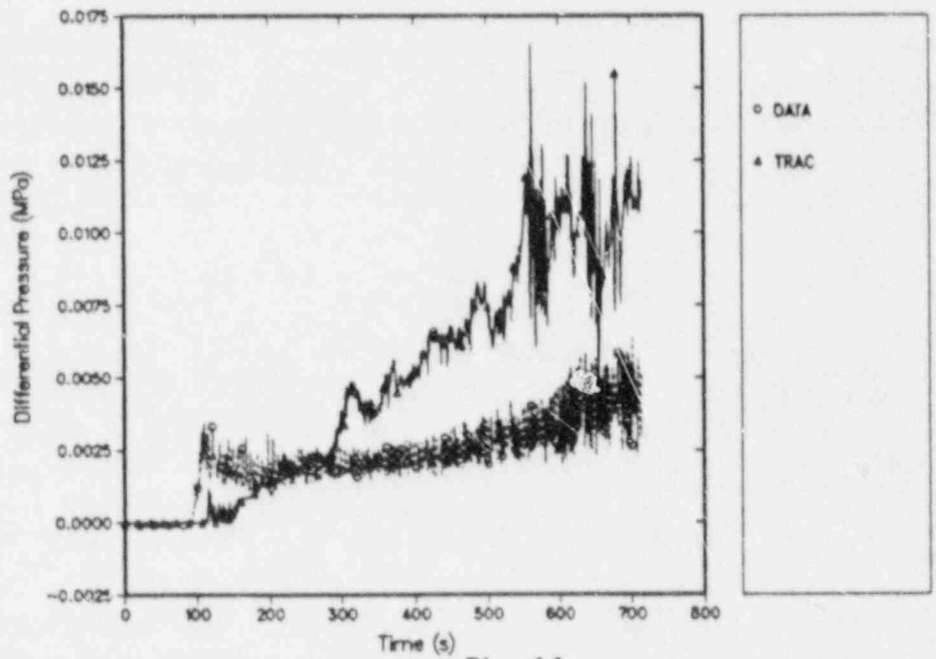

Fig. 14.
Core upper-half liquid levels for CCTF Run 58.

downcomer ECC-injection rate was uncertain as a result of oscillations in the measurement. Because of uncertainties in our knowledge of facility configuration and operation, JAERI was requested to evaluate the facility configuration and operation. They did so by specifying the status of the RVVs and providing a recommended downcomer ECC-injection rate. This value was used in the calculation but some uncertainty in this key boundary condition remains.

After revising the input model per JAERI's recommended values for the RVV status and downcomer ECC-injection rate, Los Alamos determined that the CCTF input model was adequate in that no major deficiencies were identified. We note that the input model used a lumped representation of the intact loops with three loops modeled as one. We could identify no adverse impact on the calculated result because of this modeling decision. We did note that nonphysical pressure pulses were predicted as parts of the core quenched. This calculated phenomenon was also observed for SCTF Run 714. We have postulated that this may be related to the number of nodes used to model the core; coarse noding results in large quantities of cladding surface in a given calculational cell. The impact of noding on the calculated core behavior could be examined in a noding study.

With respect to the adequacy of the code constitutive models and correlations, we draw the following conclusions: (1) TRAC generally calculates the major trends of the test with the exception of an early core quench, (2) TRAC appears to underpredict the entrainment of downcomer liquid by vapor passing from the intact loops into the broken cold leg, (3) the core void distribution shows the effect of the interface-sharpener logic previously discussed (too much liquid below the quench front and too little above), and (4) nonphysical pressure pulses may be related to the code constitutive models and correlations. However, a noding study would be a necessary prerequisite to evaluating whether or not a code deficiency exists.

UPTF PROGRAM SUPPORT

We performed a posttest analysis of UPTF test no. 11. This test investigated the countercurrent stratified flow characteristics of a full-scale PWR hot leg. This situation is similar to the conditions that are hypothesized to occur in the event of a small-break LOCA in which the core is uncovered. Steam produced as a result of boiling heat transfer flows into the steam generator, is condensed on the tubes, and then flows back towards the vessel as condensate. This phenomena is known as "reflux condensation." It is of importance to determine whether TRAC can predict the countercurrent flow (CCF) of liquid in such a situation.

Tests runs were performed at 0.3 MPa and 1.5 MPa. The test procedure first established the water flow in the hot leg by injection into the inlet plenum of the steam-generator simulator (Fig. 15). Then a steady flow of steam was introduced into the core simulator, which because of the configuration of the facility was forced to flow countercurrent to the liquid flow in the hot leg of interest. This was done for a variety of steam flows to determine the CCF characteristic. The TRAC calculations were performed in the same manner.

The comparison of the TRAC results with the data are shown in Fig. 16. The results presented are in the form of dimensionless liquid flux delivered vs the dimensionless steam flow. These coordinates are typical of those used for the presentation of CCF data. The results show that TRAC underpredicts the countercurrent flow limitation (CCFL) point and, at the lower steam flows, overpredicts the amount of liquid delivery. However, for the test

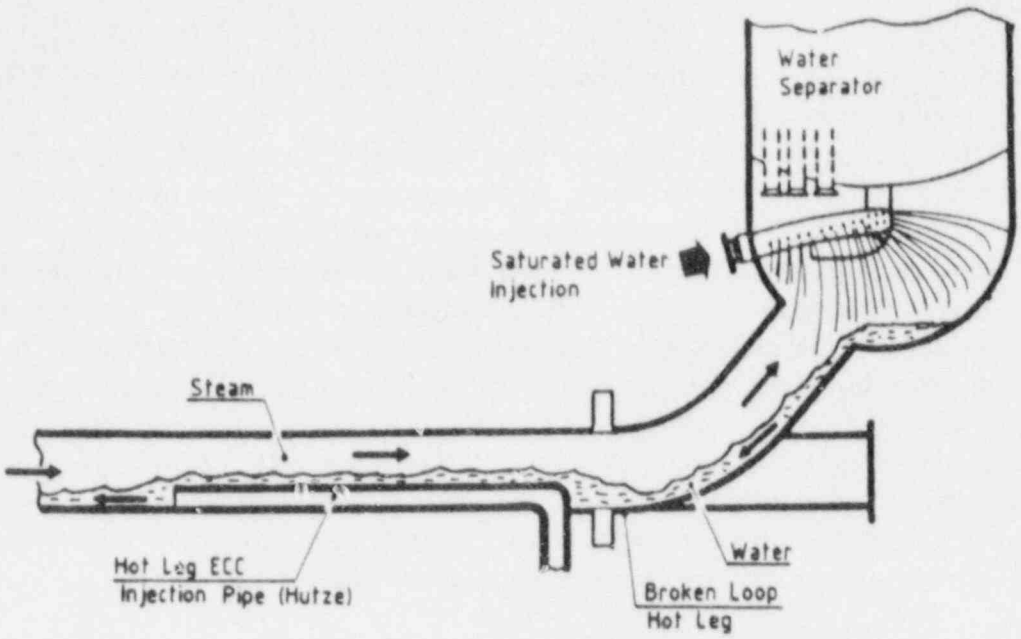

Fig. 15.
Test setup and procedure for the hot-leg CCF test in UPTF.

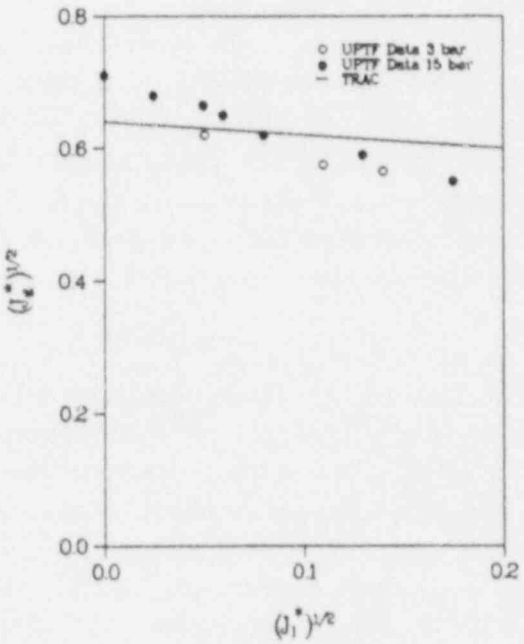

Fig. 16.
Comparison of the TRAC prediction with the full-scale hot-leg CCF data from UPTF.

run that modeled the "reflux condensation" conditions typical of a PWR small-break LOCA. TRAC accurately predicted the complete downflow of liquid.

Analysis of the calculated results shows that TRAC predicts "on-off" CCF behavior, whereas the data suggest a smooth transition. In the course of TRAC development it was decided to use a constant value for the interfacial friction factor for stratified flow. This was necessary because available friction-factor correlations developed from small-scale data did not predict reasonable values when applied to full-scale geometry. Recent assessment of alternative correlations in TRAC has shown that a new model suggested by Ohnuki[12] better predicts the CCFL point, but still overpredicts the amount of liquid delivery at the lower steam flows.

Based on our assessment, we recommend that alternative correlations be further investigated in order to better predict the CCF phenomena in full-scale hot legs. The current version of TRAC underpredicts the CCFL point, but accurately predicts the complete delivery of liquid for conditions similar to those expected during a small-break LOCA reflux-condensation transient.

TRAC CODE IMPROVEMENT

From our assessment of TRAC against large-scale reflood data, we have typically enjoyed good success in predicting the overall core liquid inventory. However, in the detailed analysis, the predicted void-fraction distribution within the core shows too much accumulation below the quench front, and too little above the quench front. Also, during the transient reflood process, the code predicts sharp discontinuities in the void fraction occurring near the quench front, whereas the data show a smooth transition. These difficulties are caused by the core-reflood model, which restricts the amount of liquid leaving a hydrodynamic mesh cell (containing the quench front) based on a pool-entrainment correlation.[13] This method of restricting the liquid flux is also referred to as the interface sharpener. To improve the prediction of the core reflood process, we investigated a drift-flux model for the void fraction[14] as an alternative to the present core-reflood model. Moreover, the model eliminated the need for the interface sharpener. We assessed the model in an experimental version of TRAC-PF1/MOD2 against the CCTF Run 14 data because this test is prototypic of the bottom-reflood tests performed in the facility.

The results of the comparison are shown in Figs. 17–22. Here, we compare the predicted pressure drop at six intervals in the core to the data. Thus, the Δp contains the effect of the static pressure of the fluid, the interfacial and wall friction, and the temporal and spatial accelerations. In a reflood transient such as this, the static pressure of the fluid dominates; therefore, the plots represent primarily the liquid content. Also, since each interval is evenly spaced (0.61m), an estimate of the liquid fraction can be made from the pressure drops presented. The results show that except for the very bottom interval, the TRAC prediction is in reasonable agreement with the data. Work is continuing to investigate other methods for the core-reflood model. Also, we are investigating alternative correlations for the dispersed-flow film-boiling regime because the large amount of liquid that is known to exist above the quench front causes a very early quench with the current correlations.

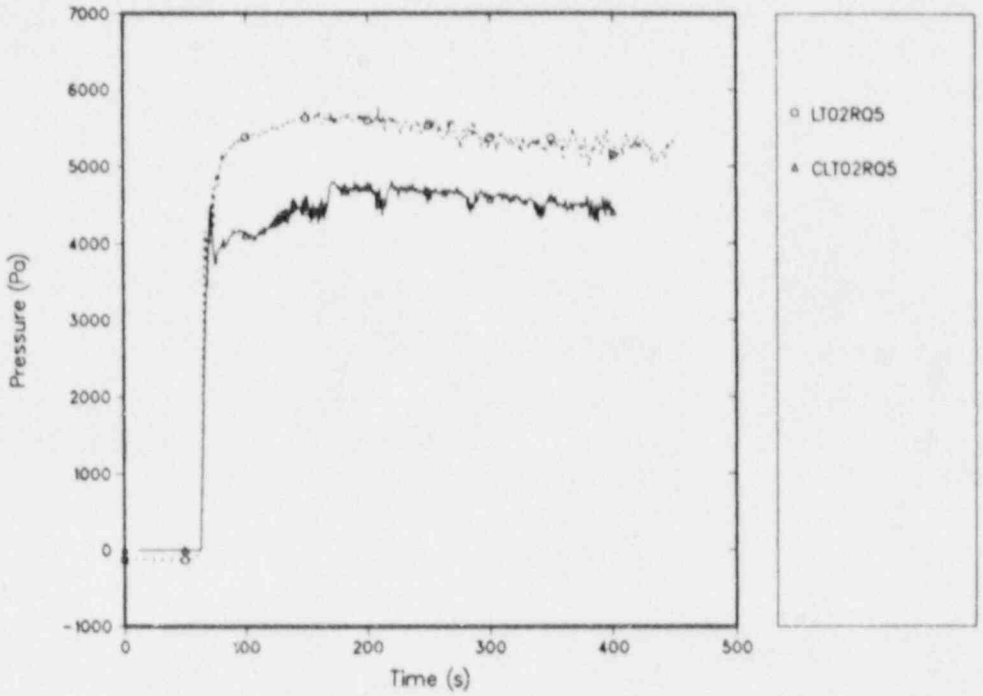

Fig. 17.

Comparison of the TRAC prediction with the CCTF Run 14 data for the core Δp at 0.0 to 0.61 m, where 0.0 m is the bottom of the core.

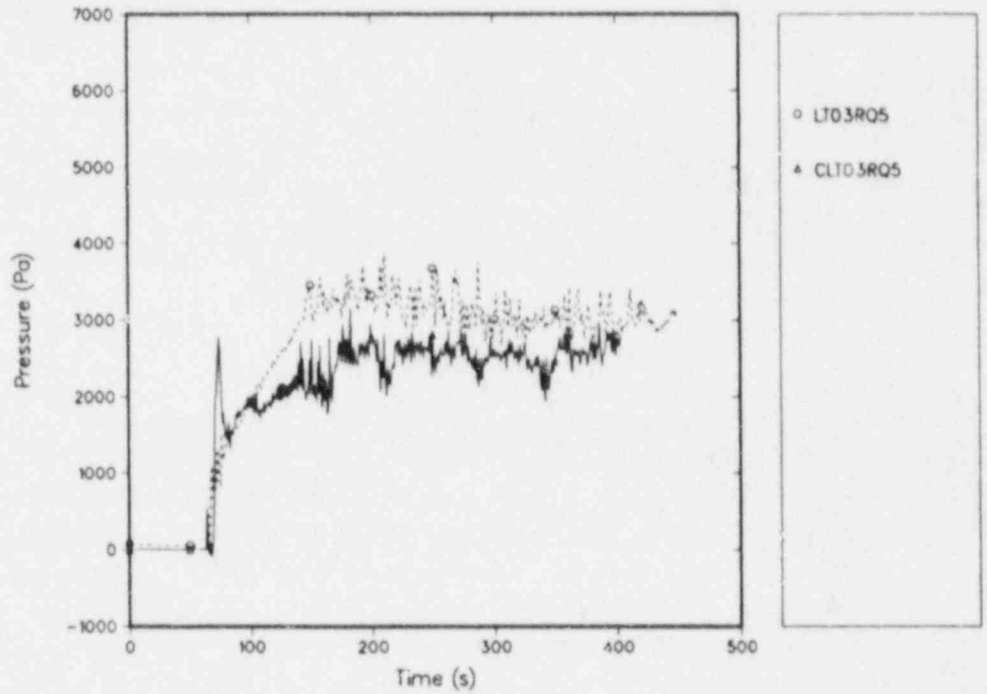

Fig. 18.

Comparison of the TRAC prediction with the CCTF Run 14 data for the core Δp at 0.61 to 1.22 m, where 0.0 m is the bottom of the core.

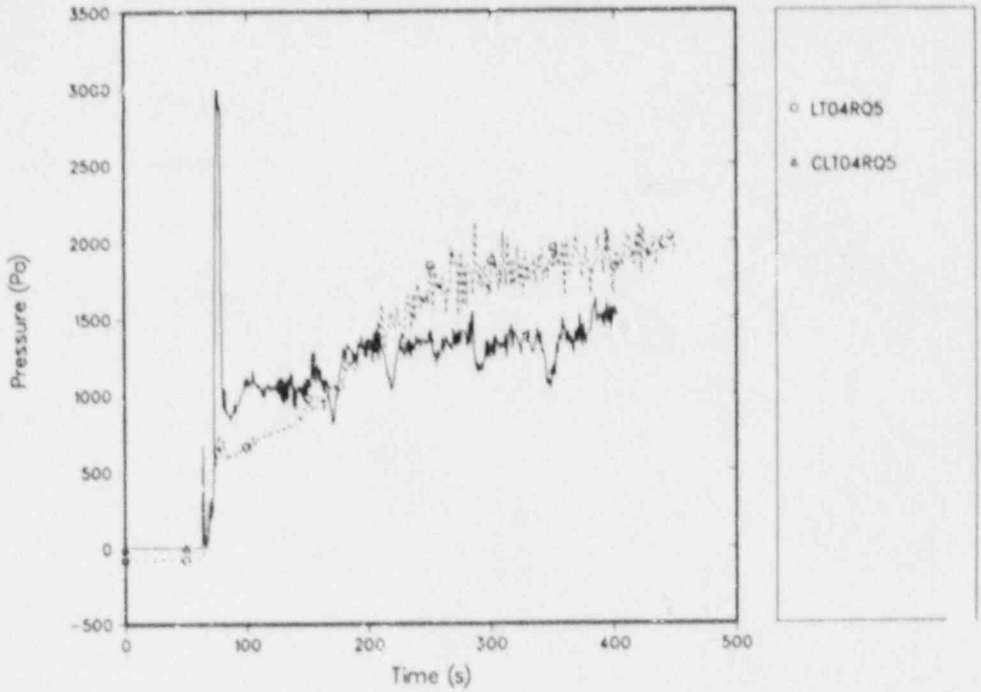

Fig. 19.

Comparison of the TRAC prediction with the CCTF Run 14 data for the core Δp at 1.22 to 1.83 m, where 0.0 m is the bottom of the core.

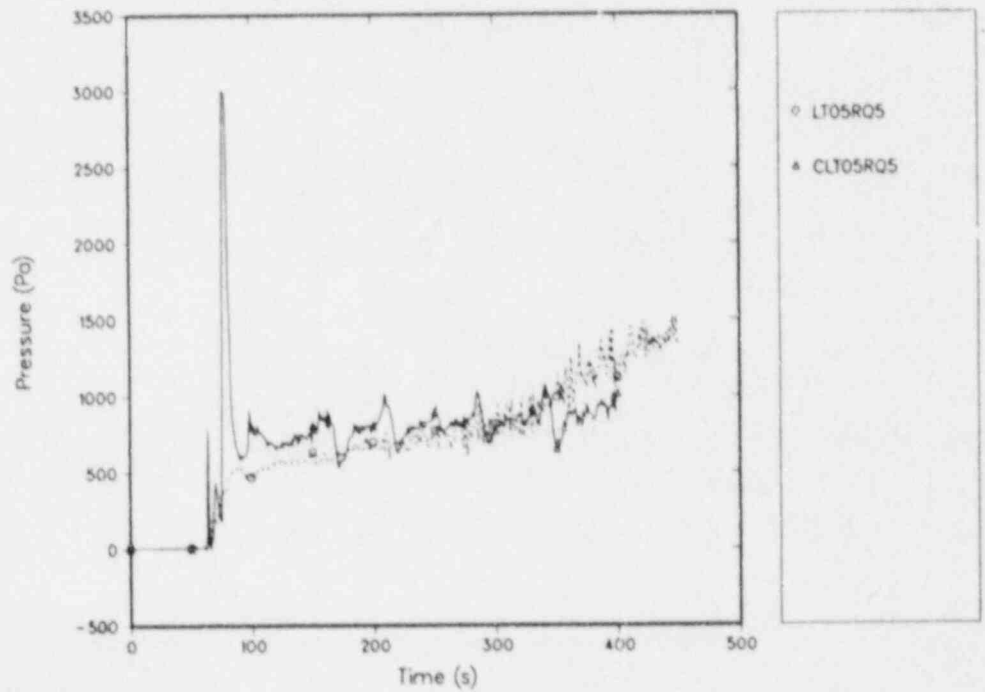

Fig. 20.

Comparison of the TRAC prediction with the CCTF Run 14 data for the core Δp at 1.83 to 2.44 m, where 0.0 m is the bottom of the core.

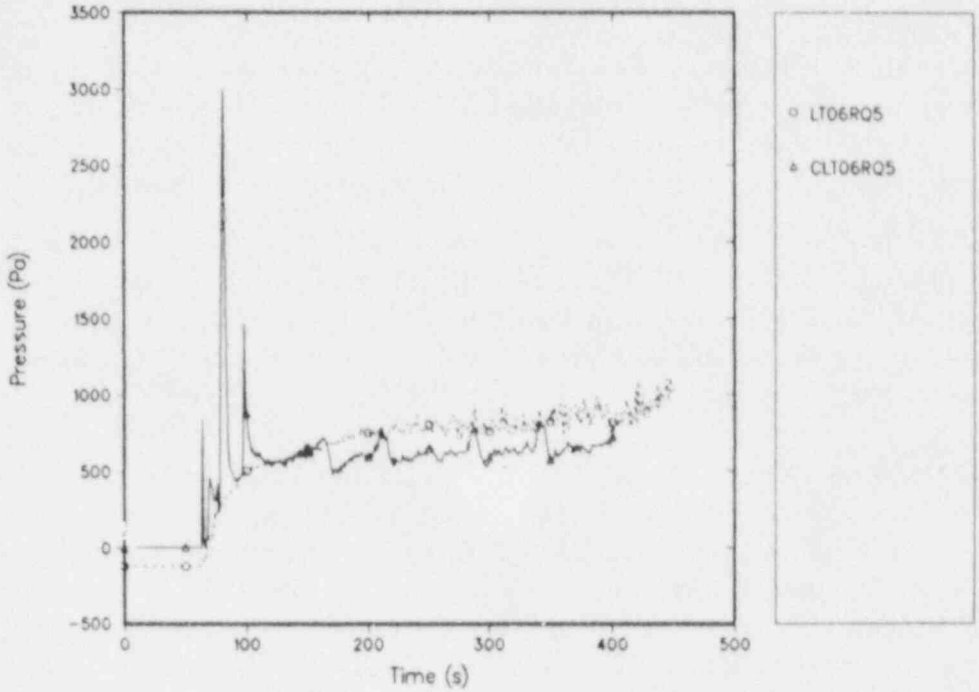

Fig. 21.

Comparison of the TRAC prediction with the CCTF Run 14 data for the core Δp at 2.44 to 3.05 m, where 0.0 m is the bottom of the core.

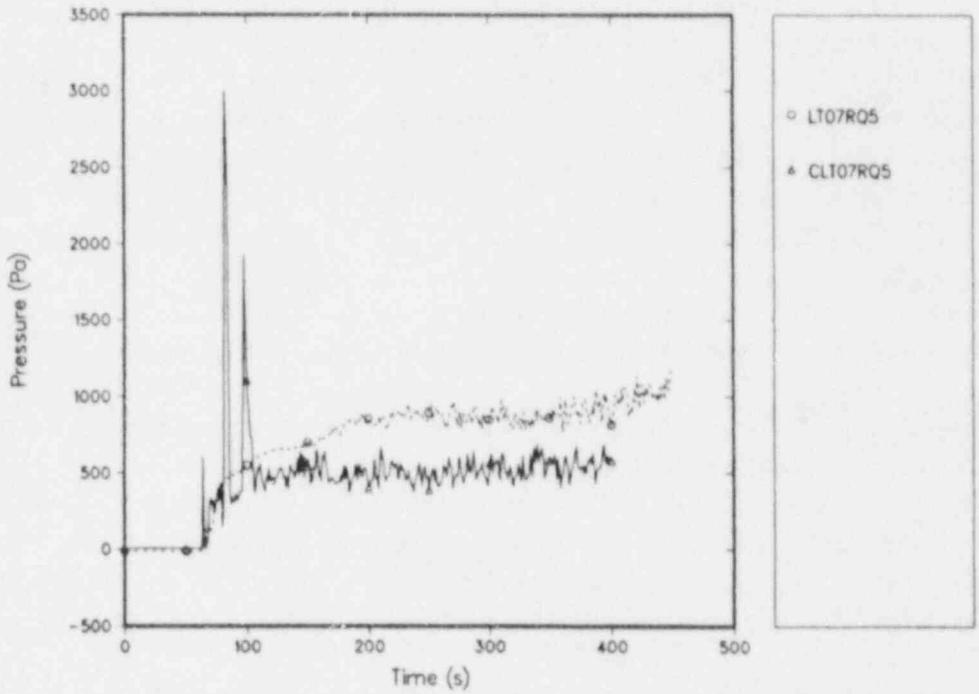

Fig. 22.

Comparison of the TRAC prediction with the CCTF Run 14 data for the core Δp at 3.05 to 3.66 m, where 0.0 m is the bottom of the core.

SUMMARY

We believe that Los Alamos is functioning as a vital participant within the 2D/3D Coordination Program. The results of our analytical efforts are being used to support test specification and design, improve understanding of phenomena occurring in tests, assess the predictive capability of TRAC, and identify needed areas of code improvement.

REFERENCES

Note: reports in the LA-2D/3D-TN and LA-CP series contain proprietary data from the Japan Atomic Energy Research Institute (JAERI) and the Federal Republic of Germany (FRG) that cannot be released to a third party without authorization from the US NRC, JAERI, and FRG representatives.

1. Safety Code Development Group, "TRAC-PF1/MOD1: An Advanced Best-Estimate Computer Program for Pressurized Water Reactor Thermal-Hydraulic Analysis." Los Alamos National Laboratory report LA-10157-MS, NUREG/CR-3858 (July 1986).
2. T. Iguchi, A. Ohnuki, T. Oyama, A. Kamoshida, Y. Niitsuma, T. Iwamura, H. Akimoto, K. Nakajima, T. Chiba, H. Watanabe, K. Komori, H. Sonobe, T. Okubo, Y. Abe, A. Owada, T. Hojo, A. Minato, I. Sakaki, H. Adachi, E. M. Feldman, and Y. Murao, "Data Report on Large Scale Reflood Test-106, SCTF Test S3-SH2 (Run 704)," JAERI memo 62-116 (March 1987).
3. B. E. Boyack and L. Mascheroni, "A Posttest Analysis of SCTF Run 704 Using TRAC-PF1/MOD1." Los Alamos National Laboratory document (to be issued).
4. P. R. Shire and B. E. Boyack, "Upper-Plenum Studies of SCTF Run 605." Los Alamos National Laboratory document LA-2D/3D-TN-86-15 (August 1986).
5. T. Okubo, T. Iguchi, A. Ohnuki, T. Oyama, A. Kamoshida, Y. Niitsuma, T. Iwamura, H. Akimoto, K. Nakajima, T. Chiba, H. Watanabe, K. Komori, H. Sonobe, Y. Abe, A. Owada, T. Hojo, A. Minato, I. Sakaki, H. Adachi, E. M. Feldman, and Y. Murao, "Data Report on Large Scale Reflood Test-115, SCTF Test S3-9 (Run 713)," JAERI memo 62-125 (March 1987).
6. T. Iwamura, M. Sobajima, T. Okubo, A. Ohnuki, Y. Abe, and H. Adachi, "Two-Dimensional Thermal-Hydraulic Behavior in Core in SCTF Core-II Forced Feed Reflood Tests (Effects of Radial Power and Temperature Distributions)," JAERI memo 60-395 (January 1986).
7. P. R. Shire, "TRAC-PF1/MOD1 Analysis of SCTF Core-III Test S3-9 (Run 713)." Los Alamos National Laboratory document (to be issued).
8. H. Akimoto, T. Iguchi, A. Ohnuki, T. Oyama, A. Kamoshida, Y. Niitsuma, T. Iwamura, K. Nakajima, T. Chiba, H. Watanabe, K. Komori, H. Sonobe, T. Okubo, Y. Abe, A. Owada, T. Hojo, A. Minato, I. Sakaki, H. Adachi, E. M. Feldman, and Y. Murao, "Data Report on Large Scale Reflood Test-S3-f10, SCTF Test S3-SH2 (Run 714)," JAERI memo 62-126 (March 1987).
9. S. C. Harmony and B. E. Boyack, "A Posttest Blind Analysis of SCTF Run 714 Using TRAC-PF1/MOD1." Los Alamos National Laboratory document (to be issued).
10. T. Okubo, T. Iguchi, K. Okabe, J. Sugimoto, H. Akimoto, and Y. Murao, "Quick-Look Report on CCTF Core-II Reflood Test C2-AA2 (Run 58), Investigation of Downcomer Injection Effects," JAERI-memo 58-386 (October 1983).

11. D. A. Siebe and B. D. Boyer, "The Analysis of CCTF Run 58 with TRAC-PF1/MOD1," Los Alamos National Laboratory document LA-2D/3D-TN-86-19 (to be issued).
12. A. Ohnuki, H. Adachi, and Y. Murao, "Scale effects on countercurrent gas-liquid flow in horizontal tube connected to inclined riser," in proceedings of the ANS 1987 National Heat Transfer Conference, Pittsburgh, Pennsylvania, August 9–12, 1987, pp. 40–49.
13. A. M. Rozen, S. I. Golub, and T. I. Botintseva, "Calculation of Droplet Carryover with Bubbling," *Teploenergetika*, **23** (11), 59–62 (1976).
14. B. Chexal, and G. Lellouche, "A Full-Range Drift-Flux Correlation for Vertical Flows (Revision 1)" NP-3939-SR, Rev. 1, EPRI (September 1986).

Analysis of UPTF Test 11 (Hot leg CCF) with a Full-Range Drift-Flux Model

H.G. Sonnenburg

Gesellschaft für Reaktorsicherheit (GRS) mbH
Forschungsgelände
D-8046 Garching
F.R.Germany

ABSTRACT

At GRS a full-range drift-flux model has been developed and verified. This model has been developed on the base of both the drift-flux theory and the envelope theory. The resulting model equation predicts the relative velocity for horizontal pipes and for inclined pipes. The model equation is implemented into the GRS system code ATHLET.

The UPTF test 11 (hot leg CCF test) produces two-phase flow in a full-scale hot leg simulator relative to a KWU reactor. Therefore, the measurement of flow parameters in that facility procures a valuable basis in order to assess the full-scale performance of the ATHLET code.

A good agreement between measured and predicted flow parameters has been reached. Even the typical flow behaviour at the onset of flooding is correctly predicted by the ATHLET code. The drastic change in water level heights which occurs when countercurrent flow limitation (CCFL) is reached could be explained by the code. Therefore, the ATHLET code can be regarded as a tool to analyze details of CCFL phenomena.

By means of comparative calculations the influence of the "Hutze" on CCFL is investigated. Based on these calculations it is shown that this influence is less than 10 % in steam mass flow rate.

1. Introduction

CCF in the hot leg of a PWR loop is an important phenomenon in the course of the 'small break loss-of-coolant accident' (SB LOCA). It was the subject of investigation in the UPTF test 11 to determine the limit of this CCF. The UPTF test 11 procures the saturated CCF limit in a 1:1 scale of a PWR hot leg.

Having these important results, the models which are used in computer

codes to determine relative velocities for such specific geometries, are challenged to show both if the measured limit could be predicted and if the scaling performance of model is sufficient. If these demands are fulfilled the code calculation based on such a verified model could give answer to the question how this flow limit is physically provoked, because these calculations provide spatial distributions of the process controlling parameters. Furthermore, these verified models allow CCF-predictions of differently designed hot legs with rather some confidence.

At GRS a full-range drift-flux model has been developed and verified. The model is implemented into the GRS system code ATHLET /1/. ATHLET will comprise in its final state different sets of equation systems. The actually in ATHLET available 4-equation system is considered to be sufficient to investigate the phenomena in the hot leg during reflux condenser mode which have been observed in UPTF test 11.

2. Theoretical Tools

The full-range drift-flux model is based on the drift-flux theory. This theory procures a generally valid expression for the relative velocity between phases in a cross-sectional flow area. This expression is generally valid because there is no restriction imposed on it.

$$\langle\langle Vv\rangle\rangle - \langle\langle V\ell\rangle\rangle = (Co - Co\ell)\,\langle J\rangle + \frac{\langle Jv\ell\rangle}{\langle Av\rangle\,\langle 1-Av\rangle} \qquad (1)$$

$$\text{with} \qquad 1 = Co\,\langle Av\rangle + Co\ell\,\langle 1-Av\rangle \qquad (2)$$

In order to determine the drift-flux $\langle Jv\ell\rangle$ the envelope theory is utilized. This theory leads to a drift-flux $\langle Jv\ell\rangle$ as a function of both CCFL-parameters and phase distribution parameter. The CCFL-parameters are the so called limiting velocities which can be read from a typical flooding diagram as the intersections with the axes (see fig. 1).

With the drift-flux deduced from envelope theory the drift-flux equation (1) can be rewritten as:

$$\langle\langle Vv\rangle\rangle - \langle\langle V\ell\rangle\rangle = (Co - Co\ell)\,\langle J\rangle + \frac{Co\;Co\ell}{\frac{Co\langle Av\rangle}{WOvgr} + \frac{Co\ell\langle 1-Av\rangle}{WO\ell gr}} \qquad (3)$$

The resulting equation (3) is generally used for all situations, for dispersed flow as well as for separated flow. The equation applies for cocurrent upflow, cocurrent downflow, and for countercurrent flow. It even predicts the relative velocity of phases in case of countercurrent flow limitation. Depending on the limiting velocities (WOvgr,WOℓgr), equation (3) predicts the relative velocity for horizontal pipes as well as for vertical or inclined pipes.

Empirical input to model equation from CCFL correlations

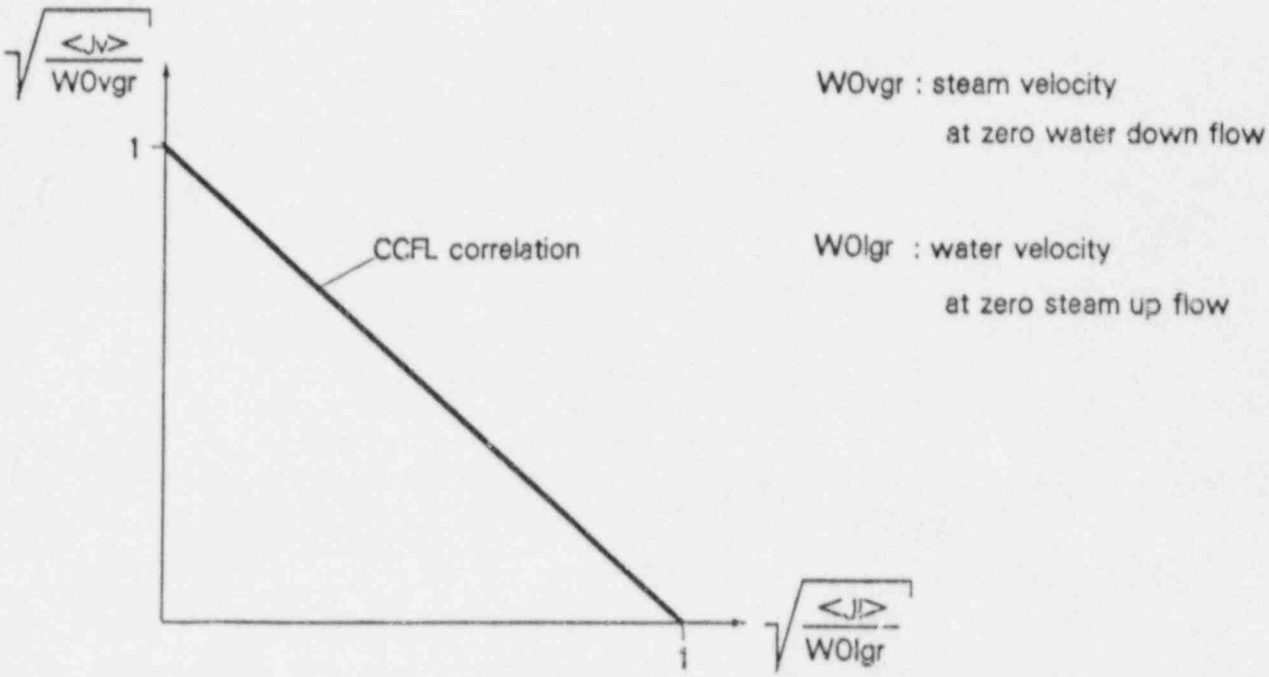

Fig. 1: CCFL correlation defined by limiting velocities

3. Empirical Input to the Full-Range Model

As indicated above the model equation (3) needs inputs for both phase distribution parameter and CCFL-parameters (WOvgr,WOℓgr) from adequate CCFL correlations.

3.1 Phase Distribution Parameter

In order to provide the model equation (3) with the phase distribution parameter Co the Co-correlation of Ishii /2/ is taken. As a result of the verification procedure this correlation was slightly modified to account for both larger diameters and pipe inclinations. The complete correlation actually used in the model is given by:

$$Co = MIN\ (Co1,\ Co2,\ Co3)$$

$$Co1 = (1+a(1-\sqrt{\rho_v/\rho_\ell}))(1-e^{-18Av}) \qquad (4)$$

$$a = 0.2 \text{ if } D \leq 0.1 \text{ m}$$
$$a = 0.4 \text{ if } D \geq 0.5 \text{ m}$$

$$Co2 = 1 + \frac{(1-Av)(1-Ed)}{Av + \left[\frac{1+75(1-Av)}{\sqrt{Av}} \frac{\rho_v}{\rho_\ell}\right]^{1/2}} \qquad (5)$$

$$Co3 = \frac{WOvgr}{Av\ WOvgr + (1-Av)\ WO\ell gr} \qquad (6)$$

The onset of entrainment (Ed>0) is supposed to occur if the vapour velocity exceeds a critical velocity. This critical velocity is given by (7):

$$2.5 \cdot 10^{-4} \frac{\sigma}{\mu_v} \sqrt{\frac{\rho_\ell}{\rho_v}} \qquad (7)$$

if the orientation of pipe is vertical or inclined.

The criterion which accounts for horizontal flows relies on Taitel & Dukler's stability criterion (8). The critical velocity is given by:

$$\sqrt{\frac{g\ \Delta\rho\ D\ \alpha}{\rho_v}} \qquad (8)$$

The first phase distribution parameter (4) applies to the churn turbulent or slug flow regime. The second phase distribution parameter (5) applies to the annular mist flow regime. The third phase distribution parameter (6) provides a maximal value. This maximum reflects the highest degree of separation which can be reasonably described by the derived model equation (3).

3.2 CCFL-parameters

In order to provide the model equation (3) with the CCFL parameters (limiting velocities: WOvgr,WOℓgr) that CCFL correlation has to be chosen for evaluation which applies for the considered geometrical situation.

In case of a horizontal flow duct the CCFL correlation of Bankoff & Lee is taken. Whereas for vertical or inclined flow ducts a modified correlation of Wallis is taken.

3.2.1 Horizontal flow duct

Bankoff & Lee /3/ measured the countercurrent flow rates in a slightly inclined flow duct. The results are presented using the Wallis parameters. Bankoff & Lee replaced the critical length scale diameter by the hydraulic diameter (Dhyd=2H) because they measured in a square channel.

They found that the effect of inclination of the channel is best described by introducing the sinus of the inclination angle in the gravity term. The resulting CCFL correlation which gives the best fit to measured data is:

$$\left(\frac{j_v^2\,\rho_v}{2\,g\,H\,\sin\vartheta\,\Delta\rho}\right)^{1/4} + 0.73\left(\frac{j_\ell^2\,\rho_\ell}{2\,g\,H\,\sin\vartheta\,\Delta\rho}\right)^{1/4} = 1.15 \qquad (9)$$

In order to utilize this empirical information (9) for equation (3) which should be applicable to flows in horizontal pipes the following assumptions are made:

1. The inclination angle of flow duct is interpreted as the liquid fraction gradient times the pipe diameter.

$$\sin(\vartheta) = \frac{\partial(1-Av)}{\partial z}\,Dhyd \qquad (10)$$

2. The channel height (H) can be replaced by the diameter of horizontal pipe.

$$H = Dhyd \qquad (11)$$

The resulting limiting velocities from that modified CCFL correlation are given by:

$$W0vgr = 1.87\sqrt{\frac{g\,D^2\,\Delta\rho}{\rho_v}\cdot\frac{\partial(1-Av)}{\partial z}} \qquad (12)$$

$$W0\ell gr = 3.51\sqrt{\frac{g\,D^2\,\Delta\rho}{\rho_\ell}\cdot\frac{\partial(1-Av)}{\partial z}} \qquad (13)$$

3.2.2 Vertical or inclined flow duct

Wallis /4/ provides a CCFL correlation for vertical pipes.

$$\left(\frac{j_v^2\,\rho_v}{g^+\,D\,\Delta\rho}\right)^{1/4} + m\left(\frac{j_\ell^2\,\rho_\ell}{g^+\,D\,\Delta\rho}\right)^{1/4} = C \qquad (14)$$

$$\text{with } C = m = 1$$

Correlation (14) applies at first for pipes with diameters within a certain range. The validity of correlation (14) has been proven for the diameter range from 0.01 m to 0.05 m. In order to extend the validity of this correlation to larger diameters and to inclination angles less than 90 degree some modifications are implemented into the original correlation

(14). Modifications which account for the extension in inclination are given by:

$$1.\quad g^{+} = g \sin(\vartheta) \tag{15}$$

$$2.\quad C = 1.31 + (1.0 - 1.31) \sin(\vartheta) \tag{16}$$

$$3.\quad m = 0.73 + (0.9 - 0.73) \sin(\vartheta) \tag{17}$$

with ϑ: inclination angle

Modifications which account for the extension in diameter are given by:

$$D = D_{equ} \tag{18}$$

$$\text{with } D_{equ} = \begin{cases} D_{hyd} \text{ if } Bo^{*} < 200 \text{ or } \sin(\vartheta) < 0.9 \\ \frac{200}{\pi} \sqrt{\frac{\sigma}{g^{+} \Delta\rho}} \text{ if } Bo^{*} > 200 \text{ and } \sin(\vartheta) > 0.9 \end{cases}$$

$$\text{where the Bond-no. } Bo^{*} = D \pi \sqrt{\frac{g^{+} \Delta\rho}{\sigma}} \tag{19}$$

The Bo*-no-limitation reflects the effect that the local drift velocity is disturbed by wall effects only if the pipe diameter falls below $200/\pi$ times the Laplace length. The recently published investigation of pool void fraction models by Kataoka & Ishii /5/ points to the fact that this limit occurs already at smaller diameters. Ishii & Kataoka propose a Bo*-no-limitation of 30. However, the limiting velocities WOvgr and WOℓgr which determine the relative velocity of phases for the inclined part of hot leg (50 degree inclination) can be read from the previously stated CCFL correlation. These limiting velocities are given by:

$$WOvgr = 1.01 \sqrt{\frac{g\, D\, \Delta\rho}{\rho_v}} \tag{20}$$

$$WO\ell gr = 1.36 \sqrt{\frac{g\, D\, \Delta\rho}{\rho_\ell}} \tag{21}$$

4. System Code ATHLET

The ATHLET code is a fusion of the codes ALMOD /6/, DRUFAN /7/, and FLUT /8/ within a single, consistent code structure. The ATHLET code is intended for LWR analyses of operational and abnormal transients, small, intermediate and large breaks and of severe accidents. Therefore, within ATHLET code different sets of equation systems will be available.

In the present state of development the ATHLET code includes among others the 4-equation system which was originally used in DRUFAN. This 4-equation system consists of mass balance for steam, mass balance for water, momentum balance for mixture and energy balance for mixture.

Because the momentum balance is evaluated for the mixture, this 4-equation system requires an algebraic equation for the relative velocity between phases. For this purpose, the previously described full-range drift-flux model (3) comes into operation.

5. Model Verification

The application of the code ATHLET to both small scale tests and large scale tests prior to the UPTF test no. 11 already demonstrate the good scaling performance of the full-range drift-flux model.

5.1 Small Scale Test Prediction

The blind prediction of the small leak test ISP18 (international standard problem 18 at LOBI test facility - small break LOCA test) with DRUFAN (same model as ATHLET) showed very good agreement of all key parameters /9/. The prediction of void fractions in both hot legs and cold legs reached excellent agreement with measured void fractions. The development of liquid contents in both the steam generators and the remaining primary system indicates an accurate prediction of mass flow rates in hot and cold legs.

5.2 Large Scale Test Prediction

The post test analysis of a large scale test (the Finnish loop seal test of IVO - diameter of pipe is 0.85 m) /10/ based on the same model equation with ATHLET leads to good agreement in the relevant parameters pressure difference and liquid content in test section.

From these encouraging results and further successful investigations in different scales we conclude that the full-range drift-flux model covers the relevant scaling range.

6. UPTF Test No. 11 (Hot Leg CCF)

Because the UPTF /11/ (upper plenum test facility) produces two-phase flow in full-scale simulators relative to a KWU reactor, the data from this facility are highly important for the assessment of the model.

The UPTF test no. 11 (hot leg CCF) investigates steam/water flow phenomena in the hot leg during reflux condensation, which is a cooling mode that may occur during a SB LOCA.

Saturated water was injected into the inlet chamber of the UPTF water separator simulating the steam generator in the broken loop hot leg and saturated steam was introduced via the core simulator system.

The injected water flows countercurrent to the steam through the hot leg back into the reactor vessel simulator.

The water flowing within the horizontal part of the hot leg had to pass the "Hutze" region. The Hutze is an elliptically shaped ECC inlet device (see fig. 2). The injection port of this device is located about 1.5 m away from the vessel. The Hutze region extends about 2 m along the hot leg. The Hutze area blocks about 10 % of the full cross-sectional area of the hot leg.

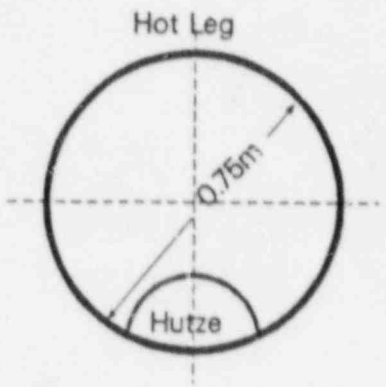

Open Flow Area = 0.3974m²

Hydraulic Diameter = 0.639m

Blocked Area by "Hutze" = 0.04438m²

Open Flow Area

without "Hutze" = 0.4418m²

Hydraulic Diameter = 0.75m

Fig. 2: Cross-sectional area of a hot leg within the Hutze region

Each test run was run until steady state conditions were reached. The established water mass flow rates which pass the hot leg against the countercurrent flowing steam, were measured by means of water level measurements in the reactor vessel simulator.

The pressure in the upper plenum simulator of the test facility was kept constant during the test run. The test runs #30 to #34 were accomplished at 0.3 MPa, whereas the test runs #37 to #45 were accomplished at 1.5 MPa. The dependence of CCFL on pressure therefore is well represented by the test.

6.1 Test Results

The results of the UPTF test no. 11 can be stated in a flooding diagram with Wallis parameters as the axes of the diagram. The Wallis parameters for the steam phase and water phase are given by:

$$j_v^* = \left(\frac{\dot{m}_v^2}{g\ D\ \Delta\rho\ \rho_v A^2}\right)^{1/2} \qquad (22)$$

$$j_\ell^* = \left(\frac{\dot{m}_\ell^2}{g\ D\ \Delta\rho\ \rho_\ell A^2}\right)^{1/2} \qquad (23)$$

If the characteristic dimensions (Dhyd, Area) in the Wallis parameters (22) and (23) refer to the Hutze region of the hot leg, the test data are best represented by the CCFL correlation of Richter (24).

$$j_v^{*1/2} + j_\ell^{*1/2} = 0.7 \qquad (24)$$

The characteristic dimensions are given by

Dhyd = 0.639 m and Area = 0.3974 m²

The characteristic dimensions outside the Hutze region are given by:

Dhyd = 0.750 m and Area = 0.4418 m²

This analysis suggests that the Hutze region is the process controlling region although the controlling region was generally expected at the transition from horizontal to inclined pipe of hot leg (see /12/ and /13/).

7. Post Test Prediction with ATHLET

GRS made a post test prediction with the code ATHLET in order to qualify the parameters of the previously described drift-flux model (3) involved.

7.1 Nodalization of Hot Leg

The code calculation restricts on the representation of the hot leg including the Hutze, the reactor simulator and the inlet chamber of steam generator simulator.

The representation of hot leg is accomplished with the most economical nodalization which just can provide a reasonable evaluation of the model equations to show the effect of Hutze on CCFL. This results in a nodalization consisting of 6 fluiddynamic zones representing the hot leg with Hutze. From these 6 zones two of them represent the Hutze region. One zone represents the bended part of the hot leg and one adjacent zone represents the inclined part of the hot leg.

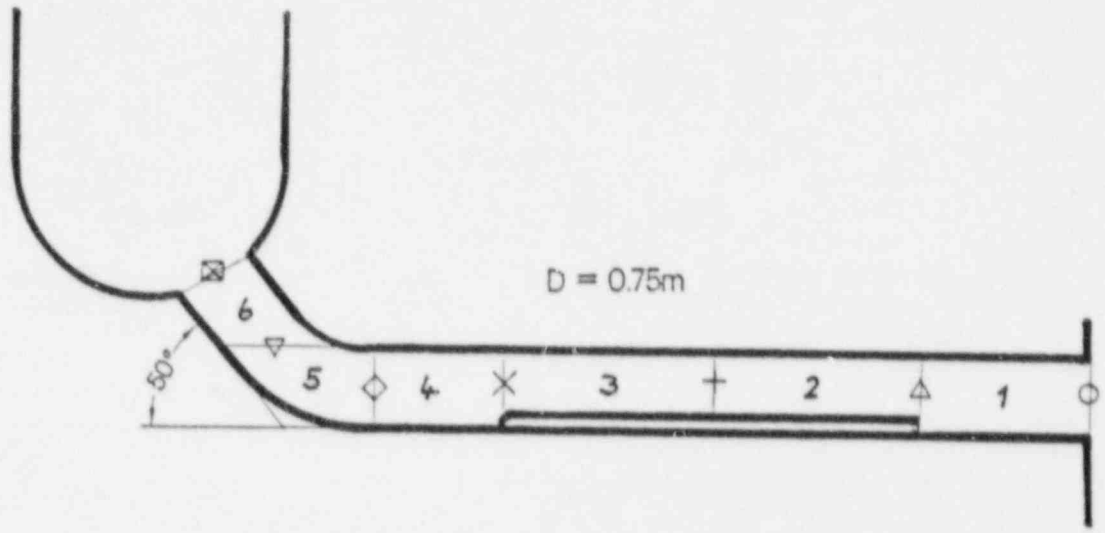

Fig. 3: Nodalization of the hot leg

The remaining components which are also represented in the code calculation are not shown because they do not contribute to the CCFL-result.

7.2 Initial and Boundary Conditions

Each calculation starts with zones which are completely filled with saturated steam at rest. After a few seconds the steam mass flow rate is ramped up to a certain value. This value is kept constant throughout the whole transient. After having reached steady state flow conditions the water mass flow rate is also ramped up to a mass flow rate of 30 kg/s.

According to this procedure a steam first mode CCFL is modeled. This mode corresponds to that one of the UPTF test procedure.

The constant steam flow rates chosen for the calculation correspond to those which are actually injected via the core simulator system into the UPTF

7.3 Calculated Results

Depending on the injected constant flow rates the simulated two-fluid system stabilizes itself within a 60 second transient time. The reached steady state flow data after that transient time are taken for comparison.

7.3.1 Typical time history of two-phase flow parameters calculated by ATHLET

Fig. 4 to fig. 8 demonstrate how the calculated flow parameters develop during that transient. Fig. 4 shows the injected water and steam mass flow rates. The following plot, fig. 5, illustrates how the calculated water and steam mass flow rates at the connection between hot leg and upper plenum react on the injected rates. Fig. 6 to fig. 7 show the flow parameters water velocity, steam velocity, and liquid fraction, respectively, at different locations within the hot leg.

7.3.2 CCFL curve in the Wallis diagram

The calculated mass flow rates at CCFL conditions are plotted together with measured rates in a Wallis diagram which uses the characteristic dimensions of the hot leg outside the Hutze region, that is:

$$\text{Area} = 0.4418\ m^2 \quad ; \quad D_{hyd} = 0.75\ m$$

Each symbol in the plot stands for one calculation or one test run, respectively.

The calculated CCFL data based on the previously described full-range drift-flux model tend to underpredict the measured CCFL data, but they are generally in good agreement with the measured data.

The measured CCFL data and calculated CCFL data for both pressures 0.3 MPa and 1.5 MPa, plotted in a Wallis diagram (fig. 9) indicate that the dependence on pressure is well represented by the Wallis parameters. Furthermore, the comparison suggests that the limiting velocities utilized in the code model for the horizontal and inclined pipe are adequate for the description of flows in such pipes.

7.3.3 Predicted water level height along the hot leg

Fig. 10 illustrates the established water level heights along the hot leg at conditions given in run #39.

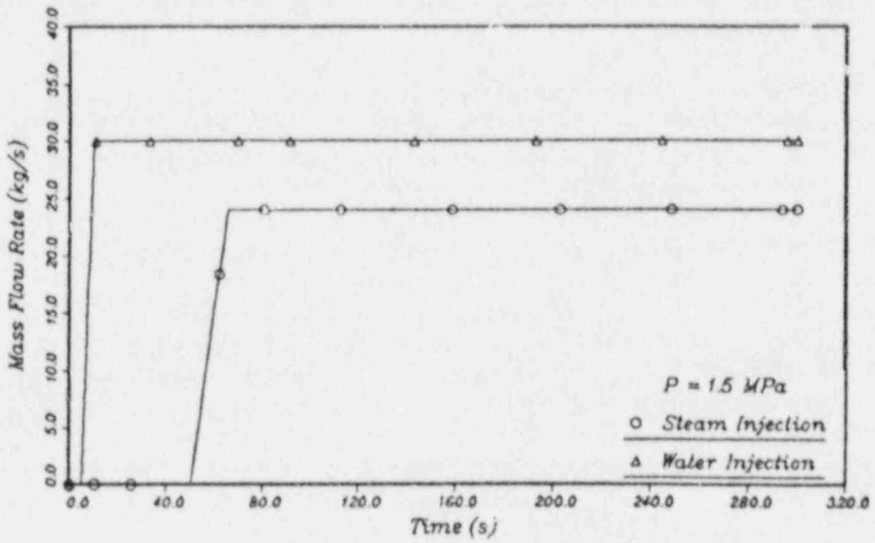

Fig. 4: Injected water and steam mass flow rate

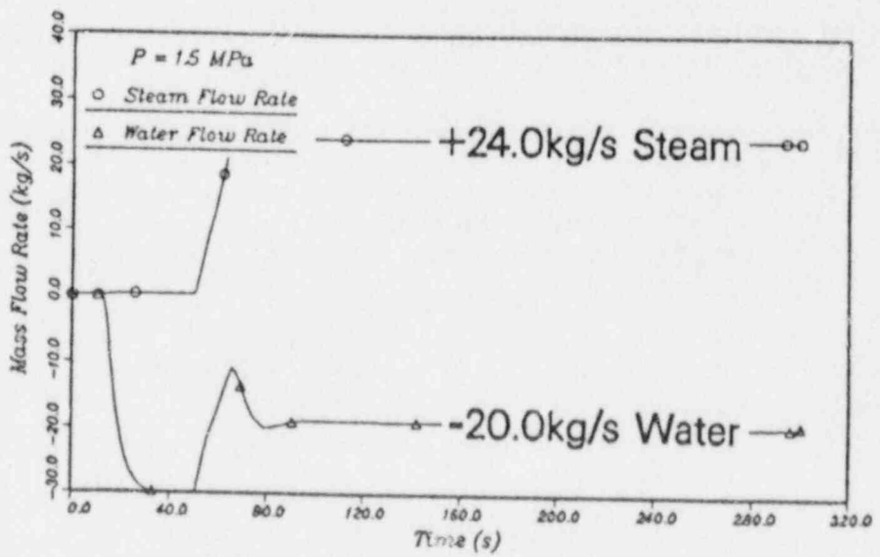

Fig. 5: Water and steam mass flow rate at
the connection between hot leg and vessel

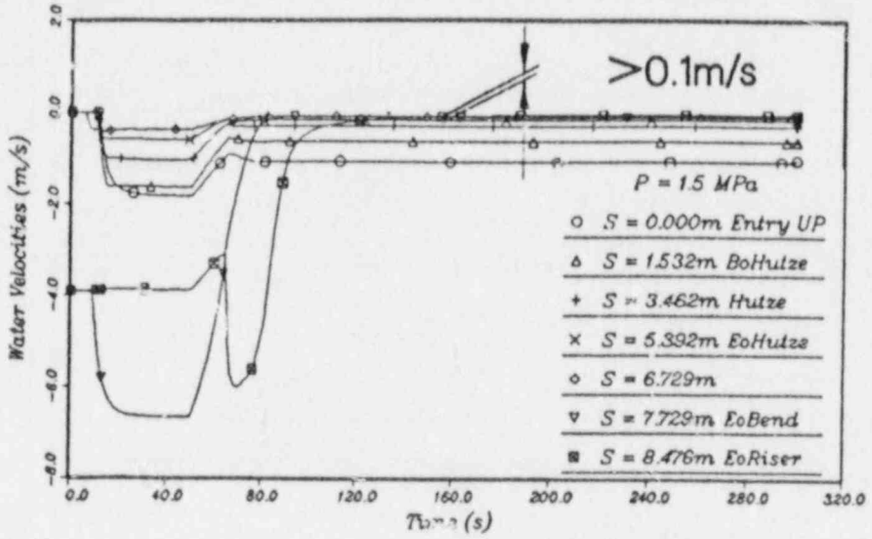

Fig. 6: Water velocities along the hot leg

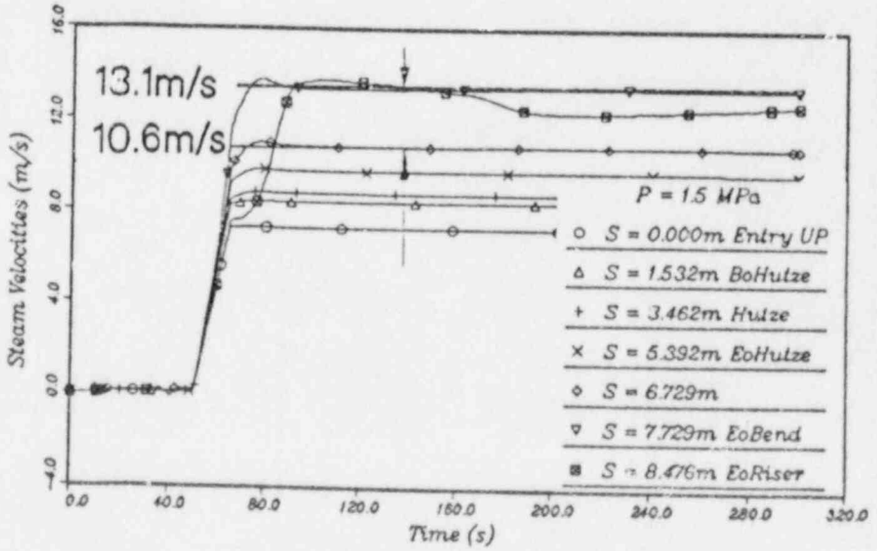

Fig. 7: Steam velocities along the hot leg

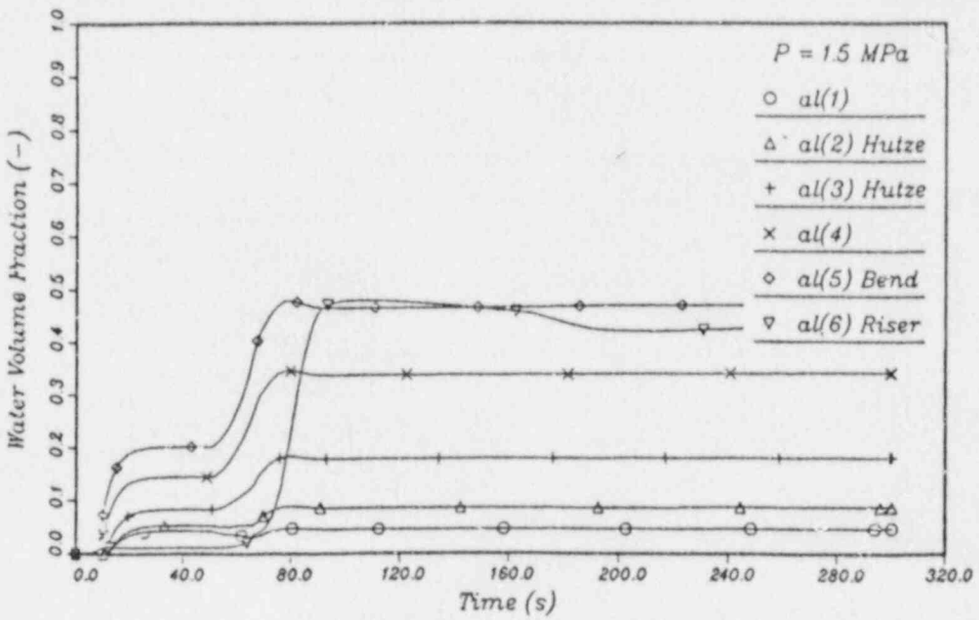

Fig. 8: Water volume fraction along the hot leg

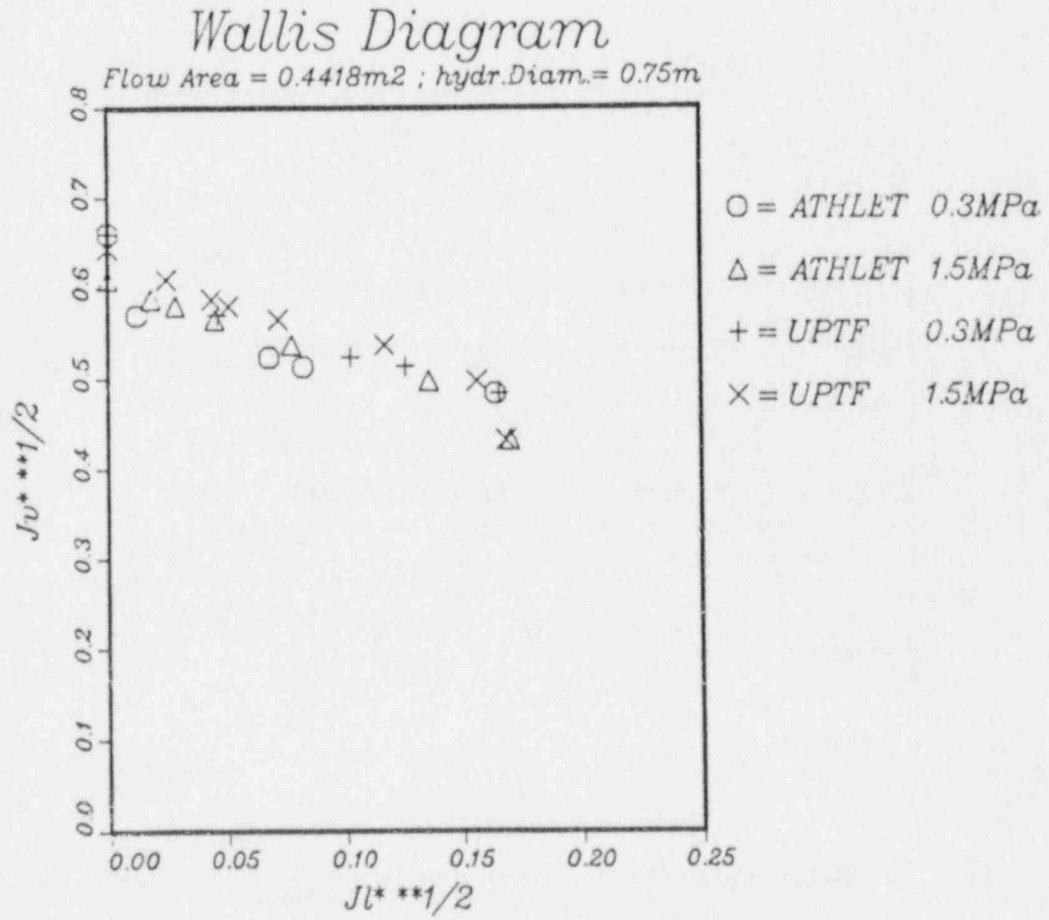

Fig. 9: UPTF and ATHLET data plotted in a Wallis diagram

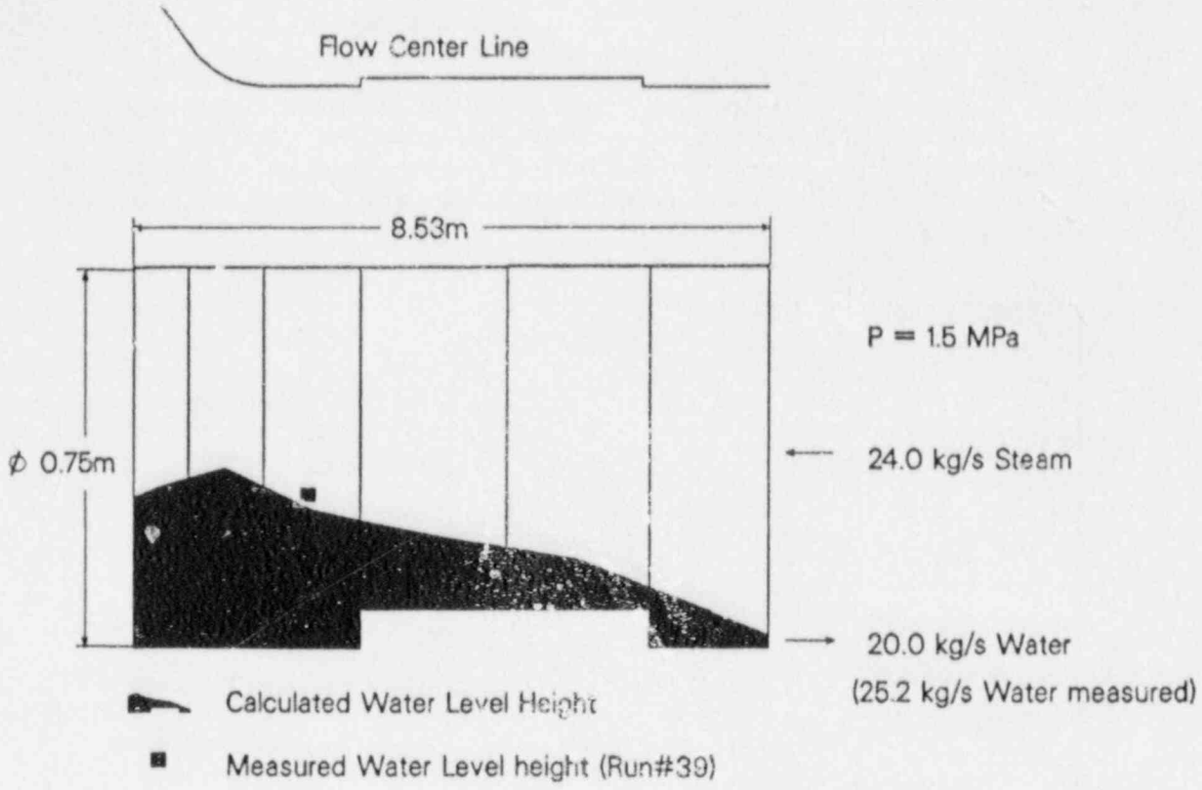

Fig. 10: Water level heights along the UPTF hot leg

Within this plot the Hutze region is indicated by an unshaded section. The calculated water level height between Hutze and the bend of the hot leg can be compared with the 3-beam-gamma-densitometer measurement located there. Because the calculated water mass flow rate is about 30 % underestimated in case of run #39, the calculated water height slightly falls below the measured one.

From fig. 10 it is evident that the CCFL controlling region is not within the Hutze region. From the calculation one could see that the largest amount of water accumulated due to the steam flowing countercurrent to the water is located at the bent part of the hot leg. Consequently, the highest steam velocities which may be able to provoke the CCFL are located at that position. If the water has passed the bent part of the hot leg the interaction at the interface between steam and water decreases significantly due to the reduced steam velocity. In case of the calculation for run #39 the steam velocity decreases from 13 m/s at hot leg position 7.729 m (End of Bend) to 10 m/s at hot leg position 6.729 m (Begin of Bend), whereas the water velocity increases with less than 0.1 m/s within the same distance (see fig. 6 and fig. 7).

A significant acceleration of the water flow within the hot leg is predicted at the end of the Hutze region, next to the exit to the upper plenum, but here the steam velocity falls below 8 m/s, which is far below a critical velocity.

7.3.4 Comparison of water level heights

A 3-beam-gamma-densitometer is mounted in the hot leg at 6 m away from the vessel. The position of this instrument is in between the Hutze and the bent part of hot leg. Assuming a stratified flow the density readings can be recalculated in water level heights. These water level heights are compared with calculated water level heights at the same position, see fig. 11 and fig. 12.

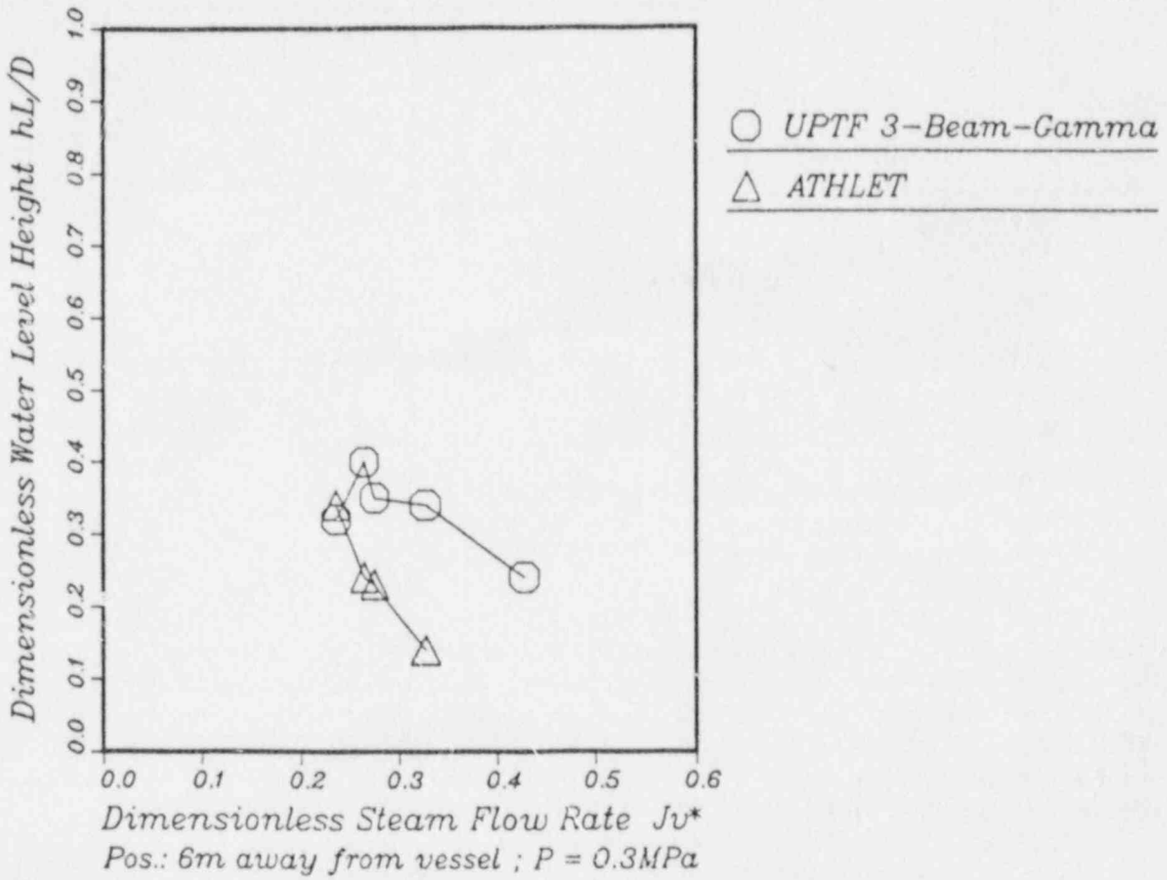

Fig. 11: Dimensionless water level height at 0.3 MPa

Although the position of the densitometer does not coincide with the CCFL locus the density readings give insight into the phenomena, if these readings are seen in combination with the ATHLET calculation. The following interpretation of the experimental data relies on the reliability of the code ATHLET.

The ATHLET calculation shows that the water level height at measurement position is generally lower than that level at CCFL locus (see fig. 10) but the level data trends with respect to the steam mass flow rate are equal to both positions. From the test readings at 6 m away from the vessel (less than 1 m away from the expected CCFL locus) one can see that as far as the countercurrent flow limit is not exceeded the water level is

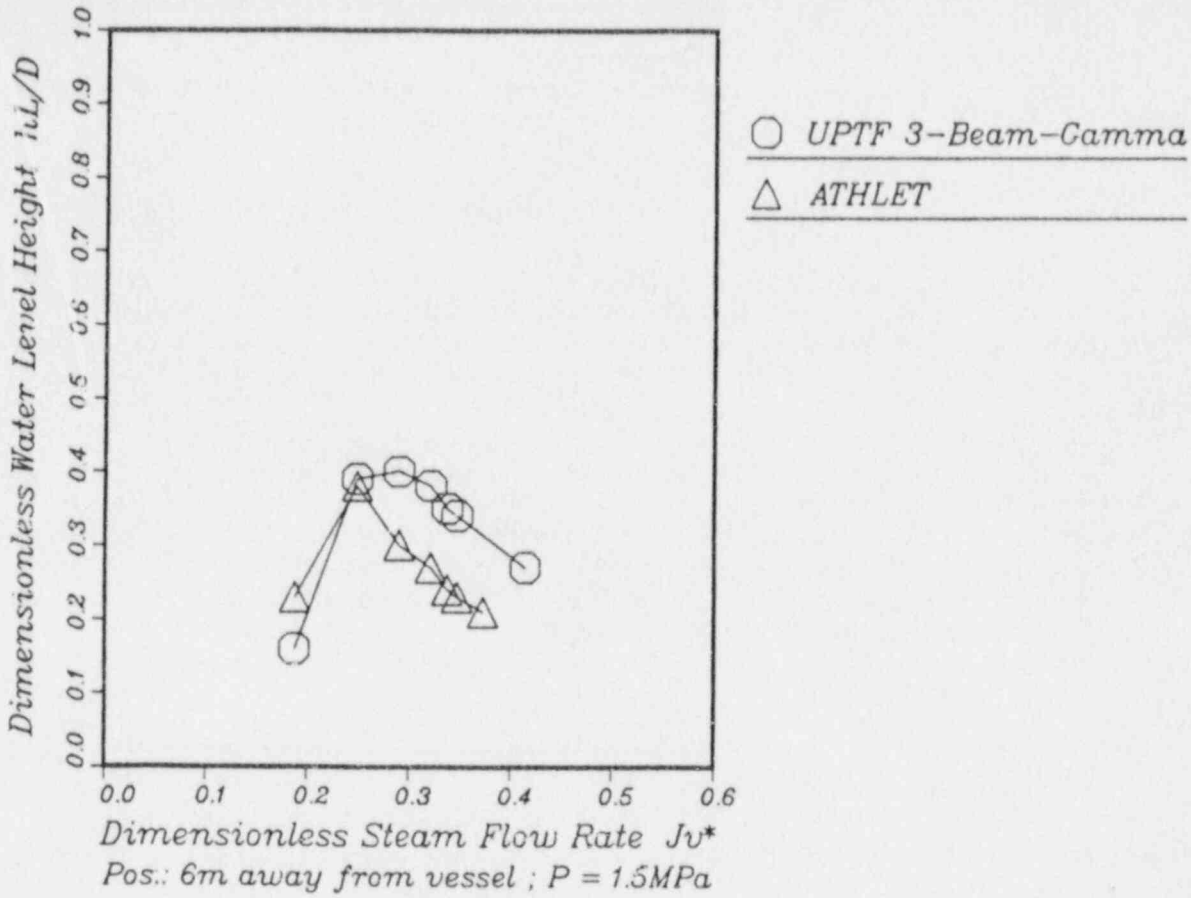

Fig. 12: Dimensionless water level height at 1.5 MPa

kept on a low level. About 0.12 m from the bottom of the hot leg at the 6 m position is covered by water.

If the steam mass flow rate reaches the CCFL the water level steeply increases to the highest level. About 0.30 m from the bottom of the hot leg at the 6 m position is covered by water under CCFL condition.

The ATHLET calculation predicts the same behaviour as it is observed in the UPTF test.

Besides this agreement in the water level data the ATHLET calculation demonstrates that under CCFL conditions the Hutze is far below the water surface.

With further increase of the steam mass flow rate beyond the CCFL the water level height decreases gradually due to the steam flow which starts to entrain water from the water surface.

Further increase of the steam mass flow rate leads to the situation that no water can pass through the hot leg towards the vessel. It is interesting to note that now a large amount of water still remains in the hot leg. The water level at measurement position indicates a water level height about 0.20 m. At the same mass flow rates ATHLET underestimates the remai-

ning water in the hot leg because zero water penetration is simulated at a steam mass flow rate which is smaller than that one observed in UPTF.

8. Influence of the Hutze on the Two-Phase Flow in the Hot Leg

Based on the excellent representation of the hot leg CCFL phenomena by ATHLET, this code may help to analyse the contribution of the Hutze to CCFL behaviour. A series of comparative calculations with a hot leg which does not contain the Hutze allows an identification of that Hutze influence.

The Hutze region of the hot leg is mainly represented by the following geometrical features:

a) the cross-sectional area is 10 % reduced compared to the full area
b) the hydraulic diameter is 20 % reduced compared to the full diameter
c) the centre line of the two-phase flow is elevated up to 0.05 m relative to the centre line outside the Hutze
d) the bottom line of the horizontal pipe is elevated up to 0.10 m relative to the bottom line outside the Hutze.

8.1 Determination of Differences

The comparative calculations are based on the same nodalization but with altered geometrical features referring to a hot leg without the Hutze.

Fig. 13 to fig. 15 demonstrate the difference in CCFL behaviour at different pressures between both hot legs with Hutze and without Hutze. Here again the data are presented in the Wallis diagram based on the dimensions of the full cross-sectional area of the hot leg.

At low pressures these differences in CCFL tend to disappear (see fig. 13: P=0.3 MPa). At 1.5 MPa the difference in steam mass flow rate at zero penetration is less than 3 %, whereas the difference in steam mass flow rate at the onset of flooding could reach 9 % (see fig. 14: P=1.5 MPa). These differences increase slightly with an increase in pressure. At 7 MPa, a typical pressure under SB LOCA conditions, the difference at the onset of flooding does not exceed 10 % (see fig. 15: P=7.0 MPa).

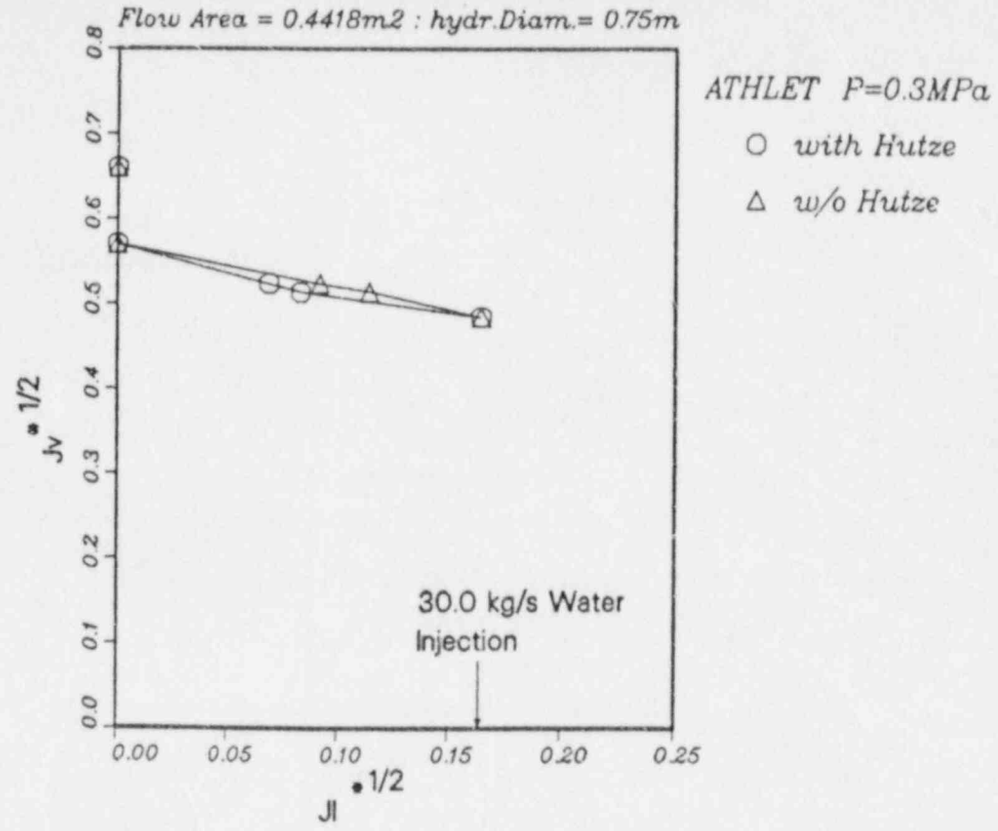

Fig. 13: Comparative ATHLET calculation for 0.3 MPa

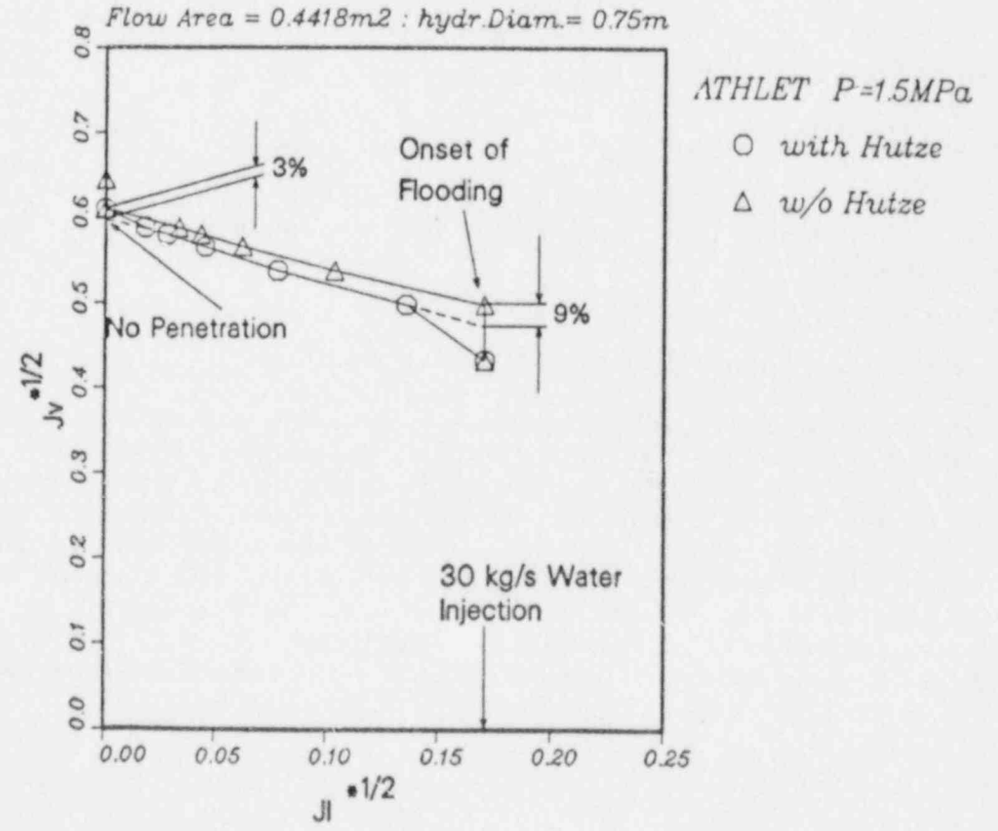

Fig. 14: Comparative ATHLET calculation for 1.5 MPa

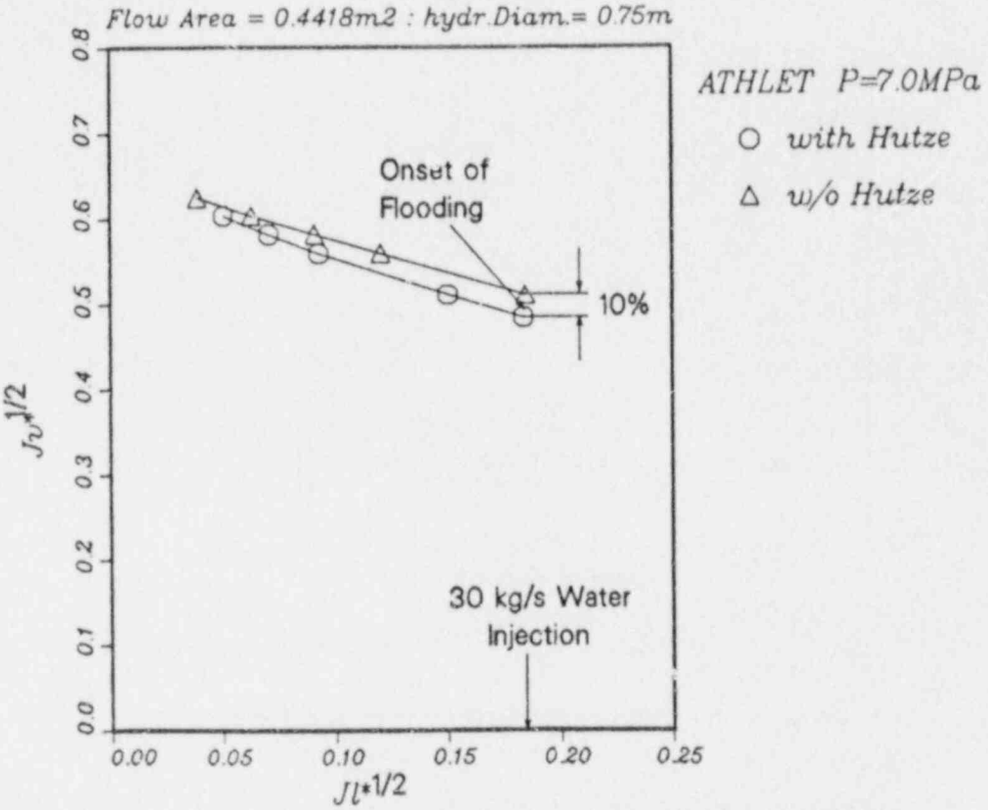

Fig. 15: Comparative ATHLET calculation for 7.0 MPa

8.2 Explanation of Differences

Steam mass flow rates which provoke CCFL in the hot leg with Hutze are expected to be lower than that one which provokes CCFL in a hot leg without Hutze.

8.2.1 Differences expected in previous investigations

The difference between the two cases was recently assessed by other investigators /14/ on the base of a Wallis methodology assuming the Hutze region as a CCFL relevant region. The resulting difference is in the order of 20 %. This 20 % difference in the steam mass flow rate is the sum of two 10 % contributions. The first one considers the area contraction within the Hutze region which is in the order of 10 %. The second contribution refers to the 20 % reduction of hydraulic diameter within the Hutze region. Because the CCFL depends on the square root of the hydraulic diameter according to Wallis parameters the reduction of diameter affects the CCFL with 10 %. Both 10 % differences summarize up to 20 %.

8.2.2 Explanation of differences as indicated by ATHLET

The ATHLET calculation contradicts this assessment because the CCFL controlling area is identified to be located at the bent part of the hot leg. At the bent part of the hot leg the water accumulation reaches its maximum there. According to the ATHLET calculations a water level height of about 0.3 m could be reached there. If steam mass flow has passed that region the interaction between steam and water decreases drastically.

The water level height at that locus does not depend on the water level heights at upwind or downwind positions because the void wave velocity under CCFL condition is zero.

Concerning the differences, variations of the water level inclination show an influence on the steam mass flow rate only. From the water level height plottings it becomes obvious that the Hutze at the bottom of the horizontal pipe elevates the water level height according to its dimensions within the

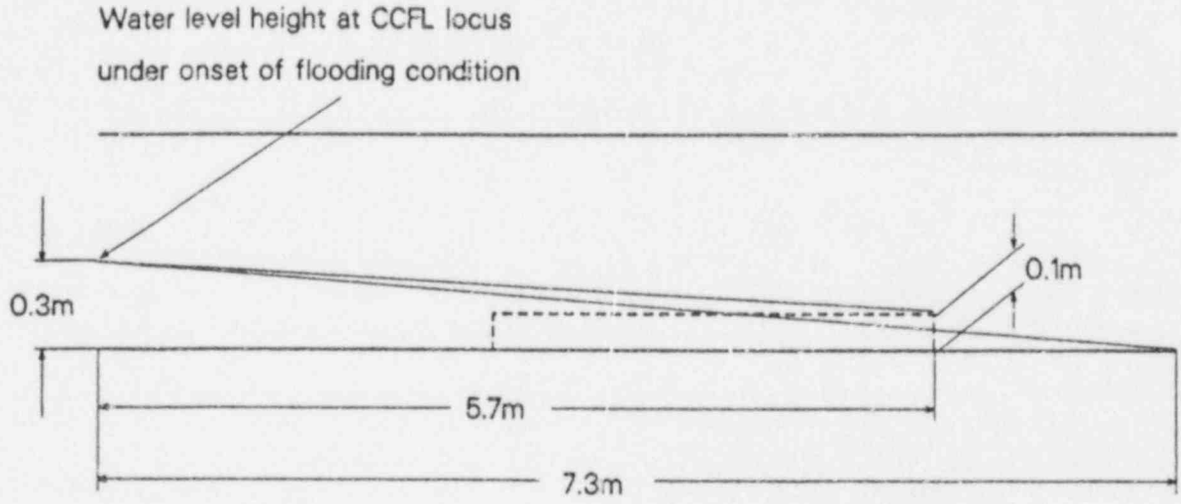

w/o Hutze : $\tan \alpha = 0.3m / 7.3m = 0.041$

with Hutze : $\tan \alpha = (0.3m-0.1m) / 5.7m = 0.035$

$$\sqrt{\frac{\tan \alpha_{\text{w/o Hutze}}}{\tan \alpha_{\text{with Hutze}}}} = \frac{Jv_{\text{w/o Hutze}}}{Jv_{\text{with Hutze}}} = 1.08$$

Fig. 16: Estimation of water level inclinations assuming a constant inclination along the hot leg

Hutze region. The elevated water level height at the Hutze contributes to a reduced level inclination and consequently affects the CCFL.

Therefore, the amount of influence on CCFL is given by the water level elevation within the Hutze region. The water displacement due to the Hutze generally depends on the water accumulation there. However, it can be estimated that relative to the horizontal pipe without the Hutze the water level inclination decreases up to 17 %.

Because the water flux Jℓ is much smaller than the steam flux Jv, it can be seen from equation (3) with (12) and (13) that the steam flux Jv depends on the square root of the inclination. Therefore, the estimated 17 % reduction in inclination leads to an 8 % reduction in steam flux and consequently to an 8 % reduction of the steam mass flow rate (see fig. 16).

9. Conclusion

The full-range drift-flux model implemented in the GRS system code ATHLET procures a realistic simulation of the hot leg CCFL. Comparisons between measured and calculated mass flow rates related to CCFL conditions are in good agreement. Even the calculated water level heights agree favourably with the 3-beam-gamma densitometer readings. The dependence of water level on steam mass flow rate is well represented by the code model.

The analysis of the UPTF test 11 (SB LOCA test) based on the ATHLET calculation indicates that the CCFL in the hot leg probably occurs at the bent part of the hot leg. The accumulation of water reaches its maximum there. Simultaneously, the largest differences in phasic velocities are predicted for this position.

The influence of the Hutze on CCFL related mass flow rates is identified to be the elevating effect of the Hutze on the water level at the Hutze region. This Hutze related elevation reduces the water level inclination along the hot leg and therefore, a reduced steam mas. flow rate already provokes CCFL.

The influence of the Hutze region on CCFL is determined by code calculations as well as by hand calculations. From these calculations we conclude that the influence on CCFL is less than 10 % in steam mass flow rate.

10. References

/1/ A. Schäfer, G. Lerchl, Topical Meeting on Anticipated and Abnormal Transients in Nuclear Power Plants, Atlanta Georgia, "Modeling of Transients with the GRS system code ATHLET" April 12-15, 1987,

/2/ M. Ishii, "One-Dimensional Drift-Flux Model and Constitutive Equations for Relative Motion between Phases in Various Two-Phase Flow Regimes", ANL-77-47

/3/ S.C. Lee, S.G. Bankoff, Topical Report to Nuclear Regulatory Commission (1982), "Steam-Subcooled Water Countercurrent Flow in an Inclined Channel"

/4/ G.B. Wallis, UKAEA Rept. AEEW-R123, 1961

/5/ I. Kataoka, M. Ishii, "Prediction of Pool Void Fraction by New Drift Flux Correlation", NUREG/CR-4657, ANL-86-29

/6/ U. Gaal et al., ALMOD/MOD1 Code Description" GRS-A-1316/I-III (1986)

/7/ F. Steinhoff, "DRUFAN-02 -Interim Program Description Part 1" GRS-A-685 (1982)
F. Steinhoff, "DRUFAN-02 -Interim Program Description Part 2" GRS-A-714 (1982)

/8/ A. Hora, C. Michetschläger, H.-G. Sonnenburg, V. Teschendorff "Analysis of Reflood Phenomena by the Two-Fluid Code FLUT", Advances in Two-Phase Flow and Heat Transfer, M. Nijhoff Publ., Den Haag (1983)

/9/ W. Kolar, L. Piplies, H. Städtke, Commission of the European Communities, Joint Research Centre Ispra Establishment, Technical Note No.1.06.C1.85.136, Volumen I and Volumen II, "OECD-CSNI International Standard Problem No.18 - Comparison of the Prediction Calculations with the Experimental Results" October 1985

/10/ H. Schickel, "Calculation of Loop Seal Experiment with DRUFAN-02" GRS Technical Note SCL-87-1, 25.02.1987/GLZ

/11/ K. Riedle et al., "Test No. 11 Countercurrent Flow in PWR Hot Leg Test", KWU Quick Look Report R 515/87/08

/12/ Naugab Lee, "Limiting Countercurrent Flow Phenomenon on small break LOCA transients", Nuclear Engineering and Design 102(1987)211-216 North-Holland, Amsterdam

/13/ A. Ohnuki, "Experimental Study of Countercurrent Two-Phase Flow in Horizontal Tube Connected to inclined Riser", Journal of Nuclear Sci. and Techn., Vol. 23, No. 3, pp. 219-232, March 1986

/14/ Enclosure to MPR letter from Paul S. Demerell to Dr. L. Shotkin (NRC) dated March 13, 1986, "US Input to Definition of Test Objectives and Conditions for UPTF Hot Leg SB LOCA Test (Test No.11)

NRC FORM 335 (2-84) NRCM 1102, 3201, 3202

U.S. NUCLEAR REGULATORY COMMISSION

BIBLIOGRAPHIC DATA SHEET

SEE INSTRUCTIONS ON THE REVERSE

1. REPORT NUMBER (Assigned by TIDC, add Vol. No., if any)
NUREG/CP-0091
Vol. 4

2. TITLE AND SUBTITLE
Proceedings of the Fifteenth Water Reactor Safety Information Meeting

3. LEAVE BLANK

4. DATE REPORT COMPLETED
MONTH: January YEAR: 1988

5. AUTHOR(S)
Compiled by Allen J. Weiss, BNL

6. DATE REPORT ISSUED
MONTH: February YEAR: 1988

7. PERFORMING ORGANIZATION NAME AND MAILING ADDRESS (Include Zip Code)
Office of Nuclear Regulatory Research
U. S. Nuclear Regulatory Commission
Washington, D. C. 20555

8. PROJECT/TASK/WORK UNIT NUMBER

9. FIN OR GRANT NUMBER
A-3283

10. SPONSORING ORGANIZATION NAME AND MAILING ADDRESS (Include Zip Code)
Same as Item 7 above

11a. TYPE OF REPORT
Proceedings of conference on safety research

b. PERIOD COVERED (Inclusive dates)
October 26-29, 1987

12. SUPPLEMENTARY NOTES
Proceedings prepared by Brookhaven National Laboratory

13. ABSTRACT (200 words or less)

This six-volume report contains 140 papers out of the 164 that were presented at the Fifteenth Water Reactor Safety Information Meeting held at the National Bureau of Standards, Gaithersburg, Maryland, during the week of October 26-29, 1987. The papers are printed in the order of their presentation in each session and describe progress and results of programs in nuclear safety research conducted in this country and abroad. Foreign participation in the meeting included twenty-two different papers presented by researchers from Belgium, Czechoslovakia, Germany, Italy, Japan, Russia, Spain, Sweden, The Netherlands and the United Kingdom. The titles of the papers and the names of the authors have been updated and may differ from those that appeared in the final program of the meeting.

14. DOCUMENT ANALYSIS - a. KEYWORDS/DESCRIPTORS
reactor safety research
nuclear safety research

b. IDENTIFIERS/OPEN ENDED TERMS

15. AVAILABILITY STATEMENT
Unlimited

16. SECURITY CLASSIFICATION
(This page) Unclassified
(This report) Unclassified

17. NUMBER OF PAGES

18. PRICE

UNITED STATES
NUCLEAR REGULATORY COMMISSION
WASHINGTON, D.C. 20555